DE-FE0028292

Final Report

ROBUST IN-SITU STRAIN MEASUREMENTS TO MONITOR CO_2 STORAGE

Project/Grant Period: 1 October 2016 – 30 June 2022

Clemson University
300 Brackett Hall
Clemson, SC 29634-5702
DUNS 04-262-9816

Principal Investigator
Larry Murdoch

Co-Principal Investigators
Scott DeWolf, Liwei Hua, Leonid Germanovich, Hai Xiao

Contributors
Xuran Zhu, Yongji Wu, Jing Guo, Robert Moak, Riley Blais, Soheil Roudini, Olivia Costantino, Grant Plunkett, Austin Smith-Jones

U.S. Department of Energy
National Energy Technology Laboratory

PREFACE

This project is the culmination of more than 10 years of research funded through three projects by the U.S. Department of Energy, National Energy Technology Laboratory to develop technology for measuring the strain tensor in geologic formations. The first project (DE-FE0004542) was an exploratory effort that involved simulations and basic field measurements that evaluated the feasibility of using strain measured in boreholes as a diagnostic tool. That project was followed by DE-FE0023313, which involved deploying one of the last remaining Gladwin strainmeters at the North Avant Field, an oil reservoir in northeastern Oklahoma operated by our industry partners, Grand Resources. The Gladwin strainmeter was the gold standard of geodetic-grade tensor strainmeters since the 1980s, so it was well-suited to demonstrate the value of strain measurements during reservoir characterization. Results from the DE-FE0023313 project demonstrated the feasibility of measuring and interpreting the strain tensor measured at shallow depths during well tests. The encouraging results of this project were tempered by the realization that it would be impossible to continue the research using Gladwin strainmeters because the Australian company making these instruments had shut down their operations.

Scott DeWolf had experience using high resolution Michelson interferometers to measure minute strains in the subsurface, and Scott thought it was feasible to use this approach to build a strainmeter with capabilities similar to those of the Gladwin strainmeter. At the same time, Liwei Hua and Hai Xiao and his students at Clemson were using microwave photonics to measure strains distributed along an optical fiber at resolutions that rivaled measurements made with fiber Bragg gratings. Liwei and Hai suspected, however, that microwave photonics methods could be refined to significantly improve performance.

Evaluating the promise of the two optical fiber sensing technologies developed by Scott and Liwei was the initial motivation for this project. While the sensing technologies were fundamental, their usefulness required packaging the optical fiber sensors into instruments that would enable the fiber to be safely coupled to subsurface formations. This led to the development of a variety of instruments that were field tested at a site near Clemson University, and at the North Avant Field. Additional testing was done using column tests in the laboratory. Another critical aspect of the project was developing quantitative methods for interpreting strain. Leonid Germanovich led this effort and developed a novel analytical solution to the strains caused by a pressurized region, and we also used numerical methods to analyze and interpret strains.

We were able to stay reasonably close to our proposed schedule until March 2020 when Clemson University and Grand Resources closed because of the COVID19 pandemic. Pandemic restrictions and problems with supply chains caused field work originally planned for spring 2020 to be delayed until March 2022. The project officially ended in June 2022, but field testing of the strainmeters at the North Avant Field continued for several more months, and data processing and analysis continued after that. Despite the delays we ultimately were able to meet all of the original project goals, and we are pleased to present them in the following report.

ACKNOWLEDGEMENTS

A wide range of people contributed to the successful completion of this project and we appreciate all of their contributions. Among the most important contributors are Marvin, Scott and Richard Robinowitz of Grand Resources, who operate the North Avant Field where much of our field work was conducted. They provided access to wells, resources and personnel that were essential to the project and we appreciate their efforts. We also appreciate the expertise of personnel at Grand Resources, including J.R. Ashby, Travis Pierce, Cody Schapansky, Tyler Schapansky and June Schmelling. Vijay Janardhan of Basin Trak set up the telemetry and controller for well 9A that enabled us to configure and monitor injection tests at the North Avant Field from our offices in Clemson. Ace McCarthy and Clark Giles and their crew from Two Eight Drilling did an excellent job creating the borings for the shallow strainmeters in Oklahoma. In South Carolina, we appreciate drilling services from Jimmy Rogers of Rogers Well Drilling, and Trever Slack at PetraTech Environmental. Justin Roye, Chase Collier and their colleagues at Schlumberger pumped the cement needed to couple the strainmeters to rock at the North Avant Field. John Leeman of Leeman Geophysical provided insights and printed circuit board design and manufacturing that we used for the optical fiber Michelson interrogators described in Chapter One. We appreciate the support and understanding of Scott Justice and John Andrae who manage and oversee agricultural research neighboring our field site near Clemson.

The project benefited from the help of several graduate students at Clemson. Riley Blais, Austin Smith-Jones, Grant Plunkett, Rob Moak, Soheil Roudini, and Olivia Costantino were partially supported by the project and they are largely responsible for the field and lab experiments. Riley Blais and Austin Smith-Jones worked on periodic well tests and their work is described in Chapter Twelve. Grant Plunkett and Olivia Costantino conducted laboratory experiments representing conditions in the vadose zone and their work is presented in Chapters Thirteen and Fourteen. Soheil Roudini developed the proxy-based inversion workflow described in Chapter Seven. Rob Moak did the simulations of strain caused by leaks in Chapter Eight and the field work and simulations in Chapter Eleven. Special thanks to Xuran Zhu, Yongji Wu, and Jing Guo for their help with the electronics used in the CMPI system described in Chapter Two.

The field deployment of strainmeters was critical to the success of the project and it inevitably occurred during the hottest days and coldest days of the year. We particularly appreciate the experience and guidance of Wade Johnson and his colleagues at the EarthScope Consortium (formerly UNAVCO). Riley Blais, Grant Plunkett and Matt Seigler helped on one of the hottest deployments, and Rob Moak and Austin Smith-Jones were there on the coldest. We appreciate their good-natured assistance.

We particularly appreciate the guidance and patience of Steve Henry, our program manager at the DOE.

CONTENTS

Preface ii
Acknowledgements iii
Major Accomplishments v
Executive Summary vii
Part One: Instrument Developments and Deployments vii
Part Two: Simulations and Inversion x
Part Three: Experiments xiii
Technology Transfer xviii
Data Management xxiii

PART ONE: INSTRUMENT DEVELOPMENTS AND DEPLOYMENTS
Chapter One: Point Instrument Development 1-51
Chapter Two: Distributed Instrument Development 2-57
Chapter Three: Deployments at the Simpson Station, Pendleton, SC 3-34
Chapter Four: Deployments at the North Avant Field, Barnsdall, OK 4-45

PART TWO: SIMULATIONS AND INVERSION
Chapter Five: Numerical Simulations of Strain in Variably Saturated Porous Media 5-32
Chapter Six: Analytical Model of the Strain Near a Pressurized Formation 6-13
Chapter Seven: Proxy-Based Bayesian Inversion of Strain During Well Tests 7-42
Chapter Eight: Using Strain to Characterize Leaks from Reservoirs 8-42
Chapter Nine: Using Strain Caused by Ambient Loading to Detect Leaks 9-7

PART THREE: EXPERIMENTS
Chapter Ten: Injection Testing at the North Avant Field 10-31
Chapter Eleven: Point Loads and Pumping Tests in Unconfined Aquifers 11-21
Chapter Twelve: Analysis of Strain During Pumping Tests with a Periodic Rate 12-138
Chapter Thirteen: Strain Caused by Air Pressure in the Vadose Zone 13-37
Chapter Fourteen: Changes in Water Pressure on Strain in the Vadose Zone 14-113

MAJOR ACCOMPLISHMENTS

The goal of this project was to develop and demonstrate robust instrumentation to monitor the in-situ strain tensor in order to improve the security of CO_2 storage in geologic formations. We met the original goals of the project and the major overarching accomplishment is the advancement of strain tensor monitoring from an intriguing concept to a commercially available technology with a solid foundation of novel instruments supported by theoretical analyses and validation experiments. Additional accomplishments include:

INSTRUMENTATION

- Designed, built and evaluated nine new optical fiber strainmeters tiltmeters using Michelson interferometers to measure deformation with ultra high resolution at both shallow and deep point locations in the subsurface. These are the *robust* strainmeters that motivated the title of the project.
- Designed, built and evaluated a novel method called CMPI of measuring distributed strain in optical fibers with nanostrain resolution, and cm-scale location, and sampling into the seismic band. CMPI technology has advantages over existing commercial DAS and DSS methods.
- Developed and demonstrated capabilities to deploy instruments in the field and used them to measure strain caused by ambient signals like barometric pressure and tides, as well as induced signals like surface loading and pore pressure changes from pumping tests.
- Deployed a working strainmeter at 1,700 ft, slightly above an active reservoir. This is to our knowledge the greatest depth a strainmeter has been deployed and the techniques we used can readily be extended to greater depths.
- Advanced the technology readiness level (TRL) of the tensor optical fiber strainmeter from the TRL 4 in the proposal to a TRL of 7, which was the goal of the project.

ANALYSES

- Developed and demonstrated a computational workflow that uses machine learning to reduce the computational requirements and make it practical to use Bayesian inversion to interpret strain tensor field data. This will improve how strain tensor data can be used during decision making.
- Evaluated the strain tensor fields and time series that would be caused by leaks of CO_2 or other fluids from reservoirs. Demonstrated that signals from leaks could be measured with instruments developed for the project, opening a potentially new method for ensuring storage security.
- Showed that strains in caprock can be used to estimate pressure in a reservoir. This avoids the need to drill monitoring wells into the reservoir, and it expands the capabilities of monitoring in the caprock.
- Derived and applied a novel analytical solution to the strains in the vicinity of a pressurized poroelastic inclusion. This solution explains field data measured during injeciton tests at the North Avant Field, and it will simplify future interpretation of strain tensor data.

EXPERIMENTS

- Characterized the strain tensor at an array three strainmeters during six injection tests at the North Avant Field, Oklahoma. Demonstrated repeatability of the strain signal. Showed similarities between the strain signal at shallow depths and pressure in the underlying reservoir.
- Demonstrated that useful strain data can be measured at reservoir depths. This confirms that strains could be measured in the caprock slightly above a reservoir at locations planned for pressure monitoring wells.
- Demonstrated the feasibility of using the strain tensor and distributed strain measured in caprock, or the vadose zone, to characterize an underlying reservoir or aquifer using a variety of different well tests. This further strengthens the validity of using strain data to characterize reservoirs and aquifers.
- Obtained strain data from above the aquifer during well tests with pumping rates that are constant, sinusoidal and positive, or a periodic square wave with zero net rate, and we showed the data are consistent with poroelastic simulations. These types of well tests have a variety of applications for characterizing and monitoring during CO_2 storage.
- Demonstrated strain data caused by small variations in air pressure can be measured with CMPI and interpreted with poroelastic simulations. Showed how strain is affected by changes in water content in the vadose zone, particularly by a rising and falling water table. These accomplishments show that high resolution distributed strain measurements hold promise for monitoring the vadose zone.

TECHNOLOGY TRANSFER

- Partially supported nine graduate students in Environmental Engineering, Hydrogeology, Electrical Engineering.
- Research described in nine journal papers, 23 talks and conference abstracts. Additional journal papers are in preparation.
- A new company called Tensora was started to provide strainmeter techology for commercial applications.
- A patent application has been filed covering the CMPI technology developed for the project.

DATA

- Strainmeter data associated with the project is publically available from several sources described below.

EXECUTIVE SUMMARY

This report summarizes the work done on project DE-FE0028292 between 2016 and 2022. The overall goal of the project was to develop and demonstrate methods to measure and interpret the strain tensor in the subsurface to better understand processes related to storing CO_2 in geologic formation. This was accomplished by developing two distinct methods of measuring strain using optical fibers, one that uses Michelson interferometers to measure strain at a point and another based on microwave photonics that measures strain distributed along a fiber. The project also involved theoretical analyses of deformation associated with fluid pressure changes and inversion methods of using those analyses to interpret strain tensor measurements. A third major topic of the project involved field and lab experiments that integrated the optical fiber measurements with the theoretical analyses.

The body of work conducted for the project is organized into three major Parts described in fourteen chapters in the following pages. Part One describes the instruments developed for the project and presents the data they generated and methods for processing the data into a usable form. Part Two outlines the simulations and inversion methods, and Part Three summarizes the experimental work.

PART ONE: INSTRUMENT DEVELOPMENTS AND DEPLOYMENTS

Understanding subsurface processes like deformations associated with fluid injection requires the use of robust monitoring technologies, which is why instrument development and testing were a major component of this research. This was motivated in part by the obsolescence of existing geodetic deformation monitoring technologies, primarily borehole tensor strain measurements, as well as the desire to create application specific instrumentation such as high compliance strainmeters for softer materials. These developments are grouped into two main categories: so-called point sensing where one or more measurements are made at a single location or over a small region and distributed sensing where one or more measurements are made over a larger spatial extent. The technology development and laboratory testing of each of these are described in Chapters One and Two, and their installation and capabilities are demonstrated at our local Simpson Station field site is covered in Chapter Three. This first part is concluded with the installation of new instrumentation at our CO_2 injection analog site in Oklahoma in Chapter Four.

Point instrument development

We developed a suite of new optical fiber instruments for deformation monitoring as well as significantly improved our ability to monitor these instruments. A new borehole deployable opto-electronic interrogation system was developed that is capable of capturing up to nine interferometers and consumes less than 2 Watts of power, which is less than one-third of the previous design. Several single-component strainmeters were developed including a compliant strain ribbon with a resolution of $8x10^{-14}$ strain, as well as two strainmeter "smart casings" designed to be deployed inline with standard well casing that are capable of measuring strains from $4\text{-}5x10^{-16}$ strain and to the best of our knowledge are the most sensitive borehole strainmeters ever developed. A full scale prototype of a novel two-axis optical fiber tiltmeter

based on fibers embedded into a flexural pendulum bob was created that is capable of measuring the horizontal tilt vector to a resolution of just over a nanoradian (~10^{-4} degrees) that is completely passive and does not require leveling. A compliant 3-component strainmeter using optical fiber Bragg gratings embedded in a urethane cylinder was developed for directional deformation monitoring in sediments, that while less sensitive than its interferometric counterparts is capable of being pushed into its host formation and measuring pressure changes of about 1 kPa. Three new optical fiber embedding approaches were evaluated for measuring directional strains at very high resolutions. This included a design with multiple fiber wrapped mandrels, inclined helical wrappings and non-circular wrapped mandrels each capable of measuring strains in the 10^{-14} to 10^{-16} range. These developments culminated in a completely new borehole strainmeter system capable of resolving four components of the strain tensor at extremely high resolution in a very robust borehole package capable of single-trip installation and grouting.

Contribution

This covers the development and testing of 9 new optical fiber based instruments for both shallow and deep borehole installations in hard rock or soft sediments. This portfolio of technologies allows for the robust monitoring of subsurface deformation over a wide range of applications that before could previously only be done using either obsolete or less robust and lower resolution systems made from sensors developed for industrial applications.

Distributed instrument development

Significant improvements were made to our existing distributed fiber sensing capabilities resulting in a faster and much higher resolution system capable of many of lab and field measurements related to subsurface deformation monitoring. This started with Optical Carrier Microwave Interferometry (OCMI), an existing distributed strain sensing (DSS) technology capable of resolving ~1 με between pairs of laser machined reflectors inside the core of an optical fiber that form as many intrinsic Fabry-Pérot interferometer cavities. Adding coherent detection to the OCMI system created the Coherence-length-gated Microwave Photonics Interferometry, or CMPI, system capable of resolving ~1 nε between reflector pairs. Other critical enabling developments included adding an external Michelson interferometer reference with a digital coherence control system to limit crosstalk between adjacent reflector pairs. We were able to incorporate a powerful fractional interference fringe counting algorithm by exploiting an inherent property of electro-optic modulators called “chirp” to generate in-phase and quadrature fringe signals for demodulation. While this DSS system is capable of collecting data at a few times per second, a sideband demodulation technique was developed to unlock distributed acoustic sensing (DAS) capabilities at sample rates in the tens of kilohertz at the same nε resolution. The hardware was reduced from a collection of bench top test and measurement equipment to an integrated rack mounted CMPI interrogator that included firmware to control the device and software to interface configure and collect data. Fibers containing multiple reflector pairs were packaged in laminated plastic and fiberglass strips to increase the strain transfer from the surface of a borehole to the optical fiber that were then used in a suite of laboratory experiments such as distributed strain measurements of direct loading, pressure wave propagation and water infiltration into sediment columns.

Contribution

The CMPI system fills an important gap in current distributed strain monitoring where both spatial coverage and high resolution are required. This new system is also capable of distributed acoustic sensing, effectively replacing both DSS and DAS in one box. While it does require engineered fiber with either weak fiber Bragg gratings or laser machined reflectors, these are commercially available products, and the system itself mostly consists of commercial hardware with the exception of one custom printed circuit board.

Deployments at the Simpson Station, Pendleton, SC

Many of the instruments developed in Chapters One and Two were field tested at our local Simpson Station facility located a few miles west of Clemson University. This included the three optical fiber tensor strainmeter prototypes that were installed with the help of a new collection of equipment for mixing and pumping the expanding grout used to couple them to the formation. While only two of the three tensor prototypes survived long term and both showed excellent noise performance, they lacked the ability to resolve strains from more than one direction. A fourth tensor strainmeter using fiber wrapped elliptical cylinders was installed that matched the noise levels of the previous but was able to resolve all three components of the horizontal strain tensor as well as the vertical strain with a resolution of $4x10^{-14}$ strain. Both high compliance strain ribbon and 3-component urethane push-in instruments were installed in the shallow subsurface and were capable of measuring strains associated with atmospheric pressure loading of the surface as well as pumping from a nearby well. Three distributed strain sensing ribbons were also installed for interrogation using the CMPI method described in Chapter Two. The first string consisted of two sensing fibers extending from ~30 to 17 feet and 14 to 7 feet below ground, however, these strings were broken during installation. The second ribbon featured 8 pairs of 15 cm reflectors separated by 85 cm that spanned the borehole from ~30 to 4 feet below ground and was subjected to a variety of tests including surface loading, constant and periodic rate pumping and seismic impulses. Ambient spectra show a strain resolution of approximately 1 nε at 0.01 Hz (100 seconds). The third and final distributed strain ribbon was deployed with 7 reflectors at 1 m spacing that was able to resolve the ~100 nε induced by repeated surface loadings from a person approaching the wellhead. A fiberglass push-in instrument with six sets of CMPI reflectors was also deployed in the shallow subsurface that showed a clear response of about 100 nε when subjected to surface loading by a vehicle.

Contribution

The field work presented in this chapter proves the viability of the technologies developed in Chapters One and Two for actual field applications. While it is difficult to evaluate some of these instruments in the lab given their extreme sensitivity, the field results show that they are capable of measuring deformations from ambient signals like barometric pressure and tides as well as induced signals like surface loading and pore pressure changes from pumping tests. These deployments also allowed us to identify robustness issues that were addressed in each subsequent iteration to increase the likelihood of success for each new installation.

Deployments at the North Avant Field, Barnsdall, OK

The ultimate test of the new tensor optical fiber strainmeter technology developed in Chapter One was to deploy them in an operational environment such as our CO_2 injection analog site at the North Avant Field in Oklahoma. This was done to build an array of tensor strainmeters encircling the injection well 9A in order to extend our capabilities for using tensor strains for interpreting deformations from subsurface injections. The installation consisted of four new elliptical ring strainmeters, three of which were deployed at shallow depths (140 feet) similar to our previous installations (~100 feet) and one in the reservoir at 1,700 feet, all of which were successful. All four installations exhibited the expected post-grouting behavior and produced data that could be calibrated in-situ using the solid earth tides to transform the gauge strains to the north-south, east-west, horizontal shear and vertical strain components of the strain tensor with outstanding fidelity. Scalar and spectral admittance estimates show these new strainmeters respond very similarly to barometric pressure as the Gladwin tensor strainmeter, as well as to surface waves from teleseismic events. While the ambient spectra of the optical fiber instruments is a few dB higher than the Gladwin, this is most likely an artifact of the relative ages of the installations and the amount of data collected thus far. We also deployed the two-axis optical fiber tiltmeter, however, issues caused by improper installation limited the usefulness of comparisons to the nearby commercial tiltmeter. We also upgraded and expanded our reservoir water level monitoring array from three autonomous logger deployments to five near real time pressure measurements with cellular telemetry.

Contribution

The success of the strainmeter installations proves that these new tensor optical fiber instruments are at least as capable as any of the previous technologies. These deployments also raise the technology readiness level (TRL) of the tensor optical fiber strainmeter from the TRL 4 in the proposal to a TRL of 7, which was the stated goal. The deployment at 1,700 feet is, to the best of our knowledge, the deepest strainmeter deployment ever attempted and successfully completed. Furthermore, it was able to be grouted into a borehole drilled over 100 years ago and still has all four horizontal gauges go into permanent compression resulting in an installation capable of measuring the strain tensor.

PART TWO: SIMULATIONS AND INVERSION

Simulating the deformation caused by changes in pore pressure is accomplished by solving equations for fluid pressures coupled to equations for displacements of the solid porous matrix. The processes of interest to this report are limited to small deformations that are assumed to be in the elastic range of material behavior, which can be evaluated using methods of linear elastic poroelasticity. Part Two of the report begins with an overview of the governing equations and constitutive relations used to analyze linear elastic poroelasticity. These equations form the basis for simulations used elsewhere in the report and are summarized in Chapter Five. Details of the governing equations vary depending on the extent of saturation, number of fluid phases present, and which fluid phases are pressurized. The most general case evaluated in this work considers porous media partially saturated with air and water where both the air and water pressure can change. These conditions occur in the vadose zone influenced by changes in barometric pressure, which is the topic of experiments in Chapter Thirteen. To support this case, Chapter

Five describes the governing and constitutive equations for partially saturated conditions with two varying fluid pressures. The analyses used for other cases can be derived by simplifying the expressions given in Chapter Five.

Strains in the vicinity of a pressurized formation

Interpreting strains caused by changing the pressure in a reservoir or aquifer is a major focus of this research and this motivated the derivation of analytical solutions that will quickly make the necessary calculations. The approach was to treat the zone where the pressure has been changed by injection or pumping as a mathematical inclusion or inhomogeneity. An *inclusion* is a pressurized zone where the elastic properties are the same as the enveloping geologic material, whereas an *inhomogeneity* is a zone where the elastic properties differ from the enveloping material. We started with the classic work of Eshelby and conducted a mathematical analysis that generates closed-form equations for the strains in the vicinity of both pressurized inclusions and inhomogeneities. The resulting equations can be solved virtually instantly using simple computers, which simplifies interpretation using inversion methods.

The results of the analytical solutions are consistent with the results of the injection tests described in Chapter Ten. Data from shallow strainmeters during the injection tests are similar to previous results and we have already shown in DE-FE0023313 that analyses similar to the ones derived here can explain the shallow strains. However, the signs of the strains measured at the deep strainmeter are opposite those at the shallow strainmeters. The analytical solution in Chapter Six explains this observation as a consequence of the strainmeter being in proximity to a reservoir boundary, which is confirmed by coring data.

Contribution

A new analytical solution is described for rapidly calculating the strains in the vicinity of poroelastic inclusions and inhomogeneities. The solution explains essential details of field data obtained during injection tests, and paves the way for fast interpretation of strain data in future applications.

Strains in the vadose zone

We solved the governing equations for the general case and used the solution to evaluate the factors affecting strain during barometric pressure fluctuations in the vadose zone. The results of these simulations show how strain caused by fluctuations in barometric pressure propagates as diffusive-like waves through the vadose zone. Propagation of the strain depends on the water content in the vadose zone. Increasing the water content reduces the air phase pressure diffusivity and this slows the propagation of both pressure and strain. Air pressure fluctuations go to zero at the capillary fringe where the relative air-phase permeability goes to zero, but the air pressure fluctuations are transferred to the water pressure and they continue to propagate.

Contribution

The analyses in Chapter Five show how strain caused by barometric pressure fluctuations depends on water content, and this implies that measuring strain could be a way to monitor changes in the vadose zone. This would generate a novel method for monitoring the vadose zone, which could have far-reaching applications. The high spatial resolution and high strain

sensitivity of the CMPI method described in Chapter Two make that method particularly well suited to this application. Experiments validating the simulations are described later in Chapters Thirteen and Fourteen.

Interpreting strain data to support decision-making

The value of strain tensor data lies in the ability to interpret them to improve the understanding of subsurface processes, and for our purposes, to improve the understanding of processes related to CO_2 storage. Interpretation of strain data can take several forms, and we show in Chapter Ten how time series of the average horizontal normal strain and the vertical strain at shallow depths are remarkably similar to time series of pressure in the underlying reservoir. This indicates that in some cases it could be feasible to interpret strain measured at shallow depths using analytical solutions developed for pressure measured in the reservoir. This finding has major implications for characterizing reservoirs and aquifers, but the analytical approach presented in Chapter Six is limited to broad, but simple insights. More detailed insights are feasible by using more detailed models of the deformation process, and the ideal model would include a wide range of processes represented mathematically in fine detail. The problem with using this type of model to interpret strain is that it requires significant computational resources simply to solve the forward model. Bayesian inversion methods provide parameter estimates along with rigorous estimates of parameter and prediction uncertainty, and these capabilities are important when the results of inversions are used to support decision making. However, Bayesian inversion requires many forward model runs to evaluate many possible parameter sets that could explain the observed strain signals and this is generally computationally infeasible using detailed poroelastic models run on computers that are readily available. To address this problem, we developed a workflow that trains a machine learning model called KNN using results from a poroelastic simulator. The KNN model learns to how to give output results that are essentially the same as those given by the numerical simulator in response to a particular set of input parameters. The workflow uses the KNN model as a fast proxy for the much slower poroelastic simulator and this makes it feasible to use Bayesian inversion to interpret strain tensor measurements.

Contribution

This chapter describes a computational workflow that will enable strain tensor measurements to be used to estimate reservoir parameters and their uncertainties. This will improve reservoir characterization, and a rigorous evaluation of uncertainties will support using the results for decision making during CO_2 storage or related applications. Supporting sound decisions is among the most important roles for geophysical data in CO_2 storage.

Using strain data to detect and characterize leaks

Leaks of CO_2 out of a storage reservoir would compromise the viability of storing CO_2 in geologic formations, and considerable effort has been devoted to identify methods for identifying and characterizing leaks. Strain responds to changes in fluid pressure, and leaks will potentially change the fluid pressure in the reservoir and the caprock, so it is inevitable that leaks will cause strain. However, for the strain signal to be useful it would need to be large enough to measure and distinct enough to recognize and interpret. To evaluate the size and pattern of strain created by leaks in Chapter Eight, we used the available literature on natural and induced leaks to

develop a conceptual framework based on leak geometry and properties. The geometries include a vertical conduit to the ground surface, a horizontal layer and a vertical conduit intersecting a horizontal layer as idealized cases, along with combinations of the basic cases. The ratio of the leak transmissivity to the reservoir transmissivity was used as a property to distinguish two types of leak behavior. The transmissivity ratio is small in a Type I leak and large in a Type II leak, and this has an important effect on the cause of strain. As a result, a Type I leak may have little effect on the pressure in the reservoir, so the resulting strain field is caused by pressure changes in the caprock caused by the leaked fluid. The large transmissivity ratio of a Type II leak means that resulting strain field is caused by a pressure change in the reservoir due to the leak.

The conceptual model was used in Chapter Eight to guide the setup of a series of poroelastic simulations that show the patterns and time series of strains caused by leaks. In general, the simulations show that leaks will create strain signals in the caprock that form distinctive patterns characteristic of the leak geometry. Pressurizing a reservoir will also create a strain signal and it is important to be able to distinguish this signal from that of a leak. One approach to doing this is to monitor strain at equal distances from a well because the signal from a leak will break the symmetry that is expected during injection into a reservoir. The strain caused by Types I and II leaks will create distinctive patterns and time series that could be recognized by manual inspection, but a better approach could be to use machine learning to automatically monitor strain time series for signals that could indicate leaks.

Earth is subjected to a variety of naturally occurring loads that vary with time, and these effects cause strain in the subsurface. Earth tides and barometric pressure changes are two examples, and the strains they cause are readily detected by the instruments described in Chapters One and Two. The strains caused by naturally occurring loads will depend on the elastic properties of the subsurface, which can change in response to a leak. For example, CO_2 accumulating in an aquifer overlying a storage reservoir will create gas bubbles, which will increase the effective compressibility of the pore fluid. We simulated this effect and found that a layer where the fluid compressibility has increased will create a strain field when loaded by barometric pressure fluctuations, and the analyses are outlined in Chapter Nine. The strain anomaly caused by the leak occurs over and adjacent to the accumulated gas. The strains are small, but they are large enough to be detected by the strainmeters outlined in Chapter One.

Contribution

Leaks of CO_2 out of a reservoir can change fluid pressures in the reservoir and caprock and this will create a strain tensor signal that could be detected using strainmeters, and characterized using analyses developed for this project. Leaks will also alter the strain response to natural loads, like Earth tides and barometric pressure. This suggests that passively monitoring the strain tensor could lead to a low-cost method of ensuring the security of CO_2 storage by rapidly detecting leaks or other anomalies associated with injection.

PART THREE: EXPERIMENTS

Part Three of the report presents a series of experiments conducted in the lab and field to evaluate the effects of pressure changes on strain. These tests include strain measurements during injection into a reservoir at constant rate, in addition to tests involving pumping rates that varied as a periodic function of time. We also evaluated point loads at the ground surface that

create strain at depth. The program also includes laboratory experiments characterizing strains caused by small periodic fluctuations of air pressure and variations of water pressure under partially saturated conditions.

Strain tensor measured during injection into a reservoir

The flagship field study of the project occurred at the North Avant Field, an oil reservoir in northeastern Oklahoma where we had access to the 9A injection well completed in a permeable lens at approximately 530 m depth. We deployed three tensor borehole strainmeters at shallow depths (~45m) and one strainmeter was deployed at reservoir depth as outlined in Chapters One and Four. A Gladwin strainmeter and strainmeters we developed and deployed earlier were in the vicinity of well 9A and data from these instruments was available. Four wells extended into the reservoir near well 9A and were used to monitor pressure.

Six injection tests were conducted in the summer and fall of 2022, and the pressure in the reservoir and the strain tensor were monitored as functions of time. The pressure increased during injection and decreased during recovery at all the monitoring wells. The horizontal strain increased (became tensile) and the vertical strain decreased (became compressive) during injection and then changed sign during recovery at the two shallow strainmeters. The opposite occurred at the deep strainmeter—horizontal strain decreased and vertical strain increased during injection. The NS strain was greater than the EW strain at a shallow strainmeter east of the injection well, but the relative magnitudes were reversed at a shallow strainmeter north of the injection well. This response is consistent with the circumferential strain being larger than the radial horiontal strain.

The pressure and strain time series are slightly non-linear with negative curvature during injection and positive curvature during recovery. A linear fit to the data indicates the reservoir was pressurized at rates from 2 to 4 kPa/hr, and this resulted in normal strain rates at shallow depths of 1-2 nε/hr. The strain rates at the deep strainmeter were slightly faster, in the range of 1.5 to 2.5 nε/hr. The data were fit using a log function of time and the t_o/r^2 values for pressure are essentially the same as t_o/r^2 for strain. The semi-log slopes for pressure are linearly correlated to the semilog slopes for pressure. The data were also fit to a power law function. Both the shallow strain data and the pressure in the reservoir are characterized by exponents generally between 0.9 and 1.0, the exponent for the data from the deep strainmeter is smaller, in the range of 0.7 to 0.8.

The new pump controller developed for this work held the injection rate constant, but the duration of the tests was long enough to encounter anomalies that caused the pump to shut off and this caused the injection rates to depart from ideal conditions. We accounted for these anomalies by weighting the values measured during each test when calculating the mean and standard deviations. This allowed us to estimate the uncertainty in the means while accounting for the inevitatble vagaries of the field tests. The weighted coefficient of variation of the shallow strain data is less than 0.17 for four of the six normal strains and 0.32 is the maximum value. The variability of normal strain data at the deep strainmeter is larger, with CoV ranging from 0.2 to 0.32. To CoV of pressure data is less than that from the strain data, ranging from 0.03 to 0.12.

Data from the tests indicates that strain data during six tests are repeatable with uncertainties with tolerances that are acceptable for field tests. Important characteristics of the pressure data

that would be used to interpret well tests are similar to, or correlated with similar characteristics of the shallow strain data. The shallow strain data are consistent with expectations from simulations, suggesting they should provide valuable constraints during inversion. The data quality from the optical fiber strainmeters developed for the project is essentially the same as from the Gladwin strainmeter.

Contribution

This test marks the first demonstration of the strainmeters developed for this project under field conditions similar to the conditions expected for applications related to monitoring CO_2 storage. We were initially motivated to develop optical fiber strainmeters as a replacement for the now unavailable Gladwin strainmeters, and the results here show that the new optical fiber strainmeters generate data of similar quality as the Gladwin strainmeter. This work also marks the first time multiple injection tests were conducted with sufficient control on the injection rate to enable comparison between tests and evaluation of uncertainty. It is also the first time a strainmeter has been deployed at reservoir depths. Perhaps the most significant result of the tests, however, is the demonstration of a tensor strainmeter array generating repeatable data that is similar to the pressure response.

Strains during well tests with a periodic rate

Periodic pumping tests involve cycling the pumping rate with a regular period and measuring the resulting response. Some of these tests involve imposing a periodic rate on a constant mean rate. However, other tests involve moving water out of, and back into the well at rates that are balanced so the net rate after each period is zero. Some zero-net-rate (ZNR) well tests use rates that follow a sinusoidal pattern, whereas others use a square wave pattern that switches between a constant rate of pumping and a constant rate of injection to achieve a zero net rate. We evaluated the pressure and strain signals during well tests with a periodic rate in Chapter Twelve. The chapter describes tests that use a zero-net pumping rate in Part 1, and it outlines tests that use a sinusoidal rate with a positive mean pumping rate in Part 2.

A ZNR periodic pumping system was constructed and used to perform tests in the unconfined aqufer in saprolite underlying our field site near Clemson, South Carolina. A series of 10 ZNR periodic pumping tests was conducted with periods ranging from 2 to 540 minutes.

The time lag of the primary period of the pressure increases as a linear function of distance from the pumping well, and it increases as the square root of the period of the ZNR test over a range of periods spanning two orders of magnitudes. The first few harmonics follow similar trends, but the higher frequency harmonics diverge from this trend. Strain and tilt data from various instruments in the vadose and saturated zones are periodic during ZNR tests. The time lags of the strain components increase roughly linearly with distance from the well. Many of the time lags of the strain data from the vadose zone are similar to the time lags observed in the pressure data from a similar distance and pumping period. These results were found for both ZNR and sinusoidal rate tests.

Analysis of the time lags of the pressure and strain indicate that hydraulic diffusivities estimated from the strain data measured in the vadose zone are similar to the estimates from the pressure data measured in the aquifer.

Strain was measured using CMPI and a vertical strain ribbon (Chapter Two) for the sinusoidal rate tests, but this system was unavailable for the ZNR tests. The phase lags of the vertical strain decrease with depth, according to data measured using the vertical strain ribbon. This indicates that vertical strain propagates upward in a wave-like pattern during the sinusoidal pumping tests.

Simulations were performed to understand how pressure and strain responds to ZNR periodic pumping. The simulations analyzed the periodic tests in the time domain and then a Fourier transform was used to evaluate the data in the frequency domain. The time lag of the average horizontal strain in the vadose zone is similar to the time lag of the pressure at a similar radial distance in the underlying aquifer, according to the simulations. The simulations support the field observations and indicate that inversion methods similar to those described in Chapter Seven could be useful for interpreting periodic well tests.

Contribution

This set of experiments demonstrates that strain in the formations overlying a permeable aquifer or reservoir will vary periodically in response to periodic variations in the pumping rate at a well. The phase lag of the strain can be interpreted using simple, type-curve methods to generate preliminary parameter estimates. The consistency between the field data and the numerical simulations indicates that numerical inversion should be a promising method for more detailed interpretations.

Periodic variations in rate during injection of CO_2 have been proposed as a method for creating pressure signals that can be analyzed continuously to evaluate characteristics of leaks and other effects. Chapter Twelve shows that strain measurements made in the formation overlying the reservoir could also be used to monitor periodic injection signals.

Strains in the vadose zone cause by changes in air pressure

Barometric pressures commonly change by a few hundred Pa on a daily cycle and variations of several 1,000 Pa accompany weather fronts and storms, and these fluctuations create loads that causes strain in the vadose zone. A simple conceptual model is to account for changes in barometric pressure by assuming it only acts at the ground surface. This explains some effects, and it is the typical assumption used to determine a barometric correction for deep strainmeters. However, the correlation between barometric pressure and shallow strain changes with time in some cases, and this appears to be a result of changes in the air pressure diffusivity caused by changes in water content. Barometric pressure could diffuse relatively deep into the subsurface when soils are dry, but pressure diffusion is negligible in wet soils because the gas phase pressure diffusivity (and relative permeability) is essentially zero. This seems to be a reasonable explanation, but little work was available describing the effects of barometric pressure on strain in the vadose zone.

This motivated a series of experiments where the air pressure was varied in the head space of a meter long sand-filled column and the air pressure and strain were monitored as functions of time at various locations along the column (Chapter Thirteen). The air pressure was varied as a sinusoidal function of time with an amplitude of 25 Pa and a frequency of 4 Hz. We conducted theoretical analyses of this process (Chapter Five) and the results indicated that the small change in pressure would create strains in the range of 10^{-7}, which varied at 4 Hz and propagated like

decaying waves down the column. Measuring this signal required measuring strains with 10^{-8} resolution or better at a frequency of more than several 10s of Hz and a spatial resolution of roughly 10 cm. This was beyond the capabilities of existing measurement technology, but we expected it could be measured with CMPI, so the experiments also served as stage for evaluating the performance of CMPI (Chapter Two).

The results of the experiments show that both air pressure and strain vary at the same frequency as the pressure in the head space. The amplitude of the pressure decreased as a negative exponential function of depth, and the phase delay of the pressure increased as a linear function of depth in uniform, dry sand. The amplitude of the vertical strain decreases and the phase if the strain also increases with depth. The maximum amplitude of strains is several tenths of a microstrain, but it decreases to several 0.01 microstrain ($\sim 10^{-8}$) at a depth of approximatley 0.5 m. Clearly measuring these small strains was an excellent demonstration of the capabilities of CMPI.

The strain in the column was clearly responding to variations in air pressure in the head space in dry sand. This was unsurprising because during well tests in saturated conditions (Chapters Ten, Eleven and Twelve) we found that the temporal characteristics of the average horizontal strains were similar to the characteristics of the fluid pressure. However, the phase delay of the strains in the column occurred significantly ahead of the phase delay of the pressure. This effect occurs because strains are a result of both the pressure applied at the ground surface and the pressure propagating through the porous medium. We developed several models that show this effect and explain the observed data for dry sand.

Changing the water content alters the air phase permeability and this changes how the air pressure propagates, which also changes how the strain propagates. Results from a series of experiments using different water contents are described in Chapter Thirteen.

Contribution

An important finding from this work is that strains in porous media caused by small fluctuations in in air pressure propagate as decaying diffusive waves, and the distribution of amplitude and phase depend on the water content of the soil. The CMPI method implemented with a strain ribbon is able to measure the variations in strain, and the results are consistent with theoretical analyses. This contributes to the fundamental understanding of earth processes, and it also suggests that measurements of vertical strains in the vadose zone could be used as a new monitoring tool to evaluate changes in the distribution of water content in the vadose zone.

Strains in the vadose zone cause by changes in water pressure

Characterizing water content and pressure changes in the vadose zone is important to understanding a variety of geologic processes, ranging from storage and drainage, to evapotranspiration, and recharge. We showed in Chapter Thirteen that small changes in air pressure cause strains that can be measured with CMPI, so we extended this work to evaluate how changes in water pressure affect strains. The investigation outlined in Chapter Fourteen used a column filled with sand that is subjected to changes in water content and pressure. An optical fiber with CMPI reflectors was laminated in a high-surface-area ribbon and deployed along the axis of the column. Experiments were conducted by filling the column from the bottom or infiltrating water from the top.

Hydrologic conditions define three zones based on the pressure magnitude and distribution: and *Ambient Zone* where the pressure heads are quasi-static, and the pressure gradient is roughly unity (head gradient of zero); a *Transition Zone* where the pressures increase from ambient to zero, are changing relatively rapidly and the pressure gradient is relatively steep, and a *Positive Pressure Zone* where the pressure is positive, the rate of change is slower than in the transition zone and the gradient is flatter.

Injection of water causes the pressure to increase and the three pressure zones to move upward. Strain signals in the range of 10s of με were observed with a noise level of generally less than 0.1 με (signal to noise ratio of greater than 100) during injection and drainage. The strain generally increases during injection and decreases during drainage. The strain rate, and how the strain relates to changes in pore pressure varied considerably, however. These changes are repeatable and were used to define four stages in the strain time series during filling and four stages during draining. An additional three stages were identified in the time series of tests that involved filling the column until water ponded on the surface of the sand.

The spatial and temporal distributions of strain caused by injection depend on the location of the moving pressure zones. The locations of the different pressure zones were determined from pressure profiles at different times and these data were transferred to strain time series. This shows that the pressure zones occur in consistent locations relative to the strain sensor during the different stages, which indicates that the changing pore pressure is controlling the strain. This was expected, but how the pressure controls the strain was unexpected. In some locations, the strain increases with increasing pressure, which is consistent with Hooke's Law. In other locations, however, the strain is unchanged or decreases when the pore pressure increases.

Details of the experiments and resulting data are presented in Chapter Fourteen.

Contribution

Results of the laboratory experiments indicate that CMPI can measure strain caused by fluid pressure changes in the vadose zone with a signal to noise ratio of 100 or more. Injection and drainage cause a strain signal that is complex, but repeatable. The magnitudes of the strain signal are consistent with magnitudes that are expected based on poroelastic calculations using independently measured properties of the sand.

These results indicate that the CMPI technique with an optical fiber laminated in a strain generates data that represent the strain distribution during hydrologic processes of imbibition and drainage in variably saturated sand. Along with the results in Chapter Thirteen, this suggests that distributed strain measurements using CMPI could be a viable approach for evaluating processes in the vadose zone, laying the groundwork for future field implementation.

TECHNOLOGY TRANSFER

The technology developed during this project has been transferred to applications for CO_2 storage through publications and education of graduate students. A new company has also been started to make the techology available commercially.

PUBLICATIONS AND EDUCATION

This project has been described in eight peer-reviewed publications (Hua et al., 2017; Hua et al., 2021;Zhu et al., 2021; Murdoch et al., 2020; Murdoch et al., 2021; Murdoch et al., 2023; Hua & Murdoch and others, 2023; Roudini et al., 2023), four completed MS theses (Costantino, 2021; Plunkett, 2021;Blais, 2023; Smith-Jones, 2023), and it will contribute to two on-going PhD dissertations by Rob Moak and Soheil Roudini. We filed one patent application (Hua et. al. 2022). We have communicated the results of the project on an ongoing basis at research conferences, including 19 presentations the AGU Fall Meeting, the Clemson Hydrogeology Symposium and other professional meetings. We gave four invited talks and we presented at the NETL Annual Review meeting from 2017 to 2020.

Journal papers and patent application

Hua, L., & Murdoch, L. C. (2023). A Microwave Photonics Optical Fiber Method for Measuring Distributed Strain for Hydrologic Applications in the Vadose and Saturated Zones. In G. Zhan (Ed.), *Distributed Acoustic Sensing in Borehole Geophysics*. American Geophysical Union. In review

Hua, L., Song, Y., Cheng, B., Zhu, W., Zhang, Q., & Xiao, H. (2017). Coherence-length-gated distributed optical fiber sensing based on microwave-photonic interferometry. *Optics Express*, *25*(25), 31362. https://doi.org/10.1364/oe.25.031362

Hua, L., Zhu, X., Dewolf, S., Lei, J., Zhang, Q., Murdoch, L., & Xiao, H. (2021). Phase Demodulation by Frequency Chirping in Coherence Microwave Photonic Interferometry. *IEEE Journal of Selected Topics in Quantum Electronics*, *27*(2). https://doi.org/10.1109/JSTQE.2020.2975575

Hua, L. H. Xiao, L.C. Murdoch. US Patent Application Entitled: "Phase Demodulation by Frequency Chirping in Coherence Microwave Photonic Interferometry"Application No.: 17/584,017. Filed: January 25, 2022

Murdoch, L. C., DeWolf, S., Germanovich, L. N., Moysey, S., Hanna, A., Roudini, S., & Moak, R. (2023). Using the Shallow Strain Tensor to Characterize Deep Geologic Reservoirs. *Water Resources Research*. https://doi.org/10.1029/2022wr032920

Murdoch, L. C., Germanovich, L. N., DeWolf, S. J., Moysey, S. M. J., Hanna, A. C., Kim, S., & Duncan, R. G. (2020). Feasibility of using in situ deformation to monitor CO2 storage. *International Journal of Greenhouse Gas Control*, *93*. https://doi.org/10.1016/j.ijggc.2019.102853

Murdoch, L. C., Germanovich, L. N., Roudini, S., DeWolf, S. J., Hua, L., & Moak, R. W. (2021). A Type-Curve Approach for Evaluating Aquifer Properties by Interpreting Shallow Strain Measured During Well Tests. *Water Resources Research*, *57*(9). https://doi.org/10.1029/2021WR029613

Roudini, S., Murdoch, L. C., Shojaei, M., & DeWolf, S. (2023). Proxy-based Bayesian inversion of strain tensor data measured during well tests. *Geomechanics for Energy and the Environment*. In review

Zhu, X., Hua, L., Lei, J., Tang, J., Murdoch, L., & Xiao, H. (2021). Microwave–photonic low-coherence interferometry for dark zone free distributed optical fiber sensing. *Optics Letters*, *46*(5), 1173. https://doi.org/10.1364/ol.414699

Theses

Costantino, O. (2021). *Evaluating the Feasibility of Measuring and Analyzing Strain Caused by Changes in Barometric Pressure in the Vadose Zone* [Master of Science]. Clemson University.

Plunkett, G. (2021). *A Novel Technique for Distributed Measuring of Strain in the Vadose Zone* [Master of Science]. Clemson University.

Riley Blais. (2023). *Evaluating the Feasibility of Using Strain Measured During Sinusoidal-Rate Pumping Tests,* [Master of Science]. Clemson University.

Smith-Jones, A. (2023). *Evaluation of Zero-Net-Rate Pumping Tests* [Master of Science]. Clemson University.

Invited talks

Scott DeWolf, Larry Murdoch, Leonid Germanovich, Stephen Moysey, Alexander Hanna, and Robert Moak, "Using the shallow strain tensor to characterize deep geologic reservoirs," G&P CCS Learning Series & Geomechanics COP Tech Talk: Near-Surface Strain for CCS Monitoring, Chevron. Houston, TX. March 7, 2023.

Scott DeWolf, Larry Murdoch, Liwei Hua, Hai Xiao, Leonid N. Germanovich, Michael Furgeson, Stephen Moysey, and Alexander Hanna, "Designs and Performance of New Optical Fiber Tilt and Strain Instruments," Planetary Science Seminar, NASA Jet Propulsion Laboratory. Pasadena, CA. September 23, 2019.

Scott DeWolf, Larry Murdoch, Liwei Hua, Hai Xiao, Leonid N. Germanovich, Stephen Moysey, and Alexander Hanna, "New Electromagnetic and Optical Fiber Strainmeters and Tiltmeters for Measuring Deformation," 2018 Incorporated Research Institutions for Seismology (IRIS) Seismic Instrumentation Symposium, Session 2: Advancements in Instrumentation. Tuscon, AZ. October 30, 2018.

Larry Murdoch, Scott DeWolf, Leonid Germanovich. 2023. Measuring and interpreting the shallow strain tensor during transient well testing. ARMA Workshop on Optical Fiber Sensing in Geomechanics, Atlanta, GA

Conference presentations

Johnson, Wade, Scott DeWolf, David Mencin, and Elizabeth Van Boskirk, "Future Strainmeter Technology," Turkish-German Symposium on Seismotectonic Research in the Marmara Region, Session 6: Fault-zone characterization based on novel seismic processing techniques. Istanbul, Turkey. August 17, 2022.

Smith-Jones, A. Lawrence C. Murdoch, and Scott DeWolf, "Evaluation of Zero-Net-Rate Periodic Pumping Tests," 2022 Clemson Hydrogeology Symposium. Clemson, SC. March 31, 2022.

Moak, R Lawrence C. Murdoch, Leonid N. Germanovich, and Scott DeWolf, "The Feasibility of Using Deformation Monitoring to Identify Leaks from Geologic Repositories," 2021 Clemson Hydrogeology Symposium. Clemson, SC. October 21, 2021.

DeWolf, S., Lawrence C. Murdoch, Leonid N. Germanovich, Robert Moak, Soheil Roudini, and Austin Smith-Jones, "An Overview of Optical Fiber Strain and Tilt Systems Developed at Clemson University," 2021 Clemson Hydrogeology Symposium. Clemson, SC. October 21, 2021.

Blais, R., Lawrence C. Murdoch, and Scott DeWolf, Liwei Hua, and Robert Moak, "Using Strain in the Vadose Zone During Sinusoidal-Rate Well Tests to Characterize an Aquifer," 2021 Clemson Hydrogeology Symposium. Clemson, SC. October 21, 2021.

Roudini, R., Lawrence C. Murdoch, Scott DeWolf, and Leonid N. Germanovich, "Interpretation of Borehole Strain Measurements Using Surrogate Modeling-Based Optimization," 2020 Fall Meeting of the American Geophysical Union, Session H036, Presentation H036-0008. San Francisco, CA. December 8, 2020.

Blais, R., Lawrence C. Murdoch, Scott DeWolf, Leonid N. Germanovich, Liwei Hua, and Robert Moak, "Using Strain in the Vadose Zone During Sinusoidal-Rate Well Tests to Characterize an Aquifer," 2020 Fall Meeting of the American Geophysical Union, Session H062, Presentation H062-0008. San Francisco, CA. December 9, 2020.

DeWolf, S., Lawrence C. Murdoch, Leonid N. Germanovich, Robert Moak, and Michael Ferguson, "Designs and Results from Three New Borehole Optical Fiber Tensor Strainmeters," 2019 Fall Meeting of the American Geophysical Union, Session S21G, Presentation S21G-0597. San Francisco, CA. December 10, 2019.

Moak, R., Lawrence C. Murdoch, Scott DeWolf, and Leonid N. Germanovich, "Framework for Characterizing Strain in the Vicinity of Leaky Reservoirs," 2019 Fall Meeting of the American Geophysical Union, Session H21H, Presentation H21H-1839. San Francisco, CA. December 10, 2019.

Murdoch, L.C., Scott DeWolf, Leonid N. Germanovich, Alexander Hanna, Robert Moak, Stephen Moysey, and Soheil Roudini, “Interpreting the Strain Tensor During Injection into a Reservoir,” 2019 Fall Meeting of the American Geophysical Union, Session H12D, Presentation H12D-04. San Francisco, CA. December 9, 2019.

Murdoch, L.C., Scott DeWolf, Leonid N. Germanovich, Alexander Hanna, and Robert Moak, "Recent Developments in Hydromechanical Well Testing," 2019 Clemson Hydrogeology Symposium. Clemson, SC. April 4, 2019.

Moak, R., Lawrence C. Murdoch, Scott DeWolf, Leonid N. Germanovich, and Riley Blais, "Characterizing the Subsurface Using Deformation from Pumping and Surface Loading Tests," 2019 Clemson Hydrogeology Symposium. Clemson, SC. April 4, 2019.

Moak, R., Lawrence C. Murdoch, Scott DeWolf, Leonid N. Germanovich, Riley Blais, and Grant Plunkett, "Characterizing the Subsurface Using Deformation from Pumping and Surface Loading Tests," 2018 Fall Meeting of the American Geophysical Union, Session H51A, Presentation H51A-07. Washington, DC. December 14, 2018.

Murdoch, L.C., Scott DeWolf, Leonid N. Germanovich, Liwei Hua, Alexander Hanna, Jianan Tang, Stephen Moysey, Hai Xiao, Robert Moak, Grant Plunkett, and Riley Blais, "Characterizing Strain During Injection to Reduce Risks During CO2 Storage," 2018 Fall Meeting of the American Geophysical Union, Session H23M, Presentation S51F-0392. Washington, DC. December 14, 2018.

Hanna, A., Stephen Moysey, Lawrence C. Murdoch, Scott DeWolf, and Leonid N. Germanovich, "A cloud computing approach to massively-parallel distributed stochastic optimization with application to geomechanical reservoir characterization," 2018 Fall Meeting of the American Geophysical Union, Session H23M, Presentation H23M-2144. Washington, DC. December 11, 2018.

Hanna, A., Scott DeWolf, Stephen Moysey, and Lawrence C. Murdoch, "Using strain tensor measurements to locate and characterize subsurface heterogeneities," European Geophysical Union General Assembly 2018, Session ERE6.1, Presentation EGU2018-19571. Vienna, Austria. April 12, 2018.

DeWolf, S., Lawrence C. Murdoch, Leonid N. Germanovich, Stephen Moysey, and Alexander Hanna, "Results from New Tensor and Areal Strainmeters for Monitoring Fluid Injection and Withdrawal," 2018 Clemson Hydrogeology Symposium. Clemson, SC. April 12, 2018.

DeWolf, S., Lawrence C. Murdoch, Leonid N. Germanovich, Stephen Moysey, Alexander Hanna, John Hu, Riley Blais, Grant Plunkett, and Wade Johnson, "New Tensor and Volumetric Strainmeters for Monitoring Fluid Injection and Withdrawal," 2017 Fall Meeting of the American Geophysical Union, Session G51B, Presentation G51B-0750. New Orleans, LA. December 15, 2017.

Murdoch, L.C., Scott DeWolf, Leonid N. Germanovich, Stephen Moysey, and Alexander Hanna, John Hu, Riley Blais, Grant Plunkett, and Wade Johnson, "Forward and Inverse Models Incorporating Strain, Tilt and Pressure Data for Monitoring Deformation During CO2 Injection," 2017 Fall Meeting of the American Geophysical Union, Session S51C, Presentation S51C-0613. New Orleans, LA. December 15, 2017.

COMMERCIALIZATION

Project personnel have recently started a company called *Tensora*, Inc (https://www.tensora.io/) to commercialize technologies developed during this project. Tensora intends to focus initially on providing the ultra-high resolution strainmeters described in Chapter One to the carbon storage market and other relevant markets.

The basis for the CMPI distributed strain technology is covered under patent application No.: 17/584,017. Filed: January 25, 2022 and cited above as Hua et al. (2023). The Clemson Technology Transfer Office is currently seeking licensees interested in commercializing the CMPI technology.

DATA MANAGEMENT

Multiple data sources were gathered throughout this project including strain, tilt, wellhead pressures and injection rate and supporting meteorological data. This required aggregating data from both commercial and project-developed instruments into a suitable database, transmitting it to several backup locations on and off campus, and making the data available to project participants and to the public. The sources of the raw and processed data are described below.

RAW DATA

All raw data from this project (DE-FE0028292) and incoming data from ongoing research are publicly available through the Seismological Facility for the Advancement of Geoscience's Data Management Center (SAGE DMC). All data managed by Clemson University are aggregated through the International Federation of Digital Seismograph Networks (FDSN) Network Code 2J, which can be found through the following listing:

DeWolf, S. and Murdoch, L. C. (2016). *Clemson University Subsurface Deformation Monitoring Network*, International Federation of Digital Seismograph Networks, Dataset/Seismic Network, http://www.fdsn.org/networks/detail/2J_2016/, DOI: 10.7914/SN/2J_2016.

Metadata (StationXML) and waveforms (miniSEED) can be found via the SAGE MetaData Aggregator at:

http://ds.iris.edu/mda/2J/

The Gladwin Tensor Strainmeter deployed in AVN2 is operated and maintained by the EarthScope Consortium (formerly UNAVCO), whose data are also made publicly available under the FDSN Network Code PB. Metadata (StationXML) and waveforms (miniSEED) can be found via the SAGE MetaData Aggregator at:

http://ds.iris.edu/mda/PB/AVN2/

PROCESSED DATA

Processed strain along with monitoring well pressures and injection pressure and rate data from the suite of 2022 injection tests can be found at the National Energy Technology Laboratory's Energy Data Exchange (EDX) at:

Lawrence C. Murdoch and Scott DeWolf, *9A Injection: July 26 thru November 21, 2022*, 2023-08-21, https://edx.netl.doe.gov/dataset/9a-injection-july-26-thru-november-21-2022, DOI: 10.18141/1995730

CHAPTER ONE
POINT INSTRUMENT DEVELOPMENT

Contents

1.1 A Review of Optical Fiber Interferometry . . . 1-1
1.2 Optical Fiber Michelson Interrogator . . . 1-3
1.2.1 Review of the Version 3 OFMI . . . 1-4
1.2.2 The Version 4 OFMI . . . 1-6
1.3 Two-Axis Optical Fiber Tiltmeter . . . 1-10
1.3.1 Design and Prototype Development . . . 1-10
1.3.1.1 Conceptual Design . . . 1-10
1.3.1.2 Static Sensitivity Model . . . 1-10
1.3.1.3 Pendulum Rod Design . . . 1-12
1.3.1.4 Pendulum Mass Design . . . 1-15
1.3.2 Prototype Calibration . . . 1-16
1.3.3 Prototype Noise Performance in the Lab . . . 1-17
1.4 Optical Fiber Michelson Strain Ribbon . . . 1-18
1.4.1 First Prototype . . . 1-18
1.4.2 Second Prototype . . . 1-19
1.4.3 Analytical Calibration Estimate . . . 1-19
1.5 Optical Fiber Smart Casings . . . 1-21
1.5.1 Open-Closed Areal Strainmeter . . . 1-21
1.5.1.1 Design . . . 1-21
1.5.1.2 Hydrostatic Calibration . . . 1-23
1.5.2 Open-Open Areal Strainmeter . . . 1-23
1.5.2.1 Design . . . 1-23
1.5.2.2 Hydrostatic Calibration . . . 1-24
1.6 Mutlicomponent Optical Fiber Bragg Grating Strainmeter . . . 1-26
1.6.1 Design . . . 1-26
1.6.2 Hydrostatic Calibration . . . 1-26
1.7 Tensor Optical Fiber Strainmeters . . . 1-28
1.7.1 Nested Mandrel TOFS . . . 1-28
1.7.1.1 Prototype Design . . . 1-28
1.7.1.2 Numerical Model . . . 1-29
1.7.1.3 Hydrostatic Calibration . . . 1-30
1.7.1.4 Directional Load Calibration . . . 1-31
1.7.2 Inclined Helix TOFS . . . 1-32
1.7.2.1 Conceptual Design . . . 1-32
1.7.2.2 Prototype Design & Assembly . . . 1-33
1.7.2.3 Hydrostatic Calibration . . . 1-34
1.7.2.4 Directional Load Calibration . . . 1-35
1.7.3 Elliptical Ring TOFS . . . 1-36
1.7.3.1 Prototype Design . . . 1-36
1.7.3.2 Hydrostatic Calibration . . . 1-37
1.7.3.3 Directional Load Calibration . . . 1-37
1.7.4 North Avant Field Strainmeters . . . 1-38
1.7.4.1 Final Design . . . 1-39
1.7.4.2 Hydrostatic Calibration . . . 1-40
1.8 Summary of Strainmeter Lab Results . . . 1-43
1.9 Load Frame Calibration System . . . 1-45

1.9.1 Background and Motivation 1-45
1.9.2 System Design and Assembly 1-45

POINT INSTRUMENT DEVELOPMENT

Point instruments can be defined as one or more sensors packaged to measure one or more variables at one location (e.g. in a borehole). This could include measurements of different physical quantities (e.g. temperature or pressure) or multiple measurements of the same variable at different orientations (e.g. horizontal and vertical strains). This is in contrast to distributed instruments designed to make measurements at multiple locations (e.g. axially along a borehole) like distributed acoustic sensing (DAS) and distributed strain sensing (DSS) that are described in Chapter 3.

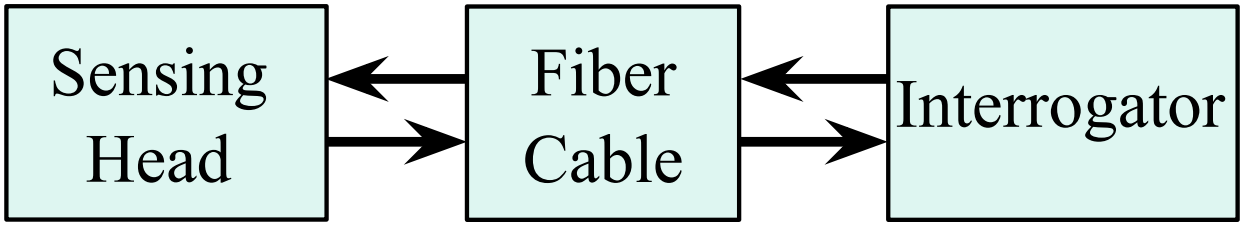

Figure 1.1: Block diagram of a basic optical fiber sensing system showing the interrelation between the sensing head and interrogator, along with the fiber cable that connects them.

A key advantage of optical fiber sensing systems is that the active and passive elements can be easily separated. The optical fiber instruments developed for this project are designed to consist of a passive "sensing head" containing one or more interferometers are used to measure some combination of the strain, tilt and temperature of its environment. This is connected to an opto-electronic interrogation system that is used to send and receive light from the sensing head using a fiber cable. The basic block diagram for this arrangement is shown in Figure 1.1, which is particularly advantageous in borehole applications where the sensing head contains no serviceable components and is often permanently installed.

This chapter describes the development of multiple sensing heads as well as a new optical fiber interrogation system. The sensing heads include a two-axis tiltmeter, a single-axis vertical strainmeter ribbon, fiber embedded "smart" casings, and several different approaches for measuring the in-situ strain tensor. These developments are preceded by a brief review of optical fiber interferometry and the interrogator developments and concludes with a novel automated loading frame to assist in laboratory calibration of the tensor instruments.

1.1 A Review of Optical Fiber Interferometry

The measurement principle used in the optical fiber strainmeters is the optical fiber Michelson interferometer. Figure 1.2 shows the most basic implementation wherein a light source of an arbitrary initial polarization state is injected into one of the four arms of a 2×2 fused optical fiber coupler where the light is split into two paths. After propagating down their respective paths, the two light rays reflect off mirrors (retroreflectors) and return back through their same paths and recombine at the 2×2 coupler to form interference fringes.

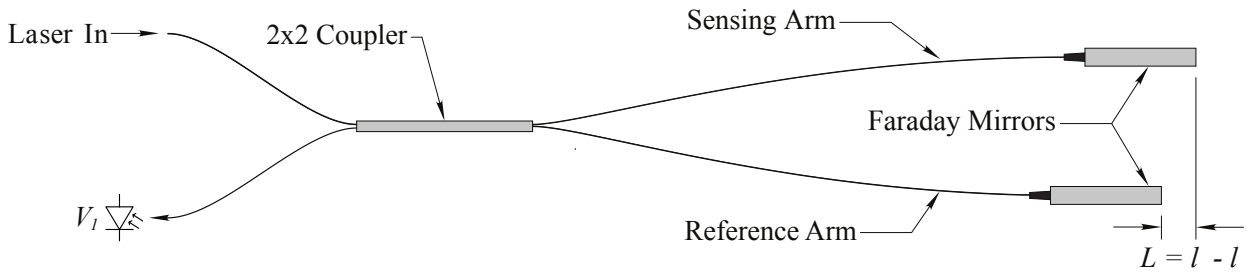

Figure 1.2: Schematic of a basic optical fiber Michelson interferometer using a single 2×2 coupler and photodetector.

The total optical phase of coherent, monochromatic light propagating in an optical fiber can be expressed as

$$\theta = \frac{2\pi n l}{\lambda} \tag{1.1}$$

where the index of refraction $n = c/v$ is the ratio of the speed of light in air c and the speed in the material v, l is the path length, and λ is the wavelength. The optical phase shift ϕ is related to the difference between the optical phase of the light propagating in the sensing arm θ_S and reference arm θ_R, respectively, as

$$\begin{aligned} \phi &= \theta_S - \theta_R \\ &= \frac{2\pi n}{\lambda}\left(l_S - l_R\right) \\ &= \frac{2\pi n L}{\lambda}, \end{aligned} \tag{1.2}$$

where $L = l_S - l_R$ is the physical length difference between the two interferometer arms.

The intensity at the output of the 2×2 coupler as seen by the output (voltage) V_1 of the photodetector can be expressed as

$$V_1 = u_1 + v_1 \cos\left(2\phi\right) \tag{1.3}$$

where u_1 is the DC offset, v_1 the fringe amplitude, and the factor of 2 is a result of the reflection (i.e., the light travels through its path twice). Therefore, changes in the optical path length difference nL between the sensing and reference arms of the interferometer manifest themselves as changes in the output voltage of the photodetector. However, there are two main limitations to this technique addressed below.

One well known difficulty with optical fiber interferometers is decreased fringe contrast caused by differential polarization changes. This occurs after the light is split in two since each pathway is then subjected to different environmental conditions (strain, temperature, pressure, etc.), and these can alter the birefringence and therefore the state of polarization in one arm relative to the other. The amplitude of the (returned) interfering light, the fringe contrast, depends upon this relative polarization state of the two returning beams; in the extreme, with orthogonal polarizations, the returning beams do not interfere with each other.

A simple remedy to employ a pair of optical components known as a phase-conjugating, or Faraday mirrors, first used in fiber interferometers by Kersey et al. (1991). These consist of a Faraday rotator (typically a rare-earth magnet surrounding a high Verdet constant optical material) and a plane mirror. This creates a non-reciprocal reflection that rotates the polarization state of the incoming light by $90°$, forcing what had been the component of the electric field propagating along the fast axis (low n) to propagate back to the coupler along the slow axis (high n) and vice-versa. The result is return-beams restored to their original polarization (rotated by $90°$) and nearly perfect fringe contrast as long as the polarization perturbations do not occur faster than the propagation time. Faraday mirrors are compact and inexpensive, and can be used in place of the retroreflectors in Figure 1.2.

The second obstacle relates to the bidirectional phase ambiguity shown in equation (1.3). Consider the case where the output intensity is a maximum, i.e., where the optical phase is $\phi = \pi/2$, or optical path length difference $nL = \lambda/2$. An increase or decrease in L results in a decrease in intensity seen by the photodetector, thereby making it impossible to discriminate between expansive and contractive path length changes.

One method involves exploiting the evanescent waveguide properties of the coupler used to split and recombine the two interferometer arms. Fused optical fiber couplers are fabricated by grinding down or melting the cladding between

a pair of adjacent fibers such that light "leaks" from one waveguide to the other when fused together. In addition to the amplitude being split, there is also a phase shift induced in proportion to the distance between the waveguides and the wavelength of light. For an ideal 3 dB 2×2 coupler (50/50 splitting ratio), the light in the second fiber is phase-shifted by $180°$; unfortunately this provides no new information since it is just -1 times the original. However, in an evenly split 3×3 fused coupler the other two fibers undergo a $120°$ phase shift. Therefore, for a (polarization-insensitive) optical fiber Michelson interferometer using a 3×3 coupler (Figure 1.3), there are three fringe signals $120°$ phase-shifted from each other. It is then possible to take advantage of this for the recombined light returning from the sensing arms for resolving directional fringe information. Sheem (1980) was among the first to publish results of a fiber optic gyroscope using 3×3 couplers, and there have been many dozens of other published works using this technique in Michelson, Mach-Zehnder and Sagnac optical fiber interferometers.

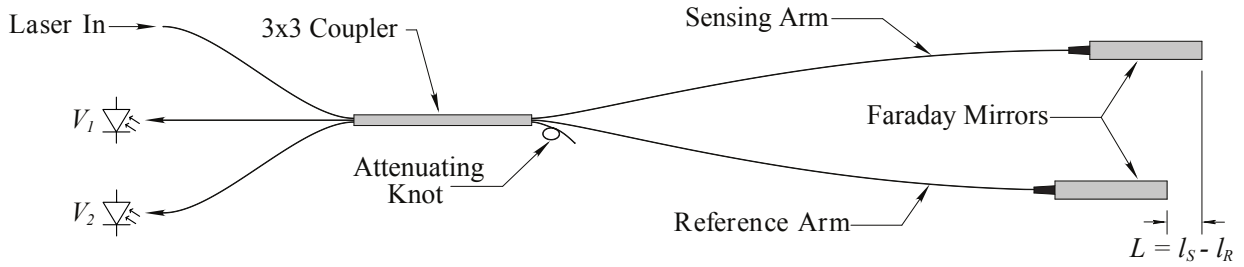

Figure 1.3: Schematic of the optical fiber Michelson interferometer using a 3×3 coupler with a 2×2 coupler tap and triple photodetector detection scheme.

The optical fiber interferometers used during this project employ a real-time digital signal processing system was developed to extract the optical phase difference ϕ from the two phase-shifted interference fringe signals output by the 3×3 coupler. This method is based on Zumberge et al. (2004), wherein equation (1.3) is adapted to accommodate both outputs $x = V_1$ and $y = V_2$ as

$$x = x_0 + a \sin(p + p_0) \tag{1.4}$$

$$y = y_0 + b \cos(p) \tag{1.5}$$

where $x_0 = u_1$ and $y_0 = u_2$ are the DC offsets, $a = v_1$ and $b = v_2$ are the fringe amplitudes, p_0 is an arbitrary starting phase and $p = 2\phi$ is the optical phase difference. These two relationships can be inverted to compute the phase p using the expression

$$p = \arctan\left[\frac{b}{a}\left(\frac{x - x_0}{y - y_0}\right)\frac{1}{\cos(p_0)} - \tan(p_0)\right]. \tag{1.6}$$

The ellipse shape parameters a, b, x_0, y_0 and p_0 are determined by a least-squares fit to a collection of x and y data sufficient to sweep out the perimeter of an ellipse (Zumberge et al., 2004). This phase estimate is linearly proportional to the strain in the fiber, and is therefore the desired output.

1.2 Optical Fiber Michelson Interrogator

The opto-electronic interrogators developed for the point instruments for this project is called the Optical Fiber Michelson Interrogator, or OFMI. While it is named for its most common application, i.e., for use with Michelson interferometers, it can also be used with any combination of Michelson, Mach-Zehnder and Sagnac interferometers. Figure 1.4 shows a block diagram of the main components of the OFMI, which is a light source that illuminates the

sensing head and a detection system for receiving the returning signals. The light source is commonly a distributed feedback (DFB) laser that emits monochromatic and coherent light, and the photodetectors consist of a photodiode whose current is converted to a voltage using a transimpedance amplifier.

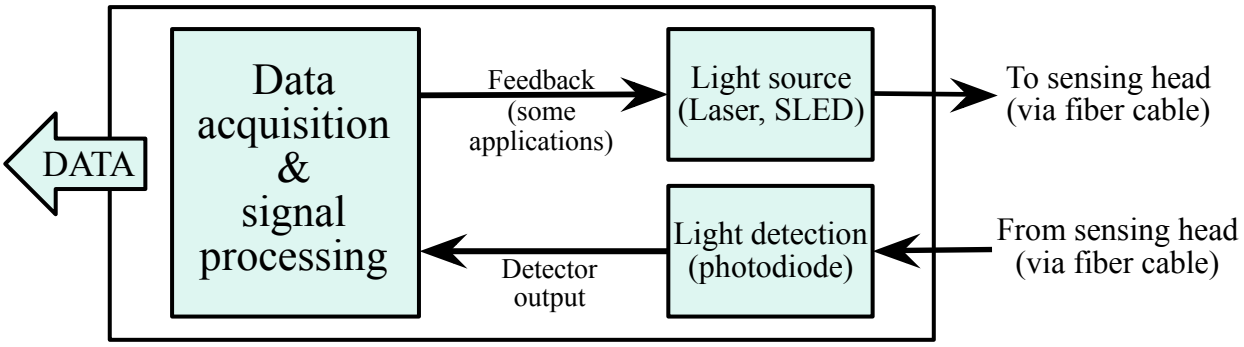

Figure 1.4: Block diagram of a simple optical fiber Michelson interrogator showing the interrelation between the sensing head and interrogator, along with the fiber cable that connects them.

A critical function of the OFMI is to convert the returning interference fringe signals into a record of the desired quantity being measured by the sensing head. This is accomplished by the interrogator by first digitizing the fringe signals using an analog-to-digital converter (ADC) and sending the results to an onboard computer that computes the strain through a signal processing algorithm often referred to as demodulation.

There was one major revision to the OFMI made during this project. This started with the Version 3 developed for the Optical Fiber Areal Strainmeter developed during the previous project (DE-FE0023313) and ended with a fully redesigned Version 4 system that was used for the Tensor Optical Fiber Strainmeter systems deployed for the demonstration part of this project. A brief review of the Version 3 OFMI is presented in the next section to provide context and motivate the development of the new Version 4 system in Section 1.2.2.

1.2.1 Review of the Version 3 OFMI

The Version 3 OFMI interrogator is shown in Figure 1.5, and consists of a power distribution system, laser driver, laser diode, photodetection system, and ADC. The electronics are a combination of off-the-shelf components and custom printed circuit boards. The power distribution board was developed in-house, and is capable of accepting an unregulated voltage from 9–36V and converts it to a regulated $+5$V for the ADC and photodetection system, and $+12$V for the laser driver. The laser system is a combination of four components: a DFB laser diode (of various models), 14-pin butterfly laser mount, laser current source/driver, and custom laser-driver-to-laser-mount adapter board. A new photodetector board was developed to read up to nine fringe signals since this system was intended for interferometers using a 3-fringe demodulation technique (Todd et al., 2002). Each channel consists of InGaAs photodiodes and operational amplifiers with potentiometers to adjust the gains of each transimpedance amplifier. These are all mounted on a daughterboard whose header plugs directly into the ADC.

The main purpose of the pressure case package is so the interrogator can be deployed $\sim$5 m deep in the borehole above the instrument. This allows the laser to use the stable temperature of the borehole environment rather than an active thermal regulation system translating to a factor of 3 to 4 in power savings. The pressure case housing is easily removed for servicing and can be replaced entirely by cutting and re-terminating the fiber and electrical connections.

Despite the innovations of the Version 3 design, it still relies on several commercial products. This means that this and subsequent OFMI designs must conform to the form factors of these products as well as adapt to changes in features imposed by their manufacturers. For example, the pressure case diameter is strictly limited by the size of the ADC board making it impossible to develop an interrogator with a narrower profile that would leave more of the open hole section available for additional instrumentation. This and other issues led to the development of the Version 4 OFMI.

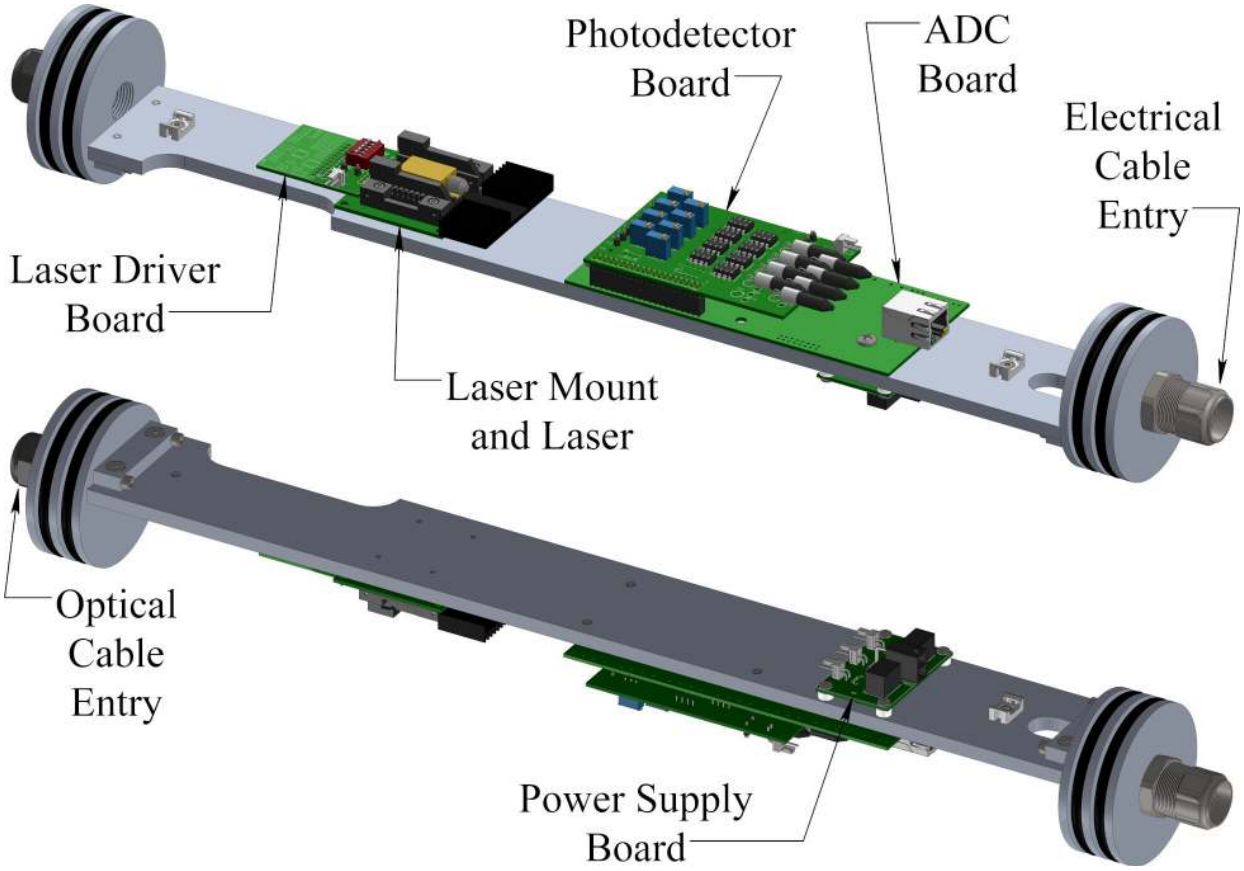

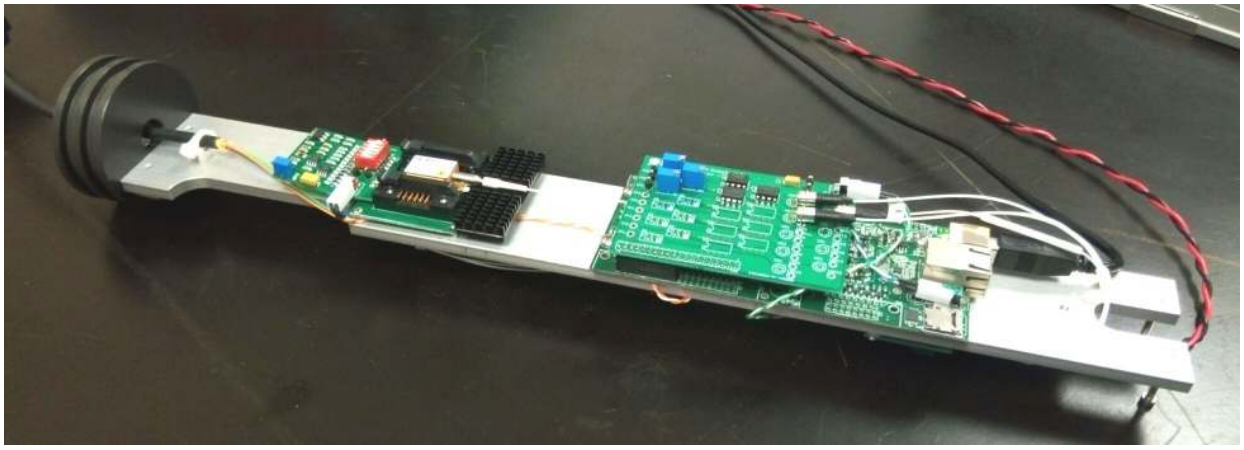

Figure 1.5: Diagrams of the top and under sides of the Version 3 OFMI showing its major components and their locations inside of the pressure case, along with a photograph of a single channel device being tested on the bench.

1.2.2 The Version 4 OFMI

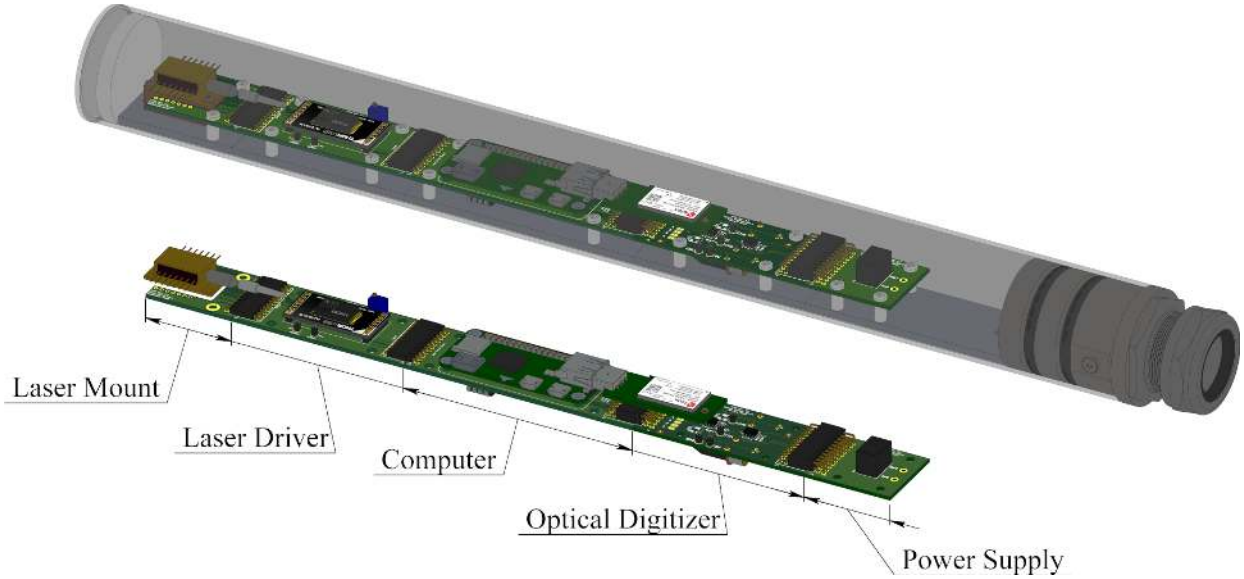

Figure 1.6: CAD rendering of the Version 4 OFMI showing its constitutive circuit boards inside (top) and outside (bottom) of the pressure case. While this design can operate up to nine optical digitizer boards, only one is shown for scaling purposes.

The Version 4 OFMI is a complete redesign of the previous interrogators featuring almost exclusively custom printed circuit boards. Figure 1.6 shows this new system that consists of a power supply, a custom laser mount and heat sink, a laser driver, an optical digitizer board for each interferometer and a commercial single board computer (Raspberry Pi Zero v1.3). This is a modular design both electronically and mechanically that can accommodate up to nine interferometers inside of a 2-inch diameter pressure case. The printed circuit boards are all 1.3" wide and are as long as needed to place the components and route their connections using a single layer on the top and bottom. Each board is held to its respective aluminum mounting tray using #4 screws on 1-inch centers.

Figure 1.7 shows the new power supply board that contains only a single 9–36V to 5V DC-to-DC converter (Traco Power TDN 5-2411WI). A considerable amount of effort was required to research the different component options to arrive at a system that could be powered off of a single 5V power supply, unlike the Version 3 OFMI that required an additional 12V converter for the laser driver. This also translates to power savings since these devices are only around 80% efficient, so the less conversion the better. While the first two revisions had a forward facing connector, this connection is not fre-

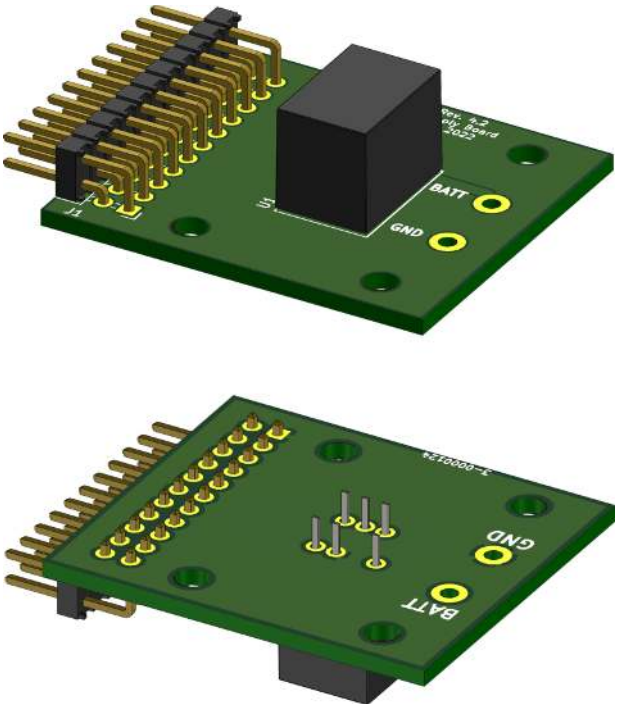

Figure 1.7: Computer renderings of the top and bottom of the power supply board.

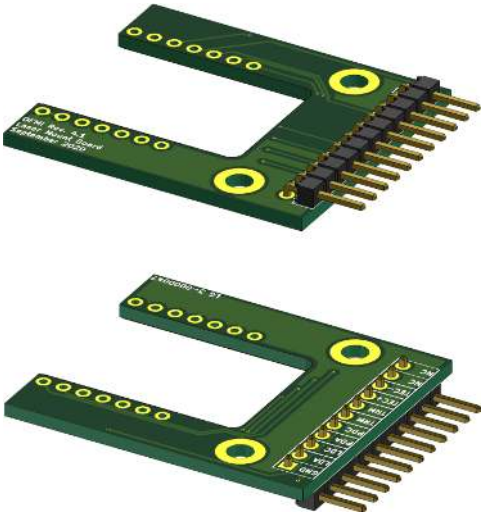

Figure 1.8: Top and bottom of the very minimal laser mount board where the 14 pins are soldered directly into the through holes.

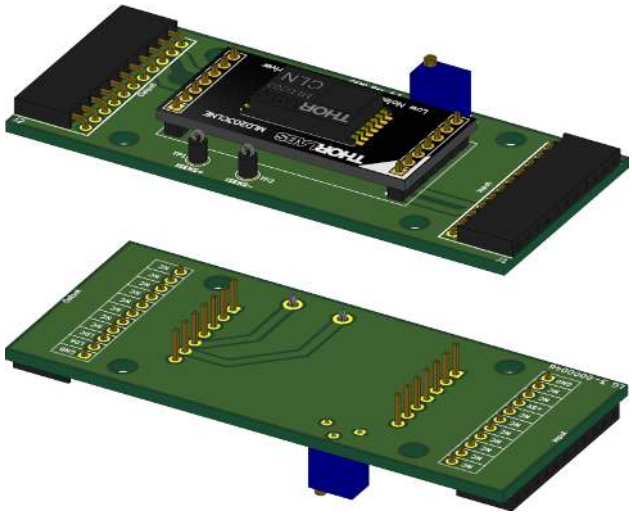

Figure 1.9: Laser driver board that hosts the laser driver daughterboard along with test points to monitor the laser current supply while adjusting the potentiometer.

quently made and unmade so the latest versions have the incoming electrical connections soldered directly to the board. The output is a 22-pin header that is needed to match the input of the first optical digitizer board, which require the extra pins to be connected in series.

Another set of new developments is how the laser is mounted and driven. The Version 3 interrogator used a commercial laser mount and heat sink (ModularOne MOT_BTSCK_HS-T) with a pair of the zero-insert-force sockets to hold the laser. While convenient, these are very bulky and as with the incoming power connections, we rarely change out lasers and opted to simply solder them directly to a very simple board (Figure 1.8). The laser mount board only has one 11-pin input header that receives only up to nine signals from the laser driver whose board is shown in Figure 1.9. This is also a very simple board since it only holds the driver chip (Thorlabs MLD203CLN) on an evaluation daughterboard (since the chip was backordered 34 weeks due to supply chain issues) along with a trim pot (Bourns 3296W-1-203LF) and a pair of test leads to adjust and monitor the current supplied to the laser. The driver board is connected on each end using 11-pin receptacles to connect to the laser on its output and ground and 5V on its input.

Perhaps the most significant design choice was to create a separate circuit board for each interferometer channel. The optical digitizer board (Figure 1.10) is responsible for converting the two phase shifted interference fringe signals from light to currents using a pair of photodiodes (Bitline Systems PD-A-25-9-1-N), converting those currents into voltages using a dual operational amplifier (Texas Instruments LM358) and from voltages to a digital number using a dual-channel ADC (Microchip MCP3202). The ADC communicates to the onboard computer using a 4-pin Serial Peripheral Interface (SPI) where three of the four pins can be shared and the individual board identified using the chip-select pin. There are nine chip-selects available that are designated by closing one of the solder bridges on the top of the board. The gains of the transimpedance amplifiers are adjusted using trim pots (Bourns 3224W-1-104E) while monitoring the outputs of the test points.

The Version 4 interrogator includes an onboard computer that performs many different functions. This is a Raspberry Pi Zero v1.3 that is soldered directly to a carrier board (Figure 1.11) that contains a 22-pin input receptacle for power and the incoming SPI communications from 1–9 optical digitizer boards. The computer board also includes a Honeywell SSCMRNN015PA3A3 digital 15-psi absolute pressure transducer for monitoring the barometric pressure via a 1/16-inch inner diameter, 1/8-inch outer diameter polyethylene tube that exits the pressure case along with the electrical connections. These data are recorded over the onboard computer's I2C bus along with the outputs of the

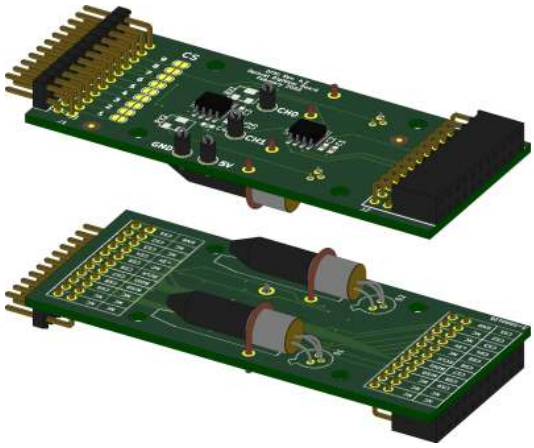

Figure 1.10: Top and bottom of the optical digitizer board showing the pair of photodiodes underneath and test points on top used to monitor the transimpedance amplifier gains.

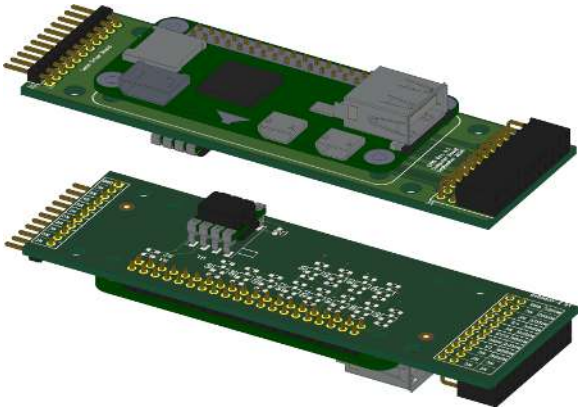

Figure 1.11: Computer carrier board showing the single board computer on top and the Honeywell SSCMRNN015PA3A3 pressure transducer on the bottom.

ADCs. A set of nine level shifting circuits are also included to convert the 5V logic of the ADCs to 3.3V, which is the only place where the single 5V supply is converted. The 11-pin output header passes only ground and 5V to the laser driver.

The onboard computer is responsible for demodulating the interference fringes and handling the data. A firmware program written in ANSI C is used to read the outputs of the ADCs and compute the optical phase differences (Eq. 1.6) and decimate the output to the desired sample rate. The phase data along with the interference fringe intensity and barometric pressure time series are stored in miniSEED format (Ahern and Dost, 2012) on a local Secure Digital (SD) card. A USB receptacle attached to the computer hosts a cellular modem to allow the data to be transmitted over a Virtual Private Network (VPN) using a cellular data connection to a cloud-based data server that is mirrored by a physical data server on campus. This cellular connection is also essential because it maintains the system time to limit clock drift during operation.

Figure 1.12 shows the mechanical assembly of the four six-channel Version 4 OFMIs that were deployed at our North Avant Field demonstration site in Oklahoma. These photos show the arrays of printed circuit boards each attached to individual aluminum trays that are linked using tray mounts. Each set of boards and trays is connected to a stainless steel end cap that uses a double o-ring to seal off the interior. A short aluminum disc is attached to the opposite end to constrain the end of the trays inside of the pressure case outer cylinder. The final length for these systems is approximately 36 inches ($\sim$91 cm).

There several penetrations through the OFMI pressure case end cap for optical and electrical connections. Figure 1.13a shows these penetrations, which includes the 18 fibers needed to send and receive light from the six interferometers inside of the tensor strainmeters developed in Section 1.7. Each board stands off of their respective trays using a 5/16" spacer that allows for the laser and photodiode fibers and splice protection sleeves to be neatly contained. This photo also shows the two 16-gauge wires used to power the device and shows the black RG174 coaxial cable for the cellular modem antenna as well as the green polyethylene tube connected to the barometric pressure sensor in Figure 1.13b.

The completed Version 4 OFMI consumes about 1.9 Watts under normal operation, including cellular. This is approximately 1.5W less than the Version 3 interrogator that does not include a computer or telemetry, which that means it should comfortably operate on only one 100 Amp-hour battery rather than two or three like the existing installations.

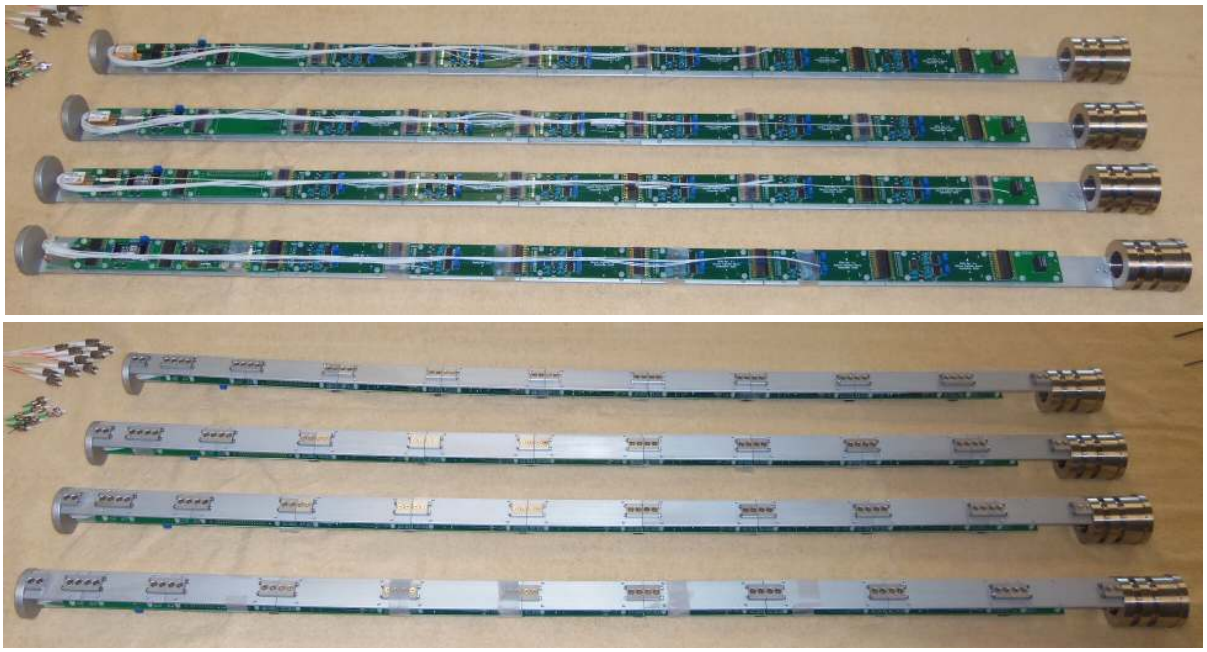

(a) (b)

Figure 1.12: Photographs of the top (a) and bottom (b) of the four full six-interferometer Version 4 OFMIs used for the North Avant Field tensor strainmeter installations.

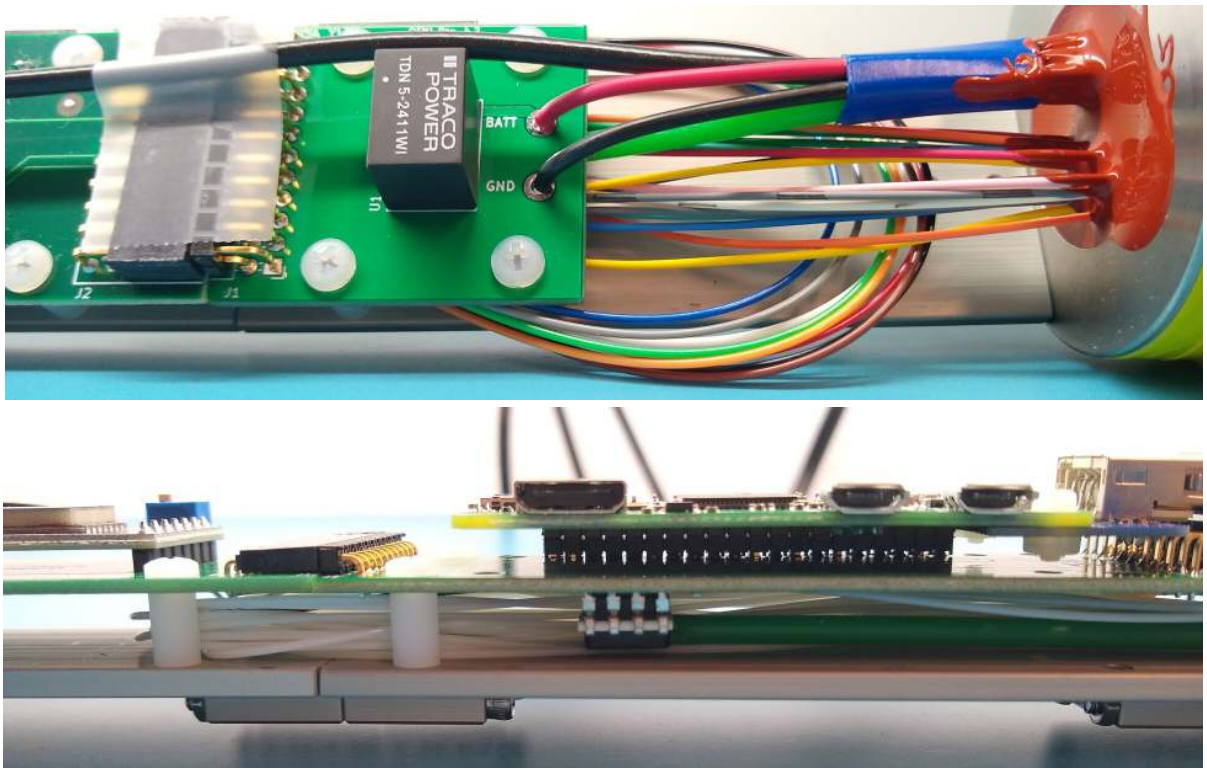

(a) (b)

Figure 1.13: (a) Fiber and electrical penetrations into the OFMI pressure case. (b) Side view of the computer board showing the green polyethylene tube connected to the digital barometric pressure sensor.

1.3 Two-Axis Optical Fiber Tiltmeter

Tilt, or inclination is a fundamental measurement and a vital part of geophysical and geotechnical monitoring since can be a simple way to measure deformation at or below the surface from any number of natural or anthropogenic processes that is relatively straightforward to interpret. There are innumerable varieties of tilt measuring devices, or tiltmeters (aka: inclinometers, clinometers, etc.), large and small for almost as many applications. However, our research interest is in the geodetic class of instruments where the focus is on very long period phenomena (i.e., signal durations from several hours to days, weeks, months, or even years) measured in shallow or deep boreholes.

We therefore proposed to develop a two-axis, or vector optical fiber tiltmeter using embedded optical fibers that can be interrogated as a Michelson Interferometer that can be deployed in a borehole. Figure 1.14 shows a photograph as well as a schematic diagram of a prototype tiltmeter developed for this project, which consists of a pressure case, pendulum rod, pendulum mass, and mounting hardware for the pendulum itself and the required optical components. The basic design principle is that if a pendulum bob: as the frame tilts, the mass bends the rod causing compressive strain along one axis of the rod and extensional strain along the other that is measured using two orthogonal pairs of optical fibers. The following subsections describe the design, calibration and benchtop performance of the prototype shown in Figure 1.14.

1.3.1 Design and Prototype Development

1.3.1.1 Conceptual Design

The basic operating principle is that of a flexural pendulum where local gravity acts against a mass, or pendulum "bob" at some distance L from the hinge point where the restoring force is the flexural bending of the pendulum rod, or cantilever (Figure 1.14). Two or more pairs of optical fibers are embedded in the pendulum rod to resolve both orthogonal components of tilt, conventionally referred to as x and y (or East-West and North-South in geographic coordinates). While only two pairs are required to uniquely determine the x and y tilt directions, one or more additional fiber pairs can be included to provide an overdetermined measurement such that common-mode instrumental and environmental effects such as laser noise, photodetector nonlinearity, and temperature gradients can be removed using principle component analysis.

1.3.1.2 Static Sensitivity Model

The bending of the flexural pendulum bob can be modeled as a cantilever beam with a circular cross section. The primary concern is how much lateral deflection of the rod occurs when the pressure case containing the pendulum bob tilts, which is related to how much the embedded fibers are strained. This is a function of the Young's modulus, diameter, and length of the rod as well as how far apart the sensing and reference fibers of a given interferometer pair are from one another (i.e., the radial separation). Fortunately it is very easy to compute the displacements and strains for a fixed-free cantilever with a circular cross section. The lateral deflection δ can be described using the relationship

$$\delta = \frac{4FL^3}{3\pi r^4 E} \tag{1.7}$$

where F is the force acting at the end of the pendulum rod, and L, r, and E are the length, radius, and Young's modulus of the pendulum rod, respectively. The strain of a fiber a distance y from the "neutral axis" (in this case it is the center of the rod given the symmetry of the cross section) as a function of the distance down the cantilever x is

$$\epsilon = \frac{4F}{\pi r^4 E} xy \tag{1.8}$$

Since the strain is being measured along the length of the rod with an optical fiber, the observation is actually the

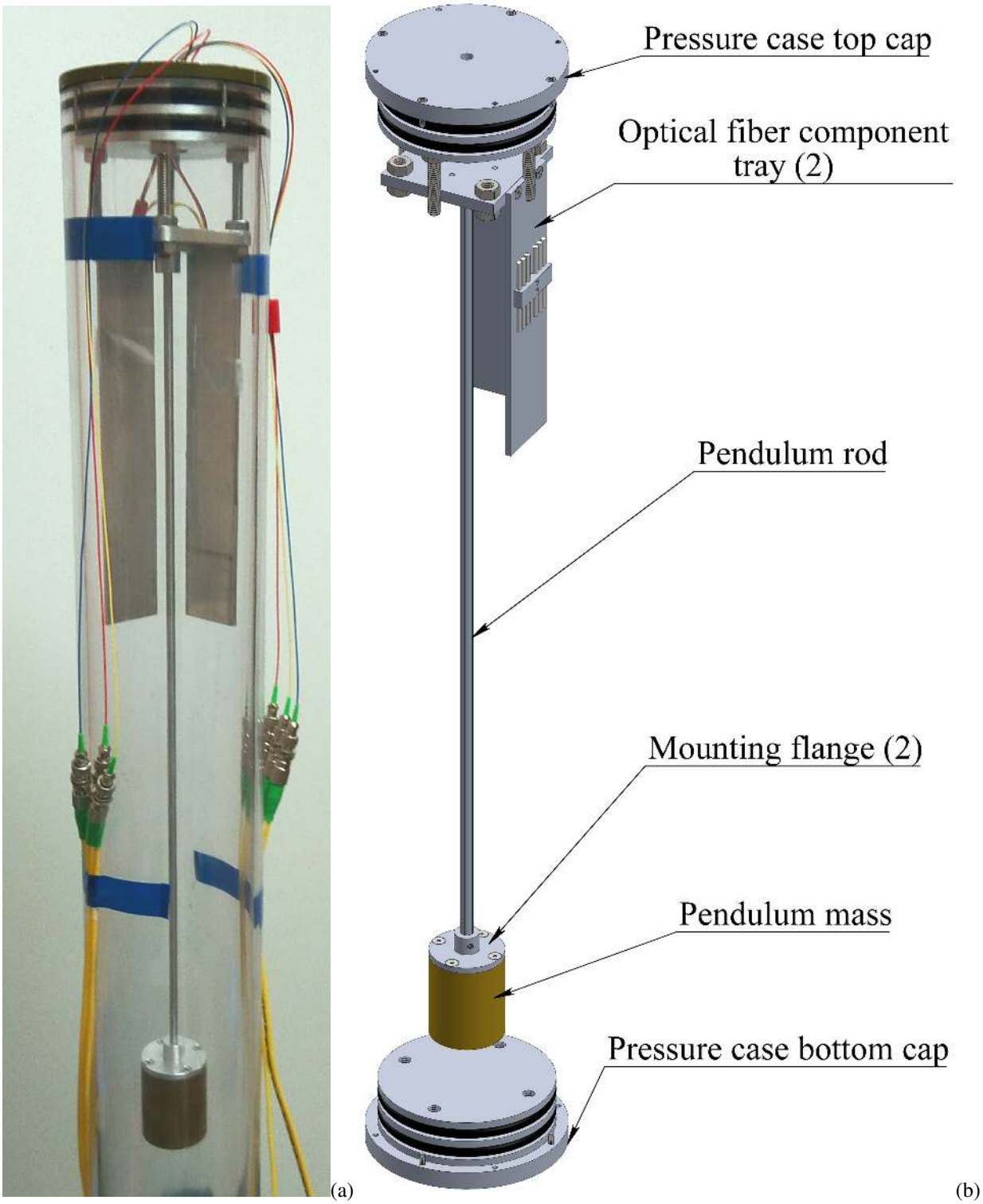

Figure 1.14: Photograph (a) and schematic diagram (b) of the two-axis optical fiber tiltmeter.

average differential strain

$$\begin{aligned}\Delta\bar{\epsilon} &= \frac{1}{L}\int_0^L \frac{4F}{\pi r^4 E} xy\, dx \Bigg|_{-r_{sep}}^{r_{sep}} \\ &= \frac{2FL}{\pi r^4 E} y \Bigg|_{-r_{sep}}^{r_{sep}} \\ &= \frac{4FL}{\pi r^4 E} r_{sep} \end{aligned} \tag{1.9}$$

where r_{sep} is the radial separation distance of the fiber pair, or the radial distance of the optical fiber from the center axis of the pendulum rod (this is the right-most dimension shown in each subplot of Figure 1.15). Equations 1.7 and 1.9 have been verified using the SolidWorks Simulation software.

The average differential strain can be converted into a strain per unit tilt (radians) by acknowledging the fact that the force acting on the pendulum mass is in fact

$$F = mg\sin(\theta)$$

where the small angle approximation $\sin(\theta) \approx \theta$ makes Equation 1.9

$$\Delta\bar{\epsilon}(\theta) = \frac{4mgLr_{sep}}{\pi r^4 E}\theta \tag{1.10}$$

This can be converted into an optical phase using the relationship derived by Butter and Hocker (1978)

$$\Delta\phi = \frac{\pi nL}{\lambda}\left\{2 - n^2\left[p_{12} - \nu\left(p_{11} + p_{12}\right)\right]\right\}\epsilon \tag{1.11}$$

where $n = 1.4682$ is the index of refraction of the fiber at $\lambda = 1550.11$ nm, and $p_{11} = 0.113$ and $p_{12} = 0.252$ are the two strain-optic (Pockel's) coefficients. The whole point of all of this is to estimate the sensitivity in terms of the optical phase difference in the pair of optical fibers as the pendulum bob reacts to the tilting of the pressure case, which can be done by inserting Equation 1.10 into 1.11

$$\frac{\Delta\phi}{\theta} = \frac{4mgnL^2}{r^4\lambda E}\left\{2 - n^2\left[p_{12} - \nu\left(p_{11} + p_{12}\right)\right]\right\} r_{sep} \tag{1.12}$$

This seems to make sense given that one would expect the optical phase to depend upon the mass, length, and radius of the pendulum rod, as well as the separation distance between the two fibers (no separation means that the fibers are coincident, and therefore see the same strain).

1.3.1.3 Pendulum Rod Design

The most important aspect of this tiltmeter is the fiber-embedded pendulum rod. This is accomplished by stretching two or more pairs of optical fiber inside of a long cylindrical tube and epoxying them in place such that the flexural bending of the rod strains the fibers in a predicable manner. One way to solve the challenge of azimuthally separating and orienting the fibers within the rod tube is to partition the tube using cylindrical rods that fill the void space not occupied by the fibers. This breaks down to a circle packing problem when viewed in cross-section.

A key limitation in designing the pendulum rod is the materials available for solving this circle packing problem. While one could have custom cylinders and rods made to fit a specific design, using readily available materials significantly reduces the cost and lead time. For example, the company MicroGroup has a very nice selection of welded stainless steel tubing in both fractional inch and metric sizes as well as standard hypodermic needle gauges. MicroGroup also offers rods (or wire) from diameters of 0.006" to 0.100" with part numbers following the 304B0xxxXRND convention, where xxx is the rod diameter in thousandths of an inch.

The first concern was the design of the rod since the other elements of the design such as the length needed to achieve a given sensitivity and borehole package (i.e., pressure case) diameter. This issue of embedding the fibers into the main rod tube with other rods boils down to a classic circle packing problem, which is constrained by material availability. An arbitrary lower bound of 1/8" was chosen for the rod diameter because anything smaller would make assembly cumbersome as well as limit the robustness of the rod. Likewise, a maximum rod diameter of 1/4" was chosen given that its stiffness would require a relatively large mass to achieve a lateral deflection similar to smaller rod sizes. This design uses 900-micron, tight-buffered optical fibers since this was the pigtail material used on the four Faraday mirrors that were readily available.

There are five different components under consideration:

1. the outer stainless tube
2. the four 900 μm diameter optical fibers
3. a central rod for the core
4. the four rods separating the fibers about the central rod ("orbit" rods)
5. the epoxy that fills the void space between items 1–4

Figure 1.15 shows two example cross sections using standard 0.180" OD 304 stainless steel tubing with two different wall thicknesses offered by MicroGroup. Table 1.1 shows the model numbers and dimensions for 10 different standard sizes for the main tube, as well as the dimensions for the central and separating/orbit rods. The distance between the center and the axis of the fiber is r_{sep}.

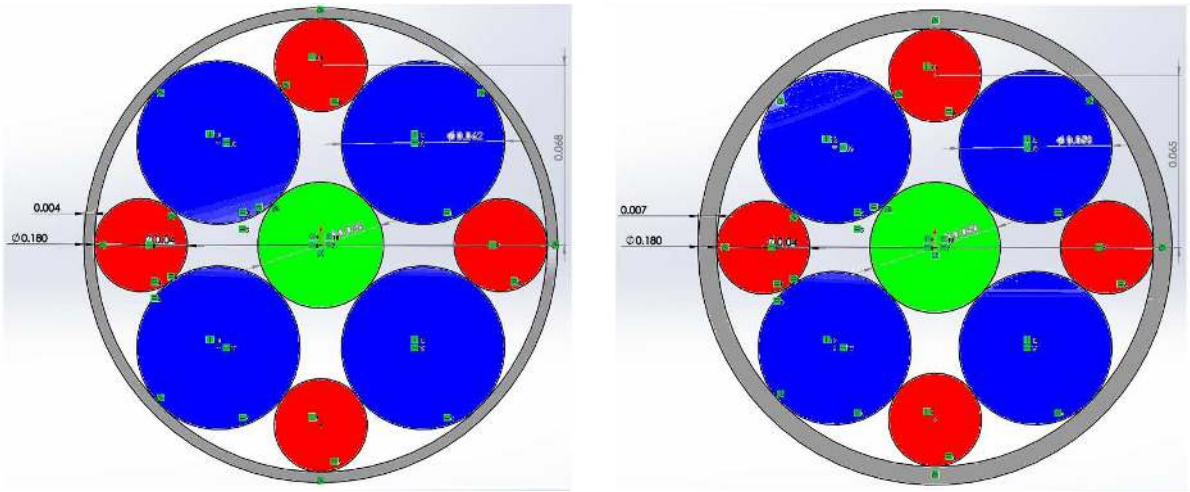

Figure 1.15: Examples of pendulum rod cross sections for two 0.180" OD tubing wall thicknesses.

It is less accurate to assume that the bulk Young's modulus is simply that of 304 stainless steel ($E_{304} = 190$ GPa) since for the smaller diameters a sizable fraction of the cross sectional area is made up of epoxy and the PVC and acrylate of the optical fiber buffer. To check the validity of this assumption Equations 1.7 and 1.9 have been computed using both a bulk Young's modulus of 304 stainless as well as a weighted average value based on the cross sectional areas of the various materials

$$\bar{E} = \frac{E_f \cdot 4A_f + E_t \cdot A_t + E_c \cdot A_c + E_o \cdot 4A_o + E_e \cdot A_e}{4A_f + A_t + A_c + 4A_o + A_e}$$

where the various Es are the Young's moduli

Table 1.1: MicroGroup model numbers and dimensions for the fractional and hypodermic tubes.

Item Number	Tube OD (in)	Tube Wall (in)	Tube ID (in)	Center OD (in)	Orbit OD (in)	r_{sep} (in)
304F10125X006SL	0.125	0.006	0.113	0.042	0.027	0.039
304H09XX	0.148	0.007	0.135	0.056	0.039	0.049
304F10156X006SL	0.156	0.006	0.144	0.055	0.045	0.054
304H08XX	0.165	0.007	0.150	0.053	0.049	0.058
304H07XX	0.180	0.004	0.173	0.048	0.062	0.068
304H07X	0.180	0.007	0.166	0.050	0.058	0.065
304F10188X006SL	0.188	0.006	0.176	0.047	0.064	0.070
304H06X	0.203	0.007	0.191	0.042	0.073	0.077
304F10219X006SL	0.219	0.006	0.207	0.035	0.086	0.086
304F10250X010SL	0.250	0.010	0.230	0.039	0.095	0.097

- $E_f = 4.6$ GPa of 900 μm diameter, tight-buffered optical fiber (also a cross-sectional area weighted average of PVC, acrylate, and glass (DeWolf, 2009))
- $E_t = 190$ GPa of the main, outer 304 stainless steel tube
- $E_c = 190$ GPa of the central, 304 stainless rod
- $E_o = 190$ GPa of the four 304 stainless rods that separate the optical fibers around the central rod
- $E_e = 2.86$ GPa for the epoxy filler

The various areas are

- $A_f = \pi r_f^2$, where $r_f = 4.5 \times 10^{-4}$ m
- $A_t = \pi \left(r_{t_o}^2 - r_{t_i}^2\right)$, where r_{t_o} and r_{t_i} are the outer and inner radii of the main surrounding tube
- $A_c = \pi r_c^2$, where r_c is the radius of the central rod
- $A_o = \pi r_o^2$, where r_o is the radius of the four rods separating the optical fibers about the central rod
- $A_e = \pi r_{t_i} - 4A_f - A_c - 4A_o$, is the cross sectional area of the ID of the main tube less the areas of the fibers, orbit rods, and central rod.

This simplifies the weighted averaged Young's modulus to

$$\bar{E} = \frac{4E_f r_f^2 - E_e\left[r_c^2 + 4\left(r_f^2 + r_o^2\right) - r_{t_i}^2\right] + E_{304}\left(r_c^2 + 4r_o^2 - r_{t_i}^2 + r_{t_o}^2\right)}{r_{t_o}^2} \tag{1.13}$$

where $E_{304} = E_t = E_c = E_o = 190$ GPa.

The results of Equations 1.7, 1.9, and 1.12 for the same 10 different standard tubing sizes from Table 1.1 are shown in Table 1.2 assuming a solid rod of 304 stainless (i.e., $E = 190$ GPa) and Table 1.3 for values of $\bar{E}$ from Equation 1.13. Both tables show the deflection, average differential strain and sensitivity assuming an acceleration due to gravity of $g = 9.8$ m/s^2 and a mass of $m = 0.4$ kg (the details of the mass are presented in Section 1.3.1.4). It is clear from comparing the results the use of $\bar{E}$ nearly doubles the deflection, average strain and therefore the sensitivity.

Another key element of the overall tiltmeter design that can be learned from the deflections in Table 1.2 and Table

Table 1.2: Deflection, average differential strain, and tilt sensitivity assuming a bulk Young's modulus of $E = 190$ GPa.

Item Number	Tube OD (in)	Tube Wall (in)	δ (mm)	$\Delta\bar{\epsilon}$ (mϵ)	$\Delta\phi/\theta$ (rad/rad)
304F10125X006SL	0.125	0.006	122.49	1.798	3,829
304H09XX	0.148	0.007	62.33	1.149	2,448
304F10156X006SL	0.156	0.006	50.17	1.020	2,171
304H08XX	0.165	0.007	40.35	0.881	1,876
304H07XX	0.180	0.004	28.49	0.729	1,553
304H07X	0.180	0.007	28.49	0.697	1,484
304F10188X006SL	0.188	0.006	24.20	0.637	1,357
304H06X	0.203	0.007	17.61	0.510	1,087
304F10219X006SL	0.219	0.006	13.06	0.423	900
304F10250X010SL	0.250	0.010	7.66	0.279	595

1.3 is how far the instrument can be tilted before the mass comes in contact with the inside of the pressure vessel. For example, a 4" OD, 1/4" wall pressure vessel has an ID of 3.5". If a mass diameter of 1.5" is chosen the resulting annulus is 1" or roughly 25 mm, which means that a pendulum rod constructed from any but the last two entries in Table 1.3 would result in the mass hitting the inside of the pressure case when set on its side. More importantly it would mean that for a 0.5 m long pendulum it would mean that the maximum tilt would be ± 0.044 radians or about $\pm 3^\circ$ before the mass would hit the side of the pressure case.

A rod diameter of 0.180" and wall thickness of 0.004" was chosen for the prototype shown in Figure 1.14 since this would result in the mass comfortably coming to rest on the inside of the pressure case when layed on its side (e.g. during transport). This was also chosen because the 0.048" center rod and 0.062" orbit rods were in stock. An end view of the pendulum rod assembly can be seen in Figure 1.16 where the yello 900 μm diameter optical fiber pigtails from the Faraday mirrors are separated by the four orbit and center rods resulting in two pairs of orthogonal fibers.

1.3.1.4 Pendulum Mass Design

One unique design feature is that the Faraday mirrors attached to each fiber are embedded into the mass resulting in a compact and robust pendulum bob. This poses a challenge, however, since the fibers exiting the mass must transition into the pendulum rod without severely bending the fiber. The solution was to have the mirror housings enter through the bottom of the mass at a 10° angle (Figure 1.17) such that the angle of this bend transition could be minimized.

Figure 1.16 shows a picture of the prototype mass with the four Faraday mirror fiber pigtails emerging and entering the pendulum rod. While the 10° tilting of the mirror housings doesn't fully compensate for the steep transition into the narrow rod, the extra room provided by the mounting flange hub (Figure 1.14) further eases this bend.

A 1.5" diameter piece of brass 1.75" long was chosen for the prototype mass. Brass is a decent material due to its relatively high density ($\sim$8.5 g/cm^3), machinability compared to tungsten ($\sim$19 g/cm^3), mechanical stability compared to lead ($\sim$11 g/cm^3) and expense compared to gold (also $\sim$19 g/cm^3). The final mass once machined weighs in at 0.4 kg.

Table 1.3: Deflection, average differential strain, and tilt sensitivity using an average Young's modulus computed using Equation 1.13.

Item Number	Tube OD (in)	Tube Wall (in)	$\bar{E}$ (GPa)	δ (mm)	$\Delta\bar{\epsilon}$ (mϵ)	$\Delta\phi/\theta$ (rad/rad)
304F10125X006SL	0.125	0.006	93	250.13	3.671	7,819
304H09XX	0.148	0.007	113	104.76	1.932	4,114
304F10156X006SL	0.156	0.006	116	81.84	1.663	3,542
304H08XX	0.165	0.007	121	63.39	1.384	2,947
304H07XX	0.180	0.004	120	45.18	1.156	2,462
304H07X	0.180	0.007	123	43.85	1.073	2,284
304F10188X006SL	0.188	0.006	125	36.87	0.971	2,069
304H06X	0.203	0.007	130	25.75	0.746	1,589
304F10219X006SL	0.219	0.006	144	17.20	0.557	1,185
304F10250X010SL	0.250	0.010	145	10.00	0.365	778

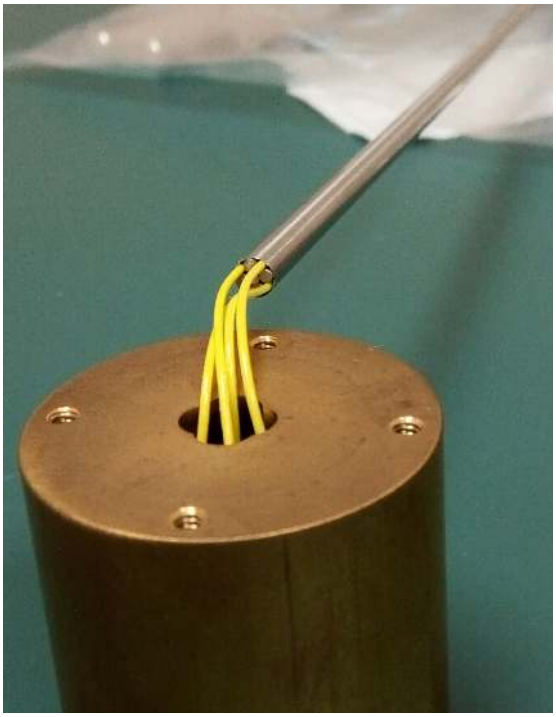

Figure 1.16: Photograph of the four Faraday mirror pigtails emerging from the pendulum mass and entering the rod.

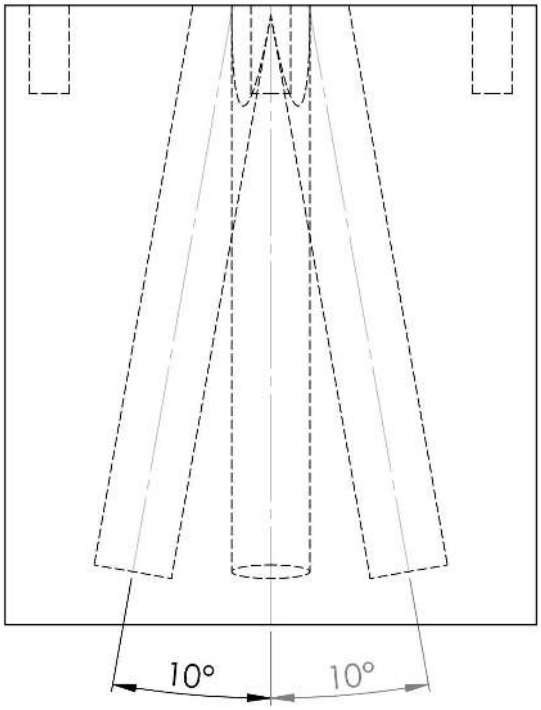

Figure 1.17: Cross sectional view of the tiltmeter pendulum mass showing the 10° angle of the embedded Faraday mirrors.

1.3.2 Prototype Calibration

The prototype tiltmeter system shown in Figure 1.14 was calibrated using a manual calibration stage. This is a 1 m long device with a pivot on one end and a micrometer head (Fowler 54-850) to raise and lower the other end resulting in a tilt resolution of 10^{-6} radians per step. The tilt platform is also equipped with a rotation stage (Thorlabs

PR01) mounted between the pivot point and the bottom of the tiltmeter pressure case that can be manually rotated in increments of 1°.

The calibration procedure was to measure the differential strain in the two pairs of orthogonal optical fiber while raising and lowering the tilt stage over a range of azimuths. The first step was to raise the stage from -14 microns to $+14$ microns in eight increments of 4 microns to estimate the tilt sensitivity in radians of optical phase change per radian of stage tilt. This was was repeated for twelve 30° azimuth increments from 0° to 330° to compute the tilt sensitivity as a function of rotation of the tiltmeter.

Figure 1.18 shows the tilt sensitivity results as a function of azimuth. We expect the tilt sensitivity of a given orthogonal pair of optical fibers to vary as the sine and cosine of the tiltmeter frame azimuth, that is the x and y components should be separated by 90°, which is clearly evident by the 90° offset in their sensitivities (i.e., peaks at $\sim 60^\circ$ and $\sim 150^\circ$).

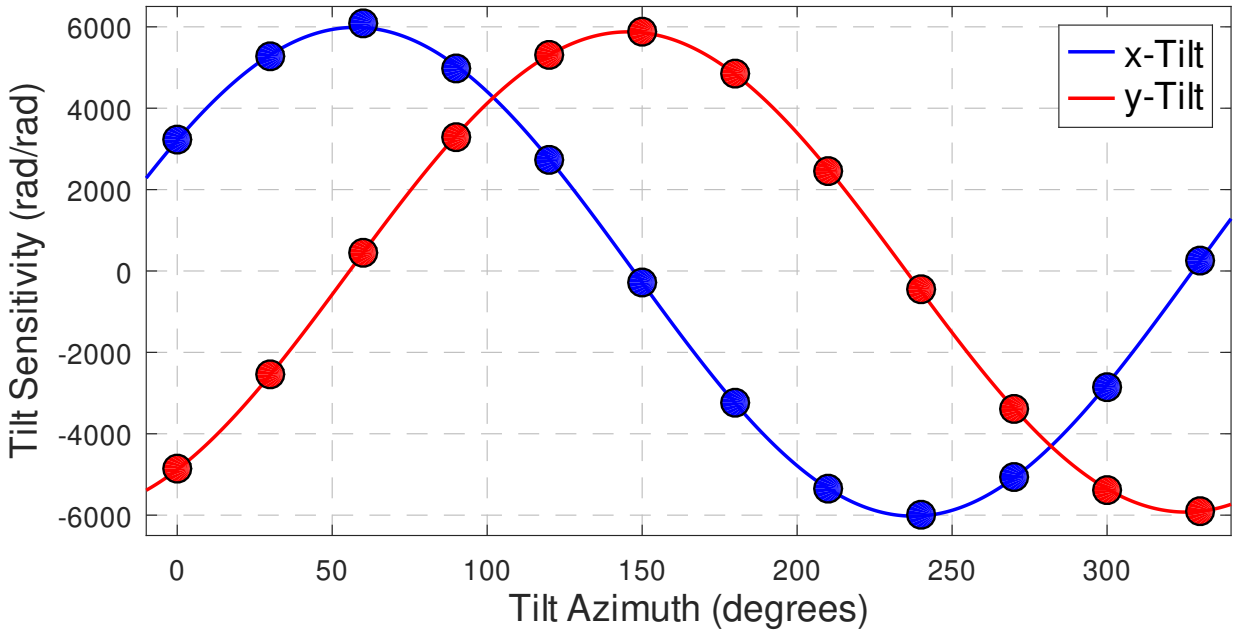

Figure 1.18: x and y tilt calibration curves as a function of azimuth.

The maximum sensitivity of each axis is approximately 6,000 radians of of optical phase change per radian of frame tilt using the 0.180" diameter, 0.004" wall stainless tubing. This is about 2.4 times more sensitive than the crude analytical model presented in row 5 of Table 1.3. However, this instrument has a least-count of 2.5×10^{-9} radians of frame tilt assuming a 16-bit digitizer. This should be adequate to measure Earth tides with a signal-to-noise of about 10, however, the real noise performance and instrument stability (drift) will have to be determined empirically in a deep borehole test.

1.3.3 Prototype Noise Performance in the Lab

Data were collected for approximately 12 hours to get a preliminary estimate of the tiltmeter performance under ambient conditions in the laboratory. Figure 1.19 shows the magnitude spectra for both the x and y tilt components assuming a nominal sensitivity of 6,000 radians of interferometric optical phase change per radian of tilt. These spectra show a clear peak on both components just over 2 Hz that is the observed free period of oscillation of the tiltmeter. (While a somewhat rigorous exposition of the static response was done in Section 1.3.1.2, a similar derivation of the dynamic response was not completed to predict the free period in advance). There appears to be a cluster of harmonics above about 7 Hz that may be the result of higher transverse and/or torsional modes, however, this behavior was not

explored since this instrument was designed for quasi-static deformation and will most likely be operated at sample rates below its free period.

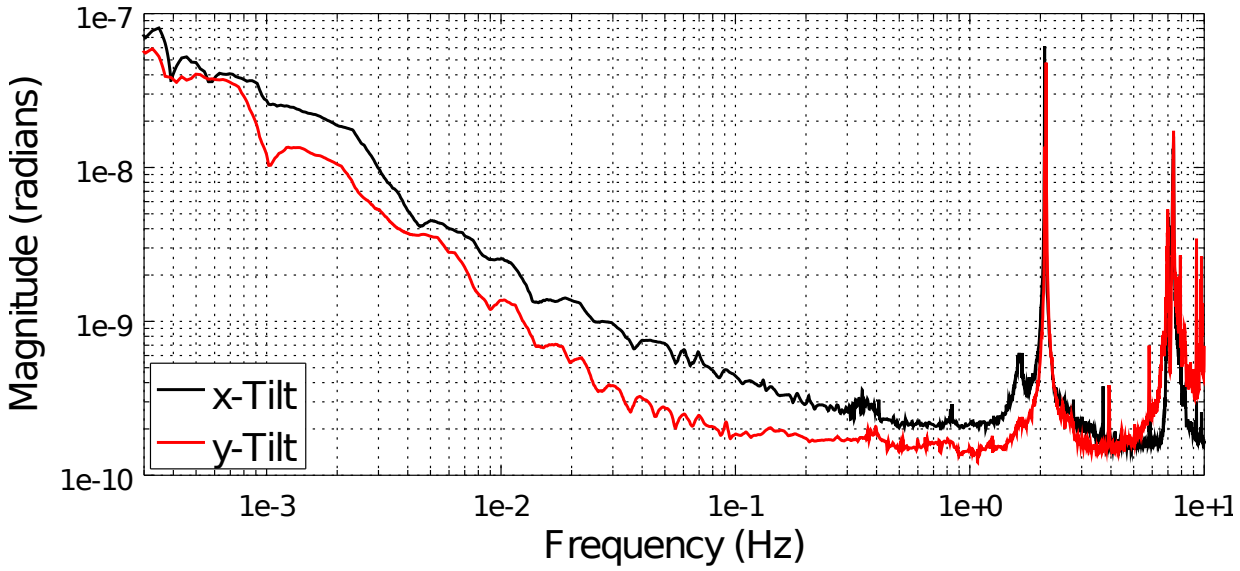

Figure 1.19: x and y tilt noise magnitude spectra under open air lab conditions.

The main takeaway from Figure 1.19 is that both components appear to be able to resolve a nanoradian at about 100 seconds (0.01 Hz). This was approximately the resolution estimated in the previous section, however, the conditions of the lab environment are very likely to be much less stable than its intended borehole environment.

1.4 Optical Fiber Michelson Strain Ribbon

Optical fiber strain gauges housed in stainless steel pressure cases are often necessary to make sure the instrument can survive installation and long term operation. However, this often results in a sensing package with a very low compliance that can be difficult to use in softer materials such as sediments. This led to the development of an optical fiber embedded in a fiberglass "ribbon" for use in softer materials, e.g. sediments in the shallow subsurface.

1.4.1 First Prototype

We developed two prototypes of an Optical Fiber Michelson Strain Ribbon to evaluate the feasibility of this new sensor concept. The first was a ribbon containing just a single embedded fiber that could be interrogated as one arm of a Michelson interferometer. Figure 1.20 shows this first prototype that is constructed from a 2-inch wide fiberglass strip base layer. $\sim$24 m of fiber epoxied on top and looped back-and-forth such that each end of the fiber exits each end of the ribbon. One end is connected to an output of a 3×3 coupler and the other to a Faraday mirror to form one half of the basic optical fiber Michelson interferometer topology shown in Figure 1.3. A spool of fiber of the same length is used as the reference arm that is also connected to the second output of the 3×3 coupler and its own Faraday mirror.

This first prototype was tested for functionality by connecting it to a Version 3 Optical Fiber Michelson Interrogator (Section 1.2.1). The embedded sensing fiber appeared to survive assembly and seemed to be robust to handling. This sensor was extremely sensitive, however, which made it impractical to calibrate in the lab since very slight temperature changes (e.g. approaching the sensor) induced a very large response and any applied load would immediately cause the interrogator to miscount. While we couldn't do much with this device, it did prove the concept of an embedded optical fiber ribbon interrogated as an interferometer.

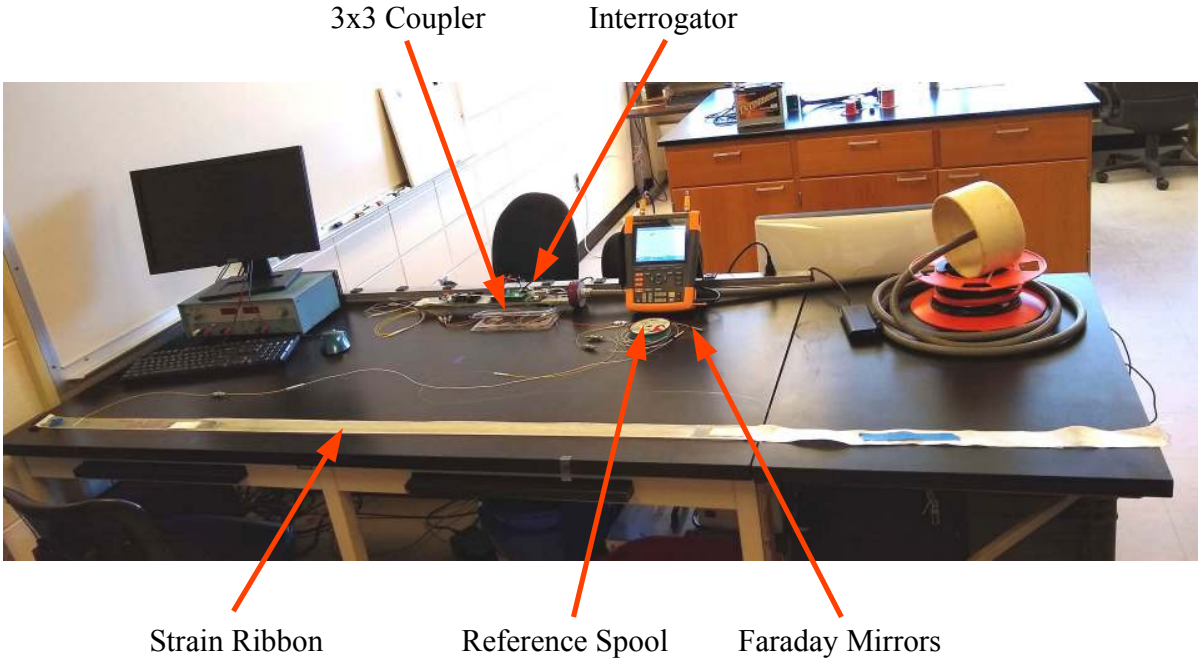

Figure 1.20: Photograph of the strain ribbon and requisite components to complete and interrogate the interferometer running as one arm of an equal-arm Michelson interferometer.

1.4.2 Second Prototype

The second ribbon prototype employed the same embedding approach and was designed and constructed to yield a fully-featured and field-deployable instrument. Figure 1.21 shows a similar 2-inch wide fiberglass base layer and embedded 24 m of optical fiber as the first prototype, however, this instrument includes an integral "component tray" that houses the components needed to make this a complete system.

The component tray is a 2" wide, 16" long, 5/16" thick piece of aluminum plate that is bonded to one end of the fiberglass ribbon. A majority of its interior is milled out 1/4" deep to form a well to embed the reference arm spool, 3×3 coupler and pair of Faraday mirrors as well as a notch to accept the input of a 4-fiber tactical cable (Fiber Instrument Sales FBSMTACCABLE4). One end of the fiber embedded in the fiberglass ribbon and the reference spool are fusion spliced to two of the outputs of the 3×3 coupler and their other ends spliced to Faraday mirrors consistent with Figure 1.20b. Three of the four fibers in the tactical cable are spliced to the three inputs of the 3×3 coupler. The fusion splice joints are protected using hermetic splice sleeves that are also housed in the component tray well (these are translucent and difficult to see in Figure 1.21). All the components are temporarily secured in the tray well using a fast curing cyanoacrylate adhesive until the well is filled using a low-viscosity epoxy.

The resulting assembly is an extremely sensitive single-component strainmeter that is robust enough for field deployments. As with the first prototype, this instrument was far too sensitive to test in the lab beyond basic functionality, but unlike its predecessor it was deployed in the field (see Section 3.1.3 for details).

1.4.3 Analytical Calibration Estimate

A preliminary estimate of the strain ribbon calibration can be made using the Butter and Hocker (1978) relationship shown Section 1.3.1.2. This is the inverse of Equation 1.11

$$\frac{\epsilon}{\Delta\phi} = \frac{\lambda}{\pi n L}\left\{2 - n^2\left[p_{12} - \nu\left(p_{11} + p_{12}\right)\right]\right\}^{-1} \tag{1.14}$$

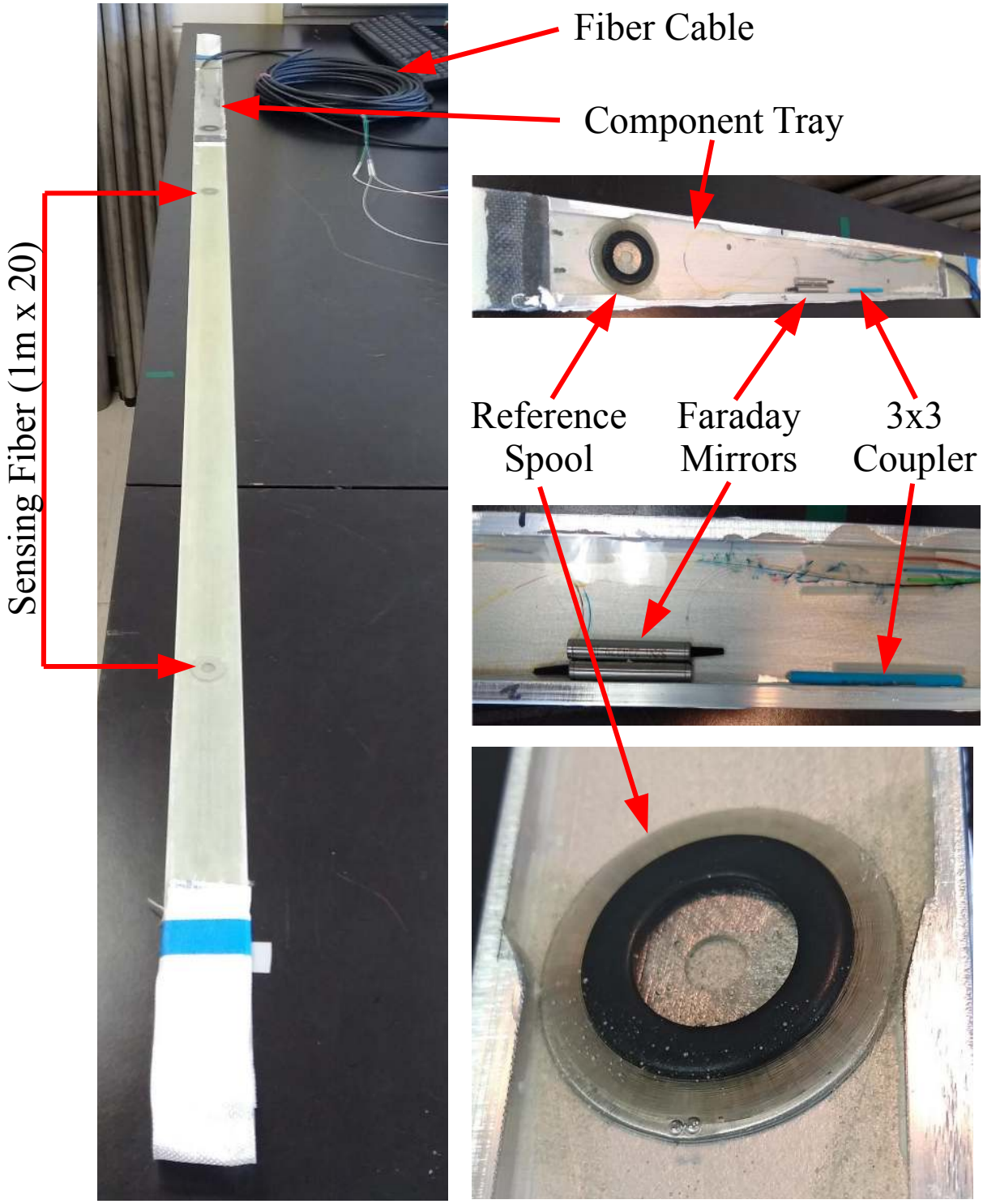

Figure 1.21: Photos of the current fully integrated Optical Fiber Michelson Interferometer Strain Ribbon, showing the full assembly (left) and close up of the component tray (top right) that contains the Faraday mirrors, 3×3 coupler (middle right), and reference spool (bottom right).

which is in units of strain per radian of optical phase change. This calculates out to about 5 nϵ per radian, which assuming a fractional fringe counting resolution of a radian to 1 part in 2^{16} (i.e., a 16-bit digitizer) implies a least-count of 80×10^{-15} strain, or 80 femtostrain.

1.5 Optical Fiber Smart Casings

One limitation of strainmeter deployments is they require a dedicated borehole designed and drilled for hosting just a single strainmeter. While some installations have been modified to include auxiliary casings inside of the main wellbore to accommodate tiltmeters and seismometers, these are rare and limited to special narrow instruments and not standard posthole or borehole seismometers. The ability to use a strainmeter installation as a multipurpose monitoring well motivated the proposed development of optical fiber "smart casings" where the interferometric strain gauges are embedded into a device that more resembles well casing than a closed pressure vessel. This form factor could enable a strainmeter to be deployed inline with standard casing, or possibly multiple strainmeters separated by standard casing segments.

1.5.1 Open-Closed Areal Strainmeter

The first optical fiber smart casing prototype developed for this project was an areal strainmeter designed to result in a device that has the same dimensions as 4-inch nominal Schedule 40 pipe (Figure 1.22). This was easiest to achieve by using the bottom of the casing to house the required interferometer components as well as the cable penetration. The principle drawback of this design is that it closes off the bottom of the casing thereby limiting its location to the bottom of a completed borehole. This device is referred to as the "Open-Closed" Areal Optical Fiber Strainmeter, or AOFS-OC, since it is open at the top and closed on the bottom, making its interior available for other instrumentation.

1.5.1.1 Design

The main body of the open-closed areal optical fiber strainmeter consists of a single helical wrap of optical fiber embedded between a pair of concentric tubes. The length of the fiber, and therefore the diameter averaged over the length of the instrument, is measured as one arm of an equal-arm Michelson interferometer (Figure 1.22a). This prototype was constructed from 6061 aluminum because it is light weight, inexpensive and easy to machine, however, this could easily be made from plain or stainless steel.

The inner and outer cylinders were designed to slide together without damaging the wrapped fiber and with an annulus that would be easy to fill with epoxy. The outer cylinder was a standard 4-inch nominal Schedule 5 pipe with a 4.5" OD and 4.334" ID. The inner cylinder was machined from a standard 4-inch nominal Schedule 40 pipe with an inner diameter of 4.026" and an outer diameter of 4.5" that was turned down on a lathe to 4.25". This left an approximate annulus of 0.083" that while large enough to accommodate a single layer wrap the 250 micron ($\sim$0.010") diameter fiber, would have been too narrow to comfortably slide the outer cylinder over without damaging the fiber. Furthermore, it would have been very challenging to wrap the fiber uniformly up and down the length of the inner cylinder. Both of these issues were solved by machining a pair of helical grooves down the length of the inner cylinder that were 0.020" apart (Figure 1.22b) to guide the embedded fiber that were also sufficiently deep to fully hide it below the ID of the inner cylinder.

Ideally both ends of the fiber wrapped around the inner cylinder would emerge from one end of the inner cylinder such that the optical components could all be attached at one end. This required that the fiber loop back, but rather than wrapping one contiguous fiber with a loop at one end we wrapped two fibers up the length of the inner cylinder and spliced the ends together. A turnaround loop was still needed, however, which was carved to connect one parallel groove to the other with a bending radius gentle enough as to not introduce significant attenuation (Figure 1.22b). This was done using two approximately 65 m lengths of 250-micron diameter Corning ClearCurve ZBL optical fiber (to limit microbending losses from the helical groove).

A cylindrical container was welded to one end of the inner cylinder to house the optical components and cable

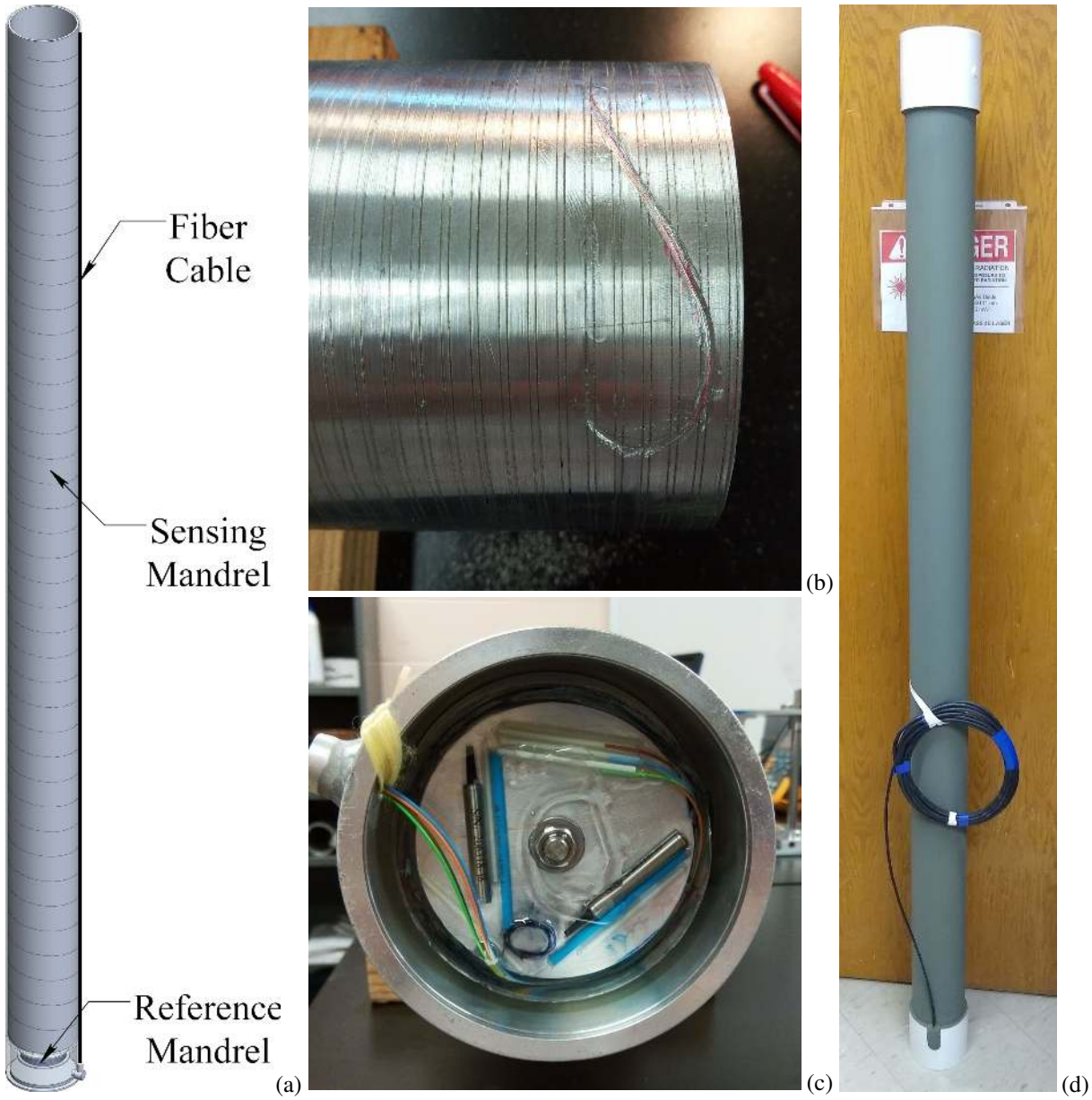

Figure 1.22: Diagram (a) and photographs (b-d) of the Open-Closed Areal Optical Fiber Strainmeter smart casing. (a) Diagram of the AOFS-OC with the outer cylinder made transparent to reveal the fiber wrapped reference mandrel at the bottom of the instrument. (b) Top of the strainmeter showing how the fiber wraps up and back down the sensing mandrel such that both ends of the sensing fiber return to the vessel at the bottom. (c) Bottom of the strainmeter showing the vessel containing the reference spool, optical components and splice protectors. (d) Photo of the completed smart casing. Note that the PVC couplings used during deployment are not represented in the diagram shown in (a).

penetration (Figure 1.22c). This was 4.5" in diameter to match the OD of a 4-inch nominal pipe and contains a 2.5" deep cavity to house an aluminum spool containing the 130 m of fiber for the reference arm of the interferometer as well as a 3×3 coupler, pair of Faraday mirrors, broken out fiber cables and the hermetic fusion splice protection sleeves used to connect all the components. The interior was potted with a low-viscosity epoxy (Henkel Loctite STYCAST 1264) after which a cap was glued to the bottom to seal it off.

The final step was to glue on the outer cylinder once all the fibers were wrapped and optical components spliced on and the device appeared to be functioning properly. The outer cylinder was centralized using layered strips of a low friction tape and the annulus was filled with a low-viscosity using a syringe and dispensing needle. Once cured the instrument was subjected to a hydrostatic calibration test (Section 1.5.1.2) whereafter PVC couplings were attached and the exterior coated with a self-etching primer (Figure 1.22d).

1.5.1.2 Hydrostatic Calibration

A simple hydrostatic pressure test was conducted to get an estimate of the sensitivity of the AOFS-OC. This test consisted of plugging the top end of the instrument with an expanding well plug that was modified with a barbed fitting such that the air inside could be pressurized using a hand pump (SKF Mityvac MV8510). This was done up to a pressure of 2,500 Pa ($\sim$0.36 psi) over a period of about 70 seconds with a pressure logger (Onset Computer Corporation HOBO model U20) placed inside as the calibrated reference (Figure 1.23). The internal pressure was allowed to bleed off at whatever leak rate the sealed cap could maintain.

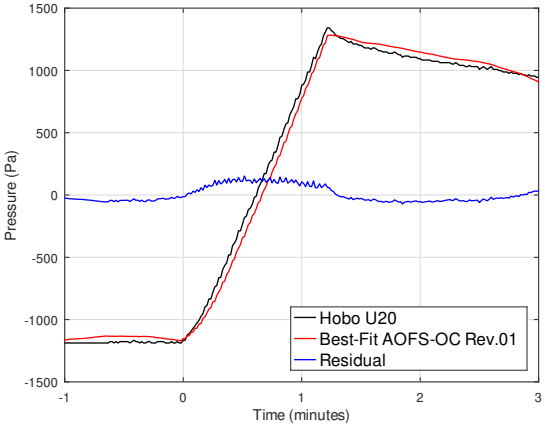

Figure 1.23: Pressure calibration time series of the AOFS-OC showing the applied pressure (black), best-fit areal strain record (red) and their difference (blue).

The pressure time series from the logger was compared to the output of the fringe counting system on the interrogator (Figure 1.23). The result was a calibration factor of 2.17 ± 0.02 Pascals per radian of optical phase change, which implies a 16-bit least-count resolution of 33 µPa. This combined with the assumption of a bulk modulus of aluminum of 70 GPa implies a strain resolution of 4.7×10^{-16}, or $\sim$0.5 femtostrain, most likely making it the most sensitive borehole strainmeter ever constructed.

1.5.2 Open-Open Areal Strainmeter

The second smart casing prototype design addresses the primary disadvantage of the first, which is the need for one end of the instrument to be closed off to the wellbore. This is the "Open-Open" Areal Optical Fiber Strainmeter (Figure 1.24a) since it is truly a well casing replacement since it can be deployed at any location in the completion.

1.5.2.1 Design

As with its open-closed counterpart, the main body of the open-open areal optical fiber strainmeter consists of a pair of concentric tubes with an embedded optical fiber that monitors the average diameter of the borehole. This was also constructed from 6061 aluminum, but unlike the AOFS-OC only the inner diameter matches the 4.026" of a standard 4-inch nominal, Schedule 40 pipe. The outer diameter of the completed instrument needed to be increased to 5" to accommodate an integral reference mandrel that is isolated as well as the requisite optical components and cable penetration. While this is only a modest ½" increase in the diameter, this is slightly smaller than the 5.050" OD as a standard 4-inch nominal, Schedule 40 coupling making it no wider than any of the connections that would be used to deploy it downhole.

The assembly of the AOFS-OO was more complex than the first prototype. The inner cylinder was turned down from a standard 4-inch nominal, Schedule 40 aluminum pipe to an OD of 4.25" and a single helical groove of 12 threads-per-inch (∼0.083" spacing) was cut into its exterior to guide and protect the sensing fiber. A pair of 4" long thin aluminum cylinders for the reference mandrel and reference mandrel cover were slid over the inner cylinder and the end sleeves were welded to each end of the inner cylinder. The outside ends of these sleeves are machined to the same dimensions as a standard 4-inch nominal, Schedule 40 pipe and contain a raised edge to centralize the outer cylinder once the interior is completed. With the mechanical assembly of the interior completed, the inner cylinder was wrapped with 256 m of 250-micron diameter Corning ClearCurve ZBL optical fiber.

The next step was to wrap the reference mandrel with a matching length of optical fiber (Figure 1.24b). Since this was to be covered by another surrounding cylinder and sealed with epoxy, care was taken to protect the fiber penetrations out of this epoxy since these can be extremely fragile. This was done using short lengths of optical fiber "furcation" tubing as shown in Figure 1.24c, after which the ends of the reference mandrel cover were sealed. With both the sensing and reference fibers secured, the 3×3 optical coupler and Faraday mirrors were spliced on and the interferometer was checked for functionality. The final step before installing the outer protective sleeve was to splice on the fiber cable that exits the top of the instrument through a well machined in the upper end sleeve and secure all of the optical components to the main tube (Figure 1.24d).

The final assembly steps were to cover the fiber wrappings, optical components, and fiber cable penetration with a thin aluminum sleeve and pot the interior with epoxy. The outer cylinder is a 5-inch OD, 1/8-inch wall tube that spans the raised ridges on the upper and lower end sleeves (seen at the right of Figure 1.24d). The annulus between the inner diameter of the outer sleeve and the outer diameter of these raised ridges was filled with an epoxy putty except for another well machined in one end sleeve. A funnel was inserted into this trough to deliver about 4 liters of Henkel Loctite STYCAST 1264 low-viscosity epoxy. This was done with the instrument in a tall cylindrical vacuum chamber, after which the instrument was put under vacuum for about an hour to remove any air bubbles in the epoxy and to ensure penetration of the epoxy around the optical fibers, components, and fiber cable penetration.

While the AOFS-OO along with its "Open-Closed" (AOFS-OC) cousin are prototypes, they are intended to be deployed in an operational environment. The choice to make these from aluminum was because it is relatively inexpensive and easy to machine and weld. However, previous experiments have shown that aluminum has a strong reaction to the post-tensioning grout we typically use to couple strainmeters to the ground. Therefore, we have coated both of the smart casings with several coats of a self-etching primer after sanding and chemically treating the exposed surfaces. PVC couplings were added to each end so they can be quickly attached to pipe during deployment using standard PVC cement. The completed AOFS-OO is shown in Figure 1.24e.

1.5.2.2 Hydrostatic Calibration

A simple pressure calibration was applied to the AOFS-OO to obtain an estimate of its sensitivity to stress. This was done by plugging both ends with expanding plugs, one of which contained a fitting such that the interior could be pressurized using a hand pump. Figure 1.25 shows the result of such a calibration where the interior was pressurized over about a 90 second time period and let to leak out. A pressure logger (Onset Computer Corporation HOBO model U20) was placed inside of the AOFS-OO was used as the calibrated reference and compared to the output of the fringe counting system on the interrogator. A linear least-squares regression was used to determine a calibration factor (inverse sensitivity) of 1.721 ± 0.008 Pascals per radian of optical phase change. Again assuming a fractional fringe reso-

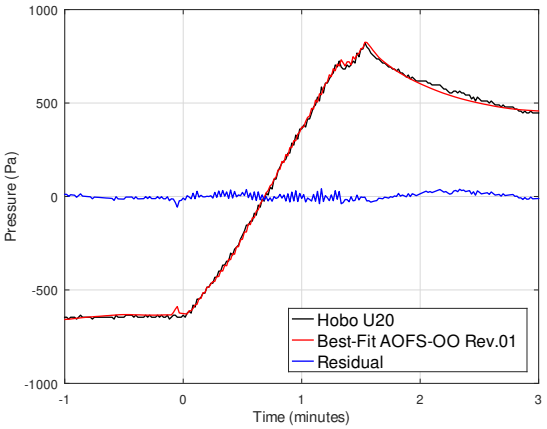

Figure 1.25: Pressure calibration time series of the AOFS-OO showing the applied pressure (black), best-fit areal strain record (red) and their difference (blue).

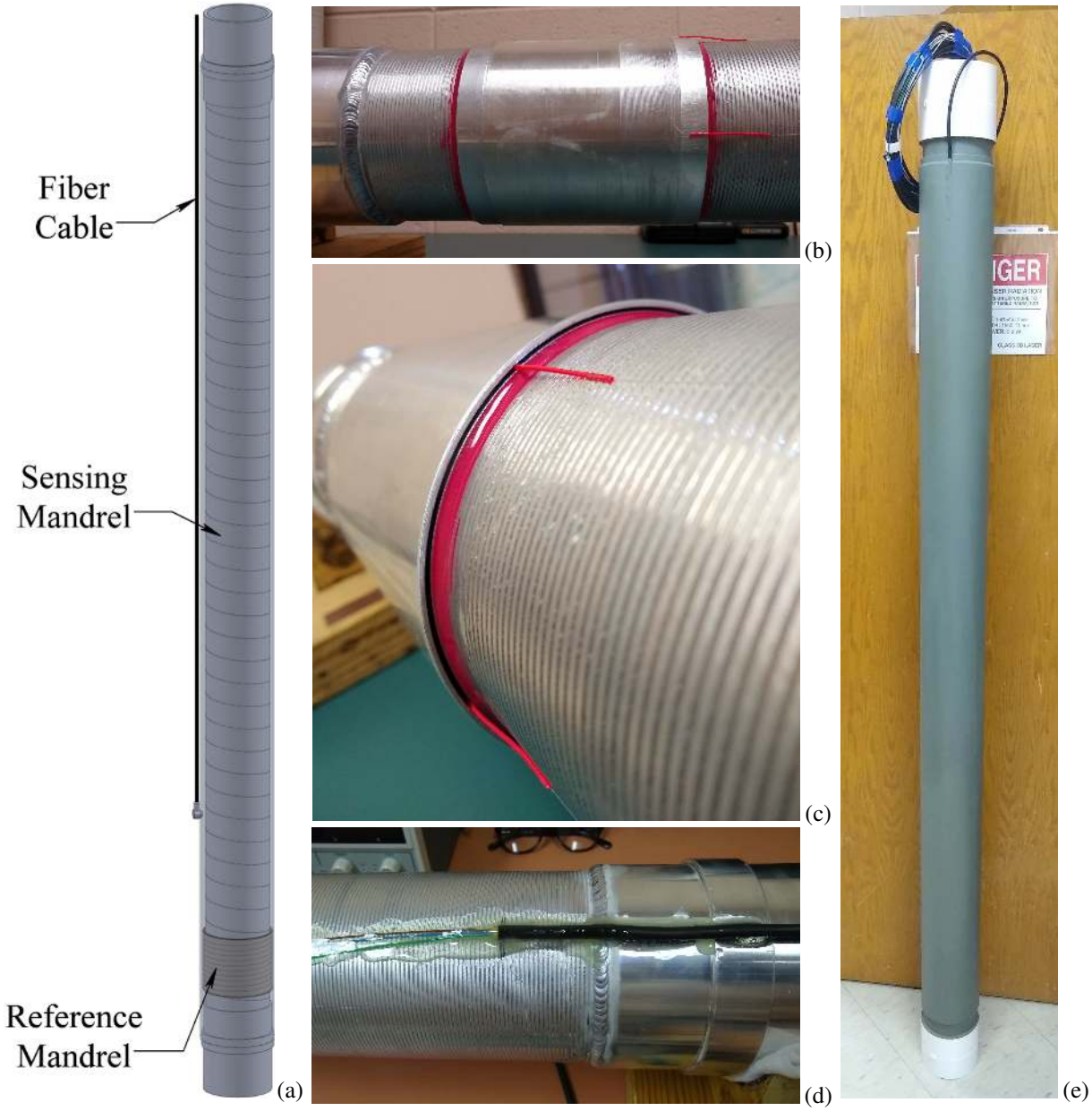

Figure 1.24: Diagram (a) and photographs (b-e) of the Open-Open Areal Optical Fiber Strainmeter smart casing. (a) Diagram of the AOFS-OO with the outer cylinder made transparent to reveal the integrated fiber wrapped reference mandrel. (b) Wrapped reference mandrel showing the furcation tubing used to protect the fiber exit from under the (c) reference mandrel cover. (d) Picture of the fiber cable exit from the fiber wrapped interior. (e) Photo of the completed smart casing. Note that the final design of the fiber cable penetration from the interior is not represented in the diagram shown in (a).

lution of 1 part in 2^{16} results in a least-count of about 26 μPa and a strain resolution of 3.8×10^{-16} or ∼0.4 femtostrain. For comparison, the AOFS-OC calibration factor from Section 1.5.1.2 is 2.17 ± 0.02 Pa/rad, which now makes the AOFS-OO the most sensitive borehole strainmeter ever constructed.

1.6 Mutlicomponent Optical Fiber Bragg Grating Strainmeter

A drawback of conventional strainmeters is that they need to be permanently grouted into a borehole to monitor deformation in the host formation. This often means that the instrument needs to be made of a rigid and inert material such as stainless steel to survive the installation and grouting making them too stiff for making strain measurements in softer materials like sediments. These two limitations and the desire to monitor deformations in the shallow subsurface led to the development of a higher compliance strainmeter that can measure multiple components of strain that can also be pushed into a hole left by a standard sediment coring tool.

1.6.1 Design

A novel high-compliance, push-in strainmeter was developed for this project that employs commercial fiber Bragg grating (FBG) sensors. Figure 1.26 shows a mature prototype featuring a compliant urethane sensing head that contains three independent sensing regions distributed uniformly around its circumference. These consist of a single fiber with three FBGs along its length that are wrapped around a previously cast inner core that is then covered by a second casting thereby embedding the fibers within the urethane matrix. This is cast around a length of threaded rod such that a cap can be attached to deflect material while being driven in using an attachment to the upper portion of the rod. An aluminum channel is used to break the bare internal fibers out into a field deployable tactical cable that is filled with epoxy.

The reflected wavelength of the FBGs inside of the urethane sensing head are monitored using a commercial interrogator (Micron Optics SM125). While this is an older interrogator (circa 2012), it is capable of resolving wavelength changes of 1×10^{-12} meters at sampling rates of up to 2 Hz. This resolution at a nominal wavelength of 1550 nm implies a strain resolution of approximately 0.6 microstrain. However, the actual relationship between wavelength and deformation of the sensing head will depend on the FBG orientation to the applied strain and the material properties, which needs to be determined empirically.

1.6.2 Hydrostatic Calibration

One method to determine the strain sensitivity of the instrument shown in Figure 1.26 was to subject it to a simple hydrostatic pressure calibration test. The instrument was placed in a tall pipe along with a calibrated pressure transducer (Onset Computer Corporation Hobo U20) that was then slowly filled with water to a height of about 2 m and then slowly drained. Data from the FBGs was recorded using a Micron Optics SM125 interrogator connected to a laptop computer. This fill-and-drain procedure was performed five times such that the temperature change during the final cycle was less than 0.2°C. Figures 1.27a–c show the time series during this final fill-and-drain cycle with the response from the reference transducer shown in black, the best-fitting push-in instrument time series in red, and their difference (residual) in blue.

Table 1.4: Least squares results from the multicomponent FBG hydrostatic pressure test showing the calibration factor in Pascals of pressure change per picometer of FBG wavelength change for each sensing element.

Gauge	Calibration Factor (Pa/pm)
S1	1188 ± 6
S2	991 ± 6
S3	1013 ± 12

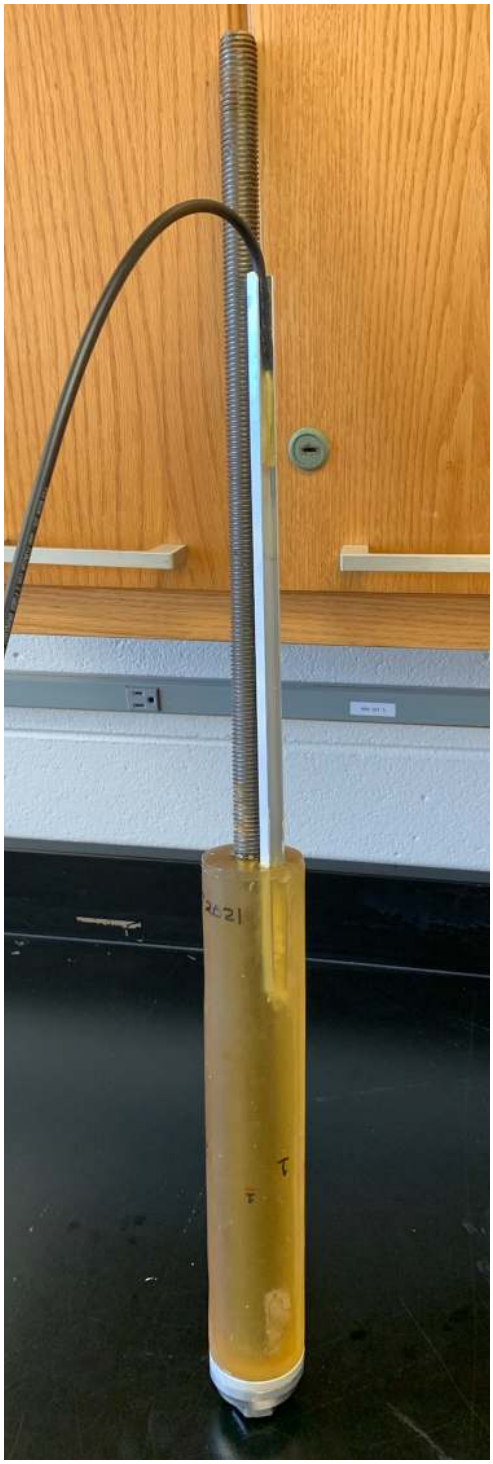

Figure 1.26: Photograph of the 3-component FBG strainmeter showing the urethane sensing head coupled to a central rod and cable.

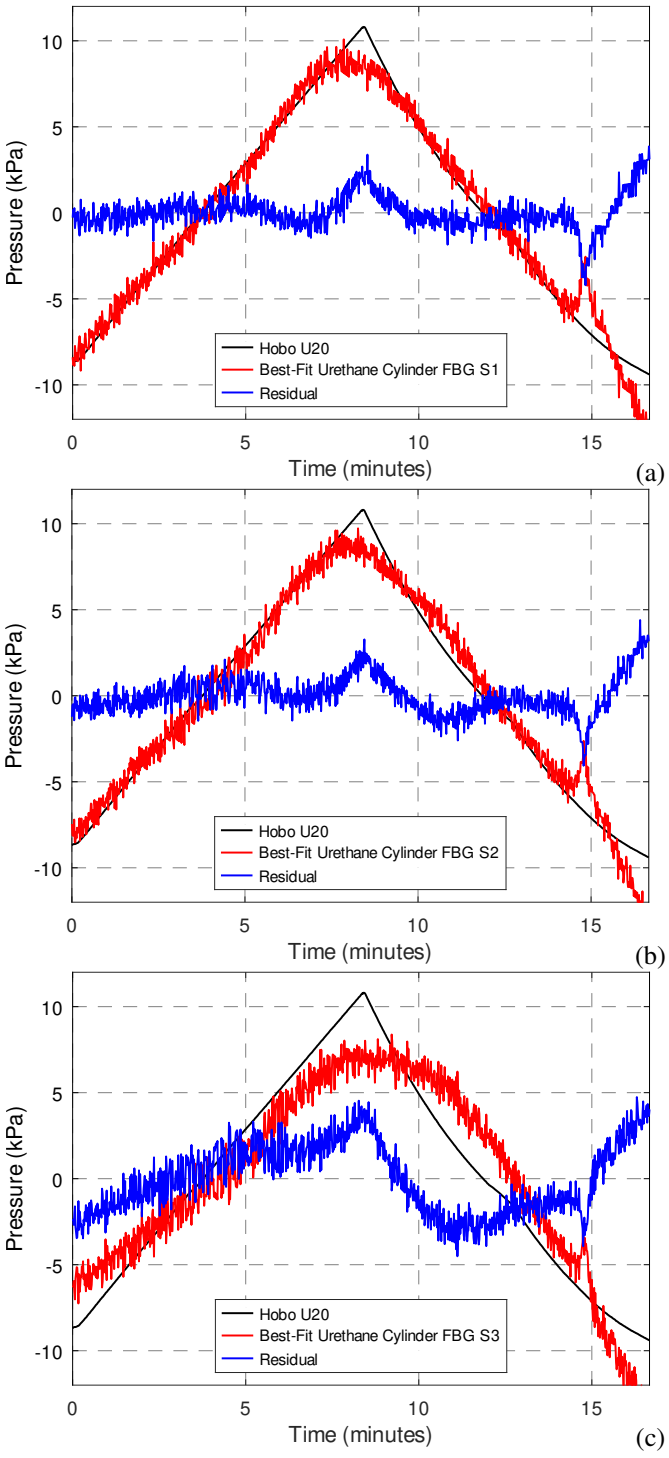

Figure 1.27: Pressure calibration time series results for the three sensing components S1–S3 shown in (a)–(c), respectively.

Results from the pressure calibration test are shown in Table 1.4, which shows an average response of approximately 1 kPa per picometer of wavelength change with an uncertainty of about 0.5–1%. Given that the least-count of the SM125 interrogator is 1 pm implies that this new instrument should be able to resolve stress changes of several kPa. Assuming a strain resolution of 1 με suggests that the bulk modulus of the instrument is around 1 GPa, which is consistent with the bulk modulus of urethane.

1.7 Tensor Optical Fiber Strainmeters

The main objective of this project was to investigate and test one or more ways to robustly measure the in situ strain using optical fibers. We developed a single component instrument in the previous project (DE-FE0023313) that was able to measure the areal strain with a fidelity that matched and in some cases exceeded the performance of the existing Gladwin Tensor Strainmeter (Gladwin, 1984). This success motivated us to develop ways to modify the areal strainmeter design concept to extend its capabilities from a single component to an instrument capable of measuring the horizontal strain tensor.

1.7.1 Nested Mandrel TOFS

Perhaps the most intuitive extension of an areal optical fiber strainmeter for tensor measurement is to embed more than one fiber wrapped cylinder into the downhole pressure case. This concept led to the design of a strainmeter incorporating three or more fiber-wrapped cylinders equally distributed around the borehole axis such that each would experience a different load stress due to its proximity to the pressure case wall and interactions with neighboring cylinders. This concept has been labeled as the Nested Mandrel Tensor Optical Fiber Strainmeter, or TOFS-NM.

1.7.1.1 Prototype Design

A scaled down prototype was designed and fabricated (Figure 1.28) that includes three fiber wrapped circular mandrels separated by three solid rods that all fit into a 3.5” diameter, 0.083” wall pressure case made from a 3-inch nominal, Schedule 5 pipe. This is referred to as the Version 5 TOFS-NM because it was the fifth concept design and not because it was preceded by four prototypes.

Figure 1.28 shows a 3D mechanical model of this Version 5 prototype that includes the trio of sensing and reference mandrel pairs, separation rods and upper and lower centralizers. The nested within each 1.25” diameter, 0.035” wall sensing mandrel

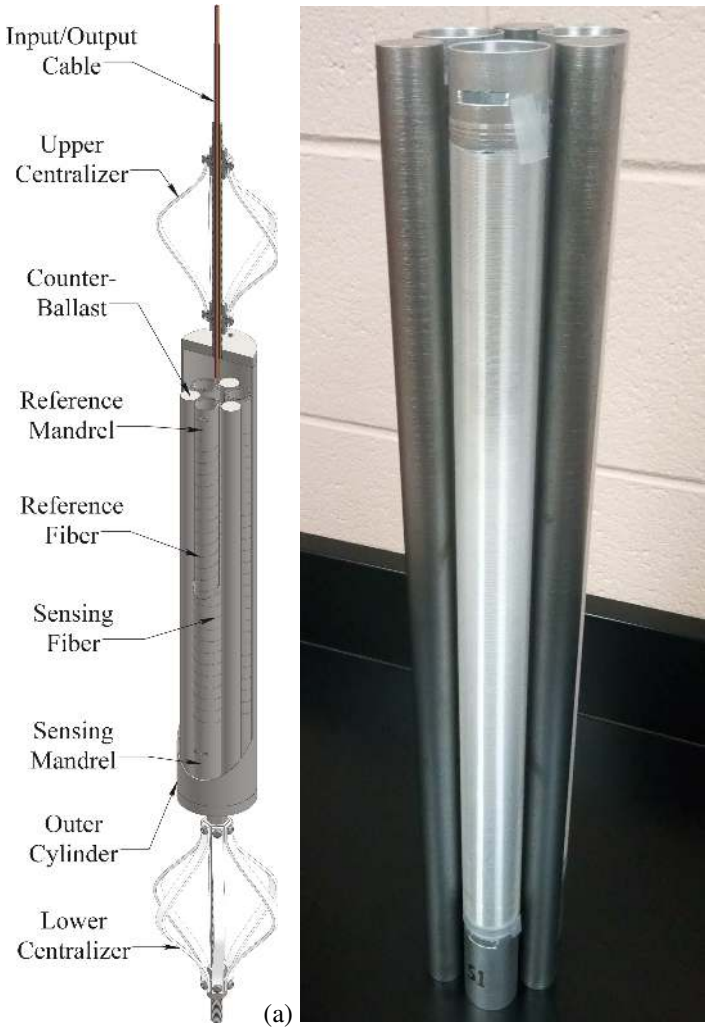

Figure 1.28: (a) Computer rendering of the triple nested mandrel tensor strainmeter design. (b) Photograph of the interior components of the triple mandrels with one of the fiber wrapped elements in the forefront.

is a 1" diameter, 0.035" wall stainless steel cylinder that holds an equal amount of optical fiber (∼165 m) that forms the reference arm of the interferometer. This leaves a 0.09" air gap between the inner diameter of the sensing mandrel and outer diameter of the reference mandrel to decouple the reference fiber from external forces. The three separation rods serve both as a means to azimuthally separate the trio of nested sensing and reference mandrel pairs as well as provide additional weight such that the assembled instrument is negatively buoyant in grout.

This design was evaluated using a numerical model and the prototype was subjected to both hydrostatic and directional loading tests before being installed at our local field site. These numerical and lab tests are described below and the deployment is detailed in Section 3.1.2.1.

1.7.1.2 Numerical Model

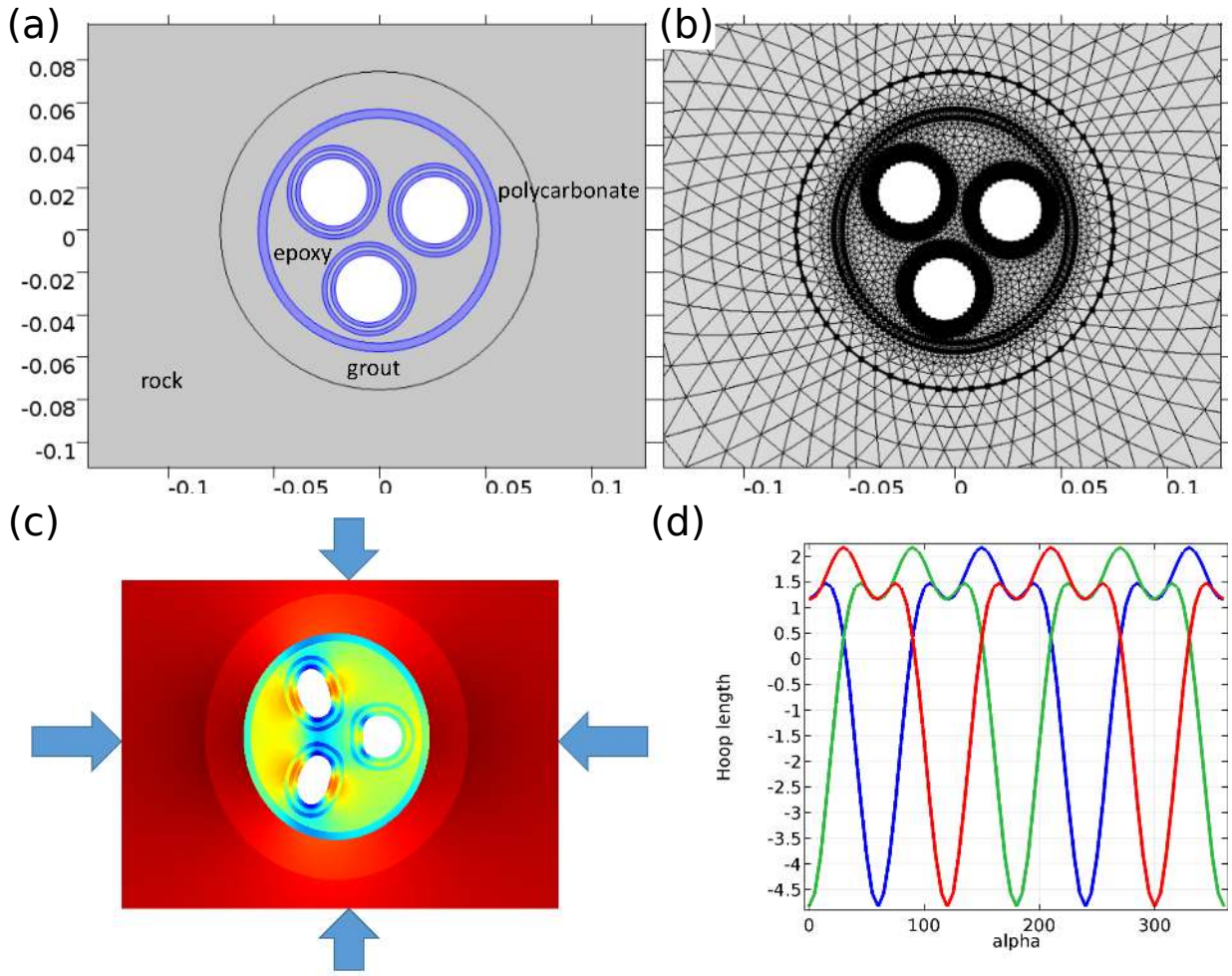

Figure 1.29: (a) Schematic of the three-cylinder in a pressure case design, and (b) the model mesh. (c) The resulting strain in each cylinder when subjected to a far-field strain in the formation. (d) The azimuthally dependent circumferential strain in each cylinder.

The main concern of the nested mandrel or any potential strainmeter design is whether the observed circumferential strain in each cylinder is unique enough to resolve directional strains. We therefore numerically evaluated this design using COMSOL. Figure 1.29 shows the model setup and results, with Figure 1.29a and Figure 1.29b showing a cross

section of the three-cylinder in a pressure case design along with the mesh geometry. The resulting strain field along one azimuth is shown in Figure 1.29c, and the circumferential strain in each cylinder shown as a function of azimuth is shown in Figure 1.29d.

The results in Figure 1.29d show a clear and unique strain response for each cylinder with azimuth, implying that this is could be a candidate for a horizontal tensor strainmeter design. However, each gauge does not show the typical $\cos(2\theta)$ response one would expect from a linear strain gauge oriented along the same azimuth and instead predicts one minor and one major peak of sensitivity per 180°, the former being of opposite sign of the latter While this could be a potential problem for this design, this is such a straightforward and easy to fabricate design we nonetheless decided to proceed with the prototype to evaluate it in the lab and field.

1.7.1.3 Hydrostatic Calibration

The completed prototype of the TOFS-NM v5 was to subjected to a simple hydrostatic pressure calibration test as a way to determine its strain sensitivity. The instrument was placed in a tall pipe along with a calibrated pressure transducer (Onset Computer Corporation Hobo U20) that was slowly filled with water to a height of about 2 m and then slowly drained multiple times in an attempt to compensate for the response due to water temperature changes. Data was recorded using a Version 3 OFMI connected to a laptop computer.

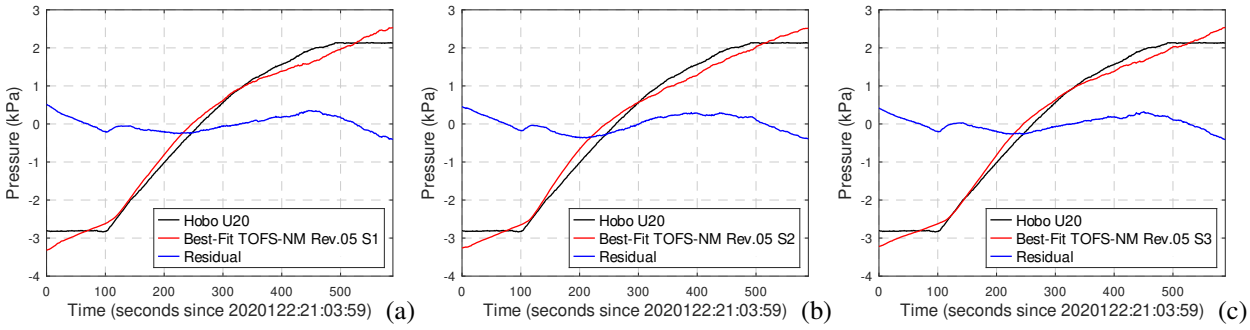

Figure 1.30: Hydrostatic water loading test of the TOFS-NM v5 for the three gauges S1 (a), S2 (b) and S3 (c).

Table 1.5: Least squares results from the TOFS-NM v5 hydrostatic pressure test showing the calibration factor in Pascals of pressure change per radian of optical phase change change for each sensing gauge.

Gauge	Calibration Factor (Pa/radian)
S1	0.48 ± 0.01
S2	0.41 ± 0.01
S3	0.46 ± 0.01

The results from the last and most temperature stable fill-and-drain hydrostatic load test are shown in Figures 1.30a–c and Table 1.5. Figure 1.30 shows the response of the reference transducer in black, the best-fitting strainmeter gauge time series in red, and their difference (residual) in blue for each of the three strain gauges (i.e., fiber wrapped tubes). While there is still considerable drift in the strainmeter data due to its high sensitivity, the results appear consistent averaging about 0.45 Pascals per radian of optical phase difference. Optimistically assuming that a radian of phase change can be measured to within 1 part in 2^{16} (the bit depth of the OFMI ADC) implies an average least-count resolution of about 7 μPa, which is four times more sensitive than the AOFS-OO in Section 1.5.2.2. Further assuming that the instrument has an average a bulk modulus of somewhere near 20 GPa (10% of its cross-sectional area is stainless steel at 166 GPa and 90% is epoxy at 3 GPa) implies an average strain calibration coefficient of

$\sim 2.3 \times 10^{-11}$ strain or 23 picostrain per radian, with the same assumed 16-bit depth results in a least-count resolution of $\sim$0.3 femtostrain, or roughly equivalent to the AOFS-OO.

1.7.1.4 Directional Load Calibration

The directional load sensitivity of the Version 5 TOFS-NM prototype was also tested in the lab using the automated load frame device described in Section 1.9, which also outlines the detailed procedure. To summarize, the strainmeter prototype was inserted into the load frame oriented along a given azimuth and subjected to repeated loads at increasing weights before being rotated by 10° and the process repeated. Each load was repeated 10 times to obtain the mean and standard deviation of the change in the optical phase between the 10 loaded and unloaded states. This was repeated for a total of 8 masses from 5 to 40 pounds in 5 pound increments. The means and standard deviations at each load were then used in a weighted linear least-squares fit to obtain the load sensitivity in radians of optical phase change per kilogram of applied load.

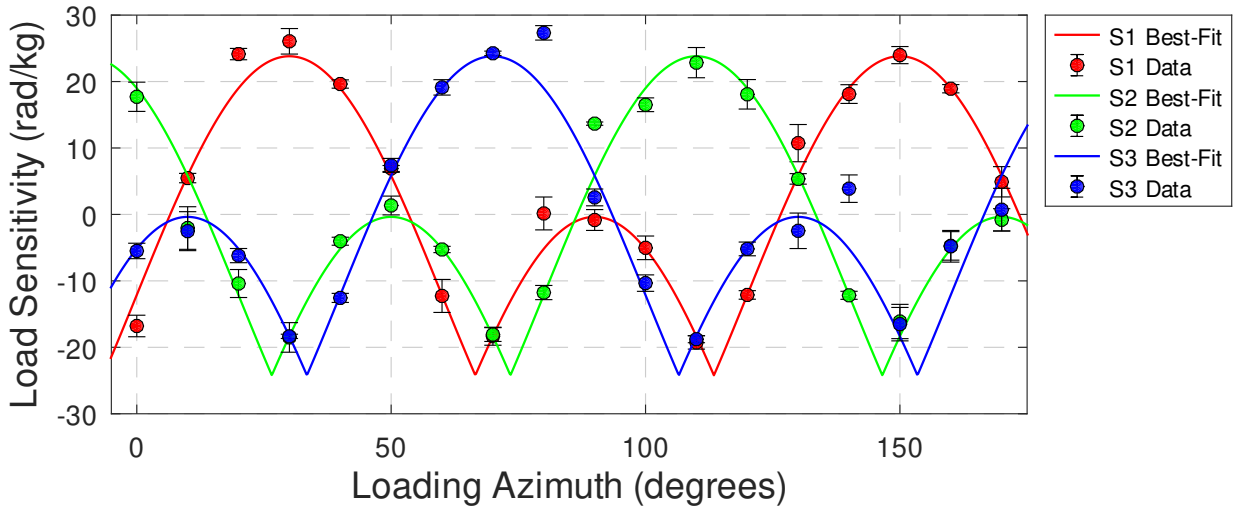

Figure 1.31: Load sensitivity as a function of azimuth for the TOFS-NM v5, showing the data (filled circles) and best-fit function (solid lines) for the three strain gauges, S1 (red), S2 (green) and S3 (blue).

Figure 1.31 shows the result of plotting the load sensitivity for each gauge as a function of the direction along which the instrument was loaded. This does not conform precisely to the numerical predicted directional load sensitivity shown in Figure 1.29d, however, a function of the form

$$S_i(\theta) = c_1 + c_2|c_3 + \cos(3\theta - c_4)| \tag{1.15}$$

appears to appropriately model the data. This partially rectified sine wave is similar to the numerical result in that there are major and minor peaks in load sensitivity, but differ in that this is not simply the absolute value of the curves shown in Figure 1.29d. It is also interesting that the functional form is proportional to 3 times the azimuth rather than 2, which means that the sensitivity is a maximum three times for every 360° implying that a given fiber wrapped cylinder strain gauge is most sensitive every 120°.

The amplitudes of the load sensitivity range over roughly ± 25 radians of optical phase change per kilogram of applied load, or about 20 grams per radian. Assuming a bit-weight of 2^{16} as was done with the pressure calibration, this implies a load resolution of about $3 \times 10{-}7$ kg.

The lack of agreement between the numerical and load frame results in their basic functional form, and the fact that the triple mandrel design doesn't follow the traditional $\cos(2\theta)$ form raises serious questions about whether data

from this instrument could be resolved into the strain tensor components in a unique way.

1.7.2 Inclined Helix TOFS

Another approach to extending the areal strainmeter concept to a tensor instrument is to modify the geometry of the fiber wraps around the sensing mandrel. One way to change the wrap geometry and still preserve the concentric circular design is to incline the wraps rather than wrap them horizontally in the plane perpendicular to the axis of the cylinder. This concept led to the design of the Inclined Helix Tensor Optical Fiber Strainmeter, or TOFS-IH. One can visualize how this is able to resolve directional strains by considering that the length of fiber in an inclined helix projected onto the plane perpendicular to the axis of the cylinder is greater when the helix is inclining and declining (going up and down the axis of the cylinder) than when the wrap transitions from inclining to declining and vice versa. This implies that a directional load applied to the inclined portions of the helix strains more fiber than when it is applied to the top and bottom of the inclines.

1.7.2.1 Conceptual Design

The conceptual design of the TOFS-IH is that of a pressure case with a thin, fiber-wrapped cylinder epoxied to its interior using inclined helices. This design is broken down graphically in Figure 1.32. There are 3 pairs of fiber wraps around the inner cylinder, each 120° from the next with the sensing and reference arms opposing each other. While there are only about 8 wraps for each interferometer shown in Figure 1.32, one could make many hundreds or thousands of wraps to get a vertical average.

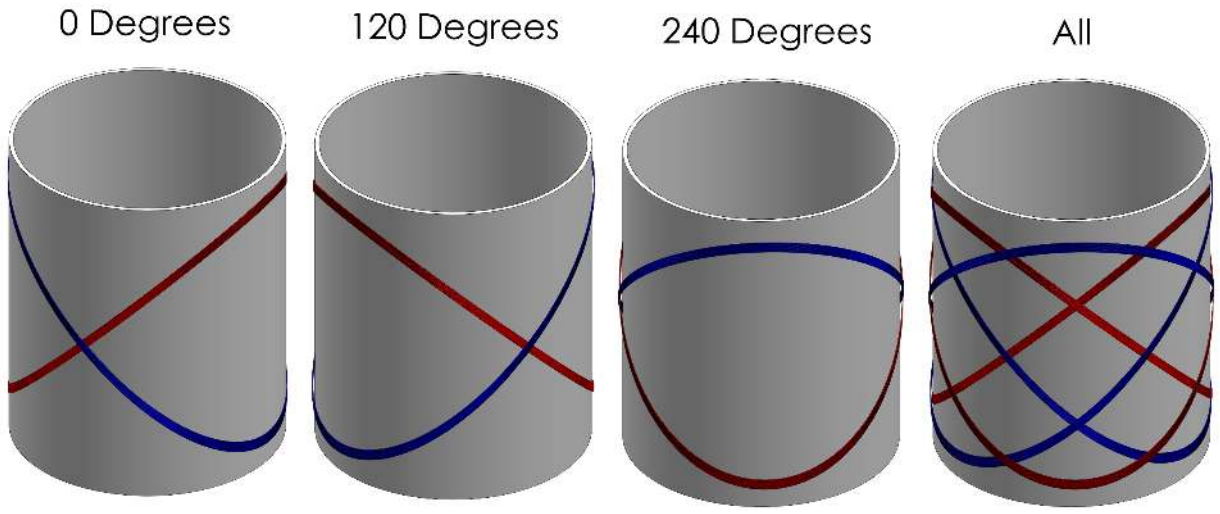

Figure 1.32: Concept design for inclined helix strainmeter, where the red and blue fibers represent the sensing and reference arms of each interferometer, respectively.

The wraps can be expressed mathematically in terms of the parametric equations for a helix

$$x_{m,n} = \left[r_c + (2m-1)\, r_f\right] \cos\left(t + \frac{2n\pi}{3}\right) \tag{1.16}$$

$$y_{m,n} = \left[r_c + (2m-1)\, r_f\right] \sin\left(t + \frac{2n\pi}{3}\right) \tag{1.17}$$

$$z_{m,n} = \frac{r_f}{\pi} t + r_c \cos\left(t - m\pi\right), \tag{1.18}$$

where $m \in 1, 2, 3, 4, 5, 6$ is the layer number, $n \in 0, 1, 2$ is the interferometer number, r_c is the radius of the cylinder being wrapped (and epoxied into the pressure case), and r_f is the radius of the optical fiber. These equations state that the outer diameter of each successive wrap layer is one fiber diameter larger than the previous. The first interferometer (at $0°$) has a sensing arm $(x_{1,0}, y_{1,0}, z_{1,0})$ and a reference arm of $(x_{2,0}, y_{2,0}, z_{2,0})$, and likewise the second interferometer is $(x_{3,1}, y_{3,1}, z_{3,1})$ and $(x_{4,1}, y_{4,1}, z_{4,1})$, and the third $(x_{5,2}, y_{5,2}, z_{5,2})$ and $(x_{6,2}, y_{6,2}, z_{6,2})$.

1.7.2.2 Prototype Design & Assembly

While using inclined wraps for directional strain gauges seems plausible in concept, actually building a device with layers of inclined wraps proved to be very challenging. The same 3-inch nominal, Schedule 5 pipe form factor as the TOFS-NM was chosen (Figure 1.28a) in order to make each prototype the same dimensions, and the plan was to use an equivalent length of fiber for each gauge in order to get a length-for-length comparison between all the prototypes. It was also decided to use a nested reference mandrel made of a thick walled stainless steel tube (2½-inch nominal, Schedule 80 pipe) for mechanical stability and counterballast, rather than to use opposing wraps like what is shown in the concept design in Figure 1.32 to save time on making the inclined wraps.

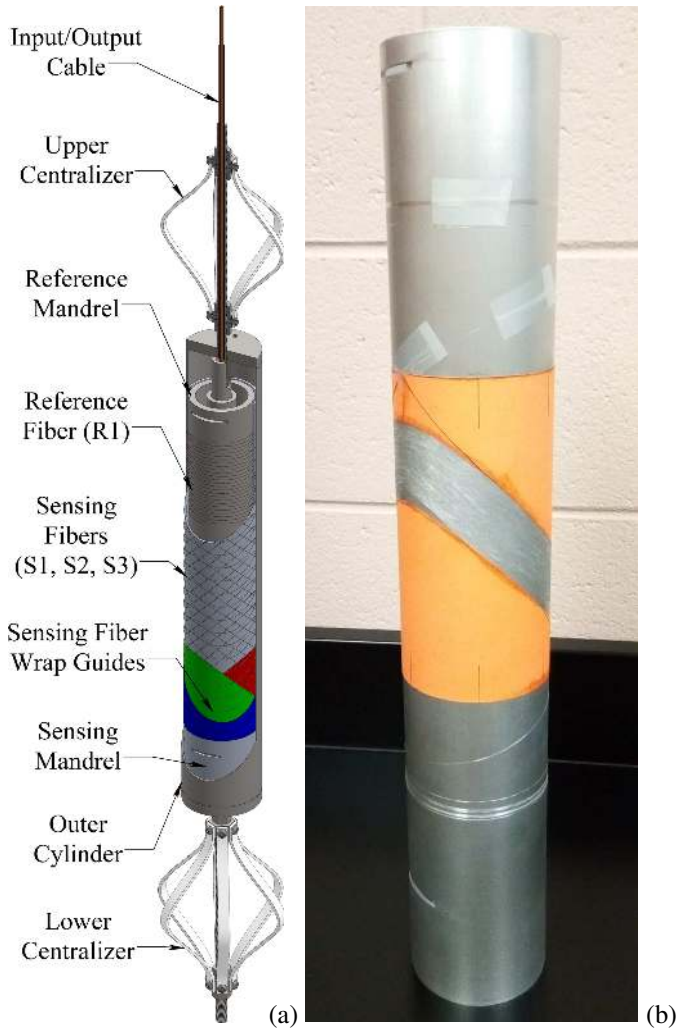

Figure 1.33: (a) Computer rendering of the inclined wrap tensor strainmeter design. (b) Photograph of the interior inclined fiber wrapped sensing mandrel with only the first wrap completed.

The solution for guiding the fibers along an inclined helical path was to use a thick sheet of paper that was close to the thickness of the optical fiber (250 μm) on which a sinusoidal curve was printed whose period was the circumference of the sensing mandrel and amplitude the height of the wrap. This proved to work well for the first layer as shown in Figure 1.33b. Winding each wrap proved to be extremely tedious since the fiber would have to be tacked in place using an instant bonding adhesive, which despite its claim of speed did require repeated wiping and a time allowance to sufficiently dry to the point where inadvertent bonding was prevented.

Given the many hours it took to complete the wrapping shown in Figure 1.33b it was decided to abandon the desire of making three TOFS prototypes with equal lengths of sensing fiber. The new approach was to use 900 μm diameter tight buffered fiber that is much more durable and easier to manipulate. The wrapping procedure was similar to the first attempt but using a stack of thick paper cut into a sinusoid to match the larger fiber diameter, and a total of 16 wraps were used for each layer resulting in a sensing fiber length of just over 7 m.

Figure 1.34a–c shows the wrapping of each layer of the sensing mandrel. This starts with the $0°$ wrap in yellow with blue guide paper (Figure 1.34a), where after the violet guide paper for the second layer is laid down over the first wrap and indexed using the printed marks and the brown fiber is wrapped (Figure 1.34b). The third and final layer is done in the same manner using red guide paper and green fiber (Figure 1.34c). The final step was to wrap the same length of optical fiber onto the reference mandrel and secure it using epoxy (Figure 1.34d).



Figure 1.34: Photographs of the completed first (a), second (b) and third (c) inclined wrap layers along with the triply wrapped reference mandrel (d).

Each wrap was attached to their requisite 3×3 couplers and Faraday mirrors and tested for functionality and the final assembly was completed. The reference mandrel was nested inside of the sensing mandrel and the penetrations and ends sealed just like the individual TOFS-NM elements, centralizers attached and inserted into the pressure case. The interior was then mostly filled with a low-viscosity epoxy before the top cap was welded on and the remaining volume filled.

The TOFS-IH v5 was then subjected to the same hydrostatic and directional loading tests as the TOFS-TM v5, the results of which are described below.

1.7.2.3 Hydrostatic Calibration

The completed prototype of the TOFS-IH v5 was to subjected to the same simple hydrostatic pressure calibration test as the TOFS-NM to determine its strain sensitivity. The instrument was placed in a tall pipe along with a calibrated pressure transducer (Onset Computer Corporation Hobo U20) that was slowly filled with water to a height of about 2 m and then slowly drained multiple times in an attempt to compensate for the response due to water temperature changes. Data was recorded using a Version 3 OFMI connected to a laptop computer.

The results from the last and most temperature stable fill-and-drain hydrostatic load test are shown in Figures 1.35a–c and Table 1.6. Figure 1.35 shows the response of the reference transducer in black, the best-fitting strainmeter gauge time series in red, and their difference (residual) in blue for each of the three strain gauges (i.e., fiber wrapped

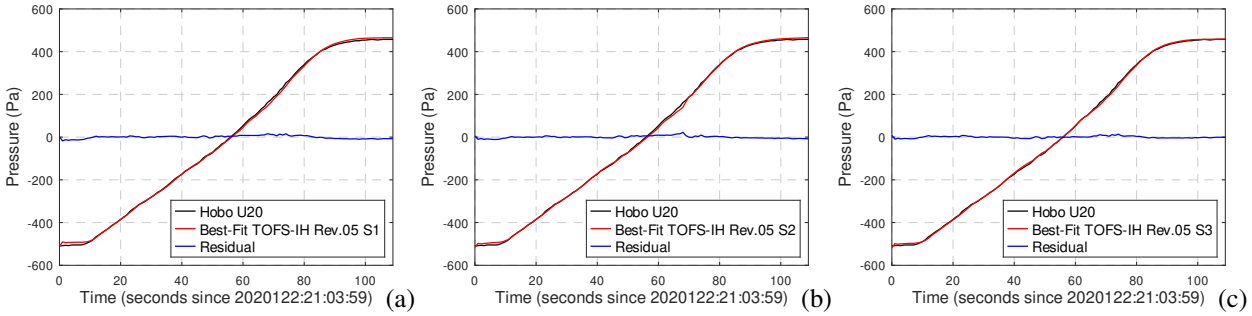

Figure 1.35: Hydrostatic water loading test of the TOFS-IH v5 for the three gauges S1 (a), S2 (b) and S3 (c).

Table 1.6: Least squares results from the TOFS-IH v5 hydrostatic pressure test showing the calibration factor in Pascals of pressure change per radian of optical phase change change for each sensing gauge.

Gauge	Calibration Factor (Pa/radian)
S1	39.0 ± 0.7
S2	39.4 ± 0.6
S3	42.1 ± 0.5

tubes). There appears to be considerably less drift in these time series compared to the TOFS-NM (Figure 1.30) evidenced by how much more closely the overall shape of the pressure and best-fit optical phase difference curves match. The average response appears to be about 40 Pascals per radian of optical phase change which is about 100 times less sensitive than the TOFS-NM (Table 1.5) despite having approximately 25 times less sensing fiber. The reason for this is subject to speculation, but the 2.5 times thicker sensing mandrel (0.090" versus 0.035" wall) may be a potential explanation since the stress-strain relationship in a thin walled cylinder is proportional to 2 times the wall thickness.

Performing a similar analyses that a radian of phase change can be measured to within 1 part in 2^{16} implies an average least-count resolution of about 610 μPa, which is about 90 times less sensitive than the TOFS-NM in Section 1.7.1.3. Further assuming that the instrument has an average a bulk modulus of somewhere near 25 GPa (10% of its cross-sectional area is stainless steel at 166 GPa, 10% is aluminum at 70 GPa and 80% is epoxy at 3 GPa) implies an average strain calibration coefficient of $\sim 2.4 \times 10^{-8}$ strain or 24 nanostrain per radian, with the same assumed 16-bit depth results in a least-count resolution of ∼0.4 picostrain. While this is the least sensitive interferometric sensor thus far, it is still more than capable of resolving the solid Earth tides at 10^{-8} strain. One potential lesson from this instrument is that its lower, but still more than adequate, sensitivity may be advantageous given the much lower drift compared to its more sensitive counterparts.

1.7.2.4 Directional Load Calibration

The Version 5 TOFS-IH was also subjected to a directional load test identical to that performed on the TOFS-NM in Section 1.7.1.4. Figure 1.36 shows the load sensitivities as a function of the applied load angle where all three curves perform as expected – they follow the $\cos(2\theta)$ functional form and the sensitivity maximum for each is 60° offset from the next. The load sensitivity ranges from roughly -5 to 1 rad/kg implying an average sensitivity of 6 rad/kg, which is about 10 times less than the ± 25 rad/kg load sensitivity of the TOFS-NM v5 (Figure 1.31). To summarize, the TOFS-IH prototype is 100 times less sensitive in pressure than the TOFS-NM but only ∼10 times less sensitive to directional loads despite having 25 times less fiber.

This result is a clear and convincing validation of the inclined wrap approach for measuring directional strains.

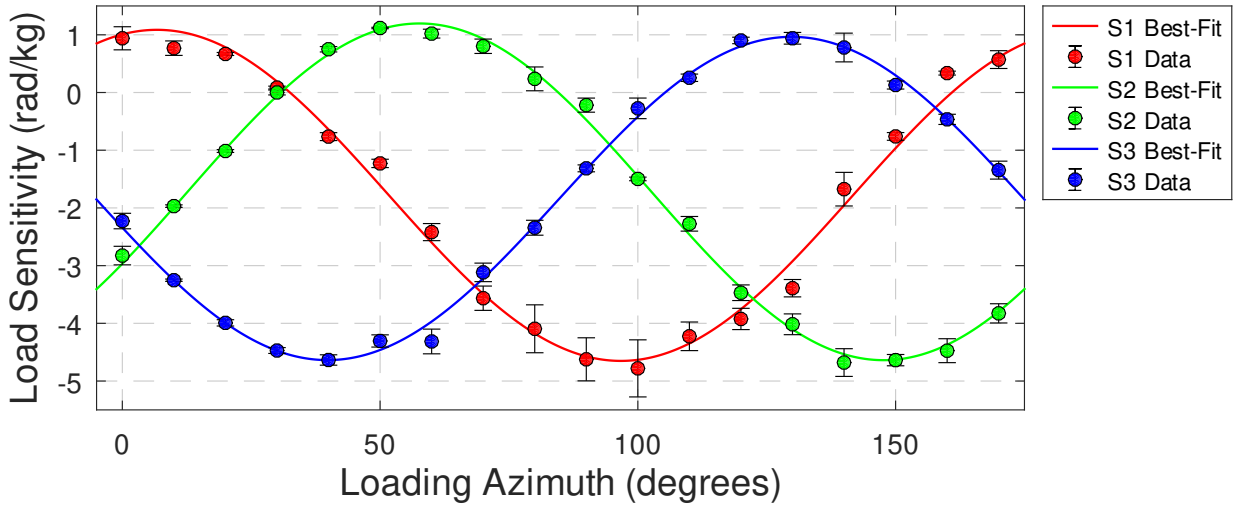

Figure 1.36: Load sensitivity as a function of azimuth for the TOFS-IH v5, showing the data (filled circles) and best-fit function (solid lines) for the three strain gauges, S1 (red), S2 (green) and S3 (blue).

1.7.3 Elliptical Ring TOFS

The final tensor strainmeter concept explored during this project departs from the circular geometry by embedding fibers wrapped on cylinders with an elliptical cross section, or Elliptical Ring Tensor Optical Fiber Strainmeter, or TOFS-ER. Fibers wrapped in a circular pattern obviously implies that the amount of fiber exposed to a directional load is the same regardless of the direction in which it is applied. However, if the fiber is wrapped around an elliptical cylinder the amount of fiber under load will vary with direction with the maximum being perpendicular to the semiminor axis of the ellipse. In other words, there is more fiber facing the applied load along the flat sides of the ellipse (where the curvature is a minimum) than on the narrow sides (where the curvature is a maximum).

1.7.3.1 Prototype Design

The TOFS-ER v5 was the third prototype in the tensor strainmeter development series that employs a stack of fiber wrapped elliptical cylinders for the directional strain gauges. This is shown in Figure 1.37, which uses the same 3.5" diameter pressure case design and centralizers as the TOFS-NM and TOFS-ER. Each aluminum elliptical ring is separated by circular cylinder that is wrapped with the same 48 m length of 250 μm diameter optical fiber (Corning ClearCurve ZBL) as the elliptical sensing

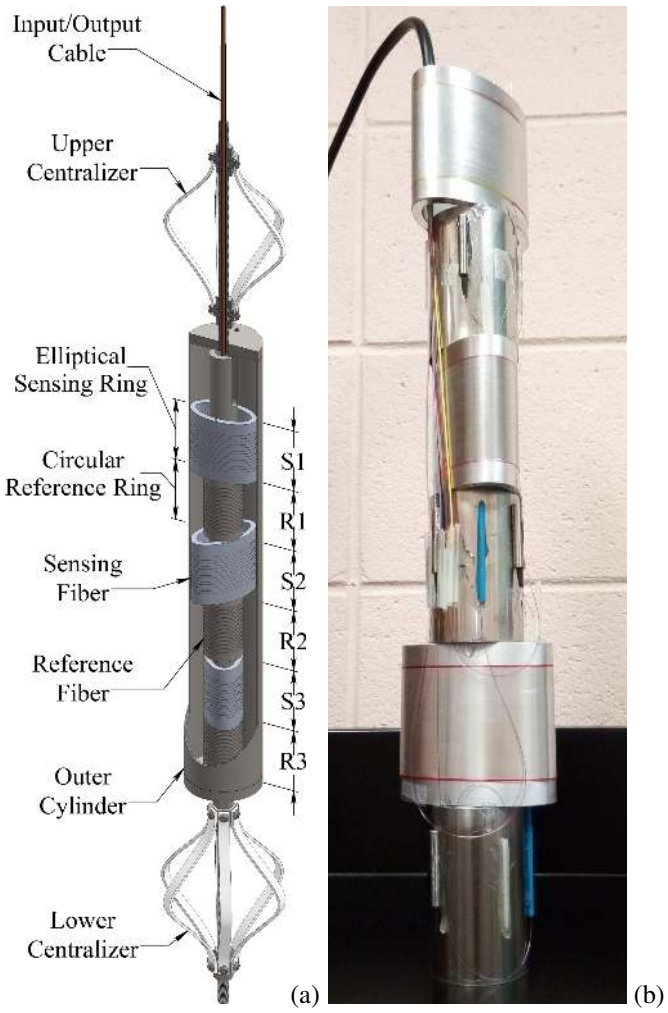

Figure 1.37: The Version 5 TOFS-ER.

mandrels. Thin walled stainless tubes cover each reference mandrel to serve as a way to seal off the reference arm fibers from external stresses as well as provide a place to attach the 3×3 couplers, Faraday mirrors and hermetic fusion splice protection sleeves (Figure 1.37b).

The completed sensing and reference gauge stack was attached to an optical fiber cable and inserted into its pressure case for potting. Most of the strainmeters we've developed use a "tactical" fiber cable (Fiber Instrument Sales FBSMTACCABLE12), which consists of a number of 900 µm tight-buffered optical fibers and a collection of aromatic polyamide (aramid) fibers for bulk filling and tensile reinforcement. With each of these care is taken to seal the end of this cable inside of the pressure case before potting the interior since the aramid fibers can absorb the low-viscosity epoxy, which can also wick up into the cable jacket. This is especially important since these are potted under a vacuum to ensure penetration and immobilization of all the fibers and interior components. Unfortunately, a small leak must have developed causing epoxy to wick up about 6 inches into the cable above the top cap of the pressure case making it more brittle and therefore susceptible to damage.

Despite this setback, the completed prototype was fully functional for the directional loading test (Section 1.7.3.3), but did become damaged before the hydrostatic calibration (Section 1.7.3.2) and deployment (Section 3.1.2.1). This was due to an accidental pulling on the cable, however, one strain gauge (S2) did survive and was able to be used.

1.7.3.2 Hydrostatic Calibration

The hydrostatic calibration test of the TOFS-NM v5 followed the exact same procedure as the TOFS-NM (Section 1.7.1.3) and TOFS-IH (Section 1.7.2.3). The time series results from the one surviving strain gauge are shown in Figure 1.38, which as in the TOFS-NM (Figure 1.30) exhibits a fairly large drift as shown by the residual. The pressure calibration factor was estimated to be 2.78 ± 0.08 Pa/rad, which implies a 16-bit least-count of about 42 µPa. Performing the same very coarse cross sectional weighted average of bulk moduli (10% stainless steel, 50% aluminum and 40% epoxy) yields about 50 GPa, suggesting a strain calibration factor of about 5×10^{-11} strain or 50 picostrain per radian of optical phase change. This implies a least-count strain resolution of ~0.8 femtostrain, which is roughly 3 times less than the TOFS-NM (Section 1.7.1.3).

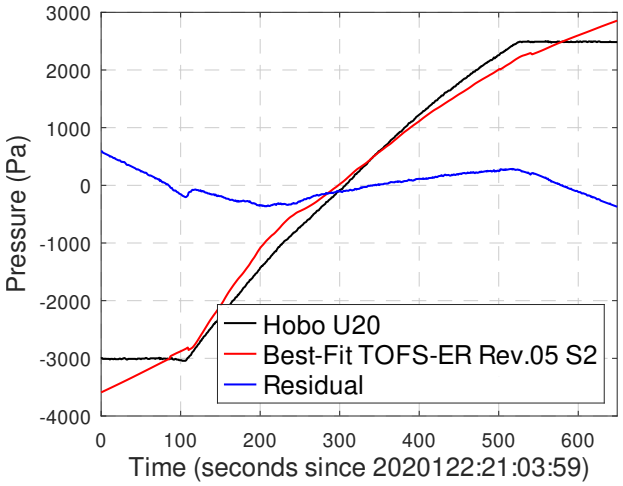

Figure 1.38: Pressure calibration time series of the surviving gauge in the TOFS-ER showing the applied pressure (black), best-fit areal strain record (red) and their difference (blue).

1.7.3.3 Directional Load Calibration

As with the two previous prototypes, the TOFS-ER v5 was subjected to the very same directional loading test using the system described in Section 1.9. Fortunately these data were collected before the hydrostatic tests and all three strain gauges were functioning, resulting in the curves shown in Figure 1.39. This instrument also obeys the $\cos(2\theta)$ functional form with 60° separating each sensitivity maximum.

The load sensitivity ranges from about 0 to -25 radians per kilogram resulting in a load calibration factor of ~0.04 kilograms per radian of optical phase change. Once again using the 1-part-in-2^{16} assumption results in a load resolution of about 6×10^{-7} kg.

As with the inclined wrap TOFS, **this result is a clear and convincing validation of the elliptical cylinder strain gauge approach for measuring directional strains**, implying that we now have two tensor strainmeter designs that conform to our expectations.

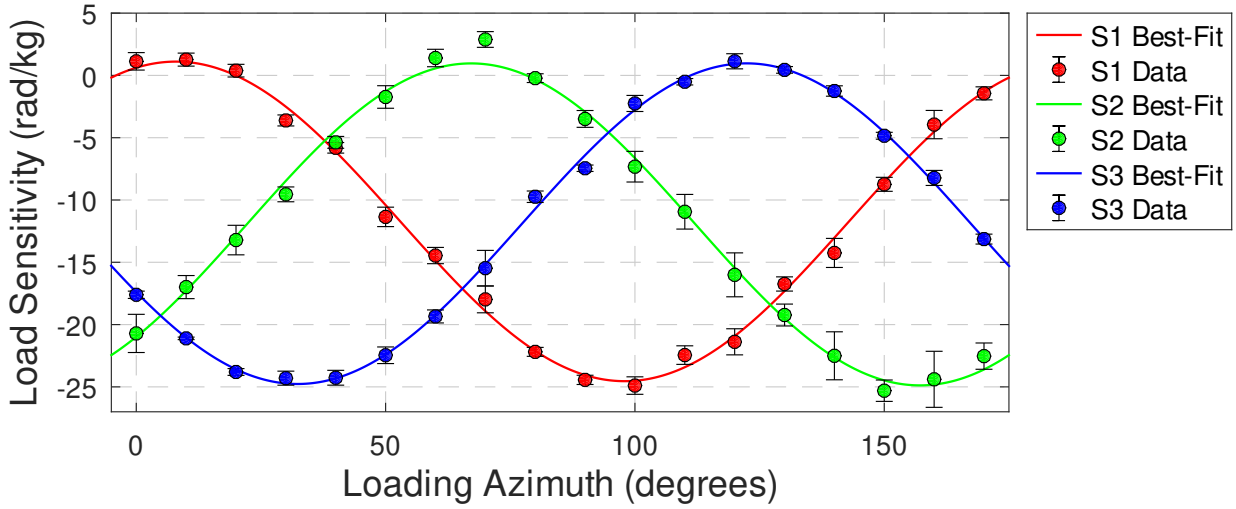

Figure 1.39: Load sensitivity as a function of azimuth for the TOFS-ER v5, showing the data (filled circles) and best-fit function (solid lines) for the three strain gauges, S1 (red), S2 (green) and S3 (blue).

1.7.4 North Avant Field Strainmeters

The choice of which of the three tensor strainmeter designs would be scaled up for deployment at our North Avant Field test site was ultimately decided by three factors:

1. Directional strain resolution
2. Ease and cost of fabrication
3. Ease of assembly

Lab tests showed that each design was capable of resolving directional loads. However, concerns about the partially rectified strain versus azimuth curve for the nested mandrel design (Figure 1.31) raises concerns about the complexity and uniqueness of the functional form of the applied load and direction. This is unfortunate since this design is very simple to fabricate and is moderately easy to assemble.

The inclined wrap and elliptical ring designs both show the expected directional load response, but present differing challenges. While the inclined wrap consists of very simple fabricated parts, it is by far the most tedious to assemble by hand. The elliptical ring is the easiest of the three designs to assemble since the sensing elements are very easy to quickly wrap by hand, however they do require CNC machining that the other designs do not. The elliptical ring design also suffers from the same limitation as the Gladwin Tensor Strainmeter (Gladwin, 1984) in that the horizontal gauges only measure the strain over a limited axial extent (i.e., the length of the gauge), whereas the other designs average the horizontal load over almost the entire length of the downhole package.

It was ultimately decided to go with the elliptical ring design because it has the desired directional response and is fast and easy to assemble. The next task was to scale up the prototype (Figure 1.37) into a full sized instrument more similar to conventional borehole strainmeters. This included other changes and improvements that are outlined in the following sections.

1.7.4.1 Final Design

The instruments developed for the North Avant Field site are the culmination of years of conceptual and computer modeling as well as prototyping and lab and field testing. This version, called the Version 6.0 Elliptical Ring Tensor Optical Fiber Strainmeter (or TOFS-ER v6) includes many long desired features in addition to the ability to measure the horizontal strain tensor. From the pressure case to the gauge layout, it both departs from and integrates ideas learned from the previous 40 years of borehole strainmeter developments.

The first departure from previous strainmeters is that the pressure case is designed to allow for pumping grout through the instrument. Existing strainmeters require a two trip deployment where the expanding grout used to couple it to the formation is emplaced in the first trip downhole using a tremie pipe or dump bailer, where the instrument is lowered into the grout after the termie or bailer are removed. This new pressure case (Figure 1.40) is designed to be deployed on a tremie pipe such that grout can be pumped and circulated around the instrument in a single trip deployment.



(a) (b) (c)

Figure 1.40: Pictures of the new tensor strainmeter pressure case design featuring an integral central pipe for pumping grout through and around the instrument during deployment.

Figure 1.40 shows several photos of this new package that features an outer cylinder with two end caps just like previous instruments (Figure 1.40a). Unlike these, the latest includes a central 1-inch nominal pipe through the center that is threaded onto two female-female straight pipe couplings. The outer diameter of each coupling is partially threaded such that each end cap can be screwed on to the ends of the pressure case (Figure 1.40b). This results in a sealed pressure vessel (Figure 1.40a) that contains the fiber-wrapped sensing and reference elements with a hole through the center (Figure 1.40c). Once assembled, the end caps are welded to the outer cylinder and the couplings.

The full design of the TOFS-ER v6 is shown in Figure 1.41a, which includes four horizontal strain gauges, a vertical strain gauge and a reference gauge. This is packaged as a stack of elliptical cylinders separated by circular cylinders along a central pipe contained in the aforementioned pressure case. Each pair of cylinders forms the directional sensing and omni-directional reference arms of an equal-arm Michelson interferometer. The top circular cylinder contains two identical wraps to form an isolated reference or “null” component. This null interferometer and the reference arms for the horizontal strain gauges are covered by stainless steel sleeves (not shown in Figure 1.41a

but visible in Figure 1.41b) that is sealed between the fiber-wrapped outer diameters of the circular cylinders and the inner diameters of the sleeves, which helps isolate these fibers from external loads on the pressure case. The vertical strain gauge is a length of fiber wrapped multiple times between a pair of circular cylinders transversely mounted at the top and bottom of the stack.

Figure 1.41b shows the completed vertical stack with each component wrapped with fiber and spliced to their respective beamsplitters and mirrors. Each element contains approximately 20 m of 900-micron tight-buffered Corning ClearCurve ZBL optical fiber whose fiber lengths are matched to within about 1 mm to limit apparent strains due to laser frequency drift. Each circular cylinder is covered with the previously mentioned thin stainless steel sleeve for securing the 3×3 couplers, Faraday mirrors, and hermetic fusion splice protection sleeves. The communications cable enters through the top cap (on the bottom of Figure 1.41b and is spliced to the inputs of the six 3×3 couplers.

The interior of the instrument is covered with a protective outer stainless steel sleeve and potted with epoxy. This is done in a manner similar to the AOFS-OO discussed above in 1.5 wherein about 6 liters of the same low-viscosity epoxy is pumped into the interior under vacuum to ensure there are no bubbles and that the epoxy penetrates all the components. The result is a completely sealed and very robust down-hole instrument package (Figure 1.41c), whose weakest point is the exit of the fiber cable from the instrument.

1.7.4.2 Hydrostatic Calibration

Pressure calibration was performed on the TOFS-ER in a manner similar to the smart casings shown in Section 1.5, however, unlike the previous test the instrument was placed in a chamber and externally pressurized. Figure 1.42 shows the pressure calibration time series, and the calibration factors (inverse sensitivities) are presented in Table 1.7. While there appears to be a fairly broad range of pressure sensitivities over the four supposedly identical gauges, they are all reasonable values given the amount of fiber and stiffness of the sensing elements. The null component appears to be not perfectly insensitive, but this was expected since it is not perfectly isolated from strains in the surrounding materials – the design goal was to have something much less sensitive, which this achieves by an order of magnitude.

While these results show that the TOFS-ER is about 200 times less sensitive than the AOFS-OO, it is still very sensitive and should be capable of resolving the strains induced by pumping at our demonstration site. Consider a calibration factor of 500 Pa/rad, for which we can estimate the optical phase to about 1 part-per-million resulting in a pressure resolution of 500 μPa. A stiff estimate of the bulk modulus of the instrument would be approximately somewhere between acrylic (∼3 GPa) and stainless steel (∼160 GPa). Therefore the strain calibration factor should be at least 3 nε per radian with a resolution of $\sim 3 \times 10^{-15}$, or 3 femtostrain.

Table 1.7: Least squares results from the TOFS-ER external pressure test showing the calibration factor for each sensing element.

Gauge	Calibration Factor (Pa/rad)
S0 (null)	2073 ± 13
S1 (0° horizontal)	301.8 ± 0.7
S2 (45° horizontal)	408.5 ± 0.8
S3 (90° horizontal)	509.7 ± 5.3
S4 (135° horizontal)	250.9 ± 2.6
SZ (vertical)	535.7 ± 3.4

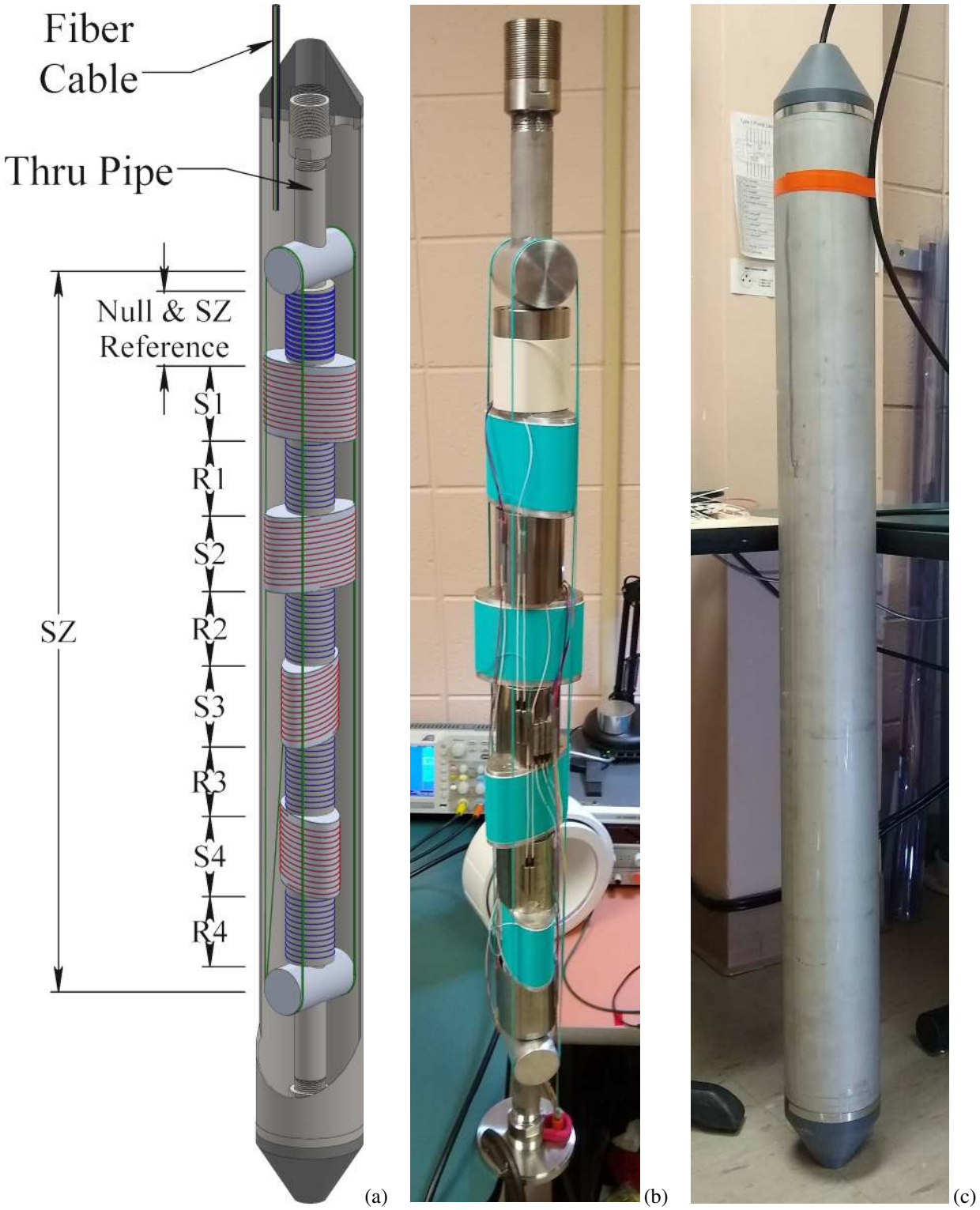

Figure 1.41: Diagram (a) and photographs of the interior (b) and exterior (c) of the Version 6 Elliptical Ring Tensor Optical Fiber Strainmeter, TOFS-ER v6. Note that the photograph in (b) shows the interior of the instrument upside-down.

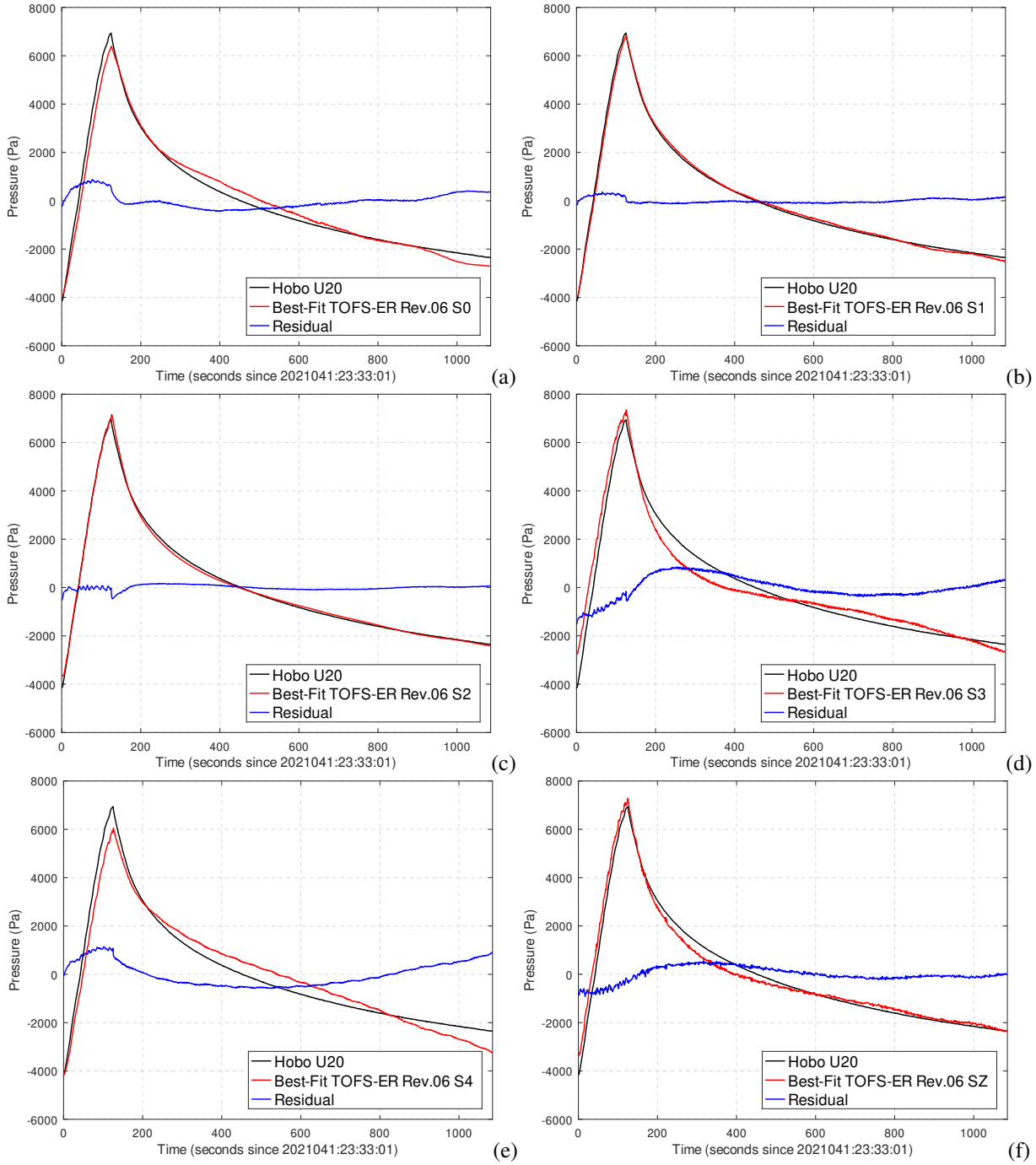

Figure 1.42: Pressure calibration curves for the six components of the Version 6 TOFS-ER showing the applied pressure (black), best-fit areal strain record (red) and their difference (blue) for the null component S0 (a), four horizontal gauges S1–S4 (b–e), and vertical strain gauge SZ (f).

1.8 Summary of Strainmeter Lab Results

There were a total of eight strainmeters developed for this project that made it through the prototyping, assembly and lab testing. This includes

1. Optical Fiber Michelson Strain Ribbon, Version 2 (OFMSR v2)
2. Open-Closed Areal Optical Fiber strainmeter, Version 1 (AOFS-OC v1)
3. Open-Open Areal Optical Fiber strainmeter, Version 1 (AOFS-OO v1)
4. Multicomponent Optical Fiber Bragg Grating Strainmeter, Version 1 (MOFBG v1)
5. Nested Mandrel Tensor Optical Fiber Strainmeter, Version 5 (TOFS-NM v5)
6. Inclined Helix Tensor Optical Fiber Strainmeter, Version 5 (TOFS-IH v5)
7. Elliptical Ring Tensor Optical Fiber Strainmeter, Version 5 (TOFS-ER v5)
8. Elliptical Ring Tensor Optical Fiber Strainmeter, Version 6 (TOFS-ER v6)

Most of these were subjected to at least a hydrostatic pressure calibration, and the three Version 5 prototypes to a directional loading test. These results are summarized in Table 1.8, which shows the pressure calibration for each (where applicable) in Pascals per native units (radians of optical phase change for the Michelson interferometers and picometers of wavelength change in the case of the FBG strainmeter). This is followed by an estimate of the pressure resolution, or least-count for each assuming 1 pm for the FBG instrument and 2^{16} bits for the Michelson interferometers. Estimates (in some cases very crude) of each instrument's bulk modulus is presented followed by an estimate of the strain calibration factor in strain per native unit, and the strain resolution assuming the aforementioned bit weights. The load calibration (inverse sensitivity) and least-counts are also shown for the three Version 5 prototypes.

Despite the diversity of strainmeter designs, all but the MOFBGS are easily capable of resolving the solid Earth tides. Even though the Version 6 TOFS-ER is much less sensitive to pressure than even its Version 5 counterpart, its 40 femtometer least-count is still 250 times more sensitive than the 10 picostrain resolution of the Gladwin Tensor Strainmeter (Gladwin, 1984). Furthermore, hydrostatic results from the less sensitive TOFS-IH (Section 1.7.2.3) suggest that dialing back the amount of embedded fiber and therefore the sensitivity may improve drift performance. This issue is may be moot since it is impossible to assess the character of the actual drift in a laboratory environment, but it may be a profitable subject for future research.

One clear area for ongoing research is estimating the effective bulk modulus to derive accurate estimates of the strain sensitivity from hydrostatic pressure tests. The hydrostatic tests are no doubt valuable to assess functionality and the relative sensitivity of each gauge, but offers little insight into the strain performance. While the directional load tests were interesting for assessing the functional form and relative sensitivity of the three main tensor strainmeter design concepts, it too is also of limited usefulness if the goal is to determine the relationship between strain in the instrument and strain in the formation in which it is designed to be coupled.

Overall each strainmeter design was a success in that it met the objective of being actually realized as a functioning instrument capable of resolving strain(s). Despite the complexity and intricacy of assembling the smart casings, the result is very robust and profoundly sensitive. The strain ribbon is a simple and highly sensitive device that can be easily deployed in shallow boreholes backfilled with native materials. Each of the tensor instruments should be perfectly capable of measuring the solid Earth tides with very high fidelity, which is essential for determining the in-situ calibration which is required to relate formation strains to the responses of the embedded directional strain gauges.

Table 1.8: Summary of the average horizontal strain gauge calibration results from the strainmeter designs presented in this chapter.

Instrument	Pressure Calibration (Pa/Native Unit)	Least-Count (Pa)	Bulk Modulus (GPa)	Strain Calibration (ϵ/Native Unit)	Least-Count (ϵ)	Load Calibration (kg/radian)	Least-Count kg
OFMSR v2	n/a	n/a	n/a	5×10^{-9}	8×10^{-14}	n/a	n/a
AOFS-OC v1	2.2	3.3×10^{-5}	70	3×10^{-11}	5×10^{-16}	n/a	n/a
AOFS-OO v1	1.7	2.6×10^{-5}	70	2×10^{-11}	4×10^{-16}	n/a	n/a
MOFBGS v1	1060	1.1×10^{3}	1	1×10^{-6}	1×10^{-6}	n/a	n/a
TOFS-NM v5	0.45	6.9×10^{-6}	20	2×10^{-11}	3×10^{-16}	2×10^{-2}	3×10^{-7}
TOFS-IH v5	40	6.4×10^{-4}	25	2×10^{-9}	2×10^{-14}	2×10^{-1}	2×10^{-6}
TOFS-ER v5	2.8	4.3×10^{-5}	50	6×10^{-11}	8×10^{-16}	4×10^{-2}	6×10^{-7}
TOFS-ER v6	370	5.6×10^{-3}	160	2×10^{-9}	4×10^{-14}	n/a	n/a

1.9 Load Frame Calibration System

It became apparent during the prototyping of the three TOFS systems shown in Section 1.7 that a reliable and repeatable way to apply loads to was essential in order to measure and compare the directional load responses of these designs. This led to the development of a novel automated load frame calibration system that was critical to the decision making process about which TOFS design would ultimately be scaled up for deployment at the North Avant Field demonstration site.

1.9.1 Background and Motivation

The very first TOFS prototypes used a very crude load frame system (Figure 1.43) such that the load sensitivity of the instrument at a given orientation could be estimated by compressing it with a graduated amount of weight. A major issue with this approach is the very large drift induced by the high sensitivity of these devices to temperature making it difficult to discern the load state.

The procedure to work around the thermal drift is to load the device repeatedly at known times for each applied mass and instrument orientation. Doing this by hand turned out to be an extremely tedious and time consuming process. For example, consider using 5 load and unload cycles where the load is applied for 30 seconds and removed for 30 seconds. This amount of time allows for a few seconds to gently lower and raise the weights without creating excessive stress and/or vibrations that induce miscounts in the interrogation system. The steady state between setting down and picking the weight up results in roughly 15 seconds of time over which to average the strain response. If a total of 5 mass increments are used to determine the load sensitivity and this is repeated for 6 orientations from 0° to 150° in 30° increments, this is approximately 2.5 hours of precicely timed actions assuming no time for setup changes to rotate the instrument.

Figure 1.44 shows an example time series of a manual loading test. This begins with a set of 5 repeated loadings at 5 different masses, the resulting time series is shown in Figure 1.44a. The data are averaged over each load and unload time interval (denoted by the red and magenta, and blue and cyan dots, respectively) and those values are differenced to get the optical phase change during each repeated load and unload cycle. These 5 differences are averaged to get the load response and its variance for that applied load. This is repeated for the remaining loads where the mass is increased after each set of load cycle repeats. The optical phase difference for each load is shown in Figure 1.44b where a linear least squares fit (weighted by the inverse of the variance) is used to determine the load sensitivity in units of interferometric optical phase change per applied load in kilograms.

The above procedure is repeated for each instrument orientation and results in the load sensitivity versus azimuth plots shown within 1.7. While this procedure seems fairly robust, it is obvious that being able to do a larger number of repeated loads over a larger number of weights would be more ideal from a statistical standpoint. However, it is totally infeasible to do this by hand, which motivated the development of an automated load frame calibration system.

1.9.2 System Design and Assembly

The automated load frame calibration system was developed to more easily measure the directional load sensitivity of the various tensor strainmeter designs in the lab. While the true test of any tensor strainmeter design is to grout it into an open borehole and collect ambient data, this is a lot of effort, expense and time to get enough data to compare different sensor configurations. Manually loading each sensor azimuth in a repeatable and statistically meaningful manner is very tedious and prone to human error.

The calibration system developed for this project includes a loading frame, a programmable stack of up to 10 weights, a mechanism for lifting these weights and an electrical control system. Figure 1.45 shows CAD models of the device in its fully assembled (a) and major component exploded view (b), and Figure 1.46 shows a photograph of the device during a calibration. The loading frame consists of two aluminum plates separated by four linear rails that are fixed to the bottom plate and allowed to slide through the top plate with the aid of four linear bearings. Each plate has a linear rail down the center that concentrates the load along a line above and below the instrument under testing

(shown in purple in Figure 1.45). A segment of angle material is used on each side of the instrument to center it under these load rails.

Sitting over the loading frame is a frame consisting of a set of platforms to hold, lift and index the amount of dead weight applied to the instrument under testing. The platform directly above the loading frame contains a stack of ten 5 pound (2.27 kg) weights that were sold as replacement parts for a personal fitness device. A custom insert is pressed into the center of each weight with tabs separated by 18° such that the shaft going through the center can be indexed by a stepper motor located on the uppermost plate to lift only the top weight, the top two weights, and so forth.

The upper plate of the main frame and the carriage (Figure 1.45b) work together to periodically lift the selected weights. This main frame is fixed relative to the table where the bottom plate of the loading frame rests, whereas the carriage is allowed to slide up and down using a pair of rails and linear bearings similar to the loading frame. A pair of cams driven by 1000:1 DC-powered gearmotors are also fixed to the main frame that push off against the carriage causing it to raise and lower as the cams rotate. The center shaft is connected to the carriage such that the selected weights are also raised and lowered as the motors turn.

Figure 1.47 shows the electronic control system that powers and operates the device. A DC power supply powered the gear motors to set the device in motion and microcontroller was used to index the stepper motor by 18° once the desired number of load cycles for that given weight was reached. The load and unload cycles were monitored with a load cell between the weight stack and top plate of the loading frame so that they could be counted and the weights indexed when there was no load on the center shaft.

The final system was fairly complex but met the design goal of being able to repeatedly apply a graduated load to the strainmeters under testing. While the cycle time was fairly long, it can be run unattended for extended periods of time with each weight increment applied tens of times before switching to the next. Logging of the load cell voltage made the processing of the time series data from these tests very easy since it can be difficult to determine whether the instrument was under load when its azimuthal response is at a minumum or has changed sign. The device can be challenging to setup and debug and it still requires the instrument to be rotated manually, however, it was an invaluable tool for evaluating the tensor strainmeter designs for this project.

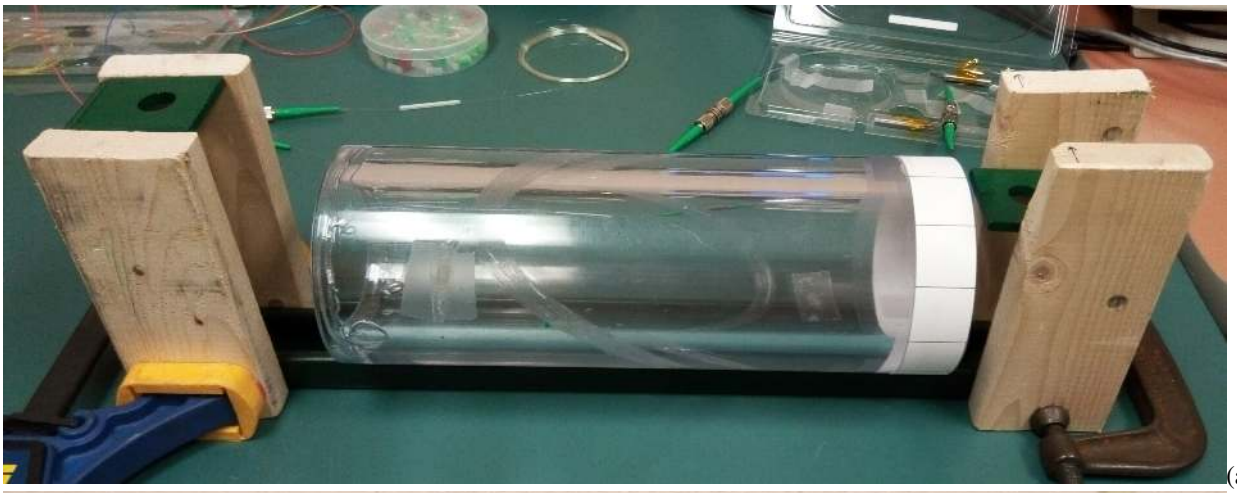
(a)


(b)

Figure 1.43: Crude load frame system used during the early prototyping phase of the TOFS development showing the Version 1 Inclined Wrap strainmeter before (a) and during (b) applied loads. The foam pad between the plate weights and upper load frame plate is to dampen unwanted shock and vibration of setting and removing the weight stack on the highly sensitive instrument under testing.

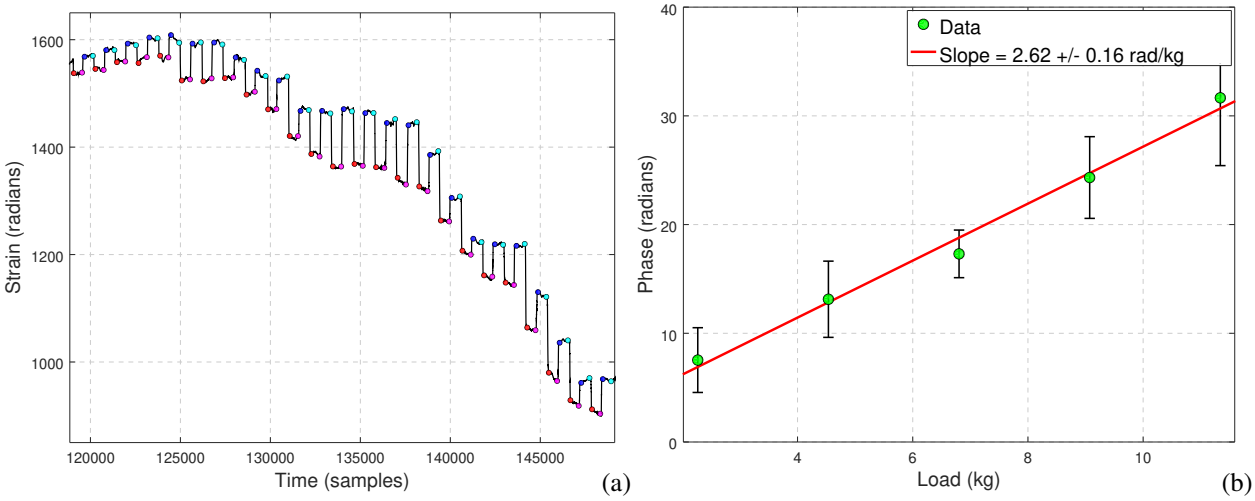

Figure 1.44: (a) Example time series from a load test using 5 repeated applications of 5 masses. The blue and cyan dots denote the time interval over which the load is removed and the red and magenta dots are when the load is applied. (b) An example of the interferometric optical phase change as a function of applied load.

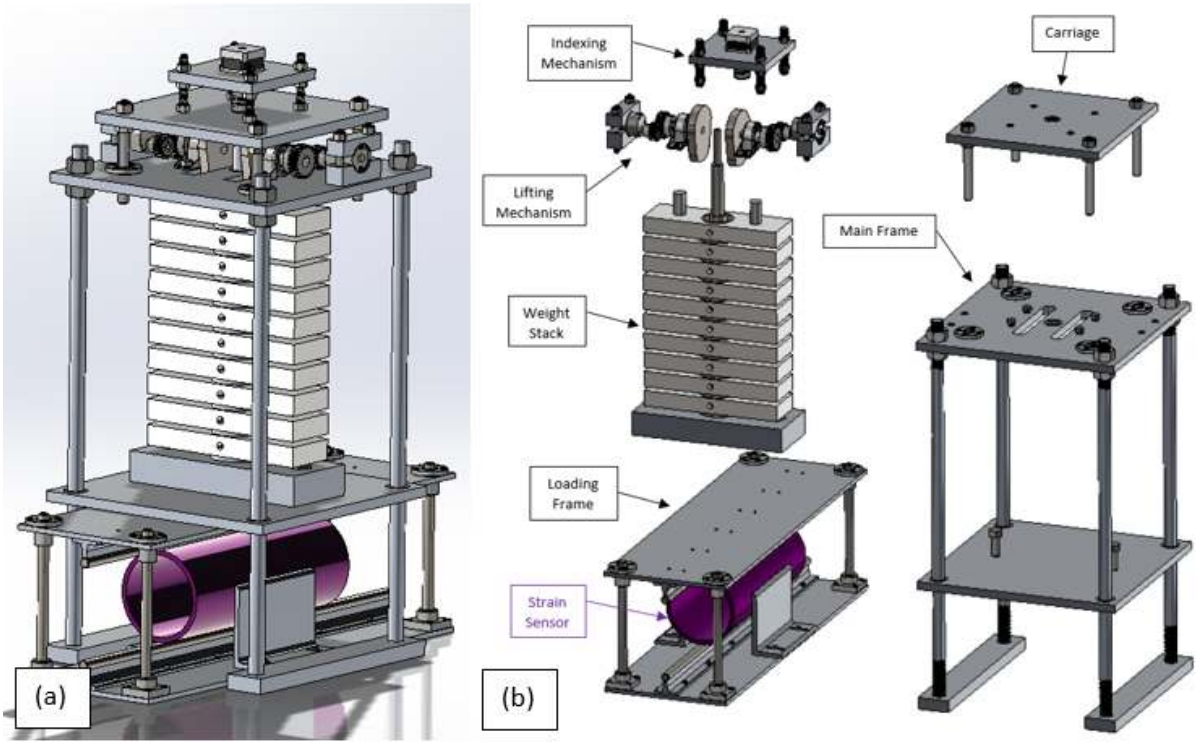

Figure 1.45: Loading device in its assembled view (a), as well as an annotated explosion of the major components (b). Device is driven by two gear motors and one stepper motor and is comprised almost entirely of aluminum and stainless steel alloys.

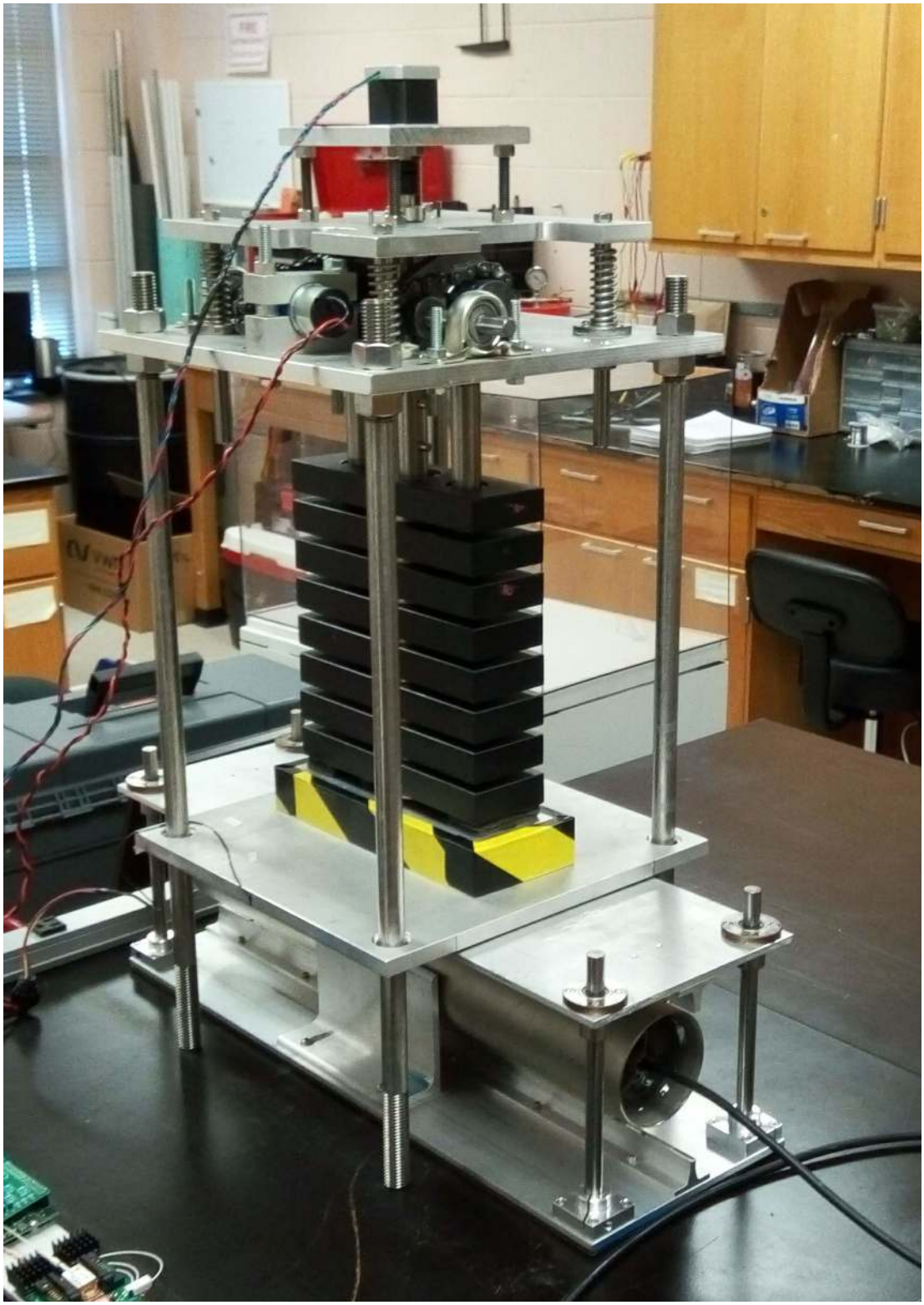

Figure 1.46: Photograph of the loading device during a calibration of one of the TOFS prototypes that was eventually deployed at the Simpson Station.

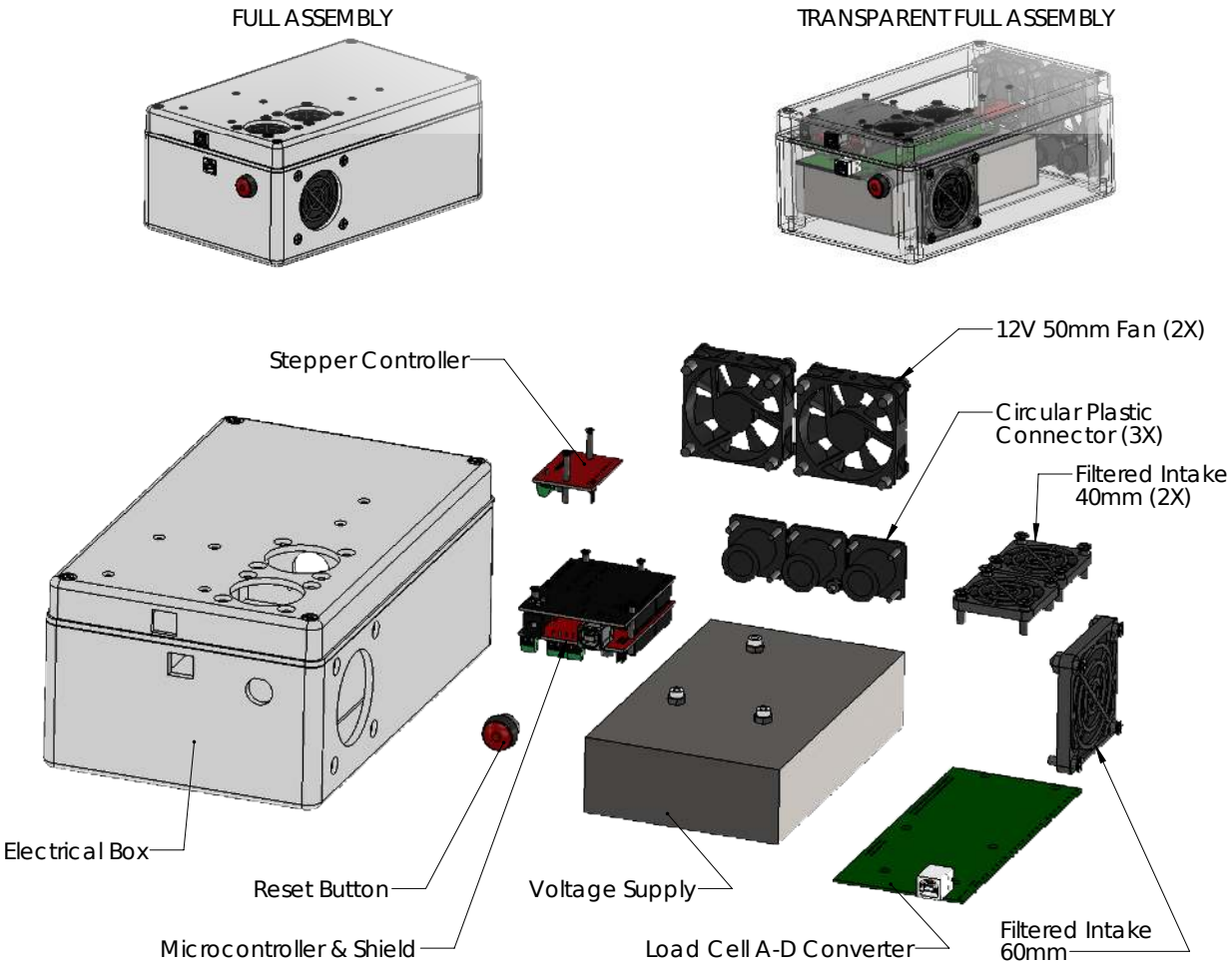

Figure 1.47: CAD realizations of the electronics enclosure that powers and controls the operation of the automated load frame calibration system.

References

Ahern, T. K. and Dost, B. (2012). Standard for the Exchange of Earthquake Data (SEED) Reference Manual, Version 2.4. Technical report, Incorporated Research Institutions for Seismology. http://www.fdsn.org/media/_s/publications/SEEDManual_V2.4.pdf.

Butter, C. D. and Hocker, G. B. (1978). Fiber optics strain gauge. *Applied Optics*, 17(18):2867–2869.

DeWolf, S. (2009). *Optical and Mechanical Behavior of the Optical Fiber Infrasound Sensor*. Master of Science in Earth Sciences, University of California San Diego. https://escholarship.org/uc/item/8652n0w4.

Gladwin, M. T. (1984). High-precision multicomponent borehole deformation monitoring. *Review of Scientific Instruments*, 55(12):2011–2016.

Kersey, A. D., Marrone, M. J., and Davis, M. A. (1991). Polarisation-insensitive fibre optic Michelson interferometer. *Electronics Letters*, 27(6):518–520.

Sheem, S. K. (1980). Fiber-optic gyroscope with [3×3] directional coupler. *Applied Physics Letters*, 37(10):869–871.

Todd, M. D., Seaver, M., and Bucholtz, F. (2002). Improved, operationally-passive interferometric demodulation method using 3×3 coupler. *Electronics Letters*, 38(15):784–786.

Zumberge, M. A., Berger, J., Dzieciuch, M. A., and Parker, R. L. (2004). Resolving Quadrature Fringes in Real Time. *Applied Optics*, 43(4):771–775.

CHAPTER TWO
DISTRIBUTED INSTRUMENT DEVELOPMENT

Contents

2.1 Distributed Sensing Principles . . . 2-1
2.1.1 Coherence-length-gated Microwave Photonics Interferometry (CMPI) . . . 2-1
2.1.1.1 Theory . . . 2-2
2.1.1.2 Lab Demonstration . . . 2-4
2.1.2 Microwave Photonics Low-Coherence Interferometry (LCI) . . . 2-4
2.1.2.1 Theory . . . 2-6
2.1.2.2 Lab demonstration . . . 2-6
2.1.3 Phase Demodulation by Frequency Chirping in CMPI . . . 2-6
2.1.3.1 Theory . . . 2-7
2.1.3.2 Lab Demonstration . . . 2-8
2.1.4 Coherence Control . . . 2-9
2.1.5 CMPI for Distributed Acoustic Sensing . . . 2-11
2.1.5.1 Theory . . . 2-12
2.1.5.2 Lab Demonstration . . . 2-13
2.2 CMPI Interrogator . . . 2-16
2.2.1 Hardware . . . 2-16
2.2.2 Software . . . 2-17
2.3 CMPI Data Storage, Transfer and Processing . . . 2-18
2.4 Sensor Fabrication . . . 2-18
2.4.1 Ultra-Fast Laser Reflector Fabrication . . . 2-18
2.4.2 Broadband Fiber Bragg Grating (FBG) . . . 2-18
2.5 Sensor Packaging . . . 2-22
2.5.1 CMPI Ribbons for Normal Strain Measurement . . . 2-23
2.5.1.1 Tape Laminated Strain Ribbon . . . 2-24
2.5.1.2 Fiberglass Strain Ribbon . . . 2-27
2.5.2 CMPI Packaging for Strain Tensor Measurement . . . 2-28
2.5.2.1 Pipe Inflating Test . . . 2-34
2.5.2.2 Dead Weight Loading Test . . . 2-34
2.5.2.3 Pipe Rotating Test . . . 2-35
2.5.2.4 Long Range Sensing . . . 2-35
2.5.2.5 Pipe Sleeve Relocating . . . 2-36
2.5.3 CMPI Direct Push Instrument . . . 2-36
2.6 Case Studies in the Lab . . . 2-36
2.6.1 5-Foot Corrugated Column . . . 2-36
2.6.2 18-inch Tall PVC Column Injection Test . . . 2-38
2.6.3 Measuring Distributed Strain from Poroelastic Processes . . . 2-40
2.6.3.1 Experimental setup . . . 2-41
2.6.3.2 Procedure, Results and Interpretation . . . 2-41
2.6.3.3 Loading Tests . . . 2-45
2.6.4 Air Pressure Column Test . . . 2-47

DISTRIBUTED INSTRUMENT DEVELOPMENT

2.1 Distributed Sensing Principles

2.1.1 Coherence-length-gated Microwave Photonics Interferometry (CMPI)

One of the unique advantages of optical fiber sensing is its ability to acquire spatially distributed information. The combination of ultra-low loss optical fibers and high-speed electronics now make it possible to continuously monitor various spatially varying parameters over tens of kilometers or even longer distance. The applications have also extended from the structural health monitoring to other areas such as the monitoring of geophysical properties , chemical/biological species and physiological parameters.

In general, distributed optical fiber sensing can be categorized into two groups. The first is the so called quasi-distributed sensing which cascades many discrete devices (e.g., fiber Bragg gratings, or FBGs) along the fiber. These cascaded sensor devices share the same signal processing instrument but sample the entire space at discrete points. It has the advantages of flexible deployment, multi-agent capability and high detection sensitivity. However, most of the existing systems can only multiplex a limited number of sensors.

Another category is the so-called fully distributed optical fiber sensing technology which is commonly based on the time domain reflectometry (TDR) of various kinds. In a traditional optical time domain reflectometry (OTDR) system, a short optical pulse launches into an optical fiber and the back scatterings of the light are recorded by the photodetector in the order of time of arrival. The scatterings can be the Rayleigh scattering of the fiber or the nonlinear signals such as Raman (ROTDR) and Brillouin (BOTDR) scatterings. The characteristics (e.g., the intensity and wavelength shift) of these scatterings are sensitive to the parameters to be measured (e.g., temperature or strain). However, the TDR based technologies have relatively low signal to noise ratio (SNR). The system needs to perform hundreds of averages to get decent sensing performance. The strain sensitivity for TDR type distributed sensing technology is generally around 10 $\mu\epsilon$.

Optical interference is very sensitive to the optical path difference (OPD) change. Phase-OTDR uses a coherent light source in a traditional OTDR system. The optical interference of the distributed Rayleigh scatterings within the duration of the light pulse is collected and processed. The strain sensitivity of phase-OTDR can be as high as 4 nϵ. However, phase-OTDR has the difficulty to quantitatively link the obtained interference signal to the specific parameters of interest unless phase recovery methods are deployed, because the random nature of the Rayleigh scattering. In addition to the traditional OTDR technique, the optical frequency domain reflectometry (OFDR) has also been developed for distributed optical fiber sensing. OFDR also uses a frequency-swept coherent light source. The time-of-arrival information is obtained by the Fourier transform of the optical signal of the frequency sweeping range. OFDR has much higher SNR and spatial resolution compared with the traditional OTDR. OFDR can resolve hundreds nϵ in strain. However, its measurement range is short.

In the past few years, microwave-photonics technologies have been investigated for optical fiber sensing. By introducing microwave modulation into the optical system, the optical detection is synchronized with the microwave modulation frequency. As a result, the system has a high SNR and thus an improved detection limit. In addition, the phase of the microwave-modulated light can be easily obtained and Fourier transformed to find the time-of-arrival information for distributed sensing. The microwave photonics technology has been demonstrated for both quasi-distributed and fully-distributed sensing. Recently, an incoherent optical carrier based microwave interferometry (OCMI) technique has been demonstrated for fully distributed sensing with high spatial resolution and large measurement range. The system used a microwave modulated incoherent (broadband) light source to interrogate cascaded intrinsic Fabry-Pérot interferometers formed by adjacent weak reflectors inside an optical fiber. When the distance between two adjacent reflectors was larger than the coherence length of the light source, the optical interference components in the received signal became zero and the microwave terms were processed to form a microwave interferogram, which was further analysed to calculate the optical path difference between any two reflectors along the fiber. Similar concept has also been successfully validated using large core multimode silica fibers and single crystal sapphire fibers. The method

has a number of unique advantages including high signal quality, relieved requirement on fabrication, low dependence on the types of optical waveguides, insensitive to the variations of polarization, high spatial resolution, and fully distributed sensing capability. However, the reported OCMI system only read the interference in microwave domain. As such the sensing resolution was low (in tens of με, limited by the long wavelength of the microwave signal and the intermediate frequency of the microwave source.

In this project, we developed a new coherent microwave-photonics interferometry (CMPI) system for distributed optical fiber sensing. The system uses a coherent light source to obtain the optical interference signal from the cascaded weak reflectors for high sensitivity sensing. The coherence length of the light source is carefully chosen or controlled to gate the signal so that distributed sensing can be achieved.

2.1.1.1 Theory

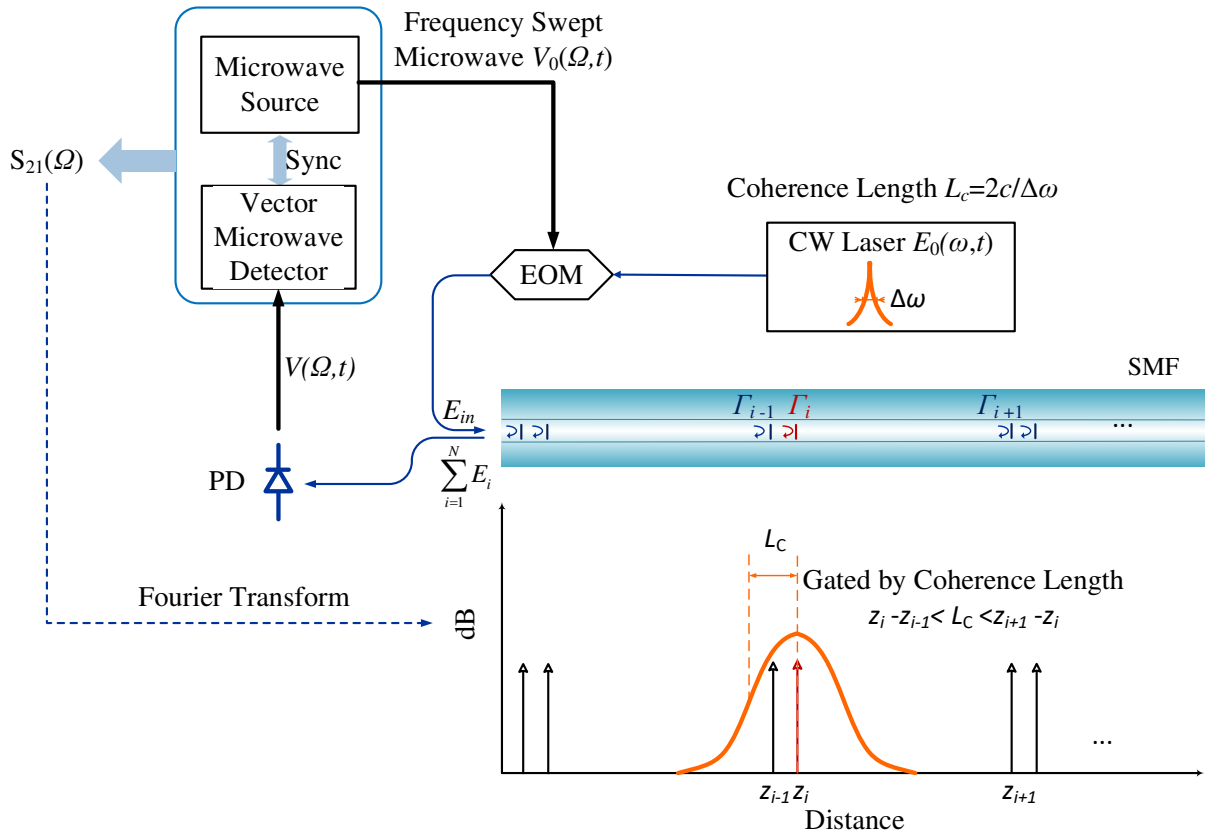

Figure 2.1: Schematic illustration of coherent microwave-photonics interferometry (CMPI).

The proposed CMPI system is schematically shown in Figure 2.1. A continuous wave (CW) laser with full width at half maximum (FWHM) of is used as the light source. The light intensity is modulated by the microwave signal and sent into a single mode fiber (SMF). There are N weak reflectors inscribed on in the core of the SMF. Light reflected by the reflectors and received by the photodetectror. The microwave photonics system synchronizes the detection and measures the amplitude and phase of the signal at the modulation frequency Ω. The complex frequency response S_{21} of the system normalized with respect to the input signal is

$$S_{21}(\Omega) = \frac{m}{2}\sum_{i=1}^{N}\int_{-\infty}^{\infty} A_{z_i}(\omega)^2\, d\omega \cdot \mathrm{e}^{-j\frac{\Omega n z_i}{c}} + \frac{m}{2}\sum_{i=1}^{N}\sum_{j=1,j\neq i}^{N}\int_{-\infty}^{\infty} A_{z_i}(\omega) A_{z_j}(\omega)\cos(\phi_i-\phi_j)\, d\omega \cdot \cos\frac{\Omega n(z_i-z_j)}{2c}\,\mathrm{e}^{-j\frac{\Omega n}{2c}(z_i+z_j)} \tag{2.1}$$

$$= \underbrace{\frac{m}{2}\sum_{i=1}^{N}\int_{-\infty}^{\infty} A_{z_i}(\omega)^2\, d\omega \cdot \mathrm{e}^{-j\frac{\Omega n z_i}{c}}}_{\text{self product term}} + \underbrace{\frac{m}{4}\sum_{i=1}^{N}\sum_{j=1,j\neq i}^{N}\int_{-\infty}^{\infty} A_{z_i}(\omega) A_{z_j}(\omega)\cos(\phi_i-\phi_j)\, d\omega \cdot \left(\mathrm{e}^{-j\frac{\Omega n z_i}{c}} + \mathrm{e}^{-j\frac{\Omega n z_j}{c}}\right)}_{\text{cross product term}} \tag{2.2}$$

By applying complex Fourier transform to $S_{21}(\Omega)$, we obtain the time domain signal

$$F(t_z) = \sum_{i=1}^{N} I_N(z_i)\,\delta\left(t_z - \frac{n z_i}{c}\right) \tag{2.3}$$

where t_z denotes the time variable and

$$I_N(z_i) = \frac{m}{2}\int_{-\infty}^{\infty} A_{z_i}(\omega)^2\, d\omega + \frac{m}{2}\sum_{j=1,j\neq i}^{N}\int_{-\infty}^{\infty} A_{z_i}(\omega) A_{z_j}(\omega)\cos(\phi_i-\phi_j)\, d\omega \tag{2.4}$$

$$= \frac{m}{2}\int_{-\infty}^{\infty} \Gamma_i^2 A_0(\omega)^2\, d\omega + \frac{m}{2}\sum_{j=1,j\neq i}^{N}\int_{-\infty}^{\infty} \Gamma_i\Gamma_j A_0(\omega)^2 \cos\frac{\omega n(z_i-z_j)}{c} d\omega \tag{2.5}$$

$I_N(z_i)$ represents the time domain pulse located at z_i. The amplitude of $I_N(z_i)$ is the sum of two parts. The first part is a constant determined by the reflectivity of the reflector and the input light power. The second part is the superposition of the optical interference among the reflected lightwaves of the ith and any other reflectors in the system. The intensity of the interference of any two waves changes sinosoidally as function of phase difference between them. The amplitude of the sinusoidal function approaches zero as the phase difference increases.

The coherence length L_c performs as a truncating function, which limits the number of reflectors contributing to the amplitude of the time domain pulse. If the OPD between the jth and i^{th} reflectors is much larger than the coherence length of the light source L_c, the jth reflector's contribution becomes very small and can be neglected. On the other hand, if the OPD between the ith and j^{th} reflector is smaller than L_c, slightly change of the OPD can change the value of the second part dramatically. Thus, the amplitude variation of the time domain pulse can provide a sensitive indication of the OPD changes.

We can engineer the system to make sure that at any fiber location there are only two reflectors within the coherence length of the light source. It becomes apparent that we can either control the linewidth ($\Delta\omega$) of the optical source or the distance between two adjacent reflectors to include or exclude the reflectors to contribute to the second term of eq. 2.5. If we further assume that the OPD between the two reflectors is much smaller than L_c, then $I_N(z_i)$ can be approximated as

$$I_2(z_i) \approx \frac{m\Delta\omega A_0^2}{16}\left[\Gamma_i^2 + \Gamma_i\Gamma_j \cdot \exp\frac{-n|z_i - z_j|}{L_c} \cdot \cos\frac{\bar{\omega}n(z_i - z_j)}{c}\right] \tag{2.6}$$

$$\approx \frac{m\Delta\omega A_0^2}{16}\left[\Gamma_i^2 + \Gamma_i\Gamma_j \cdot \cos\frac{\bar{\omega}n(z_i - z_j)}{c}\right] \tag{2.7}$$

$I_N(z_i)$ varies sinusoidally as a function of the OPD between the two reflectors. The period of the sinusoidal function equals to the average optical wavelength. A minor change in OPD between the two reflectors can produce a detectable change in the amplitude of the time domain pulses. The locations of the reflectors can be identified by their corresponding position in the time axis. Therefore, the coherence gated microwave-photonic system can be used for distributed sensing with very high sensitivity.

2.1.1.2 Lab Demonstration

To validate the signal processing method, a single pair of reflectors separated by 10 cm were fabricated on a SMF by femtosecond laser micromachining. The femtosecond laser beam was focused into the fiber core to slightly modify the refractive index of the focusing area without striping the polymer coating of the fiber. The two reflectors had very close reflectively and they formed a weak reflection FPI with a cavity length of 10 cm. The two fiber ends of the FPI were glued onto two motorized translation stages (Newport PM500) respectively. The two fixing points were separated by 1.55 m and the FPI was positioned in the middle of the two stages. Axial strains were applied to the FPI by moving one stage at 1 με (corresponding to about 0.6 με) per step. The sweeping microwave bandwidth of the VNA was from 0.1 to 4.1 GHz. The light source was a tunable laser that had a Lorentzian shape spectrum with FHWM about 100 kHz (Agilent 81640A) whose coherence length was about 0.954 km at the center wavelength of 1543 nm.

The amplitudes of the time domain signals under different applied strains are shown in Figure 2.2a. The insert shows the amplitudes of the two peaks (at the time points t_{s1} and t_{s2}) as function of the applied strain. The microwave bandwidth was large enough to separate the two reflectors as two time-domain pulses. It is obvious that the amplitudes of the two reflector pulses changed sensitively as a function of the applied strain. The changes of the two peak amplitudes were in phase. Figure 2.2b plots the real part of the signal and the insert shows the peak of the real part at the time points t_{s1} and t_{s2} as a function of the applied strain. The amplitudes of the real part of the signal were also in phase. A close comparison of the Figures 2.2a and 2.2b appears that the amplitude changed faster than the real part of the signal. The period of the sinusoidal function is 7.2 με, which is slightly larger than the theoretical period 6.5 με , where we assume the effective strain-optic coefficient P_{eff} is about 0.204. Several possibly reasons lead to the mismatch. The major reason is that the fiber was glued on the stage without striping off the coating, so the applied strain was not 100 percent transferred to the sensor due to the shear deformation at the coating and adhesive.

2.1.2 Microwave Photonics Low-Coherence Interferometry (LCI)

The CMPI technique provides high sensitivity for distributed sensing. By detecting the phase change through optical interference, nε-level sensitivity can be achieved. However, to discriminate cascaded IFPIs and avoid crosstalk among sensors, dark zones (low-sensitivity regions) need to be inserted between adjacent IFPIs, and the coherent length of the laser source also needs to be carefully controlled, which increases the system complexity.

Low-coherence interferometry (LCI) is initially used for remote absolute distance measurement, in which a local receiving interferometer (LRI) is connected in-line with the remote sensing interferometer. The optical path difference (OPD) of the LRI (length difference between two arms of the interferometer) is adjusted to match that of the sensing interferometer within the coherence length of the laser source, such that the interference occurs at the output of the LRI. Inspired by the LCI, we modified the CMPI system by adding a local Michelson interferometer (MI). The MI is utilized as the LRI in the original CMPI system. Consequently, the dark zones along the sensing fiber are eliminated, and the requirement for a laser source is also relieved. The schematic of the LCI-CMPI system is shown in Figure 2.3.

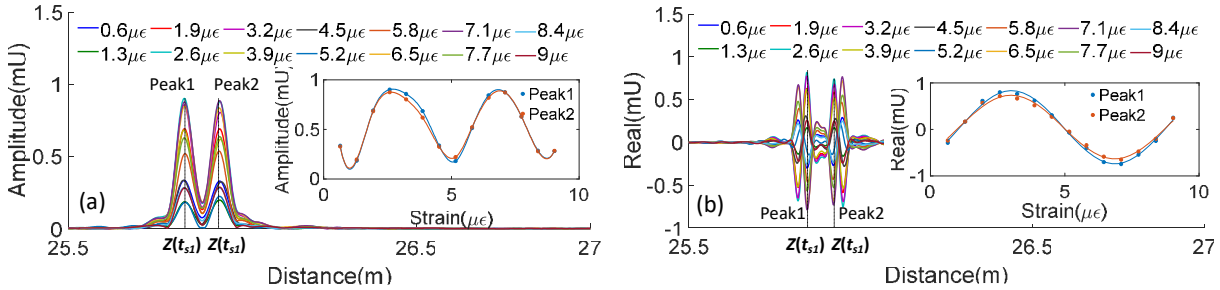

Figure 2.2: Strain response of an FPI consisting of two reflectors separated by a distance of 10 cm using a microwave bandwidth of 4 GHz. (a) Amplitude of the time-domain pulse under various applied strains. Inset: amplitudes of the two peaks as a function of the applied stain. (b) Real parts of the time-domain signals shown in (a). Inset: amplitudes of the two peaks as function of the applied stain.

The interrogation part of the LCI-CMPI system is the same as the original CMPI system. The sensor array is formed by weak reflectors with equal separations between any two adjacent reflectors. A Michelson interferometer which has the length difference between two arms very close to the gauge length of the sensors (L) is added in the system. The light reflected from each reflector would pass the MI first, and then be routed back to the detector. Instead of directly measuring the length change of each sensor, the new system measures the length difference (ΔL) change between each sensor and the length difference of the two arms of the MI. Thus, the coherence length of the light source only needs to cover the ΔL to produce high contrast signal, regardless of the gauge length of the sensors.

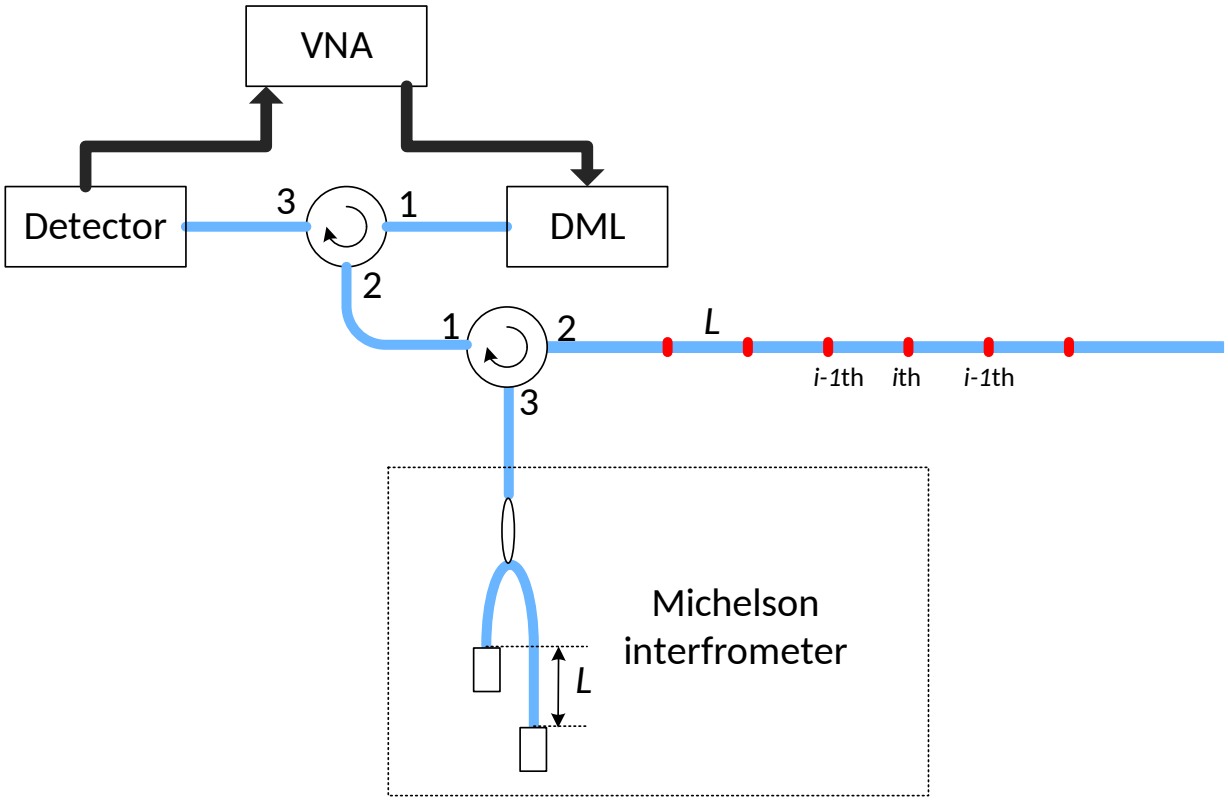

Figure 2.3: Schematic of the LCI-CMPI system.

2.1.2.1 Theory

Assume there are N reflectors along on the sensing fiber, and the distance between any two adjacent reflectors is L. After Fourier transform, there will be $N+1$ pulses showing in time domain signal as:

$$F(t_z) = I_1\,\delta\left(t_z - \frac{n\,z_1}{c} - \frac{n\,z_s}{c}\right) + \sum_{i=1}^{N-1} I_{i+1}\,\delta\left(t_z - \frac{n\,z_i}{c} - \frac{n\,z_L}{c}\right) + I_{N+1}\,\delta\left(t_z - \frac{n\,z_N}{c} - \frac{n\,z_L}{c}\right),$$

where c is the speed of light in vacuum, n is the refractive index of the fiber, z_i is the distance that the light travels from the directly modulated laser (DML) to the ith reflector and then back to the photodetector, z_s is the distance that the light travels force and back within the short arm of the MI, t_z denotes the time variable. $F(t_z)$ is the superposition of $N+1$ delta functions with different time delays nz_i/c, where the amplitude of each delta function is expresses as:

$$I_i = \begin{cases} \frac{m}{8}\Gamma_1^2 \int_{-\infty}^{\infty} A(\omega)^2\,d\omega & i = 1 \\ \frac{m}{8}\left(\Gamma_{i-1}^2 - \Gamma_i^2\right) \int_{-\infty}^{\infty} A(\omega)^2\,d\omega & i = 2, 3, ..., N \\ \frac{m}{8}\Gamma_N^2 \int_{-\infty}^{\infty} A(\omega)^2\,d\omega & i = N+1 \end{cases}$$

where Γ_i is the reflectivity of the ith reflector, ω is the frequency of the optical carrier, A is the spectrum density of the optical carrier. The amplitude of the ith delta function ($1 < i < N+1$) changes sinusoidally as function of the strain ϵ applied to the sensor formed by the $i-1^{\text{th}}$ and the ith the reflector. The strain sensitivity is proportional to the gauge length of each sensor L.

2.1.2.2 Lab demonstration

The distributed strain has been measured by using the LCL-CMPI system to demonstrate the idea. 9 reflectors were fabricated on a single mode fiber (SMF) to form the sensor array with a separation of 15 cm between adjacent reflectors (Figure 2.4a). The sensor array was fixed on two motorized linear translation stages (Newport PM 500) by using all-purpose glue. The two fixing points were 1.77 meters apart. Axial strains of 0.565 μϵ per step were applied to the reflector pairs formed Fabry-Pérot interferometers (FPIs) by moving one stage at 1 μm per step. Total strain of 11.3 μϵ was applied to the sensor. The amplitude change as function of applied strain for all of the 9 reflectors formed 8 sensors are shown in Figure 2.4b from pulse 4 to pulse 11. As the strain has been applied uniformly to the sensors, all of the respective pulses experienced the similar period of change. The experimental result showed that the measured amplitude change vs. strain fitted the mathematical model well, and there was no obvious cross talk among sensors.

2.1.3 Phase Demodulation by Frequency Chirping in CMPI

The CMPI measures the intensity of the interferometer output. The measured value would be ambiguous, in the sense that it does not yield a unique reading of phase; in addition, it would not provide a reliable indication of fringe movement direction and would thus prohibit fringe tracking. Theoretically, there are ways to calibrate sensors, but they are either not practical or too complicate for the field testing. We developed a signal processing method, which uses the current CMPI system but reads pair of signals for each sensor from the respective time pulse(s). The two signals could be either the amplitude of the two pulses, or the real and imaginary part of the one merged pulse. Due to the chirp effect of electro-optic modulator (EOM), the two signals record the intensity of the interferometer (sensor) with different adding phase. Those two signals form the quasi-quadrature fringes and could provide a suitable reading of the sensor optical phase difference (OPD).

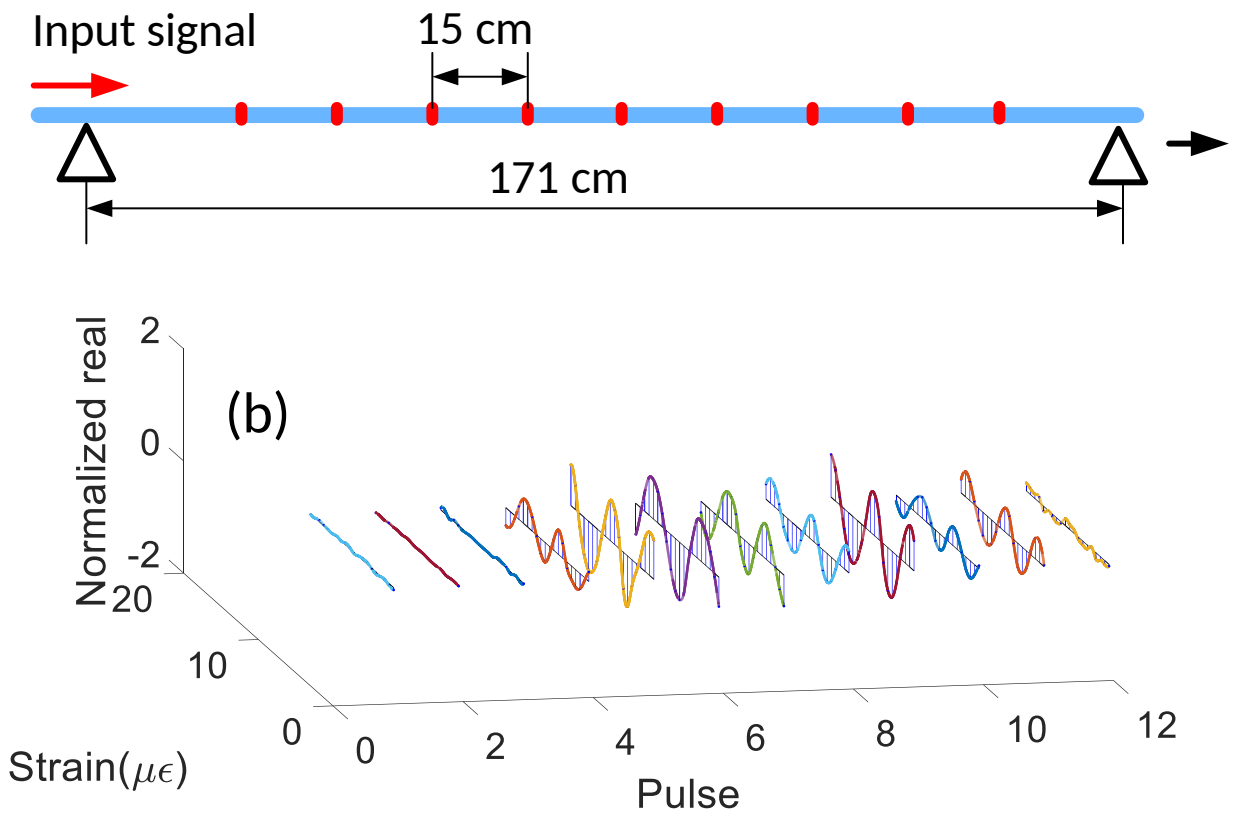

Figure 2.4: (a) Schematic of the strain measurement. (b) Amplitude change as function of applied strain for each time pulse.

2.1.3.1 Theory

A single arm modulated Mach Zehnder interferometer (MZI) type EOM is used as intensity modulator in a CMPI system. Assume there are two reflectors h, g along the fiber, and the optical distance between them is much smaller than the coherence length of the optical carrier. The reflectivity of them are A_g and A_h receptivity. The time domain signal can be expressed as:

$$\begin{aligned} F(t) \approx & -8A_h J_1(a_2)\cos\left(\frac{\Delta\phi}{2}\right)\left\{A_h\sin\left(\frac{\Delta\phi}{2}\right)+A_g\sin\left(\phi_h-\phi_g-\frac{\Delta\phi}{2}\right)\right\}\delta\left(t-\frac{nz_h}{c}\right) \\ & -8A_g J_1(a_2)\cos\left(\frac{\Delta\phi}{2}\right)\left\{A_g\sin\left(\frac{\Delta\phi}{2}\right)+A_h\sin\left(\phi_h-\phi_g+\frac{\Delta\phi}{2}+\pi\right)\right\}\delta\left(t-\frac{nz_g}{c}\right), \end{aligned} \tag{2.8}$$

where c is the speed of light in vacuum, n is the refractive index of the fiber, z_h (z_g) is the distance that the light travels from the EOM to the hth (g^{th}) reflector and then back to the photodetector, ϕ_h (ϕ_g) is the respective phase for light traveling that distance, $\Delta\phi$ is the static phase difference between the two arms of the EOM, which can be controlled by the DC voltage that applies to the EOM. Equation 2.8 shows that the amplitudes of pulses formed by the two reflectors are both decided by the OPD between the two reflectors, and both of them change sinusoidal as function of the OPD between them. There's a phase shift $\Delta\phi+\pi$ between the two changing functions. The phase shift is a constant, and it can be adjusted by changing the bias voltage of the EOM.

When the microwave bandwidth is not wide enough to separate the two paired pulses from one interferometer in time domain, the two pulses merge into one. The peak point of the merged pulse could locate at any time point between nz_h/c and nz_g/c. Assuming that the peak locates at $t_c = n\left(z_h + z_g\right)/2c$, the time domain signal at t_c is expressed as:

$$\begin{aligned} F\left(t_c\right)_{\Delta\Omega} \approx & -8A_h J_1\left(a_2\right)\cos\left(\frac{\Delta\phi}{2}\right)\left\{A_h \sin\left(\frac{\Delta\phi}{2}\right) + A_g \sin\left(\phi_h - \phi_g - \frac{\Delta\phi}{2}\right)\right\} \\ & \cdot \operatorname{sinc}\left[\Delta\Omega\frac{n\left(z_g - z_h\right)}{c}\right]\exp\left[-j\Omega_c\frac{n\left(z_g - z_h\right)}{c}\right], \\ \approx & -8A_g J_1\left(a_2\right)\cos\left(\frac{\Delta\phi}{2}\right)\left\{A_g \sin\left(\frac{\Delta\phi}{2}\right) + A_h \sin\left(\phi_h - \phi_g - \frac{\Delta\phi}{2} + \pi\right)\right\} \\ & \cdot \operatorname{sinc}\left[\Delta\Omega\frac{n\left(z_h - z_g\right)}{c}\right]\exp\left[-j\Omega_c\frac{n\left(z_h - z_g\right)}{c}\right], \end{aligned} \tag{2.9}$$

where $\Delta\Omega$ and $\Delta\Omega_c$ are the bandwidth and center frequency of the modulation microwave band. The real part of the merged time pulse is expresses as:

$$\begin{aligned} \Re\left[F\left(t_c\right)_{\Delta\Omega}\right] = & 8J_1\left(a_2\right)\cos\left(\frac{\Delta\phi}{2}\right)\operatorname{sinc}\left[\Delta\Omega\frac{n\left(z_g - z_h\right)}{c}\right]\cos\left[\Omega_c\frac{n\left(z_g - z_h\right)}{c}\right] \\ & \cdot\left\{-A_h^2 \sin\left(\frac{\Delta\phi}{2}\right) - A_g^2 \sin\left(\frac{\Delta\phi}{2}\right) + 2A_h A_g \cos\left(\phi_h - \phi_g\right)\sin\left(\frac{\Delta\phi}{2}\right)\right\}, \end{aligned} \tag{2.10}$$

and the imaginary part is expressed as:

$$\begin{aligned} \Im\left[F\left(t_c\right)_{\Delta\Omega}\right] = & 8J_1\left(a_2\right)\cos\left(\frac{\Delta\phi}{2}\right)\operatorname{sinc}\left[\Delta\Omega\frac{n\left(z_g - z_h\right)}{c}\right]\cos\left[\Omega_c\frac{n\left(z_g - z_h\right)}{c}\right] \\ & \cdot\left\{-A_h^2 \sin\left(\frac{\Delta\phi}{2}\right) - A_g^2 \sin\left(\frac{\Delta\phi}{2}\right) + 2A_h A_g \sin\left(\phi_h - \phi_g\right)\sin\left(\frac{\Delta\phi}{2}\right)\right\}. \end{aligned} \tag{2.11}$$

The optical phase terms are marked as red in the Equations 2.10 and 2.11. It is shown that there is a $\pi/2$ phase shift between the real and imaginary part, so the quadratic detection can also be achieved by using the real and imaginary part of the peak point on the merged pulse to realize. The bias voltage can be used to adjust the amplitude of the real and imaginary part to achieve better signal contrast. Slightly offset from the center point between two reflectors should cause a phase shift deviation from $\pi/2$, but the phase shift should easily be found through calibration.

The calibration and phase recovery are very similar to the Michelson interferometer strain meter which has been reported in this project. The sensors shall be placed in a room temperature lab, where low frequency environmental noise will be applied to all the sensors for long time (several hours to days) during which the peak information of each sensor will be recorded continuously. The data will be used for the ellipse fitting. Each sensor has a set of fitting coefficients which will be used for the phase recovery during the sensing.

2.1.3.2 Lab Demonstration

The bias voltage effects to the constant phase shift of two paired fringes has demonstrated through lab experiments. We have also demonstrated the feasibility of the signal processing method when use it for the multiple sensors distributed sensing.

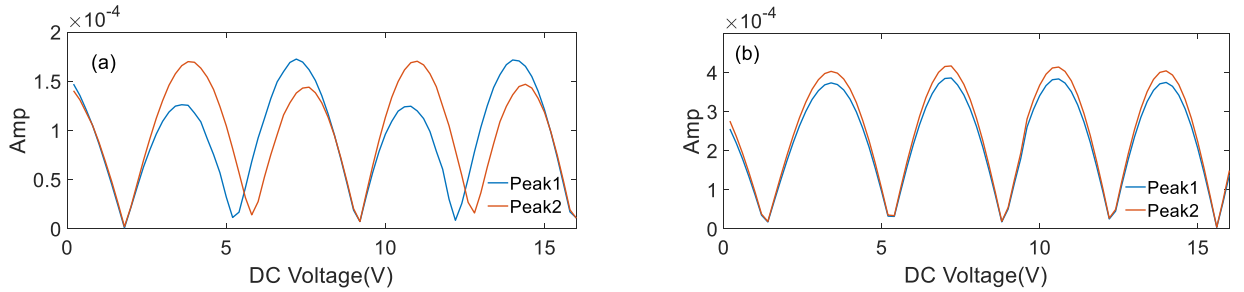

Figure 2.5: Amplitude change of the two peaks as function of applied bias voltage to the EOM when use (a) coherent light (b) incoherent light.

A 15 cm cavity IFPI has been used as a sensor in a CMPI system to demonstrate the bias voltage effects. The two reflectors formed two peaks in time domain. Figure 2.5a shows the amplitude of both time peaks changes as function of the bias voltage. Because the phase shift between two peaks changes, the amplitude ratio between them is not a constant. Note that when the coherence length of the light source is longer than the sensor cavity length, the phase shift equals zero. Therefore, when use the wide band light source, the amplitude of the two peaks always changed in phase as a function of the bias voltage as shown in Figure 2.5b.

The constant phase difference of the two paired fringes at different bias voltage was investigated. The sensor was put on a table, where the temperature varied slowly. 50 sampled data were taken at each bias voltage, and the signal were sampled at 0.1 Hz. Figure 2.6 shows the fitted ellipse and the sensor data at eight different bias voltages. It is shown that the phase delay ϕ_0 between the two quadrature fringe signals change gradually as function of bias voltage, and the phase delay of $\pi/2$ can be reached when the bias voltage is adjusted to around 3.6 V.

The distributed sensing data analyzing capability was demonstrated by using a reflector array. 8 weak reflectors were fabricated on a single model fiber, and the separation distance between two reflectors were 15 cm. The reflector array was fitted into the modified c-CMPI system, where a 15-cm cavity Michelson interferometer was used as a reference interferometer. The 8 reflectors formed 7 cascaded sensing sections. In the time domain, there were 9 pulses as shown in Figure 2.7a, where the middle 7 pulses were the sensing indicators for the respective 7 sections. The real and imaginary part of the peak point of each pulse formed the quasi-quadrature fringes. The 1st and the 8th pulses can be used as the power reference for sensor calibration and phase recovery. The sensor was put on a table, where the temperature varied slowly. 300 sampled data were taken at each bias voltage. The signal sweep interval was 10 s, and it took 3 s to finish a single microwave spectrum sweep. In this experiment all the peak values were normalized to the amplitude of the 1st peak before performing the ellipse fitting. Figure 2.7b-h shows the fitted quadrature fringe signals traced ellipses by using the 7 peak values. The constant phase offset between the two paired fringe signals for the 7 sensors were found through the fitting. As the exactly center locations between two reflectors were not easy to locate, the phase offsets for all 7 sections were different, but the fitted coefficients for each time point were close for several times of calibration. The two paired fringe signals of 3rd sensor could not cover the whole ellipse, because the calibration time was short. Longer time calibration is needed for a better result. The data acquisition time was about 3 s for each measurement, so the high frequency noise has been picked up during the data acquisition, which makes the ellipses look blurry. Faster microwave frequency sweep can help to decrease the noise.

2.1.4 Coherence Control

CMPI uses coherence length of the light source as a gate function, which only allows the reflectors with separation distance smaller than the coherence length contributes to the amplitude of the time domain pulse at each respective location, so that the distributed sensing can be achieved. Therefore, we can engineer the system to make sure that at any fiber location there are only two reflectors within the coherence length of light source to form an interferometer. The separation of adjacent two interferometers should be much larger than the coherence length to avoid cross talk, so the spatial resolution of CMPI system is decided by the coherence length. A MI can be added into the system to

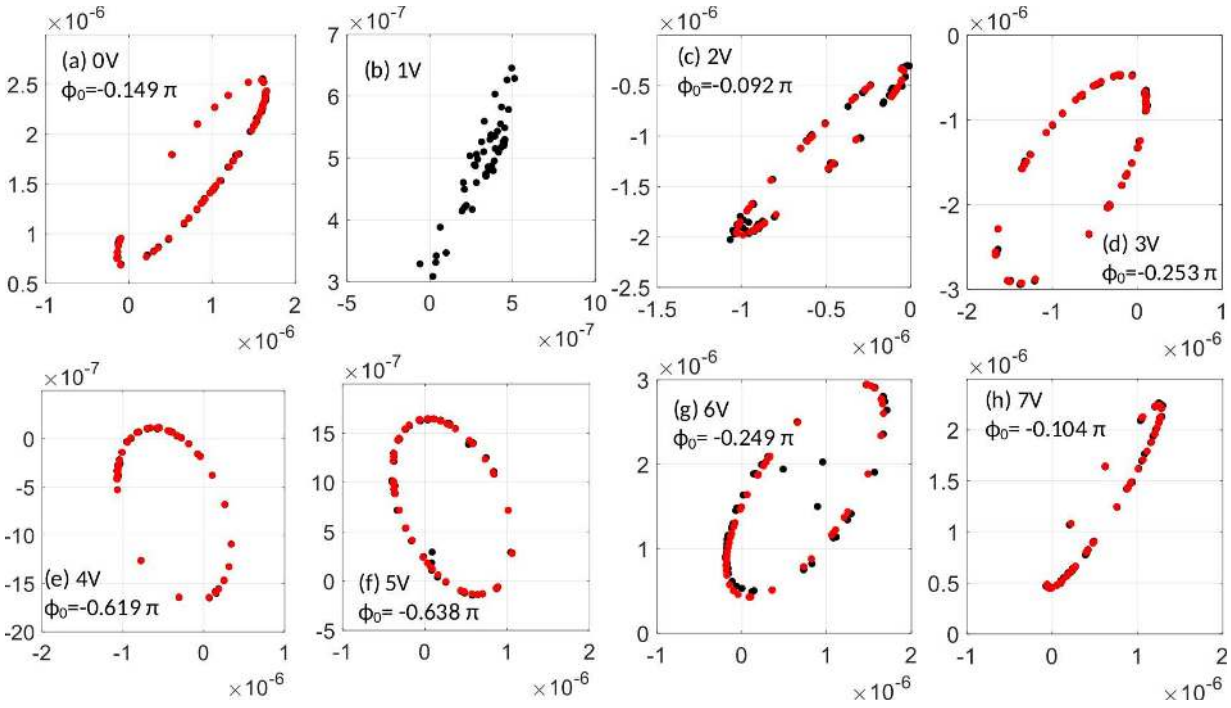

Figure 2.6: Quasi-quadrature fringe signals trace out an ellipse under bias voltage (a) 0 V, (b) 1 V, (c) 2 V, (d) 3 V, (e) 4 V, (f) 5 V, (g) 6 V, (f) 7 V. The black dots show the original signal, and the red dots show the fitted signal.

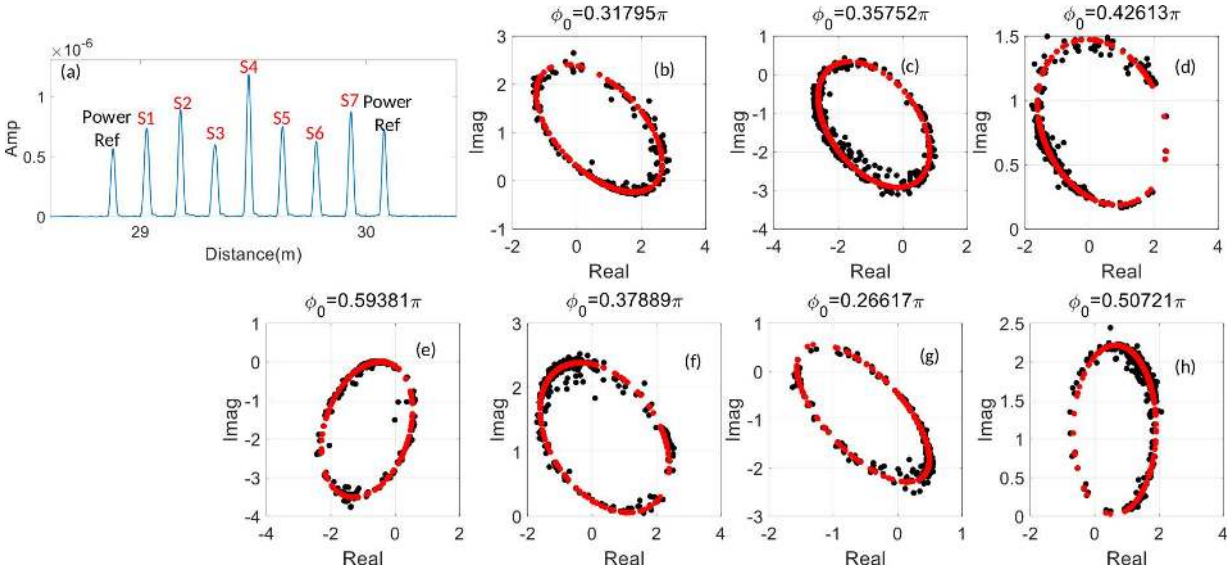

Figure 2.7: (a) Time domain signals of the 8 reflectors sensor array interrogated by the CMPI system. The quasi-quadrature fringe signals trace out an ellipse by using the real and imaginary part of the peak point data of (b) S1, (c) S2, (d) S3, (e) S4, (f) S5, (g) S6, (h) S7. The black dots show the original signal, and the red dots show the fitted signal.

realize the fully distributed sensing, and then we need to have the coherence length larger than the length difference ΔL between the gauge length of the MI and any two adjacent reflectors, but also much smaller than the gauge length. We tried to make ΔL close to zero, but limited by the accuracy of the reflector fabrication, the ΔL can be from several millimeters to 2 centimeters. On the other hand, the gauge length is needs from tens of centimeters to meters to get required strain sensitivity. Therefore, the light with coherence length of several centimeters is needed.

The coherence length is inversely proportional to the linewidth of the laser. For the coherence length of 10 cm, the respective linewidth is about 1 GHz (8 pm), but most of the commercial light source either has the linewidth smaller than 5 MHz (distributed feedback (DFB) laser) or larger than several THz (Amplified Spontaneous Emission, or ASE light source). Vertical-Cavity Surface-Emitting Laser (VCSEL) could have linewidth of 10 GHz, but it normally has low output power. In the past, we filtered one longitude mode from a Fabry-Pérot (FP) laser by using the Fiber Bragg Grating (FBG) type optical filter. However, only filtering one mode out caused at least 10 dB power loss, so it is not very practical for the field testing. We developed another way to change the coherence length of the light source by fast scanning the output wavelength of the narrow linewidth DBF Laser. Since Vector Network Analyzer (VNA) detects the time average system response at each scanning frequency, so the effective results measured by the VNA is the average of the all scanning wavelength. The effective coherence length of the light source should be shortened by this process.

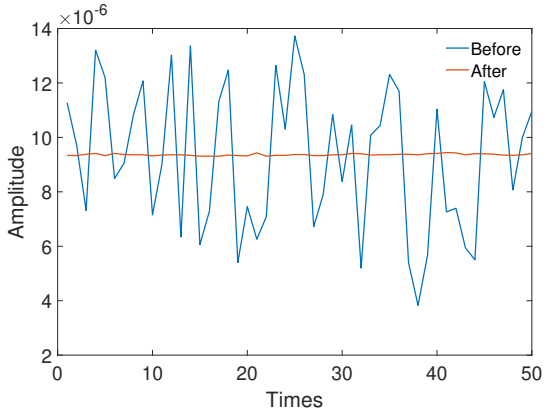

Figure 2.8: Amplitude of time pulse change as function of time before and after applying laser current modulation.

In our system, a commercial DBF laser is used in the design. The linewidth of the laser is about 2 MHz, which corresponding to the coherence length of 50 m. The center wavelength shifts 3.6 pm/mA around laser current of 170 mA, so modulate the laser current with amplitude of 2.3 mA, can shorten the coherence length to 10 cm. The output power also changes as function of the inject current, but 2.3 mA current change only induce power change of 0.08 dB which is negligible. A waveform generator (Analog Devices AD5932) is used to produce the modulation signal and send into the modulation port of the laser controller. A pair of reflectors with separation distance of 10 m were fabricated on a single mode fiber, and they formed a FP interferometer (FPI), which was used to demonstrate the coherence length control. The FPI was put on the optical table in an open area. The air flow brought temperature change and also changed the strain to the FPI randomly. The FPI was connected to the CMPI system and the data was taken every 1 s. Figure 2.8 shows the amplitude of the time pules peak formed by the FPI as function of measurement time before and after adding the current modulation. The coherence length is larger than the optical path difference (OPD) of the FPI before applying the modulation signal, so the amplitude of the time pulse changed dramatically. After applying the laser current modulation, the amplitude calmed down. The results indicate that the effective coherence length of the laser can be decreased by fast modulating the laser current.

The coherence length control capability is limited by the lowest sampling rate of VNA. As the laser center wavelength is changed due to the refractive index of the gain material in the laser changing, which is a comparatively slow process. On the other hand, the laser current oscillation rate should be several times higher than the VNA frequency sweeping rate to make sure that all the wavelengths are used at each microwave frequency, so the averaging among all wavelength can be realized.

2.1.5 CMPI for Distributed Acoustic Sensing

CMPI for distributed acoustic sensing (DAS) is a new method that we developed to measure rapid distribute strain signals. The original CMPI technique requires scanning through the entire microwave band to acquire one frame of distributed strain information. The frequency scanning time limits the measurement bandwidth to less than 5Hz. To

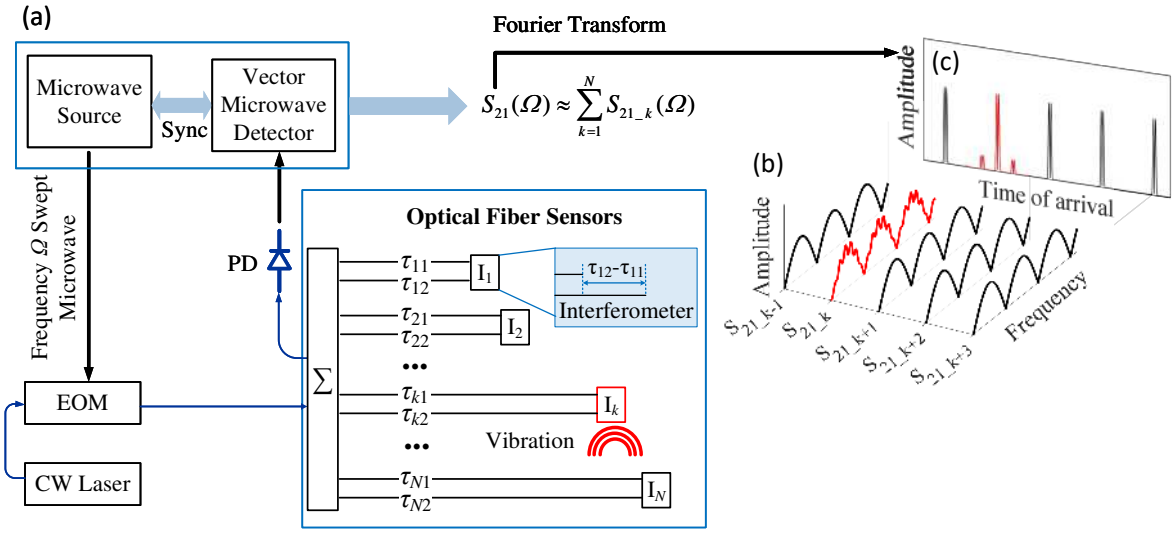

Figure 2.9: (a) Schematic illustration of the CMPI system for acoustic distributed acoustic sensing. PD: Pho-todetector, EOM: electro-optic modulator, CW laser: continuous-wave laser. (b)The amplitude of the decomposed frequency domain signal from each interferometer. (c) The amplitude of the time domain signal. .

increase the measurement bandwidth, CMPI DAS makes measurements made with the CMPI system, but process the strain signal through a different route. The method records the strains caused by acoustic signals during the microwave frequency scanning and separates the strain signals in space through a frequency-time joint approach. As a result, an acoustic detection bandwidth of tens of kilohertz for distributed sensing with centimeter-scale spatial resolution can be obtained.

2.1.5.1 Theory

A mathematical model of the CMPI system represents the main components, including a microwave source, a vector microwave detector, a light source, an electro-optical modulator, a photodetector (PD), and distributed sensors formed by interferometers (Figure 2.9(a)). A continuous-wave (CW) laser with a center frequency of ω is used as the light source. The light intensity is modulated by a microwave signal. The light launches into an optical fiber sensing network and is reflected by reflectors with respective time delays τ. Any two reflections that have a lag (τ_{k2}-τ_{k1}) much smaller than the coherence time of the laser produce optical interference, so the responsive light paths form an interferometer I_k. Light reflections are injected into a PD, which converts the light power into electric voltage and sends it back to the vector microwave detector. The frequency of the microwave signal is swept over a designed range. At each modulation frequency Ω, synchronized detection is conducted, and the amplitude variation and phase shift of the modulation envelop are measured.

The complex frequency response of the system S_{21} can be approximately expressed as

$$S_{21}(\Omega) \approx rect\left(\frac{\Omega - \Omega_c}{B_\Omega}\right) \cdot \sum_{k=1}^{N} S_{21_k}(\Omega),$$

where$B_\Omega$and Ω_c are the bandwidth and center frequency of the microwave signal and S_{21_k} is the frequency response

from the *k*th interferometer, which is expressed as

$$S_{21_k}(\Omega) = m\left[\left({A_{k1}}^2 + A_{k1}A_{k2}\cos\Delta\phi_k\right)e^{-j\tau_{k1}\Omega} + \left({A_{k2}}^2 + A_{k1}A_{k2}\cos\Delta\phi_k\right)e^{-j\tau_{k2}\Omega}\right],$$

where *m* is a constant decided by the modulation depth of the EOM; A_{k1} and A_{k2} are the amplitudes of the two reflected waves; $\Delta\phi_k$ is the optical phase difference between the two waves. If the OPD of the two reflected waves in the *k*th interferometer (L_k) changes sinusoidally as a function of time, then the optical phase difference varies accordingly and is expressed as

$$\Delta\phi_k = \left[L_k + \delta_k\cos(\Theta_k t + \Phi_0)\right]\omega/c,$$

where Θ_k and δ_k are the frequency and amplitude of the dynamic OPD changes, t is the time variable. If the microwave modulation frequency is linearly scanned with a step of $\Delta\Omega$ and a constant sampling time Δt , we can express t as

$$t = \left(\Omega - \Omega_{start}\right)/\Delta\Omega\cdot\Delta t,$$

The time domain signal is the complex inverse Fourier transform of the S_{21}, and it can be expressed as

$$F(t_z) = \left[mB_\Omega\mathrm{sinc}\left(B_\Omega t_z\right)e^{-j\Omega_c t_z}\right] * \sum_{k=1}^{N} F_k(t_z),$$

which includes 'Static' and 'Dynamic' components as

$$\begin{aligned} F_k(t_z) = {} & \left\{\left[{A_{k1}}^2 + A_{k1}A_{k2}\cos\tfrac{L_k\omega}{c}\right]\delta(t_z-\tau_{k1}) + \left[{A_{k2}}^2 + A_{k1}A_{k2}\cos\tfrac{L_k\omega}{c}\right]\delta\left(t_z-\tau_{k2}\right)\right\}_{\text{Static}} \\ & -\left\{\begin{array}{l} \frac{\delta_k\omega}{c}A_{k1}A_{k2}\sin\frac{L_k\omega}{c}\cdot\left[\delta\left(t_z-\tau_{k1}+\Theta_k\frac{\Delta t}{\Delta\Omega}\right)e^{j\Phi_{cons}} + \delta\left(t_z-\tau_{k1}-\Theta_k\frac{\Delta t}{\Delta\Omega}\right)e^{-j\Phi_{cons}}\right] \\ +\frac{\delta_k\omega}{c}A_{k1}A_{k2}\sin\frac{L_k\omega}{c}\cdot\left[\delta\left(t_z-\tau_{k2}+\Theta_k\frac{\Delta t}{\Delta\Omega}\right)e^{j\Phi_{cons}} + \delta\left(t_z-\tau_{k2}-\Theta_k\frac{\Delta t}{\Delta\Omega}\right)e^{-j\Phi_{cons}}\right] \end{array}\right\}_{\text{Dynamic}} \end{aligned}$$

The 'Static' component includes two time-pulses (main lobes) that are generated by the two reflected waves from interferometer I_k, and they are centered at τ_{k1} and τ_{k2}, respectively. The 'Dynamic' component is formed by time pulses generated by the dynamic OPD changes. The dynamic pulse pairs behave as sidelobes, which occur at both sides of the respective main lobes (Figure2.9c).

The offset between a side lobe and the corresponding main lobe (D_{offset}) is directly proportional to the acoustic frequency Θ_k with a scaling coefficient $\Delta t\Delta\Omega$. The amplitude of the dynamic OPD change δ_k is directly proportional to the amplitude of the sidelobes.

We calculate δ_k by using the sidelobe amplitude and the interference phase. The interference phase is calculated using the chirp effect of the EOM to perform quadrature-phase demodulation. This is done by tuning the EOM bias to add opposite phase shifts of $\pi/4$ to the optical interference phase, so the peak values of the two main lobes are in quadrature. The standard quadrature-phase demodulation method can be used to calibrate the conic coefficients and calculate the interference phase.

2.1.5.2 Lab Demonstration

We used an array of 12 weak reflectors 5 cm apart on a piece of SMF and an optical fiber based MI (Figure2.10) to demonstrate the idea. The MI was made with a 1x2 SMF 50:50 coupler and two Faraday rotation mirrors (FRM). The

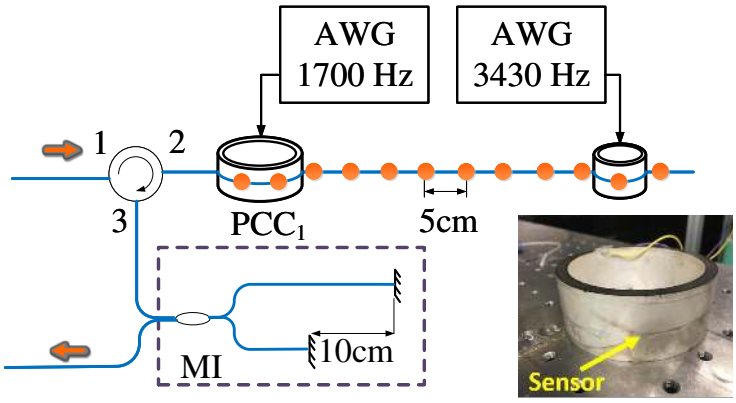

Figure 2.10: Schematic of the experiment to demonstrate CMPI for DAS.

MI was embedded in a block of epoxy to reduce the OPD change induced by environmental influences (temperature, vibration, etc.). The light was reflected by the reflectors and then reflected by the MI. The co-herence length of the light source is shorter than two times the optical interval of the reflectors, so only the reflector pairs with separation distance close to the arm length difference of the MI are selected to form the interferometers. For example, the light reflected by the 1st reflector and longer arm of MI would produce strong interference with the light reflected by the 3rd reflector and shorter arm of MI. The strain changes be-tween 1st and 3rd reflectors (2nd and 4th, 3rd and 5th, and so on) can be measured using this system . Therefore,10 sensing units along the SMF were formed for spatially continuous monitoring.

Two piezo ceramic cylinders (PCCs) were used to produce acoustic signals at two different locations. A 5-cm-long fiber section centered at 37.05m (between the 1st and 2nd reflector) was taped in the tangential direction along the outer surface of PCC1 (dim. Ø85x32mm), and another 5-cm-long fiber section centered at 37.47 m (around the 11th re-flector) was taped along the outer surface of PCC2 (dim. Ø47x40mm) as shown in Figure 2.10. The fiber between the two PCCs was freely placed on an optical table and did not substantially couple acoustic waves. Two AWGs were used to provide driving signals to the PCCs. The driving signals were synchronized and triggered by the VNA. Two driving signals with frequencies of 1700 Hz and 3430 Hz were applied to the PCC1 and PCC2, respectively.

The VNA measured the amplitude and phase of the electrical signal at the modulation frequency, which was set to 16001 sampling points in the microwave band from 0.1 GHz to 15.1 GHz. The IFBW was set to 30 kHz, so the average sampling time for each sampling point was 0.036 ms. The bandwidth for each sensing section is solely dependent on the IFBW, which was 13.8 kHz for each sensing unit. In the time do-main, the pulse reflected by the kth reflector (k<11) and the long arm of the MI were over-lapped with the pulse that was reflected by the (k+2)th reflector and the short arm of the MI. Therefore, 14 pulses were formed within the range of 36.93 m to 37.57 m, as shown in Figure2.11(a). The peak value of the 3rd, 4th, 11th, and 12th pulses was used to read the interference phase from the interferometers formed by (1,3), (2,4), (9,11), and (10,12) reflectors, respectively. The four small pulse clusters highlighted by the dashed line boxes in Figure2.11 were the sidelobes generated by the vibration from the PCCs. The two pairs of sidelobes located around 30.50m (Figure 2.11.b) and 43.61m (Figure2.11.c) were symmetrically distributed to the 3rd and 4th pulses, respectively. The two pairs of sidelobes located around 24.18m (Figure 2.11.d) and 50.72m (Figure. 2.11) were symmetrically distributed to the 11th and the 12th pulses, respectively. The vibration locations and frequencies were clearly distinguished, as shown in Figure 2.12 (a), where the processed strain was plotted as a function of frequency and distance.

The reconstructed temporal signals from the sensing units centered at 37.03 m and 37.08 m were both in phase with the driving signal to PCC1, as shown in Figure 2.12(b). The reconstructed temporal signals centered at 37.43 m and 37.48m were both in phase with the driving signal to PCC2, as shown in Figure 2.12(c). The strain amplitude was proportional to the contact length between the sensor unit and the respective PCC. The strain amplitude read from the

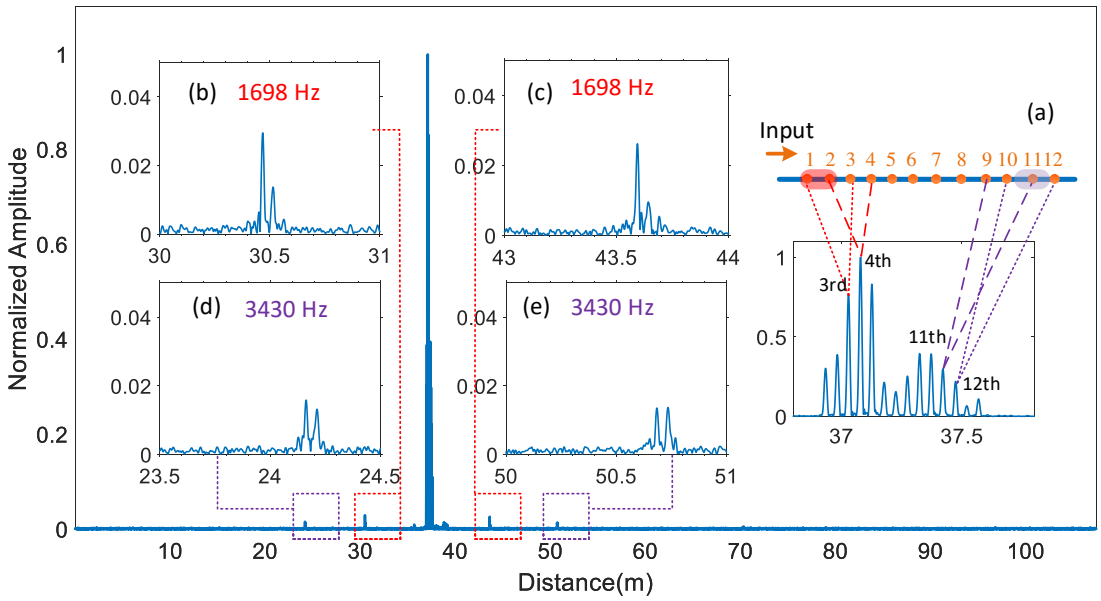

Figure 2.11: Time-domain signal when the PCCs located at 37.05 m and 37.47 m were driven at 1700 Hz and 3430 Hz. Insets: Expanded time signal. (a) The main lobes formed by the reflector array; (b)(c) sidelobes generated by the PCC1 that centered at 37.43 m and driven at 1700 Hz; (d) (e) sidelobes caused by the vibration of PCC2 that located at 37.08 m and driven at 3430Hz .

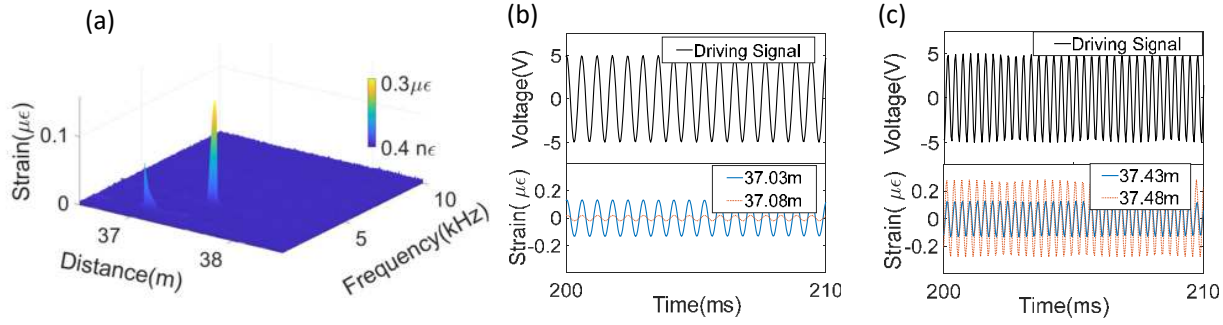

Figure 2.12: (a) Strain as functions of frequency and distance. (b) Driving signal (upper) to PCC1 and the reconstructed temporal signals centered at 37.03m and 37.08m (lower). (c) Driving signal (upper) to PCC2 and the reconstructed temporal signals centered at 37.43m and 37.48m (lower).

sensor unit centered at 37.03 m was larger than that at 37.08 m, as the PCC1 was attached to the fiber section from 36.98 m to 37.03 m. Likewise, the strain amplitude read from the sensor unit centered at 37.48 m was larger than that at 37.43 m, as more than half of the taped fiber section to PCC2 was after 37.48 m.

The results show that the phase and amplitude of the acoustic signal are well re-solved in the reconstructed temporal signals. The amplitude of 19.5 $n\epsilon$ at 37.08 m was clearly identified, indicating a lower detection limit of less than that for the experiment setting. The strains from the sensor units that are 5 cm apart are distinguishable, demonstrating a spatial resolution of 5 cm for DAS.

2.2 CMPI Interrogator

A CMPI interrogator was built during the project. Both the hardware and software were developed to incorporate all the key advantages of the CMPI.

2.2.1 Hardware

The schematic of the CMPI interrogator is shown in Figure 2.13.The interrogator includes a transmitter, optical fiber amplifiers, photodetector(PD), and a vector network analyzer (VNA). The last three components are off-the-shelf products, and they are directly integrated into the system. The transmitter produces modulated lightwave and is assembled by using off-the-shelf devices, but requires more design and control. A typical transmitter in a CMPI system contains a laser and an electro-optic modulator (EOM). However, for better spatial resolution and consistent inference phase shift, a micro controller is needed control the coherence length and the bias voltage to EOM. In our first version of the transmitter design, a STMicroelectronics STM32 was used for the microcontroller. The system works good in the field, but we had two issues. Firstly, a commercial laser driver was used, which was bulky. The feedback from the laser was not able to be read through the CMPI controlling program. Secondly, the STM32 has to be programmed and uploaded and therefore we have to upload a new program to affect any changes. The VNA scanning was not able to synchronize with the STM32, so most of the time the signal processing required some manually filtering of the bad data which were taken during the bias voltage adjusting.

The updated version of the transmitter fixed above issues. A circuit has designed to combine the laser driving and bias control, so the new transmitter is much smaller than the old version, which has dimension of $20 \times 10 \times 5$ cm as shown in Figure 2.14. It contains three layers, the first layer contains the laser diode, laser driver, STM32, photodetector, bias-T; the second layer has the EOM and 1/99 coupler; the third layer contains the circulator. Each layer contains several FC to FC adaptor fixers for easy assembling. As the former design, one D/A channel of STM32 has been used to provide the modulation (2–5 kHz) to the laser driver to produce wavelength dithering. Another D/A channel is used to provide bias voltage to EOM. One A/D channel is used to convert the 1/100 output from the EOM to calculate the desired bias voltage to EOM. The Modbus-RTU communications protocol is implemented in the STM32, so we are able to talk to it through the serial port. This new development allows user to change the laser wavelength dithering frequency and amplitude, center wavelength, and bias voltage using a script in the MATLAB programming language.

The developed interrogator has been integrated into a portable case($12.72in x 24in x 17.5in$). The upper layer (Figure 2.15(left)) inside of the case includes two EDFAs, the CMPI transmitter and receiver (transceiver), and the AC-DC power supply for the those two parts. The lower layer(Figure2.15(right)) includes the VNA and a bare-bone computer. Sensing cable and MI can be plug into the respective ports on the front panel. An external monitor can be used with the CMPI interrogator to perform the in situ monitoring. The front view of the interrogator is shown in Figure2.16(left).The blue box circled regime is the front panel. The schematic of the front panel is shown in Figure2.16(right). Users can plug in Michelson interferometer and the sensors on the front panel through the respective ports. Either external light source or internal light source can be selected for the measurement. When chose internal light source, an optical cable with FC/UPC connectors on both sides are needed to connect the INT and MOD ports (Figure 2.17(left)). When external light source is used, the light should be injected into the MOD port through a FC/UPC connector (Figure 2.17(right)). The sensor and MI are required to FC/APC connectors.

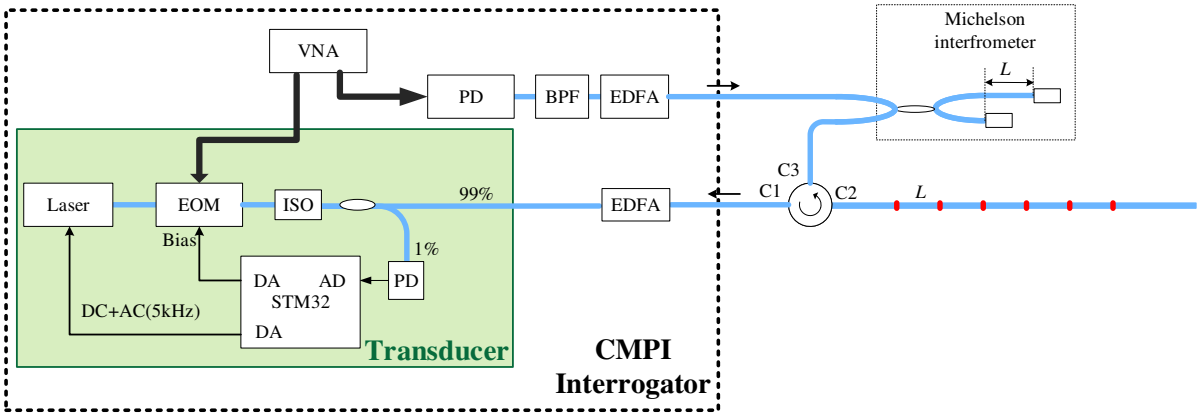

Figure 2.13: Schematic of the CMPI interrogator

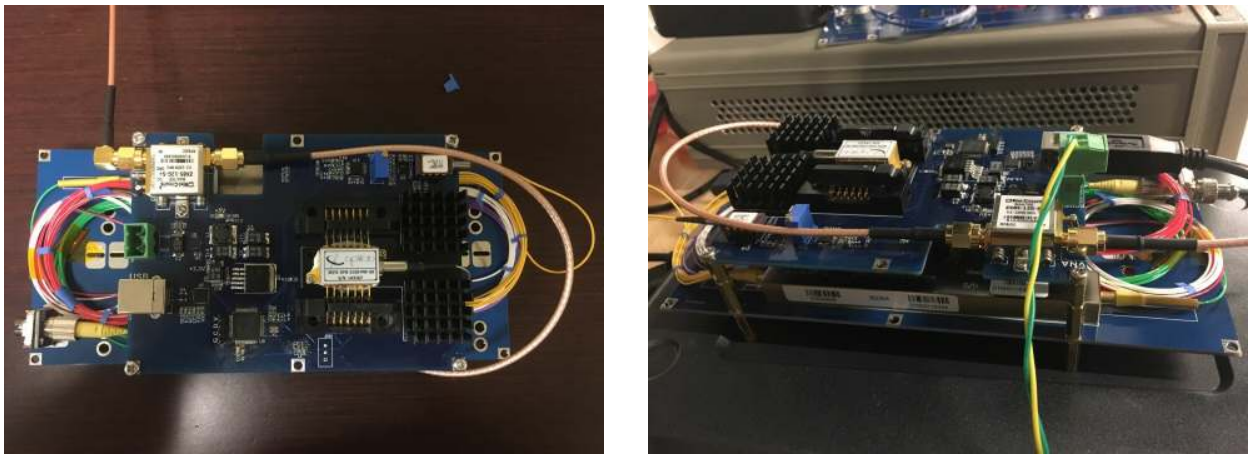

Figure 2.14: Top (left) and side (right) views of the CMPI transmitter.

2.2.2 Software

We have generated a suite of MATLAB functions for coherence length control, wavelength scanning and bias voltage control. All these functions can be called from the CMPI interrogator main function, so any controlling of the transmitter can be synchronized with the VNA sweeping. Moreover, we have added the laser temperature and output power reading function in the firmware, and they can be acquired after each measurement. The laser temperature information can be used to discriminate the signal change due to the laser wavelength drifting and the daily barometric pressure change or tides.

A user friendly CMPI measurement APP was developed. Users from different background can easily use the interrogator to perform measurement, monitor signals, download data, and process the data. The interface of the CMPI data acquisition APP is shown in 2.18. The start and stop microwave frequencies, number of sampling points, as well as the measurement time can be setup by user through the interface. The 'CALI' button is used for initial system adjustment. The 'START' button is used to trigger the measurements. Time domain signals are shown during the measurement, so the user can monitor the signals during the interrogation.

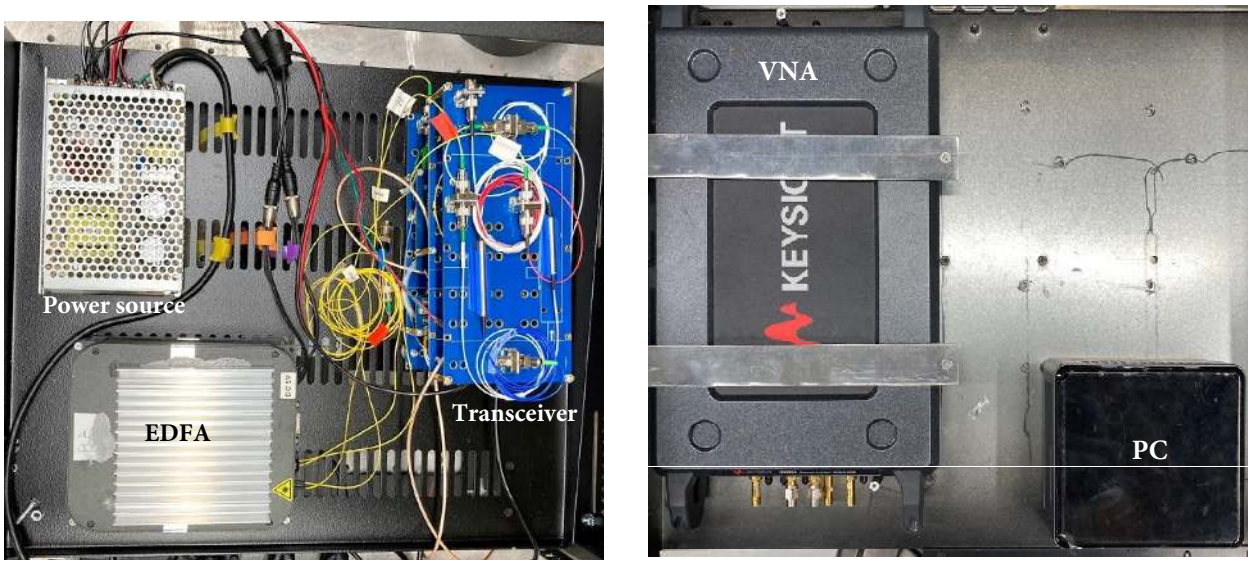

Figure 2.15: Upper (left) and lower (right) layers of the CMPI interrogator.

2.3 CMPI Data Storage, Transfer and Processing

CMPI data are stored in the google drive. The data volume is typically 1–2GHz data/day when tens of sensing units are in the system and the VNA scanning rate is 0.1 Hz. RCLONE is used to transfer the raw data to Clemson Palmettos to further process. Palmetto is Clemson University's primary high-performance computing (HPC) resource, which currently comprised of 2021 compute notes (totalling 23072 CPU cores). A user interface has been developed for end user to process the signal as shown in Figure 2.19.

2.4 Sensor Fabrication

2.4.1 Ultra-Fast Laser Reflector Fabrication

Ultra-fast laser including the femo-second laser and the pico-second laser were used to fabricate the weak reflectors along the SMF. The laser light was focused into the fiber core to slightly modify the refractive index. 100X oil immerse objective was used in the setup to get 1-μm diameter focus spot. Therefore, the reflectivity of each reflector can be fine controlled. The reflector fabricated in this way has flat reflectivity curve over the a wide spectrum, so they are easy to be implemented into the CMPI system. However, the fabrication is time consuming and there aren't commercial products to purchase.

2.4.2 Broadband Fiber Bragg Grating (FBG)

Broadband FBGs or called Chirp weak FBGs, can be used as weak reflector too. We found several vendors that make those with large volume. However, FBGs only reflect light within a certain band. The bandwidth for a chirp FBG can be up to 10 nm, but there's a trade off between the reflectively at each wavelength and the bandwidth. The larger the bandwidth, the weaker the reflectively would be. Besides, the wavelength of the peak reflection varies as function of temperature and strain. Therefore, it is comparatively harder to implement weak FBGs into the CMPI system. We have successfully implement over one thousand weak FBGs that separated 10cm into the system and the interrogated by using the CMPI interrogator. The time signal showed high SNR as shown in Figure 2.20. Ambient noise was recorded by the sensor. We were able to demodulate the interference phase for more than 90% sensors. The results indicate that the CMPI system can have sensor capacity of over thousand.

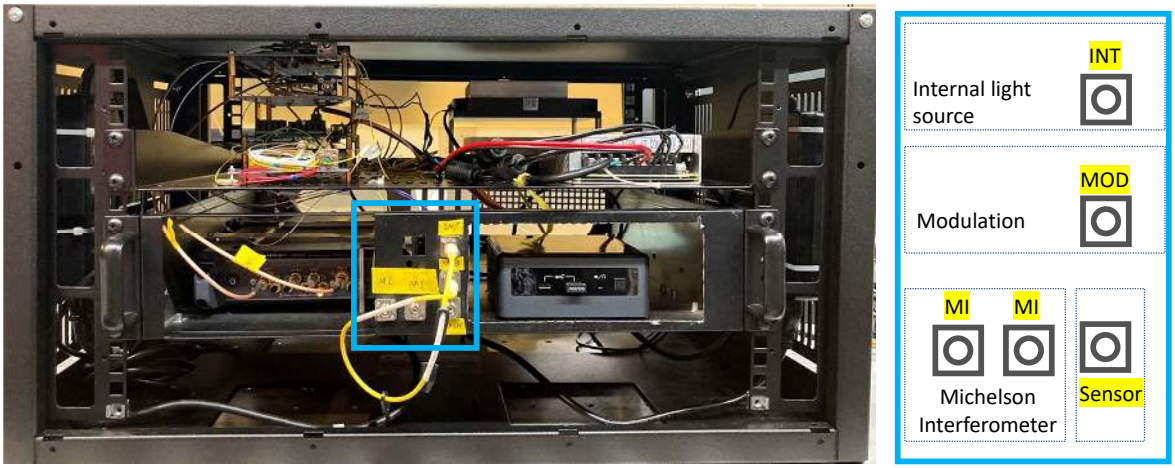

Figure 2.16: Front view of the CMPI interrogator(left) and the schematic of the front panel(right)

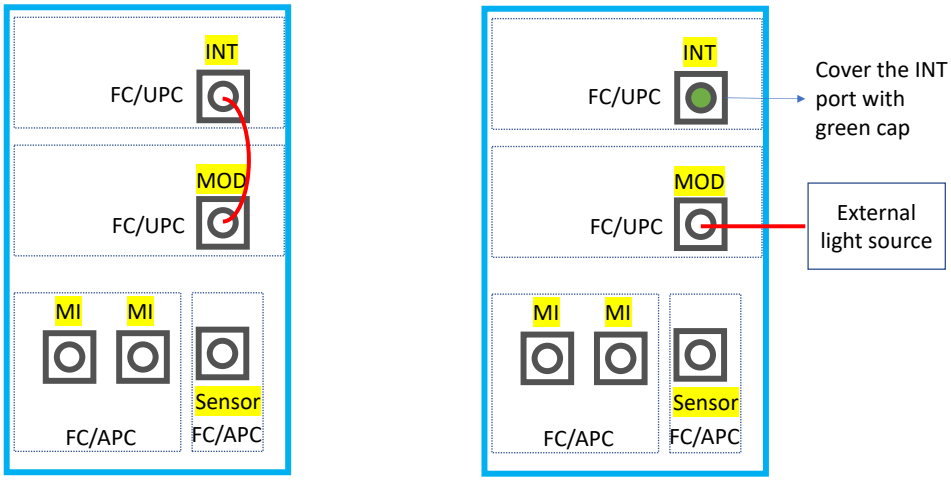

Figure 2.17: Connection guide using internal (left) and external(right)light source to perform measurement

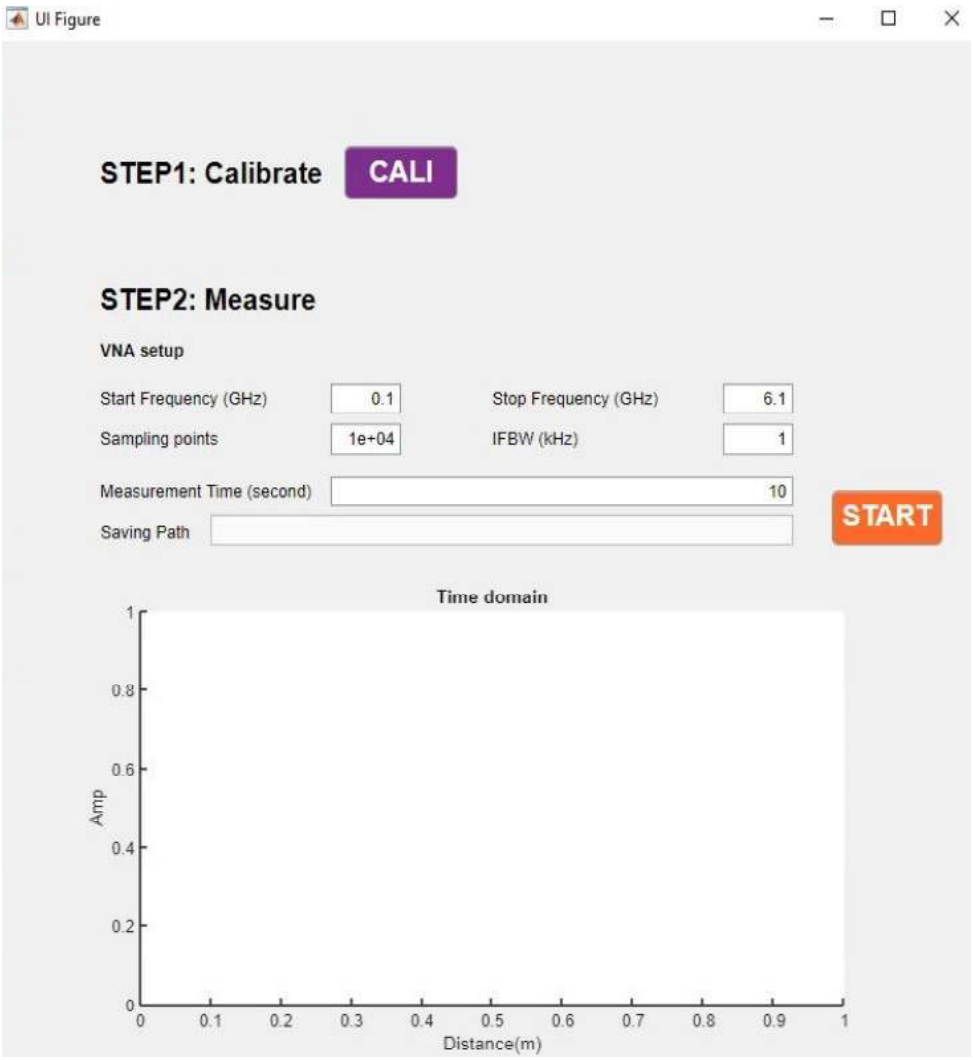

Figure 2.18: Interface of the MATLAB APP for CMPI interrogator control

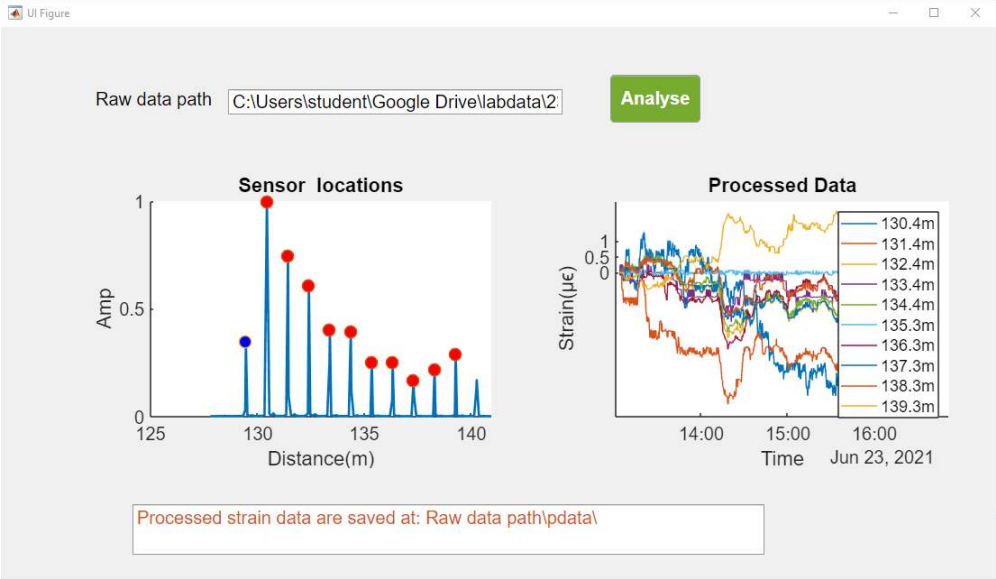

Figure 2.19: Interface of the MATLAB APP for CMPI signal processingl

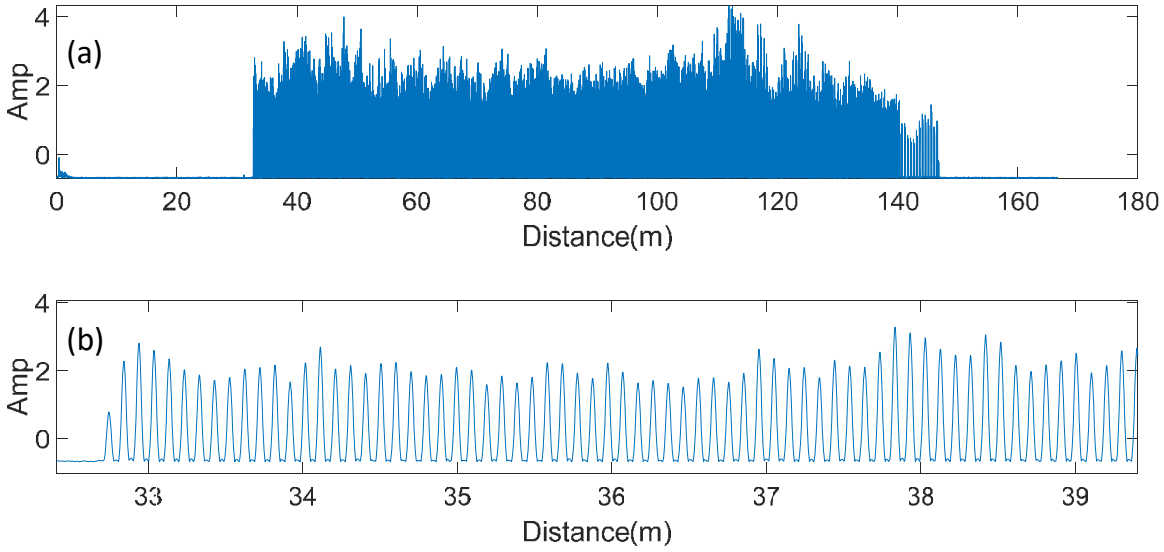

Figure 2.20: Time domain signal read by using the weak FBGs array.(a) 1100 FBGs. (b)Zoomed in signal

2.5 Sensor Packaging

We have been evaluating different methods of packaging optical fiber for strain transfer. The goal of the packaging is to protect the fiber from mechanical damage during installation, to protect the fiber from chemical or mechanical damage in the subsurface, and to couple the fiber to the formation. These goals are at odds with each other because the first two are well served by isolating the fiber from the formation as much as possible, which is best accomplished using a stiff, inert package. Indeed, this is how armoured cables are typically designed. However, mechanically isolating the fiber prevents it from measuring strain. The compromise is to provide enough protection to ensure successful deployment, but use a package that is compliant enough to transfer strain to the fiber.

Slip and stretch are two basic processes that will affect strain transfer from formation to fiber. Optical fibers are thin, but relatively stiff ($E = 42$ GPa) compared to their outer coatings ($E < 1$ GPa), and the coating may be stiffer or more compliant than the formation. As a result of the contrasts in stiffness, strain in the formation may be greater than strain in the fiber. In this case, stretching strain would vary smoothly from the formation to the fiber.

Another effect that would cause problems is when the shear stress along the wall of the fiber or packaging exceeds a critical value and slip occurs. This could happen, for example, when the fiber package was relatively stiff and the shear strength between the package and the formation was low, either because of a low friction coefficient, surface area, or normal force. In this case, slip would cause a discontinuity in the strain within the packaging.

At least three different geometries are available for packaging optical fiber that are intended for strain transfer from optical fiber to an enveloping formation (Figure 2.21). Most downhole applications use optical fiber enveloped by cylindrical shells of different materials. Optical fibers used for strain transfer are typically coated in a durable polymer intended to transfer strain. In some cases, the fiber is then enveloped in a steel tube, which may also be coated in an outer layer for additional protection. This type of packaging protects the fiber, but the compliance of the tubing can be quite low.

The helical geometry is based on a cable package designed by Baker Hughes where two optical fibers are arranged in as opposing helices (Figure 2.21). Strain is determined over short intervals and the data are used to determine axial and bending strains. Further analysis of this geometry is outlined below.

Planar geometries package fiber in long strips of material designed to create much larger surface areas in contact with the formation. In some cases, the planar package is pushed against the wall of a borehole resulting in a curved shape (Figure 2.21). In other cases, the strip may be a flat plane embedded in porous media.

Fiber packaging with low compliance (stiff) will probably perform well when it is strongly bonded to cement, which in turn is strongly bonded to a formation. However, stiff packaging in compliant formations, like unlithified sediments may slip against the formation, thereby underestimating strain. This would likely occur, for example, when fiber packaged in steel tubing was deployed in sediments. One approach to remedy this problem is to increase the compliance and surface area of the package, and this has motivated the planar package in Figure (2.21).

Factors affecting the onset of slip can be evaluated by balancing forces on the packaging (2.22). Assuming the shear stress at slip is given by the product of the normal stress, σ_N and the coefficient of friction, μ between the formation and the packaging gives the critical strain gradient required to cause slip as

$$(\nabla\varepsilon)_c = wC_p\mu\sigma_N \tag{2.12}$$

where C_p is the compliance, and w is the width of the packaged fiber.

We have been evaluating several materials to use in planar packaging and they vary in adhesion and surface texture. One type of material is a polyester film with a strong adhesive backing. Fiber is laminated between two pieces of film. Another material is woven polypropylene. The fiber is bonded to the polypropylene with adhesive. Several types of woven polypropylene and adhesive have been identified and they are being evaluated in the laboratory by measuring C_p and μ. We have also conducted strain transfer tests.

One sample of the polyester film and another of the woven polypropylene were tested on a loading frame and their compliances are remarkably similar, between 75 and 82 με/N. We have designed and built a prototype device to measure the coefficient of friction, μ. The device measures the displacement caused by applying a known shear load to two blocks with the desired surfaces. We have conducted successful proof-of-concept tests using the device, and we are currently making refinements to improve operational aspects.

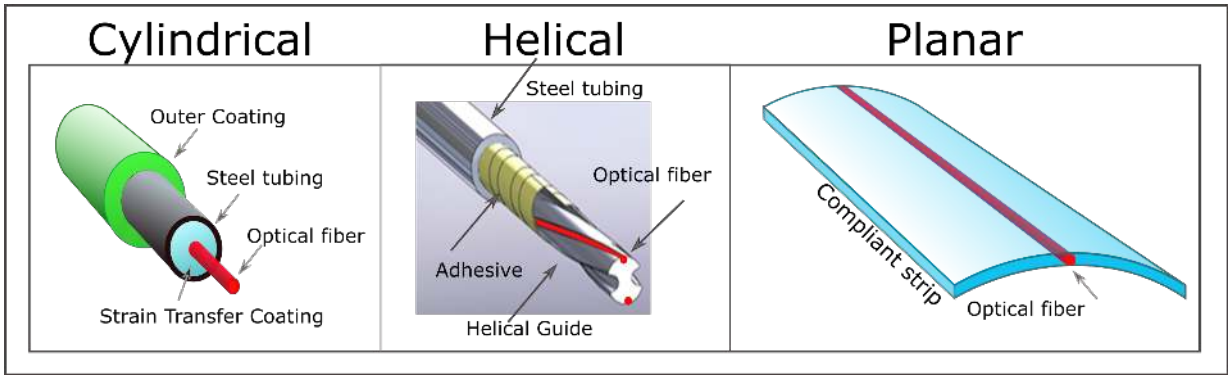

Figure 2.21: Types of packaging intended to transfer strain from formation to optical fiber. A variety of cylindrical geometries are available where a coated optical fiber is sheathed in a steel tube, in some cases, a polymer layer. The helical geometry shows a diagram of the WIRE cable where two fibers are placed in grooves in a helical guide. The planar geometry attaches fiber to compliant strip to create a large surface area for coupling to the formation.

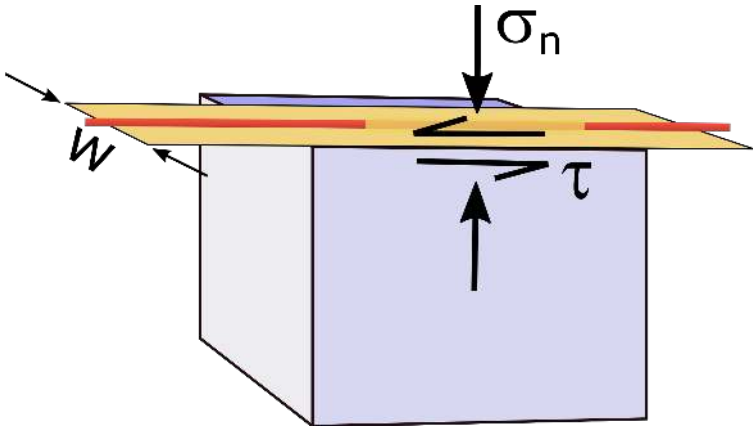

Figure 2.22: Free body diagram showing normal and shear stresses acting on a planar strip containing an optical fiber.

2.5.1 CMPI Ribbons for Normal Strain Measurement

Numerous packaging methods have been tried to pack the CMPI sensors to protect the sensor and meanwhile enhance the strain transfer. The earlier developments include packing the sensor by using Swagelok fittings and insert sensing fiber in the hot shrink tube. Though the result obtained from initial tests was good, these methods were not adopted due to the complexity. Later, we developed a method to push the low viscosity epoxy into polyethylene tube that contained the fiber. This method was not successful as the epoxy couldn't cure in the absence of air. We have also tried to pack the fiber in nylon cord and immerse the assembly in epoxy. The fiber and the cord were kept under tension while curing. We used an inner cord that is pulled inside an outer cord along with the fiber to hold the fiber tightly within the outer cord. The test results showed the applied strain could be transferred to the sensor with some reduction. The packaging works well when the sensor piece is only two or three meters long, but the performance diminished when the sensor piece is longer.

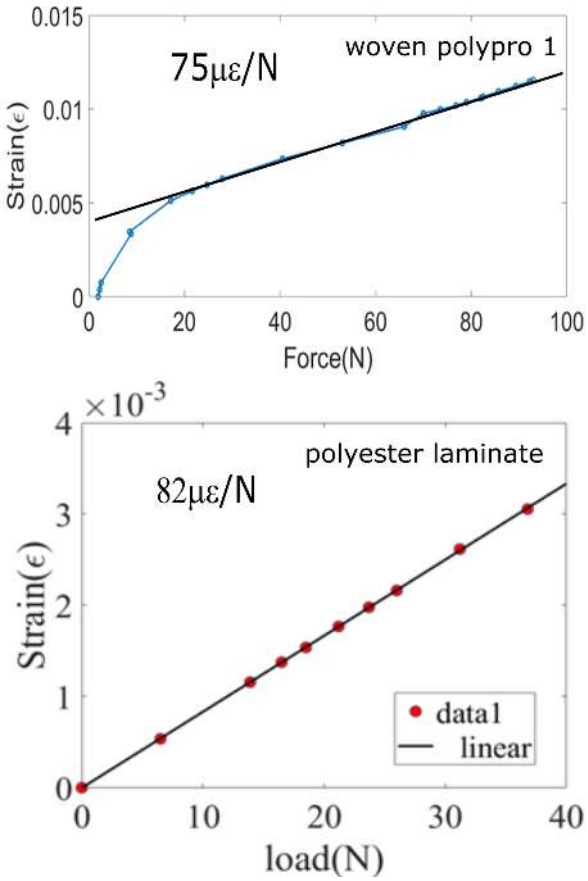

Figure 2.23: Strain as a function of load for two types of planar strips used to package optical fiber. Compliance values are between 75 and 82 με/N.

2.5.1.1 Tape Laminated Strain Ribbon

In the fourth quarter of this project, we developed a tape lamination packaging method, which is much easier to control with excellent strain transfer performance. The packaged sensor ribbon consists of an optical fiber with sensors that is pre-tensioned and sandwiched between two pieces of 1-inch-wide tape (Figure 2.24). The fiber is strongly bonded to the two sides of the tape, producing a package that is 2.5 cm wide and 100 to 200 microns thick. This packaging approach is designed to make the fiber into an assembly with a large surface area. The intent is that this will allow the package to be attached to the wall of a casing or boring by friction using a modest normal force.

Two fiber reflector pairs were used to test the strain transfer capability of the packaging. The distance between two pairs was 1 meter, and the separation of the two reflectors in one pair was 1 cm. The packaged sensor was fixed on two motorized linear translation stages (Newport PM 500) by putting a base clamp on top of each end of the fiber in the strip packaging, and using a threaded fitting to press the claps onto the stages. Axial strains were applied to the reflector pairs which formed the Fabry-Perot interferometer (FPI) by moving one stage at 5 microns per step. The measured strain was very close to the applied strain. The results showed that the new packaging method transferred strain to sensor well.

An apparatus resembling ground condition in situ conditions was used to test the packages sensor as shown in Figures 2.25 through 2.27. The apparatus consisted of a compliant cylinder filled with sand. The fiber strip was

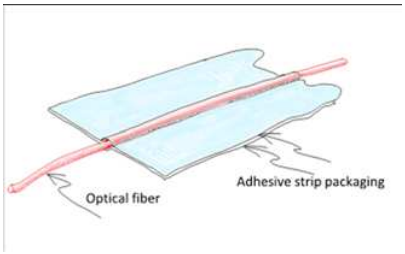

Figure 2.24: Optical fiber packaged between two adhesive strips to create a large-surface area, high compliance system.

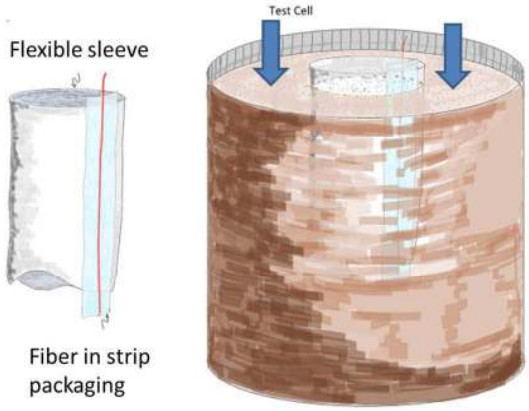

Figure 2.25: Fiber in strip packaging (blue) attached to the side of a flexible sleeve. Strip packaging is 2.5 cm wide. Assembly deployed in a cylindrical testing apparatus. Diameter of the cylinder is 15 cm. The cylinder is loaded along its axis.

attached to a flexible polyethylene tube, which was expanded by filling it with sand. The fiber strip was attached to a polyethylene sleeve (Figure 2.26), and the annular space was filled with sand to a level slightly above the top of the external tube (Figure 2.25).

This general configuration (Figure 2.26) is designed to be deployed in an open hole (Figure 2.25 and Figure 2.27). The flexible polyethylene tube, or similar, would be lowered into the borehole and the pressurized with air or water, forcing the fiber strip against the borehole wall. The poly tube would then be filled with sand. This would create a normal force on the fiber packaging (Figure 2.27]) Friction between the fiber strip and the borehole wall would hold the fiber in place so that it measured strain along the axis of the borehole.

The sensor in the packaging was a 1.2 m piece of single mode fiber containing a 1 cm cavity FPI in the middle. One end of fiber was connected to the CMPI system. The apparatus was loaded by adding 18 increments of 200 mL of sand, which weighed 310 g each. The load caused deformation of the cylinder, which was further transferred to the sensor through the movement of the sand.The load versus amplitude (real) change of the time domain pulse formed by the FPI is shown in Figure 2.28. The curve shows less than half period of the sinusoid curve. For the tape packaged 1 cm cavity FPI, the half period of peak amplitude change is corresponding to about 26 $\mu\epsilon$, so the strain induced by adding 200 mL sand to the system was less than 1.44 $\mu\epsilon$. The amplitude change was reversible, as we released the load, the amplitude of the time domain pulse changes back to the original value.

The tape lamination packaging method showed significant advantages over the other methods. However, it was difficult to put fiber within polymer by hand, especially as the fiber gets longer. Therefore, in the 10th quarter of this project, we built an adaptive auto-alignment sensor packaging system for hundreds-of-meters long sensor array packaging.

The design of the packaging system is shown in Figure 2.29. A prototype instrument based on the design was built and shown in Figure 2.30. Two rollers are attached to a slotted mounting bracket, which is slotted to accommodate several sizes of adhesive backed polymer (tape). The mounting bracket has a 3/8-inch centered hole through its length which places the fiber near the center of the tape.



Figure 2.31: Packaged fiber sensor.



Figure 2.26: Fiber packaged in a compliant strip and attached to a flexible poly tube (left). Fiber with poly tube on a roll for field testing (right).

The fiber is then further aligned to the center of the tape with a small
eyelet. The tape with the fiber passes through two plastic rollers. The plastic rollers are mounted in a vertically slotted hole and are manually tensioned using a pair of bolts. The packaged fiber is collected on a reel which is used to pull the tape through the instrument.

The instrument can provide consistent tension to the fiber and tape, and it has the capability of auto-align the fiber to the center of the tape. A 10 m long packaged sensor array is shown in Figure 2.31. The tension on both tapes was slightly different, which resulted in some buckling distributed along the packaged sensor. For further improvement of the system, we plan to measure and balance the tension on both upper and lower tapes by adjusting rolling friction of the tape dispensers.

We deployed an fiber laminated between to polyester strips in the field using procedures developed earlier. The deployment went well until the borehole back fill was at the level of the splice between the packaged fiber and tactical data cable. The fiber broke when the back fill was raised above this junction. Our analysis of this problem concluded that the fiber failed when it was loaded transversely across a small offset at the end of the splice protector. Previous design effort had focused on the split protector and the packaged fiber, but not on their junction.

After the field deployment was diagnosed, we redesigned the junction and developed a reliable way to integrate the

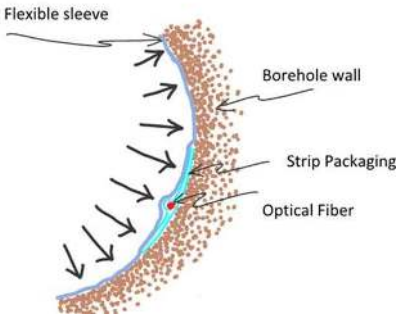

Figure 2.27: Fiber strip held in place on a borehole wall by normal force.

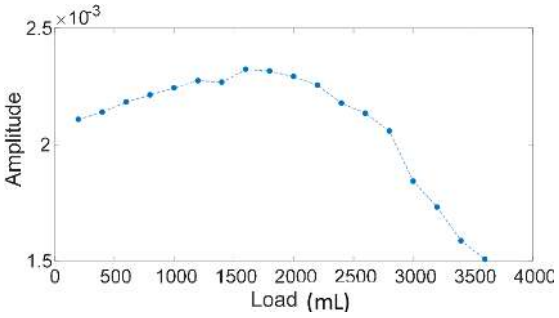

Figure 2.28: Amplitude (real part) of the time domain pulse (peak point) as a function of the adding load.

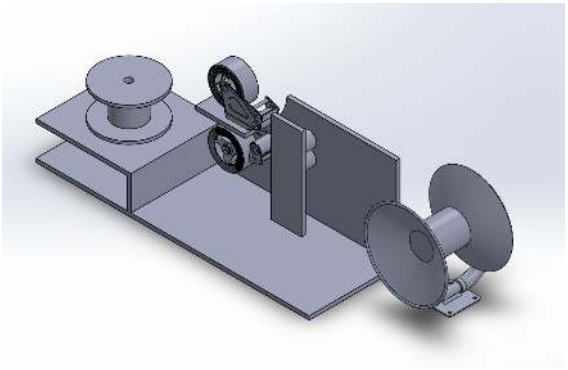

Figure 2.29: Working sketch of the packaging system.

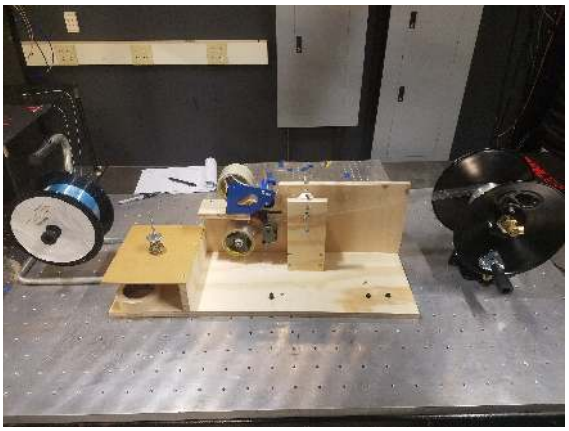

Figure 2.30: Prototype packaging instrument.

fiber–data cable transition into the fiber package. The basic packaging approach that we are using is to cast the fiber with a narrow fabric and a resin in a mold. The different fabrics and resins have been identified to achieve different stiffnesses. The splice between the fiber and the tactical data cable is cast in a separate mold and the compliance grades between the package and the splice protector.

2.5.1.2 Fiberglass Strain Ribbon

Urethane and epoxy are used for resins, and acrylic and fiberglass are used for the fabric. This allows the modulus of the strain ribbon to range from MPa to GPa. Examples of a strain ribbon created from epoxy and fiberglass are given in Figure 2.32). The fiberglass ribbon can be coiled with a 0.3m radius of curvature (Figure 2.33). Urethane resin is used to create strain ribbons with a softer elastic modulus than when epoxy is used as the resin (Figure 2.34). The new approach appears promising and we expect to move ahead with additional lab and field testing of these designs.

We have developed methods to pack the CMPI sensors in ribbons made from various materials. Those ribbons covered a wide range of compliance and provided the options for measuring strain in different surroundings. For better matching the applications with respective ribbon,we have measured the compliance of the ribbons by using a loading machine. The measured results are shown in Figure 2.35. The measured compliance ranged from 1.2×10^{-5} to 2.2×10^{-3} strain/N.

A 15 cm CMPI sensor was packed within a 1-inch wide urethane ribbon (M1). We placed the ribbon on the



Figure 2.32: Strain ribbon packaged in molded fiberglass and epoxy. a.) strain ribbon in the mold, b.) reinforced splice with data cable; c.) transition for splice to packaged fiber sensor.

cement floor and put a sandbag on top of the sensing regime. The floor was gently knocked by using the hammer. The knocking place was about 1 m away from the sensor along the ribbon direction. It showed a good repeatable pulse response, as shown in Figure 2.39. The wave frequency was about 300–400 Hz.

We developed methods and prototypes for packaging optical fiber sensors into sheets and ribbons (Figure 2.36) for field deployment. We have scaled up the methods for creating strain ribbons suitable for field scale deployment. This has involved designing and creating a frame for fabricating ribbons of suitable length. The current frame (Figure 2.37) is 9m long, but the methods can be scaled to longer lengths. The long frame can be adapted to a variety of packaging methods.

2.5.2 CMPI Packaging for Strain Tensor Measurement

We have developed methods for packaging fiber to be included as part of a cylindrical boring. This included methods for packaging fiber in thin shells designed to either span the circumference of a boring, or mounted on the side of casing. We evaluated a variety of materials in an effort to create a device that will protect the fiber during deployment, have good strain transfer characteristics, and be straightforward to deploy in the field. One encouraging approach is to embed optical fiber in epoxy

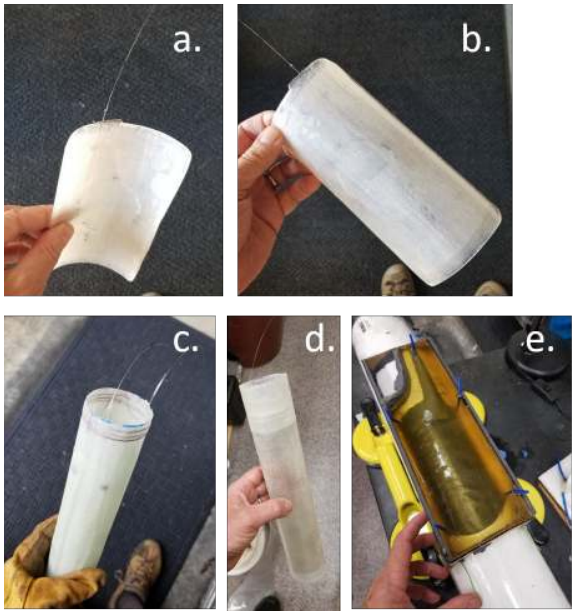

Figure 2.40: Shells and tubes with embedded optical fiber sensors.



Figure 2.33: Optical fiber packaged in a fiberglass ribbon and coiled in a 0.3m radius of curvature.

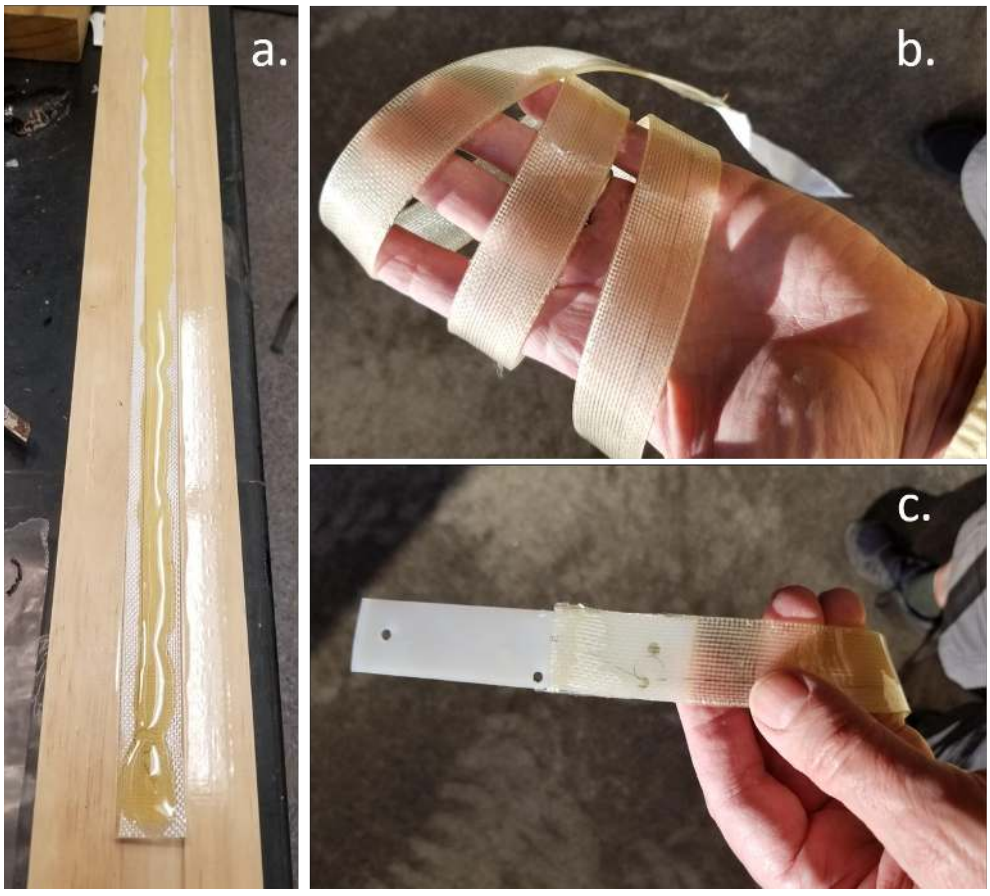

Figure 2.34: Strain ribbon molded from urethane and fiberglass.

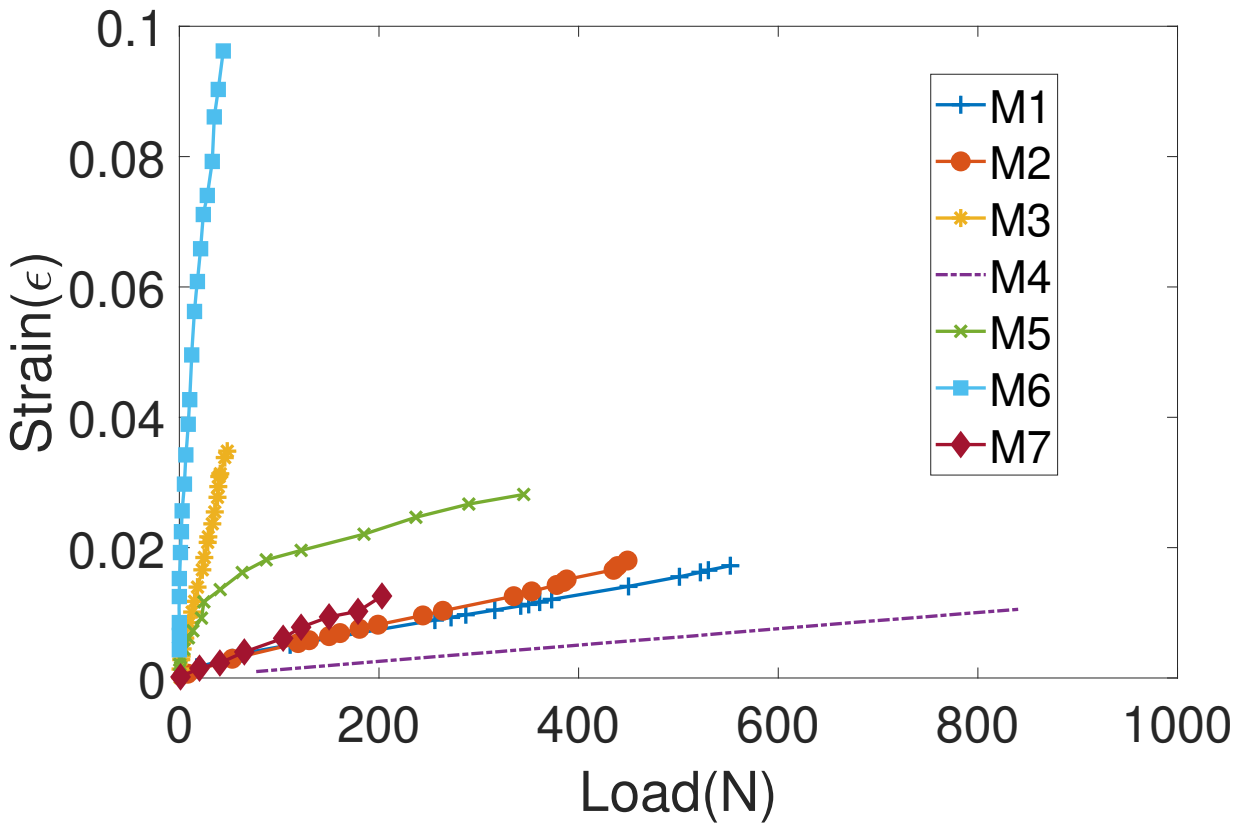

Figure 2.35: Compliance testing results for ribbons packed in seven different materials.

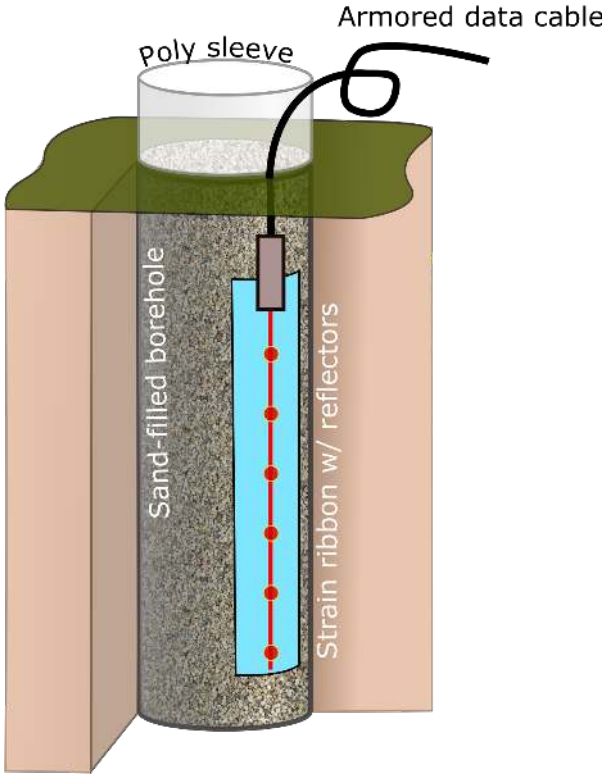

Figure 2.36: Strain ribbon completion for matching compliance in a soft formation.



Figure 2.37: Frame for building strain ribbons suitable for field-scale deployment.

and fiberglass composites (Figure 2.40a–d). We have developed techniques for wrapping fiber into various configurations and then embedding in fiberglass and epoxy composites. Most methods we have used so far are good for simple prototypes, but it is cumbersome to make more complicated shaped using these methods. One approach to making complex shapes is to cast them in a mold. We have develop urethane molds to facilitate the casting of fiber packaging (Figure 2.40).

We developed methods and prototypes of strain tensor shells for deployment on the outside of casing ((Figure 2.38)). The tensor shells are designed to be used with CMPI, but the method can be adapted to enable tensor measurements to be made with other optical fiber sensors, including DAS. We refer to this approach as "discrete, distributed tensor strain measurement." The image of the prototype multi-component strain shell is shown in Figure 2.41. The shell is formed by two layers of fiberglass and single-mode fiber (SMF) with four weak reflectors that are 15cm apart. The shell is initially built on a 4-inch diameter PVC pipe. The fiber section between the first two reflectors is placed in the angular direction around the pipe, so the interferometer formed by the two reflectors is used to measure the transverse strain.

The section between the last two reflectors is placed along the pipe in the axial direction, and the interferometer formed by the last two reflectors is used to measure the axial strain (Figure 2.41a). On the end of the fiber is spliced with an APC connector, and a splicing protection house is embedded in the shell for a robust setting. We tested the shell by applying force to the pipe from different directions. The forces were applied through pipe inflating, dead weight loading, and pipe rotating.

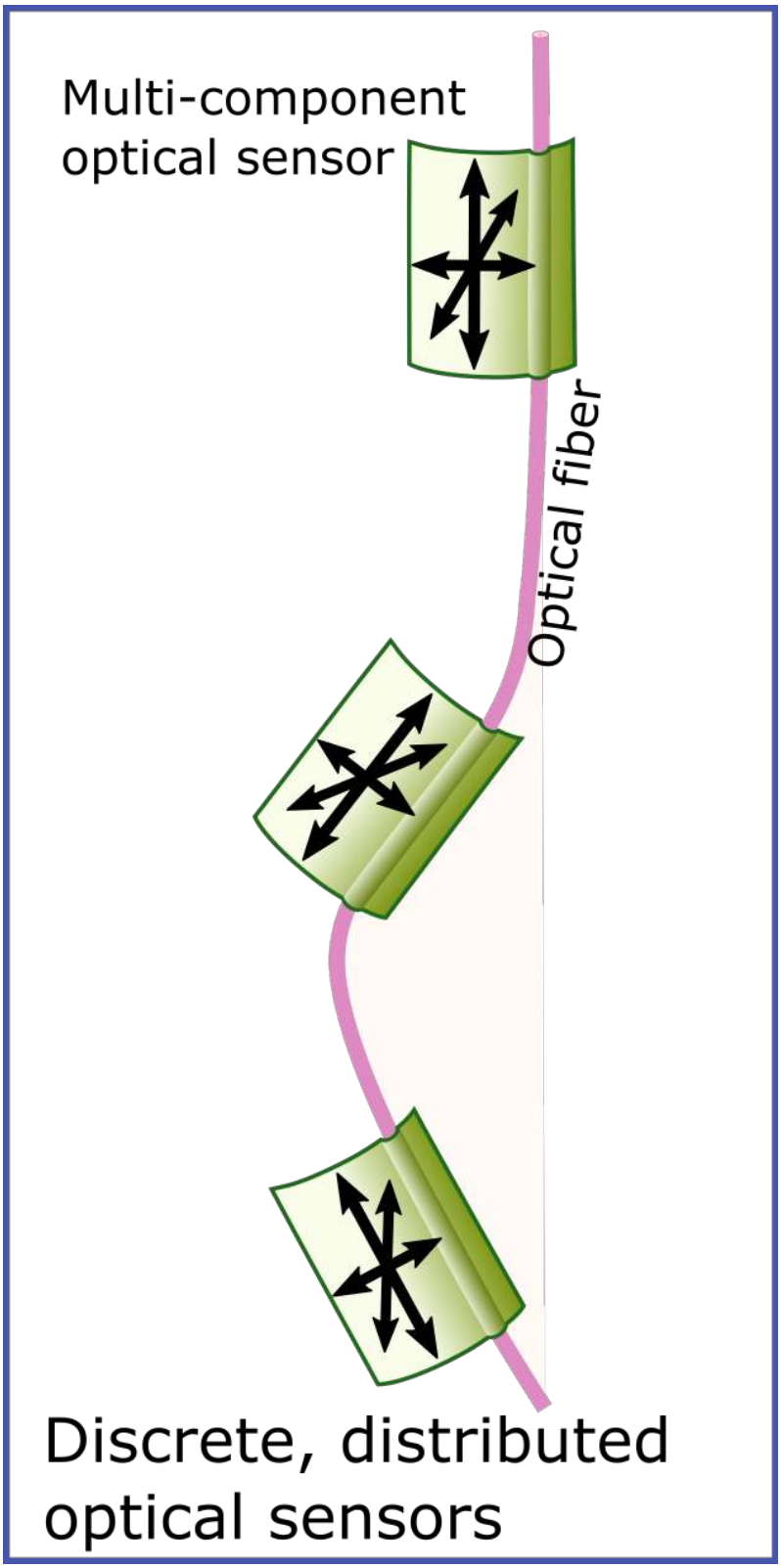

Figure 2.38: Fiber packaged in a shell for discrete, distributed strain tensor sensing.

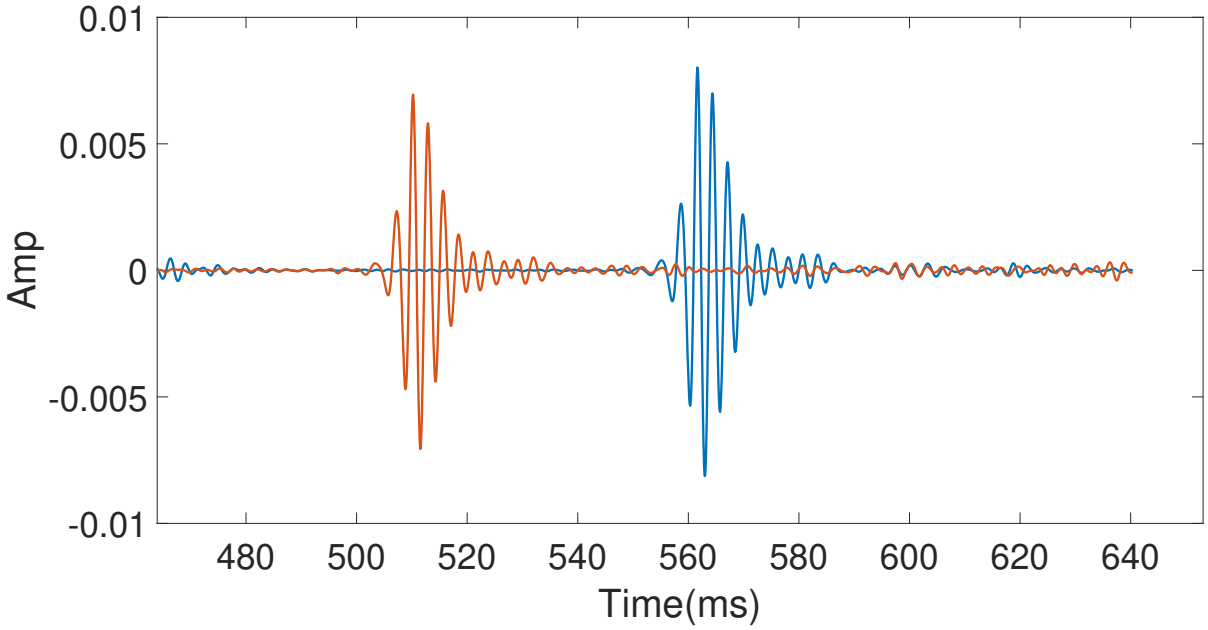

Figure 2.39: Strain signal from ground knocking measured by the neon ribbon packed sensor.

2.5.2.1 Pipe Inflating Test

We sealed the two ends of the pipe and put hooks on both ends. The pipe was hanged from the ceiling by hooking one end to the ceiling hook. A $1/4$-inch tube was used to connect the pipe and a syringe. Air with different volumes (12, 25, 30, 40, and 50 mL) was injected into and pumped out from the pipe. The test repeated at each volume for ten times. The measurement results show that the transverse and axial strain are changing in phase during the process, as shown in Figure 2.42a. The measured strains increase as increasing the volume of the injected air. A pressure transducer was used to measure the air pressure inside the column. Both transverse strain and axial strain increase linearly as a function of air pressure (Figure 2.42b). The calculated modulus by using the transverse strain reading and pipe geometries is 25 GPa, which is higher than the typical modulus of the PVC pipe.There are two cuts in the transverse direction on the pipe and the glass-reinforced plaster matrix has much higer modulus than the PVC. We think both issues might cause strain reading lower than the theoretical value. Nevertheless, the results indicating the strain was transferred to the sleeve, and the strain directions were well differentiated. Putting the sleeve to the pipe formed by materials with higher modulus can help verify the strain transfer coefficients.

2.5.2.2 Dead Weight Loading Test

The column was loaded by adding weight to the bottom end. Five different weights were used. The loading and unloading were rotated performed at each weight. As shown in Figure 2.43, the axial strain increases when the load is on and decreases when the load is off. The transverse strain changes oppositely, as it increases when the load is off and decreases when the load is on. Both strain components change linearly as a function of the increased stress. The calculated Young's modulus is similar to the calculated value from the air inflating tests.

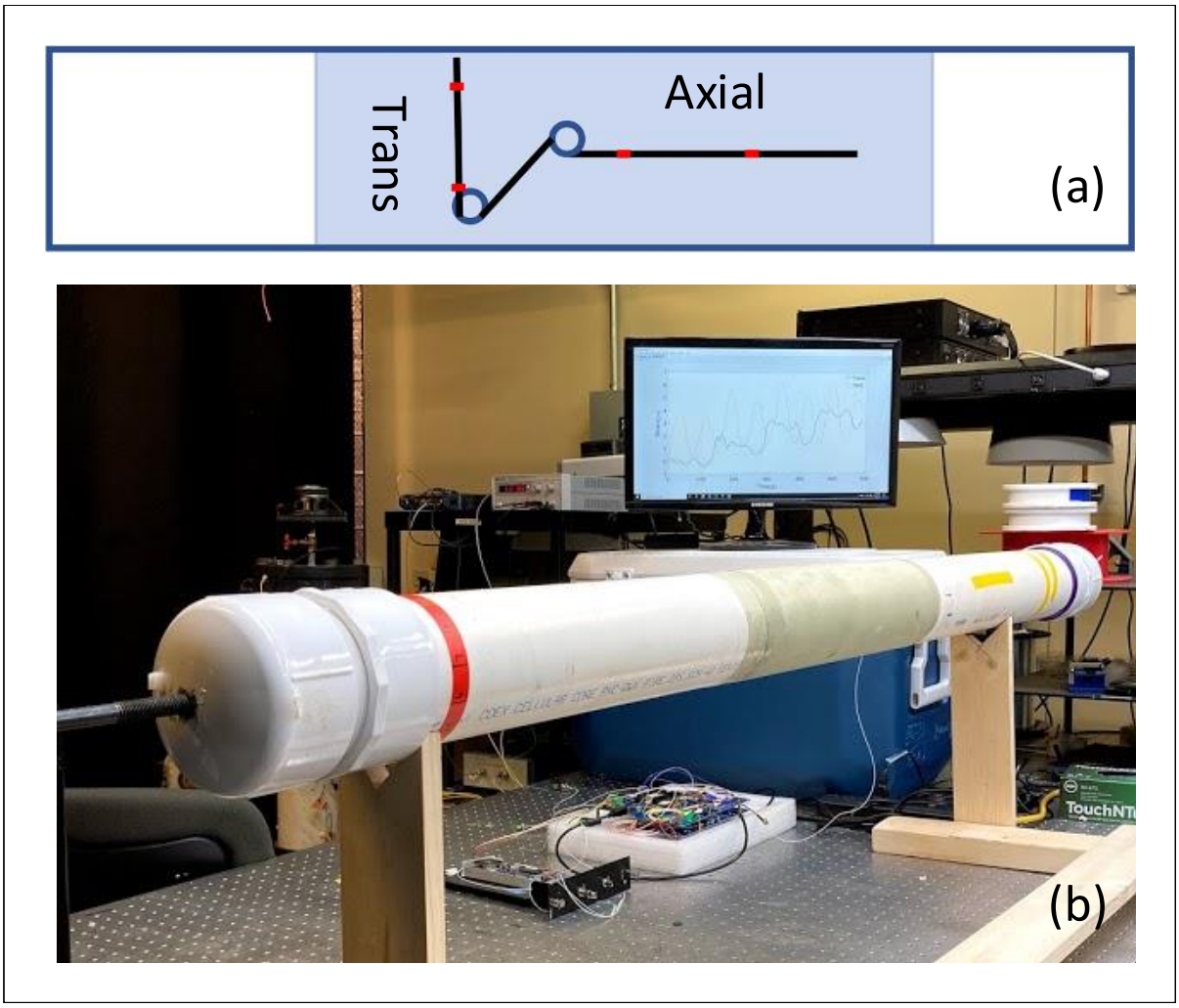

Figure 2.41: Side view diagram (a) and photograph (b) of the of the multicomponent strain shell on the pipe.

2.5.2.3 Pipe Rotating Test

We placed the pipe vertically on the pipe holder (Figure 2.41b). The pipe was rotated about the axial direction from 0 to 2π and then rotated back to 0. Data was taken every 0.15 rad, and the test was repeated four times. The self-weight of the pipe applied different forces to the two strain sensors under different rotation angles. When the strain sensors are rotated to the top, the axial sensor is compressed and shows negative strain, and the transverse sensor is stretched and shows the positive strain. When strain sensors are rotated to the bottom, the axial fiber is stretched and show positive strain, and the transverse sensors are compressed and show the negative strain (Figure 2.44a).

2.5.2.4 Long Range Sensing

A 1-km long delay fiber was put before the strain shell. The strain shell was placed on the pipe rest. Environment noise was recorded. The ellipse fitting results of the signals showed a similar noise level as the ones without delay fiber. The rotation test was repeated, and each sensor component showed a similar response as without the delay cable (Figure 2.44b). The results indicate that the multiple component strain can be resolved when the sensing range is kilometers long.

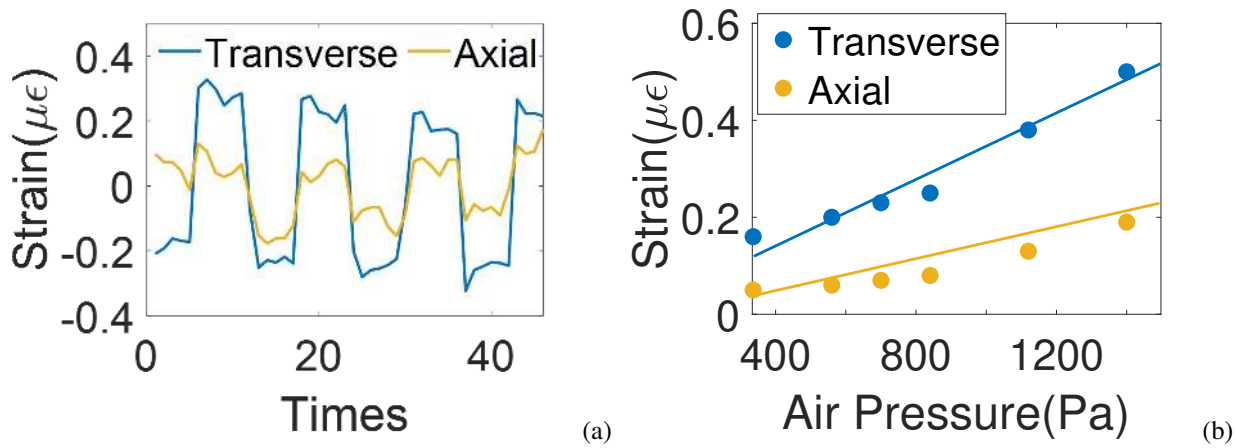

Figure 2.42: (a) Strain change along the transverse and axial directions when the 50 mL air was periodically pump into and out from the pipe. (b) Strain change along the transverse and axial directions as function of air pressure inside the column.

2.5.2.5 Pipe Sleeve Relocating

We took off the strain shell from the initial PVC pipe and attached it onto another 4-in pipe. The shell transfer was simple, and two people took about 5 minutes to complete. We wrapped tape around the shell for better strain transfer (Figure 2.45). The rotating pipe test that we performed on the initial pipe was repeated. The results show that the strain shell still can capture the small deformations of the pipe. The strain changing pattern and amplitude were similar to the same test we did before. The experiment results indicate that we can use this packaging method to build a strain shell to use in the field.

2.5.3 CMPI Direct Push Instrument

The strain shell works excellent when we attached on to the pipe. However, there are circumstances that we need the strain sensors to be underground by themselves. We have therefore developed the CMPI Direct Push Instrument (DPI), which comes with a robust aluminum case (Figure 2.46). The new design allows pushing the sensor device into the downhole without using a supporting pipe.

The installation of the DPI with loading and pumping test results are presented in Chapter 4.

2.6 Case Studies in the Lab

Several lab apparatuses have been build up and used for verifying the feasibility of the signal processing and sensor packaging of the distributed strain sensing platform in a manner similar to the field test.

2.6.1 5-Foot Corrugated Column

The first version of deformation-monitored lab apparatus consisted of a cardboard cylinder filled with earth material (sand). The fiber sensor was embedded in the sand after packaging. However, the size of the column was small. Besides, in that apparatus, cardboard column which has higher compliance than sand was used as the sand container, so it was complicated to compare the differential displacement of sand measured by the packaged sensors with deformation of the outer surface of the column measured by the reference sensors. The newly designed deformation-monitored lab apparatus used plastic corrugated tube as sand container which is more compliant to the vertical movement of the sand. Therefore, the new designed apparatus made the sensor packaging assessment more reliable.

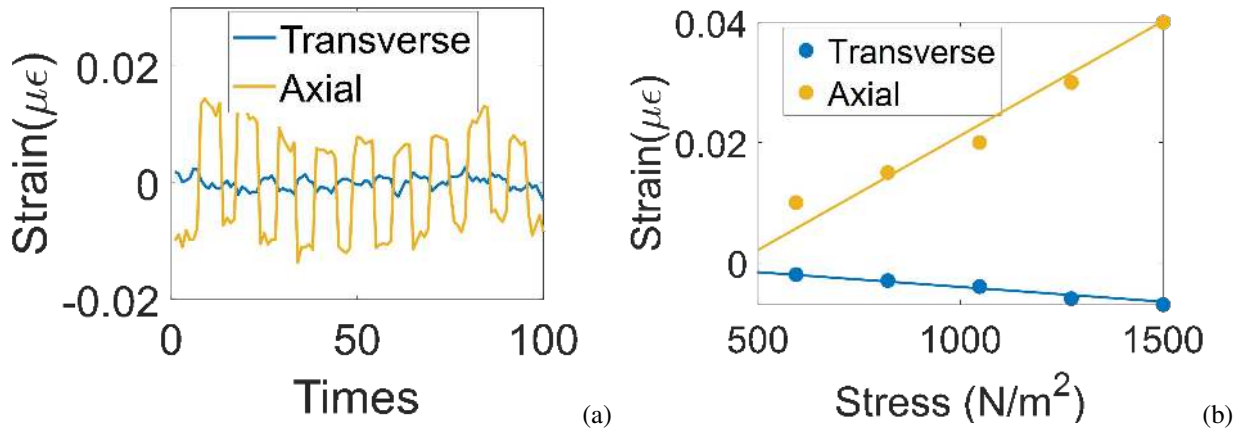

Figure 2.43: (a) Strain change along the transverse and axial directions when a 131-g weight was periodically putting on and off to the bottom end of the pipe. (b) Strain change along the transverse and axial directions as function of stress induced by the weights.

The schematic and image of the new deformation-monitored lab apparatus is shown in Figure 2.47. A 5-ft long 18-inch diameter corrugate tube was filled with sand, the bottom end of the tube was cemented into a round shape base. The based can be leveled by two jacks which were placed vertically to each other beneath the base. The button end of a 2-inch PVC pipe is fixed at the center of the base and buried in sand. A fiber with 8 reflectors on was pre-strained and attached to the PVC pipe. The separation distance between two adjacent reflectors was 0.15 m, and each fiber section between adjacent reflectors form a sensor, named S1, S2, S3, etc from top to bottom respectively. These sensors divided the entire pipe into 7 sections. The in lab coherent microwave photonics interrogator (CMPI) was connected to the top end of the fiber.

Static loads were applied to the top of the PVC pipe step by step, the signal under each loading step was recorded by the CMPI in lab interrogator and the strain at each sensor was calculated by using the signal processing method which was proposed last quarter. To exclude the temperature cross talk, 20 times of on and off measurements were performed to measure the response of the sensors under each loading weight. The measured strain as function of the applied loads for the seven sensors were plotted in Figure 2.48a. The S1 which was located most close to the top end of the PVC pipe was under the largest strain at each loading weight, and the S7 which was located most close to the bottom end of the PVC pipe was under the smallest strain at each loading weight. S1 was not buried in the sand, so loading force at S1 could be approximately equal to the gravity of the weight. The calculated Young's modulus (stress/strain) by using strain measured at S1 was 3 GPa, which is close to that of PVC pipe. The result indicates that the package method could help transfer the deformation from PVC to the sensor well.

Secondly, static loads were applied to the sand step by step by using the same loading strategy. The weights were placed next to the PVC pipe on the side where the sensors were taped on as shown in the inset of Figure 2.48b. The S1 was under the smallest strain among the 7 sensors as the sand movement was not affect the demotion of PVC pipe at that location. The strains measured by the first six sensors were smaller than the strain that measured by directly adding load on the top of the PVC pipe as shown in Figure 2.48b. We believe that the movement of sand induced small deformation of the PVC pipe because of the friction, and then the sensors measured the strain of the respective section of the PVC pipe. The experiment results indicate that, the differential displacement of sand is measurable by taping the sensor to a PVC pipe that buried in the sand, however, fixing sensor to a tube with the material compliance closer to sand would provide the sensors higher sensitivity to the sand movement.

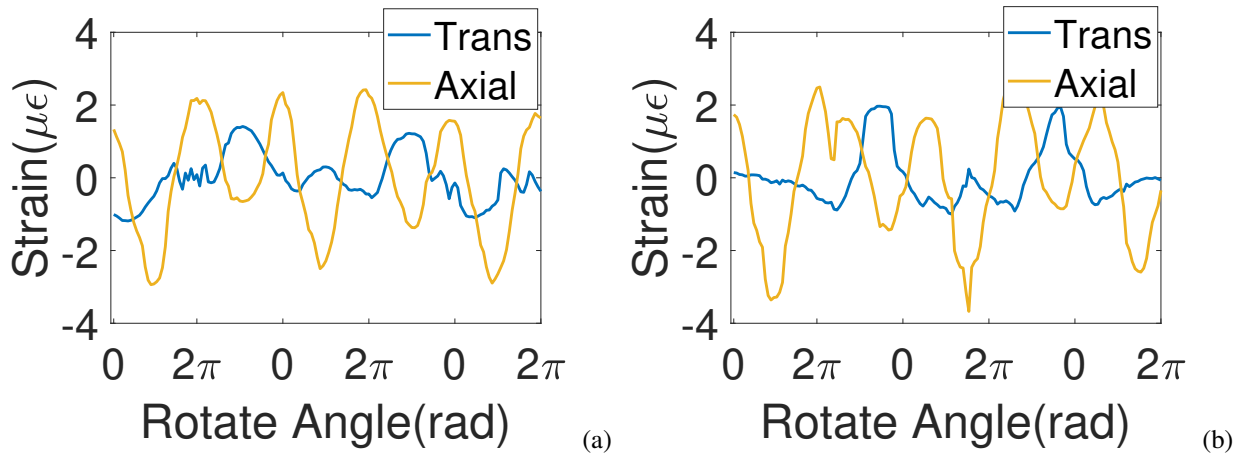

Figure 2.44: Strain change along the transverse and axial directions when the pipe was periodically rotated about the axial direction.(a)Strain shell was placed 30 m away from the interrogator.(b)strain shell was placed 1 km away from the interrogator

2.6.2 18-inch Tall PVC Column Injection Test

The objective of the test was to exam the bonding between the packaged fiber and sand. The strain measurement could be also provide guidance for the future field deployment.

The fiber sensor we used for the test has three reflectors on, and they formed two adjacent Fabry-Pérot interfrometers (FPIs). The separation between adjacent reflectors were 15 cm. The sensor was packaged by using the prototype packaging instrument, and then installed in a column. The schematic and picture of the apparatus are shown in Figures 2.49 and 2.50 respectively. The column was made from a 8-inch wide 18-inch tall PVC pipe cemented into a base. The column contains one entry 3/8-inch barb for injection and draining. A Tee was connected with the valve, and the other two ends of the Tee was connected with the pump and a stand pipe for head reading respectively. Inside the column at the base there was a threaded rod that was used to anchor the packaged sensor to the bottom. The sensor was anchored through a metal wire attached to a washer that threaded through the bottom of the packaging. The bottom of the packaging contained a rod that was used to attach the wire. The fiber array was tensioned during the filling of the column with sand. The column was periodically struck with a dead weight during the filling to compact the sand. The first reflector was 5 cm below the surface of the sand, and the third reflector was 10 cm above the bottom of the column.

A loading test was done first by adding a weight on the top of the sand. Strains at each sensor locations were negative when the weight was applied, and the absolute value of strains increased monotonously as the load increased. The ratio between the stress and measured strain was around 600 MPa for both locations. This is greater than the expected Young's modulus of sand, probably because of friction with the wall of the cylinder.

Water was injected into the base of the column. A peristaltic pump was used to inject water at a rate of $\sim$250 mL/min. Data were taken during the pumping test with sampling cycle of 0.3 s. The pumping was done step wise (0.6 L/step for the first steps, 0.4 L for last step), and head was measured during these breaks. The testing results are shown in Figure 2.51. Water flowed upward during pumping and stopped when the pump was off. The reading head after first step was 6.35 cm which was below the first reflector, so FPIs were compressed during the first step before 200 seconds due the expanding of the sand volume below the FPIs. During the second pumping step, the water level reached the bottom reflector. The head measured after the second step of pumping was 18.5 cm. At around 346 s, extension showed in the lower FPI and compression showed in the upper FPI. This is consistent with an increase in pore pressure between the lower two reflectors. During the third step of pumping, the signal indicated slight compression followed by rapid extension for the upper sensor, as the water level reached the middle reflector at around 802 s. The strain

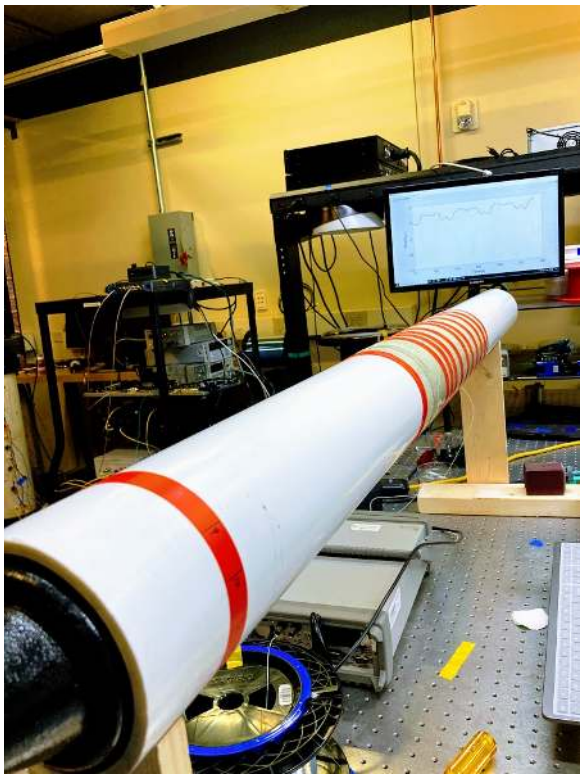

Figure 2.45: Image of the strain shell on the new pipe.

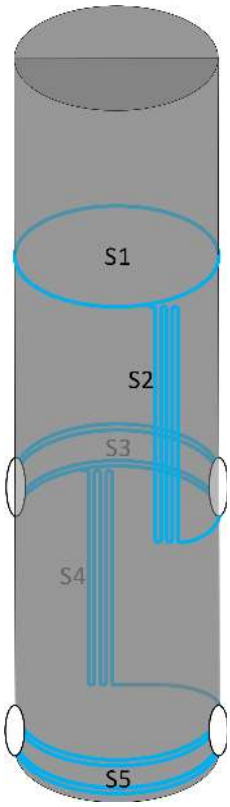

Figure 2.46: Schematic of the Direct Push Instrument. The sensing regimes are marked as S1–S6.

reached the maximum for both sensor locations at 1,327 s when the column begins to overflow, where in total of 2.2 L water were pumped into the column.

The peaks on both curves rapidly declined when the pump was turned off and the water level in the standing pipe flowed back to the column. Equilibrium was reached at 2,045 s, and the reading head at that time was 39.37 cm. Draining started at 2,045 s by opening a valve. The draining induced a rapid decrease in strain (tension) at both sensor locations, and the strain readings were both below original levels after draining. The reading from the upper sensor decreased more than the lower one. This could be due to either consolidation of the sand or temperature decreasing due to water injection. Temperature dropping may be larger at the upper sensor location because several round of water pumping had been done before this one, and the sand around lower sensor location should contain more water. Also, more sand on top of it was shielding it more from the swings temperature in the room. The slight strain increase/decline between the pumping stopping and the next step of pumping start starting was due to resettling of the grains or down flow of the water from the standing pipe to the column.

The observed strain during the injection test was consistent with expectations. This is encouraging. It suggests that method of packaging fiber in a polymer strip can protect the fiber in the high humidity underground environment, at least for a short duration. The packaging also provided good friction between the fiber and the sand because it appears that the the displacement of the sand was transferred to the fiber. This test was intended as a proof-of-concept, and we think it was successful in this regard. It also identified a need to make more accurate measurements of pressure and temperature within the column.

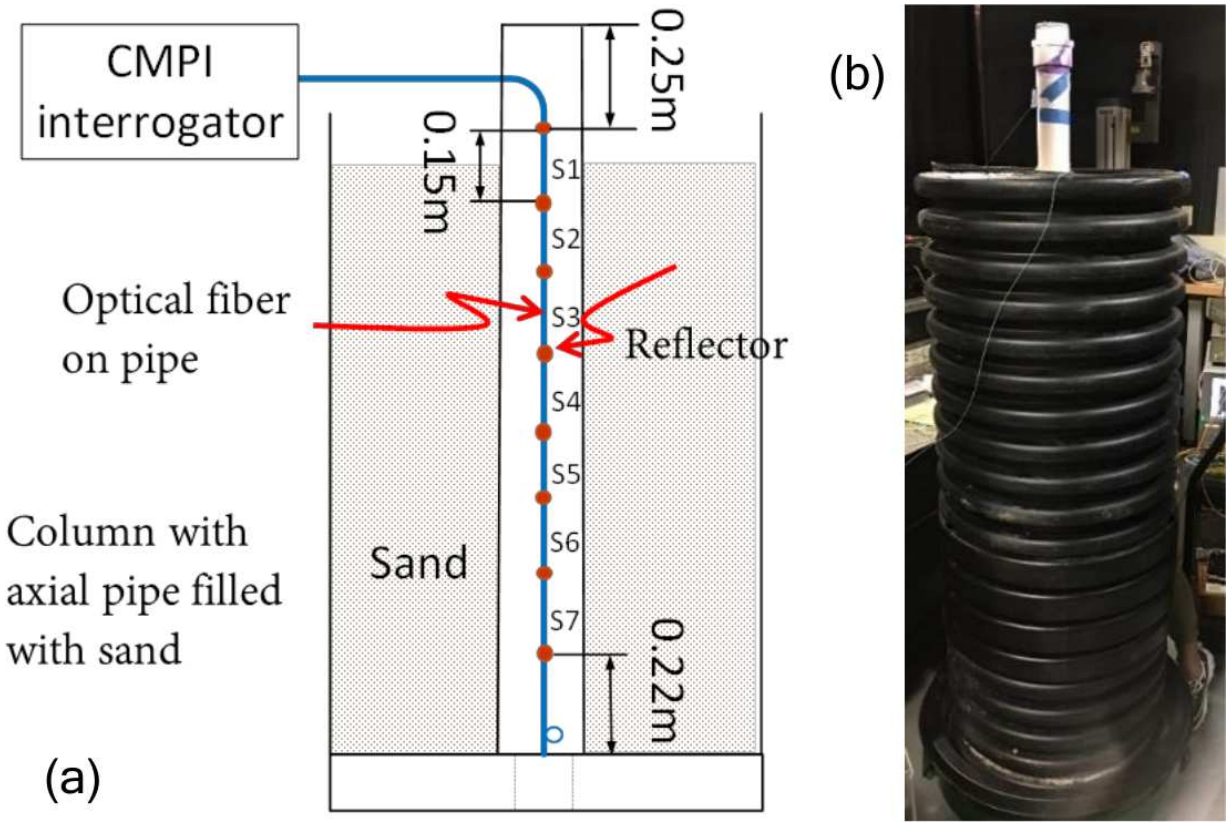

Figure 2.47: (a) Schematic and the (b) image of the deformation monitored lab apparatus.

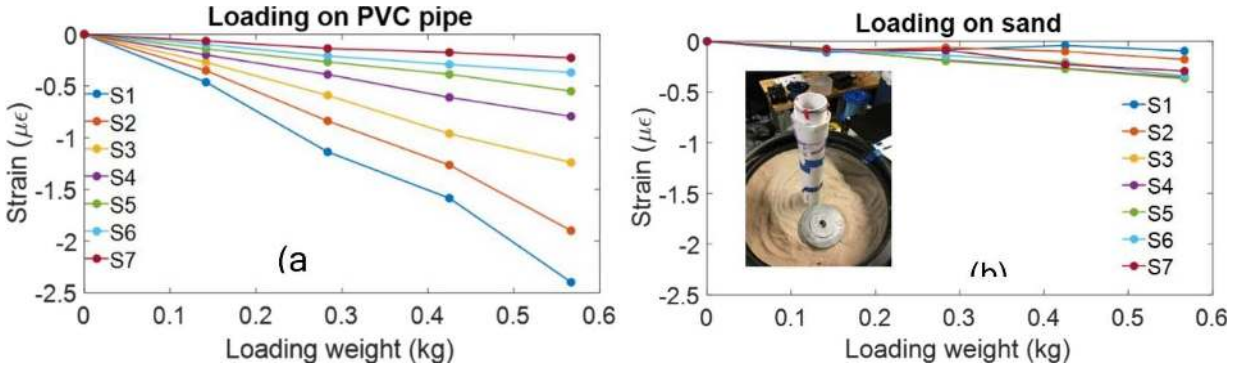

Figure 2.48: Strain versus loading weight for the seven sensors when adding load on the (a) top of the PVC pipe (b) sand.

2.6.3 Measuring Distributed Strain from Poroelastic Processes

Capabilities to measure distributed strain in the field with CMPI were advanced by conducting laboratory experiments, which allow strains during poroelastic processes to be measured in a controlled setting. The objectives of the laboratory experiments are both to advance the performance of CMPI, and to evaluate the feasibility of using CMPI to characterize poroelastic processes.

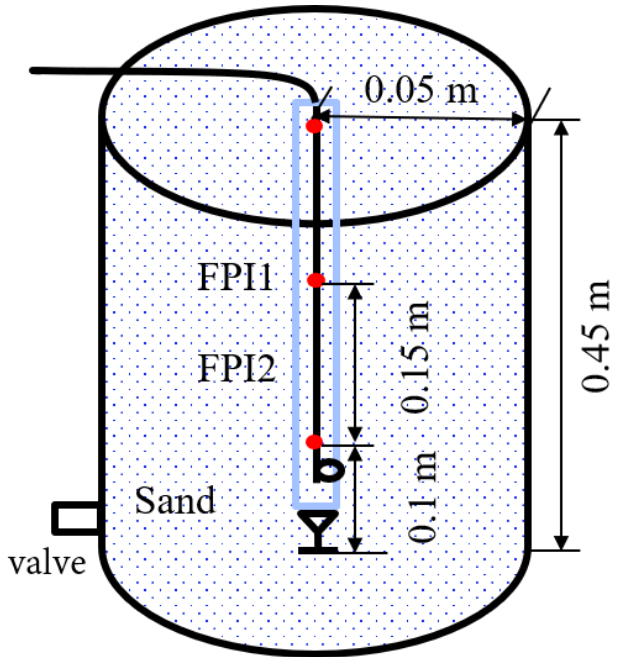

Figure 2.49: Schematic of the in lab apparatus for the pumping test.

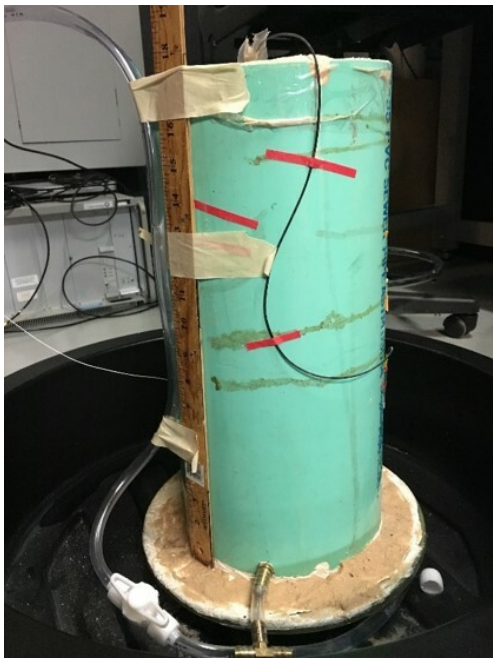

Figure 2.50: Lab apparatus for the injection test.

2.6.3.1 Experimental setup

The experiments were conducted using CMPI broadband reflectors placed along the axis of an instrumented column filled with fine-grained sand. This column, shown in Figure 2.52, is 74 cm tall and 20 cm wide in diameter. An optical fiber with 6 reflectors spaced 0.1 m apart was laminated between two pieces of polyester film, 2.5 cm wide and approximately 150 microns thick. The compliance of the film and fiber is approximately 80 $\mu\varepsilon$/N. The film was attached to the bottom of the column and tensioned with a constant force of 10N along the axis of the column. A layer of gravel 5cm deep was place on the bottom of the column to facilitate uniform distribution of injected fluid. A fine mesh was placed on top of the gravel and held in place with a thin layer of coarse-grained sand. The column was then filled with sand in lifts approximately 15cm thick and it was vibrated between the placement of each lift to promote consolidation. Figure pressure sensors and 4 temperature sensors are located around the column. The upper 4 sensors are attached to tensiometers, shown in Figure 2.53. The lower one is directly connected to the injection gravel layer.

2.6.3.2 Procedure, Results and Interpretation

Water is injected using a peristaltic pump. This water is left out overnight before the experiment to allow it to equilibrate with the air temperature. The peristaltic pump moves water at a rate of 250ml/min. Strain is measured using CMPI. The data acquisition system records pressure, temperature, weight of the water used for injection, as well as the temperature of the injected water and room temperature. When the water reaches the top of the column, it is allowed to pond for a moment then the pump is shut off to prevent the water from running over the top. After 5 to 10 minutes of stagnation, the pump is turned on in reverse and the water drains out at a constant rate. The pump is turned off when the pressure in the lowest sensor reads negative pressure. The pressures in the lower sensors will then rise due to delayed yield from storage. The pump is then turned back on and the process is repeated a couple times.

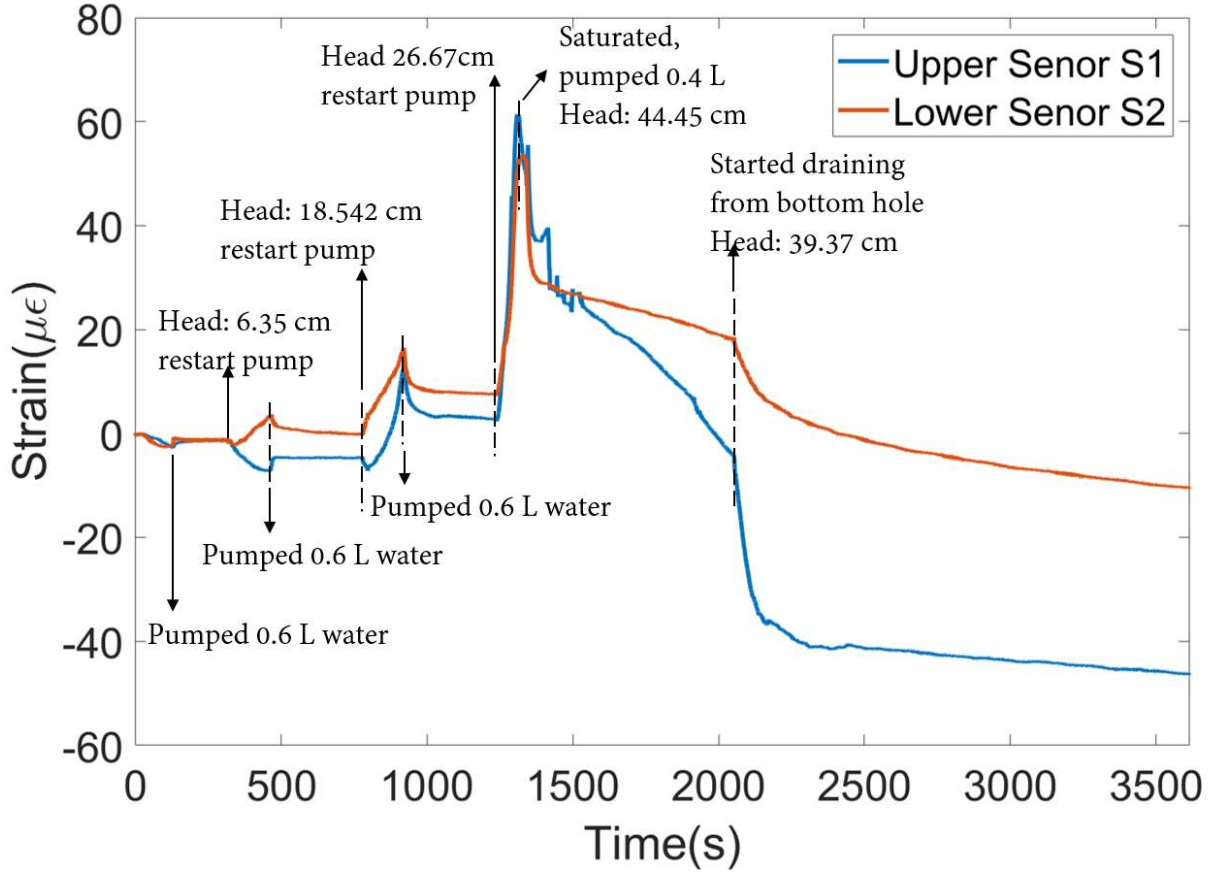

Figure 2.51: Strains at two sensor location during the lab injection test.

Several pumping out tests have been conducted. Data from a representative test are shown in the figures. Please note that the reflectors used to measure strain are named by their distances from the top of the column. i- denotes the reflectors inside the sand o- denotes reflectors taped to the outside of the column. i5cm is 5cm from the top of the column on the inside. o45cm is 45 cm from the top of the column on the outside. Reflector i45cm does not show signals as well as the other sensors, this is most likely due to a defect. It also shows oscillation related to the activity of the pump.

The representative test for the injection and pumping out shows initial compression followed by tensioning of the optical fiber (Figure 2.54). The lowest reflectors seem to go straight into extension. This is due to a residual water table and wetting front present from previous tests. The order at which the reflectors go from compression to tension is ordered by their distance from the wetting front. As the wetting front reaches the top of the column, a sharp increase in pressure and a sharp movement into compression is seen (Figure 2.58). We believe this is due to changes in capillary suction. After the sharp dip into compression, the fiber begins tensioning as the column continues to fill past the sand. The pump is turned off to prevent water from draining from the top.

After around 5 minutes for stabilization, the pump is turned on in reverse to drain. Drainage causes an initial tensioning of the fiber due to what we believe is poroelastic rebound (Figure 2.59). Eventually, compression begins, and the optical fiber goes into compression. The order which they switch over is related to their depth in the column. To allow for delayed yield from storage, further pumping cycles are carried out. A dip into compression due to this in the lower sensors is shown on Figure 2.54.

Sensors along the outside of the column also show changes in strain during these pumping events (Figure 2.55). During injection, the strains diverge from each other. The lowest strain sensor, o45cm, shows the most extension followed by the rest of the outside sensors in order of depth from the top. We believe this to be due to the column bulging out as it fills with water. When the water drains, the difference between the strain shown in the reflectors lessens.

In a another test, the water was injected until the column is approximately 2/3 full. The pump is then turned off for several minutes. After this stabilization period, called "Hold" in Figure 2.61, the pump direction is reversed and water is pumped out of the column at a rate of 250 mL/min.

The bottom of the column goes into tension at the beginning of injection. The strain rate is relatively fast over the first minute, but then it decreases and remains steady at approximately 0.03 $\mu\epsilon$/s at the lower two sensors. This is an expansion of the bottom of the column as a linear function of time. The strain rate at 25 cm increases after approximately 400 s and reaches 0.03 $\mu\epsilon$/s at 600 s. Interestingly, the strain rate at the underlying sensor (15 cm) drops and is roughly zero when the rate at the 25 cm reaches $\mu\epsilon$/s. The strain rate at the sensor 10 cm above (15 cm) reaches 0.03 $\mu\epsilon$/s at approximate 1,000 s, and a similar effect occurs at 5 cm, where the strain rate increases to 0.03 $\mu\epsilon$/s at 1,400 s. The strain signal propagates up the column at a rate of approximately 1 cm in 40 s (0.0003 m/s). This is approximately the rate at which the level of the saturated height of the column is rising.

The pressure at the bottom of the column increases at approximately 2.5 Pa/s. This is consistent with a rise in the water level at a rate of 0.25 mm/s. This is equivalent to 1 cm in 40s, which is the same rate of advance as the strain signal.

The pump is shut off at 1,600 s and the system is held constant for 20 minutes. The pressures drop and the strains become slightly compressive when pumping stops and they are roughly constant during the Hold interval.

Water is pumped out starting at 2,278 seconds. The top (5 cm) and bottom (45 cm) of the column are compressed immediately. Tensile strain occurs at the other three strain sensors at the outset of pumping, but this effect is short lived as the strain reverses and becomes tensile with time. The switch from tension to compression occurs from the top down with a lag of approximately 300 seconds between each sensor. The pump is shut off at time 3,577 seconds. The column stops compressing and tensions slightly.

The pressure drops rapidly when the pump is turned on, and then the rate of drop diminishes. The experiment shows how strain is related to changes in pressure and water content in sand. Pressure increase during injection causes expansion of the porous media and tensile strain. A strain wave progresses up the column at the same rate as the rise of the saturated zone. The bulk modulus of the can be estimated as the ratio of the pressurization and strain rates, 2.5 Pa/s divided by 0.03 $\mu\epsilon$/s, which gives $K = 83$ MPa. The rapid drop when pumping stops is accompanied by a rapid, brief compression during the Hold period. The onset of pumping causing pressure to drop rapidly and this causes compression at the bottom of the column where the pressure changes initially. However, tensile strains occur in the sand overlying the lowest sensor at the outset of pumping. This occurs in response to the tensile strain at the bottom of the column. Tensile strain also occurs at the top of the column as the water level drops. The strain reverses and becomes compressive progressively from top to bottom as the water level reaches each sensor.

These results suggest that Small scale strain measurements can be seen under laboratory conditions of injection and drainage. Packaging the fiber between tape adequately connects the sand and the optical fiber allowing for transfer of strain. Strain seems to be affected by boundaries such as the water table and the capillary barrier at the interface between the sand and the top of the column. The distributed strain measurements show variations in strain in different lengths along and inside the column. The analysis showed that the strains measured with CMPI sensors embedded in sand are reflecting strains during poroelastic deformation.

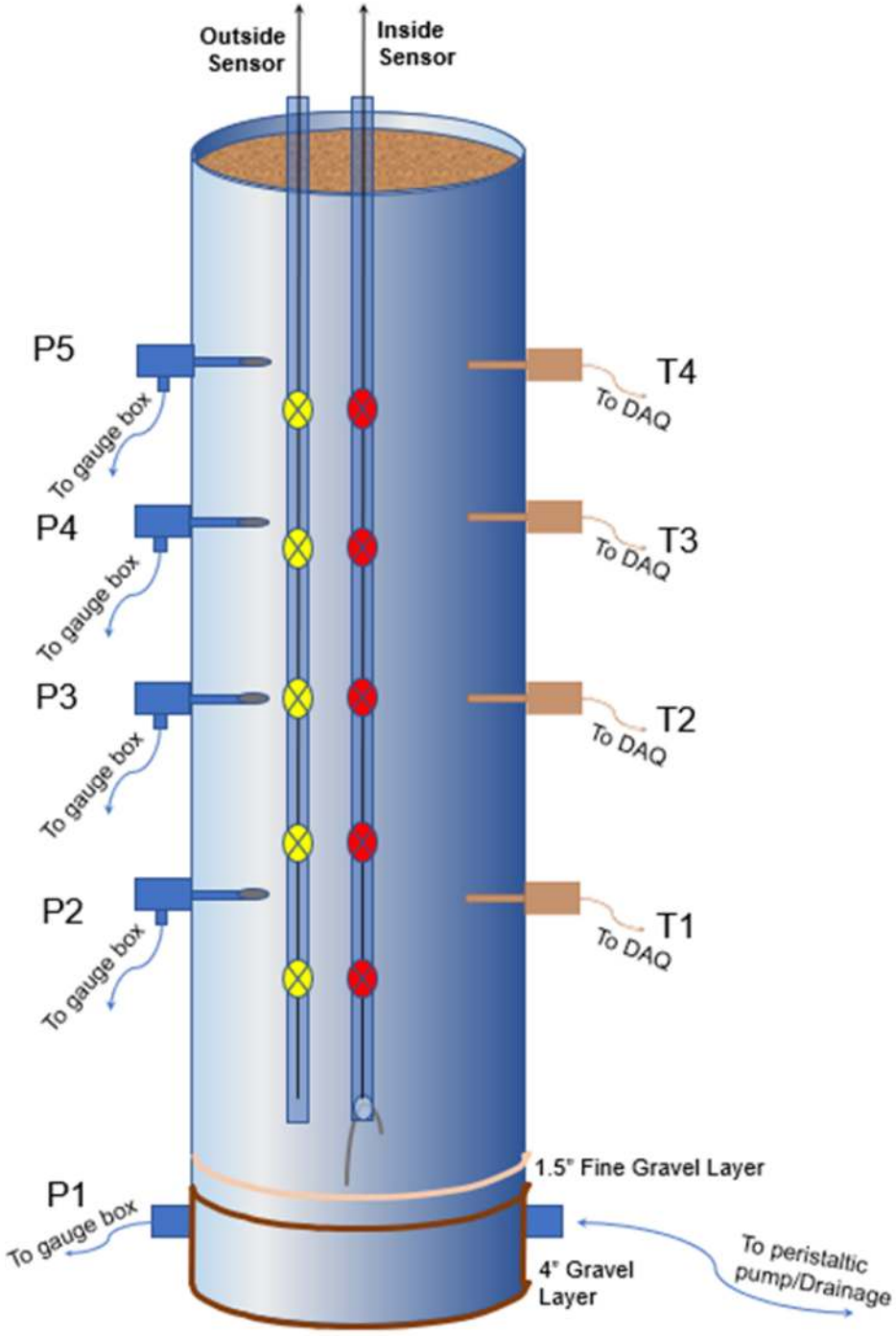

Figure 2.52: Column used for experiments to evaluate CMPI during poroelastic deformation. P1-5 are pressure sensors. T1-4 are thermistors housed in brass tubing. The five red points indicate the reflectors on fiber on the inside of the column inside the sand; yellow ones indicate the reflectors on fiber along the outside of the column.

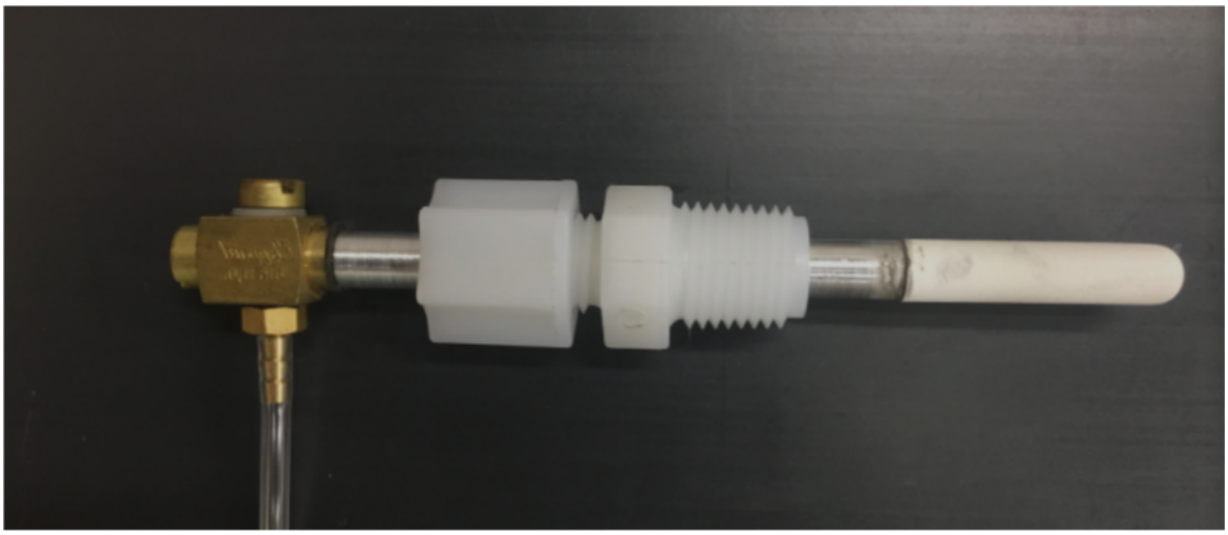

Figure 2.53: Tensiometer used to measure pressure in the sand on P2-P5. The porous cup allows negative pressure to be measured.

2.6.3.3 Loading Tests

The column was loaded with weights and the strain was measured in the sand and in the wall of the column. The load was applied by placing weights on Styrofoam cylinder with a diameter that is approximately 1 cm less than the inside of pipe. A 2.5-cm-wide slot was cut along the radius of the loading column and the strain ribbon was put in the slot during loading. This allowed the load to be applied without contacting the strain ribbon. Steel disks were placed on the loading cylinder to generate forces of 1.4, 2.8, 5.4 and 11.4 N. A loading test was conducted by placing steel disks on the loading cylinder, measuring the strain at each reflector pair for approximately 60 seconds. Then the weights were removed for approximately 1 minute, and the test was repeated approximately 10 times. This produced a step-like time series of increasing and decreasing strain. Trends in the strain also occurred during the test, presumably because of temperature changes. The average strain resulting from the applied load was determined with a trend lines that were manually fit to the upper and lower steps in the time series.

Four suites of tests were conducted using loads applied to dry sand soon after the column was filled. Three suites of tests were conducting later when the sand was completely saturated. Additional tests were conducted by applying load to the wall of the pipe instead of on the sand. The tests are named for where the load was applied (LS = load on sand; LW = load on wall)–the moisture state of the sand (DS = dry sand, WS = wet and fully saturated sand) and the applied load in grams force. So, test LS-DS-560 applied a weight of 560 gm to the dry sand.

The strains at a particular elevation increased with the applied load. This is the expected response, so the strains were normalized to the applied load to facilitate plotting (Figure 2.62). The strain in the sand increases markedly with elevation in all the tests. Strains in the saturated sand are generally greater than strains in the dry sand at the same elevation. The maximum ratio is approximately 0.7 1/N at the upper end of the column when the sand is saturated, and the ratio decreases to approximately 0.1 1/N at lower end of the column (Figure 2.62)).

In contrast, the strain ratio in the wall of the column ranges from 0.02 to 0.1 1/N. The strain ratio in the wall appears to be independent of elevation and there appears to be negligible difference between tests using dry and saturated sand (Figure 2.63).

It was assumed that the applied force was uniformly distributed at a particular elevation within the sand and within the PVC pipe. It was also assumed that the applied force could transfer from the sand to the PVC pipe. So, for

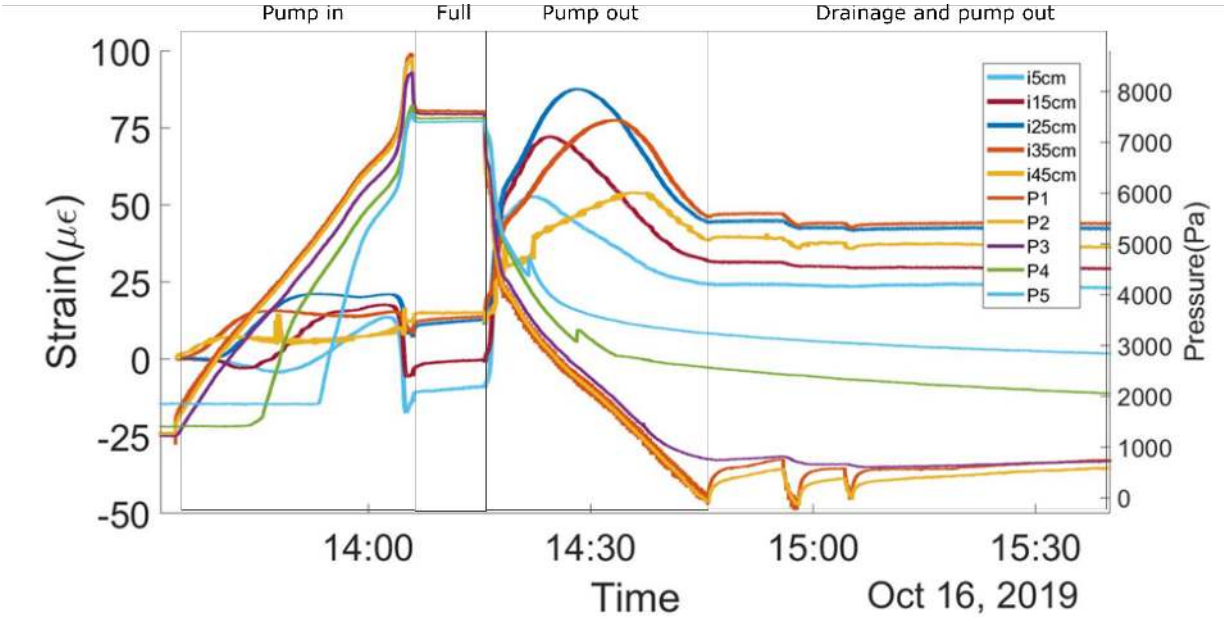

Figure 2.54: Strains measured inside the column with CMPI and pressures measured with internal gauges at different at different locations as functions of time.

example, the fraction of the load carried by the sand could increase if the fraction carried by the pipe decreased with elevation, providing the total force summed to the applied load.

A series of optimization analyses was conducted by determining the elastic moduli $E^{(\prime)}{}_{PVC}$ and the five $E^{(\prime)}{}_{si}$. The objective function was the sum of the squared residuals between the applied force and the sum of $F_s + F_w$. Analyses were conducted for all the test conducted using wet sand, all the tests conducted using dry sand, and all the tests as an aggregate.

The elastic modulus of the PVC pipe is in the range of 2 to 3 GPa, whereas the sand is in the range of 5 to 30 MPa. This causes the force carried by the PVC pipe to be greater than that in the sand, even though the weight was applied to the sand. The ratio of F_s/F_{applied} is generally less than 0.2, and it is less than 0.1 at the bottom of column, according to the analysis. Ratio of F_w/F_s decreases with elevation, which is consistent with Figure 2.62.

The ratio of $(F_w + F_s)/F_{\text{applied}}$ typically increases with elevation and it generally ranges between 0.4 and 1.6 (Figure 2.64). Ideally, this ratio would equal unity.

The optimization analysis estimates an effective elastic modulus, $E^{(\prime)}$. Poisson's ratio for sand can range from 0.25 to 0.4, which causes C_1 to range from 0.83 to 0.47, and $\nu = 0.3$ gives $C_1 = 0.75$. This allows Young's modulus to be estimated from the strain data (Figure 2.65)). The results indicate that Young's modulus is roughly uniform from the middle to the top of the column. Estimates based on all the data are in the range of $E_s = 15$ to 20 MPa, and E_{PVC} using only the data from dry sand indicate a stiffer modulus for sand, in the range of $E_s = 30$ MPa, and E_{PVC} estimate using only the data from wet sand indicate a softer modulus for sand, in the range of $E_s = 5$ to 10 MPa, and $E_{PVC} = 2.4$ GPa.

Published estimates for the Young's modulus of loose sand range from 5 to 25 MPa. Published values for E of PVC pipes range from 2.4 to 2.9 GPa.

Values of E_s and E_{PVC} are consistent with published values using strain estimates from the middle to the upper parts of the column, but estimated Es in the bottom of the column is greater than expected. This is a consequence of the strain in the sand decreasing with depth (Figure 2.62).

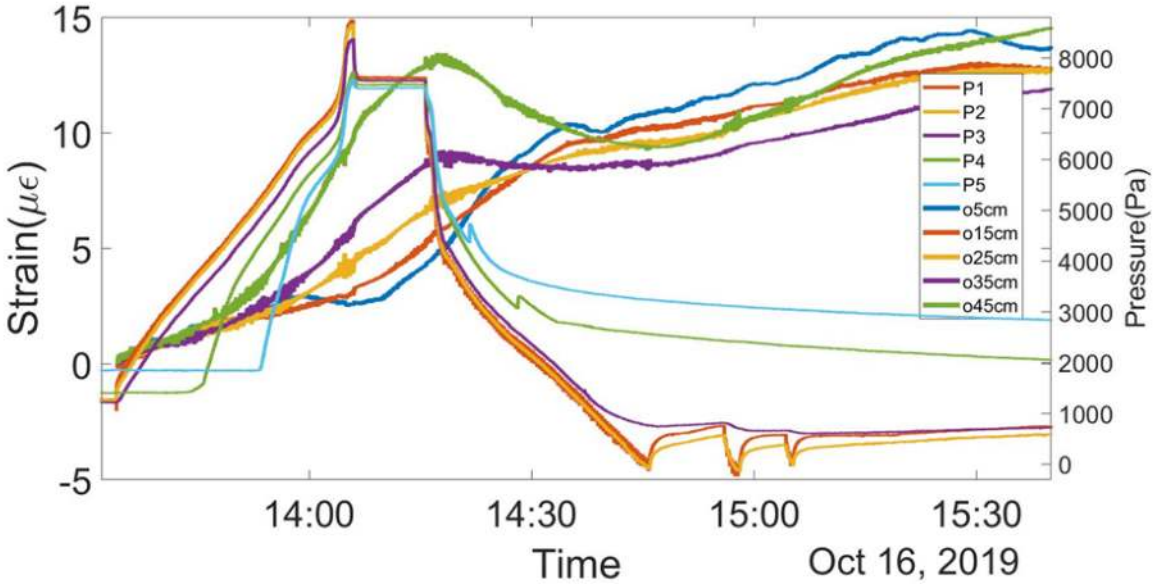

Figure 2.55: Strains measured on the outside the column with CMPI and pressures measured with different internal gauges as functions of time. Strain of the column to occurs as the column fills with water. The lowest sensor detects the most strain. As the column drains the difference between the strains decreases.

2.6.4 Air Pressure Column Test

Estimating changes in pressure or changes in gas phase permeability from strain data could be a way to monitor changes saturation. This approach has applications for detecting CO2 storage in reservoirs, or CO2 accumulation in the shallow subsurface. Evaluating the feasibility of detecting strains caused by small changes in gas pressure also provides a tool for assessing and refining the CMPI measurement method developed for the project.

The basic tools for measuring strain from barometric pressure changes and analyzing these measurements appear to be in place, but some tools are in their early stages. Coherence-Length-Gated Microwave Photonics Interferometry, or CMPI has been demonstrated to measure strain changes at various depths in the field, but most of the former measured change was due to slow pressure changes. The seismic wave we measured showed reasonable delays as a function of depth, but the results were lack comparison from reference sensors. This quarter, laboratory experiments were conducted to compare the strain signals with the fast varying air pressure signal to evaluate dynamic measuring feasibility.

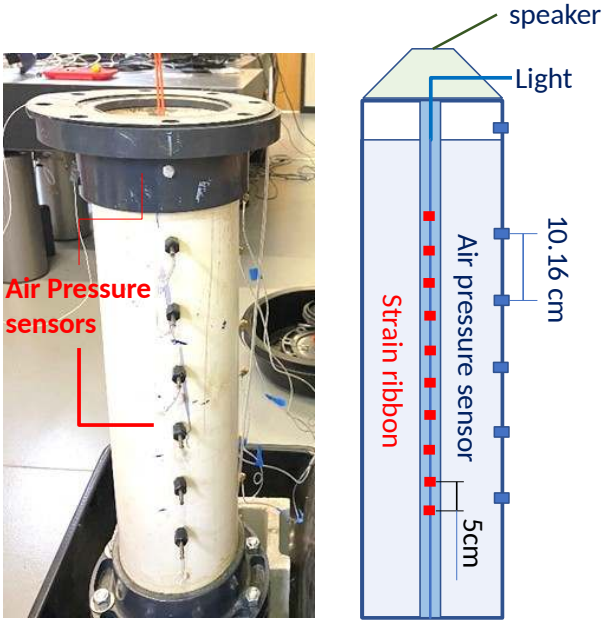

Figure 2.66: Annotated photograph and sketch of the smart column.

The laboratory experiments were set up using a PVC column filled with permeable material and configured with instrumentation to measure parameters, such as air pressure, water pressure, and vertical strain. The experiments

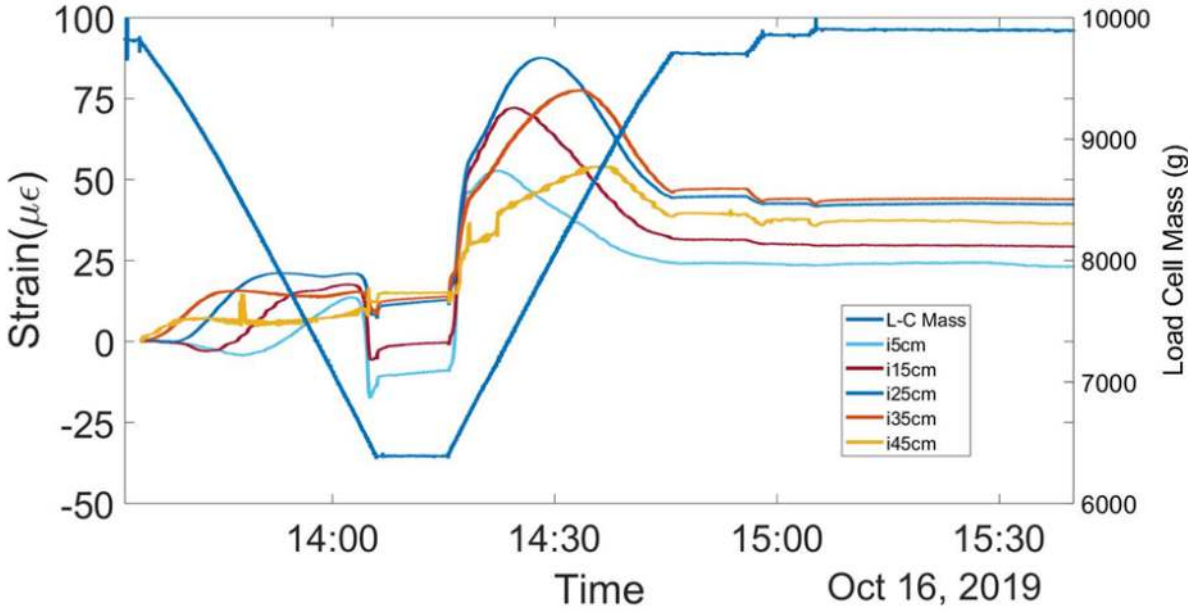

Figure 2.56: Strains measured inside the column with CMPI and the mass of water injected measured by load cells as functions of time.

consisted of changing the air pressure at the column's top and measuring pressure and strain propagation throughout the column. Figure 2.66 shows an image of the column. The PVC column is eight inches (20.32 cm) in diameter and has two flange pieces that are glued on both ends. These pieces have caps and gaskets that are bolted onto the column to ensure there is no air leakage and can be easily removed if needed. The column's total length from both ends of the flange pieces is 40.5 (115.58 cm) inches. Quarter-inch holes were drilled and tapped into the PVC column on two axes for both the air pressure and water pressure sensors.

Low-pressure air sensors were used to measure the variability of the air pressure during experimentation. These transducers use digital differential pressure sensors and a compensated analog output. They cover a pressure range of 0.15 to 1 psi, or about 1–7 kPa. The sensors were connected to a LabJack data acquisition device that produces an automatic analog and digital output used to process the pressure data. The holes that contained air pressure sensors used in this experiment are at the depths of 4.5 in (11.43 cm), 12 in (30.48 cm), 16 in (40.64 cm), 20 in (50.8 cm), 24 in (60.96 cm) , 28 in (71.12 cm). The top sensor located at 4.5 in was set to just above the sand level and has been used as the reference sensor. The other five sensors are buried in the sand.

The strain sensor was composed of single-mode fiber (SMF) and 12 weak reflectors spaced every 5 cm on the fiber. An external Michelson interferometer (MI) with a cavity length of 10 cm was used to select every other reflector to form distributed interferometers. The fiber was laminated within two pieces of one-inch wide tape to form the CMPI strain ribbon. This strain ribbon was ingrained with the sand during column installation. The ribbon was attached with a hook on the bottom piece of the column and extended to just below the sand level at the top of the column. While the sand was being installed into the column, the ribbon had tension from a pulley system with a 1 kg weight. Once the sand reached the top of the column, the tension was removed, and the cable from the ribbon was embedded into a slot cut into the top gasket. Vacuum grease was applied to this to ensure there would not be any air leakage.Further improvements to the sand-packed PVC column were made to ensure the air would not leak during the induced acoustic application. Connections between the PVC column and both air pressure and water pressure sensors were cleaned and reapplied with a Teflon tape and pipe dope to create a strong seal in the threads. This seal was tested by applying a high pressure to the column and using a pressure transducer to monitor if the pressure could be maintained. The applied

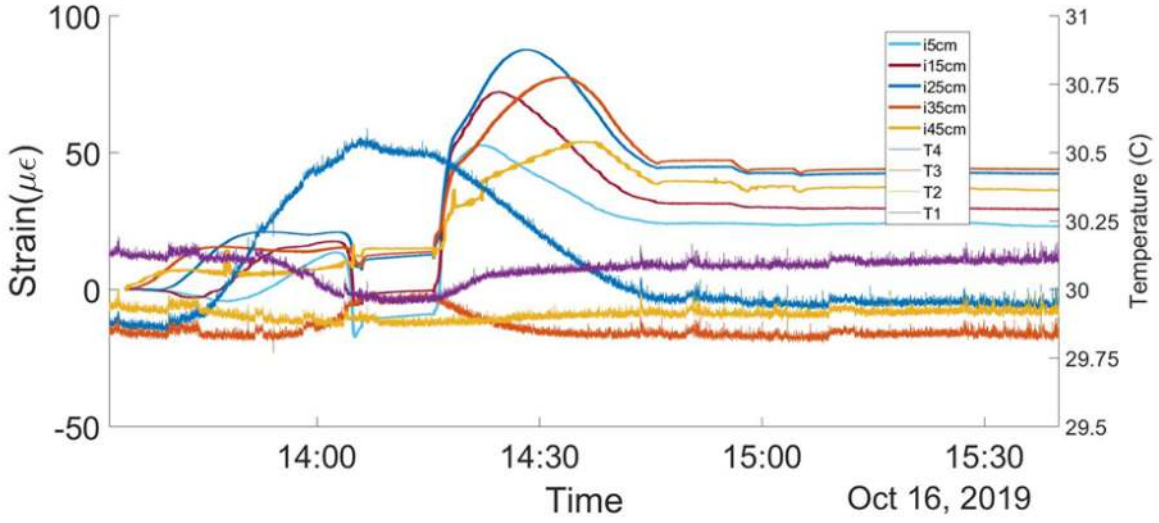

Figure 2.57: Column temperature and inside strains measured with CMPI as functions of time.

pressure was stable in the column for more than several minutes, so seal was concluded to be maintained. The column was repacked with fresh sand and a 3-inch gravel layer at the bottom. The strain ribbon was reinstalled by tensioning the ribbon with a pulley system and known weight to protect the fiber while the sand and gravel was filled within the column.

A synchronization between the air pressure data acquisition system (LABJACK T7) and CMPI system was made to better analyze the correlation between pressure and strain signals. A Python program was created to put the LABJACK on the streaming hold mode. The program starts streaming data once the external trigger signal from the CMPI interrogator is received. The synchronization allows a constant time delay between the the air pressure and the strain signals.

A 4 Hz acoustic signal was applied to the dry sand using a speaker and a function generator. The speaker was drilled into the top lid of the column so the signal could be applied directly into the head space above the sand. The 4 Hz signal was produced continuously while several rounds of data were acquired. Air pressure measurements were recorded at five different lengths of the column at 4-inch space in addition to one measurement being made above the sand level within the head space. Figure 2.67 displays the results of the raw air pressure data between two and three seconds of a test. The sensor installed in the head space is represented by s1, and the sensor furthest down the column is represented as s6. The maximum amplitude of the air pressure is observed to be perceived by s1, where the acoustic signal is the closest. As the air pres-

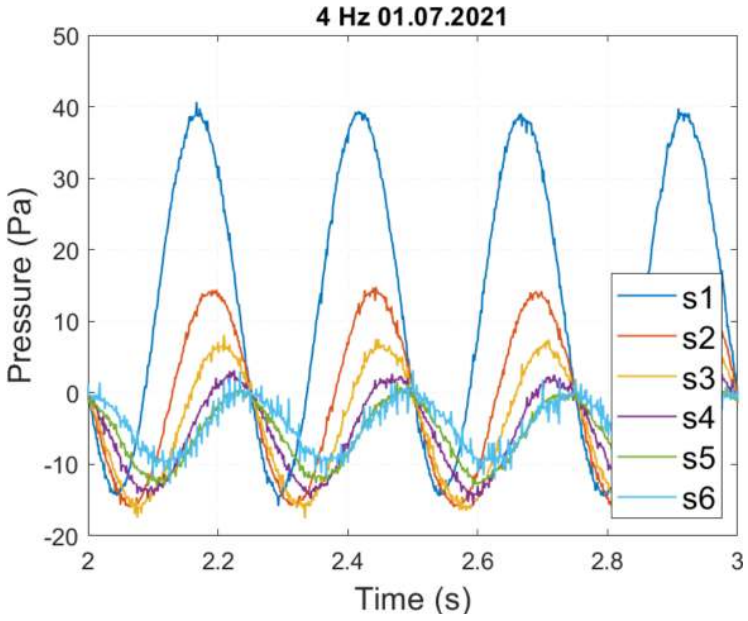

Figure 2.67: Raw air pressure data from induced acoustic signals.

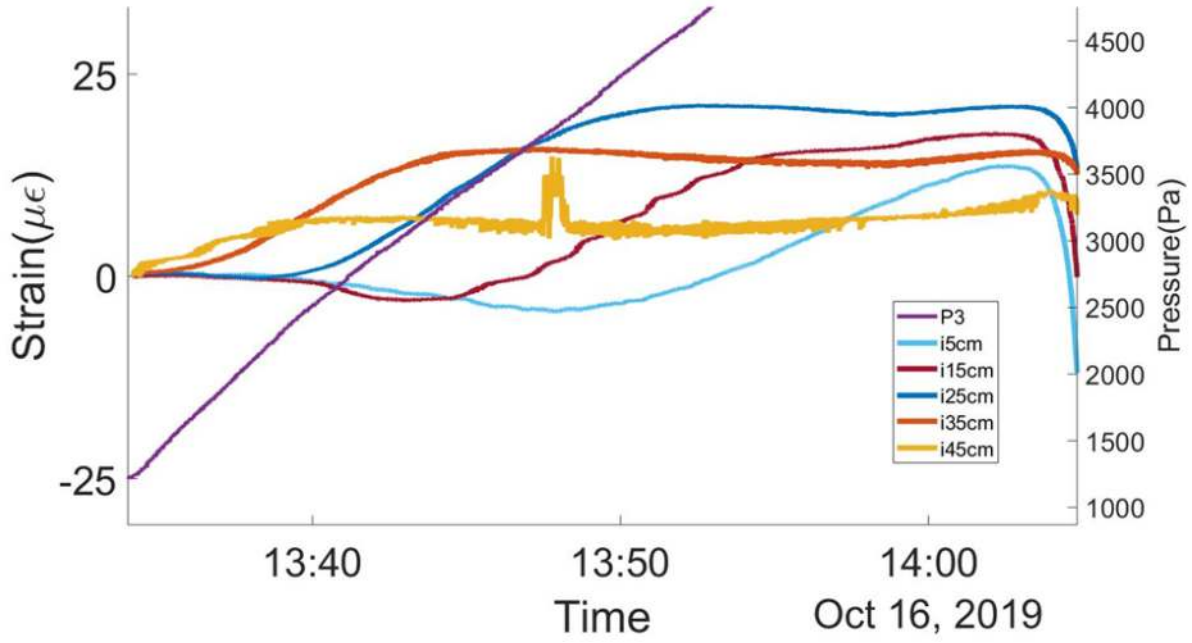

Figure 2.58: Early strain measurements made with CMPI and the pressure at P3 as functions of time. Notice the ordering of tensioning corresponds to increasing pressure and depth in the column.

sure wave travels within the sand, the magnitude of the of the air pressure is dampened as depth is increasing (the signal moving towards the other sensors). This is inferred to be caused by the air diffusivity that decreases with an increase in depth.

Phase delay analyses were done on these experiments for both the air pressure and strain measurements. It was expected that the strain would be affected by the induced air flow and the delay between the sensors would be dependent on the depth as well. The analysis for the delay in the air pressure signal was computed by subtracting the arrival times from s1, the sensor contained in the head space. Figure 2.68 shows the results from the phase analysis on both the air pressure and the strain during experimentation. The delay of the air pressure is observed to be nearly linear, while the strain measurements have some variation. The smallest time delay in the air pressure is from the spacing between s1 and s2, yielding approximately a 22 ms delay. The strain delay for the reflectors closest to the acoustic signal is 32 ms. As the depth increases, the time delay for the air pressure signal has increased to approximately 75 ms between s1 and s6 for the air pressure data and 73 ms for the strain data. Both of the parameters are trending in the same pattern, showing an increase in the time delay as depth is increased as well. This trend is implied to be a result of the air diffusivity changing as a function of depth as well.

We applied the acoustic sinusoidal signal to the dry sand material and measured both the air pressure and the vertical strain as functions of time and depth. The acoustic sinusoidal signal had a frequency of 4 Hz, and the air pressure and strain were measured. The recorded strain and air pressure data are shown in Figures 2.69 and 2.70, respectively. The air pressure signal produced from the acoustic speaker induces a response in the vertical strain. When the pressure is observed to be increasing, the vertical strain responds by compressing. In addition, when the pressure begins to decrease, the vertical strain signal moves into tension. This correlation is seen throughout the recorded data even though the figures are only currently showing less than one second. It can be inferred in this unsaturated case that the compressional strain is found when the pressure is increasing, and tensile strain is measured when the pressure is decreasing. Furthermore, the air pressure delay is observed to be the largest in this unsaturated case. There is approximately 80 ms from when the top air pressure sensor (6.6 cm) receives the acoustic signal to

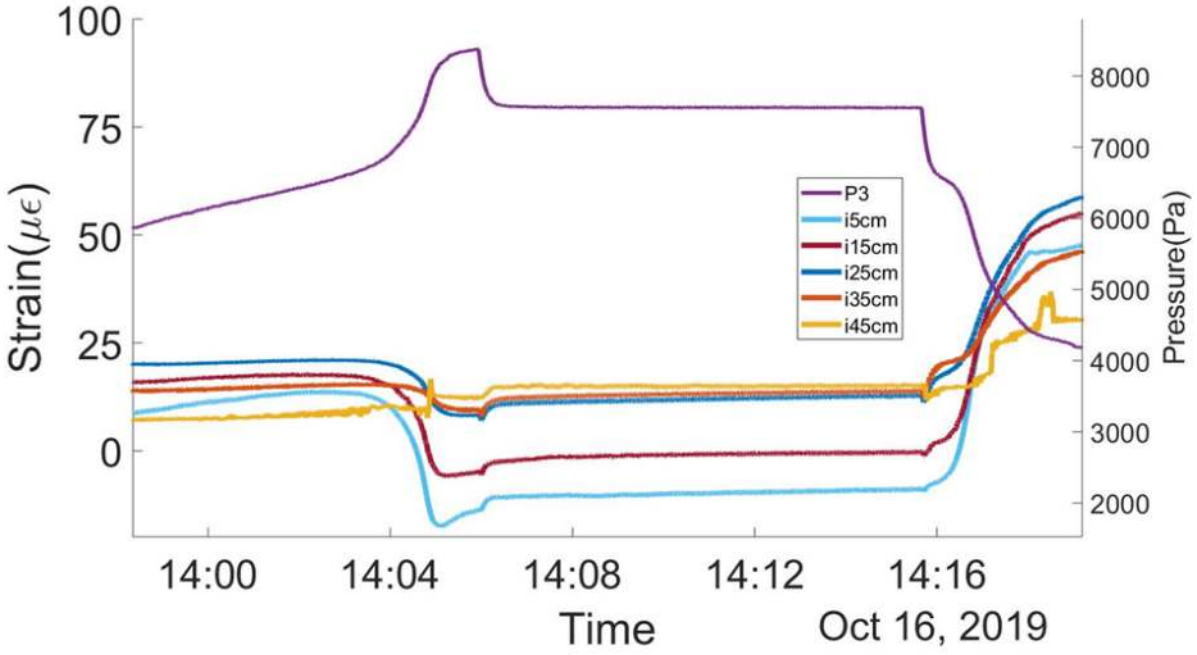

Figure 2.59: Strain measurements made with CMPI and the pressure at P3 as functions of time around the pressure jump and early draining. The amount of compression during the pressure jump decreases with depth away from the top of the column.

when it arrives at the last sensor (67.6 cm).

Further experiments took place that included injecting water into the bottom of the sand-packed PVC column and repeating by applying the acoustic sinusoidal signal. The purpose of this procedure was to observe the changes in the time delay between the air pressure sensors when the relative air permeability was changed due to the presence of water in the pore space. Water was injected into the column at a rate of 0.1 L/min until it reached the top of the column according to the water level in the standpipe. Once the water reached the top of the column, it was pumped back out at the same rate in which it was injected. The acoustic sinusoidal signal was applied once the water had been pumped out, but before enough time had taken place that gravity drained the remaining water. The strain and air pressure results for this experiment are shown in Figures 2.71 and 2.72. The presence of the water has altered the responses from both the air pressure and strain. There is still a relationship between increasing pressure causing compression and decreasing pressure causing tension, but the time delay has increased. There is now a 120 ms between when the acoustic signal reaches the top air pressure sensor to when it arrives to the bottom, increasing the delay by about 50 percent from the unsaturated conditions. The available pore space that was filled with air in the unsaturated case now contains water, which has impaired the free movement of the air. This has caused a decrease in the gas-phase diffusivity, resulting in a longer time delay between the two sensors.

Additional modifications were made to the sand material of the column to measure the effects of the changes in permeability. Soil gathered in Clemson, SC was collected, dried, and sieved so it could be added to the original sand. A silt material that was retained in the 120-mesh sieve (125 microns) was used for the experiments. The original sand and silt were then mixed by weight, where the final mixture contained 80 percent sand and 20 percent silt. This mixture was added to the top of the column, and experiments were then repeated by applying the acoustic sinusoidal signal. T he results from an unsaturated test with the addition of this material is shown in Figures 2.73 and 2.74. Figure 2.74 specifically shows the results from applying the acoustic sinusoidal signal to the unsaturated sand/silt mixture that was added to the column. As mentioned above, the delay in the sand material between the top and bottom air pressure

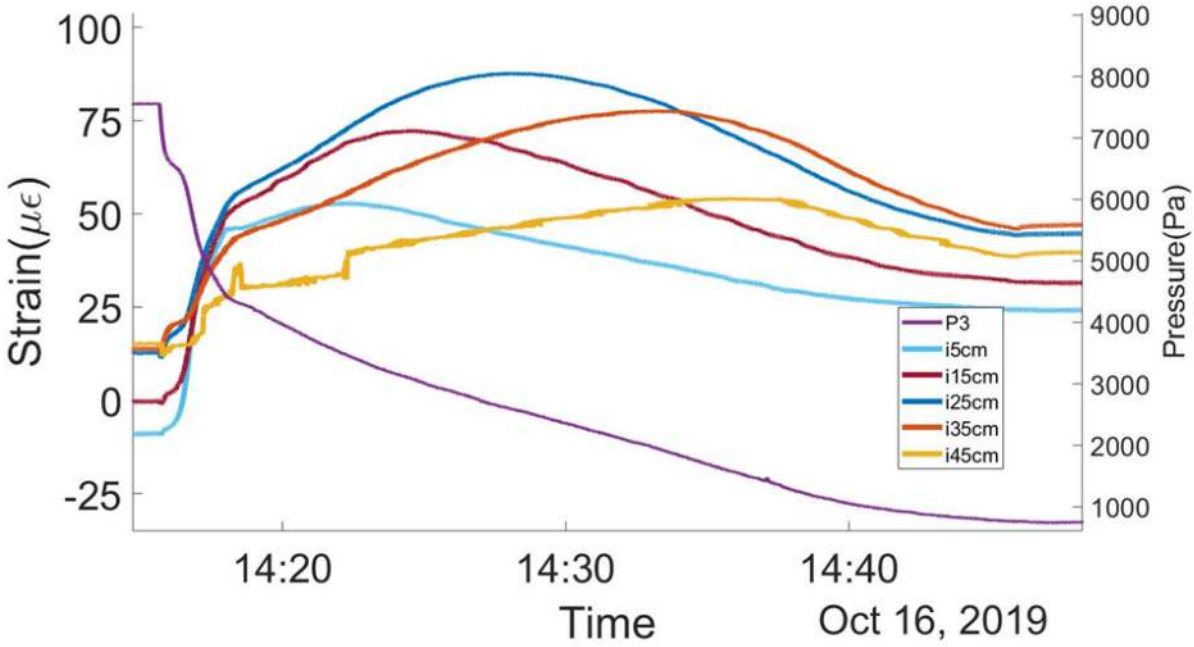

Figure 2.60: Inside strain measurements made with CMPI and the pressure in P3 as functions of time during the drainage. The change from extension to compression occur in order of decreasing depth from the top.

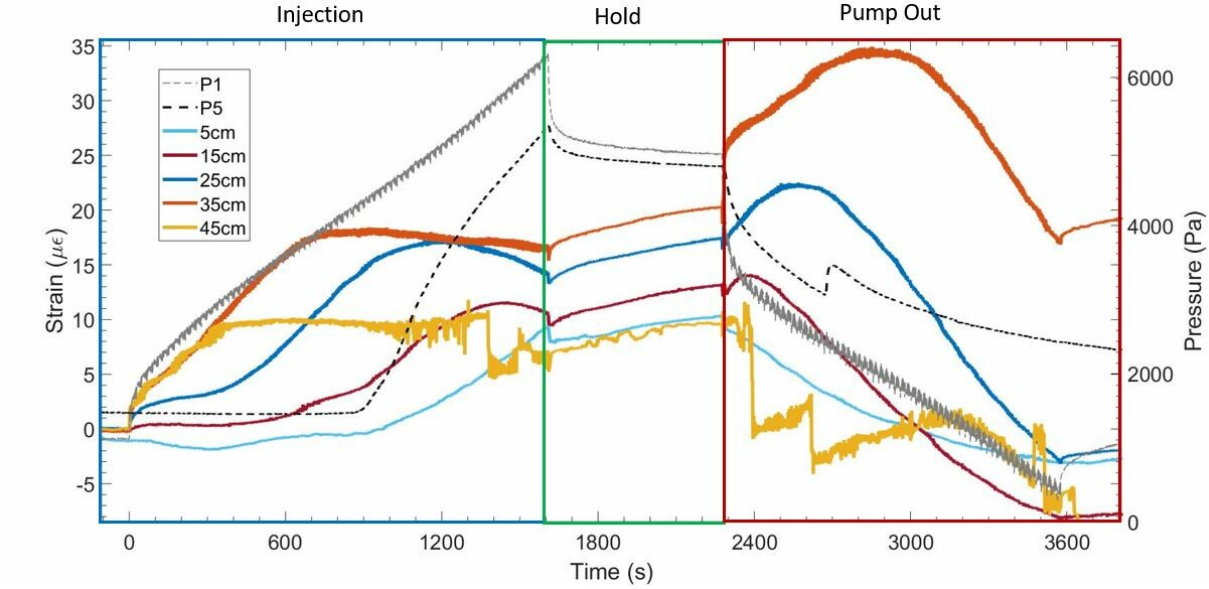

Figure 2.61: Strains measured on the inside of the column and top and bottom pressures measured as functions of time during an experiment. Strain measured at different elevations from the top as shown in legend. Pressure measured at locations P1 an P5 as shown in Figure 2.52. Water was injected at a rate of 250 ml/min until it filled roughly 2/3 of the column. Injection was zero during the "Hold" interval. Water was then pumped out at a rate of 250 mL/min.

sensor was 80 ms; however, the delay now between the top and bottom air pressure sensor is 130 ms. The increased amount of time can be contributed to the decrease in permeability from the addition of the finer grained material. Furthermore, since the sand/silt mixture is contained in the part of the column where the top three sensors are located, it is important to discuss the delay in this section of the column as well. In the sand material, the delay between the top sensor (6.6cm) and the second sensor (26.9 cm) is 20 ms. When the material is changed to the sand/silt mixture, the delay increases to 40 ms for the top two sensors. The time it takes for the sinusoidal signal to reach the second sensor doubles as a result of adding 20 percent silt material to the sand.

The preliminary results from the numerical simulations display a similar trend to the laboratory data and are important to be mentioned. More analyses from these will come, but the strain and air pressure time series appear to be promising. Figure 2.75 displays this plot. The solid lines represent the air pressure, and the dashed lines represent the vertical strain. The data displays a phase lag between the air pressure and strain which is similarly found in the laboratory data.

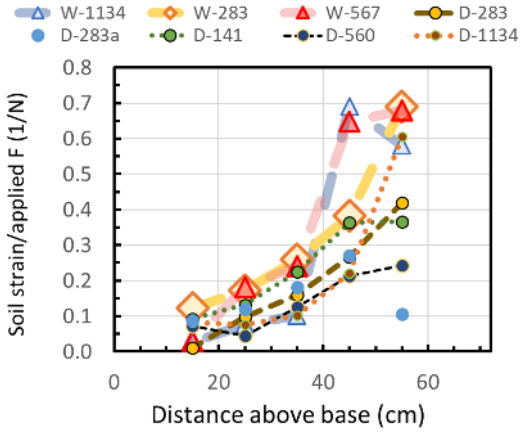

Figure 2.62: Ratio of the strain in sand to the applied force as a function of distance above the column base for tests with different applied loads and different saturation states (D = dry; W = saturated). The x axis extends over the full height of the column.

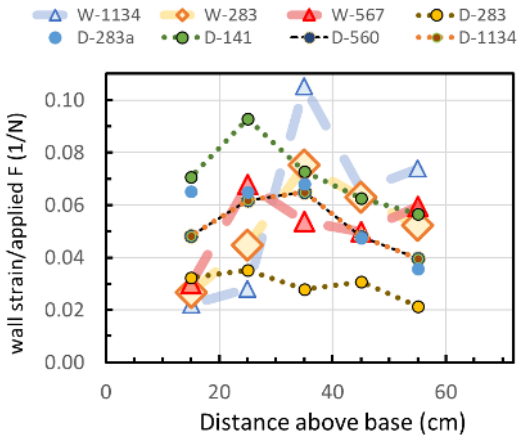

Figure 2.63: Ratio of the strain in wall of the PVC pipe to the applied force as a function of distance above the column base for tests with different applied loads and different saturation states (D = dry; W = saturated). The x axis extends over the full height of the column.

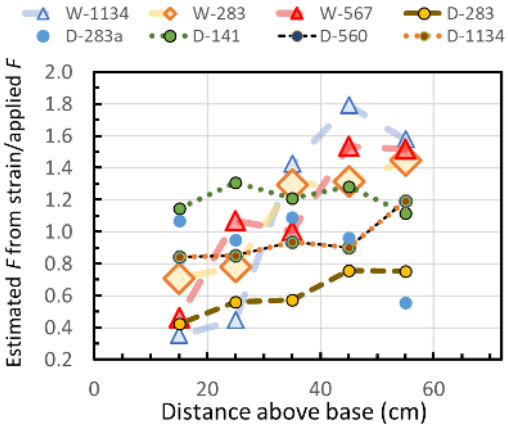

Figure 2.64: Ratio of the total force estimated from the strain to the applied force as a function of distance above the column base for tests with different applied loads and different saturation states (D = dry; W = saturated). The x axis extends over the full height of the column.

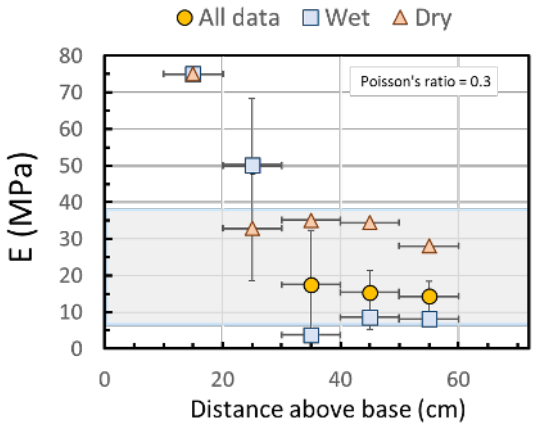

Figure 2.65: Estimated Young's modulus of sand using parameter estimation that requires internal forces to sum to the applied force. The gray band is the range of moduli in the mid to upper parts of the column.

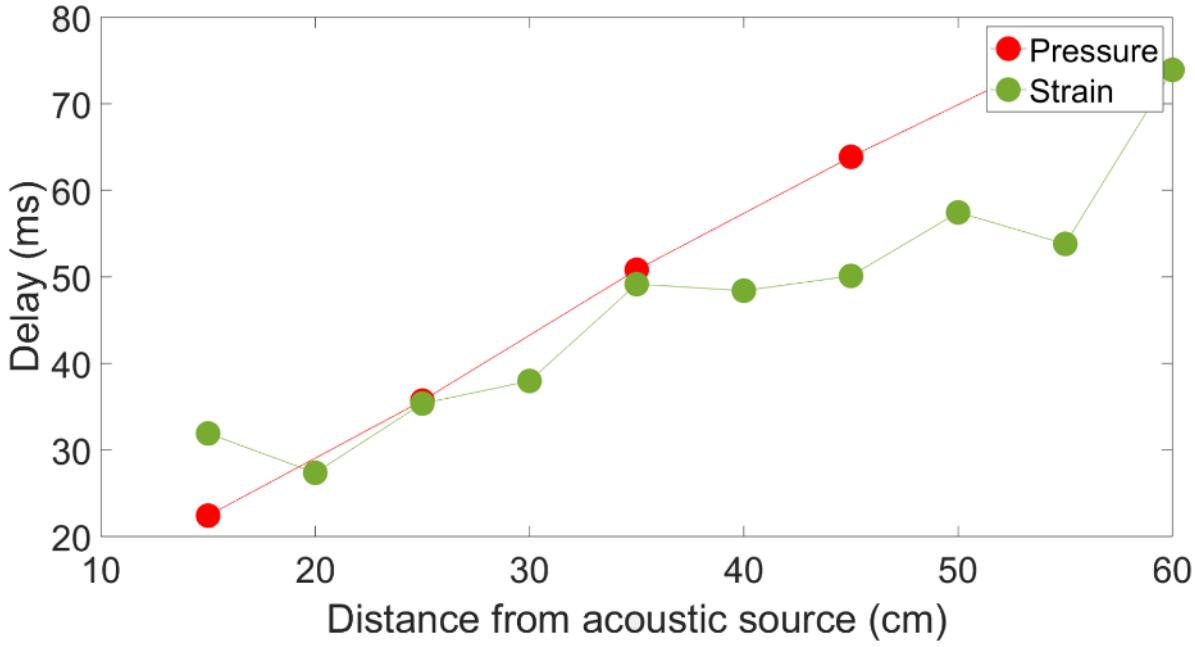

Figure 2.68: Air pressure and strain delays as a function of distance from the 4 Hz signal.

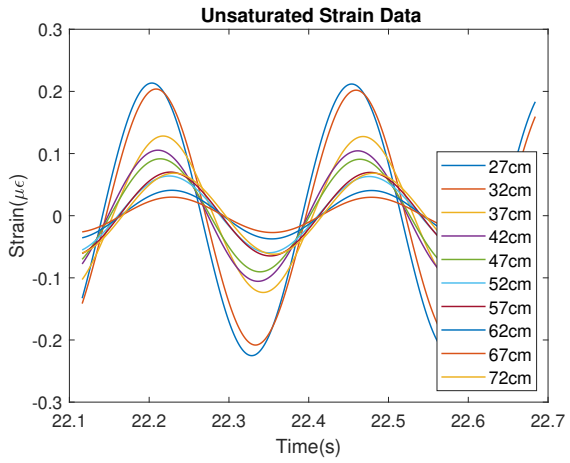

Figure 2.69: Strain signals in the dry/unsaturated sand material.

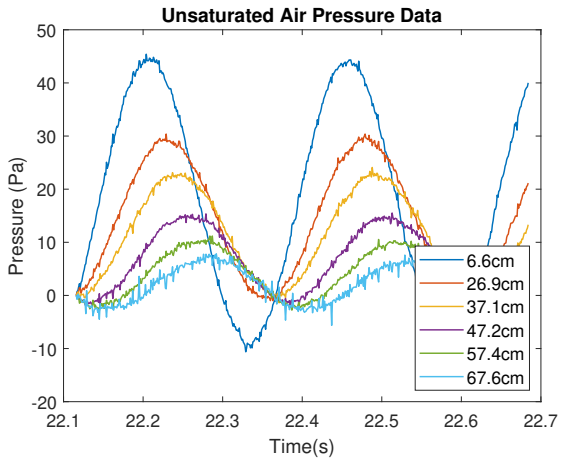

Figure 2.70: Pressure signals in the dry/unsaturated sand material.

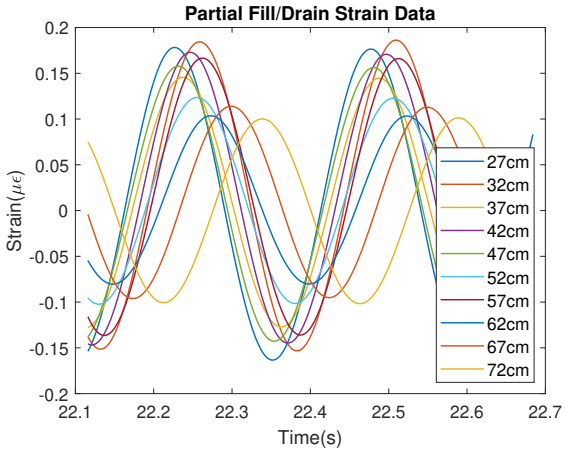

Figure 2.71: Strain signals after sand material has been filled and drained of water.

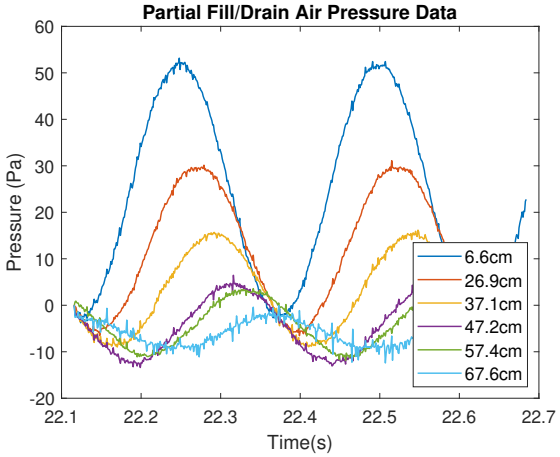

Figure 2.72: Air pressure signals after sand material has been filled and drained of water.

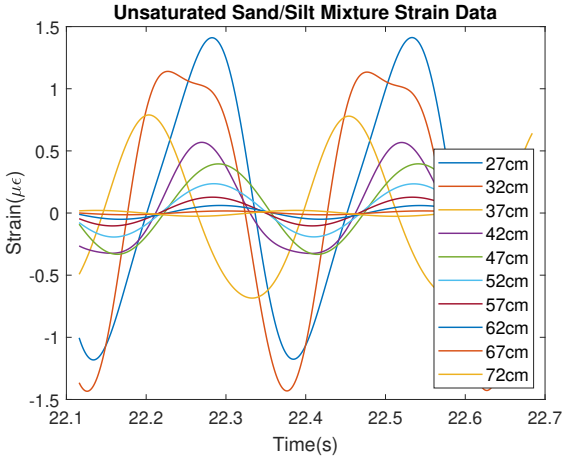

Figure 2.73: Strain signals after material was changed to sand/silt mixture.

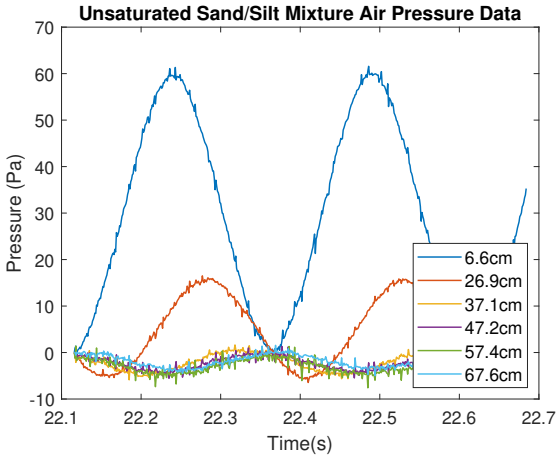

Figure 2.74: Pressure signals after material was changed to sand/silt mixture.

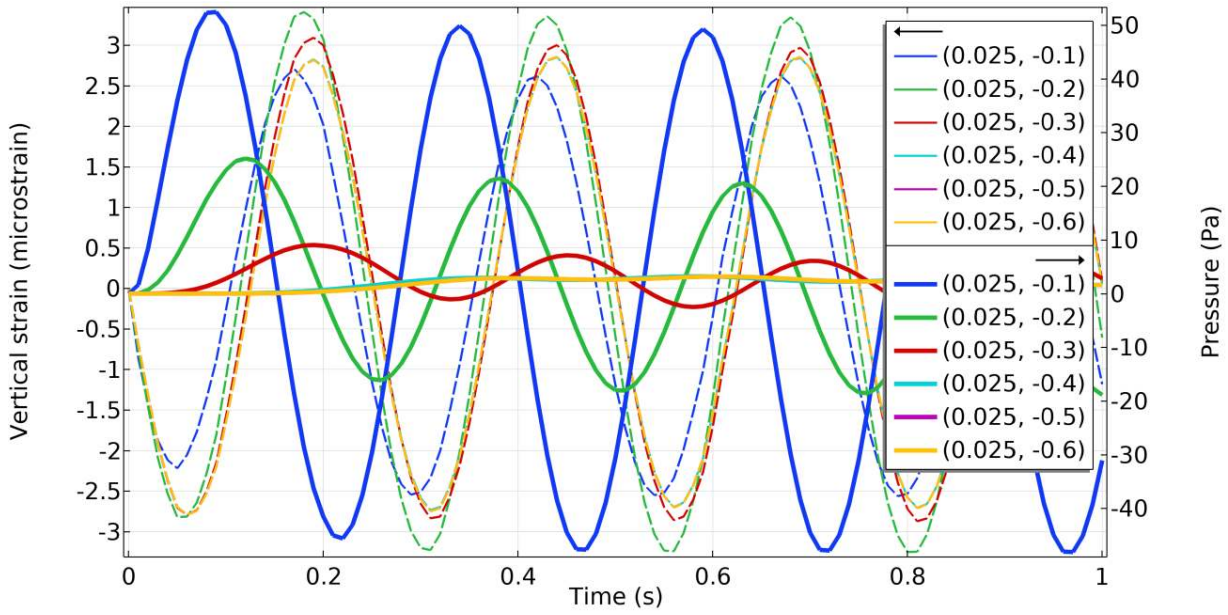

Figure 2.75: Simulation results of air pressure and vertical strain as a function of time.

CHAPTER THREE
DEPLOYMENTS AT THE SIMPSON STATION, PENDLETON, SC

Contents

3.1 Point Instruments 3-2
3.1.1 Grouting Trailer 3-2
3.1.2 Tensor Optical Fiber Strainmeters 3-3
3.1.2.1 Version 5 TOFS Prototypes 3-3
3.1.2.1.1 Installation 3-3
3.1.2.1.2 Performance & Observations 3-4
3.1.2.1.3 Conclusions 3-7
3.1.2.2 Version 6.0 Elliptical Ring TOFS 3-8
3.1.2.2.1 Installation 3-8
3.1.2.2.2 Performance & Observations 3-8
3.1.2.2.3 Conclusions 3-10
3.1.3 Optical Fiber Michelson Strain Ribbon 3-11
3.1.3.1 Installation 3-11
3.1.3.2 Performance & Observations 3-11
3.1.3.3 Conclusions 3-13
3.1.4 Muticomponent Optical Fiber Bragg Grating Strainmeter 3-14
3.1.4.1 Installation 3-14
3.1.4.2 Performance & Observations 3-14
3.1.4.3 Conclusions 3-16
3.2 Distributed Instruments 3-16
3.2.1 CMPI Strain Ribbon #1 3-16
3.2.2 CMPI Strain Ribbon #2 3-19
3.2.2.1 Ambient Noise Results 3-21
3.2.2.2 Periodic Pumping Tests 3-24
3.2.3 CMPI Direct Push Instrument 3-28
3.2.4 CMPI Strain Ribbon #3 3-28

DEPLOYMENTS AT THE SIMPSON STATION, PENDLETON, SC

The Simpson Station has been our local facility for testing a wide range of commercial and novel geophysical and environmental monitoring technologies for over a decade. It is located approximately 10 miles west of Clemson University and is roughly one-third of an acre of pasture land that has been the site of many first field deployments including the electromagnetic and optical fiber strainmeters developed for previous DOE-funded research projects.

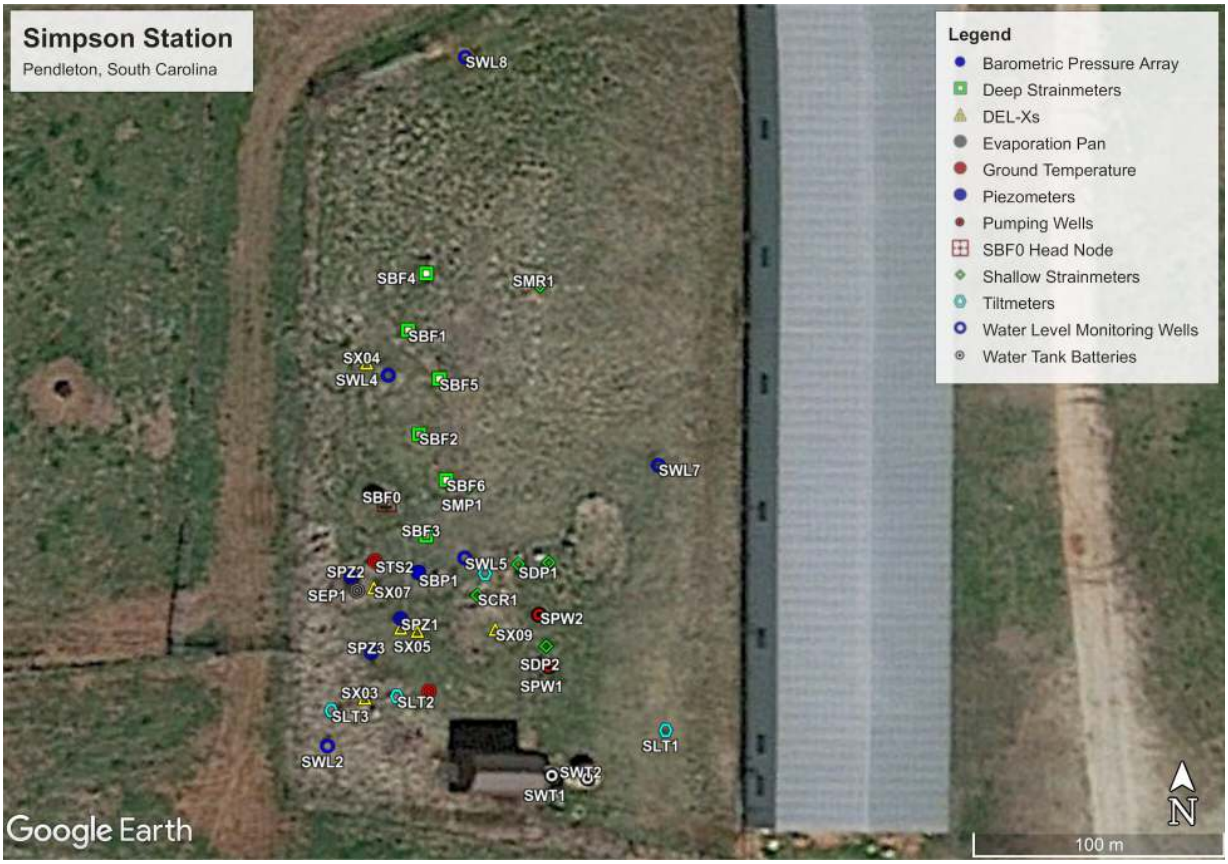

Figure 3.1: Overhead view of the Simpson Station test facility showing the plethora of sensors deployed at the site along with the project developed instrumentation.

Figure 3.1 shows an overhead view of the Simpson Station site highlighting some of the locations used to test the instruments developed during this project. This includes deep boreholes SBF1–SBF6 drilled into bedrock for tensor strainmeter prototypes described in Section 1.7. Pumping wells SPW1 and SPW2 and water level monitoring wells SWL2, SWL4, SWL5, SWL7 and SWL8 are used for the tests described in Chapters Twelve. There are multiple shallow wells for tilt monitoring, SLT1–SLT3, and an array of shallow DEL-X extensometers (Murdoch et al., 2015) in wells SX03–SX05 and SX07–SX09 as well as the Optical Fiber Michelson Strain Ribbon SMR1 described in Section 1.4 and used in experiments presented in Chapter Eleven. The three CMPI strain ribbons developed were also deployed (SCR1–SCR3) as well as the CMPI direct push instrument in well SDP1 and the multicomponent fiber Bragg grating instrument (Section 1.6) in SDP2.

This chapter describes the deployment and field results from the various optical fiber Michelson, Bragg grating, and CMPI-interrogated Fabry-Pérot based instruments developed during this project. These follow the same "point" and "distributed" sensing categories as Chapters One and Two.

3.1 Point Instruments

There were several single and multicomponent "point" instruments developed during this project that were evaluated at our local Simpson Station field site. This included all three Version 5 Tensor Optical Fiber Strainmeter prototypes and the final Version 6 Elliptical Ring TOFS designed for grouting into solid rock, in addition to the higher compliance Michelson strain ribbon and multicomponent optical fiber Bragg grating strainmeters specifically designed for making measurements in sediment. One of the first steps, however, was to develop a robust and reliable way to mix and pump the grout needed to couple the rock strainmeters to their host formations.

3.1.1 Grouting Trailer

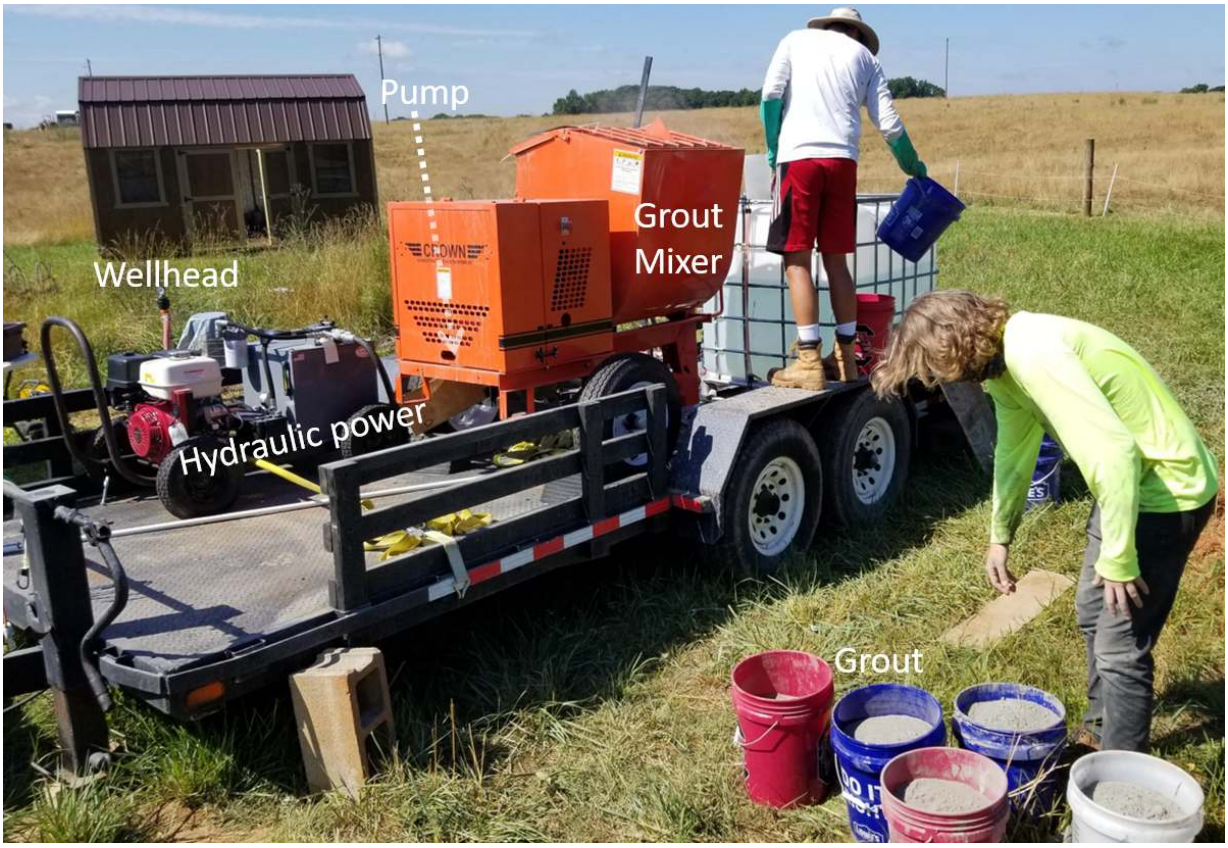

Figure 3.2: Annotated photo of the grouting trailer showing the grout mixer, pump, hydraulic power pack, pump, water tank (right side) and well head.

The first step towards grouting in strainmeters required assembling all of the equipment needed for mixing and pumping grout onto a trailer for transport and operation. These components were procured and tested in stages and includes a horizontal shaft mixer that empties into a hopper that feeds a progressive cavity grout pump connected to a hydraulic power pack. A water tank and dedicated water pump are also included to hydrate the grout and to clean out the mixer, hopper, grout pump and the hoses and pipe used to deliver the grout downhole. We have mounted these components onto a trailer such that grout can be mixed and pumped while on the trailer with only minor setup (Figure 3.2).

Deployment of the instrument prototypes required multiple trial groutings to establish procedures for mixing, pumping and cleanup (Figure 3.3). This was done using several open holes using standard Portland cement rather than the more expensive expanding grout used for the strainmeters. We were able to mix and measure the grout properties



Figure 3.3: Installing strainmeters. (a) Strainmeter at the well head ready to be lowered to depth. (b) Pipe string used for grouting. (c) Strainmeter and field crew at the wellhead.

like viscosity using a flow cone for and density using a scale and graduated container within several minutes with the new mixer, which is an order of magnitude improvement from previous mixings that took almost an hour. A series of gauges allowed us to measure the pressure at the output of the grout pump as well as at the wellhead where the high pressure hose leading from the pump transitioned into the lightweight stainless steel pipe (Flatwater Fleet Frac-Pipe™) used to deliver the grout down hole. The pumping pressure was regulated using a regulator on the hydraulic power pack. All pipe, hose and equipment were then easily disassembled and rinsed with water from the storage tank.

3.1.2 Tensor Optical Fiber Strainmeters

There were four tensor strainmeters grouted in at our Simpson Station test facility during this project. This included the three Version 5 TOFS and one Version 6 TOFS that would go on to be used at our CO2 injection analog site in Oklahoma.

3.1.2.1 Version 5 TOFS Prototypes

All three of the Version 5 TOFS prototypes were deployed and at least some preliminary analyses were able to be completed before deciding on which of the three designs would ultimately be fabricated for the North Avant Field demonstration. These were the Nested Mandrel TOFS (Section 1.7.1), Inclined Helix TOFS (Section 1.7.2 and Elliptical Ring TOFS (Section 1.7.3). Details of their installation and assessments of their performance are presented in the following sections.

3.1.2.1.1 Installation

The three Version 5 Tensor Optical Fiber Strainmeters were installed at the Simpson Station test facility in late June of 2020. While these instruments were completed over 6 months earlier, their installations were delayed due to the

COVID-19 pandemic making it difficult to mobilize the equipment and personnel needed to assist in the deployments. These installations started with the Elliptical Ring TOFS in borehole SBF2 on June 25th, 2020 and was followed four days later by the Nested Mandrel TOFS in borehole SBF5 on June 29th, 2020, and concluded with the Inclined Helix TOFS in borehole SBF6 the next day on June 30th, 2020.



(a) (b) (c)

Figure 3.4: Photographs just before the deployments of the Version 5 Nested Mandrel (a), Inclined Helix (b) and Elliptical Ring (c) tensor strainmeters into boreholes SBF2, SBF5 and SBF6, respectively.

The installation procedure was the same for each of the three deployments. Each instrument was lowered on stainless steel wire rope in tandem with the grout tremie pipe shown in Figure 3.3b. Figure 3.4 shows each strainmeter prior to installation where after approximately 4 cubic feet of grout (BASF MasterFlow 1206) was mixed to the desired consistency and pumped into each borehole with the instrument in-situ using the grouting equipment shown in Figure 3.2. The result was about 20 vertical feet of grout surrounding each strainmeter, after which the tremie was extracted from the borehole and all of the equipment cleaned and readied for the next installation.

3.1.2.1.2 Performance & Observations

There are several indications that a strainmeter has been successfully grouted into a borehole that can be seen in the time series data following installation. Figure 3.5 shows the grout "curing curves" for each of the three prototypes just prior and following each installation. The first sign is the exothermic reaction of the grout in the first 24–48 hours that can be clearly seen in each of the plots in Figure 3.5. While there is a clear exothermic signal in the elliptical ring instrument (Figure 3.5a), it appears that the remaining gauge failed about 75 hours following installation due to what is most likely stresses in the defective fiber cable (see Section 1.7.3.1). However, this is a clear signal that the grout was successfully delivered.

The other hallmark of a successful grouting and overall installation is that each strain gauge goes into permanent compression, which allows each instrument to measure positive and negative strains. While this can take anywhere from two weeks to many months following deployment, it appears that all three gauges of the two remaining strain-

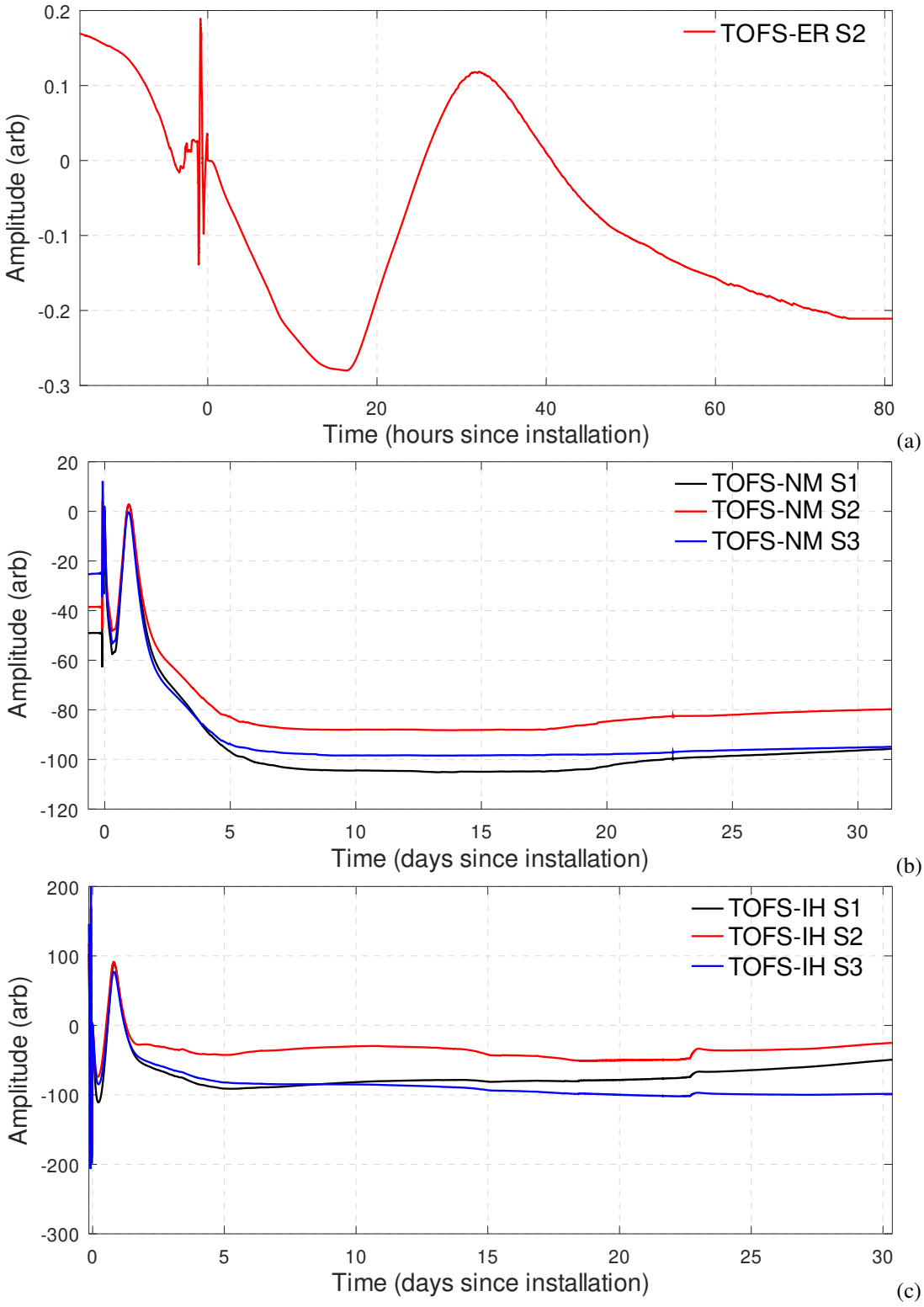

Figure 3.5: Grout cure curves for the Version 5 Elliptical Ring (a), Nested Mandrel (b) and Inclined Helix (c) TOFS prototypes from Simpson Station deployment. Note that the vertical axis for each plot is in arbitrary units.

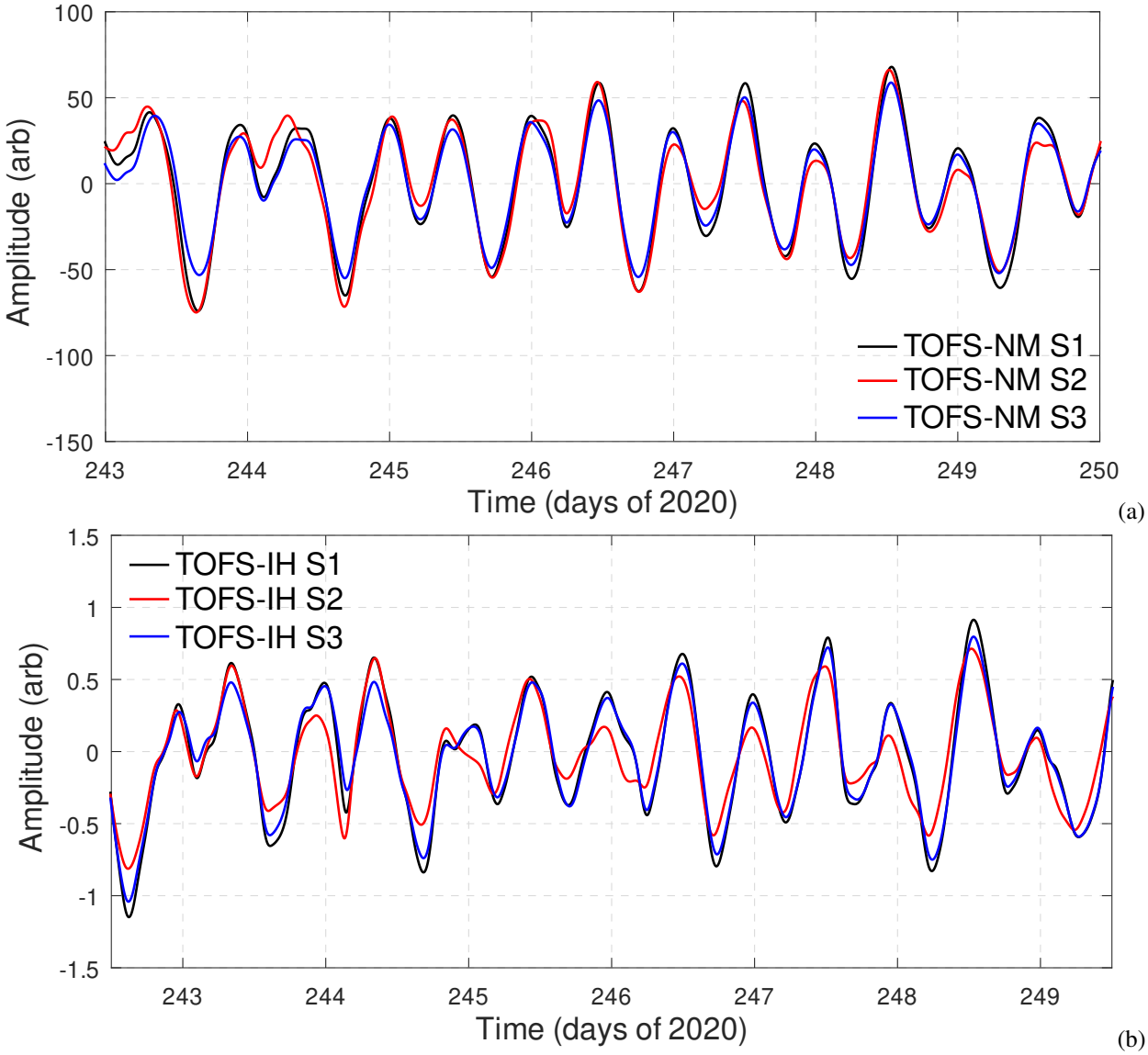

Figure 3.6: Bandpass filtered data showing the solid Earth tides for the Version 5 Nested Mandrel (a) and Inclined Helix (b) TOFS prototypes from Simpson Station deployment. Note that the vertical axis for each plot is in arbitrary units.

meter prototypes were headed toward compression and did in fact achieve permanent compression shortly after the one month shown in Figures 3.5b and 3.5c.

Next was to see if the two surviving strainmeters were able to observe the solid Earth tides. This was done by band pass filtering the raw gauge strain data between 2 days and 6 hours (roughly double the 1 CPD tides and half of the 2 CPD tides, or a 1 octave filter), the results of which are shown in Figure 3.6. While both plots show what is very much tidal like behavior, there are several concerns revealed by these plots. The primary issue is that all three components on each instrument are measuring, with minor exceptions, what appears to be the same signal. The second is that despite the time intervals not being exactly aligned (the TOFS-IH starts about a half day earlier), the two instruments seem to have distinctly different waveforms.

Considerable efforts were made to determine the cause of the similar but different tidal waveforms in Figure 3.6. These measurements were correlated and corrected for barometric pressure effects and water level fluctuations using both scalar and spectral admittances with little change in the results (in fact both Figures 3.6a and 3.6b have been corrected for both). While we were able to determine using tidal prediction software that the signals on the Nested Mandrel TOFS (Figure 3.6a) are a nearly perfect match for the areal strain, suggesting that the three fiber-wrapped mandrels are likely only sensitive to volumetric strain. More perplexing is that the filtered waveforms on the Inclined Wrap TOFS (Figure 3.6b) do not match any of the predicted tidal waveforms of any orientation.

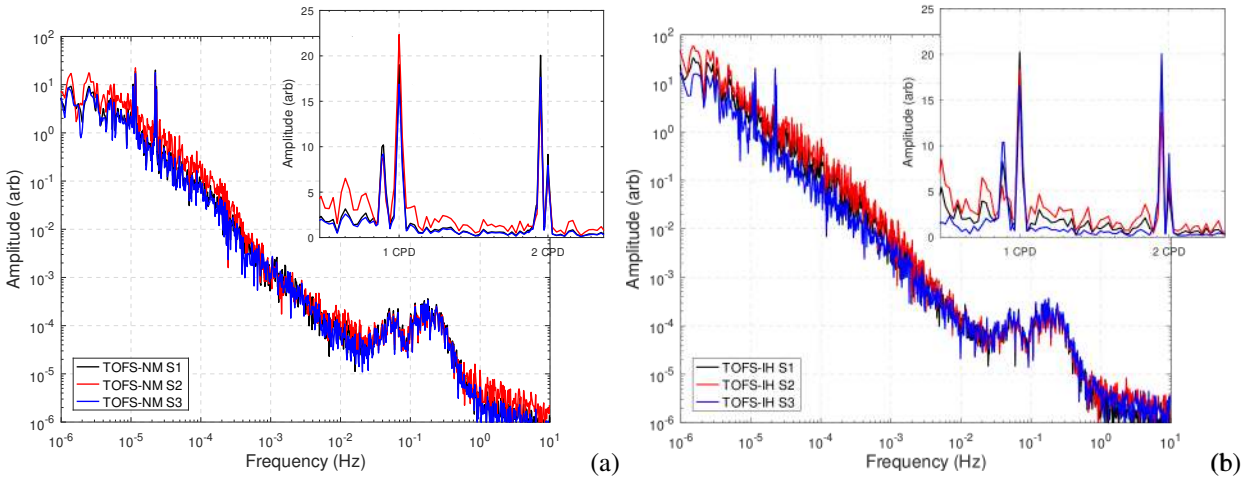

Figure 3.7: Amplitude spectrum estimates for the Version 5 Nested Mandrel (a) and Inclined Helix (b) TOFS prototype instruments. The inset plot focuses on the tidal band between 1 and 2 CPD.

The final piece of information gathered from these two Version 5 TOFS prototypes is their relative responses to ambient data. This is quantified by their amplitude spectra shown in Figure 3.7. It is important to note that both are still in arbitrary units due to the lack of a tidal calibration, but have been scaled such that the tidal peaks are more-or-less in agreement for comparison. It is intriguing to notice that both spectra are very similar despite the factor of 100 sensitivity difference observed in the lab. They also have similar increases in energy in the 10–100 second (10^{-3}–10^{-2} Hz) band from teleseismic events as well as at around a 7-second period ($\sim$0.14 Hz) from microseisms.

3.1.2.1.3 Conclusions

All three Version 5 Tensor Optical Fiber Strainmeters were successfully installed in late June of 2020. While the one remaining gauge on the Elliptical Ring TOFS did not survive long enough to quantify its performance, the post-grouting behavior on all three was consistent with proper immersion and longer term trends on all three gauges from the two remaining instruments show permanent compression trends. While the amplitude spectra show these strainmeters should compare very favorably to current strainmeters under ambient noise conditions, the inability of both the Nested Mandrel and Inclined Helix TOFSs to clearly resolve tides from distinct directions is a major concern.

It is clear that both Version 5 TOFS prototypes are measuring tides or tidal like behavior (Figure 3.6), but contain a large isotropic component that is potentially obscuring any underlying tides. It may be necessary, for example, to include more than three orientations of fiber to obtain an estimate of this isotropic signal (e.g. using principal component analysis) and remove it to get at the directional strains. This was one motivation for using four horizontal strain gauges in the up-sized Version 6 Elliptical Ring TOFS presented in the next section.

3.1.2.2 Version 6.0 Elliptical Ring TOFS

The Version 6 Elliptical Ring Tensor Optical Fiber strainmeter is the final design intended for deployment at our CO2 injection analog site in Oklahoma. It was essential to test this device at our local field site to develop some best practices for handling and deploying this new strainmeter and most importantly assess its ability to resolve directional strains. The following sections describe this deployment and the resulting data.

3.1.2.2.1 Installation

We deployed a TOFS-ER v6 system at our local Simpson Station field site on May 27th, 2021 into borehole SBF6 in the open hole section above the Version 5 Inclined Helix TOFS. The Version 6 TOFS-ER features a through-pipe design that is meant for pumping grout through the instrument in-situ, which up until this point we have only pumped grout around the side of a downhole instrument. This deployment differed in that we also employed our new electric hoist system to lower the strainmeter on pipe rather than wire rope.

The TOFS-ER v6 strainmeter adapts to 1-inch nominal pipe above and below the instrument. Figure 3.8a shows the instrument with the 4-foot upper pipe installed, along which a centralizer was used to keep the top of the instrument concentric with the borehole. Another 4-foot pipe was attached to the bottom (Figure 3.8b) that was capped on the bottom since this end is likely to become obstructed upon contact with the bottom of the wellbore. Figure 3.8b also shows that bottom pipe has two rectangular openings cut into it to let grout out through the bottom, and it contains another centralizer. A support cable was used to lower the instrument with these pipes until the top of the upper pipe was just above the surface whereupon a fitting that traps the foam cleanout ball, or "pig" was attached along with a left-hand threaded Acme screw coupling (Figure 3.8c). This coupling connected to the right-hand threaded frac pipe that was used to pump the grout down hole and through the instrument, after which the Acme coupling could be released with a few turns and the frac pipe recovered. Figure 3.8d shows the final coupling that connected to the grouting pump.

We were able to successfully lower the strainmeter on pipe using our new electric winch and collapsible mast system and pump grout through and around the instrument in-situ. While we did use a wire rope attached to the upper grout pipe that remained downhole with the instrument, this was primarily for safety purposes given this was the first time this procedure was executed. Approximately 4 cubic feet of grout was mixed to the proper viscosity and specific gravity and pumped down the tremie after which it was detached from the upper pipe on the instrument and all of the equipment was meticulously cleaned for reuse at a later date.

3.1.2.2.2 Performance & Observations

It is essential to note that this first TOFS-ER v6 was deployed with a modified Version 3 Optical Fiber Michelson Interrogator (Section 1.2.1) since the Version 4 systems (Section 1.2.2) were still undergoing revisions. Unfortunately, the OFMI v3 can only record up to four interferometers so it was decided to capture only the horizontal components to test for directional strain resolution that was lacking in the Version 5 TOFS prototypes.

Figure 3.9 indicates a successful grout emplacement since all four gauges are showing compression before the nominal 28-day cure time, with three out of the 4 gauges in compression about one week after deployment, where the third gauge (S3) takes almost the full four weeks. A slug test was performed several days following installation (Figure 3.10) to check the functionality and the sign of the four horizontal gauges.

By far the most important test of the new full sized TOFS-ER v6 is whether it can resolve more than one component of the strain tensor. A least-squares fitting algorithm was applied to the band pass filtered data to obtain the coefficients needed to transform the four horizontal gauge strains into the east-west (ϵ_{xx}), north-south (ϵ_{yy}), horizontal shear (ϵ_{xy}) and possibly the vertical strain (ϵ_{zz}). The results of this fitting algorithm are shown in Figure 3.11 where much to our



Figure 3.8: Photographs taken during the deployment of the TOFS-ER v6 instrument at the Simpson Station. (a) Strainmeter with upper pipe, centralizer, and support cable attached. (b) Grout slot in the lower pipe for the bottom of the instrument. (c) Top of the upper pipe with pig trap and frac pipe attached before lowering into the well. (d) Instrument lowered and grout injection fitting and pressure gauge attached.

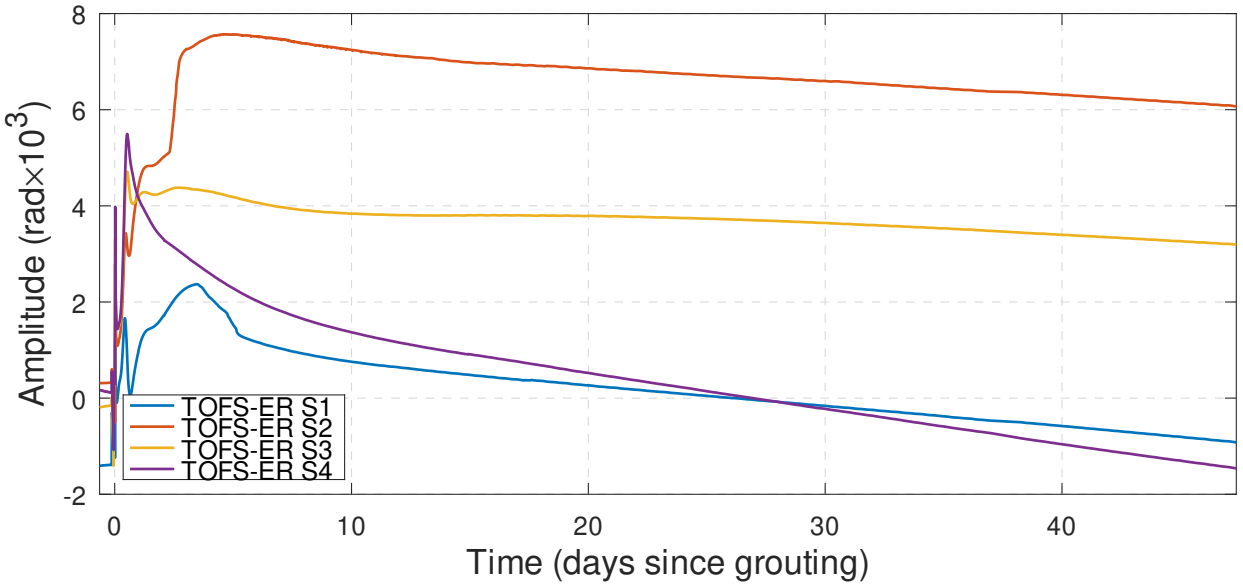

Figure 3.9: Grout cure time series from the full scale Version 6 TOFS-ER showing all four horizontal gauges in compression almost immediately after grouting.

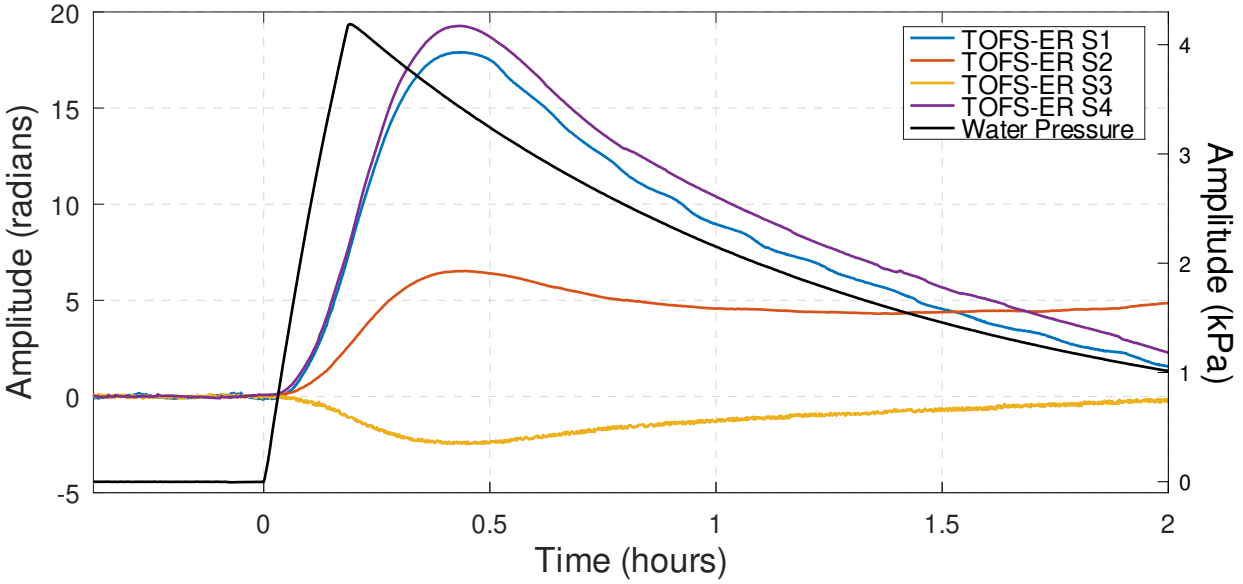

Figure 3.10: Time series of a slug test done days after installation and grouting.

relief the fits are excellent. There even turns out to be enough residual strain in the principal components to estimate the vertical strain without data from the discrete vertical strain gauge.

3.1.2.2.3 Conclusions

The excellent tidal calibration results from the TOFS-ER v6 installation at the Simpson Station (Figure 3.11) prove beyond any doubt that this design is capable of resolving four components of the strain tensor. It also demonstrates the

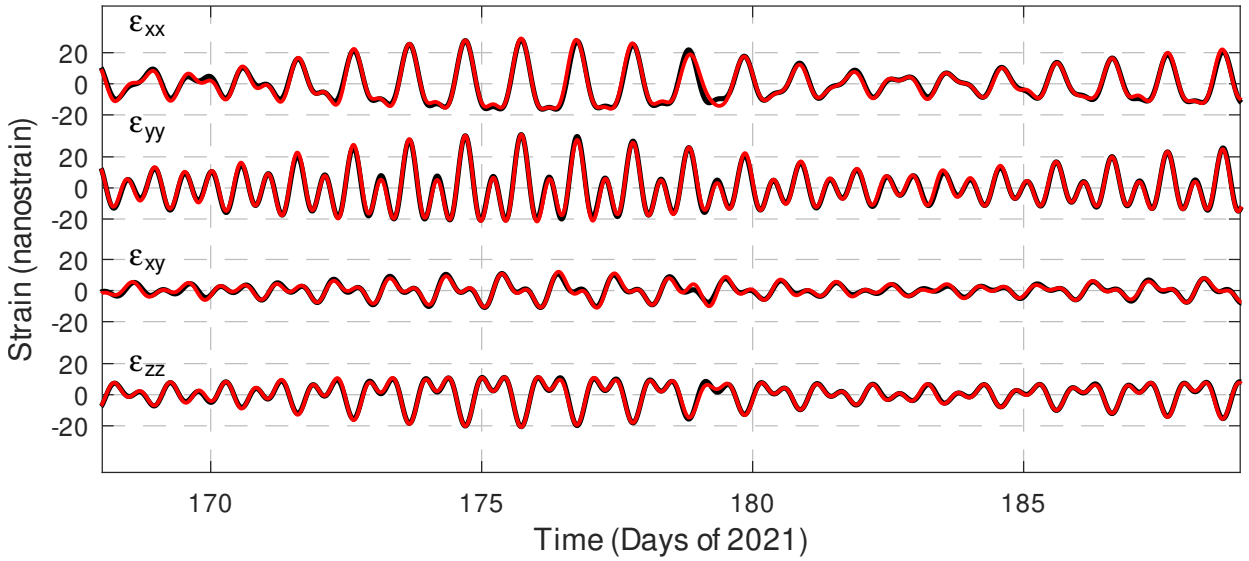

Figure 3.11: Time series results from the tidal calibration of the TOFS-ER v6 in borehole SBF6.

power of principal component analysis in breaking up the data from the individual strain gauges to obtain not only the strains directly resolved on each gauge, but the signal common to all four gauges, which in this case is proportional to the vertical strain.

3.1.3 Optical Fiber Michelson Strain Ribbon

The development of the Version 2 Optical Fiber Michelson Strain Ribbon (OFMSR v2) was motivated by the need to be able to make high resolution vertical strain measurements in the shallow subsurface. This is similar to the DEL-X extensometers described in Murdoch et al., 2015, but with an easier installation method and much higher resolution. Details of the development of the OFMSR are described in Section 1.4, and its installation and post-installation performance are described below.

3.1.3.1 Installation

The OFMSR v2 was installed on November 17th, 2021 into the freshly drilled borehole SMR1 (Figure 3.1) at the Simpson Station test site. The installation started by drilling a 20 foot deep hole using our Geoprobe 5410 drill rig equipped with 4-inch diameter augers. Once drilled, the ribbon was attached to about 5 pounds of ⅜" diameter steel rods and lowered into the hole whereupon sand was packed into the hole to force the ribbon up against the wall of the borehole until the instrument was covered. The remaining hole was re-filled with native material and a Bentonite plug was added just below the ground surface to prevent preferential water flow into the loosened sediment and sand above and around the instrument.

A tactical fiber cable was run from the wellhead into an enclosed shed where the OFMSR was connected to an interrogator. The instrument recorded data from its installation until about 8 months later on July 20th, 2022 when its interrogator was repurposed for other experiments.

3.1.3.2 Performance & Observations

Changes in atmospheric pressure can have a very significant impact on the vertical strain and therefore it is critical to understand the relationship between the barometric pressure and the strain measured by the OFMSR. There are two

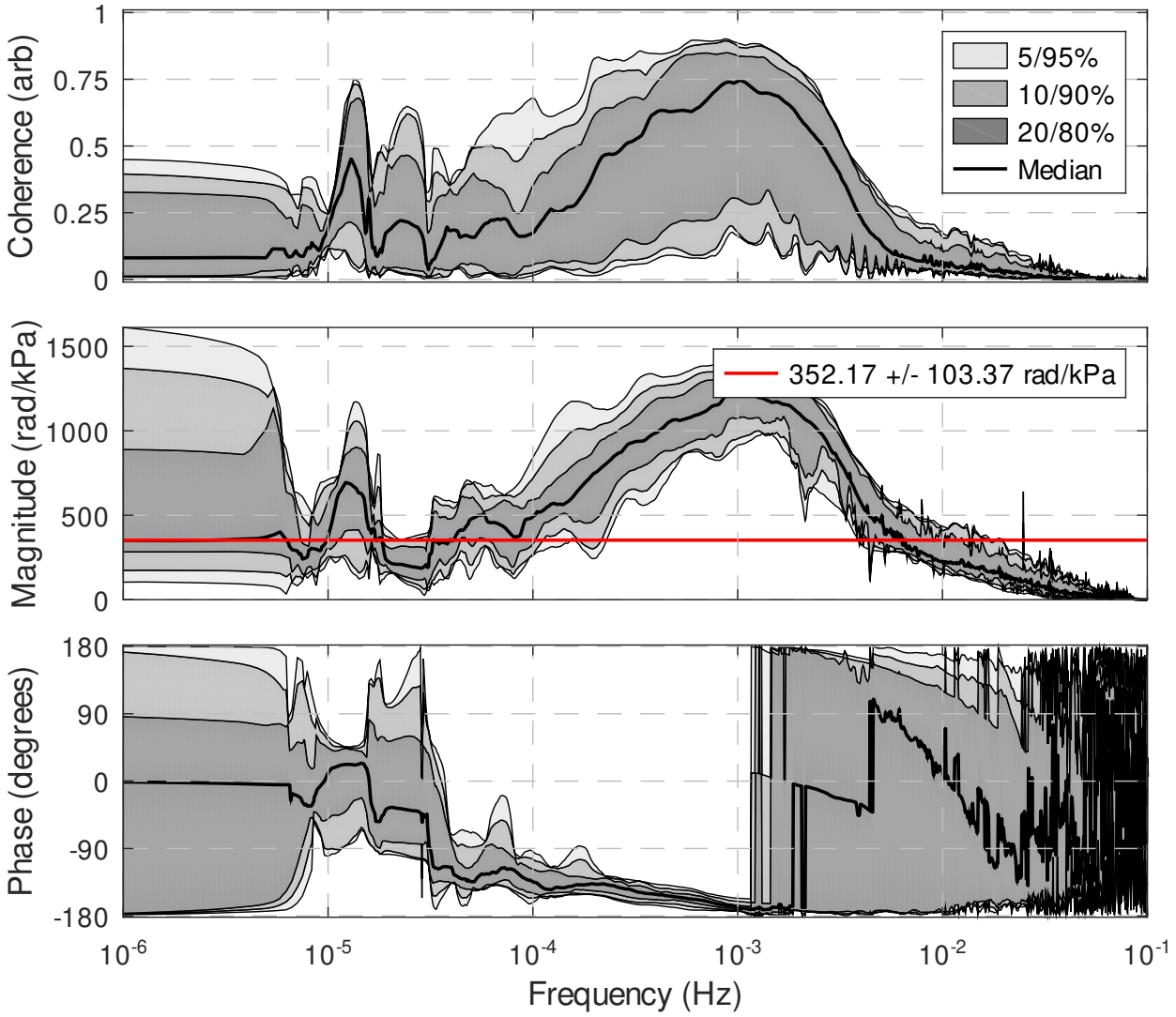

Figure 3.12: Cross spectrum of the OFMSR and barometric pressure showing the coherence (top), magnitude (center) and phase (bottom) relationship between the vertical strain and atmospheric pressure as functions of frequency. The scalar admittance value determined by least-squares is shown as a red horizontal line superimposed on the magnitude plot. The central black lines show the median of each estimate along with $5^{th}/95^{th}$, $10^{th}/90^{th}$ and $20^{th}/80^{th}$ percentile confidence bands in shades of gray.

main ways to estimate the influence of one signal on the other, the first is just to estimate the linear correlation between them. This was done using a linear least-squares fit of the barometric pressure to the vertical strain, resulting in a scalar admittance (i.e., the best value to scale the barometric pressure by to minimize the variance in the strain time series) of 352 ± 103 radians of optical phase change per kiloPascal of pressure change. Assuming a nominal calibration factor of 5 nϵ per radian results in a calibrated scalar admittance of approximately 1.8 μϵ/kPa. This is a very large value compared to typical borehole strainmeters that are typically 20–30 nϵ/kPa (see Section 4.2.2.2).

The main issue with the scalar admittance is that it only captures how the strain and barometric pressure are related irrespective of their frequency content. This can be estimated by computing the cross spectrum of the two signals, which is shown in Figure 3.12 that shows the coherence (squared correlation), magnitude and phase as a function of frequency. The coherence shows how much of the strain signal can be explained by changes in barometric

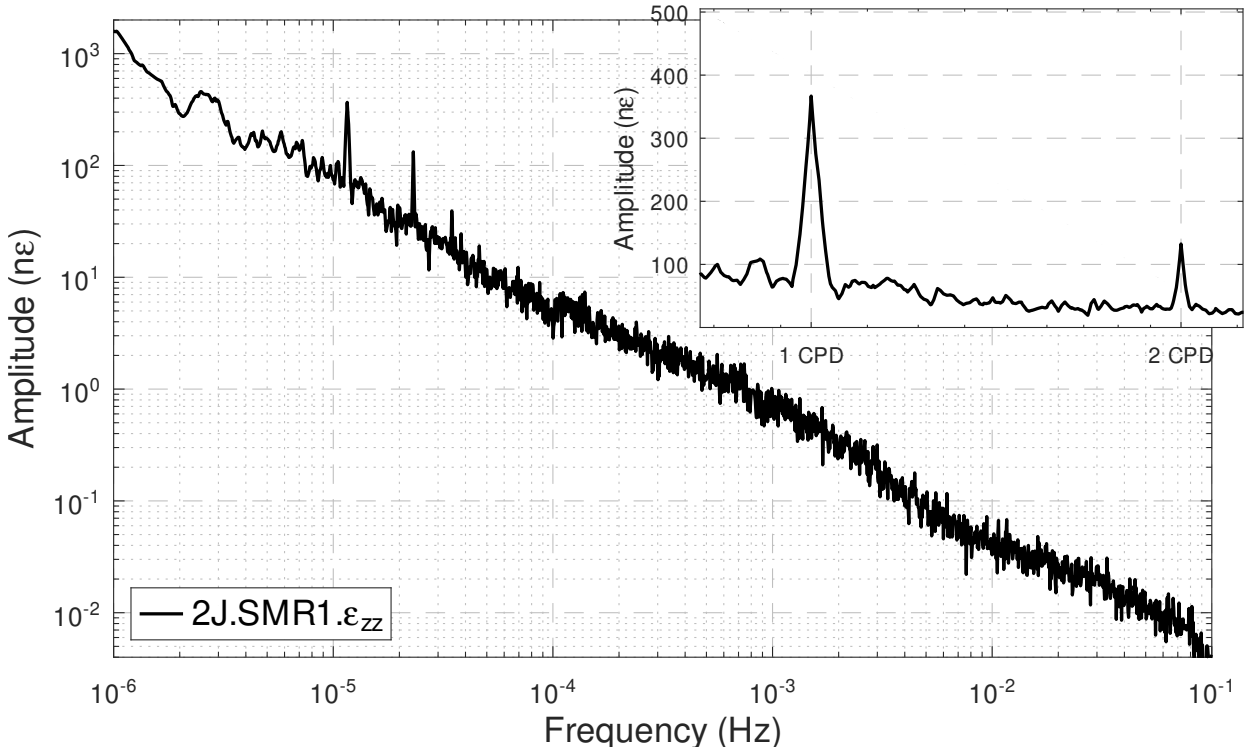

Figure 3.13: Amplitude spectrum for the vertical strain as recorded by the Michelson strain ribbon. The inset plot focuses on the 1 and 2 CPD tidal band.

pressure, which in this case is a rather complicated relationship that peaks near 1 cycle-per-day (CPD), slightly less so at 2 CPD and has its highest coherence around 1×10^3 Hz, or 1,000 seconds. This is most likely do to changes in atmospheric pressure due to convective storms that cause abrupt changes on the order of a few minutes to tens of minutes.

The magnitude and phase of the vertical strain and barometric pressure relationship is also highly frequency dependent. The spectral admittance agrees quite closely with the scalar admittance over the lowest frequencies but almost doubles to 700 radians/kPa at 1 CPD and is almost four times larger at 1,000 seconds (1×10^3 Hz) before heading towards zero along with the coherence. It is important to note that the sign of the barometric pressure was flipped during these calculations such that the lowest frequency phase estimates would be near $0°$, but slowly heads toward $-180°$ as the frequency increases.

This complex spectral admittance was used to filter and remove the effect of barometric pressure on the vertical strain record before computing the amplitude spectrum shown in Figure 3.13. There are clear peaks at exactly 1 and 2 CPD at amplitudes of $\sim$350 and $\sim$150 nϵ. The lower frequency peak is no doubt the diurnal response of thermal stresses in the near surface, which is sufficiently strong to induce the 2 CPD as a second harmonic. These peaks are also much too large to be related to the solid Earth tides which are in the 10–20 nanostrain range.

3.1.3.3 Conclusions

The Version 2 Optical Fiber Michelson Strain Ribbon is a highly sensitive vertical strainmeter designed for near surface deformation monitoring. Cross spectrum estimates of the vertical strain and barometric pressure are complex and strongly frequency dependent (Figure 3.12), requiring a full spectral admittance correction to the data for observing

signals less than a few minutes in duration with optimal fidelity. Amplitude spectrum results (Figure 3.13) show that the effect of diurnal thermal heating and cooling of the surface is large (hundreds of nanostrain) that is likely obscuring the solid Earth tides (low tens of nanostrain), making an in-situ calibration impossible. However, this strain ribbon appears to be more than sensitive enough with a least-count resolution of 8×10^{-14} strain for even the most demanding near surface strain measurements.

3.1.4 Muticomponent Optical Fiber Bragg Grating Strainmeter

The Mutlicomponent Optical Fiber Bragg Grating Strainmeter was another instrument motivated by the desire to measure directional strains in sediments where traditional, grout-in strainmeters would be far too rigid. The details of the design and results from lab tests are presented in Section 1.6, and the following sections detail the installation and field performance of this high-compliance, three-component strainmeter in the shallow subsurface.

3.1.4.1 Installation

The MOFBG strainmeter was installed at the Simpson Station test site on November 10th, 2021 and ran almost continuously until June of 2022. It was installed into a new borehole designated as SDP2 (Figure 3.1) that was first drilled with the same Geoprobe 5410 rig and 4-inch augers to a depth of 15 feet. A core sampling tool was used to create a smooth boring several feet below this to a 2.38" diameter matching the diameter of the instrument. This was intended to make a snug, but not quite press fit between the instrument and the surrounding saprolite material, and the instrument was lowered and seated into this cored hole by hand on several 1-inch diameter push rods made for this purpose.

3.1.4.2 Performance & Observations

The first step to understanding the behavior of the MOFBG strainmeter is to quantify its response, if any, to barometric pressure. Three scalar and spectral admittance estimates were made, the plots from which are shown in Figure 3.14. The scalar results are shown in Table 3.1 in both native units (picometers of wavelength change per Pascal of pressure change) and calibrated units using the results of the hydrostatic pressure test (Table 1.4).

Table 3.1: Barometric pressure scalar admittance estimates for the three gauges within the MOFBG strainmeter.

Gauge	Admittance (pm/Pa)	Admittance (Pa/Pa)
2J.SDP2.S1	2.3 ± 1.2	2.7 ± 1.7
2J.SDP2.S2	2.9 ± 2.2	2.9 ± 2.2
2J.SDP2.S3	2.4 ± 1.3	2.4 ± 1.3

The scalar (Table 3.1) and spectral (Figure 3.14) indicate a fairly small but not insignificant barometric pressure sensitivity. The coherence plots show that most of this is focused on the 1 CPD for gauge S2 and both 1 and 2 CPD for gauge S3, while there is much lower coherence on gauge S1. This lower sensitivity is also borne out by the lack of stability in the phase estimate in the tidal band.

The scalar admittance results from Table 3.1 and pressure calibration results from Table 1.4 were then used to make the amplitude spectrum plots shown in Figure 3.15. These show several notable features, the first being the clear 1 and 2 CPD peaks at $\sim$1.5 and $\sim$0.5 Pascals on gauges S2 and S3 that are mostly absent on gauge S1. These are most likely from thermal stresses in the near surface from daily heating and cooling. The other interesting result is the spectral flattening from approximately 1×10^{-2} Hz (100 seconds) up to the Nyquist frequency (0.1 Hz), which is a telltale indication of insufficient numerical precision, i.e., the instrument is measuring the smallest possible pressure it is capable of resolving.

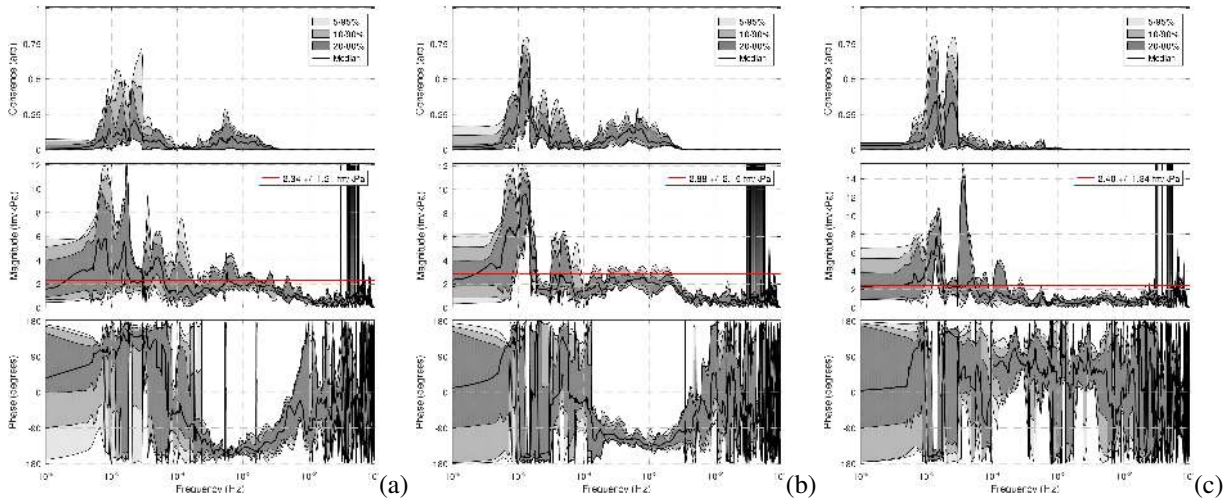

Figure 3.14: Cross spectrum of the MOFBG strainmeter and barometric pressure showing the coherence (top), magnitude (center) and phase (bottom) relationship between the vertical strain and atmospheric pressure as functions of frequency for each strain component S1–S3 (a–c). The scalar admittance value determined by least-squares is shown as a red horizontal line superimposed on the magnitude plot. The central black lines show the median of each estimate along with 5th/95th, 10th/90th and 20th/80th percentile confidence bands in shades of gray.

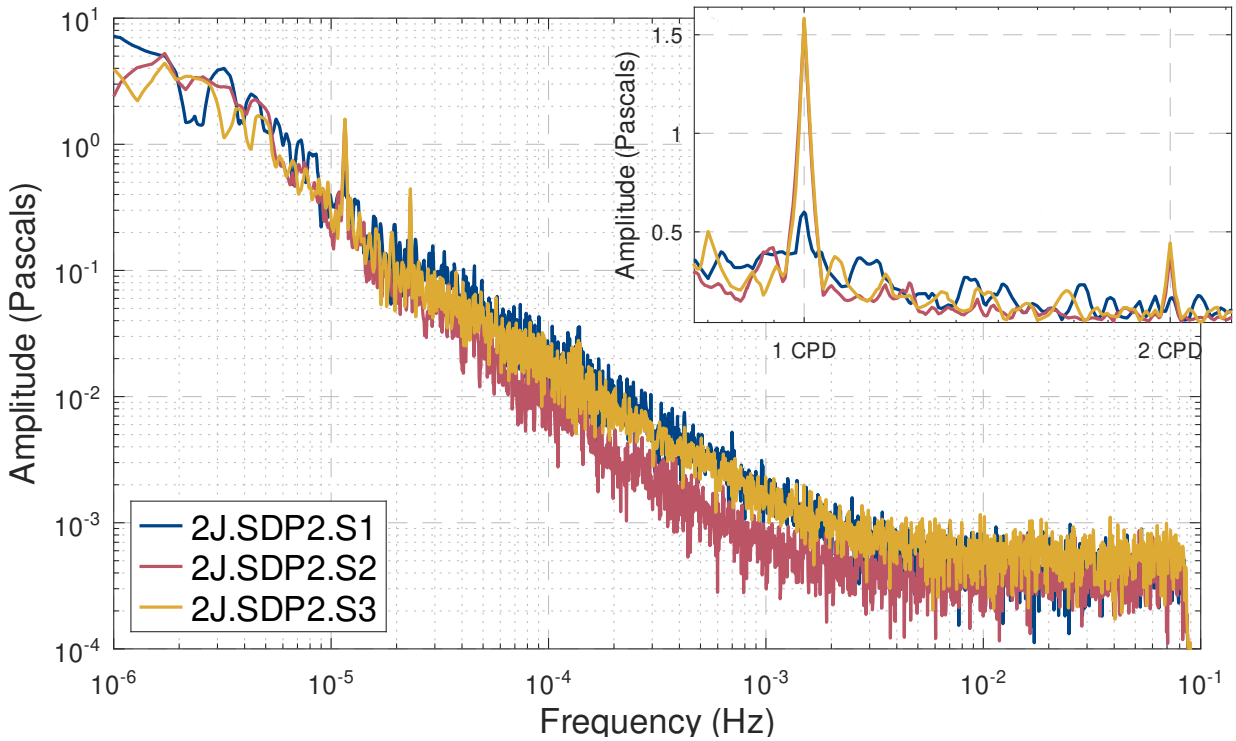

Figure 3.15: Amplitude spectrum for the three strain components measured by the MOFBG strainmeter. The inset plot focuses on the 1 and 2 CPD tidal band.

3.1.4.3 Conclusions

The high compliance Multicomponent Optical Fiber Bragg Grating strainmeter survived its installation and appears to be mostly coupled to the formation. While the spectral results (Figure 3.15) show clear signals at 1 and 2 CPD for strain gauges S2 and S3, gauge S1 seems to lack this feature. This is also present in the low coherence (Figure 3.14(a)) across the frequency band on S1 relative to the other two gauges. All three gauges do show clear responses to pumping tests in the nearby well SPW2 (Figure 3.1) as shown in upcoming Section 12.4.3.7, which further demonstrates the success of this proof-of-concept instrument.

3.2 Distributed Instruments

Three CMPI strain ribbons and one multicomponent "direct push" strainmeter were installed at the Simpson Station test facility during this project. These utilize the CMPI distributed strain sensing technology described in Chapter 2, and their installation and results are described in the following sections.

3.2.1 CMPI Strain Ribbon #1

We installed an pair of fibers packaged in a compliant strip and designed to be used with the CMPI system at the Clemson University Simpson Station field test site. The goal of this effort was to evaluate the feasibility of deploying and operating a CMPI in the field.

The installation process involved boring a hole in saprolite to a depth of 40 ft using a 4-inch diameter solid stem auger (Figure 3.17). The auger was advanced to depth and then rotated for a few minutes in an effort to remove cuttings and reduce the potential for collapse. This follows practice in the well drilling industry in the area. The augers were removed and a rod was lowered in the hole to confirm it remained open to the total depth. The water table was at a depth of 29 ft and the rod met mild resistance below the water table, which occurred because the hole was filled with water with a high content of suspended solids (muddy water). This is consistent with the state of the hole drilled using solid stem augers previously.

A polyethylene sleeve that was closed at the bottom was attached to a 6-inch long piece of 2-inch PVC pipe, and the fiber was also attached to the pipe. Tubing (1-inch diameter thin-walled stainless steel with pressed threads) was used to push the piece of pipe, with the sleeve and fiber to the bottom of the hole. The poly sleeve was folded axially as it was advanced into the hole. This reduced the profile and wall friction. The poly sleeve was 7-inch layflat tubing, which expands to a diameter slightly larger than the boring. The field configuration involved laying extending the fiber and poly tubing in different directions from the boring (Figure 3.18) The tubing met with resistance when the water table was reached, but it was successfully pushed to total depth.

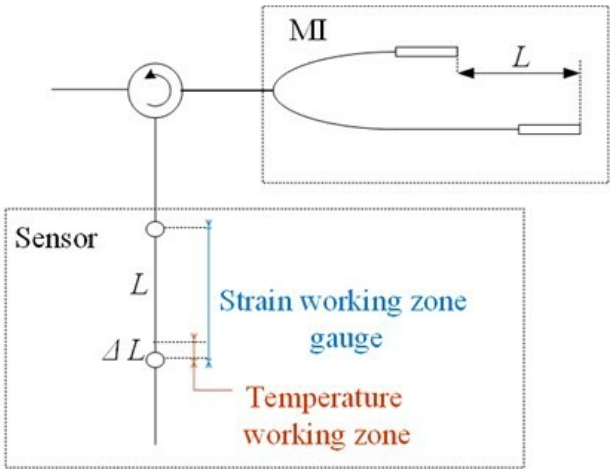

Figure 3.16: Schematic of sensor with Michelson Interferometer reference.

Two strings of optical fiber packaged in compliant polymer strip were advanced into the hole. Reflectors on lower string extended from the bottom of the hole to a depth of approximately 17 ft. Reflectors on the upper string extended from a depth of 14 to 7 ft.

The same tubing was extended into the sleeve and water was added to the top of the sleeve at a rate of approximately 5 to 10 gpm in an effort to open the sleeve against the water pressure in the hole. The tubing reached a total depth of 35.3 ft before meeting significant resistance. We assumed that the sleeve had been closed by water pressure below this

depth. The bottom of the sleeve had been perforated so that water pressure would equilibrate between the inside and outside of the sleeve during operation. As a result, water added to the sleeve could flow out through the perforations and into the formation. This limited the pressure that could be achieved inside the sleeve and this limited the extent to which the sleeve could be opened below the water table.


(a)
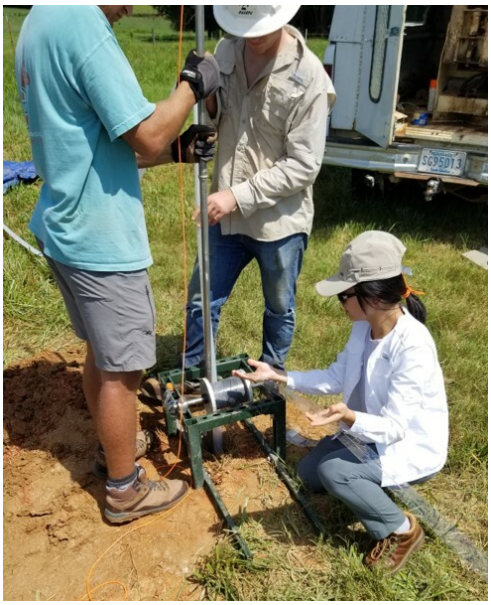
(b)

Figure 3.17: Field installation of CMPI fiber at the Clemson hydromechanics research site. (a) packaged fiber on table on right, tubing on table on left, poly sleeve on left side, project personnel are around the borehole where fiber is installed. (b) view of the head of the boring. Fiber is in transparent strip on lower left and it passes over roller at top of boring, poly sleeve is behind the vertical stainless steel tube.

Coarse-grained, well sorted sand used as filter pack in wells was added to the sleeve to open it and push the fiber against the wall of the boring. One half a cubic ft of sand should fill the sleeve by approximately 4.3 ft. We added 1 bag of sand and the level of the sand in the bottom of the hole increased by 4 ft to approximately 31.5 ft. This is the expected response. The sand level increased by 2.5 ft when the next bag of sand was added. The sand level increased by 0.4 ft when the next bag (0.5 cubic ft) of sand was added. The sand level was at approximately 29 ft, which is the depth of the water table. The water level in the sleeve was approximately 25 ft depth. We then added approximately 0.5 cubic ft of saprolite and the level at the bottom increased by approximately 0.3 ft. The level was determined by the level of resistance to the stainless steel rod. The tubing was lifted by 5 to 10 ft periodically to avoid, or detect bridging. We dropped a tape to depth and it extended to 28 ft, so it seems unlikely that bridging explains the apparent loss of material.

All the reflectors were working when the fiber was initially installed, and we checked the functionality of the fibers periodically during completion. At this point, it was reported that the bottom two reflectors on the lower string were not working. The break is at a depth of approximately 22 ft, which is above the level of the bottom of the rod.

We continued added saprolite and find that the saprolite has accumulated around the rod over a depth range of 24 to 28 ft. The rod was retracted above 24 and the top of the bridge could be felt. The top of the bridge appears to be at, or slightly below the location of be break in the fiber. The bridge was also detected after the break was detected. The water level in the sleeve was at approximately 25 ft, so the bridge occurred in the vicinity of the water level in the sleeve.

We continued to add saprolite to the sleeve. Saprolite was used after the first 3 bags of sand in order to try to match the material on the outside of the sleeve. The sand was washed into place with water from a hose at the ground surface.

Washing was used with the first few buckets of saprolite, but it was discontinued when the level of the saprolite was above 25 ft. Saprolite was added in volumes of approximately 4 to 5 gallons, slightly more than a half foot. The level of the saprolite increased by 4 to 5 ft with each bucket of saprolite once the level reached approximately 20 ft.

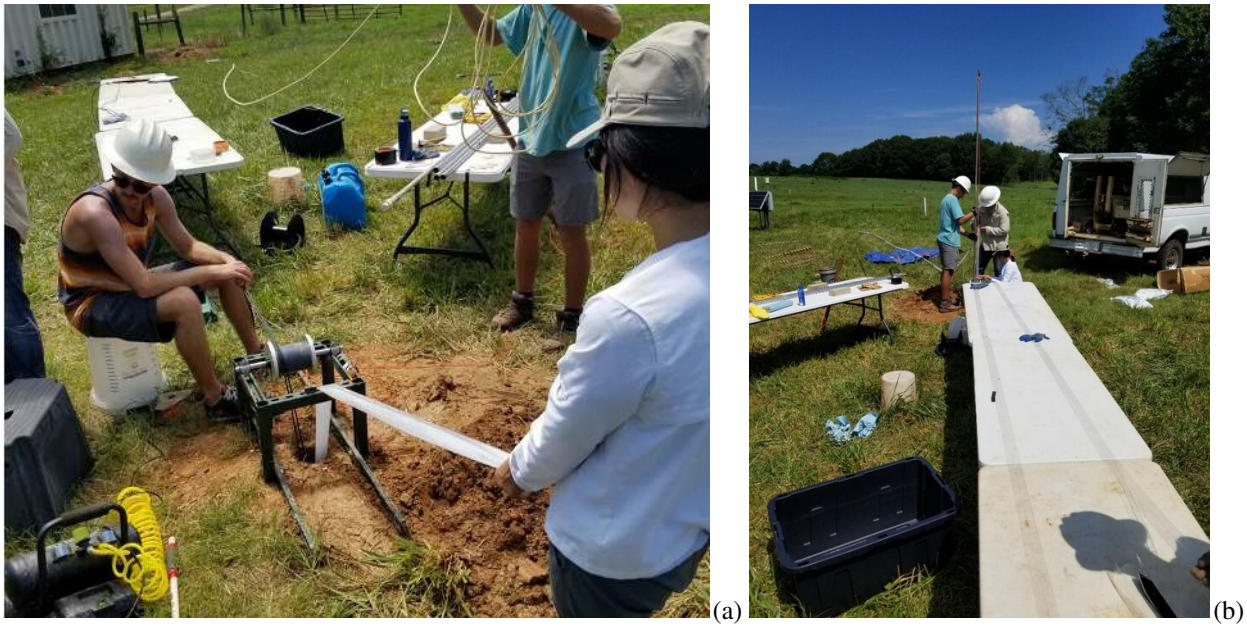

(a) (b)

Figure 3.18: Field installation of CMPI fiber at the Clemson hydromechanics research site. (a) Top of boring after installation. White band is poly sleeve. Fibers are in tactical cable extending over grey roller. (b) Fiber packaged in transparent strip on table during deployment.

The upper fiber string was reported broken when the saprolite was being added. The string was broken at a depth of approximately 12 ft when the level of saprolite was in the range of 18 to 20 ft.

The cause of the breaks in the fiber appears to be related to the use of the tubing during completion. The tubing was moved up and down to locate the top of the solid material in the sleeve. The movement was smooth and controlled. The threads on the tube have a protruding ridge, which houses the o-ring. One possibility is that solid material added to the sleeve pushed the tube to the side of the hole. The tube was lifted and lowered regularly and it is possible that the ridge on the side of the tube rubbed against the side of the hole. If the fiber was resting on a protruding rock, then contact with the ridge on the tube could break the fiber. This would explain why the breaks occurred 5 to 7 ft above the current bottom of the hole.

Measurements made after completion indicated that two reflector pairs were working. Data over the first day or so indicated a diurnal variation of approximately 50 microstrain. This signal appears to be largely a result of temperature variations of the interrogator and associated electronic equipment. In the field, the temperature is averaged at 26 degree C during summer, and the variation was about ± 5 degrees C. The surrounding temperature change induces a laser wavelength drift (0.094 nm/degree C) and results in an interference phase change from the sensors. For a regular interferometer, the strain temperature cross talk ratio is 60 $\mu\epsilon$/degree C (@ 1550 nm). However, CMPI uses a Michelson interferometer (MI) as a reference interferometer which has cavity length close to the sensor cavity length (less than 1cm difference). The phase change for each sensor is read from the interference phase difference between the sensor and the MI. Since, wavelength drifting causes interference phase change for both sensor and MI, the wavelength drift induced phase change only along the ΔL as shown in Figure 3.16. The strain-temperature cross talk is $\Delta L/L$ 60 $\mu\epsilon$/degree C, which is at least 10 times less than the conventional interferometer when the sensor cavity is about 15 cm. To further compensate the temperature induced interference phase change, we can have one sensor attached to the high compliance material, so it will be isolated from the movement of the soil and only records the phase changed due

to the laser wavelength drifting. Since all the sensors have similar sensitivity, the measured phase change can be used to do the temperature compensation for the rest sensors.

The field effort was successful in creating two working reflectors in the subsurface. We deploying the CMPI interrogator and associated electronics in the field for the first time. These are significant accomplishments, and we also learned some important lessons related to completion and deployment. Problems associated with breaking fibers during completion appear to be a result of how the material filling the sleeve is placed.

3.2.2 CMPI Strain Ribbon #2

The sensors packaged in a compliant strip were installed in a 30 ft deep hole in the bull farm and buryied in saprolite. There are 8 reflectors that are 15 cm apart every 85 cm on the fiber. A 15 cm cavity Michelson interferometer (MI) is used as a reference, which has been installed in a 10 m dry hole 5 m away from sensor hole. The schematic of sensing system is shown in Figure 3.19a. CMPI testing system has been installed in the barn 5–10 m away from the holes. Measurements were taken every 70 seconds.

Each reflector pair form 3 pulses in time domain. The first pulse is the reflections from closer reflector and reflected by the short arm of the MI. The third pulse is the reflection from farther reflector and reflected by the longer arm of the MI. The center pulse is the sensing pulse, which is the merged pulse of the refection from both reflectors and then reflected by the longer and shorter arms of the MI respectively. A loading tested has been done after installation by measuring the strain change between a person (∼160 lb) stand close and far away from to the hole. The measured stain as function of depth is shown in Figure 3.19b, where the red dots are the strain read at the respective locations, and the blue curve shows the estimated strain value at each location.

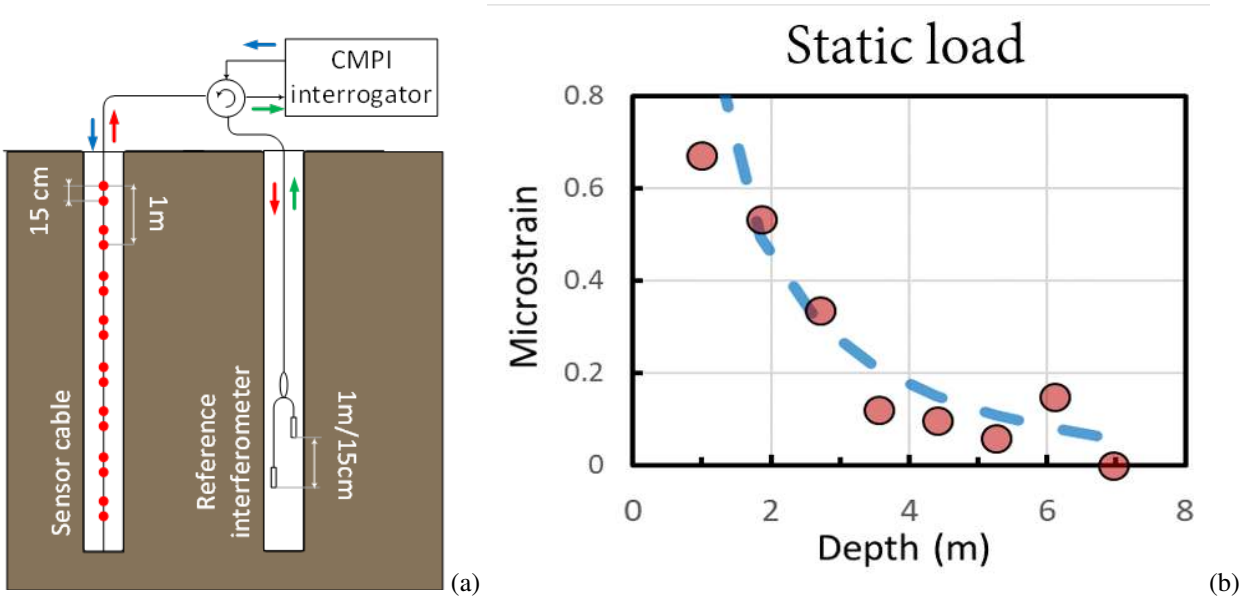

Figure 3.19: (a) Schematic of sensing system in the Clemson Bull Farm. (b) Strain measured at each sensor location during static loading.

CMPI is used under assumption of that the microwave phase of each reflection is a constant. However, when the measurement distance is long, the microwave phase change of each reflection becomes substantial over time, which mainly due to the daily temperature change. Distance compensation is needed to find the right sensor location. As the location reading from the sensing peak varies due to strain induced the OPD change, the good way to know the sensor location changes would be from the nearby reference pulses. The location change of each sensor as function of measurement time are plotted in the Figure 3.20a. The location shift for reference peaks are discrete, so the location

shifting compensation still gives abrupt sensor phase change. Figure 3.20b shows the location shift modified strain under a pump testing, where abrupt strain changes are observed at multiple time due to the signal processing error. Microwave phase shifting of the reference peaks changes continuously as shown in Figure 3.20c and reflects the change of location of the reflections. Subtracting the microwave phase change of the reference peaks from the sensor peaks can well compensate the location change of the sensors. Strain changes during pumping calculated by frequency shifting compensation is plotted in Figure 3.20d, where most of the abrupt phase change due to the time point jumping in Figure 3.20b are removed.

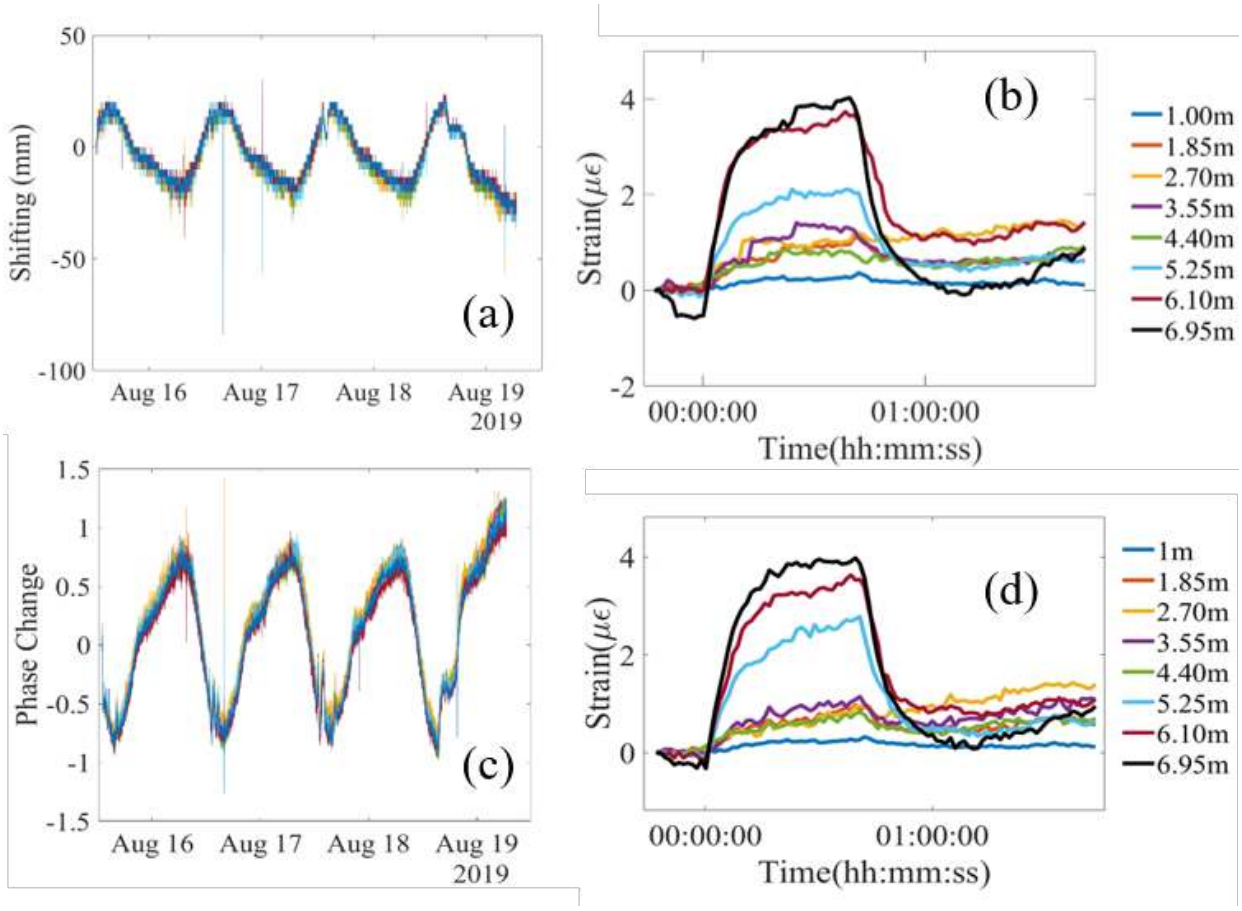

Figure 3.20: (a) Locations shifting of reference. (b) pumping testing results (location compensation). (c) Phase shift of the reference peaks. (d) Pumping test results calculated using phase shifting compensation.

The microwave phase compensation method has been used to correct the long term strain measurements day. (Figure 3.21) shows the strain data where taken from the installation August 15–27, 2019. Due to the consolidation, large strains were observed after the installation on Aug. 15. Pumping test was done on the evening of Aug. 18 where the pulses are shown on the strain vs. time curves. Small daily periodical strain changes were observed. Those changes are mainly due to the daily temperature change and barometric pressure change. More data analyze will be performed in the coming quarter. Splicing point between the sensor array and armor cable was broken due to a heavy rain fall on Aug. 27. We are designing the splicing protection housing to protect the splicing points for the new sensor arrays.

A 1-meter-long Michelson interferometer (MI) is used as reference to increase the strain sensitivity. The MI selects the reflectors that are 1 m apart, so 7 pairs of reflectors were selected and formed seven sensing sections as shown in Figure 3.22. There was 15 cm overlap between any two adjacent sensing sections. The top five sensors and the

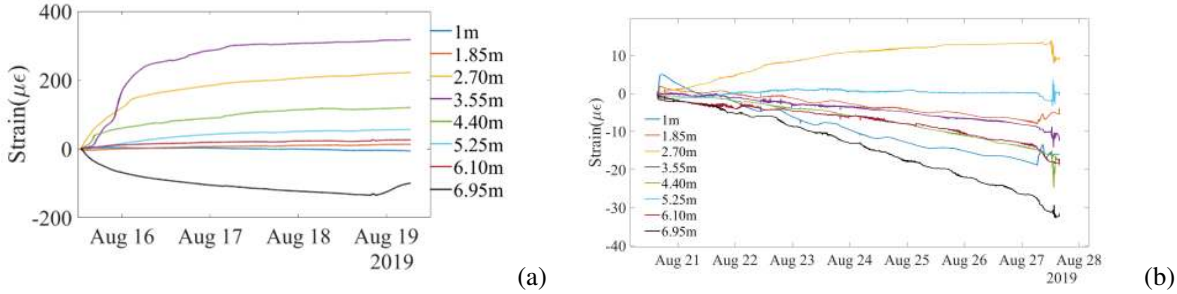

Figure 3.21: (a) Strain measured at each sensor location from Aug.15 to Aug.20, 2019. (b) Strain measured at each sensor location from Aug.20 to Aug.28, 2019.

bottom sensor showed acceptable ellipse fitting when processing the signal. The fitting noise was mainly due to the unbalanced reflections from the sensors, which could be a result of reflector fabrication. A 3-hour-long pumping test was performed on Dec. 17th, 2019. The average strains as function of time within the 6 sections are shown in Figure 3.23. The strain was tensile and increased during pumping. Strain magnitude increased as a function of depth. As the pumping well was closer to the sensor array compare with the pumping test that performed in August, the maximum strain at each location during pumping was about 2 times larger than the former test.

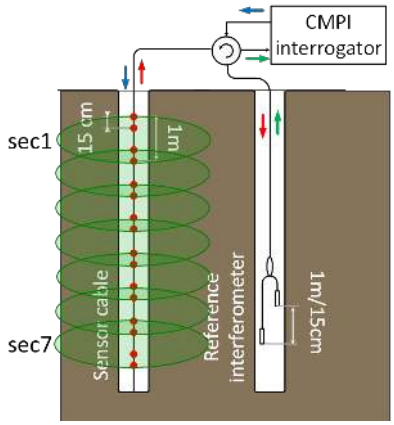

Figure 3.22: Schematic of sensor array installed in the field.

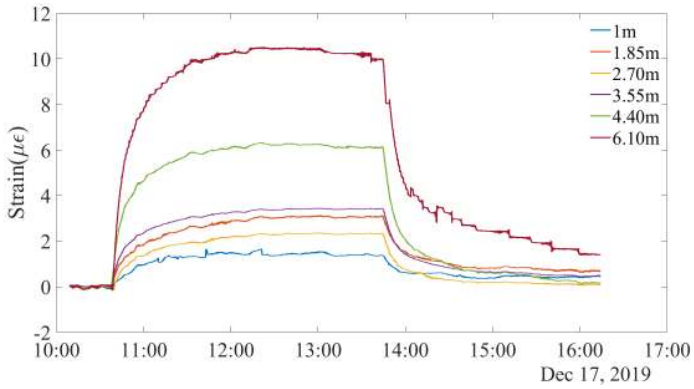

Figure 3.23: Strain response as function of time during pumping test.

Some preliminary seismic tests were conducted on December 18th by using this vertical array of strain sensors descried above. The source was made by hitting a plate with a hammer. The test performed several times. The sampling rate of the system was set as 9.871 kHz. A DC–37.55 Hz frequency window was applied to each sensor during the post data processing. The sensor response during two times of tests were shown in Figures 3.24a,b. Figure 3.24c shows the response from sensors when no hitting was performed. A burst signal showed up at all the locations after hitting. A slight time delay (∼23.5 ms) of the strain response between the top sensor and bottom sensor was observed. The experiments showed that the system has the capability of capturing the seismic signal.

3.2.2.1 Ambient Noise Results

Five days of CMPI strain measurement data were used to compare with the barometric pressure data. The barometric pressure data were recorded by a HOBO barometric pressure logger that is set on the surface at the Simpson Station ∼10 meters away from the CMPI sensor array. Strong correlation is shown between the pressure data and

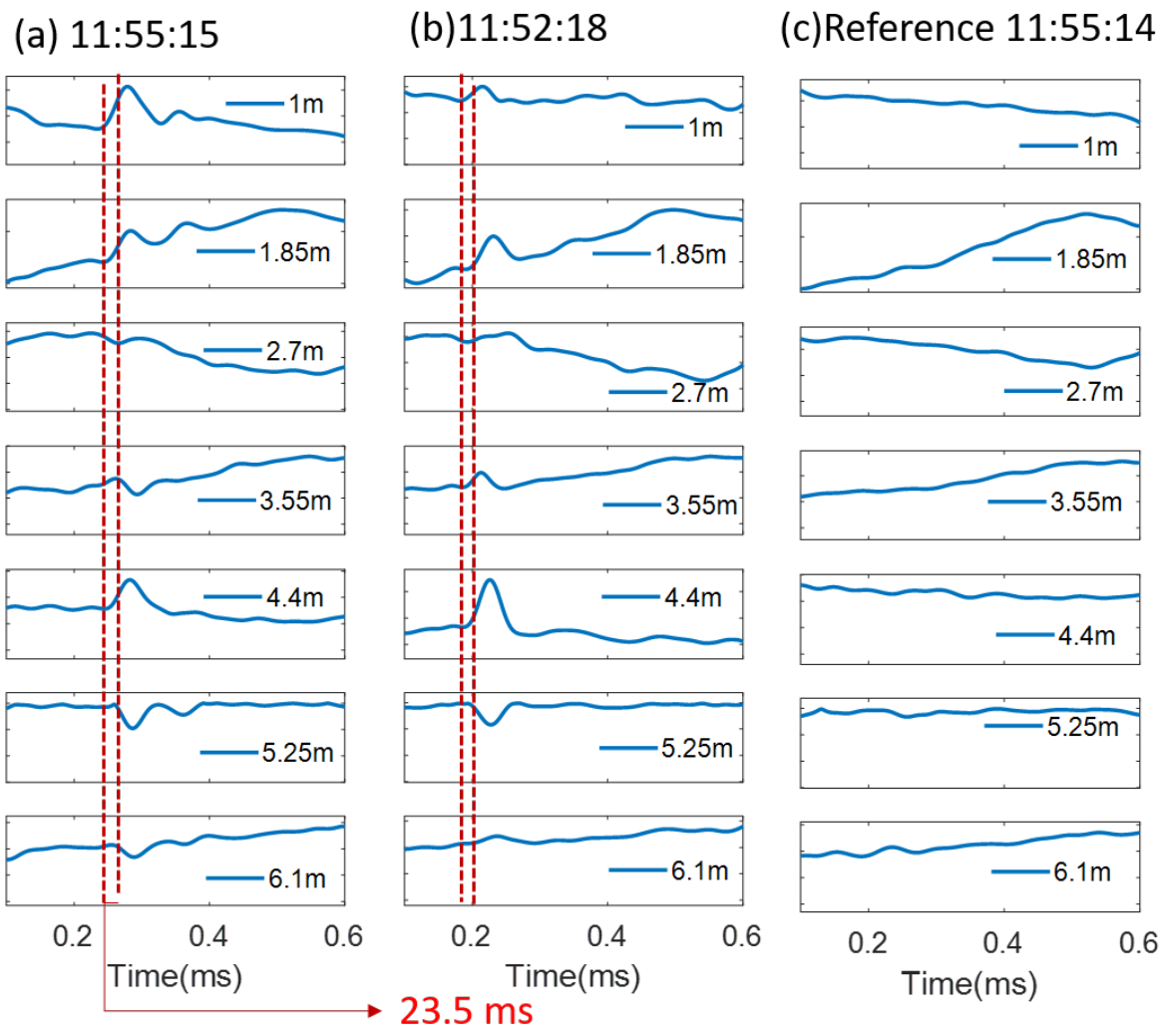

Figure 3.24: Response from sensors when a plate with a hammer hit the ground at (a) 11:55:15 and (b) 11:53:18. (c) Reference response from sensors when the ground was not hit.

strain data. Figure 3.25 shows the zoomed in one day data which were taken on March 15th, 2020. The top plot shows the pressure (kPa) as function of time. The S1–S6 are strain (in units of microstrain) from the CMPI sensors that are located at depths of 1, 1.85, 2.7, 4.4, 5.25 and 6.95 meters respectively. There were two sudden barometric pressure change around 6:00 am and 12:00 pm local time as marked with red dash line in the figure. Positive net strain showed from reading of all CMPI sensors when barometric pressure decreased, and vice versa.

Spectrum analyses were performed to investigate the similarity of the frequency components between the strain signals and barometric pressure. A 5-hour window with 99 percent of overlap between adjacent windows has been applied to the 5 day data set. 50th and 95th percentiles of results at each frequency were chosen, and the plots are shown in Figure 3.26. In the process, we assume the modulus of the sand in the sensor hole is 50 MPa. The spectra show similarity between the strain signals and pressure signal within the frequency range from 0.1 to 10 mHz. The results indicate the noise level of the CMPI sensors at shallow depth maybe dominated by the ambient noise.

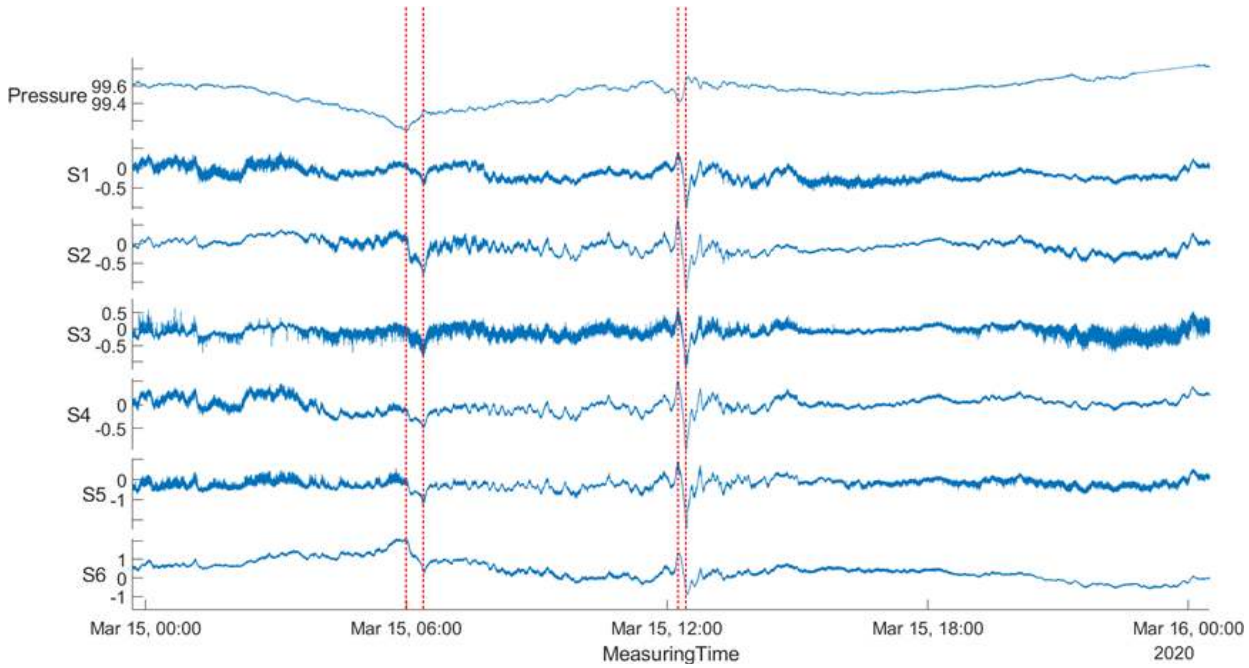

Figure 3.25: Barometric pressure (top plot) and strain measured at depth of 1 m (S1), 1.85 m (S2), 2.7 m (S3), 4.4 m (S4), 5.25 m (S5), and 6.95m (S6) on 15-Mar-2020.

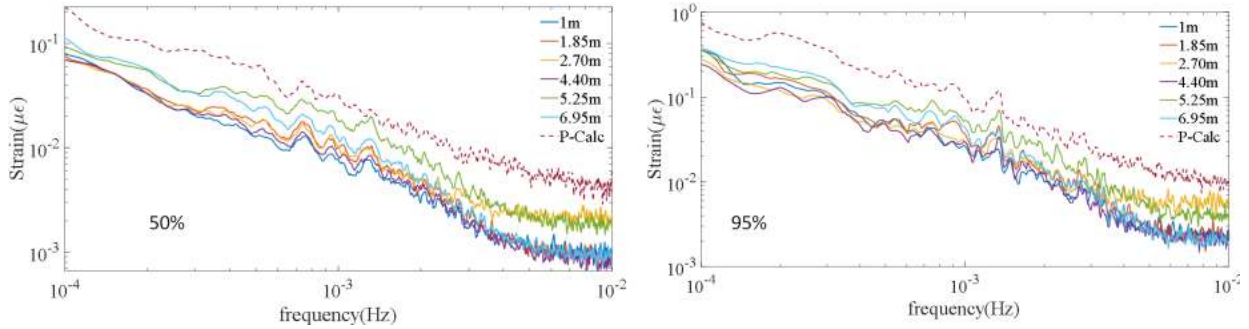

Figure 3.26: Median (left) and 95th percentile (right) strain spectra at each depth calculated from 5 days CMPI strain data. The brown color line shows the spectrum of the strain which is converted from Barometric pressure where the sand modulus of 50 MPa is assumed.

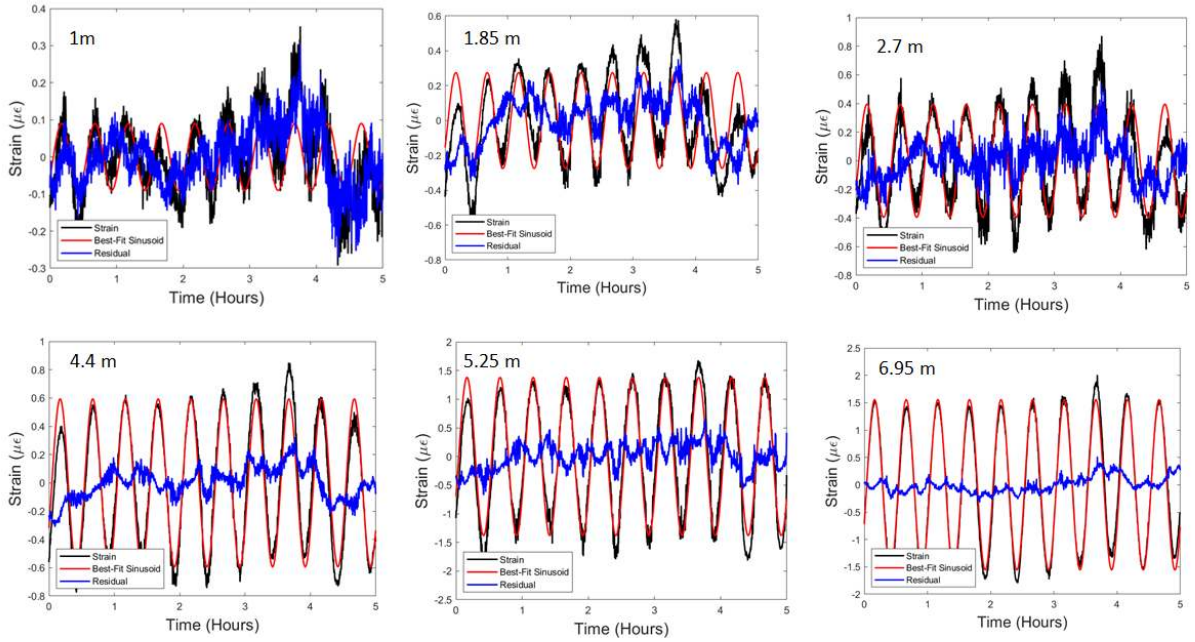

Figure 3.27: Recorded strain at different depth during pumping test with sinusoidal pumping rate (black), the best-fit to the strain signal (red) and their residual (blue).

3.2.2.2 Periodic Pumping Tests

An array a CMPI sensors was installed at our local Simpson Station field site in November 2019 that has been functional for the past five months. The sensors were packaged in a compliant ribbon and were installed in a 30 ft deep hole. There were 8 reflectors that were 15 cm apart every 85 cm on the fiber. A 3-hour-long pumping test with constant rate was performed on Dec. 17th, 2019. Results showed that the strain was tensile and increased during pumping. Strain magnitude increased as a function of depth. Our theoretical analysis shows that underground strain distribution from pumping tests with sinusoidal rate can be utilized for leak detection, and this method could be used at the North Avant Field demonstration site for the current project.

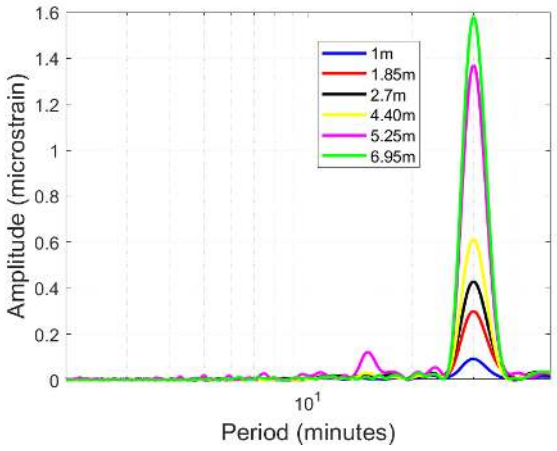

Figure 3.28: Magnitude spectrum plot during a sinusoidal pumping test.

To demonstrate the feasibility of measuring the distributed sinusoidal strain signals by using CMPI sensing system, pumping tests with sinusoidal rate were performed at the Simpson Station. In these tests, water was pumped from the aquifer using a sinusoidal rate with a constant period of 30 minutes. The sinusoidal rate is controlled by a function generator (Tektronix AFG1022) which outputs a sinusoidal varying signal. This signal is read by a variable frequency drive to control a single phase 0.5 horsepower submersible pump. Each pumping test was performed for 6 hours, allowing 12 periods to be recorded. The amplitude of the driving signal was varied across 6 different tests to observe the effect pumping rate amplitude has on the sensitivity of the instrument. Flow rate was recorded using an Omega FP-5600 Flow meter. The recorded amplitude of the flow rates was 1.5 gpm, 0.7 gpm, 0.5 gpm, 0.25 gpm,

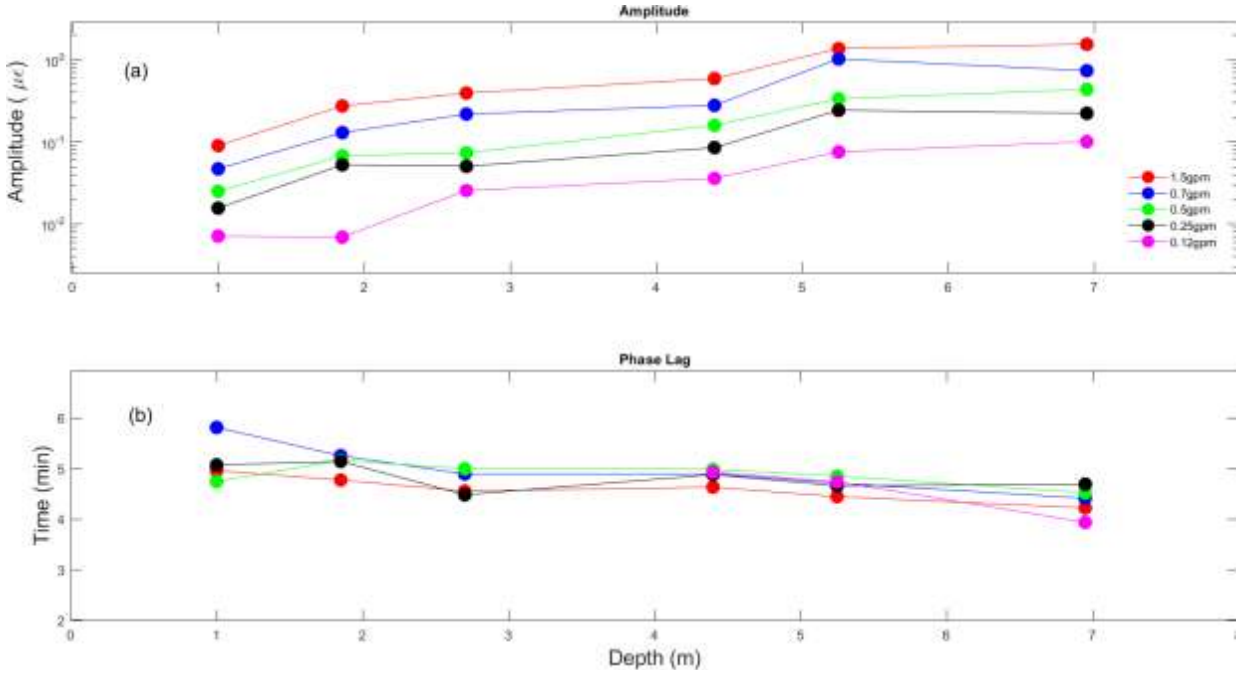

Figure 3.29: Amplitude and phase lag as a function of depth in the vadose zone during the six sinusoidal pumping tests.

and 0.12 gpm respectively for the six tests respectively. The hydraulic head of 3 monitoring wells were collected too by using HOBO data loggers. Strain was measured using CMPI sensors above the aquifer between 1 and 6.95 meters below the surface. The sampling rate was set as 0.2 Hz.

Figure 3.27 shows an example of the strain change at 6 sensor locations over one 6 hours pumping, where the amplitude of pumping rate was 0.5 gpm. The raw strain data is shown in black, the best fit to the strain data is shown in red, and the residual between the two is shown in blue. When the pumping rate increases during the test, the vadose zone goes into tension (positive net strain). When the pumping rate decreases, the vadose zone goes into compression (negative net strain). The magnitude spectra of strain signals got from the 6 sensors (Figure 3.28) show that the strain signals have the same changing period as the pumping signal, as the large spikes at the 30 minutes on each spectrum coincidence with the known pumping period.

The best fit line of strain data is used to calculate the approximate amplitude of the strain and the phase lag between the driving signal and the strain response. Figure 3.29(a) shows the amplitude at different depth for all the 6 times of tests. All the 6 plots show that the amplitude of the sinusoidal strain signal was increased as function of depth. The amplitude of the strain decreasing as the pumping rate decreasing, but the changing trends are similar. When the pumping rate decreased to 0.12 gpm, the strain read by the top sensor was around 5 nϵ which is barely readable. The 5 nϵ noise level could be from the CMPI interrogation and the ambient noise induced strain change. The phase lags are plotted as function of depth as shown in Figure 3.29(b). The phase lag was between 4–5 min. The lag is slightly larger for the sensors at shallow depth and smaller for the sensors at deep depth. This trend is clearer when the driving voltage was large where the strain signal was much higher than the noise level for the upper sensors.

Further tests were done by alter the period of the pumping signal. The pumping with a 15, 30, and 60-minute period were used. The flow rate for all these tests varied from 5.7 to 0.9 gallons-per-minute (gpm). Each pumping test was performed for a minimum of 6 hours or up to 12 hours, keeping consistent the recording of at least 12 periods. This resulted in 24 cycles recorded for the 15-minute period test and 12 cycles recorded for the 30-minute and 60-minute period tests. The amplitude of the control signal was held constant for each test to isolate the effect of the

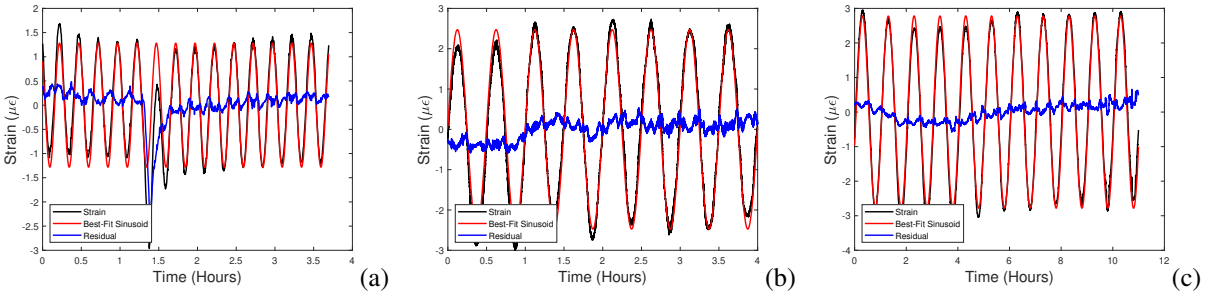

Figure 3.30: Strain change at 6.95 m during the (a) 15-minute, (b) 30-minute and (c) 60-minute period of sinusoidal pumping.

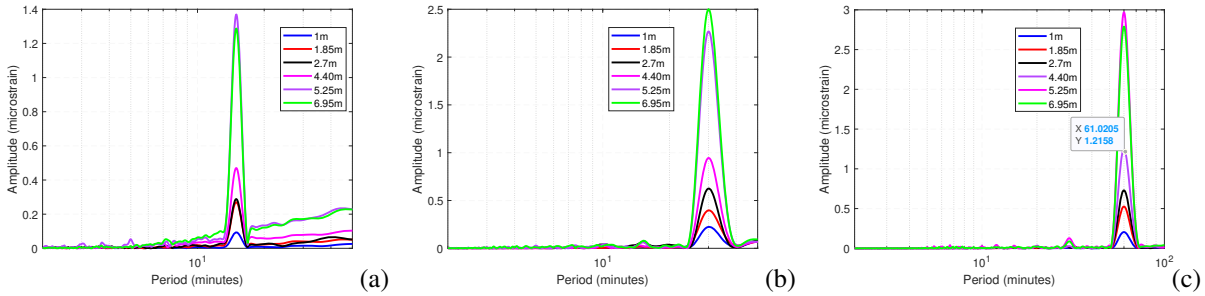

Figure 3.31: Magnitude spectrum plot during a sinusoidal pumping test with (a) 15-minute, (b) 30-minute and (c) 60-minute period of sinusoidal pumping.

varying period on the sensitivity of the instrument and to observe and frequency dependent responses. The flow rate was recorded using an Omega FP-5600 Flow meter. The hydraulic head of 3 monitoring wells were collected using HOBO data loggers. Strain was measured using CMPI sensors above the aquifer between 1 and 6.95 m below the surface. The sampling rate was set as 0.5 Hz for the 30 minute period test and 0.1 Hz for the 15 and 60 minute period tests.

Figure 3.31 shows an example of the strain change at the 6.95 m sensor location for each of the different sinusoidal periods. All three tests were performed at the same control maximum and minimum input resulting in flow rates ranging from 0.9 to 5.7 gpm. The raw strain data is shown in black, the best fit to the strain data is shown in red, and the residual between the two is shown in blue. As seen in the multi-amplitude tests, when the pumping rate increases during the test, the vadose zone goes into tension (positive net strain). When the pumping rate decreases, the vadose zone goes into compression (negative net strain). The magnitude spectra of strain signals observed in Figure 3.30 shows that the strain signal can be observed and filtered at multiple different frequencies, all depending on the input period. Each spike in the plots corresponds with the input period for that specific test.

The best fit line of strain data is used to calculate the approximate amplitude of the strain and the phase lag between the driving signal and the strain response. Figure3.32 shows the amplitude at different depths for all three tests. Each test shows that the amplitude of the sinusoidal strain increases with depth and the greater the period, the greater the amplitude of strain. With the phase lag there is a range of delay from 3 to 7 minutes. The trends for the amplitude and phase is similar between all three tests. Phase and amplitude dependence on periodicity is a phenomenon observed in pressure data when using sinusoidal pressure to characterize aquifers. The analyzed data indicate that the current developed CMPI field sensing networking can be combined with sinusoidal pumping tests to explore the elastic soil property in vadose zone at multiple depths.

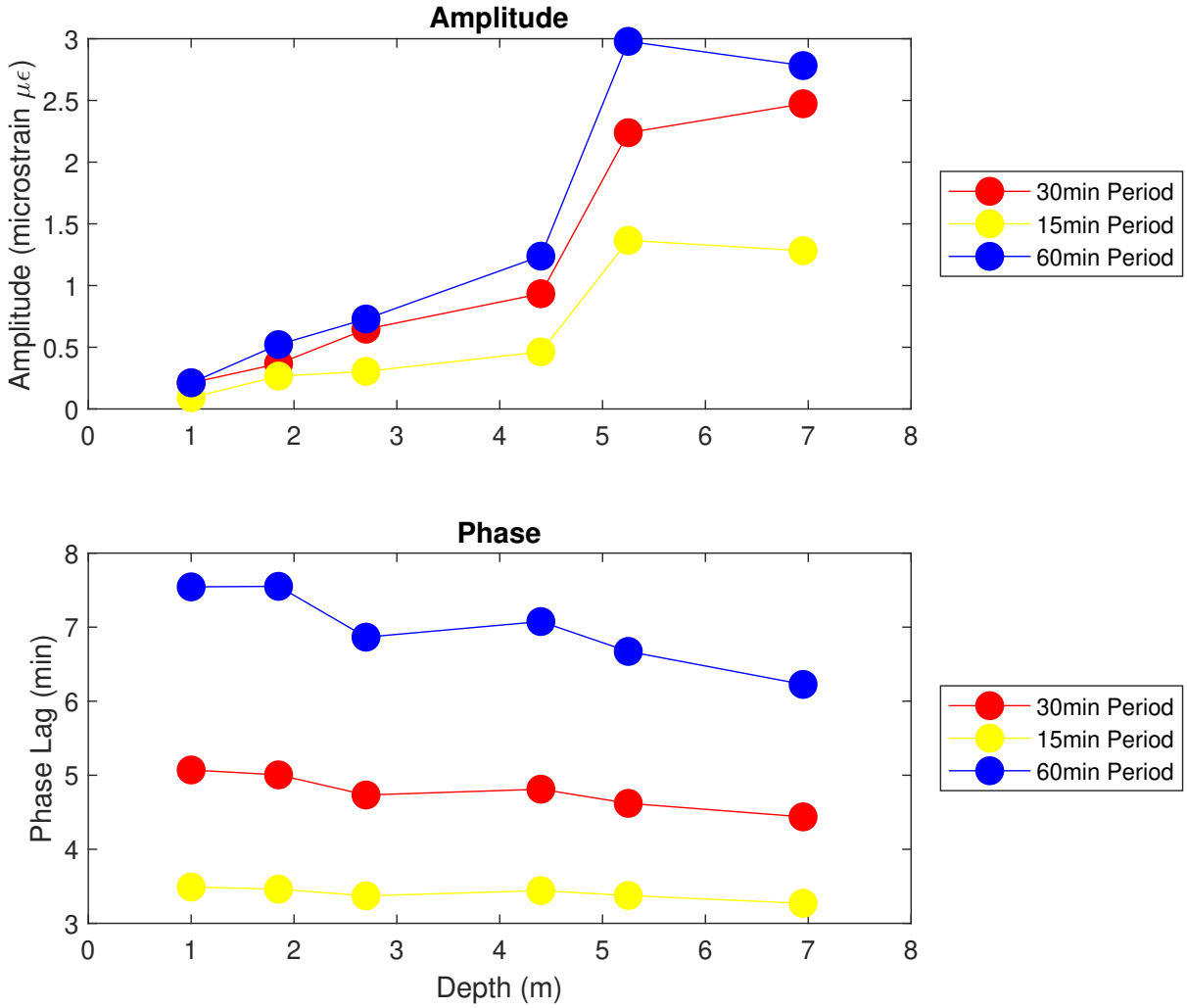

Figure 3.32: Amplitude and phase lag as a function of depth in the vadose zone during the three sinusoidal pumping tests.

3.2.3 CMPI Direct Push Instrument

We have successfully been installed the Direct Push Instrument (DPI) at our local Simpson Station field site (Figure 3.33). The DPI contains six sensing components that measure average horizontal strain (S1), the vertical strain on the SW side (S2), the horizontal strain on the NW side (between 9–2 o'clock)(S3), the vertical strain on the NE side (S4), the horizontal strain on SW side (between 5–10 o'clock) (S5) (Figure 2.46.

Loading test was performed by driving a vehicle periodically away and close to the installation well. The vehicle was at the SE of the well. Sensing data (Figure 3.34) show that when the vehicle moved close to the well, the average horizontal strain (S1) and the vertical strain (S2, S4) decreased due to the compression, the horizontal strain on the NW side (S3), and the horizontal strain on SW side (between 5–10 o'clock)(S5) increased due to the unsymmetrical loading.

3.2.4 CMPI Strain Ribbon #3

A third newly developed 9-m-long CMPI strain ribbon was installed at our local Simpson Station field site (Figure 3.35). Seven reflectors are 1 m apart, along with the ribbon to form 6 continuous sensing regimes.

Loading tests and pumping tests were performed after the installation. All the six sensing regimes showed reasonable responses to soil displacement due to the activities. In the loading test, a person walked away and close to the installation hole periodically. The movement of the person caused compression and relaxing of the soil and results in the vertical strain change (Figure 3.36). In the pumping test, the water was pumped out from well for half an hour and pumped back in to the well for half and hour. The strain change curves (Figure 3.37) were similar to the other pumping tests we did when use different types of sensors. The results indicate that the new packaging method allows small strain transfer and could be one good option for making the strain ribbons.



Figure 3.33: Direct-push strainmeter (a) during fabrication (b) during fabrication showing reflectors (c) instrument in the field (d) preparing to install (e) pushing the instrument in place using a small drilling rig.

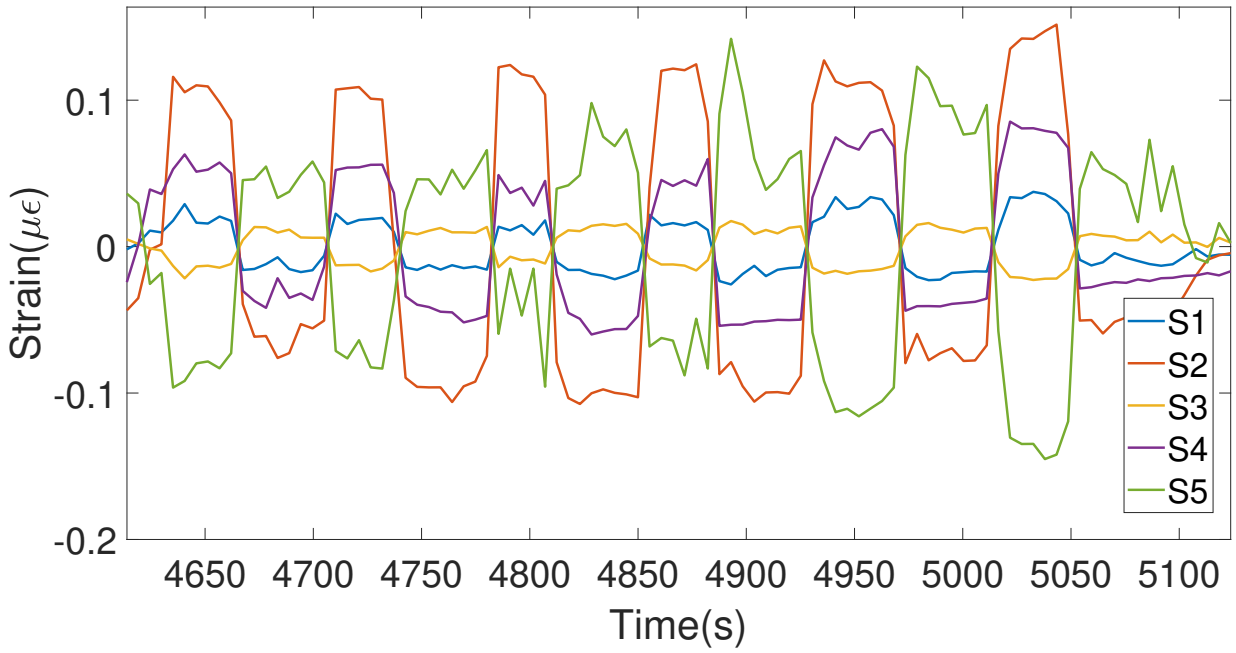

Figure 3.34: Strain response of 5 sensing sections of the pushing instrument during the vehicle loading test.

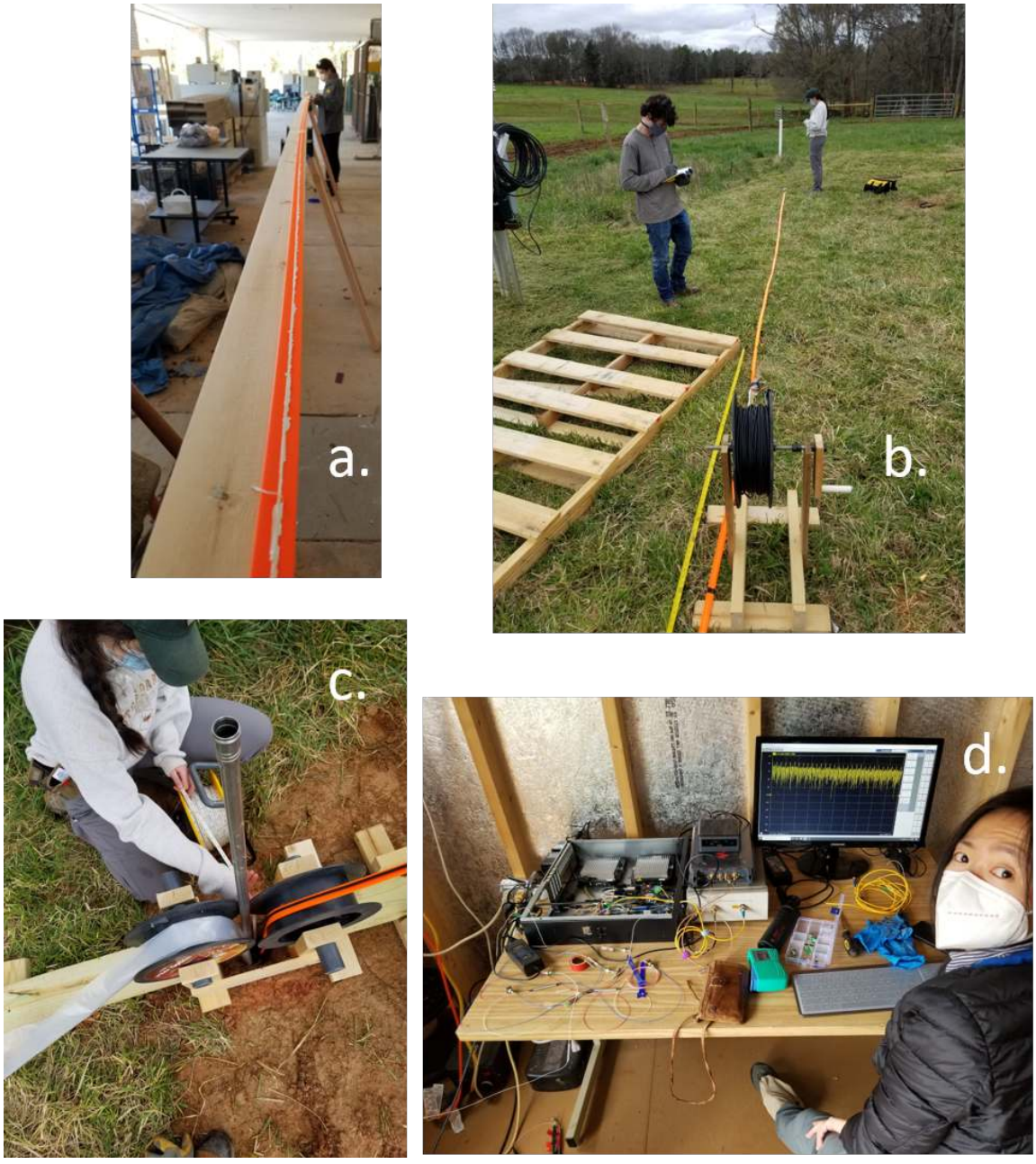

Figure 3.35: Strain ribbon (a) during fabrication (b) preparing to install (c) deploying ribbon in a borehole (d) monitoring the signal during deployment.

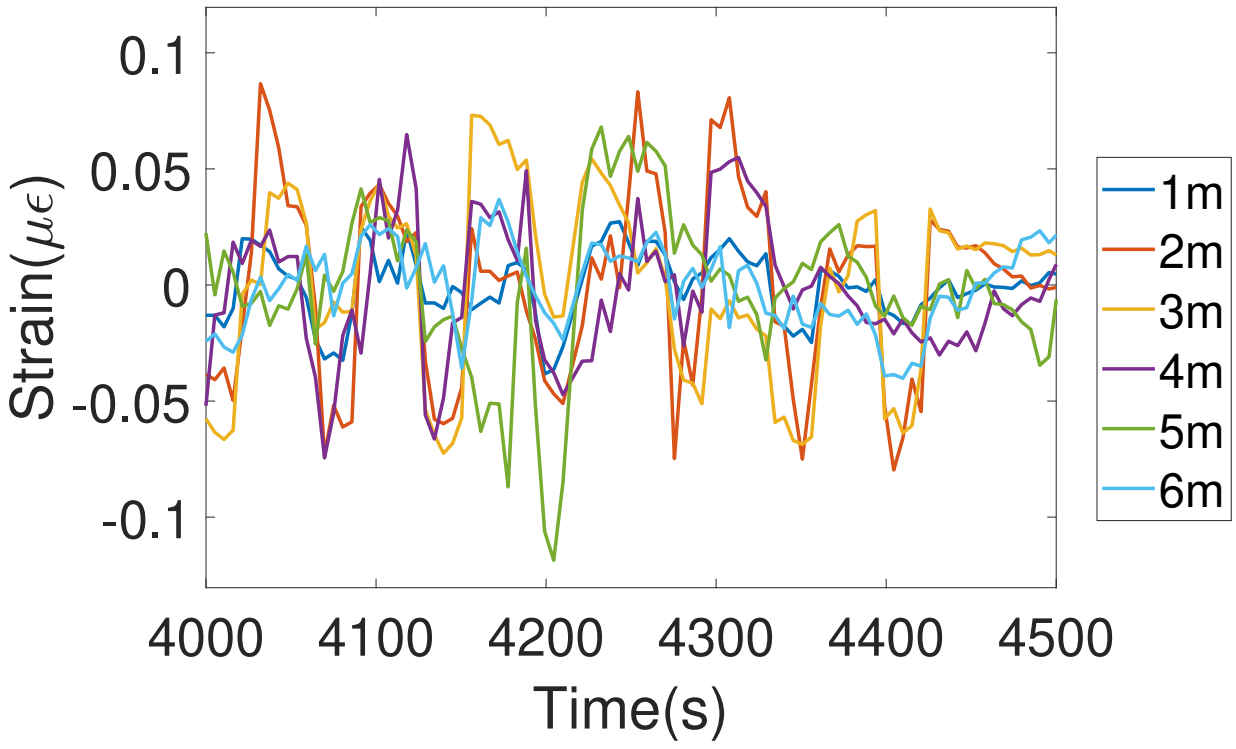

Figure 3.36: Strain response of 6 sensing sections of the strain ribbon during the person loading test.

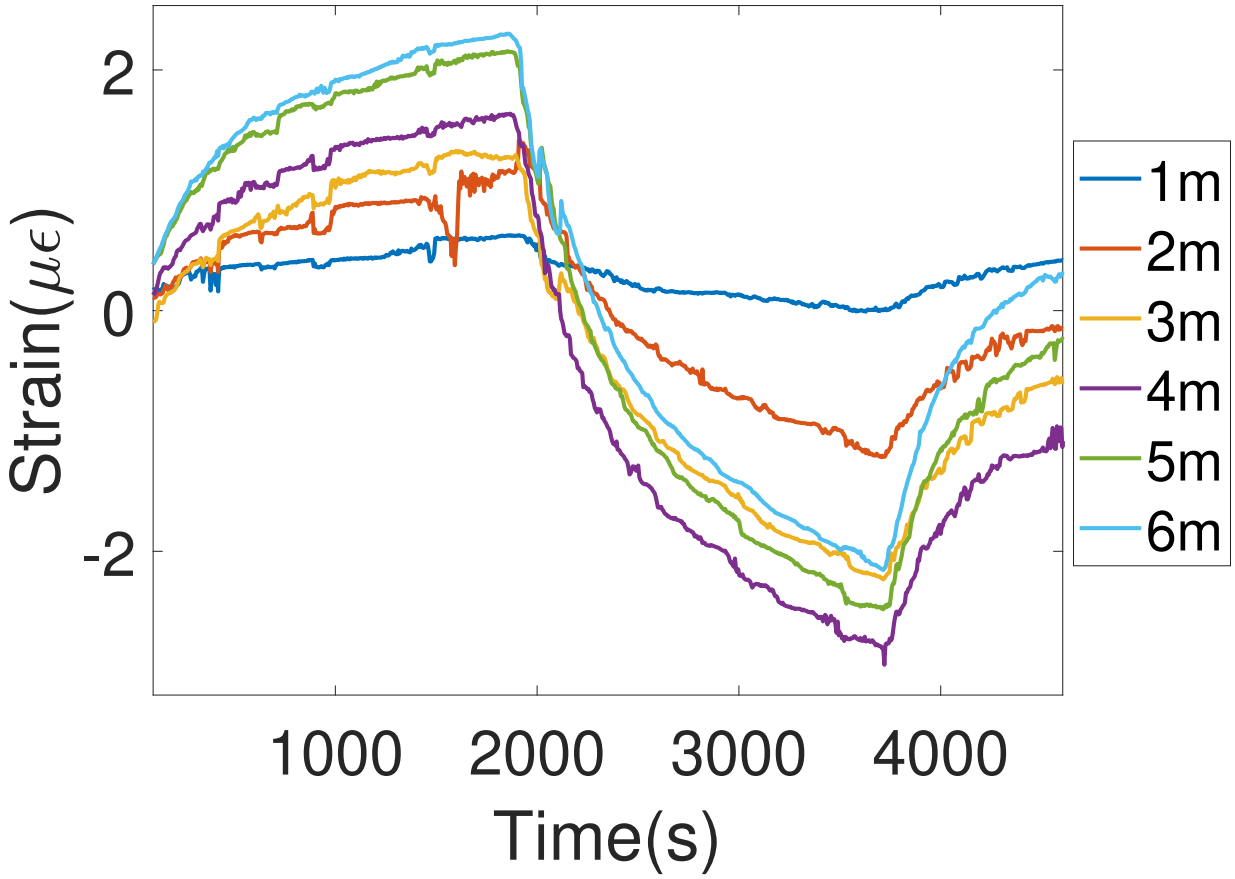

Figure 3.37: Strain response of 6 sensing sections of the strain ribbon during the pumping test.

References

Murdoch, L. C., Freeman, C. E., Germanovich, L. N., Thrash, C., and DeWolf, S. (2015). Using in situ vertical displacements to characterize changes in moisture load. *Water Resources Research*, 51(8):5998–6016.

CHAPTER FOUR
DEPLOYMENTS AT THE NORTH AVANT FIELD, BARNSDALL, OK

Contents

4.1 Two-Axis Optical Fiber Tiltmeter 4-2
4.1.1 Deployment 4-2
4.1.1.1 Preparations 4-2
4.1.1.2 Installation 4-2
4.1.2 Performance & Observations 4-5
4.1.2.1 Barometric Pressure Admittance 4-5
4.1.2.2 Calibration 4-7
4.1.2.3 Ambient Spectra 4-7
4.1.2.4 Teleseismic Events 4-9
4.1.2.5 Conclusions 4-9
4.2 Tensor Optical Fiber Strainmeters 4-14
4.2.1 Deployment 4-14
4.2.1.1 Drilling 4-14
4.2.1.2 Installation 4-14
4.2.1.2.1 Shallow Strainmeters 4-14
4.2.1.2.2 Deep Strainmeter 4-15
4.2.1.3 Grouting 4-17
4.2.1.4 Supporting Infrastructure 4-20
4.2.2 Performance & Observations 4-22
4.2.2.1 Grout Cure 4-22
4.2.2.2 Barometric Pressure Admittance 4-22
4.2.2.3 Calibration 4-26
4.2.2.4 Ambient Spectra 4-28
4.2.2.5 Teleseismic Events 4-35
4.2.2.6 Conclusions 4-38
4.3 Reservoir Pressure Monitoring Stations 4-42
4.4 Upgrades to Existing Infrastructure 4-44

DEPLOYMENTS AT THE NORTH AVANT FIELD, BARNSDALL, OK

The North Avant Field is our CO_2 injection analog test site about 30 miles north of Tulsa, Oklahoma, just north the unincorporated town of Avant and south of the town of Barnsdall, OK. This was the test site of our previous demonstrations for the project DE-FE0023313 whose geographic and geologic details along with its production history are described in detail in that final report (Murdoch et al., 2019).

One of the goals was to update and upgrade our current monitoring infrastructure and deploy an array of our new tensor strainmeters to support the demonstration part of this project. Figure 4.1 shows an overhead view of the North Avant Field infrastructure as of the end of the project. Upgrades and updates to the existing infrastructure included:

- Upgraded supervisory control and data acquisition (SCADA) system and updated cellular data telemetry on injection well WW9A
- Upgraded data acquisition along with new solar and cellular telemetry systems for pressure monitoring wells WW29 and WW60
- Upgraded data acquisition and new cellular telemetry for pressure monitoring well WW27
- Upgraded solar and new cellular telemetry systems for AVN3 (eddy current tilt and vertical strain) and AVN4 (areal strain, vector tilt and meteorological)



Figure 4.1: Overhead view of the North Avant field showing the upgraded and new systems deployed as a part of the demonstration component of this project.

The new installations included:

- New solar, data acquisition and cellular telemetry systems for pressure monitoring wells WW32[1] and WW87
- New Version 6 Elliptical Ring Tensor Optical Fiber Strainmeters equipped with Version 4 Optical Fiber Michelson Interrogators and cellular telemetry installed in new wells AVN22, AVN32 and AVN87 and existing well AVN31
- New Two-Axis Optical Fiber Tiltmeter deployed in well AVN1

Details of these upgrades and new deployments will be covered in this chapter.

4.1 Two-Axis Optical Fiber Tiltmeter

The prototype Two-Axis Optical Fiber Tiltmeter presented in Section 1.3.1 was repackaged and deployed in borehole AVN1 at the North Avant Field in September of 2019. The goal of this installation was to deploy it in an operational environment and to compare its performace to a commercial electrolytic tiltmeter (Applied Geomechanics, now Jewell Instruments LILY) located in borehole AVN4 approximately 35 m away. The following sections describe the preparations for its deployment followed by its installation, which is then followed by quantitative assessments of its performance.

4.1.1 Deployment

4.1.1.1 Preparations

The prototype Two-Axis Optical Fiber Tiltmeter was repackaged from the polycarbonate enclosure used for lab tests to a much more robust stainless steel pressure case. This was an essential step to ensure its long term survival in a wet, uncased borehole. Figure 4.2 shows some of the details of this assembly starting with the pressure case complete with lifting eyes (Figure 4.2a). The main input fiber cable (Fiber Instrument Sales "Blue Tactical", FBSM-TACCABLE12) is sealed on the exterior using a standard submersible cable gland and using a low viscosity epoxy on the underside of the pressure case top cap (Figure 4.2d), which should be suitable for pressures well exceeding any foreseeable deployment scenario. A key feature of this pressure case is the bottom plug (Figure 4.2c) that is used to partially evacuate the pressure case prior to deployment to limit the interaction of the pendulum bob with air molecules. This plug is also be used to pressurize the interior to remove the top or bottom cap without the need of jack-off screws or pry-off pliers.

4.1.1.2 Installation

The prototype of the Two-Axis Optical Fiber Tiltmeter was deployed at the North Avant Field during the second week of September, 2019. This took advantage of the existing unused borehole AVN1 as well as the nearby eddy current and electrolytic tiltmeters deployed in AVN3 and AVN4, respectively. AVN1 is located about 12 meters north-by-northwest from AVN3, which is also along the same line as AVN2 and AVN4 to the south, and was drilled to a depth of just under approximately 240 feet and cased with steel to a depth of $\sim$110 feet. It was originally drilled almost exactly three years prior in September 2016 at the same time as AVN2, however, the latter was determined to be a better geologic setting for the Gladwin Tensor Strainmeter (GTSM).

AVN1 was sounded prior to installation to measure the depth-to-water and total depth. The water level was found to be 104' 8" below-ground-surface (bgs), with a soft tag about 236' 10" that settled to $\sim$237'. This soft bottom was unacceptable for the tiltmeter, so about 2.5 feet of coarse gravel was added to the bottom that was then covered with

[1]This is considered a new installation because we failed to collect any usable data from several autonomous data logger deployments during the previous project



Figure 4.2: Photographs of the new optical fiber tiltmeter pressure case. (a) The completed package. (b) Upside-down shot of the tiltmeter attached to the underside of the pressure case top cap. (c) Bottom cap of the pressure case revealing the sealing plug and o-ring (bottom) and counter-bored recess. (d) Close-up of the tight-buffered optical fiber passing through a reservoir of epoxy into the pressure case interior.

play sand to a final depth of 233' 8". This resulted in a satisfactory hard tag off of the bottom that was deemed suitable for setting the tiltmeter.

The tiltmeter was prepared for deployment and lowered to the bottom. The bottom of the pressure case was removed to extract two pieces of soft foam used to surround the pendulum bob to protect it during shipment (Figure 4.3a). The cap was replaced and the interior of the pressure case was evacuated to about -50 kPa using a hand pump. A tripod and winch was set up over the hole and the winch cable (⅛" 7 $\times$ 19 304 stainless wire rope) was attached to a bridal connected to three eye bolts secured to the top of the tiltmeter pressure case (Figure 4.3b). The tiltmeter was then lowered to the bottom while slowly paying out the optical fiber cable. Once at the bottom, the support cable was attached to an eye bolt located in the well casing just above the ground surface.

Optical and electrical connections were made after lowering the tiltmeter. The optical fiber cable was fed into and spliced to a 2-channel (Version 3) Optical Fiber Michelson Interrogator. Power and Ethernet connections were made at the other end of the interrogator and both optical and electrical penetrations were potted with epoxy. The interrogator was then lowered into the wellbore approximately 3 m and the electrical conduit containing the power and Ethernet cables was fed through a cast iron well cap that was then secured to the casing stick up (Figure 4.3c). This conduit was then run to the AVN3 electrical enclosure and tested for functionality, whereupon the conduit was trenched in (Figure 4.3d) by an employee of our industry partner Grand Resources.



Figure 4.3: Photographs taken during the installation of the Two-Axis Optical Fiber Tiltmeter deployment. (a) Removal of the lower cap of the tiltmeter pressure case in order to extract the foam surrounding the pendulum bob to protect it during transit. (b) Winch holding the tiltmeter just before lowering into the wellbore. Note the electrical enclosures for AVN2, AVN3 and AVN4 in the background. AVN1 wellhead cap (c) and conduit trench to the AVN3 electrical box (d).

4.1.2 Performance & Observations

The Two-Axis Optical Fiber Tiltmeter operated in borehole AVN1 at the North Avant Field site from its installation in September 2019 until January of 2021. This provides an ample time window over which to perform analyses to quantitatively assess its behavior relative to the electrolytic Applied Geomechanics LILY tiltmeter deployed in AVN4. Details of their responses to barometric pressure, solid Earth tides and earthquakes are presented in the following sections along with a comparison of their spectral responses to ambient signals.

4.1.2.1 Barometric Pressure Admittance

It is critical to carefully examine the response of each tiltmeter to deformations associated with barometric pressure changes since the most energetic component of the signal is often coincident with the tides used to perform an in-situ calibration. There are several ways to estimate the magnitude of the barometric pressure effect, or admittance. A common and perhaps most straightforward approach is to simply to fit the barometric pressure time series to the strain data using least-squares, resulting in an estimate of the scalar admittance. This was done for both the x and y components of each tiltmeter resulting in the scalar barometric pressure admittance values shown in Table 4.1.

Table 4.1: Least squares results of the barometric pressure scalar admittances for the Two-Axis Optical Fiber Tiltmeter in AVN1 and the commercial tiltmeter in AVN4.

Instrument & Component	Scalar Admittance (native units per /kPa)	Scalar Admittance (nanoradians/kPa)
2J.AVN1.θ_{xx}	0.09 ± 0.29	-30 ± 650
2J.AVN1.θ_{yy}	0.05 ± 0.01	18 ± 76
2J.AVN4.θ_{xx}	0.04 ± 0.04	-105 ± 730
2J.AVN4.θ_{yy}	0.09 ± 0.05	20 ± 835

The scalar admittance values in Table 4.1 are also shown in calibrated units using the results from upcoming Section 4.1.2.2. All of the estimates have very large uncertainties due to the very poor fit results making it difficult to estimate the true impact of the barometric pressure record on the tilt measurements.

The second and more sophisticated approach is the estimate the spectral admittance, i.e., the scalar admittance as a function of frequency. This was done using cross spectrum analyses implemented using the adaptive sine multitaper approach of Riedel and Sidorenko (1995). While this data adaptive approach works well for reducing the variance in a given cross spectrum estimate, it is also very useful to obtain a statistically meaningful estimate of how the cross spectra vary. This was implemented by dividing the data into partially overlapping windows of 28 days (i.e., Welch's method (Welch, 1967)), estimating the cross spectra of each window and stacking them to compute the 5th, 10th, 20th, 50th, 80th, 90th and 95th percent confidence intervals.

The cross spectrum results are shown in Figure 4.4 for the optical fiber tiltmeter and Figure 4.5 for the commercial tiltmeter. Each component plotted shows three separate estimates. The top plot in each panel is the magnitude squared coherence, which is an estimate of the frequency dependent correlation between the tilt and barometric pressure, i.e., what fraction of the tilt record is a result of the barometric pressure at a given frequency. The middle plot shows the magnitude of this effect in native units per kiloPascal along with a horizontal red line indicating the scalar admittance estimate. The final plot on the bottom of each panel is the phase relationship between the tilt and barometric pressure with 0° being in-phase and 180° being out-of-phase.

Figure 4.4 and Figure 4.5 show the median along with the aforementioned confidence intervals for the stacked windows of cross spectrum estimates. The medians are shown as a thick black line and each confidence band is shaded according to the 5th/95th, 10th/90th and 20th/80th confidence intervals. This provides a graphical way to identify not

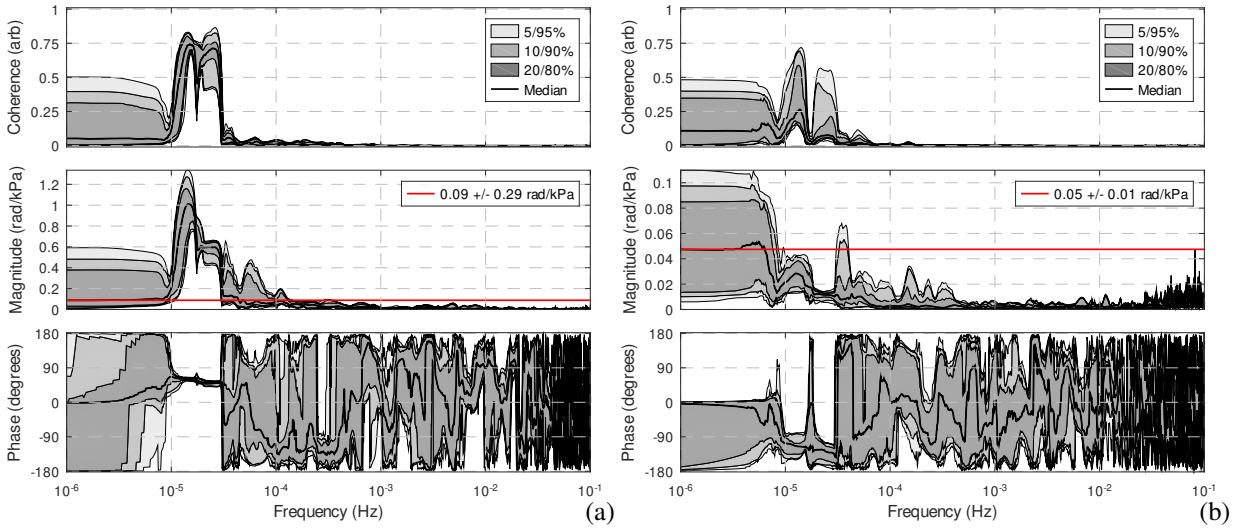

Figure 4.4: Barometric pressure spectral admittances for the Two-Axis Optical Fiber Tiltmeter deployed in AVN1.

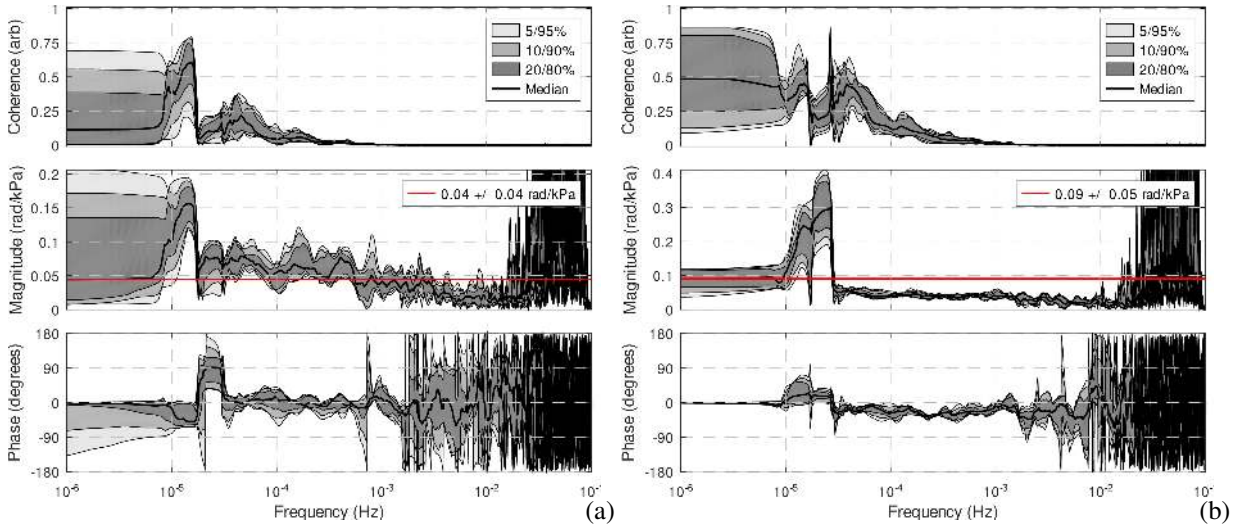

Figure 4.5: Barometric pressure spectral admittances for the commercial tiltmeter deployed in well AVN4.

only the central tendency (median) of each estimate, but also see how variable each is by the width of the confidence bands.

It is critical when evaluating spectral admittance plots like Figure 4.4 and Figure 4.5 to first consider the coherence since the magnitude and phase estimates are only statistically meaningful where the data are correlated. The coherence appears to be very low for anything above about 10^{-4} Hz (10,000 second, or $\sim$3 hour period and longer) with the highest at 1 cycle-per-day (1 CPD). In most cases this is where the admittance is the highest (excluding the y-component on the optical fiber tiltmeter, Figure 4.5b), from 3 to 10 times larger than the least-squares result that appears to faithfully capture the lowest frequency part of the spectrum.

The scalar and spectral admittance estimates imply show that it is easy to over or under correct for the influence of the barometric pressure on the tilt records. For example, if the least-squares result is used, the energy at 1 CPD could be under corrected for by up to a factor of 10, whereas if the result at 1 CPD would over correct the low frequencies by

the same amount. The remedy for this is to apply a coherence-weighted spectral admittance correction following the method outlined in Crawford and Webb (2000), which uses the magnitude and phase to create a filter that is applied to the barometric pressure. This filtered barometric pressure data is then subtracted from the tilt record and the result is ready for comparing to the tides.

4.1.2.2 Calibration

While the optical fiber tiltmeter was been calibrated in the lab (Section 1.3.2) and the commercial tiltmeter outputs data in microradians, it is often useful to compare the data to the predicted solid Earth tides. This also provides a way to estimate the orientation of the instrument in geographic coordinates, which simplifies data interpretation.

Data from both tiltmeters were compared to the north-south and east-west components of the solid Earth tides. The predicted tides were computed using the FORTRAN program `ertid`, which is a part of the SPOTL software package (Agnew, 2012). The x and y tilt data from each instrument were compared to the predicted tides using least-squares fit to determine their amplitudes. This fit was repeated for the predicted tides for each 1° rotation to get the mean-squared error for each angle, and the angle with the lowest residual was deemed to be the orientation of the instrument.

Table 4.2: Earth tide calibration results for the Two-Axis Optical Fiber Tiltmeter in AVN1 and the commercial tiltmeter in AVN4.

Instrument & Component	x Amplitude (nanoradians per native unit)	y Amplitude (nanoradians per native unit)	Angle ($^\circ$ CW from north)
2J.AVN1.θ_{xx}	-184 ± 16	-289 ± 304	237 ± 129
2J.AVN1.θ_{yy}	1 ± 10	364 ± 143	270 ± 802
2J.AVN4.θ_{xx}	-115 ± 10	-1113 ± 6	84.1 ± 0.5
2J.AVN4.θ_{yy}	962 ± 30	-229 ± 19	346.6 ± 1.2

The tide fit time series are shown in Figure 4.6 for the optical fiber tiltmeter and Figure 4.6 for the commercial tiltmeter. It is clear that both fits for the Two-Axis Optical Fiber Tiltmeter are very poor, with the east-west (θ_{xx}) being somewhat better than the north-south (θ_{yy}) results. This is in contrast to the commercial tiltmeter where the east-west fit is excellent, however, similar to the previous in that the north-south is not as well matched.

The numerical results from the tide fits are summarized in Table 4.2, which show quantitatively what is shown qualitatively in the graphical results (Figure 4.6 and Figure 4.7). The calibration coefficients for the commercial tiltmeter come out to be almost exactly 1,000 nanoradians per microradian (the nominal calibration) with the θ_{yy} component about -13° from true north. the component separation is $\sim 98^\circ$, which is slightly more than 90°, but is still acceptable. Results from the optical fiber tiltmeter are uniformly poor with several of the statistical uncertainties being several times larger than the estimates themselves. The calibration factors completely disagree with the lab results (Section 1.3.2) of about 6,000 radians of optical phase change per radian of tilt, or $\sim$170,000 nanoradians per radian of optical phase change. The resulting angle calculations are useless since the statistical uncertainties very large.

4.1.2.3 Ambient Spectra

Magnitude spectra are often useful for evaluating the performance of an instrument since it shows the amplitude of what the device is recording as a function of frequency. Figure 4.8 and Figure 4.9 show the magnitude spectra from ambient data for the optical fiber and commercial tiltmeters, respectively. These were computed using the median of

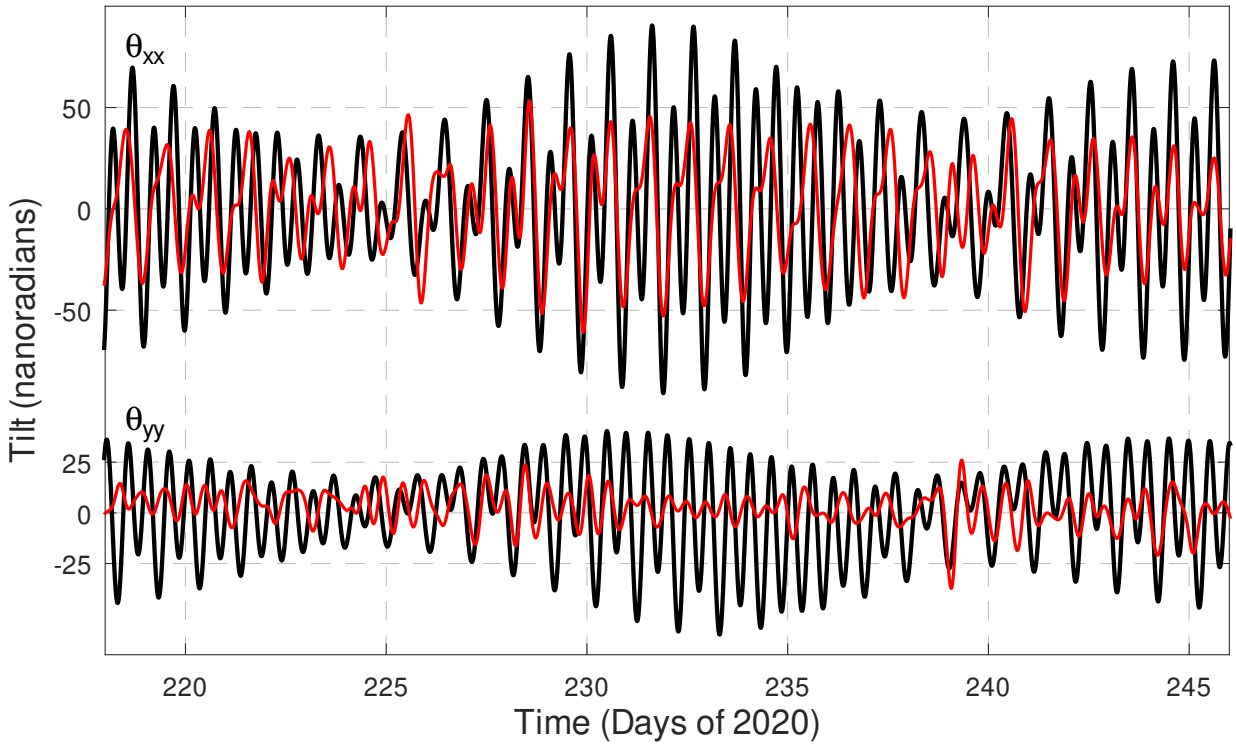

Figure 4.6: Earth tide calibration for the Two-Axis Optical Fiber Tiltmeter deployed in AVN1.

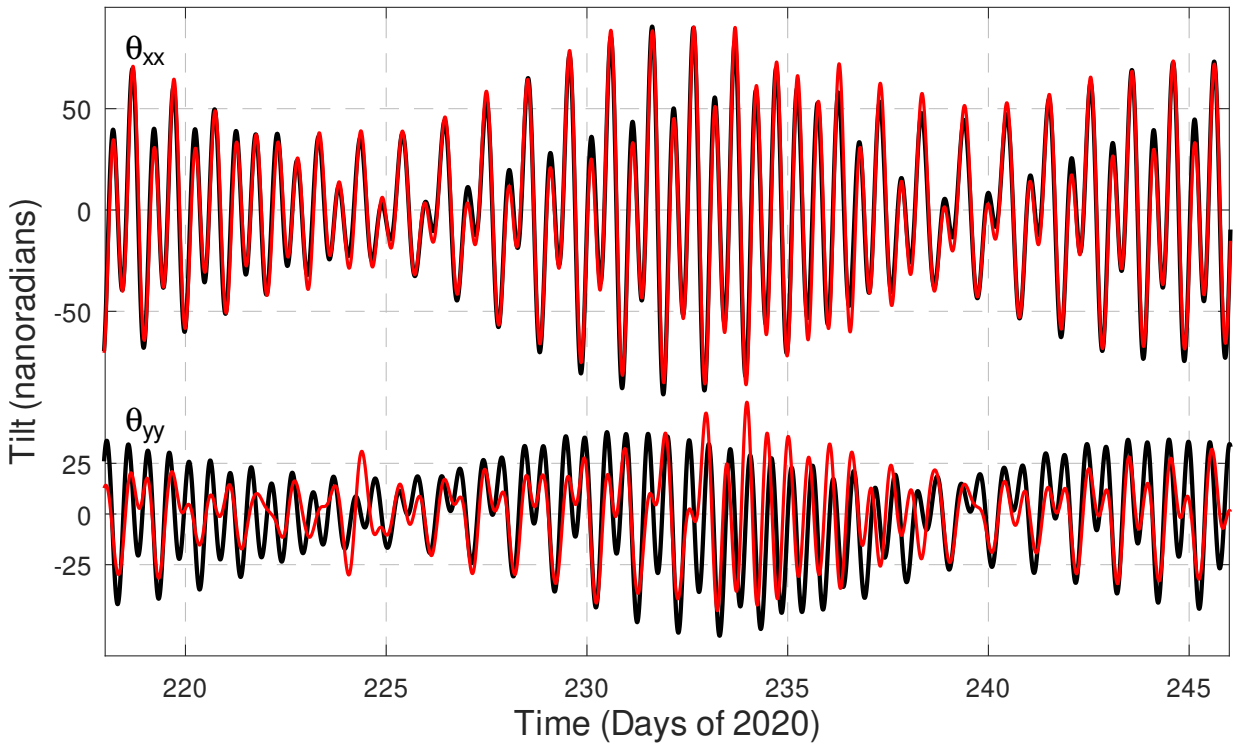

Figure 4.7: Earth tide calibration for the commercial tiltmeter deployed in well AVN4.

a stack of partially overlapping 56-day data windowed periodograms where the data were tapered using a Hamming window. The results are shown in Figure 4.8 for the optical fiber tiltmeter and Figure 4.9 for the commercial tiltmeter.

While both spectra seem to line up at the 1 CPD peak (not surprising since they were both rescaled to the tides) their characteristics are quite different. The optical fiber tiltmeter spectra (Figure 4.8) shows clear peaks at 1 and 2 CPD (1.15×10^{-5} and 2.31×10^{-5} Hz), but no indications of either the O1 and M2 tides at 1.08×10^{-5} and 2.24×10^{-5} that are clearly evident in the commercial tiltmeter specra (Figure 4.9). The east-west and north-south spectra from the two tiltmeters are compared in Figure 4.10 and Figure 4.11, respectively. These show that the optical fiber tiltmeter has a steeper slope than the commercial instrument, and lacks the spectral "hump" from about 1×10^{-2} (100 seconds) onward from the presence of earthquakes.

4.1.2.4 Teleseismic Events

The final comparison between the optical fiber and commercial tiltmeters is in their response to surface waves from teleseismic events. While both appear to clearly record these events, the optical fiber tiltmeter exhibits some interesting behavior not seen in the commercial instrument. Comparison time series for two earthquakes are show, the first one was the M7.8 earthquake located 99 km SSE of Perryville, Alaska on July 22, 2020 (Figure 4.12) and the second a few months later from the M7.6 earthquake located 99 km SE of Sand Point, Alaska on October 19, 2020.

Both instruments show a number of consistencies. For example, they both have a larger response on the north-south component than the east-west. The main surface wave signals are a nearly wiggle for wiggle match starting at about 6:28 on July 22nd (Figure 4.12 and about 21:28 on October 19th (Figure 4.13).

There are several striking and interesting differences between these two nearly collocated tiltmeters. While there are subtle differences in the beat pattern in the main part of the surface wave signals, the most fascinating is the first arrival of the S wave that is barely visible in the commercial tiltmeter signal and is very prominent in the optical fiber instrument. Two figures are provided to show that this a repeatable effect and the mechanism behind it is unknown.

4.1.2.5 Conclusions

There are several factors contributing to the poor results from the Two-Axis Optical Fiber Tiltmeter as deployed at the North Avant Field. First is the sensitivity, since the 16-bit least count is only 2.5 nanoradians, which implies that it should be able to measure the tides with a signal-to-noise ratio of about 20, however, this is clearly not the case. The clear peaks at 1 and 2 CPD indicate very significant environmental contamination, since diurnal thermal effects usually manifest as a 24 hour peak in the spectra. The 2 CPD signal is most likely the second harmonic of the very large 24-hour signal. This contamination is evident in the time series, primarily in the x component, which is caused by improper deployment.

Ineffective cable management and a lack of a physical device constraint (e.g., clamp) are the most probable causes of the much more noisy signal in the optical fiber tiltmeter compared to the commercial tiltmeter. The optical fiber cable from the tiltmeter pressure case to the interrogator pressure case and the electrical conduit coming from the other end of the Version 3 OFMI (Section 1.2.1) didn't have enough slack to prevent temperature changes at the exposed wellhead (Figure 4.3c) from pulling on the cable and therefore the tiltmeter pressure case. While care was taken to ensure the pressure case had a firm place to rest on the bottom of the borehole, it was otherwise completely unconstrained. The pressure case should have been clamped or sanded in, which may have offset some of the thermally induced pulling from the cables.

This noise is what made the decision to stop data acquisition over a year before the instrument was extracted. While this deployment was less than a success, it still functions and is being prepared for re-deployment. Issues like the enhanced S wave arrival response remain a complete mystery, but hopefully a collocated deployment with another commercial tiltmeter and additional seismometer will help better understand the dynamic behavior of this novel device.

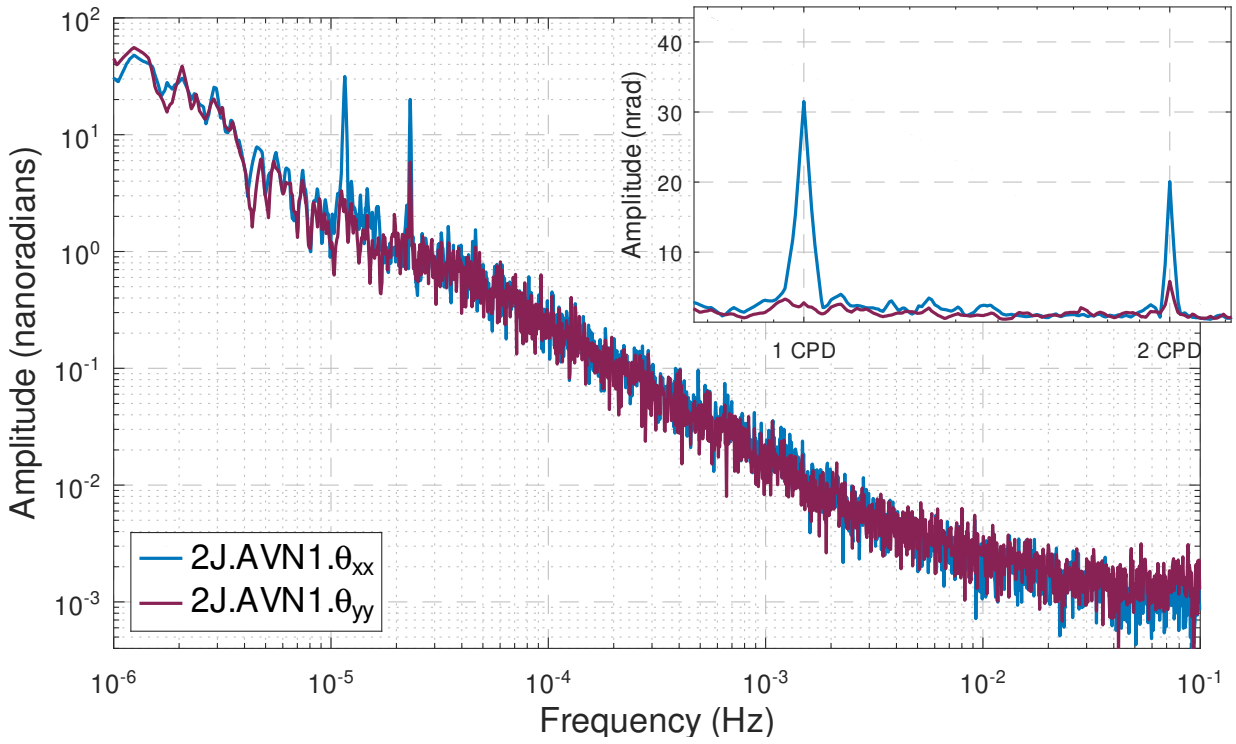

Figure 4.8: Magnitude spectra for both calibrated components of the Two-Axis Optical Fiber Tiltmeter in AVN1.

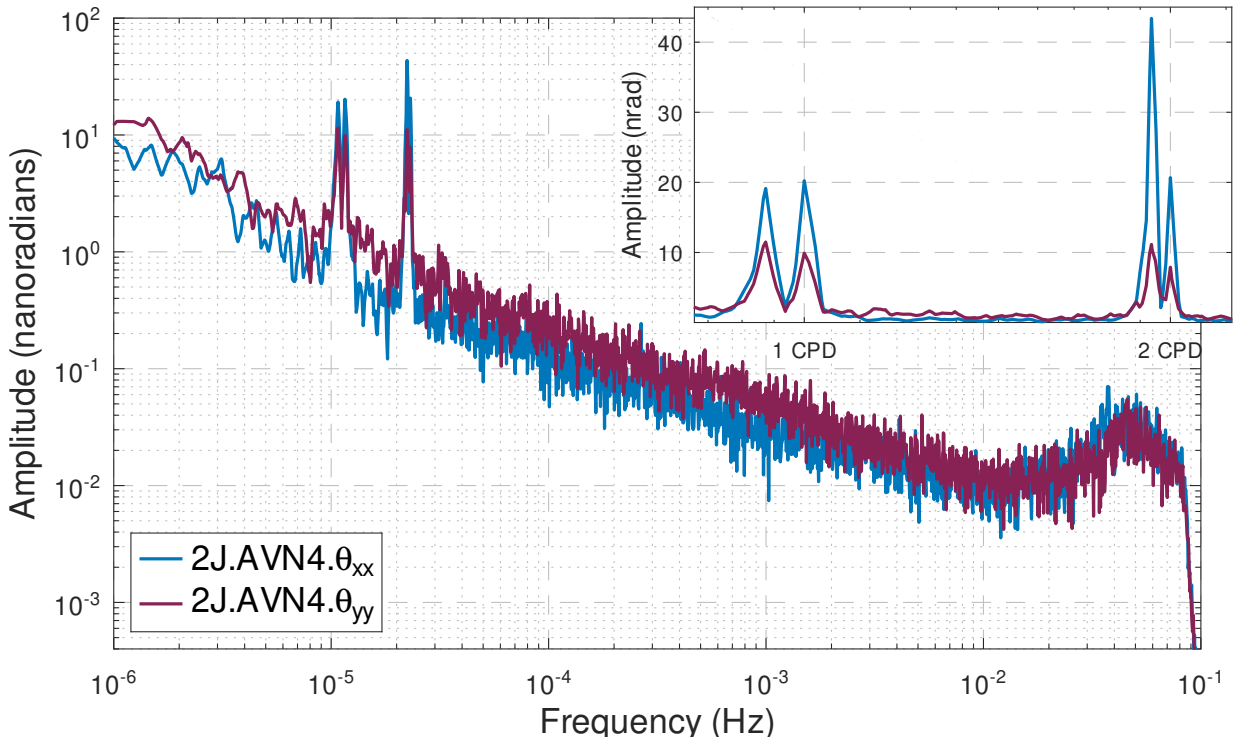

Figure 4.9: Magnitude spectra for both calibrated components of the commercial tiltmeter AVN4.

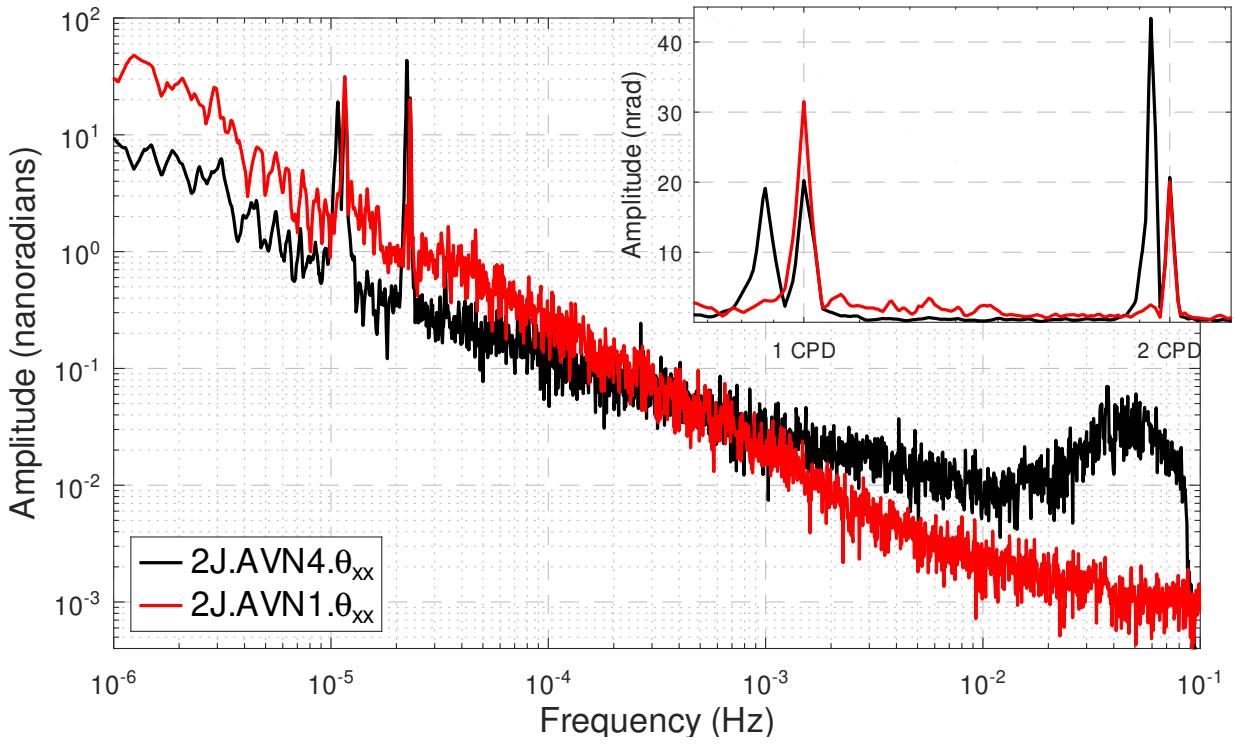

Figure 4.10: Magnitude spectra for all four calibrated components of the TOFS-ER v6 at AVN32.

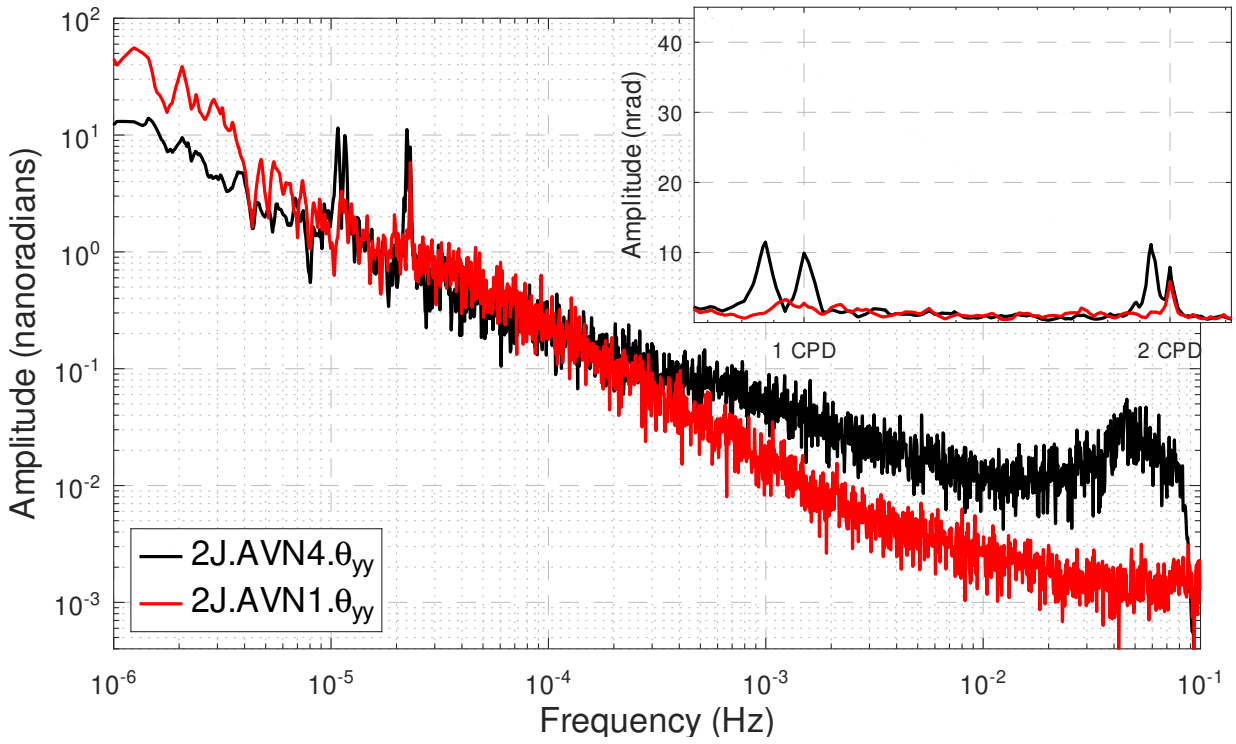

Figure 4.11: Magnitude spectra for all four calibrated components of the TOFS-ER v6 at AVN87.

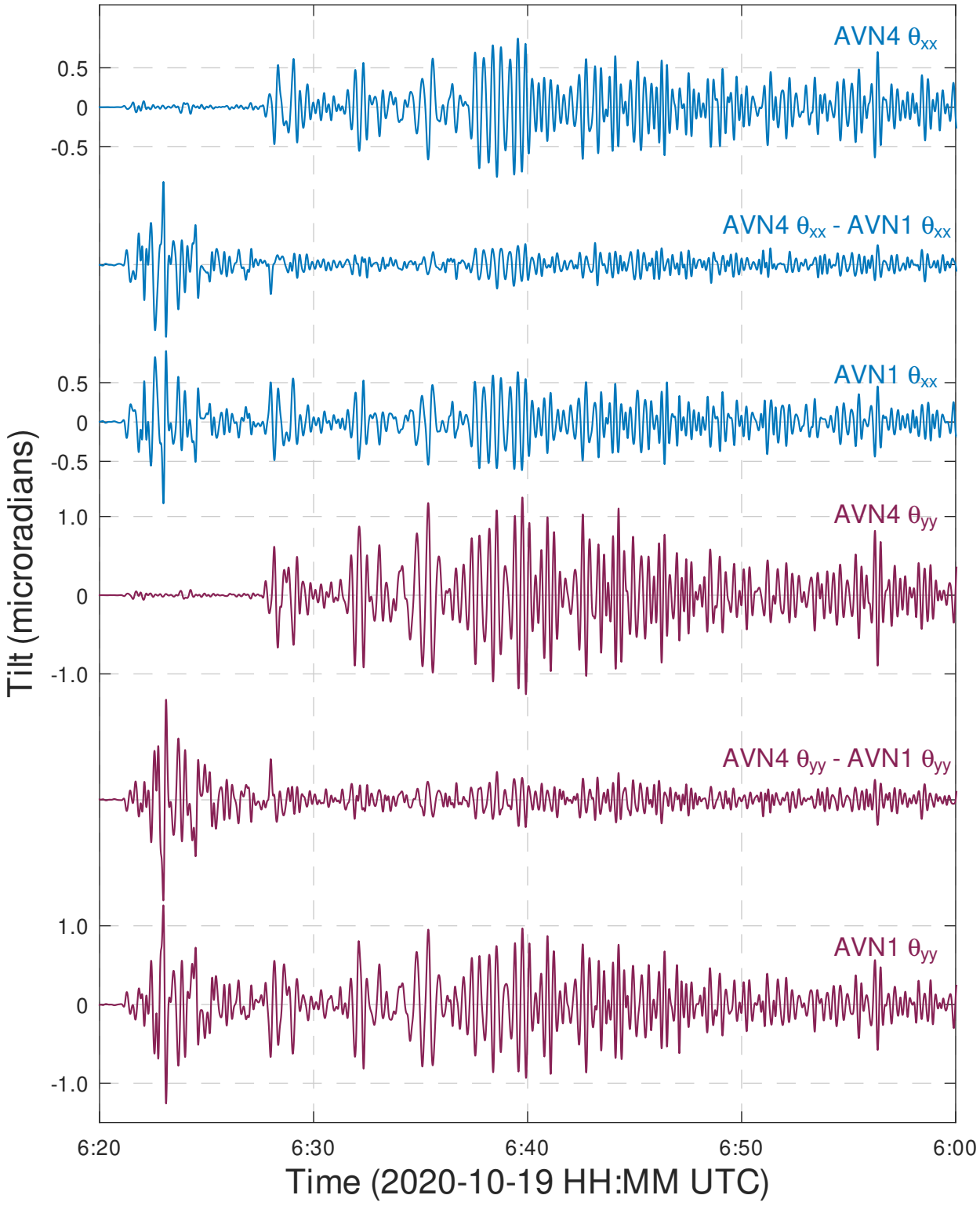

Figure 4.12: Teleseismic waveforms for the commercial tiltmeter in AVN4 compared to the TAOFT v1 in AVN1, showing each of the two vector components for the M7.8 earthquake located 99 km SSE of Perryville, Alaska on July 22, 2020.

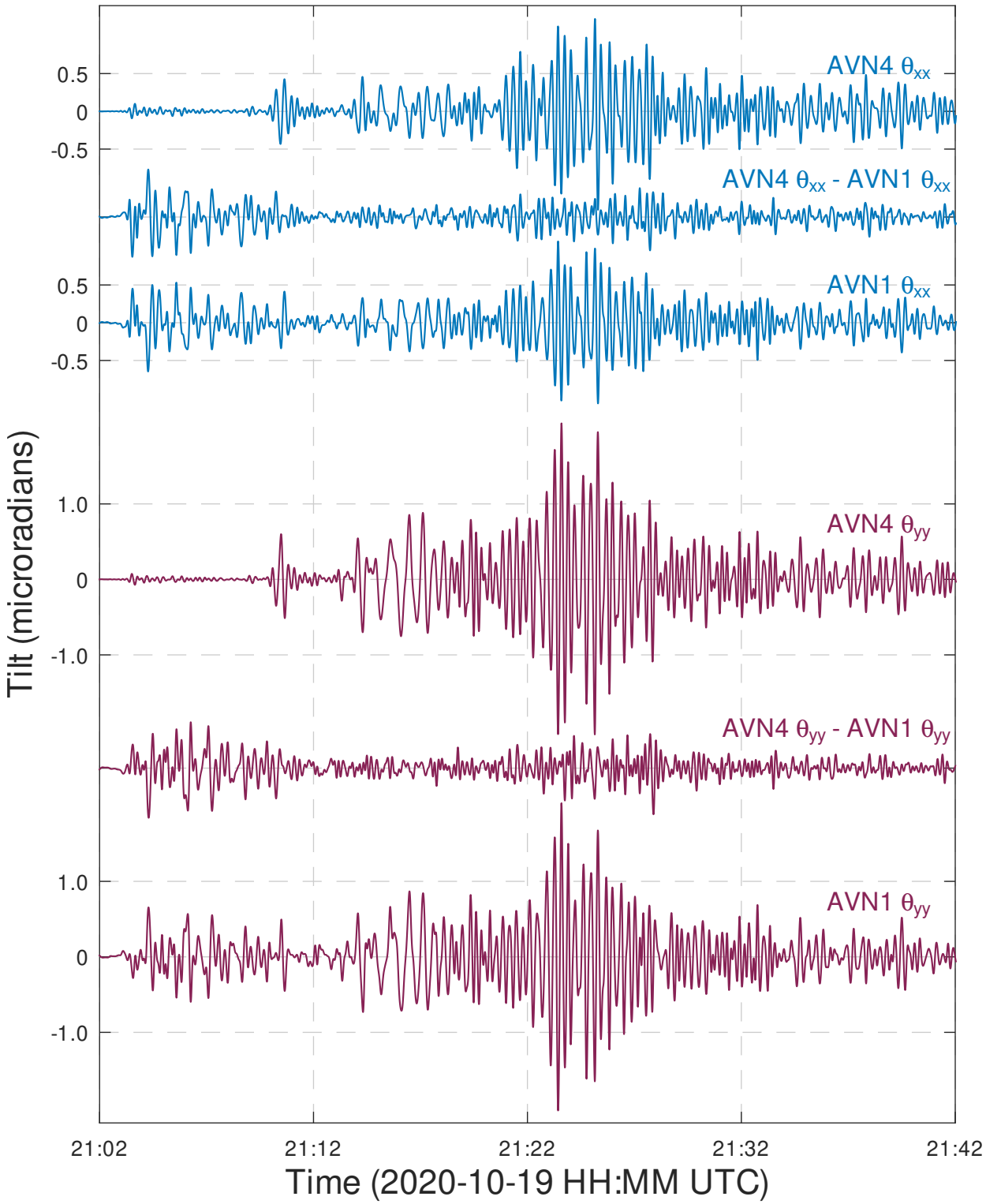

Figure 4.13: Teleseismic waveforms for the commercial tiltmeter in AVN4 compared to the TAOFT v1 in AVN1, showing each of the two vector components for the M7.6 earthquake located 99 km SE of Sand Point, Alaska on October 19, 2020.

4.2 Tensor Optical Fiber Strainmeters

The tensor optical fiber strainmeters developed for the demonstration part of this project are the outcome of years of evaluating multiple designs through prototypes and laboratory and field testing. Details of the final design, called the Version 6 Elliptical Ring Optical Fiber Strainmeter (TOFS-ER v6), are shown in Section 1.7.4. Four strainmeters, in conjunction with as many Version 4 Optical Fiber Michelson Interrogator (OFMI v4), were assembled for deployment at our North Avant Field test facility. These were to be partitioned between three shallow instruments at roughly 140 feet in depth, and one in the reservoir at a depth of 1,700 feet – the deepest strainmeter deployment ever attempted.

The following sections detail the deployment and post-deployment performance and observations of the four TOFS-ER v6 installations at the North Avant Field. This includes the drilling, installation and grouting of these four instruments along with their supporting infrastructure. Qualitative and quantitative analyses are then used to evaluate the performance of these new instruments compared to previously installed strainmeters.

4.2.1 Deployment

Deployment of the four tensor strainmeters developed for this project was performed over two trips. The drilling and deployment of the three shallow instruments was completed and preparations for the deployment of the deep strainmeter were started during the first mobilization in December of 2021. Unfortunately, getting the deep well ready for a strainmeter proved to be more difficult than anticipated and we had to return after the holiday break. This was further delayed by a series of winter storms that made access to the site by heavy equipment very difficult. We were able to deploy the deep instrument and get our grouting contractor to each well resulting in four successful deployments in March of 2022.

4.2.1.1 Drilling

Three new shallow wells were drilled and cased for the three new shallow strainmeters at wells AVN22, AVN32 and AVN87 (Figure 4.1). This was done using the same drilling contractor we used in 2016 and 2017 during the previous project. The procedure was also very similar to the previous strainmeter installations. Each new well was drilled and cased to 50 feet, rather than to 70 feet with 6-inch steel pipe, and drilled to a final depth of 140 feet, leaving a 70 foot open hole section. After drilling the casing annulus was grouted and a weld flange installed (Figure 4.14).

The 140-foot total depth is a notable difference between these three new shallow wells and the three previous strainmeter wells. The earlier wells AVN2, AVN3 and AVN4 were intended to target a limestone layer between roughly 90–100 feet because of concerns installing these relatively low compliance strainmeters in the softer shale material that bounds this layer. While this was a concern for the new installations, they are at three different elevations that made targeting a specific zone impossible or more expensive. Furthermore, we wanted to be able to evaluate the performance of the strainmeters in a softer material for applications where there may be no choice.

4.2.1.2 Installation

While one of the project objectives was to build out our shallow strainmeter array to surround the injection well 9A, another key goal was to deploy a strainmeter at reservoir depths. The preparations for, and the installations of the strainmeters at these two depths was different as a result and are discussed in the following sections.

4.2.1.2.1 Shallow Strainmeters

Installation of the shallow strainmeters followed a procedure somewhat different than past installations (for example, those in Sections 3.1.2.1.1 and 3.1.2.2.1). As before, a 4-foot section of 1-inch pipe was added to the top and bottom of each strainmeter, where the same slot was cut into the bottom of the lower pipe to allow grout to exit (e.g.


(a)

(b)

Figure 4.14: Photographs showing the drilling of well AVN87 (left) and attachment of the weld flange to the casing stickup on well AVN22.

Figure 3.8). Centralizers were then added to these upper and lower pipes, whereafter a 1½-to-1 inch polyethylene weld adapter fitting was screwed onto the top steel pipe. This was then welded to 1½ poly tubing whose length was measured such that the strainmeter would be suspended in the borehole by approximately 1 foot from the bottom (Figure 4.15).

Figure 4.16 shows several key details of the typical shallow strainmeter installation. First is the steel "U" block that allows the strainmeter connected to the poly pipe to hang in the wellbore by the 1½-to-2 inch NPT adapter that will be used to connect to the grout pumping rig. This adapter was small enough to fit inside of the 4-to-2 inch reducing adapter that was screwed into the upper flange such that the solar system mast can be fully deployed leaving everything in place. There was also sufficient room to lower the interrogator into the wellbore next to the poly tubing, where the power and communications cabling was pulled through the center mast pipe and into the main enclosure. All three shallow strainmeters were deployed in this manner and were left running and producing data.

These three new shallow installations were designated station names based on their proximity to other nearby wells. The first, AVN22 (AVN being the abbreviation for Avant, which is a shortened name for the North Avant Field site) is located a few meters from production well WW22 (WW is the abbreviation for Wolco West, a designation given to this lease by the oilfield operator since these are west of the unincorporated town of Wolco, OK). The others are AVN32 and AVN87 that are similarly located next to what would become pressure monitoring wells WW32 and WW87, respectively (Section 4.3).

4.2.1.2.2 Deep Strainmeter


(a)

(b)

Figure 4.15: Pictures showing the plastic welding of the 1½" polypropylene tubing to the weld fitting attached to the upper strainmeter pipe (a) and the fully assembled instrument shortly before being lowered into the wellbore (b).

The plan for the deep installation was to use one of the existing oil wells owned and operated by industry partner Grand Resources. While this saved the expense of drilling a new well into the reservoir at ∼1,700 feet, it did pose other challenges since these were drilled in the 1910s (or earlier) and each had unique histories of completion, development and repairs. We eventually decided on well AVN31 (Figure 4.1) since it was largely unobstructed by secondary casings used to seal off leaks in the casing.

The caliper log indicated that there was an open interval in the vicinity of 1,680 feet that should be well suited to deploying the strainmeter. However, there was an open cavity called a "shot hole" from about 1,700 to 1,740 feet deep that was created by an explosion to induce fractures to enhance oil production. The plan was for the operator to fill the cavity with sand prior to installing the strainmeter. The size of the cavity was unknown, so we wanted to fill it with sand before cementing. There are many wells like this at the North Avant Field and filling these cavities with sand is a routine operation. The operator filled the cavity with sand prior to our arrival and they measured the depth as 1,700 feet using a logging truck.

Some weeks later when we arrived, rigged up and ready to deploy the strainmeter, the operator decided to run a tool string to the bottom of the hole to verify the depth. This showed that the hole was 1,740 ft deep, which indicated that the cavity was still open. We stood down while more sand was brought in and the hole was filled to what we thought was the proper depth. Then we ran the strainmeter into the well on 2⅜" external upset (EU) pipe and it reached the bottom (Figure 4.17). However, the bottom of the hole was now at 1,600 ft, which was shallower than expected since more sand was added than was needed. This meant that the strainmeter was inside casing, above the bottom of the open interval. While it is possible that the strainmeter could work in these conditions, the condition of the casing and cement are unknown and this raises concern about how well the strainmeter would be coupled to the formation.


(a)

(b)

Figure 4.16: (a) Photo of the casing stickup and weld flange with the 2-inch NPT adapter being supported by the steel "U" block from which the strainmeter and poly tube assembly is hanging. The pipe tee and horizontal pipes screwed into this adapter was used during the lowering process and removed before erecting the solar mast. (b) Picture of the completed solar system attached to the well casing stickup.

We pulled the strainmeter out of the borehole and the operator brought in a hydraulic bailer to remove the sand. Several runs of the hydraulic bailer removed some sand, but not enough to install the strainmeter. It was now a few days before Christmas and the field effort had taken more than a week longer than expected. The operator had their pulling rig and all their field personnel tied up on our project and they had fallen behind on several critical projects that needed to be done to keep their field operating. So, we decided to take a break and return to remove the remaining sand and complete the installation at a later date.

We returned to the North Avant Field in March of 2022 to resume preparations of the deep well and deploy the strainmeter. We began by gearing up to remove the excess sand using a large pump and a dummy drill bit called a "mule shoe" to flush the sand. However, when this tool was deployed the hole depth was found to be the original depth of the hole before any sand was washed into the well. We decided to forego further efforts to sand in the shot hole and after discussions with the grouting contractor decided to rely on a two-stage grouting procedure to seal the well before pumping the expanding cement. The strainmeter was then lowered to a depth of 1,680 feet on multiple lengths of 2⅜" EU pipe, excluding the final length of 2⅞" EU pipe to house the interrogator, and suspended in the hole to await grouting.

4.2.1.3 Grouting

Preparations for grouting the three shallow strainmeters was simple since we had left these setup for easy access. This required going to each well, removing the battery, unbolting the solar panel mast flange from the weld flange


(a)

(b)

Figure 4.17: Pictures of the strainmeter on its way into the deep well (a) and being run in on pipe (b), which also shows the spool of fiber cable in the foreground.

on the casing stickup, and laying the assembly on the ground (see Figure 4.18a), which exposed a 2-inch NPT bell reducing coupler that connected to the top of each polyethylene tremie pipe. After this we reconnected the battery so data would be logged during the grout pumping and removed the interrogator from the wellbore. We then to deployed a 20-foot long, 2-inch PVC pipe in each well to house the interrogator, which obviated the more difficult task of ensuring that the wellbore wasn't overfilled with cement during pumping and leaving no place to install the interrogator.

Our grouting contractor Schlumberger arrived to do the grouting on Wednesday, March 9th, 2022, which started with the three shallow wells and ended with the deep instrument. Each well followed the same basic procedure where the pump and cement hopper trucks backed up near each well (as in Figure 4.18a), connected their hose to the top of the tremie using a 2-inch NPT to 2⅜" EU adapter, mixed and pumped the cement, and washed out the pump and hoses with water into a nearby holding pit dug next to each well for that purpose. A volume of 4.5 to 5 barrels of expanding cement was pumped into each well followed by a small volume to clear the hose and a portion of the tremie pipe of grout. Figure 4.18c shows the monitoring panel the pump operator (Figure 4.18b) used during the cementing operation. This volume of cement filled each of the shallow borings to within 20 feet of the ground surface.

The grouting procedure was more elaborate for the deep instrument since we first had to attempt to seal the well such that the expanding grout would not be lost to the same place where the sand must have disappeared. After consulting with an engineer at Schlumberger the day before and with the field manager at the site, we decided to pump 38 barrels of neat Portland cement along with a stop-loss additive and wait 30 minutes (using the existing brine as an accelerator) before pumping 10 barrels of the expanding grout. Figure 4.19a shows the pump truck connected to the 2⅞" EU adapter and pipe emerging from the wellhead. The first pumping operation with the stop-loss material appeared to have worked as planned since water began to flow out of the wellhead during the pumping of the expanding grout (Figure 4.19b). This second volume would have been lost to the formation if the first batch of neat cement grout


(a)


(b)


(c)

Figure 4.18: Photographs of grout pumping for the shallow strainmeter wells. (a) Trucks backed up to well AVN87 with the pump truck on the left connected to the tremie pipe, the cement hopper truck on the right, and the strainmeter pedestal laying down in the foreground. (b) Pump truck operator at work. (c) Control panel in the pump truck.


(a)

(b)

Figure 4.19: Photographs of grout pumping for the deep strainmeter. (a) Water and pump trucks backed up to well AVN31 with the pump truck on the left connected to the tremie pipe. (b) Water being displaced from the well by the expanding grout.

had not sealed the well.

While there were some difficulties with the trucks maintaining traction at several of the sites, the actual grout mixing and pumping went very smoothly. All four of these groutings did end up being successful as indicated by the data shown in Section 4.2.2.

4.2.1.4 Supporting Infrastructure

The cementing was followed the next day with the re-installation of the strainmeter supporting infrastructure. This was basically the reverse order of the day before grouting where we removed the 2-inch NPT reducing adapter from the tremie pipe, trimmed this and the 2-inch PVC casing flush with the weld flange, inserted the interrogator into this 2-inch casing, and stood the mast back up. Figure 4.20 shows each completed installation in the order they were grouted.

While all four strainmeters were operational and transmitting data prior to departure, telemetry had been intermittent at best. Another trip in June of 2022 was made to install directional antennas that improved communications for all but AVN87, which has been intermittent.



Figure 4.20: Photographs of the final strainmeter installations for the shallow wells (a) AVN22, (b) AVN32, (c) AVN87 and the deep well (d) AVN31.

4.2.2 Performance & Observations

The post-grouting performance of the four installations can be assessed in multiple ways from visually inspecting the data to more advanced signal processing and statistical methods. The following sections describe the immediate post-grouting behavior followed by estimates of the scalar and spectral barometric pressure admittances that are then used to perform an in-situ Earth tide calibration. This is followed by estimating the relative noise present on each strainmeter through their magnitude spectra and a brief comparison of the response of the shallow Gladwin Tensor Strainmeter (GTSM), a shallow TOFS-ER and the deep TOFS-ER.

4.2.2.1 Grout Cure

One indicator of the likely success of a strainmeter installation can be seen in the hours just after grouting. The main characteristics of a typical strainmeter grout cure is a very large transient in the first 24 to 36 hours from the exothermic reaction of the grout followed by a much longer exponential trend where ideally each of the horizontal strainmeter gauges go into long term compression. This compression is essential since this is the best indication that the strainmeter is properly coupled, i.e., the expansive grout annulus is pushing outward against both the instrument and the formation.

Time series plots of the first two months after grouting are shown for the three shallow installations AVN22 in Figure 4.21, AVN32 in Figure 4.22 and AVN87 in Figure 4.23, with the deep instrument at AVN31 in Figure 4.24. Of these four AVN32 in Figure 4.22 is the most representative of an ideal post-grouting time series with all four horizontal gauges going into compression. This squeezing on the diameter of the strainmeter leads to the opposite trend for the vertical component, which, to the best of our knowledge, is the first grout cure time series for an integrated vertical strain gauge in a borehole strainmeter.

The time series for AVN22 (Figure 4.21) and AVN31 (Figure 4.24) depart from the ideal, but not necessarily due to issues with their installations. While there are several prolonged data gaps that have been interpolated over in the first 24 hours on AVN22, the main issue is related to the phase demodulation. Recall that the relationship between the x (Equation 1.4) and y (Equation 1.5) contains five ellipse shape parameters in order to compute the optical phase difference (Eq. 1.6). These parameters are fixed prior to installation and for some reason the heat generated by the exothermic reaction of the grout curing caused these parameters to vary rapidly, resulting in inaccurate estimates of the strain. This was most likely caused by thermal stress induced changes to the internal optical components, which are specifically designed to be shielded from this effect. Despite this, however both AVN22 and AVN31 show the compression on the horizontal gauges and extension on the vertical indicating successful installations.

The post-grouting behavior of AVN87 (Figure 4.23) departs from the ideal case in several ways. First is that gauge S1 became non-functional as a result of water ingress into the interrogator pressure case in the time between their installation in December 2021 and grouting in March 2022. While two of the remaining three gauges, S2 and S3, go into compression shortly after grouting, the horizontal strain gauge S4 has a slightly extensive trend. The other anomaly is the vertical strain that runs exactly the opposite of the other three strainmeters, perhaps due to a simple inversion of which channel was selected as x and y inside of the interrogator. These departures from the nominal behavior do not necessarily disqualify AVN87 from being a successful installation because this is one of several metrics.

4.2.2.2 Barometric Pressure Admittance

Successfully removing the barometric pressure signal from the strain records is essential before performing an in-situ calibration. This is due to the large 1 CPD signal in the barometric pressure whose energy, along with any harmonics, that can be easily misinterpreted as strain tides using a blind fitting algorithm like linear least-squares. The problem then becomes being able to obtain a robust estimate of the magnitude of the barometric pressure effect on each gauge.

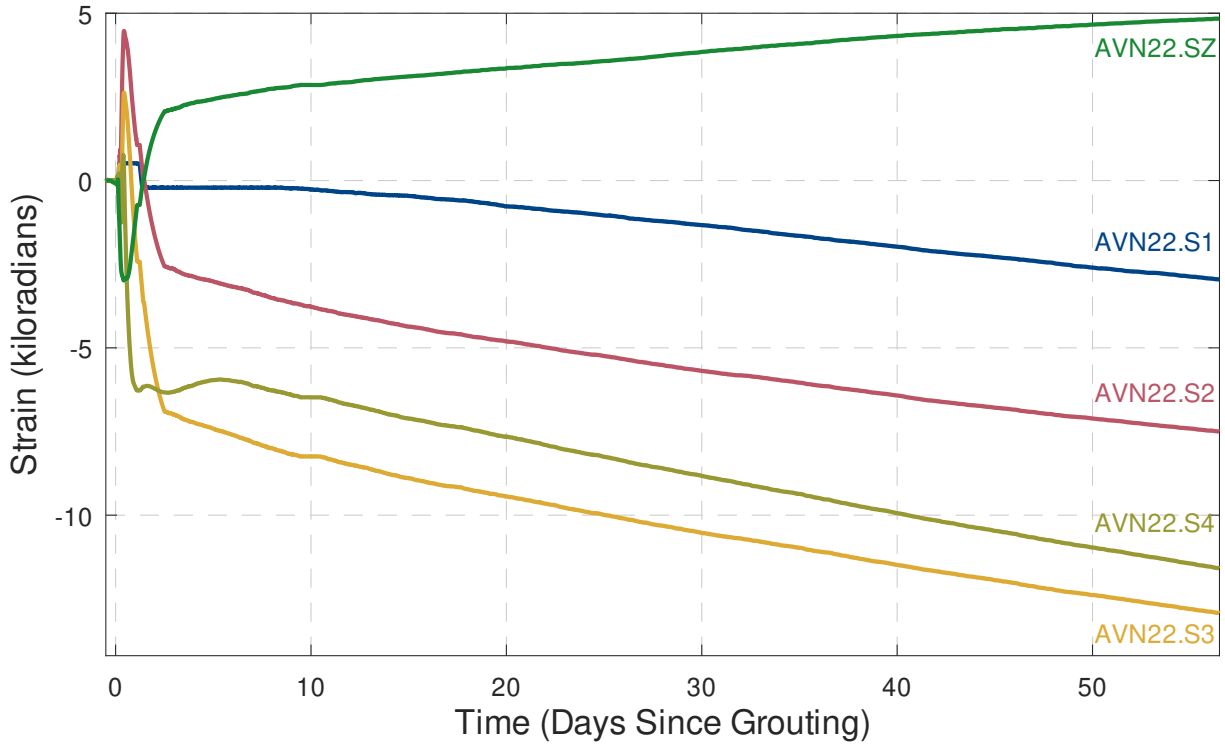

Figure 4.21: Grout cure time series for AVN22.

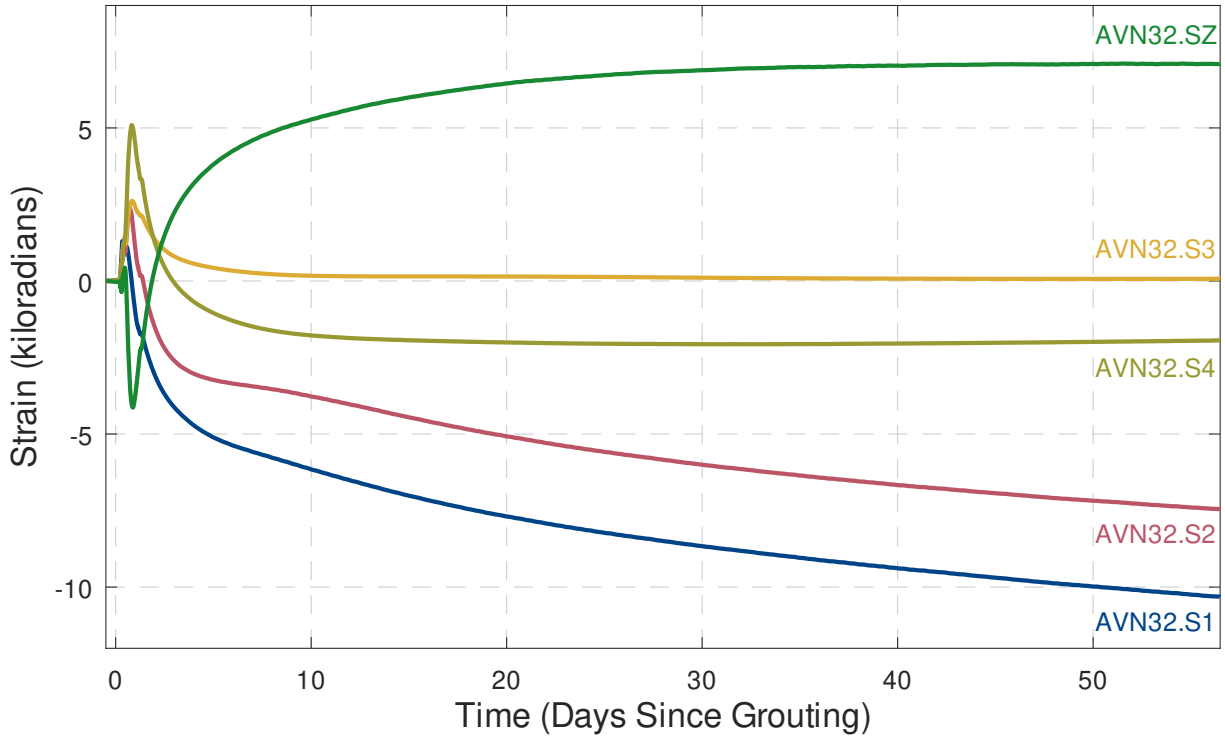

Figure 4.22: Grout cure time series for AVN32.

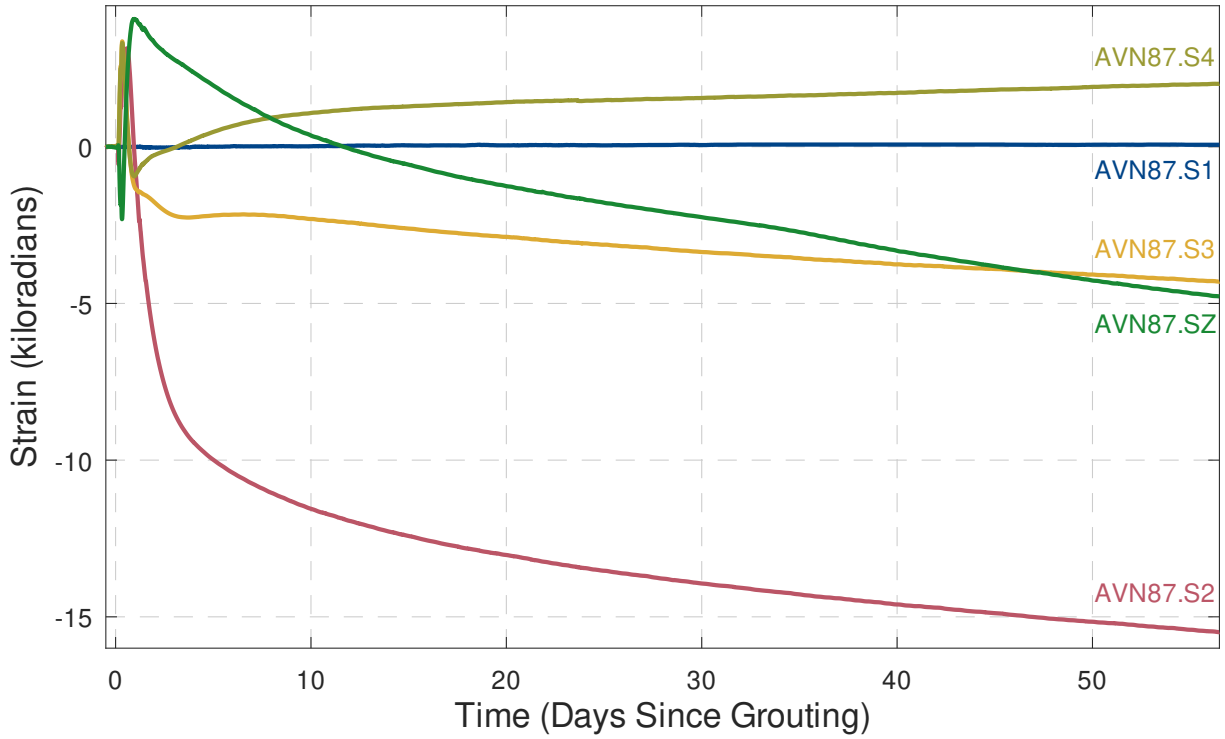

Figure 4.23: Grout cure time series for AVN87.

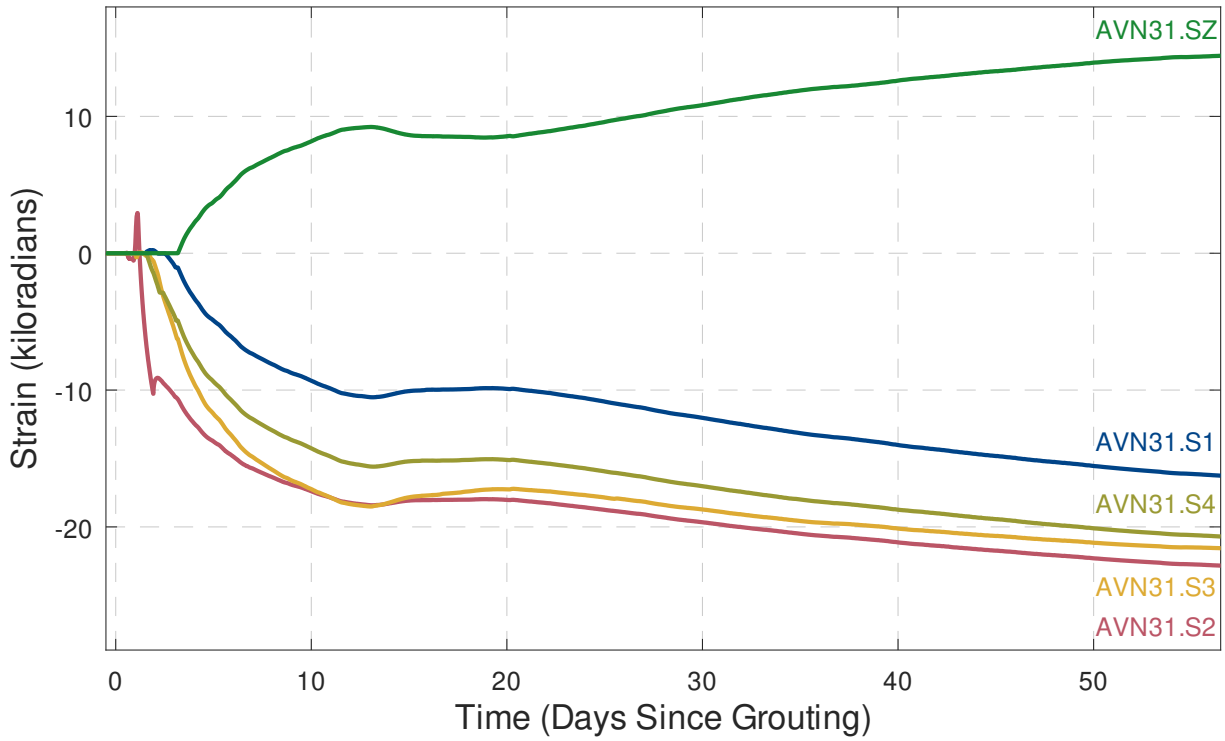

Figure 4.24: Grout cure time series for AVN31.

Table 4.3: Barometric pressure scalar admittances for each of the four horizontal strain gauges for the shallow GTSM in well AVN2.

Instrument & Component	Scalar Admittance (nϵ/kPa)
PB.AVN2.S1	27 ± 25
PB.AVN2.S2	29 ± 3
PB.AVN2.S3	20 ± 18
PB.AVN2.S4	28 ± 18

Table 4.4: Uncalibrated barometric pressure scalar admittances for the null, four horizontal and vertical strain gauges within the shallow TOFS-ER in well AVN22.

Instrument & Component	Scalar Admittance (radians/kPa)
2J.AVN22.S0	0.18 ± 0.06
2J.AVN22.S1	9.8 ± 3.1
2J.AVN22.S2	8.1 ± 2.4
2J.AVN22.S3	8.7 ± 1.9
2J.AVN22.S4	10.0 ± 1.9
2J.AVN22.SZ	8.9 ± 4.0

Table 4.5: Uncalibrated barometric pressure scalar admittances for the null, four horizontal and vertical strain gauges within the shallow TOFS-ER in well AVN32.

Instrument & Component	Scalar Admittance (radians/kPa)
2J.AVN32.S0	0.13 ± 0.04
2J.AVN32.S1	25.7 ± 7.9
2J.AVN32.S2	19.6 ± 5.3
2J.AVN32.S3	3.5 ± 1.0
2J.AVN32.S4	9.0 ± 3.0
2J.AVN32.SZ	40 ± 14

Table 4.6: Uncalibrated barometric pressure scalar admittances for the null, four horizontal and vertical strain gauges within the shallow TOFS-ER in well AVN87.

Instrument & Component	Scalar Admittance (radians/kPa)
2J.AVN87.S0	0.34 ± 0.04
2J.AVN87.S1	1.15 ± 0.15
2J.AVN87.S2	14.1 ± 1.8
2J.AVN87.S3	9.0 ± 1.6
2J.AVN87.S4	7.9 ± 2.0
2J.AVN87.SZ	21.1 ± 5.7

Table 4.7: Uncalibrated barometric pressure scalar admittances for the null, four horizontal and vertical strain gauges within the deep TOFS-ER in well AVN31.

Instrument & Component	Scalar Admittance (radians/kPa)
2J.AVN31.S0	0.44 ± 0.07
2J.AVN31.S1	26 ± 10
2J.AVN31.S2	23.7 ± 9.1
2J.AVN31.S3	31 ± 13
2J.AVN31.S4	30 ± 12
2J.AVN31.SZ	27.7 ± 8.6

As with the tiltmeter (Section 4.1.2.1) this was done using least-squares for the scalar admittance and adaptive multitaper cross spectrum analysis for the spectral admittance. The scalar admittance values for the individual strain gauges in native units (i.e., uncalibrated) are shown in Table 4.3 for the shallow GTSM in AVN2, Table 4.4 for the shallow TOFS-ER in AVN22, Table 4.5 for the shallow TOFS-ER in AVN32, Table 4.6 for the shallow TOFS-ER in AVN87 and Table 4.7 for the deep TOFS-ER in AVN31. For the GTSM, the scalar admittance values agree reasonably with the published values of 22, 26, 26 and 27 nϵ/kPa. The null component on each of the TOFS-ER installations appears to be relatively insensitive to barometric pressure with values ranging from 0.13–0.44 radians/kPa, which is expected since these reference fibers are designed to be sealed off from external stresses. AVN22 (Table 4.4) seems to have the most consistent scalar admittance among all of the five active strain gauges at around 10 radians/kPa, but the others range from about 3–30 radians/kPa. AVN31 (Table 4.7) appears to have the highest average admittance values and therefore the lowest sensitivity to barometric pressure, which is plausible given its 12 times greater depth.

An interesting note is the similarity between the values in Tables 4.4–4.7 and the average value of found during the hydrostatic calibration done in the laboratory (Section 1.7.4.2). The average was found to be approximately 400 Pa/rad, which inverting and multiplying by 1,000 yields ∼2.5 rad/kPa. While this is on the low side of the TOFS-ER scalar admittance values, it is within a factor of 3–10 times smaller.

The scalar admittance values for the four calibrated strain tensor components for each strainmeter are shown in Tables 4.8–4.12 for AVN2, AVN22, AVN32, AVN87 and AVN31, respectively. These were computed using the uncalibrated scalar admittance values from each gauge (Tables 4.3–4.7) and the in-situ calibration factors found in the next section (Section 4.2.2.3). Results from the GTSM (Table 4.8) are around 10–20 nϵ/kPa for the horizontals and vertical and just under 1 nϵ/kPa for the shear. This lower value for the shear also appears to be shared by AVN22 (Table 4.9), AVN87 (Table 4.11) and especially AVN31 (Table 4.12) whose shear admittance is up to 70 times lower than the other horizontal strains. Looking at the shallow installations, AVN32 (Table 4.10) and AVN87 (Table 4.11) seem to have admittances much larger than either AVN2 (Table 4.8) and AVN22 (Table 4.9).

While the scalar admittance can provide some insights into the influence of barometric pressure on the strain gauges, the spectral admittance is a much more comprehensive look at this complex interaction. As a first example, consider the coherence, magnitude and phase plots for the shallow GTSM in borehole AVN2 as shown in Figure 4.25. Each of the four strain gauges share coherent energy near 1 CPD and in the band above 2 CPD up to about 5×10^{-4} Hz (∼2,000 seconds) where the coherence is negligible at higher frequencies and the scalar admittance estimates (shown as red horizontal lines) track the longest period part of the signals. The final important feature is that while there is significant energy in the strain signal from the semidiurnal tides (2 CPD), the coherence is low indicating that the strain and barometric pressure , while each have energy at that frequency, are uncorrelated.

These spectral admittance characteristics on AVN2 (Figure 4.25) are also consistent across the other shallow strainmeters, AVN22 (Figure 4.26), AVN32 (Figure 4.27) and AVN87 (Figure 4.28). Of course this excludes the null component S0 that shows essentially zero coherence across the entire frequency band, which is the desired outcome since it means that it is in fact uncoupled from the stresses induced by atmospheric pressure changes. The coherence extends up into higher frequencies than AVN2, however, this is most certainly due to the fact that the AVN2 barometer is sampled once every 30 seconds ($5.6 \times 10^{-}4$ Hz) rather than at the same rate as the strainmeters, which was deliberate in the design of the interrogators accompanying each strainmeter.

The deep strainmeter at AVN31 (Figure 4.29) has spectral admittances that differ significantly from the shallow installations. There is very low coherence across the entire frequency band, in fact, the 95th percentile line appears to at best make it to a coherence of 0.5 at 1×10^{-6} Hz. This also shows up as very poor phase stability for each of the strainmeter gauges.

4.2.2.3 Calibration

An in-situ calibration was performed on each strainmeter, which included a re-calibration of the GTSM at AVN2. This was done using the same method as with the tiltmeters (Section 4.1.2.2) but with multiple components of strain

Table 4.8: Barometric pressure scalar admittances for the four strain tensor components as measured by the shallow GTSM in well AVN2.

Instrument & Component	Scalar Admittance (nϵ/kPa)
PB.AVN2.ϵ_{xx}	22.0 ± 6.4
PB.AVN2.ϵ_{yy}	10.3 ± 3.0
PB.AVN2.ϵ_{xy}	0.85 ± 0.25
PB.AVN2.ϵ_{zz}	10.8 ± 3.1

Table 4.9: Barometric pressure scalar admittances for the four strain tensor components as measured by the shallow TOFS-ER in well AVN22.

Instrument & Component	Scalar Admittance (nϵ/kPa)
2J.AVN22.ϵ_{xx}	9.4 ± 1.3
2J.AVN22.ϵ_{yy}	9.2 ± 1.3
2J.AVN22.ϵ_{xy}	0.53 ± 0.07
2J.AVN22.ϵ_{zz}	0.38 ± 0.05

Table 4.10: Barometric pressure scalar admittances for the four strain tensor components as measured by the shallow TOFS-ER in well AVN32.

Instrument & Component	Scalar Admittance (nϵ/kPa)
2J.AVN32.ϵ_{xx}	375 ± 53
2J.AVN32.ϵ_{yy}	38.5 ± 5.4
2J.AVN32.ϵ_{xy}	57.6 ± 8.1
2J.AVN32.ϵ_{zz}	92 ± 13

Table 4.11: Barometric pressure scalar admittances for the four strain tensor components as measured by the shallow TOFS-ER in well AVN87.

Instrument & Component	Scalar Admittance (nϵ/kPa)
2J.AVN87.ϵ_{xx}	67.9 ± 6.1
2J.AVN87.ϵ_{yy}	58.5 ± 5.3
2J.AVN87.ϵ_{xy}	11.7 ± 1.1
2J.AVN87.ϵ_{zz}	41.4 ± 3.7

Table 4.12: Barometric pressure scalar admittances for the four strain tensor components as measured by the shallow TOFS-ER in well AVN31.

Instrument & Component	Scalar Admittance (nϵ/kPa)
2J.AVN31.ϵ_{xx}	551 ± 93
2J.AVN31.ϵ_{yy}	694 ± 117
2J.AVN31.ϵ_{xy}	9.6 ± 1.6
2J.AVN31.ϵ_{zz}	426 ± 72

rather than tilt. The calibrated components include the east-west strain ϵ_{xx}, north-south strain ϵ_{yy}, horizontal shear strain ϵ_{xy} and vertical strain ϵ_{zz}. While the GTSM does not have a dedicated strain gauge, it does have four horizontal gauges leading to an overdetermined system of equations whose common mode component can be extracted as the vertical strain coupling.

The predicted and best-fit strainmeter time series for all five strainmeters are shown in Figures 4.30–4.34. These plots show the modeled output in black and the band pass filtered strainmeter data in red for each of the four strain tensor components. Different time windows were chosen for each calibration based on the best-fitting 28 days within the overall time range of the data. Overall the results are excellent and the predicted and filtered data match almost exactly over the selected time window. There are some small anomalies causing some minor disruptions in AVN87

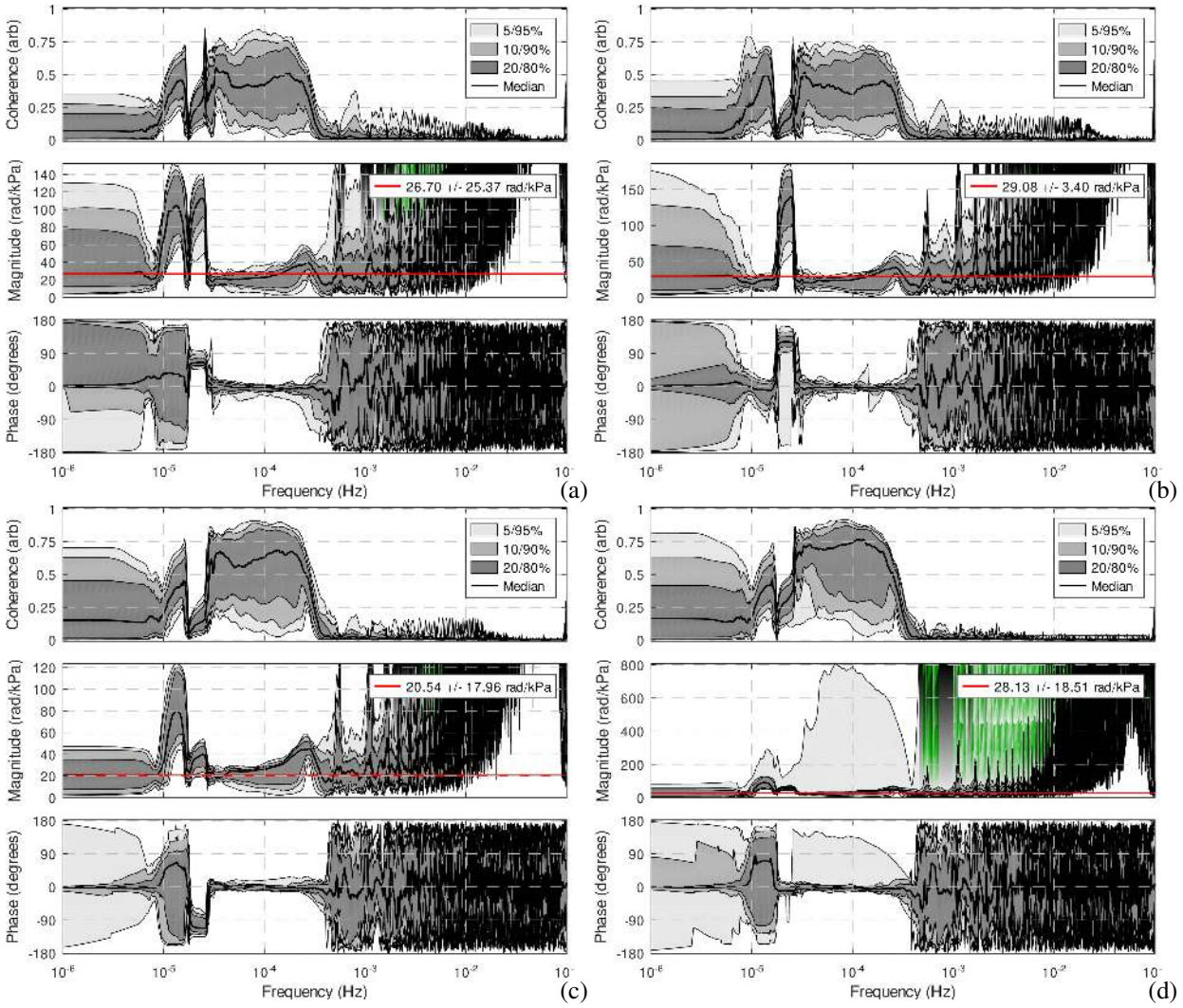

Figure 4.25: Barometric pressure spectral admittances for the GTSM at AVN2.

(Figure 4.33), however, these fits were using only three of the four gauges.

The deep strainmeter at AVN31 (Figure 4.34) appears to have several more noticeable anomalies. First is there appear to be some phasing issues with the east-west (ϵ_{xx}) component since while the major tides seem to line up very well, the minor tides appear stronger in the data than in the prediction. The fitting process appears to have difficulty matching the shear strain with the data collected from the four horizontal gauges, and is largely absent in the deeper instrument. The reason for these effects is unknown and the subject of ongoing research.

4.2.2.4 Ambient Spectra

Armed with the in-situ calibration data from the previous section, we estimated the magnitude spectral densities for all five strainmeters. These were computed in a manner identical to the tiltmeters in Section 4.1.2.3. The results for the shallow GTSM in borehole AVN2 are shown in 4.35, followed by the three shallow TOFS-ER in AVN22 (Figure 4.36), AVN32 (Figure 4.36) and AVN87 (Figure 4.38), and then finally the TOFS-ER in the deep well AVN31

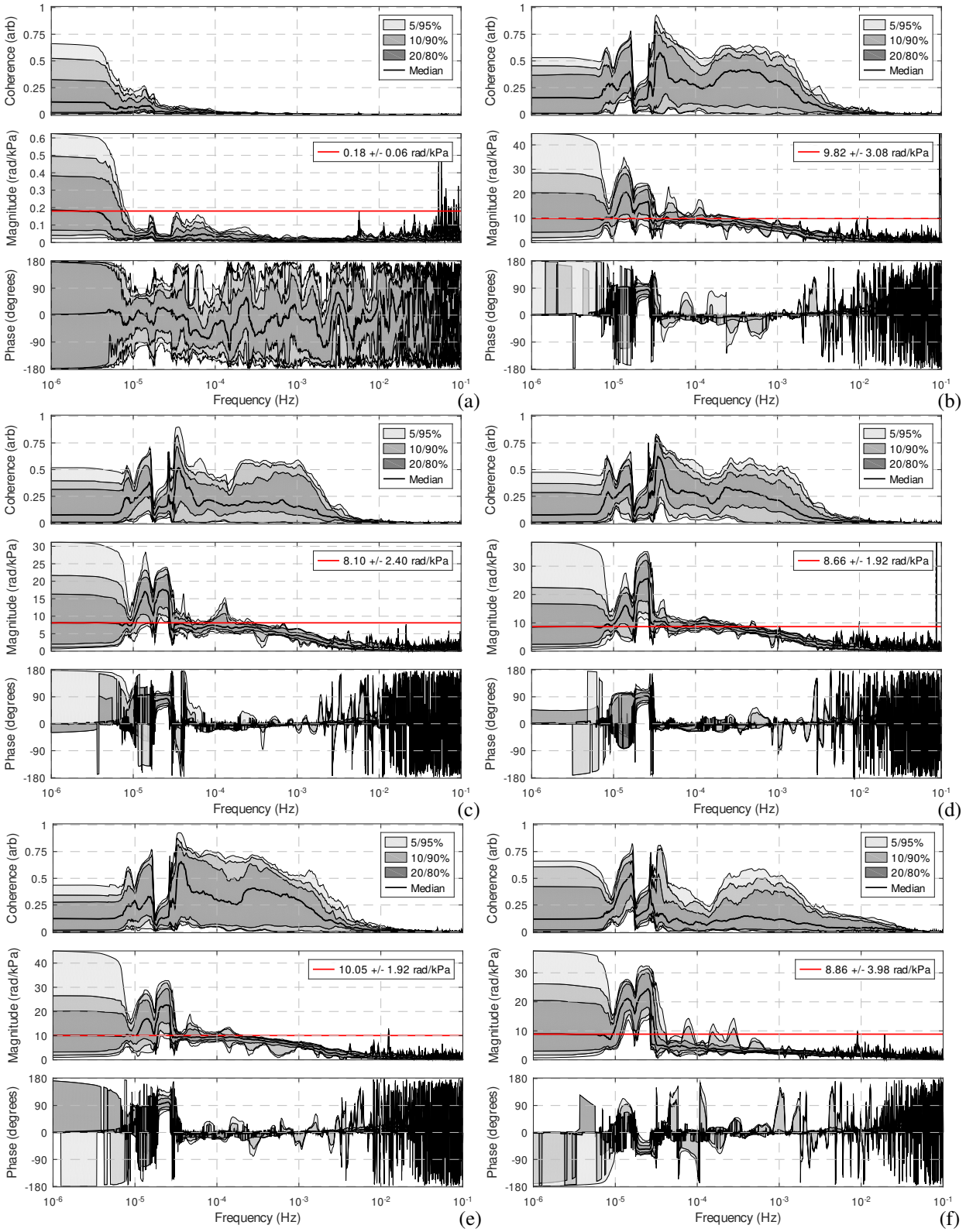

Figure 4.26: Barometric pressure spectral admittances for the TOFS-ER v6 at AVN22.

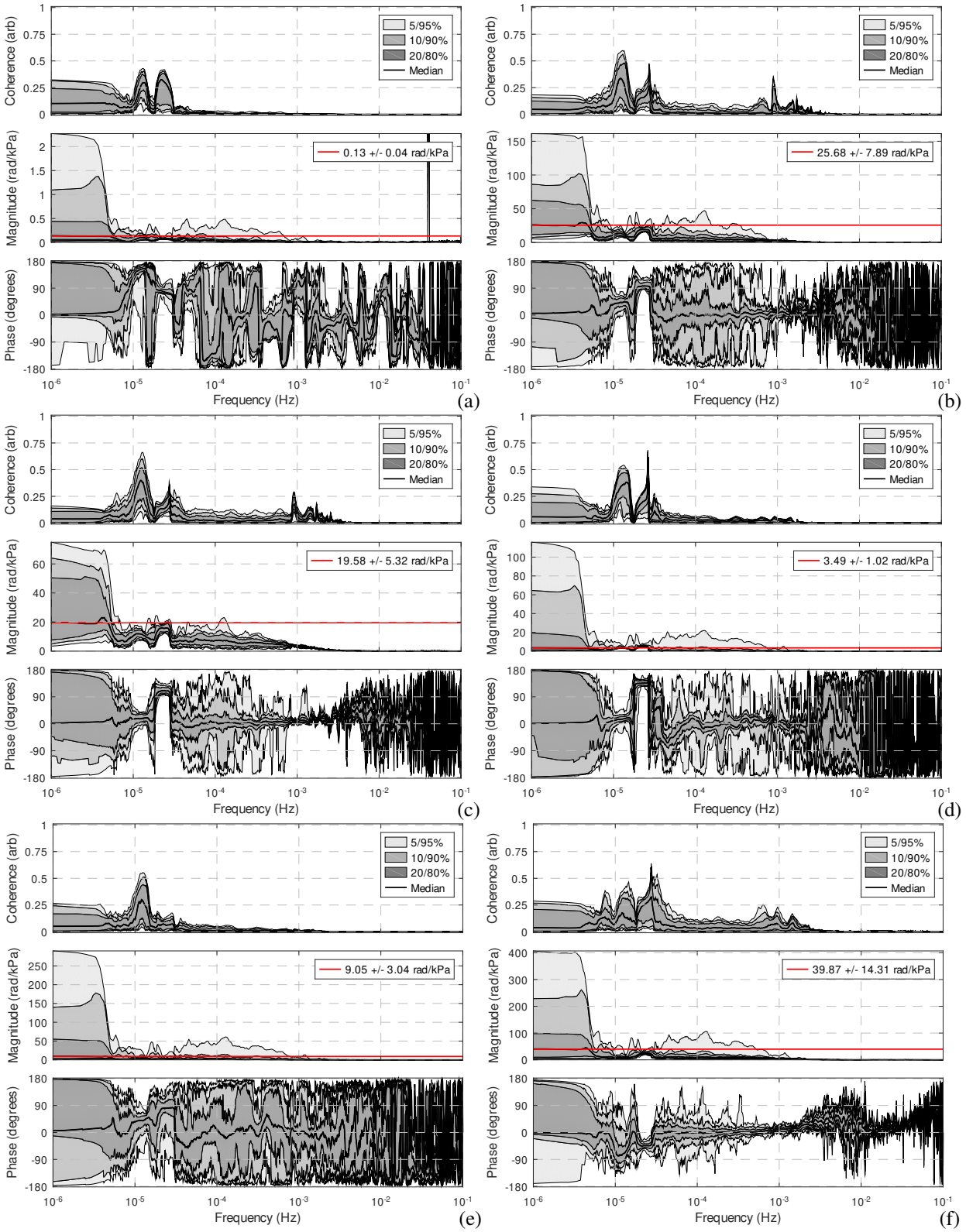

Figure 4.27: Barometric pressure spectral admittances for the TOFS-ER v6 at AVN32.

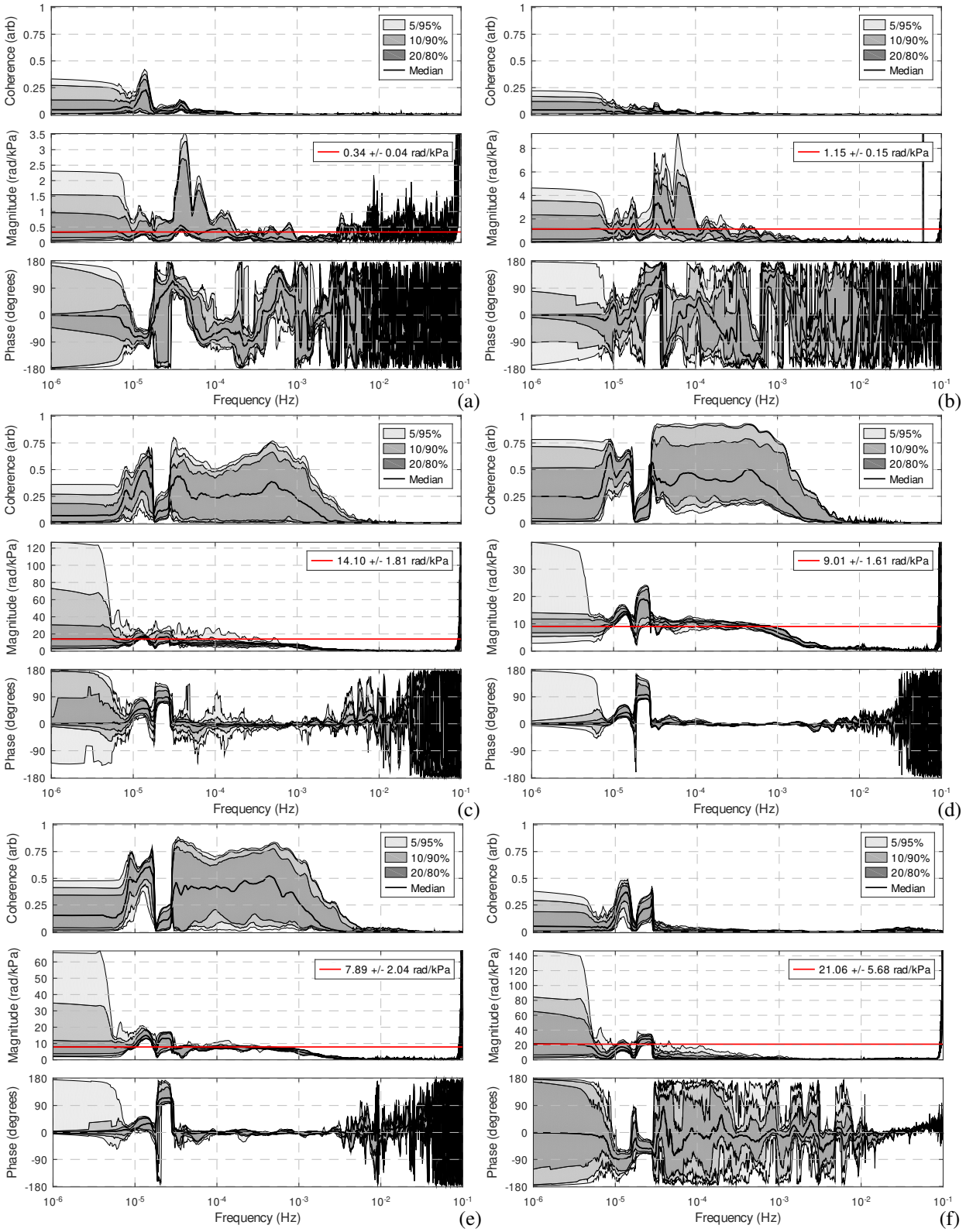

Figure 4.28: Barometric pressure spectral admittances for the TOFS-ER v6 at AVN87.

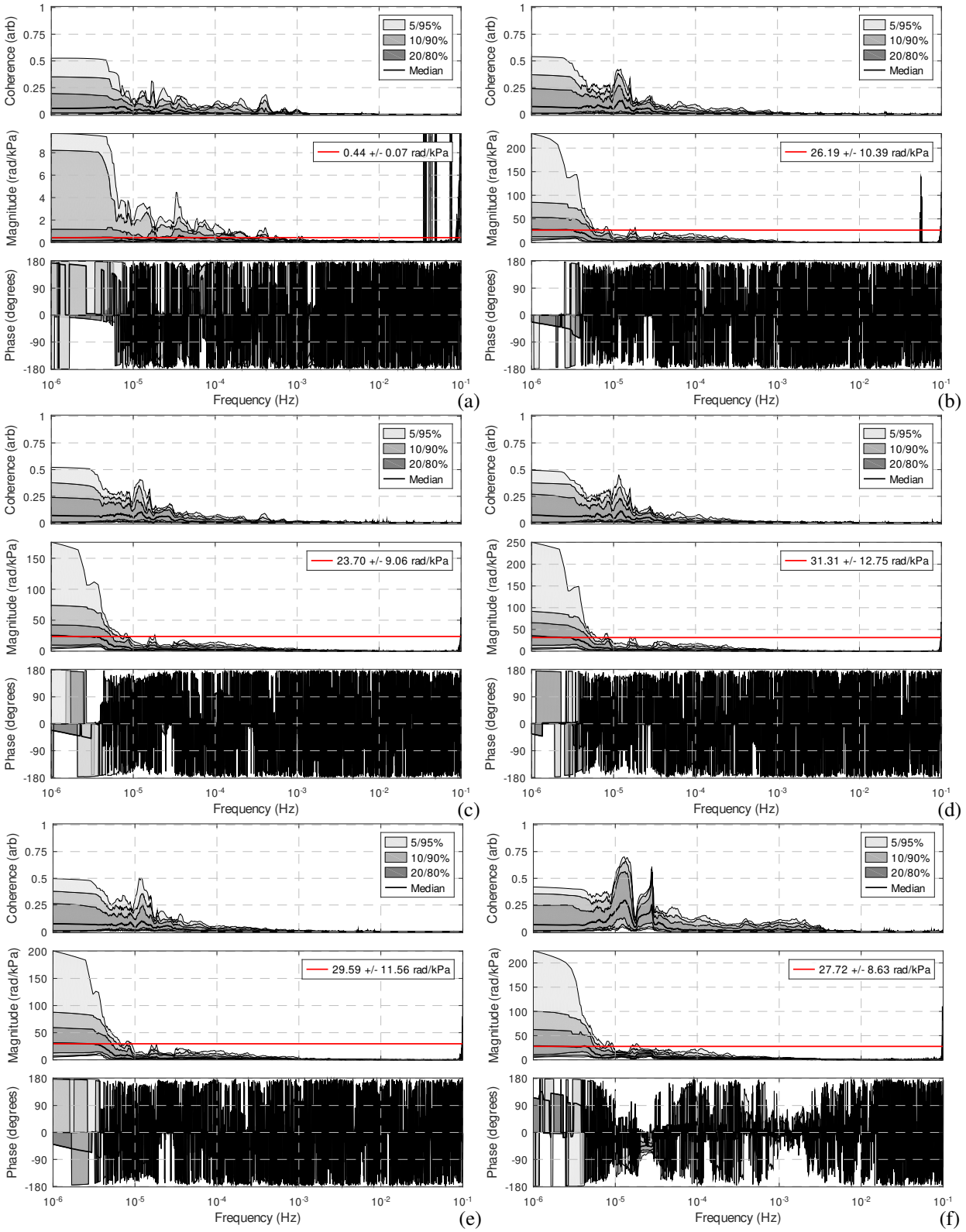

Figure 4.29: Barometric pressure spectral admittances for the TOFS-ER v6 at AVN31.

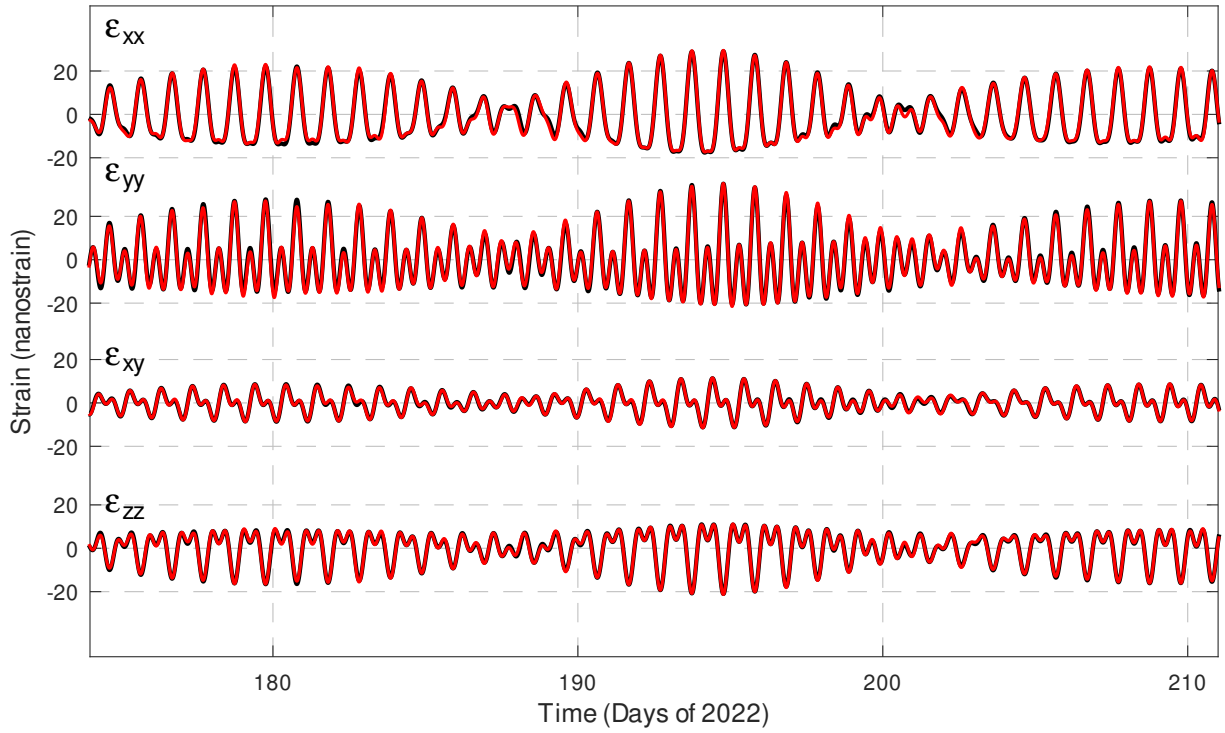

Figure 4.30: Earth tide calibration time series for the GTSM in AVN2 showing the predicted tides in black and best-fitting strainmeter data in red.

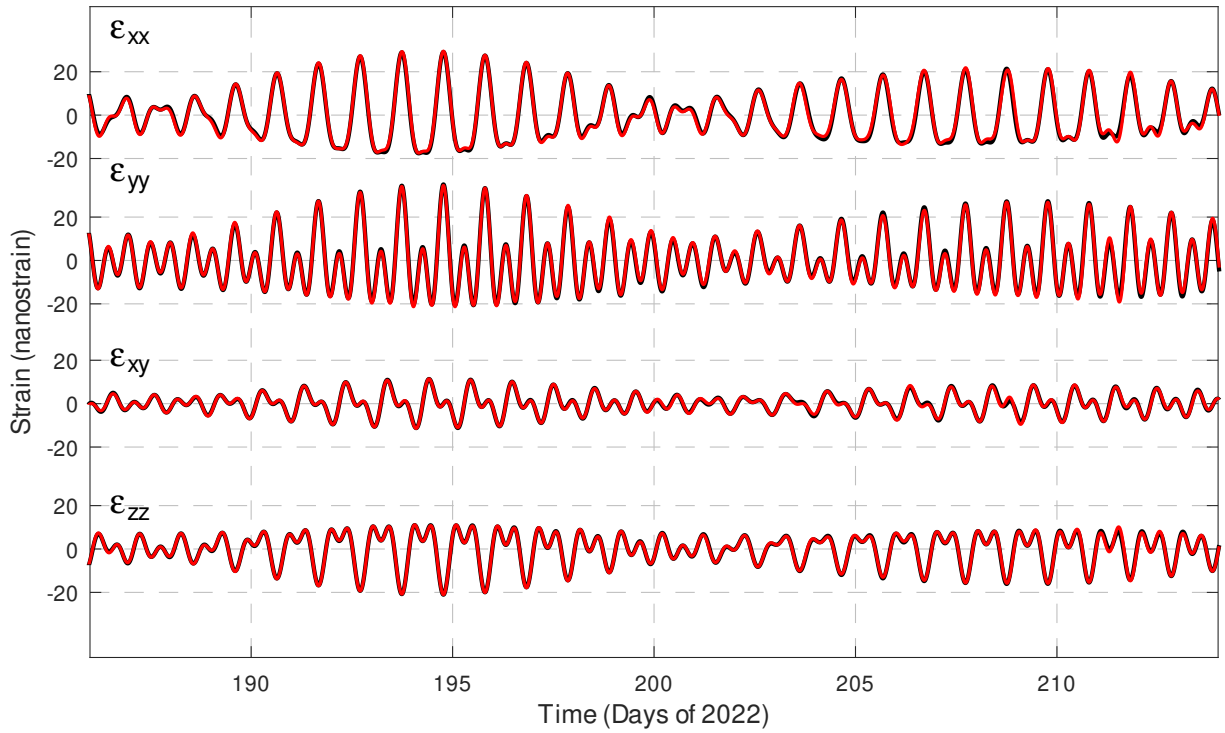

Figure 4.31: Earth tide calibration time series for the TOFS-ER v6 in AVN22 showing the predicted tides in black and best-fitting strainmeter data in red.

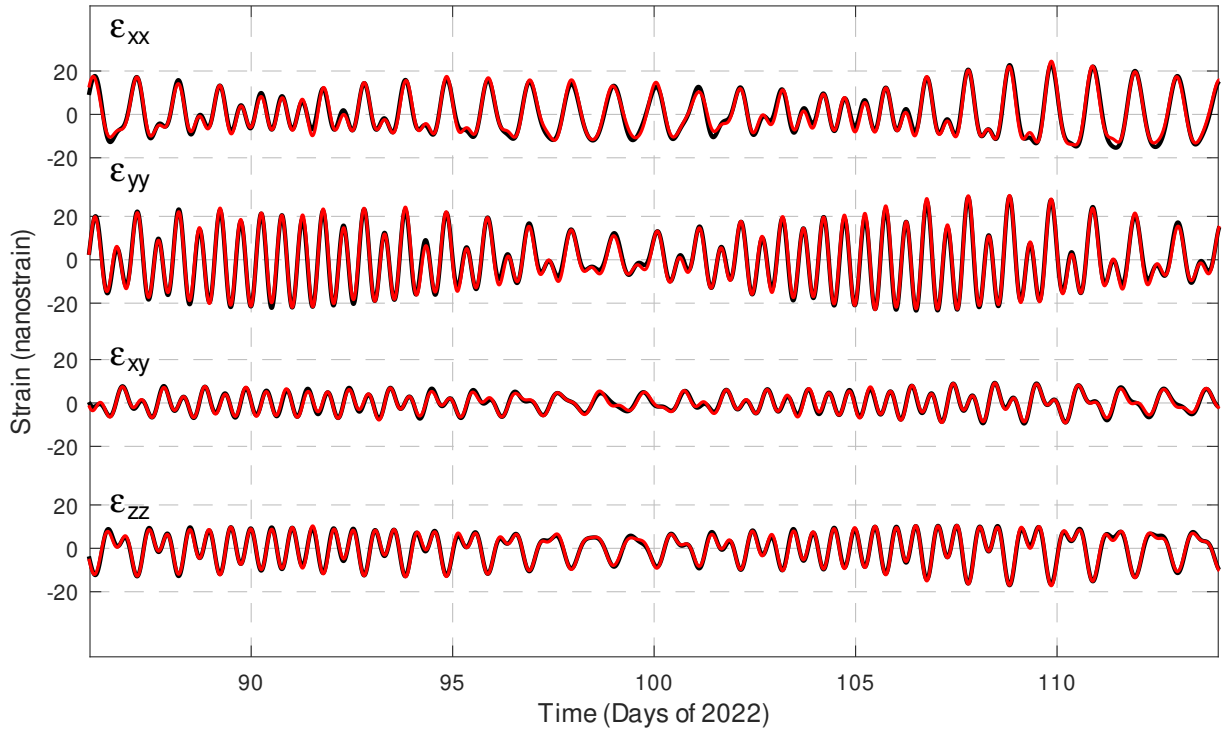

Figure 4.32: Earth tide calibration time series for the TOFS-ER v6 in AVN32 showing the predicted tides in black and best-fitting strainmeter data in red.

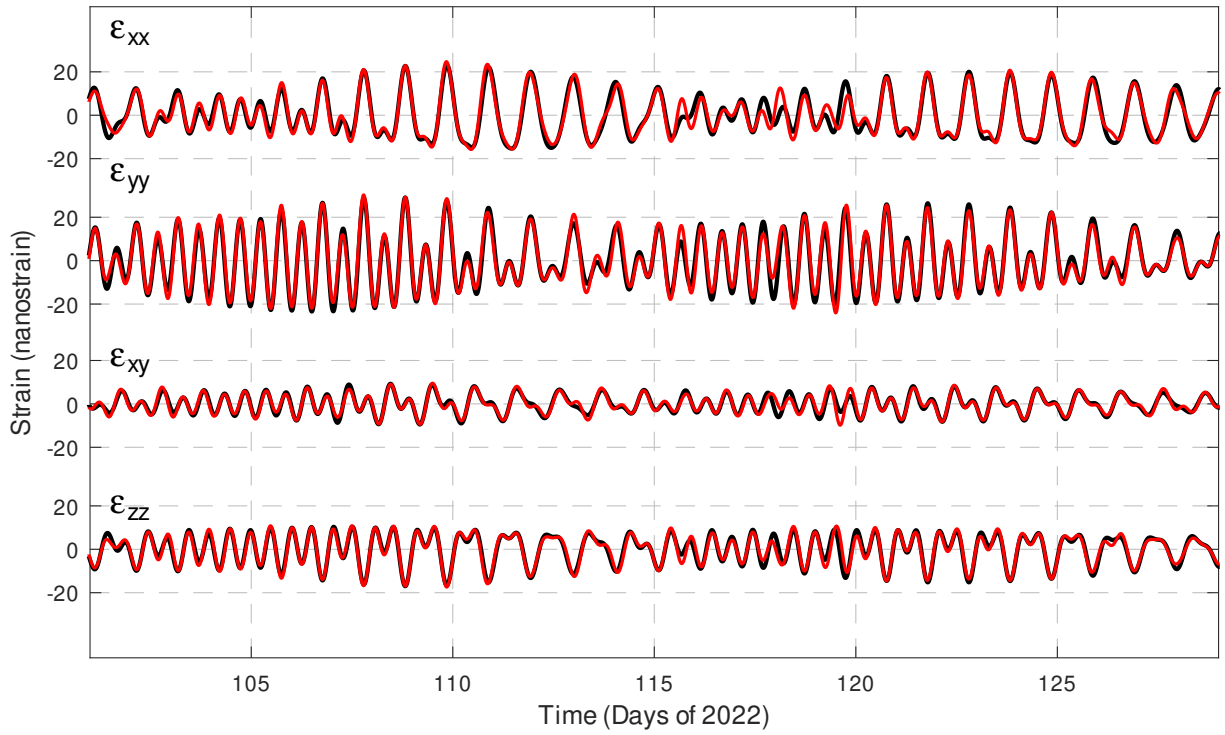

Figure 4.33: Earth tide calibration time series for the TOFS-ER v6 in AVN87 showing the predicted tides in black and best-fitting strainmeter data in red.

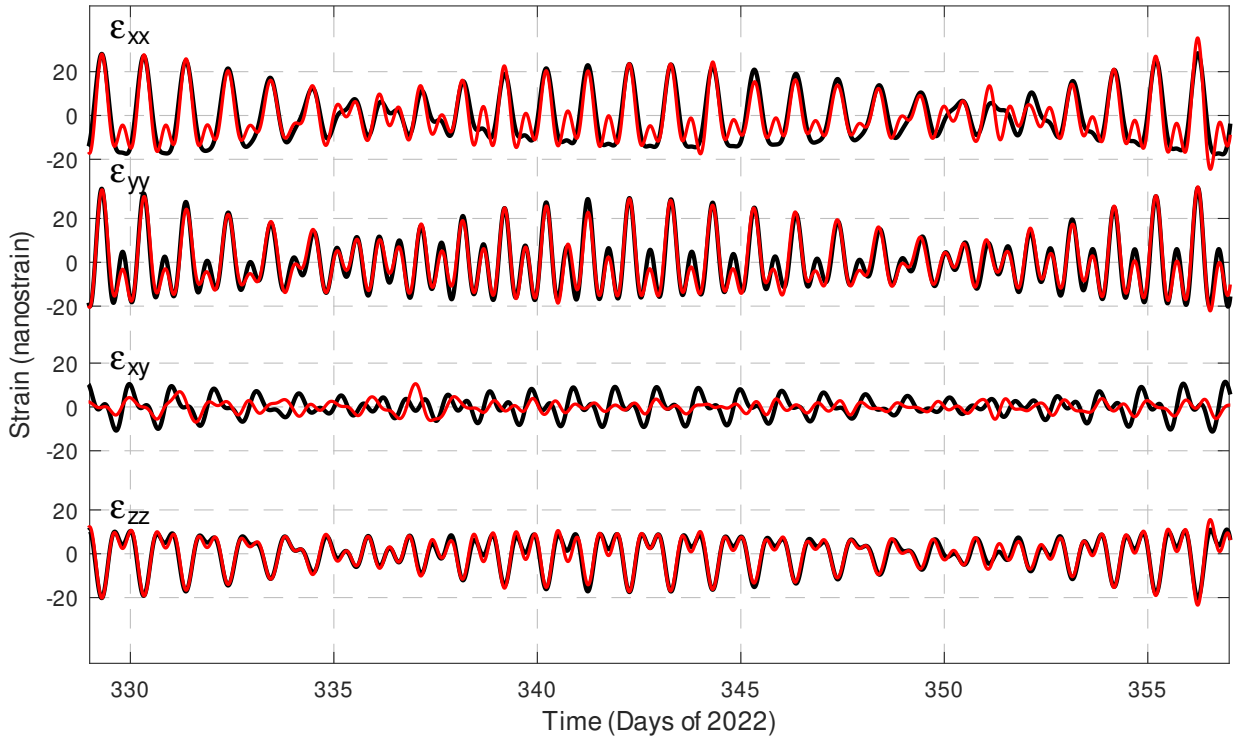

Figure 4.34: Earth tide calibration time series for the TOFS-ER v6 in AVN31 showing the predicted tides in black and best-fitting strainmeter data in red.

(Figure 4.39). Each contains an inset plot highlighting the 1 and 2 CPD tidal bands that have a rather coarse frequency resolution since the data window length (and therefore the frequency spacing) was shortened (increasing the frequency spacing) in order to average the results enough to visually compare the spectra.

The similarities and differences in these spectra are perhaps best illustrated in Figures 4.40–4.43. These show the magnitude spectra for each instrument separated by strain tensor component, for example, the east-west strain ϵ_{xx} in Figure 4.40, the north-south strain ϵ_{yy} in Figure 4.41, the horizontal shear strain ϵ_{xy} in Figure 4.42 and the vertical strain ϵ_{zz} in Figure 4.43. There is very good agreement across all shallow instruments in the amplitudes of both the diurnal and semidiurnal tides.

The most noticeable difference in these plots is that the TOFS-ER spectrum estimates have a higher variance and are systematically 3–9 dB higher noise than the GTSM. The variance is most likely the result of the fact that the GTSM has been installed over 5 years longer than the TOFS-ER instruments and is undoubtedly more stable as a result. The systematic amplitude difference is especially pronounced in the horizontal shear (Figure 4.42) where the amplitudes of the tides seem to line up quite well indicating very good calibration results, the GTSM is inexplicably much lower noise when resolving the shear compared to the other components (Figure 4.35).

4.2.2.5 Teleseismic Events

The final comparison between the existing shallow GTSM at AVN2 and the other TOFS-ER is their response to surface waves propagating from distant earthquakes, or teleseisms. While these strainmeters routinely record seismic waves, surface waves from Alaska seem to provide the clearest waveforms for comparison. Figure 4.44 shows the time series of the four strain tensor components during the M7.0 earthquake located 18 km SW of Malango, Solomon Islands on November 22, 2022. Rather than plotting the waveforms from all five strainmeters, only the shallow

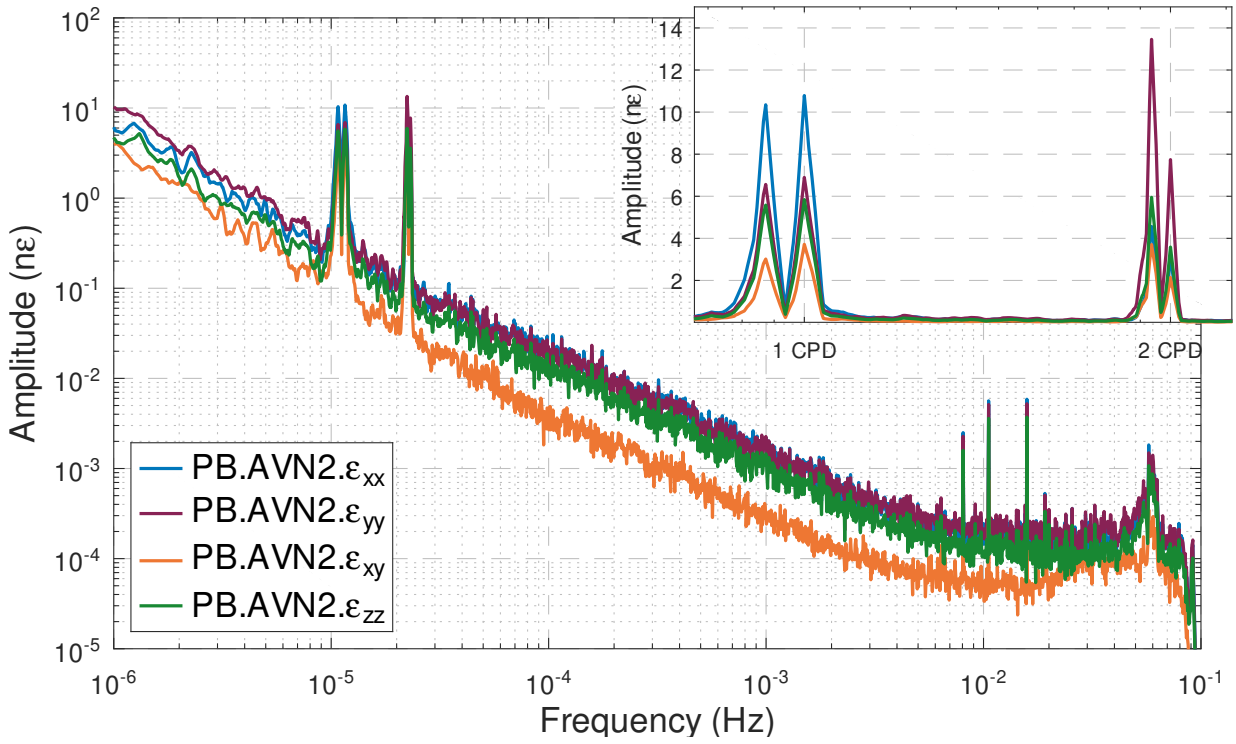

Figure 4.35: Magnitude spectra for all four calibrated components of the GTSM at AVN2.

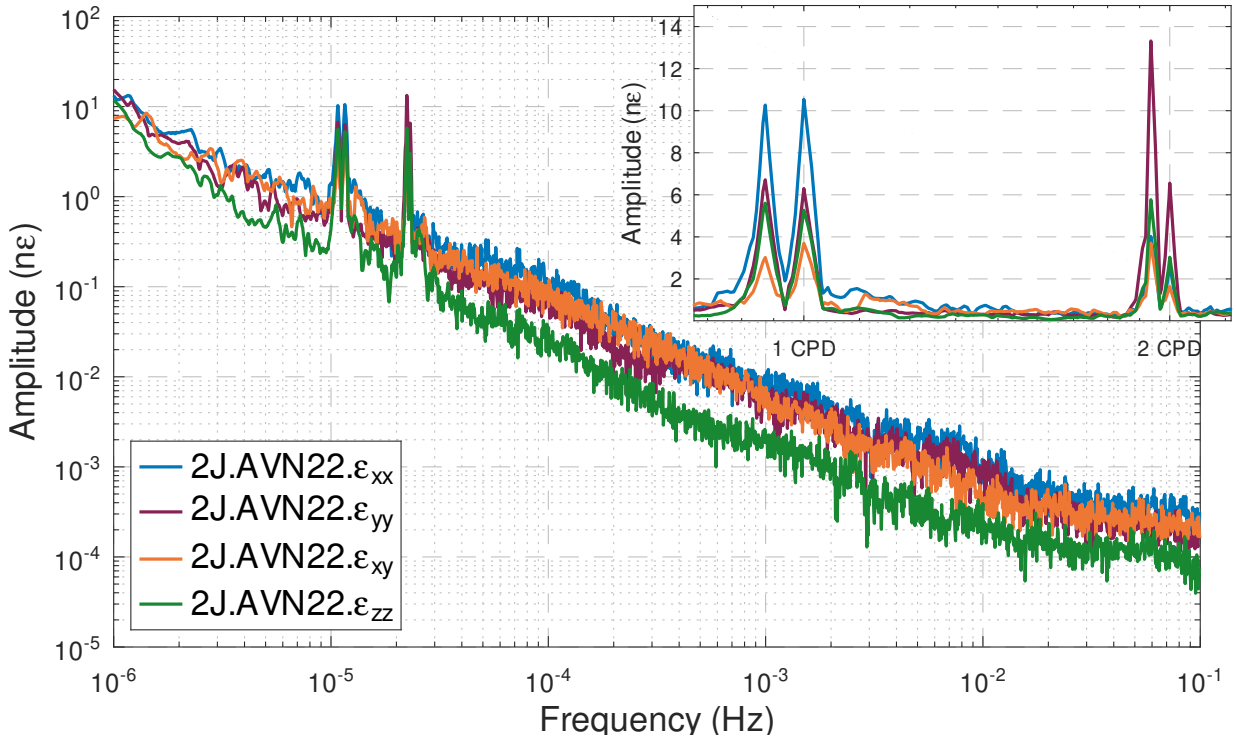

Figure 4.36: Magnitude spectra for all four calibrated components of the TOFS-ER v6 at AVN22.

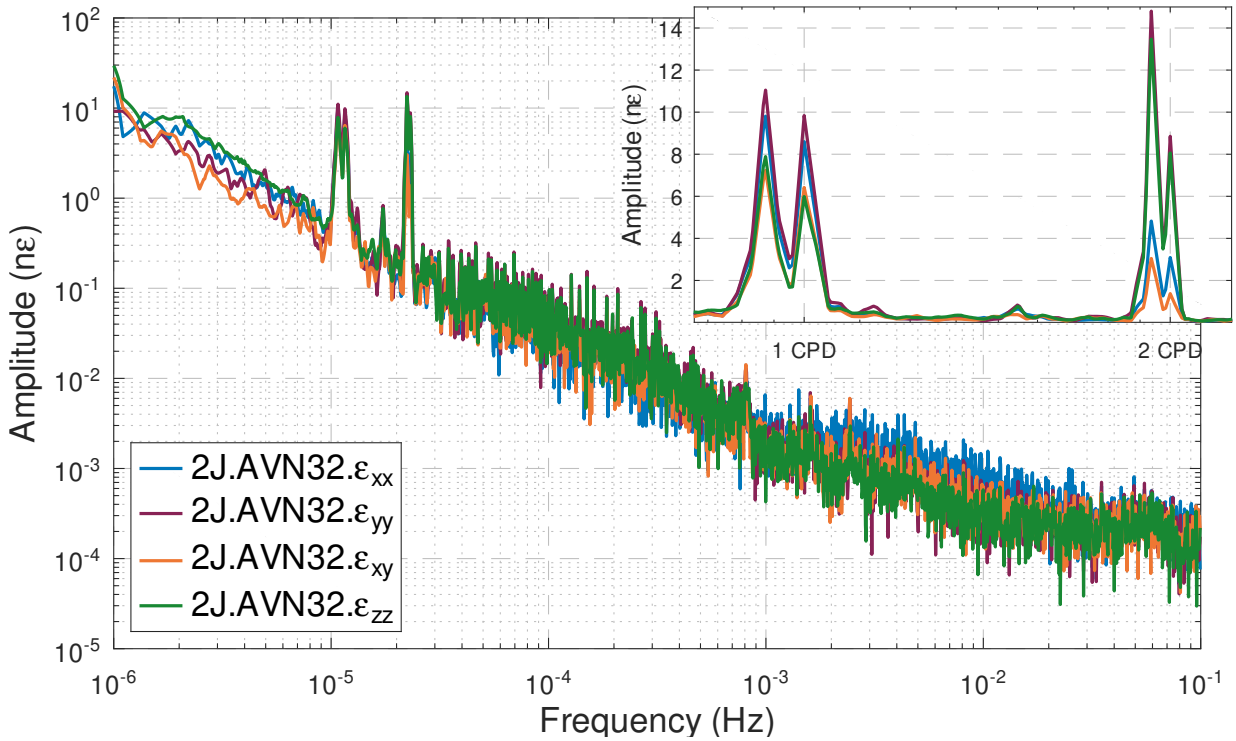

Figure 4.37: Magnitude spectra for all four calibrated components of the TOFS-ER v6 at AVN32.

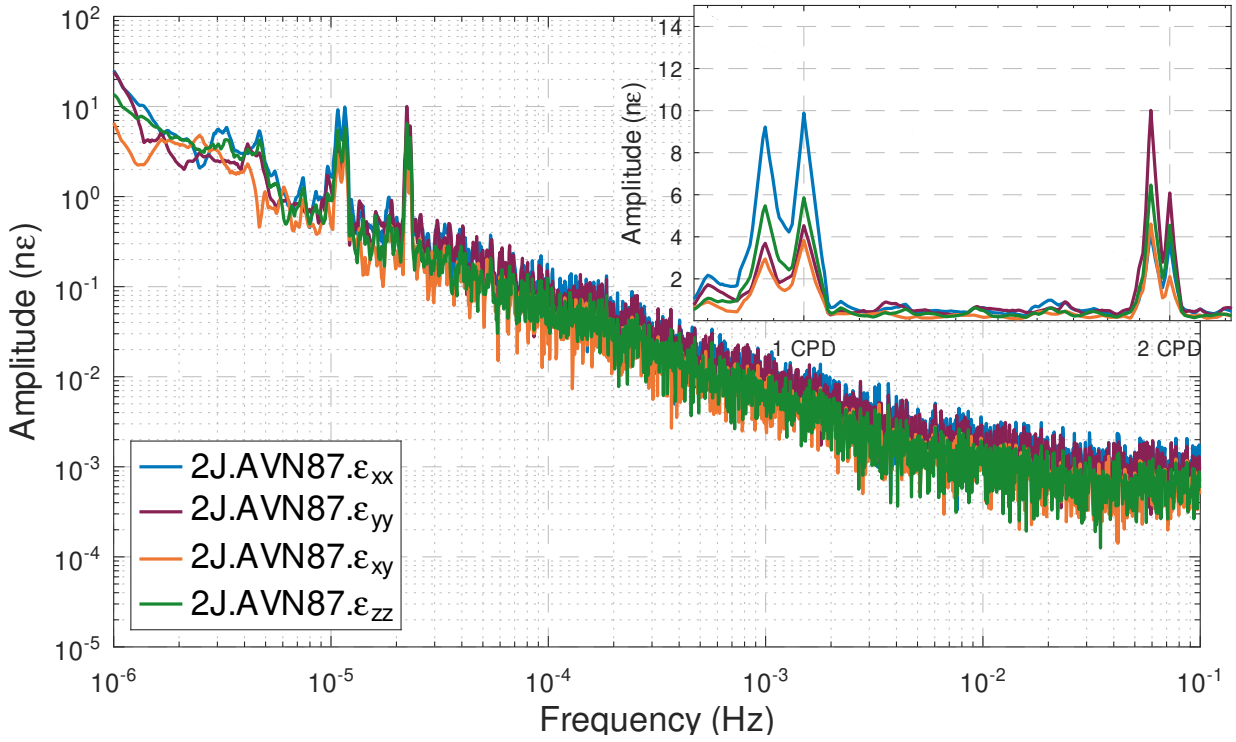

Figure 4.38: Magnitude spectra for all four calibrated components of the TOFS-ER v6 at AVN87.

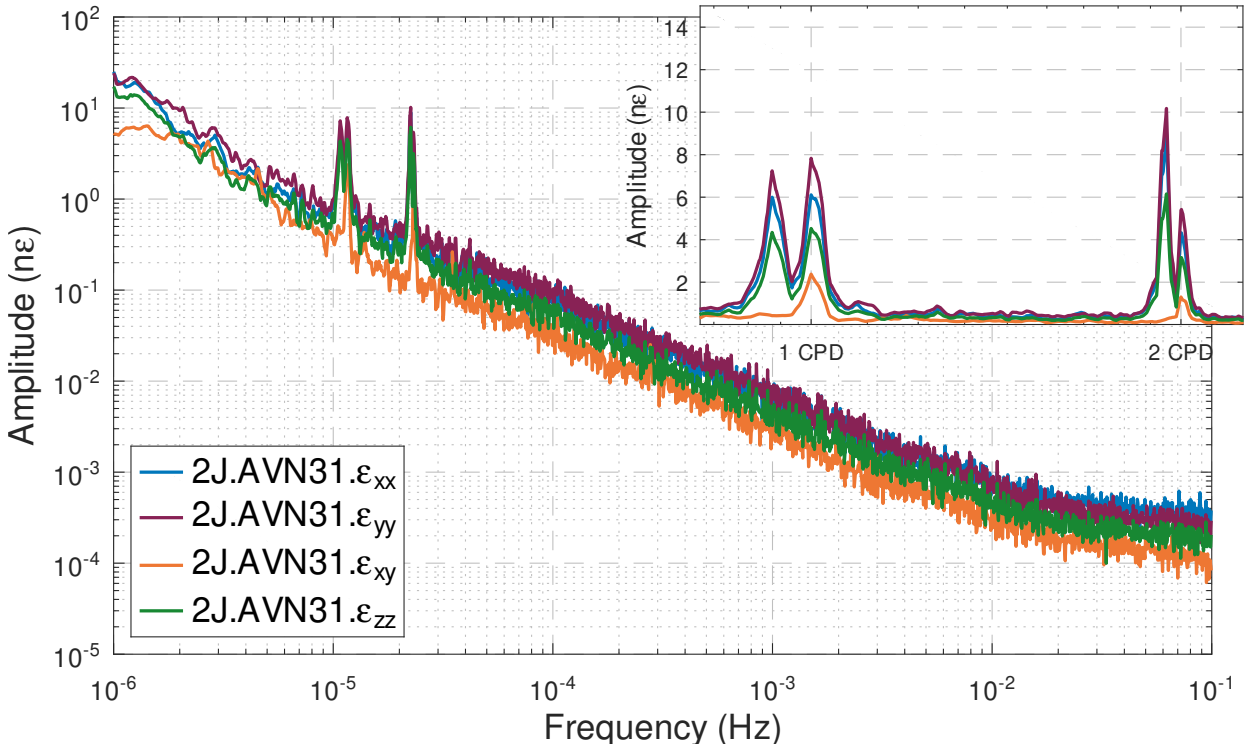

Figure 4.39: Magnitude spectra for all four calibrated components of the TOFS-ER v6 at AVN31.

GTSM from AVN2, shallow TOFS-ER from AVN22 and deep TOFS-ER from AVN31 are shown since it compares the existing strainmeter technology (GTSM) to the new instruments developed during this project in both comparable shallow (AVN22) and deep (AVN31) settings as well as a comparison between the two identical instruments (AVN22 and AVN31) at two different depths.

The waveforms in Figure 4.44 are grouped in color by the each tensor component and stacked with the GTSM at AVN2 on top, shallow TOFS-ER at AVN22 in the middle and deep TOFS-ER in AVN31 at the bottom. While there are some very subtle differences, each component waveform is nearly identical across all three instruments shown. The one exception is the shear component on AVN31, which seems to be mostly absent as previously discussed.

4.2.2.6 Conclusions

It is clear from the results described above that the four Version 6 Elliptical Ring Tensor Optical Fiber Strainmeters deployed at the North Avant Field were a huge success. The grout cure time series (Figures 4.21–4.24) all show the expected post-grouting behavior with all but one of the horizontal strain gauges going into permanent compression indicating that all four strainmeters were successfully grouted and are coupled to their host formations. This includes the deep strainmeter at AVN31 where considerable effort was made to ensure a successful installation (see Sections 4.2.1.2.2 and 4.2.1.3). The overwhelming majority of the in-situ tidal calibration results show excellent agreement with the predicted tides (Figures 4.31–4.34), which is corroborated by the very close overlap in the amplitudes of the tidal peaks in the strain tensor component spectra (Figures 4.40–4.43).

There are still some challenges remaining, however, such as the systematic level difference in the ambient spectra of the TOFS compared to the GTSM and the difficulty in resolving the horizontal shear strain on the deep instrument. We are confident that given enough time both the variance and overall spectrum levels will clean up and more closely match the GTSM. The lack of shear resolution in the deep strainmeter may simply be a result of the depth since we may

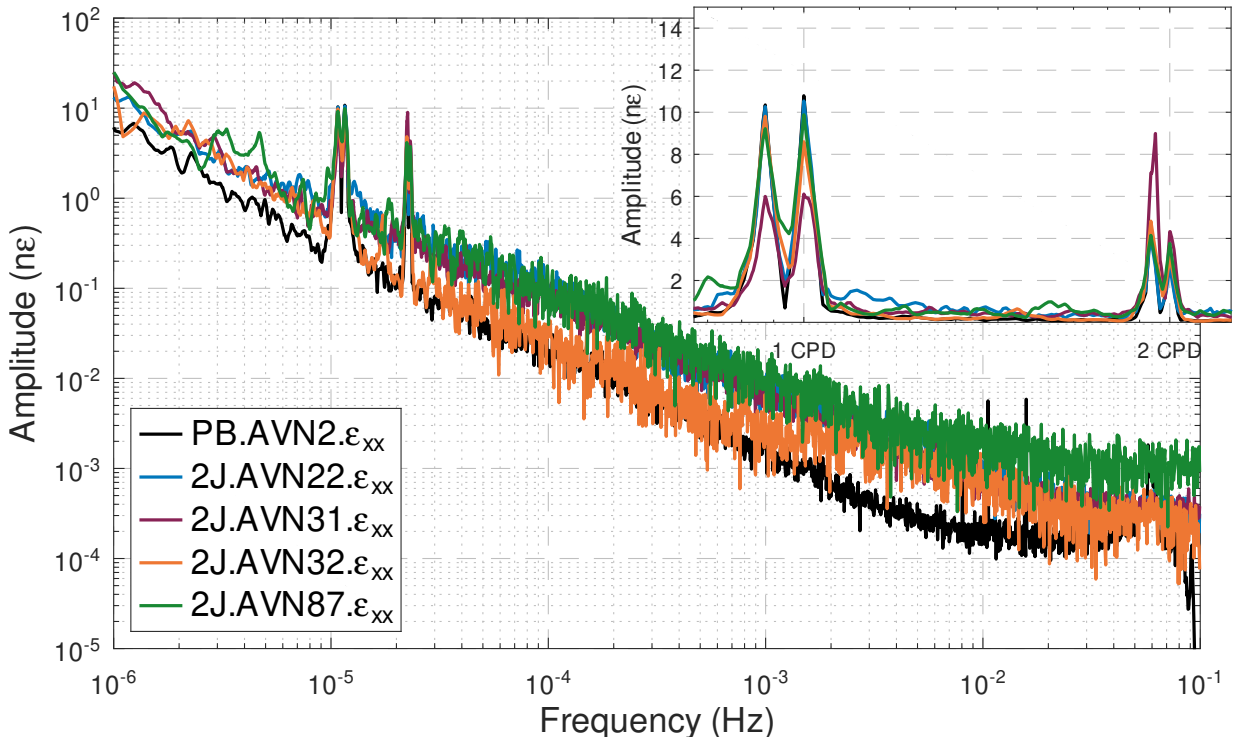

Figure 4.40: Magnitude spectra for the east-west strain component (ϵ_{xx}) as measured by all five strainmeters.

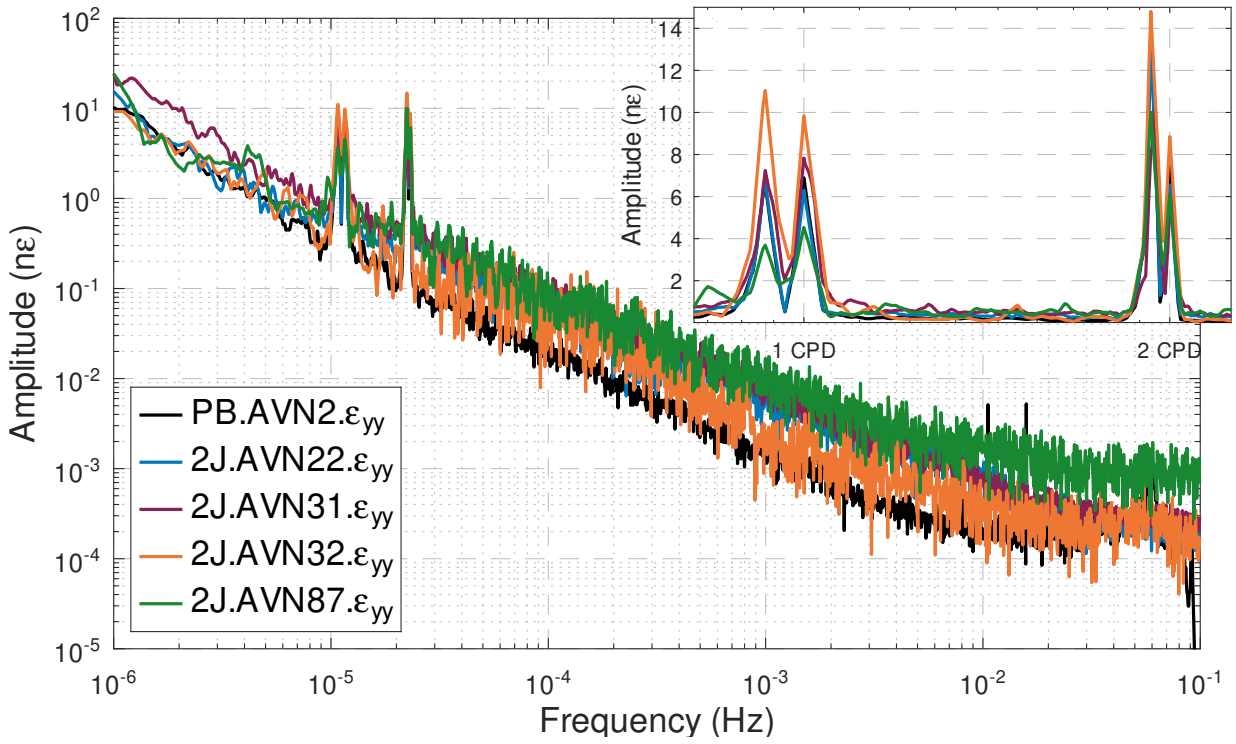

Figure 4.41: Magnitude spectra for the north-south strain component (ϵ_{yy}) as measured by all five strainmeters.

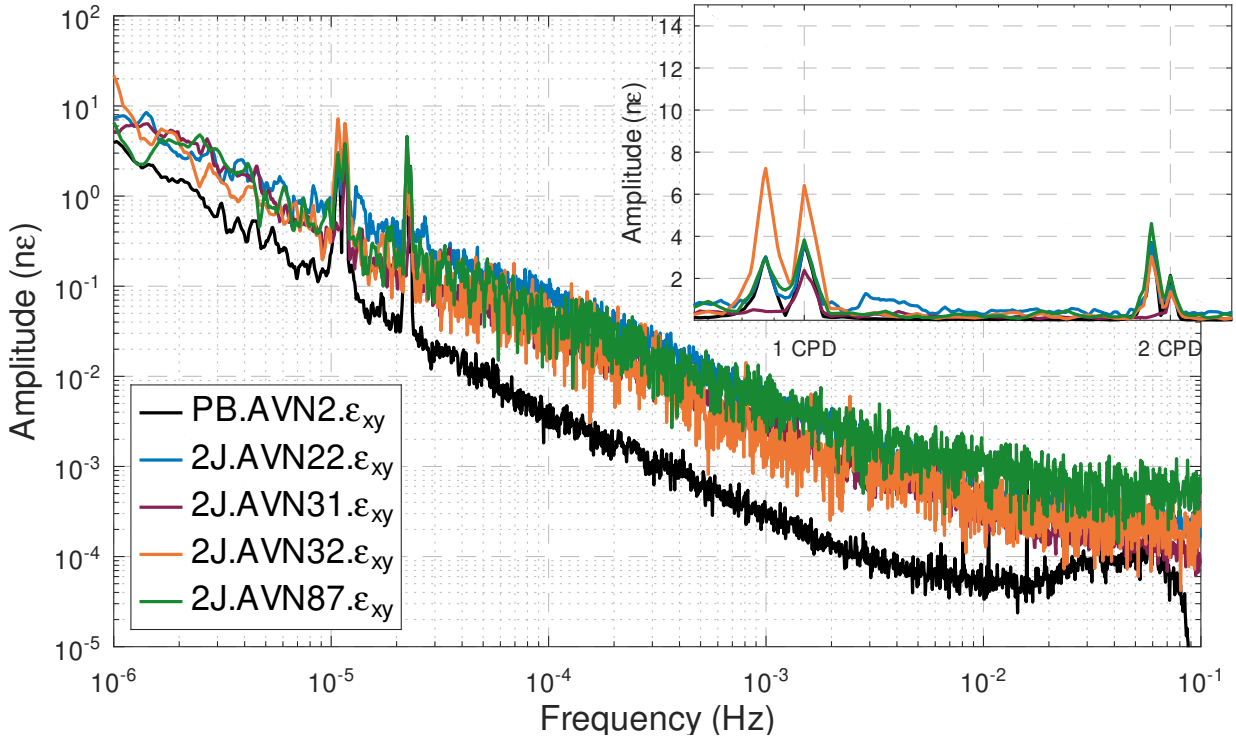

Figure 4.42: Magnitude spectra for the horizontal shear strain component (ϵ_{xy}) as measured by all five strainmeters.

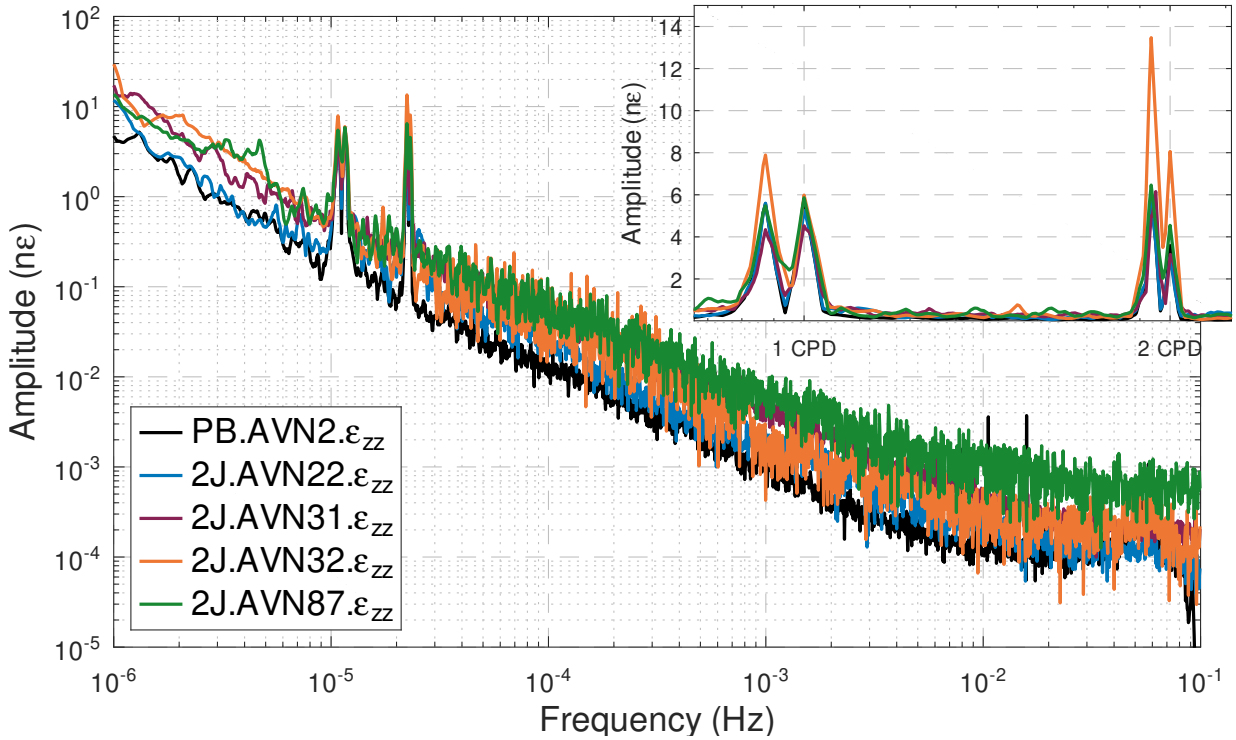

Figure 4.43: Magnitude spectra for the vertical strain component (ϵ_{zz}) as measured by all four TOFS-ER strainmeters and inferred from the GTSM.

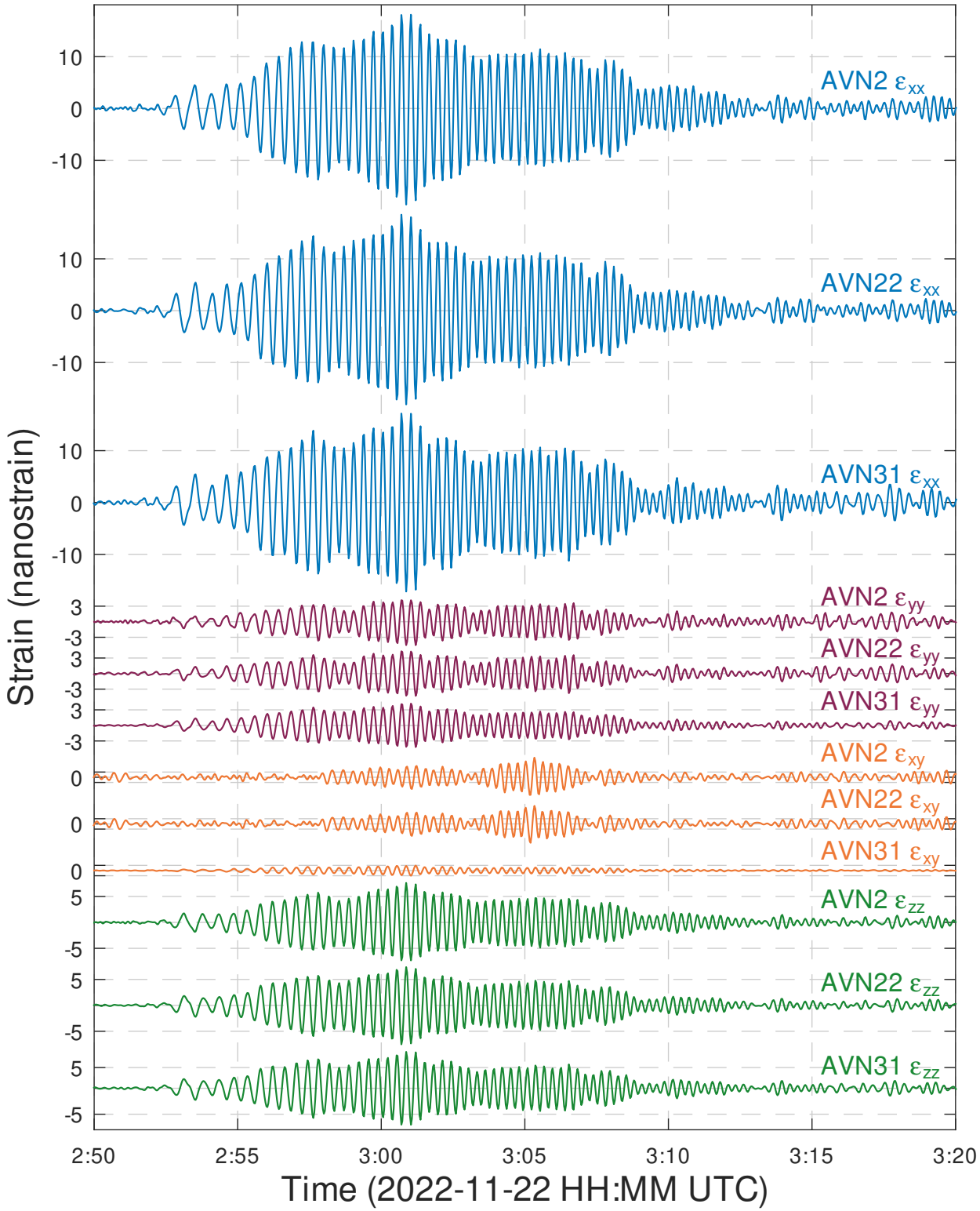

Figure 4.44: Teleseismic waveforms for the shallow GTSM at AVN2, the shallow TOFS at AVN22 and the deep TOFS at AVN31, showing each of the four tensor strain components during the M7.0 earthquake located 18 km SW of Malango, Solomon Islands on November 22, 2022.

be violating the assumption of a traction free elastic half-space that is implicit in the predicted strain tide calculations.

4.3 Reservoir Pressure Monitoring Stations

We constructed four new pressure transmitter boxes for installation at the North Avant Field. Figure 4.45 shows the assembly of these new boxes that will be attached to 5-foot pipes on top of wells WW29, WW32, WW60 and WW87 (Figure 4.1). These are updated versions of the transmitter box installed at WW27 during the previous project DE-FE0023313, which includes a simpler and more robust mounting system for the solar panels.



Figure 4.45: Photograph of the new pressure transmitter boxes to be installed at our demonstration site at the North Avant Field in Oklahoma.

The main improvement to these new transmitter boxes is a new cellular telemetry system. The previous system deployed at WW27 used a RS485-to-WiFi (802.11b/g/n) converter and transmitter that is received by the WiFi system at the AVN3 head node. This system has proven to be unreliable despite the addition of power-hungry amplifiers and cumbersome and expensive directional antennas. The new approach is to use a low power single-board computer and RS485 translator along with a dedicated cellular modem such that instead of having each well transmit its data to the head node, each system will operate autonomously. This has the advantage that each system will continue to collect data if the head node goes down or communications become unreliable, but will also reduce the power consumption of each installation as well as the head node and will require fewer dedicated components.

Three of the four new pressure monitoring stations were deployed during the December 2021 trip, with the final one during March of 2022. This included wells WW29 and WW32 where we have collected data in the past using autonomous data loggers manually deployed on fishing line where we had to reel them in and out of the wellbore to retrieve and collect data. We were also finally able to get a transducer into well WW32 where we have twice failed to deploy an autonomous logger. A new station was added to well WW87 next to one of the new shallow strainmeter installations where we have no previous pressure data. Preparations were made to deploy a fifth station at WW60 where we have collected very high quality data in the past, however, we ran out of time during the December 2021 trip. This station was completed during the March 2022 trip, however, unlike the fluid level gauges other wells (Keller Acculevel 0507.13807.051337.54) this monitors the gas pressure (Keller Preciseline 0308.00302.051949.54).

Pictures of the four new pressure monitoring stations are shown in Figure 4.46. As with the strainmeter installations, the telemetry was unreliable until directional antennas were added in June of 2022.



Figure 4.46: Photographs of the final new pressure monitoring installations at (a) WW29, (b) WW32 (with AVN32 shown in the background), (c) WW60, and (d) WW87 (with AVN87 in the background).

4.4 Upgrades to Existing Infrastructure

We leveraged the September 2019 visit to the North Avant Field, OK to deploy the Two-Axis Optical Fiber Tiltmeter (see 4.1) to make several improvements to our existing infrastructure in preparation for upcoming field tests. This included changes to the solar infrastructure at wells AVN3 and AVN4. The 120 Watt solar panel was removed from AVN4 and added to just below the existing and identical 120 Watt panel at AVN3 (Figures 4.47a and b). A new 150 Watt panel was then installed at AVN4, and both charge controllers were upgraded to new "smart" charge controllers (Morningstar SunSaver MPPT-15L) such that the battery voltage and temperature as well as charge and load currents can be logged along with the other strain, tilt, and weather instruments.

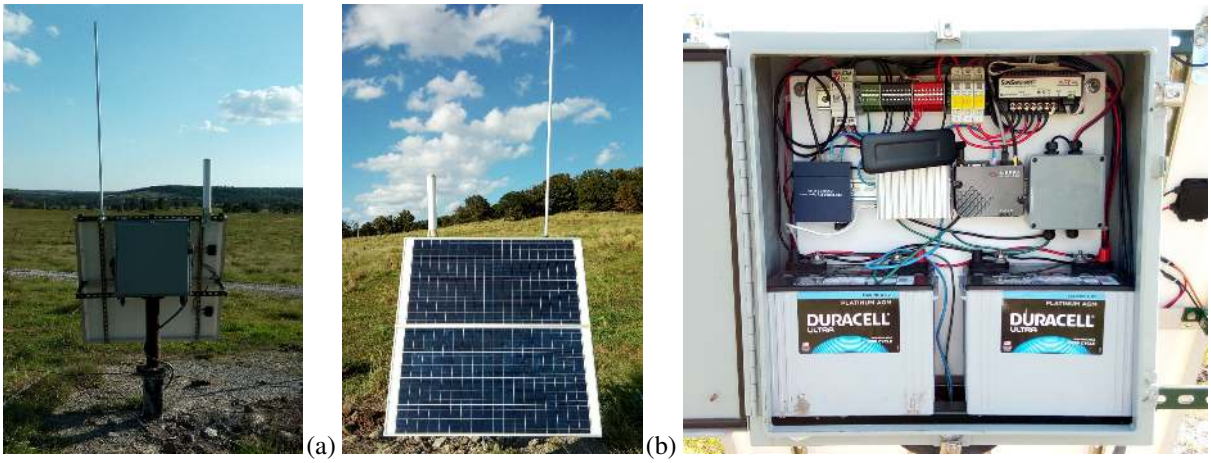

(a) (b) (c)

Figure 4.47: Photographs of communications and power upgrades to the AVN3 head node showing the front (a) and back (b) of the enclosure with the additional solar panel and larger 802.11x wireless antenna. (c) Picture of the inside of the enclosure with the new "smart" solar charge controller and cellular diversity antenna.

The wireless data transmission system on WW27 was replaced during the December 2021 deployment with a standalone data acquisition and cellular telemetry system identical to the other pressure monitoring wells. The existing pressure transmitter (In-Situ Rugged TROLL 200) was found to be defective and was replaced with a Keller Acculevel 0507.13807.051337.54, which is the same transducer used in WW29, WW32 and WW87.

Other upgrades were made to the supporting infrastructure on boreholes AVN3 and AVN4 in June of 2022. This included replacing the station computers and wireless communication systems with much lower powered devices, as well as the same directional antennas. The batteries in AVN3 were also replaced.

References

Agnew, D. C. (2012). SPOTL: Some Programs for Ocean-Tide Loading. Technical Report 954322pg, University of California San Diego Scripps Institution of Oceanography. https://escholarship.org/uc/item/954322pg.

Crawford, W. C. and Webb, S. C. (2000). Identifying and removing tilt noise from low-frequency (< 0.1 hz) seafloor vertical seismic data. *Bulletin of the Seismological Society of America*, 90(4):952–963.

Murdoch, L. C., DeWolf, S., Germanovich, L. N., Hanna, A., Moak, R., and Moysey, S. (2019). Characterizing and interpreting the in situ strain tensor during co2 injection. Technical Report DE-FE0023313, Clemson University, SC (United States).

Riedel, K. S. and Sidorenko, A. (1995). Minimum bias multiple taper spectral estimation. *IEEE Transactions on Signal Processing*, 43(1):188–195.

Welch, P. (1967). The use of fast fourier transform for the estimation of power spectra: a method based on time averaging over short, modified periodograms. *IEEE Transactions on Audio and Electroacoustics*, 15(2):70–73.

CHAPTER FIVE

NUMERICAL SIMULATIONS OF STRAIN IN VARIABLY SATURATED POROUS MEDIA

Contents

5.1 Introduction 5-2
5.2 Analysis of Partially Saturated, Two-phase Porous Media 5-2
5.2.1 Deformation of the solid 5-8
5.2.2 Configuration to represent experiments 5-10
5.3 Application to Strain in the Vadose Zone 5-12
5.3.1 Conceptual Model 5-12
5.3.2 Gravity Drained Sand 5-14
5.3.3 Dry Sand 5-19
5.3.4 Filled to 20 cm depth 5-27

5.1 INTRODUCTION

This report includes several numerical analyses of strain caused by changes in pore fluid pressure. There are slight variations among the analysis, but they all are based on general principles from the theory of linear poroelasticity. In the first section of this chapter we show the basis for the governing equations in partially saturated material where either the gas or liquid phase can be pressurized because this is the most general case and the others can be obtained by simplification. In the second section, the numerical analyses are used to simulate the strain caused by fluctuations of air pressure at the top of a vertical column of partially saturated porous media. The simulations are generally motivated by the potential to use strain in the vadose zone caused by fluctuations in barometric pressure, but they are configured based on experiments conducted in Chapter 9. Some of the results from the simulations described here are used in Chapter 9 to understand the experiments, but a more detailed description of the experiments are described in this chapter.

5.2 ANALYSIS OF PARTIALLY SATURATED, TWO-PHASE POROUS MEDIA

Changes in fluid pressure will deform porous media, and in variably saturated media the deformation can involve changes in the pressure of either water or gas, or both. Variable saturation is common in the vadose zone where water pressure can change due to infiltration or drainage, and air pressure can change due to barometric pressure fluctuations. Deformation caused by this process can be analyzed by determining the total stress, σ_{ij}, in a porous solid containing an effective fluid pressure, P, that is the weighted sum of the air and water pressures. We will assume the fluid mass conservation and the solid deformation are coupled, and the water content in the porous medium can vary from fully to partially saturated conditions. This requires governing equations that satisfy,

1. Mass and momentum conservation of the fluid
2. Constitutive laws relating saturation, pore pressure, elastic modulus and permeability
3. Momentum conservation of the solid
4. Constitutive law relating stresses, strains and pore pressure

Mass conservation of the fluid can be expressed as,

$$-\nabla \cdot q_i = \frac{\partial \phi S_i \rho_i}{\partial t} = S_i \rho_i \frac{\partial \phi}{\partial t} + \phi \frac{\partial S_i \rho_i}{\partial t} \tag{5-1}$$

where subscript i is the phase designation (i = g = gas, i = l = liquid), q_i is the fluid mass flux vector, S_i is phase saturation (volume of phase i per pore volume), ρ_i is density of the fluid (mass/volume of fluid), f is the porosity (pore volume/total volume), t is time. Fluid compressibility can be defined as,

$$\beta_i = \frac{1}{\rho_i} \frac{\partial \rho_i}{\partial P_i} \tag{5-2}$$

and capillary pressure is,

$$P_c = P_g - P_l \tag{5-3}$$

where *P* is pressure. Substituting into equation (3-1) and expanding results in,

$$-\nabla \cdot q_i = S_i \rho_i \frac{\partial \phi}{\partial t} + \phi S_i \beta_i \rho_i \frac{\partial P_i}{\partial t} + \rho_i \phi \frac{\partial S_i}{\partial P_c}\left(\frac{\partial P_g}{\partial t} - \frac{\partial P_l}{\partial t}\right) \tag{5-4}$$

The volumetric gas content, θ_g, (volume gas/volume total) is related to the volumetric water content through,

$$\theta_g = \phi - \theta_l \tag{5-5}$$

and the volumetric water content is related to the capillary pressure using (van Genuchten, 1980),

$$\theta_l = \phi S_r + \phi(1 - S_r)[1 + (\alpha P_c)^n]^{-m} \tag{5-6}$$

$$m = 1 - \frac{1}{n} \tag{5-7}$$

The liquid phase saturation is described as,

$$S_l = \frac{\theta_l}{\phi} \tag{5-8}$$

and the liquid and gas saturations are related by,

$$S_l + S_g = 1 \tag{5-9}$$

Equation (5-6) can therefore become,

$$S_l = S_r + (1 - S_r)[1 + (\alpha P_c)^n]^{-m} \tag{5-10}$$

$$S_g = (1 - S_r)\{1 + [1 + (\alpha P_c)^n]^{-m}\} \tag{5-11}$$

where S_r is irreducible liquid saturation, and *n* and α are fitting parameters. The change of θ_l as a function of capillary pressure is the specific moisture capacity and is expressed as,

$$C_m = \frac{\partial S_l}{\partial P_c} = -\frac{mn}{P_c}(1 - S_r)[1 + (\alpha P_c)^n]^{-m-1}(\alpha P_c)^n \tag{5-12}$$

From equation (5-9) we get

$$\frac{\partial S_g}{\partial P_c} = -\frac{\partial S_l}{\partial P_c} \tag{5-13}$$

Then, equations (5-2) and (5-9) can be combined and expressed as,

$$-\nabla \cdot q_l = S_w \rho_w \frac{\partial \phi}{\partial t} + \theta_l \beta_l \rho_l \frac{\partial P_l}{\partial t} + \rho_l \frac{\partial \theta_l}{\partial P_c}\left(\frac{\partial P_g}{\partial t} - \frac{\partial P_l}{\partial t}\right) \tag{5-14}$$

$$-\nabla \cdot q_g = S_g \rho_g \frac{\partial \phi}{\partial t} + \theta_g \beta_g \rho_g \frac{\partial P_g}{\partial t} + \rho_g \frac{\partial \theta_g}{\partial P_c}\left(\frac{\partial P_g}{\partial t} - \frac{\partial P_l}{\partial t}\right) \tag{5-15}$$

Assuming that the rate of change of the porosity is equal to the volumetric strain rate implies that the mineral grains are incompressible. This results in,

$$\frac{\partial \phi}{\partial t} = \alpha_b \frac{\partial \varepsilon_{kk}}{\partial t} \tag{5-16}$$

where α_b is the Biot-Willis parameter. Expanding, rearranging, and using the specific moisture capacity from (5-12) gives

$$\nabla \cdot q_l + \rho_l(\theta_l \beta_l - C_m)\frac{\partial P_l}{\partial t} = -\rho_l C_m \frac{\partial P_g}{\partial t} - \alpha_b S_l \rho_l \frac{\partial \varepsilon_{kk}}{\partial t} \tag{5-17}$$

$$\nabla \cdot q_g + \rho_g\left(\theta_g \beta_g - C_m\right)\frac{\partial P_g}{\partial t} = -\rho_g C_m \frac{\partial P_l}{\partial t} - \alpha_b S_g \rho_g \frac{\partial \varepsilon_{kk}}{\partial t} \tag{5-18}$$

The first terms on the right-hand side of equations (3-17) and (3-18) are sources that couple the pressure changes in the phases. The second terms account for the changes in storage as a result of deformation.

Equations (5-17) and (5-18) can be simplified for special cases. This will provide simplified expression for specific applications, and it can serve as a check for the general expressions above. The first case to be considered will assume the porous medium is saturated, so $C_m = 0$ and $S_w = 1$, while the changes in the gas phase are ignored. Equation (5-17) becomes,

$$\nabla \cdot q_l = -\alpha_b \rho_l \frac{\partial \varepsilon_{kk}}{\partial t} - \rho_l \phi \beta_l \frac{\partial P_l}{\partial t} \tag{5-19}$$

or,

$$\nabla \cdot q_l = -\alpha_b \rho_l \frac{\partial \varepsilon_{kk}}{\partial t} - \rho_l \frac{1}{M} \frac{\partial P_l}{\partial t} \tag{5-20}$$

where the Biot Modulus for a porous medium with incompressible grains is,

$$M = \frac{1}{\phi \beta_l} \tag{5-21}$$

Equation (3-20) is commonly used to analyze fully coupled poroelastic problems in saturated porous media (Wang, 2000, eq. 4.65; Bai and Elsworth, 2000 eq. 2.32; Cheng, 2016).

Another special case occurs when the fluid pressures are coupled from the volumetric strain. The porous media is assumed to deform in response to local changes in fluid pressure, so the rate of change of porosity can be approximated as,

$$\frac{\partial \phi}{\partial t} = \left(\frac{1}{K} - \frac{1}{K_s'}\right) \frac{\partial P_l}{\partial t} \tag{5-22}$$

where K is the drained bulk modulus of the porous material, and K_s' is the bulk modulus of the solid grains. Substituting,

$$\nabla \cdot q_l + \rho_l (\theta_l \beta_l - C_m) \frac{\partial P_l}{\partial t} = -\rho_l C_m \frac{\partial P_g}{\partial t} - S_l \rho_l \left(\frac{1}{K} - \frac{1}{K_s'}\right) \frac{\partial P_l}{\partial t} \tag{5-23}$$

and grouping terms that depend on the fluid change results in,

$$\nabla \cdot q_l + \rho_l \left(S_w \left[\phi \beta_l + \left(\frac{1}{K} - \frac{1}{K_s'}\right)\right] - C_m\right) \frac{\partial P_l}{\partial t} = -\rho_l C_m \frac{\partial P_g}{\partial t} \tag{5-24}$$

Recognizing that the term in square brackets is the unconstrained specific storage, $S_{\sigma l}$, for the liquid phase gives,

$$\nabla \cdot q_l + \rho_l (S_w S_{\sigma l} - C_m) \frac{\partial P_l}{\partial t} = -\rho_l C_m \frac{\partial P_g}{\partial t} \tag{5-25}$$

and,

$$S_{\sigma l} = \phi \beta_l + \left(\frac{1}{K} - \frac{1}{K_s'}\right) \tag{5-26}$$

A similar expression can be developed for the gas phase. This can be expressed as,

$$\nabla \cdot q_g + \rho_g \left(S_g S_{\sigma g} - C_m\right) \frac{\partial P_g}{\partial t} = -\rho_g C_m \frac{\partial P_l}{\partial t} \quad (5\text{-}27)$$

$$S_{\sigma g} = \phi \beta_g + \left(\frac{1}{K} - \frac{1}{K_s'}\right) \quad (5\text{-}28)$$

Equation (5-25) is a form of Richard's equation that includes an expression related to the change in air pressure on the right-hand side. Ignoring changes in gas pressure gives the mass conservation expression used in the Richard's equation. Equations (5-25) through (5-28) describes the fluid mass conservation in a two-phase system that includes storage changes due to local pressure changes. It omits storage changes from non-local stress changes. These effects are negligible for this problem because of the high compressibility of the pore fluid.

The fluid flow also needs to be considered in this analysis. Conservation of momentum gives a form of Darcy's Law written in terms of mass flux is described as,

$$q_i = -\frac{\rho_i k k_{ri}}{\mu} \nabla (P_i + \rho_i g z) \quad (5\text{-}29)$$

where k is permeability, k_r is relative permeability, z is the elevation, μ is viscosity, and g is acceleration due to gravity. Relative permeabilities for each phase are characterized using (van Genuchten, 1980) and are written as,

$$k_{rl} = S_e^{\frac{1}{2}} \left[1 - \left(1 - S_e^{\frac{1}{m}}\right)^m\right]^2 \quad (5\text{-}30)$$

$$k_{rg} = S_g^{\frac{1}{2}} \left(1 - S_e^{\frac{1}{m}}\right)^{2m} \quad (5\text{-}31)$$

$$S_e = \frac{S_l - S_r}{1 - S_r} = \frac{\theta - \theta_r}{1 - \theta_r} \quad (5\text{-}32)$$

where S_l the liquid saturation, S_g is the gas saturation, and S_e is the effective liquid saturation.

The equations listed above can be written in terms of diffusion. Using a form of equations (5-17) and (5-18) that includes the specific storage as in equation (5-25) and substituting into equation (5-29), this produces,

$$-\nabla \cdot \frac{\rho_l k k_{rl}}{\mu} \nabla (P_l + \rho_l g z) + \rho_l (S_w S_\sigma - C_m) \frac{\partial P_l}{\partial t} = -\rho_l C_m \frac{\partial P_g}{\partial t} \quad (5\text{-}33)$$

$$-\nabla \cdot \frac{\rho_g k k_{rg}}{\mu} \nabla \left(P_g + \rho_g g z\right) + \rho_g \left(S_g S_\sigma - C_m\right) \frac{\partial P_g}{\partial t} = -\rho_g C_m \frac{\partial P_l}{\partial t} \quad (5\text{-}34)$$

The storage terms can then be divided out and this results in,

$$-\nabla \cdot \frac{k k_{rl}}{\mu (S_w S_\sigma - C_m)} \nabla (P_l + \rho_l g z) + \frac{\partial P_l}{\partial t} = -\frac{C_m}{(S_w S_\sigma - C_m)} \frac{\partial P_g}{\partial t} \quad (5\text{-}35)$$

$$-\nabla \cdot \frac{k k_{rg}}{\mu (S_g S_\sigma - C_m)} \nabla \left(P_g + \rho_g g z\right) + \frac{\partial P_g}{\partial t} = -\frac{C_m}{(S_g S_\sigma - C_m)} \frac{\partial P_l}{\partial t} \quad (5\text{-}36)$$

This system has the form of non-homogeneous diffusion equations with the terms on the right side serving as source terms written as,

$$-\nabla \cdot D_l \nabla (P_l + \rho_l g z) + \frac{\partial P_l}{\partial t} = -\Gamma_l \quad (5\text{-}37)$$

$$-\nabla \cdot D_g \nabla \left(P_g + \rho_g g z\right) + \frac{\partial P_g}{\partial t} = -\Gamma_g \quad (5\text{-}38)$$

where the diffusivities of the liquid and gas pressure are respectively,

$$D_l = \frac{k k_{rl}}{\mu (S_w S_\sigma - C_m)} = \frac{k k_{rl}}{\mu (S_w S_\sigma + |C_m|)} \quad (5\text{-}39)$$

$$D_g = \frac{k k_{rg}}{\mu (S_g S_\sigma - C_m)} = \frac{k k_{rg}}{\mu (S_g S_\sigma + |C_m|)} \quad (5\text{-}40)$$

The fluid pressure coupling terms on the right side are,

$$\Gamma_l = \frac{C_m}{(S_w S_\sigma - C_m)} \frac{\partial P_g}{\partial t} \quad (5\text{-}41)$$

$$\Gamma_g = \frac{C_m}{(S_g S_\sigma - C_m)} \frac{\partial P_l}{\partial t} \quad (5\text{-}42)$$

5.2.1 Deformation of the solid

Momentum conservation of the solid assumes quasi-static conditions, so

$$\frac{\partial \sigma_{ij}}{\partial x_i} = -F_i \tag{5-43}$$

where σ_{ij} is the total stress tensor, and F_i is the body force vector. The *ij* subscript assumes Einstein notation where repeated subscripts indicate summation.

The total stress depends on the effective stress on the solid, σ_{eij} and the effective pore pressure, P (Borja, 2006 eq. 3.42)

$$\sigma_{ij} = \sigma_{eij} - \alpha P \tag{5-44}$$

where the Biot-Willis parameter is,

$$\alpha = 1 - \frac{K}{K_s} \tag{5-45}$$

With K as the bulk modulus of the porous material and K_s as the bulk modulus of the solid grains, and α=1 in soils. The sign convention is that positive stress is tensile and negative stress is compressive. According to equation (5-44), an increase in P will cause the effective stress to become tensile (increase) when the total stress remains unchanged.

The effective pressure in the unsaturated zone is weighted between the water and the air pressures (Borja, 2006 eq. 3.24 and Lu et al., 2010 eq. 18). This can be written as,

$$P = S_e P_l + (1 - S_e) P_g \tag{5-46}$$

where the effective saturation is defined in equation (5-32). Under saturation conditions, equation (5-44) reduces to the Biot effective stress to,

$$\sigma_{ij} = \sigma_{eij} - \alpha P_w \tag{5-47}$$

and can be used in saturated linear elastic poroelasticity (Wang, 2000; Cheng, 2006).

Hooke's Law relates to stress to strain, and pressure to displacement. This can be expressed as,

$$\sigma_{ij} = 2G\varepsilon_{ij} + \lambda \varepsilon_{kk} \delta_{ij} - \alpha P \delta_{ij} \tag{5-48}$$

where G is the shear modulus, ε_{kk} is the volumetric strain, and δ_{ij} is the dirac operator. The Lame constant, λ, and G are related to other elastic properties using

$$\lambda = \frac{E\nu}{(1+\nu)(1-2\nu)} \tag{5-49}$$

$$G = \frac{E}{2(1+\nu)} \tag{5-50}$$

where E is Yonng's Modulus and ν is Poisson's ratio. The strains are related to displacement gradients as,

$$\varepsilon_{xx} = \frac{\partial u}{\partial x}; \varepsilon_{yy} = \frac{\partial v}{\partial y}; \varepsilon_{zz} = \frac{\partial w}{\partial z}; \varepsilon_{xy} = \frac{1}{2}\left(\frac{\partial u}{\partial y} + \frac{\partial v}{\partial x}\right); \varepsilon_{yz} = \frac{1}{2}\left(\frac{\partial v}{\partial z} + \frac{\partial w}{\partial y}\right); \varepsilon_{zx} = \frac{1}{2}\left(\frac{\partial w}{\partial x} + \frac{\partial u}{\partial z}\right)$$

(5-51)

The volumetric strain is

$$\varepsilon_{kk} = \varepsilon_{xx} + \varepsilon_{yy} + \varepsilon_{zz} \tag{5-52}$$

The elastic properties of the soil vary with the water content. According to Lu and Kaya (2012), Young's modulus can be described as a power function expressed as,

$$E = E_d + (E_w - E_d)\left(\frac{\theta-\theta_d}{\theta_w-\theta_d}\right)^{m1} \tag{5-53}$$

where E_w is Young's modulus under wet conditions characterized by the moisture content θ_w, and E_d is Young's modulus at moisture content θ_d. The parameter ml is a parameter that depends on the soil. According to Lu and Kaya, $ml < 0.3$ is for sand, $0.3 < ml < 1.1$ is for silt, and $ml > 0.8$ is for clay.

Poisson's ratio also changes with saturation. According to Thota et al. (2021), Poisson's ratio can be described as,

$$\nu = \nu_d + (\nu_s - \nu_d)\left[\left\{\left(\frac{(1+(\alpha P_c)^n)^{\frac{1}{n-1}}}{S_{fun}}\right)^{n_1}\right\}^{\frac{1}{n_1-1}}\right] \tag{5-54}$$

where n and α are parameters in the water retention function in equation (5-6), v_d and v_s are the Poisson's ration under dry and saturated conditions, and n_1 and S_{fun} are fitting parameters introduced by Thota et al. (2012). Thota et al. (2012) used data describing Poisson's ratio as a function of water content to estimate parameters for different soil textures. Average values are v_d=0.19, v_s=0.38, S_{fun}=0.3, and n_1=3.7.

The body force for this problem is the total unit weight of the soil. It acts in the -z direction and is written as,

$$F_z = \left(\rho_b + \theta_l \rho_l + \theta_g \rho_g\right) g \qquad (5\text{-}55)$$

where ρ_b is the dry bulk density of the soil, θ_l and θ_g are the volumetric fluid contents, and ρ_l and ρ_g are the liquid and gas densities. The dry bulk density is the mass of the solid grains of soil per total volume of soil.

5.2.2 Configuration to represent experiments

Solving the governing equations requires configuring a geometry and selecting boundary and initial conditions that represent the experiments.

5.2.2.1 Geometry

The column using in the experiments is represented as a rectangular domain 0.2 m in the horizontal and 1 m in the vertical direction. The analysis is done in 2D cartesian coordinates.

This geometry was assumed in order to account for friction on the walls of the column. Preliminary analyses were conducted using 1D geometry, which would be appropriate for a half space with a uniformly distributed load. However, results from the 1D analysis show that the strains increase with depth. This occurs because the surface load causes strains that are independent with depth. However, the magnitude of the strain decreases with depth in the experiments. The geometry of the simulation was expanded to 2D in order to include friction on the walls of the column. The strain in the 2D simulation that included friction decreased with depth, so this geometry was adopted.

5.2.2.1.1 Boundary conditions

The problem requires three sets of boundary conditions, one for each of the gas and liquid fluid phases, and another for the displacements. Boundary conditions are required on each of the four sides of the rectangular domain. The four scenarios considered in the analysis (Dry, Drained, Filled to 35 cm depth, and Filled to 20 cm depth) differ by their boundaries and initial conditions.

Top boundary: Gas: zero fluid pressure initial, variable pressure during the transient; liquid: no flow; solid: zero total stress

Bottom boundary: Gas: no flow; liquid: No flow for dry initial condition, specified pressure head for other scenarios: P=0.01 for drained, p=0.65 m for filled to 35 cm depth, p=0.8 m for filled to 20 cm depth; solid: zero displacement.

Right and left side: Gas: no flow; liquid: no flow; solid: zero displacement.

Preliminary analyses were evaluated that considered a roller-type boundary (zero normal displacement) on the right and left side. This type of boundary condition could represent a case where the sand was free to slip along the wall of the column. The strain increased with depth when this boundary condition was used, but the strain was observed to decrease with depth. The strain decreases with depth when the zero displacement condition was used, which implies that there were negligible slip between the sand and infinitely stiff wall of the column.

5.2.2.1.2 Initial Conditions

It was assumed that the fluid and solid were in static equilibrium at the start of the simulation.

5.2.2.1.3 Parameters

The parameters used in the simulation were estimated based on independent tests or assumed from published values. The permeability was increased by a factor of three from the compared lab tests to better match the observed pressures, and slight adjustments were made to the function describing the elastic modulus. Other parameters were unchanged from their initial estimate.

Table 1: Parameters used to describe fluids and solid in the simulation	
Young's Modulus	
Dry, E_d	12 MPa
Saturated, E_s	20 MPa
Elastic modulus power, --	0.25
Poisson's ratio	
n_d, Dry	0.19
n_s, Saturated	0.38
S_{fun}	0.3
n_l	0.37
Permeability, k	8×10^{-11} m^2
Water retention	
Saturated water content, q_s	0.28
Residual water content, q_r	0
Van genuchten, a	4x10-4 (1/Pa)
Van genuchten, $_n$	4
Fluid properties	
r_l	1000 kg/m^3
r_g	$(P_g+P_{atm})/(RT)$
m_g	1.8×10^{-5} Pa s
m_l	1.0×10^{-3} Pa s

5.2.2.2 Solution Method

The governing equations and configuration outlined above were solved using the Galerkin finite element method. The rectangular problem domain was discretized using a mapped mesh with 12 columns and 800 rows. The resulting system of equations was solved using the Multifrontal Massively Parallel sparse direct Solver (MUMPS) (Amestoy et al., 2000).

The simulations included several scenarios that involved different initial conditions and material properties. Each simulation was solved in four steps with adjustments for each scenario.

1. Steady solution of the initial static fluid pressures. The lower boundary condition was set to either no-flow, or specified pressure depending on the scenario.

2. Steady solution of the initial static pressure air pressure and displacements using the static fluid pressure as input. This gives the equilibrated initial conditions.

3. Transient solution of the air and water pressures using a periodic air pressure boundary condition.

4. Transient solution of the displacements and strains using the air and water pressures.

The solution approach assumes a one-way coupling of the fluid pressure to strain. The back coupling from the strain to the fluid pressure is included using a specific storage term.

5.3 APPLICATION TO STRAIN IN THE VADOSE ZONE

The analyses outlined in the preceding section cover the conditions used in experiments throughout the report. Many of the simulations elsewhere in the report assume saturated conditions to simulate tests conducted in aquifers and reservoirs. Chapter 14 describes tests conducted in partially saturated conditions where the air pressure is constant. This case requires using constitutive models that describe how properties vary with pore pressure, as outlined above, but it only requires simulating one pore pressure. The experiments in Chapter 13 describe conditions where the air pressure in the vadose zone are changing with time and space, and this causes changes in water pressure. Simulating these experiments requires using all the conditions outlined above, with the other simulations following as simplifications.

This following subsection describes the simulation of strain in the vadose zone caused by changes in air pressure, following the conditions described in Chapter 13. The simulations described here provide additional context and sensitivity analyses for the experiments in Chapter 13.

5.3.1 Conceptual Model

The boundary conditions were adjusted to develop simulations that show the components of strain in the conceptual model. This involved conducting a simulation where the boundary load was omitted, but the internal pressure was included. This simulation is called “pressure load only.” Another set of simulations was done by omitted the coupling between the pore pressure and the strain. These simulations are called “surface load only.” Additional simulations include the complete analysis where both the pressure and surface loads are included.

Two sets of the conceptual model simulations were conducted, one for uniform dry sand material and another that include partial fill to 65 cm of depth. The results show that total vertical strain results from contributions from the surface load and pressure load (Figure 3.2), as outlined in the conceptual model (Figure 5.1). The effects of the two components are most clearly seen when the sand is dry and at 0.2 m depth (Figure 5.2a). As the pressure on the surface increase, the surface load component of the vertical strain decreases (compresses). The magnitude of this

component is fluctuating between +/- 0.4 με while the pressure fluctuates between +/- 25 Pa. The pressure load component of strain is delayed behind the pressure wave and is slightly less than the surface component. The surface load component dominated the sign and the total vertical strain compresses as a result of the pressure wave. It is also lagged behind the pressure wave by approximately 65 ms.

The phase of the two components moves closer together at 0.4 m and they are nearly in phase from one another at 0.6 m (Figure 5.2b and Figure 5.2c). The magnitude of the strain from surface load also decreases with depth. This is because the friction that is occurring from the walls of the column is increasing as depth increases. In addition, the pressure load component had a sign change at these depths and begins to compress from a pressure increase like the surface component does. The resulting total strain at 0.4 m is approximately half of that from the 0.2 m depth while the resulting total strain at 0.6 m is barely fluctuating at all.

The surface load and pressure load components behave similarly even when there is water present in the sand (Figure 5.2). The overall effect from the addition of water into the pore space is that the two components are less out of phase from one another. In addition, both strain components compress when the surface air pressure increases and tension when the pressure decreases. The largest strain is still occurring closest to the surface at 0.2 m and decreases to nearly zero by 0.6 m on the column.

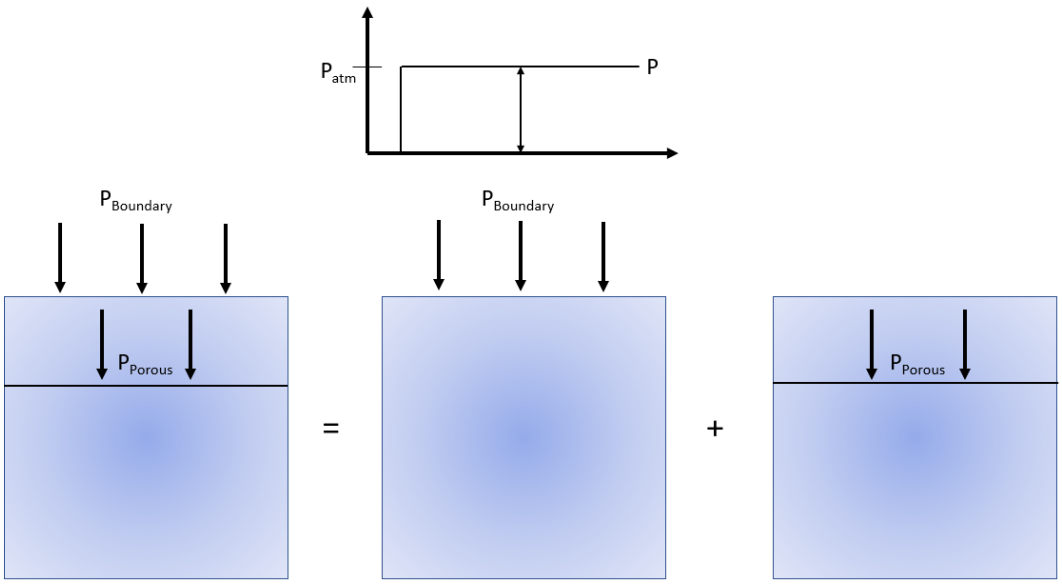

Figure 5.1: Conceptual model of the barometric pressure that is loading the ground surface and propagating in the subsurface. The strain caused by the two components is added to get the total strain.

These components explain the vertical strain that is observed from the simulations and the measured laboratory data as well. The data from these components show that the strain from the surface load is only decreasing with depth due to the friction on the walls of the column. In

addition, the phase delay between the surface pressure fluctuations and the vertical strain is the combination of the two components, and it shows that the strain is lagged behind the pressure in these cases. This shows how the vertical strain can sometimes appear to be preceding the air pressure wave. Because of this, it can be difficult to look at the recorded strain signal by itself and immediately interpret what is happening in the subsurface. It is valuable to know the effects of both of these components rather than simply the raw vertical strain signal that is measured.

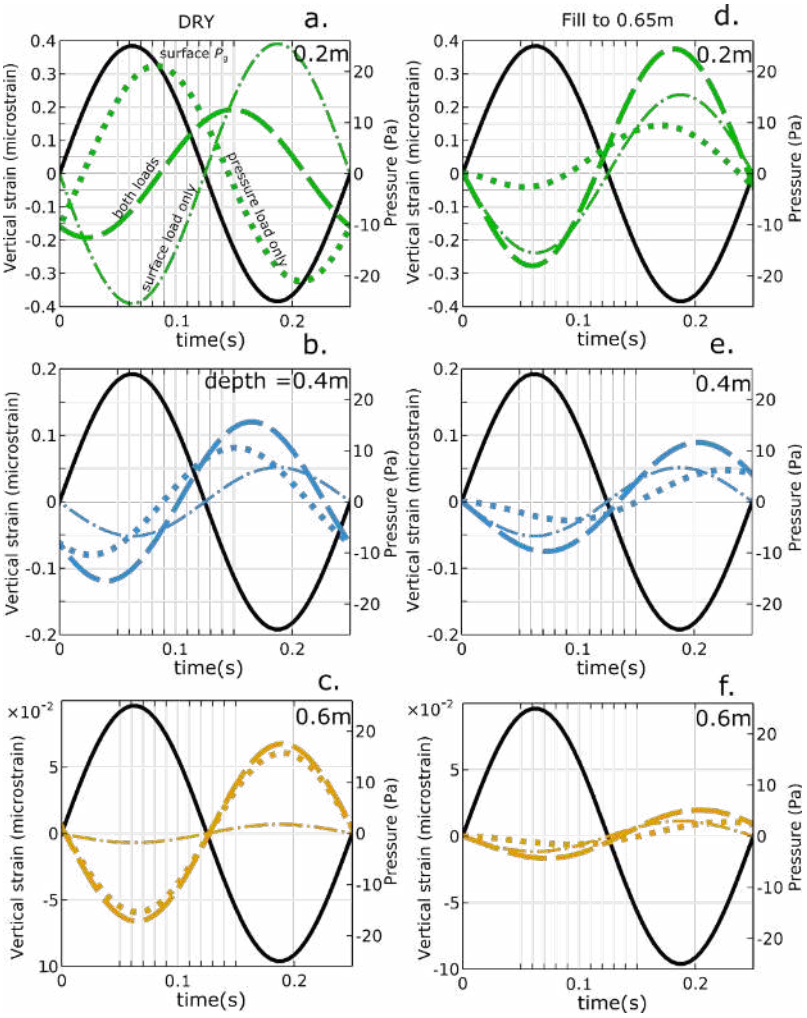

Figure 5.2: Components of the vertical strain from an air pressure fluctuation on the surface. The black solid line is the pressure at the ground surface, dashed-dot line is the component from surface loading only, the dotted line is the pressure load in the porous media only, and thick dashed line is the total from those two components.

5.3.2 Gravity Drained Sand

Sand that has been saturated and drained by gravity is considered the baseline analysis for the simulations. This section will detail the initial conditions and effects from the addition of a periodic signal.

5.3.2.1 Initial Conditions

A steady-state simulation was conducted to define the initial conditions for the transient model. The pressure head at the bottom of the model was assumed to be 0.01 m, which causes the bottom of the model to be saturated (Figure 5.3). The saturation zone extends up to a depth of 0.9m, so the air entry pressure head is approximately 0.1m. Gravity drainage leaves a residual saturation in the pore space. The water content is largest at the bottom of the column where the sand is saturated and decreases to nearly zero at the top (Figure 5.3a). There is an inverse relationship between the air and water content as functions of depth in this condition. The air content is largest at the top of the column as a result. This relationship is similar for the water and gas saturation (Figure 5.3b). The air saturation that is in the sand decreases to zero at about 0.90 m whereas the water saturation reaches one at the same location.

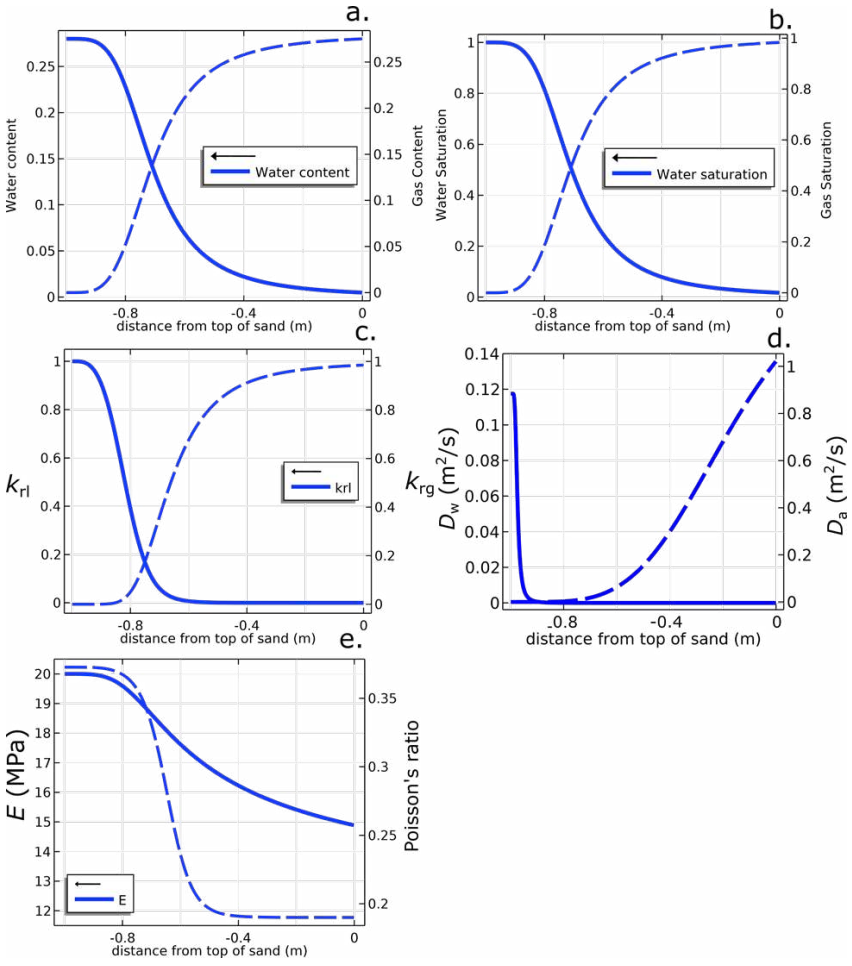

Figure 5.3: Initial conditions as functions of depth for the gravity drained scenario a.) water content, b.) water and gas saturation, c.) water and gas permeability, d.) pressure diffusivity, and e.) Youngs Modulus and Poisson's ratio.

The changes in water/gas content and the saturations also affect the relative permeabilities of the water and air (Figure 5.3c). The relative permeabilities affect the rate at which fluid mass moves through the porous media. The gas-phase relative permeability

gradually decreases from 1.0 at the top to a value of essentially zero at approximately 0.85 m depth, slightly above the top of the capillary fringe. The liquid-phase relative permeability is negligible above 0.6 m of depth, and it sharply increases to 1.0 between 0.6 < depth < 0.9 m. The gradual decrease in the air permeability with depth follows the same trends as the air content and air saturation. The liquid-phase permeability also increases as the water saturation and water content increase.

The water and air diffusivities control the rates at which fluid pressure moves through the porous media. This is important because the fluid pressures cause strain. The air diffusivity (Figure 3.3d) is zero at the bottom of the column and then increases nearly linearly above a depth of 0.75 m. It reaches a maximum of approximately 1.0 m^2/s at the top of the column where the sand is dry. The water diffusivity is greatest at the bottom of the column, where it is approximately equal to the air diffusivity at the top of the column (Figure 5.3d) The water diffusivity sharply decreases above approximately 0.9 m of depth. This is because the water content decreases above this same depth, causing the diffusivity to decrease to zero as well.

The Young's Modulus (E) ranges from 20 MPa at the bottom of the column to approximately 15 MPa at the top. The sand material is the stiffest at the bottom of the column when it is 20 MPa, and it softens upward. Poisson's ratio follows a similar trend by increasing from approximately 0.175 to 0.375 as depth on the column increases. The changes in elastic properties are because the properties are assumed to be function of water content, as outlined above.

5.3.2.2 Profiles as functions of time

Pressure and strain data were measured along the length of the column, so data from the analysis were plotted to simulate the expected distribution during the experiments. The air pressure fluctuates by +/- 25 Pa at the surface and the magnitude of the variability decreases to essentially zero at the bottom of the column (Figure 5.4a). At each time, the pressure change is greatest at zero depth and diminishes to zero downward. The pressure is roughly zero at the start of the cycle and increases (blue-green-red) and then decreases (red, cyan, purple, yellow, black) and then increases again to complete the cycle. This lag of an internal peak within the column indicates that the wavelength of the pressure variation is at least several times longer than the column.

The pattern in the change in water pressure (Figure 5.4b) is similar to the change in the air pressure (Figure 3.4a). This occurs because the changing air pressure affects the water pressure. Both cases show that the greatest amount of change is occurring at the top of the column and the changes are decreasing as depth increases. There is zero change in both air and water pressure at 0.8 cm and deeper on the column.

Strain is affected by both the air and water pressures, and the contribution from each of the pressures is weighted by the saturation. The distribution of the weighted pressure resembles that of the air pressure (Figure 5.4c). The greatest changes are occurring closer to the top of the column and fluctuate between +/- 25 Pa. The weighted pressures diminish to zero at 0.8 m on the column.

Fluctuations in the air pressure change the water saturation (Figure 5.4d). In general, increasing air pressure decreases the saturation. The changes in saturation are small, however, the changes in pressure are small for this example (+/- 25 Pa). For comparison, the daily

variation in barometric pressure is often 250 Pa or more. Nevertheless, the simulations indicate that the air pressure variations of 25 Pa cause the water saturation to change by roughly 10^{-5}.

The vertical strain is affected by the variations in pressure (Figure 5.4e). Increases in pressure at the beginning of the cycle (blue-green-red) cause compressive strain (negative). The magnitude of the comparison increases at the beginning of the cycle (blue-red), but then it decreases at the top of the column (green-red). The strain becomes tensile (positive) when the pressure at zero depth decreases (blue-purple-yellow). The vertical strain is affected by both the pressure at zero depth and throughout the column. An increase in pressure at zero depth causes compressive strain (decrease, or contraction), whereas an increase in pressure at a point within the column causes tensile strain (increase, or expansion). Moreover, the contraction resulting from a large compressive strain at one location can cause expansion in the form of tensile strain in neighboring regions. The resulting strain profile is a combination of these effects.

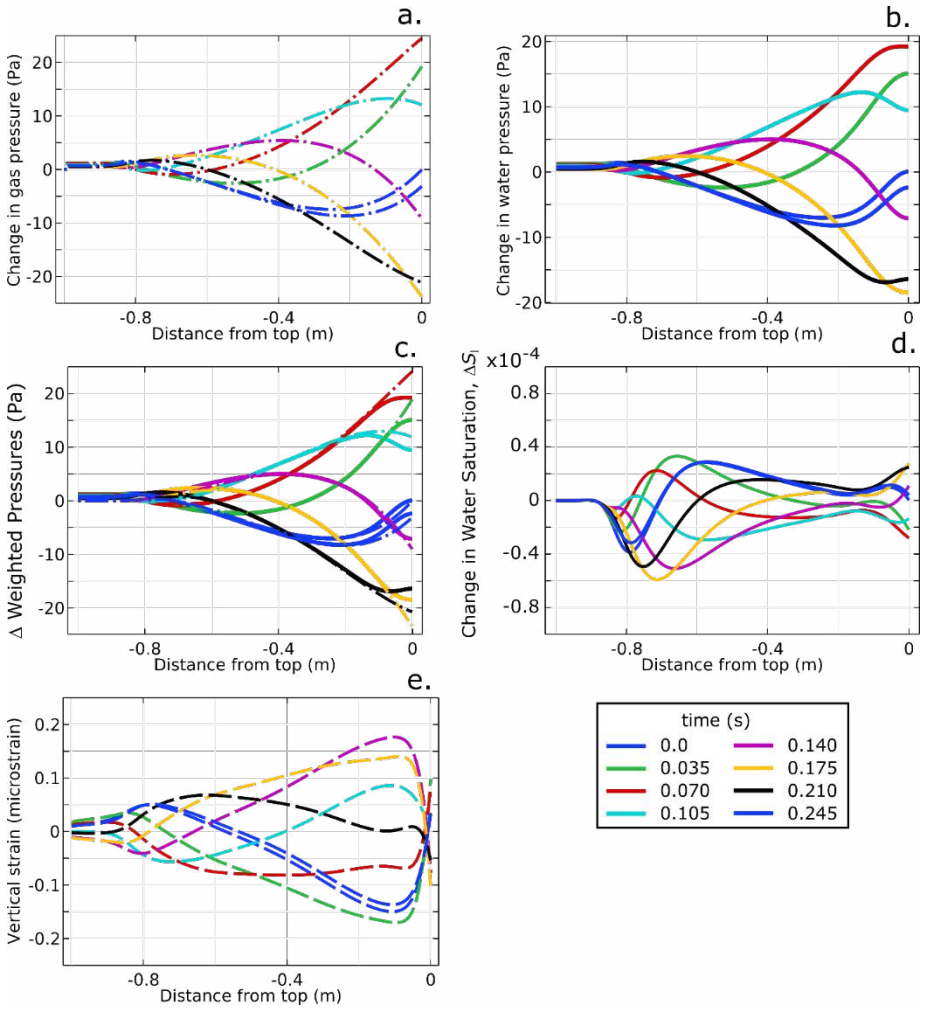

Figure 5.4: Pressure, saturation, and strain as function of distance from the top of the sand for different times during one period (0.25s) of a pressure variation (colors shown on key). a.) change in gas pressure; b.) change in water pressure; c.) change in weighted pressures; d.) change in water saturation; e. vertical strain.

5.3.2.3 Time series as functions of depth

A periodic air pressure signal was applied to the top of the sand while the saturation varied from the gravity drained scenario (Figure 5.5a). The largest fluctuations are between approximately +/- 25 Pa in the head space just above the sand level (black line). As the signal travels throughout the sand, the magnitude of the fluctuations decreases with depth and drops to approximately +/- 2.5 Pa at 0.6 m on the column (yellow line).

The periodic signal induces a response from the vertical strain in the sand (Figure 5.5b). An increase in the pressure causes the vertical strain to decrease, or compress, while a decrease in the pressure leads to positive strain, or tension. The magnitude of the vertical strain follows a similar pattern to the air pressure and decreases with depth (Figure 5.5c). The largest fluctuation is at 0.1 m depth and is between approximately +/- 0.15 με. Additionally, the smallest fluctuations are deeper on the column at 0.6 m depth and are between +/- 0.07 με.

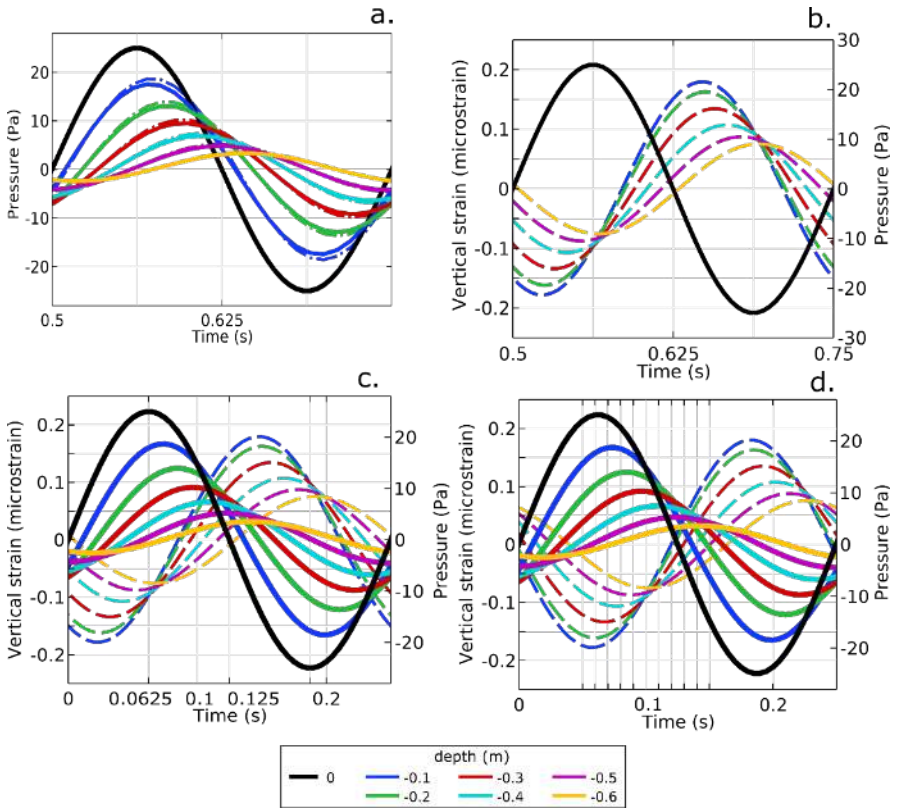

Figure 5.5: Time series of pressure and vertical strain at depths along the center of the column. Periodic fluctuation of air pressure at the top of the column with amplitude of 25 Pa and period of 0.25s (Thick black lines). Data from the third pressure cycle (0.5<t<0.75s). a.) gas (dash-dot) and water (solid line) pressures. B.) vertical strain (dashed) c.) pressure and strain at different depths; d.) pressure and strain with time scale for the strain advanced by 35ms to account for synchronization of the data acquisition system.

There is also an offset, or a lag time between the induced air pressure signal and the observed vertical strain. Figure 5.5c is showing that the vertical strain is preceding the air pressure wave by approximately 40 ms. The increase in pressure on the surface is being perceived at depth in the sand before the pressure wave arrives at the same depth, causing the strain to appear to occur before the air pressure signal. This is the signal predicted to occur in the experiments. However, there was synchronization delay between the data acquisition that measures the pressure and the system the system that measures the strain, and this added an offset in the relative timing of the two signals. We estimate this delay to be approximately 35 ms. This time was added to the time scale (Figure 5.5c) in an effort to represent the results in the experiments.

5.3.3 Dry Sand

Simulations also included a scenario where the sand was completely dry, and the water content was zero. This section will outline the effects of the dry sand in both the initial conditions and the addition of the periodic signal.

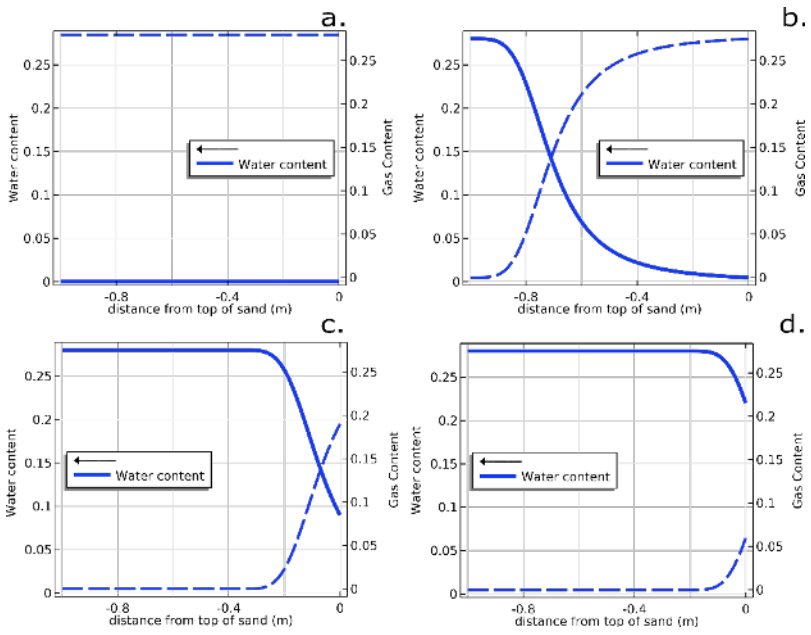

Figure 5.6: Initial water content as a function of depth for different initial conditions. a.) dry. b.) gravity drainage. c.) PZP at d =0.35m. d.) PZP at d = 0.2m.

5.3.3.1 Initial Conditions

The dry sand presented a unique case when analyzing the effects of the water content and the vertical strain. Unlike the gravity drained scenario, the water content and the water saturation are both zero (Figure 5.6a and Figure 5.7a). Without the injection of the water into the sand, the gas content is uniform at the assigned 0.28 value and the gas saturation value is 1.0. The pore space is completely filled with the air and there is no water changing the gas saturation. This relationship also holds true

for the relative permeabilities as a function of depth (Figure 5.8a). Without any water present in the sand, the relative permeability of the liquid was zero. Because the sand was completely dry, the gas permeability remains at 1.0 initially and will when the periodic signal is applied as well. As long as the sand is dry, the relative permeability of the water will remain zero.

Additionally, the water diffusivity is zero, and the air diffusivity is uniform at approximately 1.45 m^2/s (Figure 5.8a). The air diffusivity is greater when the sand is dry than when the sand had been filled and drained by gravity. It only reached a maximum of 1.0 m^2/s when the sand was partially saturated, and the water content was varying with depth. The air diffusivity was lower in that scenario because the varying saturation did not allow the air to diffuse as quickly throughout the sand. Lastly, because the saturation is not changing or varying throughout the sand column, the elastic properties are uniform as well (Figure 5.10a). The Young's Modulus is 12 MPa and the Poisson's Ratio remains constant at 0.16. Both of these parameters are affected by the water content, and they are lower and constant because there is no water present in the sand.

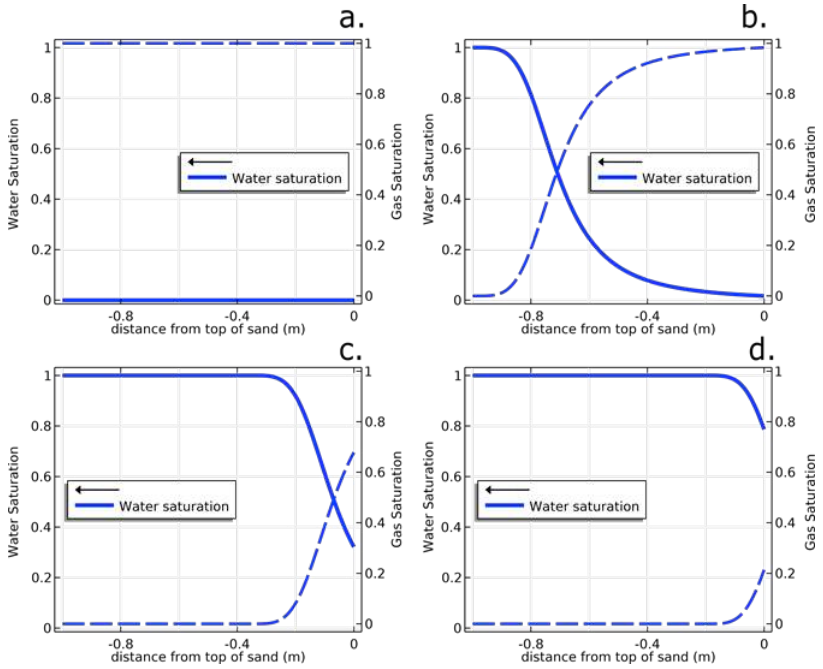

Figure 5.7: Initial water saturation, Sl, and gas saturation, Sg, as a function of depth for different initial conditions. a.) dry. b.) gravity drainage. c.) PZP at d = 0.35m. d.) PZP at d = 0.2m

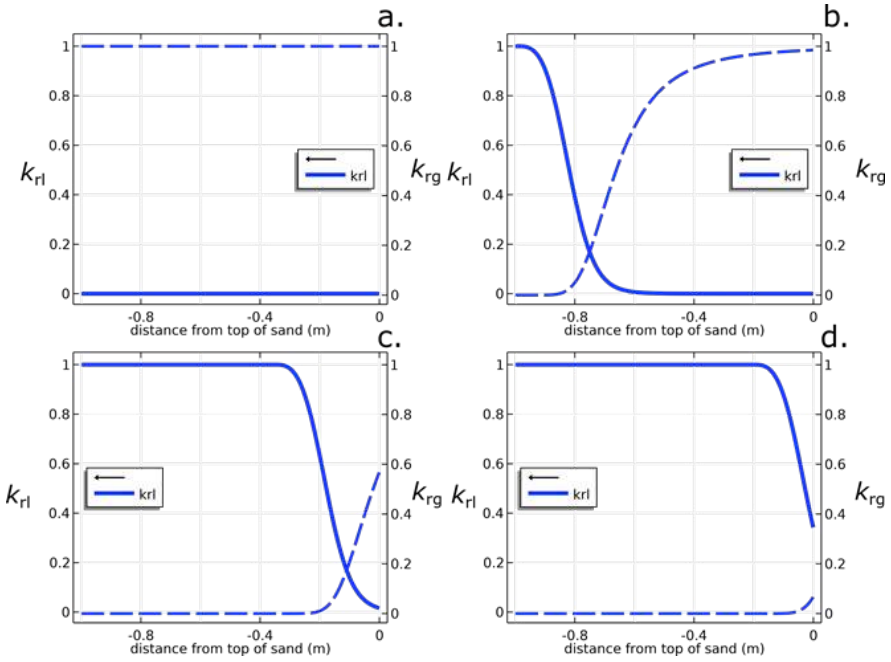

Figure 5.8: Initial relative water permeability, krl, and gas permeability, krg, as a function of depth for different initial conditions. a.) dry. b.) gravity drainage. c.) PZP at d = 0.35m. d.) PZP at d = 0.2m

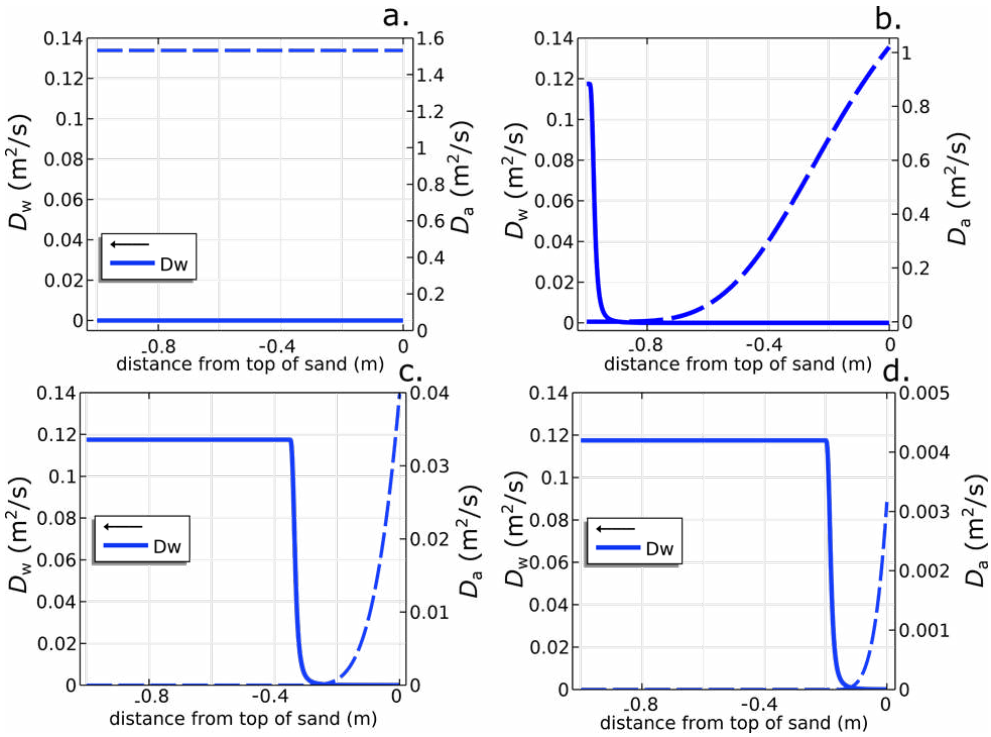

Figure 5.9: Initial pressure diffusivity for water, Dw, and are, Da,, as a function of depth for different initial conditions. a.) dry. b.) gravity drainage. c.) PZP at d = 0.35m. d.) PZP at d = 0.2m

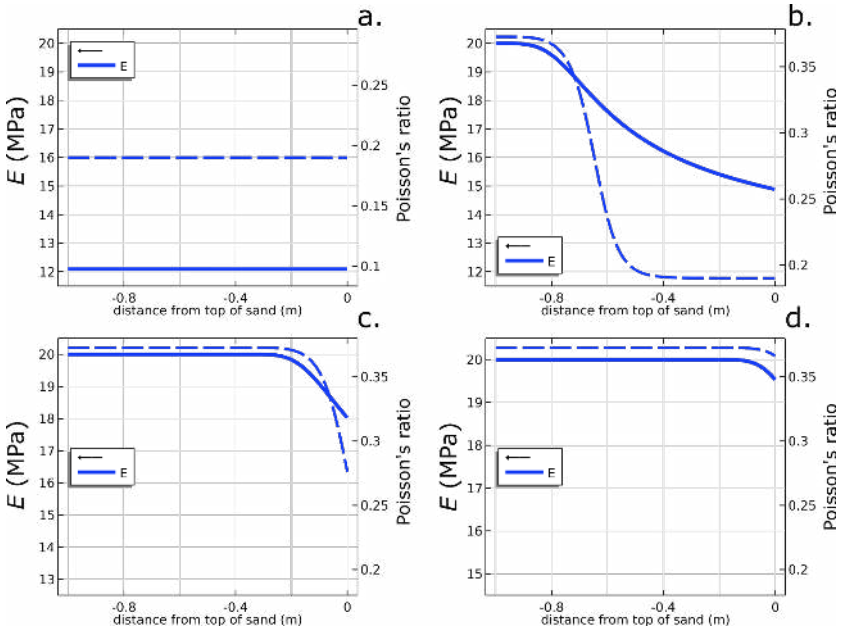

Figure 5.10: Initial drained Young's modulus, E, and drained Poisson's ratio, n, as a function of depth for different initial conditions. a.) dry. b.) gravity drainage. c.) PZP at d = 0.35m. d.) PZP at d = 0.2m

5.3.3.2 Profiles as functions of depth

The pressure profiles fluctuate between +/- 25 Pa, even when the sand is completely dry (Figure 5.11a). Unlike the gravity drained scenario, the pressure signal is still present at the bottom of the column and is fluctuating between +/- 5 Pa. There is no water saturation at the bottom of the column, so the air pressure signal is able to continue to travel through the sand. The changes in air pressure did not have any effect on the changes in water saturation. The water pressure and the change in water saturation remains constant at zero because there was no water injected into the sand in this scenario (Figure 5.12a and Figure 5.13a).

The weighted pressures mimic the air pressure profiles because there is no contribution from the water pressure (Figure 5.14a). This causes the strain to only be affected by the changes in air pressure in this scenario. The vertical strain is fluctuating as a result of the fluctuating air pressure (Figure 5.15a). The increases in the beginning of the cycle are still causing a compressive strain while the decreases in pressure cause a tensile response. The magnitude of the strain signal in the dry sand scenario are slightly higher than those in the gravity drained case. The compressive and tensile fluctuations are between +/- 0.21 με. The vertical strain is still affected by the changes in air pressure that are happening on the surface of the sand (0.0 m depth) and also throughout the sand. In general, air pressure increases on the surface will lead to a compressive response in the strain while an increase in air pressure within the subsurface can cause a tensile response in that same location. The profiles represent the combination but still without any effects of changing water pressure because the sand is fully dry.

5.3.3.3 Time series as functions of depth

Applying the air pressure signal on the surface causes the air pressure to change in the sand (Figure 5.16a). The pressure moves between +/- 25 Pa on the surface but decreases as depth increases. The magnitude of the fluctuations decreases to approximately +/- 18 Pa at 0.1 m, and decreases to less than +/- 3 Pa at 0.6 m. There is also a noticeable delay in the maximums and minimums. The pressure wave at depth is lagged behind the signal being applied in the head space.

The air pressure wave on the surface induces a change in the vertical strain that can be perceived at various depths along the column (Figure 5.17a). This shows that the increase in air pressure on the surface causes compression in the subsurface and a decrease in pressure leads to tension. There is also a noticeable change in magnitude as depth is increased as well as a lag time between the surface pressure and the perceived strain (Figure 5.18a). The strain is still occurring before the air pressure at specific depths. This is again because the strain in the sand is not only affected by the changing surface pressure but is also a combination of the changes in strain occurring at depth. In order to correct for this and to only see the changes in strain caused by the surface loading, the additional strain that is perceived at depth can be subtracted out (Figure 5.19a).

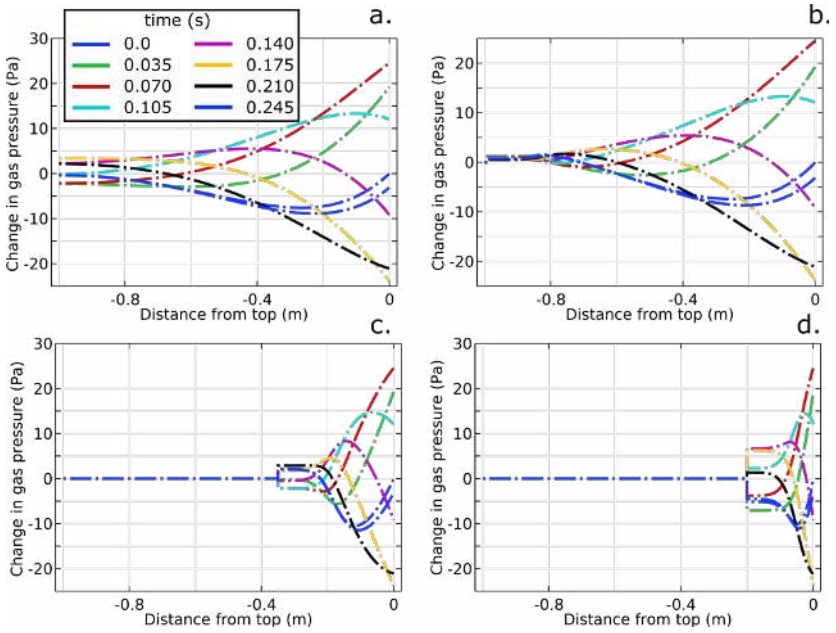

Figure 5.11: Changes in gas pressure relative to initial conditions as functions of time and depth for different initial conditions during periodic air pressure fluctuations with an amplitude of 25 Pa and a 25 s period at the ground surface. Initial conditions a.) dry. b.) gravity drainage. c.) PZP at d = 0.35m. d.) PZP at d = 0.2m.

Without water present in the sand, the dry sand scenario experienced minor changes. The magnitude of the air pressure and the strain saw small changes from the gravity drained case. The magnitude of the vertical strain only increased by approximately 0.01 με and the air pressure still fluctuated around +/- 25 Pa. This shows

that the changes were small when the saturation is varying throughout the sand. The gravity drained case only had a small amount of water present, and it did not have a significant impact on the parameters. The vertical strain is a combination of the air and water pressure, but the simulations seem to show that the changes in air pressure have a much larger effect on the strain than that of the water pressure.

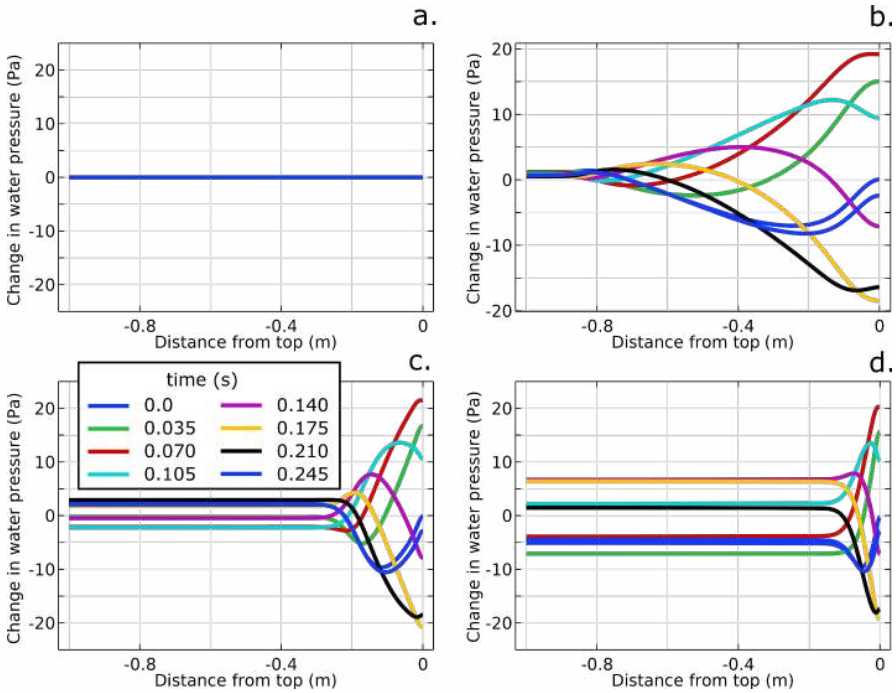

Figure 5.12: Changes in water pressure relative to initial conditions as functions of time and depth for different initial conditions during periodic air pressure fluctuations with an amplitude of 25 Pa and a 25 s period at the ground surface. Initial conditions a.) dry. b.) gravity drainage. c.) PZP at d = 0.35m. d.) PZP at d = 0.2m.

5.3.3.4 Filled to 35 cm depth

The next scenario describes the changes in air pressure and vertical strain when the water level was increased to 0.35 m depth below the top of the column and held there when the periodic signal was applied.

5.3.3.5 Initial Conditions

The pressure head at the bottom of the column was held at 0.65m. This caused the point of zero pressure (PZP) to be at d=0.35m. The air entry pressure head is approximately 0.1m, so this means that the sand is fully saturated below 0.25 m depth, so the gas content and saturation are in and below this zone but increases above it. The initial water content and water saturation support this idea (Figures Figure 5.6c and Figure 5.7c).

The varying water saturation and water content in the sand changes the relative permeabilities (Figure 5.8c). The relative gas permeability at the top of the column is just below 0.6 and quickly decreases to zero by 0.2 m. The relative gas permeability is increasing at a point above the water level because of the capillary zone that is just above 0.35 m. As the water saturation is increasing but remaining below 1.0, the relative gas permeability begins to decrease

because the gas cannot travel through the sand. This is similar to the drained sand conditions because the points on the column that still had varying saturation caused the gas permeability to decrease as well. The sand being fully saturated at 0.35 m causes the liquid relative permeability to remain uniform at 1.0. The water pressure diffusivity increases to a maximum at 0.12 m^2/s and sharply decreases above 0.35 m depth (Figure 5.10c). The air pressure diffusivity is large at the top of the column where the sand is dry but also sharply decreases to zero at the 0.35 m depth. The abrupt change in saturation at this point causes the sharp increases and decreases in both pressure diffusivities. The drained case presents more gradual changes, unlike the sharp changes in this filled experiment. The air diffusivity decreased much more gradually along the column because the sand had varying saturation that increased with depth as well.

The elastic properties in this experiment are greater than in the other experiments where the water content is saturated (Figure 5.10c). An increase in water in the sand causes the stiffness of the material to increase, causing the elastic properties to be higher than when the sand was fully dry. Young's Modulus is approximately 18 MPa at the top of the column and increases to 20 MPa at 0.25 m. It remains uniform at this location. Poisson's ratio is 0.27 at the top of the sand (d = 0.07 m) and increases sharply to approximately 0.40 at d =0.18 m. These properties are also effected by the capillary fringe zone because they change as soon as water in present in the sand, which is above the fill location at 0.35 m.

5.3.3.6 Profiles as functions of depth

When the periodic signal is applied to the sand, the gas pressure profiles decrease where the sand is fully saturated (Figure 5.11c). This is the point where the gas saturation is zero and the gas pressure is uniform. The changes in gas pressure vary at the top of the column where the saturation is moderate, but the sand is fully saturated below 0.35 m depth and causes the gas pressure to be zero below that point. This is also true for the water pressure below that point (Figure 5.12c). There are no changes in the water pressure below 0.35 m depth. The water pressure changes only will occur when the saturation would decrease. This is similar to the gravity drained case. The changes in water pressure vary because the saturation varies throughout the sand and is only partially saturated anywhere except the very bottom of the column. Additionally, air and water pressure below the 0.35 m filling point remain constant, the weighted pressure is uniform as well (Figure 5.13c).

The pressure head being held constant at 0.65 m will still allow for there to be changes in water saturation slightly above this location due to the capillary fringe zone (Figure 5.14c). There are not any changes in water saturation from approximately 0.22 m and deeper. Because the point of zero pressure is at d = 0.35 m, the water saturated in capillary fringe zone is constant. The water content is varying above this point while the saturation is consistent above this point. Lastly, the vertical strain is changing from the top of the column to the bottom as an effect of the increased water level (Figure 5.15c). The periodic signal still causes compression at the top of the sand and tension at the bottom of the sand even through the sand is saturated. In addition, there is still vertical strain occurs within the saturated zone. The vertical strain is about 0.5 m on the column, or halfway down. This supports that vertical strain is not only affected by the air pressure but the water pressure as well.

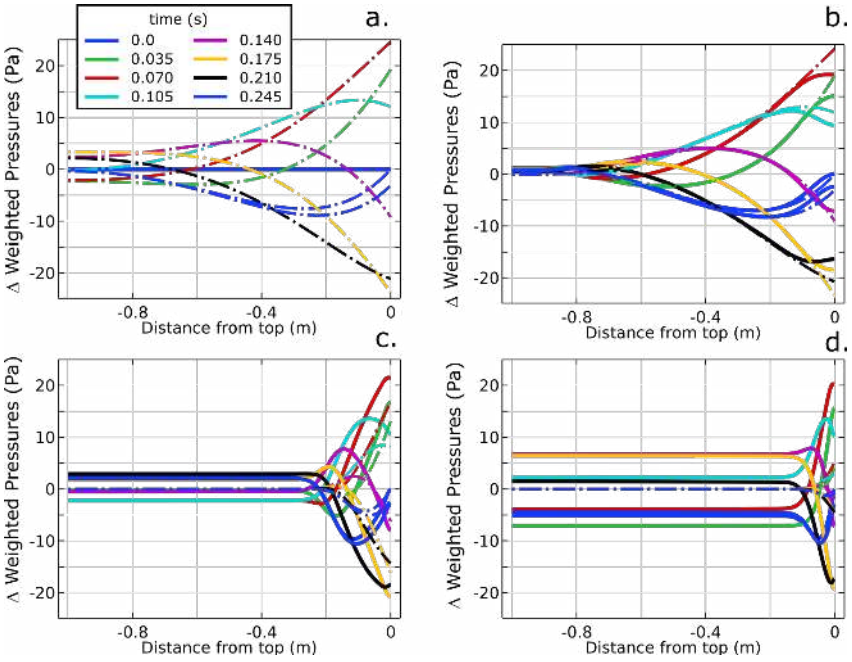

Figure 5.13: Changes in weighted air and water pressure relative to initial conditions as functions of time and depth for different initial conditions during periodic air pressure fluctuations with an amplitude of 25 Pa and a 25 s period at the ground surface. Initial conditions a.) dry. b.) gravity drainage. c.) PZP= at d = 0.35m. d.) PZP at d = 0.2m.

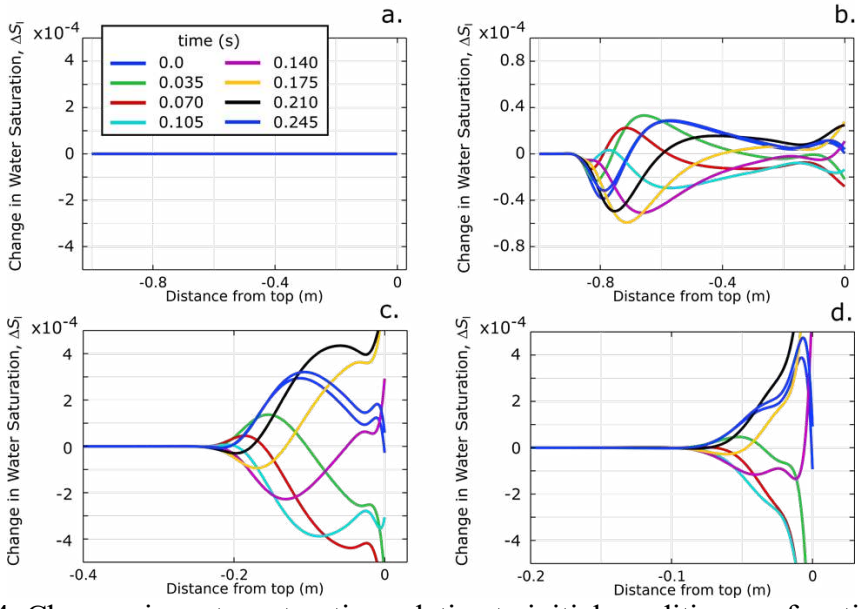

Figure 5.14: Changes in water saturation relative to initial conditions as functions of time and depth for different initial conditions during periodic air pressure fluctuations with an amplitude of 25 Pa and a 25 s period at the ground surface. Initial conditions a.) dry. b.) gravity drainage. c.) PZP at d = 0.35m. d.) PZP at d = 0.2m.

5.3.3.7 Time series as functions of depth

The periodic air pressure signal decreases overall as a result of the water level at 0.35 m (Figure 5.16c). The air pressure at d = 0.1 m is comparable to the dry sand scenario, but the points below this have a decrease in amplitude and an increase in phase lag. All of the points from d = 0.3 m and deeper follow the trend of the 0.6 m point (yellow line). The air pressure wave only moves through the partially saturated sand and not where the sand is fully saturated. This is supported by the initial permeability and diffusivity data. The magnitude of the strain also experiences changes when the periodic signal is applied to the sand (Figure 5.17c). The magnitude of the vertical strain has doubled from the drained and dry sand scenarios. The vertical strain is now fluctuating between +/- 0.4 με and still remains lagged between the pressure wave that is at 0.0 m depth. Furthermore, the initial pressure wave is still lagged behind the vertical strain. (Figures Figure 5.18c and Figure 5.19c). This is because the loading component and the subsurface propagation are both affecting the total strain.

5.3.4 Filled to 20 cm depth

5.3.4.1 Initial Conditions

The water in the sand column is raised to 0.20 m depth and held constant there after reaching an equilibrium. The results from raising the water level in this experiment are similar to those from the 'filled to 35 cm depth' case. The increase water level to 20cm on the column causes the water content and water saturation to raise to this point as well (Figure 5.6d and Figure 5.7d). Because of the capillary fringe zone above the water level, the sand is saturated throughout the entire column. The capillary fringe zone causes there to be varying levels of saturation up to the top of the sand (d = 0.0 m). The water content and saturation are always less than 1.0 because of this, and the gas content and saturation are essentially zero for the entire length of the column.

The relative gas permeability is nearly zero along the entire column (Figure 5.8d). The relative liquid permeability dominates this scenario because the sand is saturated along the entire length. The relative liquid permeability is 0.4 at the top of the sand and quickly increases to 1.0 by 0.18 m depth. It remains 1.0 below this point. Both diffusivities behave similarly to the 35 cm filled scenario except their sharp changes take place at a higher depth on the column (Figure 5.8d). The water diffusivity reaches its maximum of 0.12 m^2/s at 0.20 m and the air diffusivity is only present for the top 0.05 m at 0.003 m^2/s. This air diffusivity is much smaller than in the 35 cm filled case. Lastly, the elastic properties are large and nearly constant all throughout the sand (Figure 5.10d). Young's modulus is 20 MPa and Poisson's ratio is 0.35, which are both the same in the 35 cm filled case. When the sand is fully saturated, these elastic properties reach their maximums and stay constant.

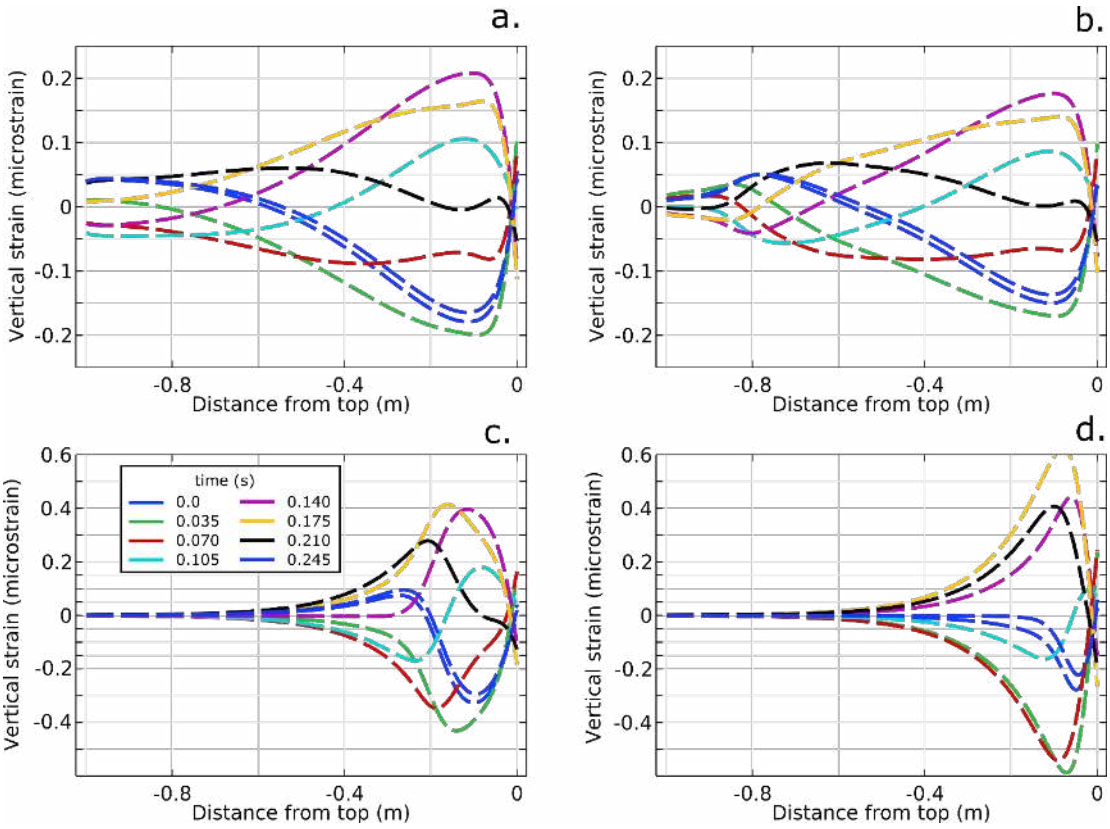

Figure 5.15: Vertical strain as functions of time and depth for different initial conditions during periodic air pressure fluctuations with an amplitude of 25 Pa and a 25 s period at the ground surface. Initial conditions a.) dry. b.) gravity drainage. c.) PZP at d = 0.35m. d.) PZP at d = 0.2m.

5.3.4.2 Profiles as functions of depth

The patterns of change in gas, water and weighted pressure are similar to the other cases where the sand is saturated (Figures Figure 5.11d, Figure 5.12d and Figure 5.13d). Above d = 20 cm, these pressures are increasing and decreasing from the applied periodic signal, but they decrease to zero when interacting with the boundary at zero pressure. The changes in water pressure and weighted pressure still reflect a capillary fringe zone because they decrease to zero before the 20 cm fill location. This shows that the saturation is uniform in this zone and has reached a point of equilibrium (Figure Figure 5.14d).

The vertical strain goes to zero at the same location in this experiment as the 35 cm filled case (approximately 0.70 m), but the changes above this point are larger than all of the other three cases (Figure 5.15d). Raising the water level to d = 20 cm has caused the magnitude of the vertical strain to fluctuate between +/- 0.6 με. This is the largest amount of strain that is observed between the dry, drained, and filled to 35 cm case.

5.3.4.3 Time series as functions of depth

The periodic pressure signal on the surface remains the same and only slightly fluctuates throughout the sand (Figure 5.16d). The amplitude of the pressure decreases below +/- 10 Pa and much more lagged behind the wave on the surface. Because the water level is raised to 20 cm, the air pressure wave only moves throughout the sand to this point. It is expected that the pressure is still responsive at these depths from the loading that is taking place on the surface rather than the air pressure being transmitted through the sand. The vertical strain diminishes to nearly zero by 0.5 m (Figure 5.17d). Although the vertical strain is reaching its maximum in this scenario, it is impeded by the saturated in the sand. The strain at depths 0.2 m and below fluctuates between +/- 0.3 με, which is half of what is observed at 0.1 m (Figure 5.18d and Figure 5.19d). The air pressure wave is diminished below this point, so this component of the vertical strain is not being applied and it is solely contributed from the water pressure. The increased water level decreases the vertical strain.

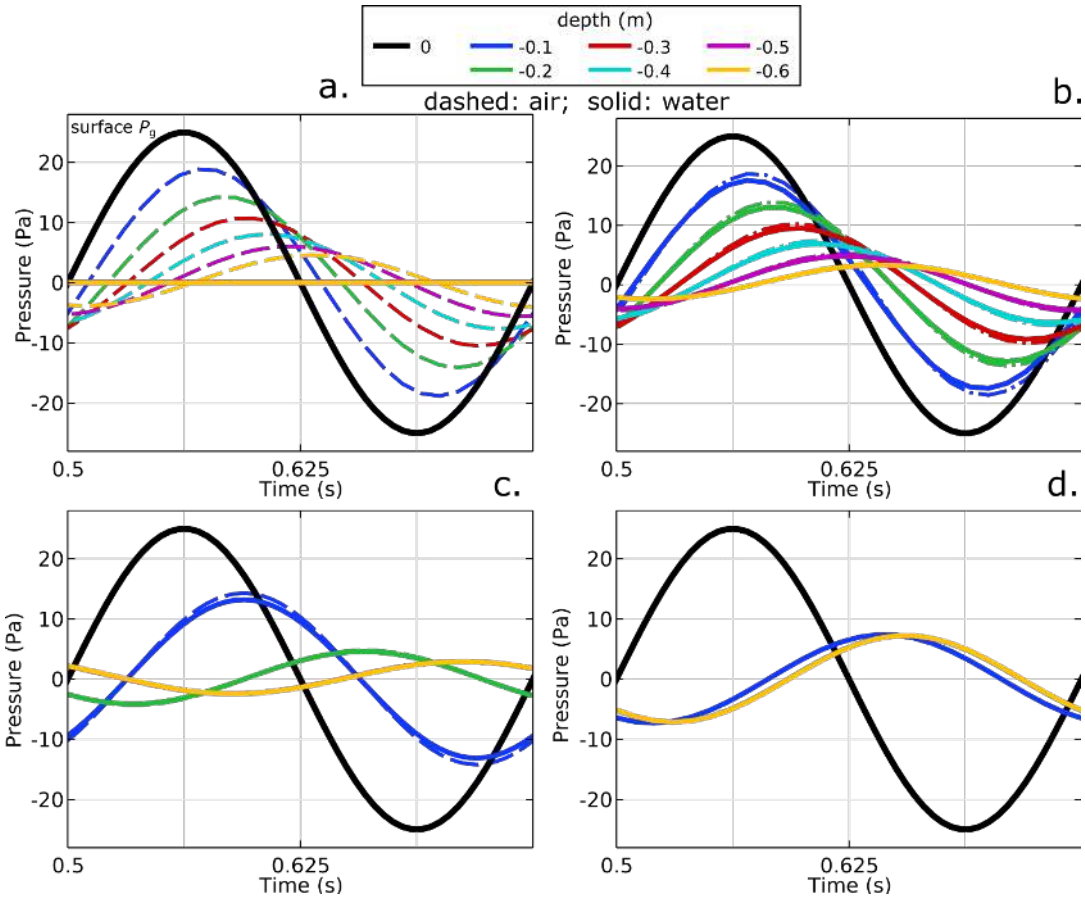

Figure 5.16: Time series of water (solid line) and air pressure (dashed line) at different depths (colors in legend) for different initial conditions during periodic air pressure fluctuations with an amplitude of 25 Pa and a 25 s period at d = 0 (thick black line). Initial conditions a.) dry. b.) gravity drainage. c.) PZP at d = 0.35m. d.) PZP at d = 0.2m. Air pressure at the upper surface (d=0) as thick black line.

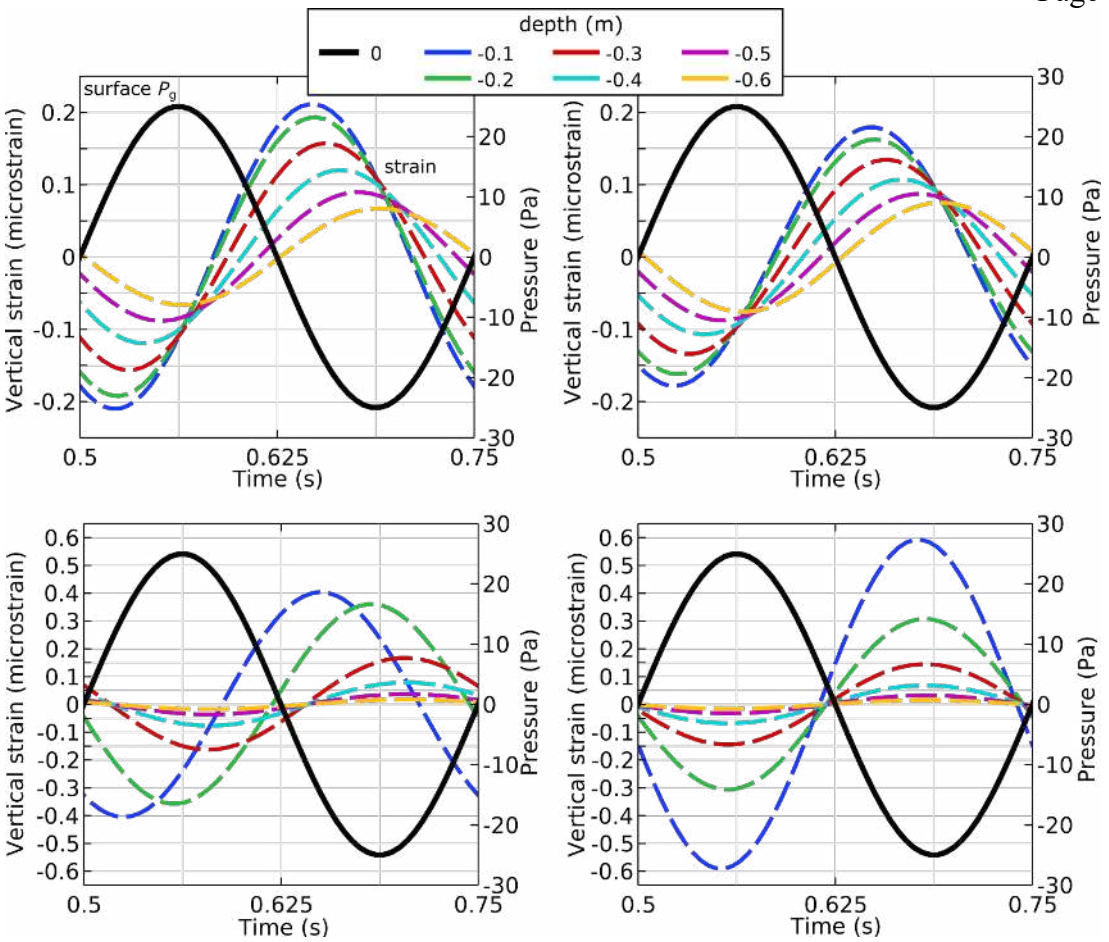

Figure 5.17: Time series of vertical strain at different depths (colors in legend) for different initial conditions during periodic air pressure fluctuations with an amplitude of 25 Pa and a 25 s period at d = 0 (thick black line). Initial conditions a.) dry. b.) gravity drainage. c.) PZP at d = 0.35m. d.) PZP at d = 0.2m. Air pressure at the upper surface (d=0) as thick black line.

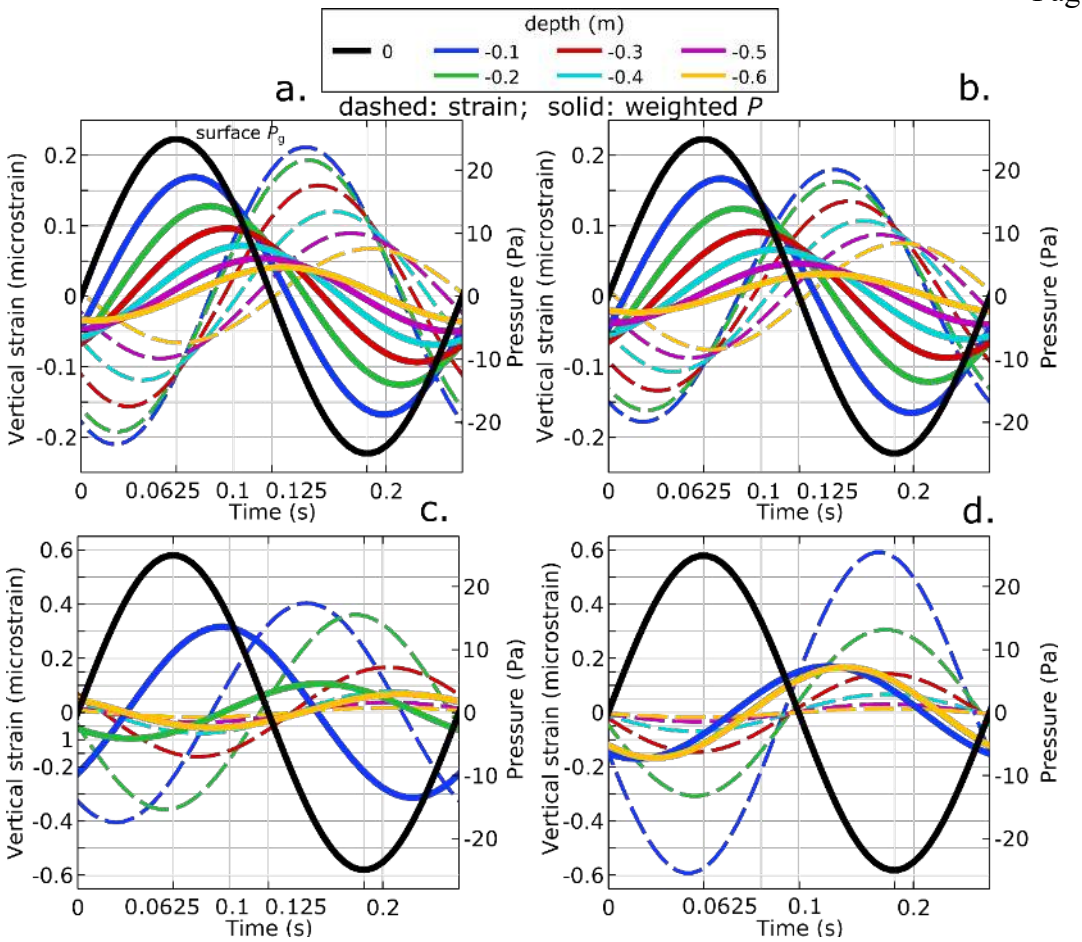

Figure 5.18: Time series of vertical strain (dashed lines) and weighted pressure (solid lines) at different depths (colors in legend) for different initial conditions during periodic air pressure fluctuations with an amplitude of 25 Pa and a 25 s period at d = 0 (thick black line). Initial conditions a.) dry. b.) gravity drainage. c.) PZP at d = 0.35m. d.) PZP at d = 0.2m.

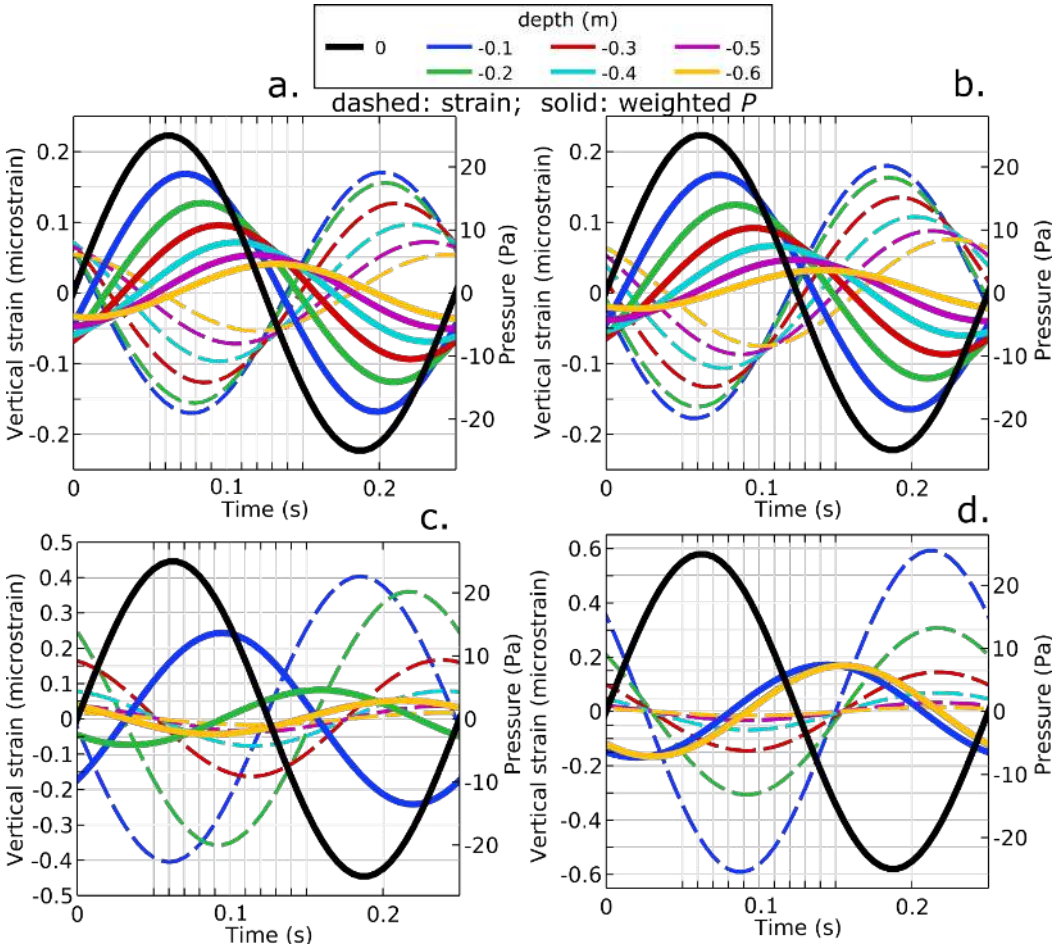

Figure 5.19: Same data as Figure 3.16 – but with the time scale of the strain advanced by 0.035s to account for a synchronization error between the pressure and strain data.

CHAPTER SIX

ANALYTICAL MODEL FOR STRAINS IN THE VICINITY OF A PRESSURIZED FORMATION

Contents

6.1 Analytical model 6-2
6.1.1 Inclusion model 6-3
6.1.2 Inhomogeneity model 6-4
6.1.3 Transformation strain 6-4
6.2 Strains on the inclusion Boundary 6-5
6.2.1 Inclusion of arbitrary shape 6-5
6.2.2 Ellipsoidal inclusion 6-6
6.2.3 Thin ellipsoidal inclusion 6-6
6.3 Strains on the inhomogeneity Boundary 6-9
6.3.1 Ellipsoidal inhomogeneity 6-9
6.3.2 Thin ellipsoidal inhomogeneity 6-11
6.4 Concusions 6-13
6.5 References 6-14

ANALYTICAL MODEL FOR STRAINS IN THE VICINITY OF A PRESSURIZED FORMATION

Analytical solutions are a mainstay of techniques for evaluating pressure signals measured during well tests, and similar methods can be used to evaluate the poroelastic response. This type of solution is much faster than the numerical solutions used in Chapter Five, so it is well suited to making interpretations using inversion methods. Moreover, analytical solutions can often generate physical insights that are obscured by numerical calculations. Despite their value, analytical solutions for poroelastic problems are limited and currently only a handful of published solutions is available for evaluating strain during injection into, or production from a reservoir or aquifer. The objective of this chapter is to fill this gap and develop the analytical expressions needed to interpret strains in the vicinity of a pressurized formation.

The analysis outlined in the following pages was an important task throughout the project, but final details of the analysis were motivated by the need to interpret strains observed during the injection tests outlined in Chapter Ten. Those tests showed that the horizontal strain was tensile and the vertical strain was compressive at shallow strainmeters overlying the pressurized reservoir (Figure 1a). The ratios of the radial and circumferential horizontal strains differed at two locations, and previous work suggested this ratio was affected by the location of a reservoir boundary. Results from the deep strainmeter, AVN31, show that vertical strain was tensile and the horizontal strains were compressive, signs that are opposite from the strains at shallow depth. The deep strainmeter is slightly outside of a high permeability lens (Figure 1a).

The main goal of the analytical model is to provide a basis for preliminary interpretation of strains during well tests, with a particular motivation coming from the well tests in Chapter Ten. More detailed analyses can be accomplished using numerical methods outlined in Chapter Seven, but those methods are complex and may be out of reach for some applications.

6.1 ANALYTICAL MODEL

The approach we used is to consider the portion of the aquifer or reservoir affected by a well as a pressurized poroelastic region, V, in a homogeneous, isotropic elastic half-space (Figure 1b). The half space geometry allows the effects of the ground surface to be included. The pressurized region has a characteristic thickness, h, and characteristic horizontal dimension, a. It is embedded at depth, H, in uniform matrix with low permeability. The region is assumed to be thin ($h/a \ll 1$) and deep ($h/H \ll 1$).

The simplest case is to represent the region as a pressurized *inclusion* where the elastic properties are the same as those of the enveloping half-space (host) material. The properties of the reservoir may actually be different from those of the confining unit, so the next step is to represent the region as a pressurized *inhomogeneity* where the elastic properties differ from the enveloping host material. The inclusion model will be outlined first, followed by the inhomogeneity model. Unless stated otherwise, in both cases, the pore pressure change, Δp, in the region is assumed to be uniform and equal to the pressure data from the monitoring wells. As an example, pressure data from monitoring wells at our field site are given in Chapter Ten.

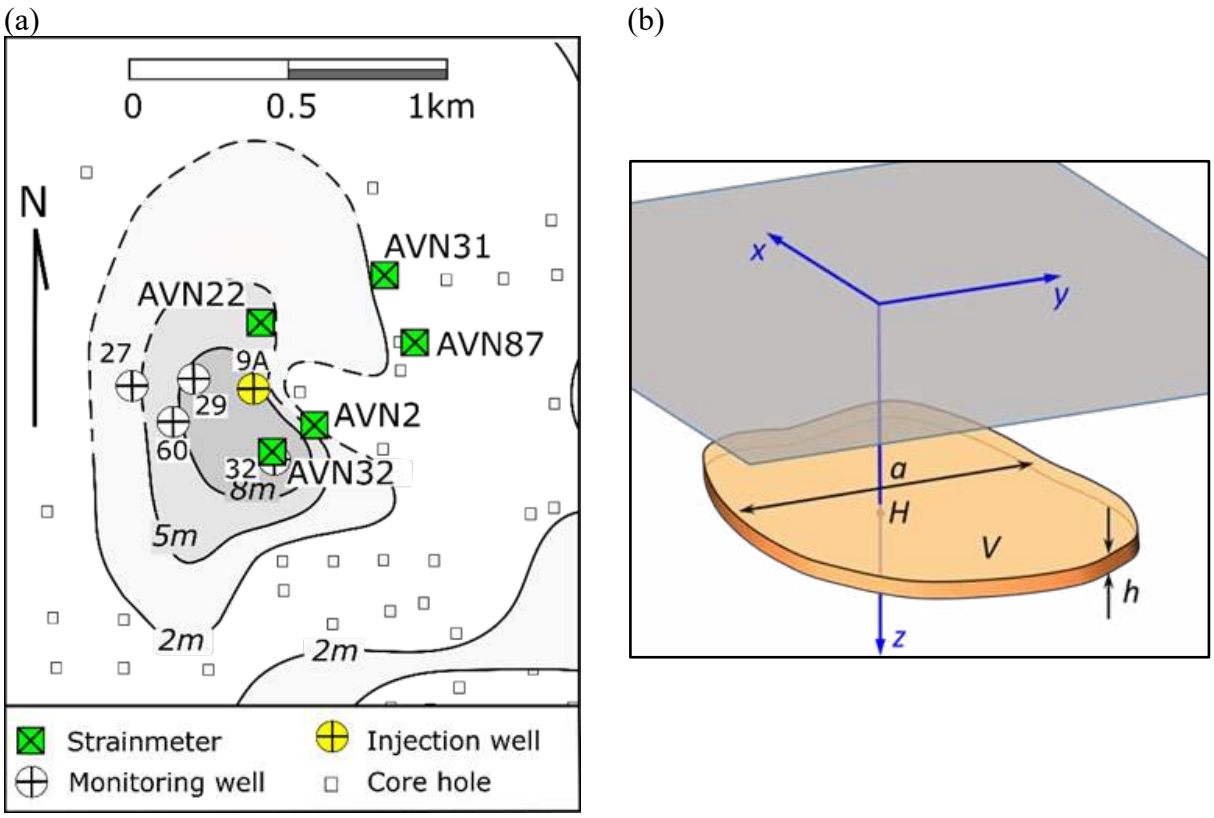

Figure 1. (a) Map of the North Avant Field with locations of strainmeters, injection well and monitoring well. Contours are thickness in m of permeable lens at the base of the Bartlesville Formation. AVN31 is a deep strainmeter at the boundary of the permeable lens. The other strainmeters are shallow. (b) Conceptual model of a pressurized reservoir represented by a poroelastic inclusion (the same properties of reservoir and host rock) or inhomogeneity (different properties of reservoir and host rock) in an elastic half space.

6.1.1 Inclusion model

When the pressurized region has the same properties as those of the host material, the deformation induced in the half-space (Figure 1b) by the pressure change can be found by using Mindlin and Cheng's (1950) results. They studied the elastic effect of a non-uniform distribution of temperature in a half-space, but thanks to the mathematical similarity between the thermoelastic and poroelastic constitutive laws (Cheng, 2016), one only needs to replace parameter β in the Mindlin and Cheng (1950) equation (2) with $\beta = \alpha\Delta p/(\lambda + 2\mu)$, where Δp is the pressure change distribution, α is the Biot-Willis coefficient, $\mu = E/[2(1+\nu)]$ and $\lambda = 2\mu\nu/(1-2\nu)$ are the Lame parameters, E is the Young Modulus, and ν is the Poisson ratio. Equation (2) in Mindlin and Cheng (1950) expresses the induced displacement vector at the arbitrary point in the half-space through a full-space Newtonian potential. For a uniform pressure change, Δp, in the inclusion, zero pressure change in the enveloping material, and canonical inclusion shapes such as a rectangular prism or an ellipsoid this potential is expressed in closed form (e.g., Kellogg, 1929; MacMillan, 1958; Nowacki, 1986; Mura, 1987; Ru, 1999;

Germanovich et al., 2012). Once the displacement field is known, the induced tilts and strains are found in closed form by differentiating displacements (Timoshenko and Goodier, 1970). This method allows for determining the deformation field both in the inclusion and surrounding matrix.

6.1.2 Inhomogeneity model

If the pressurized region and the host material have different properties, the former is called an inhomogeneity (Eshelby, 1957). The vertical deformation of a *thin* pressurized inhomogeneity (Figure 1b) follows from the solution outlined in Germanovich and Chanpura (2002) as

$$\varepsilon_{zz} = \frac{\Delta h}{h} = \frac{3\lambda_0 + 2\mu_0}{\lambda_0 + 2\mu_0}\alpha_0 \Delta p \tag{1}$$

All other strains in the inhomogeneity are negligible in the leading order, which implies the uniaxial strain state. Hereafter, subscript "0" denotes material properties of the inhomogeneity whereas the lack of subscript indicates properties of the enveloping material.

According to (1), the vertical deformation caused by a thin pressurized *inclusion* is

$$\varepsilon_{zz} = \frac{\Delta h}{h} = \frac{3\lambda + 2\mu}{\lambda + 2\mu}\alpha \Delta p_* \tag{2}$$

whereas other strains in the inclusion are negligible in the leading order. The final step is to recognize that the analysis for the homogeneous case can be applied to the heterogeneous case by equating (1) and (2). This gives the pressure change

$$\Delta p_* = \frac{\alpha_0(\lambda + 2\mu)(3\lambda_0 + 2\mu_0)}{\alpha(\lambda_0 + 2\mu_0)(3\lambda + 2\mu)}\Delta p \tag{3}$$

that should be used in the homogeneous case to account for contrasts in elastic properties between the inhomogeneity and matrix. Deformations determined in this way will be accurate in the leading terms and used below to analyze the strain state in the vicinity of the pressurized reservoir.

6.1.3 Transformation strain

In isotropic material, transformation strain tensor, ε_{ij}^T, is defined by the constitutive relation

$$\sigma_{ij} = 2\mu(\varepsilon_{ij} - \varepsilon_{ij}^T) + \lambda(\varepsilon_{kk} - \varepsilon_{kk}^T)\delta_{ij} \tag{4}$$

where σ_{ij} and ε_{ij} are the stress and strain tensors, respectively, and Kronecker delta $\delta_{ij} = 1$ when $i = j$ while $\delta_{ij} = 0$ when $i \neq j$. Therefore, the transformation strain is a particular case of the Robinson-Eshelby stress-free strain (Robinson, 1951; Eshelby, 1957), which the inclusion or inhomogeneity would experience in the absence of the matrix (confining unit).

Transformation strain is called isotropic, dilational, or hydrostatic if

$$\varepsilon_{ik}^T = \varepsilon_0^T \delta_{ik} \tag{5}$$

where ε_0^T is the *linear* transformation strain. The *volumetric* transformation strain $\varepsilon_v^T = \varepsilon_{kk}^T = 3\varepsilon_0^T$. In the case of a pressurized inclusion or inhomogeneity,

$$\varepsilon_0^T = \frac{\alpha_0 \Delta p}{3K_0} = \frac{\alpha_0 \Delta p}{3\lambda_0 + 2\mu_0} \tag{6}$$

where $K = (3\lambda + 2\mu)/3$ is the bulk modulus. Thus, equation (1) for a strain state inside a thin inhomogeneity can be written as

$$\varepsilon_{33} = \frac{3\lambda_0 + 2\mu_0}{\lambda_0 + 2\mu_0}\varepsilon_0^T, \quad \varepsilon_{ij} = 0 \text{ if } \quad ij \neq 33 \tag{7}$$

6.2 STRAINS ON THE INCLUSION BOUNDARY

6.2.1 Inclusion of arbitrary shape

Using properties of harmonic and by-harmonic potentials that undergo a jump on crossing a boundary surface, Eshelby (1957) found the strains, $\varepsilon_{ij}(\text{out})$, just outside the inclusion from their values, $\varepsilon_{ij}(\text{in})$, just inside (Figure 2). Combining expressions (2.13) in Eshelby (1957) yields

$$\begin{aligned}\varepsilon_{iq}(\text{out}) = \varepsilon_{ij}(\text{in}) + \frac{1}{1-\nu}\varepsilon_{jk}^T n_j n_k n_i n_q - \varepsilon_{ik}^T n_k n_q - \varepsilon_{qk}^T n_k n_i \\ + \frac{1}{3}\left(n_k n_q \delta_{ik} + n_i n_k \delta_{qk} - \frac{1+\nu}{1-\nu} n_k n_q - \frac{1}{1-\nu} n_i n_j n_k n_q \delta_{jk}\right)\varepsilon_{kk}^T\end{aligned} \tag{8}$$

where n_i are the direction cosines of the outward normal to the inclusion surface, δ_{ij} is the Kronecker delta, and ε_{ij}^T is the tensor of transformation strain in the inclusion. Henceforth, repeated tensor indices imply summation over these indices, and indices 1, 2, and 3 correspond, respectively, to x, y, and z coordinate axes. The transformation strain does not need to be homogeneous in the inclusion as only its value on the inclusion surface at a given point affects the strains just outside the inclusion surface (Figure 2).

If the transformation strain is dilational (i.e., isotropic), that is, $\varepsilon_{ik}^T = \varepsilon_0^T \delta_{ik}$ (equation (6)), expression (8) simplifies to

$$\varepsilon_{iq}(\text{out}) = \varepsilon_{ij}(\text{in}) - \frac{1+\nu}{1-\nu}\varepsilon_0^T n_i n_q \tag{9}$$

Thus, to determine the strain immediately outside an inclusion, one only needs to know the strains in the corresponding point, adjacent to the boundary, inside the inclusion (Figure 2).

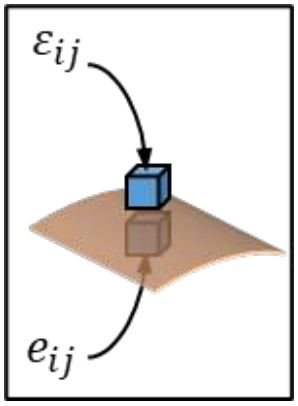

Figure 2. Strains $e_{ij} = \varepsilon_{ij}(\text{in})$ and $\varepsilon_{ij} = \varepsilon_{ij}(\text{out})$ at, respectively, inner (lower) and outer (upper) elementary representative volumes (points) adjacent to the inclusion surface.

6.2.2 Ellipsoidal inclusion

In the case of an ellipsoidal inclusion (Figure 3a) and homogeneous transformation strain, ε_{ij}^T, strain inside the inclusion is also homogeneous and related to ε_{ij}^T by (Eshelby, 1957, eq. (3.6))

$$\varepsilon_{ij} = S_{ijkl}\varepsilon_{kl}^T \tag{10}$$

where S_{ijkl} is the Eshelby tensor. This tensor depends on the Poison ratio and inclusion semiaxes, but not on the transformation strain. In the homogeneous elastic material, Eshelby tensor has 12 non-zero independent components while all other components are determined by the symmetry properties (e.g., Mura, 1987)

$$S_{ijkl} = S_{klij} = S_{jikl} = S_{ijlk}, \tag{11}$$

For an ellipsoidal inclusion, Eshelby (1957, eq. (3.23)) provides expressions for the normal at point (x, y, z) on the ellipsoid surface

$$n_1 = \frac{x}{a^2 h}, \quad n_2 = \frac{y}{b^2 h}, \quad n_3 = \frac{z}{c^2 h}, \quad h = \left(\frac{x^2}{a^4} + \frac{y^2}{b^4} + \frac{z^2}{c^4}\right)^{1/2} \tag{12}$$

where a, b, and c are the ellipsoid semiaxes. Expressions (12) are to be used in (8) and .

6.2.3 Thin ellipsoidal inclusion

For a thin ellipsoidal inclusion ($c \ll a$ and $c \ll b$), the only non-zero independent components of the Eshelby tensor are

$$S_{2323} = S_{3131} = \frac{1}{2}, \quad S_{3311} = S_{3322} = \frac{\nu}{1-\nu}, \quad S_{3333} = 1 \tag{13}$$

Substituting these in (10) yields non-zero strains in the inclusion

$$\varepsilon_{33} = \varepsilon_{33}^T + \frac{\nu}{1-\nu}(\varepsilon_{11}^T + \varepsilon_{22}^T)\,, \quad e_{13} = \varepsilon_{13}^T\,, \quad e_{23} = \varepsilon_{23}^T \tag{14}$$

which in the case of dilational transformation strain reduces to

$$\varepsilon_{33} = \frac{1+\nu}{1-\nu}\varepsilon_0^T\,, \quad e_{ij} = 0 \text{ if } \quad ij \neq 33 \tag{15}$$

Together with (9), this equation yields strains

$$\varepsilon_{33}(\text{out}) = \frac{1+\nu}{1-\nu}\varepsilon_0^T\,(1-n_3^2), \quad \varepsilon_{ij}(\text{out}) = -\frac{1+\nu}{1-\nu}\varepsilon_0^T n_i n_j \text{ if } \quad ij \neq 33 \tag{16}$$

immediately outside the inclusion surface (in the leading order).

Because quantities n_i are direction cosines, equation (16) implies that $\varepsilon_{zz} = \varepsilon_{33}(\text{out})$ is always tensile (positive or zero) while other normal strains, $\varepsilon_{xx} = \varepsilon_{11}(\text{out})$ and $\varepsilon_{yy} = \varepsilon_{22}(\text{out})$, are both compressive (negative or zero).

Consider, for example, the *xy*-trace of the ellipsoid surface (Figure 3b)

$$\frac{x^2}{a^2} + \frac{y^2}{b^2} = 1, \quad z = 0 \tag{17}$$

For this trace, equation (12) returns

$$n_1 = \frac{x}{a^2 h}\,, \quad n_2 = \frac{y}{b^2 h}\,, \quad n_3 = 0\,, \quad h = \left(\frac{x^2}{a^4} + \frac{y^2}{b^4}\right)^{1/2} \tag{18}$$

In this case, the strain tensor, $\varepsilon_{ij}(\text{out})$, along the *xy*-trace (immediately outside the ellipsoid, Figure 3b) is given by (16) with (18). In the matrix form,

$$\begin{pmatrix} \varepsilon_{xx} & \varepsilon_{xy} & \varepsilon_{xz} \\ \varepsilon_{xy} & \varepsilon_{yy} & \varepsilon_{yz} \\ \varepsilon_{xz} & \varepsilon_{yz} & \varepsilon_{zz} \end{pmatrix} = -\frac{1+\nu}{1-\nu}\varepsilon_0^T \begin{pmatrix} n_1^2 & n_1 n_2 & 0 \\ n_1 n_2 & n_2^2 & 0 \\ 0 & 0 & -1 \end{pmatrix} \tag{19}$$

and the corresponding principal strains along the *xy*-trace (also immediately outside the ellipsoid, Figure 3b) are

$$\begin{pmatrix} \varepsilon_1(\text{out}) \\ \varepsilon_2(\text{out}) \\ \varepsilon_3(\text{out}) \end{pmatrix} = \frac{1+\nu}{1-\nu}\,\varepsilon_0^T \begin{pmatrix} -1 \\ 0 \\ 1 \end{pmatrix} \tag{20}$$

Here $\varepsilon_3(\text{out})$ and its direction (along *z*-axis) is vertical while $\varepsilon_1(\text{out})$ is always compressive and horizontal. Its direction in the horizontal plane changes along the *xy*-trace, but the magnitude remains constant. This and that $\varepsilon_2(\text{out})$ is zero everywhere along the *xy*-trace are interesting facts, the strain tensor components are generally measured not in a principal coordinate set as the principal stress directions are not known a priory.

For an ellipsoidal inclusion with semiaxis ratios of $a/b = 2$, $c/a \ll 1$, and $c/b \ll 1$ (Figure 3a), the strain distributions along the *xy*-trace of the ellipsoid surface on plane $z = 0$ (Figure 3b) are plotted in Figure 4a in rectangular coordinates (Figure 3a). Strains in normal and tangential directions to the *xy*-trace are plotted in Figure 4a. Because the strains inside an ellipsoidal inclusion are uniform, one of them can be used to normalize the outside strains. For a thin inclusion, the only non-zero leading-order strain is ε_{33} (equation (15)). This is why strains in Figure 4 are normalized by $e_0 \equiv \varepsilon_{33} = (1+\nu)\varepsilon_0^T/(1-\nu)$. The resulting normalized strains do not depend on the Poisson ratio. All normal horizontal strains are indeed compressive (in the leading order), while the vertical normal strain, $\varepsilon_{zz} = \varepsilon_{33}(\text{out})$, is tensile according to (19).

It is interesting to note that the normal strains in *z* direction immediately outside and inside the inclusion boundary are equal ($\varepsilon_{33}(\text{out}) = e_{33}(\text{in})$) on the *xy*-trace. This is expected and follows from the traction continuity conditions on the boundary.

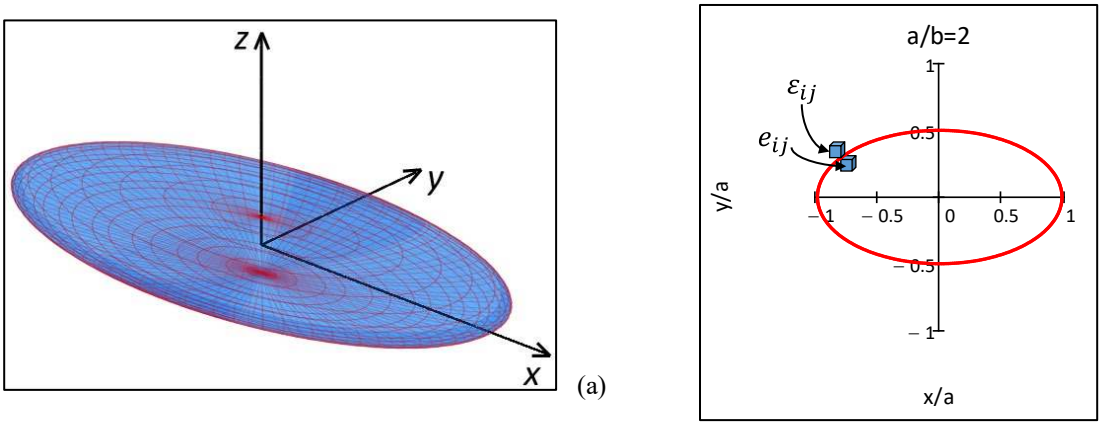

Figure 3. (a) Inclusion shaped as a thin ellipsoid with semiaxis ratios $a/b = 2$, $c/a \ll 1$, and $c/b \ll 1$. Coordinate axes are shown by black lines. (b) Intersection of the ellipsoid surface with plane $z = 0$ (*xy*-trace of the ellipsoid). Strains $e_{ij} = \varepsilon_{ij}(\text{in})$ and $\varepsilon_{ij} = \varepsilon_{ij}(\text{out})$ at, respectively, inner and outer points, immediately adjacent to the *xy*-trace (inclusion surface).

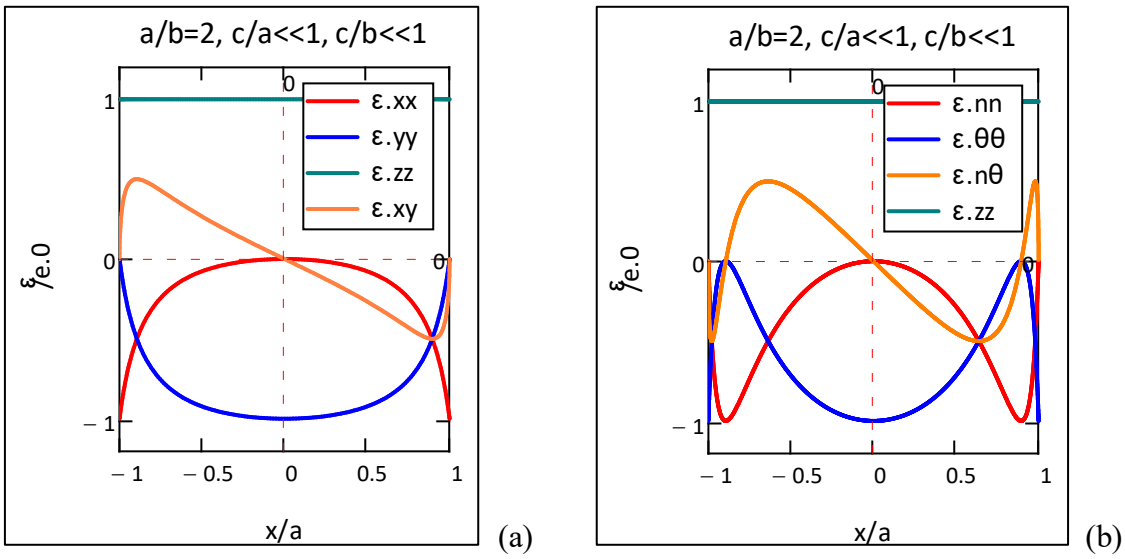

Figure 4. Distributions of strains $\varepsilon_{ij} = \varepsilon_{ij}(\text{out})$ along the upper part of the ellipsoid *xy*-trace, $y > 0$ (Figure 3b), immediately outside the trace. Due to the symmetry, strain distributions along the lower part, $y < 0$, are the same except the shear strain changes its sign. Strains are normalized by $e_0 = (1+\nu)\varepsilon_0^T/(1-\nu)$, which is equal to the vertical strain, ε_{33} (equation (15), inside the thin ellipsoid (a) Strains in rectangular coordinates (Figure 3a). (b) Strains in normal and tangential directions to the *xy*-trace of the ellipsoid (Figure 3b).

6.3 STRAINS ON THE INHOMOGENEITY BOUNDARY

6.3.1 Ellipsoidal inhomogeneity

Eshelby's (1957) method transforms an inhomogeneity to an equivalent inclusion. The shape of the equivalent inclusion is identical to that of the original inhomogeneity, but its elastic properties are the same as those of the matrix. The transformation strains in the equivalent inclusion, ε_{ij}^*, however, differ from the transformation strains in the original inhomogeneity, ε_{ij}^T. The former are adjusted to make the strains and stresses generated by the inclusion transformation equal to those generated by the transformation of the inhomogeneity (both in the inhomogeneity and in the matrix). Determining the equivalent transformation strains, ε_{ij}^*, effectively provides the solution of the original inhomogeneity problem, which is also written in the form of (10) as

$$\varepsilon_{ij} = S_{ijkl}\varepsilon_{kl}^* \tag{21}$$

where S_{ijkl} is the Eshelby tensor. This tensor is the same as in (10) and depends on the Poisson ratio of the matrix material, but not on the inhomogeneity material properties and not on the transformation strain. The inhomogeneity properties though are accounted for in the equivalent transformation strain, ε_{kl}^*. Thus, once ε_{kl}^* is found, equation (21) reduces the inhomogeneity

problem to determining the Eshelby tensor.

It turns out that for an *ellipsoidal* inhomogeneity in an *unbounded* matrix and with *uniform* ε_{ij}^{T}, the strains and stresses, generated by the transformation inside the inhomogeneity, are also uniform (Eshelby, 1957). This greatly simplifies the solution, and for a general ellipsoid, the tensor S_{ijkl} has only 12 independent non-zero components. For several cases, they are tabulated in the closed form (Mura, 1987) and simple numerical algorithms are available for their fast evaluation (e.g., Reches, 1998; Meng et al., 2012). The number of independent components of S_{ijkl} can be reduced by assuming ellipsoid symmetries (e.g., oblate spheroid).Given ε_{ij}^{T}, the transformation strains, ε_{ij}^{*}, in the equivalent inclusion can be found from the set of linear algebraic equations

$$\begin{aligned} 2\mu_1\left(S_{ijkl}\varepsilon_{kl}^{*} - \varepsilon_{ij}^{T} + \varepsilon_{ij}^{\infty}\right) + \lambda_1\left(S_{kkmn}\varepsilon_{mn}^{*} - \varepsilon_{kk}^{T} + \varepsilon_{ij}^{\infty}\right) \\ = 2\mu\left(S_{ijkl}\varepsilon_{kl}^{*} - \varepsilon_{ij}^{*} + \varepsilon_{ij}^{\infty}\right) + \lambda\left(S_{kkmn}\varepsilon_{mn}^{*} - \varepsilon_{kk}^{*} + \varepsilon_{ij}^{\infty}\right) \quad (i = j) \end{aligned} \tag{22}$$

that expresses the equality of strains and stresses in the problems for the original inhomogeneity and for the equivalent inclusion. Expression (22) is only slightly more general than that in Mura (1987) as it includes the remote strain tensor, $\varepsilon_{ij}^{\infty}$, specified at infinity. In the case of $i \neq j$, the shear transformation strains follow directly from (22) and can be written as

$$\varepsilon_{\alpha\beta}^{*} = \frac{\mu_1\varepsilon_{\alpha\beta}^{T} - (\mu_1 - \mu)\varepsilon_{\alpha\beta}^{\infty}}{\mu + 2(\mu_1 - \mu)S_{\alpha\beta\alpha\beta}} \quad (\alpha \neq \beta) \tag{23}$$

Hereafter, there is no summation over Greek tensor indices. In the case of $i = j$, equation (22) is considered as an implicit definition of the normal transformation strains.

To compare strains in the asymptotic equation (1) to the exact solution for the ellipsoidal inhomogeneity in the infinite space (Eshelby, 1957), further consider equation (22) for $i = j$. In this case, (22) has three unknowns ($\varepsilon_{11}^{*}, \varepsilon_{22}^{*}, \varepsilon_{33}^{*}$). Rearranging its terms yields the equivalent set

$$\begin{cases} (2\mu + \Lambda_{11})\varepsilon_{11}^{*} + \Lambda_{12}\varepsilon_{22}^{*} + \Lambda_{13}\varepsilon_{33}^{*} = \mathrm{A}_1 \\ \Lambda_{21}\varepsilon_{11}^{*} + (2\mu + \Lambda_{22})\varepsilon_{22}^{*} + \Lambda_{23}\varepsilon_{33}^{*} = \mathrm{A}_2 \\ \Lambda_{31}\varepsilon_{11}^{*} + \Lambda_{32}\varepsilon_{22}^{*} + (2\mu + \Lambda_{33})\varepsilon_{33}^{*} = \mathrm{A}_3 \end{cases} \tag{24}$$

where

$$\begin{cases} \Lambda_{\alpha\alpha} = \lambda + 2S_{\alpha\alpha\beta\beta}\Delta\mu + S_{kk\beta\beta}\Delta\lambda \\ \mathrm{A}_{\alpha} = 2\mu_1\varepsilon^{\mathrm{T}}_{\alpha\alpha} + \lambda_1\varepsilon^{\mathrm{T}}_{kk} - 2\Delta\mu\varepsilon^{\infty}_{\alpha\alpha} - \Delta\lambda\varepsilon^{\infty}_{kk} \end{cases} \tag{25}$$

and parameters $\Delta\mu = \mu_1 - \mu$, $\Delta\lambda = \lambda_1 - \lambda$ represent the property contrasts.

The linear algebraic equation set (24) has a unique solution for any physically-permissible combination of material properties, transformation strains, and remote strains. This solution can be written as

$$\varepsilon^{*}_{11} = \frac{\dfrac{A_3(2\mu + \Lambda_{22}) - A_2\Lambda_{32}}{(2\mu + \Lambda_{22})(2\mu + \Lambda_{33}) - \Lambda_{32}\Lambda_{23}} + \dfrac{A_2\Lambda_{12} - A_1(2\mu + \Lambda_{22})}{\Lambda_{13}(2\mu + \Lambda_{22}) - \Lambda_{23}\Lambda_{12}}}{\dfrac{\Lambda_{31}(2\mu + \Lambda_{22}) - \Lambda_{32}\Lambda_{21}}{(2\mu + \Lambda_{22})(2\mu + \Lambda_{33}) - \Lambda_{32}\Lambda_{23}} + \dfrac{\Lambda_{12}\Lambda_{21} - (2\mu + \Lambda_{22})(2\mu + \Lambda_{11})}{\Lambda_{13}(2\mu + \Lambda_{22}) - \Lambda_{23}\Lambda_{12}}} \tag{26}$$

for ε^{*}_{11} while strains ε^{*}_{22} and ε^{*}_{33} are obtained from (26) by the cyclic permutation $1 \to 2 \to 3 \to 1$ of indices. This yields the normal transformation strains in the equivalent inclusion. The shear transformation strains are given by (23) (when $\varepsilon^{\infty}_{ij} = 0$). The actual strains in the inhomogeneity are equal to those in the equivalent inclusion and are given by equation (21).

Taking into account remote strains, the tensor expression (21) can be written in the usual matrix form as

$$\begin{pmatrix} \varepsilon_{11} \\ \varepsilon_{22} \\ \varepsilon_{33} \\ \varepsilon_{23} \\ \varepsilon_{13} \\ \varepsilon_{12} \end{pmatrix} = \begin{pmatrix} \varepsilon^{\infty}_{11} \\ \varepsilon^{\infty}_{22} \\ \varepsilon^{\infty}_{33} \\ \varepsilon^{\infty}_{23} \\ \varepsilon^{\infty}_{13} \\ \varepsilon^{\infty}_{12} \end{pmatrix} + \begin{pmatrix} S_{1111} & S_{1122} & S_{1133} & 0 & 0 & 0 \\ S_{2211} & S_{2222} & S_{2233} & 0 & 0 & 0 \\ S_{3311} & S_{3322} & S_{3333} & 0 & 0 & 0 \\ 0 & 0 & 0 & S_{2323} & 0 & 0 \\ 0 & 0 & 0 & 0 & S_{1313} & 0 \\ 0 & 0 & 0 & 0 & 0 & S_{1212} \end{pmatrix} \begin{pmatrix} \varepsilon^{*}_{11} \\ \varepsilon^{*}_{22} \\ \varepsilon^{*}_{33} \\ 2\varepsilon^{*}_{23} \\ 2\varepsilon^{*}_{13} \\ 2\varepsilon^{*}_{12} \end{pmatrix} \tag{27}$$

where the 6×6 matrix (called *S* below) represents the Eshelby tensor S_{ijkl}. All other non-zero components of the Eshelby tensor are obtained from those in S using the Eshelby tensor symmetries $S_{ijkl} = S_{jikl}$ and $S_{ijkl} = S_{ijlk}$ indicated in (11).

Equations (23) and (25) – (27) give explicit expressions for the uniform strains in an ellipsoidal inhomogeneity generated by its uniform transformation (transformation strains).

6.3.2 Thin ellipsoidal inhomogeneity

Let the ellipsoid semi-axes be $a \geq b \geq c$. In general, for an isotropic inhomogeneity, components of the Eshelby tensor, S_{ijkl}, depend upon a, b, c and the Poisson ratio. In a particular case of a *thin* ellipsoidal inclusion, $c \ll b \leq a$, and in the leading order (Mura, 1987),

the non-zero Eshelby tensor components are given by (13), while all other components of *S* in (27) are zeros. Substituting *S* and (13) in (23) and (25) – (27) yields (uniform) strains within the inhomogeneity

$$\varepsilon_{11} = \varepsilon_{11}^{\infty}, \quad \varepsilon_{22} = \varepsilon_{22}^{\infty}, \quad \varepsilon_{33} = \varepsilon_{33}^{\infty} + \frac{2\mu_0\varepsilon_{33}^{T} + \lambda_0\varepsilon_{kk}^{T} - 2\Delta\mu\varepsilon_{33}^{\infty} - \Delta\lambda\varepsilon_{kk}^{\infty}}{2\mu_0 + \lambda_0}$$
$$\varepsilon_{12} = \varepsilon_{12}^{\infty}, \quad \varepsilon_{23} = \varepsilon_{23}^{\infty} + \varepsilon_{23}^{T}, \quad \varepsilon_{13} = \varepsilon_{13}^{\infty} + \varepsilon_{23}^{T} \tag{28}$$

In the case of isotropic, dilatational transformation strain (5) and in the absence of remote strain,

$$\varepsilon_{ij}^{\infty} = 0, \;\; \varepsilon_{12}^{T} = \varepsilon_{23}^{T} = \varepsilon_{13}^{T} = 0, \;\; \varepsilon_{kk}^{T} = \; 3\varepsilon_{33}^{T} \tag{29}$$

In this case, all strains in (28) but ε_{33} are zeros, and we have

$$\varepsilon_{33} = \frac{3\lambda_0 + 2\mu_0}{\lambda_0 + 2\mu_0}\varepsilon_0^{T} = \frac{1+\nu_0}{1-\nu_0}\varepsilon_0^{T}, \quad e_{ij} = 0 \;\text{ if }\; ij \neq 33 \tag{30}$$

which is identical to (7).

It is worth noting that in the leading order, the equivalent transformation strain tensor

$$\begin{pmatrix} \varepsilon_{11}^{*} \\ \varepsilon_{22}^{*} \\ \varepsilon_{33}^{*} \end{pmatrix} = \varepsilon_0^{T}\frac{\mu_1(\lambda_1 + 2\mu_1)}{\mu(3\lambda_1 + 2\mu_1)}\begin{pmatrix} \dfrac{\lambda + 2\mu}{3\lambda + 2\mu} \\ \dfrac{\lambda + 2\mu}{3\lambda + 2\mu} \\ \dfrac{\mu}{\mu_1} - \dfrac{2\lambda}{3\lambda + 2\mu} \end{pmatrix}, \quad \varepsilon_{12}^{*} = \varepsilon_{23}^{*} = \varepsilon_{13}^{*} = 0 \tag{31}$$

where we again assumed dilational transformation strain (5) and zero remote strains, ε_{ij}^{0}. Expression (31) illustrates that while the equivalent shear transformation strains are all zero, the equivalent normal transformation strains are not equal. In other words, the equivalent transformation strain is not dilational even if the actual transformation strain is.

Finally, take into account that strains are the same in the inhomogeneity and equivalent inclusion problems. This allows the inclusion solution (9) to be used for the case of the inhomogeneity. Accordingly, inserting (30) in (9), find strains

$$\varepsilon_{33}(\text{out}) = \left(\frac{1+\nu_0}{1-\nu_0} - \frac{1+\nu}{1-\nu} n_3^2\right)\varepsilon_0^T, \quad \varepsilon_{ij}(\text{out}) = -\frac{1+\nu}{1-\nu}\varepsilon_0^T n_i n_j \text{ if } ij \neq 33 \tag{32}$$

immediately outside the ellipsoidal inhomogeneity (Figure 3b). Comparing (32) to the case of thin inclusion (equation (16), observe that the only changed strain component is $\varepsilon_{33}(\text{out})$, which now depends on both Poisson's ratio of inhomogeneity and that of the enveloping matrix.

As the inhomogeneity and equivalent inclusion have identical shapes, equations (18) for the outward normal, n_i, to the inclusion surface also apply for the inhomogeneity. In particular, $n_3 = 0$ on the *xy*-trace of the inhomogeneity (Figure 3b), so ε_{33} in (32) rewrites as

$$\varepsilon_{33}(\text{out}) = \varepsilon_{zz} = \frac{1+\nu_0}{1-\nu_0}\varepsilon_0^T \tag{33}$$

Since this is the only change compared to the case of inclusion (equation (19), all plots in Figure 4 but ε_{zz} are also valid in the case of inhomogeneity. Although ε_{zz} changed its magnitude, it remains tensile everywhere on the *xy*-trace.

Similar to the inclusion, the principal stresses just outside the *xy*-trace of inhomogeneity are obtained from (33) and can be written as

$$\begin{pmatrix}\varepsilon_1(\text{out})\\ \varepsilon_2(\text{out})\\ \varepsilon_3(\text{out})\end{pmatrix} = \varepsilon_0^T \begin{pmatrix} -\dfrac{1+\nu}{1-\nu} \\ 0 \\ \dfrac{1+\nu_0}{1-\nu_0}\end{pmatrix} \tag{34}$$

6.4 CONCUSIONS

Simple closed form expressions are obtained for strains in the vicinity of a pressurized formation using *Eshelby*'s (1957) solution for the ellipsoidal inclusion (the same properties of reservoir and host rock) or ellipsoidal inhomogeneity (different properties of reservoir and host rock). Especially simple expressions are found in the case of a thin inclusion, when one of the semi-axes is much smaller than the other two. Our analysis shows that the strain changes caused by the formation pressurization are tensile for the vertical normal strain and compressive for normal horizontal strains everywhere along the formation boundary.

In Capter 10 we observed that our deep strainmeter was slightly outside of a high permeability lens. The deep strainmeter results show that vertical strain was tensile and the horizontal strains were compressive. Thus, our analysis explains the results from the deep strainmeter (Chapter 10), which otherwise would be difficult to explain because the sign of the

strains are opposite from the strainmeters at shallow depth.

Our findings are significant also because they allow for complementing the forward model and inverse analysis by including robust closed from considerations of the deep strain measurements.

In addition, a deep, thin ellipsoidal inhomogeneity provides a benchmark for the inhomogeneity that is not necessarily thin or ellipsoidal. Because the leading terms of our asymptotic analysis in the former case agree with those obtained from the exact Eshelby solution, this increases the confidence of the asymptotic consideration. This also suggests that findings for the ellipsoidal inhomogeneity could be extended to more complex geometries representing geologic heterogeneities and to not uniform pressure distributions.

6.5 REFERENCES

Eshelby, J. D., 1957, The determination of the elastic field of an ellipsoidal inclusion and related problems, Proceeding of the Royal Society London A, Proceedings of the Royal Society of London, Series A, Mathematical and Physical Sciences, Vol. 241, No. 1226, pp. 376-396.

Germanovich L.N., and R.A. Chanpura, 2002, Modeling Thin Inclusions in Poroelastic Medium by Line Discontinuities, IUTAM Symposium on Analytical and Computational Fracture Mechanics of Non-Homogeneous Materials, B.L. Karihaloo (ed.), Kluwer, Dordrecht, Boston, London, pp. 133 – 142.

Germanovich, L.N., Gence, G., Lowell, R.P., Rona, P.A., 2012, Deformation and surface uplift associated with serpentinization at mid-ocean ridges and subduction zones, J. of Geoph. Research, Vol. 117, Issue B7, July 2012, DOI: 10.1029/2012JB009372.

Helms, L.L., 2014, Potential theory, Universitext, Springer-Verlag, London, 485 pp.

Kellogg, O.D., 1929, Foundations of potential theory, Verlag Von Julius Springer, Berlin, 1929, 406 pp. (reprinted by Dover, New York, 1953).

Li, Q., and Anderson, P.M., 2001, A Compact Solution for the Stress Field from a Cuboidal Region with a Uniform Transformation Strain, Journal of Elasticity, Vol. 64, pp. 237–245.

MacMillan, 1958, The theory of the potential, Dover Publications, Inc., New York, New York, 384 pp.

Mindlin R.D., and D.H. Cheng, 1950, Thermo-Elastic Stress in the Semi-Infinite Solid, J. Applied Physics, 21(9), pp. 931-933.

Mura, T., 1987, Micromechanics of Defects in Solids, Martinus Nijhoff Publishers, Dordrecht, 587 pp.

Nowacki, W. (1986). Thermoelasticity, 2nd edition. PWN-Polish Scientific Publishers, Warsaw; Pergamon Press, Oxford.

Ru C.Q.,1999, Analytic solution for Eshelby's problem of an inclusion of arbitrary shape in a plane or half-plane, J. Appl. Mech, 66, 315–322. (doi:10.1115/1.2791051)

Timoshenko, S.P. and Goodier, J.N., 1970, Theory of Elasticity, 3rd edition, McGraw-Hill, New York.

CHAPTER SEVEN

PROXY-BASED BAYESIAN INVERSION OF STRAIN TENSOR DATA MEASURED DURING WELL TESTS

Contents

7.1 Abstract 7-2
7.2 Introduction 7-2
7.2.1 Overview 7-3
7.2.2 Inversion with uncertainty estimates 7-4
7.2.3 Proxy Models 7-4
7.2.4 Our Approach 7-5
7.3 Method 7-5
7.3.1 Conceptualization 7-6
7.3.2 Initialization 7-7
7.3.3 Exploration 7-10
7.3.4 Solution 7-11
7.4 Workflow validation using idealized model 7-13
7.4.1 Conceptualization 7-13
7.4.2 Initialization 7-16
7.4.3 Exploration 7-18
7.4.4 Solution 7-20
7.5 Field Application 7-22
7.5.1 Conceptualization 7-23
7.5.2 Initialization 7-24
7.5.3 Exploration 7-26
7.5.4 Solution 7-26
7.6 Discussion 7-30
7.7 Conclusion 7-31
7.8 List of Symbols 7-32
7.9 References 7-37

7.1 ABSTRACT

Recent instrument developments have made it possible to measure the strain tensor caused by injecting or pumping fluid from aquifers or reservoirs, but the full value of these data is limited because the long runtimes of poroelastic forward models makes it impractical to use many inversion schemes. This limits the interpretation of strain data for managing the recovery of resources or storage of wastes in the subsurface. This paper describes a method of inverting deformation data using a poroelastic numerical simulator so the results can be used to manage reservoirs or aquifers. We developed a workflow designed to reduce the number of simulations sufficiently to make it feasible to use DREAMzs, an advanced Bayesian inversion method that translates the uncertainties from different sources into unbiased posterior parameter distributions and uncertainty envelopes around the field data. Using a KNN proxy model for the poroelastic simulator is key to reducing the overall computations, and the workflow includes a strategy for ensuring the proxy model results converge on the results from the simulator. The workflow is tested using an idealized example that verifies the ability to correctly identify parameters and characterize noise used to perturb the data. Field data from an injection test at an oil reservoir near Tulsa, Oklahoma, and described in our previous report for DE-FE0023313 are also used to evaluate the efficacy of the workflow with a real dataset. The workflow identified 265 history matching solutions out of 1240 total simulation runs (21% acceptance ratio), where the results were used to characterize posterior parameter distribution and evaluate the prediction uncertainty. This workflow is significant because it enables strain tensor, or other geomechanical measurements to be interpreted to guide decision-making during energy and environmental processes in the subsurface.

7.2 INTRODUCTION

Matching the history of data from transient well tests to the results from simulations is widely used to characterize subsurface properties like permeability, rock stiffness or facies boundaries (Bourdet, 2002; Doherty, 2015; Foroud et al., 2014; Hill & Tiedeman, 2006; Horne, 1995; Istok & Dawson, 1991; Rana et al., 2018). We have developed techniques for measuring multiple components of the subsurface strain tensor that are caused by pumping or injection (Murdoch et al., 2020), and this has led to a need to develop history matching techniques to interpret hydromechanical well tests (where strain and pressure data are measured). Interpretations that can estimate the distribution of reservoir parameters and their uncertainties would have particularly important applications.

The forward model for this problem couples fluid flow and deformation, and this leads to a system of non-linear equations from poroelasticity (Detournay and Cheng, 1991). Different inversion techniques have been used with poroelastic forward models to address a variety of problems, but a particularly common application is to analyze data describing the deformation of the ground surface caused by fluid injection or extraction from wells (Iglesias & McLaughlin, 2012; Morris et al., 2011; Rinaldi & Rutqvist, 2013; Shi et al., 2012; Vasco et al., 2001), or volcanic activities (Nunnari et al., 2005; Velez et al., 2011). Many of these studies are designed to find a single, best-fit solution to the data, and they provide limited information about uncertainty in parameters and model prediction (Santhosh & Sangwai, 2016). Several other studies use methods designed to identify multiple solutions that fit deformation data within an acceptable tolerance. For example, Murdoch et al. (2023) used a stochastic inversion (NGSAII) to interpret subsurface strain data, whereas other researchers employed Bayesian algorithms to invert InSAR

data (Alghamdi et al., 2021; Bagnardi & Hooper, 2018; Jha et al., 2015; Ramirez & Foxall, 2014). Results from these inversions provide an adequate number of realizations to evaluate parameter and prediction uncertainties, but stochastic or Bayesian inversions can be cumbersome or intractable when the forward model requires lengthy execution times. For example, a stochastic inversion of strain data required roughly 70,000 simulations (Murdoch et al., 2023), and Bayesian inversion of InSAR data measured at the In Salah oilfield converged after a similar number of simulations (Ramirez & Foxall, 2014). This type of computational problem is feasible to conduct, but it is expensive and technically challenging and limits the applicability of using strain data to understand reservoirs.

Techniques for analyzing complex reservoir problems have been evolving rapidly with the refinement of inversion methods and the integration of machine learning techniques to reduce computational requirements (Jaber et al., 2019). We suspected that these techniques could be used to analyze hydromechanical well tests, so we evaluated the current state-of-art and developed a workflow for this application. The objective of this chapter is to describe the workflow and demonstrate its performance. This chapter is based on Roudini et al. (2023).

7.2.1 Overview

Difficulties with the long-run times required by complex forward models underly many problems associated with matching the time series, or history of measurements made in response to pumping or injection into aquifers or reservoirs (Asher et al., 2015). The simplest history matching (HM) approach is to change one or more parameters and manually compare model results to historical data until a sufficient match is achieved (Gilman & Ozgen, 2013). This approach is easy to implement and it can be a useful starting point, particularly when the number of parameters is small. However, this approach is typically limited to a small range of the parameter space (Costa et al., 2014) and is unable to describe model prediction uncertainties, for example, from errors in the conceptual model, field measurement, or other sources (Hill & Tiedeman, 2006).

Recent work has given rise into the development of Assisted History Matching (AHM) workflows that couple a numerical model with optimization-based or Bayesian-inference-based algorithms to automatically search a parameter space and identify acceptable solutions (Oliver & Chen, 2011). Deterministic and stochastic methods are two main classes of optimization-based algorithms (Liberti & Kucherenko, 2005). Deterministic optimization-based AHM workflows typically include gradient descent algorithms that are capable of finding optimal solutions with a limited number of simulations (Burrows & Doherty, 2016), which makes them relatively fast. They are vulnerable to converging on local minima, however, and this obstructs the ability of gradient descent methods to find global minima in complex HM problems. Stochastic optimization methods can avoid converging on local minima and are better suited to non-linear and complex objective functions (Rana et al., 2018). Simulated annealing, particle swarm optimization and genetic algorithms are well-known stochastic optimization methods used in HM applications in water resources (Gill et al., 2006; Hill & Tiedeman, 2006; Perozzi et al., 2016; Tongal & Booij, 2022) and petroleum engineering (Foroud et al., 2014; Khatoon et al., 2021; Schulze-Riegert et al., 2002). Optimization-based methods can effectively identify parameters from an HM analysis, but they are unable to quantify the uncertainty in predictions made with the parameters they have identified. This shortcoming can limit the value of optimization methods in design and evaluation problems where estimating uncertainty is important.

7.2.2 Inversion with uncertainty estimates

Bayesian inference-based methods address the problem of quantifying prediction uncertainty by estimating parameters as a probabilistic distribution, known as a posterior (Vrugt, 2016), target (Ward & Fox, 2012), joint (Zheng & Han, 2016) or stationary distribution (Liu et al., 2000). Ensemble Kalman filter (EnKf) and Markov Chain Monte Carlo (MCMC) methods are well-known algorithms (Araujo et al., 2019) that incorporate prior knowledge and the likelihood of similar model parameters to identify a suite of acceptable solutions, each of which is defined by a set of parameters. Each parameter has a suite of values from the acceptable solutions that define a probability distribution characterizing the uncertainty of the parameter. The uncertainties of all the parameters define the prediction uncertainty.

The EnKf algorithm sequentially modifies model parameters until a posterior distribution is obtained (Houtekamer & Mitchell, 2005). This method has been used successfully in a variety of earth science applications (Jeong et al., 2010; Liu & Oliver, 2005), but it can fall short in highly non-linear or complex problems (Evensen, 2003).

MCMC algorithms use a Monte Carlo approach to draw samples from a parameter space, and a Markov scheme to generate chains of parameter sets that eventually converge on a posterior distribution (Dellaportas & Roberts, 2003). The classic approach (Andrieu et al., 2003) is to use the Metropolis-Hasting algorithm (Chib & Greenberg, 1995) to form Markov chains as random walks from one parameter set to another. This avoids calculating the difficult-to-estimate normalization factor in Bayes theorem, but the Metropolis-Hasting algorithm makes no assumptions about the orientation and jump rate of random walks, resulting in convergence difficulties for some complex problems (Vrugt & Ter Braak, 2011). These problems were addressed by determining the orientation and jump rate for each chain with a differential evolution operator that uses results from multiple other chains (Ter Braak & Vrugt, 2008). This causes the orientation and jump rate of each chain to evolve and identify potential posterior distributions with higher accuracy. This differential evolution approach was further refined and used to create a code called DREAM (Vrugt, 2016) by only updating randomly selected parameters rather than the entire parameter set, and eliminating outlier chains. A recent refinement (DREAMzs) uses an improved sampling scheme that further reduces the number of chains and iterations required for the convergence of the MCMC algorithm (Vrugt, 2016).

Applications of DREAMzs to HM problems by Zheng et al. (2016) and Pourreza-Bilondi et al. (2017) required approximately 10^4 simulations for convergence. This is significantly fewer simulations than required by other MCMC methods, which is encouraging. However, the runtime of numerical simulations that include multiple, coupled processes is often many tens of minutes to several hours or more. It could require significant computational resources to use these simulators even with an efficient algorithm like DREAMzs, and this has made it impractical to use large numerical simulators directly with MCMC inversions.

7.2.3 Proxy Models

One approach to reducing the computational demand during inversion is to use artificial intelligence methods to create a proxy model that replaces many of the runs of the numerical simulator (Maschio & Schiozer, 2014; Mirghani et al., 2012; Singh et al., 2008; Tripoppoom et al., 2020). One example of this approach is the use of the *K*-Nearest Neighbors (KNN) artificial intelligence method to create a proxy model for a standard MCMC inversion. This approach was

used to create a proxy model of pressure and flow data from a well field completed in shale, for example (Dachanuwattana et al., 2018). The KNN proxy model reduced the number of simulations required by the numerical simulator in this example from approximately 10^6 to 5000 (Dachanuwattana et al., 2018). This approach has also been used to optimize a wellfield design to minimize the effects of saltwater intrusion (Hussain et al., 2015). This strategy was expanded by Tripoppoom et al. (2020), who used both KNN and an Artificial Neural Network (ANN) to analyze pressure and flow data from a shale gas well.

7.2.4 Our Approach

The previous results are encouraging, but to our knowledge, none of them include the analysis of coupled fluid pressure and deformation. This will increase the complexity and duration of the forward simulations compared to simulations of pressure alone, and this will make the inversion more cumbersome. Furthermore, previous HM proxy model applications have not taken advantage of DREAMzs, which could streamline the inversion enough to make it practical to include deformation data.

We developed a workflow designed to facilitate the inversion of hydromechanical well test data using a poroelastic simulator and DREAMzs in order to identify parameters and their uncertainties from pressure and strain tensor data. The components of the workflow will be described, and then it will be demonstrated with two examples, one that uses synthetic data and another that uses real field data.

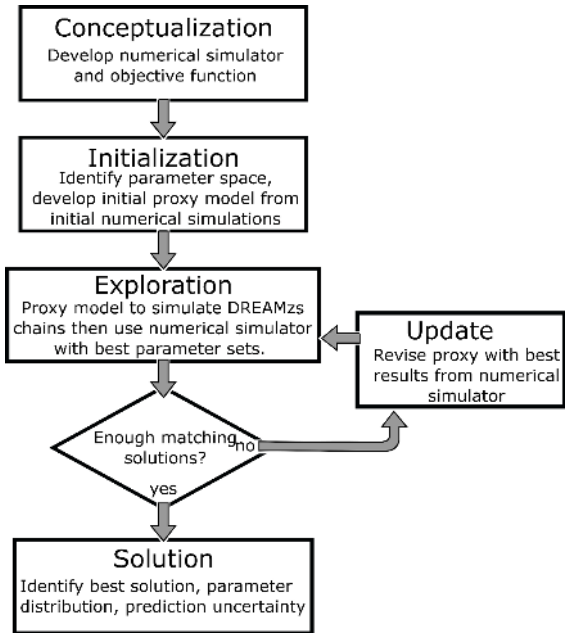

Figure 1. Workflow for doing Bayesian inversion using proxy model.

7.3 METHOD

The inversion workflow was motivated by the need to solve hydromechanical well testing problems, but it could be used to address a variety of related problems so we will describe the method in general terms and specific examples will follow. Figure 1 shows the four workflow phases: 1.) Conceptualization; 2.) Initialization; 3.) Exploration; and 4.) Solution.

Conceptualization involves identifying the physical problem, characterizing it mathematically and developing a solution. Suitable datasets are identified and used to define an objective function. The initialization phase identifies the parameters that are important and bounds the parameter space, and it includes an initial training of the proxy model using parameters randomly sampled from the parameter space. In the exploration phase, the initialized proxy model is used by DREAMzs to explore the parameter space with multiple chains. The chains are combined and parameters in the best solutions are used in the numerical model to update the proxy model. The updated proxy model is used by DREAMzs and the process is repeated until a stopping

criterion is reached (Figure 1). The solution is a suite of parameter sets and associated simulation results from the numerical model that fit the data within a convergence threshold.

7.3.1 Conceptualization

The workflow begins by conceptualizing the physical problem and identifying a numerical simulator to represent it.

7.3.1.1 Numerical simulator

There are a variety of reservoir simulators or multiphysics differential equation solvers that are suitable for the poroelastic problem we are interested in. We used the code COMSOL Multiphysics because it can simulate poroelastic processes and it is closely integrated with MATLAB, which we used to perform the inversion calculations. Other numerical simulators that can accommodate batch input and output could easily be used in the workflow.

7.3.1.1.1 Definitions

The dependent variables in the numerical simulator will be referred to as *system response* variables in keeping with the terminology used in inversion (Yeh, 1986). The transient system response variables will be designated as $\theta_{i,j,k}$ where i is the time index, j is the variable type and location, and k is the source index for the response variable value (parameters used in the analysis are summarized in the List of Symbols table at the end of the paper). The time index, i, includes all the times used in the field dataset. The variable type and location index, j, refers to measurements made with different sensors at various locations. The source index includes $k = D$ for field data, $k = M$ for response variables modeled using the numerical simulator, and $k = K$ for variables that are estimated using the proxy model.

The analysis identifies material properties that appear as parameters in the numerical simulator. Parameter sets will be designated as $\Pi_{p,q}$ where p is the parameter index and q is the parameter set index. For example, the poroelastic example analysis that follows includes five parameters E_a, E_c, b_a, k_a, and ν_a, (Table 4) and the workflow will identify 86 sets of these parameters that fit the field data, $\theta_{i,j,D}$, within a threshold, so $1 < p < 5$ and $1 < q < 86$.

7.3.1.1.2 Objective Function

The objective function characterizes the mismatch between a response variable observed in the field and the variable calculated by either the simulator or proxy model (Dachanuwattana et al., 2019; Tripoppoom et al., 2019). The system residual error (SRE) is an average mismatch at each time step

$$SRE_{i,k} = \sqrt{\frac{1}{m}\sum_{j=1}^{m}\left[\frac{100\times(\theta_{i,j,k}-\theta_{i,j,D})}{\zeta_j}\right]^2} \quad (1)$$

where m is the number of response variables. $SRE_{i,M}$ is calculated using the numerical simulator and $SRE_{i,K}$ is calculated using the proxy model. ζ_j is the range of a response variable over the duration of the field data and is defined as

$$\zeta_j = \left(\theta_{i,j,D}\right)_{max} - \left(\theta_{i,j,D}\right)_{min} \quad (2)$$

The global objective error (GOE) is the sum of squared system residual errors over all the timesteps (Hassanzadeh et al., 2019; Schoups & Vrugt, 2010; Vrugt, 2016)

$$GOE_{\mathrm{k}} = \sum_{i=1}^{n} SRE_{i,k}^{2} \quad (3)$$

where $k = M$ or K. The relative residual error (RRE) is the average relative residual for a response variable for all the time steps (Tripoppoom et al., 2020)

$$RRE_j = \frac{1}{n}\sum_{i=1}^{n}\left[\frac{|\theta_{i,j,M} - \theta_{i,j,D}|}{\theta_{i,j,D}}\right] \quad (4)$$

where n is the number of timesteps in both equations (3) and (4). The SRE, GOE and RRE will be used in the workflow, but the GOE will be the primary objective function.

7.3.2 Initialization

The initialization phase is designed to identify parameters that are important to the solution, and to establish bounds for the parameter space containing suitable solutions (Tripoppoom et al., 2021). It also develops an initial proxy model. These actions will reduce the computations required during inversion while helping to ensure the results include solutions near the global optimum.

Initialization begins by using the conceptual geologic model, available data (e.g., cores, well logs, and seismic records) and scientific judgment to identify a conceptual computational model and to bound the maximum and minimum values of all the parameters included in the simulation. This results in $\Pi_{p,max}$ and $\Pi_{p,min}$.

7.3.2.1.1 Parameter Identification

An analysis similar to a two-level factorial experimental design (Elarbe et al., 2022; White et al., 2001) is used to identify parameters, or interactions between parameters that have a significant effect on the forward model (Tripoppoom et al., 2019; Wantawin et al., 2017). The approach includes identifying input parameters within the upper and lower limits of the parameters and evaluating them using experiments or mathematical models (Ilzarbe et al., 2008; Jamshidnezhad, 2015). In our application, the numerical simulator is then used to calculate the GOE for each parameter set, and the GOEs are used to calculate the influence that each parameter has on the solutions from model.

Consider an example problem with $f = 2$ parameters, A and B. Two values of A and B (the max and min) are used to create $h = f^2 = 4$ parameter sets, $\Pi_{p,g}$ where p= 1 to 2 and g = 1 to h. The simulator is used to calculate the GOE_M for each parameter set. Each of the parameters has an associated unit parameter, A^* and B^*, that only carries a sign. So, for example: A^* = +1 to represent A_{max}, and A^* = -1 to represent A_{min}. Parameter interaction is characterized by the product, $AB^* = A^*B^*$. This results in vectors of unit parameters and GOEs, which are shown in Table 1 for the example. The total influence of the parameters and the parameter interactions on the GOE is the dot product of the unit parameter and GOE vectors, so the influence factor for parameter A is: $I_A = A_g^* \cdot Y_g$. A t-value for the bth influence factor is calculated using

$$t_{Ib} = \frac{I_b - \bar{I}}{SE_n} \quad (5)$$

where $\bar{I}$ is the mean influence factor and SE_n is the standard error of the simulation noise. We determined SE_n using the ANOVA approach outlined by Montgomery (2017). The *t*-values are ranked and *t*-values greater than the Bonferonni limit (Bonferroni, 1936) are assumed to identify parameters, or groups of interacting parameters that are important to the solution and that should be used in the subsequent analysis. Parameters or groups of parameters with *t*-values less than the Bonferonni limit are ignored.

A two-level factorial analysis requires simulations to account for all *f* parameters and their interactions. A two-level full factorial analysis (2FFA) requires 2^f simulations to evaluate all parameter interactions. However, parameter interactions involving more than 3 parameters can typically be ignored, which requires $2^{f-\tau}$ simulations where τ is determined based on the *f*. This leads to two-level partial factorial analysis (2PFA) that is more computationally efficient than 2FFA for problems with more than 6 or 7 parameters, but without notable loss of resolution (Chobisa, 2021).

Table 1. Unit parameters and system response for datasets created from maximum and minimum values of parameters *A* and *B*.

	Parameter sets	Unit Parameters		Interaction	System Response
g		A_g^*	B_g^*	AB_g^*	Y_g
1	$\Pi_{p,1}$	-1	-1	+1	GOE_1
2	$\Pi_{p,2}$	-1	+1	-1	GOE_2
3	$\Pi_{p,3}$	+1	-1	-1	GOE_3
4	$\Pi_{p,4}$	+1	+1	+1	GOE_4

7.3.2.1.2 Solution Feasibility Evaluation

The feasibility of finding a HM solution that matches the data is evaluated with an initial sampling of the important parameters identified with the two-level factorial analysis. Latin Hypercube Sampling (McKay et al., 2000) is used to generate sets of uncorrelated, random parameters with a uniform density within the bounds defined by $\Pi_{p,max}$ and $\Pi_{p,min}$. In the examples that follow, LHS was used to obtain 40 samples of each parameter, resulting in $\Pi_{LHS\,p,g}$ where $1 < g < 40$. These datasets are used in the simulator and the resulting simulated response variables are plotted along with the observed data. The plots are inspected to ensure that the observed data, $\theta_{i,j,D}$, are contained within the envelopes defined by the simulated response variables, $\theta_{LHS\,i,j,M,g}$. The plots are also inspected to ensure that the trends, or shapes of the predicted time series resemble the data. These checks ensure that acceptable solutions are contained within the parameter bounds (Tripoppoom, Xie, et al., 2020). The conceptual model

and parameter bounds may need to be revised until the trends and values of the response variables are consistent with the data.

7.3.2.1.3 Initial proxy model

A proxy model that can represent the numerical simulator is selected and initialized to ensure proper functionality prior to data analysis. Our approach requires using a proxy model with predictive capabilities, and we selected a simple, fast machine learning algorithm called KNN (Altman, 1992) for the HM application described here. The KNN method estimates values at unknown points using values measured at points that are nearby in parameter space. The method can use a selected number, termed *K*, of nearest neighbors, and this gives rise to the acronym, *K*-Nearest Neighbors (KNN). The KNN method avoids the need to assume a prior distribution of the observed data, so it is classified as non-parametric (Lee et al., 2019). It searches for the similarity between measured points, which is a hallmark of a memory-based machine learning method (El Bilali et al., 2021).

7.3.2.1.4 Algorithm

The KNN method uses a suite of h simulations, each of which has a parameter set, $\Pi_{K\,p,1<g<h}$, and corresponding response variables, $\theta_{K\,i,j,M,1<g<h}$. The KNN algorithm estimates the response variable for an arbitrary parameter set, Π_p^{ε}, using a weighted average of $\theta_{K\,i,j,M,g}$. The algorithm uses values of the parameters that are normalized to the range of parameters in all the datasets to avoid biases caused by large differences in the mean values of different parameters. Parameter sets that are normalized to the ranges are designated with a hat, $\widehat{\Pi}_{K\,p,g}$.

The Euclidian distance in normalized parameter space is calculated using

$$L_g = \left\{\sum_{p=1}^{f}\left(\widehat{\Pi}_p^{\varepsilon} - \widehat{\Pi}_{K\,p,g}\right)^2\right\}^{1/2} \tag{6}$$

for all *h* parameter sets and ranked, and then indices for the *K* parameter sets with the shortest Euclidian distances are used to create a vector, a_e, where $1 < e < K$.

The response variables from the parameter sets identified in a_e are used to predict the response variables using

$$\theta_{i,j,K}(\Pi_p^{\varepsilon}) = \sum_{e=1}^{K}\gamma_e\,\theta_{K\,i,j,M,a_e} \tag{7}$$

where the weight vector is based on the inverse of the normalized Euclidian distance

$$\gamma_e = \frac{\sum_{e=1}^{K} L_{a_e}}{L_{a_e}} \tag{8}$$

A separate KNN analysis is used to calculate each response variable at each time step.

7.3.2.1.5 Selecting K

Performance of the KNN method is affected by the value of *K,* the number of nearest measured points used in the weighting term. A cross-fold validation analysis is used to estimate

the optimal value of K, which is expected to be an integer between 1 to 1.5 times the square root of the number of measured points (Tripoppoom et al., 2019; Yu et al., 2018).

The first fold in the cross-fold analysis starts by selecting training ($0.8h$) and validation ($0.2h$) datasets from the simulated datasets. Response variables, $\theta_{i,j,K}$, for each validation parameter set are calculated using the selected training dataset. The Root Mean Squared Errors (RMSEs) between $\theta_{i,j,K}$ and $\theta_{i,j,M}$ are calculated using all response variables and all the validation parameter sets and then the RMSE values for the same response variable are summed to obtain the total RMSE, $RMSE_{T,j}$. This process is repeated for all possible values of K for the first fold.

The second fold is calculated much the same as the first, except the datasets are shuffled and different sets are used for training and validation. The process is repeated for five folds and $RMSE_{T,\mathrm{j}}$ for each value of K is averaged across the five folds. The value of K with the lowest average $RMSE_{T,\mathrm{j}}$ is used to explore the parameter space.

7.3.3 Exploration

The exploration phase uses DREAMzs to search the parameter space within bounds defined by $\Pi_{p,max}$ and $\Pi_{p,min}$. This phase starts by using random parameter estimates generated internally to create three computational chains that are populated by DREAMzs. A threshold GOE, GOE_{MT}, is defined and used to identify valid HM solutions.

The exploration process is conducted as follows:

7.3.3.1 Conduct a DREAMzs Iteration

A1. Estimate a trial parameter set, Π_{Tp}, which includes an estimate of the variance of the system residual error, $\sigma^2_{SRE_T}$. This is done by randomly selecting between the parallel direction and snooker updaters described by Ter Braak & Vrugt, (2008) and Vrugt (2016). These updating algorithms are optimized to draw on archived parameter sets in the chains to estimate candidate Π_{Tp} with a high likelihood of generating acceptable results.

A2. Use the current KNN proxy model to evaluate the $\theta_{T_{i,j,K}}$ using Π_{Tp}, and then calculate the $GOE_{K,T}$ using equation (3).

A3. Determine whether the trial parameter set should be accepted as the current parameter set. Do this by calculating the Metropolis-Hastings factor

$$\omega = \min\left[1, \frac{\sigma_{SRE_C}}{\sigma_{SRE_T}} \exp\left[\frac{GOE_{K,C}}{2\sigma^2_{SRE_C}} - \frac{GOE_{K,T}}{2\sigma^2_{SRE_T}}\right]\right] \quad (9)$$

which is based on the Likelihood function (Vrugt, 2016). Then calculate a random number in the interval, $0 \leq \beta \leq 1$. If $\omega > \beta$ then Π_{Tp} is accepted as the new current parameter set and the chain is extended. This involves saving Π_{Tp} and $\sigma^2_{SRE_T}$ as the iith member of the chain, so $\Pi_{C,ii} = \Pi_{Tp}$ and $\sigma^2_{SRE_C,ii} = \sigma^2_{SRE_T}$. If $\omega \leq \beta$ then Π_{Tp} is discarded.

A4. Return to A1 until Λ members have been accepted into each chain. Λ is determined for each problem. For example, Zheng et al. (2016) used Λ = 45,000. We assumed that Λ is large enough to ensure the chains converge, and we verified convergence for selected chains at the end of the inversion.

This routine ends by combining the three chains to give response variables, $\theta_{Cp_{i,j,K,ii}}$, parameter sets and estimated variances, $\Pi_{Cp,ii}$ and values of $GOE_{K,Cp,ii}$ from each of the three chains, where $1 < ii < 3\Lambda$.

7.3.3.2 Update Proxy Model

B1. Use the GOE to rank the best 10% datasets from the combined chains and then divide the ranked list into quartiles. Randomly select 10 solutions from each quartile (40 datasets total). Let *kk* be the indices identifying the 40 top representative datasets selected from the quartiles, so the best parameter sets are $\Pi_{Cp,kk}$.

B2. Use the numerical simulator to calculate $\theta_{Cp_{i,j,M,kk}}$ using $\Pi_{Cp,kk}$. Calculate $GOE_{M,Cp,kk}$ using equation (3).

B3. Evaluate the performance of the proxy model by comparing $GOE_{M,Cp,kk}$ with $GOE_{K,Cp,kk}$.

B4. Adding parameter sets from $\Pi_{Cp,kk}$ and response variables, $\theta_{Cp_{i,j,M,kk}}$, to the current training set and update KNN using the new training set with equations (6) thru (8).

B5. Select an updated *K* using the same approach described for initialization in 2.2.3.2.

7.3.3.3 Search and Refine

C1. Conduct a DREAMzs iteration as in 2.3.1

C2. Update the proxy model as in 2.3.2

C3. Identify valid history matching (HM) solutions where $GOE_{M,Cp,kk} < GOE_{MT}$. Save results as $\theta_{HM_{i,j,M,mm}}$, $\Pi_{HM_{p,mm}}$ and increment a history matching counter, *mm*, for each valid solution.

C4. Increment the workflow counter and return to C1 until either of the following stopping criteria is reached:

a.) The number of workflow iterations is greater than a threshold value (100 in our examples), or
b.) The number of valid history matching solutions is greater than a problem-specific target value, Σ.

7.3.4 Solution

The solution phase consists of updating, so the findings are internally consistent, and then compiling and summarizing the results.

7.3.4.1 Posterior Parameter Distributions

The population of $\Pi_{HM_{p,mm}}$ is typically too small to characterize the posterior distribution (Tripoppoom et al., 2019). A more thorough sampling is obtained using parameter sets drawn from the iteration that includes the most contributions to $\Pi_{HM_{p,mm}}$, and that has converged according to the *R*-statistic< 1.2 (Gelman & Rubin, 1992). This ensures that the chains sample from the posterior distribution and they are almost irreducible (Toft et al., 2007). The chains in the selected iteration are merged and the parameters in the last 10% of the merged chains are used to characterize the posterior distribution, $\Pi_{PO_{p,qq}}$.

7.3.4.2 SRE Variance and HM Solutions

The exploration phase refined the estimate of the system residual error variance, σ^2_{SRE}, and this requires an update to the identification of the HM solutions. The set of all σ^2_{SRE} values in $\Pi_{PO_{p,qq}}$ is used to calculate a mean $\bar{\sigma}^2_{SRE}$, which is then used to update the GOE_{MT} as

$$GOE_{Mt} = n(3\bar{\sigma}_{SRE})^2 \quad (10)$$

The updated GOE_{MT} is then used to re-identify the valid HM solutions, revising the datasets identified in section 2.3.3. The re-identified HM solutions are used to update $\theta_{HM_{i,j,M,mm}}$ and $\Pi_{HM_{p,mm}}$.

7.3.4.3 Statistical Summary

a) The results are summarized using
b) Most accurate parameter values The most accurate solution, $\theta_{A_{i,j,M}}$, is the HM solution with the least GOE. The most accurate solution is determined with the simulator using the most accurate parameter set, Π_{Ap}.
c) Mean parameter values The parameter means are defined as the mean values in $\Pi_{PO_{p,qq}}$, which is determined using proxy-based parameter sets that satisfy convergence.
d) Parameter Uncertainty Uncertainty in the parameter estimates is determined by characterizing an idealized distribution that represents the posterior distribution. For example, this is the standard deviation or 95% confidence interval of a normal or log-normal distribution fit to $\Pi_{PO_{p,qq}}$.

7.3.4.4 Prediction Uncertainty

The parameter variability in $\Pi_{HM_{p,mm}}$ dataset allows for estimating the posterior prediction uncertainty by calculating the 5th and 95th percentile values (P5 and P95, respectively) at each time step from $\theta_{HM_{i,j,M,mm}}$ (Vrugt, 2016). These values bound the 90% confidence band for the observed data.

The total uncertainty is estimated by evaluating the signal noise along with the posterior prediction uncertainty. This is done by assuming the datasets from $\theta_{HM_{i,j,M,mm}}$ represent the normally distributed noise about the most accurate dataset, $\theta_{A_{i,j,M}}$. We first characterize the noise distribution at each time step. The noise characteristics are then used to generate 10,000 random

points at each time step and for each HM dataset in $\theta_{HM\,i,j,M,mm}$. The randomly generated points about the values of $\theta_{HM\,i,j,M,mm}$ are compiled for each time step, and the P5 and P95 values are calculated for that time step. Combining the P5 and P95 values for all the time steps gives the band of total uncertainty for the response variable. Posterior prediction uncertainty with associated total uncertainty represents the prediction uncertainty.

7.4 WORKFLOW VALIDATION USING IDEALIZED MODEL

A model of an idealized aquifer with an injection well was developed and used to evaluate the workflow when the parameters are known *a priori*. A fully coupled poroelastic numerical model (Cheng, 2016; Detournay & Cheng, 1993; Wang, 2000) was used to create data describing pressure in the aquifer and strain in an overlying confining unit. These datasets were perturbed by adding normally distributed error with a mean of zero to the pressure and strain data. The perturbed datasets were then used as field data in the workflow.

7.4.1 Conceptualization

The idealized model is composed of a permeable aquifer layer (5 m thick) and an overlying confining unit (100 m thick). The aquifer and confining unit are separated by a thin, impermeable layer to restrict flow out of the aquifer (Figure 2). The lateral boundaries assume no-flow and zero normal displacement at r = 30 km, which is essentially an infinite lateral extent. Water is injected at a rate of 0.5 l/s (8 gpm) for 334 hours (206 timesteps) in an injection well that fully penetrates the aquifer. The properties are assumed to be constant and uniform and the values are similar to a sandstone aquifer with shale confining units (Murdoch et al., 2016).

These assumptions are the basis for two-way coupling between pressure and deformation in poroelasticity (Detournay & Cheng, 1993). The equations describing poroelasticity are applied over a domain that includes the reservoir and overlying and underlying confining units. The domain extends to the ground surface because some strain measurements are made at shallow depths. Boundary conditions and parameter distributions are inferred from the geologic conceptual model and used to define an analysis that forms the basis of the numerical simulator (Figure 2).

7.4.1.1.1 3.1.1 Numerical Simulator

The analysis includes two sets of conservation equations, one for the fluid and one for the porous solid (Detournay & Cheng, 1993). Momentum conservation for the solid is (Cheng, 2016)

$$\frac{\partial \sigma_{ij}}{\partial x_j} = F_i \tag{11}$$

where σ_{ij} is the total stress tensor, and F_i is the body force vector. Repeated subscripts indicate summation using the Einstein convention. Hooke's Law for a linear poroelastic solid is (Wang, 2000)

$$\sigma_{ij} = 2G\varepsilon_{ij} + \lambda\varepsilon_{kk}\delta_{ij} - \alpha P\delta_{ij} \tag{12}$$

where ε_{ij} is the strain tensor, ε_{kk} is the volumetric strain, δ_{ij} is the dirac operator, α is the Biot-Willis parameter, λ is a Lame constant, and G is the shear modulus. Using $\lambda = \frac{E\nu}{(1+\nu)(1-2\nu)}$ and $G = \frac{E}{2(1+\nu)}$ and substituting (12) into (11)

$$\frac{E}{2(1+\nu)}\frac{\partial^2 u_i}{\partial x_k^2} + \frac{E}{2(1+\nu)(1-2\nu)}\frac{\partial \varepsilon_{kk}}{\partial x_i} = \alpha\frac{\partial P}{\partial x_i} \tag{13}$$

where u_i is displacement of the solid in the ith direction, E is drained Young's modulus, ν is drained Poisson's ratio. The strain tensor is determined using displacement gradients (Cheng, 2016).

Conservation of mass of the fluid gives (Wang, 2000)

$$-\frac{\partial q_i}{\partial x_i} = \frac{1}{M}\frac{\partial P}{\partial t} + \alpha\frac{\partial \varepsilon_{kk}}{\partial t} \tag{14}$$

where q_i is the volumetric flux vector, P is the pore pressure, α is the Biot-Willis coefficient, and M is the Biot modulus

$$\frac{1}{M} = \frac{(\alpha-\phi)(1-\alpha)3(1-2\nu)}{E} \tag{15}$$

where ϕ is porosity. Volumetric flux is

$$q_i = -\frac{k}{\mu}\frac{\partial}{\partial x_i}(P + \rho g x_3) \tag{16}$$

where k is the permeability, ρ is the fluid density, μ is the dynamic viscosity, g is the gravitational acceleration, and x_3 is upward coordinate.

The governing poroelastic equations are solved using the Galerkin finite element method. The finite element mesh consists of small rectangles (~1 m radial and 0.3 m vertical) adjacent to the well screen (r = 0.1 m) and their radial dimension increases progressively to ~4 m at r = 400 m. The mesh increases in both radial and vertical directions for a total of 12,025 elements and a minimum element quality of 0.95.

The assembled Jacobian matrix was solved using the MUMPS solver (Amestoy et al., 2000) with a relative tolerance of 0.01 used for convergence. Adaptive time stepping was enabled to allow the code to increase the size of the time step to reduce execution time. Run times were in the range of 7 to 10 minutes. The numerical forward model was formulated and solved using COMSOL Multiphysics.

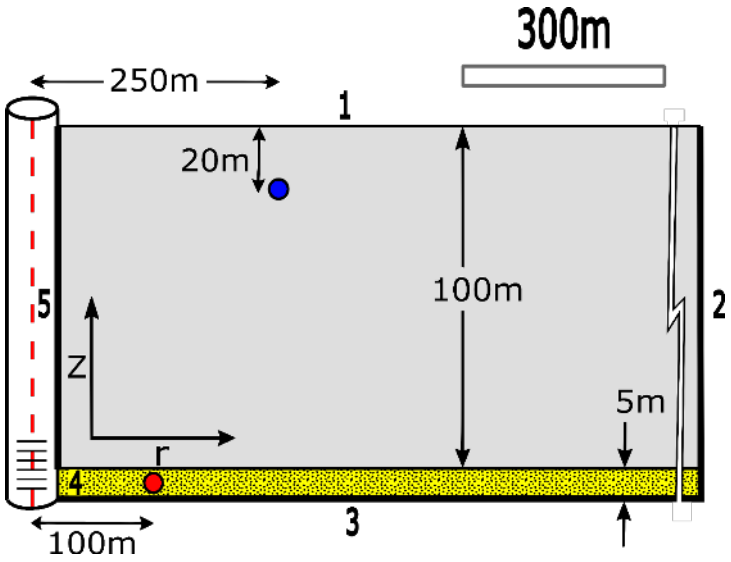

Figure 2. Cross section of idealized model geometry that is axially symmetric about injection well. Boundary 1: no-flow and zero traction; boundary 4: specified flux, no shear traction, and normal traction is equal to the pressure change on well screen face; all other boundaries, including 2, 3, 5 are no-flow and roller (zero displacements normal to the boundary). The blue dot is the shallow strainmeter (d = 20 m and r = 250 m), the red dot is the location of the downhole pressure transducer installed in monitoring well (d = 102.5 m and r = 100 m).

Table 2. Initial values used for model parameters. Parameters in boxes bordered with a single line were fixed, whereas the seven parameters bordered by a double line are the parameter set initially considered for estimation, $\Pi_{p,initial}$.

Model Parameter	Units	Aquifer	Confining unit
Young's Modulus	GPa	$E_a = 5$	$E_c = 6$
Porosity	—	$\phi_a = 0.2$	$\phi_c = 0.2$
Thickness	m	$b_a = 5$	$b_c = 100$
Permeability	mD	$k_a = 150$	$k_c = 0.00001$
Poisson's Ratio	—	$\nu_a = 0.25$	$\nu_c = 0.3$
Fluid viscosity	Pa s	$\mu_a = 0.001$	$\mu_c = 0.001$
Fluid density	kg/m^3	$\rho_a = 1000$	$\rho_c = 1000$
Biot-Willis parameter	—	$\alpha_a = 0.95$	$\alpha_c = 0.95$

7.4.1.2 Definitions

The three response variables for the idealized model include the pore pressure at a monitoring well in the aquifer and the circumferential and vertical strain at a shallow strainmeter (Figure 2). Data that are noise-free were obtained by solving for the pressure and strains using the methods described above and the parameters in equations (11) thru (16). The time series from the simulator were then perturbed by Gaussian noise with a standard deviation of 5 nε for circumferential strain, 7 nε for vertical strain, and 5.5 kPa for pressure. The noisy time series at the monitoring locations, P, $\varepsilon_{\theta\theta}$, ε_{zz}, are considered as transient data observed in the field, $\theta_{i,j,\mathrm{D}};\ \theta_{i,1,\mathrm{D}} = \varepsilon_{\theta\theta};\ \theta_{i,2,\mathrm{D}} = \varepsilon_{zz};\ \theta_{i,3,\mathrm{D}} = P$.

The governing equations identify seven material parameters (E, ν, α, k, μ, ρ, ϕ) in each of the two units, the aquifer and confining unit. We also include the geometric parameter, b, the layer thicknesses as a parameter. This gives 16 parameters. We fix the values of 9 parameters, and consider the other 7 as candidates for estimation (f = 7; Table 2). The ranges of parameter values ($\Pi_{p,max}$ and $\Pi_{p,min}$) are estimated from values for sandstone reservoirs and shale confining units (Table 3).

7.4.1.3 Objective Function

The objective function for this problem is the GOE (equation 3) for the three response variables calculated over 17 representative times (n = 17).

7.4.2 Initialization

7.4.2.1 Parameter Identification

Parameters were screened using a full factorial design because the limited number (seven) of parameters requires 2^7 = 128 simulation runs, which is tractable for this problem. $\Pi_{p,max}$ and $\Pi_{p,min}$ (Table 3) are used to form possible parameter combinations, which are then evaluated using the numerical simulator. The simulation results indicate that a log transform is needed to make the influence factors (I_i) homoscedastic with a normal distribution, which is required for the two-factorial analysis (Montgomery, 2017).

Table 3. Bounds on values of model parameters and their alphabetical code using the two-factorial design.

Code	Parameter	Units	Minimum, $\Pi_{p,min}$	Maximum, $\Pi_{p,max}$
A	E_a	GPa	1	10
B	E_c	GPa	1	8
C	b_a	m	1	30
D	k_a	mD	50	250
E	ν_a	—	0.1	0.49
F	ν_c	—	0.1	0.49
G	ϕ_a	—	0.1	0.50

The 2FFA results identify 15 parameters or groups of parameters that are above the Bonferroni limit (Figure 3). This indicates that the GOE is sensitive to five of the parameters, E_a (A), E_c (B),

b_a (C), k_a (D), and ν_a (E), but insensitive to ϕ_a (G), and ν_c (F). The GOE is also sensitive to interactions between six pairs of parameters, three groups of three parameters, and one group of four parameters (Figure 3). The interactions only include combinations of the five individual parameters that are ranked above the Bonferroni limit, so those are the parameters that will be used in the subsequent analysis. Moreover, the majority of four-way interactions and all other interactions with a greater number of parameters fall below the Bonferroni limit, confirming the assumption that high-order interactions are negligible.

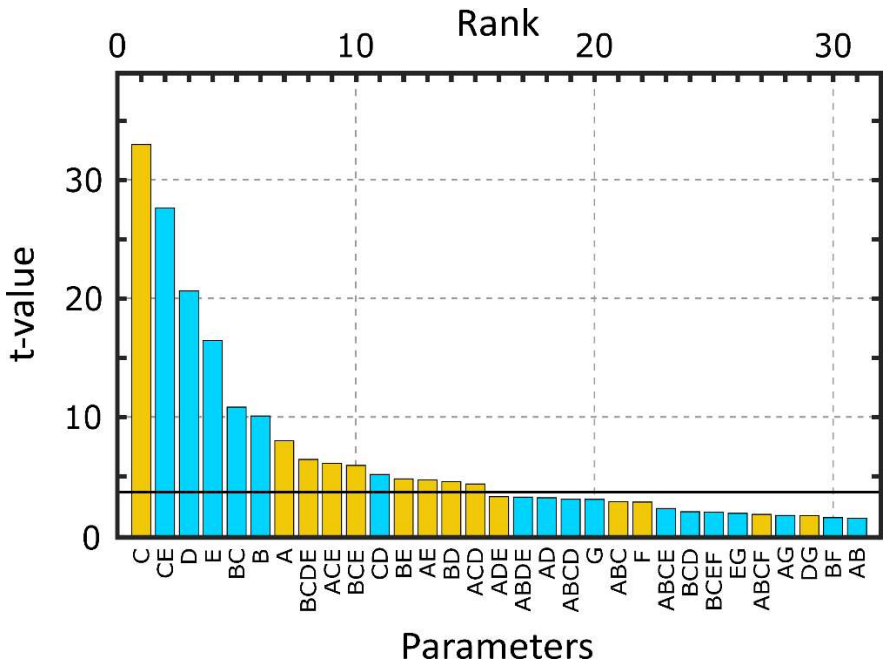

Figure 3. *t*-value ranking for two-level full factorial design. Parameters C, D, E, B, A, and interactions between parameters CE, BC, CD, BE, AE, BD, ACE, BCE, ACD and BCDE are above the Bonferroni limit (horizontal black line). The alphabetical code for the parameters is given in Table 3. Orange represents an increase; blue is a decrease in GOE.

7.4.2.2 Solution Feasibility Evaluation

The screening evaluation reduced the number of important parameters from seven to five, and then LHS was used to select 40 parameter sets, $\Pi_{LHS_{p,g}}$, that were used in the simulator to create initial simulated results, $\theta_{LHS_{i,j,M,g}}$ ($1 < i < 17$, $1 < j < 3$; $1 < p < 5$; $1 < g < 40$). The trends of the pressure and strains from the initial simulated results are similar to the idealized field data, and the envelopes of results contain the data (Figure 4). This analysis indicates that suitable HM solutions are feasible using the initial conceptual model and assumed parameter bounds.

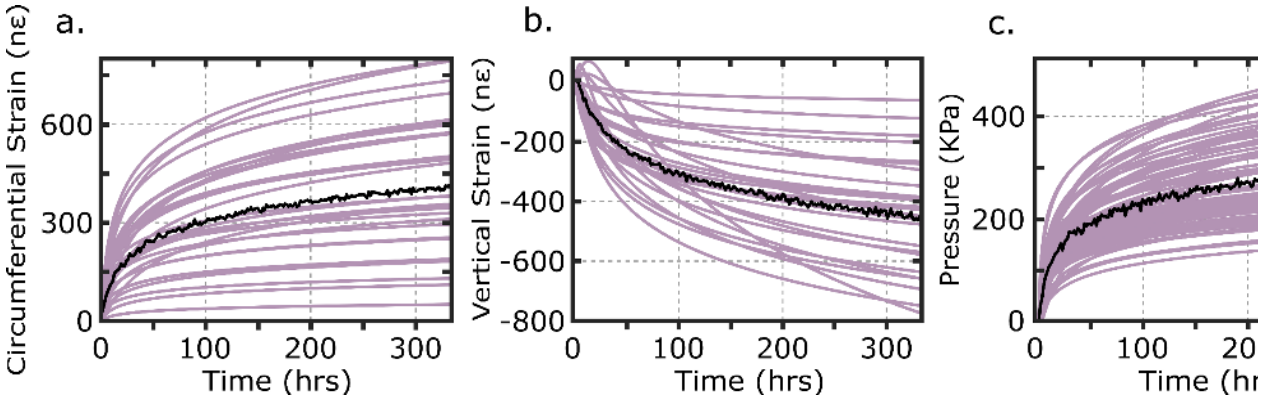

Figure 4. (a) Circumferential strain field data (black) and simulated LHS samples results (purple) (b) Vertical strain field data (black) and simulated LHS samples results (purple) (c) Pressure field data (black) and simulated LHS samples results (purple).

7.4.2.3 Initial Proxy Model

An initial proxy model is developed using three response variables at 17 times. These data generate 51 individual proxies (3 x 17) and each one is trained using $\Pi_{LHS_{p,g}}$ and $\theta_{LHS_{i,j,M,g}}$ from last step and equations (6-8). This approach creates an initial proxy model with resolution across the entire parameter space, which improves the efficiency and convergence of the subsequent workflow. A cross-fold analysis indicates initial values of K for the response variables: $K = 3$ for $\varepsilon_{\theta\theta}$; $K = 2$ for ε_{zz}; and $K = 6$ for P.

7.4.3 Exploration

The exploration phase was initiated by setting a tolerance envelope of ±3σ to accept results as valid HM solutions. σ is approximately 2% of the maximum of each response variable, which leads to GOE_{MT} = 330 using equation (3).

The parameter space is explored using three chains in DREAMzs to estimate new parameter sets, and the $\theta_{T_{i,j,K}}$. The iterations were terminated after 135,000 parameter sets (Λ was set to 45,000 in each of 3 chains according to Zheng et al., 2016), $\Pi_{Cp,ii}$ were evaluated and the results were sorted based on the GOEs from the proxy model. Representative solutions were selected (e.g., section 2.3.2. B1) and re-evaluated using the numerical simulator to obtain the actual GOEs.

Parameter sets that satisfied $GOE_M < GOE_{MT}$ were saved as HM solutions, and another iteration was conducted if the total number of parameter sets that met the GOE_{MT} was less than Σ = 85. The GOE_M generally decreases during the first 300 simulations and it is roughly constant after that, but it is highly variable throughout the analysis, ranging over 2 to 3 orders of magnitude within each iteration (Figure 5a). The first datasets to qualify for $\Pi_{HM_{p,mm}}$ were identified during simulation 320 in iteration 8 (Figure 5a and b), and 13 datasets were identified by simulation 400 (Figure 5a). Each iteration typically identified 4 to 10 acceptable datasets, but the results were variable and a few iterations identified more than 10 and two iterations identified no acceptable datasets (Figure 5b). Occasionally DREAMzs initializes chains that explore part of parameter space that is far from the regions with high-fidelity proxy models (Zhang et al., 2020), which

explains why some workflow iterations fail to find HM solutions. The workflow was terminated after 21 iterations and 880 simulations, and a total of 86 HM solutions were identified. The acceptance ratio (the number of HM solutions/total number of simulations) is approximately 0.1 (10%).

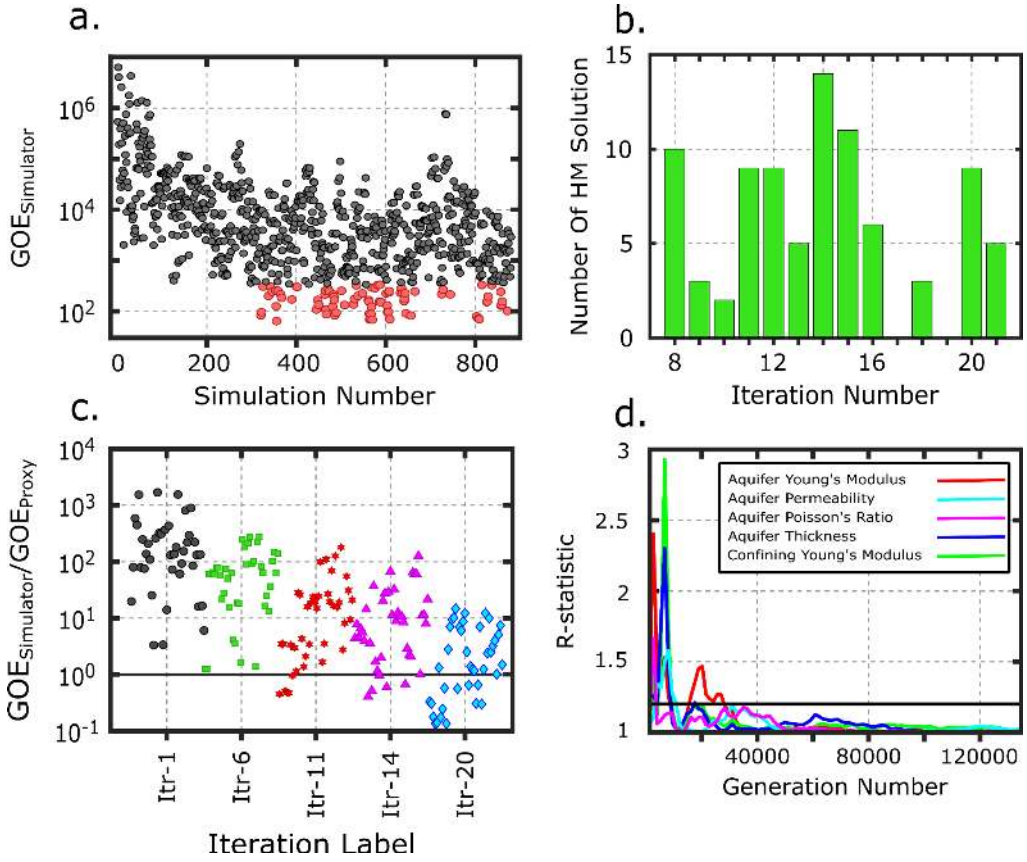

Figure 5. (a) Simulated GOE_M as function of simulation number. Red points are simulations with $GOE_M < 330$, the acceptance threshold. (b) The number of HM solutions as a function of workflow iterations. (c) Ratio of (GOE_M/GOE_K) for five representative iterations during the exploration phase. (d) R-statistic for 5 parameters (colored lines) as a function of the chain generations in iteration number 14. The solid black line is threshold of 1.2 for convergence to the posterior distribution.

The ability of the proxy model to identify datasets with a low GOE_M was evaluated using the ratio of GOE_M/GOE_K for selected iterations (Figure 5c). The GOE ratios are between 10 and 1000 after iteration 1, but they progressively decrease with the number of iterations (Figure 5c). This indicates that the accuracy of the proxy model improves as the workflow progresses. Ultimately, the proxy model calculates a GOE that is similar to that calculated with the numerical simulator.

7.4.4 Solution

The solution consists of the posterior parameter distribution along with an assessment of prediction and parameter uncertainty.

7.4.4.1 Posterior Parameter Distribution

Workflow iteration 14 found 14 solutions with acceptable GOE that compose the largest portion of $\Pi_{HM_{p,mm}}$ population (Figure 5b), so the chains in iteration 14 were used for the *R*-statistic diagnostic test. The *R*-statistic decreases with the chain generations and is less than 1.2 (the convergence threshold) after approximately 28,000 generations (Figure 5d). The last 10% of the generations gives 13,500 solutions generated with the proxy model that provide detailed samples of the parameter space in the vicinity of the global optima.

The results include a parameter distribution from the HM solutions, $\Pi_{HM_{p,mm}}$, along with the posterior distribution, $\Pi_{PO_{p,qq}}$. The posterior distribution is flatter and broader than that from $\Pi_{HM_{p,mm}}$. For example, the aquifer permeability value falls in the range of 140-150 mD for 80% of probability in the distribution from HM solutions, whereas this range is extended to 130-170 mD in the posterior distribution (Figure 6).

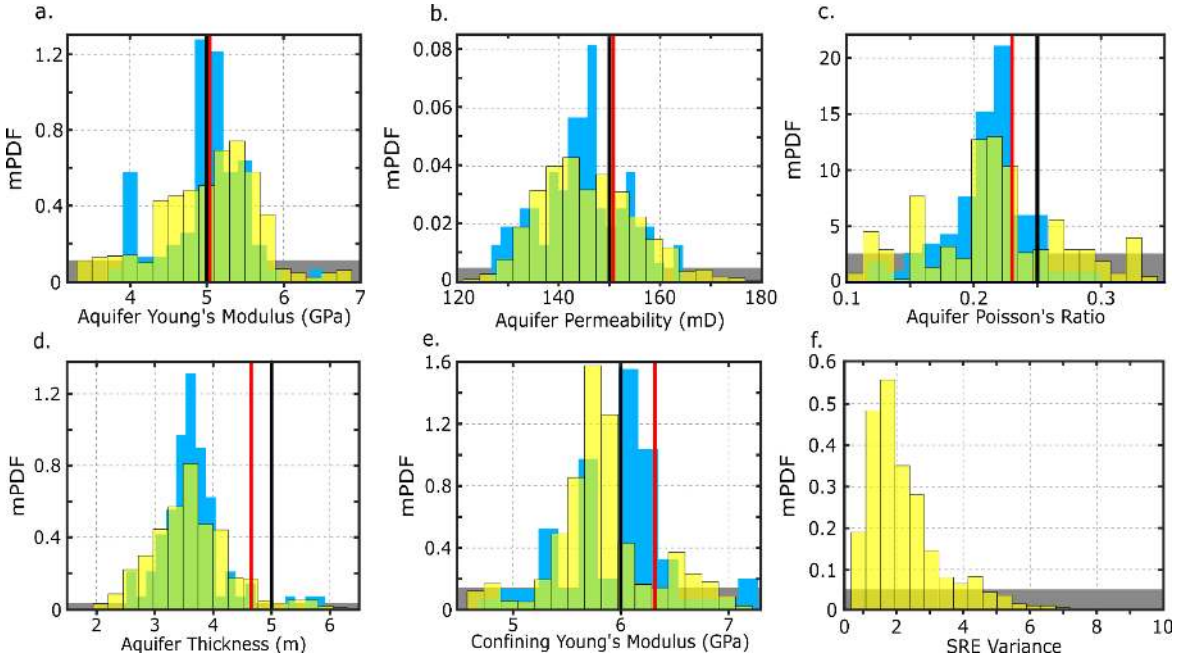

Figure 6. Marginal probability distributions for parameters identified in history matching dataset, $\Pi_{HM_{p,mm}}$(dark blue bars) and posterior distribution, $\Pi_{PO_{p,qq}}$ (yellow bars). The grey background rectangle is prior uniform distribution. The solid red lines are the most accurate value from HM solutions and the black line is the correct value.

7.4.4.2 SRE Variance and HM Solutions

The σ^2_{SRE} is derived jointly with the other parameters and shown as the SRE variance distribution in Table 4 and Figure 6. In this example, the noise is synthetic and characterized by the original $GOE_{MT} = 330$, so there is no need to update the value. Instead, we can use this step for verification. The mean value of SRE variance $\bar{\sigma}^2_{SRE}$ = 2.267 (Figure 6f) gives GOE_{MT} = 345 using equation (10). The small relative error (0.04) between these GOE values confirms the ability of the workflow to generate a reliable estimate of the prediction uncertainty.

7.4.4.3 Statistical Summary

The most accurate solution is derived from parameters with errors that range from less than 0.01 to approximately ±0.08 of the actual parameter value (Table 4). The errors for means of the posterior distribution are similar to those of the most accurate solution, with the exception of the aquifer thickness and Poisson's ratio. The means of the posterior distribution underestimate the actual values of b_a and ν_a with a relative error of roughly -0.25 (Table 4). The standard deviation and CoV for b_a and ν_a are also greater than for the other parameters, indicating relatively high uncertainty b_a and ν_a.

Table 4. Estimated parameter values and their distributions and errors. R.E: relative error. Std.dev/CoV: the standard deviation and coefficient of variation of the posterior parameter distribution. N: normal distribution, L-N: log-normal distribution.

Parameter	Actual	Most Accurate/RE	Distribution	Mean of Posterior/RE	Std. dev/CoV of Posterior
	Π_E	Π_{Ap}	$\Pi_{PO_{p,qq}}$	$\Pi_{PO_{p,qq}}$	$\Pi_{PO_{p,qq}}$
E_a	5	5.02/0.004	N	5.03/0.006	0.67/0.14
k_a	150	150.3/0.0038	N	146/-0.03	9.72/0.07
ν_a	0.25	0.23/-0.08	N	0.19/-0.24	0.04/0.21
b_a	5	4.6/-0.07	N	3.6/-0.28	0.70/0.19
E_c	6	6.3/0.05	N	5.8/-0.03	0.47/0.08
σ^2_{SRE}	—	—	L-N	2.27	1.30/0.57

7.4.4.4 Prediction Uncertainty

The 90% confidence interval is narrow relative to the magnitude of each signal (Figure 7). For example, the 90% confidence interval for pressure is ±0.050 of the $\theta_{A_{i,j,M}}$ value at 150 hrs (shown as the orange line in Figure 7), and it is ±0.065 and ±0.083 of the $\theta_{A_{i,j,M}}$ values at 150 hrs for circumferential and vertical strain, respectively. The narrow confidence interval occurs because this idealized example assumes the reservoir properties are uniform and constant, whereas properties are expected to be heterogenous and possibly change with time in real applications. Moreover, this example is free of epistemic error because the deployed conceptual model is almost

exact and makes accurate predictions of response variables. However, this kind of error could occur when a field application differs from the assumed conceptual model.

The total uncertainty is also estimated by including the noise along with the posterior prediction uncertainty. This is accomplished by assuming the $\theta_{HM\,i,j,M,mm}$ dataset describes the noise distribution about $\theta_{A_{i,j,M}}$ as outlined in Section 2.4.4. This gives the band of total uncertainty in Figure 7. The magnitude of total uncertainty for this example was characterized using the average of the ratio of P95/P5 at three representative times (t = 100 hr, 200 hr, and 300 hr). This gives average P95/P5 values of 1.39 for circumferential strain, 1.45 for vertical strain and 1.34 for pressure at the monitoring well. These ratios provide a basis for the evaluation of total uncertainty results from field example that follows.

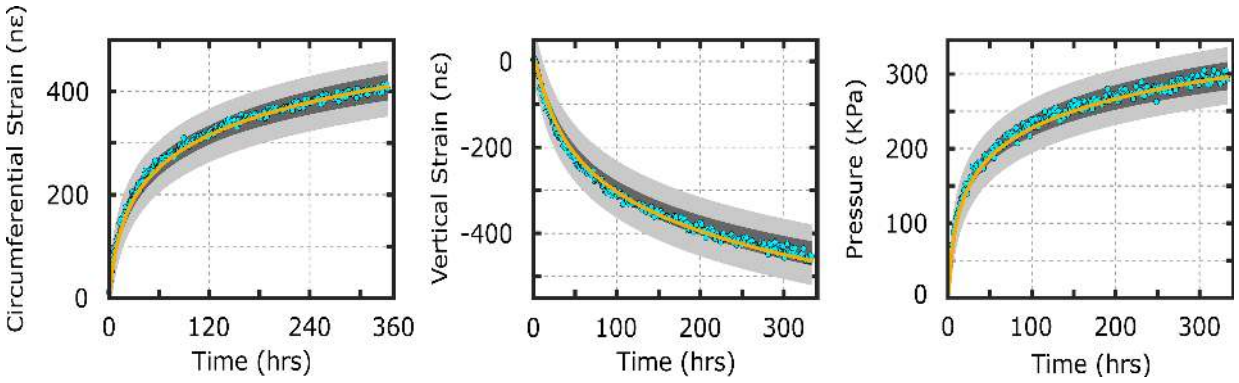

Figure 7. Uncertainty envelopes for response variables circumferential strain, vertical strain and pressure. The dark grey band = posterior prediction uncertainty, the light grey = total uncertainty, the solid orange line indicates the most accurate solution ($\theta_{A_{i,j,M}}$) and the cyan dots are the assumed field data ($\theta_{i,j,D}$) for the idealized model.

7.5 FIELD APPLICATION

The workflow is used to analyze strains and pressures measured during an injection test at the North Avant Field, in Osage County, Oklahoma (Murdoch et al, 2019 and 2023). The North Avant Field includes wells completed in permeable lenses at the base of the Bartlseville sandstone, a Pennsylvanian sandstone overlain by low permeability shale at a depth of 530 m.

Water was injected into well 9A for 6 days and the rate fluctuated between 8 and 14 gpm, with an average rate of 11 gpm.

Pore pressure was measured in the permeable lens and horizontal strain tensor ($\varepsilon_{rr}, \varepsilon_{\theta\theta}, \tau_{r\theta}$) and the vertical strain (ε_{zz}) were measured using strainmeters cemented into a 3-m-thick limestone bed at a shallow depth in the confining unit (Figure 8). The circumferential strain from the horizontal strain tensor and vertical strain were used in the inversion. Strain data were measured during the injection test (Murdoch & DeWolf, 2019).

7.5.1 Conceptualization

The field site is modeled using fully coupled poroelastic physics to predict the field data using equations 11 through 16. The model domain uses 2D axisymmetry that includes a permeable lens of unknown extent and thickness underlying a 30-m-thick layer of full lateral extent representing the Bartlesville sandstone (Figure 8). Pressure is measured in the permeable lens, and strain is measured at a shallow depth in the confining unit (Figure 8).

Core data indicate there is a large contrast in permeability between the permeable lens and the Bartlesville sandstone, and there is also a large contrast between the permeability of Bartlesville sandstone and the overlying and underlying confining units. We assume that the permeabilities of these three formations are different from each other, but are uniformly distributed and represented by average values.

All flow boundaries are defined as no-flow except where a uniform flux of water is applied to the left side of the permeable lens to represent the injection well. Mechanical boundary conditions on the upper boundary are set to no traction. Other model boundaries are assumed as zero normal displacement (roller) except the wellbore face where the normal traction is equal to the fluid pressure (Murdoch et al., 2021).

The model domain is discretized using 196,629 mesh elements with a minimum element quality of 0.98 and 146,629 DoF. The runtime for this model is 13-15 min using an i-7 processor with 8 Gb of RAM. The runtime is slightly longer and the DoF slightly larger than the synthetic model (7-10 min runtime and 85,614 DoF).

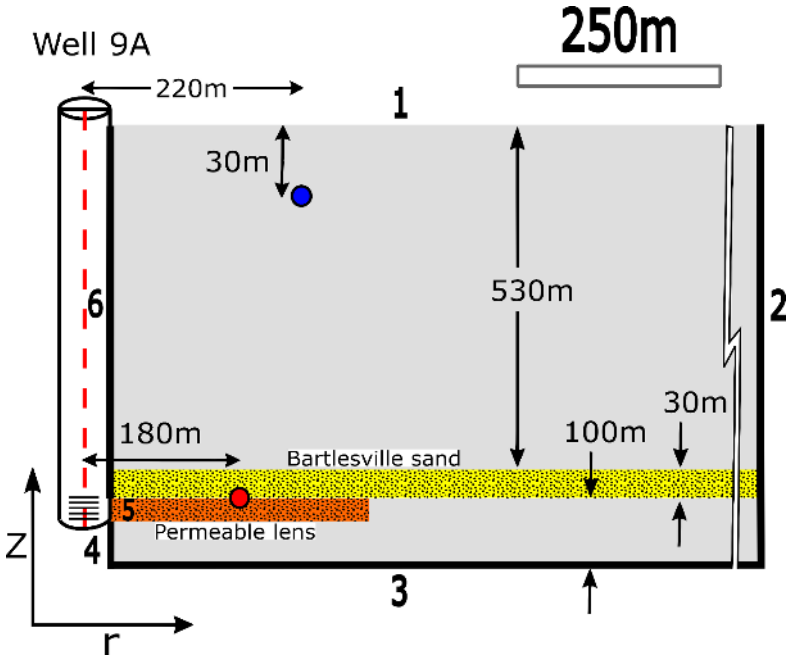

Figure 8. Cross section of the conceptual model for the field case study in North Avant Field, Oklahoma. Axial symmetry with a radius of 10 km and well 9A at the axis of symmetry (red dashed). Boundary 1: no-flow and zero traction;

boundary 5: specified flux, no shear traction, and normal traction is equal to the fluid pressure change on wellbore face; boundaries 2, 3, 4 and 6: no-flow and roller (zero displacements normal to the boundary). The blue dot is the location of shallow strain measurement (d = 30 m and r = 220 m), the red dot is the downhole pressure transducer installed in well 29 (d = 560 m and r = 180 m) (Murdoch et al., 2021).

7.5.2 Initialization

7.5.2.1 Parameter Identification

The model includes 24 material parameters in four geologic units, but we assumed that pressure and strains at the monitoring locations were affected by no more than 12 parameters (Table 5).

A partial two-factor analysis (2PFA) was used to evaluate the feasibility of reducing the number of parameters used in the inversion even further. A 2PFA was used because a full factorial analysis would require 2^{12} simulations, which is computationally impractical for this problem. A log transform was applied to the influence factors (I_i) to make them homoscedastic and normally distributed.

Table 5. Parameter names, alphabetical code and bounds on values of parameters used in 2PFA

Code	Name	Parameter	Units	Minimum, $\Pi_{p,min}$	Maximum, $\Pi_{p,max}$
A	Aquifer Young's Modulus	E_a	GPa	1	25
B	Confining Young's Modulus	E_c	GPa	1	15
C	Lens Young's Modulus	E_l	GPa	1	15
D	Aquifer Permeability	k_a	mD	0.01	1
E	Lens Thickness	b_l	m	1	20
F	Lens Radius	r_l	m	50	1000
G	Limestone Young's Modulus	E_s	GPa	20	60
H	Fluid Compressibility	Z_a	1/Pa	0.1	2
J	Aquifer Poisson's Ratio	ν_a	—	0.1	0.4
K	Confining Poisson's Ratio	ν_c	—	0.1	0.4
L	Lens Poisson's Ratio	ν_l	—	0.1	0.4
M	Lens Permeability	k_l	mD	1	300

The 2PFA results identify seven parameters E_a, E_c, k_a, r_l, E_s, ν_a and k_l that individually impact the GOE (Figure 9). The results are also sensitive to three other parameters, E_l, b_l and ν_c that appear in significant parameter interactions. The parameters Z_a and ν_l, have a trivial impact on the GOE so they will be excluded from the inversion process (Figure 9). The 2PFA analysis

could have been conducted with more than 12 parameters, for example, if the user was unwilling to eliminate parameters based on experience, but the *t*-value of these parameters would have been below the Bonferroni limit and this would eliminate them from further consideration in the inversion.

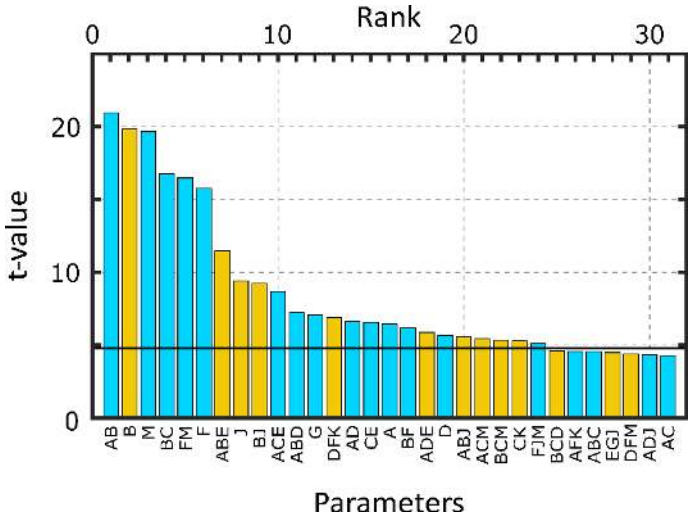

Figure 9. *t*-value ranking for different parameters and groups of parameters calculated using 2PFA. Parameters B, M, F, J, G, A, D, and several groups of interacting parameters are above the Bonferroni limit (horizontal black line). The alphabetical code for the parameters is given in Table 5.

7.5.2.2 Solution Feasibility Evaluation

LHS was used to create 40 parameter sets, $\Pi_{LHS_{p,g}}$, and the numerical simulator was used to create simulated response variables, $\theta_{LHS_{i,j,M,g}}$ ($1 < i < 16$, $1 < j < 3$; $1 < p < 10$; $1 < g < 40$). The trends in $\theta_{LHS_{i,j,M,g}}$ are similar to the field data and the results form broad envelopes around the data (Figure 10). These results indicate that it should be feasible for the numerical model and parameter bounds to give suitable HM solutions.

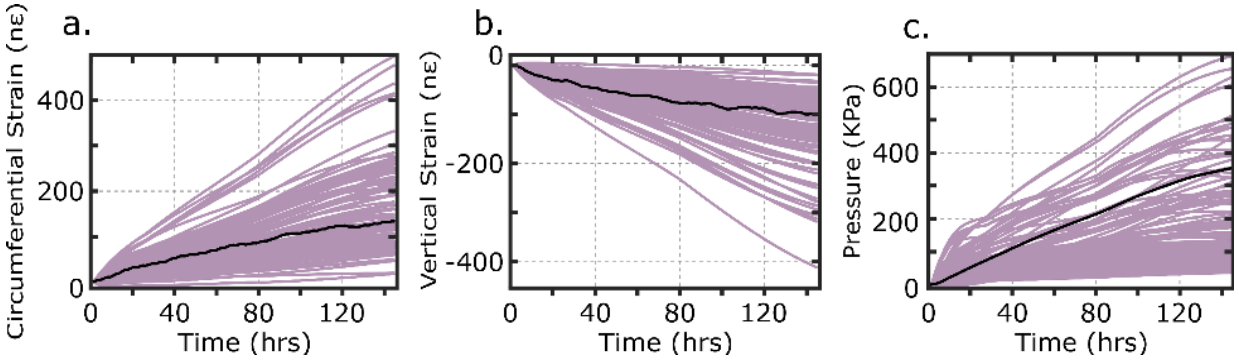

Figure 10. Comparison of field data with the initial simulations to evaluate solution feasibility (a) Circumferential strain field data (black) and realizations from model simulations (purple) (b) Vertical strain field data (black) and realizations from model simulations (purple) (c) Pressure field data (black) and realizations from model simulations (purple).

7.5.2.3 Initial Proxy Model

An initial proxy model was created for three response variables and 16 different times, which requires 48 individual proxies. Datasets $\Pi_{LHS_{p,g}}$ and $\theta_{LHS_{i,j,M,g}}$ from LHS sampling was utilized to train each proxy. Cross-fold validation was conducted to identify the optimum initial values of *K* for the response variables, and we found *K* = 6 for $\varepsilon_{\theta\theta}$; *K* = 4 for ε_{zz}; and *K* = 2 for *P*.

7.5.3 Exploration

The workflow requires an initial threshold GOE to identify HM solutions, but this is challenging because there is limited information on the various (epistemic, measurement, aleatory, or other) sources of noise and uncertainty. The lack of information about uncertainty is common for well testing, and many other field problems, so we developed an approach that uses an initial assumption followed by a revision. We reasoned that the uncertainty of each response variable should be in the range of 25-30% or less (equation 4). This is consistent with Figure 10, and it assumes that enough information about the site geology and other factors is available to limit the uncertainty to this range.

This gives GOE_{MT} = 3200 to initiate the exploration phase, however, this value can be modified later when SRE variance values are inferred by the workflow, and a revised set of HM solutions is then identified based on the updated GOE_{MT}.

The workflow was conducted with three parallel chains and Λ = 25,000 generations in each chain. This resulted in 75,000 generations in each iteration, which was verified as sufficient for convergence using the *R*-statistic after the workflow iterations were complete (Figure 11c).

The workflow identified 145 HM solutions after 30 iterations and 1240 total simulations. This gives an acceptance ratio of about 0.11 (11%) based on our initial assessment of uncertainty, however it will be updated later using σ^2_{SRE} determined from the posterior distribution.

The ratio of GOE_M/GOE_K was between 10 to 1000 early in the workflow, but it decreased and reduced to approximately unity at iteration 28 (Figure 11a). This shows that the proxy model predictability is refined as the workflow evolves and it is similar to the numerical simulator late in the analysis. Each workflow iteration identified between 2-10 acceptable solutions, except for the first three iterations that identified no acceptable parameter sets (Figure 11b).

7.5.4 4.4 Solution

The solution uses the workflow results to create the posterior parameter distribution and evaluate the predictive uncertainties.

7.5.4.1 4.4.1 Posterior Parameter Distribution

Workflow iteration 26 identified the most acceptable HM solutions to $\Pi_{HM_{p,mm}}$ dataset (10 acceptable solutions in Figure 11b), which makes it the best candidate for characterizing the posterior distribution, $\Pi_{PO_{p,qq}}$. The R-statistic test was then conducted to evaluate the convergence of chains within iteration 26. The results indicate that the R-statistic initially drops below the convergence threshold at about 13,000 generations, but it then increases above the threshold for two parameters (Confining and limestone Young's modulus) at about 28,000 generations (Figure 11c). The R-statistic again drops below the convergence threshold after 33,000 generations and continues to decrease after that. These results demonstrate that Λ = 25,000 generations (75,000 generations total) are sufficient for convergence. The last 10% of solutions from iteration 26 (7500 solutions evaluated by proxy model) were used to represent the posterior parameter distributions.

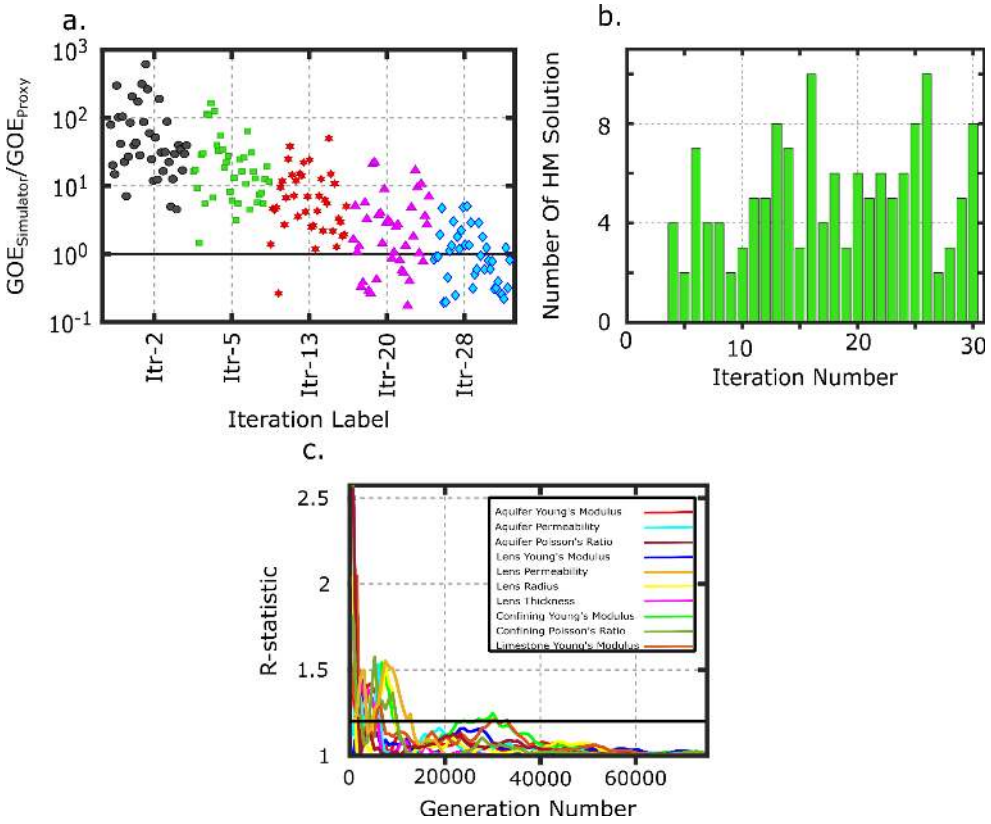

Figure 11. (a) Ratio of (GOE_M/GOE_K) for five representative iterations during the exploration phase (b) The number of HM solutions identified from each workflow iteration during the exploration phase (c) The evolution of R-statistic for 10 parameters (colored lines) with the number of chain generations in iteration 26. The solid black line is the convergence threshold of 1.2.

The change from the prior to posterior distribution is proportional to the parameter sensitivity. For example, the 2PFA analysis shows that the sensitivity of the solution to Poisson's ratio of the confining unit, ν_c, was relatively low and only entered as a combination with other

parameters (Figure 9), and the posterior distribution of ν_c is only slightly refined from the initial value assumed in the prior distribution (Figure 12i).

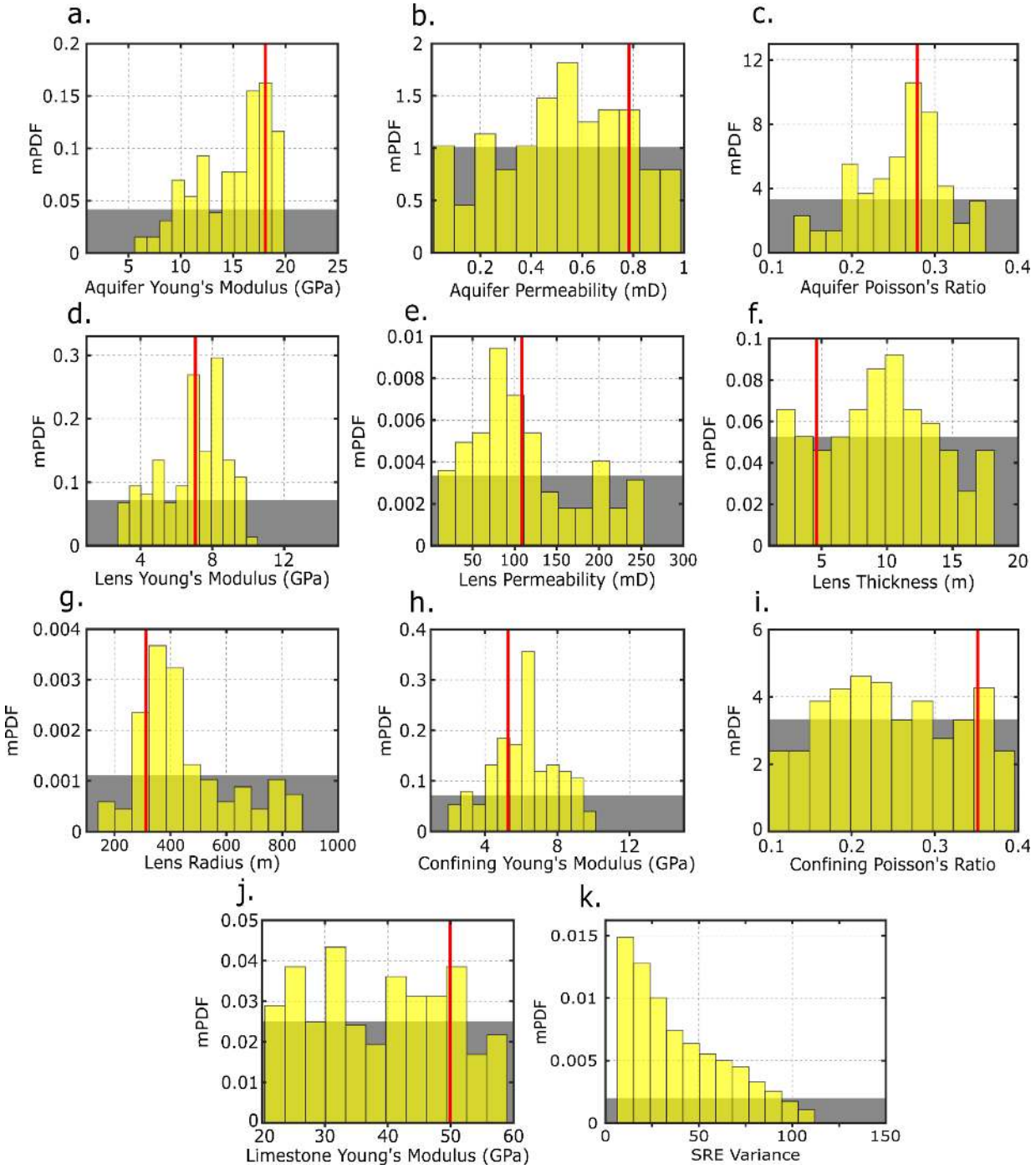

Figure 12. Posterior distribution for the parameters used for the inversion process, $\Pi_{PO_{p,qq}}$. The grey background rectangle is the prior distribution at the beginning of inversion. The solid red lines represent the values from the most accurate solution, Π_{Ap}.

7.5.4.2 SRE Variance and HM Solutions

The σ^2_{SRE} was obtained from the posterior distribution (Figure 12k and Table 6) and then used to re-calculate the threshold GOE (equation 10). This caused the GOE_{MT} to increase from an initial estimate of 3200 to GOE_{MT} = 4700. The GOE_{MT} was underestimated because some factors affecting uncertainty were unknown initially. The initial underestimation of GOE_{MT} means that some solutions that were initially discarded should now qualify as HM solutions. The new GOE threshold nearly doubled the number of HM solutions from 145 to 265, increasing the workflow acceptance ratio from 0.11 (11%) to 0.21 (21%). Moreover, the quantification of prediction uncertainty would also be conducted based on updated $\Pi_{HM\,p,mm}$ with 265 members.

7.5.4.3 Statistical Summary

Parameter values from the most accurate solution and the mean and median values from the posterior distribution (Table 6) are consistent with measurements of formation properties and estimations from other independent methods (Murdoch et al., 2023), so the inversion appears to have identified a reasonable representation of the field conditions. Parameters from the most accurate solution are generally within a factor of 2 of the mean or median values (Relative Error of 1.0) from the posterior distribution, and most are significantly closer to each other (Table 6). Most of the posterior distributions are approximately normally distributed with coefficients of variation from 0.18 to 0.48 (Table 6). These variations are considerably larger than those in the idealized case because there is more uncertainty in the conceptual model used to model the field problem. The distributions of some parameters (E_a, k_l and r_l) are skewed (Figure 12a, e and g) so summary statistics based on normal distributions were avoided.

Table 6. Parameter values from most accurate solution and summary statistics for the posterior distribution. R.E: relative error with most accurate. Std.dev/CoV: the standard deviation and coefficient of variation. N: normal distribution; L-N: log-normal distribution; U: uniform distribution; SR: skewed right; SL: skewed left.

Parameter	Most Accurate	Distribution	Mean of Posterior/RE	Median of Posterior/RE	Std. dev/CoV of Posterior
	Π_{Ap}	$\Pi_{PO\,p,qq}$	$\Pi_{PO\,p,qq}$	$\Pi_{PO\,p,qq}$	$\Pi_{PO\,p,qq}$
E_a	17	SR	—	15/0.15	—
k_a	0.77	N	0.52/-0.33	—	0.25/0.48
ν_a	0.28	N	0.27/-0.04	—	0.05/0.18
E_l	7.2	N	6.4/-0.11	—	1.5/0.23
k_l	110	SL	—	144/0.30	—
b_l	4.5	N	9.5/1.1	—	4.5/0.47
r_l	317	SL	—	364/0.15	—
E_c	5.3	N	6.1/0.15	—	1.5/0.24
ν_c	0.35	U	0.25/-0.29	—	0.09/0.36
E_s	50	U	40/-0.20	—	12/0.30

σ^2_{SRE}		—	L-N	32.6	—	20/0.61

7.5.4.4 Prediction Uncertainty

The modified HM dataset, $\theta_{HM_{i,j,M,mm}}$, with 265 solutions was used to evaluate the posterior prediction uncertainty by comparing the 90% confidence interval with $\theta_{A_{i,j,M}}$ values at the selected time step. For example, the 90% confidence interval for pressure is ±0.35 of the $\theta_{A_{i,j,M}}$ value at 75 hrs (shown as the orange line in Figure 13), and it is ±0.25 and +0.30/-0.20 of the $\theta_{A_{i,j,M}}$ values at 75 hrs for circumferential and vertical strain, respectively.

The prediction uncertainty envelope around field data (Figure 13) is wider than for the idealized case (e.g. Figure 7). A likely reason for this additional uncertainty is because the simple conceptual model used to set up the numerical simulation is unable to represent the aquifer heterogeneities in the field or measurement noise from strainmeters (Schoups & Vrugt, 2010).

The magnitude of total uncertainty is summarized using the P5/P95 ratio averaged over three representative times (t = 60 hr, 100 hr, and 140 hr). This results in average P95/P5 values of 3.70 for circumferential strain, 3.10 for vertical strain and 6.50 for pressure at well 29. These values are approximately 2-3x greater than the total uncertainties calculated in the idealized case, which seems reasonable.

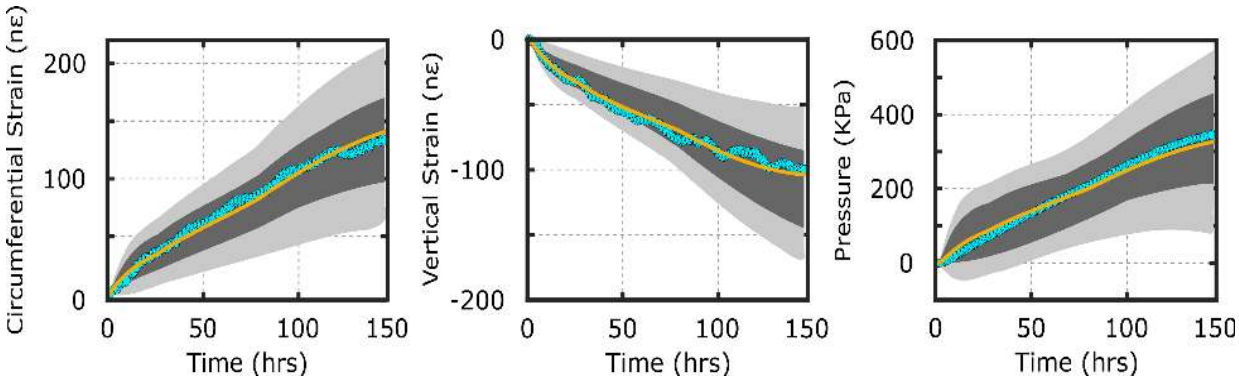

Figure 13. The posterior prediction (dark grey) and total (light grey) uncertainty bounds for each response variable from the field test, circumferential strain, vertical strain and pressure. The most accurate solution is shown using solid orange line and cyan dots represent datasets from the field.

7.6 DISCUSSION

The proxy-based workflow outlined here significantly reduces the computational requirements for conducting Bayesian inversions with a poroelastic simulator. Inversion of the field-based example required 1240 simulations. While, an analysis of a similar dataset using a genetic algorithm required 60x more simulations of the computationally demanding simulator (Murdoch et al., 2023), and this significantly increased the overall computational burden. The examples shown here utilized a 2D axisymmetric forward model to illustrate the performance of the workflow. This simplistic forward model was adopted for convenience, but we have also

evaluated the workflow with 3D poroelastic models and the overall reduction in computational requirements are similar to those described here.

Enabling the use of a 3D poroelastic reservoir simulator in a Bayesian inversion of strain data has important implications for monitoring the production of resources or the storage of wastes. For example, geologic storage of CO_2 will require that ongoing monitoring data be integrated into operational decision-making to minimize risks associated with leakage, seismicity or other processes related to reservoir pressure (Rutqvist, 2012). Most geologic storage sites will have a 3D reservoir model that could serve as the basis for predicting how operational decisions, like the injection rate schedule, affect the reservoir pressure and resulting strain in the caprock. Any realistic decision will be made in the context of balancing the severity and likelihood of risks. For example, a decision to increase the rate of injection to improve the benefits of CO_2 storage would be balanced against the likelihood, or uncertainty of causing leakage. The Bayesian inversion workflow enables strain measurements in the caprock to contribute to this decision-making process by providing predictions of pressure change with uncertainty.

The results of the inversion of the field data in Section 4 are considerably more uncertain than the results from the idealized example (Section 3). For example, the P5/P95 total uncertainty in the idealized case is about 1.4, whereas it is 3.1 to 6.5 in the field case. This is reasonable because the noise in real field data is likely larger than the noise in the idealized case. The actual instrument noise from the strainmeters is quite small (Murdoch et al., 2019), however, suggesting the relatively large uncertainty in the field case is a result of a mismatch between the distribution of aquifer parameters in the field and the simple, axially symmetric distribution assumed in the conceptual model. This type of conceptual model error is common with models of geologic systems (Vasco et al., 2010), and a common approach is to evaluate alternative conceptual models that could improve performance. Values of σ_{SRE}^2 can be used to assess the overall performance, and *t*-values in the 2PFA can be used to assess the importance of individual or groups of interacting parameters affecting the performance of alternative conceptual models.

7.7 CONCLUSION

Deformation during well tests conducted to evaluate reservoirs or aquifers causes strain that can be measured in the field and interpreted through inversion, but this technique has been limited by long run times of poroelastic forward models that make inversion computationally prohibitive. We describe a workflow that uses KNN to create proxy models that run several orders of magnitude faster than the poroelastic forward models used to train them. The fast proxy models are used by DREAMzs to do a Bayesian inversion of strain data with associated estimates of uncertainty. The proxy models are refined with additional training simulations until the goodness of fit from the poroelastic models is the same as from the proxies. This workflow finds sets of parameters that give results within an acceptable range of the original data with far fewer runs of the poroelastic simulator than required by other inversion methods. The final results include a rigorous estimate of parameter and prediction uncertainties.

This workflow is significant because it enables measurements made by ultra-high resolution strainmeters to be interpreted quickly and with uncertainties so they can be used to guide decision-making during the recovery of resources, like hydrocarbons, water or heat, or the storage of wastes, like CO_2, in the subsurface.

7.8 LIST OF SYMBOLS

Variable	Description	Location
Response variables		
$\theta_{i,j,k}$	Response variable	2.1.2
$\theta_{i,j,\mathrm{K}}$	Response variable calculated using the proxy model	2.1.3
$\theta_{i,j,\mathrm{M}}$	Response variable calculated using the numerical simulator	2.1.3
$\theta_{i,j,\mathrm{D}}$	Response variable from the field data	2.1.3
$\theta_{LHS\,i,j,M,g}$	Simulated response variables from LHS samples	2.2.2
$\theta_{K\,i,j,\mathrm{M,g}}$	Response variable set calculated by the simulator and used to train the proxy model	2.2.3.1
$\theta_{T_{i,j,K}}$	Response variable from trial parameter set calculated using the proxy model	2.3.1-A1
$\theta_{Cp\,i,j,K,ii}$	Proxy-based response variables from the combined DREAMzs chains, $1<ii<3\Lambda$	2.3.1-A4
$\theta_{Cp\,i,j,M,kk}$	Response variables calculated by simulating the top representative datasets selected from the quartiles.	2.3.2-B2
$\theta_{HM\,i,j,\mathrm{M,mm}}$	Simulated response variables from history matching solutions	2.3.3-C3
$\theta_{A_{i,j,\mathrm{M}}}$	Simulated response variable from the most accurate history matching solution with the least GOE_M	2.4.1-(a)
$\varepsilon_{\theta\theta}$	Circumferential strain	3.1.2
ε_{zz}	Vertical strain	3.1.2
P	Fluid pressure change from ambient pressure	3.1.2
ε_{rr}	Radial strain	4
$\tau_{r\theta}$	Horizontal shear strain	4
Parameter sets		
$\Pi_{p,q}$	Parameter sets estimated by the workflow	2.1.2
$\Pi_{p,max}$	Maximum values of parameters	2.2
$\Pi_{p,min}$	Minimum values of parameters	2.2
$\Pi_{p,g}$	Parameter sets used in parameter identification	2.2.1
$\Pi_{LHS\,p,g}$	Parameter sets selected with LHS and used by the initial proxy model	2.2.2

$\Pi_p^{\varepsilon};\ \widehat{\Pi}_p^{\varepsilon}$	Set of user-specified parameters. The proxy model finds the response variables for these parameters. The hat indicates parameter values normalized to their range.	2.2.3.1
$\widehat{\Pi}_{K\,p,g}$	Parameter sets normalized to their range and used for training the proxy model.	2.2.3.1
$\Pi_{K\,p,g}$	Parameter sets used for training the proxy model, 1<*g*<*h*	2.2.3.1
Π_{Tp}	Trial parameter set used in DREAMzs	2.3.1-A1
$\Pi_{C,ii}$	Parameter sets in the DREAMzs chain, 1<*ii*<Λ	2.3.1-A1
$\Pi_{Cp,ii}$	Parameter sets in the combined DREAMzs chains, 1<*ii*<3Λ	2.3.1-A1
$\Pi_{Cp,kk}$	Top representative parameter sets selected from the quartiles	2.3.2-B1
$\Pi_{HM\,p,mm}$	Parameter sets from HM solutions with $GOE<GOE_{MT}$	2.3.3-C3
Π_{Ap}	Parameters from the most accurate history matching solution defined by the least GOE_M	2.4.1-a
$\Pi_{PO\,p,qq}$	Posterior distribution of parameters, 1< q <0.1Λ	2.4.1-b
$\Pi_{p,initial}$	Initial values of parameters	Table 2
Π_E	Actual parameter values used in the idealized example	Table 4
Global objective errors		
GOE_{k}	Global error used as an objective function	2.1.3
GOE_{MT}	Threshold GOE for result from the simulator to qualify as a history matching dataset	2.3
$GOE_{K,T}$	Global error of trial parameter set calculated using the proxy model	2.3.1-A2
$GOE_{K,C}$	Global error of current parameter set calculated using the proxy model	2.3.1-A2
$GOE_{K,Cp,ii}$	Global errors of the members in the combined DREAMzs chains calculated using the proxy model, 1<*ii*<3Λ	2.3.1-A4
$GOE_{M,Cp,kk}$	Global error of the top representative datasets selected from the quartiles calculated from the simulator	2.3.2-B2
$GOE_{K,Cp,kk}$	Global error of the top representative datasets selected from the quartiles calculated from the proxy model	2.3.2-B3
$GOE_{M,mm}$	Global error of history matching solutions calculated with the simulator	2.4
GOE_M	Global error calculated with the simulator	3.3
GOE_K	Global error calculated with the proxy model	3.3

Model parameters		
$E_{\text{a or c}}$	Young's modulus of aquifer or confining unit	Table 2
$\nu_{\text{a or c}}$	Poisson's ratio of aquifer or confining unit	Table 2
$\alpha_{\text{a or c}}$	Biot-Willis parameter of aquifer or confining unit	Table 2
$k_{\text{a or c}}$	Permeability of aquifer or confining unit	Table 2
$\mu_{\text{a or c}}$	Fluid viscosity of aquifer or confining unit	Table 2
$\rho_{\text{a or c}}$	Fluid density of aquifer or confining unit	Table 2
$\phi_{\text{a or c}}$	Porosity of aquifer or confining unit	Table 2
$b_{\text{a or c}}$	Thickness of aquifer or confining unit	Table 2
$E_{\text{l or s}}$	Young's modulus of lens or limestone	Table 5
ν_{l}	Poisson's ratio of lens	Table 5
k_{l}	Permeability of lens	Table 5
b_{l}	Thickness of lens	Table 5
r_{l}	Radius of lens	Table 5
Z_a	Fluid compressibility	Table 5
Residual Errors		
$SRE_{i,k}$	System residual error	2.1.3
$SRE_{i,M}$	System residual error calculated with the simulator	2.1.3
$SRE_{i,K}$	System residual error calculated with the proxy model	2.1.3
m	Number of response variables	2.1.3
n	Number of time steps	2.1.3
ζ_j	Range of a response variable in the field data	2.1.3
RRE_j	Relative residual error	2.1.3
$\sigma^2_{SRE_T}$	Variance of SRE for trial parameter set used in DREAMzs	2.3.1-A1
$\sigma^2_{SR_C}$	Variance of SRE for current parameter set used in DREAMzs	2.3.1-A2
$\sigma^2_{SRE_C,ii}$	Variance of SRE for the members in the DREAMzs chain, $1<ii<\Lambda$	2.3.1-A3
σ^2_{SRE}	Variance of SRE	2.4.1-d
$\bar{\sigma}^2_{SRE}$	Mean value for SRE variance	2.4.2
σ	Standard deviation used to generate synthetic Gaussian noise	3.3
Two-level factorial analysis		

$A,B,\ldots$	Example parameters	2.2.1
$A^*,B^*\ldots$	Normalized example parameters	2.2.1
A_{max}, B_{max}, …	Upper limits for example parameters	2.2.1
A_{min}, B_{min}, …	Lower limits for example parameters	2.2.1
f	Number of parameters	2.2.1
τ	Reduction factor used in 2PFA	2.2.1
t_{Ib}	*t*-value for influence factor	2.2.1
I_b	Influence factor	2.2.1
$\bar{I}$	Mean influence factor	2.2.1
SE_n	Standard error from simulation noise	2.2.1
Y_g	GOE calculated for parameter sets from Table 1	Table 1
Proxy model parameters		
L_g	Euclidian distance in parameter space	2.2.3.1
a_e	Vector of indices identifying the K nearest neighbors to a particular parameter in $\widehat{\Pi}_p^{\varepsilon}$	2.2.3.1
γ_e	Normalized inverse Euclidian distance used as a weighting factor in KNN model	2.2.3.1
$RMSE_{T,\mathrm{j}}$	Total mean squared error used for selecting *K* values	2.2.3.2
DREAMzs parameters		
ω	Metropolis-Hastings factor	2.3.1-A3
β	Random number used in DREAMzs	2.3.1-A3
Λ	Total number of generations in the DREAMzs chain	2.3.1-A4
Σ	Target number of history matching solutions	2.3.3-b
Poroelastic conceptualization		
σ_{ij}	Total stress tensor	3.1.1
ε_{ij}	Strain tensor	3.1.1
ε_{kk}	Volumetric strain	3.1.1
F_i	Body force	3.1.1
u_i	Displacement of solid	3.1.1
q_i	Volumetric fluid flux vector	3.1.1
λ	Lame constant	3.1.1

G	Shear modulus	3.1.1
E	Drained Young's modulus	3.1.1
M	Biot modulus	3.1.1
α	Biot-Willis coefficient	3.1.1
v	Drained Poisson's ratio	3.1.1
ϕ	Porosity	3.1.1
k	Permeability	3.1.1
μ	Dynamic viscosity	3.1.1
ρ	Fluid density	3.1.1
g	Gravitational acceleration	3.1.1
x_3	Upward coordinate	3.1.1
r	Radial distance	3.1.1
d	Depth of the top of aquifer	3.1.1
Abbreviation		
HM	History Matching	1.1
AHM	Assisted History Matching	1.1
EnKf	Ensemble Kalman filter	1.2
MCMC	Markov Chain Monte Carlo	1.2
KNN	*K*-Nearest Neighbors	1.3
ANN	Artificial Neural Network	1.3
SRE	System Residual Error	2.1.3
GOE	Global Objective Error	2.1.3
RRE	Relative Residual Error	2.13
2FFA, 2PFA	Two-level Full Factorial Analysis, Two-level Partial Factorial Analysis	2.2.1
LHS	Latin Hypercube Sampling	2.2.2
RMSE	Root Mean Squared Error	2.2.3.2
mPDF	marginal Probability Density Function	3.4.1
Std	Standard deviation	Table 4
CoV	Coefficient of Variation	Table 4
DoF	Degree of Freedom	4.1

7.9 REFERENCES

Alghamdi, A., Hesse, M. A., Chen, J., & Ghattas, O. (2020). Bayesian poroelastic aquifer characterization from InSAR surface deformation data. Part I: Maximum a posteriori estimate. *Water Resources Research*, *56*(10), e2020WR027391.

Alghamdi, A., Hesse, M. A., Chen, J., Villa, U., & Ghattas, O. (2021). Bayesian Poroelastic Aquifer Characterization From InSAR Surface Deformation Data. 2. Quantifying the Uncertainty. *Water Resources Research*, *57*(11), e2021WR029775.

Altman, N. S. (1992). An introduction to kernel and nearest-neighbor nonparametric regression. *The American Statistician*, *46*(3), 175-185.

Amestoy, P. R., Duff, I. S., & L'excellent, J.-Y. (2000). Multifrontal parallel distributed symmetric and unsymmetric solvers. *Computer methods in applied mechanics and engineering*, *184*(2-4), 501-520.

Andrieu, C., De Freitas, N., Doucet, A., & Jordan, M. I. (2003). An introduction to MCMC for machine learning. *Machine learning*, *50*(1), 5-43.

Araujo, M., Chen, C., Gao, G., Jennings, J., Ramirez, B., Xu, Z., Yeh, T.-h., Alpak, F. O., & Gelderblom, P. (2019). Benchmarking of advanced methods for assisted history matching and uncertainty quantification. SPE Reservoir Simulation Conference,

Asher, M. J., Croke, B. F., Jakeman, A. J., & Peeters, L. J. (2015). A review of surrogate models and their application to groundwater modeling. *Water Resources Research*, *51*(8), 5957-5973.

Bagnardi, M., & Hooper, A. (2018). Inversion of surface deformation data for rapid estimates of source parameters and uncertainties: A Bayesian approach. *Geochemistry, Geophysics, Geosystems*, *19*(7), 2194-2211.

Bonferroni, C. (1936). Teoria statistica delle classi e calcolo delle probabilita. *Pubblicazioni del R Istituto Superiore di Scienze Economiche e Commericiali di Firenze*, *8*, 3-62.

Bourdet, D. (2002). *Well test analysis: the use of advanced interpretation models*. Elsevier.

Burrows, W., & Doherty, J. (2016). Gradient-based model calibration with proxy-model assistance. *Journal of Hydrology*, *533*, 114-127.

Cheng, A. H.-D. (2016). *Poroelasticity* (Vol. 27). Springer.

Chib, S., & Greenberg, E. (1995). Understanding the metropolis-hastings algorithm. *The American Statistician*, *49*(4), 327-335.

Chobisa, D. (2021). Design of Experiments for the Development of Injectable Drug Products. In *Design of Experiments for Pharmaceutical Product Development* (pp. 69-96). Springer.

Costa, L. A. N., Maschio, C., & Schiozer, D. J. (2014). Application of artificial neural networks in a history matching process. *Journal of Petroleum Science and Engineering*, *123*, 30-45.

Dachanuwattana, S., Jin, J., Zuloaga-Molero, P., Li, X., Xu, Y., Sepehrnoori, K., Yu, W., & Miao, J. (2018). Application of proxy-based MCMC and EDFM to history match a Vaca Muerta shale oil well. *Fuel*, *220*, 490-502.

Dachanuwattana, S., Yu, W., & Sepehrnoori, K. (2019). An efficient MCMC history matching workflow using fit-for-purpose proxies applied in unconventional oil reservoirs. *Journal of Petroleum Science and Engineering*, *176*, 381-395.

Dachanuwattana, S., Yu, W., Zuloaga-Molero, P., & Sepehrnoori, K. (2018). Application of assisted-history-matching workflow using proxy-based mcmc on a shale oil field case. *Journal of Petroleum Science and Engineering*, *167*, 316-328.

Dellaportas, P., & Roberts, G. O. (2003). An introduction to MCMC. In *Spatial statistics and computational methods* (pp. 1-41). Springer.

Detournay, E., & Cheng, A. H.-D. (1993). Fundamentals of poroelasticity. In *Analysis and design methods* (pp. 113-171). Elsevier.

Doherty, J. (2015). *Calibration and uncertainty analysis for complex environmental models*. Watermark Numerical Computing Brisbane, Australia.

El Bilali, A., Taleb, A., & Brouziyne, Y. (2021). Comparing four machine learning model performances in forecasting the alluvial aquifer level in a semi-arid region. *Journal of African Earth Sciences*, *181*, 104244.

Elarbe, B., Elganidi, I., Ridzuan, N., Yusoh, K., Abdullah, N., & Vijaya Kumar, S. (2022). Application of full factorial design to screen the factors influencing the wax deposition of Malaysian crude oil. *Journal of Petroleum Exploration and Production Technology*, *12*(7), 1829-1839.

Evensen, G. (2003). The ensemble Kalman filter: Theoretical formulation and practical implementation. *Ocean dynamics*, *53*(4), 343-367.

Foroud, T., Seifi, A., & AminShahidi, B. (2014). Assisted history matching using artificial neural network based global optimization method–Applications to Brugge field and a fractured Iranian reservoir. *Journal of Petroleum Science and Engineering*, *123*, 46-61.

Gelman, A., & Rubin, D. B. (1992). Inference from iterative simulation using multiple sequences. *Statistical science*, 457-472.

Gill, M. K., Kaheil, Y. H., Khalil, A., McKee, M., & Bastidas, L. (2006). Multiobjective particle swarm optimization for parameter estimation in hydrology. *Water Resources Research*, *42*(7).

Gilman, J. R., & Ozgen, C. (2013). *Reservoir simulation: history matching and forecasting*. Society of Petroleum Engineers Richardson.

Hassanzadeh, Y., Afshar, A. A., Pourreza-Bilondi, M., Memarian, H., & Besalatpour, A. A. (2019). Toward a combined Bayesian frameworks to quantify parameter uncertainty in a large mountainous catchment with high spatial variability. *Environmental monitoring and assessment*, *191*(1), 1-22.

Hill, M. C., & Tiedeman, C. R. (2006). *Effective groundwater model calibration: with analysis of data, sensitivities, predictions, and uncertainty*. John Wiley & Sons.

Horne, R. N. (1995). Modern well test analysis. *Petroway Inc*, *926*.

Houtekamer, P. L., & Mitchell, H. L. (2005). Ensemble kalman filtering. *Quarterly Journal of the Royal Meteorological Society: A journal of the atmospheric sciences, applied meteorology and physical oceanography*, *131*(613), 3269-3289.

Hussain, M. S., Javadi, A. A., Ahangar-Asr, A., & Farmani, R. (2015). A surrogate model for simulation–optimization of aquifer systems subjected to seawater intrusion. *Journal of Hydrology*, *523*, 542-554.

Iglesias, M. A., & McLaughlin, D. (2012). Data inversion in coupled subsurface flow and geomechanics models. *Inverse Problems*, *28*(11), 115009.

Ilzarbe, L., Álvarez, M. J., Viles, E., & Tanco, M. (2008). Practical applications of design of experiments in the field of engineering: a bibliographical review. *Quality and Reliability Engineering International*, *24*(4), 417-428.

Istok, J. D., & Dawson, K. J. (1991). *Aquifer testing: design and analysis of pumping and slug tests*. CRC Press.

Jaber, A. K., Al-Jawad, S. N., & Alhuraishawy, A. K. (2019). A review of proxy modeling applications in numerical reservoir simulation. *Arabian Journal of Geosciences*, *12*(22), 1-16.

Jamshidnezhad, M. (2015). *Experimental design in petroleum reservoir studies*. Gulf Professional Publishing.

Jeong, H., Ki, S., & Choe, J. (2010). Reservoir characterization from insufficient static data using gradual deformation method with ensemble Kalman filter. *Energy Sources, Part A: Recovery, Utilization, and Environmental Effects*, *32*(10), 942-951.

Jha, B., Bottazzi, F., Wojcik, R., Coccia, M., Bechor, N., McLaughlin, D., Herring, T., Hager, B. H., Mantica, S., & Juanes, R. (2015). Reservoir characterization in an underground gas storage field using joint inversion of flow and geodetic data. *International Journal for Numerical and Analytical Methods in Geomechanics*, *39*(14), 1619-1638.

Khatoon, S., Phirani, J., & Singh Bahga, S. (2021). Accelerated Bayesian inference-based history matching of petroleum reservoirs using polynomial chaos expansions. *Inverse Problems in Science and Engineering*, *29*(13), 3086-3116.

Lee, T. R., Wood, W. T., & Phrampus, B. J. (2019). A machine learning (kNN) approach to predicting global seafloor total organic carbon. *Global Biogeochemical Cycles*, *33*(1), 37-46.

Liberti, L., & Kucherenko, S. (2005). Comparison of deterministic and stochastic approaches to global optimization. *International Transactions in Operational Research*, *12*(3), 263-285.

Liu, J. S., Liang, F., & Wong, W. H. (2000). The multiple-try method and local optimization in Metropolis sampling. *Journal of the American Statistical Association*, *95*(449), 121-134.

Liu, N., & Oliver, D. S. (2005). Ensemble Kalman filter for automatic history matching of geologic facies. *Journal of Petroleum Science and Engineering*, *47*(3-4), 147-161.

Maschio, C., & Schiozer, D. J. (2014). Bayesian history matching using artificial neural network and Markov Chain Monte Carlo. *Journal of Petroleum Science and Engineering*, *123*, 62-71.

McKay, M. D., Beckman, R. J., & Conover, W. J. (2000). A comparison of three methods for selecting values of input variables in the analysis of output from a computer code. *Technometrics*, *42*(1), 55-61.

Mirghani, B. Y., Zechman, E. M., Ranjithan, R. S., & Mahinthakumar, G. (2012). Enhanced simulation-optimization approach using surrogate modeling for solving inverse problems. *Environmental Forensics*, *13*(4), 348-363.

Montgomery, D. C. (2017). *Design and analysis of experiments*. John Wiley & Sons. New York.

Morris, J. P., Hao, Y., Foxall, W., & McNab, W. (2011). A study of injection-induced mechanical deformation at the In Salah CO2 storage project. *International Journal of Greenhouse Gas Control*, *5*(2), 270-280.

Murdoch, L. C., & DeWolf, S. (2019). *9A Injection: October 11 thru October 17, 2017*. DOI: 10.18141/1505374.

Murdoch, L. C., DeWolf, S., Germanovich, L. N., Hanna, A., Moak, R., & Moysey, S. (2019). *Characterizing and Interpreting the In Situ Strain Tensor During CO2 Injection*. Final Report for DOE Project DE-FE 0023313, 252 p. DOI: 10.2172/1529100.

Murdoch, L. C., DeWolf, S., Germanovich, L. N., Moysey, S., Hanna, A., Roudini, S., & Moak, R. (2023). Using the Shallow Strain Tensor to Characterize Deep Geologic Reservoirs. *Water Resources Research*, *59*(2), e2022WR032920.

Murdoch, L. C., Germanovich, L. N., DeWolf, S. J., Moysey, S. M., Hanna, A. C., Kim, S., & Duncan, R. G. (2020). Feasibility of using in situ deformation to monitor CO2 storage. *International Journal of Greenhouse Gas Control*, *93*, 102853.

Murdoch, L. C., Germanovich, L. N., Roudini, S., DeWolf, S. J., Hua, L., & Moak, R. W. (2021). A Type-Curve Approach for Evaluating Aquifer Properties by Interpreting Shallow Strain Measured During Well Tests. *Water Resources Research*, *57*(9), e2021WR029613.

Murdoch, L., Moysey, S., Germanovich, L., & Hughes, B. (2016). *Proof-of-feasibility of using well bore deformation as a diagnostic tool to improve CO2 sequestration*. DOI: 10.2172/1240376

Nunnari, G., Puglisi, G., & Guglielmino, F. (2005). Inversion of SAR data in active volcanic areas by optimization techniques. *Nonlinear Processes in geophysics*, *12*(6), 863-870.

Oliver, D. S., & Chen, Y. (2011). Recent progress on reservoir history matching: a review. *Computational Geosciences*, *15*(1), 185-221.

Perozzi, L., Gloaguen, E., Giroux, B., & Holliger, K. (2016). A stochastic inversion workflow for monitoring the distribution of CO2 injected into deep saline aquifers. *Computational Geosciences*, *20*(6), 1287-1300.

Pourreza-Bilondi, M., Samadi, S. Z., Akhoond-Ali, A.-M., & Ghahraman, B. (2017). Reliability of semiarid flash flood modeling using Bayesian framework. *Journal of Hydrologic Engineering*, *22*(4), 05016039.

Ramirez, A., & Foxall, W. (2014). Stochastic inversion of InSAR data to assess the probability of pressure penetration into the lower caprock at In Salah. *International Journal of Greenhouse Gas Control*, *27*, 42-58.

Rana, S., Ertekin, T., & King, G. R. (2018). An efficient assisted history matching and uncertainty quantification workflow using Gaussian processes proxy models and variogram based sensitivity analysis: GP-VARS. *Computers & Geosciences*, *114*, 73-83.

Rinaldi, A. P., & Rutqvist, J. (2013). Modeling of deep fracture zone opening and transient ground surface uplift at KB-502 CO2 injection well, In Salah, Algeria. *International Journal of Greenhouse Gas Control*, *12*, 155-167.

Roudini, S., Murdoch, L. C., Shojaei, M., & DeWolf, S. (2023) Proxy-based Bayesian inversion of strain tensor data measured during well tests. . *Geomechanics for Energy and the Environment*. In review

Rutqvist, J. (2012). The geomechanics of CO 2 storage in deep sedimentary formations. *Geotechnical and Geological Engineering*, *30*, 525-551.

Santhosh, E. C., & Sangwai, J. S. (2016). A hybrid differential evolution algorithm approach towards assisted history matching and uncertainty quantification for reservoir models. *Journal of Petroleum Science and Engineering*, *142*, 21-35.

Schoups, G., & Vrugt, J. A. (2010). A formal likelihood function for parameter and predictive inference of hydrologic models with correlated, heteroscedastic, and non-Gaussian errors. *Water Resources Research*, *46*(10).

Schulze-Riegert, R., Axmann, J., Haase, O., Rian, D., & You, Y.-L. (2002). Evolutionary algorithms applied to history matching of complex reservoirs. *SPE Reservoir Evaluation & Engineering*, *5*(02), 163-173.

Shi, J.-Q., Sinayuc, C., Durucan, S., & Korre, A. (2012). Assessment of carbon dioxide plume behaviour within the storage reservoir and the lower caprock around the KB-502 injection well at In Salah. *International Journal of Greenhouse Gas Control*, *7*, 115-126.

Singh, A., Minsker, B. S., & Valocchi, A. J. (2008). An interactive multi-objective optimization framework for groundwater inverse modeling. *Advances in water resources*, *31*(10), 1269-1283.

Ter Braak, C. J., & Vrugt, J. A. (2008). Differential evolution Markov chain with snooker updater and fewer chains. *Statistics and Computing*, *18*(4), 435-446.

Toft, N., Innocent, G. T., Gettinby, G., & Reid, S. W. (2007). Assessing the convergence of Markov Chain Monte Carlo methods: an example from evaluation of diagnostic tests in absence of a gold standard. *Preventive veterinary medicine*, *79*(2-4), 244-256.

Tongal, H., & Booij, M. J. (2022). Simulated annealing coupled with a Naive Bayes model and base flow separation for streamflow simulation in a snow dominated basin. *Stochastic Environmental Research and Risk Assessment*, 1-24.

Tripoppoom, S., Ma, X., Yong, R., Wu, J., Yu, W., Sepehrnoori, K., Miao, J., & Li, N. (2020). Assisted history matching in shale gas well using multiple-proxy-based Markov chain Monte Carlo algorithm: The comparison of K-nearest neighbors and neural networks as proxy model. *Fuel*, *262*, 116563.

Tripoppoom, S., Xie, J., Yong, R., Wu, J., Yu, W., Sepehrnoori, K., Miao, J., Chang, C., & Li, N. (2020). Investigation of different production performances in shale gas wells using assisted history matching: Hydraulic fractures and reservoir characterization from production data. *Fuel*, *267*, 117097.

Tripoppoom, S., Yu, W., Huang, H., Sepehrnoori, K., Song, W., & Dachanuwattana, S. (2019). A practical and efficient iterative history matching workflow for shale gas well coupling multiple objective functions, multiple proxy-based MCMC and EDFM. *Journal of Petroleum Science and Engineering*, *176*, 594-611.

Tripoppoom, S., Yu, W., Sepehrnoori, K., & Miao, J. (2021). *Assisted History Matching for Unconventional Reservoirs*. Gulf Professional Publishing.

Vasco, D., Karasaki, K., & Kishida, K. (2001). A coupled inversion of pressure and surface displacement. *Water Resources Research*, *37*(12), 3071-3089.

Vasco, D., Rucci, A., Ferretti, A., Novali, F., Bissell, R., Ringrose, P., Mathieson, A., & Wright, I. (2010). Satellite-based measurements of surface deformation reveal fluid flow associated with the geological storage of carbon dioxide. *Geophysical Research Letters*, *37*(3).

Velez, M. L., Euillades, P., Caselli, A., Blanco, M., & Díaz, J. M. (2011). Deformation of Copahue volcano: inversion of InSAR data using a genetic algorithm. *Journal of Volcanology and geothermal research*, *202*(1-2), 117-126.

Vrugt, J. A. (2016). Markov chain Monte Carlo simulation using the DREAM software package: Theory, concepts, and MATLAB implementation. *Environmental Modelling & Software*, *75*, 273-316.

Vrugt, J. A., & Ter Braak, C. J. (2011). DREAM (D): an adaptive Markov Chain Monte Carlo simulation algorithm to solve discrete, noncontinuous, and combinatorial posterior parameter estimation problems. *Hydrology and Earth System Sciences*, *15*(12), 3701-3713.

Wang, H. (2000). *Theory of linear poroelasticity with applications to geomechanics and hydrogeology* (Vol. 2). Princeton university press.

Wantawin, M., Yu, W., & Sepehrnoori, K. (2017). An iterative work flow for history matching by use of design of experiment, response-surface methodology, and markov chain monte carlo algorithm applied to tight oil reservoirs. *SPE Reservoir Evaluation & Engineering*, *20*(03), 613-626.

Ward, N. D., & Fox, C. (2012). Identification of aquifer parameters from pumping test data with regard for uncertainty. *Journal of Hydrologic Engineering*, *17*(7), 769-781.

White, C. D., Willis, B. J., Narayanan, K., & Dutton, S. P. (2001). Identifying and estimating significant geologic parameters with experimental design. *SPE Journal*, *6*(03), 311-324.

Yeh, W. W. G. (1986). Review of parameter identification procedures in groundwater hydrology: The inverse problem. *Water Resources Research*, *22*(2), 95-108.

Yu, W., Tripoppoom, S., Sepehrnoori, K., & Miao, J. (2018). An automatic history-matching workflow for unconventional reservoirs coupling MCMC and non-intrusive EDFM methods. SPE Annual Technical Conference and Exhibition,

Zhang, J., Zheng, Q., Chen, D., Wu, L., & Zeng, L. (2020). Surrogate-based Bayesian inverse modeling of the hydrological system: An adaptive approach considering surrogate approximation error. *Water Resources Research*, *56*(1), e2019WR025721.

Zheng, Y., & Han, F. (2016). Markov Chain Monte Carlo (MCMC) uncertainty analysis for watershed water quality modeling and management. *Stochastic Environmental Research and Risk Assessment*, *30*(1), 293-308.

CHAPTER EIGHT

USING STRAIN TO CHARACTERIZE LEAKS FROM RESERVOIRS

Contents

8.1 Abstract 8-2
8.2 Introduction 8-2
8.2.1 Characteristics of leaks 8-3
8.2.2 Conceptual Models 8-4
8.2.3 Detection 8-5
8.3 Deformation Caused by a Leak 8-12
8.3.2 Patterns 8-15
8.3.3 Horizontal Transects 8-23
8.3.4 Vertical Profiles 8-26
8.3.5 Deformation at Points 8-27
8.4 Deformation Caused by a Leaky Reservoir 8-32
8.4.1 Patterns 8-32
8.4.2 Horizontal Transects 8-33
8.4.3 Vertical Profiles 8-35
8.4.4 Deformation at Points 8-36
8.5 A Hypothetical FieLd Case at the Avant Field 8-37
8.5.1 Vertical Profiles 8-38
8.5.2 Patterns 8-38
8.5.3 Deformation at Points 8-39
8.6 Discussion 8-41
8.7 References 8-42

USING STRAIN TO CHARACTERIZE LEAKS FROM RESERVOIRS

8.1 ABSTRACT

A leak of CO_2 or other fluid from a reservoir will change the pressure in the reservoir and the confining unit, and these pressure changes which will cause strain. We evaluated the feasibility of using strain to detect and characterize leaks by first developing a conceptual framework for the poroelastic behavior of leaky geologic storage reservoirs. The framework is based on a review of natural and industrial analogues of leakage and vertical flow in geologic settings. It includes a vertical conduit to the ground surface, a horizontal layer and a vertical conduit intersecting a horizontal layer as idealized cases, along with combinations of the basic cases. The poroelastic deformation produced by pressurizing each of these scenarios is characterized using numerical simulation to devise strategies for leak detection and characterization. These strategies are evaluated through a hypothetical case study of water injection into a disposal reservoir at the North Avant Field in Oklahoma by introducing a hypothetical leakage conduit into a calibrated geomechanical model. Two basic types of leaks are recognized based on the ratio of the leak transmissivity to the reservoir transmissivity. This ratio is small in a Type I leak so leakage can have little effect on the pressure in the reservoir and the resulting strain field is caused by pressure changes in the caprock. The transmissivity ratio is large in a Type II leak and the resulting strain field is caused by a pressure change in the reservoir due to the leak. In general, the simulations show that leaks will create strain signals in the caprock that form distinctive patterns characteristic of the leak geometry. Pressurizing a reservoir will also create a strain signal and it is important to be able to distinguish this signal from that of a leak. One approach to doing this is to monitor strain at equal distances from a well because the signal from a leak will break the symmetry that is expected during injection into a reservoir. High resolution strain tensor instruments as described in Chapter Two should be capable of detecting the strain signals expected to be caused by leaks, which could help ensure the reliability of geologic storage.

8.2 INTRODUCTION

Geologic reservoirs are used to store a variety of fluids, including natural gas, hazardous waste, and carbon dioxide, which may be obtained from industrial facilities, Direct Air Capture technologies or as a byproduct of hydrocarbon production (Vasco et al., 2019). In some cases, the storage is meant to be temporary, such as the seasonal storage and removal of natural gas, whereas waste fluids, including CO_2, are intended to be stored permanently. In all cases, leakage of a fluid out of its intended reservoir will cause problems, either because of the loss of a valuable fluid that cannot be economically recovered, or because of the potenntial environmental damage that can be caused by leakage of waste into the environment. Indeed, ensuring the permanence of CO_2 stored in underground reservoirs is critical to moving forward with a viable strategy for CO_2 storage.

There is general consensus that leaks from geologic storage reservoirs typically occur through either wells or fractures penetrating the caprock seal. Faults and fractures are ubiquitous in the Earth's crust. Over a century of hydrocarbon production has reactivated faults (Gurevich & Chilingarian, 1993; Segall, 1989; Segall et al., 1994), and created millions of orphaned, abandoned, and active wells throughout the sedimentary basins proposed for CCS (Kang et al., 2021). Fault reactivation may lead to permeability increase (Meguerdijian & Jha, 2021; Rinaldi

et al., 2014; Rutqvist et al., 2016; Wiprut & Zoback, 2002), and it is therefore important to evaluate the storage integrity of depleted reservoirs that once stored hydrocarbons over geologic timescales.

Analyses indicate that the probability of injected CO_2 encountering a leaky well (Gasda et al., 2004) or a leaky fault (Jordan et al., 2011) is quite high in many basins. The approach to evaluating risks is to (1) understand the characteristics of leaks in natural and engineered settings; (2) develop conceptual and mathematical models that characterize leak behavior; (3) develop field methods for detecting and characterizing leaks.

Leaks have the potential to alter the subsurface fluid pressure, which will cause strain that can be used to detect and chacterize leaks. This possibility has motivated an evaluation of the feasibility of using strain to characterize leaks from reservoirs. The objective of the following chapter is to describe this evaluation.

8.2.1 Characteristics of leaks

Although geologic storage of fluids has been used successfully for decades, leakage has been known to occur and there remains a lack of agreement on how best to detect leaks prior to storage or how to monitor for leaks after a fluid has been sequestered. The design of effective strategies for leak detection and characterization should incorporate as much existing information on leaks as possible, and there have been a considerable number of studies characterizing sites of known leakage. Many natural and industrial analogues, along with the mechanism and results of leakage, have been summarized by Lewicki et al. (2007).

8.2.1.1 Examples

Industrial analogues to leakage from CO_2 storage reservoirs include leakage from wells in hydrocarbon reservoirs or gas storage facilities due to blowouts, cracked or corroded well casings, or improper or damaged cement completions. Leakage along wells completed in both natural and engineered reservoirs is known to occur, as evidenced by the number of leaking wells from methane reservoirs (Kang et al., 2021), and salt dome storage caverns (Bérest et al., 2019). Well leakage could occur along the annulus at rates that can range from a subtle seeps to a catastrophic torrent, such as the Deepwater Horizon incident (Hsieh, 2011). Flows can create a striking novelty in some cases, such as the periodic eruption of the Crystal Geyser, a CO2-fueled geyser created be an abandoned well in Utah (Han et al., 2013).

Natural analogues to leakage from CO_2 storage reservoirs include leakage from CO_2 reservoirs created by magmatic off-gassing, thermal decomposition of carbonates or other natural processes (Lewicki et al., 2007). Oftentimes, leakage in these settings occurs along faults or fractures triggered by seismic activity (Lewicki et al., 2019) or from fault reactivation or hydraulic fracturing of the caprock seal due to pressurization. The impact of faults on fluid flow is complicated by the fact that faults can act as barriers, conduits or mixed conduit/flow barriers with complex and heterogenous architecture and permeability pathways (Annunziatellis et al., 2008).

Much of what is known about leaks along faults is based on conceptual models for fault zone architecture and hydrogeology (Bense et al., 2013; Caine & Evans, 1996; Faulkner et al., 2010; Wibberley & Shimamoto, 2003). In general, faults are typically characterized by a narrow fault core, along which dilation and offset is likely to have occurred, and a wider damage zone

with smaller fractures and faults where the host rock is relatively unaltered. The zone in which flow occurs depends on the permeability structure resulting from various mechanical and chemical processes of permeability enhancement or reduction. Mechanical closure or dilation of the dislocation can occur through changes in effective stress on the walls of the fault or fracture, which can be influenced by the presence of asperities and the stiffness of the fault. Permeability may also be reduced through chemical reactions, such as clay formation from the hydrolysis of silicate minerals. These physical and chemical interactions may cause the flow along a fault to be concentrated along narrow conduits, even in faults that may extend for kilometers in the direction of strike. These conduits may sometimes occur where two or more faults or fractures intersect (Annunziatellis et al., 2008).

8.2.2 Conceptual Models

Important geometric characteristics affecting strain are related to the distribution of physical properties, primarily the permeability and elastic modulus. A convenient approach is to consider three basic geometries of features that are more permeable than their enveloping material; a horizontal layer, vertical conduit, and a vertical conduit overlain by a horizontal layer (Figure 8-1). These geometries can be evaluated to determine the strain fields that they create in response to a load. Alternatively, the basic geometries can be combined to create composite structures, such as a horizontal layer with a vertical conduit, or with a vertical conduit leading to a layer (Figure 8-1d and e).

The strain fields created by simple composite geometries may have contributions from each of the basic geometries. For example, the strain field in the vicinity of a vertical leak overlying a reservoir may have strain contributions from pressure changes in the underlying horizonal layer as well as from the vertical conduit. These effects are superimposed and may cause the pattern of the strain field to be complicated. As a result, it will be convenient to characterize strain fields associated with the basic geometries, and then evaluate strains from composite geometries.

8.2.2.1 Loading

Strain results from a change in applied or body loads. Three types of loads are relevant to the interpretation of strains caused by leaks; fluid pressure change in the reservoir, natural processes, fluid pressure change outside of the reservoir (Figure 8-2).

8.2.2.2 Pressure change in the reservoir

Fluid pressures will increase during injection and decrease as they equilibrate when injection stops. Changes in fluid pressure during injection will cause strain in the overburden that forms the baseline strain signal. Fluid pressure within the reservoir may migrate into an overlying conduit, and this would be the hallmark of a leak (Figure 8-2).

There are two end-member scenarios where a leak will affect pressures that result in strain. One scenario is where the rate of fluid flow up the conduit is large compared to flow in the vicinity. In this case, the leak could be a major effect on the pressure within the reservoir. For example, a strong leak may prevent the pressure from changing beyond the leak. This would cause the baseline strain signal from pressurization of the reservoir to differ from what it would be without a leak. Another end member is where the pressure in the reservoir is unaffected by the leak, but the pressure in the leak itself is sufficient to cause strain. In this case, the measured

strain will be the superposition of the strain caused by the underlying reservoir and the strain from the leak.

An important aspect of this type of loading is that it can be controlled by the use of wells and pumps. Changes in the injection rate are expected to accompany maintenance or other operations, and this would change the pressure in the reservoir. Moreover, it would be feasible to intentionally change the injection rate to cause strain that would be used for diagnostic purposes. A periodic fluctuation superimposed on an average value is one way the injection rate could be varied to create a load that would cause strain.

8.2.2.3 Natural processes

Another type of load considers natural processes, such as changes in barometric pressure or Earth tides (Figure 8-2). Changes in water content in soil from rainfall or evapotranspiration will also affect loading.

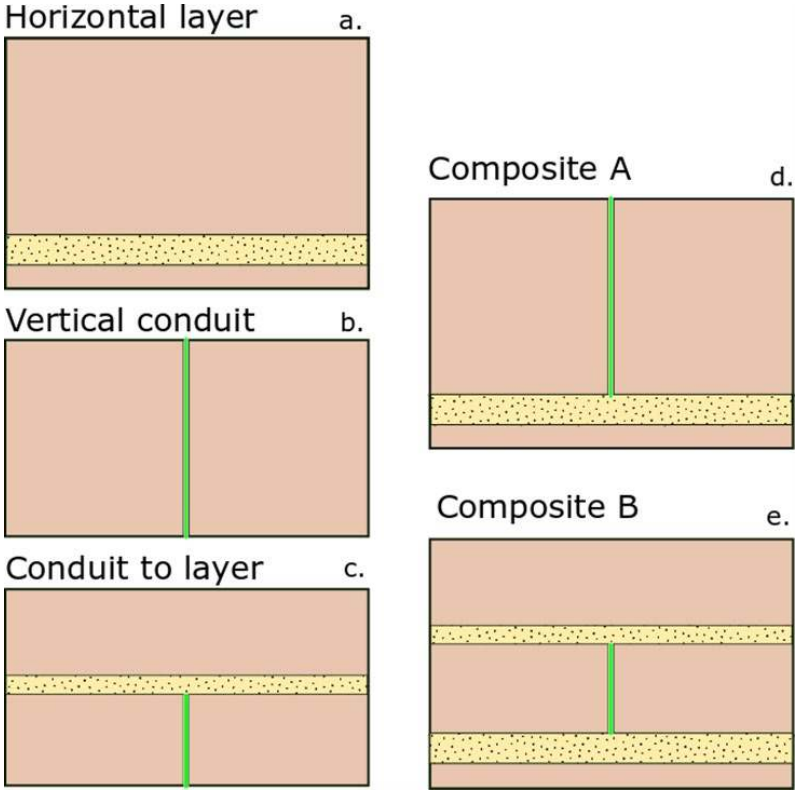

Figure 8-1. Geometries used to characterize strain fields. Basic geometries include a.) a horizontal permeable layer representing a reservoir or aquifer; b.) a vertical conduit such as a fracture, sand-pipe, or well; c.) a vertical conduit overlain by a horizontal permeable bed. Basic geometries are combined to create more realistic composite geometries; d.) and e.).

8.2.3 Detection

Carbon Capture and Storage (CCS) is cited to have the potential to play a major role in meeting emissions reduction targets established by the IPCC, but there remains uncertainty on how best to assess and mitigate the primary risk of this technology: leakage out of the intended reservoir. The two primary mechanisms for leakage out of geologic storage reservoirs are along

wells or along faults or fractures penetrating the caprock seal. Faults and fractures are ubiquitous in the Earth's crust and over a century of hydrocarbon exploration has resulted in reactivation of faults (Segall, 1989; Segall et al., 1994; Wiprut & Zoback, 2002) and creation of new ones (Gurevich & Chilingarian, 1993), along with millions of orphaned, abandoned, and active wells throughout many sedimentary basins proposed for CCS (Kang et al., 2021). Methods have been developed for estimating the probability of an injected CO_2 or pressure plume encountering a leaky well (Gasda et al., 2004) or a leaky fault (Jordan et al., 2011; Zhang et al., 2010) and indicate that the likelihood could be quite high in many cases. It is therefore crucial to establish a comprehensive caprock integrity assessment and monitoring strategy that is designed to:

(i) detect existing leaks during the site selection and characterization phase, and
(ii) monitor for leaks that have developed after the initiation of operations or those that were not identified during initial characterization.

In following section we briefly review current strategies and proposed methods for leak detection and evaluate the feasibility of using in situ deformation measurements to identify leakage conduits out of the reservoir. This is accomplished by evaluating the far-field hydromechanical behavior in the overburden due to vertical flow and leakage from geologic storage reservoirs.

8.2.3.1 Strategies

The ultimate goal in any caprock integrity assessment and monitoring program is to identify leaks early in their development while mitigation is possible, and impact could be minimized. Ideally, existing leaks would be identified in the site selection and characterization stage prior to the initiation of storage operations (Plasynski et al., 2011). After storage operations have begun, it will be important to have a diverse portfolio of monitoring technologies to detect any evidence of leakage so that proper action could be taken in a timely manner. Strategies for leak detection include direct detection of leakage conduits, leaked fluids, or leaked pressure. Evidence of leakage could also be detected indirectly by measuring deformation caused by leaked pressure.

8.2.3.2 Detecting a Leakage Conduit

Existing leakage conduits may be detected through various methods. Preexisting faults may be identified through the review of core data, wireline logging, or seismic reflection surveys, while other geophysical methods, such as magnetic surveys (Frischknecht et al., 1985) or Ground Penetrating Radar (GPR), and electrical resistivity (Aller, 1984), may be used to identify unmapped wells. Core and wireline data could be valuable for determining the orientation and hydraulic information for a fault; however, well bores and cores are often sparse, but could be available in heavily drilled sedimentary basins, such as depleted oil and gas fields. Direct detection of faults could also be accomplished through seismic reflection surveys like those conducted at the In Salah CO_2 storage reservoir in Algeria (Vasco et al., 2019). However, many faults may be below seismic detection thresholds, and these methods provide little information on whether a fault is sealing or non-sealing.

8.2.3.3 Detecting Leaked Fluid

Fluid that has leaked out of a reservoir creates a zone of anomalous composition, pressure and temperature, and these characteristics are the bases for detection methods.

8.2.3.3.1 Geochemical Monitoring

After storage operations have begun, leaks could be identified through the direct detection of leaked CO_2 or other stored fluids, which could be accomplished by geochemical composition monitoring or imaging of the injected plume through seismic reflection surveys. Geochemical leak detection methods consist of monitoring for CO_2 breakthrough concentrations in groundwater (Yang, 2014), soil-gas (Kim, 2019; Schacht, 2014), or air at the ground surface (Lewicki, 2009). These methods have been valuable in characterizing the extent and rate of leakage at many natural and industrial GCS analogues. Soil gas monitoring has been used to quantify CO_2 emissions at Mammoth Mountain (Farrar et al., 1995; Lewicki et al., 2019), along the San Andreas Fault (Lewicki & Brantley, 2000) and Latera caldera (Annunziatellis et al., 2008). Off-gassing of CO_2 at Yellowstone has been monitored with eddy covariance (Lewicki et al., 2017), and dissolved CO_2 concentrations in groundwater have been monitored at Soda Springs, ID (Lewicki et al., 2013). Indeed, continuous geochemical monitoring has been useful for characterizing the leakage dynamics of many natural analogues to CO_2 storage, and will likely be a part of any geologic storage project; however, these techniques require that a leak has already occurred and that the leaked fluid has had time to reach the monitoring point. The reduction in detection time is thus a key motivating factor in the development of many geophysical leak detection methods.

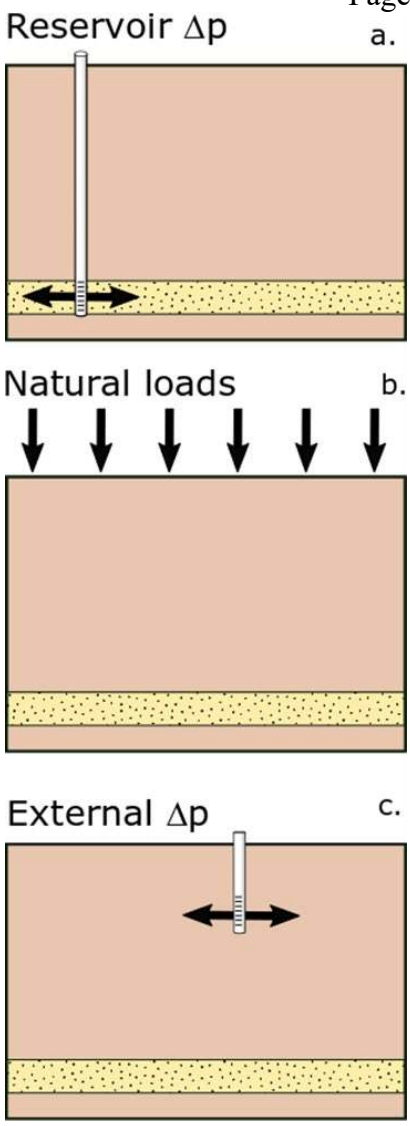

Figure 8-2. Types of loads that could cause strain. a.) fluid pressure change in a reservoir, typically from injection or pumping; b.) natural loads, such as barometric pressure, Earth tides, or changes in water content near the ground surface; c.) fluid pressure change overlying the reservoir, typically from injection or pumping.

8.2.3.3.2 Seismic Imaging

Subsurface imaging through timelapse active seismic surveys has proven to be valuable for tracking the extent of the injected plume of CO_2 or CO_2/CH_4 mixtures at many storage projects, such as Sleipner (Chadwick et al., 2014), Snhovit (Grude et al., 2013), Aquistore (White et al., 2014, 2015), and the CO2CRC Otway Project in Australia (Correa et al., 2017; Pevzner, Urosevic, Popik, et al., 2017; Pevzner, Urosevic, Tertyshnikov, et al., 2017). Many of these projects demonstrated the ability to resolve CO_2 plumes with injected volumes as small as 2-4 kt at depths greater than 800 m (Chadwick et al., 2014; Pevzner et al., 2021), while other projects, such as the Decatur project in the Illinois Basin, have had difficulty detecting a 70 kt CO_2 plume (Coueslan et al., 2014). Improvements to seismic detection thresholds have been achieved through advancements in permanent installations of both sources and receivers.

Surface Orbital Vibrators (SOVs) may serve as an active source combined with Distributed Acoustic Sensing (DAS) and permanently installed Geophone seismic receivers. These techniques will likely be invaluable for monitoring the plume of injected fluids, but may be limited in their ability to monitor the much larger pressure plume that develops as a result of injection.

8.2.3.3.3 Changes in Fluid Compressibility

The compressibility of CO_2, methane, and other fluids commonly stored in geologic reservoirs is often several orders of magnitude higher than water, leading small changes in the gas saturation to result in significant changes in the pore fluid compressibility. This effect has been utilized to detect the presence of CO_2 from changes in compressibility observed by interpreting pore pressures signals from Earth tides (Sato, 2006) or from timelapse pumping tests (Hosseini & Alfi, 2016; Shakiba & Hosseini, 2016). One study demonstrated how this effect can be used to create timelapse tomography maps of the diffusivity in a formation to detect leaks (Shakiba & Hosseini, 2016). This was accomplished by analyzing Harmonic Pulse Tests (HPTs), where the injection rate is modulated at a known period, and the corresponding periodic pressure response is recorded in an array of monitoring wells. These signals are then interpreted in the frequency domain to obtain estimates of the hydraulic diffusivity of the formation between the pulsing and observation wells. If a change in diffusivity is detected, the test is repeated using a cluster of pulsing and observation wells closer to the detected change to refine estimates of the geometry of the diffusivity anomaly.

8.2.3.4 Detecting Leaked Pressure

Pumping or injection in a well will cause a change in pressure that propagates away from the well in the formation and along any fluid-saturated permeable conduits. As a result, many researchers have explored both passive and active leak detection methods by monitoring the pressure in the target reservoir, referred to as the Injection Zone (IZ), and overlying formations comprising the Above Zone Monitoring Interval (AZMI).

Pressure monitoring in the IZ can reveal useful information on the fluid behavior in the storage formation. However, interpretation of these pressure signals for leak detection has been cited as a challenging task due to its sensitivity to several parameters, such as background pressure trends, injection rate, formation rock and fluid properties, reservoir boundaries, well completion type, and far-field well operations (Hosseini et al., 2019). Active testing strategies have been investigated for boosting the signal to noise ratio or detectability of the leakage signal. These methods include modulation of the injection rate to produce a periodic signal that could be more easily identified and interpreted in the frequency domain (Sun et al., 2015).

Many studies have investigated the potential for detecting leaks by monitoring the pressure in the AZMI for anomalies and history-matching a calibrated site model to estimate a location and rate of leakage to explain the observed anomaly (Cameron et al., 2016). There are three basic assumptions to this approach: (i) that the leakage signal is detectable and identifiable from the background, (ii) that the forward model is well calibrated without the effect of the leak or leaks, and (iii) that the leak could be properly parameterized in the inversion scheme with no knowledge of the leakage conduit or leaking fluids (e.g., whether the leak is a fault or a well, whether there are multiple leaks, the composition of the leaking fluid, etc.).

The validity of the first assumption - that increases in pressure due to leakage could be discriminated from natural fluctuations in the background pressure – will depend on the strength of the leakage signal, the resolution of the sensor, and the ability to identify and filter out all background sources, such as atmospheric loading, Earth and ocean tides, and any known or unknown active wells in the monitoring formation. Numerous studies have investigated the factors controlling the magnitude of the pressure perturbation in overlying aquifers due to leakage (Nordbotten, Zeidouni, Nuefeld, Pegler, etc.). In general, the magnitude will depend on the hydraulic diffusivity of the monitoring interval, the distance to any boundaries and boundary type, the distance to the leak(s), the rate of leakage, and any heterogeneities. All these factors could have a significant impact on the observed signal and should be considered in the design of any monitoring strategy. The resolution of pressure transducers can vary widely depending on cost with standard pressure gauges typically able to resolve changes on the order of 10 Pa, with state-of-the-art sensors capable of 10^{-3} Pa. The ability to filter out background signals will depend on the quality and amount of data on input signals, such as barometric pressure monitoring, windspeed, known pumping rates, etc.

The validity of the second assumption - that an adequately calibrated forward model for the reservoir-caprock-monitoring interval system exists – will depend on the magnitude of the effect the leak will have on the type of signal inverted to estimate model parameters. For instance, a model of the monitoring formation calibrated to pumping data may be contaminated by the effect of any existing leaks, allowing existing leaks to essentially be calibrated into the site model. However, the effect of the leak could be absent or different if the model was calibrated using a different input signal, such as barometric loading (van der Kamp & Gale, 1983) or Earth tides (Hsieh et al., 1987) instead of pumping.

The validity of the third assumption – that the leak could be properly parameterized in the inversion scheme with no knowledge of the leakage conduit or leaking fluid – could depend greatly on the nature of the leak. If there is a detectable leakage signal in three or more monitoring wells from a single point source, such as a leaky well, then the inversion scheme could be straightforward. However, if the leakage is distributed among several sources or a complex leakage pattern along a fault, then the inversion could be more difficult.

While direct detection of leaked pressure has been demonstrated to be a promising approach to identify the presence and location of leaks, this requires that a monitoring well is completed along the flow path of the leaking pressure in a fluid-saturated, permeable formation, and that the pressure has had time to reach the observation point. Furthermore, since pressure is a scalar measurement, a minimum of two wells are required to obtain useful information on the location of the leak, with three or more wells being optimal.

8.2.3.5 Detecting Deformation from Leaked Pressure

Another approach to characterizing the leaked pressure is to measure deformation. Changing the pressure in a reservoir through well operations will deform the reservoir, overburden and ground surface at great distances from the zone of pressure perturbation. In some cases, such as over-pumping in the Central Valley Aquifer of California, this can result in noticeable amounts of subsidence and inelastic deformation, while in other cases, the deformation is elastic and only detectable by sensitive measurements taken *in situ* (Murdoch et al., 2021; Schuite et al., 2017; Schweisinger et al., 2011). Deformation may be characterized by the strain tensor, which holds a rich amount of information on the magnitude and orientation of

perturbed stresses and the elastic properties of the subsurface materials. Incorporating deformation measurements into joint inversion schemes with pressure data has been demonstrated to improve the speed of convergence and decrease the time required to detect a leak (Jung et al., 2013). Deformation from well operations may be characterized by measuring the vertical displacement of the ground surface, or gradients of displacement in the subsurface by measuring tilt or strain. Further details on how these approaches could be used to identify leaks are provided below.

8.2.3.5.1 Uplift

Researchers at the In Salah carbon storage site in Algeria were able to detect evidence of leakage by identifying unusual uplift patterns using Interferometric Synthetic Aperture Radar (InSAR) (Vasco et al., 2019). The uplift near the injection well was characterized by two parallel ridges forming a distinct double-lobe pattern, which has been associated with the pressurization of a vertical planar conduit, such as a fault or fracture (Pollard & Holzhausen, 1979). This discovery prompted further investigation through review of seismic data and CO_2 breakthrough concentrations in monitoring wells, which led the operators to conclude that leakage had occurred and the well was shut in (Vasco et al., 2019). While these results demonstrated that deformation measurements could be used to detect pressure distributions indicative of leakage or pressurized faults, remote sensing methods are limited to observations of the ground surface at a frequency of usually no more than once per day. Real-time monitoring of high resolution in situ deformation, such as tilt or strain, could be a valuable supplement to the broad spatial scale measurements provided by remote sensing.

8.2.3.5.2 Tilt

Tilt is a standard in situ deformation measurement defined as the gradient of displacement normal the direction of displacement. Currently available borehole tiltmeters have resolutions as high as 10^{-8} radians and have been used to characterize deformation from well tests (Fabian, 2004) and hydraulic fracturing (Warpinski et al., 1997). Tilt data has been found to outperform vertical displacement data in inversion schemes designed to characterize reservoir well operations (Monfared et al., 2011). These researchers found that introducing an error of 0.55% in the vertical displacement data increased the RMSE of the analysis by a factor of 13, while a 20% increase in the error in the tilt data only increased the RMSE by a factor of 7 (Monfared et al., 2011). The value of tilt data in imaging reservoir dynamics has also been demonstrated by measuring tilt at 12 locations at a depth of approximately 12 m during injection into a granodiorite at a depth of over 2 km (Vasco

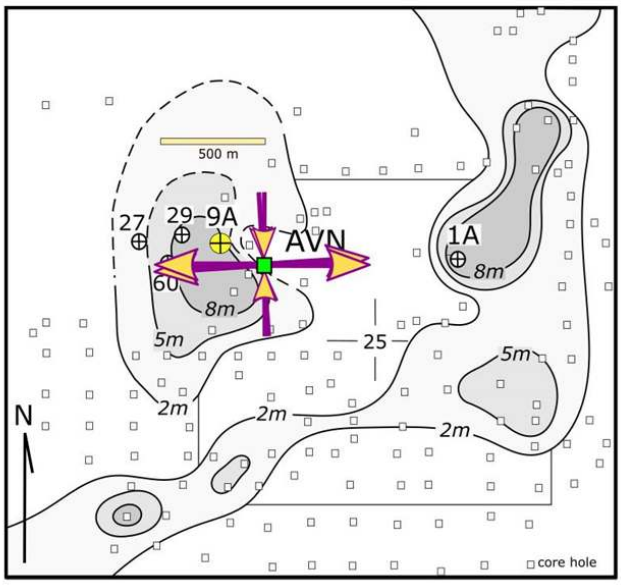

Figure 8-3. Principal strain components recorded at strainmeters installed at AVN from shut-in at Well 1A in the Avant field, Oklahoma.

et al., 2000). The pattern of the resulting tilt data indicated pressurization of a north-northwest trending zone, which is aligned with the orientation of mapped faults in the area.

8.2.3.5.3 Strain

Like tilt, strain is also a standard in situ deformation measurement. Strain is a measure of the parallel component of the gradient of displacement. Borehole strainmeters and extensometers designed to measure one or more components of the strain tensor have been used to characterize reservoir properties and fluid pressures (Murdoch et al., 2021), monitor the change in aperture of hydraulic fractures due to pumping (Hisz et al., 2013), and estimate changes in soil moisture contents over broad spatial scales (Murdoch et al., 2015).

The feasibility and advantages of using deformation measurements to monitor CCS and other geologic storage operations was investigated by (Murdoch et al., 2020b). In this study, the authors demonstrated the rich amount of information contained in the strain tenor in the overburden and identified three basic classes of instruments based on their method of deployment that could be used to characterize this behavior. These include annulus strain sensors that are cemented into the annulus of a well casing, portable borehole instruments that may be temporarily anchored inside a well casing or borehole, and grout-in borehole strainmeters that are permanently installed in a dedicated boring. Each class of sensor has their own set of advantages and limitations based on cost, logistics of use, as well as the sensitivity and spatial scale of the measurement. Annulus sensors are capable of distributed measurement of a single component of the strain tensor and have minimal affect on well operations. Portable strainmeters have the lowest sensitivity, but their ability to measure multiple components of the strain tensor could allow for more detailed analysis, and their ability to be removed and reused could reduce costs. Grout-in borehole strainmeters provide the highest sensitivity of point-scale strain measurements but require a dedicated boring.

The high resolution of grout-in borehole strainmeters and the ability to measure multiple components of the strain tensor make these instruments attractive for monitoring the complex pattern of small strains expected in the overburden during geologic storage operations. Moreover, their ability to be permanently installed at shallow depths could allow for valuable long-term reservoir monitoring at modest cost. One of the most intriguing capabilities enabled from interpretation of the strain tensor is the ability to determine the orientation of the applied stress field. For instance, shallow strain tensor measurements in the North Avant Field in Oklahoma were used to identify both the presence of, and direction towards, a production well nearly 1 km away that had recently been shut-in (Figure 8-3). This capability could have many implications for CCS and geologic storage monitoring, such as the ability to identify unknown active wells that could affect reservoir pressures, and the potential to identify and locate leaks out of the storage formation.

Although the value of strain tensor measurements could be quite high for applications in reservoir characterization and monitoring, high instrument costs and logistics of installation, as well as challenges in data interpretation have hindered their use and there are currently no instruments commercially available. We have developed a fiber optic deformation sensor capable of measuring the full strain tensor using Michelson interferometry, the same revolutionary strain sensing technology used by LIGO to detect gravitational waves (Barish & Weiss, 1999). The instrument noise is essentially zero and the resolution is limited only by our ability to remove background signals. This was accomplished by developing novel designs for

both the Michelson interrogator and strain-sensing element. The interrogator was designed with a compact formfactor that allows for deployment inside a well casing where the temperature is stable, and the sensing element is composed of optical fibers wrapped into various geometric configurations to obtain multiple components of the strain tensor.

These capabilities in deformation measurement and interpretation, along with the findings that deformation measurements could be used to detect pressure distributions caused by leakage or pressurized faults at the In Salah carbon storage facility in Algeria, have motivated us to evaluate how strain tensor measurements in the overburden could be used to detect and characterize leaks in geologic storage reservoirs.

8.3 DEFORMATION CAUSED BY A LEAK

The conceptual model for a reservoir with a leak will consists of a horizontal layer of infinite extent with a vertical planar conduit (e.g., fault zone, etc.) that extends to the ground surface (Figure 8-1). A well in the reservoir injects at constant pressure, and the leak is set a distance, L, away from the well. The caprock will be assumed to be impermeable and to extend from the top of the reservoir to the ground surface. This two-dimensional conceptual model is similar to models used to analyze fluid flow along leaks in reservoirs (Pegler, 2014; Nuefeld, 2009; Pritchard, 2001), but to our knowledge, it has not been used to analyze deformation.

The approach is to simplify the reservoir and the leak into two idealized components; 1.) a horizontal layer, and 2.) a vertical planar conduit. The deformation caused by pressurizing each component will be analyzed separately, and then they will be combined and analyzed as a composite. A central challenge will be to distinguish the deformation caused by the vertical planar conduit from the deformation that will inevitably be caused by pressurizing the horizontal layer. The analysis will first consider the transient patterns of the normal strains and tilt in cross section to understand the general deformation behavior for each case. This will be followed by an evaluation of time series signals distributed along transects and at points to identify signals that could potentially be measured with available in-situ sensors.

Table 8-1. Material properties used in the analyses.

Property	Reservoir	Conduit
Layer Thickness [m]	10	1
Young's Modulus [GPa]	10	1
Layer Stiffness [GPa/m]	1	1
Hydraulic Diffusivity [m^2/s]	11.6	11.6
Characteristic Time [days]	1	1

8.3.1.1 Case 1: Injection into a Horizontal Layer (Baseline)

Injection into a horizontal layer serves as the baseline case. This could represent a reservoir or aquifer with a competent caprock. The reservoir is represented as a uniform layer of infinite extent in 2D cartesian coordinates assuming plane strain. The overburden is assumed to be fully saturated and impermeable. This creates undrained conditions and an effective Poisson's ratio of 0.5 in the overburden. An important consequence of these assumptions is that the magnitudes of the horizontal and vertical strains are equal and opposite in sign. One

component of the normal strain is sufficient to characterize the strain tensor in this idealized case.

Injection is simulated by increasing the pressure by 1 MPa above hydrostatic over the reservoir thickness along the boundary. The geometry is idealized, but it broadly resembles the configuration of a horizontal well held at constant pressure. Injection at constant pressure could be used to maximize an injection rate while avoiding unwanted effects of excessive pressure like hydraulic fracturing of the caprock seal. The material properties used for this analysis are typical of values in saline aquifers (Table 8-1).

8.3.1.2 Case 2: Leakage along a Vertical Planar Conduit

The deformation field for this case was evaluated in plane strain with undrained conditions, as in Case 1. This configuration resembles an idealized vertical fault zone where the pressure is applied over a long lateral distance. A similar configuration was proposed for a hypothetical vertical fault or hydraulic fracture intersecting an injection well at the In Salah carbon storage site in Algeria (White, 2014; Morris, 2011; Ringrose, et al, 2013); however, the conduit in this case extends to the ground surface, whereas the hypothetical conduit at In Salah is inferred to be terminated at depth. The properties of the conduit are assumed to be uniform and constant, and the pressure is initially uniform and equal to 0 (gravity is ignored because only the pressure change is of interest). The upper boundary condition on the conduit is $p_L^u = 0$ and the pressure at the lower boundary is $p_L^L = 1$ MPa. The mechanical boundary conditions for the conduit consist of a boundary load applied normal to the conduit walls with a total stress equal to the fluid pressure. The analysis considered conduit stiffnesses ranging from 0.1 to 100 GPa/m to evaluate the effect on the deformation.

The conduit is characterized as a layer with permeability, specific storage (defined by E and ν, eq --), and thickness that are uniform and constant, and the fluid pressure in the conduit is one-way coupled to the deformation. We evaluated representing the conduit as a deformable fracture (Murdoch and Germanovich, 2006) with an aperture that varies with the fluid pressure. This fully coupled representation gives strains that differ in detail from the approach used here particularly at the leading edge of the pressure (Murdoch and Germanovich, 2006), but those differences are negligible at length and time scales that are important to characterizing strains from leaks. Using the deformable fracture approach significantly increases run times, so the equivalent porous medium approach was used instead. We also ignored changes in fracture compliance, or elastic modulus, with depth. The stiffness of some fracture zones probably increases with depth, but this effect is difficult to generalize so we decided to address it in a later analysis. The conduit was discretized with one column of a rectangular mesh, and it was bounded by edge elements with essentially zero permeability to ensure flow was 1D along the layer and to eliminate fluid exchange with the matrix. These simplifying assumptions were used to reduce computational resource requirements for the analysis and to establish a first-order approximation of the hydromechanical behavior for horizontal and vertical flow.

8.3.1.3 Pressure distribution

The pressure distribution is 1D in both cases and they share a specified pressure boundary condition at the origin. Case 1 assumes a reservoir of infinite extent, so the pressure can be described by (Carslaw & Jaeger, 1959).

$$p(x,t) = p_0\,[1 - \mathrm{erf}\,(x^*(4t^*)^{-1/2})\,] \quad (8\text{-}1)$$

where

$$x^* = \frac{x}{x_c} \quad (8\text{-}2)$$

and

$$t^* = t\frac{D}{x_c^2} \quad (8\text{-}3)$$

and p_0 is the applied pressure, D is the hydraulic diffusivity, and x_c is the characteristic length, which is equal to the depth of the reservoir, d, in this example. It follows that the extent of the pressurized interval (x_p) advances along the layer with time according to

$$x_p \sim 2\sqrt{Dt} \quad (8\text{-}4)$$

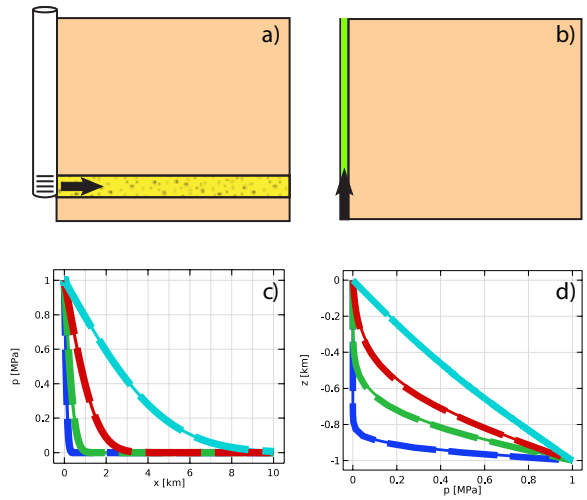

Figure 8-4. Conceptual models and pressure distributions along a layer with time for a & c) a horizontal layer, and b & d) a vertical planar conduit. Numerical solution (dashed), analytical solution (solid) for representative times.

The pressure in the vertical planar conduit is held at $p = 0$ at the ground surface, $x^* = 0$, which causes the pressure to differ from (1a). This boundary condition can be considered by modifying (1) using an infinite series (Carslaw & Jaeger, 1959), but at early times the effect of the boundary is negligible and (1) will be a reasonable approximation. One important difference between the two cases, however, is that the pressure in the vertical conduit reaches a steady state at approximately t*> -- when it is linear from the reservoir to ground surface. The pressure in the horizontal layer is always transient, however.

The numerical solution is essentially identical to the analytical solution for both cases (Figure 8-4c and d).

The pressure transient controls the evolution of the strain field, so we will use the dimensionless distance and time from the pressure analysis to characterize the strain field. The analysis was initially conducted using actual dimensions and realistic properties, and the results were configured into dimensionless terms in post processing. Results presented in dimensioned form can be easier to visualize, whereas results in dimensionless form are more easily generalized to other conditions. Both dimensioned and dimensionless form have their

merits, so results will be presented using both forms. The use of a characteristic length equal to the depth of the reservoir of 1 km means that a dimensionless distance of $x^*=1$ is equivalent to x = 1km. Similarly, a hydraulic diffusivity of D = 11.6 m^2/s, causes a dimensionless time of $t^*=1$ to be equivalent to t = 1d.

8.3.2 Patterns

Pressurization of a horizontal layer or vertical planar conduit (Case 1 or 2) creates patterns of deformation that evolve with time as the extent of the pressurized interval expands. At early times ($t^*<0.01$) the extent of the pressurized interval in the layer is small compared to the depth ($x_p << d$), and the normal strains and tilt patterns are lobes of contrasting sign (Figures 8-5 and 8-6a).

The lobes of the normal strains are symmetric about vertical and horizontal planes, whereas the symmetry planes of the lobes of tilt are inclined at approximately 45°. The sign convention is that positive strains are tensile and negative strains are compressive, and positive and negative values of tilt indicate tilting oriented in the positive and negative x-coordinate directions, respectively. Since the injection well is located at x = 0, positive values of tilt on the left side of the well will be oriented towards the well and positive values on the right side of the well are oriented away from the well.

Interestingly, the patterns of normal strain and tilt caused by a pressurized horizontal layer are essentially the same as the patterns caused by a vertical layer when the pressurized interval is small. The patterns change and symmetry about the horizontal plane is lost, however, as the deformation expands and interacts with the ground surface. Details of how the deformation patterns evolve once interaction with the ground surface occurs differ for the two cases and are described below.

8.3.2.1 Horizontal Layer (Case 1)

The horizontal strain in the overburden consists of a tensile lobe overlying the pressurized interval, and a compressive lobe in front of it (Figure 2a). The tensile lobe rapidly propagates upward, with a lobe of nanostrain magnitude reaching the ground surface within roughly the first minute (x_p ~ 25 m), and a 100 nanostrain ($\varepsilon = 10^{-7}$) lobe reaching the ground surface within the first day (x_p = 715 m) (Figure 8-5f). The pattern of vertical strain is the same as that of the horizontal strain in this case, but the sign is reversed. It follows that the strain field expands as the pressure propagates, but the strain field caused by the pressurized horizontal layer propagates much faster vertically than the pressure propagates horizontally.

The vertical strain in the pressurized layer is always tensile, whereas the horizontal strain in the layer is tensile where the pressure is greater than ~0.4p_{well} and compressive beyond. The layer is too thin in Figure 2 to visualize the strain directly, but the horizontal strain in the layer can be determined indirectly because it is continuous with the strain in the overburden. As a result, the lobe of horizontal strain in the overburden intersects the layer at the same extent of the horizontal strain in the layer. It follows that the strain in the overburden may be used to estimate the pressure distribution and strain in the layer.

As the extent of the pressurized interval increases, the lobes of normal strain expand and intersect the ground surface (Figure 2d). The strain goes to zero between the two lobes, resulting in an inclined band of zero strain, the strain *crossover band*, which extends from the reservoir up

towards the ground surface. The crossover band is inclined approximately 45° for the first day of injection (t = ~0.3 t_R*) and the angle decreases to 30° after about 10 days of injection (t = ~3 t_R*).

Like the normal strain, the lobes of tilt expand and interact with the ground surface. During injection, the tilts overlying the reservoir are towards the well, and they are away from the well at shallow depths, resulting in a crossover band in the tilt. Unlike the normal strain crossover band, the crossover band in the tilt never intersects the ground surface. Additionally, the location of the crossover band remains fairly constant throughout injection and is shallowest near the well and becomes progressively deeper with distance. The maximum tilt at the surface occurs at a distance between 0.5 and 2 km (0.5-2x*) and is approximately 100 μrad for the parameters considered in this example.

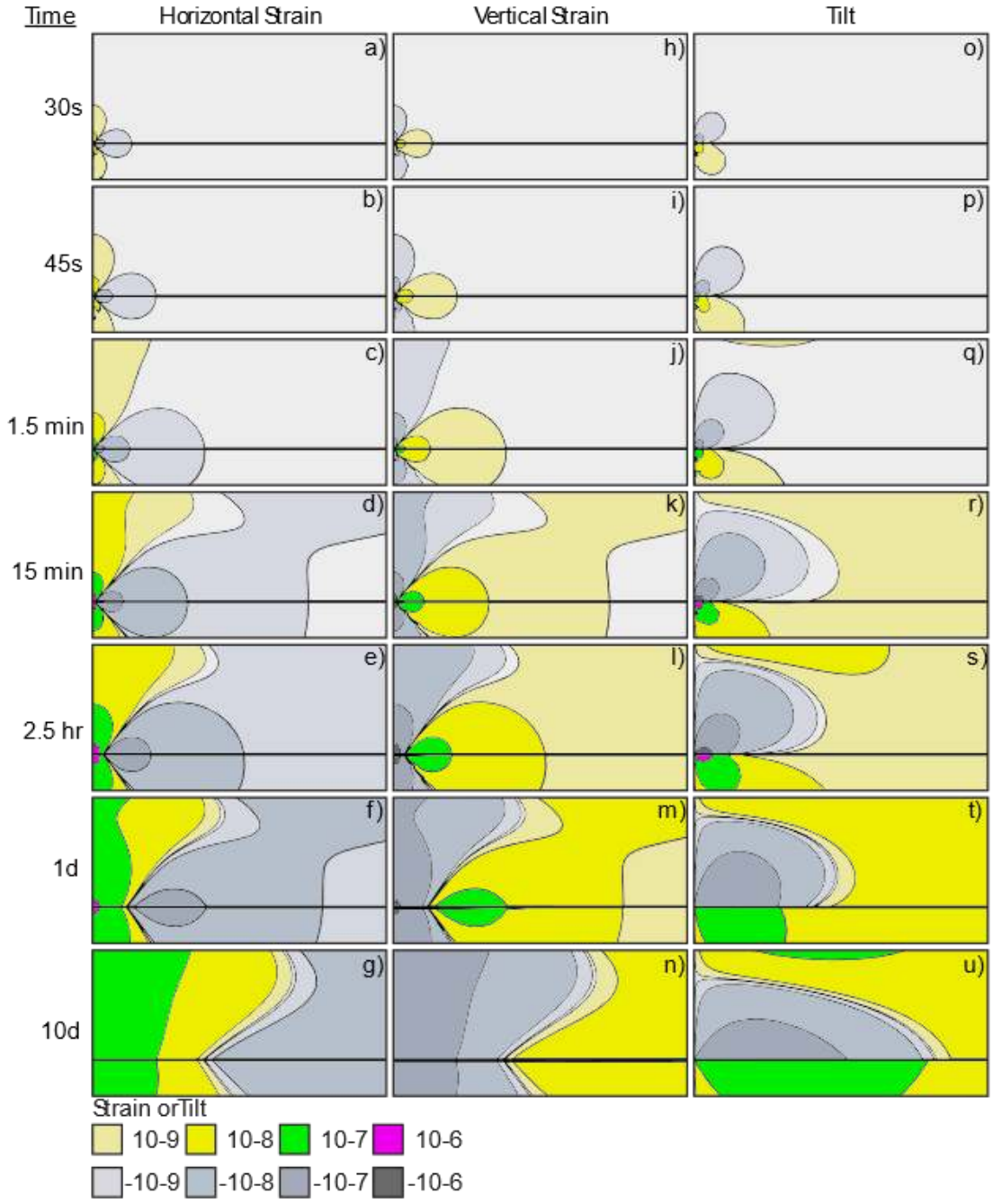

Figure 8-5. Vertical cross-section of deformation fields produced by pressurization of a horizontal layer.

The horizontal and vertical normal strains are equal and opposite in sign because the effective Poisson's ratio is 0.5. Decreasing ν reduces the magnitude of the vertical strain relative to the horizontal strain. For example, when ν=0.25 the vertical strain is -1/3 that of the horizontal strain. Relaxing the plane strain assumption further reduces the strains in the *x* and *z* directions, whereas it increases the strain in the *y* direction (normal to the plane shown in Figure 8-5). Nevertheless, the sign of the vertical strain remains opposite that of the horizontal strain

and the general patterns of the strain fields in Figure 8-5 are similar to the patterns when other values of ν and 3D conditions are used. As a result, it seems reasonable to use these conditions for an initial evaluation of strain fields. The patterns of strain in Figure 2 are also similar to the strain in axisymmetric conditions shown in Figure 3 in Murdoch et al. (2020).

8.3.2.2 Vertical Planar Conduit (Case 2)

Pressurization of the vertical conduit produces a deformation pattern that resembles the pattern created by the horizontal layer in some aspects, but in other aspects the pattern is distinct. The patterns in the normal strain and tilt in cross-section were evaluated for an applied pressure of 1 MPa with conduit stiffness ranging from 0.1 to 100 GPa/m to establish the effect on the patterns and magnitudes of deformation. In general, the magnitude of deformation and interaction with the free surface increase as the as the stiffness of the conduit decrease.

At early times, orthogonal lobes of normal strain develop around the vertical conduit that resemble the lobes around a horizontal layer (e.g. Figure 8-6a, $t^* = 0.01$). As the length of the pressurized interval increases, the extent of the lobes expand and they intersect the ground surface, creating a region of tensile horizontal strain at shallow depths and compressive horizontal strains beyond, with a crossover band of zero strain between. The lateral extent of the compressive horizontal strains is much greater than that of the tensile, and magnitudes are generally smaller in the near surface and increase with depth (Figure 8-6).

When the lobe of normal strain ahead of the conduit intersects the ground surface, the normal strains are amplified along a band that extends diagonally from the advancing pressure front toward the surface at an angle of approximately 45º (highlighted with a dashed line in Figure 8-6c at $t^*=0.01$). As the pressure front advances upward, the distance between the band of high strain and the conduit decreases. This causes the maximum strain in the near-surface caused by a vertical conduit to migrate *towards the conduit*.

Once the pressure in the conduit has reached a steady state with a linear profile between the surface and the applied pressure, the greatest tensile horizontal strains occur at shallow depths near the conduit and decrease with distance and depth. Conversely, the greatest compressive horizontal strains occur at the base of the leak where the pressure is greatest.

The tilt patterns from pressurization of the vertical planar conduit also differ from those caused by a horizontal reservoir. Like the normal strains, the tilt at the onset of pressurization forms two sets of symmetric lobes of opposite sign situated orthogonal to each other. However, unlike the normal strains, this pattern is rotated 45º from the orientation of the conduit. As the pressurized front advances, the tilt field expands and interacts with the ground surface, causing it to become asymmetric about a horizontal plane. At all times, tilt in the vicinity of the conduit is towards the conduit, but it goes to zero and is oriented away from the conduit at further distances. The distance to the change in sign at steady state decreases as the stiffness increases. This distance is greatest at a depth equal to the center of the conduit ($z^* = 0.5$) and shortest at the ends. This pattern in the tilt is reflected in the uplift as a trough centered above the conduit with parallel ridges at lateral distance – the hallmark of deformation along a free surface from an asymmetric, uniform pressure gradient applied to a vertical plane as described by Pollard and Holzhausen (1979) and observed at the In Salah carbon storage facility (White et al., 2014; Morris et al., 2011).

There are three key differences between the deformation caused by a vertical planar conduit and a horizontal layer:

1) the presence of two diagonal bands of high normal strain that extend to the surface with a separation that scales with the depth of the pressure front and converge at a rate that scales with the diffusivity of the conduit,
2) a normal strain crossover band that migrates vertically through the overburden, and
3) the occurrence of both positive and negative tilt in the near-surface formed by the double-ridge and trough uplift pattern.

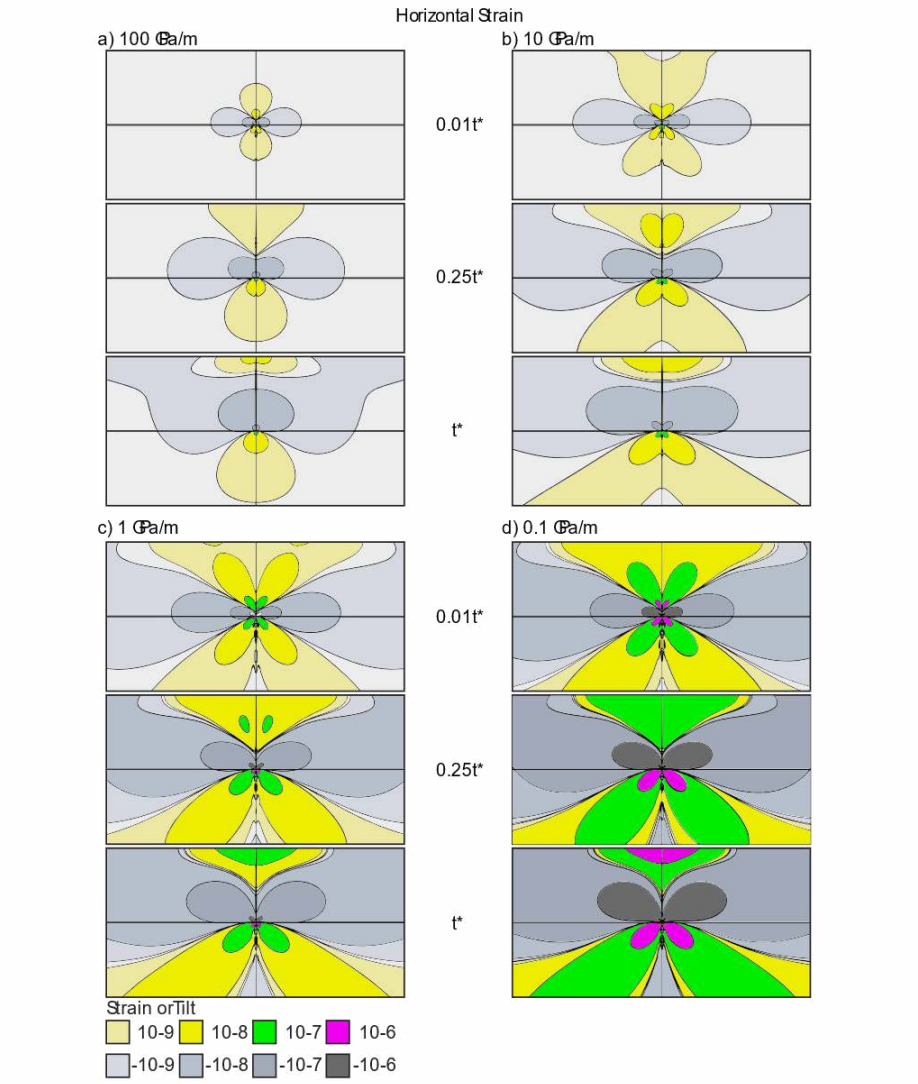

Figure 8-6. Vertical cross-section of transient horizontal strain field produced by pressurization and fluid flow along a vertical planar conduit intersecting a free surface. Results are shown for layer stiffness of a) 100 GPa/m, b) 10 GPa/m, c) 1 GPa/m and d) 0.1 GPa/m at three times relative to the characteristic time (t^*) required for the pressure distribution in the conduit to reach a linear, steady-state distribution

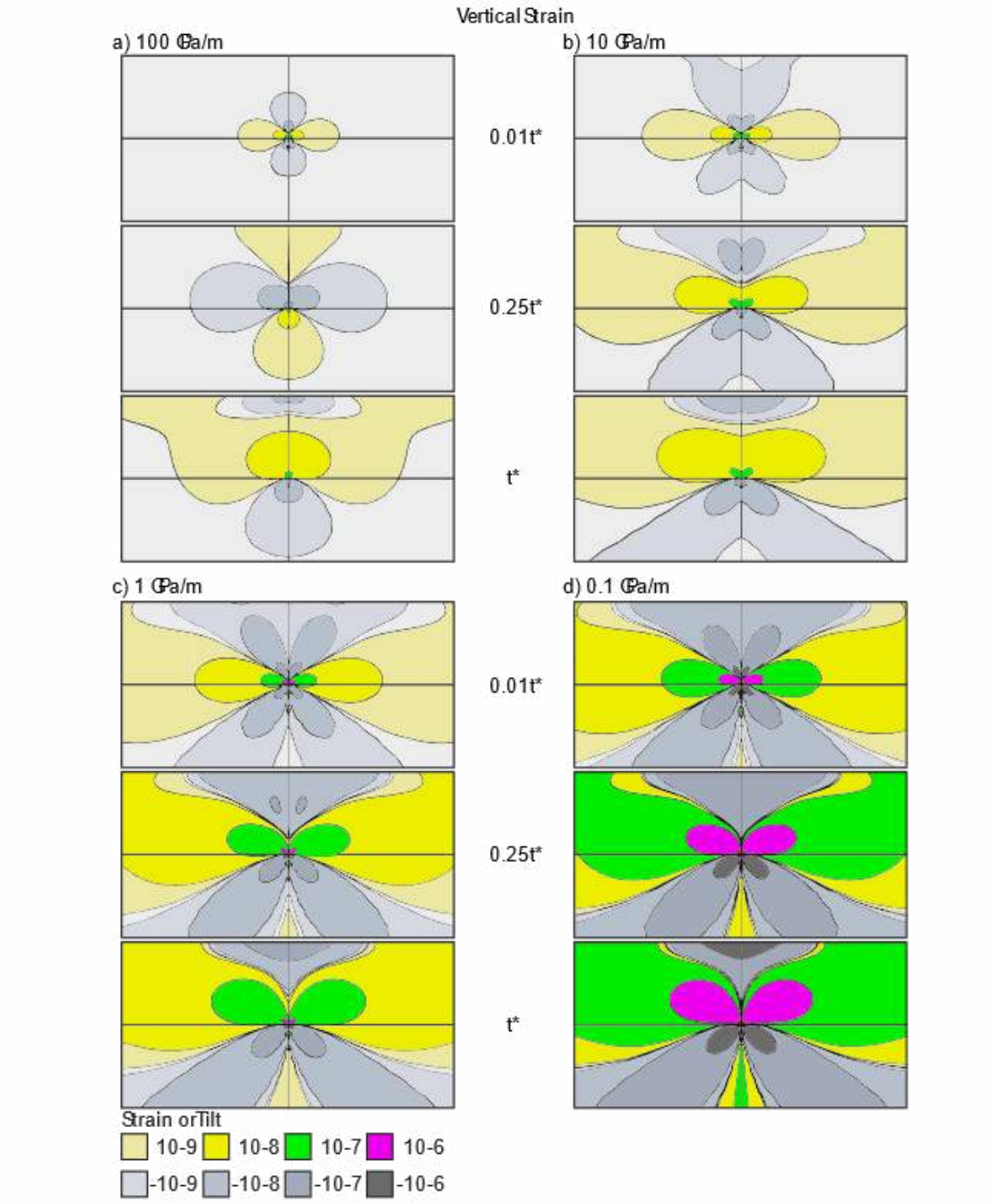

Figure 8-7. Vertical cross-section of transient vertical strain field produced by pressurization and fluid flow along a vertical plane intersecting a free surface. Results are shown for layer stiffness of a) 100 GPa/m, b) 10 GPa/m, c) 1 GPa/m and d) 0.1 GPa/m at three times relative to the characteristic time (t^*) required for the pressure distribution in the conduit to reach a linear, steady-state distribution.

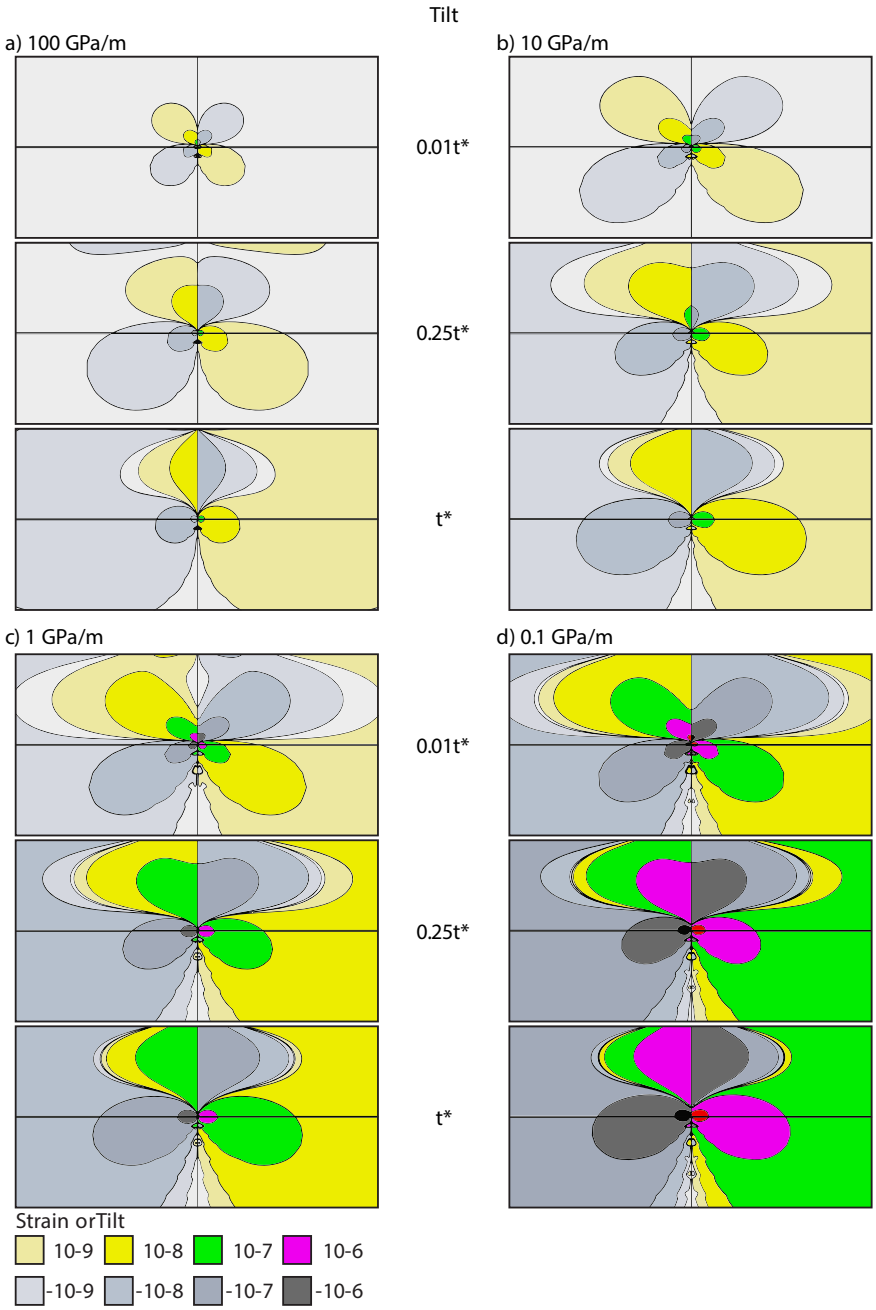

Figure 8-8. Vertical cross-section of transient tilt field ($\partial u/\partial z$) produced by pressurization and fluid flow along a vertical planar conduit intersecting a free surface. Results are shown for layer stiffness of a) 100 GPa/m, b) 10 GPa/m, c) 1 GPa/m and d) 0.1 GPa/m at three times relative to the characteristic time (t^*) required for the pressure distribution in the conduit to reach a linear, steady-state distribution.

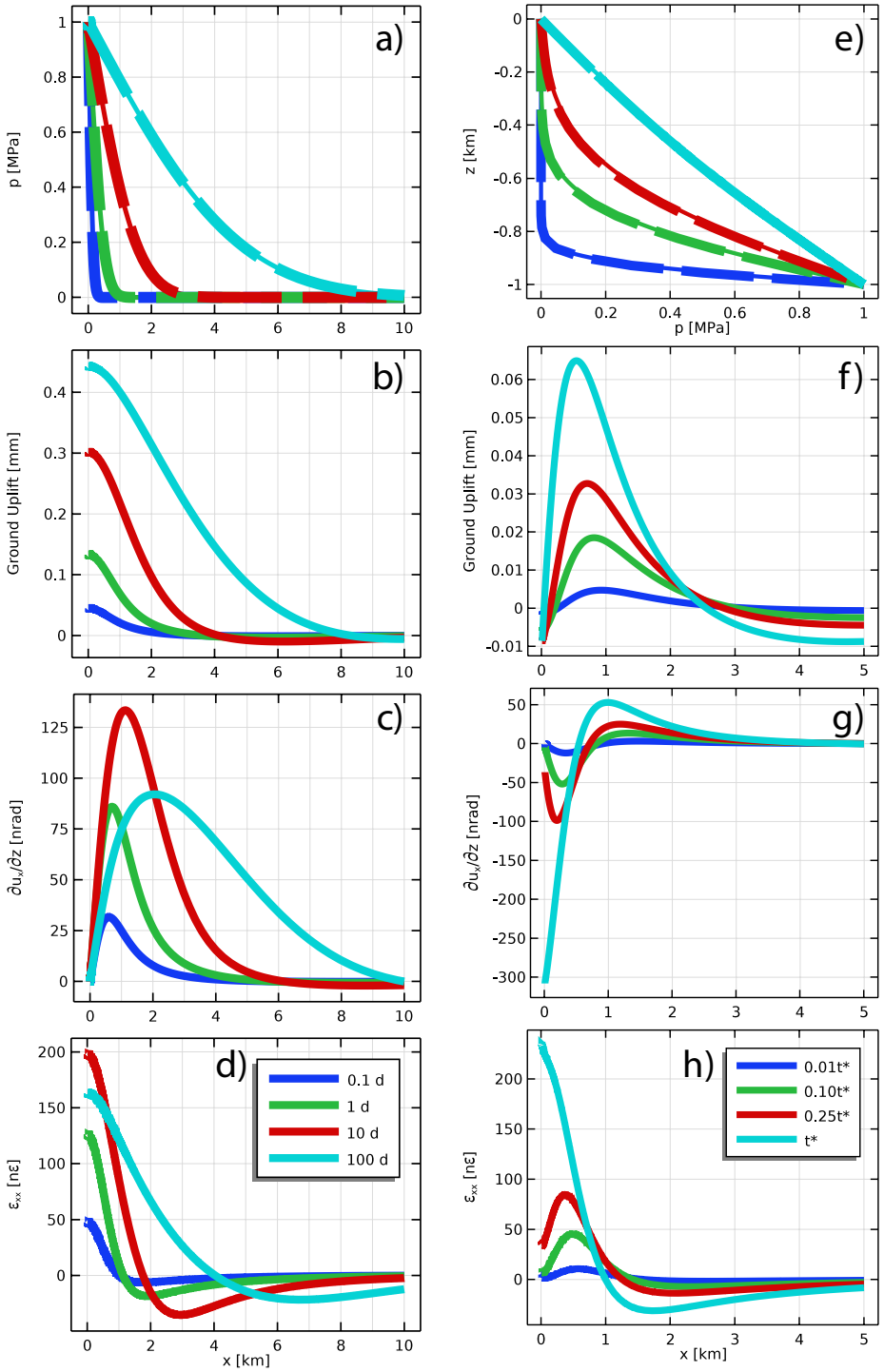

Figure 8-9. Profiles of pressure in a horizontal layer (a) and vertical conduit (b) at different times. Deformation along shallow (10-m-deep) transects created at different times by pressurization of a horizontal layer (left column, b-d) and a vertical planar conduit (right column, f-h).

8.3.3 Horizontal Transects

Deformation along shallow horizontal transects were evaluated to estimate signals that could potentially be measured with sensors at the ground surface, or in the shallow subsurface (Figure 8-9). Various components of deformation were simulated at a depth of 10 m using parameters in Table 1.

8.3.3.1 Vertical Displacement

Pressurization of a horizontal layer (Case 1) results in upward vertical displacement (uplift) at the ground surface, with the maximum occurring above the point of injection and a lateral extent greater than the pressure in the reservoir (x_p), especially at early times (Figure 8-9d). This would create a ridge above a horizontal injection well, or a dome above a vertical well. The uplift produced by the vertical planar conduit (Case 2), however, is characterized by two peaks creating a trough centered on the conduit and minor subsidence occurring at distances beyond 2.5 km ($x^* = 2.5$) (Figure 8-9f). The lateral distance to the peaks decreases with time and they migrate towards the conduit. The peaks are associated with the inclined bands of high normal strain (Figure 8-9).

The magnitude of uplift decreases with the stiffness of the vertical planar conduit. Increasing the stiffness from 0.1 to 1 GPa/m ($E = 10$ GPa/$b = 10$m) reduces the maximum vertical displacement by roughly an order of magnitude from 0.6 to 0.07 mm (Figure 8-10). Further increases in conduit stiffness will further reduce the displacement, but the relative effect is diminished. However, the conduit stiffness also affects the displacement pattern by reducing the depth of the trough between the peaks. The depth of the trough diminishes with conduit stiffness, and the trough is absent over the stiffest conduit (100 GPa/m).

8.3.3.2 Tilt

Tilt reflects the horizontal gradient in the vertical displacement, so the tilt is zero above the well in Case 1 and is always positive (away from the well) at greater distances (Figure 8-9b). This reflects the single ridge or dome uplift pattern centered above the well (Figure 8-9c). The distance to the maximum tilt increases with time and occurs at distances of approximately 0.5, 1, 1.5 and 2 km after 0.1, 1, 10 and 100 days of injection, respectively. The maximum value of the tilt increases for the first 10 days of injection to roughly 125 nrad, and decreases to less than 100 nanoradians after 100 days.

In comparison, the tilts above a vertical planar conduit (Case 2) are towards the conduit at distances less than 800 m and oriented away from the conduit beyond. As the pressure migrates to shallower depths, the tilts increase on either side of this crossover point reaching maxima of -300 and 50 nanoradians (Figure 8-9g).

8.3.3.3 Horizontal Strain

Horizontal strain along a shallow transect could be measured using optical fibers deployed at shallow depths in trenches. The signal that could potentially be measured with this type of sensor during injection into a horizontal layer (Case 1) shows that the lateral extent of the horizontal strain along a shallow transect is greater than the extent of the pressure in the layer for the first 10 days of injection (Figure 8-9d). Tensile horizontal strains (ε_{xx}) occur above the pressurized zone. They decrease and go to zero with distance and the horizontal strain is compressive in the far field. The strain crossover point advances ahead of the pressure front in

the horizontal layer, occurring at approximately $x_p + d$, for the first 10 days (Figure 8-9d). However, the strain crossover slows and lags behind the pressure at later times. The extent of pressure is at x_p = 8 km, while the crossover is at approximately 4 km after 100 days of injection in the example in Figure 6. The greatest horizontal strains occur above the well and reach a maximum of 200 nε after 10 days of injection, but then they decrease and are 160 nε after 100 days (Figure 8-9d).

The horizontal strain caused by a vertical planar conduit (Case 2) along a shallow transect (Figure 8-9h) is also tensile near the conduit and compressive at distances greater than 1 km (x = x^*), so in this respect it generally resembles the strain profile from a horizontal conduit (Figure 6d and h). However, the maximum tensile strain is offset from the conduit and it moves toward the conduit with time. The maximum horizontal strain in the shallow profile is associated with the inclined bands of high normal strain (Figure 8-6). Moreover, the maximum horizontal strain above the conduit continuously increases with time, whereas it decreases for t^*>10 above the horizontal layer (Figure 8-9).

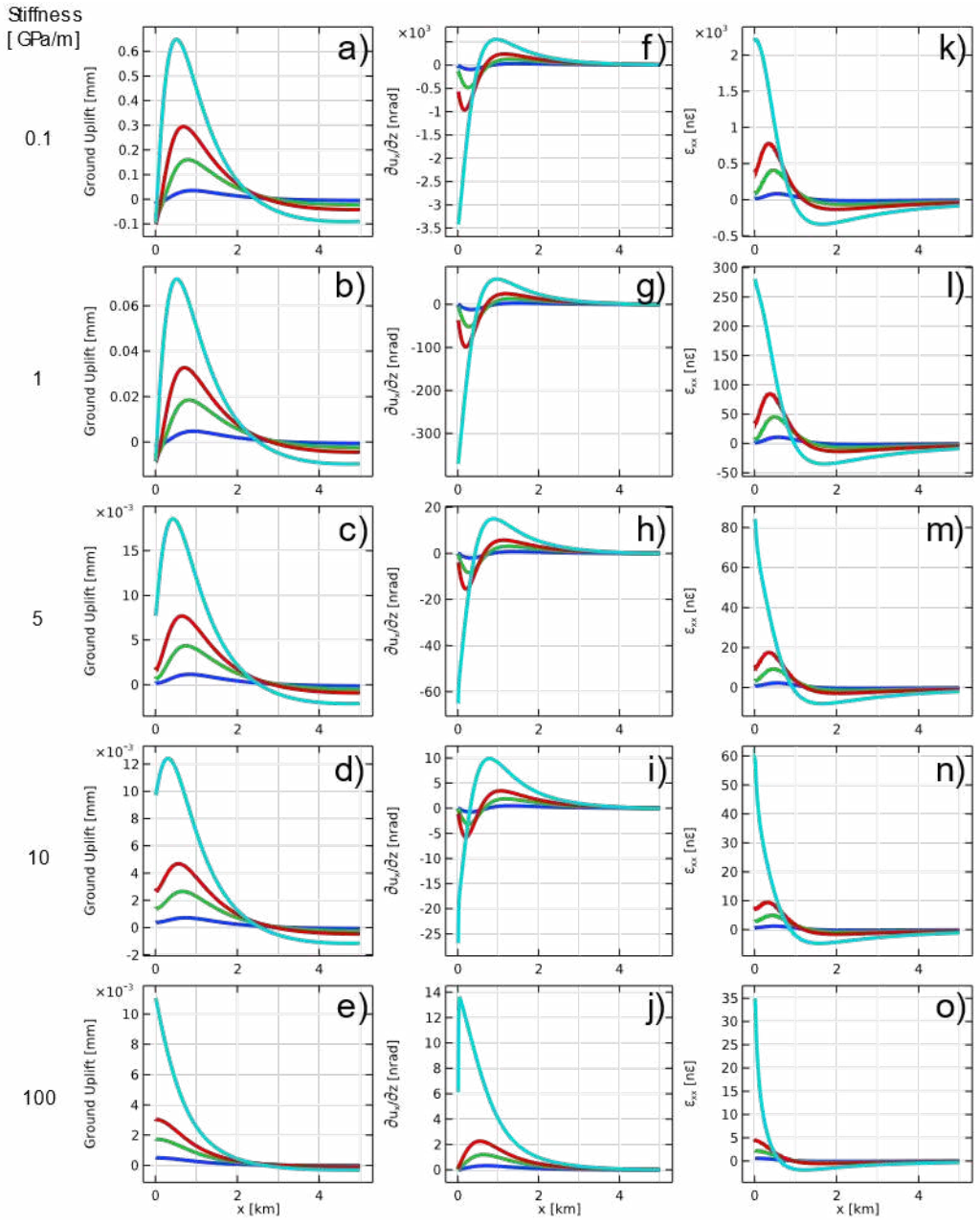

Figure 8-10. Horizontal profiles in deformation from pressurization of vertical planar conduit for stiffnesses ranging from 0.1-100 GPa/m

8.3.3.4 Effects of Conduit Stiffness

The results given above use a baseline conduit stiffness of 1 GPa/m, but deformation is sensitive to changes in stiffness. The double-ridge uplift pattern (Figure 8-10a-d) occurs above conduits with stiffnesses ranging from 0.1 to 10 GPa/m, but the height of the ridge and the depth of the trough decrease with stiffness, and the there is only one peak in this example when the stiffness is 100 GPa/m (Figure 8-10e). Negative vertical displacement (subsidence) occurs in the trough when the conduit is soft (stiffness of 0.1 and 1 GPa/m), but positive displacement (uplift) occurs above the conduit when the stiffness is 10 GPa/m or more.

The maximum magnitudes of vertical displacement are inversely proportional to the conduit stiffnesses and range from 0.6 mm to 0.01 mm of uplift for stiffnesses of 0.1 and 100 GPa/m, and -0.1 to -0.01 mm of subsidence for stiffnesses of 0.1 and 10 GPa/m, with negligible subsidence observed at 100 GPa/m. The distance to the crossover point from uplift to subsidence is not sensitive to the conduit stiffness and occurs at approximately 2.5 km from the conduit ($x^* = 2.5$).

In this idealized example, the slope of the ground surface, which is the horizontal gradient of the vertical displacement ($\partial w/\partial x$) is equal to the tilts, so the patterns in the uplift are reflected in the tilt, with tilting toward the leak at distances less than 1 km ($x = x^*$) where the double-ridge pattern is present (Ka < 100 GPa/m and p = 1 MPa) and away from the leak beyond (Figure 8-10f-j). The magnitude of the tilt is also inversely proportional to the stiffness and ranges from -2.3 μrad (towards the leak) to 14 nrad (away from the leak) for a stiffnesses of 0.1 and 100 GPa/m, respectively.

The pattern of the horizontal strain in profile at a depth of 10 m is also sensitive to the conduit stiffness, with maximum tensile strains occurring at distance from the conduit at early times during pressurization for stiffnesses less than 10 GPa/m, which corresponds to the presence of the double-ridge uplift pattern (Figure 8-10k-o). Like the uplift and tilt, the magnitude of the horizontal strain is also inversely proportional to the conduit stiffness and range from maximums of 2 με to 35 nε for stiffnesses of 0.1 and 100 GPa/m, respectively.

8.3.4 Vertical Profiles

Vertical transects, or profiles of vertical strain were analyzed to estimate signals that could be observed using distributed strain sensors in vertical boreholes, such as those described in (Murdoch et al., 2020). Vertical profiles of the vertical strain were analyzed from the ground surface to a depth of 900 m ($z^* = 0.9$) at lateral distances from the well or conduit of 50, 500 and 1,000 m ($x^* = 0.05$, 0.5, and 1). A depth of 900 m was chosen to evaluate signals that could be observed without compromising the caprock seal.

The vertical strain is compressive along profiles in the overburden overlying the pressurized region of a horizontal layer (Case 1) and tensile at greater distances ahead of the pressure front (Figure 8-11). At the closest location (x = 50 m), the vertical strain is compressive at all the times shown, and reaches a maximum of -750 nε during the first day of injection at a depth of 900 m, before decreasing to approximately -250 nε and becoming roughly uniform with depth between 10 and 100 days (Figure 8-11).

Further out, at a distance of 500 m, the profile of the vertical strain evolves in an interesting pattern. After the first two hours of injection (t = 0.1 d), the least vertical strain (greatest compressive strain) ($\varepsilon_{zz} \approx$ -25 nε) occurs at the ground surface and increases downward to a crossover point at a depth of approximately 600 m (Figure 8b). It continues to increase with depth and reaches a maximum of 100 nε at 900 m depth. The strain decreases with time, so the crossover point moves downward, and it is at 800 m depth at t = 1 day and it is absent after that because the strain is negative everywhere along the profile. A similar effect occurs at x = 1 km, where the crossover point moves downward from 200m to 400m during the first day, and is absent by day 10 in Case 1 (Figure 8-11c).

Locally, vertical strain along a profile near a vertical planar conduit (Case 2) is similar in sign and magnitude to the vertical strain caused by a horizontal layer (Case 1), but there are some important differences. For example, the vertical strains at x = 50m and above 0.6 km depth are in the range of -100 nε for both cases. However, the vertical strain in Case 2 becomes sharply positive below 0.6km at x=50m, but it is always negative above the horizontal layer in Case 2 (Figure 8-11).

Perhaps the clearest distinguishing features are the sign of the change in vertical strain and the direction of migration of the strain crossover. The vertical conduit creates positive strain at depth that migrates upward and this causes the crossover point to move upward in all three profiles (Figure 8-11). This occurs as the pressure in the conduit propagates upward. In contrast, pressure in the horizontal layer moves outward horizontally and this causes the vertical strain to become more compressive and decrease with time. The strain crossover over the horizontal layer moves downward, whereas it moved upward along vertical transects in the vicinity of a vertical planar conduit. The vertical migration of the crossover point is a clear indicator of vertical flow.

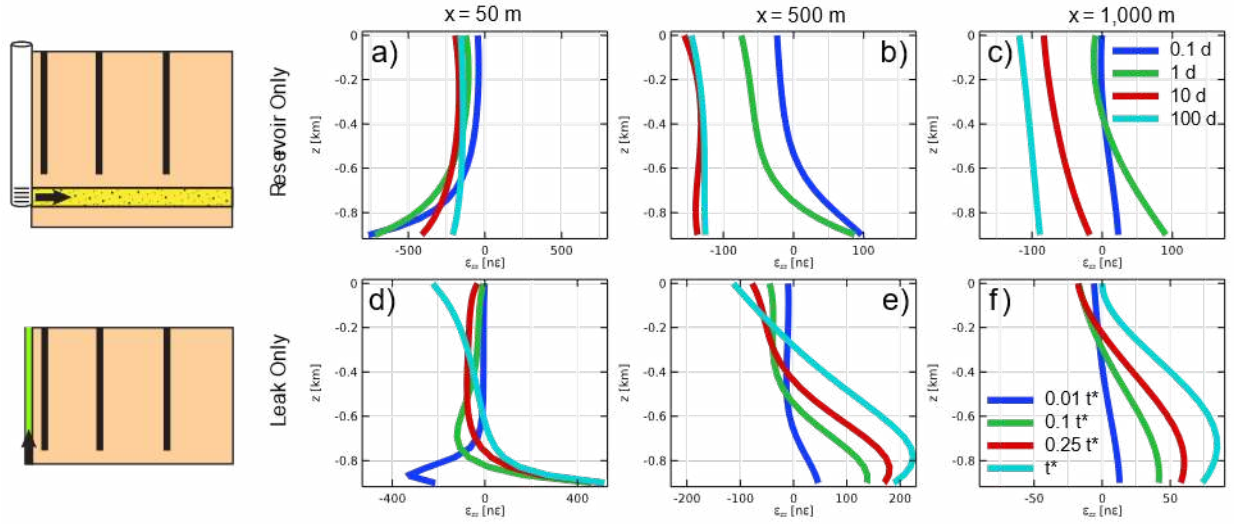

Figure 8-11. Vertical profiles in the vertical strain with distance from pressurization of a horizontal layer (top row) and a vertical planar conduit (bottom row).

8.3.5 Deformation at Points

Time series at selected locations were analyzed to predict the normal strains and the tilt that could be expected from finstruments in a field setting (Figure 8-13). . Five locations were selected at lateral distances of 50, 250, 500, 1,000 and 1,500 m (x^* = 0.05, 0.25, 0.5, 1.0 and 1.5) from the applied pressure and all are at a depth of 10 m (z^* = 0.01). These locations were selected to evaluate the feasibility of detecting and characterizing strain caused by leaks using instruments deployed at shallow depths.

Pressurizing a horizontal layer (Case 1) causes tensile horizontal strain at proximal locations (x^*<1), and compressive strain at the most distant location of 1.5 km (x^* = 1.5; Figure 8-13). After one day of injection, for example, the horizontal strain is greatest (ε_{xx} = 125 nε at x = 50m, it progressively decreases with distance, and is approximately ε_{xx} = -15 nε at the most

distant location (x = 1500m). m. The strain continues to increase at x = 50m, reaching a maximum of 200 nε after 10d, and it decreases after that. The times series at the next adjacent location, x = 100m, follows a similar pattern but it is lagged in time and smaller in magnitude than the strain at x = 50m. The lag increases, and the magnitude progressively decreases with distance from the well in the horizontal layer (Case 1, Figure 8-13). The sign of the strain reverses at x = 1500m at t=5d as the crossover point reaches that location. (Figure 8-13a). .

The horizontal strain caused by a vertical conduit also increases with time in the vicinity of the conduit and decreases at the most distant point, but details of the signal are distinct from the signal caused by the horizontal layer (Figure 8-13a and c). The strain caused by the vertical conduit initially increases fastest at the x = 500 m location, instead of near the well in the horizontal layer. The strain rate at x = 250 m increases with time and this causes the strain magnitude to overtake the magnitude at x = 500m at t* =0.3, and a similar effect occurs at x = 50m (e.g Figures 8-13d and e). In contrast, the strain rate during Case 1 decreases with time and distance, with the except of the x =1000m location (Figure 8-13b). These effects are the manifestations of the different responses of the strain tensor field outlined inFigures 8-5 thru 8-8.

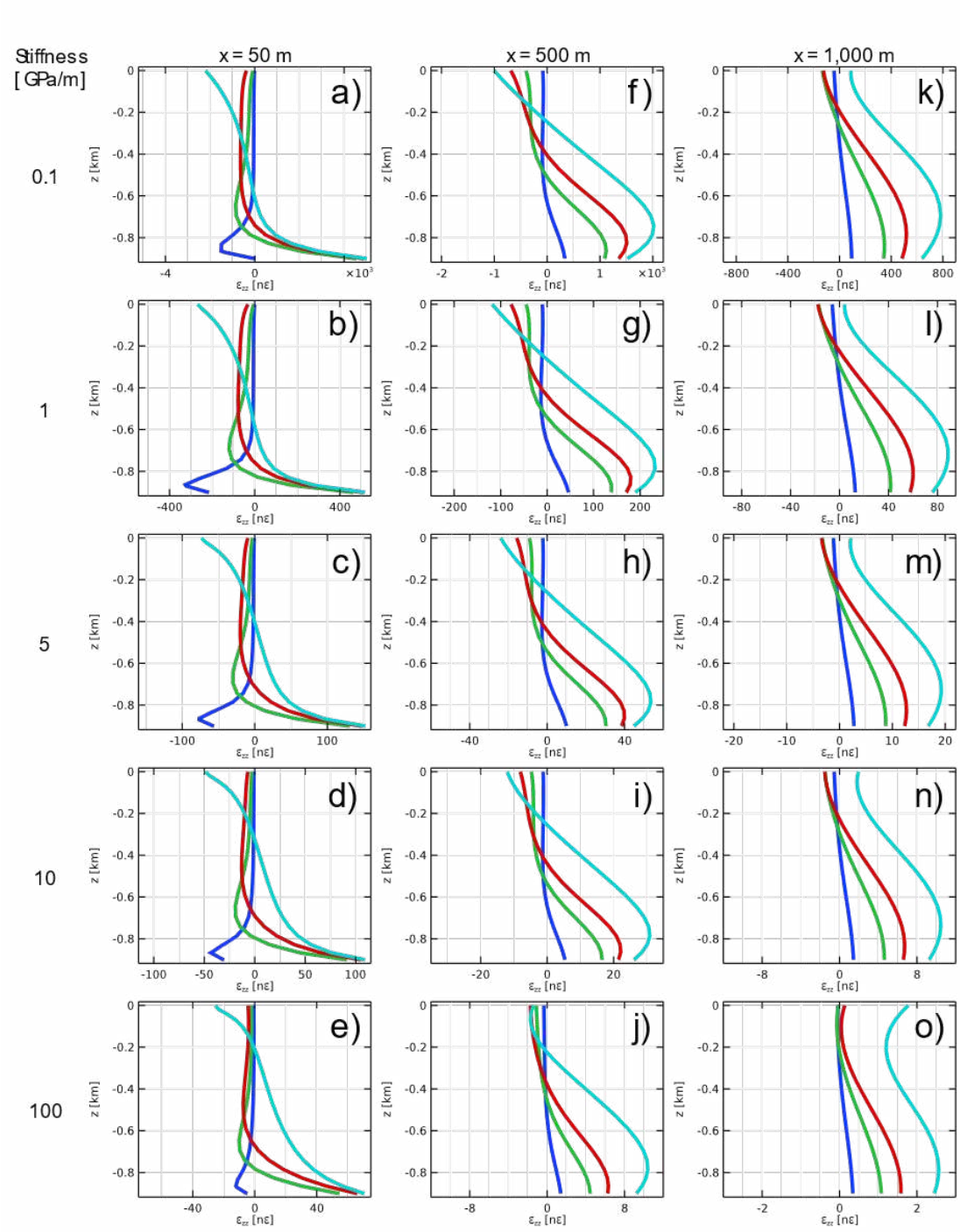

Figure 8-12. Vertical profiles of axial strain observed for various conduit stiffness at distances of 50 m (left column), 500 m (middle column), and 1,000 m (right column) from the conduit

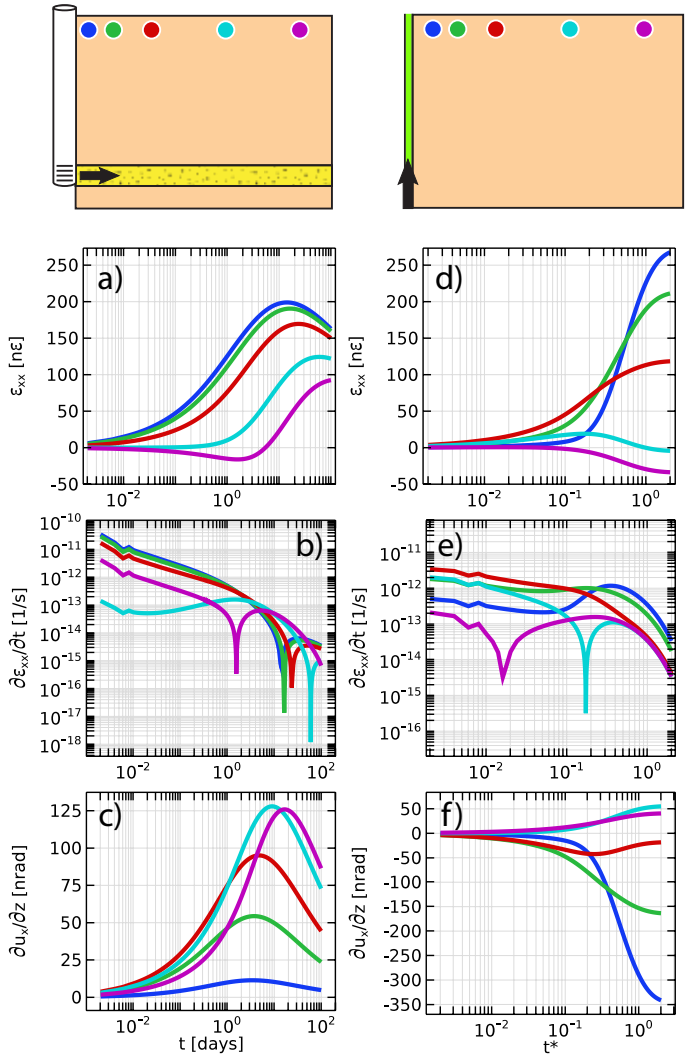

Figure 8-13. Time series of the horizontal strain, strain rate and tilt for injection into a horizontal layer, Case 1 (a-c) and from a vertical planar conduit, Case 2 (d-f).

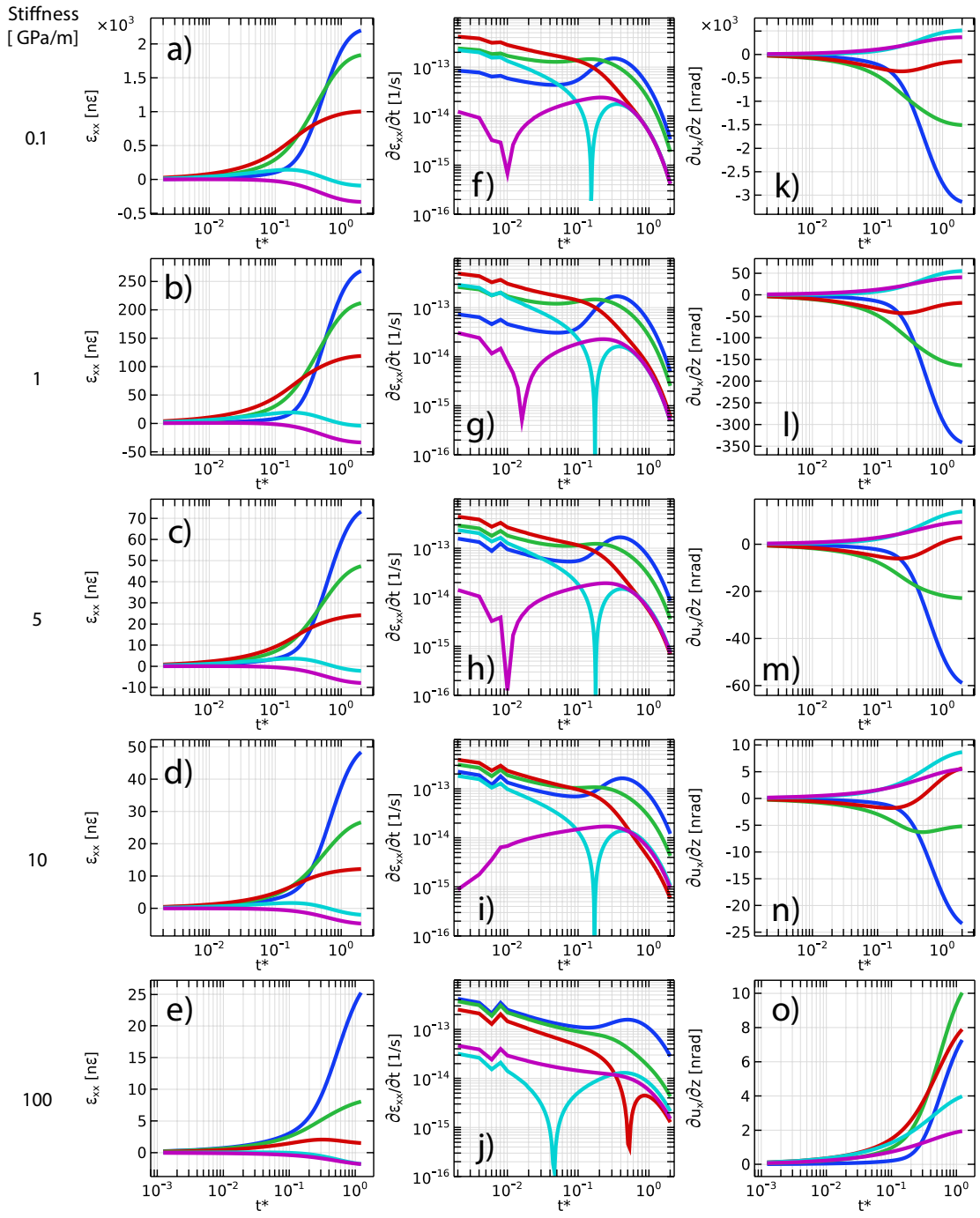

Figure 8-14. Timeseries of the horizontal strain (left column), strain rate (center column) and tilt (right column) for various conduit stiffnesses

8.4 DEFORMATION CAUSED BY A LEAKY RESERVOIR

The components evaluated in Cases 1 and 2 were combined to create a composite geometry intended to represent injection into a reservoir with a vertical leak to the ground surface at an offset lateral distance. Constant pressure boundaries were used at both the point of injection and the point of leakage at the ground surface. This approach was used to evaluate if the patterns and signals identified for the components were valid for the more realistic composite geometry of a leaky reservoir. The layer thickness and stiffnesses used for both the reservoir and leak in this example were kept the same as the previous cases, but the leak transmissivity was evaluated for a range of values to determine the effect of leak strength. For this scenario, the leak strength is expressed as the ratio of the leak transmissivity (T_L) to that of the reservoir (T_{Res}), and is given by

$$T^* = \frac{T_L}{T_{Res}} \tag{8-5}$$

We evaluated the effect of leak strength for values of T^* = 0.001, 0.01. 0.1, 1, and 10 and found that there were two end-member leakage scenarios based on the deformation response, which we will refer to as Type I and Type II leaks.

Type I leaks have a leakage flux that is low relative to that in the reservoir and therefore the leak has relatively little effect on the reservoir pressure (Figure 8-15a). Type II leaks, on the other hand, have a leakage flux that is high relative to that in the reservoir, which causes the reservoir pressure to be significantly lower than expected (Figure 8-15c). For Type I leaks, vertical migration of the pressure through the caprock is slow relative to the pressure propagation in the reservoir, which allows a nonlinear vertical pressure gradient through the caprock to develop after the pressure front in the reservoir has advanced past the leak (Figure 8-15b), while the pressure in a Type II leaks equilibrates quickly with reservoir pressures and maintains a roughly uniform pressure gradient between the reservoir and point of leakage (Figure 8-15d).

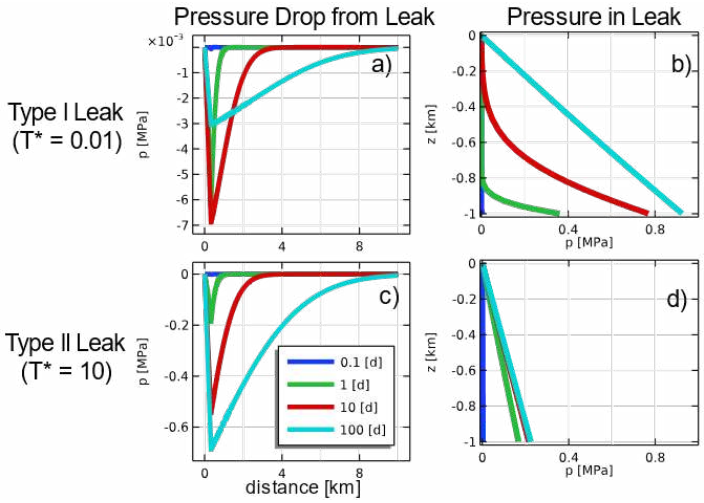

Figure 8-15. Pressure drop in reservoir caused by leak and pressure in leak for Type I (a-b) and Type II leaks (c-d).

8.4.1 Patterns

The pressure and deformation responses for Type I and Type II leaky reservoirs were evaluated for the combined effects of injection and leakage, as well as the individual effect of leakage alone. The pressure and deformation response from leakage was isolated by taking the residual between the leaking and nonleaking simulation results. Type I leak behavior was

observed for leak strengths of $T^* \leq 0.1$, and Type II leak behavior was observed for leak strengths of $T^* \geq 1$.

Since the drop in reservoir pressure observed for Type I leaks is small, the reservoir pressure remains symmetric about the well and the deformation due to leakage is mainly from an increase in pressure along the leak in the overburden. For the injection pressure and leak stiffness used in this example, the deformation caused by the leak is small compared to that from the reservoir pressurization and has little effect on the deformation pattern (Figure 8-16a-c). Removing the effect of reservoir pressurization reveals the deformation pattern observed for a Type I leak (Figure 8-16d-f), which resembles that of Case 02 described above, where a tensile wedge of horizontal strain and compressive vertical strain migrates vertically towards the surface.

For Type II leaks, the leakage flux is high and results in both a decrease in reservoir pressure and an increase in overburden pressure. These combined effects cause both the reservoir pressure distribution and overburden deformation patterns to be asymmetric about the well, with compressive horizontal strains observed downstream from the leak (Figure 8-16g-i). The deformation observed for Type II leaks is characterized by tensile vertical strains and compressive horizontal strains near the leak and in the downstream direction (Figure 8-16j-l) – a pattern that resembles that caused by a pumping well.

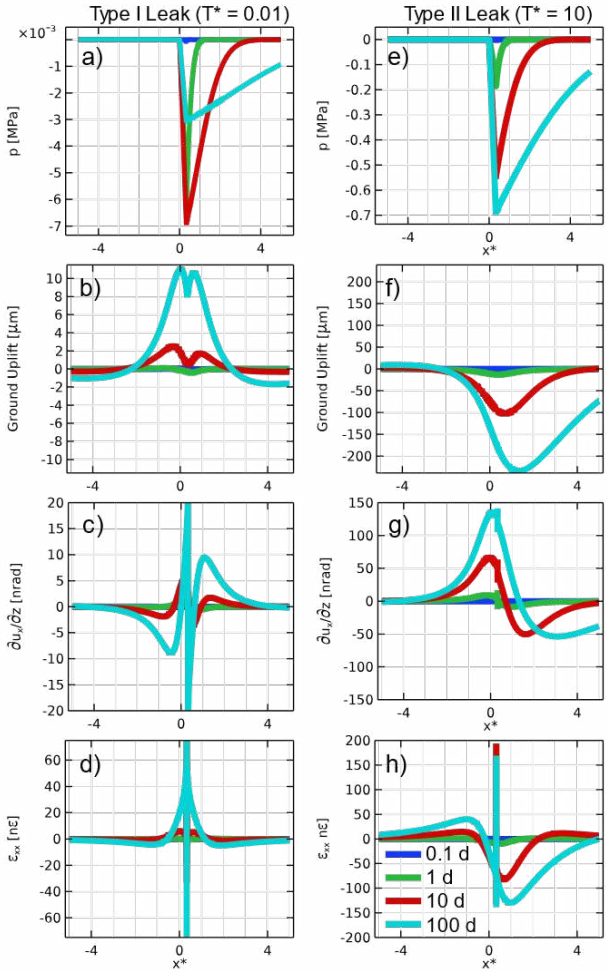

Figure 8-16. Horizontal profiles of pressure and deformation produced by leakage for Type I (left column) and Type II (right column) leaks. Data shown above consists of reservoir pressure (a&e), subsidence/uplift (b&f), tilt along the ground surface (c&g), and horizontal strain at a depth of 10 m ($z^* = 0.01$).

8.4.2 Horizontal Transects

Horizontal transects of the deformation from leakage were evaluated in comparison to those from Section 01 to identify patterns that could guide the development of leak detection strategies. As in Section 01, the transects evaluated included the vertical ground displacement (uplift/subsidence), tilt, and the horizontal strain at a depth of $z^* = 0.01$.

For Type I leaks, the horizontal transects of deformation closely resembled those for pressurization of a vertical conduit as described for Case 02. The vertical ground displacement

for the Type I leak after 100 days of uplift was characterized by 10 μm of uplift in the characteristic double-ridge pattern from pressurization of a vertical planar conduit (Figure 8-17b). This uplift pattern caused the tilts to be oriented towards the well inside the trough created by the leak, and away from the well at greater distances with maximum tilts of approximately 10 nrad after 100 days of injection (Figure 8-17c). The horizontal strains appear similar in profile to those from uplift for the first 10 days of leakage, with a double-lobe pattern symmetric about the leak and maximum strains occurring roughly 500 m from the leak. At later times when the pressure distribution in the leak is linear between the surface and the reservoir, the horizontal strain is tensile and greatest near the leak (Figure 8-17d).

For the Type II leak evaluated (T* = 10), the drop in reservoir pressure (Figure 8-17e) caused 100 μm of subsidence near the leak after 10 days, and 200 μm approximately 1 km downstream from the leak after 100 days (Figure 8-17f). This trough of subsidence migrating downstream from the well is reflected in the tilt (Figure 8-17g), and forms a roughly 4 km wide region of compressive horizontal strain of up to 150 nε after 100 days (Figure 8-17h). The leak also causes tensile horizontal strains of up to 50 nε approximately 1 km upstream from the leak after 100 days.

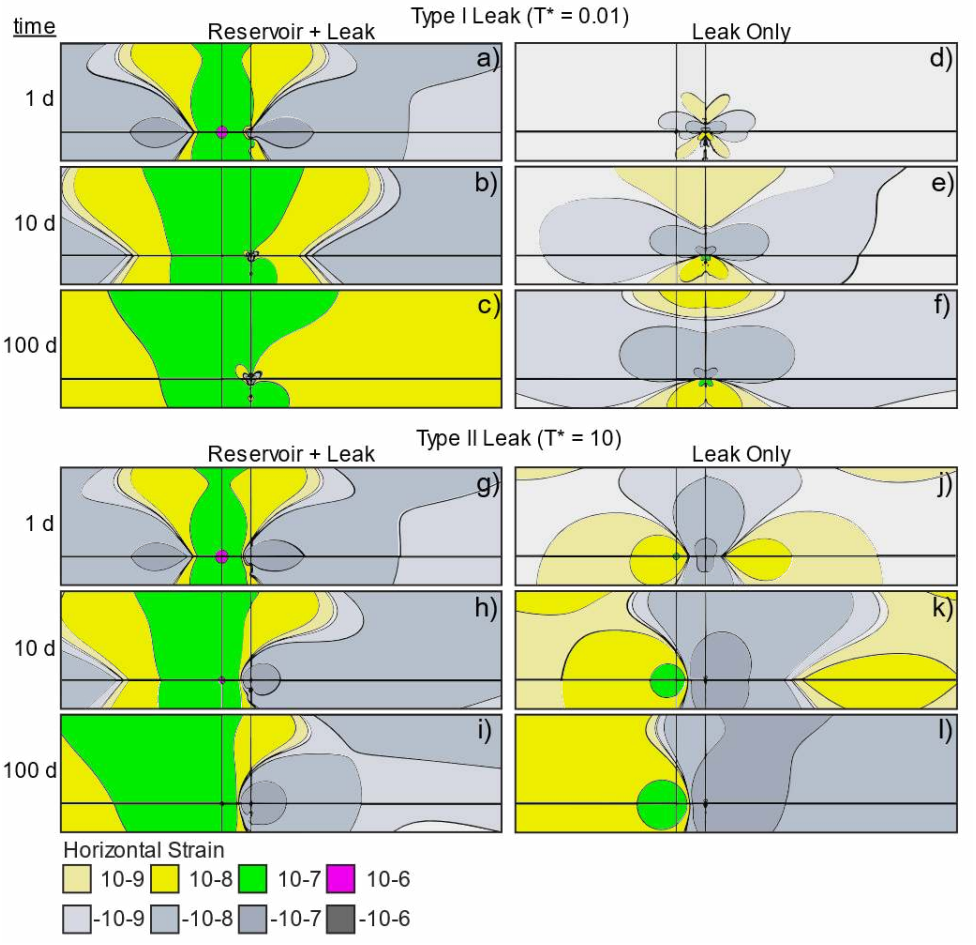

Figure 8-17. Horizontal strain from injection into leaky reservoir for a Type I (a-f) and a Type II leak (g-l). The deformation produced by injection and leakage is shown in the left column, while the deformation for the leak is shown in the right column.

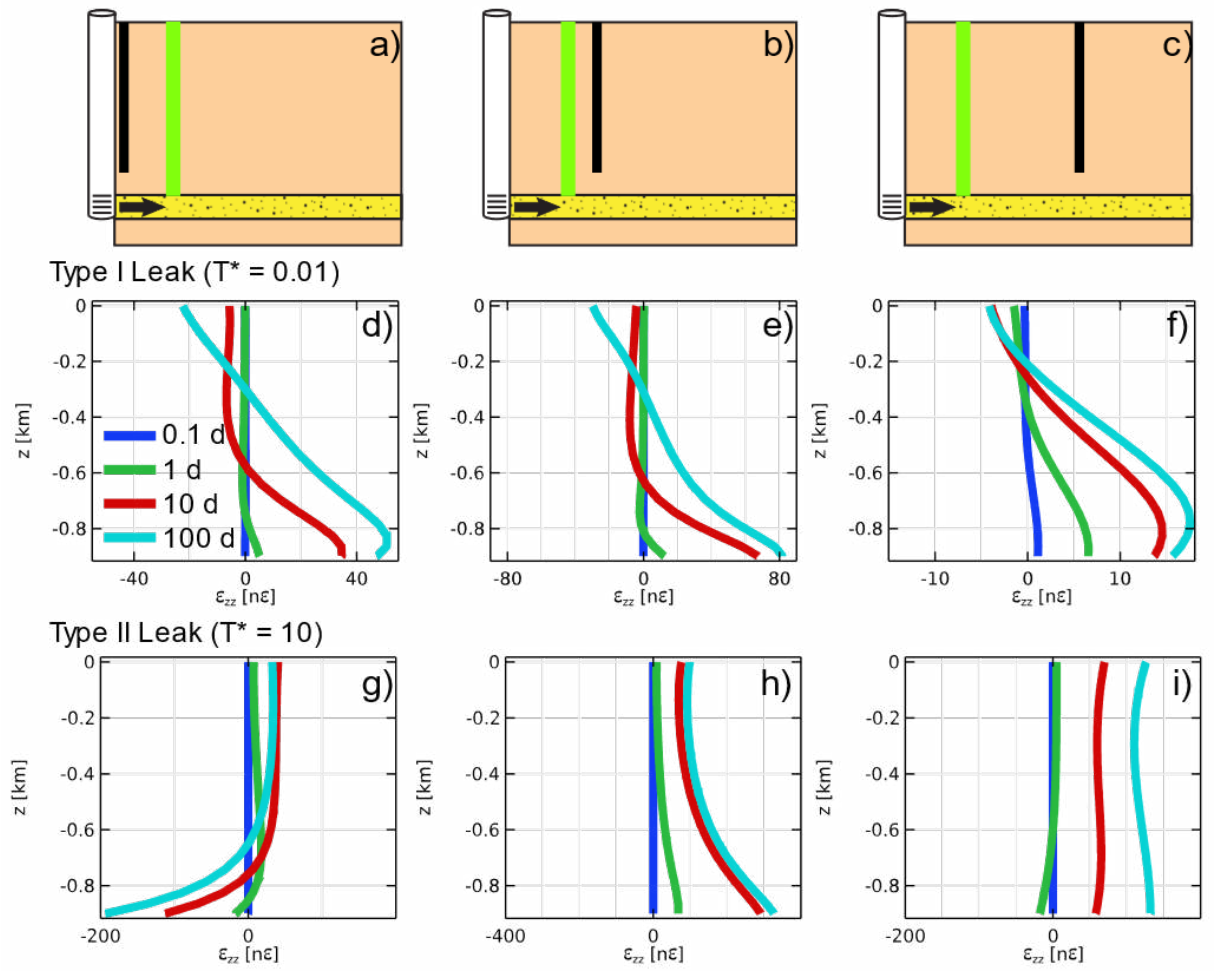

Figure 8-18. Vertical strain with time produced by leakage. The measurement locations are shown in the conceptual models (a-c) for Type I (d-f) and Type II leaks (g-i).

8.4.3 Vertical Profiles

Vertical profiles of vertical strain from Type I and Type II leaks were evaluated from the ground surface to a depth of 900 m at distances of 50, 500, and 1,000 m from the well for 100 days of injection (Figure 8-18). For Type I leaks, the vertical strain at all distances follows a pattern of being compressive near the surface and tensile at depth. This creates a crossover point in the vertical strain that is deepest near the leak and becomes progressively shallower with distance. At each location, the crossover point migrates vertically towards the surface with time as the pressure wave travels through the caprock (Figure 8-18d-f). The total distance traveled by the crossover point decreases with distance from the leak.

For Type II leaks, the vertical strain exhibits a different pattern at each location. At the closest location (x = 50 m), the vertical strain becomes increasingly compressive at depth and increasingly tensile near the surface with time, creating a crossover point that migrates vertically (Figure 8-18g). Further out at 500 m, the vertical strain is tensile at all depths and no crossover point is observed. The strain is roughly uniform to a depth of approximately 400 m, and then becomes increasingly tensile with depth (Figure 8-18h). At the furthest location (x = 1,000 m), the vertical strain is tensile at all depths and is mostly uniform with depth at all times (Figure 8-18i).

8.4.4 Deformation at Points

The time series of the horizontal strain was evaluated at distances of 50, 250, 500, 1,000 and 1,500 m from the injection well for both Type I and Type II leaks (Figure 8-19). For Type I leaks, the horizontal strain from injection was relatively unaffected by the leak, due to the low leakage flux (Figure 8-19a). Removing the effect of the reservoir revealed that the horizontal strain was tensile at all times for locations less than 1 km from the well, but was compressive at greater distances. The strain increased with distance from the well to a distance of 250 m, before decreasing and becoming compressive between 1 and 1.5 km (Figure 8-19b).

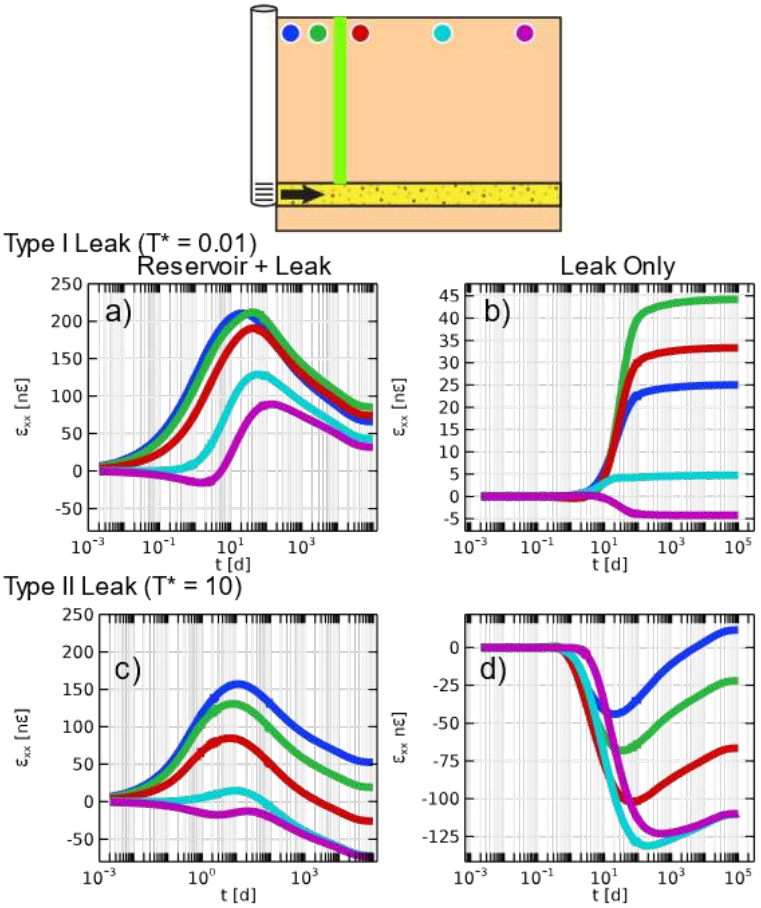

Figure 8-19. Time series of horizontal strain at 10 m depth produced by leakage for Type I (a-b) and Type II leaks (c-d). Measurements are shown for distances of 50 (blue), 100, 500 (green), 1000 (red), and 1500 m (cyan) from the injection well.

The time series of horizontal strain during injection into a Type II leaky reservoir was noticeably different than the baseline, with a decrease in the total strain observed at each location, and compressive rather than tensile strains at locations beyond 500 m from the well (Figure 8-19c). The deformation time series produced by the leak was characterized by compressive strains with magnitudes that were greater with distance from the well (Figure 8-19d).

8.5 A Hypothetical FieLd Case at the Avant Field

We have been monitoring reservoir pressure and shallow deformation signals during oil field operations in the North Avant Field in Osage County, Oklahoma for over five years. A series of water injection tests were performed to serve as an analog to CO2 storage. The deformation signals from these tests were inverted to calibrate a poroelastic site model and obtain estimates of the material properties and reservoir geometry using a type-curve approach similar to that used in conventional well test analyses (Murdoch et al., 2021). Results from these analyses were corroborated with core samples and geophysical well logs.

The North Avant Field is underlain by the Bartlesville sandstone reservoir at a depth of approximately 530 m and is ~30 m thick. A high permeability sandstone lens with a thickness of 5 m is located at the base of the Bartlesville. Brines produced from nearby oil recovery wells are injected into Well 9A, which is completed in the high permeability lens. The Bartlesville Formation is overlain by a confining layer of interbedded shales and limestones that extends to the surface. There are no above-zone aquifers or sources of drinking water in the vicinity of North Avant Field.

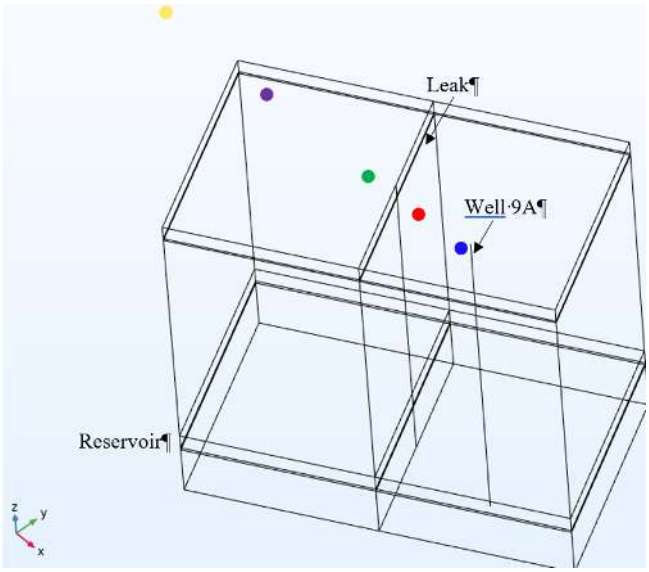

Figure 8-20. Geometry and monitoring array for North Avant Field poroelastic model.

A hypothetical leak was introduced to the calibrated poroelastic site model to predict the deformation response from a leak. The leak is represented by a vertical planar conduit from the high permeability lens to the ground surface (Figure 8-20) using the same equivalent porous medium approach, discretization methods and boundary conditions as the previous cases. This conceptual model was used to maintain consistency with the idealized scenarios in the previous sections and to determine if the patterns and signals of deformation from the 2D cases were observed for a more realistic 3D case. Similar methods for representing a leak have been used elsewhere. Deformation of the leaky reservoir was evaluated for 100 days of injection at a constant pressure

of 1 MPa in Well 9A. The deformation was analyzed for both Type I (T* = 0.01) and Type II leaks (T* = 1). Properties used in the model are in Table 2.

Table 8-2. Properties of leaks simulated in the North Avant Field

Property	Type I Leak (T* = 0.01)	Type II Leak (T* = 1)
Layer Thickness [m]	1	1
Young's Modulus [GPa]	10	10
Stiffness [GPa/m]	10	10
Hydraulic Diffusivity [m^2/s]	0.06	5.8
Characteristic Time [d]	13.4	0.13

8.5.1 Vertical Profiles

Vertical profiles of the fluid pressure in the leak and the vertical strain along the casing of Well 9A were evaluated at several times after injection (Figure 8-21). For a Type I leak, a nonuniform pressure gradient develops for a given change in reservoir pressure (Figure 8-21a). This causes the vertical strain to be tensile at depths where the leak is pressurized compressive at shallower depths (Figure 8-21b). This creates a crossover point in the vertical strain that migrates vertically towards the surface with time.

For Type II leaks, the diffusivity is high and pressure equilibrates between the constant pressure boundaries at the top and bottom of the leak in a matter of hours. This causes the pressure gradient along the leak to be roughly uniform between the reservoir and the atmosphere (Figure 8-21c). Vertical strains in the caprock produced by this pressure signal are tensile everywhere and increase with depth (Figure 8-21d).

8.5.2 Patterns

The deformation produced by leakage in most cases is expected to be small compared to that from injection. As a result, the residual between the leaking and nonleaking cases was evaluated to remove the effect of injection and isolate the deformation produced only by the leak. This is a useful approach for theoretical analyses to build an intuitive understanding of the effect of leakage on deformation.

For the Type I leak, the vertical strain in the caprock is tensile after 1 day of injection, which roughly corresponds with the onset of leakage (Figure 8-22e). At later times, a zone of compressive vertical strain extends ahead of the pressure front in the caprock, while tensile vertical strains extend out laterally from the pressurized region in the leak. The wedge of

compressive vertical strain advancing ahead of the pressure in the leak extends laterally to a distance approximately equal to the depth after 50 days of injection (Figure 8-22g). This creates a crossover band of vertical strain that migrates towards the surface.

The vertical strain in the caprock from the Type II leak is always tensile above the high permeability lens, except for a small region centered about the leak near the surface (Figure 19m-p). These tensile strains indicate that the deformation caused by the decrease in reservoir pressure from leakage is large than that due to pressurization of the caprock. As time continues, the pattern remains relatively unchanged, but increases in magnitude. A similar deformation pattern would be expected for a pumping well in the lens.

8.5.3 Deformation at Points

Time series of the vertical strain was evaluated at five points at a depth of 30 m and distances of 5, 25, 50, 75, 100, and 150% of the depth of the reservoir (d = 530 m) from Well 9A (Figure 8-23).

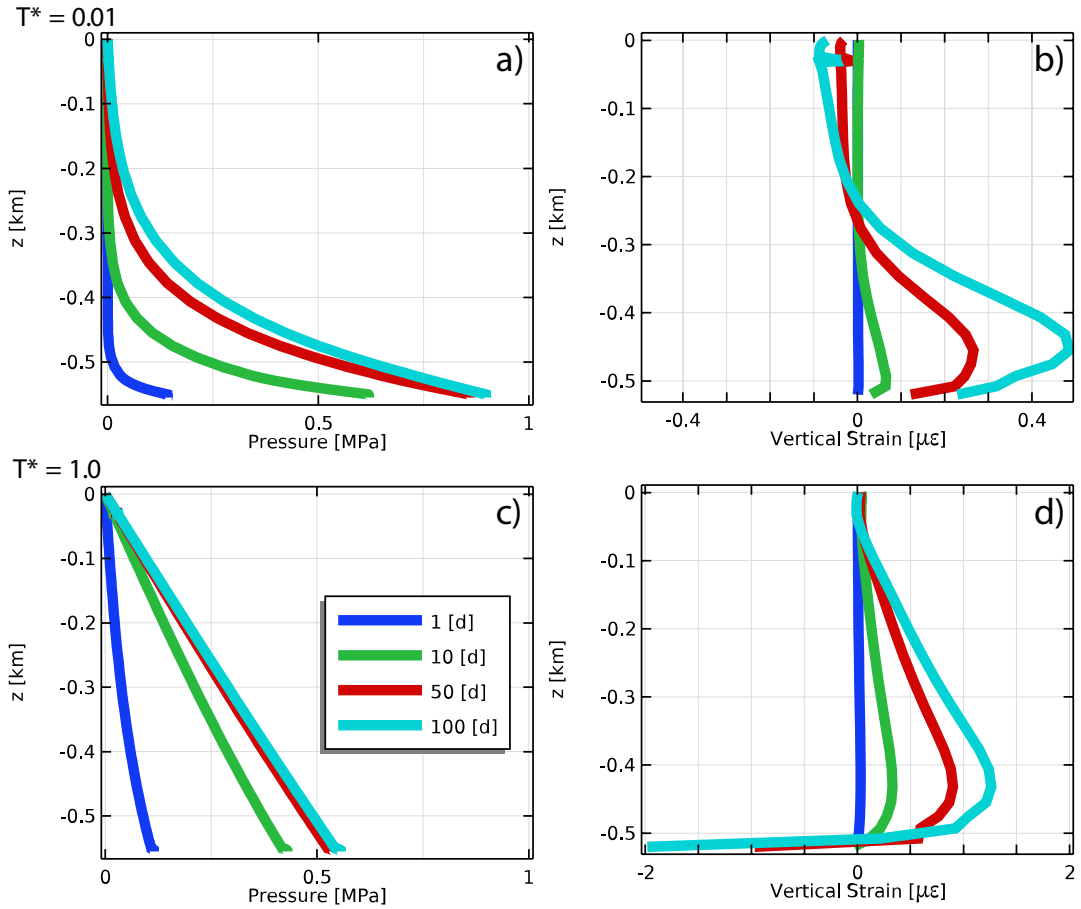

Figure 8-21. Vertical profiles of fluid pressure in the leak (a & c), and vertical strain along Well 9A (b & d) for Type I (top row) and Type II leaks (bottom row).

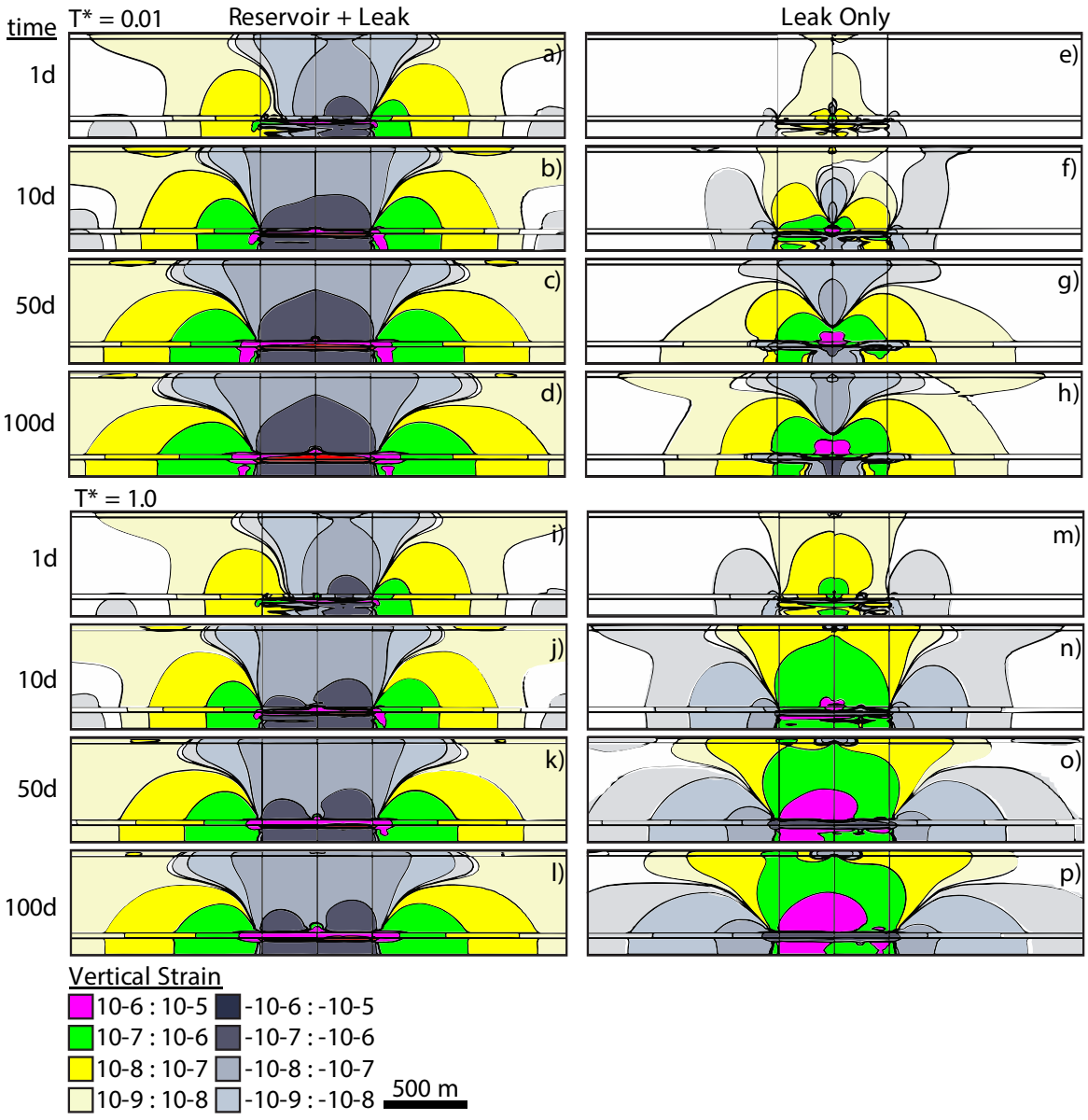

Figure 8-22. Vertical strain pattens as a function of time from injection and leakage (left column) and from leakage with the effect of injection removed (right column). Deformation shown for both Type I (a-h) and Type II leaks (i-p). Tensile strains are shown in color and compressive strains in greyscale.

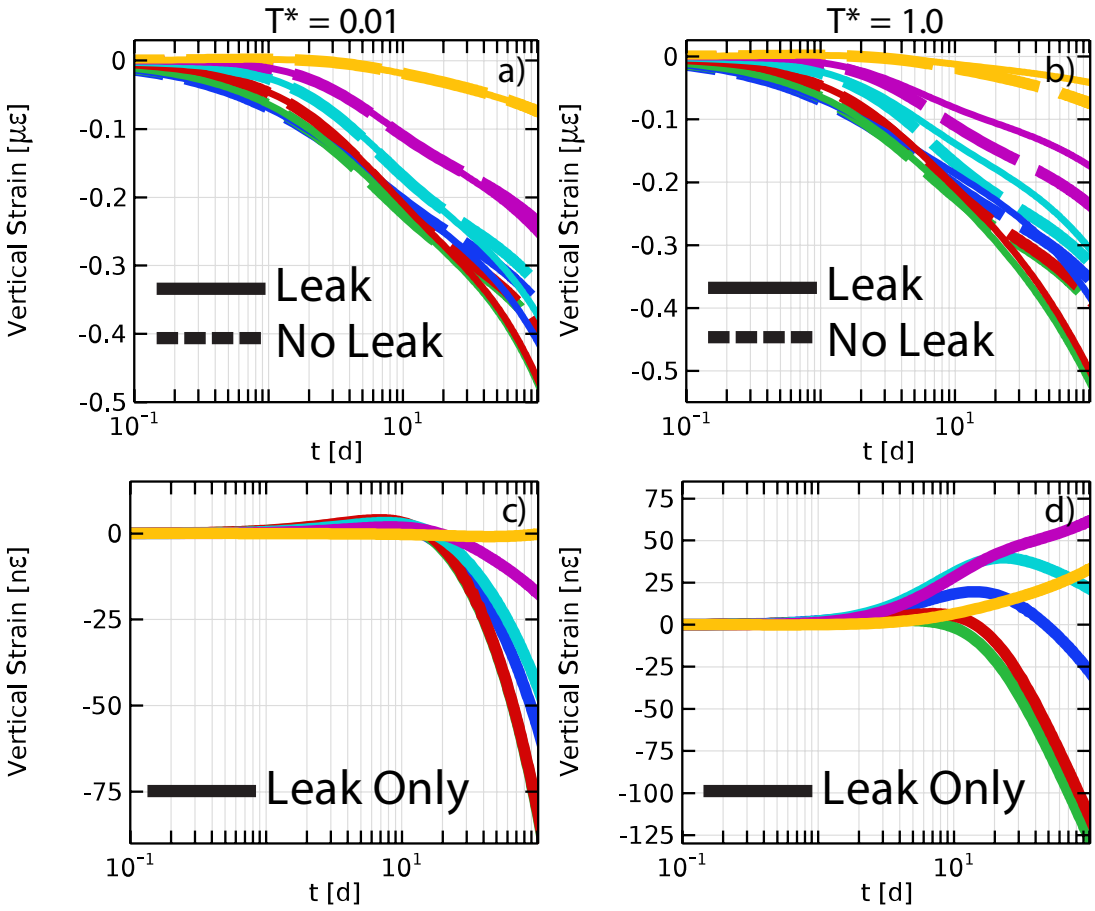

Figure 8-23. Time series of vertical strain for Type I (left column) and Type II leaks (right column). (a & b): Vertical strain signals from injection into a leaky (solid) reservoir are compared to the baseline scenario (dashed). (c & d): Vertical strain signals from leakage with the effect of the reservoir removed.

8.6 DISCUSSION

Leakage out of a reservoir along a planar conduit, such as a fault, results in deformation, the pattern of which is strongly influenced by the strength of the leak relative to the flux in the reservoir. Two end-member leakage cases, referred to as Type I and Type II, have been established based on this observation, with characteristic deformation patterns associated with each.

Type I leaks are characterized by compressive vertical, and tensile horizontal strain in the overburden centered about the leak. Strain signals in the shallow subsurface produced by this transient deformation pattern are characterized by a delayed increase in the strain and strain rate, with the delay being more pronounced for locations proximal to the leak. This progression of deformation towards the leak occurs due to the migration of the pressure to shallower depths and

is important as it provides information about the hydraulic diffusivity and location of the leak. A similar feature associated with Type I leaks is a double-ridge uplift pattern of the ground surface. This feature has been described by Pollard and Holzhausen (1979) and has also been documented at the In Salah carbon storage site in Algeria, with the uplift pattern believed to be from the pressurization of a blind, vertical planar conduit above and striking perpendicular to the injection well (White, 2014).

Type II leaks are characterized by tensile vertical strain and compressive horizontal strain in the overburden above and downstream from the leak, a pattern that resembles that of a pumping well. The similarity in reservoir pressure and overburden deformation patterns produced by Type II leaks and pumping wells could be exploited to develop a test that evaluates the effectiveness and sensitivity of a monitoring strategy to detect certain types of leaks at a given storage site.

If the leak truly has no observable effect on the reservoir pressure, then the strain from the leak could be obtained by subtracting that predicted by a calibrated site model from the observed strain signal. This is a tempting strategy but is likely not a reliable detection method as there is always the potential to calibrate the site model with information provided by existing leaks and a Type II or intermediate-type leak would certainly contaminate data used for calibration.

The difficulty to detect leaks using shallow strain data decreases significantly for cases where leakage occurs in the absence of injection or if leakage begins when the flux in the reservoir is relatively stable. In these cases, the strain from the leak would likely be much higher than background and would be noticeable in the raw timeseries data without the need for deconvolution or sophisticated detection algorithms.

8.7 REFERENCES

Carslaw, H., & Jaeger, J. (1959). *Conduction of Heat in Solids* (2nd ed.). Clarendon Press.

Morris, J. P., Hao, Y., Foxall, W., & Mcnab, W. (2011). A study of injection-induced mechanical deformation at the In Salah CO2 storage project. *International Journal of Greenhouse Gas Control*, *5*(2), 270–280. https://doi.org/10.1016/j.ijggc.2010.10.004

Murdoch, L. C., Germanovich, L. N., DeWolf, S. J., Moysey, S. M. J., Hanna, A. C., Kim, S., & Duncan, R. G. (2020). Feasibility of using in situ deformation to monitor CO2 storage. *International Journal of Greenhouse Gas Control*, *93*(August 2019), 102853. https://doi.org/10.1016/j.ijggc.2019.102853

Murdoch, L. C., Germanovich, L. N., Roudini, S., DeWolf, S. J., Hua, L., & Moak, R. W. (2021). A Type-Curve Approach for Evaluating Aquifer Properties by Interpreting Shallow Strain Measured During Well Tests. *Water Resources Research*, *57*(9). https://doi.org/10.1029/2021WR029613

White, J. A., Chiaramonte, L., Ezzedine, S., Foxall, W., Hao, Y., Ramirez, A., & McNab, W. (2014). Geomechanical behavior of the reservoir and caprock system at the in Salah CO_2 storage project. *Proceedings of the National Academy of Sciences of the United States of America*, *111*(24), 8747–8752. https://doi.org/10.1073/pnas.1316465111

CHAPTER NINE

USING STRAIN CAUSED BY AMBIENT LOADING TO DETECT LEAKS

Contents

9.1 Introduction 9-2
9.2 Conceptual Model 9-2
9.3 Objective 9-3
9.4 Analysis 9-3
9.5 Results 9-3
9.6 Summary 9-6

USING STRAIN CAUSED BY AMBIENT LOADING TO DETECT LEAKS

9.1 Introduction

Loading from barometric pressure fluctuations and Earth tides will cause transient strain signals that should respond to changes in material properties in the subsurface. Leaks of CO_2 out of a reservoir may cause rapid upward flow and release of CO_2 to the atmosphere. However, it is possible that upward transport of CO_2 will be inhibited by barriers, or traps that cause the CO_2 to accumulate. Methane accumulates in natural gas reservoirs in a similar process. It is possible, therefore, that CO_2 leaks could be characterized by an accumulation of gas.

9.2 Conceptual Model

An increase in barometric pressure compresses the underlying geologic materials by an amount that depends on the magnitude and rate of the pressure increase and the effective elastic modulus of the underlying material. The effective modulus will depend on both the stiffness of the rock matrix and the compressibility of the pore fluid. Fluid compressibility will be affected by the presence of CO_2. Using simple mixture theory, the effective compressibility of a pore fluid that consists of water and CO_2 is

$$\chi_f = \frac{1-S_{CO_2}}{K_w} + \frac{S_{CO_2}}{K_{CO2}} \tag{9.1}$$

where S_{CO2} is the fraction of pore space occupied by CO_2, the CO_2 saturation, K_w is the bulk modulus of water, and K_{CO2} is the bulk modulus of CO_2. Assuming CO_2 behaves as an ideal gas, which is sufficient for our application,

$$K_{CO2} = p_{ambient} \tag{9.2}$$

The bulk modulus of CO_2 gas will be much less than the modulus of water, so the accumulation of CO_2 will increase the compressibility of the pore fluid, according to .

CO_2 will likely accumulate in a flat-lying layer, or lens, trapped beneath an overlying confining unit. The compressibility of fluid in the lens will be greater than that of neighboring regions, and as a result, it will behave like a soft inclusion. This will cause deformation of the lens due to changes in barometric pressure to be greater than deformation in neighboring regions. Localized deformation of the lens will create strains in the overlying rock or sediments, and it is possible that this deformation could be measured and used to detect the underlying gas lens.

The conceptual model appears to be sound, but the characteristics of the resulting strain signal are unclear.

9.3 Objective

The objectives of this analysis are to characterize an example case showing how an accumulation of CO_2 gas can affect the strain caused by barometric loading, and evaluate the feasibility of interpreting the strain signal.

9.4 Analysis

An analysis was set up using a poroelastic formation in 2D cartesian coordinates with governing equations described in Chapter Five. It was assumed that CO_2 accumulated in a lens at a depth of 600m. The lens is shaped like a half ellipse, with semi-axes of 500m and 15m, on the top of a permeable aquifer at the contact with an overlying confining unit (Figure 9-1).

The upper surface of the model is loaded uniformly by a pressure that varies as a periodic function of time (Figure 9-1). The amplitude of the pressure fluctuation is 1 kPa, and the period is 8 days. This type of pressure variation is intended to represent a series of atmospheric pressure fronts. The amplitude and period of this example are larger than most diurnal variations, but fluctuations like this are common in South Carolina and elsewhere. Boundary conditions and geometric configurations are given in Figure 9-1.

9.5 Results

A periodic load on a uniform half-space causes uniform vertical subsidence when the pressure increases, and uniform uplift when the pressure drops relative to the mean, but this changes when a heterogeneity is present. The CO_2 lens in this example is assumed to contain a gas saturation of 0.2, which causes the compressibility of the pore fluid to increase by two orders of magnitude ($3x10^{-8}$ 1/Pa) compared to water with no gas ($4x10^{-10}$ 1/Pa). This causes the lens to behave as a soft inclusion, subsiding more than adjacent areas when the pressure increases and lifting more when the barometric pressure drops (Figure 9-2). In general, the ground surface is displaced 10-20 με more when the lens is present (Figure 9-2). The region affected by the larger displacements overlies the CO2 lens, and it extends roughly 500 m beyond the lateral extent of the lens (roughly an additional radial length of the lens).

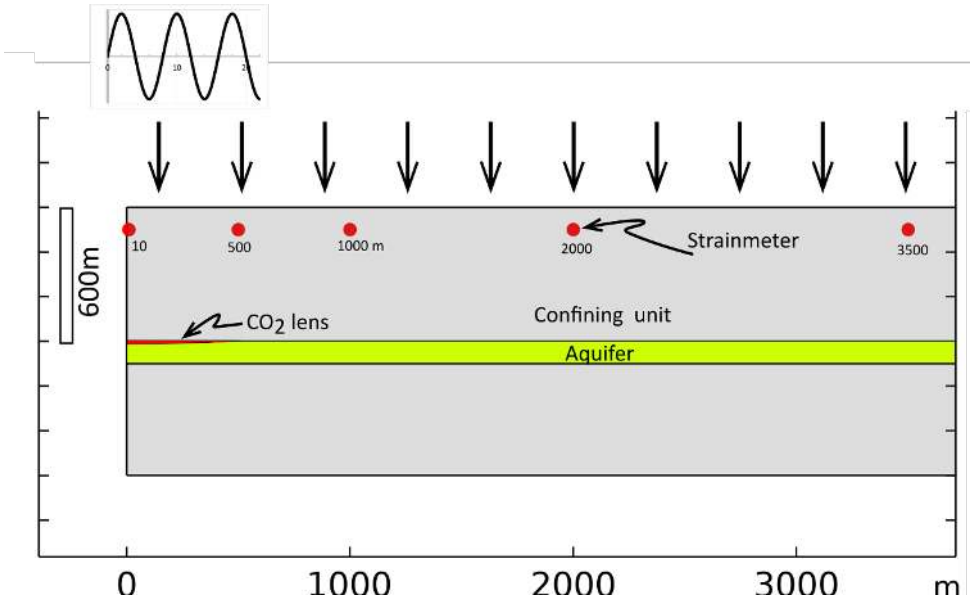

Figure 9-1. Cross-section of the simulation configuration with a CO_2 lens in an aquifer at 600m depth with an array of strainmeters at 100m depth. CO_2 lens is shown to scale. Symmetry about x=0. The model domain is 10,000m wide. Boundary conditions on the sides and bottom are no flow and roller. A pressure is applied to the top surface as a sinusoidal function of time (amplitude 1 kPa and period of 8 days) to represent barometric pressure fronts. Young's modulus = 1 GPa, Poisson's ratio = 0.25, porosity = 0.25. permeability of the aquifer = $10^{-13}m^2$, permeability of the confining unit = 10^{-16} m^2. The CO_2 lens is represented as a half ellipse with S_{CO2} = 0.2, which affects the compressibility following eq. 9.1.

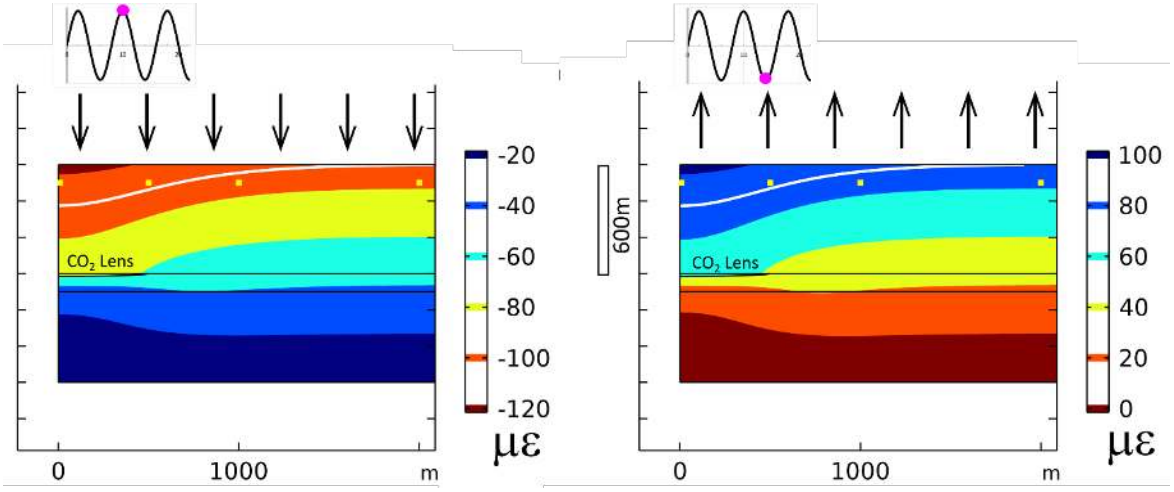

Figure 9-2. Vertical displacement field (in microns) caused by a uniform pressure at the ground surface that varies with time. Vertical displacement is greater over a lens with 0.2 CO_2 saturation. Yellow dots are strainmeters. Left side is displacement at maximum pressure relative to the mean pressure. Right side is displacement at minimum pressure in the cycle.

The displacement anomaly caused by the soft CO_2 lens causes strain at shallow depths that varies periodically with the barometric pressure. For example, strain measured at 100m depth at various radial distances by several 10s of nε over the same period as the barometric pressure (Figure 9-3). Compressive vertical strain (negative) occurs when the barometric pressure increases (Figure 9-3b). This implies that the phase of the vertical strain differs by half a period (π radians) from the barometric pressure. The magnitude of the vertical strain overlying the CO_2 lens roughly 80 percent of the strain at a reference location at 3500 m. The phase of the vertical strain overlying the lens also differs from the phase at a reference location, but the differences are small (more details are below).

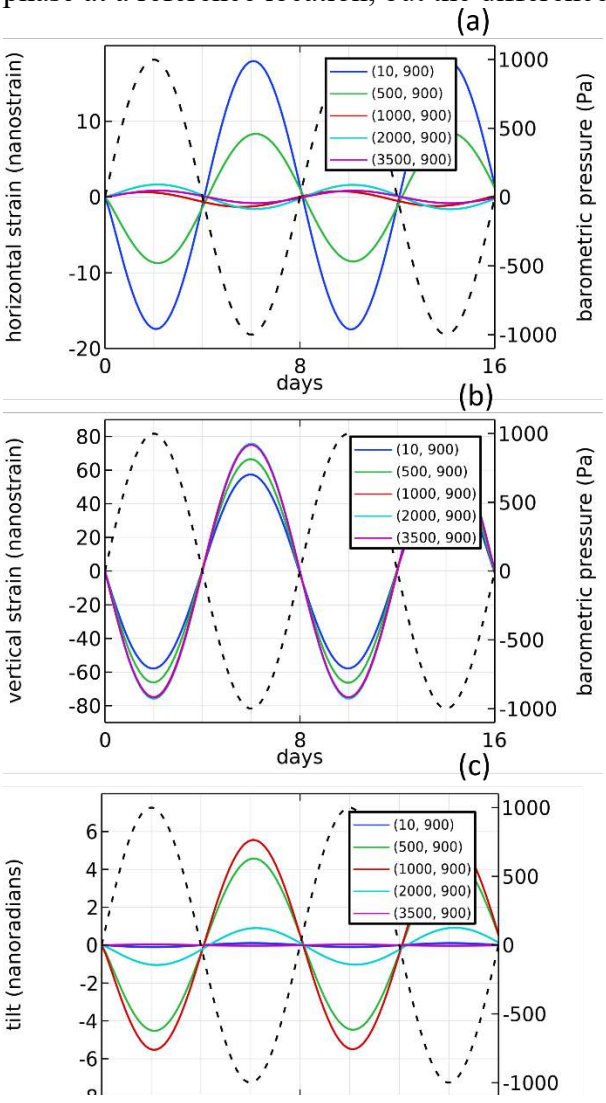

Figure 9-3. Horizontal and vertical strain, and tilt as functions of time at strainmeter locations. Numbers in the legend are coordinates of the strainmeters in Figure 9-1. Dashed line is barometric pressure in Pa.

The response of the horizontal strain is much different than that of the vertical strain (Figure 9-3a). The amplitude of the horizontal strain overlying the lens is strongly negative when the barometric pressure is positive, but the amplitude is positive at radial distances beyond the extent of the lens (x>500m). This implies that the phase of horizontal strain changes abruptly in the vicinity of the extent of the lens. The amplitude of the horizontal strain is much larger over the lens than it is beyond the lens extent (Figure 9-3a).

Tilt is also affected by the location of the lens. It is greatest in the vicinity of the the lens extent, and is significantly less over the middle of the lens and in the reference location beyond the lens extent (Figure 9-3c).

These results indicate that the magnitude and phase of the horizontal strain relative to either the vertical strain or the barometric pressure are significantly affected by the presence of an underlying CO_2 lens. The presence of the lens affects the phase over a broad region that overlies and extends slightly beyond the extent of the lens (Figure 9-4c). The phase of the vertical strain also affected by the presence of the lens, but the effect is much smaller than it is for the horizontal strain (Figure 9-4 a and c).

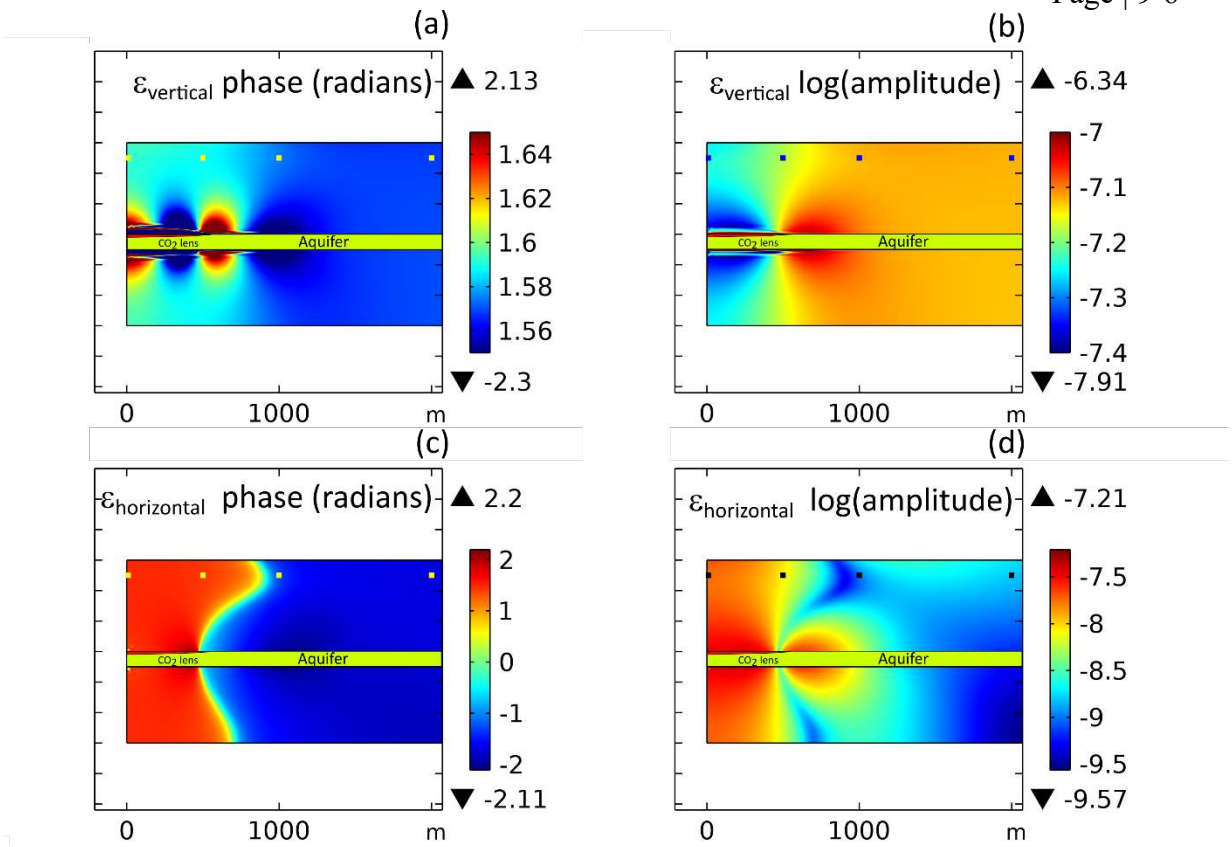

Figure 9-4. Characteristics of periodic strain signals in the vicinity of a CO_2 lens. (a) phase of vertical strain in radians. Phase of barometric pressure = $-\pi/2$ (-1.57). (b) amplitude of vertical strain, log scale (c) phase of horizontal strain in radians (d) amplitude of horizontal strain, log scale.

9.6 Summary

The results outlined above show the strain caused by barometric pressure fluctuations acting on a lens with a gas saturation of 0.2. The magnitudes of the variations in strain in the example should be readily measured using strainmeters described in Part 1. The most significant finding is that the phase of horizontal strain caused by barometric fluctuations is altered significantly by the presence of the lens. This occurs when increasing barometric pressure causes a depression over the lens, which results in horizontal stretching.

The phase of periodic signals should be readily detected by standard signal processing methods. As a result, it should be straightforward to identify the phase difference in the horizontal strain shown above, and it may also be possible to identify the much smaller phase differences in the vertical strain (Figure 9-4d). Ideally, changes in strain could be measured at shallow strainmeters throughout the life of a project, detecting the effects of accumulating CO_2. This would allow differences in phase caused by CO_2 accumulation to be distinguished from phase differences caused by other heterogeneities.

The magnitude of the effect outlined here will depend on material properties (e.g. elastic modulus, poisson's ratio, permeability), geometry of the CO_2 lens (depth, thickness,

lateral extent), and the magnitude and period of the barometric fluctuations. The example shown here demonstrates proof-of-concept, and further analyses will be required to evaluate the effects of different properties, geometries and pressure characteristics. It is also worth noting that strain caused by changes in gravitational acceleration during Earth tides may reflect changes in compressibility caused by CO_2 gas accumulation.

CHAPTER TEN

TRANSIENT STRAIN TENSOR MEASUREMENTS DURING INJECTION TESTING AT THE NORTH AVANT FIELD

Contents

10.1 Abstract 10-2
10.2 Introduction 10-3
10.3 Overview 10-3
10.3.1 AVN2 10-4
10.3.2 AVN22 10-6
10.3.3 AVN31 10-6
10.4 Injection Tests 10-6
10.4.1 Injection test T1 10-8
10.4.2 Injection test T2 10-8
10.3.2 Injection test T3 10-9
10.3.2 Injection test T4 10-12
10.3.2 Injection test T5 10-13
10.3.2 Injection test T6 10-14
10.5 Responses at instruments during different tests 10-15
10.5.1 AVN2 10-15
10.5.2 AVN22 10-15
10.5.3 AVN31 10-19
10.5.4 Pressure 10-19
10.6 Synthesis 10-21
10.6.1 Linear approximation and average rates 10-21
10.6.2 Log transform and reservoir of infinite extent 10-24
10.6.3 Power function approximation 10-24

TRANSIENT STRAIN TENSOR MEASUREMENTS DURING INJECTION TESTING AT THE NORTH AVANT FIELD

10.1 ABSTRACT

Six injection tests were conducted at the North Avant Field oil reservoir, and the pressure in the reservoir and the strain tensor were monitored as functions of time. The strain tensor was measured at two shallow strainmeters (40m depth) in the overburden and one deep strainmeter (500m depth) near the reservoir. The pressure increased during injection and decreased during recovery at all the monitoring wells. The horizontal strain increased (became tensile) and the vertical strain decreased (became compressive) during injection and then changed sign during recovery at the two shallow strainmeters. The opposite occurred at the deep strainmeter—horizontal strain decreased and vertical strain increased during injection. The NS strain was greater than the EW strain at a shallow strainmeter east of the injection well, but the relative magnitudes were reversed at a shallow strainmeter north of the injection well. This response is consistent with the circumferential strain being larger than the radial horiontal strain.

The pressure and strain timeseries are slightly non-linear with negative curvature during injection and positive curvature during recovery. A linear fit to the data indicates the reservoir was pressurized at rates from 2 to 4 kPa/hr, and this resulted in normal strain rates at shallow depths of 1-2 nε/hr. The strain rates at the deep strainmeter were slightly faster, in the range of 1.5 to 2.5 nε/hr. The data were fit using a log function of time and the t_o/r^2 values for pressure are essentially the same as t_o/r^2 for strain. The semi-log slopes for pressure are linearly correlated to the semilog slopes for pressure. The data were also fit to a power law function. Both the shallow strain data and the pressure in the reservoir are characterized by exponents generally between 0.9 and 1.0, the exponent for the data from the deep strainmeter is smaller, in the range of 0.7 to 0.8.

A new pump controller developed for this work held the injection rate constant, but the duration of the tests was long enough to encounter anomalies that caused the pump to shut off and this caused the injection rates to depart from ideal conditions. We accounted for these anomalies by weighting the values measured during each test when calculating the mean and standard deviations. This allowed us to estimate the uncertainty in the means while accounting for the inevitatble vagaries of the field tests. The weighted coefficient of variation of the shallow strain data is less than 0.17 for four of the six normal strains and 0.32 is the maximum value. The variability of normal strain data at the deep strainmeter is larger, with CoV ranging from 0.2 to 0.32. To CoV of pressure data is less than that from the strain data, ranging from 0.03 to 0.12.

Data from the tests indicates that strain data during six tests are repeatable with uncertainties with tolerances that are acceptable for field tests. Important characteristics of the pressure data that would be used to interpret well tests are similar to, or correlated with similar characteristics of the shallow strain data. The shallow strain data are consistent with expectations from simulations, suggesting they should provide valuable constraints during inversion.

10.2 INTRODUCTION

A suite of six injection tests was conducted during summer 2022 at well 9A to evaluate the peformance of tensor strainmeters. The duration of the tests ranged from 77 to 337 hrs (Table 10-1) and each test was separated from the others by several days to weeks (Figure 10-1).

A centrifugal pump at Well 9A was configured with a variable speed drive, which was set to 0.0019 m^3/s (30 gal/minute). This is the injection rate during most of the tests. In a few cases, injection occurred at slower rates. This occurred because the pump stopped inadvertently. The water handling system at the site was configured to provide continuous positive pressure to the pump. As a result, water could flow through the pump and into the well when the pump was off but the valve at the wellhead was open. This occurred at the end of T2 (Figure 10-1) when the power to the pump was interupted because of a lightning strike, for example. Several other outages occurred through the testing period.

Pressure at monitoring wells WW27, WW29, WW32, and WW60 was measured thoughout the testing period. The pressure at all the monitoring wells except WW60 was measured with submersible transducers suspended below the water level in the well. Pressure was measured in the head-space of WW60 because it could not be opened to deploy a transducer at depth. All the wellheads were sealed during testing. The pressure at the injection well, 9A, was measured at the wellhead.

Strain was measured using tensor strainmeters at three locations. Horizontal strain was measured at AVN2 using a Gladwin strainmeter and vertical strain was measured a few meters away in an adjacent borehole. Four components of strain were measured at AVN22 and AVN31 using elliptical ring tensore strainmeters developed for the project. Data from the strainmeters was processed using calibration methods described elsewhere in this report, and the data from calibration 2023187 decimated to 1 hr intervals was used here.

Table 10-1. Start and end times of injection in the well 9A, North Avant Field.

	Start		End		Elapsed
Test	date	time (hr)	date	time (hr)	hrs
T1	7/30/2022	14	8/2/2022	19	77
T2	8/10/2022	16	8/18/2022	2	178
T3	8/29/2022	16	9/12/2022	17	337
T4	9/23/2022	17	9/27/2022	14	93
T5	10/21/2022	19	10/25/2022	13	90
T6	11/1/2022	12	11/11/2022	18	246

10.3 OVERVIEW

The injection tests are characterized by increasing pressure at well 9A and at the four monitoring wells in the vicinity (Figure 10-1a). The well head pressure decreases sharply at well 9A and drops below 0 soon after the well is shut-in. The pressures at the monitoring wells drop gradually and they all were dropping when the next test was started (Figure 10-1a).

The pressure change at wellhead of 9A reached maximum values of more than 1500 kPa. The greatest pressure change occurred at WW29 and ranged up to 800 kPa, and was roughly 0.2 to 0.4 of the wellhead pressure change at well 9A (Figure 10-1a). The pressure change at WW29 was followed closely by the pressure at WW32 and then by the pressure at WW27. That is the order of distance from well 9A. The pressure change at WW60 was less than at the other monitoring wells (a maximum of 300 kPa), likely because it was being measured in the head space of the well.

The pressure increases with a slight negative curvature, whereas it decreases with slight positive curvature (Figure 10-1a). These signs of curvature are typical of well behavior, although the curvature is less than expected when a well injects into a reservoir of infinite lateral extent. This creates a general sawtooth pattern in the pressure time series (Figure 10-1a).

10.3.1 AVN2

The strain tensor at AVN2 changes systematically by several 100 nε during each injection test, and it varies by approximately 400 nε durign the full suite of tests (Figure 10-1b). Typically the horizontal strains increase while the vertical strain decreases durign injection and the opposite occurs during shut in. There is a slight curvature with the same sign as the pressure. The general pattern of the horizotnal strain timeseries resembles the sawtooth pattern of the pressure changes in the monitoring wells, whereas the pattern of vertical strain resembles that of horizontal strains with an opposite sign. The NS strain is generally greater than the EW strain throughout most of the timeseries (Figure 10-1b).

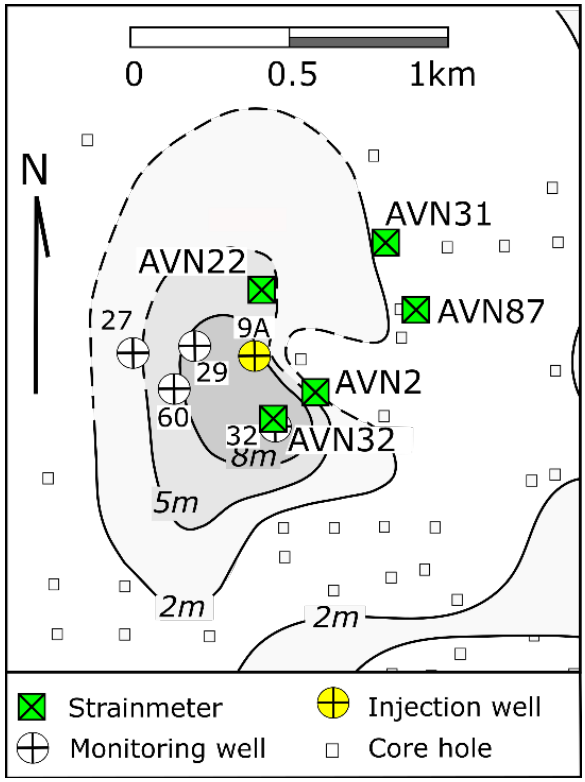

Figure 10-1. Map of the North Avant Field with locations of strainmeters, injection well and monitoring well. Contours are thickness in m of permeable lens at the base of the Bartlesville Formation.

The horizontal shear strain is less than the normal strains varying by less than 100 nε. The shear strain typically increases during injection (Figure 10-1b).

The EW and vertical strains during the shut-in period between T4 and T5 are anomalous (Figure 10-1b). The vertical strain increases during the other shut-in periods, but it is constant until day 70 and then it decreases. The EW strain increases during injection and it continues to increase through day 70 instead of starting to decrease when shut-in occurs. The slope of the NS strain and the sign of the slope of the shear strain also change on day 70. There are also anomalies during the start of T5 (Figure 10-1b). The vertical strain decreases and the EW strain increases approximately 1 day before the start of T5, whereas the NS strain increases at the start of injection. The reason for these effects is unclear.

(a)

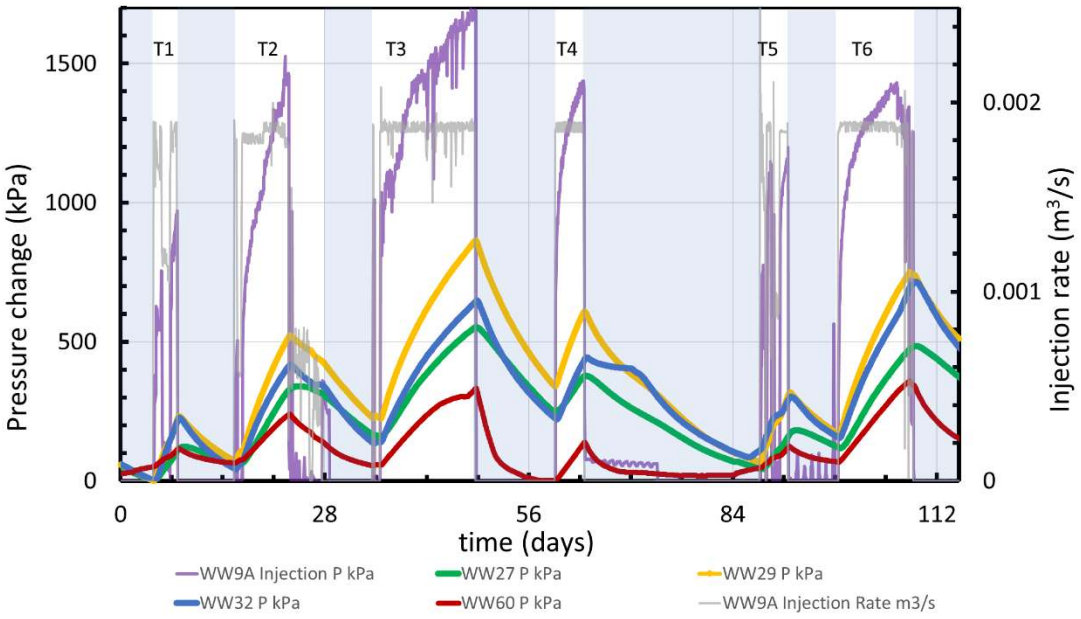

(b)

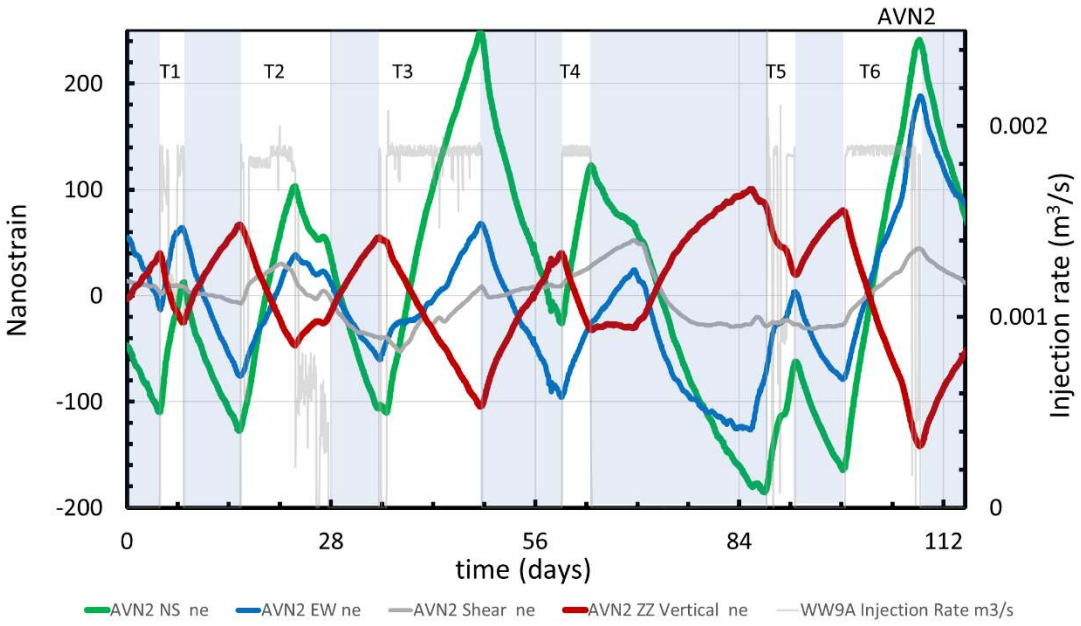

Figure 10-2. Pressure and strain during injection into well 9A at North Avant Field, summer 2022. (a) Pressure change at well 9A and at monitoring wells WW27, WW29, WW32, and WW60. (b) Four strain components at strainmeter AVN2. Injection rate as thin grey line. Six injection tests labeled T1-T6 with injection rate as thin grey line. Light blue bands are when well 9A was shut in.

10.1.1 AVN22

The strain components at AVN22 generally resemble those at AVN2 where the horizontal strains increase during injection and decrease during shut-in, while the vertical strain decreases during injection and increases during shut-in (Figure 10-2a). Sharp changes in slope occur when injection starts or stops, giving the timeseries a consistent sawtooth pattern. The strain magnitudes are similar to, or slightly less than at AVN2, ranging up to 300 nε over the suite of tests. The shear strain continuously increases up to T5 and then it stablizes (Figure 10-2a).

The anomalous behavior observed at AVN2 between T4 and T5 is absent from the data from AVN22.

10.1.2 AVN31

Strain components at the deep strainmeter AVN31 also vary systematically during injection and shut-in, but the patterns are different than at the two shallow strainmeters. Generally, the horizontal strains decrease and the vertical strains increase during injection and they change sign during shut-in. The overall magnitudes are up to 500 ne for most of the tests, but the strains vary by up to 1000 nε at the end of the suite of tests durign T5 and T6, several times larger than the strains at the shallow strainmeters.

Slopes of the strain records are generally associated with with changes in the pumping rate, but the timing of these changes is variable. During the beginning of T2, T4 and T6, for example, the slope of the strain changes at the start of injection, and it changes at the end of injection during most of the tests. These changes follow the behavior at the shallow strainmeters. However, the change in slope precedes the start of injection during by several days at T3 and by longer than this at T5. The slope remains constant through the end of T2, but the slopes change sign earlier in T2 when the rate drops at day 22.

10.4 INJECTION TESTS

The data from each tests were compiled and evaluated individually to provide more resolution than is available from the overall timeseries. Trends in the data preceding each test were matched with an exponential function and extrapolated through the duration of the tests. The same exponential function was used for all the datasets and the parameters were identified using least squares. A constant was added so all data were positive throughout the domain, and the sign of negative data was changed prior to fitting the trend. The constant and the sign change were selected manually so the exponential function was a good representation of the data. The domain of the data used to characterize the trend was selected manually and ranged from 50 to 190 hours before the start of each test. The predicted data were subtracted from observed data to give the expected response that would have occurred in the absence of ambient variations. The timescale was offset to start at zero at the start of injection during each test. This process resulted in data values that are roughly zero prior to and at the start of injection ($t<=0$). In a few cases, there were variations in the data before the start of injection and this caused the trend-corrected data to differ from zero at $t = 0$.

(a)

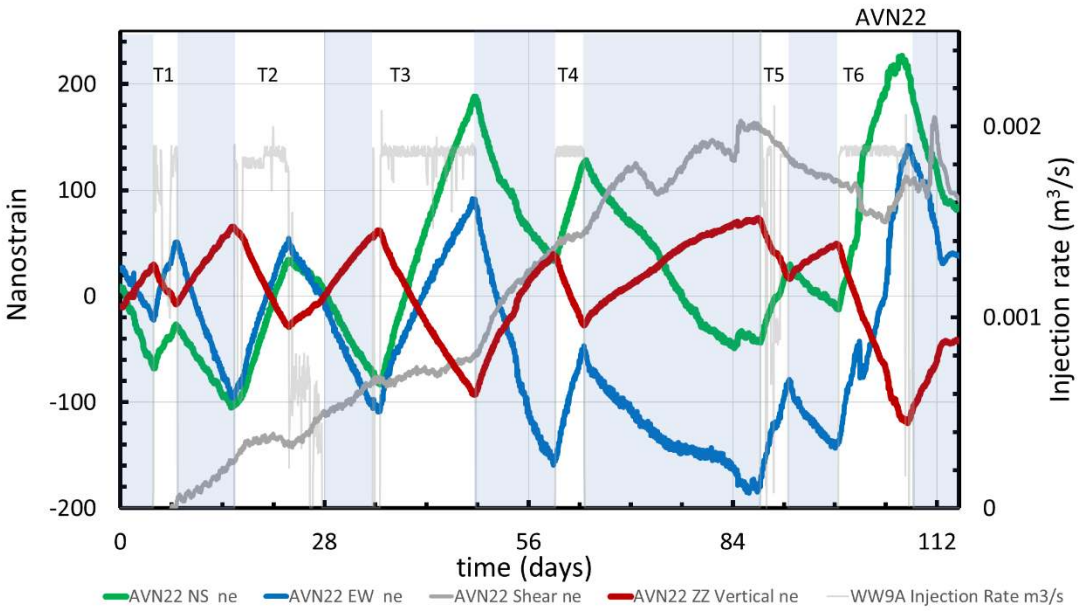

(b)

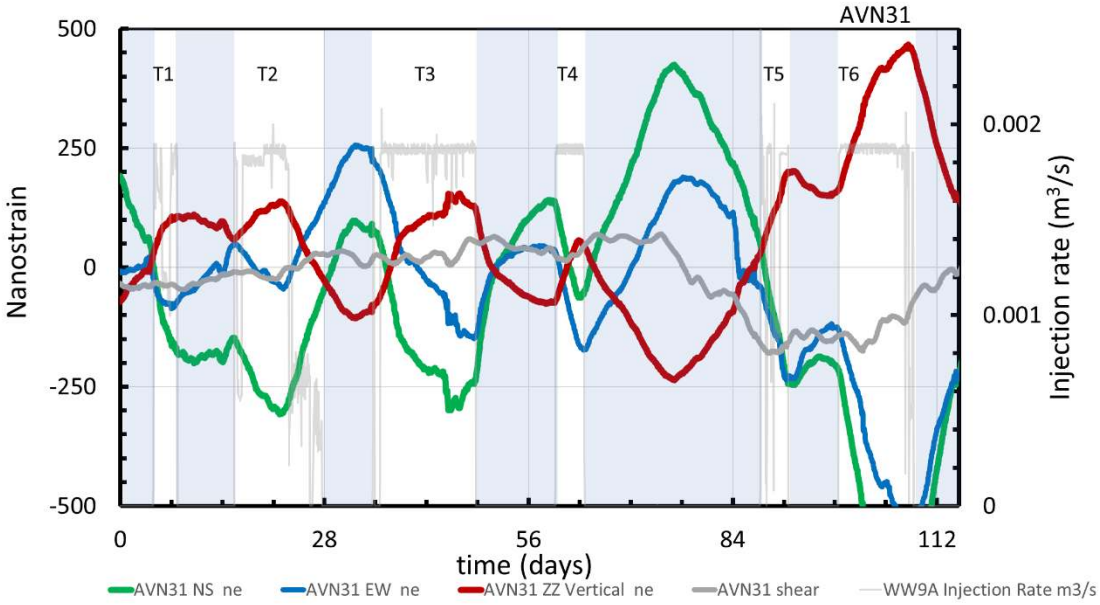

Figure 10-3. Strain during injection into well 9A at North Avant Field, summer 2022. (a) Four strain components at strainmeter AVN22. (b) Strain components at strainmeter AVN31. Six injection tests labeled T1-T6 with injection rate as thin grey line. Light blue bands are when well 9A was shut in.

10.4.1 Injection test T1

The first injection test lasted slightly longer than 3 days and it is marked by a drop in the rate in the middle of the test (Figure 10-3). Nevertheless, it is characterized by patterns that will be repeated in subsequent tests. Pressure at WW29 and WW32 increase at a rate of approximately 3.2 kPa/hr.

The vertical strain at AVN31 increases at a rate of 1.5 ne/hr and the horizontal strains decrease at 2.2 ne/hr during the first 40 hrs of the test and then the slopes flatten when the rate drops (Figure 10-3). The slopes stay flat when the rate increases again, and then the start to decrease gradually when pumping stops. The strains start to change approximately 24 hrs before the start of injection at AVN31, an atypical response that also occurred during T5.

The NS strain at AVN2 increases at 2.2 ne/hr whereas the EW strain increases slightly slower at 1.6 ne/hr on average. The vertical strain decreases at a rate slightly slower than the EW strain (Figure 10-3).

At AVN22 the relative rates of the EW and NS strains are reversed compared to AVN2 (Figure 10-3). The EW strain increases at approximately 2 nε/hr, whereas the NS strain rate is 1.6 nε/hr and the vertical strain rate is slightly slower (Figure 10-3).

10.4.2 Injection test T2

Injection started for a few hours and then stopped for approximately one day before the injection was started again. The main period of injection (18×10^{-4} m^3/s) was from approximatetly 20 to 180 hrs, and then the rate dropped by roughly a third until hr 290 when the well was shut-in(Figure 10-4).

The strain at AVN31 was similar to test 1 except the rates were slighly slower during main period (0.9 to 1 nε/hr). The strain rates were maintained until the injection rate dropped and then they all changed sign (Figure 10-4). In contrast, the strain rate at AVN31 decreased when the injection rate decreased during T1, but the sign remained the same.

The strain rates at the shallow strainmeters were also slightly slower than during T1, with the rate at NS AVN2 decreasing from 2.2 to 1.9 nε/hr and the rate at EW AVN2 strain dropping from 1.6 to 1.1 nε/hr (Figure 10-4). The magnitudes of the strains relative to each other during T1 are similar to T2, however. For example, the NS strain is greater than the EW strain at AVN2, but the EW strain is greater at AVN22 (Figure 10-4).

The strain rate changes sign or goes to approximatley zero when the injection rate drops by 1/3 at t = 180 hrs. A similar response occurs with the pressure (Figure 10-4).

10.3.2 Injection test T3

A brief, 4-hr-long, period of injection occurred at the start of this test. It was followed by a doy-long shit-in and then the injection rate resumed and was constant unti 320 hrs. Strains appearred to respond to the brief initial period of injection, so it was used as the initial time of the test.

The pressure increased at 2.2 kPa/hr, on average, which is similar to the previous tests. The negative curvature of the pressure plot is better developed during this test than the previous ones, probably because this is the first test with a constant rate.

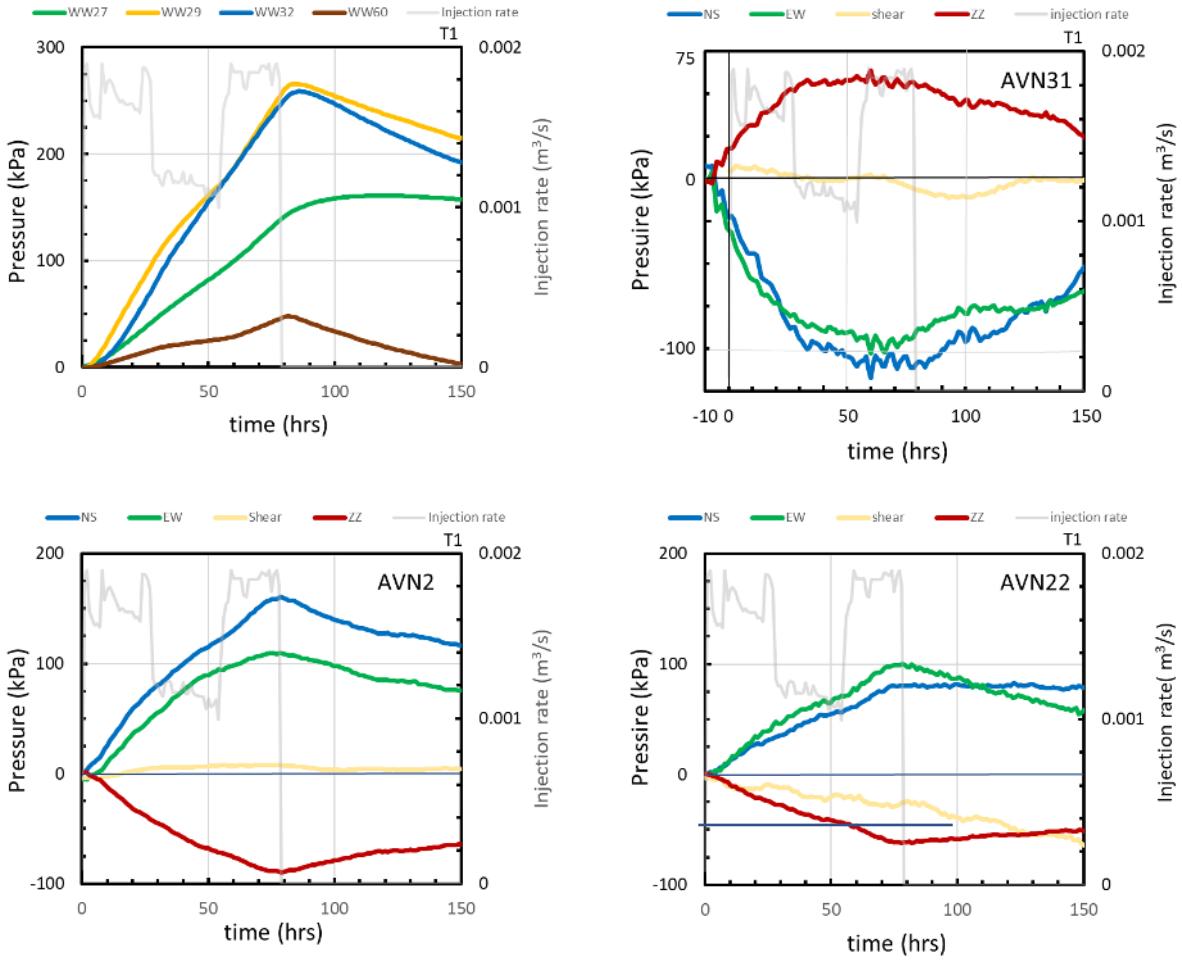

Figure 10-4. Test 1. Pressure at monitoring wells WW27, WW29, WW32 and WW60 (upper left), and transient strain tensors at AVN 31, AVN 2 and AVN22 at North Avant Field, summer 2022. Calibration 2023187.

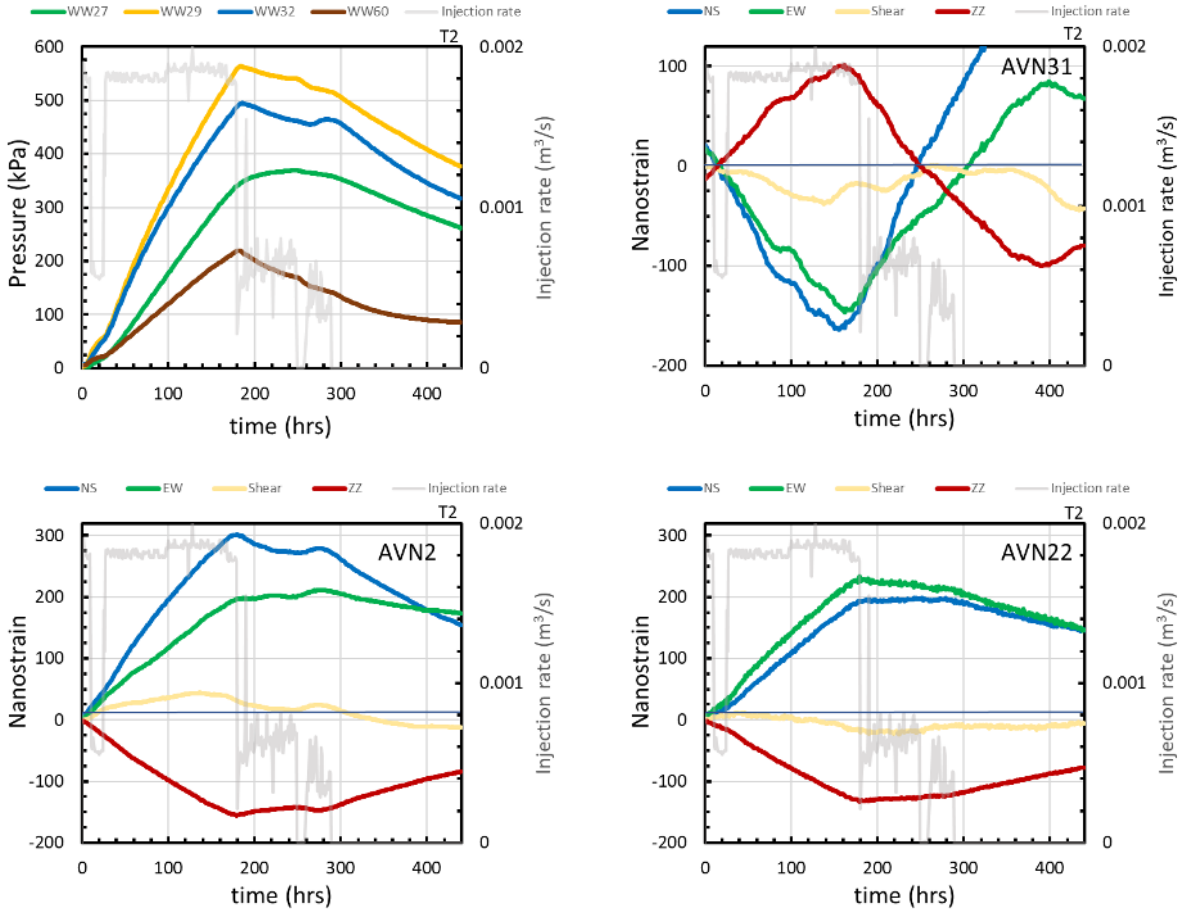

Figure 10-5. Test 2. Pressure at monitoring wells WW27, WW29, WW32 and WW60 (upper left), and transient strain tensors at AVN 31, AVN 2 and AVN22 at North Avant Field, summer 2022. Calibration 2023187.

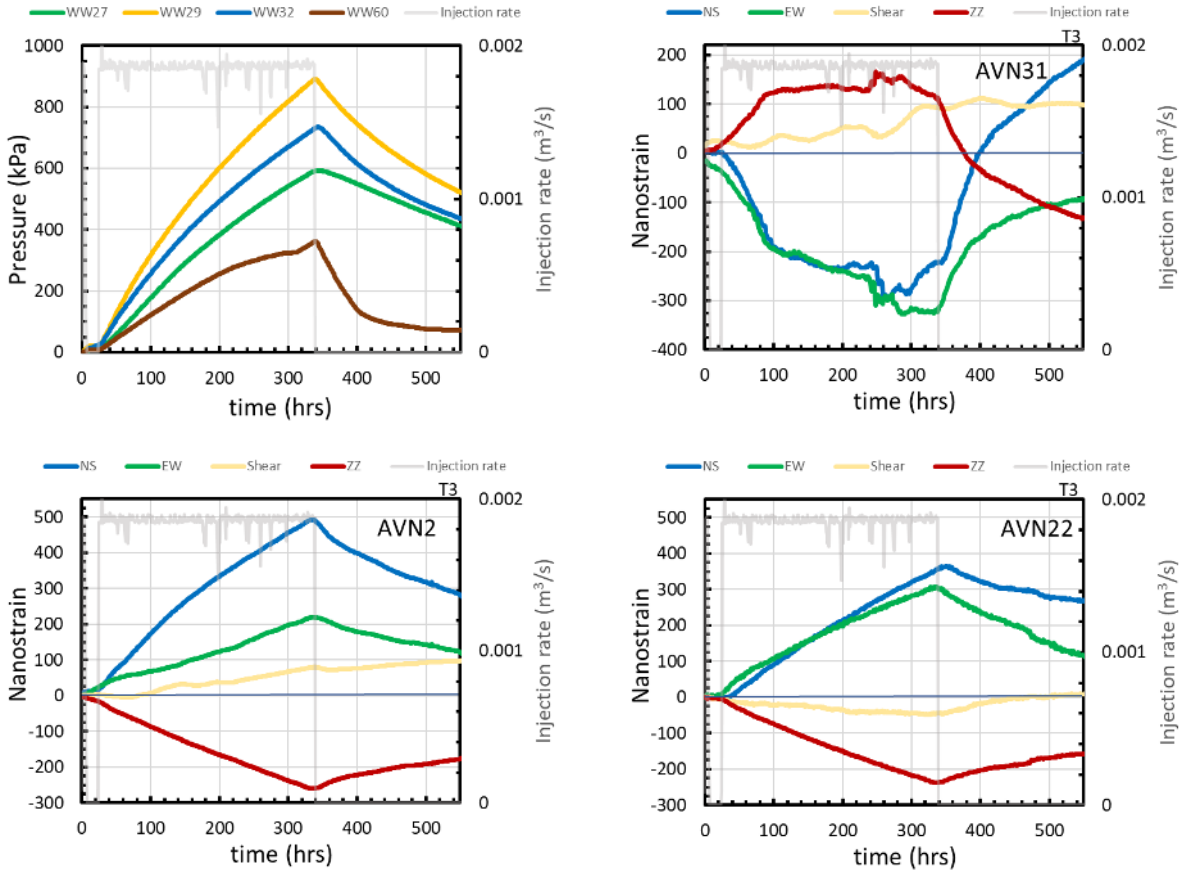

Figure 10-6. Test 3. Pressure at monitoring wells WW27, WW29, WW32 and WW60 (upper left), and transient strain tensors at AVN 31, AVN 2 and AVN22 at North Avant Field, summer 2022. A brief period of injection occurred during the first 4 hrs of the test, but it can be difficult to see on the plots. Calibration 2023187.

The vertical strain at AVN31 increased at a rate of 1.5 ne/hr and then flattened at a constant value of approximately 130 ne after 100 hrs. The horizontal strains drop at roughly the same rate and their rate also diminishes at around 100 hrs. The vertical strain increases by 20-40 ne and the horizontal strains decrease by similar amounts at $220 < t < 300$ hrs. All the strain rates change abruptly when the pump is turned off.

At AVN2 the NS strain increases at 1.5 ne/hr and the EW strain rate is roughly half this value. The vertical strain is compressive at a rate that is roughly the average of the horizontal strains, 1.25 ne/hr. The sharp fluctuations at AVN31 starting at $t = 240$hrs are absent from the horizontal strains. The exception is a slight increase in the rate of the EW strain at AVN2 at 240 hrs.

One difference between this and other tests is the relative magnitude of the horizontal strains at AVN22. The EW strain was greater than the NS strain at AVN22 during the first 100hrs, but then the EW strain diminishes and the NS strain is greater than the EW strain at the end of the test. The EW strain was greater than the NS strain during the previous tests, but those tests were shorter than this one. It is possible that the change in the relative magnitude of the horizontal strains occurs with extended pumping and T1 and T2 were too short to see this effect.

10.3.2 Injection test T4

Injection test T4 used a constant flow rate for 93 hrs. The pressure response was similar to the previous tests except at WW32 where the pressure continued to increase slightly after shut-in (Figure 10-6).

The strain response at AVN31 was remarkably consistent for the first 80 hrs of injection with the vertical strain increasign at 2 nε/hr and the horizontal strains decreasing at -2.5 nε/hr. The strain rates go to zero at approximately t = 80 hrs, roughly 13 hrs before the well is shut-in (Figure 10-6).

The strain rate is 2.2 at AVN NS and it is half this value at AVN EW. The magnitude of the vertical strain rate is similar to the EW value, -1.1 nε/hr.

The strain rate at AVN22 EW is slightly greater than that at AVN22 NS. The rates are rouhgly 14. nε/hr, which similar to the mean of the horizontal rates at AVN2. The vertical strain rate is -1.1 nε/hr, which is also the same as at AVN2.

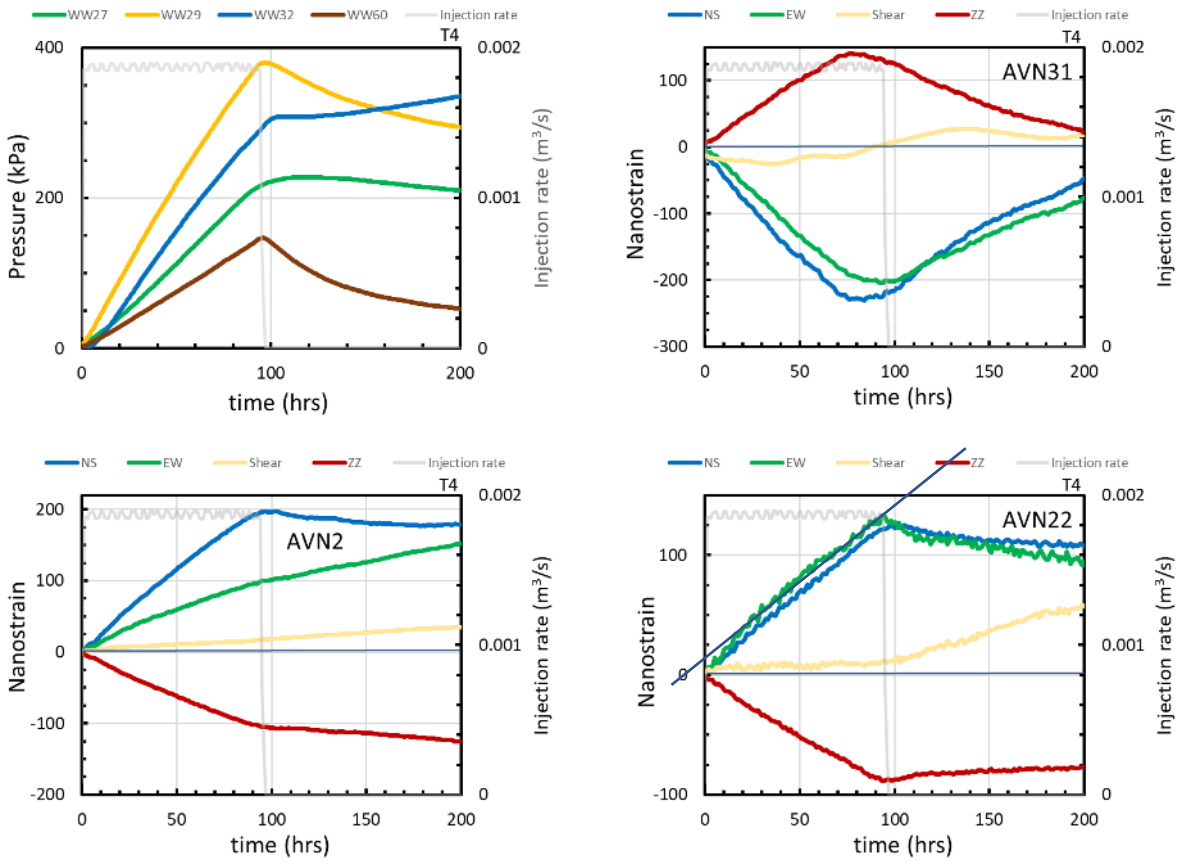

Figure 10-7. Test 4. Pressure at monitoring wells WW27, WW29, WW32 and WW60 (upper left), and transient strain tensors at AVN 31, AVN 2 and AVN22 at North Avant Field, summer 2022. Calibration 2023187.

10.3.2 Injection test T5

The injection rate during Test T5 is erratic due to mechanical problems. The general themes that emerged from the earlier tests are consistent during this one, although the rates are more variable. The average strain rates are between 1 and 2 ne/hr, and the strain rates decrease with the injection rate at all the strainmeters (Figure 10-7).

Data from AVN2 are consistent with strain starting approximatley 50 hrs before the start of injection. This is mechanically impossible and the strain during the other tests start to change at the onset of pumping, so a physical explanation remains elusive. Nevertheless, this is the response that occurs using the trend-removal procedure used during the other tests, so we show those results here.

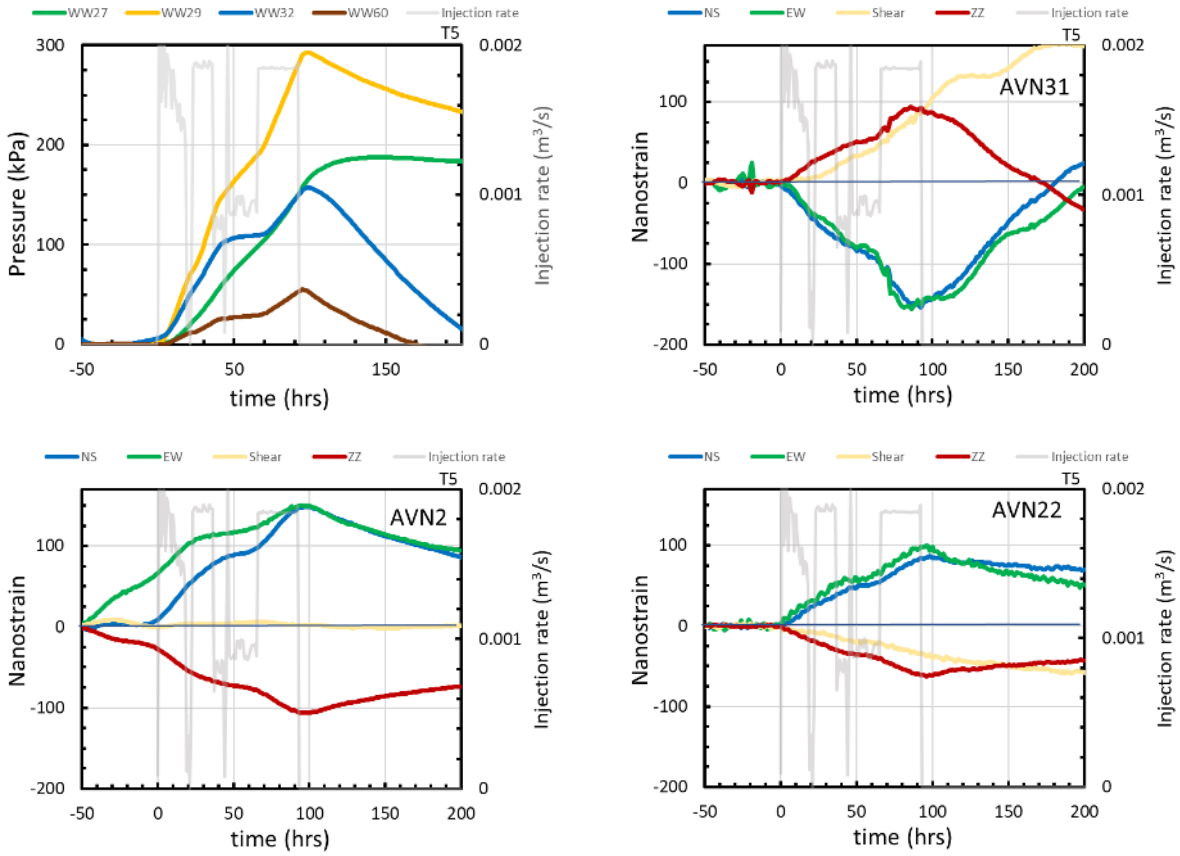

Figure 10-8. Test 5 Pressure at monitoring wells WW27, WW29, WW32 and WW60 (upper left), and transient strain tensors at AVN 31, AVN 2 and AVN22 at North Avant Field, summer 2022. Calibration 2023187.

10.3.2 Injection test T6

The injection rate during this test was constant for 220 hrs and then it fluctuated until it was concluded at t = 246 hrs (Figure 10-8). This is the second longest test next to T3 and the behavior is similar to that during T3. The strain rates at AVN31 are constant durign the first 100 hrs and then they decreases by roughly half, and then they change sign when the rate fluctuates at the end of the test.

The strain rate at AVN2 NS is similar to the rate at AVN31 vertical, and the rate at AVN2 EW is roughly 0.6 that of AVN2 NS during the first 200 hrs. The strain rates increase slightly from t = 200 hrs until shut-in at AVN2 (Figure 10-8).

The relative magnitudes of the horizontal strain rates at AVN22 are similar to earlier tests, with the EW strain rate larger than the NS rate early in the test (Figure 10-8). However, the rates abruptly change and this causes a shift in the relative magnitude of the horizontal strains at approximatley t = 80 hrs. The NS strain rate diminishes gradually, whereas the EW rate increases at t = 16 hrs and this causes the relative magnitudes of the strains to change again for t >180hrs.

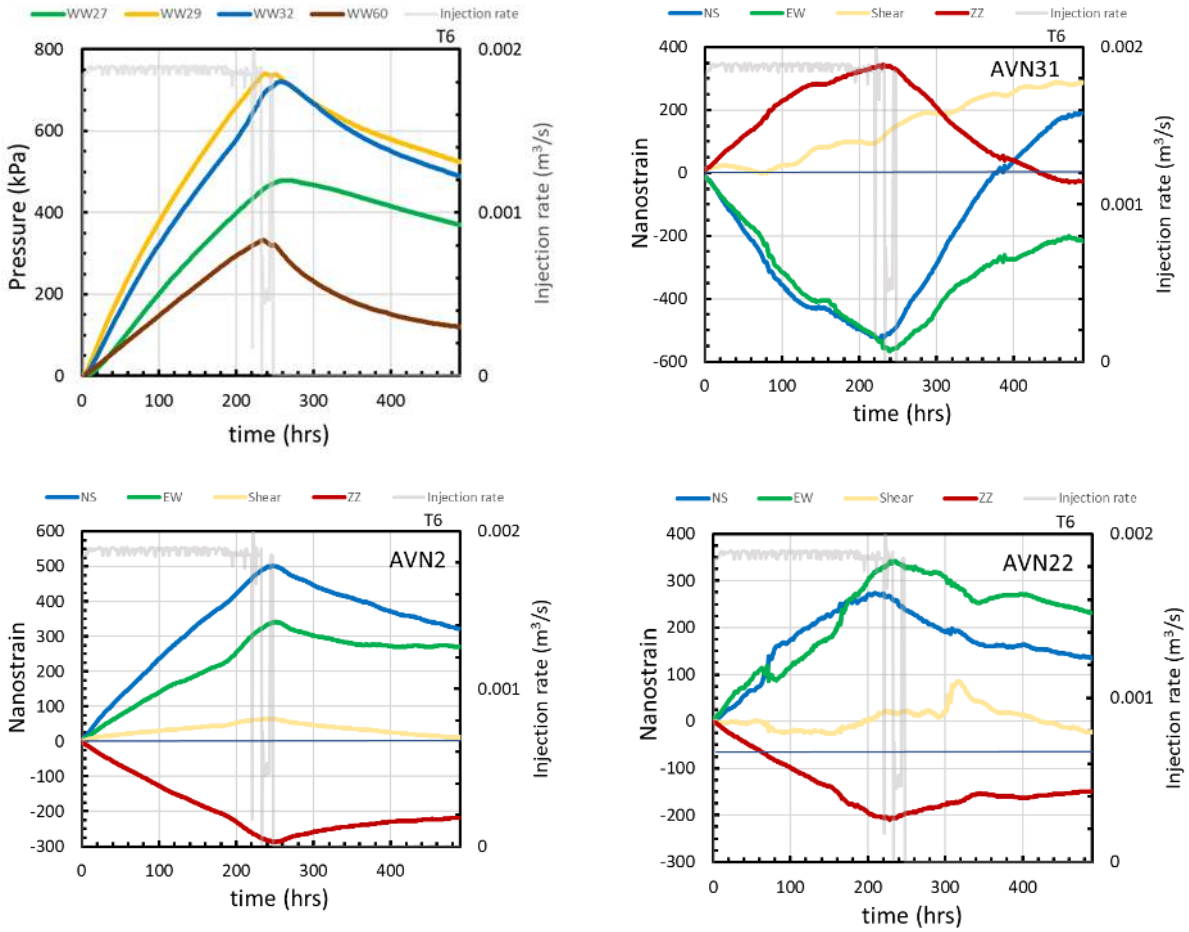

Figure 10-9. Test 6. Pressure at monitoring wells WW27, WW29, WW32 and WW60 (upper left), and transient strain tensors at AVN 31, AVN 2 and AVN22 at North Avant Field, summer 2022. Calibration 2023187.

10.5 RESPONSES AT INSTRUMENTS DURING DIFFERENT TESTS

The responses of each instrument during different tests provide insights into the consistency and reproducibility of the measurement (Figures 10-9 to 10-12).

10.5.1 AVN2

The relative magnitudes of the strain responses are consistent between the six tests with the exception of T5 where the NS strain is less than the EW strain (Figure 10-9). This occurs because of the anomalous start of the test, but the relative magnitudes of the slopes would cause the NS strain to be greater than the EW strain if they started at the same time.

The strain rate at AVN2 NS was between 2-2.2 nε/hr during tests with a consistent injection rate.

The ratio of the EW/NS strain was 2/3 during the first two tests, T1 and T2, and during the last one, T6. It was 0.4 during T3 and increased to 0.5 during T4.

The magnitude of the vertical strain rate was similar to the EW rate.

Shear strain varied more slowly and less consistently than the normal strains. The general trend is that the shear strain increased slowly during injection at rates less than 0.2 nε/hr.

Strain rates during shut-in generally changed sign compared to injection, but the rates of fall-off were slower than the increases during injection. Similar changes in the rate occurred with the pressure. T4 is an exception. The strain rate changes sign at AVN2 NS, but it did not change sign at the other channels at AVN2.

10.5.2 AVN22

The strain at AVN22 is remarkably similar to the data measured at AVN2. The strain rates are slightly slower than at AVN2, with maximum rates of approximately 1.5 nε/hr (Figure 10-10).

The EW strain is typically larger than the NS strain at AVN22, particularly during the first 100 hrs of injection. The ratio of NS/EW is between 0.8 and 0.9. The relative magnitudes may change with time, according to results from T3 and T6.

There is some high frequency variation at the several ne level in most of the tests that is absent from the results from AVN2.

Shear strain rate is slow and negative during all but one of the tests.

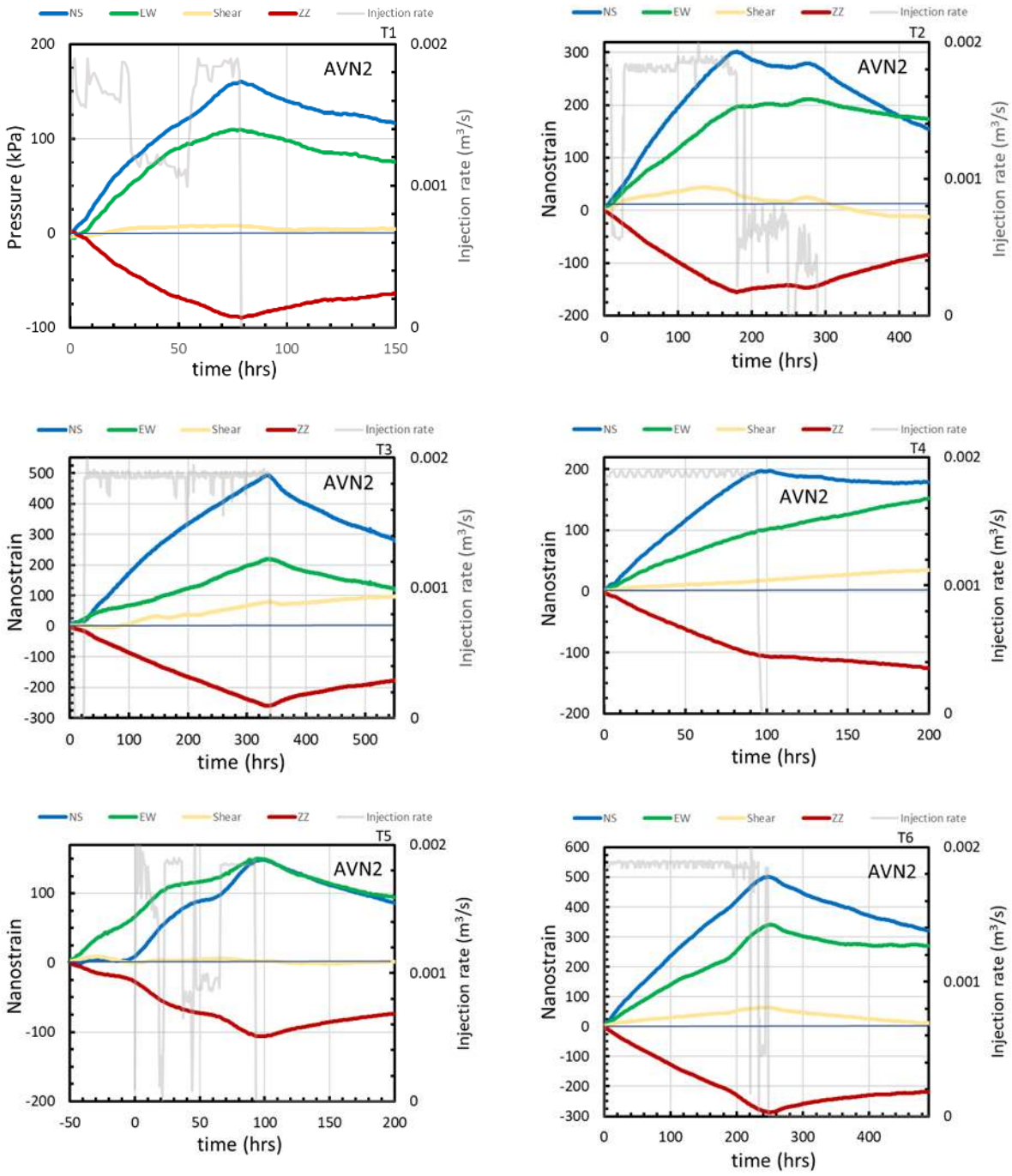

Figure 10-10. Transient strain tensor at AVN2 for six injection tests, labeled T1-T6, using well 9A at North Avant Field, summer 2022. Time is hours since injection started. Calibration 2023187.

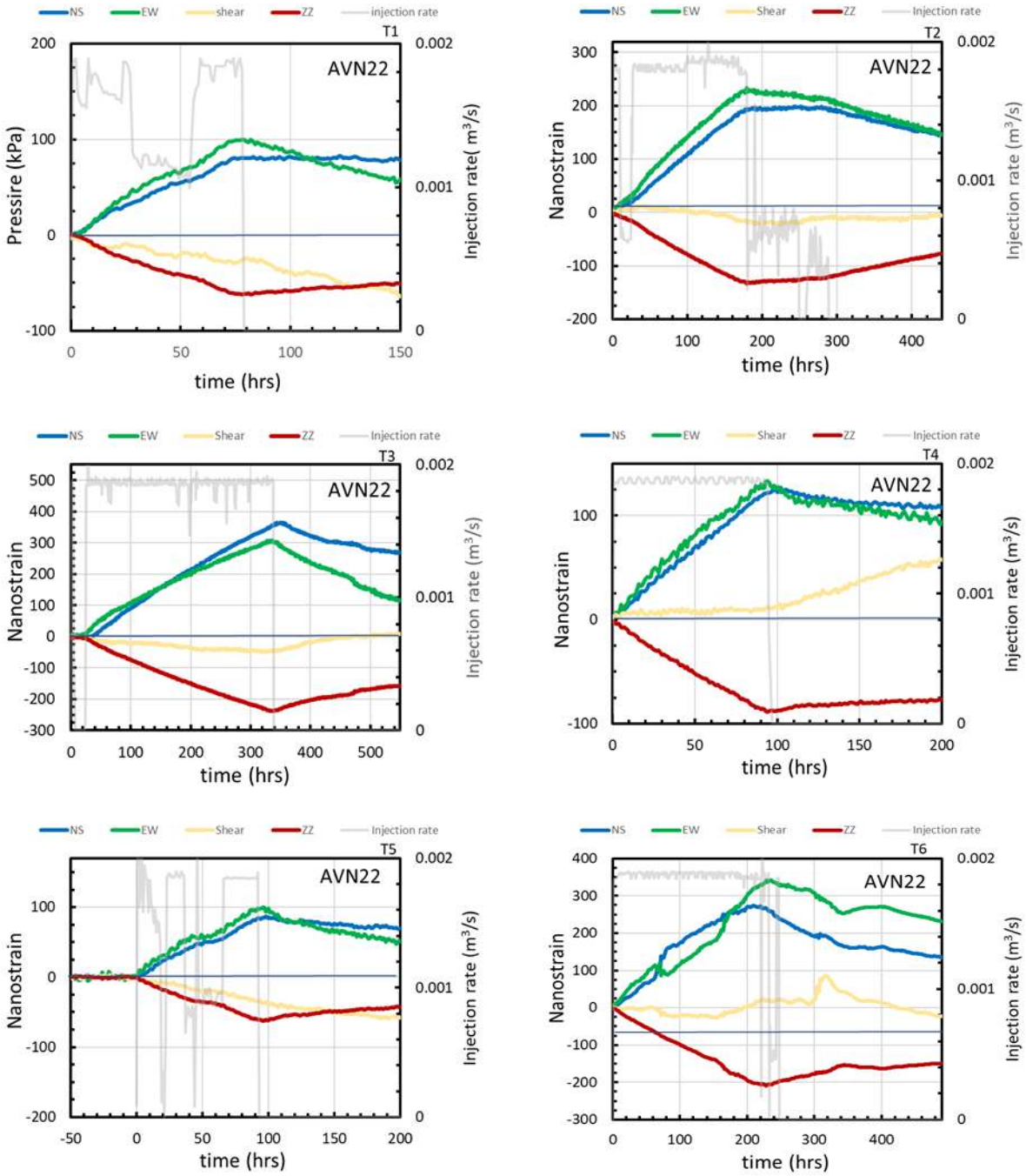

Figure 10-11. Transient strain tensor at AVN22 for six injection tests, labeled T1-T6, using well 9A at North Avant Field, summer 2022. Time is hours since injection started. Calibration 2023187.

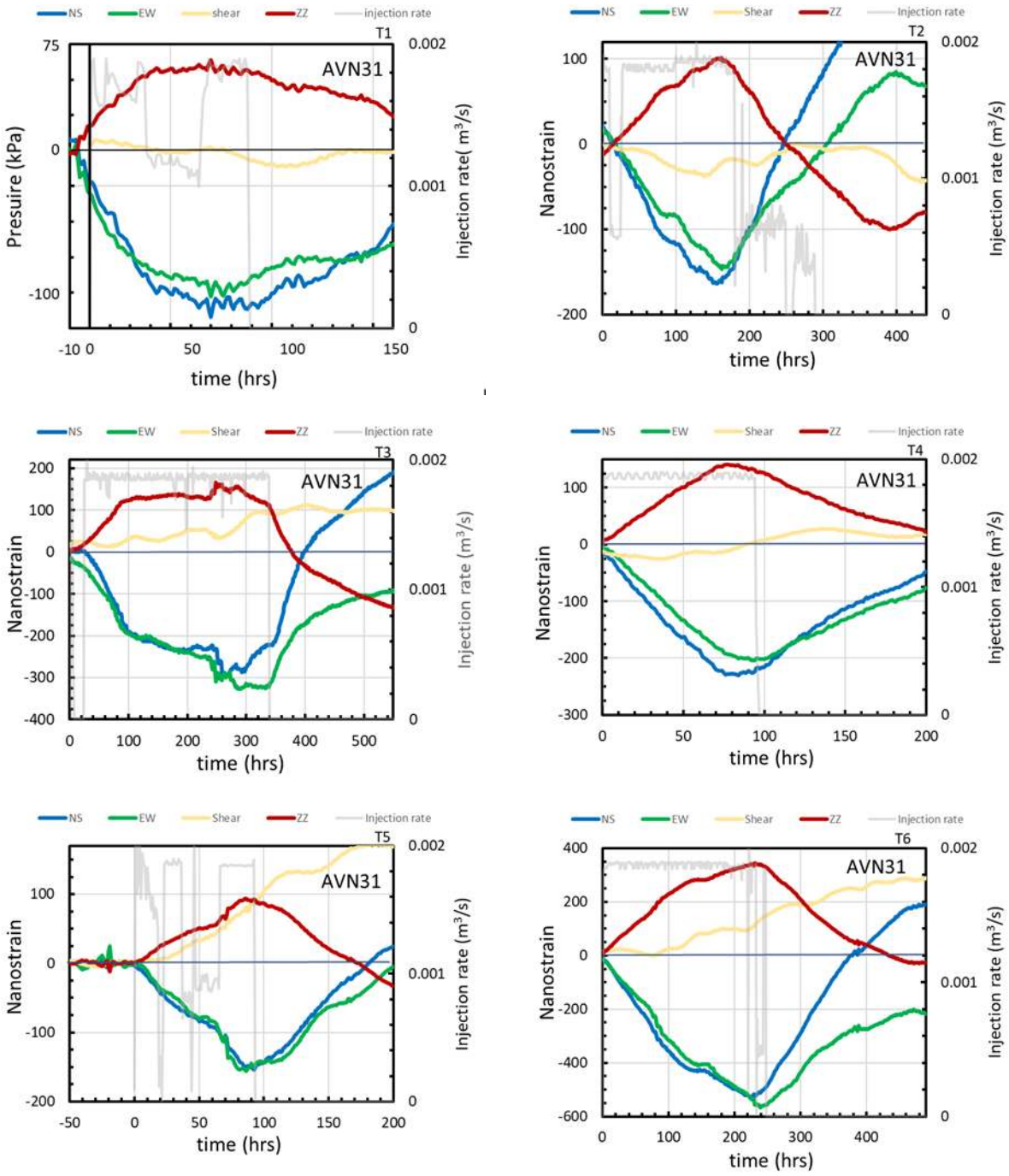

Figure 10-12. Transient strain tensor at AVN31 for six injection tests, labeled T1-T6, using well 9A at North Avant Field, summer 2022. Time is hours since injection started. Calibration 2023187.

10.5.3 AVN31

The response at AVN31 is more erratic than at the two shallow strainmeters, but the response during injection is consistent across all the tests (Figure 10-11). The vertical strain is positive and the horizontal strains are negative and the rates are in the range of 1.5 to 2 nε/hr. The strain rate diminishes after 50 to 100 hrs of injection during T1, T3 and T6, and it diminishes slightly after 100 hrs during T2.

The shear strain rate is small and variable.

10.5.4 Pressure

The relative magnitudes of the pressure changes are consistent between the tests (Figure 10-12). The pressure increases with a slight negative curvature and then decreases during shut-in. The rate of decrease at WW27 is slower than at the other wells and in some cases (T2, T3, T4, T5) the pressure continues to increase slightly after shut in, but it reaches a maxium after a few 10s of hours and then decreases. The pressure continued to increase after shut-in at WW32 during T4, but it decreased during the other tests. The pressurization rate varies slightly during changes in pumping rate.

There appears to be a lag of one to several hours between a rate change at well 9A and the pressure at the monitoring wells. This was difficult to characterize with this dataset, which was decimated at 1 hr intervals.

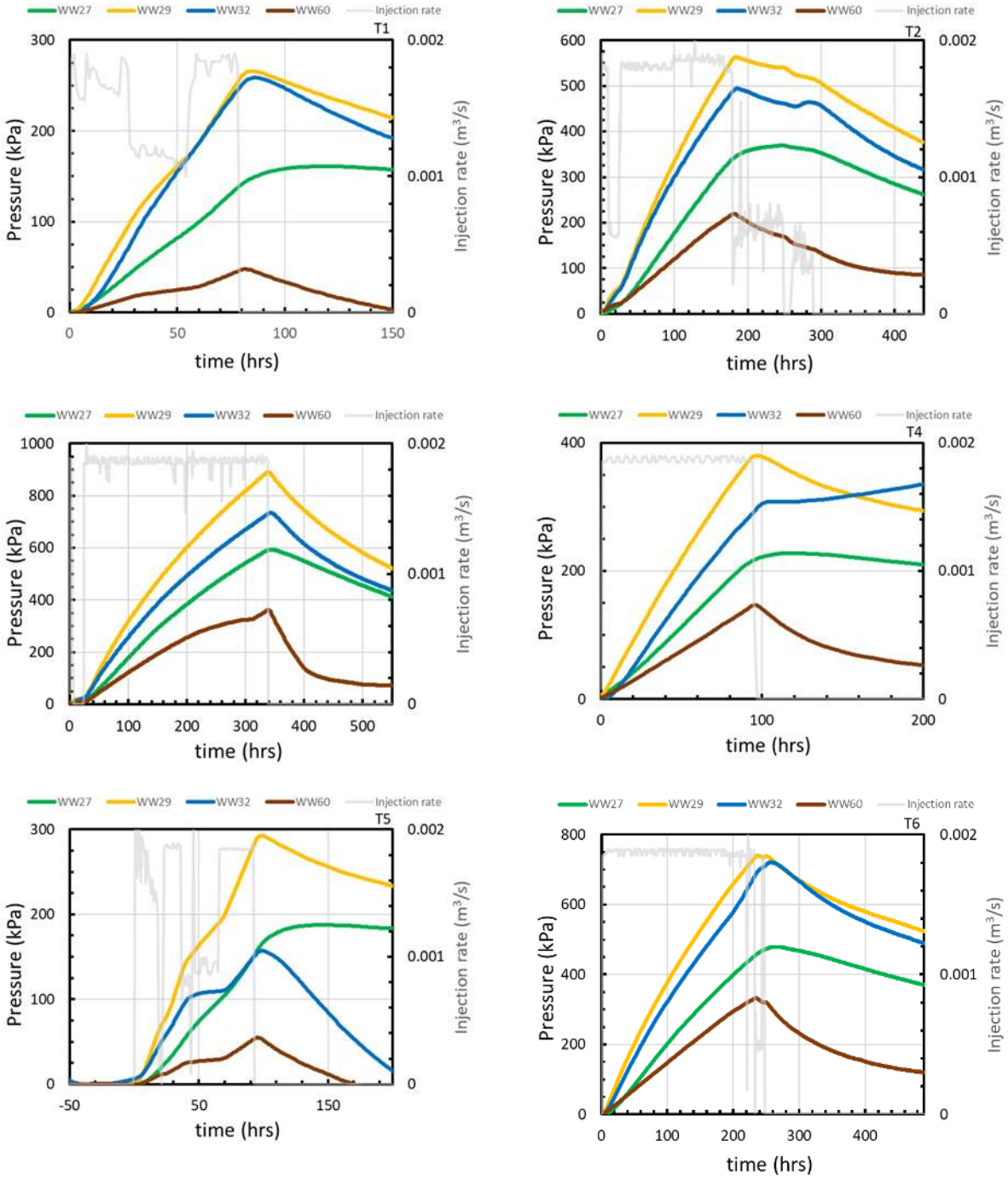

Figure 10-13. Pressure at monitoring wells WW27, WW29, WW32, and WW60 for six injection tests, labeled T1-T6, using well 9A at North Avant Field, summer 2022. Time is hours since injection started. Calibration 2023187.

10.6 SYNTHESIS

Data from the six injection tests were combined to estimate the average response and uncertainty of the estimate of the average. This was done by assuming that the pressure and strain response could be characterized by a simple function. Many of the datasets were nearly linear during injection and their slope reversed during recovery, so the initial characterization assumed the data were linear and could be characterized by a constant strain rate, or pressurization rate during injection and another rate during recovery. The rates typically decrease with time, so we also evaluated approximating the data as functions of the logarithm of time. Pressure varies as the log of time in a reservoir of infinite lateral extent, which motivated using this approximation. A power function was also used to approximate the data.

The rate at the injection pump was held constant during the tests, but the injection pump ceased operation intermittently and this caused the injection rate to fluctate. We accounted for this by rating the quality of the test from 1 to 10 and using this to weight calculations of the average and standard deviation of the strain rates.

Each test was analyzed by determining the strain rate that characterized the first 100 hrs of the data during injection and the rate that characterized the following shut-in. A weighted average and a weighted standard deviation was calculated, and the coefficient of variation was determined as their ration. The weighted average strain rate was calculated using

$$\bar{\varepsilon} = \frac{\sum_{i=1}^{n} w_i \dot{\varepsilon}_i}{\sum_{i=1}^{n} w_i} \tag{10-1}$$

here n is the number of observations and weights (6 in this case), w is the weight and $\dot{\varepsilon}$ is the strain rate. The weighted standard deviation was calculated using

$$\sigma_{\varepsilon} = \frac{n \sum_{i=1}^{n} w_i (\bar{\varepsilon} - \dot{\varepsilon}_i)^2}{(n-1) \sum_{i=1}^{n} w_i} \tag{10-2}$$

This procedure generates an average strain rate for injection and recovery for each strain component at each strainmeter (Table 10-2), and this is sufficient to generate average strain time series (Figure 10-13). Envelopes that are +/- 1 standard deviation of the mean strain rate were assumed to characterize the uncertainties in the time series (Figure 10-13).

10.6.1 Linear approximation and average rates

Data from this analysis indicate the magnitudes of the average normal strain rate range from 0.9 to 2.5 nε/hr (1 nε/hr ~ 3×10^{-13} 1/s) during injection at 0.0019 m^3/s (Table 10-2). The signs of the horizontal strains are opposite those of the vertical strains. The horizontal strains at both shallow strainmeters, AVN 2 and AVN22, are tensile, while the vertical strains are compressive. Both horizontal strains at the deep strainmeter AVN31 are compressive and the vertical strain is tensile. The magnitude of the mean horizontal strain rate is slightly larger than the vertical strain rate in all three cases.

The average magnitude of the normal strain rate is fastest at AVN31 (~2 nε/hr), and slowest at AVN22 (~1.2 nε/hr), and the intermediate value is 1.5 nε/hr at AVN2. The average shear

strains are an order of magnitude slow than the normal strains. The average shear strain rate at AVN2 (0.23 nε/hr) is larger than its standard deviation so it appears to be a non-zero rate, but the shear strain rate at the other two strainmeters are smaller than their standard deviation so they cannot be distinguished from zero.

The relative magnitudes of the horizontal strains can be affected by boundaries in the underlying reservoir, according to our earlier analyses (Murdoch et al. 2023). The ratio between the EW/NS strain rates is 0.5 at AVN2, but it is 1.2 at AVN22. The uncertainties in these average rates is small. The ratio EW/NS strain rate at AVN31 is 0.9, but the uncertainty is significantly larger than at the shallow strainmeters.

The strain rate changes sign at shut-in and the rates during recovery at the shallow strainmeters are slower than during injection (Table 10-3). For example, the rates at AVN2 and AVN22 during recovery are typically 0.2 to 0.5 that during injection. However, at the deep strainmeter (AVN31) the strain rates during recovery are similar in magnitude but opposite in sign to those during injection.

The variability of the normal strain rate data is in the range $0.1 < CoV < 0.4$ during injection, and it is more variable during recovery $0.3 < CoV < 0.75$. The shear strain rates are much more variable, with CoV>1 in most cases. The exception is shear during injection at AVN2 where the CoV is 0.028 (Table 10-3).

These characteristics generate synthetic time series that are similar in character, but with features that are unique to each strainmeter (Figure 10-13).

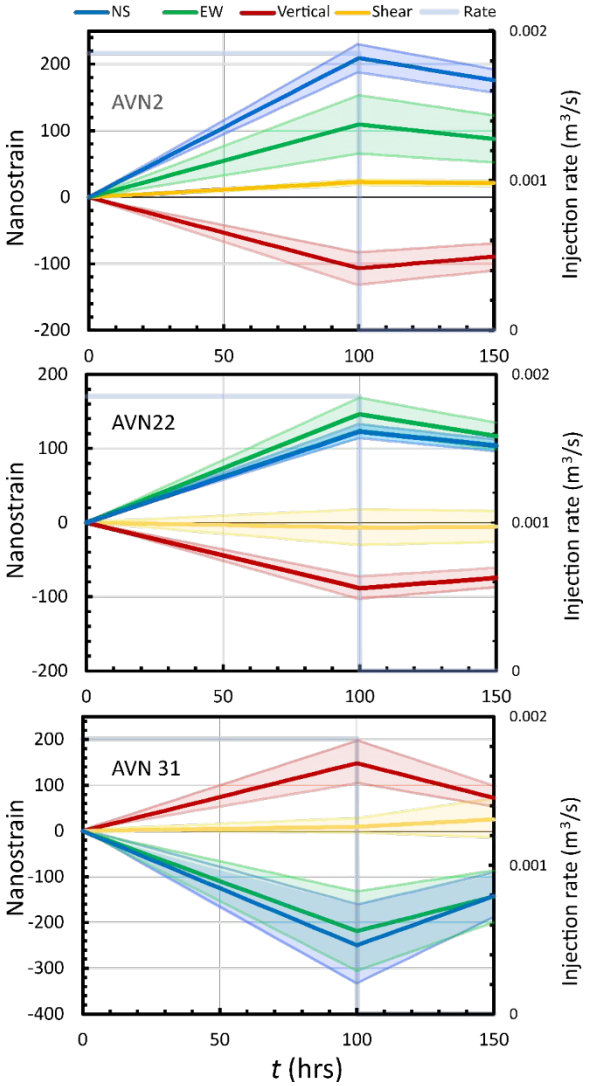

Figure 10-14. Strain components (colored lines) and injection rate (grey line) with time during an idealized injection test 100 hr long, based on weighted average values of linear fits from six tests during summer 2022 at North Avant Field. Shaded envelopes are 1 standard deviation from the mean.

Table 10-2. Strain rates during injection in nanostrain/hr for different strain components and different strainmeters during the summer 2022 injection tests at the North Avant Field.

		AVN2				AVN22				AVN31			
Test	wt	$\dot{\varepsilon}$NS	$\dot{\varepsilon}$EW	$\dot{\varepsilon}$ZZ	$\dot{\varepsilon}$Sh	$\dot{\varepsilon}$NS	$\dot{\varepsilon}$EW	$\dot{\varepsilon}$ZZ	$\dot{\varepsilon}$Sh	$\dot{\varepsilon}$NS	$\dot{\varepsilon}$EW	$\dot{\varepsilon}$ZZ	$\dot{\varepsilon}$Sh
1	1	2.8	2.4	-1.6	0.25	1.5	2	-1	-0.6	-2.4	-2.5	1.5	0.2
2	3	1.8	1.2	-1.0	0.25	1.15	1.4	-0.8	0	-1.25	-1	0.75	-0.25
3	8	2	0.8	-0.8	0.25	1.2	1.25	-0.7	-0.15	-2	-1.5	1.4	0.13
4	10	2.25	1.1	-1.2	0.2	1.25	1.5	-1	0.15	-2.7	-2.5	2	0
5	1	2	1.4	-0.75	0.1	1.4	1.15	-0.8	-0.4	-1	-0.9	1.25	0.5
6	8	2	1.25	-1.25	0.25	1.2	1.7	-1	-0.15	-3.5	-3.2	1.1	0.2
wt ave		2.09	1.12	-1.09	0.23	1.23	1.48	-0.90	-0.06	-2.52	-2.23	1.45	0.08
wt stdev		0.22	0.41	0.23	0.04	0.10	0.22	0.15	0.24	0.92	0.91	0.48	0.17
CoV		0.11	0.37	-0.21	0.17	0.08	0.15	-0.16	-3.95	-0.36	-0.41	0.33	2.08

Table 10-3. Strain rates during recovery after shut-in in nanostrain/hr for different strain components and different strainmeters during the summer 2022 injection tests at the North Avant Field.

		AVN2				AVN22				AVN31			
Test	wt	$\dot{\varepsilon}$NS	$\dot{\varepsilon}$EW	$\dot{\varepsilon}$ZZ	$\dot{\varepsilon}$Sh	$\dot{\varepsilon}$NS	$\dot{\varepsilon}$EW	$\dot{\varepsilon}$ZZ	$\dot{\varepsilon}$Sh	$\dot{\varepsilon}$NS	$\dot{\varepsilon}$EW	$\dot{\varepsilon}$ZZ	$\dot{\varepsilon}$Sh
1	1	-0.6	-0.5	0.35	-0.1	-0.1	-0.7	0.15	-0.5	0.7	0.35	-0.4	-0.25
2	2	-0.75	-0.25	0.35	-0.25	-0.3	-0.45	0.25	0.05	1.8	1.1	-1.0	0.2
3	10	-1.0	-0.45	0.4	0.15	-0.6	-0.9	0.45	0.25	3.0	2.5	-2.5	0
4	1	-0.25	0.6	-0.25	0.2	-0.25	-0.4	0.1	0.6	1.9	1.25	-1.2	0.5
5	1	-0.7	-0.7	0.35	0	-0.15	-0.4	0.25	-0.2	1.8	1.5	-1.8	0.8
6	6	-0.75	-0.3	0.3	-0.2	-0.9	-0.7	0.45	-0.1	3.7	2.4	-2.2	0.7
wt ave		-0.84	-0.35	0.33	0.00	-0.60	-0.74	0.39	0.09	2.87	2.13	-2.08	0.27
wt stdev		0.27	0.28	0.17	0.19	0.36	0.26	0.18	0.27	1.18	0.96	0.91	0.38
CoV		-0.32	-0.78	0.53	-41	-0.60	-0.34	0.45	3.0	0.41	0.45	-0.44	1.4

10.6.2 Log transform and reservoir of infinite extent

The data were analyzed using a log transform and the best fit straight line was estimated using the approach for analyzing a type curve for an infinitely acting reservoir. The t_o time intercept was determined along with the semi-log slope.

The results indicate that the values of to and semi-log slope range broadly and they generally increase with the duration of pumping. This is inconsistent with the response from a reservoir of infinite extent, but it is a likely response with interactions with multiple reservoir boundaries, which steepen the drawdown response relative to that occurring in a reservoir of infinite extent. This complicates the interpretation of to and semi-log slope, but nevertheless, we assume that to and semi-log slope from the pressure are characteristic values that could be used to interpret the test using the appropriate conceptual model.

The t_o/r^2 values determined from the shallow strain tensor data are essentially the same at the values determined from the pressure data (Figure 10-14). However, t_o/r^2 at the deep strainmeter AVN31 only increases slightly with t_o/r^2.

The semi-long slopes of the strain data are correlated to slopes from the pressure data. The correlation is approximately 0.48 nε/kPa (Figure 10-14).

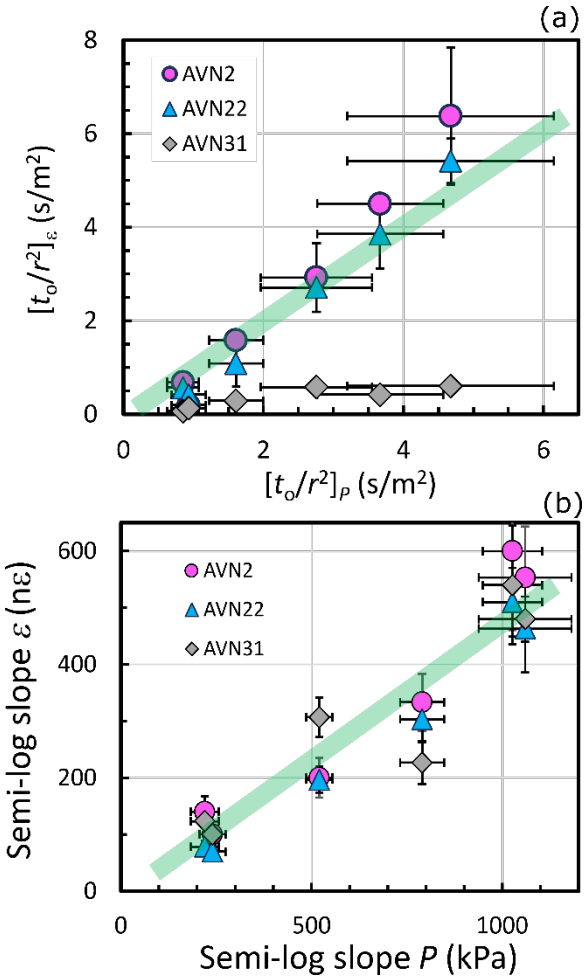

Figure 10-15. Result of log transform analyses of pressure and strain data from six injection tests at North Avant Field. (a) The ratio t_o/r^2 determined from strain tensor data at different locations as a function of the ratio determined from pressure data, where r is the radial distance from the injection well to the observation point. Data are mean values from three normal strains at each strainmeter and the pressures from four monitoring wells. Error bars are 1 standard deviation. Green line has a slope of unity. (b) Semi-long slopes of strain and pressure data. Means and standard deviations determined as in (a). Green line has a slope of 0.48 nε/kPa.

10.6.3 Power function approximation

The pressure and strain data during injection were manually fit with a power function, $y = ax^b$, by plotting the data using a log-log transform. The fits in most cases were quite good, but data in the vicinity of t = 100 hrs was used preferrrentially when some variation existed over the duration of the test. The coefficient, a, and exponent, b, were determined for each dataset and weighted averages and standard deviations were calculated (Tables 10-4 thru 10-7). Tests with irregular injection rates or anomalous behavior were weighted less than other tests. The weighted average

values for *a* and *b* were used to calculate an expected response for an injection of 0.0019 m^3/s for a 100 hr duration (Figure 10-15). Envelopes about the average strain and pressure responses were estimated using +/- one standard deviation of *a* while fixing *b* to the average value.

Both the pressure and the strain are slightly non-linear with a negative curvature as indicated by $b < 1$ (Tables 10-4 and 10-6). For example, $0.87 < b < 0.99$ for the normal strains at the shallow strainmeters, and it is smaller at the deep strainmeter $0.71 < b < 0.79$. The exponents describing the pressure response are in the same range as that of the strain from the shallow instruments ($0.93 < b < 1.06$).

The variability in the coefficients controls the uncertainty, or the height of the colored envelopes in the idealized data (Figure 10-15). The coefficient of variation, CoV, in ranges up to 0.32, but it is less than 0.17 for four of the six datasets from the shallow strainmeter, and it is generally larger, in the range of $0.27 < (CoV)_a < 0.32$ at the deep strainmeter, AVN31 (Table 10-4). The CoV from the pressures is considerably smaller than for the strains, in the range of $0.03 < (CoV)_a < 0.12$.

The relative magnitudes of the different strain components at each instrument in Figure 10-15 are similar to those shown in the idealized time series determined using the average strain rates (Figure 10-13). The results in Figure 10-13 are probably a slightly better representation of the data because they have the negative curvature that characterizes most of the injection data.

The data shown in Figure 10-15 after the pump was turned off are linear and they are the same results used in Figure 10-13. In general, there is a positive curvature to both the strain and pressure during recovery. The curvature is small, however, and the variability during recovery is larger than during injection, so we elected to ignore the curvature and characterize recovery using average rates.

Table 10-4. Exponents, *b,* in power function approximation ($n\varepsilon = at^b$) of strain tensor data from six injections tests at North Avant Field, summer 2022.

test	wt	AVN2, *r* = 222 m			AVN22, *r* = 240 m			AVN31, *r* = 520 m		
		NS	EW	ZZ	NS	EW	ZZ	NS	EW	ZZ
		222	222	222	240	240	240	520	520	520
1	1	1.1	1.4	1.2	1	1.15	0.9	0.4	0.2	0.3
2	2	0.8	0.8	0.8	1	1	1	0.7	0.7	0.78
3	6	0.87	1	0.9	1.1	0.85	0.9	0.4	0.3	0.12
4	10	0.9	0.9	0.9	0.95	0.8	0.85	0.85	1.1	0.9
5	0	0.8	0.3	0.4	1.1	0.7	0.85	1.1	1.7	1.4
6	10	0.9	0.9	0.9	0.95	0.9	0.9	1	0.85	0.9
wt average		0.89	0.93	0.90	0.99	0.87	0.89	0.78	0.79	0.71
wt std dev		0.05	0.11	0.07	0.07	0.09	0.04	0.26	0.35	0.36
CoV		0.06	0.12	0.08	0.07	0.10	0.05	0.33	0.44	0.51

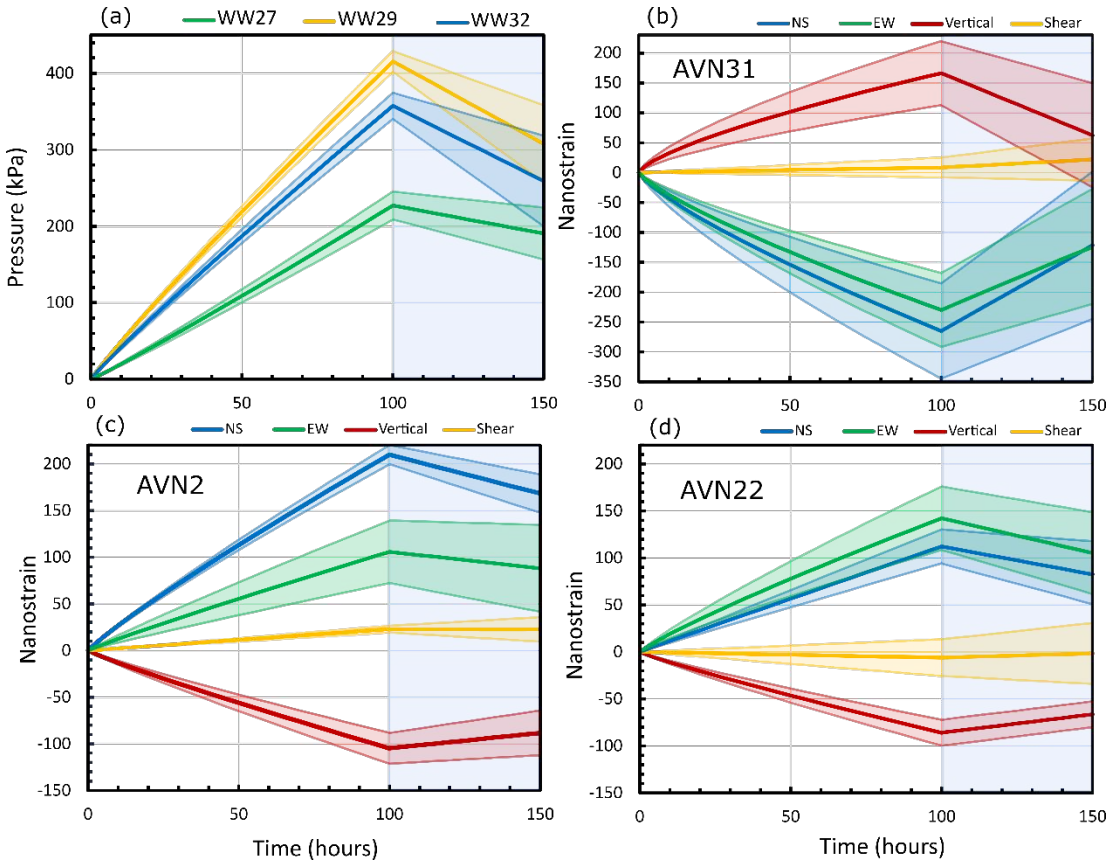

Figure 10-16. Time series determined by fitting power functions $y = ax^b$ to strain and pressure data during the injection phase of a well test. Injection occurs for 100 hrs long at a rate of 0.0019 m^3/s. Solid lines are from weighted mean values of coefficient, *a*, and exponent, *b*. Lines bounding the colored regions enveloping each line are determined using +/- 1 weighted standard deviation of the coefficient. No injection occurs after t=100hrs (light blue shaded region). Linear functions are assumed for shut-in. (a) Pressure at monitoring wells; (b) Strains at AVN31; (c) strains at AVN2; (d) strains at AVN2. Based on data in Tables 10-4 thru 10-7.

Table 10-5. Coefficients, *a*, in power function approximation ($n\varepsilon = at^b$) of strain tensor data. Units are in $n\varepsilon/hr^b$

		AVN2			AVN22			AVN31		
test	wt	NS	EW	ZZ	NS	EW	ZZ	NS	EW	ZZ
1	1	3.75	2.75	2.34	1.28	3.08	1.41	4.90	3.42	4.19
2	2	3.26	1.65	1.56	1.17	3.08	1.33	3.26	2.37	2.67
3	10	3.26	0.96	1.40	0.96	1.81	1.16	5.44	5.27	4.57
4	8	3.42	1.44	1.56	1.39	2.72	1.50	8.16	6.32	7.62
5	0	1.63	1.79	2.81	0.85	1.81	1.00	3.54	3.69	3.43
6	10	3.59	1.79	1.87	1.28	3.08	1.66	9.25	7.64	8.00
wt average		3.42	1.45	1.64	1.20	2.58	1.43	7.21	6.06	6.33
wt std dev		0.17	0.46	0.26	0.19	0.61	0.23	2.17	1.63	2.04
CoV		0.05	0.32	0.16	0.16	0.24	0.16	0.30	0.27	0.32

Table 10-6. Exponents, *b*, in power function approximation of pressure data during injection from six tests at North Avant Field, summer 2022.

test	wt	WW27	WW29	WW32	WW60
1	1	1.3	2	1.3	1.3
2	2	1.22	1.1	1.1	1.2
3	6	1	0.85	0.85	0.78
4	10	1.1	0.9	0.95	1.05
5	0	1.85	1.15	1.15	1.85
6	10	1	0.85	0.9	1
wt average		1.06	0.92	0.93	1.00
wt std dev		0.09	0.24	0.10	0.14
CoV		0.08	0.26	0.11	0.15

Table 10-7. Coefficients, *a*, of power function approximation of pressure data during injection from six tests at North Avant Field, summer 2022.

test	wt	WW27	WW29	WW32	WW60
1	1	1.37	5.67	5.41	0.71
2	2	1.67	5.96	5.14	1.43
3	10	1.59	5.96	5.00	1.53
4	8	1.82	6.10	4.60	1.63
5	0	1.52	5.67	4.06	0.76
6	10	1.82	5.67	4.73	1.53
	wt average	1.72	5.89	4.83	1.52
	wt std dev	0.14	0.19	0.23	0.18
	CoV	0.08	0.03	0.05	0.12

CHAPTER ELEVEN

EVALUATION OF STRAIN FROM POINT LOADS AT THE GROUND SURFACE AND PUMPING TESTS IN UNCONFINED AQUIFERS

Contents

11.1 Abstract 11-2
11.2 Introduction 11-3
11.3 Strain from point loads 11-3
11.3.1 Simulations 11-5
11.3.2 Field Experiments 11-12
11.4 Strain in an Unconfined Aquifer During Well Tests 11-13
11.4.1 Field Experiments 11-15
11.4.2 Simulations 11-18
11.4.3 Conclusion 11-20
11.5 References 11-21

EVALUATION OF STRAIN FROM POINT LOADS AT THE GROUND SURFACE AND PUMPING TESTS IN UNCONFINED AQUIFERS

11.1 ABSTRACT

Point loads applied at the ground surface and pumping tests in unconfined aquifers will cause strain that reflects subsurface material properties, so in principle it should be feasible to use these tests to evaluate the subsurface. Point load tests are particularly easy to conduct, so we evaluated the feasibility of conducting and evaluating these tests. The results indicate that vertical strain measurements from point load tests can be used to estimate the average elastic modulus of the subsurface, and strain tensor data should be capable of estimating poisson's ratio. A procedure for measuring strain caused by point loads applied to various different locations appears to be a viable method for estimating spatial variations in elastic properties. Transient strain measurements made during point loading in saturated material vary increase as a function of time apparently in response to pore pressure changes. This suggests that transient strain responses to point loads in saturated groud could be used to characterize permeability. Strain measurements in the vadose zone during a pumping test in an underlying unconfined aquifer change with time in a pattern that resembles the pressure change in the aquifer. The vertical strain in the vadose zone increases (becomes more tensile) with time during pumping, and reverses during recovery. The magnitude of the strain response is greatest slighly above the aquifer and it decreases with distance above the water table. A strain response was measured throughout the 9-m-thick vadose zone. Strain at the deepest measurement point was an exception to the general behavior. The strain there was greatest after pumping for ½ hr, but then it increased steadily throughout the remainder of the test. This response appears to be caused by pumping-induced changes in the pore pressure propagating upward into the vadose zone. The pressure changes reached the deepest strain sensor, but not the next one above it. Pressure propagation upward above the water table will be controlled by the relative permeability and water retention functions. This finding suggests that strain measurements in the vadose zone made during pumping in an unconfined aquifer could be used to estimate hydrologic properties of both the aquifer and the overlying vadose zone.

EVALUATION OF STRAIN FROM POINT LOADS AT THE GROUND SURFACE AND PUMPING TESTS IN UNCONFINED AQUIFER

11.2 INTRODUCTION

We conducted preliminary work evaluating the use of strain data caused by point loads at the ground surface and pumping tests in unconfined aquifers to characterize the subsurface. The work consists of simulations to evaluate parameter sensitivity and preliminary field tests. The measurements were made using the Michelson Interferometers and the CMPI technique developed for the project. Results from these tests serve to identify potential applications for strain measurements to characterize the subsurface, and they were also used by us to refine the measurement methods.

The field experiments conducted for this investigation took place at the Clemson Bull Farm field testing site, which is located near Pendleton, SC in the Piedmont Physiographic province on undeveloped pastureland. The topography is gently rolling and the soil column consists of a thin A horizon with a low permeability B horizon that extends to approximately 2.5 m below ground surface (bgs). Beneath the soil profile is an unconfined aquifer composed of biotite gneiss-derived saprolite to a depth of approximately 30 m, with crystalline bedrock below. The average water table depth is approximately 9 m bgs.

Ambient environmental data, including precipitation, evapotranspiration, air temperature, barometric pressure, water table elevation and temperature, and the subsurface temperature from the ground surface to a depth of 10 m is monitored at the site.

Strain sensing technologies deployed at the site include, five DEL-Xs (Murdoch et al., 2015), two of which are in the saturated zone, a CMPI tensor strainmeter, a CMPI-Fiber Optic Extensometer (FOX), and a Michelson-FOX. There is also a Michelson tensor strainmeter installed in the bedrock. The locations of the instruments are shown in cross section in Figure 11-1.

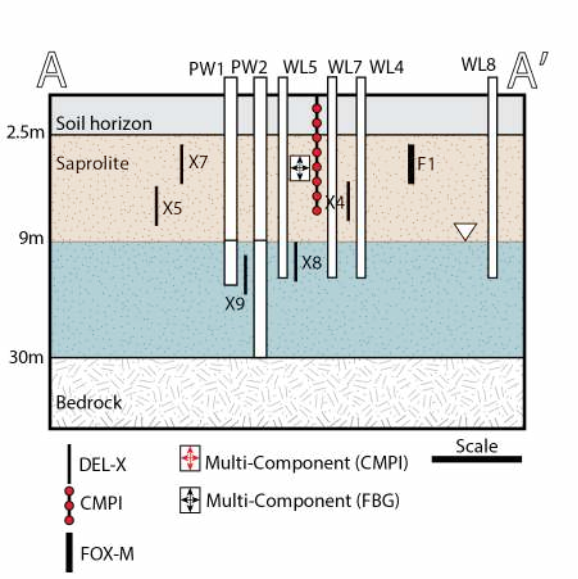

Figure 11-1. Cross section of the Simpson Station field site.

11.3 STRAIN FROM POINT LOADS

Point loads at the ground surface are typically created by moving an object with a known weight to a known location in the vicinity of the strainmeter and then removing it. This process is repeated several times as a cycle to account for background trends.

One application of this type of test is to vary the magnitude of the point load and measure the resulting change in strain. These data could be evaluated to estimate average elastic

properties of the subsurface. This approach can be extended by applying a load at multiple locations and then using the results to estimate heterogeneities in elastic properties.

The strain resulting from a sudden application of load may change with time in response to poroelastic processes. It may be feasible to characterize poroelastic processes, such as fluid flow caused by mechanical loading, by interpreting the transient strain following a sudden application of load.

Point load tests were first conducted at the Clemson field site using DEL-X extensometers (Murdoch, et al., 2015). These instruments record the relative vertical displacements between two cylindrical anchors in frictional contact with the surrounding material. The anchors are separated by a distance of 1.5 m and the vertical strain may be obtained by dividing the observed relative displacement by this gauge length.

Mechanical point load experiments were used to evaluate the sensitivity of these instruments and characterize the stiffness of the enveloping material (Freeman, 2012; Thrash, 2016). These tests were performed by repeatedly approaching the casing in which the instrument was installed. The relative displacement between the anchors decreased during loading and increased when unloaded (Figure 11-2), indicating compressive and tensile vertical strains, respectively. These data have been used to provide estimates of the Young's modulus in the vadose zone at the field site (Thrash, 2016). Interestingly, the estimates of the Young's modulus by Thrash (2016) were found to vary with time, but the mechanism explaining this variation remains uncertain. Subsequent laboratory testing has revealed that the Young's modulus of the saprolite at the field site varies with water content, and the values differ for two samples. In one sample, the modulus is E = 57 MPa for nearly saturated conditions ($\theta = 0.44$, porosity = 0.45) and it increases to E = 72 MPa for drained conditions ($\theta = 0.30$). In another sample, E = 42 MPa for nearly saturated conditino ($\theta = 0.53$; porosity = 0.56) and the modulus increases to E = 48 MPa for drained conditions, $\theta = 0.40$.

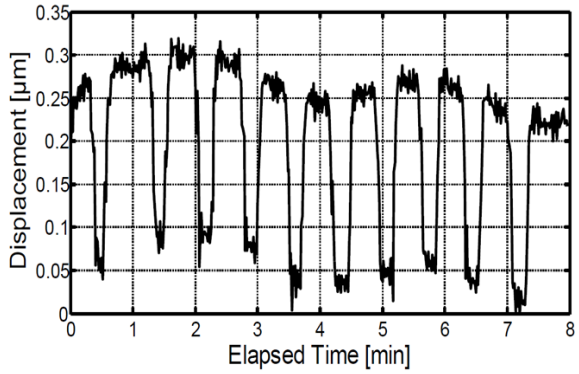

Figure 11-2. Displacements during repeated applications and removal of a point load cause by a person walking over the extensometer and then retreating. Top of the extensometer is at 6 m (Thrash, 2016).

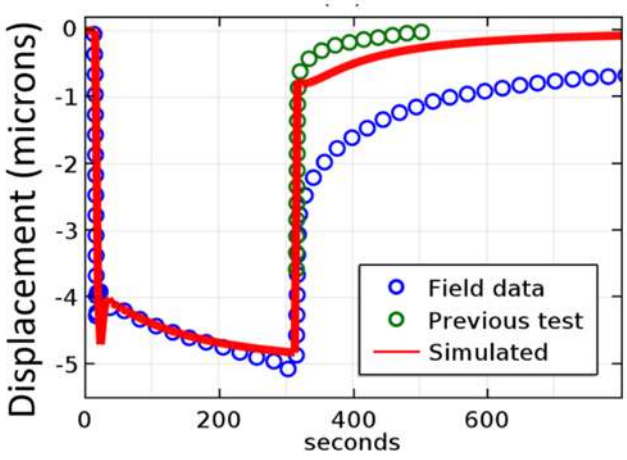

Figure 11-3. Vertical displacement data from DEL-X extensometer installed in saturated zone at depth of 3m during vehicle loading test. Transient following the initial displacement caused by poroelastic effects.

Mechanical load tests have also been performed to evaluate the response of extensometers deployed in saturated conditions using the weight of a vehicle (Moak et al., 2016). For this test, the DEL-X extensometer was installed at a depth of approximately 3 m in loess at a site near Pullman, WA. The water table was located between the two anchors of the extensometer at a depth of approximately 3.5 m, and the capillary fringe extended near the top anchor, creating saturated conditions.

As with the body weight load tests, compression was observed during loading and extension during unloading; however, additional displacement at a much slower rate was observed after the instantaneous displacement from changing the load (Figure 11-3). Numerical analysis revealed that this response is due to a pressure transience caused by the changing load. When a load is applied to a fluid saturated porous medium, the compression of the solid skeleton pressurizes the pore fluid, inducing a pressure gradient that causes flow. The resulting drainage and imbibition controls the rate of deformation. This is a well-known poroelastic phenomenon called the Skempton effect (Wang, 2000b), where the Skempton coefficient (β) relates changes in pore pressure, p, to changes in applied stress

$$\beta = \frac{\partial p}{\partial \sigma} \qquad 11\text{-}1$$

This effect has been used to understand fluctuations in water levels caused by passing trains (Jacob, 1939), or the mechanical loading of aquifers from changes in the stage of overlying streams (Boutt, 2010).

11.3.1 Simulations

Applying a point load at the ground surface, such as from the weight of a person, results in compression and extension of the underlying material in a predictable pattern that spreads laterally with depth. This behavior is well known for elastic solids, but little work has been done to characterize this effect for porous materials with variable saturation. We used the methods in Chapter Five and analyzed the poroelastic response of a 30 m thick layer of saprolite with variable saturation from a 68 kg (150 lb.) point load at the ground surface (Figure 11-4). The model was intended to represent conditions at the field site and used material properties obtained from laboratory and field tests. Three separate horizons were included in the site model: the B-horizon, saprolite (both saturated and unsaturated), and the underlying bedrock at 30 m depth bgs.

The model used properties for saprolite that were either measured in the laboratory or estimated (Table 11-1). Underlying rock was represented as a stiff, low permeability basement with E = 20 GPa, $k = 10^{-25}$ m^2 and $\phi = 0.01$.

Table 11-1. Material properties of saprolite from laboratory measurements and used in simulations.

Parameter	Unit	Lab	Simulations
Permeability (k)	m^2	9×10^{-13}	7×10^{-13}
Van Genuchten (α)	1/m	0.6	0.6
Van Genuchten (n)	dim	1.3	1.5
Porosity, ϕ	dim	Sample 1: 0.45 Sample 2: 0.56	0.5
Residual water content, θ_r	dim	0.0 0.07	0.0
Pore Fluid Compressibility (C_f)	1/Pa	--	8×10^{-8}
Young's Modulus (E) sample 1	MPa	57 MPa; $\theta = 0.44$, $\phi = 0.45$ 72 MPa, $\theta = 0.3$	Lu and Kaya E_{s1}: 57 Mpa; $\theta_1 = 0.44$ E_{s2}: 72 Mpa; $\theta_2 = 0.3$ $m = 1$
Young's Modulus (E) sample 2	MPa	42 MPa; $\theta = 0.53$, $\phi = 0.56$ 48 MPa, $\theta = 0.4$	

11.3.2 Strains beneath a point load

Results indicate that normal, areal and volumetric strains, as well as tilts, occur within the resolution of our instruments beneath the load at depths ranging from the ground surface to the bedrock at 30 m (Figure 11-4a-e). Additionally, modest pressure perturbations on the scale of 1-10 Pa occur near the water table and capillary fringe (Figure 11-4f). Identification of these pressure signals in monitoring wells would be difficult due to the effect of wellbore storage, but isolating the screened interval with a hydraulic packer could minimize this effect.

Compressive vertical strains occur beneath the load and extend all the way to the bedrock at a depth of 30 m, and extend laterally to a distance of roughly 15 m, or half the total depth (Figure 11-4a). The radial strains are more complex, with a narrow lobe of tensile strains beneath the load extending to the bedrock, and a compressive band extending diagonally beneath the load, with some tensile strains along the ground surface adjacent to the point of loading (Figure 11-4b).

The areal strains produced by the load are tensile and spread laterally with depth down to the bedrock (Figure 11-4c), whereas the volumetric strains are compressive and spread laterally with depth to the water table. Interestingly, volumetric strains are predicted to be less than 1 ne in the saturated zone (Figure 11-4d).

Directly beneath the load, tilting is oriented outwards and this pattern spreads laterally with depth. At greater distances, tilting is oriented towards the load and is greatest near the surface (Figure 11-4e).

A time series of the normal strains directly beneath the load compresses vertically and extends radially (Figure 11-5), with the vertical compression in the saturated zone (depths ≥ 9m) is transient after the load is applied (Figure 11-5b). This is due to the Skempton effect (eq. 11-1).

The elevation in pore pressure caused by compression of the solid skeleton creates a pressure gradient that diffuses at a rate proportional to the hydraulic diffusivity of the formation, resulting in further axial compression until the background pressure is reached. Thus, the instantaneous compression upon loading is related to the undrained Young's modulus (E_u) of the formation and the total compression after diffusion of the pore fluid is related to the drained Young's modulus (E) with a timescale determined by the diffusivity (D). Interestingly, a delayed tensile axial strain is observed at a depth of 12 m after the load is applied, before resuming compression (Figure 11-5b). This is due to the depth of the measurement point being 3 m below the water table, which results in a delayed arrival of the pressure wave initiating at the capillary fringe with a timescale of arrival related to the depth and diffusivity (D), given by:

$$t_p = \frac{L^2}{4D} \qquad 11\text{-}2$$

where t_p is the time of arrival of the pressure wave and L is the distance between the measurement point and origin of the diffusive pressure wave.

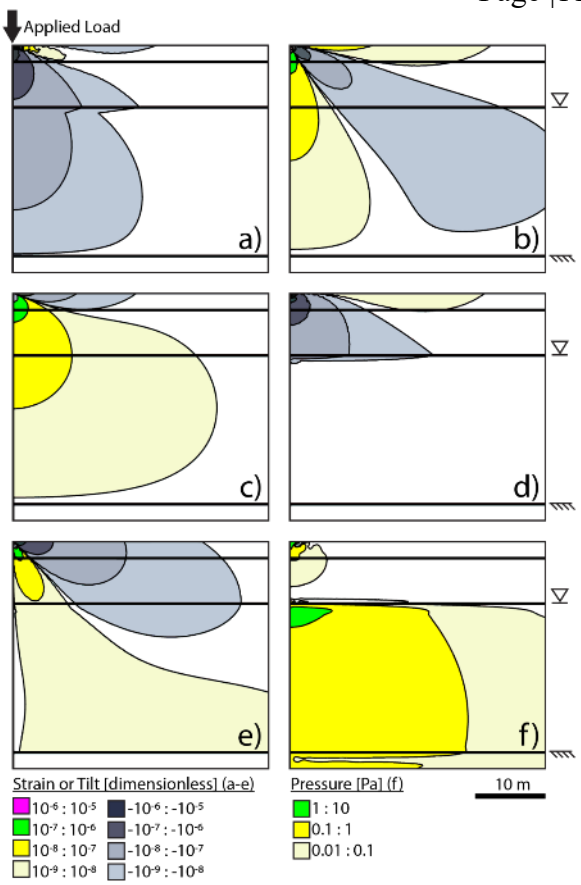

Figure 11-4. Patterns of deformation and pressure from a point load. Included are a) Vertical Strain, b) Radial Strain, c) Areal Strain, d) Volumetric Strain, e) Tilt, and f) Pressure. The lower horizontal line is the contact between saprolite and rock (the lower boundary of the model is not shown), but middle black line is the initial location of the water table, and the upper black line is not relevant to the simulations.

11.3.3 Sensitivity analysis

To better understand the factors controlling the deformation observed in response to point loads, a sensitivity analysis was performed by sweeping through different values of the key model parameters, namely: water table elevation, z_{WT}, the van Genuchten retention curve parameters α and *n*, the drained Young's modulus, *E,* and drained Poisson's ratio, ν, as well as the hydraulic conductivity, *K*.

The results from the analysis (Figure 11-6) indicate that vertical strains in the vadose zone from mechanical loading are sensitive to the Young's modulus, and pore size distribution parameter *n*, while the vertical strains in the saturated zone are most sensitive to the elevation of the capillary fringe, Young's modulus, the hydraulic conductivity and are moderately sensitive to the Poisson's ratio.

The vertical strain signals from the sensitivity analysis were evaluated at a depth of 5 and 10 m below ground surface (bgs), with the water table located at a depth of 9 m bgs unless specified otherwise.

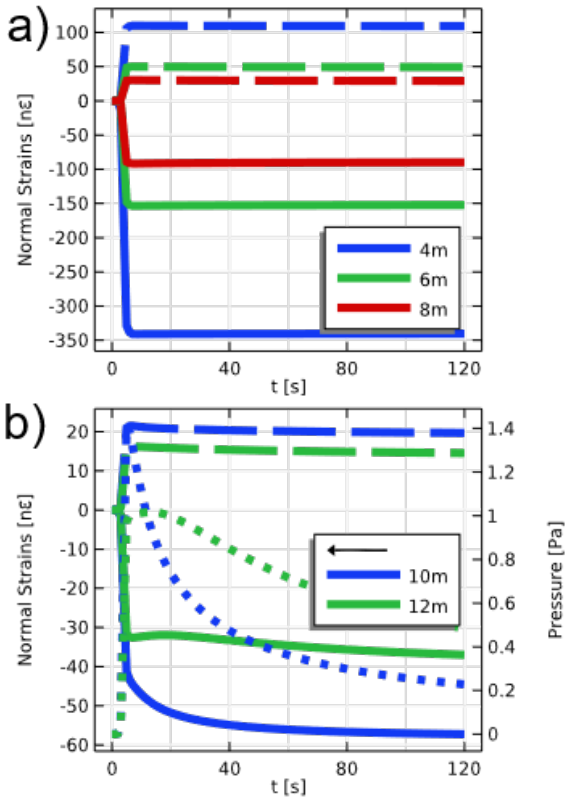

Figure 11-5. Time series of vertical strain (solid), radial strain (dashed) and fluid pressures (dotted) in a) the vadose zone and b) the saturated zone from the weight of a person.

The Young's modulus was varied between 50 and 75 MPa (Figure 11-6a and b), which is the range obtained from laboratory testing for ambient and saturated water contents (Table 11-1). At 5 m depth, the vertical strains range from 175 nε for a modulus of 75 MPa, to 275 ne for a modulus of 50 MPa. At 10 m depth, vertical strains range from approximately 45 to 70 nε for the same values of Young's modulus. This results in a sensitivity of approximately 4 nε/MPa at 5 m depth and 1 nε/MPa at 10 m depth from a 68 kg point load.

The Poisson's ratio was evaluated for the full range of 0 to 0.5. The average value for most rocks and soils is around 0.2-0.3, and a value of 0.5 indicates an incompressible material. The vertical strain showed little variation in either the vadose or saturated zone from application of a point load (Figure 11-6c and d), but the sensitivity of the radial strain would likely be much higher.

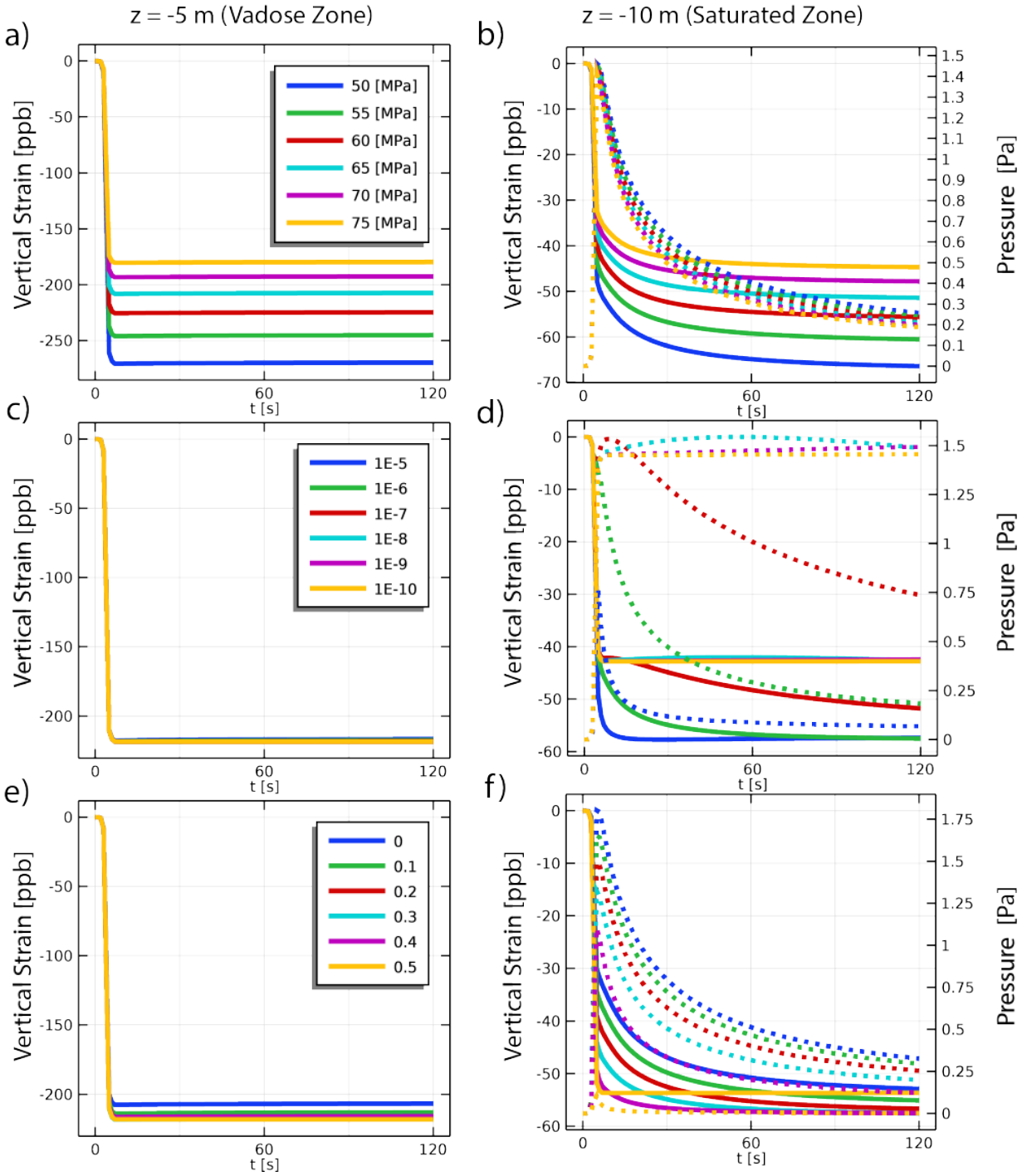

Figure 11-6. Sensitivity of vertical strain (solid lines) and pressure (dotted lines) signals in the vadose and saturated zones from a 68 kg (150 lb.) point load to changes in Young's modulus (a-b), Poisson's ratio (c-d), and hydraulic conductivity (e-f).

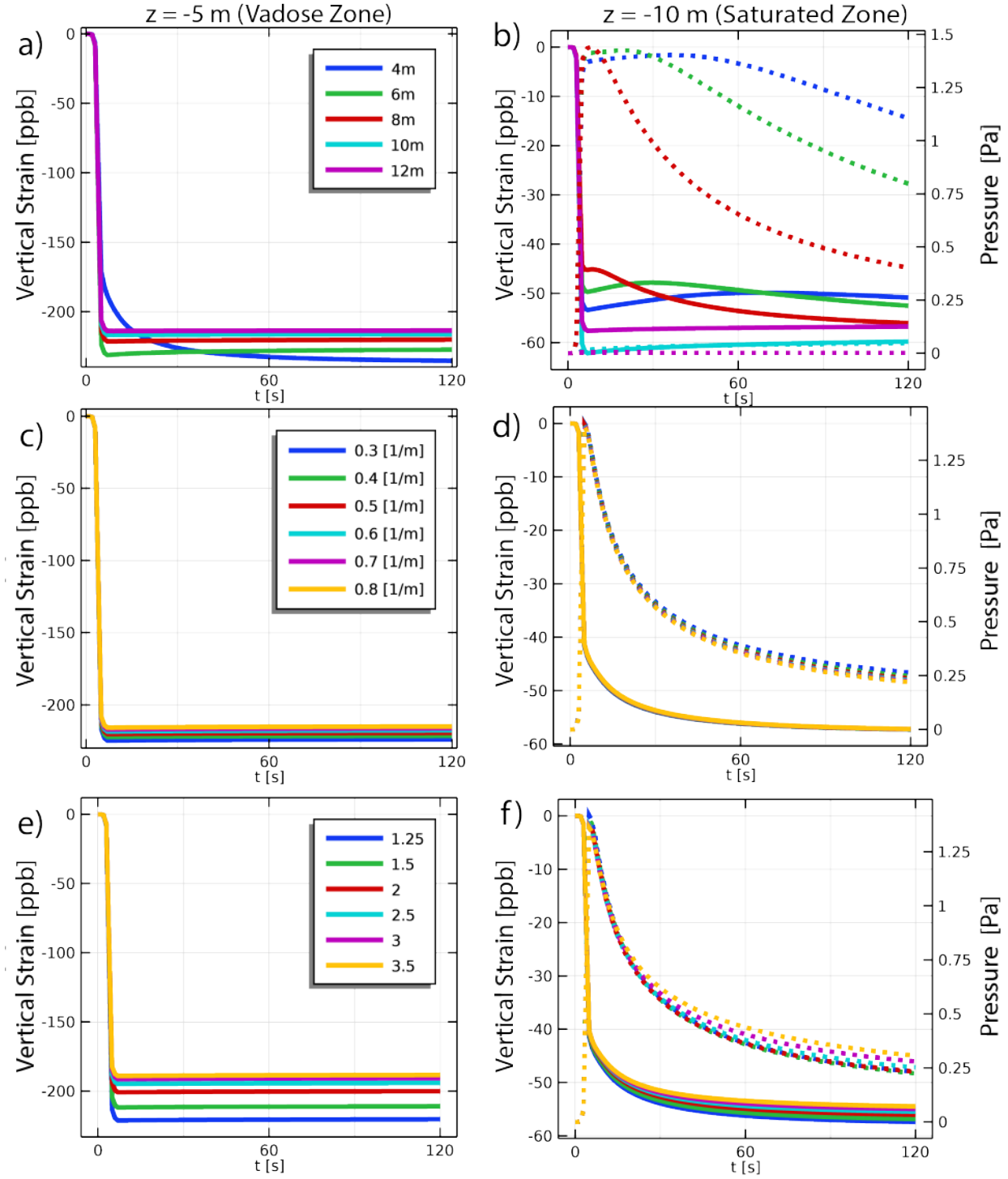

Figure 11-7. Vertical strain (solid lines) and pressure (dotted lines) signals in the vadose and saturated zones caused by a 68 kg (150 lb.) point load. (a-b) effects due to changes in water table elevation, (c-d) α in van genuchten equation, and (e-f) *n* in van genuchten equation.

The effect of the permeability was evaluated for values ranging from 10^{-12} to 10^{-17} m^2, which corresponds to a saturated hydraulic conductivity ranging from 10^{-5} to 10^{-10} m/s, which are values typical of silty sands and low permeability clays, respectively. Due to the compressibility of the pore fluid, the vertical strain in the vadose zone is insensitive to changes in the permeability or hydraulic conductivity (Figure 11-6e). In the saturated zone, however, decreases in the hydraulic conductivity caused the rate of compression to decrease markedly (Figure 11-6f). Equilibrium was reached nearly instantly compared to the timescale of the simulation for a hydraulic conductivity of 10^{-5} m/s, and the pressure remained essentially unchanged for values of K less than 10^{-8} m/s (Figure 11-6f).

The sensitivity of the vertical strain to the water table elevation was evaluated for values between 4 and 12 m bgs (Figure 11-7a and b). The water table elevation relative to the measurement point determined whether a change in the axial strain was observed Additionally, measurement points located 2 m or more from the water table observed a delayed tensile strain related to the arrival of the pressure wave, with the timescale increasing with increasing distance (Figure 11-7b). This indicates that mechanical loading tests could potentially be used to estimate the elevation of the water table and the diffusivity of the formation.

In general, the retention curve parameters only had a modest effect on the vertical strain in the vadose zone. Higher values of the pore size distribution parameter (n) led to a decrease in the observed axial strain in the vadose zone (Figure 11-7e), but had little effect on strains in the saturated zone (Figure 11-7f), whereas α, which is related to the air entry pressure, had little to no effect on the pressure or strain signals during loading (Figure 11-7c and d).

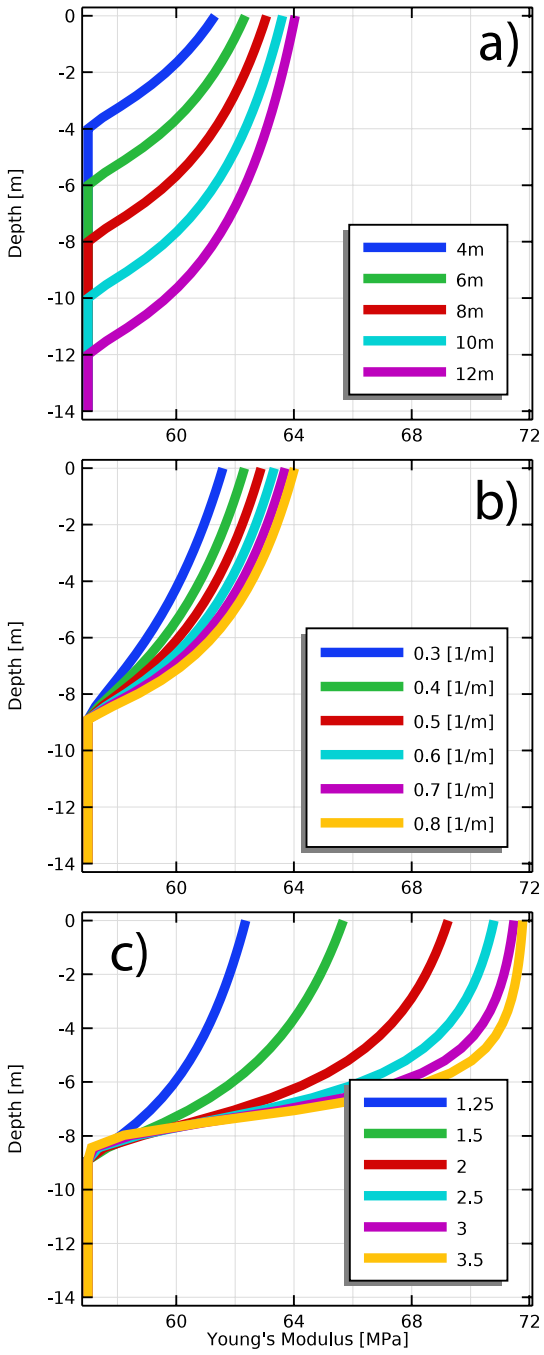

Figure 11-8. Saturation-dependent Young's modulus with depth for changes in a) water table elevation, b) α in the van genuchten equation, and c) n in the van genuchten equation.

Sensitivity of the strain to changes in the elevation of the capillary fringe and the retention curve parameters is in part due to the effect

these values have on the saturation profile through the vadose zone, which in turn leads to a change in the saturation-dependent Young's modulus (Figure 11-8). This is an intriguing concept, as deformation in response to known loads could provide an estimate of the degree of saturation, the stiffness of the material, and the state of stress in the vadose zone - all of which are used to predict the strength and stability of soils for geotechnical applications (Lu & Likos, 2004). For instance, increases in the degree of saturation increase the body force load, pore pressure and effective stress, while decreasing the stiffness. These effects will produce tensile strains in the zone of imbibition. Additionally, the load caused by the weight of the water will produce a mechanical load on the underlying material, which will decrease the effective stress, leading to compression.

11.3.4 Field Experiments

A series of mechanical loading experiments were performed using the weight of a person to evaluate the response of the Michelson fiber-optic strain ribbon that functions as a vertical extensometer (MR-1) deployed at 3.35 m depth at the Simpson Station field site. The purpose of the test was to evaluate the sensitivity of the instrument to mechanical point loads at the ground surface, and to characterize the local elastic material properties.

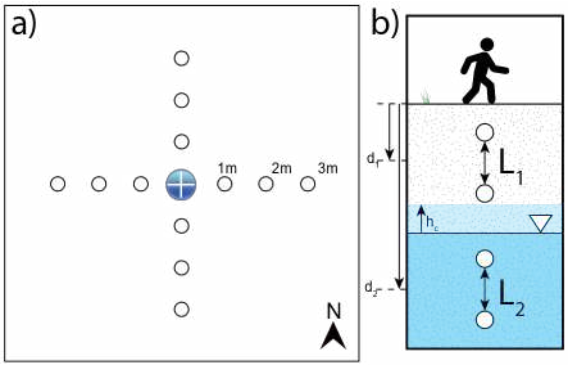

Figure 11-9. a) Map view of loading test locations. b) Conceptual model of load test design. Strain at depth d is taken as the change in gauge length L due to the applied load. The height of capillary rise is indicated by h_c.

Mechanical loading at the ground surface from the weight of a person or vehicle offers a convenient method for characterizing the instrument response of shallow deformation sensors. The magnitude, rate and location of loading may be controlled, allowing for determination of the instrument load sensitivity, and there are many analytical solutions that may be used for interpretation and estimation of the local material properties. We have designed a mechanical loading experiment to characterize the instrument response function of a shallow fiber-optic extensometer. The experiment consists of loading the ground above the instruments with a known force at a known location (Figure 11-9).. The procedure was to step back-and-forth between two points separated by 1 m at a period of 30 s. The weight of the person doing the test provides the load. This process is repeated multiple times at distances of 1, 2, 3, 4, 5, and 6 m from the instrument in each of the four cardinal directions to obtain robust test statistics.

As an example, moving the point load from r = 1m to r = 2m causes the strain at depth to increase abruptly, overshoot slightly and then stablize. Moving the load back from r = 2m to r = 1m, causes the strain to drop as the ground is compressed. Repeating this process multiple times results in a sequence of steps with magnitudes that are fairly consistent and that drift slightly with time. The magnitude of the step in the 1-2m range is approximately 100 nε and it decreases with distance to roughly 5 nε at a distance of 5-6m (Figure 11-11). The response at each location is generally repeatable, and longer period trends reflect fluctuations in barometric pressure

loading. These data are analyzed by correcting for the longer period trend and then measuring the amplitude of each step. This gives a dataset of approximately 24 values for calculating the mean and uncertainty.

The results from the loading test were interpreted using the Boussninesq solution for a point load on an elastic half-space with a known Young's modulus and Poisson's ratio. The Boussinesq solution gives the displacements in an elastic medium in a 2D axisymmetric coordinate system. The resulting strains are obtained by taking the derivative of the displacements. Vertical strain from the analytical solution using a Young's modulus of 100 MPa and a Poisson's ratio of 0.25 is similar to the strain observed in the field (Figure 11-11). This value for Young's Modulus is consistent with values obtained using other field methods and from triaxial tests.

11.4 Strain in an Unconfined Aquifer During Well Tests

Most of the applications for strain monitoring for carbon storage are focused on projects where CO_2 is stored in a permeable layer that is overlain by a low permeability, confining formation or a caprock. As a result, there is typically a sharp discontinuity in permeability between a confined aquifer and the overlying confining unit.

Surficial aquifers are bounded on the top by the water table, not by a contrast in permeability. The permeability of an ideal surficial aquifer is uniform across the water table, so the top of the aquifer is only defined by a change in saturation marking the transition to the overlying vadose zone.

The differences in the upper boundary between confined and unconfined aquifers affects processes of storage change during injection or pumping from a well. Storage change in confined aquifers is controlled by the compressibility of the fluids and solids in the aquifer, whereas, whereas storage in unconfined aquifers can be affected by pore drainage or imbibition as the water table fluctuates in response to pumping.

In previous work (Murdoch et al. 2019, 2020, 2021, 2023) we evaluated the effects of well testing on strain in the formations over confined aquifers. We also assumed the aquifers were confined in the poroelastic simulations presented in Chapters 9 and 12 in this report. The aquifer at the Clemson field testing site is unconfined, so our assumption that it is confined was made to simplify the analysis. We are confident that this assumption has negligible effect on the important conclusions derived from the analyses in Chapter 12. Nevertheless, to our knowledge, little work is available describing simulations of strain in unconfined aquifers.

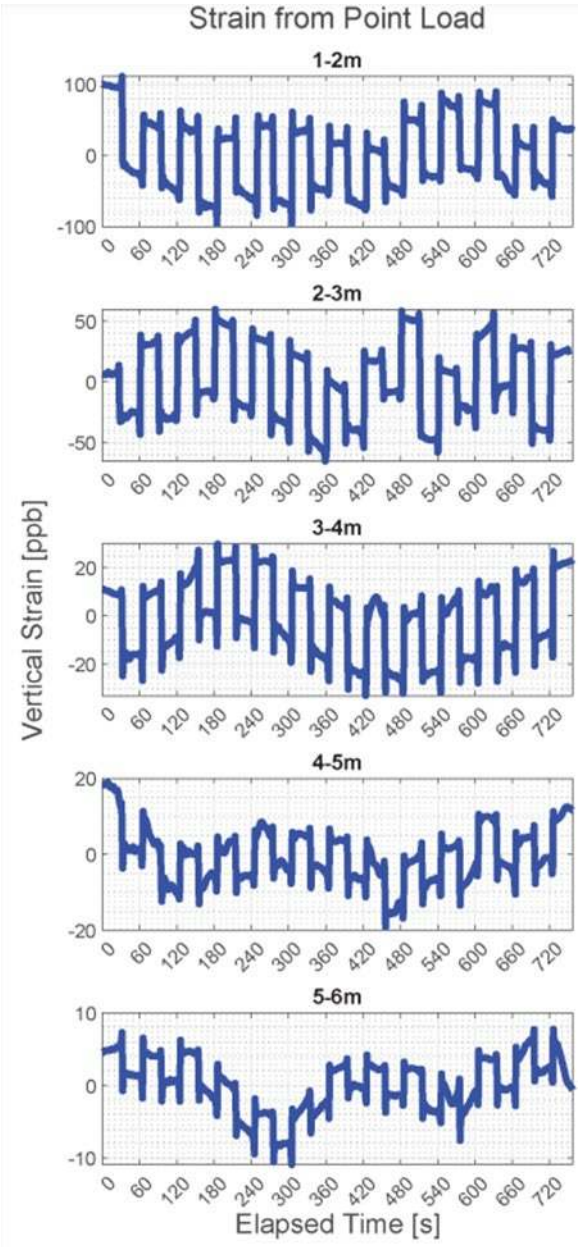

Figure 11-11. Strain caused by from moving point load between two radial distances every 30 seconds at 5 pairs of radial distances along one of the radial lines in Figure 11-9

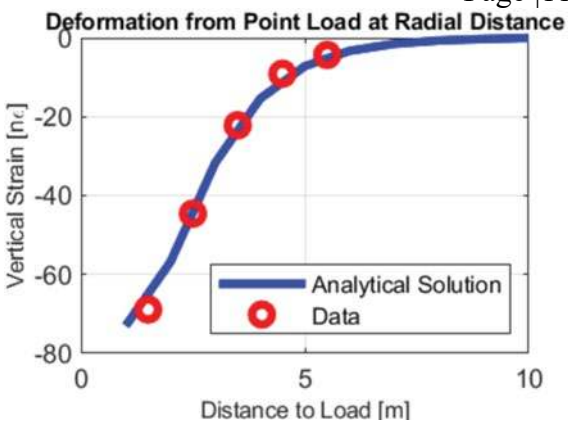

Figure 11-10. Vertical strain averaged from repeat measurements in the field (points) and calculated using an analysis based on the Boussinesq solution where E = 100 MPa and ν = 0.25.

The reason for the lack of poroelastic simulations of unconfined aquifers is that the including both saturate and unsaturated conditions increases the complexity of the poroelastic analysis. In saturated conditions, all the material parameters are constant and the equations are linear and, in some cases, the equations for pressure and displacement are fully coupled. For problems that involve partially saturated conditions, the high compressibility of the air causes the coupling of the solid strain to the pore pressure to be small, and in cases where the air pressure is constant it can be ignored and the displacement can be uncoupled from the fluid pressure.

However, this is problematic in cases where both saturated and unsaturated conditions occur. In these cases, the fully coupled conditions used in the saturated zone are extended continuously into the vadose zone. This is accomplished using a coupling term that varies with the saturation, as outlined in Chapter 5. This is the approach we used to analyze this problem.

11.4.1 Field Experiments

We performed many pumping tests in the unconfined aquifer at the Clemson field site and recorded strain at multiple locations in both the saturated and unsaturated zone, as well as the underlying bedrock. In one set of examples, pumping was conducted at a rate of 3 GPM from PW-1 for 2 hours and drawdown was measured at WL-5 (r = 6.4 m) and WL-7 (r = 11m). Vertical strain was measured at X9 (r = 3.2m) and X8 (r = 10m) in the saturated zone (Figure 11-12). Another set of tests was conducted using 3 gpm of pumping for 30 minutes followed by injection at a similar rate and time period. Vertical strain was measured at multiple depths in the vadose zone at the CMPI ribbon (r = 4.4m) during these tests (Figure 11-12).

Maximum drawdown at the pumping well was approximately 5 m, and it decreased to 11 cm at WL-5 and 6 cm at WL-7 (Figure 11-12). The test was repeated three times and the maximum drawdown varied by a factor of approximatley +/- 0.05.

Deformation occurred rapidly following the onset of pumping with compressive vertical strains during pumping in the saturated zone at X8 and X9. The strain decreased rapidly at the start of pumping and then the rate diminished with time. A similar behavior with opposite sign occurred when pumping stopped and the strain recovered. As a result, the general shape of the time series resembles that of the drawdown curves (Figure 11-12), and like the drawdown data, the strain measurements are consistent among the three tests. The strain reached minimum values of approximately -1.4 με at X8 and -7 με at X9 (Figure 11-12).

Vertical strains measured with a CMPI strain ribbon in the unsaturated zone also followed a pattern similar to the pressure, but their sign is opposite that of the strain in the saturated zone. In the vadose zone, tensile vertical strain occurs during pumping and compressive strain occurs during injection (Figure 11-12). The maximum strain occurs at the greatest depth (6m) and it reached a maximum value of approximately 2.2 με after 30 minutes of pumping (Figure 11-12). The strain decreased progressively upward and reached a maximum of approximately 0.4m at a depth of 1m. The drawdown underlying the CMPI strain ribbon would have been approximatley 5 to 8 cm after pumping for 30 minutes.

The strain changes abruptly to compression when the test switches from pumping to injection. The strain at 4 m depth drops the fastest and it surpasses strains at 5 and 6m to reach the greatest strain value at the end of 30 minutes of injection (Figure 11-12). The strain at 5m is slightly greater than that at 4m and the strain at 6m is even greater, similar to strain at 3m.

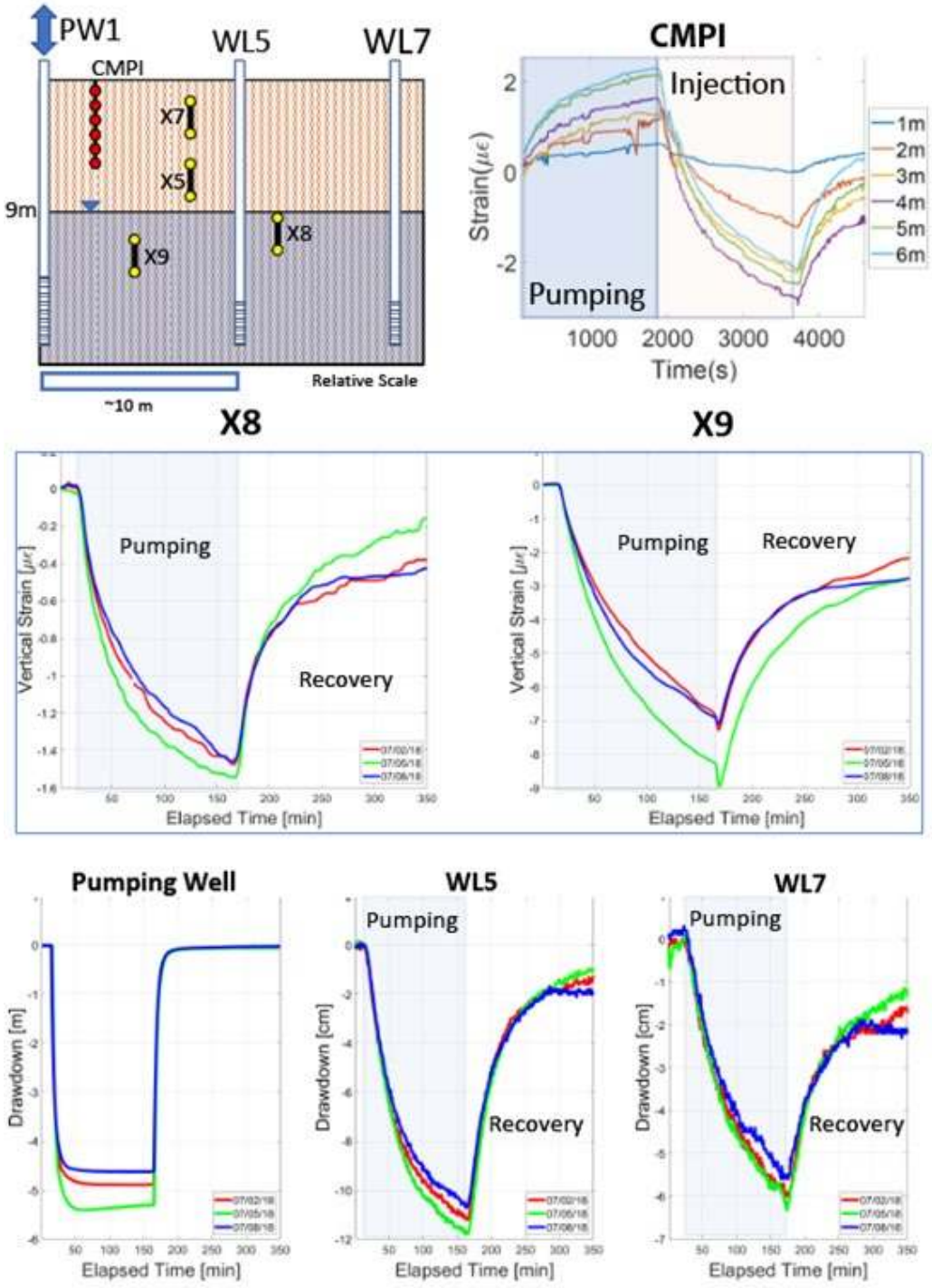

Figure 11-12. Pressure head and vertical strain during pumping tests at the Clemson field site. Data in the lower row are mis-labeled as drawdown, but they are pressure head, or water level.

Switching the relative order of the maximum vertical strains appears to be a repeatable effect. Another pumping test was conducted for a longer period, approximately 6 hrs, and the vertical strains were measured continuously using the CMPI ribbon. More information about

this test is in Chapter 12, Section 12.10. The strain data during this pumping test are presented in Figures 12-75 and 12-76, and Figure 12-75 is reproduced here as Figure 11-13. Vertical strain during this test increases to a maximum of approximately 6 με during the first 30 minutes of pumping, which is slighly more tensile strain than occurred during the test shown in (Figure 11-12). The relative magnitudes of the strains follows their depth during the first 30 minutes, but then the magnitude of the vertical tension starts to fall off at the deepest sensor. It continues to decrease through the test it is only 2 με at the end of the test. The strain at 5m depth is the greatest after 6 hrs of pumping (Figure 11-12).

The field data highlight some important similarities and differences between strain in unconfined and confined aquifers. In both types of aquifers, the vertical strain is compressive during pumping in the saturated zone and tensile in the the overlying formations above the water table. The primary difference occurs in the vicinity of the water table and appears to involve a time-dependent reversal from tensile to compressive strain. The behavior is consistent with the pressure drop caused by pumping migrating upward into the vadose zone with time.

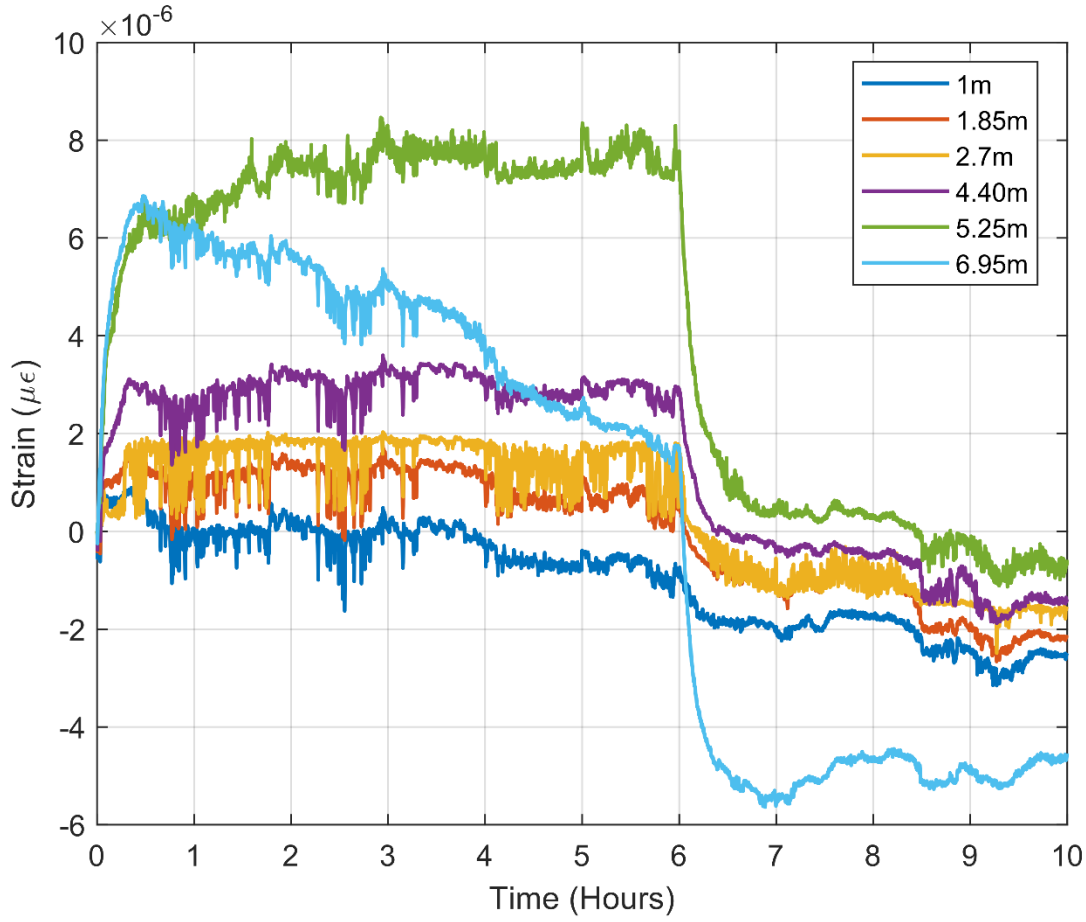

Figure 11-13. Vertical strain between reflector pairs measured as a function of depth and time in the vadose zone during a constant-rate pumping test. Positive strain is tensile. Depths indicated on the legend are the midpoint between reflector pairs separated by 15 cm. Pumping was conducted from 0-6 hours. No correction for barometric pressure.

11.4.2 Simulations

Simulations were conducted to evaluate strains during pumping tests in unconfined aquifers using the methods outlined at the beginning of this chapter and in Chapter 5. The results from a preliminary set of simulations show how the pressure evolves from a partially penetrating well (Figure 11-14). The pressure drop from pumping quickly spreads radially outward and vertically downward, but little change occurs upward across the water table during the first few hours of pumping. However, after 13 hours of pumping the pressure drop has propagated roughly 1 meter upward into the vadose zone.

There is a sharp boundary at the water table between compressive vertical strain in the saturated zone and tensile vertical strain above it in the vadose zone (Figure 11-14). This boundary moves upward with the pressure however, so it has moved upward by 1 m after 13 hrs of pumping, according to the simulations in Figure 11-14.

The tilt field also evolves with time, but there appears to be little effect at the water table compared to the other strains (Figure 11-14). Tilt is the vertical gradient of the horizontal displacement. Pumping causes aquifer material to be displaced toward the wellscreen and the extent of this displacement diminishes upward and downward, giving rise to two lobes of tilt that are roughly symmetric about the wellscreen and opposite in sign. This effect is particularly evident early in the pumping (t = 3 min. in Figure 11-14). Pumping also causes vertical displacements and this leads to subsidence of the ground surface and negative tilts. The grey zone that grows with time at the ground surface (Figure 11-14) is a result of this effect. There is a small perturbation in the contours of tilt across the water table, but this effect is difficult to discern and would likely be difficult to detect.

Another set of simulations of a pumping test in an unconfined aquifer was conducted using a more detailed model. These simulations assumed the fluid and mechanical properties are constant when the pressure is positve and vary as a function of pressure when the pressure is negative. Moreover, these simulations used an underlying zone of low permeability and high elastic modulus to represent the unweathered bedrock beneath the field site.

The pressure during this set of simulations decreases in the vicinity of the well at early times but there is little effect of pressure change at the water table (Figure 11-15a-d). The pressure change migrates upward with time and it covers more than half the vadose zone at the end of the simulation (Figure 11-15d).

Radial strain quickly becomes compressive near the wellscreen and tensile at further radial distances (Figure 11-15e-h). The crossover from compressive to tensile strain propagates outward with time in the saturated zone. A similar effect occurs in the vadose zone, although the crossover extends further from the well in the vadose zone than it does at the level of the well screen. This effect occurs at early time when there is no change of pressure in the vadose zone, so it appears to be unrelated to the upward migration of pressure change.

In contrast, the vertical strain does change with the upward migration of pressure change in this simulation (Figure 11-15i-l), just as it does in Figure 11-14.

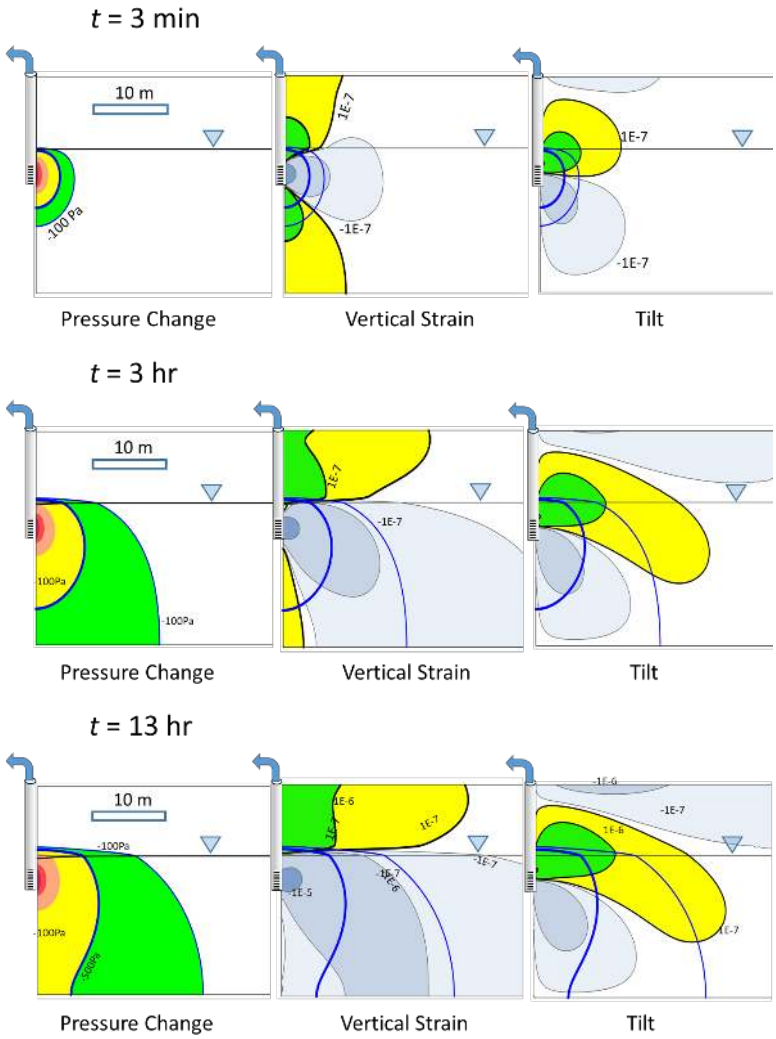

Figure 11-14. Pressure, vertical strain and tilt at three representative times durign a pumping test in an unconfined aquifer. Colors are negative pressure and positive strain, grey tones are negative strain. Tilt is the vertical gradient of the horizontal displacement. Positive tilt is similar to leaning leaning from the borehole.

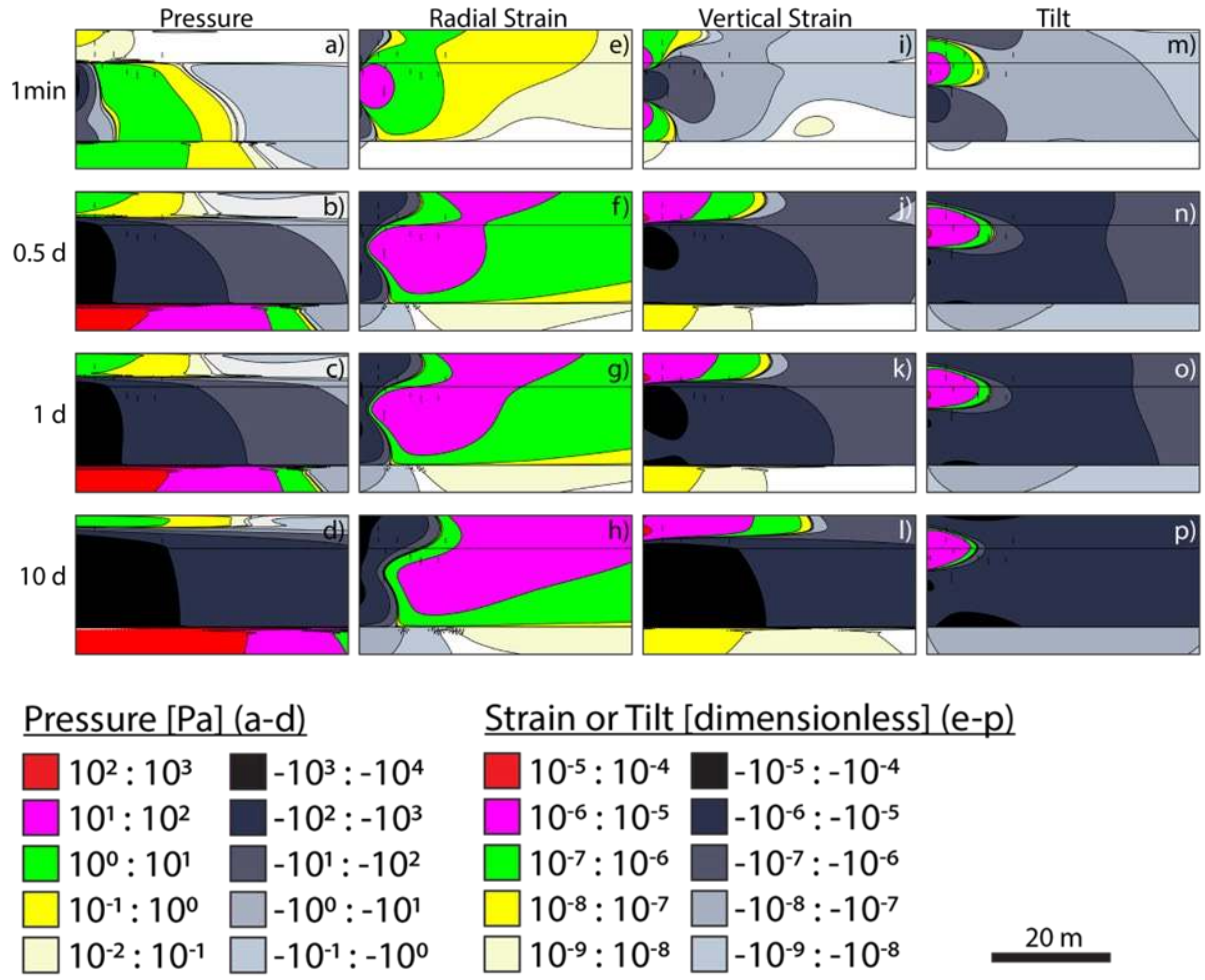

Figure 11-15: Pressure (a-d) and deformation (e-p) from constant rate pumping at 3 GPM in an unconfined aquifer for 10 days. The top row is after 1 min, second row is 12 hr, third row is 24 hr, and lowest row is 10 day. Positive pressure change and tensile strain are shown with color, a pressure drop and compressive strain are shown with grey scale. Each color band is an order of magnitude.

11.4.3 Conclusion

The field data and simulations show that strain in the vadose zone should respond to pumping with a time series that resembles pressure in the underlying aquifer. A similar conclusion will be reached in Chapter 12 where we will show that the vertical and the average horizontal strains in particular are similar, but not identicial to the pressure in the saturated zone.

The results from this study indicate that the strain at the base of the saturated zone will respond as the pressure change in the underlying aquifer migrates upward. This process is slower than pressure diffusion in the aquifer because the pressure diffusivity decreases with saturation so it is less in the vadose zone than in the saturated zone. It follows that the transient change of strain at the base of the vadose zone could be used to evaluate the change of pressure in partially

saturated conditions. One potential application would be to use the strain data to estimate the parameters of the retention curve, which are difficult to estimate in-situ.

11.5 REFERENCES

Borja, R. I. (2006). On the mechanical energy and effective stress in saturated and unsaturated porous continua. *International Journal of Solids and Structures*, *43*(6), 1764–1786. https://doi.org/10.1016/j.ijsolstr.2005.04.045

Freeman, C. (2012). *Estimating Water Flux and Storage Using Displacement Measurements in Saprolite at Depth*. http://tigerprints.clemson.edu/all_theses

Moak, R., Murdoch, L., Thrash, C., Germanovich, L., DeWolf, S., & Jun, F. (2016). Characterizing Subsurface Deformation During Loading Experiments. *AGU Fall Meeting*.

Murdoch, L. C., Freeman, C., Germanovich, L. N., Thrash, C., & Dewolf, S. (2015b). Using in situ vertical displacements to characterize changes in moisture load. *Water Resources Research*, *51*, 5998–6016. https://doi.org/10.1002/2015WR017335.

Murdoch, L. C., & Germanovich, L. N. (2006). Analysis of a deformable fracture in permeable material. *International Journal for Numerical and Analytical Methods in Geomechanics*, *30*(6), 529–561. https://doi.org/10.1002/nag.492

Murdoch, L. C., Germanovich, L. N., DeWolf, S. J., Moysey, S. M. J., Hanna, A. C., Kim, S., & Duncan, R. G. (2020a). Feasibility of using in situ deformation to monitor CO_2 storage. *International Journal of Greenhouse Gas Control*, *93*(August 2019), 102853. https://doi.org/10.1016/j.ijggc.2019.102853

Murdoch, L. C., Germanovich, L. N., Roudini, S., DeWolf, S. J., Hua, L., & Moak, R. W. (2021). A Type-Curve Approach for Evaluating Aquifer Properties by Interpreting Shallow Strain Measured During Well Tests. *Water Resources Research*, *57*(9). https://doi.org/10.1029/2021WR029613

Murdoch, L. C., Xie, S., Falta, R. W., & Ruprecht, C. (2015). Effects of increased upward flux of dissolved salts caused by CO2 storage or other factors. *Journal of Hydrology*, *527*, 776–787. https://doi.org/10.1016/j.jhydrol.2015.05.022

Thota, S. K., Cao, T. D., & Vahedifard, F. (2021). Poisson's Ratio Characteristic Curve of Unsaturated Soils. *Journal of Geotechnical Geoenvironmental Engineering*, *147*(1). https://doi.org/https://doi.org/10.1061/(ASCE)GT.1943-5606.0002424

Thrash, C. (2016). *Measuring and Interpreting Vertical Displacements related to Shallow Hydrologic Processes*. M.S Thesis, Clemson University

CHAPTER TWELVE

ANALYSIS OF STRAIN DURING PUMPING TESTS WITH A PERIODIC RATE

Contents

12.1 Abstract 12-2

Part 1 Well Tests with a Periodic Square Wave and Zero-Net Pumping Rate

12.2 Part 1 Introduction 12-4
12.2.1 Zero-Net-Rate Periodic Pumping Tests 12-7
12.2.2 Application to Detecting Gas in Aquifers 12-9
12.2.3 Strain measurements during well tests 12-10
12.3 Part 1 Methods 12-12
12.3.1 Instrumentation 12-12
12.3.2 Data Analysis 12-23
12.3.3 Numerical Experiments of ZNR tests 12-30
12.4 Part 1 Results 12-40
12.4.1 Slug Tests 12-40
12.4.2 Constant-Rate Pumping Test 12-41
12.4.3 ZNR Tests 12-44
12.5 Part 1 Discussion and Conclusions 12-72
12.6 References 12-131

Part 2 Well Tests with a Sinusoidal Pumping Rate

12.7 Part 2 Abstract 12-76
12.8 Part 2 Introduction 12-77
12.9 Part 2 Methods 12-79
12.9.1 Equipment 12-79
12.9.2 Data Collection and Storage 12-90
12.9.3 Site Description 12-90
12.9.4 Geology and Hydrogeology 12-90
12.9.5 Wells and Sensors 12-91
12.9.6 Field Experiments 12-92
12.9.7 Sinusoidal Variation 12-93
12.9.8 Data Processing and Analysis 12-94
12.10 Part 2 Results 12-95
12.10.1 Constant Rate Pumping Test 12-95
12.10.2 Sinusoidal Pumping Tests 12-100
12.11 Part 2 Discussion 12-120
12.11.1 Aquifer Properties 12-121
12.11.2 Simulations of Pressure and Strain 12-122
12.11.3 Implications 12-129

12.1 ABSTRACT

Periodic pumping tests involve cycling the pumping rate with a regular period and measuring the resulting response. Some of these tests involve imposing a periodic rate on a constant mean rate. However, other tests involve moving water out of and back into the well at rates that are balanced so the net rate after each period is zero. Some zero-net-rate (ZNR) well tests use rates that follow a sinusoidal pattern, whereas others use a square wave pattern that switches between a constant rate of pumping and a constant rate of injection to achieve a zero net rate.

Periodic pumping tests are typically evaluated through pressure responses at monitoring wells. Field measurements and simulations in Murdoch et al. (2021) and elsewhere in this report demonstrate that the strain field in the vadose zone responds to pressure changes in the underlying aquifer.

The objective of this chapter is to evaluate the feasibility of using strain in the vadose zone to evaluate pumping tests with a periodic rate. Part 1 of this chapter is based on Smith-Jones (2023) and it will evaluate zero-net-rate pumping tests that use a periodic square wave, whereas Part 2 is based on Blais (2023) and it will evaluate tests that use a sinusoidal rate with a positive mean rate.

A ZNR periodic pumping system was constructed and used to perform tests in the Clemson, South Carolina area. The system was designed to pump and inject with a periodic square-wave, so pumping occurs at a constant rate for half the period and is followed by injection at the same rate for half the period resulting in no net gain or loss of water from the aquifer. The system is designed to generate flow rates from 1 to 3.5 gallons per minute (gpm) with a capacity of 875-gallon per half period. Pressure and strain monitoring points are located in the vicinity of the pumping well.

A series of 10 ZNR periodic pumping tests was conducted with periods ranging from 2 to 540 minutes. Pressure data were measured in four monitoring wells, and vertical and horizontal strain and tilt data were recorded in various locations around the pumping well. Conventional aquifer tests, including slug tests and constant-rate pumping tests were conducted at the field site to provide a baseline of aquifer parameter estimates that are compared the results of ZNR tests.

Hydraulic diffusivity and transmissivity were estimated from the time lag and amplitude of the pressure signal utilizing an analytical solution (Streltsova, 1988) that assumes a confined, uniform aquifer of infinite extent. The time lags and amplitudes of the pressure signals were estimated using a Fourier transform.

The time lag of the primary period of the pressure increases as a linear function of distance from the pumping well, and it increases as the square root of the period of the ZNR test over a range of periods spanning two orders of magnitudes. The first few harmonics follow similar trends, but the higher frequency harmonics diverge from this trend. Strain and tilt data from various instruments in the vadose and saturated zones are periodic during ZNR tests. The time lags of the strain components increase roughly linearly with distance from the well. Many of the time lags of the strain data from the vadose zone are similar to the time lags observed in the pressure data from a similar distance and pumping period.

Theoretical experiments were performed to understand how pressure and strain responds to ZNR periodic pumping. The time lags of the simulated pressure responses match the field data trends. The results were used to validate the Streltsova (1988) solution for periodic pumping to estimate hydraulic diffusivity.

Hydraulic diffusivity was estimated to be 1.8×10^{-2} $m^2s^{-1} < D_h < 9.0 \times 10^{-2}$ m^2s^{-1} using pressure data from all the wells during ZNR tests. Transmissivity was estimated to be 0.8×10^{-4} $m^2s^{-1} < T < 4.3 \times 10^{-4}$ m^2s^{-1}. Assuming Storativity = T/D_h gives $1.1 \times 10^{-3} < S < 19 \times 10^{-3}$. Transmissivity is used to estimate the hydraulic conductivity, K, by dividing by the assumed aquifer thickness.

Two constant-rate pumping tests were conducted and analyzed using two conceptual models: the Hantush (1961) solution assuming confined conditions and the Neuman (1974) solution assuming unconfined conditions. The Hantush (1961) solution estimated transmissivity to be 1.6×10^{-4} $m^2s^{-1} < T < 1.8 \times 10^{-4}$ m^2s^{-1} when using data from all the wells. Storativity was estimated to be $4.4 \times 10^{-3} < S < 8.2 \times 10^{-3}$. Assuming $D_h = T/S$ gives 0.22×10^{-2} $m^2s^{-1} < D_h < 3.6 \times 10^{-2}$ m^2s^{-1}. The Neuman (1974) solution estimated transmissivity to be 0.80×10^{-4} $m^2s^{-1} < T < 0.84 \times 10^{-4}$ m^2s^{-1}. Total storativity ($S + Sy$) was estimated to be $22 \times 10^{-3} < S < 110 \times 10^{-3}$. Storativity excluding the S_y term was estimated to be $2.2 \times 10^{-3} < S < 2.5 \times 10^{-3}$. Assuming $D_h = T/S$ gives 0.073×10^{-2} $m^2s^{-1} < S < 0.36 \times 10^{-2}$ m^2s^{-1}.

Two slug tests were performed on the pumping well, PW-2. The Bouwer and Rice (1976) solution for slug tests was used to analyze the data. This solution works for both confined and unconfined conditions, so both conceptual models were covered through the analysis. Hydraulic conductivity was estimated to be 1.95×10^{-6} $ms^{-1} < K < 2.49 \times 10^{-6}$ ms^{-1}.

Statistical comparison show generally no significant difference in the estimates of D_h, K, or S made using ZNR and conventional pumping tests. However, the total storage estimated by the Neuman (1974) solution for unconfined settings is larger than that estimate using the Streltsove analysis applied to the ZNR tests. This is likely because the Neuman solution considers delayed yield from storage that the water table, whereas the Streltsova (1988) solution assumes confined conditions. The analysis also indicates that there is a statistically significant difference between parameters estimated with conventional slug tests and those measured with either constant-rate pumping tests or ZNR tests.

Hydraulic diffusivity is estimated from the time lag and the distance from the well. The time lags of the strain data from the vadose zone are similar to the lags of the pressure data from a similar distance. This indicates that hydraulic diffusivities estimated from the strain data measured in the vadose zone would be similar to the estimates from the pressure data measured in the aquifer. There appear to be sign reversals in some of the strain data that were corrected to estimate the time lag.

Chapter 12, Part 1

Wells Tests with a Periodic Square Wave and Zero Net Pumping Rate

12.2 PART 1 INTRODUCTION

Periodic pumping tests originated from the idea of interference tests where the rate of pumping during production is altered and the pressure response at observation wells is measured and analyzed (Johnson et al. 1966). A pulse test is an interference tests where the pumping well is alternated between shut-in and production, which creates a periodic square-wave pressure signal that can be detected in observation wells (Johnson et al. 1966). This idea was expanded to include a sinusoidal variation of pumping/injecting and periodic tests with multiple flow rates (Kuo 1972).

The sinusoidal technique developed for the oil industry by Kuo (1972) was adapted for use in hydrogeological applications (Black and Kipp 1981). Solutions were derived for two scenarios: the steady-periodic response to (1) a point source located within an unbounded, homogenous, isotropic 3D aquifer volume with elastic storage and (2) a fully penetrating line source located within a laterally unbounded, but finite thickness homogenous isotropic confined aquifer. This approach uses a ratio of either the phase shift or amplitude from two observation wells to determine the aquifer diffusivity (ratio of Transmissivity/Storativity). An important drawback is that this analysis is unable to independently determine transmissivity and storativity (Black and Kipp 1981).

Streltsova (1988) derives solutions for pressure drawdown for a well producing at a variable rate, including pressure response to a periodically changing production rate in a confined setting. Streltsova (1988) used Bessel function solutions by Businov and Umrichin (1960, 1964) to develop basic relationship between amplitude and phase and aquifer parameters. Streltsova (1988) gives solutions for ZNR or production only with sinusoidally, co-sinusoidally, or square-wave production rate. An approximate solution for a square-wave production rate is given using only the delay time of the fundamental frequency to estimate the hydraulic diffusivity. In addition, Streltsova (1988) presents an approximate method for solving for transmissivity using the amplitude of the pressure signal in an observation well.

Rasmussen et al. (2003) built on Black and Kipp's (1981) analysis. They provided a framework for estimating hydraulic properties using periodic sinusoidal rate of change with a zero-mean rate of change (ZNR). The framework consists of deriving analytical solutions for confined, leaky, and partially penetrating conditions, comparing analytical solutions to a finite element model, establishing a field protocol for conducting sinusoidal aquifer tests, and estimating aquifer parameters using the analytical solutions that were derived. In deriving their analytical solutions, they showed a new method that allows for the distinction of transmissivity and storativity from the diffusivity term. They found that the transmissivity and storativity determined from sinusoidal tests matched those estimated from a constant-rate pumping test. A sinusoidal pumping test conducted in a surficial aquifer produced reasonable aquifer parameter estimates for transmissivity but produced an unreasonable estimate of storativity when compared to results from constant rate tests. They concluded that a sinusoidal well test, where the net pumping equals the net injection rate, would cause limited fluctuations of the water table and that the change in storage is primarily due to an elastic response characterized by specific storage. This implies that sinusoidal tests with a zero net rate could be only weakly sensitive to specific storage, even when they are conducted in an unconfined aquifer.

Analytical solutions for periodically changing drawdown are available for confined aquifers (Black and Kipp 1981, Streltsova 1988, Bruggeman 1999), unconfined aquifers (Rabinovich et al. 2015), partially penetrating wells (Haborak 1999, Rasmussen et al. 2003), leaky aquifers (Haborak 1999, Rasmussen et al. 2003, Tang and Jiao 2011), one-dimensional aquifers (Carr and van der Kemp 1969, Townley 1995), two-dimensional aquifers (Sun 1997), composite aquifers (Trefry 1999) and near cylindrical heterogeneities (Bakker 2009).

Dagon and Rabinovich (2014) present an analytical solution for the hydraulic head field in an unconfined aquifer of finite depth under assumptions of linearized water table conditions, different vertical and horizontal constant permeabilities, constant specific-storage and water-table drainable porosity, and a small well radius to length ratio. A method was derived for estimating equivalent aquifer properties including hydraulic conductivity, specific storage, and specific yield in an unconfined setting using field test data (Rabinovich et al. (2015). They found that hydraulic conductivity and specific storage estimated using the analysis increase with inverse of the period. They also found that values of specific yield estimated through periodic tests are much less than those from constant-rate pumping tests and they increase with the period. This trend was attributed to a capillary fringe effect acting to limit the exchange of fluids between the saturated and unsaturated zones, and the exchange increases with a longer period. However, they concluded that the capillary effect cannot fully explain the specific yield and more investigation is required to fully understand specific yield with periodic pumping tests. They note the possibility of utilizing periodic pumping tests to locate heterogeneities, as a period dependence of aquifer parameters can be a heterogeneity effect (Renner and Messar 2006).

One approach to a periodic pumping test is to use a constant rate that varies periodically between injection and pumping with a mean rate of zero (Renner and Messar 2006). Periodic pumping tests were conducted with periods ranging from 10 seconds to 5,400 seconds (90 minutes) by Renner and Messar (2006). They created a square wave pumping signal consisting of (1) injection, (2) no pumping, (3) production, and (4) no pumping. They present two types of analysis for periodic pumping: Injectivity analysis and Interference analysis. An Injectivity analysis is based on the determination of the amplitude ratio and phase shift between the periodic flow rate and pressure records from the pumping well; and an Interference analysis is based on an evaluation of attenuation and phase shift between the periodic pressure signals at the pumping and monitoring wells. They explored the sensitivity of results to subsurface heterogeneities. The injectivity tests results suggest that heterogeneities with different effective hydraulic diffusivities cause variations in phase shifts in observation wells. They observed an almost constant transmissivity with strongly varying storativity. They note that storativity is associated with a characteristic timescale and variations in transmissivity will always cause an apparent variation in storativity.

Recently, further analysis has evaluated the specific yield issue. Analytical solutions were derived for both transient and steady-periodic analysis in both confined and unconfined aquifers (Huang et al. 2019). Transient analysis involves data from all periods whereas the steady-period analysis discards the first two periods to simplify computations. They wanted to analyze both instantaneous gravity drainage (IGD) and delayed gravity drainage (DGD). They identified a delayed yield coefficient, which can be related to the water retention curve. Using field data presented by Rabinovich et al. (2015), they found that the water-table acts as a no-flow boundary with periods less than 10,000 seconds, so the short period tests are independent of specific yield. They

concluded that hydraulic conductivity, specific storage, and period of periodic pumping rate significantly effect head in the entire aquifer, however, specific yield only affects the head in the vicinity of the water table.

Data from monitoring wells in the vicinity of the pumping well can, in principle, be used to estimate the distribution of heterogeneities using periodic pumping tests. Heterogeneities can be manifested as spatial variations in transmissivity and storage coefficient. Cardiff et al. (2013) and Fokker et al. (2013) both investigated methods for determining heterogeneities through inversion of a forward model. Fokker et al. (2013) utilized a numerical simulator in the Fourier space developed by Fokker et al. (2012) and applied this analysis to the field study of Renner and Messar (2006). Fokker et al. (2013) concluded that the various effective transmissivity results from Renner and Messar (2006) were caused by heterogeneities in the subsurface. Through an optimization algorithm, they were able to identify zones of different transmissivity in 2-dimensional space and they showed that data from bore logs were consistent with their findings. Cardiff et al. (2013) introduced the idea of Multifrequency Oscillatory Hydraulic Imaging in which periodic pumping tests of several frequencies are used to provide information on subsurface heterogeneities. They showed that a heterogeneity can be spatially located outside of the area between a pumping well and observation well.

An analytic-element solution for a well with sinusoidal pumping near cylindrical heterogeneities was developed by Bakker (2007). He presents a solution for 2-dimensional transient hydraulic head in an aquifer with heterogeneities, however, the amplitude and phase shift of the head varies in a complicated manner, and which makes it a challenge to analyze with limited periods and an imprecise idea of heterogeneity locations. Bakker (2007) found that block-shaped discharge functions may be approximated with a Fourier series in combination with Cesaro summation. Bakker's presented solution may be combined to simulate flow to a finite-radius well with wellbore storage and skin effect. He notes that the solution approach can be applied to two-dimensional periodic unsaturated flow and three-dimensional periodic flow.

Periodic pumping tests have been used to estimate hydraulic properties in aquifer settings controlled by fractures, such as bedrock or karstic aquifers (Fischer et al., 2018a and 2018b). Their study was able to separate three different types of responses: a conduit connectivity response, a matrix connectivity, and a dual connectivity, which is the response of a point in the matrix but close to a conduit. Fischer et al. (2018) found that a high frequency signal is sensitive to the conduit flows, whereas a low frequency signal is more sensitive to the matrix diffusive flows. They also demonstrate that the results from simulations in the frequency domain are similar to the results of simulations in the time domain.

Water levels measured in an observation well are the result of a combined action of aquifer pressure response and wellbore effects (Xing et al. 2022). Different types of aquifer disturbances require different methods of handling the wellbore effects. Xing et al. (2022) developed a general-purpose numerical model that integrates different types of periodic signals to investigate the impact of wellbore effects on the water level fluctuations. The modeling shows that the amplitude and phase are most sensitive to the distance to the disturbance source, and to the hydraulic conductivity, respectively. The sensitivity analysis shows that the wellbore effects are relatively insensitive to the distance of the disturbance source. They also conclude that the disturbance period significantly weakens the wellbore effects.

Guidance has been published on the best approach to conduct periodic pumping test analyses. Rasmussen et al. (2003) conclude that guidance is needed on the selection of the appropriate pumping frequency, as well as the utility of pumping at multiple frequencies. Cardiff and Barrash (2014) provide a method for choosing testing frequencies and flowrates that will maximize the signal amplitude. They also developed a semi-analytical method for computing sensitivity of oscillating signals to spatially distributed aquifer flow parameters. Methods to successfully denoise a periodic signal, including a discrete Fourier transform (Renner and Messar, 2006, Hollanender et al 2002) and least squares (Rasmussen et al. 2003) have been demonstrated. Bakhos et al. (2014) provided a framework for signal denoising. Patterson and Cardiff (2021) provide a general workflow that relates extracted Fourier coefficients for observation signals with single and multifrequency components to aquifer flow properties and their associated uncertainties. Cardiff and Sayler (2016) outline methods to avoid a common error with periodic pumping tests, phase wrapping, meaning the signal is delayed by more than one period.

The following chapter is based on work done by Austin Smith-Jones (2023) and Riley Blais (2023) in fulfillment of their MS theses in hydrogeology.

12.2.1 Zero-Net-Rate Periodic Pumping Tests

A zero-net-rate (ZNR) pumping test is a periodic pumping test consisting of equal pumping and injecting rates and times, resulting in a no net gain or loss of water. Although the term ZNR pumping test is not used in literature, Black and Kipp (1981) note the benefits of using equal pumping and injecting rates and times to minimize the costs through purge water disposal. Renner and Messar (2006), Rasmussen et al. (2003), and Rabinovich et al. (2015) present field tests of periodic pumping tests, with equal parts pumping and injecting with square wave and a sinusoidally changing rate, respectively. In addition, Fokker (2013) and Cardiff and Barrash (2015) present theoretical tests using a periodic test with a zero-mean rate of change. A periodic pressure signal is produced at the production/injection well and the pressure response is recorded at monitoring points surrounding the pumping well. The main benefits of a ZNR pumping test, when compared to constant-rate pumping tests, include: (1) there is no net extraction of water avoiding possible costs and risks associated with handling and treating contaminated water, (2) the pumping method causes less net contaminant plume movement since the average flow velocity induced by such pumping is zero in all directions, and (3) the oscillation signal of a known frequency can be distinguished from changing background pressure using filtering.

Streltsova (1988) derived a solution for a confined, non-leaky aquifer with square-wave periodic pumping/injecting. This analysis is governed by

$$\frac{\partial^2 p}{\partial r^2} + \frac{1}{r}\frac{\partial p}{\partial r} = \frac{1}{D_h}\frac{\partial p}{\partial t} \tag{12-1}$$

where p is pressure head, r is radial distance, D_h is hydraulic diffusivity, and t is time.

The initial condition is

$$p(r, t = 0) = p_1 \tag{12-2}$$

The outer boundary condition for an aquifer with infinite radial extent is

$$\lim_{n\to\infty} p(r,t) = p_1 \tag{12-3}$$

The inner boundary condition for the well pumping and injecting at a given flow rate, *q(t)*, is

$$qB = q_{res} + (qB)_{storage} \tag{12-4}$$

where *B i*s the formation volume factor, reservoir volume/standard volume, and q_{res} is the rate through the reservoir. Darcy's law for volumetric flow through a cross-sectional area to produce a flow rate is

$$q = -\frac{k}{\mu}\nabla P \tag{12-5}$$

where q is the volumetric flow rate through a cross-sectional area (Q/A), k is the permeability, μ is the dynamic viscosity, and P is pressure. The periodically changing rate*, q(t),* for a square wave can be represented as

$$q(t) = \frac{4\Delta q}{\pi}\sum_{n=0}^{\infty}\frac{1}{2n+1}\sin(\omega_n t) \tag{12-6}$$

where $\omega_n = (2n+1)\omega$ and is the angular frequency. λ is the pumping period, and Δq is the amplitude of the square wave.

Streltsova then applies the superposition principal and the response to a sinusoidal production rate to get the pressure response to the flow rate, *q(t)*. The quasi-steady state result is given in terms of Kelvin functions (Streltsova, 1998; eq. 3.60). The Kelvin functions can be approximated using trigonometric functions when the pressure is measured at radial distances that satisfy

$$r > \sqrt{\frac{\lambda\eta}{2\pi}} \tag{12-7}$$

The solution is limited to the first term because the fundamental frequency (n = 1) contributes most to the sum, according to Streltsova (1988, p. 131).

The time lag and pressure amplitude are important to the analysis because they can be measured in the field and used to estimate parameters. Time lag, t_L, is the delay between the pressure response in the pumping well and an observation well. Pressure amplitude, Δp, is the amplitude of the periodic variation in pressure in the reservoir.

The hydraulic diffusivity is a function of delay time (Streltsova, 1988, eq. 3.81)

$$D_h = \frac{r^2\lambda}{4\pi {t_L}^2} \tag{12-8}$$

The aquifer transmissivity is given by (Streltsova, 1988, eq 3.82)

$$T = \frac{0.671\Delta q}{\pi\Delta p} \frac{\exp\left\{-\left[\frac{\pi r^2}{\eta\lambda}\right]^{\frac{1}{2}}\right\}}{\left[\frac{\pi r^2}{\eta\lambda}\right]^{\frac{1}{4}}} \tag{12-9}$$

Estimating the delay time, t_L, and Δp are key to using eq. 1.8 and 1.9. One approach to estimating these variables is to apply a Fourier transform. A Fourier transform will separate all the periodic signals of the data into a sum of sinusoidal functions, or harmonics. The fundamental frequency, or first harmonic is used in the Streltsova (1988) analysis for the time lag of the pressure response in a monitoring well, as well as the amplitude of the pressure response in a monitoring well. Theoretical results have shown that a multi-frequency signal provides additional information about aquifer properties compared to a single frequency (Cardiff et al. 2013 and Cardiff and Barrash 2015). A square-wave, eq. (12-6), is a sum of an infinite number of sinusoids, so it is inherently multi-frequency. For example, a ZNR test with a period of 240 minutes will have an amplitude and time lag value for the first harmonic n=1 (λ = 240 minutes), third harmonic n=3 (λ = 80 minutes), fifth harmonic n=5 (λ = 48 minutes). Higher frequency harmonics are also present, although the ability to detect them will depend on site conditions. A full description of a Fourier transform is included in Section Analyzing ZNR Test Delay and Amplitude.

12.2.2 Application to Detecting Gas in Aquifers

As the Earth's climate is changing due to an influx of CO_2 to the atmosphere, it is becoming more important to develop carbon storage techniques that store CO_2 in subsurface geologic formations overlain by low permeability caprock. Leakage of CO_2 through a caprock threatens the integrity of geologic storage, and a variety of methods have been developed to detect leakage. They include 4-D seismic (Arts et al. 2004), vertical seismic profiles (Ajo-Frankin et al. 2013), the reservoir saturation tool (Butsch et al. 2013), distributed temperature sensors (Hovorka et al. 2013), and InSAR and GPS-based methods for surface-deformation measurements (Ramirez et al. 2014).

Downhole pressure measurements have been utilized to monitor CO_2 gas leakage (Hosseini et al. 2016, Shakiba and Hosseini 2016, Sun et al. 2017) through periodic pumping and pressure pulse testing, a type of periodic pumping test. Water compressibility is constant in an aquifer, however, the presence of a CO_2 gas will increase the compressibility of the pore fluid, which will affect the hydraulic diffusivity according to

$$D_h = \frac{k}{(\phi\beta' + \alpha)\mu} \tag{12-10}$$

where k is the permeability, ϕ is porosity, uniaxial aquifer compressibility, β' is fluid compressibility, α is the aquifer compressibility and μ is fluid viscosity. The compressibility of a fluid that contains a small fraction of gas is

$$\beta' = S_w\beta_w + (1 - S_w)\beta_g \quad (12\text{-}11)$$

where S_w is the water saturation, β_w is the compressibility of water and β_g is the compressibility of gas. Increasing the gas saturation will both reduce the water phase permeability k and increase the fluid compressibility, both of which will reduce η according to eq. 1.10

Shakiba and Hosseini (2016) found that the presence of CO_2 gas pockets would affect the hydraulic diffusivity, which would affect the time lag at a monitoring well. This allowed spatial distribution of CO_2 pockets to be estimated from the results of periodic pumping tests.

This implies that periodic pumping tests could be used to identify lenses of CO_2 in aquifers, a technique that could be applied to monitor for leaks above CO_2 storage facilities, or other facilities that store gas (e.g. natural gas storage). ZNR periodic tests would be particularly useful because they could be done by pumping water to and from a tank, so they would not deplete the aquifer of water, which would limit applicability in some locations.

12.2.3 Strain measurements during well tests

Borehole strainmeters capable of measuring small deformations are available, and new designs are under development (Murdoch et al., 2019). Technology presented by Murdoch et al. (2019) and in Chapters One to Three has the potential to measure strains at shallow depths that result from pumping or injecting into much deeper formations. This is appealing because the costs of deploying instruments at shallow depths could be significantly less costly than the drilling of monitoring wells into a reservoir or a deep aquifer.

Recent results have shown the functionality of strain measurements in laboratory experiments involving flow in columns (Plunkett 2021 and Costantino 2021). Strain sensors have been deployed at a field site with wells completed in saprolite, and preliminary tests have investigated the use of a strain signal in aquifer characterization (Blais 2020). Blais (2020) conducted a series of sinusoidal pumping tests with a net positive pumping rate, and his results indicate that vadose zone strain responses to pumping in an underlying aquifer and he found that hydraulic diffusivity estimates from pressure and strain are similar. Blais's work is encouraging, but it involved pumping at a net positive rate, which depleted the underlying aquifer. This motivated additional investigation into analyzing strain signals from ZNR tests.

Strain at different depths and the same radial distance was recorded during a preliminary ZNR test on April 7, 2021. The strain measurements were in the vadose zone above a water table at about 9 meters below the ground surface. A clear periodic signal can be observed in the strain data. The amplitude of the strain signal decreases, but the phase appears to be unaffected by depth (Figure 12-1). This suggests that strain measurements could be used to characterize ZNR periodic pumping tests.

The primary objective of Part 1 of Chapter 12 is to evaluate the feasibility of utilizing ZNR periodic pumping tests to estimate aquifer parameters using pressure and strain data. Part 1 is based on Smith -Jones (2023).

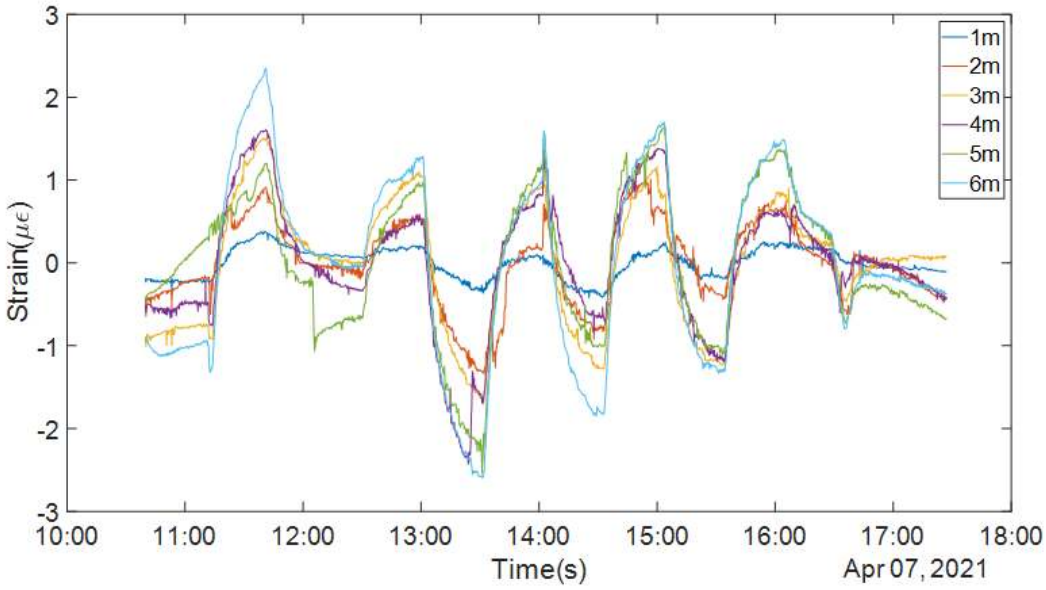

Figure 12-1. Strain response from test conducted on April 7, 2021 at the Simpson Station Hydro-mechanical Test Facility. Strain measured at depths from 1 to 6 meters using Coherence-length-gated Microwave Photonics Inteferometry (CMPI). The water table was at 9 meters below the ground surface during the test.

12.3 PART 1 METHODS

The primary focus of this chapter is to describe various aquifer tests, including slug tests, constant-rate pumping tests, and Zero-Net-Rate (ZNR) periodic pumping tests, at a field site near Clemson, South Carolina. A variety of data-collecting instruments that record pressure, vertical strain, and horizontal strain are installed at the field site. A series of procedures were followed conduct, process, and analyze the field tests.

12.3.1 Instrumentation

Various instruments and devices (**Error! Reference source not found.**) were utilized to create a closed-loop system that can control the injection and pumping rate. The pump flow rates are controlled by Variable Frequency Drives (VFDs). A holding tank collects water produced from the pumping well and then feeds another pump that injects the water back into the same well. The pumping system can be configured to conduct constant-rate pumping tests. Pressure data and strain

Table 12-1. Equipment used during the field tests.

Text Name	Device	Uses	Specifications
HOBO	HOBO U20L-04 (13'), HOBO U20L-02 (100')	Pressure data logger	Resolution < 0.014kPa, 0.14 cm water, Storage capacity: 21,700 measurements
Well Pump	Pentair Flowtec FP3212	Pump situated in pumping well	1/2 HP, 3-wire, 4-inch, depths up to 150', 0-15 gpm, 230V
Well VFD	GK3000-1S0004	Controls the power feeding into the well pump, can adjust the flow rate through changing Hz output	1/2 HP, 4 Amp, single-phase 220V, 0-50 Hz output
Tank Pump	KoolAir PM500	Pumps water out of the holding tank	0-8.5 GPM, single-phase, 230V, 4.3 m of max head, 50 Hz, Run dry protected
Tank VFD	GK3000-2S0015	Controls the power feeding into the tank pump	2 HP, 7.5 Amp, single-phase 220-240V, 0-50 Hz output
Timer Switch	InkBird 39120000	Dictates power schedule to VFDs. For a ZNR test, the timer switch cycles between equal parts of power to A (pump VFD) and to B (tank VFD)	0.01s - 99h99m time range with twin timer set value, one shot or cycle time mode, output: 2 relay
Flow meter	HOBO Onset UX90	Measures and records flow-rate through a pulse counter	Resolution: 1 second Storage Capacity: 84,650 measurements
AquaTroll	AquaTroll 500	Records water quality parameters at a set interval through a flow-through cell	Water quality parameters include temperature, DO, conductivity, pH, ORP, barometric pressure, and density
Holding Tank	Storage Tanks	Stores water from pumping portion of period to be used for injection portion of period	275 gallons and 500 gallons, connected via manifold

data were collected using data-logging pressure transducers (HOBO) and various strain recording instruments.

Strain signal investigations are an important part of this project, and a variety of strain instruments were utilized to collect field test data. The Bull Farm site in Clemson, South Carolina is an experimented field site where strain instruments are tested and evaluated. The result is that several different types of strain instruments were available for use during this study, including DEL-X instruments, a Michelson strain ribbon, an FBG direct-push instrument, and a LILY tiltmeter.

A DEL-X is an instrument developed to measure the deformation in the subsurface caused by a change in applied load (Freeman 2012, Thrash 2016, Murdoch et al. 2015). A DEL-X is composed of two cylindrical anchors positioned coaxially one above the other and separated by an interval of one meter. The anchors grip the soil, and a fiberglass rod fixed to the bottom anchor extends up through the top anchor, which is a tube. A transducer measures displacement between the upper anchor and the rod connected to the lower anchor. An aluminum sleeve prevents soil from contacting the rod to reduce friction, according to Murdoch et al. (2015). The anchors are designed to move with the soil and the high-resolution transducer measures the displacement. DEL-X instruments can resolve several nanostrain, which is one part per billion. Four DEL-X instruments are installed at the field site (DEL-X4, DEL-X5, DEL-X8, and DEL-X9) (**Error! Reference source not found.**Fiber Bragg Grating sensors, or FBGs, are readily available optical fiber sensors that can be configured to measure strain. An FBG include bands of contrasting refractive index at a uniform spacing in the core of an optical fiber. The FBG reflects wavelengths of light proportional to the spacing of the bands (FBGS and Micron Optics). The wavelength of the reflected light changes in proportion to axial strain, which changes the spacing between the bands. The wavelength of the reflected light can be measured with a resolution of approximately 1 pm, with gives a strain resolution of 1με when using light with a wavelength in the range of 1550 nm.

An optical fiber containing three FBGs spaced at 120° was embedded around the circumference of a urethane cylinder 2.25-inch in diameter and 12 inches long. The three FBGs are indicated by different channels, DPS1, DPS2, and DPS3. The top of the cylinder was attached to a 3-ft-long fiberglass tube (4 ft long total), and the bottom was attached to an aluminum cone-shaped point. The diameter of the device is several mm larger than the diameter of a hole created by a standard Geoprobe Macro-Core sampler (GeoProbe). The device was pushed into a hole made with a Geoprobe Macro-Core sampler in saprolite between 10 and 14 ft depth. This expanded the hole and caused the saprolite to compress the urethane cylinder containing the FBGs. Friction couples the saprolite to the urethane and embedded FBGs. The FBG direct-push instrument uses a Micron Optics sm125 interrogator with a resolution of approximately 0.2 με. The FBG direct-push instrument was developed for another project and the first prototype to be deployed in the field was available during the ZNR tests.

The Michelson ribbon is a 1-m-long instrument that consists of 20 m of optical fiber wrapped as a sensing coil and embedded in a 1-m-long, 5-cm wide, and 1-2 mm thick fiberglass composite ribbon. Another coil of optical fiber was wrapped on a steel disk isolated from external strain and embedded in the composite material to serve as a reference. The strain ribbon was suspended between 4 and 5m depth in a 4-inch-diameter borehole, which was then filled with dry sand. The upper two ft of the hole was sealed with bentonite to limit inflow of water.

The sensing and reference coils are joined with an optical coupler to an optical fiber that serves as a data cable extending to an electronic interrogator at the ground surface. Each coil is terminated

with a Faraday mirror. A laser in the interrogator shines light down the data cable where it is split at the coupler and reflected at each of the Faraday mirrors. The reflected light combines again at the coupler and travels back up the data cable and the intensity is measured using a photodetector in the interrogator. The path length of light traveling along the reference coil is fixed, but the path length on the sensing arm changes as a result of strain in the formation. An increase in path length of the sensing arm delays the arrival of light at the coupler and this changes the interference of the light traveling up the data cable. An increase in path length caused by strain in the formation increases the interference and reduces the intensity of light measured at the photodetector. This forms the essence of an equal-arm optical fiber Michelson interferometer. The instrument deployed in the field has a resolution of several femtostrain (10^{-15}), which is significantly greater than any of the other instruments used in the study.

The LILY self-leveling borehole tiltmeter (Applied Geomechanics/Jewel Instruments) was designed for volcanic and tectonic research and monitoring hydraulic fracturing and other subsurface processes in the oil and gas industry (Althen Sensors and Controls). The LILY tiltmeter is a dual axis-tiltmeter that senses angular movement in two vertical planes using electrolytic tilt sensors. The instrument records tilt, azimuth, temperature, and clock time. The noise floor of the tiltmeter is approximately 0.01 microradians.

Another important aspect of this project is to investigate the introduction of dissolved oxygen (DO) to the aquifer through ZNR tests. An AquaTroll 500 (In-Situ) was used for several ZNR tests and a constant-rate pumping test to monitor water quality parameters throughout the tests, including DO.

A pumping system was designed to conduct ZNR tests (Figure 12-2). The pumps are controlled by the variable frequency drives (VFD), which are turned on and off by an electronic timer switch. The timer switch is set to alternate power every half period. For example, for a 60-minute period test, the timer switch will be set to 30 minutes of pumping then 30 minutes of injecting, cycling until the test is manually stopped. Data-logging transducers (HOBO U20L-02 and U20L-04, Onset Computer) are set in the holding tanks, pumping well (PW-2) and observation wells (WL-2 WL-4, WL-5, and WL-7) to collect the total pressure head, and on the ground collecting ambient atmospheric pressure (Figure 12-2). Data from the transducers was downloaded between tests. Strain measuring instruments are deployed in various locations around the pumping well (Figure 12-2; Table 12-1).

The period of the pumping stage of a ZNR test is determined by the ratio of the tank capacity to the pumping rate. The initial tank capacity was 275 gallons and the pumping rate was 3 gpm, which limited the period to 180 minutes. To increase the duration of the pumping period, a 500-gallon tank was acquired and plumbed into the existing system through a two-inch PVC manifold, resulting in a holding tank capacity of 775 gallons. The system was designed such that both tanks are the same height and fill and drain at similar rates.

The pump and tank VFDs control the flowrate of the pumps by controlling the frequency of the AC power from 0 to 50 Hz. The flowrate produced by a given Hz output was calibrated. Several calibration tests were conducted throughout the project because the correlation between flow rate and frequency changed with use.

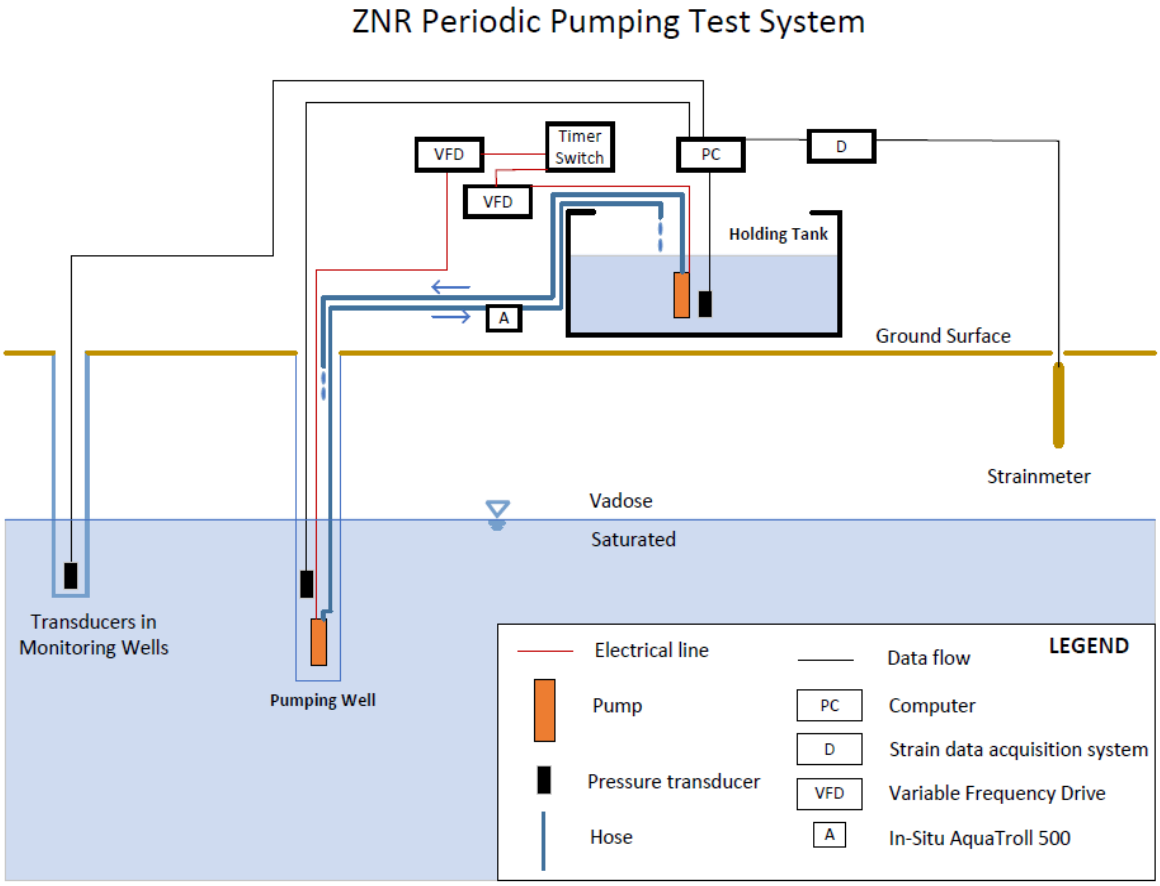

Figure 12-2. Diagram of ZNR pumping system

The pump calibration process involved conducting a 60-minute periodic test, with varying flowrates each period. Data-logging transducers are set to record pressure readings once every minute and are deployed both in the holding tank to record the sum of fluid and barometric pressure and next to the holding tank to record only barometric pressure. The barometric pressure is subtracted from the holding tank pressure. The holding tank data are then used to calculate the average rate between reading using finite differences. The rate is multiplied by the cross-sectional area of the tank(s) to give a volumetric rate for each minute. The volumetric rate is averaged over the 30-minute half period to produce a flowrate for the respective Hz output. Each Hz output used in the calibration process is plotted against its corresponding flowrate. A line of best fit is added and can be used to determine the appropriate Hz output for a desired flow rate (Table 12-2).

Pump calibration tests were conducted on March 10, 2021, April 13, 2021, November 23, 2021, November 26, 2021, January 13, 2022, March 15, 2022, March 27, 2022, May 11-12, 2022, May 15, 2022, June 8, 2022, and July 14, 2022. The results from these tests were used strictly to determine the Hz output for the Tank VFD and Well VFD for a desired flowrate used in other ZNR periodic tests.

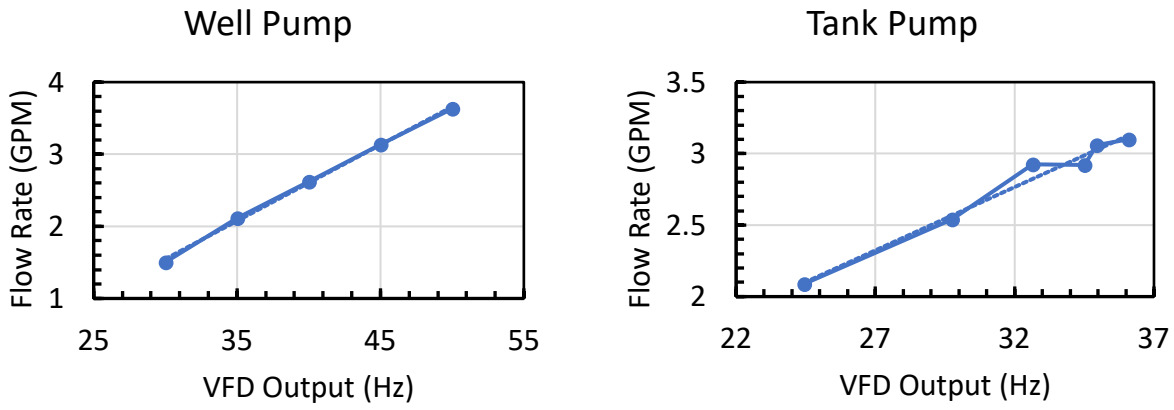

Figure 12-3. Summary of well pump and tank pump calibrations conducted on March 10, 2021.

12.3.1.1 Field Setup

The Bull Farm research field site is located on Bishop Branch Road in Pendleton, South Carolina. The Bull Farm is located within the Piedmont physiographic province, which is characterized by crystalline bedrock overlain by varying thicknesses of primarily sand, silt and clay derived from the weathering of the bedrock (Murdoch et al. 2006 and Hack 1982). The site is underlain by the Caesar's Head granite, a light gray, medium-grained, discontinuously banded to nonbanded biotite granitoid gneiss or gneissic granitoid (Nelson et al. 1998). The granitoid is strongly weathered to saprolite at depths shallower than 10 m (Murdoch et al. 2006). At approximately 2.5 m bgs, the relic structure of the saprolite is overlain by the soil B horizon, which can be classified as reddish, sandy, clayey, silt at approximately 2.5 m depth. Grain-size analysis characterize the B horizon as mostly fine-grained sand to silt with lesser amounts of clay and sand (SM to MH), and the saprolite as mostly fine-grained sand with lesser amounts of silt-sized grains (SM) (Murdoch et al. 2006). The saprolite retains some of the structure of the parent rock, which can have a significant effect on groundwater flow rates and direction.

The formation is unconfined with depth to groundwater of the surficial aquifer typically ranging between 25 and 35 ft below ground surface (bgs) (Figure 12-4). An unconfined aquifer consists of a capillary fringe between the saturated zone (positive pressure) and vadose zone (negative pressure). It is assumed that the saprolite transitions to a more competent parent-rock around 100 ft bgs, and this transition will act as a no-flow boundary for the purpose of this project. The aquifer is also assumed to be uniform and infinite lateral extent.

Ambient water levels in observation well shows that the hydraulic head gradient is to the south, which indicates groundwater flow is to the north. Groundwater flow direction was estimated using water levels from WL-4, WL-5, and WL-7. A three-point problem approach was utilized to estimate a groundwater flow azimuth of 355 degrees, assuming the aquifer is homogeneous and isotropic.

The observation wells are spread out around the pumping well, PW-2 (Figure 12-4 and Figure 12-5). The radial distances of the observation wells to the pumping well, the total depth of the wells, and the screen length of each well (Figure 12-4Table 12-1) are used in analysis. WL-2 was previously utilized for injection fracturing with another project and was drilled to a depth of 40 feet. WL-2 is an unscreened well that has developed a good connectivity to the aquifer, so there

will be no wellbore effects on the water level response. WL-4 and WL-7 were drilled to depths of about 45 feet and 40 feet, respectively. WL-5 was drilled by a professional drilling company to a depth of 60 feet. The two pumping wells, PW-1 and PW-2 were drilled by a professional drilling company and four-inch diameter wells were installed to a depth of 60 feet and 100 feet, respectively. PW-2 is the only pumping well utilized for this project. WL-8 was drilled in the fall of 2021 on the far north side of the Bull Farm field site to a depth of 35 feet bgs, with a piezometric level of 25 feet bgs. The purpose of this well was to monitor pressure at the furthest radial distance from PW-2 at the field site.

The various strain instrument locations are mapped over an aerial image (Figure 12-5) and shown in cross-section (Figure 12-4). A full list of strain measuring instruments and their depths is summarized in Table 12-1. A LILY Tiltmeter measure data during various tests and was installed in SX03 at a depth of 20 feet. DEL-X7 was not functioning during this project.

Table 12-1. A summary of data monitoring points at the Bull Farm field site. The 'Map Name' indicates the location on Figure 12-4,Figure 12-5Figure 12-6. The groundwater well depths have the screen length in parentheses.

Map Name	Description (Text Name)	Depth (screen length) (ft)	Radial Dist. from PW-2, *r* (ft)
SPW1	PW-1	60 (20)	NA
SPW2	PW-2	100 (60)	NA
SWL2	WL-2	40 (NA)	74
SWL4	WL-4	45 (5)	68
SWL5	WL-5	60 (10)	21.3
SWL7	WL-7	40 (5)	37.4
SWL8	WL-8	35 (5)	129
SX03	DEL-X3	19	52
SX04	DEL-X4	20	75
SX05	DEL-X5	19	30
SX07	DEL-X7	10	45.5
SX08	DEL-X8	30	33
SX09	DEL-X9	35	10.5
SDP2	Direct-Push FBG	14	9
SMR1	Michelson Ribbon	17	73
SLT1	LILY Tiltmeter well 1	10	38
SLT2	LILY Tiltmeter well 2	10	39
SLT3	LILY Tiltmeter well 3	10	54

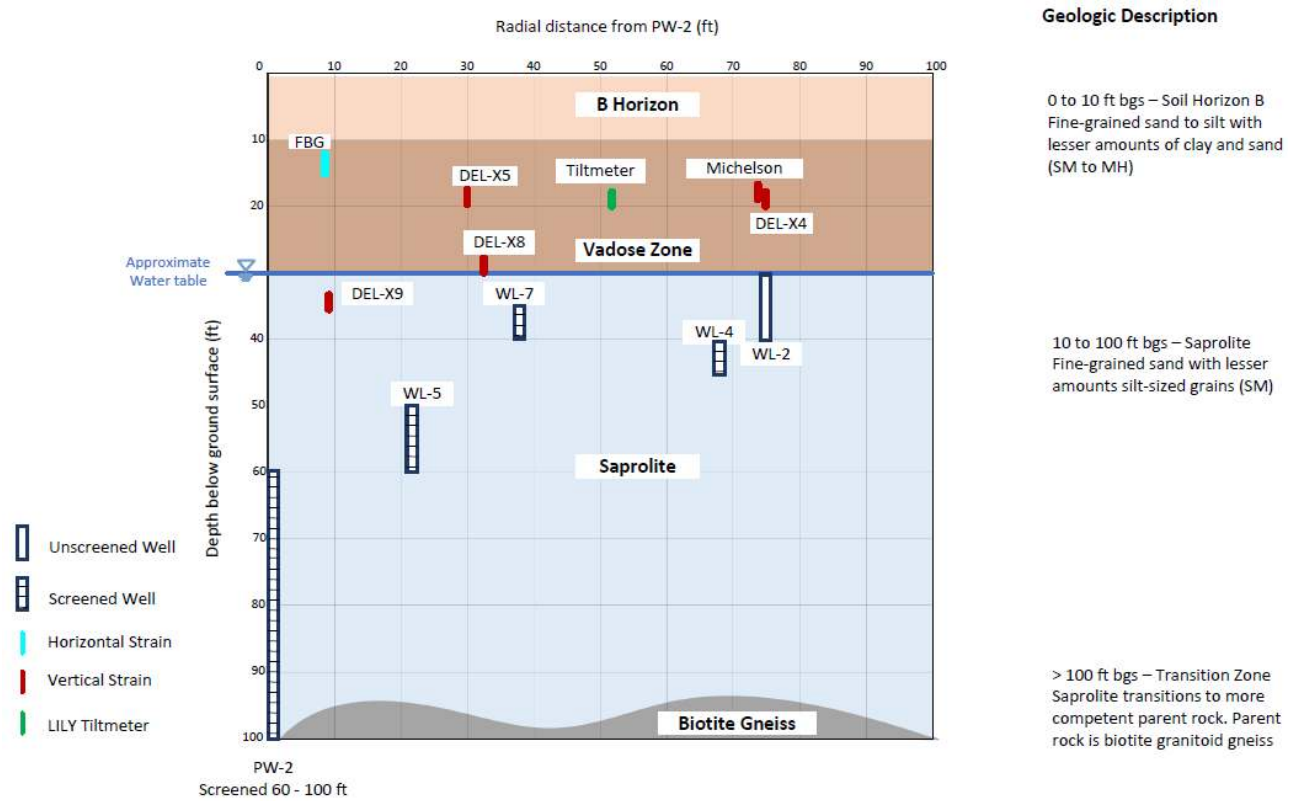

Figure 12-4. Axisymmetric cross-sectional diagram of field site instrument and well locations. The pumping well, PW-2, is located at $r = 0$ and the monitoring well screens and instrument locations are shown in relation to the pumping well. WL-2 is unscreened and was installed and developed through hydraulic fracturing.

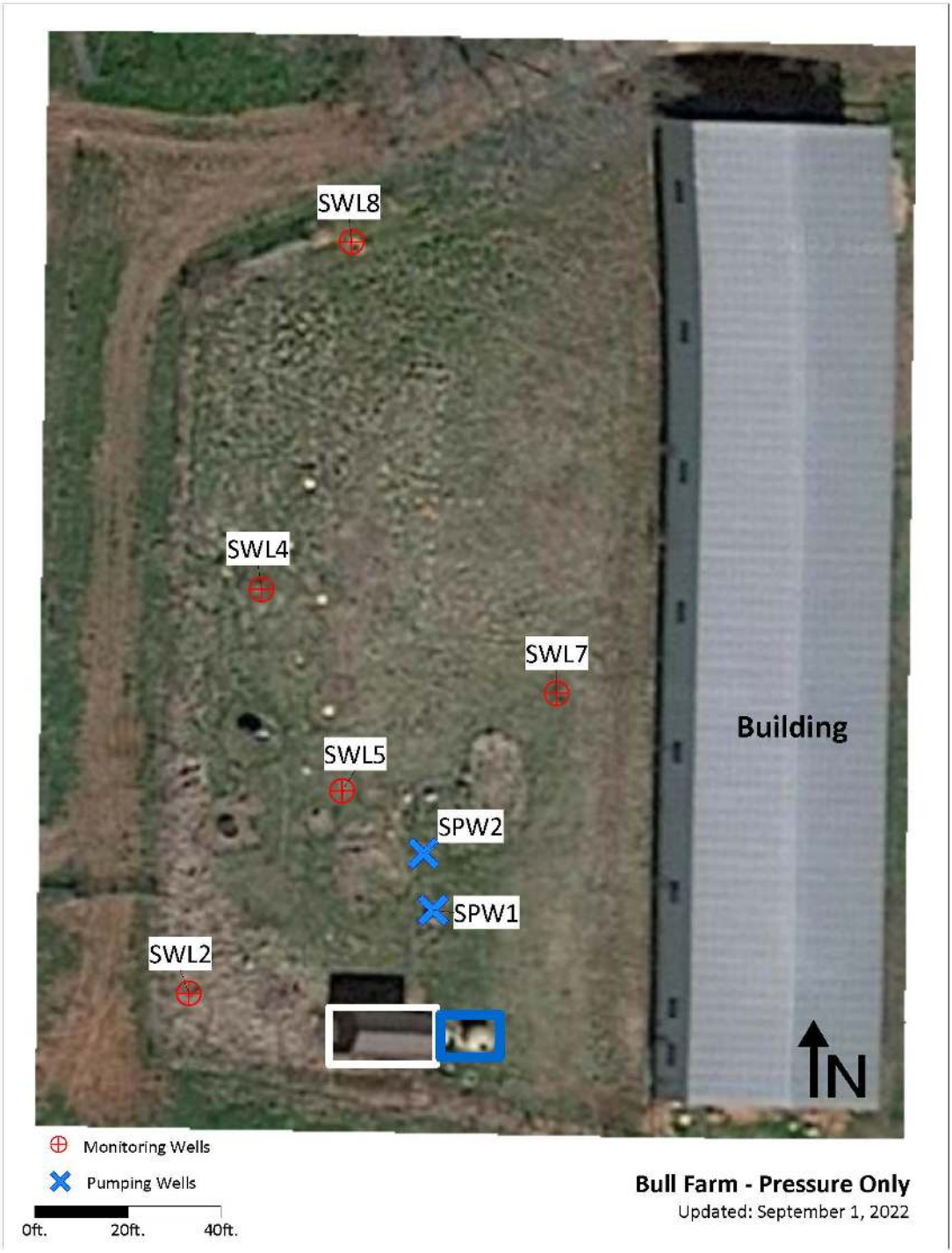

Figure 12-5. Map of Bull Farm field site showing pressure data collection points over an aerial image. Blue X's indicate pumping wells and red symbols indicate observation wells. The power is sourced in a shed indicated by the white rectangle. The holding tank(s) location is indicated by the blue rectangle. The well details are included in Table 12-1.

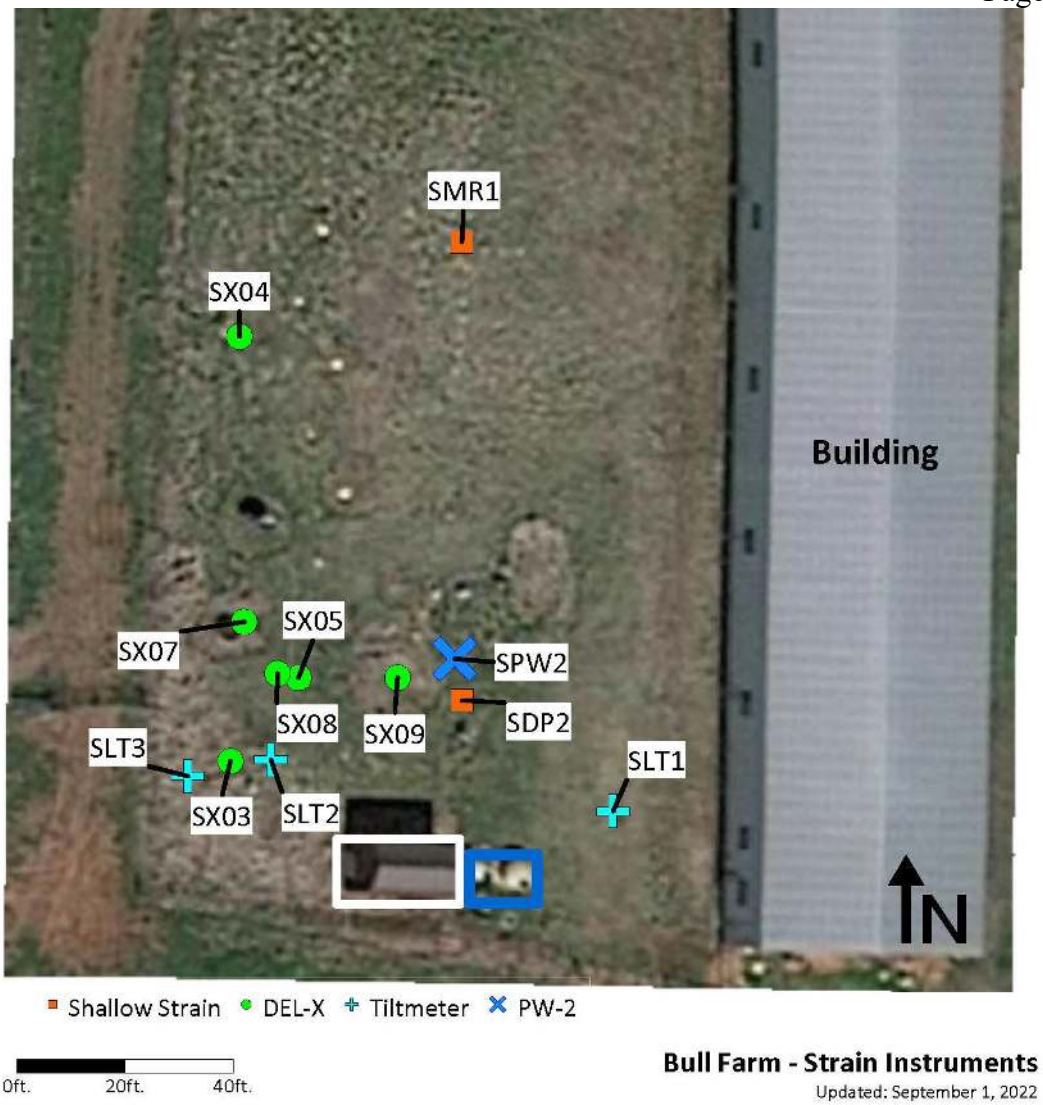

Figure 12-6. Map of Bull Farm field site showing strain data measurement locations over an aerial image. The power is sourced in a shed indicated by the white rectangle. The holding tank(s) location is indicated by the blue rectangle. A summary of the different instruments is in Figure 12-2. A LILY Tiltmeter was installed in SX03 at a depth of 20 feet.

12.3.1.2 Aquifer Test Setup

Slug tests and constant-rate pumping tests were conducted at the Bull Farm site to establish a baseline of aquifer parameters that could be compared to the results of ZNR tests. A series of ZNR tests, with periods ranging from 2 to 540 minutes were conducted and analyzed. A transducer in WL-5 was monitored throughout the duration of this project to record long-term water level trends.

12.3.1.3 Slug Test Setup

Two slug tests were conducted at the Bull Farm field site to estimate the hydraulic conductivity of the aquifer. In addition to providing a baseline of parameter estimates, an investigation into underestimating hydraulic conductivity through slug tests was conducted by comparing slug test aquifer parameter estimates to those of a constant-rate pumping test.

The slug tests were completed in PW-2 utilizing a two-inch diameter, five-feet long cylindrical slug. The volume of this slug was 0.11 ft^3 resulting in an expected initial displacement of 1.25 feet. A transducer was deployed in the well to a depth that would not interfere with the slug test, around 50 feet bgs. A second transducer was placed on the ground to record atmospheric pressure. The transducers were set to record pressure data every 10 seconds. The two slug tests were conducted consecutively on September 23, 2021. The first one was initiated at 9:52 am and the second one was initiated at 10:22 am. The duration of the slug tests are determined by the amount of time required for the well to equilibrate hydraulic head.

12.3.1.4 Constant-Rate Pumping Test Setup

Two constant-rate pumping tests were conducted at the Bull Farm field site. Constant-rate pumping tests are proven to estimate transmissivities, storage terms, and well efficiencies in confined and unconfined settings. The ZNR pumping system was modified such that the pump VFD was directly connected to the power source, bypassing the timer switch. The hose from the well pump drained into a ravine several hundreds of feet away to the north and downgradient, and a paddlewheel flowmeter was used to measure and record flowrate. The tests were started and stopped manually.

A constant-rate pumping test was completed on November 7, 2021. The flowrate was set to approximately 3 gallons per minute. Transducers were set in PW-2, WL-4, WL-5, WL-7, and on the ground to record pressure data every minute. The goal of this test was to run the constant-rate pumping test for four hours.

A second constant-rate pumping test was completed on May 25, 2022. The flowrate was increased to approximately 5 gallons per minute. Transducers were set in the same locations, recording pressure every minute. The goal duration of this test was 24 hours. The longer duration was used to evaluate the release of water from storage.

12.3.1.5 Zero-Net-Rate Periodic Pumping Test Setup

Several ZNR periodic pumping tests were conducted at the Bull Farm field site. The notable frequency dependence of aquifer parameter estimates in literature motivated ZNR tests to be conducted with periods ranging from 2 to 540-minutes.

The flowrate was nearly constant throughout the ZNR tests. The flowrate was reduced for the final two low frequency tests to 1.5 gpm, as the holding tank was at its capacity. The ZNR tests were conducted for a minimum of 3 periods, so the first two periods can be discarded to avoid transient effects during test startup. As a result, the duration of tests varied depending on the number of cycles and the period.

A timer switch was utilized for these tests to allow for automatic cycling between pumping and injecting. The timer switch is set to duration of each stage (half of the period). For example, with a 2-minute period ZNR test, the timer switch is set for a one minute pumping stage and one minute injection stage, cycled until the test is stopped manually. The AquaTroll was utilized to record water quality data during the last two tests on June 9 and July 15, 2022 (Table 12-2).

Table 12-2. Summary of ZNR tests conducted at the Bull Farm field site.

Period (mins)	Start Time	Stop Time	Number of cycles	Flowrate (gpm)
2	1/15/2022 15:16	1/15/2022 16:36	50	3
5	1/25/2022 14:35	1/25/2022 17:15	32	3
10	1/8/2022 13:00	1/8/2022 16:40	22	3
30	1/14/2022 15:00	1/15/2022 9:00	18	3
60	4/16/2022 7:46	4/16/2022 15:46	8	3
60	1/24/2022 10:30	1/24/2022 19:30	9	3
120	3/27/2022 15:31	3/28/2022 9:31	9	3
240	3/28/2022 12:00	3/29/2022 0:00	3	3
240	6/9/2022 16:45	6/10/2022 16:45	6	1.5
540	7/15/2022 12:01	7/19/2022 6:01	10	1.5

Transducers were set in PW-2, WL-4, WL-5, WL-7, WL-8, Holding Tank, and on the ground to record pressure. A transducer was utilized in WL-2 to record pressure during the March 27, March 28 and June 9, 2022 ZNR tests. The transducers were set to record pressure data once every minute for the first test completed on April 16, 2021. An initial analysis of the first ZNR test motivated a higher sampling frequency of pressure data. The HOBO transducers were set to record pressure data once every 10 seconds for the tests of 30-minute periods or less, once every 30 seconds for the 60-minute through 240-minute, and once every minute for the 540-minute. The transducer in the Holding Tank allows for a flowrate calculation and the procedure to calculate the flowrate is outlined in Section 2.1.

The various strain instruments at the Bull Farm site are hardwired to a data logging and telemetry system that allows the data to be recorded and examined in real time from a connected computer. There were some isolated issues that resulted in some instruments not recording data during particular tests, but overall, several strain instruments were functional during each of the ZNR tests. A complete list of which instruments were functional during which tests is provided in Chapter 4.

12.3.2 Data Analysis

The transducer pressure data from all field tests were uploaded into the HOBO brand software. The software plots the raw pressure and temperature data which allows for a quick inspection, ensuring the test was successful before analysis can be conducted. Strain data were retrieved at the end of the field-testing campaign. Once the data is collected from a successful test, data can be processed and analyzed.

12.3.2.1 Barometric Pressure and Long-Term Trend Corrections

The pressure data measured in the pumping or observation wells is the sum of the water pressure and barometric pressure. The first step in processing pressure data is to subtract the barometric pressure from the groundwater pressure data. The result is a pressure dataset that represents the water level pressure response. This step was done for every field test.

Aquifer tests that take place over long periods could be affected by long-term groundwater trends, and this can have a significant impact on the results. The long-term background trends of groundwater must be considered when analyzing aquifer tests of long durations. Tests in which the long-term trend has been considered included the 24-hour constant-rate pumping test on May 25, 2022, and the ZNR tests with a period > 240 minutes. Long-term pressure data is measured from a transducer in WL-5. The trends are observed for the week prior to a test, the duration of a test, and the week after a test. The pressure data is plotted as a time-series and a line of best fit is drawn to connect the pre-test data with the post-test data. The slope of this line is calculated and then the pressure data from field tests is corrected by this slope. This is done by multiplying the slope by the elapsed time to get an interpolated change of pressure that would likely occur if the test was not being conducted. This interpolated change is then subtracted out from the field pressure data.

12.3.2.2 Slug Test Analysis

The barometric corrected pressure data from PW-2 needs to be processed further for analysis. The data from the two tests are separated. Next, the data needs to be trimmed such that only the duration of the slug-in portion of the test is represented. The time data needs to be adjusted such that the start of the test equals 0 seconds. The pressure data needs to be put in terms of feet of drawdown. This is done by converting pressure (psi) to feet of head through a conversion factor of 2.31, and then subtracting out the initial head value at time = 0 seconds. A comma-delimited file is saved with time in the first column and drawdown in the second column.

The comma-delimited file is imported into well-test analysis software AQTESOLV. Aquifer and well parameters are entered, following the conceptual model. The conceptual model dictates the appropriate solutions to be used. The aquifer was assumed to be uniform and infinite lateral extent with a fully or partially penetrating well. A confined solution is used to be able compare similar analyses when looking at ZNR test results. An unconfined solution is used as the Bull Farm setting is unconfined, and any differences in results between confined and unconfined results should be noted. The Bouwer-Rice (1976) solution was originally developed for unconfined settings, but Bouwer determined that this model for slug testing could be applied to confined aquifers (Bouwer 1989). This is because the water-table boundary in an unconfined aquifer has little effect on slug test response unless the top of the screen is in the vicinity of the boundary (Bouwer 1989). Since the Bouwer-Rice (1976) solution can be utilized for both confined and unconfined settings, the analysis only needs to be run once per test.

The Bouwer and Rice (1976) solution requires an estimate of hydraulic conductivity anisotropy, K_h/K_v, to complete the analysis. A generally accepted value for this is 10, so the horizontal hydraulic conductivity is often 10 times greater than the vertical hydraulic conductivity. The slug tests analyses were completed with an anisotropy value of both 1 and 10, resulting in 4 total analyses.

The Bouwer and Rice (1976) solution is selected and then the curve matching is done manually as the early data holds the most weight in analyzing slug tests. A good representative line is drawn, and aquifer parameters are estimated based on the slope and the of the line. A summary of aquifer parameters used in analysis, the graph with a best-fit line over displacement data, and aquifer parameter estimates are exported.

12.3.2.3 Constant-Rate Pumping Test Analysis

The barometric-corrected pressure data from PW-2, WL-4, WL-5, and WL-7 was trimmed and units converted to drawdown per elapsed time. The pressure drawdown was converted to feet of head. The long-term trends for the May 25, 2022 test resulted in a trend of -0.01 $ft\,d^{-1}$. A comma-delimited file is saved with time in the first column and drawdown in the second column. This process was followed for both constant-rate pumping tests and produces a file that can be used with AQTESOLV. The well locations were surveyed, and a grid was created with PW-2 at the origin.

The flowmeter records a pulse for each unit of volume. The pulses were totaled every 30 minutes and normalized to give an average flowrate. The comma-delimited file is imported into AQTESOLV and aquifer parameters are entered following the conceptual model of the field site (Section Field Setup). The aquifer was assumed to be uniform and infinite lateral extent.

The Neuman (1974) solution for a pumping test in an unconfined aquifer and the Hantush (1961) solution for a pumping test in a confined aquifer were used to analyze the data. The Neuman (1974) solution is for a fully or partially penetrating well in a homogenous, anisotropic unconfined aquifer with delayed gravity response. This solution estimates transmissivity, storativity, specific yield, and hydraulic conductivity anisotropy ratio (Neuman 1974). Hantush (1961) extended the Theis (1935) solution for flow to a fully penetrating well in a confined aquifer, which neglects wellbore storage. Hantush (1961) modified the solution for a partially penetrating well. This solution estimates transmissivity, storativity, and hydraulic conductivity anisotropy ratio.

For constant-rate pumping tests, the curve-matching software is utilized to determine a best fit line while estimating the most representative aquifer parameters. AQTESOLV estimates parameters that minimize the residuals between the field data and the type curve. The approach was to first estimate parameters using data from WL-4, WL-5, and WL-7 individually because the results from ZNR tests were analyzed for individual wells. Next, parameters were estimated that best match the data from all the wells. For the two constant-rate pumping tests, there is a result for WL-4, WL-5, WL-7, and all three wells together.

The final calculation performed is determining well efficiency. Drawdown from the observation wells at a particular time is plotted as a function of radial distance, with drawdown (ft) plotted on the y-axis and the radial distance (ft), r, plotted on the x-axis with a logarithmic scale. A line of best fit is drawn from the observation wells to the x-intercept, where an expected drawdown on the pumping well is interpolated. The well efficiency is the ratio of expected to actual drawdwon (Kruseman and de Ridder 1990).

12.3.2.4 ZNR Test Data Processing

The data from ZNR tests are measured and analyzed in the time-domain. The pressure data from PW-2, WL-2, WL-4, WL-5, WL-7, and WL-8 are processed by discarding the first two to five periods, so early transients are omitted, and the response being analyzed is steady-periodic. For higher frequency tests, more periods are discarded as the transient response may extend past

the first two periods. The time-series data were examined on a test-by-test basis to determine the cycles used for analysis.

The data are trimmed such that the data ends on whole periods. For example, if there is a 30-minute test conducted, the data should end on minute 30, 60, 90, etc. This was done to avoid errors in the Fourier transform when using a partial period.

The time data are transformed from time of day to elapsed time since start of test, with the start of the steady-periodic data corresponding to time = 0. The pressure data (psi) are put in terms of feet of head. The hydraulic head (ft) data are then averaged over the whole test. The average is subtracted from the head values, to get an oscillating head response that is normalized to 0 ft. An example of the plotted processed data is included in Figure 12-7. The initial drop in head indicates the start of the pumping period, where pressure is lowered. In PW-2 there is a flattening of the curve through the duration of the half period, indicating a release from storage.

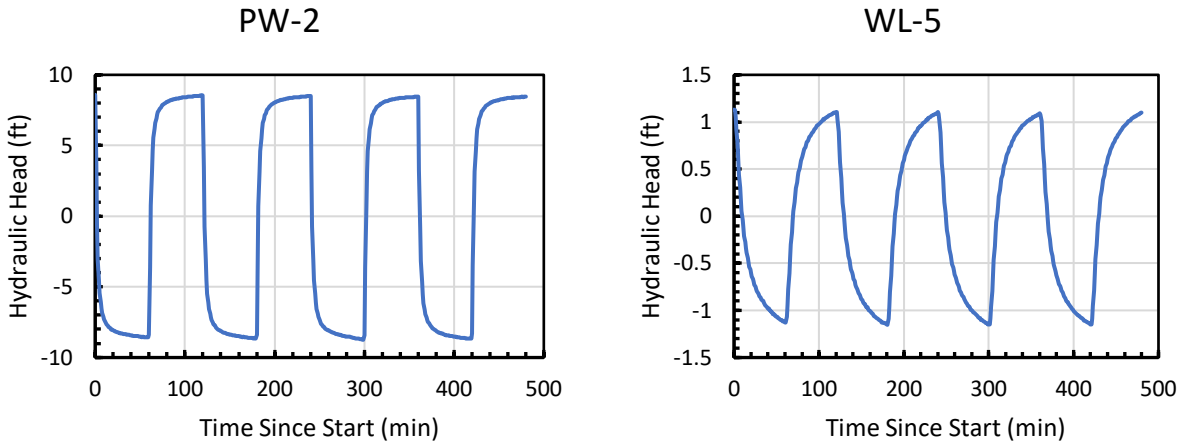

Figure 12-7. time-series of 120-minute ZNR test hydraulic head response in (a) PW-2 (left) and (b) WL-5 (right). The data are trimmed to end at minute 480, so this test has four periods ready for analysis.

Changes in head due to background trends are small over the duration of the short period tests so they are ignored. Changes in head due to background trends during the two 240-minute tests and the 540-minute test were considered. The background trends were determined to be negligible, with rates less than 0.003 ft d^{-1}.

12.3.2.5 Analyzing ZNR Test Delay and Amplitude

Trimmed and processed pressure data were analyzed to determine amplitude and delay of the fundamental period and a series of harmonics, and these data were used to estimate formation properties. The time delay, t_L, of the fundamental period during a ZNR test in a uniform confined aquifer is related to the period, λ, after some approximation (Streltsova, 1988) as

$$t_L = C_s\sqrt{\lambda r^2} \qquad (12\text{-}12a)$$

where r is the radial distance, and the constant is related to the hydraulic diffusivity

$$C_s = \sqrt{\frac{1}{4\pi D_h}} \qquad (12\text{-}12b)$$

This suggests that the delay is a function of the square root of the scaled period, λr^2, so the data should have a ½ slope on a log:log plot and the intercept is related to the D_h when the conditions required for the approximation are valid.

One condition of the approximation requires (Streltsova, 1988, 3.10.1)

$$r\sqrt{\frac{2\pi}{\lambda D_h}} > 1 \qquad (12\text{-}13)$$

This leads to a threshold value of λr^2 for eq. 12-12a to be valid

$$\lambda r^2 > \frac{D_h \lambda^2}{2\pi} \qquad (12\text{-}14)$$

One of the goals of this investigation is to evaluate the feasibility of using ZNR tests to estimate formation properties, so the preceding analyses will be used to guide the description of the data.

The periodic data from the monitoring wells were analyzed using a discrete Fourier transform (Strang 1994; Fourier, 1822) that generated a set of amplitudes and phase delays for sinusoids at the fundamental period and for harmonics (period of test / harmonic number). A discrete Fourier series assumes that an arbitrary function can be represented as

$$f(x) = A_o + \sum_{n=1}^{m} A_n \cos\left(\frac{2n\pi t}{\lambda} - \varphi_n\right) \qquad (12\text{-}15)$$

where A_o is the mean value, n is the harmonic number and m is the total number of harmonics used in the approximation, A_n is the amplitude of the nth harmonic, λ is the fundamental period, t is time and φ_n is the phase shift of the nth harmonic. The fundamental period is the first harmonic, or lowest frequency of the periodic waveform. A_1 and φ_1 are the amplitudes and phases of the first harmonic. $1/\lambda$ is the fundamental frequency.

A discrete Fourier transform is used to estimate the amplitudes, A_n, and phases , φ_n, of the fundamental period and harmonics from observed data $f(x)$. The phase values were converted to a time delay, t_{Ln}, (minutes), by dividing by the angular frequency $\omega = \frac{2\pi}{\lambda}$. In general, the amplitudes of harmonics with even values of n were small and these values were ignored. The amplitudes of harmonics with odd values of n decreased with increasing n. Time lag and amplitudes of odd harmonics $1 \leq n \leq 19$ were recorded.

The Fourier transform was limited to determining phases in the range $-2\pi < \varphi < 2\pi$. Phases of high frequency harmonics exceeded this limit in some cases. Phase calculations in these cases were adjusted to account for wrapping onto a following period, and the phases of some high fre-

quency harmonics were omitted when the results were ambiguous. Negative phases were converted to positive values by adding 2π. As a result, the delay values are the times that the monitoring well signal is delayed behind the pressure signal in the pumping well. The Fourier transform was limited to the first 20 harmonics.

A Visual Basic (VBA) computer code was written and implemented to calculate the Fourier transform in a Microsoft Excel Workbook, called FT Workbook. The time-series data and period length are entered in the FT Workbook, and then the Fourier coefficients are calculated for n=1 to n=20. The program plots the first n harmonics of the Fourier series and the raw data to facilitate visual inspection. An example of the fundamental period of the Fourier series, n = 1, and the addition of other harmonics, n = 1 - 3, and the field data plotted together is in Figure 12-8.

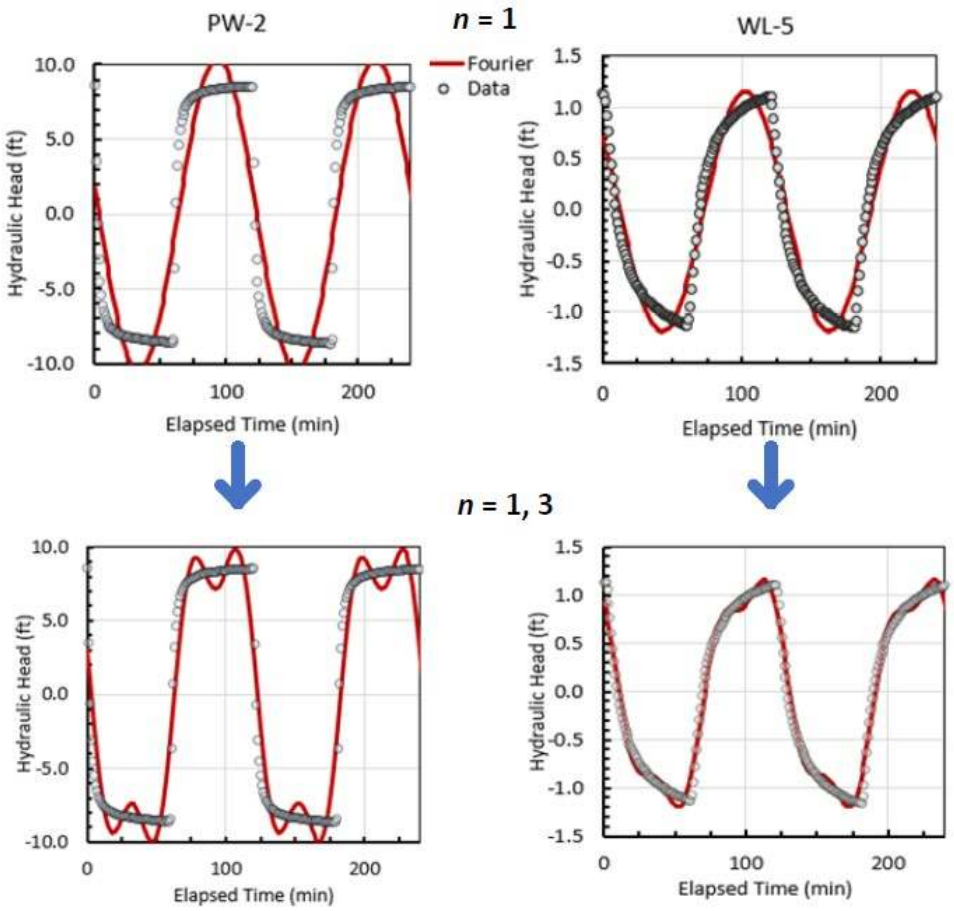

Figure 12-8. Steady-periodic hydraulic head response for the 120-minute ZNR test with two periods shown for (a) in PW-2 (left) and (b) WL-5 (right). The dots represent the field data and the red lines are the Fourier series representing the data. The fundamental period, n = 1 is shown in red in the upper row, and the fundamental period and the 3rd harmonic, n = 1,3, is shown in red in the lower row.

The FT Workbook has multiple summary tables that display the Fourier lag and amplitude results of two datasets. The Fourier results are used for parameter estimation through the Steltsova

(1988) solution. The full description of this solution is outlined in Chapter 1.1.3. Streltsova's solution results in an equation that relates time lag to the formation hydraulic diffusivity (equation 1.7), and an equation uses both time lag and amplitude to estimate transmissivity (equation 1.8). Those results can be used to estimate Storativity.

Streltsova (1988) indicates the analysis should focus on the fundamental period term since the fundamental frequency contributes most to the sum, but an investigation into higher frequency harmonics is also performed. Time lag and amplitude values of odd-numbered harmonics are recorded for each ZNR test for each monitoring location. FT Workbook allows for the visual inspection of the time lag for the first harmonics by plotting the two data. The x-axis (time) can be adjusted so that an area of interest, such as the time between two peaks, can be observed. This is a good way to check the table results and confirm time lag and amplitude values Figure 12-9.

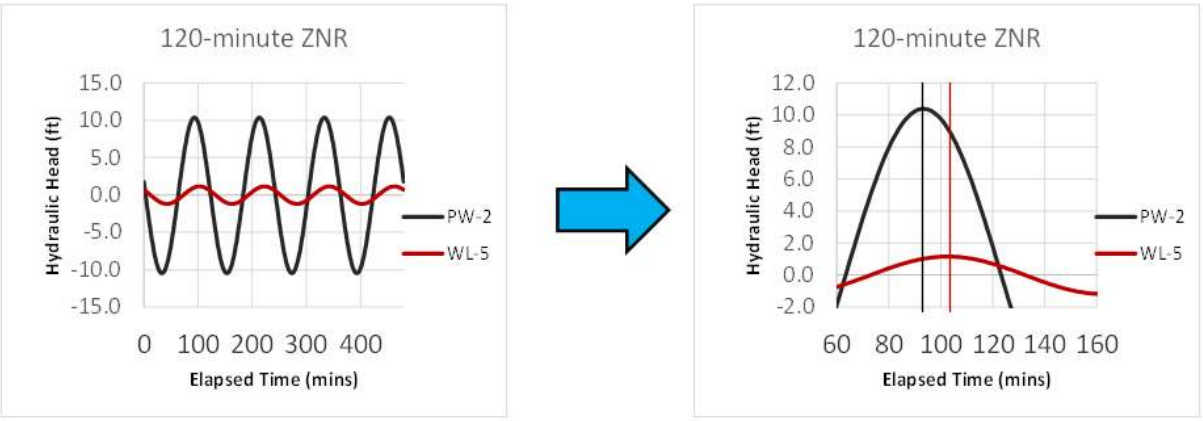

Figure 12-9. Fundamental period Fourier function for PW-2 (black) and WL-5 (red) for (a) 120-minute ZNR test (left) and a (b) zoomed in view of the same data (right), to allow for visual inspection of the time lag of signals. From the graph, the time lag between the two peaks looks to be about 10 minutes and the Fourier summary table produced a value of 9.4 minutes.

12.3.2.6 ZNR Periodic Pumping Test Strain Analysis

The strain data are measured using instruments described in Chapter Instrumentation, and stored on a server. Strain data were inspected during the testing program to verify the instruments were functioning, and then the data from each test was retrieved from the server after the field-testing campaign was complete. Periods of strain data were discarded to use the same steady-periodic that was used for the pressure analyses. The end data are trimmed at the end of the last whole periods to match the pumping data. Long-term strain data were not collected to investigate the possible need to detrend data due to background trends. Some of the strain data was clearly affected by barometric pressure variations, but no barometric pressure corrections were used. The processed strain data are processed through the FT Workbook code, and then amplitude and delay values are produced for each harmonic.

12.3.2.7 Well Efficiency of ZNR Tests

Well efficiency is calculated for the first period of every ZNR test with periods greater than 30 minutes using the same method described in Section Constant-Rate Pumping Test Analysis for

the constant rate tests. These results will be compared to the results of constant-rate pumping tests to evaluate the accuracy of this method.

12.3.2.8 Statistical Analysis

Statistical analyses of the field data were conducted to compare the results of the various types of aquifer tests. A *t*-test is used to compare the mean values of aquifer properties determined using ZNR and other well tests (Rice 2006). The null hypothesis is that means of the two datasets are equal, and it follows that any difference between the means is simply because the sampling of the datasets is incomplete. A *p*-value determined through the *t*-test is used to determine whether the null hypothesis is accepted or rejected. A *p*-value less than 0.05 is assumed to be sufficient to reject the null hypothesis and conclude that the difference between the means is significant with 95% confidence (Rice 2006).

Independent two-sample t-tests were run by assuming two-tail distribution and equal variance. The distributions were assumed two-tailed because this approach is appropriate if the objective is determining any difference between two groups (Riffenburgh 2012). The variances can be assumed equal because the usual approach is to assume no difference in variances when there is a lack of evidence of such difference (Riffenburgh 2012). Assuming unequal variance can affect the error rate and lead to false positives (Minitab 2016).

Datasets that were compared include: slug test K vs. constant-rate test K, constant-rate tests D_h vs ZNR test D_h, constant-rate test K of individual wells vs ZNR test K of individual wells, all K values from slug tests and constant-rate tests vs all K values from ZNR tests, and constant-rate test S values vs ZNR test S values. A series of *t*-tests was also run to compare the results of values of D_h determined using harmonics to the results using the fundamental period.

12.3.3 Numerical Experiments of ZNR tests

Simulations of the pressure and strain response to a square-wave, periodic pumping rate were simulated to provide a perspective on the field data. This approach utilized fluid flow through a porous media and deformation coupled through poroelasticity, representing a confined aquifer with a vadose zone above it. The governing equations are described in Chapter 5.

12.3.3.1 Pressure and Strain Experiments Setup

The analysis was set up in axial symmetry using two rectangular domains where the physics in each domain are related, but different (Figure 12-10). The lower domain includes fluid flow through porous media and deformation coupled through poroelasticity and it represents the aquifer. The upper rectangular domain is the vadose zone. It includes elastic deformation, but the fluid pressure is assumed to be constant. This is justified for short well tests because the relative liquid phase permeability in the vadose zone would limit pressure diffusion from the aquifer, and the air phase would create a highly compressible pore fluid that would limit pressure changes due to deformation. We have conducted simulations where fluid pressure in the vadose zone is allowed to change and it is represented by the Richards equation. Results of this model shows that pressure changes in the lower part of the vadose zone can be affected by pressure changes in the underlying aquifer, but those changes are small and limited to the lower few meters so they will be ignored here.

The pumping well is represented using a boundary condition that includes wellbore storage. This is accomplished by assuming water volume is conserved in a wellbore of finite volume, where

the diameter was assumed to be 0.1 m. The hydraulic head is assumed to be uniform over a fully penetrating well screen, and the head in the well bore is above the top of the screen so the change in head is equal to the change in storage in the well bore. The fundamental sinusoids of the wellbore

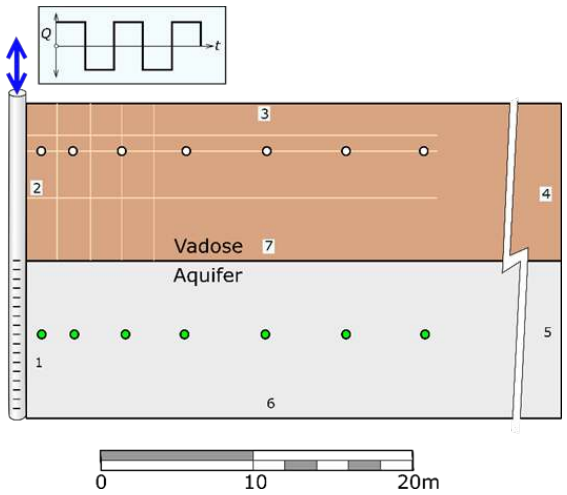

Figure 12-10. Conceptual model of simulation in axial symmetric coordinates with a well at the axis. Pressure analyzed in the aquifer. Pressure assumed constant in vadose. Strain occurs everywhere and is coupled to the fluid pressure in the aquifer. Light colored lines in vadose zone are section lines used for plotting. White circles are locations of strain and green circles are location of pressure time series. Boundary conditions for pressure and mechanics: (1) periodic flux as shown in inset from wellbore with storage, normal traction equal to pressure; (2) zero normal displacement (roller); (3) zero normal traction (4) roller @ r=10km (5) roller, specified head @ r = 10km (6) no flow, roller (7) no flow, continuity.

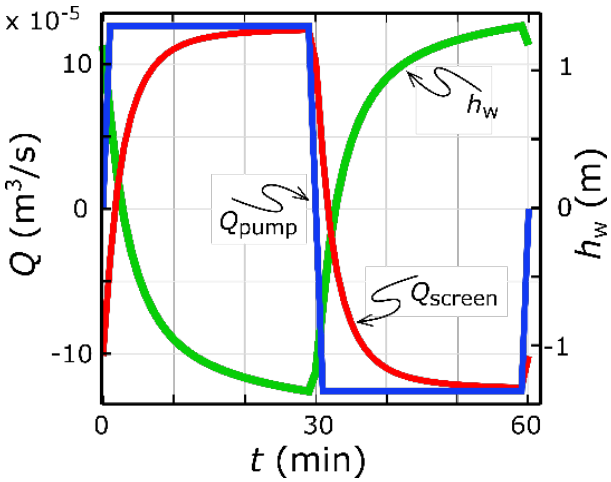

Figure 12-11. Flowrate and pressure at the wellbore. The flowrate pumped from the well (Q_{pump}) is a square wave with zero net rate. The flowrate through the well screen (Q_{screen}) is exchanged between the well and the aquifer. It differs from Q_{pump} because of wellbore storage. The head in the wellbore, h_w, is used as a phase reference in the analyses.

pressure and the pumping rate have a phase difference of $\pi/2$ when wellbore storage is absent. Including wellbore storage delays the change of pressure in the wellbore compared to the pumping rate, and this increases the phase difference between wellbore pressure and rate (Figure 12-11).

The thickness of the aquifer and vadose zones are both 10 m, which is similar to the field site, and the lateral extent is 10 km, which is large enough to eliminate effects of lateral boundaries. Other boundary conditions for the fluid and displacements are standard and summarized in

The rate varies periodically, starting with a pumping stage followed by an injection stage of equal rate, but opposite sign (Figure 12-11). This gives a net pumping rate of zero after every completed ZNR cycle of pumping and injection. Changes in wellbore storage cause the flowrate leaving the wellbore and entering the aquifer to be less than the pumping or injection rate, particularly early in a pumping or injection cycle (red line in Figure 12-11). The hydraulic head in the well drops with time during the pumping cycle and reaches a minimum at the end of the pumping stage. It then increases and reaches a maximum at the end of the injection stage (blue line in Figure 12-11).

12.3.3.2 Pressure and Strain Experiments Results

The pressure head at the well is between +/- 1 m, and this value decreases to less than 10 percent of the value at the well at r = 20m (Figure 12-12). The strains along a horizontal line at a depth of 3 m in the vadose zone fluctuate between approximately +/- 4 me at the well and they also decrease with distance but at a slightly slower rate than the pressure. The sign of the radial strain, e_{RR} changes with distance and reaches a peak of roughly 1 me that is opposite in sign from that at the well at 20m < *r* <25m (Figure 12-12).

The pressure and strains vary periodically at reference points in the aquifer and vadose zone (Figure 12-13). The shapes of the times series are generally similar—they all change rapidly at the beginning of a stage and reach a maximum or minimum at the end of the stage. The delays of pressure and strain components all increase with distance from the well, and this is manifested by a delay in the time when the maxima or minima occur in the time series (Figure 12-13). Even though they share similar general characteristics, the shapes, magnitudes and delays of each strain component are distinct from each other and from the pressure (Figure 12-13).

The injection stage of the ZNR cycle causes the vadose zone to be displaced upward and away from the well (Figure 12-14). The displacements are predominantly upward near the well and the horizontal component increases as the overall magnitude of the displacement (color of the vectors) decreases with distance from the well (Figure 12-14). The vadose zone drops near the well at the onset of the pumping stage and at $t/\lambda = 0.2$ there are downward displacements within *r* <10m of the well and the upward displacements from the earlier stage persist at *r* > 10m (Figure 12-14). The displacements are all downward and toward the well at the end of the pumping stage ($t/\lambda = 0.5$), roughly opposite the displacements at the end of the injection stage $t/\lambda = 0$ or 1.

Displacements create a rich, varying vector field in the vadose zone, but the magnitudes are relatively small and would be difficult to measure with available field equipment. However, gradients in the displacement field creates a strain tensor field, which is equally rich and varied. This is important because instruments are available to measure very small components of the strain tensor.

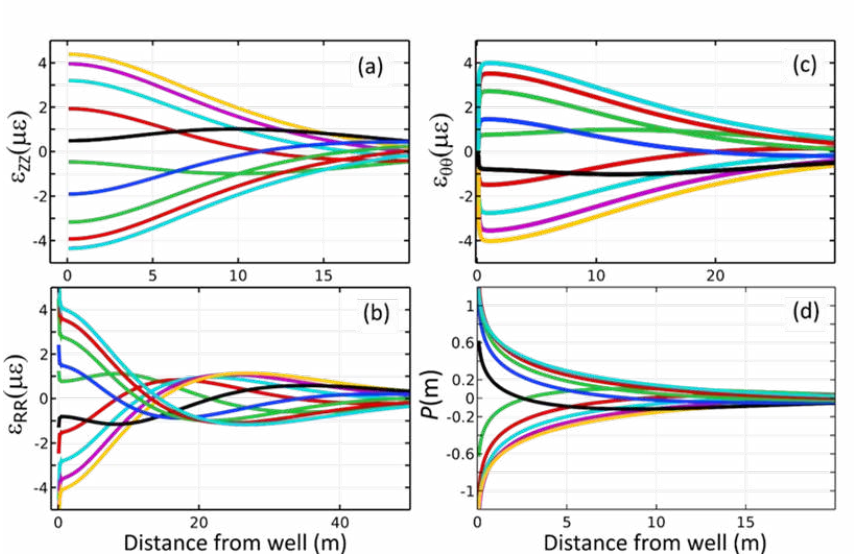

Figure 12-12. Strain components and pressure along horizontal lines shown in Figure 12-10. Strains are at z = -3m in the vadose zone, pressures are at z = -15 m (mid height in aquifer). Colors are at a particular time during one representative ZNR cycle.

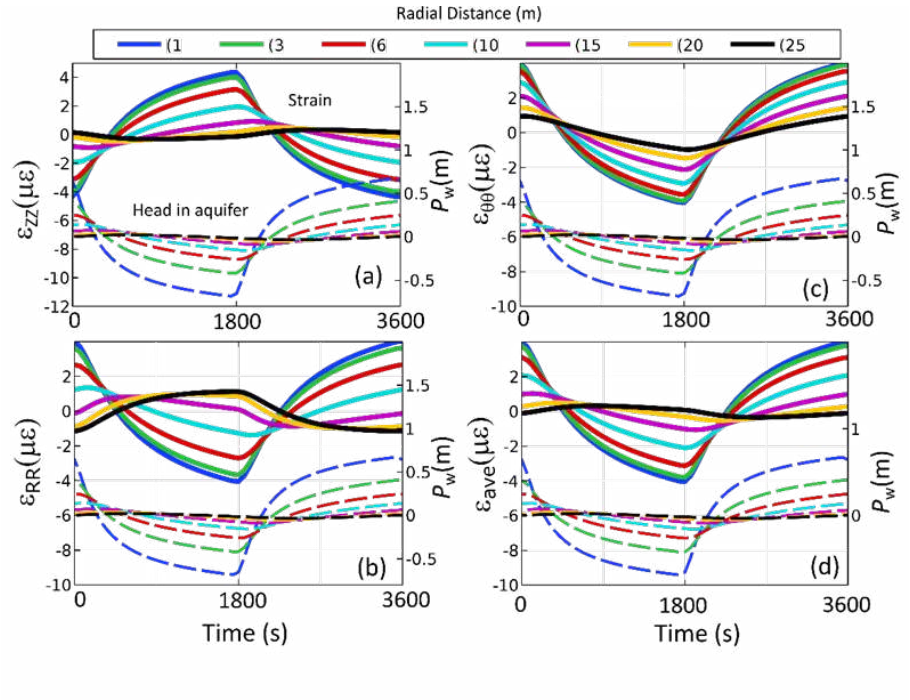

Figure 12-13. Strain components (solid lines) at reference points at different radial distances indicated by color in the vadose zone (z = -3m) and hydraulic heads (dashed lines) in the aquifer (z = -15m) at radial distances indicated by color. Reference points in Figure 12-10.

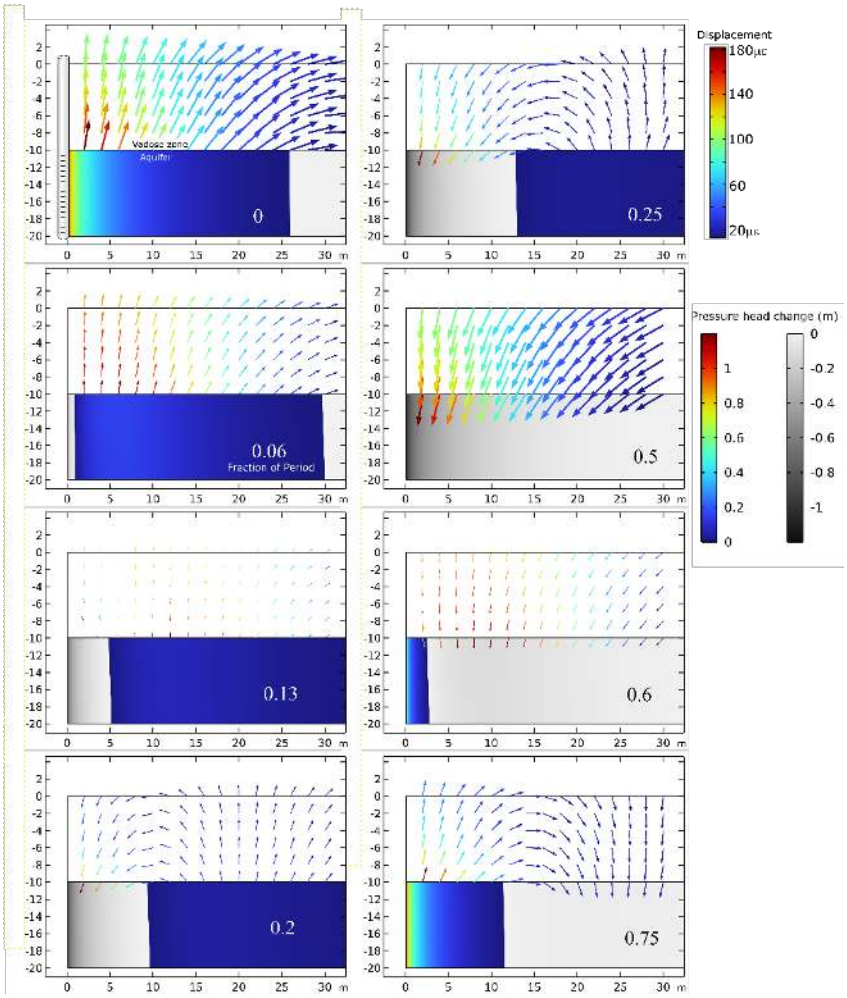

Figure 12-14. Displacements in the vadose zone and pressure in an underlying aquifer experiencing a ZNR cycle, cross-section view. The numbers are the time as fractions of a period, t/λ. Pumping occurs during $0 < t/\lambda < 0.5$, and injection occurs during $0.5 < t/\lambda < 1.0$. Displacements and pressure head change magnitudes shown in legend.

The strain tensor field at the end of the injection stage, $t/\lambda = 0$, ranges from roughly -10 με to 10 με and each component forms a unique pattern (Figure 12-15). The maximum strains are in the lower left corner, slightly above the well screen, and they decrease upward and radially within approximately 5 m of the well. In the mid-distance of $5 < r < 15$m, the strains decrease in approximately a horizontal direction (the contours are roughly vertical). At larger radial distances the strains decrease downward. Both the vertical and radial strains, and the horizontal average

strain change sign with distance, but the sign of the circumferential strain remains positive during $t/\lambda = 0$ (Figure 12-15).

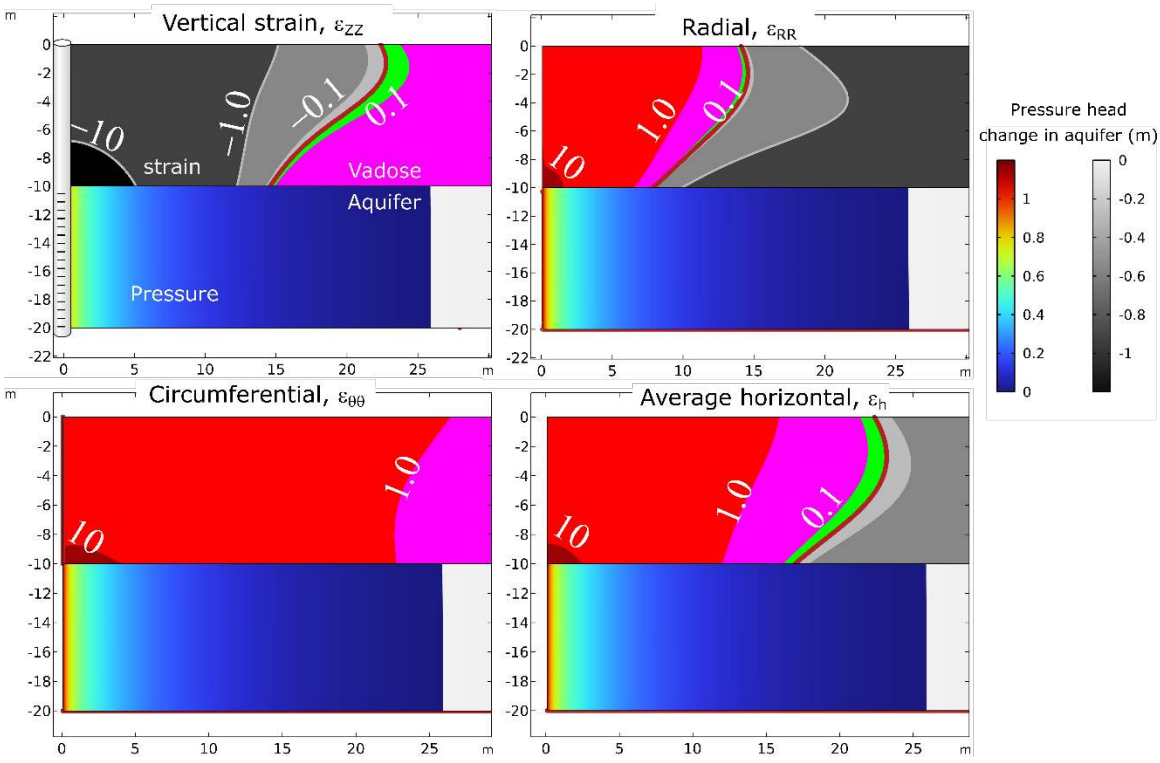

Figure 12-15. Strain components in the vadose zone and hydraulic head change in the aquifer in cross-section at the end of the injection stage of a ZNR cycle, $t/\mathrm{l} = 0$. Simulation for a period of 1 hr.

The patterns of the strain components evolve through a ZNR cycle (Figure 12-16), but in general, the onset of each stage generates strain contours that grow upward and outward in the vicinity of the well (r <~ 5m). The contours wrap upward and are subvertical in a mid-distance area ($5 < r < 15$m), and the contours continue to rotate clockwise and are inclined far from well ($r > 15$ m).

A unifying pattern emerges that appears to persist in the strain field throughout a ZNR cycle (Figure 12-16 and Figure 12-17). In general, there are four regions in the vadose zone where the direction of decreasing strain is consistent, whereas the direction of decrease pressure is always horizontal away from the well in the aquifer (Figure 12-17). Strain decreases upward in the Near Well region, whereas it decreases in a horizontal direction in the Shallow and Mid-Distance regions. Strain decreases downward in the region that is far from the well (Figure 12-17)

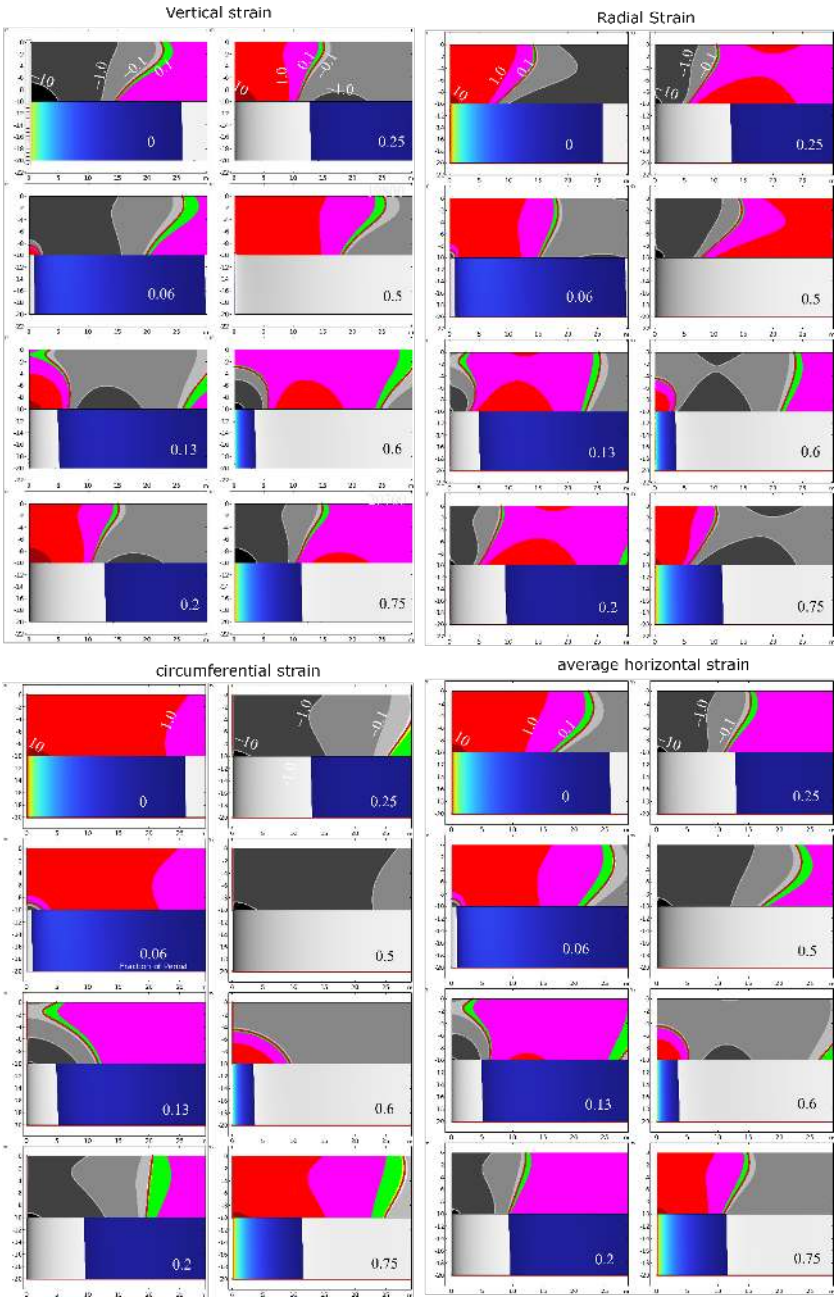

Figure 12-16. Strain components in the vadose zone and hydraulic head change in the aquifer in cross-section at different times during a ZNR cycle indicated by the fraction of a period as inset in each panel. The cycle starts with pumping and injection starts when the fractional period $t/\lambda = 0.5$. Simulations are for a period of 1 hr.

Phases of the strain components in the vadose zone were calculated using a Fourier transform. The phase of the pressure at the well face was taken as zero and phases were converted to time delay following the pressure. A half period was added to the phase of ε_{zz} to facilitate plotting with the other strains.

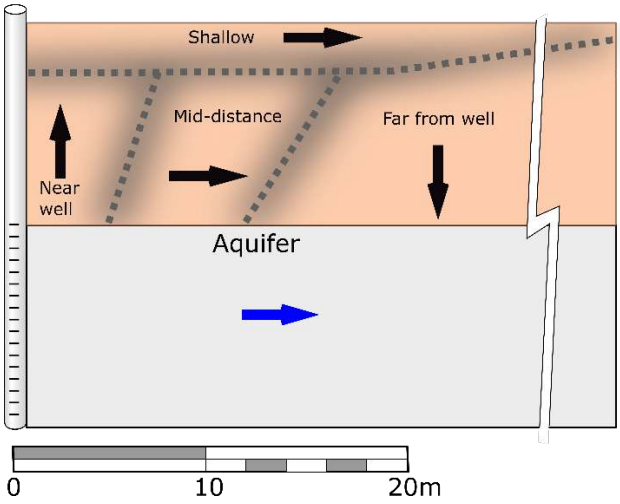

Figure 12-17. Conceptual model of regions of different hydraulic head and strain gradients in the vadose zone and aquifer. Arrows show direction of decreasing strain (black) or hydraulic head (blue).

The delay of the pressure increases as a roughly linear function of distance from the well (blue lines in Figure 12-18. The delay of the vertical and average horizontal strains, ε_{ZZ} and ε_h, at shallow depth (3m) in the vadose zone are non-linear functions of distance, but they cross the delay of the pressure at two locations and they are generally within 20 percent of the delay of the pressure within 25 m of the well (Figure 12-18a). The delay of the circumferential strain $\varepsilon_{\phi\phi}$ is significantly less and that of the radial strain ε_{RR} is significantly greater than the pressure delay. This suggests that the pressure delay in the aquifer could be estimated to within roughly 20 percent using the delay of ε_{ZZ} or ε_h measured at shallow depth in the vadose zone.

The delays of the ε_{ZZ} and ε_h are similar to the delay of p at mid-depth and near the bottom of the vadose zone in proximity to the well, but the delays for those strains exceeds that of the pressure at $r > 10$ to 15m (Figure 12-18b and c). The simulation used here assumes the pressure change in the aquifer is isolated from the vadose zone, whereas in most cases a pressure change in the aquifer is expected to propagate upward into the overlying vadose zone. This will affect the strains in the vadose zone, particularly at the bottom of the vadose zone. The strains shown in Figure 9c do not include this effect.

The patterns of the delays of the strain components are broadly consistent, but each one is distinct from the others (Figure 12-19). The delays generally increase upward and horizontally from a point in the vadose zone closest to the well screen. This gives rise to upward phase velocities within a few meters of the well (Figure 12-24). Contours of the delays are roughly vertical in the range of $6 < r < 10$m, and they curve upward and outward away from the well at greater radial distances (Figure 12-19).

The phase velocity of the strain is normal to the contours shown Figure 12-18, and this supports the general conceptual model in Figure 12-17. The horizontal phase velocity of the pressure is 1.1 m/min. The upward velocity of the ε_{zz} is approximately 2 m/min at $r = 2$m, but it drops to roughly 0 at $r = 8$m and it is downward at -0.6 m/min at $r = 14$m (Figure 12-24 and Figure 12-20).

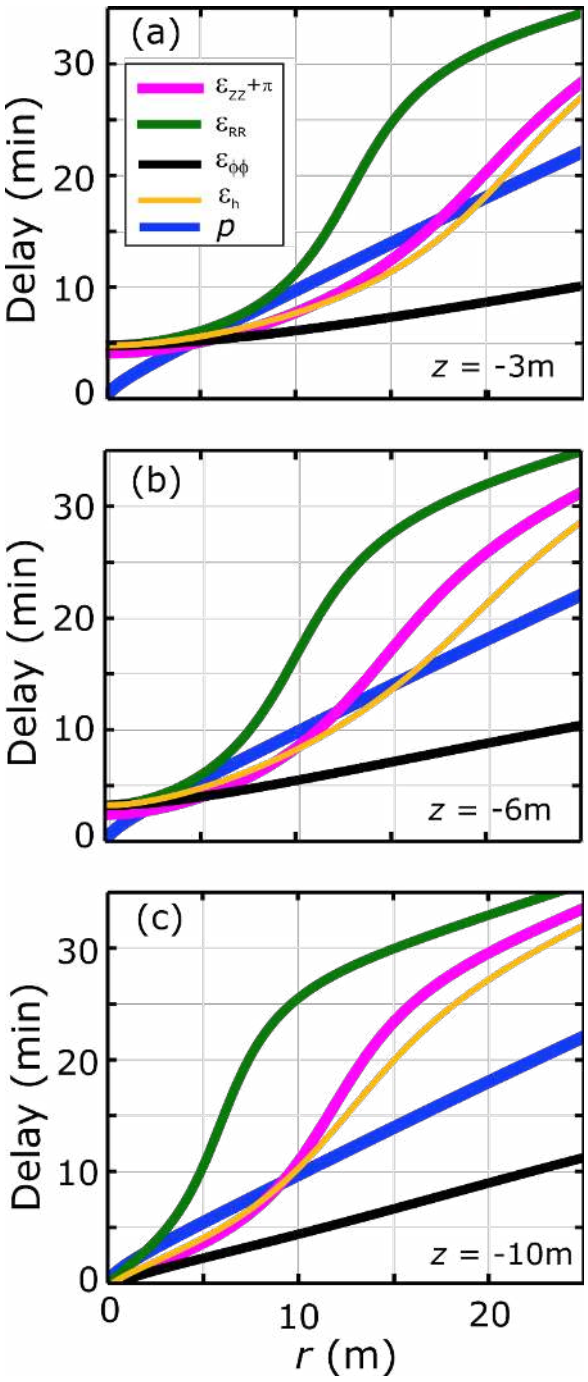

Figure 12-18. Delay of the strain and pressure along horizontal lines at different depths. Pressure measured at mid-height in aquifer. (a) strain at 3m depth and (b) strain at 6m depth. (c) strain at 10m depth, bottom of vadose zone. Period = 1 hr. The delay of the vertical strain, ε_{ZZ}, is shifted by one half a period so it plots with the other strains.

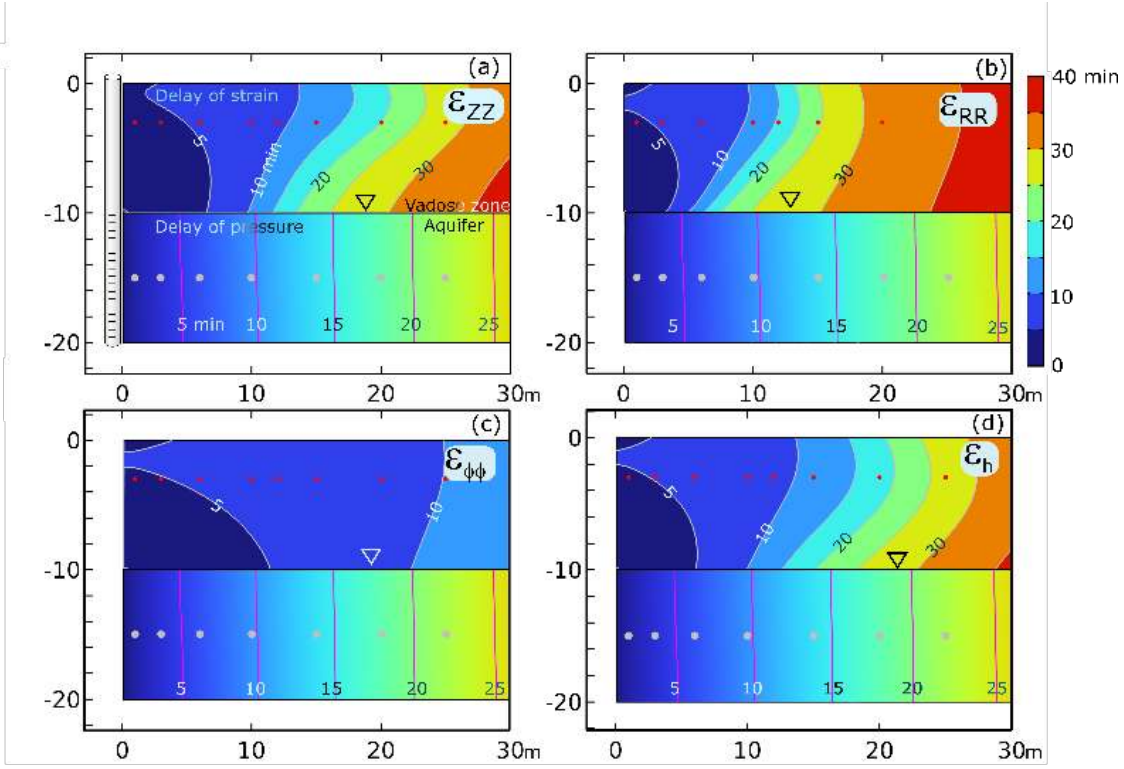

Figure 12-19. Delay of the pressure and different strain components in minutes behind the pressure at the well face for simulations that used a period of 60 min. Delay of strain in the vadose zone with filled contours, delay of pressure in aquifer with color flood. Dots are locations of time series in Figure 12-13. The delay of the vertical strain, ε_{ZZ}, is shifted by one half a period.

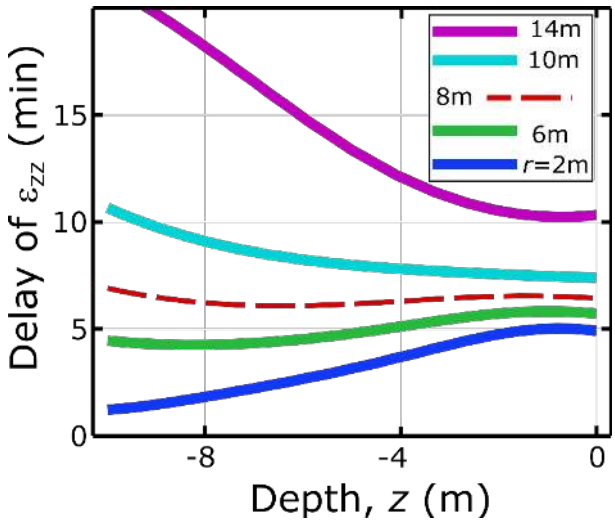

Figure 12-20. Delay of strain as function of depth along vertical lines at different radial distances (legend). Positive slope indicates strain advancing upward, negative indicates strain advancing downward. Phase velocity of the strain at r = 2m is 2 m/min, and phase velocity at r = 14m is –0.6 m/min.

12.4 PART 1 RESULTS

This chapter describes results from 13 well tests conducted in 2021 and 2022 (Table 12-3) at a field site near Clemson, SC. The field tests include slug tests, constant-rate pumping tests, and ZNR tests of various periods with pressure, strain, and dissolved oxygen measured at different locations. No pressure response occurred at WL-8 so data from this well was omitted.

Table 12-3. Summary of data obtained during zero-net-rate periodic well tests identified by the date they were conducted and the period that was used during pumping. "LTPT" refers to a long-term pumping test conducted at constant rate. 'ST1' and ST2' refer to slug tests completed in the pumping well, PW-2. WL-2, WL-4, WL-5, and WL-7 are the pressure data locations. DPS1, DPS2, and DPS3, are horizontal strain measurements, DEL-X4, DEL-X5, DEL-X8, DEL-X9 and Michelson are vertical strain data instruments. Tilt NS and Tilt EW components of the LILY Tiltmeter. The DO column indicates tests in which dissolved oxygen was measured. No data were collected for the grey cells.

Date	Test period, l	WL-5	WL-4	WL-7	WL-2	DPS1	DPS2	DPS3	DEL-X4	DEL-X5	DEL-X8	DEL-X9	Tilt NS	Tilt EW	Michelson	DO
4/20/2021	60-min	X	X	X												
1/8/2022	10-min	X	X	X		X	X	X	X	X	X	X	X	X	X	
1/14/2022	30-min	X	X	X		X	X	X	X	X	X	X	X	X	X	
1/15/2022	2-min	X														
1/24/2022	60-min	X	X	X		X	X	X	X	X	X	X	X	X	X	
1/25/2022	5-min	X	X	X												
3/27/2022	120-min	X	X	X	X	X	X	X	X	X	X	X	X	X	X	
3/29/2022	240-min	X	X	X	X	X	X	X	X	X	X	X	X	X	X	
6/9/2022	240-min	X	X	X	X				X	X	X	X	X	X	X	X
7/15/2022	540-min	X	X	X					X	X	X	X	X	X	X	X
5/25/2022	LTPT	X	X	X												X
9/23/2021	ST1															
9/23/2021	ST2															

12.4.1 Slug Tests

Two slug tests were conducted on PW-2 on September 23, 2021. The data were processed and analyzed using curve matching software, AQTESOLV. The PW-2 hydraulic head equilibrated

after about 7 minutes for each test. The Bouwer and Rice (1976) solution was utilized to analyze the slug test data, using hydraulic conductivity anisotropy values of 1 or 10 to estimate hydraulic conductivities for the two tests. The hydraulic conductivity is estimated to be $1.95\text{x}10^{-6}\ ms^{-1} \leq K \leq 3.12\text{x}10^{-6}\ ms^{-1}$ (Table 12-4) depending on the anisotropy. The AQTESOLV test summaries are included in Appendix A.

Table 12-4. Hydraulic conductivity estimated using Bouwer and Rice solution for two slug tests conducted at PW-2. K_h/K_v is 1 or 10, y-intercept is estimated to be $1.182 \leq$ y-intercept ≤ 1.473, and K is estimated to be $1.95\text{x}10^{-6} \leq K \leq 3.12\text{x}10^{-6}$

Test	K_h/K_v	y-intercept (ft)	K (m s^{-1})
#1	1	1.473	$1.95 \text{ x } 10^{-6}$
#1	10	1.443	$2.46 \text{ x } 10^{-6}$
#2	1	1.247	$2.49 \text{ x } 10^{-6}$
#2	10	1.182	$3.12 \text{ x } 10^{-6}$

12.4.2 Constant-Rate Pumping Test

A constant-rate pumping test was conducted with a duration of 163 minutes. The flowrate was 3.17 gallons per minute throughout the test. Hydraulic head was measured at WL-5, WL-4, and WL-7 at a one-minute interval.

The hydraulic head dropped in PW-2 as the pump was turned on. The maximum drawdown in PW-2 was 9.25 feet when the test was concluded (Figure 12-21). The hydraulic head dropped in WL-5 about a minute into the test and there was a maximum head drop of about 1.5 feet when the pump was turned off. The hydraulic head in WL-7 responded to the pumping about two minutes after the pump was turned on with a maximum drop of about 0.4 feet. The head at WL-4 started to drop around 5 minutes into the test and it fell about 0.25 feet during the test.

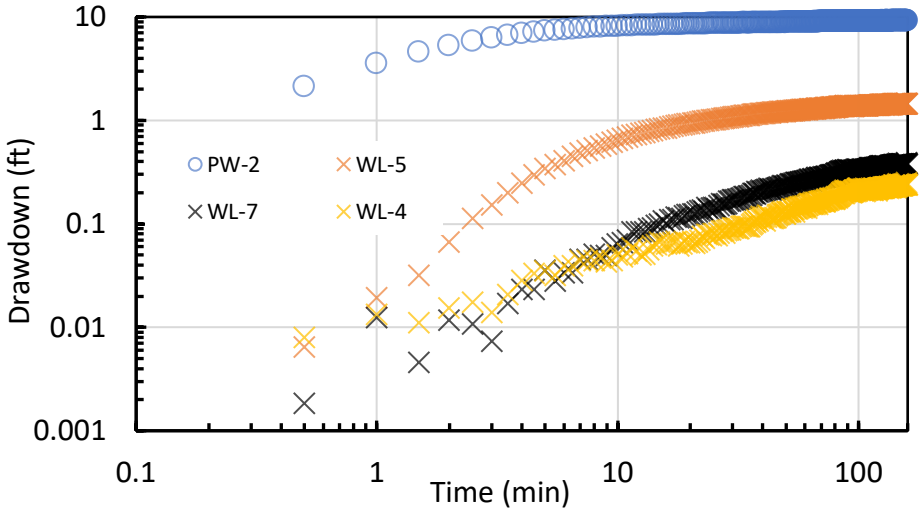

Figure 12-21. Drawdown as a function of time during a constant-rate pumping test. The pumping well, PW-2, response is shown by blue circles. The monitoring wells are shown through X's, where WL-5 is orange, WL-4 is yellow, and WL-7 is black.

Hydraulic head data were processed and then analyzed using AQTESOLV. The aquifer was assumed to be uniform and infinite lateral extent. The semi-log slope of the drawdown curve flattened with time, which suggests the water table was involved in release from storage. An unconfined aquifer is consistent with the hydrogeologic conceptual model for the site, so the solution for a well test in unconfined conditions (Neuman, 1974) was used for the analysis. In addition, a solution for a leaky, compressible aquitard (Hantush, 1961) was used. The Neuman (1974) solution was used for an unconfined setting and the Hantush (1961) solution was used for a confined setting. Confined conditions can be justified when the release from storage at the water table is small, and it is consistent with the analysis used for the ZNR tests. The drawdown data from all wells were analyzed simultaneously using the two different methods, as these solutions assume a homogenous setting. The drawdown data at each well were analyzed independently using the two different methods because the analysis used for the ZNR tests is conducted individually for each well.

Transmissivity is estimated to be $0.16x10^{-4}\ m^2s^{-1} \leq T \leq 6.3x10^{-4}\ m^2s^{-1}$ and storativity is estimated to be $1.4x10^{-5} \leq S \leq 4.4x10^{-3}$, depending on which well and which method of analysis was used (Table 12-5). The standard error associated with the transmissivity estimations are typically around +/- $2x10^{-5}$ ms^{-1} and for storativity is +/- 0.001. The parameter estimation for the unconfined case for WL-5 failed to converge and produced a low Storativity estimate. The standard error for this parameter is +/- 0.004, compared to an estimate of $1.4x10^{-5}$, which indicates a low confidence level in the estimate. AQTESOLV produces a '*t*-ratio', which is calculated by dividing the parameter estimate by the standard error. A high '*t*-ratio' value indicates a relatively small error and a small '*t*-ratio' value indicates a high error. For WL-5, the storativity '*t*-ratio' is 3 x 10^{-2}, whereas the transmissivity 't-ratio' is 22 (estimate of $1.4x10^{-4}$ m^2s^{-1} and standard error of 1.3 x 10^{-5}). So, although a very low storativity value was estimated in WL-5, there is a high error associated with this estimate, and the true value could be much higher. In general, the transmissivity estimates had the highest confidence, and the storativity and specific yield estimates

had the lowest confidence. The specific yield estimate when all wells are run together is significantly higher than the estimates when wells are run individually. The standard error for this estimate is +/- .014, producing a '*t*-ratio' of 2.8.

Table 12-5. Summary of parameter estimates from a constant-rate pumping test conducted on November 7, 2021. Specific Yield values are not estimated the Hantush (1961) solution because it assumes confined conditions.

Well	Solution	Transmissivity, T (m^2s^{-1})	Storativity, S	Specific Yield, S_y
WL-4	Hantush	$6.3x10^{-4}$	$1.9x10^{-3}$	
WL-4	Neuman	$4.3x10^{-4}$	$4.0x10^{-4}$	$2.5x10^{-3}$
WL-5	Hantush	$1.5x10^{-4}$	$1.8x10^{-3}$	
WL-5	Neuman	$1.4x10^{-4}$	$1.4x10^{-5}$	$1.0x10^{-3}$
WL-7	Hantush	$3.8x10^{-4}$	$5.1x10^{-3}$	
WL-7	Neuman	$0.16x10^{-4}$	$4.3x10^{-4}$	$1.5x10^{-2}$
All	Hantush	$1.6x10^{-4}$	$4.4x10^{-3}$	
All	Neuman	$0.82x10^{-4}$	$2.2x10^{-3}$	0.02

The drawdown of WL-5, WL-7, and WL-4 was plotted as a function of radial distance and a best fit line was used to infer the expected drawdown in the pumping well. The expected drawdown is compared to the observed drawdown to estimate well efficiency. The well efficiency was calculated to be 75% for this test. Transmissivity was divided by the saturated thickness, 75 ft, to estimate hydraulic conductivity, *K*.

A second constant-rate pumping test was conducted to duration of 24 hours. The flowrate was 5.4 gallons per minute throughout the test. Pressure data was processed and then analyzed using AQTESOLV. Hydraulic head was measured at WL-5, WL-4, and WL-7 at a one-minute intervals.

The hydraulic head dropped in PW-2 as the pump was turned on. The maximum drawdown in PW-2 was 16 feet when the test was concluded, which is slightly less than double the drawdown of the previous, shorter test. The maximum drawdowns at the monitoring wells were also slightly less than double those during the previous test (2.75 ft in WL-5, 1 ft in WL-7 and 0.45 ft in WL-4). The times until the first observed drawdown during this test were approximately the same at all monitoring wells. The Neuman (1974) solution was used for an unconfined setting and the Hantush (1961) solution was used for a confined setting.

Transmissivity is estimated to be $0.80x10^{-4}m^2s^{-1} \leq T \leq 5.4x10^{-4}\ m^2s^{-1}$ and storativity is estimated to be $6.9x10^{-6} \leq S \leq 1.8x10^{-2}$ (Table 12-6). Again, the unconfined case in WL-5 failed to converge a solution, and the estimates presented have a larger than acceptable error associated with them. The storativity 't-ratio' is $1.3x10^{-4}$ (standard error of 0.05), whereas the transmissivity 't-ratio' is 8.5 (standard error of $2.3x10^{-5}$ ms^{-1}). Like the first test, transmissivity had the highest confidence and storativity and specific yield had the lowest confidence. The typical standard error of transmissivity estimates is around +/- $2x10^{-5}$ ms^{-1} and of storativity is around +/- 0.001. The specific yield estimate when all wells are run together is significantly higher than the estimates when wells are run individually. The standard error for this estimate is +/- .028,

producing a 't-ratio' of 7.5, compared to a 't-ratio' of 15.8 for transmissivity and 15.1 for storativity.

Table 12-6. Summary of parameter estimates from a constant-rate pumping test conducted on May 25, 2022. Estimates are produced from both the individual well data and from all the wells analyzed together. Specific Yield values are not estimated the Hantush (1961) solution because it assumes confined conditions.

Well	Solution	Transmissivity, T (m^2s^{-1})	Storativity, S	Specific Yield, S_y
WL-4	Hantush	5.3×10^{-4}	1.8×10^{-2}	
WL-4	Neuman	5.4×10^{-4}	1.7×10^{-2}	1.0×10^{-3}
WL-5	Hantush	2.2×10^{-4}	1.2×10^{-3}	
WL-5	Neuman	2.0×10^{-4}	6.9×10^{-6}	1.0×10^{-3}
WL-7	Hantush	3.9×10^{-4}	9.6×10^{-3}	
WL-7	Neuman	4.0×10^{-4}	6.2×10^{-3}	1.0×10^{-3}
All	Hantush	1.8×10^{-4}	8.2×10^{-3}	
All	Neuman	0.8×10^{-4}	2.5×10^{-3}	0.11

Drawdown data from WL-5, WL-7, and WL-4 were used to calculate a well efficiency of 73%. The results from the two constant-rate pumping tests are consistent and provide a baseline of aquifer parameter estimates. Transmissivity is converted to terms of *K* for comparison to slug tests and ZNR tests results.

12.4.3 ZNR Tests

ZNR tests were conducted using periods that ranged from 2 to 540 minutes and flow rates between 1.3 and 3 gpm (Table 12-3 and Table 12-7). The flowrate is averaged over the whole test duration to produce a 'Q_avg' value, which indicates that average rate of gain or loss of water during a ZNR test. The absolute value of the injection and pumping rates gives the average amplitude of the flowrate, which is used to estimate Transmissivity.

The data were processed to steady-periodic responses by ignoring the first few periods. This gives pressure data with a mean value of approximately zero and avoids initial trends. The total duration of the tests ranged from 50 to 1080 minutes, and this resulted in a few to more than 20 periods that were used in the analysis (Table 12-7).

Table 12-7. Specifications of the ZNR tests.

Test	Start	Stop	Periods Used (total minutes)	Q_avg (gpm)	Δq (gpm)
2-minute	1/15/22 15:16	1/15/22 17:15	6-30 (50)	0.00	2.73
5-minute	1/25/22 14:35	1/25/22 17:15	5-24 (100)	0.08	3.02
10-minute	1/8/22 13:00	1/8/22 16:40	6-20 (150)	0.00	2.94
30-minute	1/14/22 15:00	1/15/22 9:00	4-34 (930)	-0.03	2.98
60-minute	4/16/22 7:46	4/16/22 15:46	5-8 (240)	0.00	3.07

60-minute	1/24/22 10:30	1/24/22 19:30	3-9 (420)	-0.01	3.04
120-minute	3/27/22 15:31	3/28/22 9:31	3-9 (840)	0.00	3.39
240-minute	3/28/22 12:00	3/29/22 0:00	2-3 (480)	-0.02	3.43
240-minute	6/9/22 16:45	6/10/22 16:45	3-4 (480)	-0.01	1.65
540-minute	7/15/22 12:01	7/19/22 6:01	4-5 (1,080)	-0.02	1.34

The basic signals consist of the flow rate from the well and the hydraulic heads in the pumping and monitoring wells (Figure 12-22). The ZNR tests consists of a pumping stage and an injection stage of equal duration and magnitude. Each stage lasts for one half period. The head in the well increases during the injection stage (pumping rate is negative), and the rate of increase diminishes with time in a pattern that resembles a constant rate test (Theis, 1935). The head in the pumping well reaches a maximum at the end of the injection stage, and then it abruptly drops when the rate changes sign. The head reaches a minimum at the end of the next stage (Figure 12-22).

The hydraulic head in the monitoring well resembles the head in the pumping well, but it is delayed in time and reduced in magnitude. The signal from monitoring well WL-5 is delayed behind that of the pumping well by a few minutes and this appears as a brief delay compared to the 60-minute period used during the test shown in Figure 12-22. The delay of the signal and reduction of signal amplitude is more apparent in monitoring wells that are further from the pumping well. For example, the delay is 6 minutes and the amplitude is 1.0 feet at WL-5 (r = 22 ft), whereas the delay is 40 minutes and the amplitude is 0.2 feet at WL-4 (r = 68 ft) (Figure 12-23).

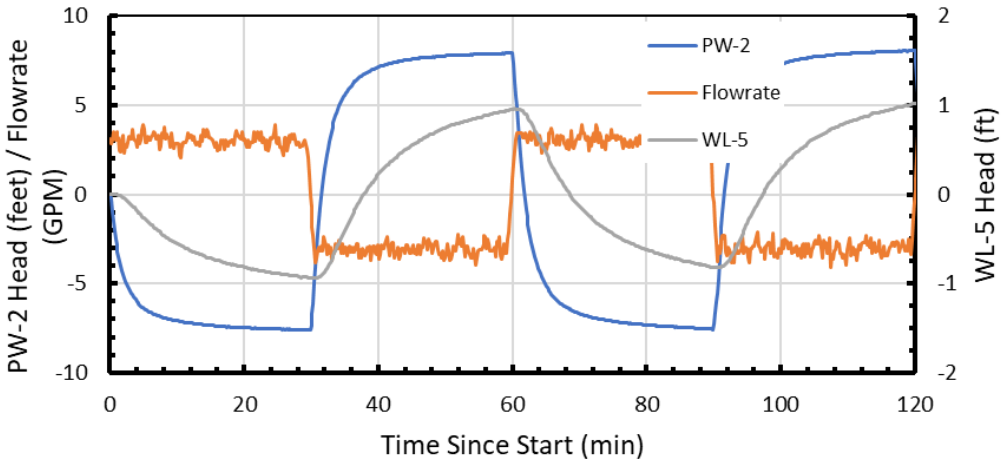

Figure 12-22. Hydraulic head and flow rate (orange) as functions of time during a ZNR test with a 60-minute period. Head in monitoring well WL-5 (gray) lags slightly behind the head in the pumping well (PW-2) by about 6 minutes.

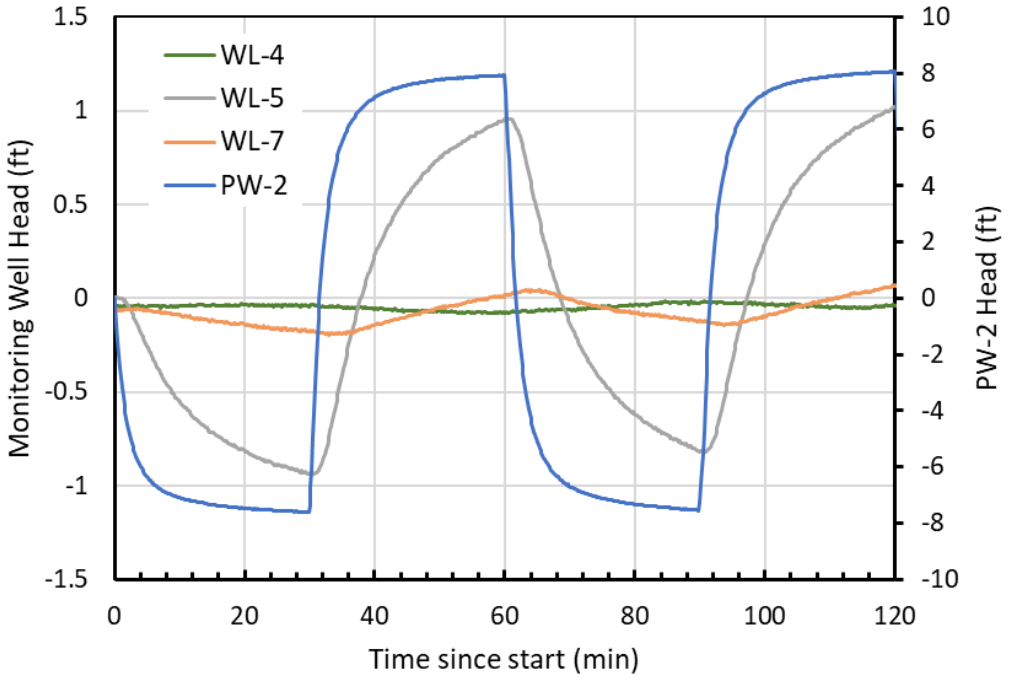

Figure 12-23. Hydraulic heads as functions of time during a ZNR test with a 60-minute period. PW-2 head is plotted on the secondary axis. Head in monitoring well WL-5 (gray) lags slightly behind the head in the pumping well (PW-2) by about 6 minutes. Head in WL-7 (orange) lags behind the head in PW-2 by about 14 minutes. Head in WL-4 (green) lags behind by about 41 minutes. The head amplitude is decreasing with increasing radial distance.

The amplitude of the hydraulic head signal decreases with distance from the pumping well, and the rate at which the amplitude falls off increases as the period of the ZNR test shortens, or the frequency increases. For example, during a test with a 60-minute period, the head in the well changes rapidly during the first 30 minutes but then it levels out and becomes nearly constant, similar to the long-term constant rate test. The rate of change of the head also decreases with time in the closest monitoring well, WL-5, but the slope at the end of each period is significantly steeper than it is in data from the pumping well (Figure 12-23). Nevertheless, the shape of the drawdown curve at WL-5 is markedly asymmetric during each period. The amplitude of the periodic signal drops by a factor of 1/8 between the pumping well and WL-5 (from 8 ft to 1 ft), and it drops by a factor of about 1/80 between the pumping well and WL-7 (from 8 ft to 0.09 ft) and by about 1/400 at WL-4 (from 8 ft to 0.02 ft) (Figure 12-23). The lag of the signal, when using the pumping well as a reference, is 6 minutes in WL-5, 14 minutes in WL-7 and 41 minutes in WL-4, for the 60-minute period test.

Reducing the period to 10-minutes changes the magnitude and shape of the drawdown curves. The magnitude of drawdown in the pumping well is 6 ft, but drops by a factor of 1/30 to 0.2 ft at WL-5 and by 3/2,000 to 0.009 ft at WL-7. The slope of the drawdown curve at the pumping well is significantly steeper at the end of each period than it is during the test with a 60-minute period. The shape of the drawdown curve at WL-5 during the 10-minute period test is nearly symmetric, resembling a sine curve, whereas it is markedly asymmetric during the 60-minute-period test

(Figure 12-23 and Figure 12-24). The lag time observed in monitoring wells is also shorter. For the 10-minute period test, WL-5 lags by 3 minutes and WL-7 lags by 6 minutes.

The noise in the drawdown signal is roughly constant and appears to be +/- 0.005 ft. For comparison, the accuracy of the transducer is 0.005 ft, according to the manufacturer. As a result, the signal to noise ratio is in the range of 40 to 1,200 at the pumping well and WL-5, but it is significantly less in the more distance monitoring wells, especially during the tests with shorter periods. For example, during the 10-minute period test the ratio of the amplitude to noise is 1.8 at WL-7 and less than 1 at WL-4,so the noise amplitude is larger than the signal amplitude.

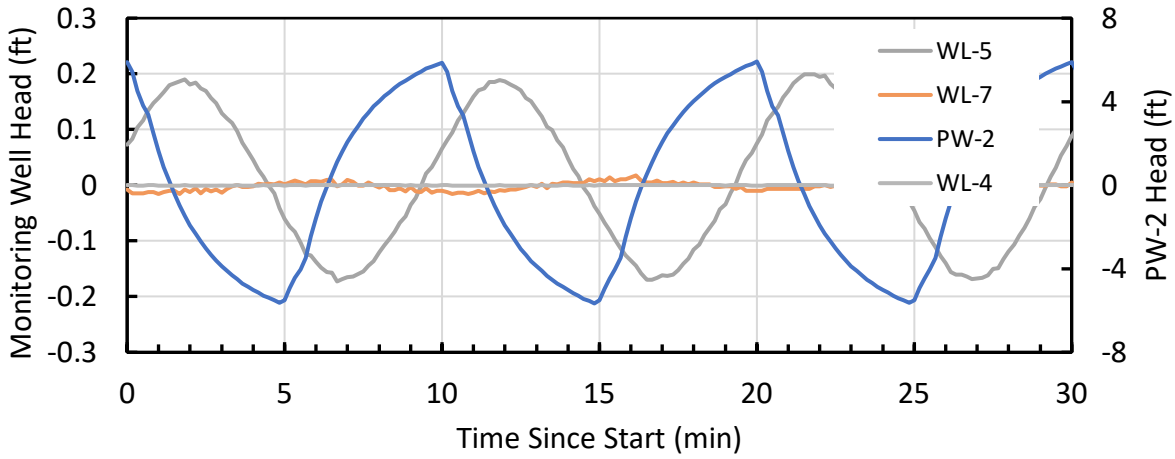

Figure 12-24. Hydraulic head as a function of time during a ZNR test with a period of 10 minutes. PW-2 (blue) head is plotted on the secondary axis. Head in monitoring well WL-5 (gray) lags behind the head in the pumping well (PW-2) by about 3 minutes. Head in WL-7 (orange) lags behind the head in PW-2 by about 6 minutes. The signal in WL-4 has a high noise amplitude and the lag could not be determined.

Increasing the period to 540-minutes changes the magnitude and shape of the drawdown curves as well. This test was performed with a flowrate of about half of that in the shorter-period tests, so the amplitude magnitude difference can be attributed to the change in rate. However, the reduction of amplitude magnitude when compared to the amplitude magnitude of the pumping well follows a similar trend. The magnitude of drawdown in the well is 4 ft, but drops by a factor of 1/8 to 0.5 ft at WL-5, by 1/40 to 0.11 ft at WL-7, and by 3/400 to 0.031 ft at WL-4. The slope of the drawdown curve at the pumping well is significantly gentler at the end of each period than it is during the test with a 10-minute period. The shape of the drawdown curve at WL-5 during the 540-minute period test resembles the asymmetrical shape observed in the 60-minute period test (Figure 12-23 and Figure 12-25). The amplitude reduction factor in WL-5 is about the same for both the 60-minute and 540-minute test, whereas the amplitude reduction factor in WL-7 and WL-4 is greater. The longer period test results in higher lag times of the signal in the monitoring wells. For the 540-minute period test, the lag was 18 minutes at WL-5, 61 minutes at WL-7 and 131 minutes in WL-4 (Figure 12-25).

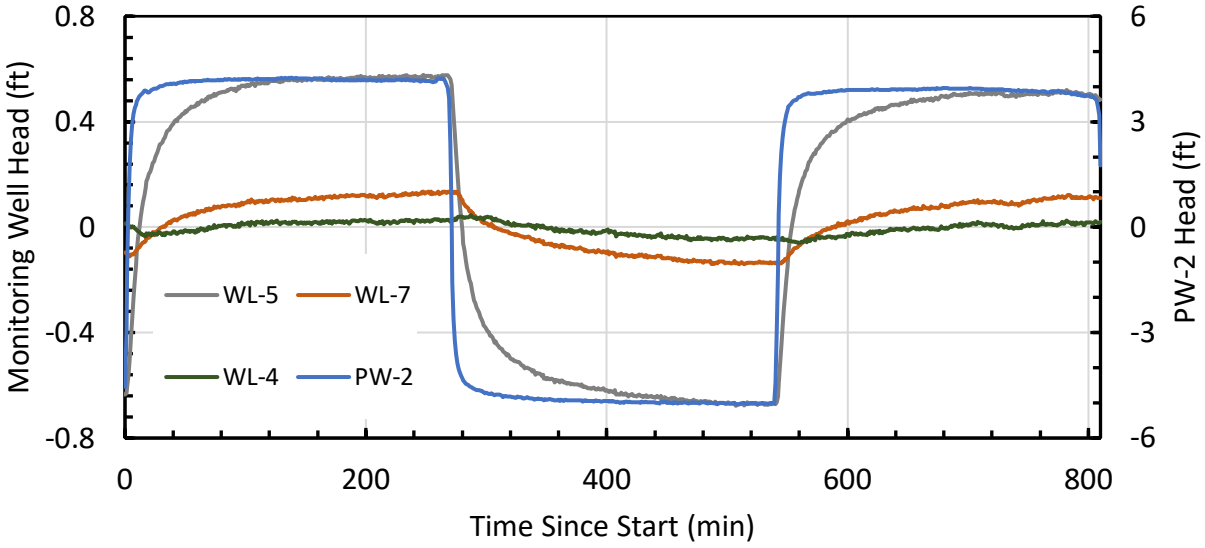

Figure 12-25. Hydraulic head as a function of time during a ZNR test with a period of 540 minutes. PW-2 (blue) head is plotted on the secondary axis. Fourier transform analysis indicates heads in the monitoring wells lag behind heads in the pumping well by the following WL-5 (grey) lags by 18 minutes. WL-7 (orange) lags by 61 minutes. Head in WL-4 (green) lags by 131 minutes.

Basic relationships between the flow rate and head data can be visualized by fitting the data with a sinusoid with the same period as the flow rate. The flow rate during a test with a 60-minute-period can be fit with a sinusoid with a maximum at t =15 minutes and a minimum at t = 45 minutes (Figure 12-22). This sinusoid has a phase delay of zero using the time scale shown in Figure 12-22. The head in the pumping well in Figure 12-22 can be fit with a sinusoid with maxima or minima every 30 minutes. This sinusoid is offset by 30 minutes compared to the pumping rate. This is a phase delay of 1/2 period or π radians.

The phase of the head in the pumping well was used as the reference when calculating the, or time lag, of the pressure signal in monitoring wells. The head in the monitoring wells are delayed from the pumping well, and the pressure signal time lag is used for aquifer parameter estimation.

The analysis outlined in the preceding paragraphs can be extended by assuming that the data can be approximated by a discrete Fourier series, which is outlined in Section 12.3.2.5. The FT Workbook is used to calculate the lag and amplitude of the fundamental period, and odd harmonics $1 \leq n \leq 19$.

One of the goals of this investigation is to evaluate the feasibility of using ZNR tests to estimate formation properties, so the analyses outlined in Section 12.3.2.5 will be used to guide the description of the data. Time lag data of the monitoring wells are linear with a slope of roughly ½ on a log:log plot when lr^2 is used on the abscissa (Figure 12-26), following 12-12a. Data from WL-2 and WL-5 follow the same trend, whereas t_L data from WL-4 and WL-7 are longer than the WL-2 and WL-5 data (Figure 12-26). The longer time lag indicates D_h estimated using WL-4 and WL-7 will be less than that estimated using WL-2 and WL-5.

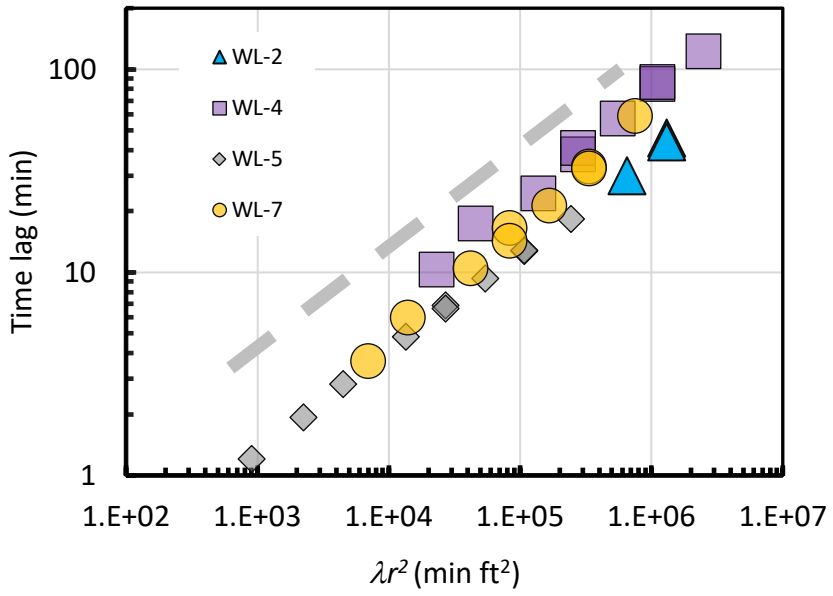

Figure 12-26. Time lag of the fundamental frequencies as a function of scaled period, λr^2 (min m^2) for WL-2, WL-4, WL-5 and WL-7. Grey line is a square root function.

Differences in time lag, and implied values of D_h may be due to heterogeneities, or they may result from well skin effects at the monitoring wells (Xing et al., 2022). WL-5 is the closest well to the pumping well, and well skin effects on monitoring wells have been shown to be most sensitive at further radial distances (Xing et al., 2022). So, although WL-5 may have a well skin, the proximity to PW-2 minimizes the effect of the well skin on the time lag.

12.4.3.1 Effects of pumping period

The amplitude and time lag of the periodic pressure signals varied with both pumping period and location. Time lag increases with both the duration of the pumping period and the distance from the pumping well. For example, the time lag of the pressure signal in WL-5 (r = 21 ft) is 18 minutes for a ZNR test with a period of 540 minutes, and the time lag of the pressure signal at WL-7 (r = 37 ft) is 61 minutes. Reducing the pumping period to 60 minutes causes the time lag to decrease from 18 minutes to 6 minutes at WL-5 and from 61 minutes to 14 minutes at WL-7.

The amplitude follows a similar trend, where the largest amplitudes occur at the closest radial distances and longest periods. The amplitude of the pressure signal also increases with the flow rate, but the amplitude reduction ratio accounts for this variable change. The amplitude reduction ratio, when using the PW-2 signal as a baseline, increases with increasing period.

12.4.3.2 Time lag

The effects of pumping period on time lag were evaluated in two ways. The baseline approach is to plot the time lag of the fundamental period from ZNR tests conducted using periods that range

from 2 to 540 minutes. A square wave consists of a fundamental sinusoid and harmonics, so the other approach was to evaluate the harmonics from the Fourier transform of individual ZNR tests. These two datasets were plotted on log-log axes with lr^2 as the abscissa following 12-12a (Figure 12-27 to Figure 12-30).

The results indicate that the time lag is characterized by a power law function of lr^2

$$t_L = C_1(\lambda r^2)^w \qquad (12\text{-}16)$$

where C_1 and w are parameters that are constant over certain intervals of lr^2. $w \approx ½$ for the fundamental period. The other harmonics generally follow $w \approx ½$, when lr^2 is greater than a threshold value. The threshold values change as the period changes, and are in the range of $2 \times 10^3 < lr^2 < 2 \times 10^5$ min ft^2 (blue bands in Figure 12-27 to Figure 12-30). This is illustrated by the linear trends of the data with ½ slope on Figure 12-27 to Figure 12-30. It follows that above the threshold, t_L is proportional to $\sqrt{\lambda}$ at fixed value of r (a particular well). Moreover, t_L is a linear function of r at fixed λ. This implies that the phase velocity of the pressure is uniform but is proportional to $1/\sqrt{\lambda}$.

Time lag data at values less than the lr^2 threshold at each well are less than that expected when extrapolating the trend from above the threshold. The time lag values tend to be less than expected particularly for the higher harmonics, $n > 7$. This causes the dataset to curve downward with decreasing λr^2 (Figure 12-27 to Figure 12-30). The data are generally contained within an envelope bounded by $w = 3/2$. This suggests that data from either short period tests or from monitoring wells close to the pumping well (small values of r) may differ from the ideal relationships that characterize the data above the threshold.

12.4.3.3 Amplitude

The amplitude of the periodic signal varies with both period and distance, just as the time lag does (Figure 12-31). The pressure oscillations dampen as they travel through the subsurface, so the amplitude decreases with distance. In addition, the pressure amplitude at the pumping well increases with period when the pumping rate is held constant, and this causes the amplitude in the monitoring wells to increase with period. For periods ranging from 10 minutes to 240 minutes, the pumping well has the largest change in amplitude, from 6 feet to 10 feet. However, the largest relative change is in the furthest monitoring well, WL-4, where the amplitude changes just under two orders of magnitude, compared to the amplitude change in PW-2 of just under one order of magnitude.

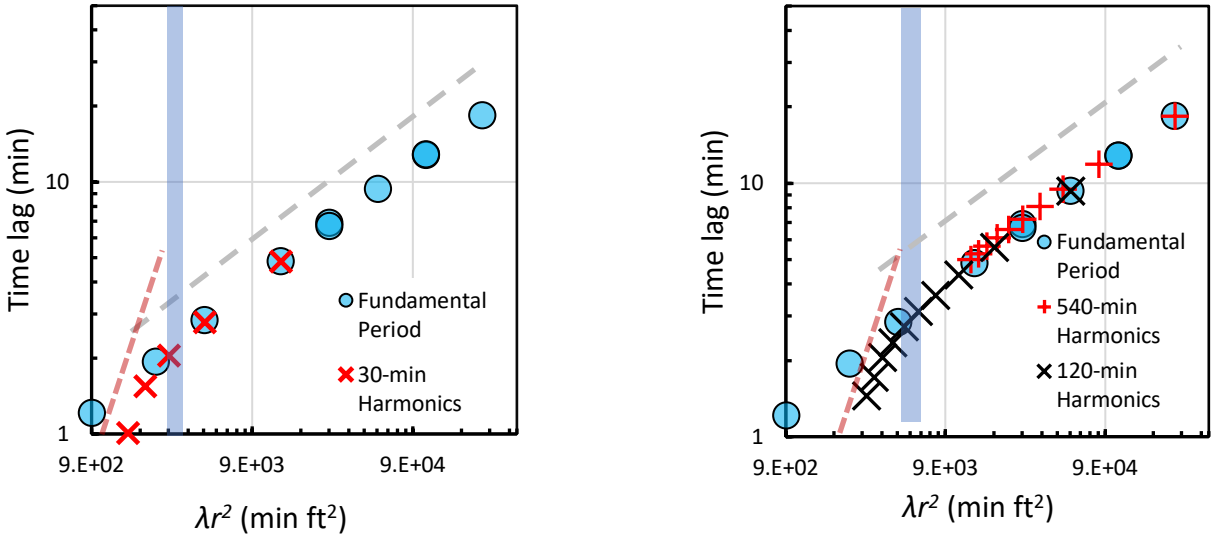

Figure 12-27. Time lags from hydraulic head data at WL-5 for the fundamental periods from all ZNR tests and all harmonics from the 30-minute ZNR test (left) and fundamental periods and the 120-minute and 540-minute ZNR tests (right). The lr^2 threshold is $lr^2 \approx 2 \times 10^3$ min ft^2 (blue band) for the 30-minute test, with harmonics $n = 7, 9$ below the threshold; and $lr^2 \approx 5 \times 10^3$ min ft^2 for the 120-minute test, with harmonics $n = 11, 13, 15, 17, 19$ below the threshold. All odd harmonics of the 540-minute test follow the fundamental period trend. Slope of grey dashed line = 1/2, slope of red dashed line = 3/2. Grey dashed line is a square root function for reference.

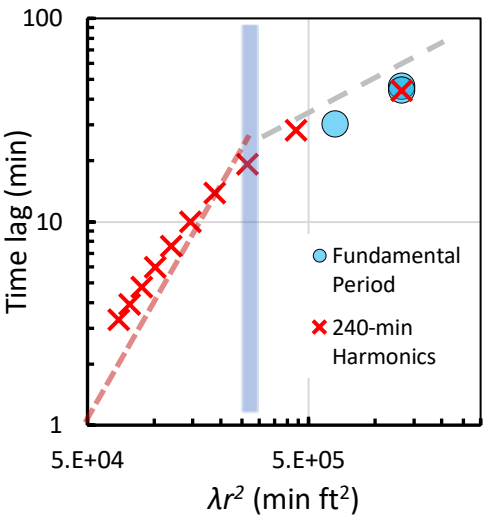

Figure 12-28. Time lags from hydraulic head data in WL-2 from fundamental periods and all harmonics measured for the 240-minute test. The lr^2 threshold is $lr^2 \approx 1 \times 10^5$ min ft^2. Slope of grey dashed line = 1/2, slope of red dashed line = 3/2.

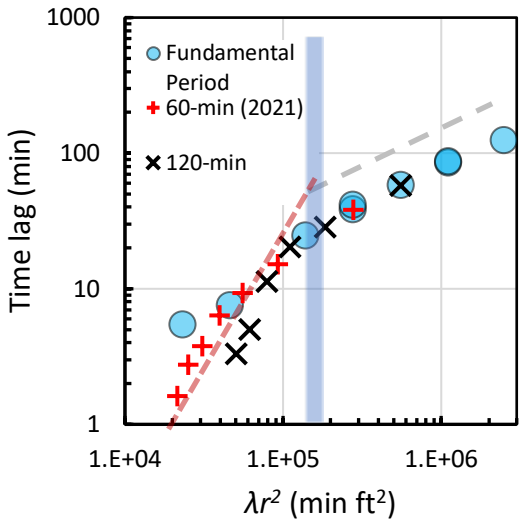

Figure 12-29. Time lags from hydraulic head data in WL-4 from fundamental periods and all harmonics measured for the 60-minute and 120-minute tests. The lr^2 threshold is $lr^2 \approx 2 \times 10^5$ min ft^2 (blue band). Slope of grey dashed line = 1/2, slope of red dashed line = 3/2.

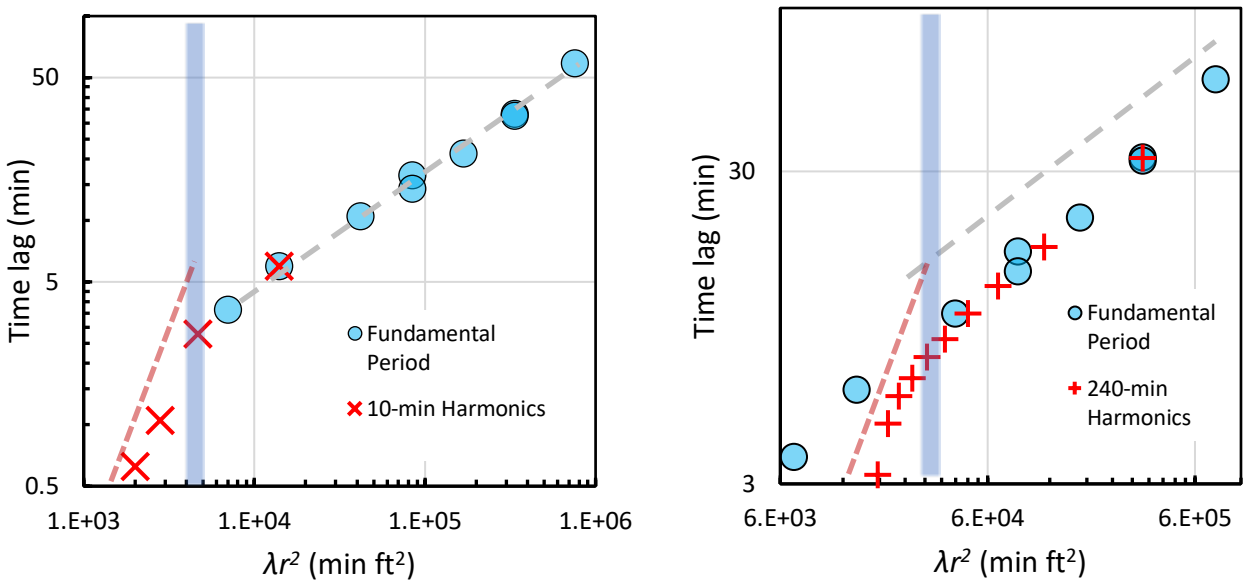

Figure 12-30. Time lags from hydraulic head data in WL-7 for the fundamental periods as a function of scaled period, λr^2, for (a) the 10-minute test harmonics (left) and (b) the 240-minute test harmonics (right). The λr^2 threshold is $\lambda r^2 \approx 5 \times 10^3$ min ft^2 (blue band) for the 10-minute harmonics, with harmonics n = 5 and 7 being below the threshold. The λr^2 threshold is $\lambda r^2 \approx 1 \times 10^4$ min ft^2 (blue band) for the 240-minute harmonics, with harmonics n =11, 13, 15, 17, and 19 being below the threshold. Slope of grey dashed line = 1/2, slope of red dashed line = 3/2.

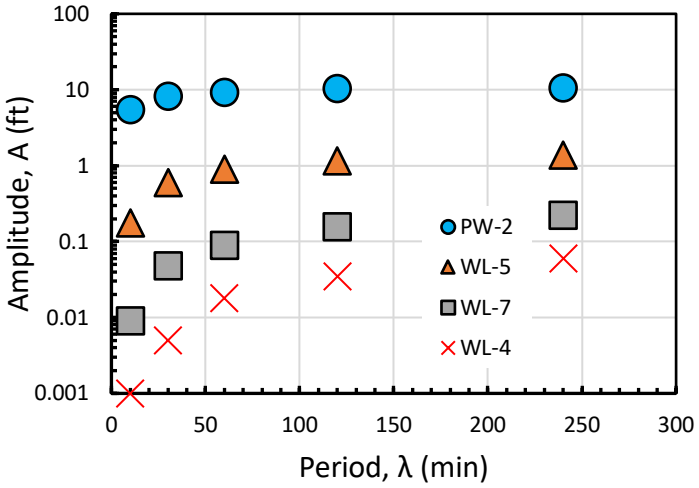

Figure 12-31. Head amplitude as a function of period for ZNR tests with periods ranging from 10 minutes to 240 minutes.

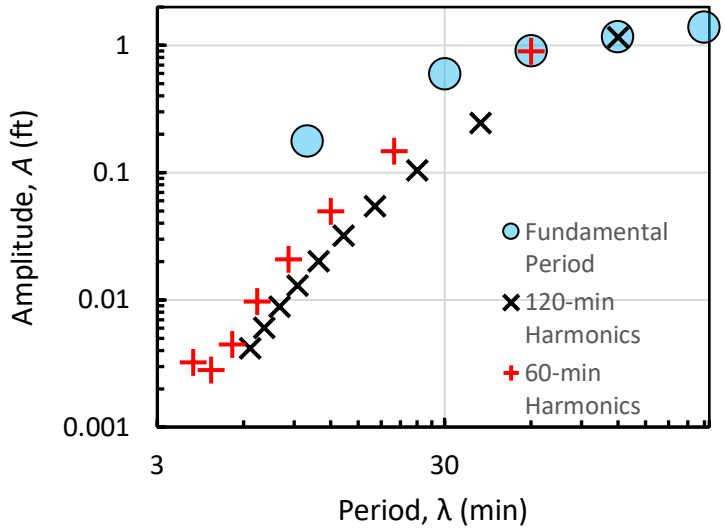

Figure 12-32. Amplitudes of pressure data at WL-5 for the fundamental periods and harmonics of ZNR tests with periods of 60 minutes and 120 minutes. The amplitudes of harmonics $n > 1$ decrease at a greater rate compared to the rate of change in amplitude of the fundamental periods.

Amplitude increases with both the fundamental period of the test, and with the period of the harmonics composing the longer-periods tests (Figure 12-32). However, the change in amplitude for higher harmonics is much greater relative to the fundamental period amplitudes change (Figure 12-32). In WL-5, the fundamental period head amplitude for the 10-minute ZNR test is 0.18 feet. In comparison, the 5th harmonic of the 60-minute ZNR test has a period of 12 minutes and has a head amplitude of 0.05 feet and the 11th harmonic of the 120-minute ZNR test has a period of 10.9 minutes and has a head amplitude of 0.02 feet. The change in amplitude for higher harmonics does not follow the same trend as the fundamental period amplitudes, and therefore these amplitudes will produce inconsistent T and S estimates utilizing eq. 1.8.

12.4.3.4 Parameter Estimates

The time lag and amplitude values were recorded and utilized in eq. 1.7 and 1.8 to estimate values for hydraulic diffusivity (D_h), transmissivity (T), and storativity (S). Hydraulic conductivity (K) is estimated from T and the saturated thickness. The datasets from each well were used individually to estimate parameter values.

D_h estimates generally range over a factor of 4, from 2 x 10^{-2} to 9 x10^{-2} m^2s^{-1} across all the ZNR tests (Table 12-8). The range of D_h values determined using data at each well spans a much smaller range, typically +/- 10^{-2} of the mean, and the mean values determined for a well account for the overall variability. D_h is estimated to be 7.6 x10^{-2} to 9.0 x10^{-2} m^2s^{-1} from data from WL-2, 1.8 x10^{-2} to 2.8 x10^{-2} m^2s^{-1} from WL-4, 7.0 x10^{-2} to 8.9 x10^{-2} m^2s^{-1} from WL-5, and 2.7 x10^{-2} to 6.4 x10^{-2} m^2s^{-1} from WL-7. The variation in estimates is the greatest in WL-7 and the smallest in WL-4.

K estimates range over about an order of magnitude across all the data, from 2 x10^{-6} to 2 x 10^{-5} ms^{-1}, when excluding estimates produced with amplitudes below the transducer resolution of 0.005 ft (Table 12-8). In some cases, aquifer parameters were estimated using an amplitude as low as 0.001 ft, and these values have a much higher uncertainty. The amplitudes with a high

uncertainty are highlighted red in Table 12-8. *K* is estimated to be 1.5 $x10^{-5}$ to 1.9 $x10^{-5}$ ms^{-1} using data from WL-2, 2.0 $x10^{-6}$ to 1.7 $x10^{-5}$ ms^{-1} from WL-4, 3.5 $x10^{-6}$ to 7.0 $x10^{-6}$ ms^{-1} from WL-5, and 7.6 $x10^{-6}$ to 1.4 $x10^{-5}$ ms^{-1} from WL-7. Again, the largest range of estimates is in data from WL-4, and the smallest range of estimates is in data from WL-2, likely due to the smaller amount of test data collected at this location (3 datasets from WL-2 compared to 9 in WL-4 and WL-7 and 10 in WL-5).

S estimates had a similar span as *K* estimates, ranging over about an order of magnitude, from 2 $x10^{-3}$ to 2 $x10^{-2}$, while ignoring the estimates produced through a high uncertainty amplitude (Table 12-8). The highest variation in *S* estimates occurred in WL-4, ranging from 2.0 $x10^{-3}$ to 19 $x10^{-3}$. The smallest variation in *S* estimates occurred in data from WL-5, ranging from 1.1 $x10^{-3}$ to 2.1 $x10^{-3}$. *S* estimates in data from WL-2 ranged from 3.9 $x10^{-3}$ to 5.1 $x10^{-3}$ and from WL-7 ranged 3.6 $x10^{-3}$ to 1.1 $x10^{-2}$.

Repeatability and effects of flowrate variability were evaluated by comparing results from two 60-minute ZNR tests and two 240-minute ZNR tests. The parameter estimate results are shaded for the 60-minute test (light blue) and for the 240-minute test (orange) in Table 12-8. Results from the two 60-minute tests results are consistent, with slightly more variability as radial distance increases. The 240-minute test conducted in March had a flowrate about double the one used during the June test, so it follows that the amplitudes of the March test are consistently about double the June test results. However, all the aquifer parameter estimates produced are consistent, confirming that flowrate does not affect the results. However, a very low flowrate will create a lower amplitude pressure signal, which could cause some problems with parameter estimates because of pressure transducer resolution and a higher noise ratio.

Table 12-8. Summary of apparent aquifer parameters estimated using ZNR tests. The time lag and amplitude values were used to estimate the parameters using eq. 1.7 and 1.8. The red values indicate inconsistent *T* and *S* estimates. The blue highlighted (60-minute tests results) and the orange highlighted (240-minute tests results) rows are duplicate tests with the same periods.

WL-2

t Date	Period, λ (minutes)	Time-lag, t_L(minutes)	Amplitude, Δp (ft)	Hydraulic Diffusivity, $D_h x\ 10^{-2}$ $(m^2 s^{-1})$	Transmissvity, $T x\ 10^{-4} (m^2 s^{-1})$	Storativity, $S x\ 10^{-3}$	Hydraulic Conductivity $K x\ 10^{-6} (m s^{-1})$
/2022	120	30.0	0.071	8.99	3.51	3.90	15.3
/2022	240	46.2	0.108	7.60	3.83	5.04	16.8
/2022	240	44.1	0.050	8.35	4.26	5.10	18.6

WL-4

t Date	Period, λ (minutes)	Time-lag, t_L(minutes)	Amplitude, Δp (ft)	Hydraulic Diffusivity, $D_h x\ 10^{-2}$ $(m^2 s^{-1})$	Transmissvity, $T x\ 10^{-4} (m^2 s^{-1})$	Storativity, $S x\ 10^{-3}$	Hydraulic Conductivity $K x\ 10^{-6} (m s^{-1})$
/2022	5	10.4	0.000	2.64	0.002	0.009	0.001
/2022	10	17.5	0.001	1.87	0.007	0.03	0.003
/2022	30	24.6	0.005	2.83	0.73	2.58	3.19
/2021	60	38.3	0.026	2.34	0.47	2.01	2.06
/2022	60	41.3	0.018	2.01	0.47	2.32	2.04
/2022	120	57.5	0.035	2.07	1.22	5.89	5.34
/2022	240	84.8	0.060	1.91	1.86	9.75	8.13
/2022	240	86.7	0.027	1.83	1.84	10.1	8.05
/2022	540	123.3	0.031	2.03	3.83	18.9	16.7

WL-5

t Date	Period, λ (minutes)	Time-lag, t_L(minutes)	Amplitude, Δp (ft)	Hydraulic Diffusivity, $D_h x\ 10^{-2}$ $(m^2 s^{-1})$	Transmissvity, $T x\ 10^{-4} (m^2 s^{-1})$	Storativity, $S x\ 10^{-3}$	Hydraulic Conductivity $K x\ 10^{-6} (m s^{-1})$
/2022	2	1.2	0.002	7.63	7.19	9.43	31.5
/2022	5	1.9	0.047	7.42	1.60	2.15	6.98
/2022	10	2.8	0.178	6.97	0.94	1.35	4.10
/2022	30	4.9	0.597	7.12	0.79	1.11	3.47
/2021	60	6.9	0.916	7.06	0.85	1.20	3.71
/2022	60	6.7	0.906	7.53	0.88	1.17	3.87
/2022	120	9.4	1.168	7.65	1.12	1.47	4.91
/2022	240	12.8	1.390	8.15	1.35	1.65	5.90
/2022	240	12.9	0.679	8.10	1.32	1.63	5.78
/2022	540	18.4	0.705	8.90	1.46	1.64	6.40

WL-7

t Date	Period, λ (minutes)	Time-lag, t_L(minutes)	Amplitude, Δp (ft)	Hydraulic Diffusivity, $D_h x\ 10^{-2}$ $(m^2 s^{-1})$	Transmissvity, $T x\ 10^{-4} (m^2 s^{-1})$	Storativity, $S x\ 10^{-3}$	Hydraulic Conductivity $K x\ 10^{-6} (m s^{-1})$
/2022	5	3.7	0.001	6.44	4.49	6.97	19.6
/2022	10	6.0	0.009	4.78	1.73	3.63	7.59
/2022	30	10.5	0.048	4.66	2.03	4.36	8.88
/2021	60	16.6	0.084	3.75	2.15	5.73	9.39
/2022	60	14.4	0.089	5.02	2.75	5.47	12.0
/2022	120	21.4	0.156	4.54	2.96	6.52	12.9
/2022	240	33.3	0.225	3.75	3.02	8.07	13.2
/2022	240	32.6	0.103	3.91	3.28	8.39	14.4
/2022	540	59.1	0.119	2.67	3.03	11.3	13.3

The higher frequency odd harmonics, $n > 1$, were also utilized with the Strelstova (1988) solution to estimate aquifer properties. The Streltsova solution assumes aquifer properties are independent of period, so the results of this analysis yields apparent properties.

Most apparent D_h estimates from high frequency harmonics are consistent when the amplitude of that signal is greater than 0.005 ft, the resolution of the HOBO transducers. This excludes the fundamental period, where D_h estimates were consistent with every test and amplitude, including amplitudes as low as 0.001 ft. The D_h estimates of higher frequency harmonics range from 2 x10^{-2} m^2s^{-1} to 2 x10^{-1} m^2s^{-1}, while excluding the frequencies whose amplitudes were < 0.005 ft. The high frequency harmonic D_h estimates are compared to fundamental period estimates for a statistical significance of difference.

Although the D_h estimates are relatively consistent for all harmonics, the *T* and *S* values are inconsistent and increasing with the frequency of the period (Figure 12-27 and Figure 12-32). The higher frequency harmonic *T* and *S* results for all monitoring wells followed a similar trend and do not produce consistent values. An example of the higher frequency *T* and S estimate trends are shown by the results of WL-5 during the 540-minute ZNR test (Table 12-9).

Table 12-9. Summary of WL-5 results from harmonics of the 540-minute ZNR test. *A* is the amplitude (ft), D_h is calculated using eq. 1.7, *T* is calculated using eq. 1.8, and *S* is calculated using the ratio of T to D_h.

Harmonic, n	Period, λ	Time lag (minutes)	*A* (ft)	D_h (ft^2min^{-1})	*T* (ft^2min^{-1})	*S*
1	540	18.4	0.705	57.5	0.095	0.002
3	180	11.9	0.195	45.6	0.20	0.004
5	108	9.5	0.103	43.1	0.29	0.006
7	77	8.1	0.065	42.4	0.37	0.009
9	60	7.2	0.046	41.3	0.45	0.010
11	49	6.6	0.035	40.7	0.51	0.013
13	41.5	6.1	0.027	40.0	0.58	0.014
15	36	5.7	0.023	40.4	0.62	0.015
17	31.8	5.3	0.020	41.1	0.66	0.016
19	28.4	5.0	0.016	40.9	0.75	0.018

The apparent D_h, *T*, and *S* results estimated from ZNR tests show a possible dependence of the period. The D_h estimates from data in WL-5 trend higher for the longer period tests, particularly tests with periods > 60 minutes (Figure 12-33a). However, one condition of the approximation requires (Streltsova, 1988, 3.10.1):

$$r\sqrt{\frac{2\pi}{\lambda D_h}} > 1 \qquad (12\text{-}17)$$

For WL-5, the condition is not met for periods > 30 minutes. The condition was met for all other tests and wells, excluding the 540-minute ZNR test with WL-7.

The D_h estimates from longer period tests with data from WL-4 and WL-7 are generally consistent and they trend higher with shorter period tests (Figure 12-33b and d). These shorter period tests trends could be an effect of the higher uncertainty associated with these tests. The D_h estimates from data in WL-5 for the shortest tests did start to increase, but on a much smaller scale than WL-7 (Figure 12-33a and b). The increasing D_h for shorter period tests is also shown through the λr^2 threshold outlined in the previous time lag plots (Figure 12-27 to Figure 12-30). Data was recorded in WL-2 for only three tests, so a trend of frequency dependence cannot be determined (Figure 12-33c).

Like the fundamental period trends, the harmonics' D_h estimates trended higher for the shorter periods. Harmonics where the amplitude is less than the pressure transducer resolution were not considered. Both D_h estimates from harmonics data in WL-5 and WL-7 show an increasing trend with shorter period (Figure 12-33a and Figure 12-33b). The D_h estimates from harmonics n > 9 were sometimes inconsistent, particularly with the shorter period tests where the amplitude had a higher uncertainty ratio. In contrast, the longer period test harmonics D_h estimates were generally consistent. For example, the 540-minute test D_h estimates from data in WL-5 decrease through harmonics 1 to 5, and then are consistent through harmonic 19 (Table 12-9). The D_h values from harmonics 1 to 19 from the 540-minute test are all within the range of D_h values produced through fundamental period ZNR test results. WL-2 and WL-4 are the furthest radial distances from the pumping well, and therefore had the smallest amplitude of pressure signals. This results in a small number of harmonic lag values that were above the transducer threshold, when compared to the results of WL-5 and WL-7.

T and *S* fundamental period results also indicated a possible dependence on period length (Figure 12-34). Both *T* and *S* increase with longer periods, notably from data in WL-2, WL-4, and WL-7. There is an effect where *T* and *S* increase with the shortest tests run, however, these tests had the smallest amplitude, around or less than the pressure transducer resolution, so there is a much greater possible relative error associated with these estimates. The increasing *S* with longer periods can be explained by a prolonged release from storage that occurs as a longer period progresses. However, D_h is consistent with longer period tests, so as S increases, so does *T* and *K*. Interestingly *S* and *T* both increase at such a rate that D_h remains consistent. The most sensitive well to the frequency dependence is WL-4 (furthest radial distance) and the least sensitive is WL-5 (shortest radial distance).

The well efficiencies from ZNR tests were estimated using a similar method as a constant-rate pumping test, by plotting drawdown in WL-5, WL-7, and WL-4 as a function of radial distance for the first half period of a test. The expected drawdown in the pumping well is inferred and then compared to the recorded drawdown to estimate well efficiency. Well efficiency was calculated for ZNR tests with a fundamental period > 30 minutes. Well efficiencies were estimated to be $66\% \leq WE \leq 81\%$, with no trends of frequency dependence. There was also no difference of well efficiencies estimated from tests with a flowrate of 3 gpm or 1.5 gpm.

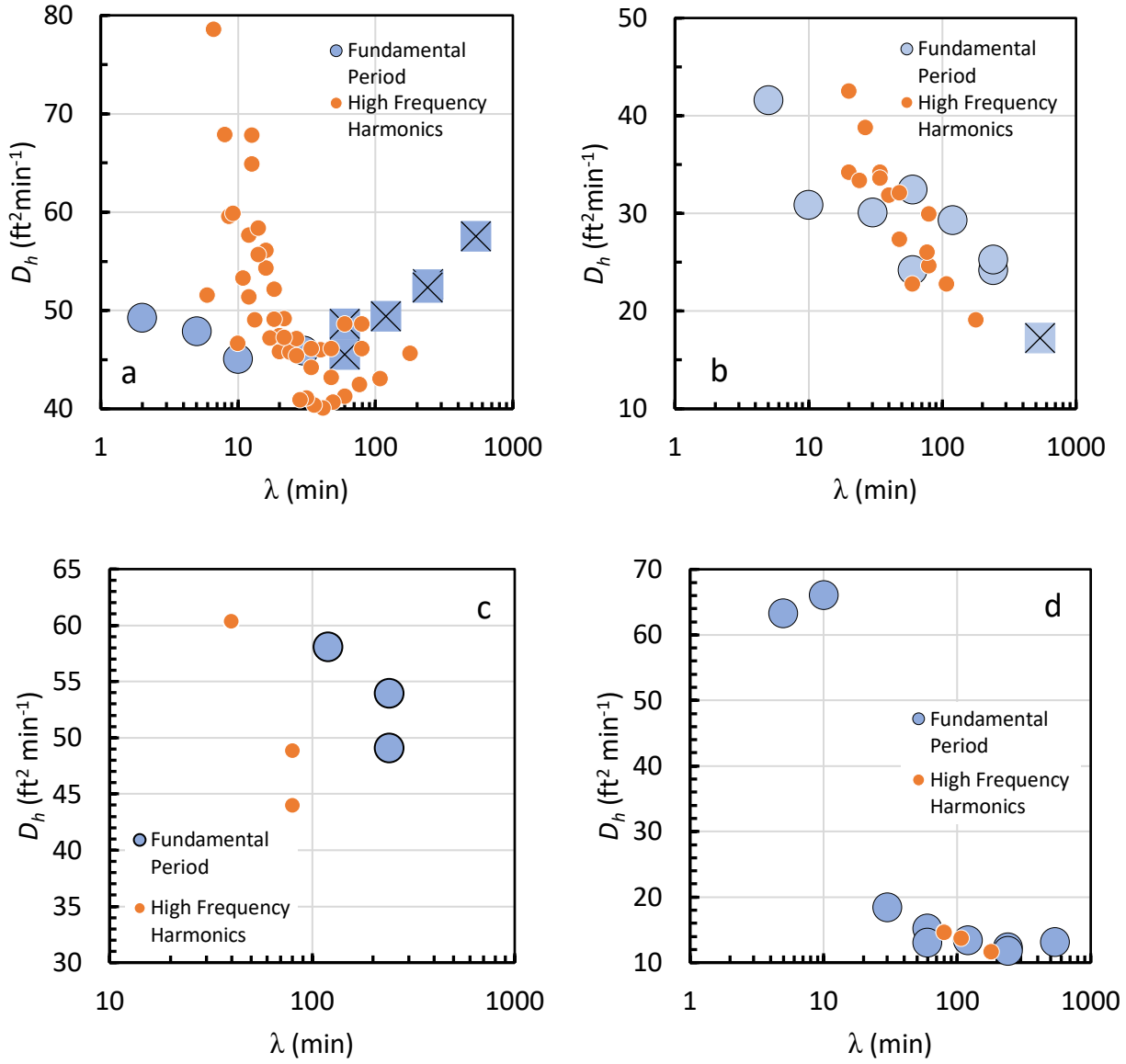

Figure 12-33. Apparent hydraulic diffusivity as a function of period for fundamental periods where the condition is met (blue dots), where the condition is not met (blue squares with black X's), and harmonics from tests with periods greater than 10 minutes and amplitude greater than 0.005 ft (orange dots). (a) data from WL-5 (top left side); (b) data from WL-7 (top right side); (c) data from WL-2 (bottom left side); and (d) data from WL-4 (bottom right side).

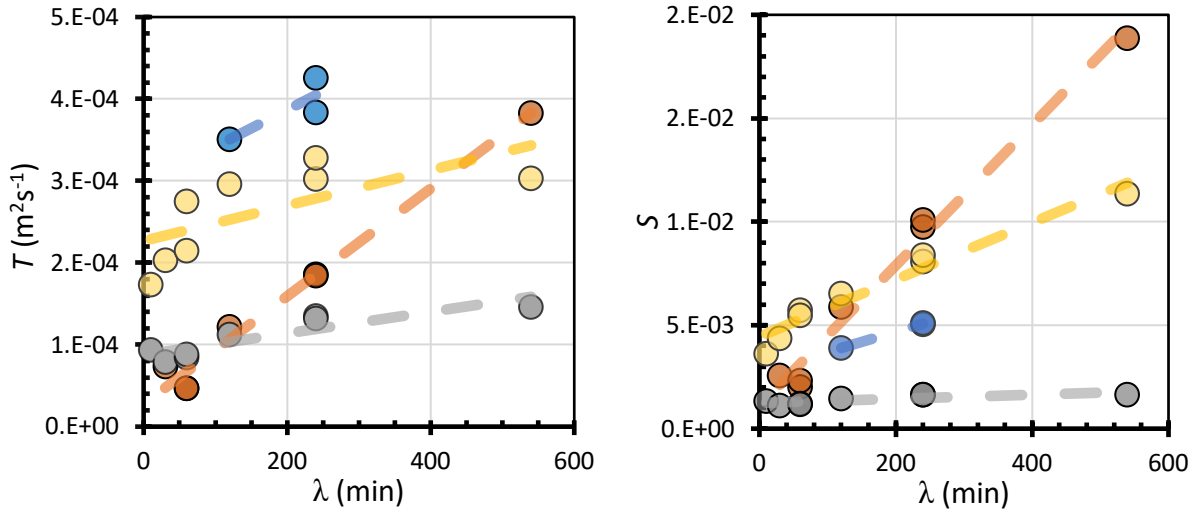

Figure 12-34. Apparent transmissivity as a function of period (left) and Storativity as a function of period (right). WL-2 (blue), WL-4 (orange), WL-5 (grey) and WL-7 (yellow). Linear trend lines from regression (dotted lines).

12.4.3.5 **Comparison of ZNR tests to traditional aquifer tests**

The D_h, K, and S values estimated through ZNR tests are compared to the results from slug tests and constant-rate pumping tests to evaluate the efficacy of using ZNR tests to characterize an aquifer. The K estimates from ZNR tests from data in WL-5 and WL-7 are similar to the estimates from constant-rate tests (Table 12-10). The average K from WL-4 data is similar to results from other ZNR tests K estimates, but they are about 4 times less than those estimated from the constant-rate test. Although the K estimates from constant-rate and ZNR tests are similar, the pumping test estimates are consistently higher when analyzing data from an individual well. However, when comparing the ZNR results to the constant-rate test results analyzed from data in all the wells, the ZNR values in the range of constant-rate values. The K estimates from slug tests are consistently less than the K estimates through ZNR or constant-rate tests, ranging from about 2 to 10 times less. This confirms Butler and Healey's (1998) idea that slug tests can often underestimate K values due to a well skin.

The S estimates from ZNR tests are similar and in the range of the those estimated through the two constant-rate tests, both for the Hantush (1961) solution and the total S estimated using the Neuman (1974) solution (Table 12-11). When looking at the two constant-rate tests analyzed by the individual well, the total S estimates, where unconfined settings are assumed (S + Sy), are similar to the S estimates where a confined setting is assumed (Table 12-11). However, when all the wells are analyzed together, the S estimates through the Neuman (1974) solution for an unconfined aquifer are consistently higher than those estimated through the Hantush (1961) solution for a confined case. In addition, the S estimates from the longer constant-rate test are larger than those estimated through the shorter constant-rate test. The D_h estimates from ZNR tests are similar to those estimated through constant-rate tests, when analyzing the data from the wells individually. There is a wide range of D_h estimates from constant-rate tests, due to the range of S estimates with the two different conceptual models.

Table 12-10. Summary of *K* values estimated through various aquifer tests. The 'ZNR Avg' values represent the average of ZNR test results. 'PT1 H' is the four-hour constant-rate test Hantush (1961) solution, 'PT2 N' is the 24-hour constant-rate test Neuman (1974) solution, 'ST1' is the first slug test and 'ST2' is the second slug test. All Wells is the results of constant-rate tests when data from all wells were analyzed together.

Hydraulic Conductivity, K ($\boldsymbol{ms^{-1}}$)

Test	WL-2	WL-4	WL-5	WL-7	PW-2	All Wells
ZNR Avg	$1.7x10^{-5}$	$0.65x10^{-5}$	$0.50x10^{-5}$	$1.2x10^{-5}$		
PT1 H		$2.8x10^{-5}$	$0.66x10^{-5}$	$1.7x10^{-5}$		$0.70x10^{-5}$
PT2 H		$2.3x10^{-5}$	$0.96x10^{-5}$	$1.7x10^{-5}$		$0.79x10^{-5}$
PT1 N		$1.9x10^{-5}$	$0.61x10^{-5}$	$0.087x10^{-5}$		$0.35x10^{-5}$
PT2 N		$2.4x10^{-5}$	$0.87x10^{-5}$	$1.7x10^{-5}$		$0.35x10^{-5}$
ST1					$0.20x10^{-5}$	
ST2					$0.25x10^{-5}$	

Table 12-11. Summary of S and D_h values estimated using various aquifer tests. The 'ZNR Avg' values represent the average of ZNR test results. 'PT1 H' is the four-hour constant-rate test Hantush (1961) solution, 'PT2 N' is the 24-hour constant-rate test Neuman (1974) solution, 'ST1' is the first slug test and 'ST2' is the second slug test. All Wells is the results of constant-rate tests when data from all wells were analyzed together.

Storativity, S

Test	WL-2	WL-4	WL-5	WL-7	All Wells
ZNR Avg	$4.9x10^{-3}$	$7.4x10^{-3}$	$1.5x10^{-3}$	$6.7x10^{-3}$	
PT1 H		$1.9x10^{-3}$	$1.8x10^{-3}$	$5.1x10^{-3}$	$4.4x10^{-3}$
PT2 H		$18x10^{-3}$	$1.2x10^{-3}$	$9.6x10^{-3}$	$8.2x10^{-3}$
PT1 N		$2.9x10^{-3}$	$1.0x10^{-3}$	$15x10^{-3}$	$22x10^{-3}$
PT2 N		$18x10^{-3}$	$1.0x10^{-3}$	$7.2x10^{-3}$	$110x10^{-3}$

Hydraulic Diffusivity, $\boldsymbol{D_h}$ ($\boldsymbol{m^2s^{-1}}$)

Test	WL-2	WL-4	WL-5	WL-7	All Wells
ZNR Avg	$8.3x10^{-2}$	$2.2x10^{-2}$	$7.7x10^{-2}$	$4.4x10^{-2}$	
PT1 H		$33x10^{-2}$	$8.3x10^{-2}$	$7.5x10^{-2}$	$3.6x10^{-2}$
PT2 H		$2.9x10^{-2}$	$18x10^{-2}$	$4.1x10^{-2}$	$0.22x10^{-2}$
PT1 N		$15x10^{-2}$	$14x10^{-2}$	$2.5x10^{-2}$	$0.36x10^{-2}$
PT2 N		$3.0x10^{-2}$	$20x10^{-2}$	$5.6x10^{-2}$	$.073x10^{-2}$

Estimates of D_h, K, and S through ZNR tests are all within an order of magnitude of results estimated using slug tests or a 24-hour constant-rate test. A *t*-test is a statistical analysis utilized to

evaluate a significant difference between two sets of populations (Rice 2006). Several populations are compared using a *t*-test, and *p*-value results are recorded to determine a statistical significance. The *t*-tests run for these datasets are two-tailed. The null hypothesis states that true difference between two population means is zero. With a 95% confidence, a *p* value greater than 0.05 states the result is insignificant, and a *p* value less than 0.05 the result is statistically significant. In other words, if the *p* value is less than 0.05, the populations are different.

Several *t*-tests were performed with similar populations. For *K*, populations of ZNR tests by wells are compared to constant-rate tests by well and the slug test results. In addition, all of the *K* ZNR results for all wells are compared to the slug test results with the constant-rate results when all wells are analyzed together. For *S* and D_h, similar comparisons are made, without the slug test results. The D_h estimates from results using the fundamental period by well are compared to the harmonics results, where amplitude is greater than 0.005 ft. And finally, the two well efficiencies estimated through the two constant-rate tests are compared to the well efficiency estimates through the first pumping stage of ZNR tests, where the period is greater than 30 minutes.

Most of the *p* values from the *t*-test are greater than 0.05, indicating that we fail to reject the null hypothesis and the values from the two test methods are not from different populations (Table 12-12). With a $p < 0.05$, the null hypothesis can be rejected, and a statistical difference between the populations is concluded. The null hypothesis is rejected when comparing all the of ZNR S estimates to constant-rate S estimates when all wells are analyzed together, WL-5 ZNR Dh compared to WL-5 constant-rate Dh, and all ZNR Dh compared to constant-rate Dh when all wells are analyzed together (red text in Table 12-12). For tests where $p > 0.05$, we can accept the null hypothesis, however, this does not necessarily mean that the alternative hypothesis is true. Similarly, where $p > 0.05$, it cannot be concluded that the populations are the same, but it can be concluded that there is not statistical difference between the populations.

Slug tests and constant-rate pumping tests are generally accepted methods of estimating *K*. Estimating aquifer properties through the Streltsova (1988) analysis of a ZNR periodic test is under review by comparing results of ZNR tests to constant-rate and slug tests, both through data from individual wells and through results that use all the well data. For both cases, there is no statistically significant difference of the groups.

The well efficiencies from ZNR tests were estimated visually using the drawdown data from the first pumping stage of the test. The two well efficiency estimates from constant-rate tests were compared to those estimated through ZNR tests, resulting in a *p*-value of 0.689 (Table 12-12). There is not a statistically significant difference between the two populations.

Table 12-12. Summary of *t*-test results. 'ZNR n = 1' indicates all the fundamental period results for a particular well and parameter are included in the population. 'CR' indicates constant-rate pumping test results for a particular well and parameter are included in the population. 'CR all' indicates results calculated from analyzing WL-4, WL-5 and WL-7 together. 'ST' indicates slug test results. 'ZNR HFH, amp > 0.005 ft' indicates D_h estimates calculated from high frequency harmonic time lag values where the amplitude of that harmonic is > 0.005 ft. Red values indicate *t*-tests where the null hypothesis is rejected.

The three tests where the null hypothesis is rejected all include the comparison of *S* terms, through the direct comparison of *S*, or through the comparison of D_h, which includes a ratio of *T* to *S*. The constant-rate results include both the Hantush (1961) estimates of *S* and Neuman

(1974) estimates of *S* + *Sy*. The Neuman (1974) analysis could be skewing the data, as the *Sy* estimates contribute heavily to the mean. The ZNR results assume confined conditions and do not have an *Sy* value. ZNR test S results have also shown a frequency dependence, where larger period tests produce large S estimates. The population of ZNR test *S* estimates includes all periods of ZNR tests, and shorter period tests could be skewing the ZNR data to a lower mean. This has motivated additional *t*-tests to be performed, where the constant-rate results are separated by conceptual model, and ZNR Dh and S estimates are only used for ZNR tests with periods of 60 minutes or greater (Table 12-13).

t-Test Results

Parameter	Population 1	Population 2	*p*-value
K	WL-5 ZNR n = 1	WL-5 CR + ST	0.454
K	WL-7 ZNR n = 1	WL-7 CR + ST	0.515
K	WL-4 ZNR n = 1	WL-4 CR + ST	0.062
K	All ZNR n = 1	CR all + ST	0.086
S	WL-5 ZNR n = 1	WL-5 CR	0.273
S	WL-7 ZNR n = 1	WL-7 CR	0.216
S	WL-4 ZNR n = 1	WL-4 CR	0.545
S	All ZNR n = 1	CR all	0.003
D_h	WL-5 ZNR n = 1	WL-5 CR	0.001
D_h	WL-7 ZNR n = 1	WL-7 CR	0.356
D_h	WL-4 ZNR n = 1	WL-4 CR	0.055
D_h	All ZNR n = 1	CR all	0.006
D_h	WL-5 ZNR n = 1	WL-5 ZNR HFH, amp > 0.005 ft	0.214
D_h	WL-7 ZNR n = 1	WL-7 ZNR HFH, amp > 0.005 ft	0.224
D_h	WL-4 ZNR n = 1	WL-4 ZNR HFH, amp >0.005 ft	0.819
D_h	WL-2 ZNR n = 1	WL-2 ZNR HFH, amp > 0.005 ft	0.659
WE	CR test	ZNR Tests > 30 minute period	0.689

Table 12-13. Summary of additional t-test results. 'ZNR All Period > 60' indicates ZNR results with periods of 60 minutes or greater, using data from all wells. 'Confined CR' indicates results from the Hantush (1961) solution and 'CR unconfined' indicates results form the Neuman (1974) solution. 'WL-5 ZNR n=1 period > 60' indicates ZNR results with periods of 60 minutes or greater, using data from WL-5. Red values indicate *t*-tests where the null hypothesis is rejected.

Parameter	Population 1	Population 2	*p*-value
S	ZNR All Period > 60	Confined CR	0.873
S	ZNR All Period > 60	Unconfined CR	0.000
D_h	WL-5 ZNR n=1 period > 60	Confined CR	0.066
D_h	WL-5 ZNR n=1 period > 60	Unconfined CR	0.000
D_h	ZNR All Period > 60	Confined CR	0.173
D_h	ZNR All Period > 60	Unconfined CR	0.001

It is clear from these results that ZNR tests have no statistical differences of S or D_h when compared to the confined assumption of the Hantush (1961) solution. In contrast, there are p-values less than 0.05 of every comparison between ZNR test results and the Neuman (1974) solution that assumes confined conditions, indicating statistical differences between the populations. This makes sense as the Streltsova (1988) solution for ZNR tests assumes confined conditions, however, the conceptual model of the bull farm does assume unconfined conditions, so it would be reasonable to assume that ZNR tests are statistically different that the true parameter values for S and D_h.

It is important to keep in mind that when comparing populations such as D_h and S, estimates from ZNR tests to D_h and S estimates from other aquifer tests, the populations from the other aquifer tests have small populations of four values when compared together, and only two values when compared by their respective conceptual models. The low population numbers can skew the means of the data, and to further evaluate the significant differences, larger populations should be considered.

12.4.3.6 Strain Data During ZNR Tests

Strain has been shown to respond to constant rate pumping and injection tests, and the objective of this phase of the research is to evaluate the feasibility of using strain to characterize ZNR tests. Measuring strain in the vadose zone can present less risk and expense than measuring pressure in a monitoring well, so using strain could improve the resolution of ZNR tests, as well as make these tests potentially cheaper.

Strain data were obtained from four DEL-X extensometers that measure vertical strain, one instrument (FBG) that measures horizontal strain, and a Michelson strainmeter that measures vertical strain. Deformation was also measured using a LILY tiltmeter. Most of the instruments were in the vadose zone within 75 ft of the pumping well, with the exception of DEL-X8 and DEL-X9, which were in the saturated zone or capillary fringe.

These instruments were deployed during ZNR tests and the data they measured was used to evaluate the feasibility of including strain data in the analysis of ZNR tests. The strain data were processed and trimmed to match the pressure data intervals from PW-2. For the Fourier transform, the first couple cycles of the test were omitted and the last several were used to characterize the response. This approach minimizes the effect of the transient at the start of test on the strain, an approach this is similar to the analysis of the pressure data. The time-series of the data were characterized, and the harmonics were evaluated using a Fourier transform.

The field site has been used as a testing ground for instruments for more than 10 years, and the instruments used in this study were developed and deployed for other projects. The DPS1 and Michelson instruments were developed and deployed within the past two years, whereas the DEL-X instruments were installed 8 to 10 years earlier. The DEL-X instruments were well past their expected service life at the time of this study. Both the DPS1 and vertical Michelson strainmeters are the first examples of their technology that were deployed in the field. They were originally intended to be used for an initial proof-of-concept evaluation, and the application here exceeds our initial expectations. These factors have caused some variability in the strain data that could be tightened up with future deployments, but, nevertheless, the data will serve for a proof-of-concept evaluation.

12.4.3.7 FBG DPS1 Time series

The FBG strainmeter has three channels that represent the directional orientation of the horizontal strain. Since PW-2 is directly due north of the FBG instrument, the first channel is analyzed. The first channel, DPS1, is 9 ft from the pumping well and it measures the horizontal strain at 13 ft depth approximately along, a radial line with the pumping well. The instrument produces data in terms of picometers (10^{-12} m) and this can be converted into units of Strain, ε, through a conversion factor of 1.2 picometers to 1 microstrain (10^{-6} ε).

The strain time series at DPS1 is clearly periodic, decreasing during the pumping stage in increases during injection. The slope is steep at the beginning of each stage and flattens with time to create a shape that resembles the pressure in PW-2. The strain amplitude of each stage is approximately +/-500 nε, and the strain appears to be delayed slightly behind the pressure in PW-2.

The Fourier transform of the DPS1 data indicates a fundamental period of 60 minutes with a delay of 3.3 minutes. The amplitudes of the odd harmonics are larger than the even harmonics, similar to the spectrum of the pressure in PW-2.

There is a high frequency signal of approximately +/- 50 nε, which is the expected magnitude of random instrument noise at the resolution limit of the instrument. This gives a signal to noise ratio of approximately 10 to 1.

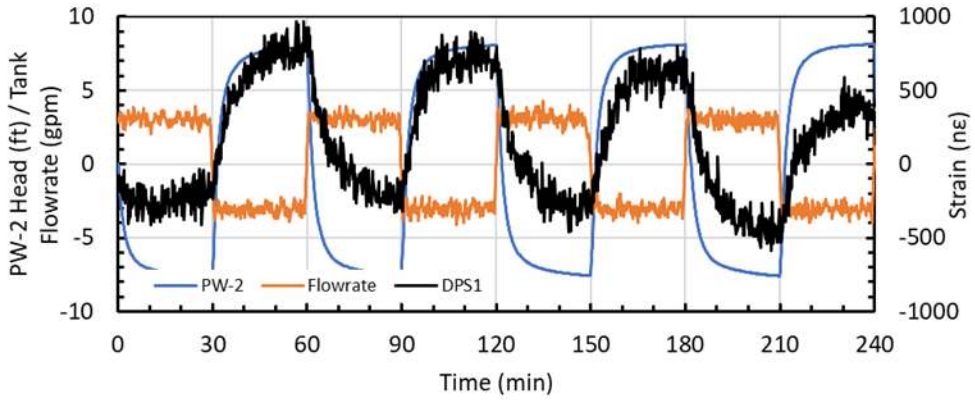

Figure 12-35. First four cycles from a 60-minute ZNR test. Horizontal strain from DPS1 (black), head in pumping well, PW-2 (blue), and flow rate pumped out of the well through tank pressure data (orange) as functions of time. Amplitude = 486 nε and delay = 3.3 min, according to Fourier transform analysis.

The FBG channel 3, DPS3, data are periodic as well, with a flipped sign to DPS1. The amplitude of the 60-minute test is +/- 0.5 picometers, or about +/- 400 nε (Figure 12-36). DPS3 data were consistently opposite sign as DPS1, and the lag estimates were about half a period longer than DPS1. Interestingly, DPS1 and DPS3 had similar amplitudes for the 10-minute, 30-minute and 60-minute tests; however, DPS3 amplitudes remained constant for tests with periods > 60 minutes and DPS1 amplitudes continued to increase with period (Table 12-14). The DPS2 showed a similar trend as DPS3, where the 60-minute test had the largest amplitude and the 120-minute

and 240-minute test amplitudes were generally constant. The DPS2 lag values indicate that the signal is arriving just before the PW-2 signal, resulting in a potential phase-wrap effect. DPS2 has a similar phase to DPS1 (Figure 12-36), despite the lag estimates showing quite different results (Table 12-14).

12.4.3.8 Michelson Time series

The Michelson strainmeter is73 ft from the pumping well and it measures vertical strain at a depth of between 13 and 17 ft. It is the furthest strainmeter from the pumping well and it has the highest precision and lowest noise.

The data from the Michelson strainmeter are clearly periodic, but the sign of the change is opposite that of horizontal strain measured at DPS1. The strain becomes increasingly compressive as the pumping well pressure increases during the injection stage, and it becomes tensile during pumping. The amplitude of the strain cycle is around 150 to 200 nε.

The average slope of the strain time series is nearly constant during each stage. The slope changes abruptly between stages in some cases, but it flattens during the last 10 minutes in other cases. The signal fluctuates by several 10s of nε at period of a few minutes throughout the test, presumably as a result of fluctuations in barometric pressure. It is possible that the flattening of the strain at the ends of some of the stages may be an artifact of barometric pressure variations and unrelated to the pumping test.

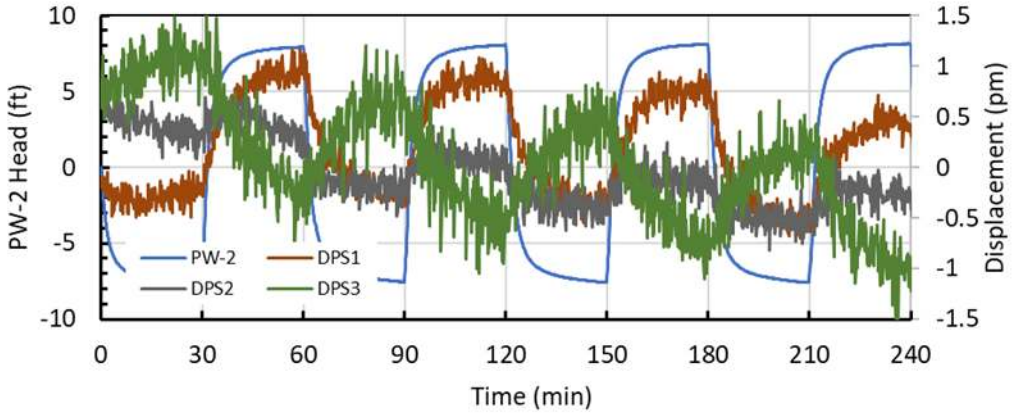

Figure 12-36. First four cycles from a 60-minute ZNR test. Horizontal strain from DPS1 (brown), from DPS2 (grey), from DPS3 (green), and head in pumping well, PW-2 (blue) as functions of time.

Table 12-14. Summary of direct-push FBG Fourier results from data collected during ZNR tests.

	DPS1		DPS2		DPS3	
λ (min)	T_L	A (pm)	T_L	A (pm)	T_L	A (pm)
10	1.2	0.23	10.2	0.07	6.6	0.11
30	2.3	0.47	30.1	0.20	18.8	0.34
60	3.3	0.58	59.2	0.26	36.2	0.51
120	2.8	0.96	98.8	0.16	71.5	0.48

240	6.8	1.12	207.2	0.18	134.1	0.48

The instrument noise is difficult to estimate from these data because it appears to be smaller than variations caused by barometric pressure. The data were not corrected for barometric pressure variations. There is a general increase in the strain throughout the test. This appears to be due to external factors, possibly a gradual decrease in barometric pressure, that are unrelated to the ZNR test.

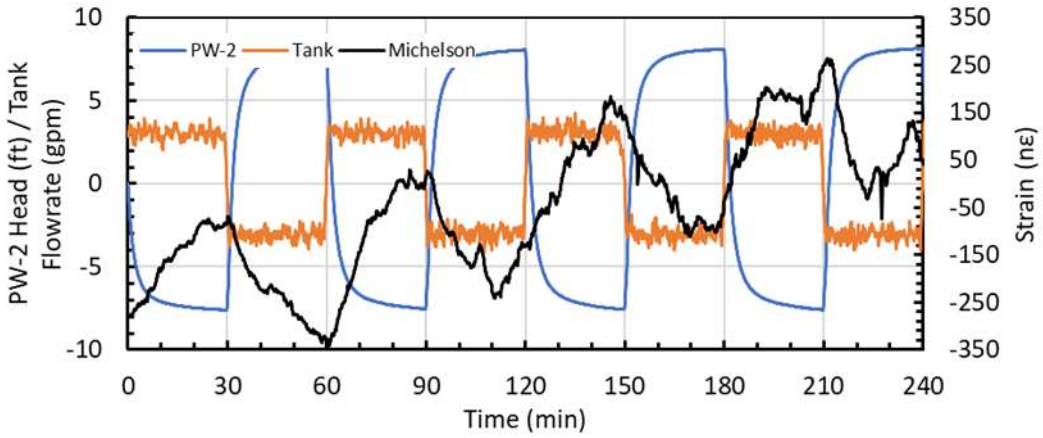

Figure 12-37. First four cycles from a 60-minute ZNR test. Vertical strain from Michelson (black), head in pumping well, PW-2 (blue), and flow rate pumped out of the well through tank pressure data (orange) as functions of time. Amplitude = 133 nε and delay = 35 min, according to Fourier transform analysis.

12.4.3.9 DEL-X Time series

The DEL-X9 (r = 10.5 feet) measures vertical strain in the saturated zone in close proximity to the well. The strain signal varies in the range of +/- 20 με during the test, and there is a clear periodic component that is similar to PW-2—that is, the vertical strain increases (expansion) when the pressure in PW-2 increases (Figure 12-38). There is a high frequency noise of approximately +/- 10 ne that complicates the signal and is likely a result of barometric pressure fluctuations. The data were not corrected for barometric pressure, but the 60-minute period in the signal is clear.

The strain data appear to respond more clearly to the injection stage and increasing pressure than to the pumping stage. The response during the start of the pumping stage is less clear, but this may be a result of sharp increases in strain that occur at the start of second and third pumping stages.

The strain appears to increase a few minutes after the start of the injection stages, suggesting the strain is delayed a few minutes behind the pressure in PW-2. This is in contrast to the results from the Fourier transform, where the fundamental component of the strain is before the PW-2 signal.

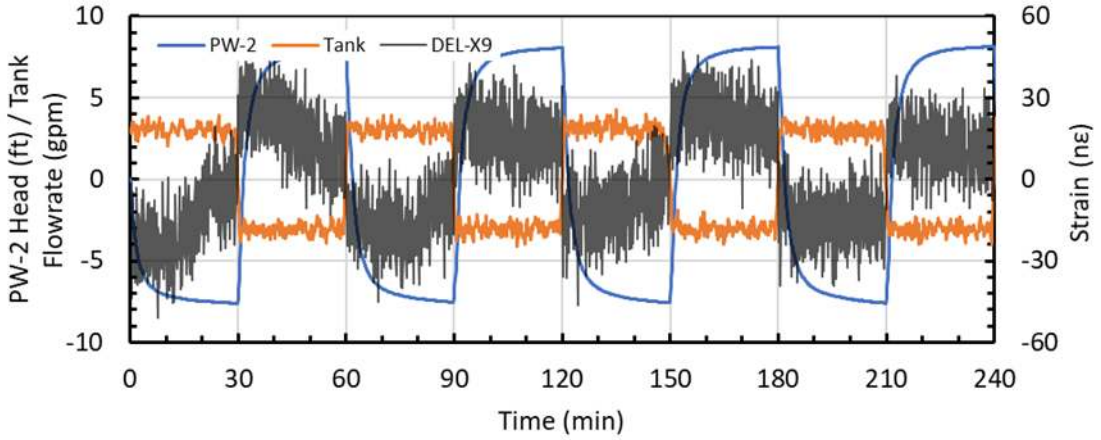

Figure 12-38. First four cycles from a 60-minute ZNR test. Vertical strain from DEL-X9 (black), head in pumping well, PW-2 (blue), and flow rate pumped out of the well through tank pressure data (orange) as functions of time. Amplitude = 19 nε and delay = 56 min, according to Fourier transform analysis.

The Fourier transform analysis indicates the fundamental wave in the DEL-X9 strain data occurs before the PW-2 pressure signal (Figure 12-39). This may be meaningful, but it may be a result of uncertainty introduced by the large noise in the data. For example, the lag during the 60-minute period ZNR test is 56 minutes, or if a full cycle is subtracted, the signal is arriving 4 minutes before the PW-2 peak. In contrast to the pressure signals, the Michelson, and the FBG DPS1, the DEL-X9 reaches the maxima and minima during the early part of the pumping and injecting stages. This could skew the Fourier transform towards the early part of the stage, altering the arrival time.

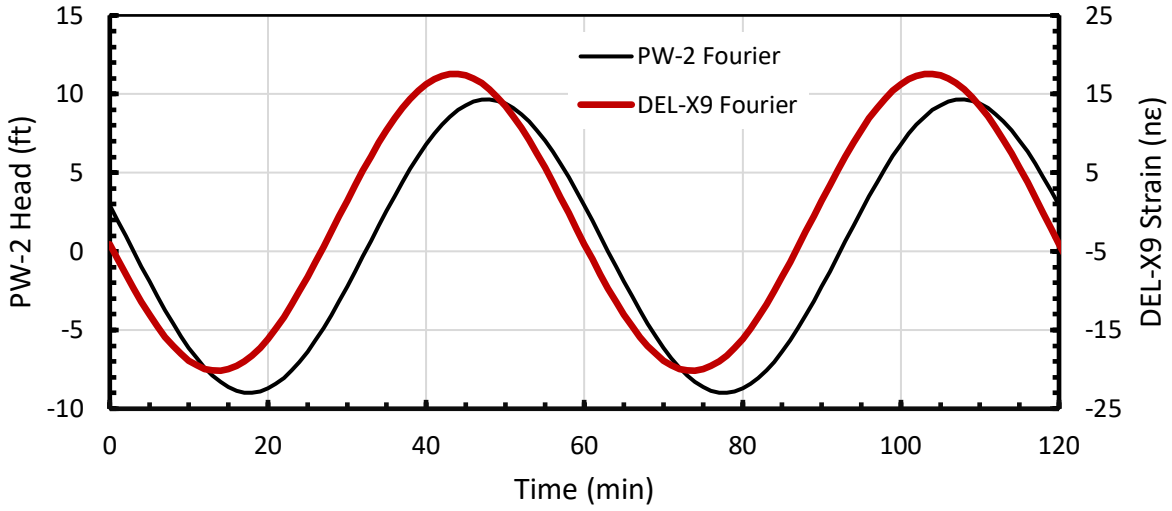

Figure 12-39. Fourier transform of 60-minute ZNR test. The DEL-X9 (red) arrives a few minutes before the PW-2 (black) pressure signal.

The DEL-X8 (r = 33 ft) is set to a depth of 30 ft and is situated around the capillary fringe. The PW-2 depth to water ranges from 25 to 35 ft below the ground surface. The strain data at DEL-X8 varies over the range of +/- 20 nε during the 60-minute ZNR test (Figure 12-40). The noise of the signal is about a few nε. relatively low when compared to the DEL-X9.

The strain signal from DEL-X8 is responding to the pumping signal in a similar manner to the Michelson, where the strain becomes increasingly compressive as the pressure increases during the injection stage, and it becomes tensile during pumping. This contrasts with how the DEL-X9 responded, indicating the DEL-X8 instrument is responding like it is in the vadose zone.

The average slope of the strain time series is nearly constant during each stage. Generally, there is a sharp slope change as the stage changes, then the slope flattens during the last 15 minutes of the stage. Like the Michelson, there is a general increase in the strain throughout the test. This appears to be due to external factors, possibly a gradual decrease in barometric pressure, that are unrelated to the ZNR test.

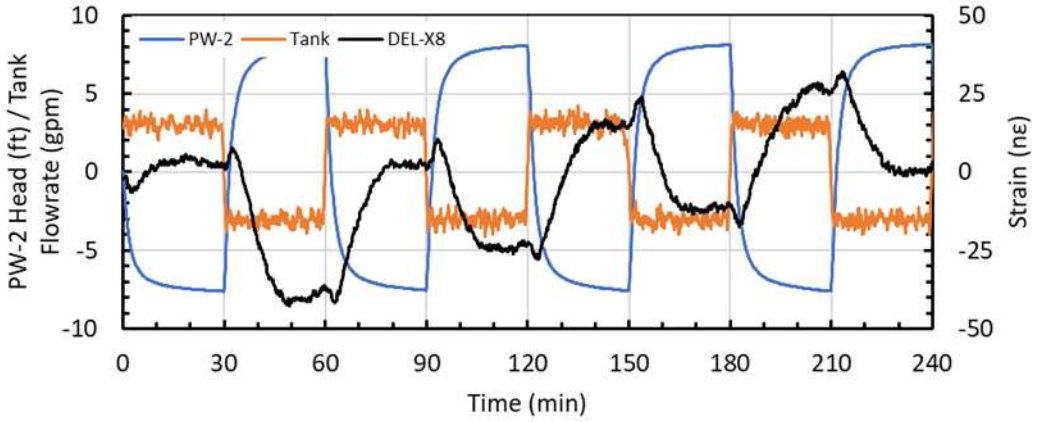

Figure 12-40. First four cycles from a 60-minute ZNR test. Vertical strain from DEL-X8 (black), head in pumping well, PW-2 (blue), and flow rate pumped out of the well through tank pressure data (orange) as functions of time. Amplitude = 19 nε and delay = 38 min, according to Fourier transform analysis.

The DEL-X4 (r = 75 ft) and DEL-X5 (r = 30 ft) are in the vadose zone, installed at depths of 20 ft and 19 ft, respectively. The strain data at DEL-X4 varies over around +/- 3 nε throughout the 60-minute test (Figure 12-40). The noise of the signal is around +/- 2 nε, resulting in a high noise ratio. Nonetheless, there is a clear periodic signal occurring. The data are saw-tooth shaped with the peaks occurring at the end of the pumping stage and the troughs occurring at the end of the injection stage. This instrument is responding similarly to the DEL-X8 and the Michelson, where the data increasing compression during the injection stage and tension during the pumping stage. According to the Fourier, the lag is about 40 minutes, and the amplitude of the signal is +/- 2.1 nε. The Michelson is a similar radial distance but has an amplitude about 60 times greater than that of the DEL-X4.

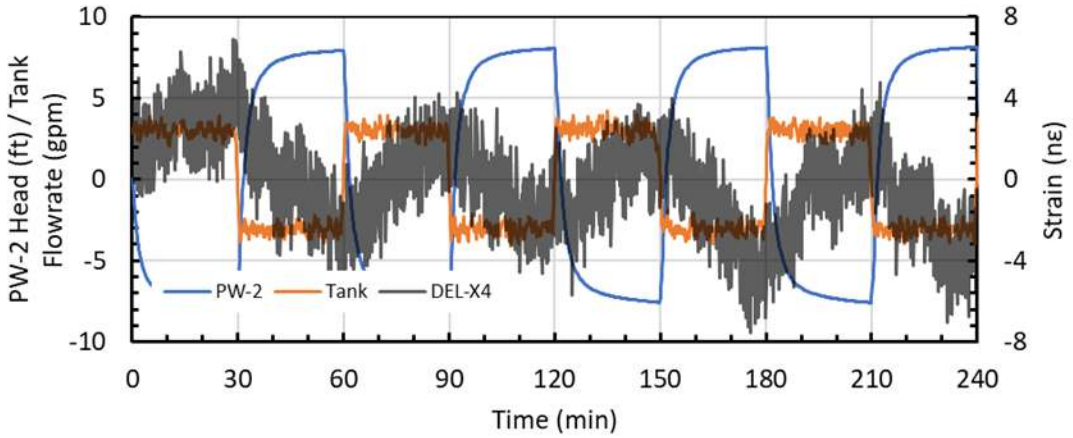

Figure 12-41. First four cycles from a 60-minute ZNR test. Vertical strain from DEL-X4 (black), head in pumping well, PW-2 (blue), and flow rate pumped out of the well through tank pressure data (orange) as functions of time. Amplitude = 2.1 nε and delay = 40 min, according to Fourier transform analysis.

The DEL-X5 (r = 30 ft) is located at a similar radial distance as the DEL-X8 (r = 33 ft). Like the DEL-X4, the amplitude varies minimally, about +/- a few nε during the 60-minute test. The early data has a high noise ratio is approaching 1 to 1, but a clear periodic signal is present during the later periods. Interestingly, the sign change is similar to the FBG DPS1. The strain time series at DEL-X5 is increasing during the injecting stage and decreasing during pumping. It is unclear why this vertical strain measuring instrument has a flipped sign to all the other vadose zone strain measuring instruments. The Fourier transform of the DEL-X5 data indicates a fundamental period of 60 minutes with a delay of 10 minutes and an amplitude of +/- 3.6 nε.

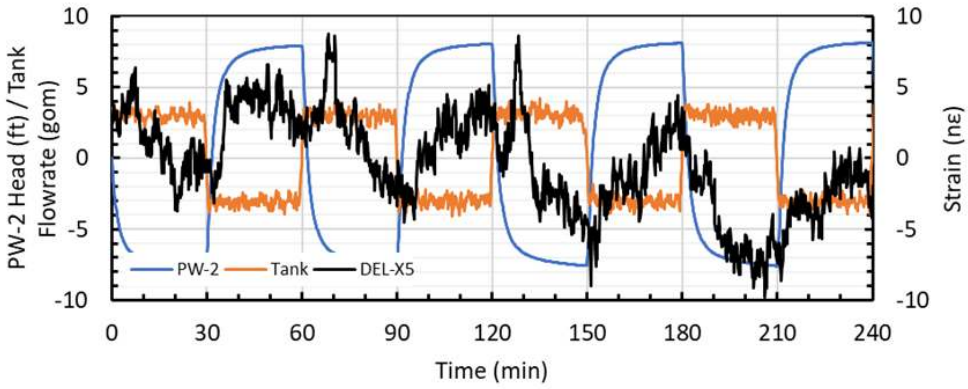

Figure 12-42. First four cycles from a 60-minute ZNR test. Vertical strain from DEL-X5 (black), head in pumping well, PW-2 (blue), and flow rate pumped out of the well through tank pressure data (orange) as functions of time. Amplitude = 3.6 nε and delay = 10 min, according to Fourier transform analysis.

The LILY Tiltmeter signals were periodic with low noise (Figure 12-43). The maximum positive tilt occurs at the end of pumping and the maximum negative tilt occurs at the end of injecting. The Tilt north/south signal has a larger amplitude than the Tilt east/west, with amplitudes of 1 microradian and 0.5 microradian, respectively. The tilt vector is calculated by adding the squared components and taking the square root. The maximum tilt vector is 1.1 microradian and occurs at the end of each stage.

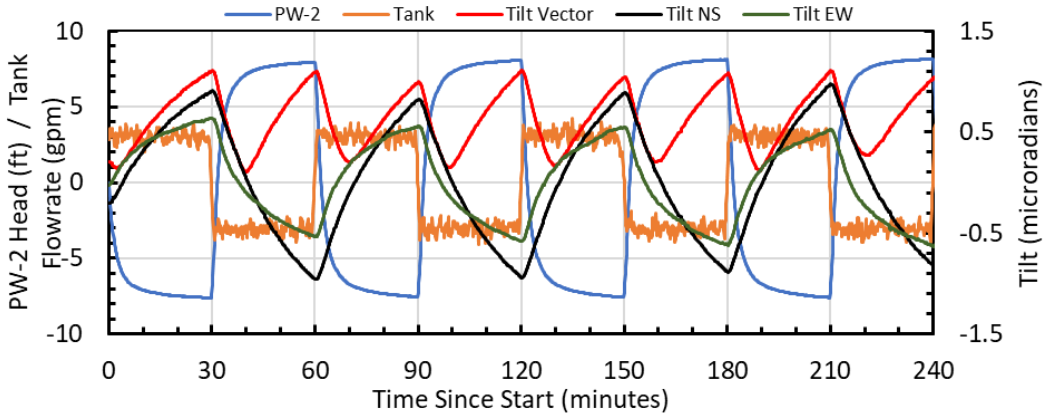

Figure 12-43. First four cycles from a 60-minute ZNR test. Tilt from the North-South channel (black), the East-West channel (green), head in pumping well PW-2 (blue), and flow rate pumped out of the well through tank pressure data (orange) as functions of time. North-South Amplitude = 0.8 microrad and delay = 39 min, and East-West Amplitude = 0.5 microrad and delay = 36 min, according to Fourier transform analysis.

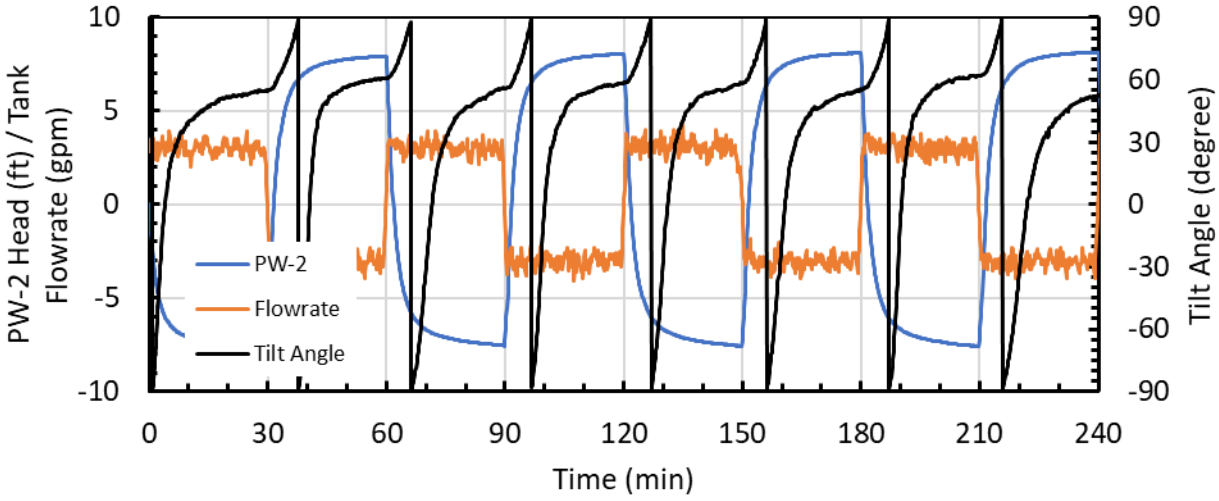

Figure 12-44. First four cycles from a 60-minute ZNR test. Tilt from the North-South channel and the East-West channel used to calculate orientation angle (black), head in pumping well PW-2 (blue), and flow rate pumped out of the well through tank pressure data (orange) as functions of time. Only quadrants I and IV are included here.

The two tilt components were used to determine the azimuth of the tilt and the results included with time series. The azimuth is relatively constant at approximately 60 at the end of a pumping or injection stage (Figure 12-44). It increases to 90 following the change in sign of the rate at the well, and then it abruptly changes orientation by 180 and continues to rapidly increase. The azimuth time series reflects the periodic change in tilt angle during periodic pumping. Additional processing would show the azimuth changing by 180 between stages, but the current analysis only resolves +/- 90º.

12.5 PART 1 DISCUSSION AND CONCLUSIONS

There was no statistical difference between hydraulic conductivities measured with ZNR tests and those measured with pumping tests. Similarly, slug test *K* estimates have no statistical difference to constant-rate test *K* estimates. However, ZNR tests have a benefit of easily estimating well efficiency and storage terms when compared to slug tests.

All the strain instruments recorded signals that varied with the same period as the pumping rate, and the time lag of the strain was generally similar to that of the pressure at a similar radial distance. However, the time lag of several of the vertical strain measurements appear to be shifted by a half period. Vertical strain should be shifted by approximately ½ period compared to the pressure at a similar radial distance, according to the simulations (Figure 12-18). This occurs because an increase in pressure in the aquifer causes a decrease in the vertical strain. However, the time lag of the vertical strain at DEL-X4 (r = 75 ft) and the Michelson instrument (r = 73 ft) are similar to that of the pressure at WL-4 (r = 68 ft) as shown in Figure 12-45. This differs from the expected response, so we evaluated the response during the long-term pumping test and the results were consistent with Figure 12-45. The reason for this shift is unclear, but we used the sign of the response from the long-term pumping test as a baseline when determining the time lag during the periodic tests.

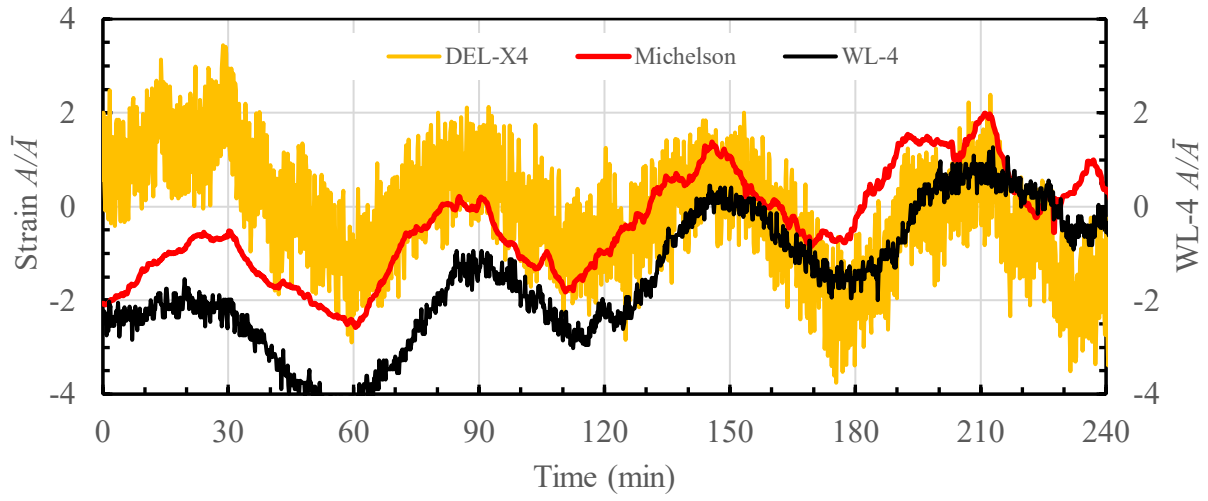

Figure 12-45. First four cycles of a ZNR test with a 60-minute period for strain data measured with the Michelson and DEL-X4 and pressure data measured in WL-4.

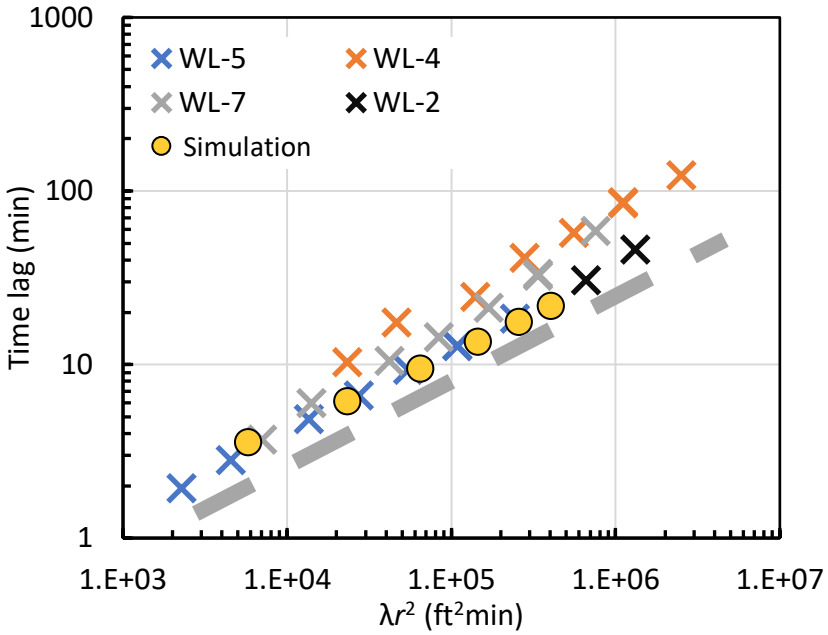

Figure 12-46. Time lag as a function of scaled period, λr^2, for field pressure data (X's) and simulations (circles). Grey dotted line is a square-root function for reference.

The permeability in the simulations was adjusted so the predicted lag times are similar to the observed lag times at WL-5 (Figure 12-45Figure 12-46). The lag times at the other piezometers are slightly greater than those at WL-5, probably because of non-ideal conditions that are not included in the simulations.

The time lag of the vertical strain measured at DEL-X4 and the Michelson instrument are similar to the simulations for the 60 minute period (Figure 12-47).

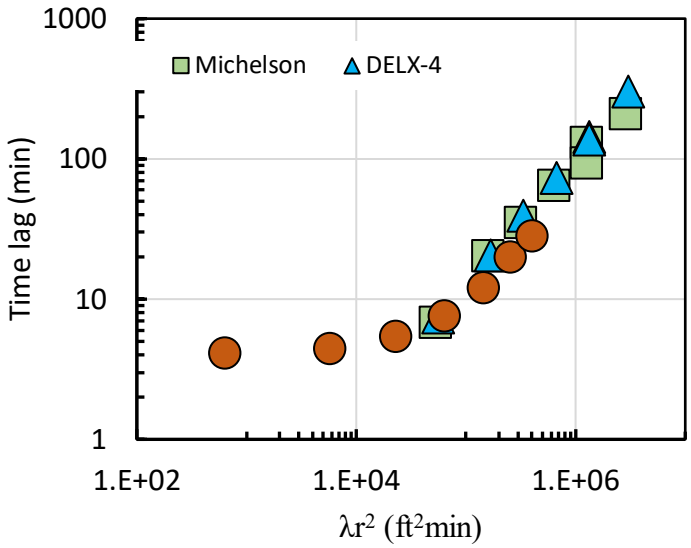

Figure 12-47. Time lag from vertical strain as a function of scaled period. The field data consists of the DEL-X4 (triangles) and the Michelson (squares). The theoretical vertical strain (circles) was corrected by subtracting half a period.

The lag time of the vertical strain in the vadose zone is generally similar to the pressure at the same value of scaled period, λr^2 (Figure 12-47). The trend of the strain data is steeper than that of the pressure, and this causes the strains from most of the instruments to be similar to, or less than that of the pressure at small values of λr^2, and greater than the pressure at large values of λr^2. This is consistent with the theoretical results in Figure 12-18.

The lag times of vertical strains at DEL-X8 and DEL-X9 are significantly greater than those of the pressure and the other strains, and that causes these data to plot above the others on Figure 12-47. DEL-X9 is in the aquifer, and DEL-X8 straddles the water table, so their behavior is not described by the model, which only includes strains in the vadose zone. In general, the sign of the vertical strain in the aquifer is opposite that in vadose zone and this likely accounts for the large difference in phase between DEL- X8 and X9 and the other data.

The lag time data from DEL-X5 for small values of scaled period follow trends that are typical of the other vertical strain instruments and the pressure, whereas data from DEL-X5 for larger values of λr^2 follow the trend from DEL-X8. The phase of the data from the three larger values of λr^2 appears to be shifted by one half period compared to the other data. The reasons for this behavior are unclear, and additional well tests would be needed to evaluate the reproducibility of this effect.

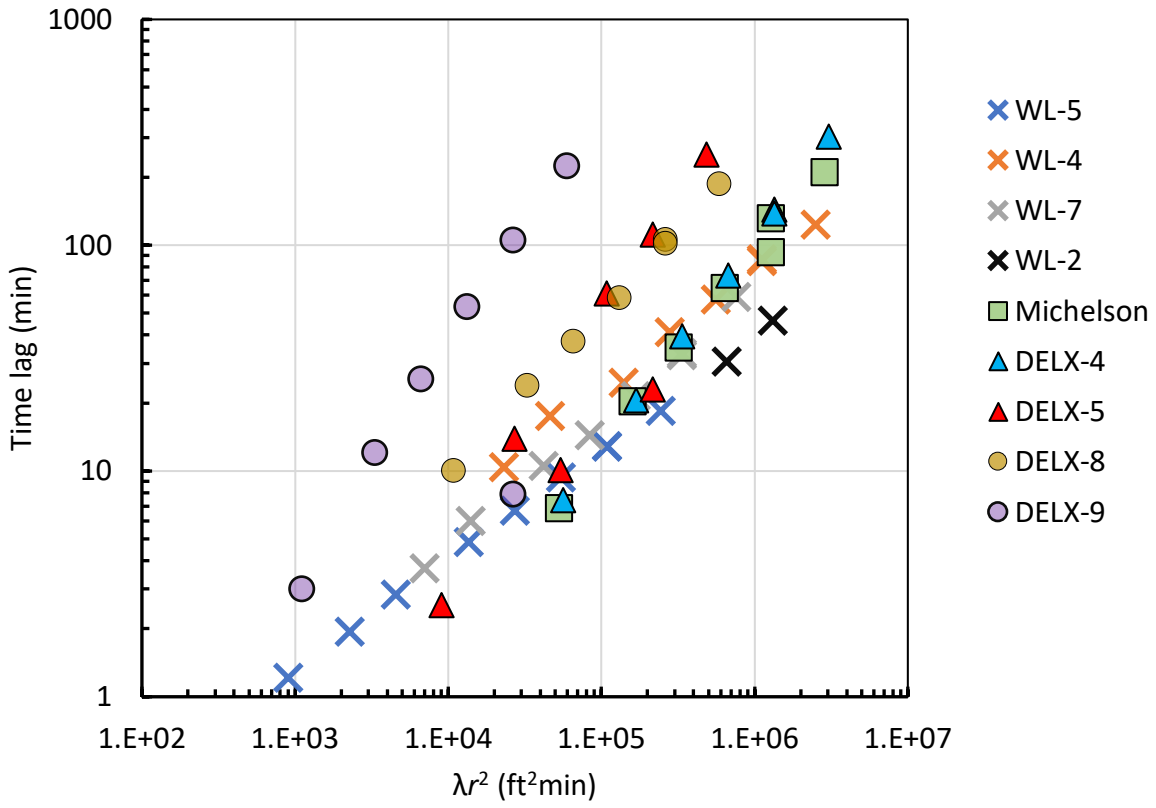

Figure 12-48. Time lag from field vertical strain and field pressure as a function of scaled period. The field data are from DEL-Xs in vadose zone (triangle), DEL-Xs in saturated zone (circle), Michelson strainmeter (square), and pressure (X).

The time lag of the average horizontal strain is similar to the pressure, but the lag for the circumferential and radial strains are quite different (Figure 12-18). The lag time of the circumferential strain is much less than, and that of the radial strain is much greater than that of the pressure. Three horizontal strains were measured at one instrument, FBG DPS1 (r = 9 ft), and the lag times from these three sensors varied considerably. The lag time from channel DP S1 is essentially the same as the pressure (Figure 12-49b), whereas the lag times at the other two channels are considerably longer.

The difference in response of the horizontal strain is likely due to the large changes in strain magnitude with orientation. This can be an important advantage because the horizontal strain tensor is expected to be sensitive to characteristics of heterogeneities. The strainmeter FBG D1 is the first prototype of a new design and further work will be needed to evaluate the individual strain components.

One important insight from the simulations in Figure 12-18 is that the lag time of the average horizontal strain is quite similar to that of the underlying pressure. It is possible to determine the average horizontal strain from the thee horizontal components, but an approach that is potentially more reliable is to use a strainmeter that measures the average horizontal strain directly. This type of instrument is described in Murdoch et al. 2020 and 2021 where it is called an areal strainmeter.

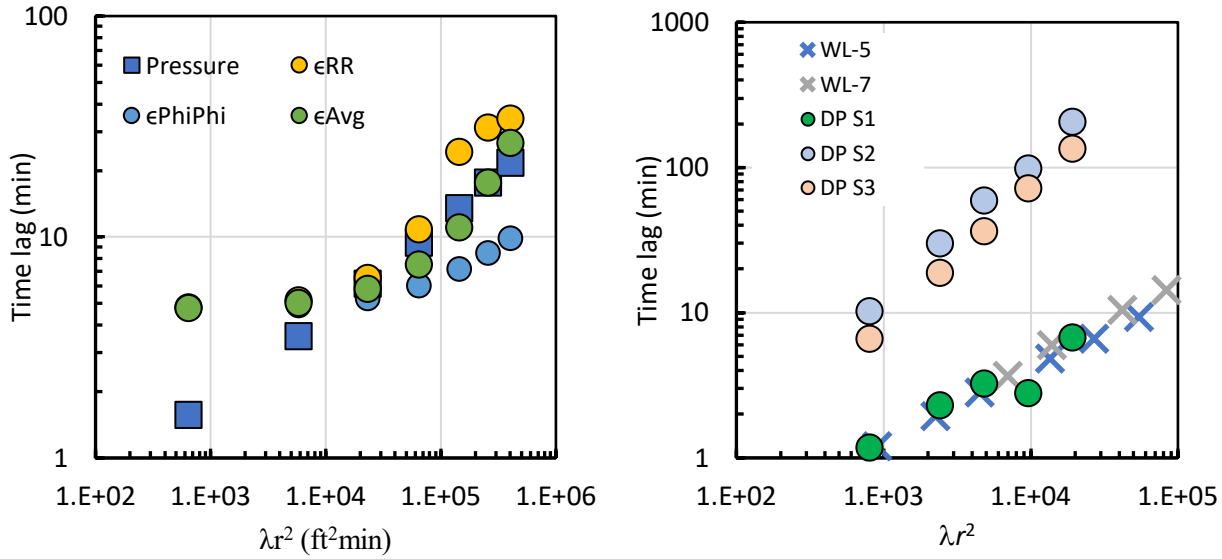

Figure 12-49. Lag from horizontal strain as a function of scaled period for (a) theoretical data and (b) field data compared to pressure. Radial and circumferential strain were average to estimate the average horizontal strain. DPS3 data (lighter circles) and corrected data (darker circles) are plotted.

Chapter 12, Part 2

Well Tests with a Sinusoidal Pumping Rate

12.6 PART 2 ABSTRACT

The objective of Part 2 of this chapter is to evaluate the feasibility of measuring and interpreting the vertical strain in the vadose zone generated during pumping tests that use a rate that varies as a sinusoidal function of time to estimate aquifer and/or overburden properties. Part 2 is based on Blais (2023). Pumping tests were performed at the Simpson Station site with a water table at 9 m and saturated saprolite from 9 to 30m depth. Sinusoidal pumping tests in the saprolite used different pumping amplitudes and periods while pressure was measured at three piezometers and vertical strain was measured in the vadose zone from 1 to 7 m depth. This set of tests used the CMPI method to measure strain.

The delay time of the pressure increased linearly with distance, and it increased with the square root of the period, while the amplitude of the pressure decreased with distance and increased with amplitude. Vertical strain in the vadose zone varied with the same period as the pumping rate and the delay times were similar to those for pressures measured at similar radial distances. Delay times for the strain increased upward. The hydraulic diffusivity was estimated using delay times for pressure and strain, and the results were compared with the values estimated from a constant-rate pumping test. The hydraulic diffusivity from the constant rate test was 0.039 m^2/sec, whereas it was 0.053 (±0.05) m^2/sec and 0.035 (±0.03) m^2/sec from the pressure data and 0.08 (±0.022) m^2/sec and 0.035 (±0.001) m^2/sec from the strain data from sinusoidal tests of various periods and amplitudes. There is no statistical difference among these values. Simulations of the pressure and strain are consistent with field observations.

12.7 PART 2 INTRODUCTION

Sinusoidal pumping tests are a form of hydraulic testing in which the well is pumped at a sinusoidal rate, either with a net removal of water, or paired with injection to have no net removal of water. Sinusoidal pumping tests are also called harmonic well test, oscillatory well test, cyclic well test, periodic well test (Sun et al. 2015, Cardiff and Barrash, 2015, Horne 1997, Mehnert et al. 1999). The test originated from the idea of pulse interference tests in the oil industry. The interference tests work just as constant rate pumping tests do, changing the fluid pressure in a reservoir to estimate reservoir properties. In industry, interference tests are performed by altering the rate of pumping during production or injection into a reservoir and measuring pressure changes at other observation wells (Johnson et al. 1966). The pulse test was introduced as an alternate interference test due to its limited interruption of production. It involves a sequence of pumping and shut in cycles, while measuring the pressure change at the pumping well and pressure response in surrounding wells. The pressure response data is in the time domain. The pulse testing method creates a cyclic pressure response, which can be separated from the background pressure (Johnson et al. 1966, Kuo 1972). This idea was expanded to harmonic pulse testing that can be performed by either: (a) sinusoidal variation of flow, or (b) periodic multiple rates (Kuo 1972). The flow rate and pressure response for this test are recorded but the key defining feature is that the data is processed in the frequency domain (Fokker, et al. 2018). By pumping/ injecting at a known frequency, the data can be processed in at a specific frequency. This helps to isolate the generated signal from possible background noise because of other production wells or other natural harmonic signals such as those mentioned above. The frequency domain analysis of the pressure response also allows the possibility of locating heterogeneities in the subsurface (Kuo, 1972). Using the frequency and subsequently the phase lag between the flow and the observed pressure, the *kh* value (the product of formation permeability, *k*, and reservoir thickness, *h*) and the skin factor can be estimated (Kuo, 1972).

The sinusoidal technique developed for the oil industry was adapted for hydrogeological applications (Black and Kipp 1981). Solutions were generated for a confined, non-leaky aquifer with both a point source and a line source. The analytical solution by Black and Kipp uses the ratio of the phase shift or amplitude between two different observation wells in order to estimate the hydraulic diffusivity. They did not provide a way to separate the hydraulic conductivity/ transmissivity and the storage components. New solutions have been derived that allow both diffusivity and transmissivity to be estimated (Rasmussen, et al. 2003a).

The pumping rate can be described as

$$Q(t) = Q_1 \cos(\omega t) + Q_2 \sin(\omega t) \qquad (12\text{-}18)$$

where ω = the angular frequency. The pressure responses measured in observation wells are are characterized using

$$s(t) = s_1 \cos(\omega t) + s_2 \sin(\omega t) \qquad (12\text{-}19)$$

These two solutions are then related to each other to generate unit drawdown amplitudes per pumping amplitude and unit phase lags between observed drawdown and the flow rate (Rasmussen et al. 2003b).

$$s_o = \frac{|s|}{|Q|} = \frac{\sqrt{s_1^2+s_2^2}}{\sqrt{Q_1^2+Q_2^2}} \tag{12-20}$$

$$\varphi_o = \varphi_s - \varphi_Q = atan\frac{s_2}{s_1} - atan\frac{Q_2}{Q_1} \tag{12-21}$$

where φ_s= the phase of the observed drawdown, φ_Q= the phase of the flow rate,

Once phase lag (φ_o) is calculated, the relationship:

$$\varphi_o = F(u) = arg\{K_o(\sqrt{iu})\} \tag{12-22}$$

can be solved through inversion to find u, where K_o is the zero-order modified Bessel function of the second kind.

The inverse function is approximated using a fifth-order logarithmic polynomial:

$$\ln(u) = \int_{i=o}^{5} c_i(ln\varphi)^i \tag{12-23}$$

where the coefficients are c_i = [-0.12665, 2.8642, -0.47779, -0.16586, -0.076402, 0.03089]. It follows that the aquifer diffusivity (D) and transmissivity (T) are (Rasmussen et al. 2003b)

$$D = \frac{\omega r^2}{u} \tag{12-24}$$

$$T = \frac{|K_o(\sqrt{iu})|}{2\pi s_o} \tag{12-25}$$

where r = radial distance from the pumping well [L].

12.8 PART 2 METHODS

This phase of the investigation includes deploying a new optical fiber strain sensor and using it to evaluate the performance during sinusoidal pumping tests. This required developing equipment and techniques for packaging and deploying an optical fiber sensor, and for pumping water from a well at a precisely controlled variable rate and measuring the flow rate from the pump and the pressures in nearby monitoring wells.

Numerical and field experiments were performed to test the viability of using a fiber optic strain ribbon and interpreting the strain signal measured in the vadose zone during sinusoidal-rate pumping to estimate aquifer properties.

12.8.1 Equipment

The equipment developed for this investigation consists of a system to pump water from a well at variable rate, and a sensor system to measure strain during pumping.

12.8.1.1 Pumping System

A system was developed to pump water from a well at a variable rate. The system uses a Berkeley JP Composite Series downhole pump model B5P4JP05231 with a downhole check valve (Figure 12-50). The pump is 4-inch in diameter and was installed in the well at a depth of 75 feet below ground surface. A pump curve for the pump is in Figure 12-51.

The pump motor is powered by 220 VAC and rate of the pump is controlled by altering the frequency of the AC power using a variable frequency drive (VFD). The system uses an ATO model GK3000 VFD, which is designed for ½ horsepower, single-phase 220 VAC power. A 1000W step-up transformer (SEYAS AT-1000) was used to convert the 120V power available at the field site to 220V. The output of the VFD is controlled by a DC input voltage generated with a Tektronix AFG1022 Arbitrary Function Generator. The function generator was configured to create a 0-5 volt sinusoidal signal with adjustable amplitude and period. The sinusoidal voltage generated by the function generator is converted to a variable frequency by the VFD, which in turn results in a flow rate at the downhole pump that varies as a sinusoidal function of time.

Flow rate was measured using a paddlewheel-type flow meter (Omega Engineering FP-5600) in the discharge hose from the downhole pump (Figure 12-51). The flow meter has a flow velocity range of 0.3 to 20 feet per second with an accuracy of ±1%. The flow meter was mounted in a ¾-inch Schedule 80 PVC pipe, which resulted measurable flow rates from 0.5 gallons per minute (gpm) to 34 gpm. The output of the flow meter was an amplified square voltage pulse. The pulse was converted to a flow rate using a conversion factor for a ¾-inch Schedule 80 PVC pipe, which is 583.19 pulse/gal, according to the manufacturer calibration specs. The calibration factor was verified in the field.

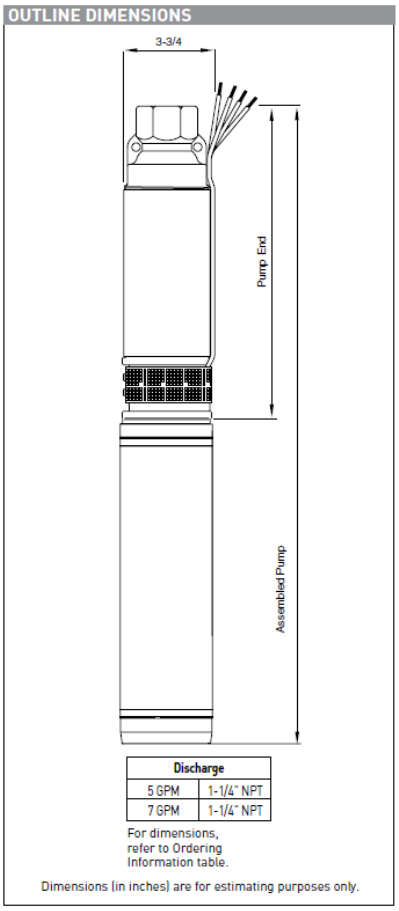

Figure 12-50: Berkeley pump schematic

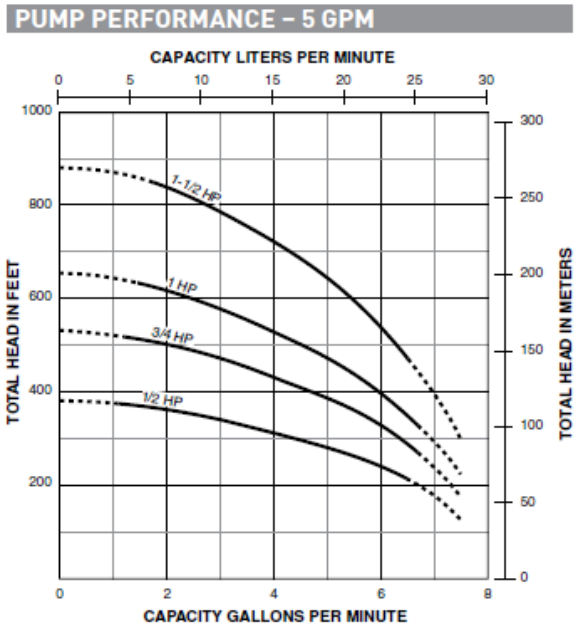

Figure 12-51:Berkeley pump performance curve

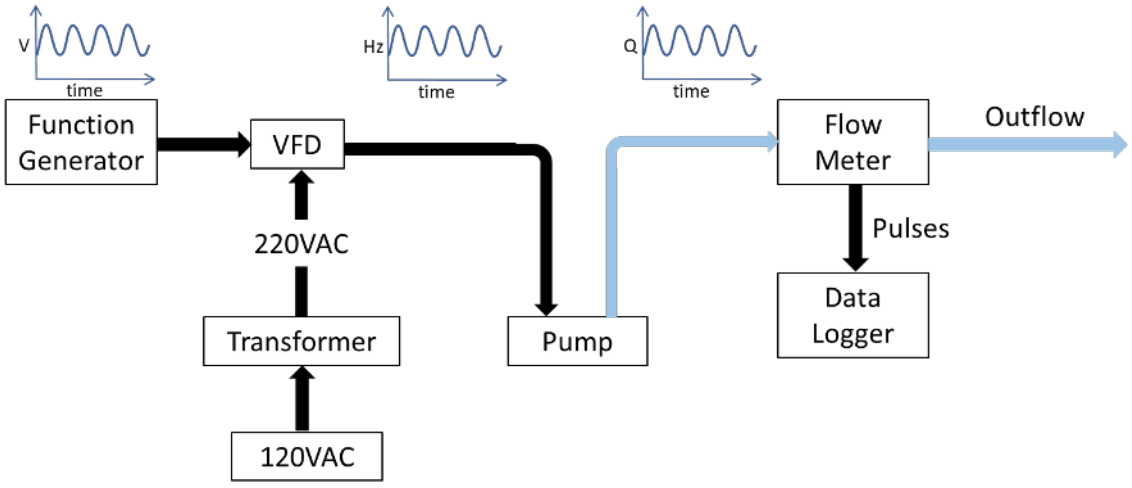

Figure 12-52: Schematic of the pumping system for flow rate control.

12.8.1.1.1 Strain measurements using CMPI

Strain in the subsurface was measured using a method called Coherence-length-gated Microwave Photonics Interferometry (CMPI), which is described in Hua, et al. (2017) and elsewhere in this report. The method measures strain along a single-mode optical fiber with internal broadband reflectors. Prior to this project, applications of CMPI to field settings were limited, so methods for deploying sensors in the field were unavailable. As a result, this project included a task to design and package optical fiber sensors used by CMPI for field deployment.

12.8.1.2 Coherence-length-gated Microwave Interferometry

The Coherence-length-gated Microwave Interferometry (CMPI) method measures the displacement between pairs of weak reflectors along an optical fiber using an electronic interrogator and Michelson interferometer reference. The system uses microwave modulated low coherence light as the probe, which is injected into the sensing fiber. The backscattering from the weak reflectors is recorded in the microwave frequency domain through down conversion. The microwave spectrum is further processed to obtain the distributed strain signals.

The CMPI methods use communication-grade, 250-micron-diameter, single-mode optical fiber with an acrylate coating and a glass core 9 microns in diameter. Reflectors are fabricated by focusing the beam of a femtosecond laser onto the core of the fiber. This modifies the refractive index over a small region within the core, which is designed to create an imperfection that reflects approximately -35 to -45 dB of light. Each reflector returns a small fraction of the light from the laser, so many reflectors can be used before the outgoing signal strength is diminished. However, the strength of the reflection is much greater than the reflections from Raleigh scattering, which increases the signal to noise ratio compared to measurement methods that use Raleigh scattering (e.g. Distributed Acoustic Sensing).

CMPI is implemented using an interrogator and reference interferometer. The interrogator includes a microwave source and detector, a laser, an electro-optic modulator, and a photodetector (PD). The light from the laser source is intensity-modulated by a microwave signal using an electro-optic modulator (EOM). The modulated light is launched into the sensing fiber, and the reflections are detected by the PD. The demodulated signal is received by the microwave detector, which measures the amplitude and phase of the signal at the modulation frequency. After the microwave source sweeps through the designated microwave bandwidth, the S_{21} spectrum is obtained, which is used to read the sensing signal. The resulting data are processed to determine the strain using methods described in Hua et al. (2017 and 2020).

An external optical fiber Michelson Interferometer (MI) with arm length difference of 15 cm is used as a reference. The MI is sealed in a metal tube and suspended in a borehole (Figure 12-53) to minimize the optical path difference (OPD) change. The deformation experienced by the sensing fiber is independent of the reference fiber, so the MI acts as a stable reference.

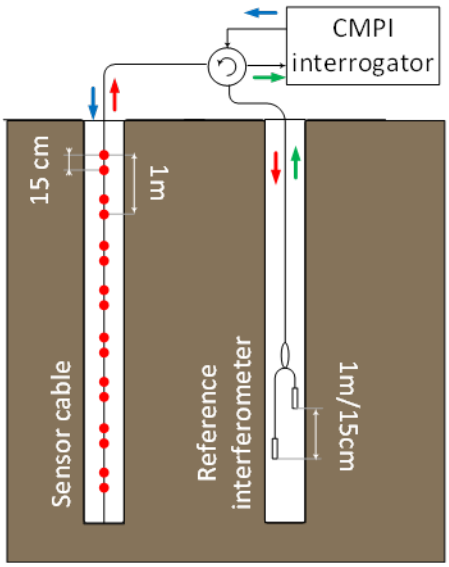

Figure 12-53: Conceptual model cross section of the sensor cable and reference interferometer in the field

12.8.1.3 Strain ribbon

The tensile strength of the 250-micron diameter optical fiber used to measure strain with CMPI is approximately 100kpsi (0.69 GPa), which is strong enough to limit breakage during careful handling in the lab, but it is too weak for field applications. This problem occurs for all applications of optical fiber and it has resulted in a variety of methods of packaging fiber into reinforced cable. Some reinforcement consists of a polymer coating, or buffer, that increases the diameter of the fiber to 900 microns. This produces tight-buffered optical fiber, which is stronger than the 250-micron-diameter fiber, but it remains too fragile for many field applications. Another cable design consists of multiple, tight-buffered fibers wrapped in braided Kevlar and coated in polymer. This is called "tactical" optical fiber cable. Tactical cable provides significant tensile and bending strength and it can protect optical fiber during many routine field applications, including in the shallow subsurface. Optical fiber armored in stainless steel tubing is also available to protect fiber under more severe conditions downhole.

Protecting optical fibers can be at odds with strain sensing. Most standard optical fiber cables protect fiber by decoupling it from external strains, which is the role of the Kevlar braid in tactical cable, for example. However, using optical fiber as a strain sensor requires that it is coupled to the formation, and it also requires that the strain field in the formation is unaltered by the presence of the fiber. For example, one possibility is to put optical fiber in a borehole and then fill the borehole with cement grout that bonds to both the fiber and the formation. This could be effective where the borehole is in competent rock with an elastic modulus similar to that of cement grout ($E \sim 10$ GPa). However, if the borehole is in unconsolidated sediment or saprolite (E

< 0.1 GPa) the cement grout would be a stiff inclusion, and this would likely cause the strain measured by the fiber to be less than the strain in the formation.

A method of packaging the optical fiber was developed that addresses the dual problem of protecting the fiber and coupling it to the formation. The approach is to encase the 250-micron fiber in a thin, flat strip of material that is strong enough to offer protection, but compliant enough to transfer strain. Optical fiber packaged in a long, flat strip of material will be called a "strain ribbon."

12.8.1.3.1 Borehole completion

The strain ribbon developed for this project was coupled to the formation using friction. This was accomplished by placing the ribbon along the axis of a borehole. A polyethylene sleeve extending the length of the borehole was then inflated and filled with sand to press the ribbon against the borehole wall (Figure 12-54). The elastic modulus and density of the sand filling the sleeve are similar to that of the saprolite at the field site. Matching the elastic modulus and density limits the perturbations in the strain field caused by the sand-filled borehole.

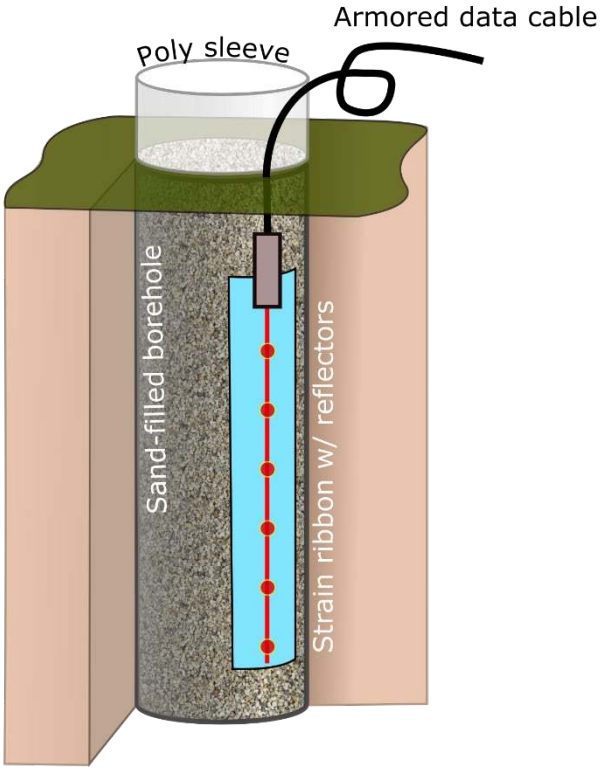

Figure 12-54: Perspective view of strain ribbon wellbore completion.

12.8.1.3.2 Conditions for slip

The strain ribbon is designed to couple the optical fiber to the formation through friction. We assumed that the frictional strength between the ribbon and the formation is

$$\tau = (\sigma_n - p)\mu \tag{12-26}$$

where σ_n is the normal stress (positive is compression), p is the pore pressure in the formation, and μ is the coefficient of friction between the ribbon and the formation. The normal force is assumed to be created from the weight of the sand in the polyethylene sleeve. Assuming the strain at the wall is negligible and the diameter of the sleeve is large enough to limit bridging, the normal force on a vertical wall is

$$\sigma_n = \frac{\nu}{1-\nu}\gamma_s d \tag{12-27}$$

where γ_s is the unit weight of the sand, ν is Poisson's ratio, and d is depth.

The problem of slip between the ribbon and the formation was analyzed using a force balance, which gives the critical strain gradient in the direction of the ribbon that can cause slip

$$\frac{d\varepsilon}{dz} = wC_T\tau \tag{12-28}$$

where C_T is the axial compliance (strain/axial force) of the ribbon, and w is the width of the ribbon. It follows that the strain gradient that would cause slip increases as a linear function of depth

$$\frac{d\varepsilon}{dz} = \frac{\nu}{1-\nu}wC_T\mu\gamma_s d - wC_T\mu p \tag{12-29}$$

12.8.1.4 Polyester film strain ribbon

The strain ribbon used in this investigation was formed by laminating optical fiber between two strips of transparent polyester film. The film is 140 microns thick, and is coated with a strong contact adhesive (ASTM D3330 peel strength of 15.3 N/cm according to the manufacturer). The film is available in rolls and is marketed as 3M™ Super Bond Film Tape 396.

A strain ribbon was created by adhering the optical fiber to the center line of one piece of film and then bonding them to another piece of film. The adhesive sides of both films contacted the fiber and each other to form a single strip with the optical fiber along the center axis. Prototypes and short ribbons were created manually to establish proof-of-concept, but this process was only capable of creating ribbons up to 1 m long. The films could become misaligned or wrinkled, or the tension in the two sides of the film could be unequal, which caused the ribbon to bend or

buckle. A packaging device was developed to avoid some of these problems. The device contains two spools of the polyester film along with a spool of optical fiber containing reflectors. The polyester films are passed through rollers and pressed together as the fiber is aligned along their centerline. The assembled ribbon is then wound on a spool (Figure 12-56). Strain ribbons up to 10 m long were created with the packaging device, and it would be possible to create even longer ribbons.

Light is transmitted from the laser in the interrogator to the strain ribbon through a tactical optical fiber cable. A fusion splice is used to couple optical fiber in the tactical cable to the fiber in the ribbon. The splice is particularly fragile, so it is encased in a block of epoxy and reinforced with aluminum.

Data was developed to evaluate conditions that could cause slip of the polyester ribbon using eq. (12-29). The ribbon was put in a loading frame to measure displacement as a function of axial load (Figure 12-55). These data show that the strain is a linear function of applied load. The data in Figure 12-55 were measured using a ribbon that was 2.5 cm, but the width of the ribbon used in the field is $w = 5$ cm. As a result, the compliance of the ribbon used in the field is half that measured in Figure 12-55, so the compliance of the ribbon used in the field is $C_T = 45$ με/N. The unit weight of the sand used in field deployments is 18000 Pa/m, and Poisson's ratio is assumed to be between 0.25 – 0.4. The coefficient of friction between the polyester film and sand was measured in the laboratory to be in the range $0.2 < \mu < 0.3$.

The pore pressure where the ribbon was deployed at the field site is negative because the ribbon is above the water table. A negative pore pressure will increase the shear stress required to cause slip, which will improve performance. However, it is possible that pressures in the vadose zone could reach zero if the water table were to rise significantly, or if there was extensive infiltration. Accordingly, pressure was set to $p = 0$ in 12-29 to provide a conservative estimate of the strain gradient that could cause slip.

The results (Figure 12-55) indicate that the strain gradient that would cause slip increases from zero at the ground surface to 0.01 1/m at approximately 2 m depth and 0.05 1/m at 10 m depth. The strain gradients expected to occur during pumping tests will be evaluated in the following pages, but they are expected to be much less than 0.01 1/m. As a result, this analysis indicates that friction should keep the strain ribbon coupled to the formation.

12.8.1.4.1 Field Deployment of Strain Ribbon

The strain ribbon was deployed at the field site in a four-inch-diameter borehole. The borehole was drilled using a Geoprobe drill rig and a solid stem auger. The borehole was drilled to 7.6 m below the surface, which is above the water table at 9 m depth. The augers were removed, and the depth of the open hole was verified by lowering a weighted tape into the hole.

The strain ribbon and polyethylene sleeve were attached to a weight and arranged on opposite sides of the borehole. The sleeve was folded along its axis to create a bundle approximately 5 cm in diameter. The weight was then lowered into the borehole and this pulled the strain ribbon and the folded sleeve down with it. The ribbon was directed over a roller at the top of the hole to limit the potential for sharply bending the ribbon as it curved downward into the hole (Figure 12-57a). The sleeve was directed into the borehole manually (Figure 12-57b).

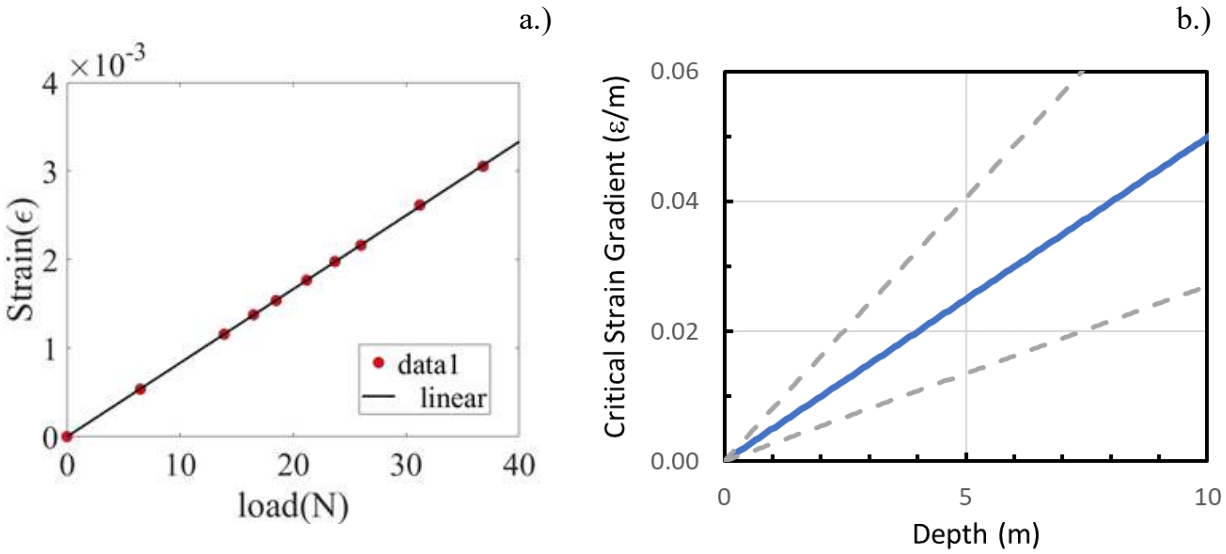

Figure 12-55 a.) strain as a function of applied axial load for two-layer, 2.5 cm wide polyester ribbon. b.) Critical strain gradient as a function of depth using the range of parameters given in text (dashed line) and using the average values of parameter (solid line).

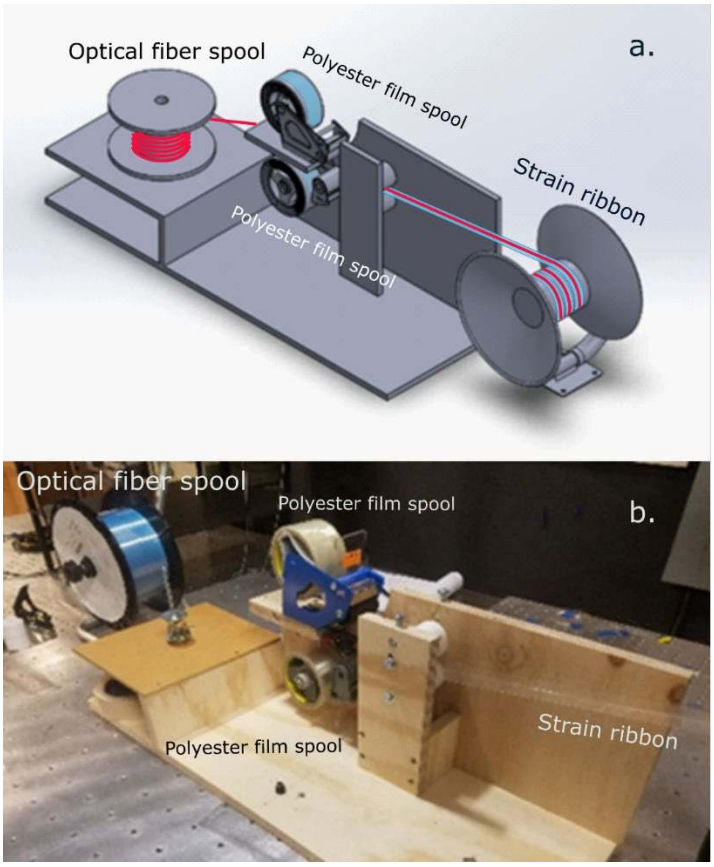

Figure 12-56: Device for creating a strain ribbon by laminating an optical fiber between two pieces of polyester film. a.) design; b.) prototype.

a.) b.)

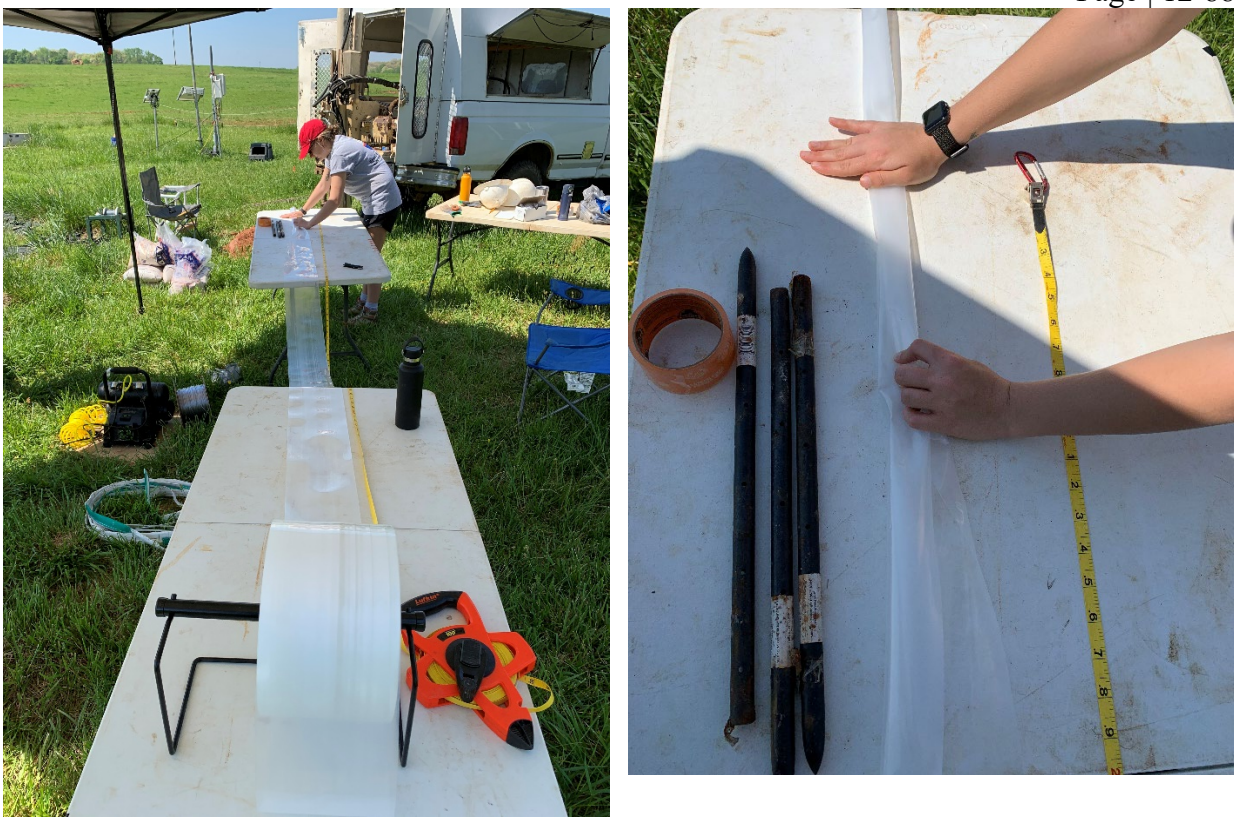

Figure 12-57: Polyethylene sleeve being prepared for installation in the borehole. a: Tubing meaning measured. b: Tubing being folded.

The polyethylene sleeve was inflated with approximately 5kPa air pressure after it was lowered to the bottom of the borehole (Figure 12-58). The open sleeve was filled with dry, well-sorted, medium- to fine-grained sand. To avoid bridging, sand was poured slowly, and the depth to the top of sand was measured with each 50-pound bag of sand added. The sleeve was then pressurized to between 5 and 10 kPa for approximately 1 minute to compact the sand before another bag of sand was added.

The data cable from the strain ribbon was attached to the interrogator and data acquisition system during deployment. Data that indicated the strain ribbon had broken could be obtained in real time as the break occurred. This allowed us to identify and revise procedures and designs that resulted in fiber breakage.

a.)



b.)



Figure 12-58: Installation of the polyethylene tubing in the borehole. a.) Strain ribbon (transparent) passing over a roller at the top of the borehole. Folded polyethylene sleeve is the white band at the top of the image; b.) Close up of the borehole with the transparent strain ribbon and the folded polyethylene sleeve.

c.)



Figure 12-58c: Polyethylene sleeve is pressurized using a shop-vac pushing the strain ribbon onto the borehole wall.

12.8.2 Data Collection and Storage

For each pumping test experiment, there were three different measurements that were recorded: water pressure, strain, and flow rate. The water pressure in monitoring wells and the pumping well was measured using Onset HOBO U20 Series transducers. Each monitoring well was equipped with a U20L-04 data-logging pressure transducer capable of measuring pressure head over a span of 4 meters with a typical error of ±0.4 cm and a resolution of 0.14 cm. The pumping well used a U20L-02 logging transducer capable of measuring pressure head of up to 30.6 m with a typical error of 3.0 cm and a resolution 0.41 cm. The larger error in the transducer used in the pumping well was deemed acceptable because of the relatively large head change in the well during the pumping tests. Hydraulic head was monitored continuously at the site at a sampling rate of one reading per minute in the monitoring wells and two samples per minute in the pumping well. The water level data were manually collected one day after each test, or every 15 days when no tests were being conducted. When redeployed into a well, a minimum of one day was allotted for the transducer to generate a baseline signal before another test was performed.

Data from the paddle wheel flowmeter was measured and stored in the field on a Campbell CR1000 data logger. The data logger was programmed to count the number of pulses every 10 seconds resulting in an accuracy of ±0.1 pulse per second. The data was collected immediately following the termination of the pumping test and the pulse count was converted to a flow rate.

12.8.3 Site Description

The field site used for this research is at the Clemson University Simpson Station in Pendleton, SC (34.670018, 282.729311). The site is a 0.25 ha subsection of a 12-ha pasture used for grazing cattle. The primary vegetation is fescue grass (*Festuca arundinacea*).

12.8.4 Geology and Hydrogeology

The site is underlaid by the Caesar's Head granite, which is a biotite-granitoid gneiss, at a depth of approximately 30 m (Murdoch et al. 2006). Saprolite derived from the gneiss occurs from approximately 2.5m to 30m depth. The hydraulic conductivity of the saprolite is $2.4x10^{-5}$ m/s at 3m depth (Murdoch et al. 2006). Constant-rate pumping tests indicate the hydraulic conductivity is an order of magnitude less, approximately $1.3x10^{-6}$ m/s, in the saturated zone below 10m depth. The upper 1.5 to 2.5m is a poorly structured clay to sandy clay loam soil, which has been mapped as the Cataula sandy loam (Soil Survey Staff). The soil is tight, with a hydraulic conductivity of less than 10^{-9} m/s, according to measurements made using a Guelph permeameter (Murdoch et al. 2006).

The depth of the water table is approximately 9 m. The hydraulic head gradient indicates groundwater flow is to the northeast toward Little Garvin Creek, which is 500 m east of the site. Big Garvin Creek is 800 m west of the field site.

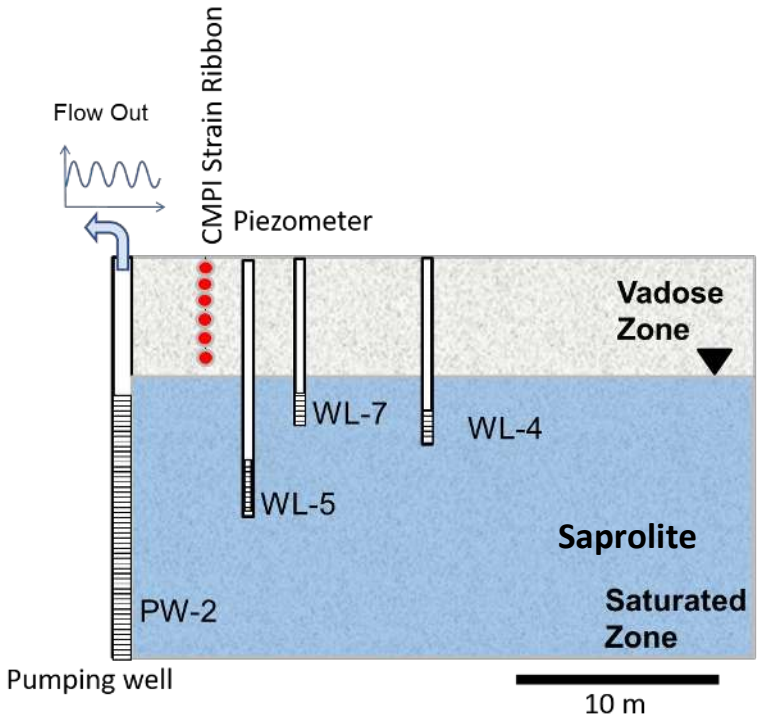

Figure 12-59: A conceptual model of the subject field site including the pumping well (PW-2), the CMPI strain ribbon, and the piezometers.

12.8.5 Wells and Sensors

The field site includes several dozen borings and sensors that have been used for a variety of projects, but only a subset of wells, piezometers, and strain sensors were used for this investigation (Figure 12-60). Groundwater well PW-2 was used for pumping, and piezometers WL-4, WL-5, and WL-7 were used to monitor hydraulic head. Well PW-2 was drilled to approximately 30m depth, which is the depth to top of competent rock. The borehole was drilled using an 8-inch diameter air rotary bit. The filter pack extends from the bottom of the borehole to 10m below ground surface, with the intent to capture then entire saturated zone. Bentonite was used to seal the annulus above the screen zone, and the remaining annulus was filled with a neat cement grout. The casing and screen are made from 4-inch diameter flush-joint PVC pipe. The slots in the well screen are 0.010 inch wide. Each piezometer (WL-4, WL-5, and WL-7) was installed using a 4-inch outer diameter solid -stem auger. WL-4 was installed to a depth of 15.3 m and is completed with 2-inch PVC casing and screen. It is screened from 13.8 m to 15.3 m with a total screen length of 1.5 m. WL-4 is located 20.9 m from PW-2. Well WL-5 is 21.1-m deep and is completed with 2-inch PVC pipe. It is screened from 18.1 m to 21.1 m with a total screen length of 3.0 m. WL-5 is 6.7 m from PW-2. Well WL-7 is screened from 11.39 m to 13.45 m with a screen length of 1.5 m, and it is completed with 1 ½-inch PVC casing and screen. WL-7 is 9.1 m from PW-2.

The piezometers were equipped with Onset HOBO U20L-04 pressure transducers, which have a span of 0 – 4 m and a resolution of 0.14 cm. They were programmed to measure pressure every one minute during each pumping test.

Strain was measured at SR-2, which is 4.4m from PW-2. The strain ribbon at SR-2 was built with reflectors spaced 15 cm apart with the midpoint of the reflectors at depths of 1.0 m, 1.85 m, 2.7 m, 4.4 m, 5.25 m, and 6.95 m.

Flow rate data were logged with a Campbell CR-1000 located on the western edge of the field site. The interrogator and data acquisition system for the CMPI system were housed in the building to the east of the field site (Figure 12-60).

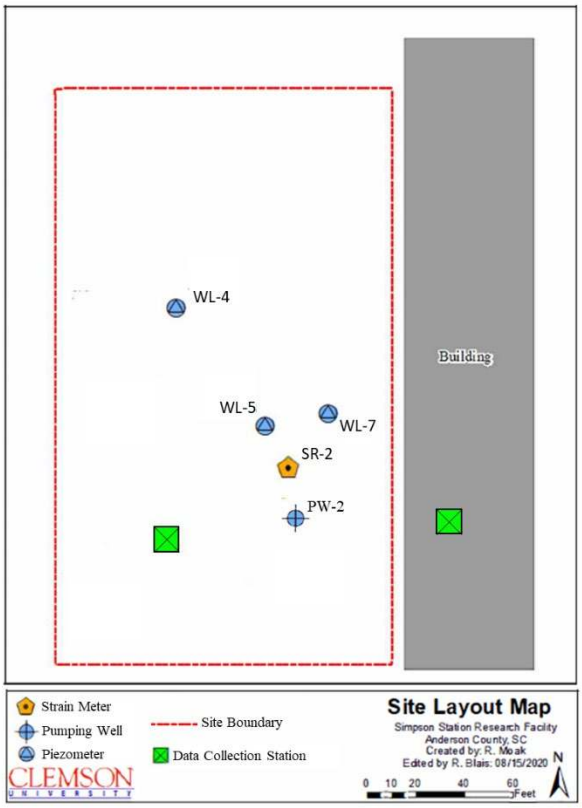

Figure 12-60: A map of the field site at Clemson University Simpson Station showing the locations of the pumping well, piezometers, strain ribbons, and other features of the site.

12.8.6 Field Experiments

Field experiments at the field site were performed to observe the frequency and amplitude response of the strain to the flow rate. The strain data were measured as well as water levels in the pumping and monitoring wells.

12.8.6.1 Calibration

The pumping system was calibrated to establish a relationship between voltage output from the VFD and flow rate. This was achieved by changing the voltage from 2.0V to 5.0V in increments of 0.5 V. Each voltage was held for five minutes, and the rate measured by the flowmeter was averaged over that time. The data were nearly linear, and they were characterized with a best fit line. The flow rate was also manually verified using a graduated five-gallon bucket during each test.

12.8.6.2 Constant Rate Pumping Test

The maximum and minimum limits of the voltage inputs of the VFD were determined from the calibration experiment. It was found that any voltage input below 1.8V would result in zero flow. This set the maximum and minimum value that could be used. A constant rate test was performed at the midpoint between 1.8V and 5V, which was 3.44V. The achieved flow rate was 3.28 gpm. This rate was held for 6 hours as the water level and strain were recorded.

12.8.7 Sinusoidal Variation

Sinusoid-rate tests were conducted using different amplitudes and periods.

12.8.7.1 Amplitude Dependent Tests

The first round of tests evaluated different amplitudes of pumping rate. Amplitude change was determined as a percentage from test 1 (Table 12-15). The purpose of this series of tests was to evaluate the strain as a function of amplitude and to evaluate the lower limit of strain amplitude that could be evaluated. By incrementally decreasing the amplitude of the pumping rate, the resulting strain and hydraulic head amplitudes would also decrease. This also decreased the signal to noise ratio of the strain and water level.

Table 12-15. Variable amplitude testing conditions

Test	Flow Rate (gpm)			Voltage Input (V)		Period (min)	Pumping Duration (hrs.)
	High	Low	Average	High	Low		
1	5.46	0.35	3.15	5.00	1.8	30	6
2	4.64	1.67	3.21	4.46	2.33	30	6
3	3.96	2.52	3.25	3.93	2.87	30	6
4	3.78	2.88	3.33	3.781	3.119	30	6
5	3.54	3.1	3.33	3.616	3.285	30	6
6	3.41	3.17	3.3	3.53	3.37	30	6

The first pumping test used the maximum and minimum voltage inputs that the function generator could produce. This resulted in an average flow rate of 3.15 gpm with a maximum flow rate of 5.46 gpm and a minimum flow rate of 0.35 gpm. A sinusoid was fit to all the data (outlined in data analysis section) and amplitude of the best fit sinusoid was taken as the average amplitude. average flow rate amplitude. For Test 1, the average flow rate amplitude was 2.45 gpm. Test 2 was designed to have a flow rate amplitude of 50% of Test 1. The best fit amplitude was 1.46 gpm, which was 57% of the amplitude of Test 1. The best fit amplitude of Test 3 was 0.7 gpm, which was 28% of Test one. The best fit amplitude of Test 4 was 0.43 gpm, which is 17% of Test 1. The best fit amplitude of Test 5 was 0.21 gpm, which is 9% of test one. The least flowrate amplitude was 0.1 gpm during Test 6, which was 4% of Test 1.

12.8.7.2 Period Dependent Tests

The second round of tests varied periods over 15, 30, and 60 minutes while using a consistent amplitude determined by the input voltage range of 1.8-5 V (Table 12-16). The goal of these experiments was to evaluate a period dependence on aquifer parameters.

Table 12-16. Variable period test conditions

Test	Period (min)	Flow Rate (gpm)			Pumping Duration (hrs.)
		High	Low	Average	
1	15	5.31	0.3	3.12	6
2	30	5.46	0.35	3.15	6
3	60	5.32	0.56	3.17	12

The pumping duration was chosen so there would be at least 6 periods available for the analysis. The pumping periods needed to be long enough so that multiple periods of pumping would not be performed prior to the first period reaching the strain sensor, making the evaluation of phase lag difficult, and (2) wouldn't be so long that the frequency generated from the VFD and function generator would became unstable and produce an improper sinusoid. Condition 1 was a limitation because of the data processing technique used and the dependence of looking at the data in the frequency spectrum. This will be covered in depth in the data processing section.

12.8.8 Data Processing and Analysis

Each pumping test generated 6 unique files, which were identified using a file naming system that followed the form "MM.DD.YYYY_DataType". Each sensor or instrument had an independent clock, which was synchronized to local time between each test. All time data was converted to Unix time, or seconds since 00:00:00 January 1st, 1970 at UTC. Unix time was used because it converted all date and time data into a single scalar value which simplified processing.

MATLAB was used to process and plot the data. Plots of the original data were inspected for anomalies, such as missing data or abnormal values due to testing procedures or data collection errors. If there was a major problem with the data, the results that were measured were archived, and the test was repeated.

Pressure and strain data varied approximately as sinusoids, and these data were analyzed to determine the frequency, magnitude, amplitude, and phase lag. For each series of sinusoidal data, a fast Fourier transform (FFT) was performed and plotted as a magnitude spectrum plot. The inputs required for the FFT were the detrended data vector and the sample rate frequency in Hz. For all the water level data, the HOBO data loggers recorded at a rate of 1 sample per minute with a resulting frequency of 1/60 Hz. The CMPI recorded data at three different frequencies among the tests, 0.1 Hz, 0.2 Hz, and 0.5 Hz. The FFT was applied to the collected data to verify that the applied periodic pumping rate was observable in the measurements taken. The output of the FFT would show any other harmonics affecting data besides the generated frequency as barometric fluctuations or earth tides. The results of the FFT were plotted as a periodogram.

The next step in processing the data is to obtain the amplitude and phase of all the sinusoidal data. This was done by generating a best fit sinusoid to the data. The first hour from each pumping test was omitted to reduce the transient effect from the start of pumping. The remaining time during the pumping test was assumed to be steady periodic flow. The data vector was then detrended to remove remaining signal drift. A Vandermonde matrix was constructed for the sine and cosine components of the best fit. Then, using the least squares approximation, a sine wave is generated that most closely fits the data.

The best fit sinusoids are calculated for the flow rate from the well, hydraulic head, and distributed strain all independently. Each sinusoid is verified manually to ensure the best fit is reasonable. The difference between the phase of the flow rate and the observed signals is calculated and used to estimate u in (12-23) and then D and T from eqs (12-24) and (12-25).

An alternate method to estimate hydraulic diffusivity from the phase delay during a sinusoidal pumping test in a uniform confined aquifer relating to the period, after some approximation (Streltsova, 1988)

$$D = \frac{\lambda r^2}{4\pi t_L^2} \tag{12-30}$$

12.9 PART 2 RESULTS

Nine pumping tests were performed during the field experiment. One test used a constant pumping rate, whereas the other eight used a pumping rate that varied as a sinusoidal function of time with different amplitudes and periods.

12.9.1 Constant Rate Pumping Test

A baseline pumping test was conducted on March 22, 2020. The pumping test lasted for 6 hours at a rate of 3.3 gallons per minute (Figure 12-61). Drawdown was recorded in the three piezometers, and strain was measured along the strain ribbon. Barometric pressure data was unavailable, so the total pressure was used to calculate drawdown.

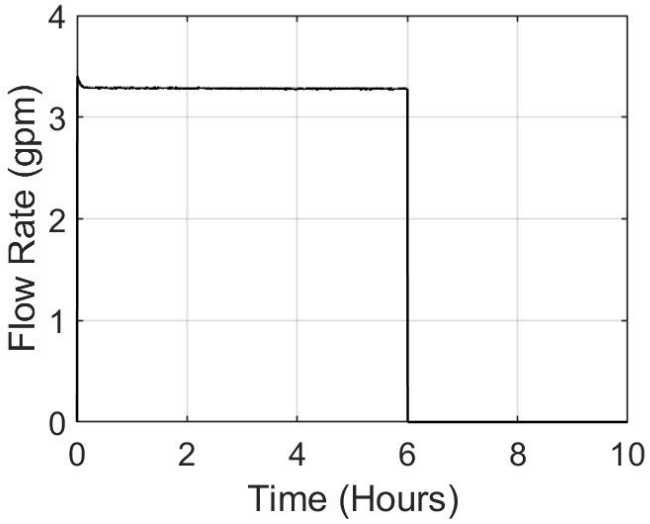

Figure 12-61: Flow rate measured during the constant-rate pumping test.

12.9.1.1 Pressure Data

The drawdown increases soon after the pump is turned on, and the rate of increase gradually diminishes until the pump is turned off at hour 6 (Figure 12-62). The greatest drawdown is 0.55m at WL-5. The maximum drawdown is 0.1m at WL-7 and 0.05m at WL-4.

The drawdown at WL-5 increases sharply at a rate of approximately 1 m/min during the first 0.5 hour of pumping. The drawdown rate slows significantly between 0.5 to 1.5 hours of pumping, and the drawdown rate is approximately 0.05 m/min (decreasing slowly with time) during the last 3 hours of the test.

The drawdown at WL-7 is slow to change at the start of pumping, in contrast to the rapid initial drawdown at WL-5. The drawdown increases sharply after 15 minutes of pumping, however, and then the rate decreases gradually until the end of pumping, reaching a maximum of 0.1 m. The drawdown at WL-4 follows a similar pattern, except the early period of slow drawdown is even longer and the maximum drawdown (0.05 m) is even less than at the other two piezometers.

The blue bands mark the time when the maximum drawdowns occur in each piezometer. The maximum drawdowns in WL-7 and WL-4 appear to lag slightly behind the drawdown in WL-5. The lag is approximately 4 to 16 minutes (in WL-7 and WL-4 respectively).

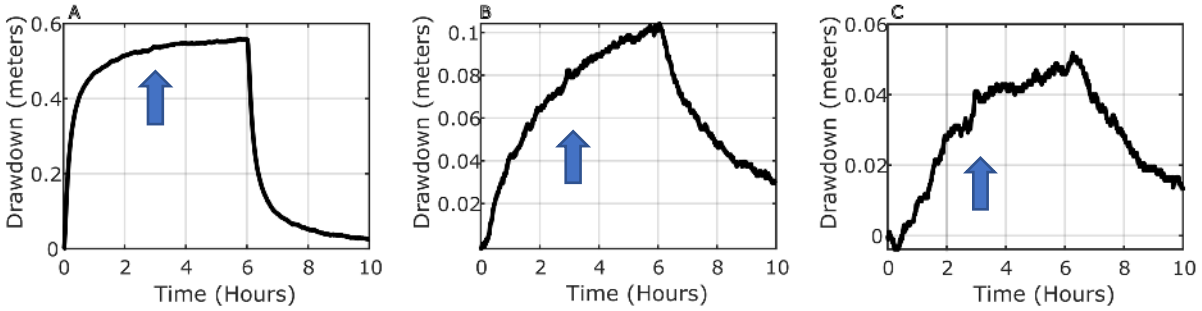

Figure 12-62: Drawdown measured at WL-5 (A), WL-7 (B), and WL-4 (C) during the constant rate pumping test. Blue arrows are examples of a similar fluctuation in all the datasets

The drawdown curves are marked by small fluctuations of up to a few cm in amplitude over periods of tens of seconds to tens of minutes or longer (Figure 12-62). The peaks are subtle in the data from WL-5, but they are more apparent in the data from WL-7. The peaks are even more apparent in data from WL-4 where they have amplitudes of one to a few mm of head, which is a larger fraction of the total drawdown than in data from the other piezometers.

The fluctuations in drawdown could be a result of small changes in the pumping rate, fluctuations in the barometric pressure, or other factors. The pumping rate was measured with a flow meter and it is remarkably steady (Figure 12-61). The drawdown data was measured with a sealed transducer. An example fluctuation in all three drawdown occurs at hour 3 and is marked in Figure 12-62, but other smaller fluctuations are also apparent (Figure 12-62). The consistency of the fluctuations across all three piezometers is likely related to changes in barometric pressure during the test.

The Neuman (1974) solution for an unconfined aquifer was selected to estimate the hydraulic properties from the observed drawdown. The Neuman solution assumes the aquifer is unconfined,

homogeneous and anisotropic, the pumping well is fully penetrating, and storage in the well is neglected. The aquifer at the study site is an unconfined saprolite aquifer. The screened section of the pumping well is 18.3m long which spans most of the approximately 20m saturated zone of the aquifer. The drawdown measured in the three (3) piezometers, WL-5, WL-7, and WL-4 were fit to a Neuman type curve using the software AQTESOLV v4.5. The solution that best fits all data from the three piezometers was used to estimate aquifer properties (Table 12-17).

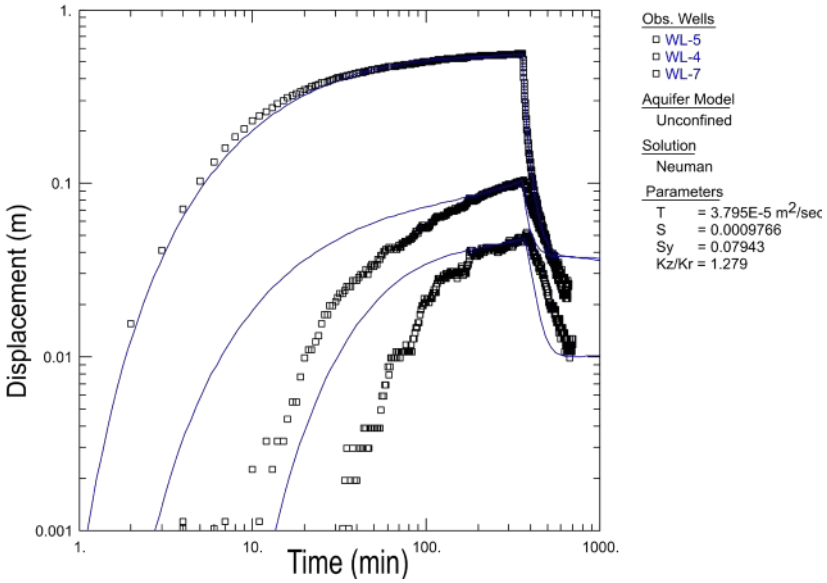

Figure 12-63. Neuman type curve overlaying drawdown (displacement) data in the three monitoring wells. WL-7 has the greatest drawdown, and WL-4 has the least drawdown.

Table 12-17. Aquifer parameters estimated from the constant rate pumping test using the Neuman solution.	
Transmissivity (T) [m^2/s]	$3.8x10^{-5}$ ($\pm 7.7x10^{-7}$)
Storativity (S)	$9.7x10^{-4}$ ($\pm 1.3x10^{-5}$)
Specific Yield (S_y)	0.08 ($\pm 1.9x10^{-3}$)

The hydraulic diffusivity of a confined aquifer is estimated using

$$D_h = \frac{T}{S} \qquad 12\text{-}31$$

Substituting the values of T and S from the Neuman Solution into the equation gives D_h = 0.039 m^2/sec. A well-defined confining unit is absent from the vicinity of the well, so storage change will be affected by drainage or filling of pores at the water table. In general, storage change caused

by pore drainage or filling will occur in addition to storage change from water and aquifer compressibility, so (12-31) could be viewed as

$$D_h = \frac{T}{S+S_p} \qquad 12\text{-}32$$

where S_p is the contribution to storage from pore drainage. The magnitude of S_p will increase with the duration of a well test because more time will be available for pores to drain. Likewise, S_p may increase with the period of a sinusoidal well test. Values of S_p will approach the specific yield, S_y, during long well tests, so S_y will serve as an upper bound on S_p. Using the value of S_y estimated from the Neuman solution gives a lower estimate of the hydraulic diffusivity of D_h = 4.8x10^{-5} m^2/sec.

12.9.1.2 Strain Data

Vertical strain was measured in the vadose zone at six locations below ground surface: 1m, 1.85m, 2.7m, 4.4m, 5.25m, and 6.95m (Figure 12-64 and Figure 12-65).

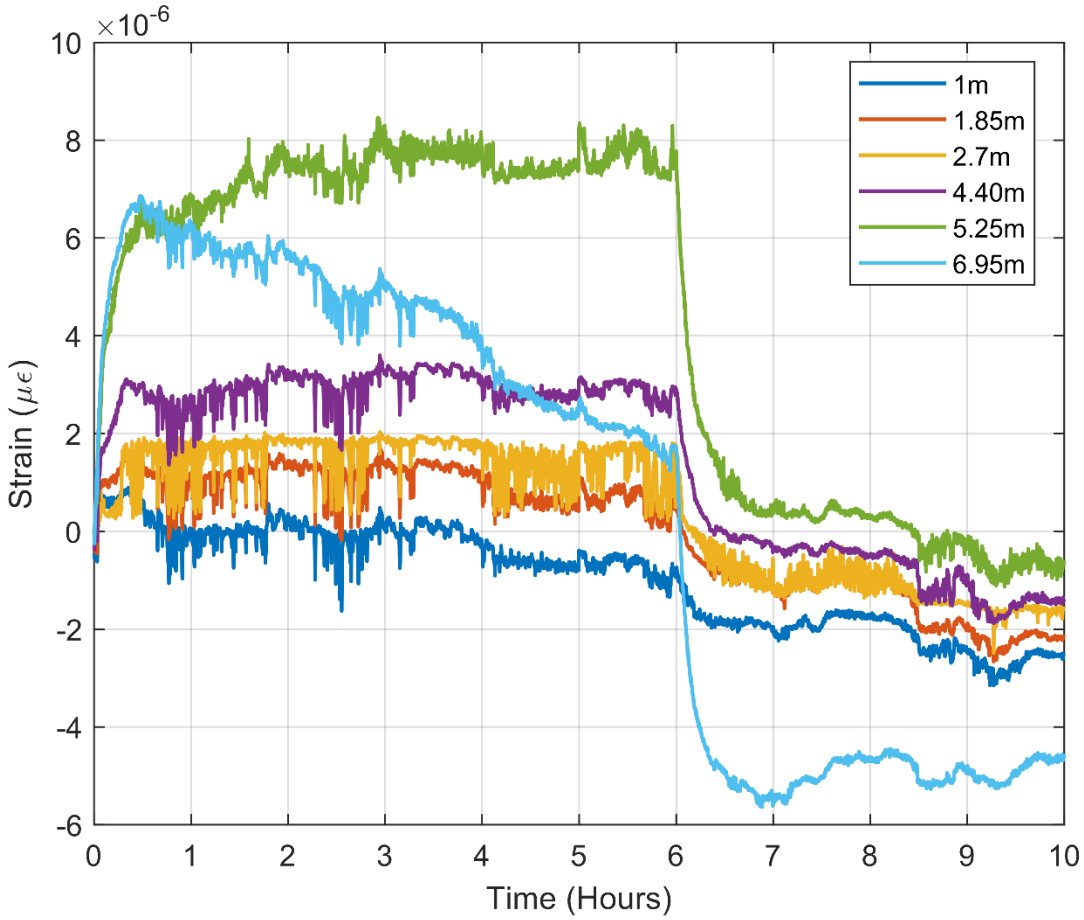

Figure 12-64. Vertical strain between reflector pairs measured as a function of depth and time in the vadose zone during a constant-rate pumping test. Positive strain is tensile. Depths indicated on the legend are the midpoint between reflector pairs separated by 15 cm. Pumping was conducted from 0-6 hours. No correction for barometric pressure.

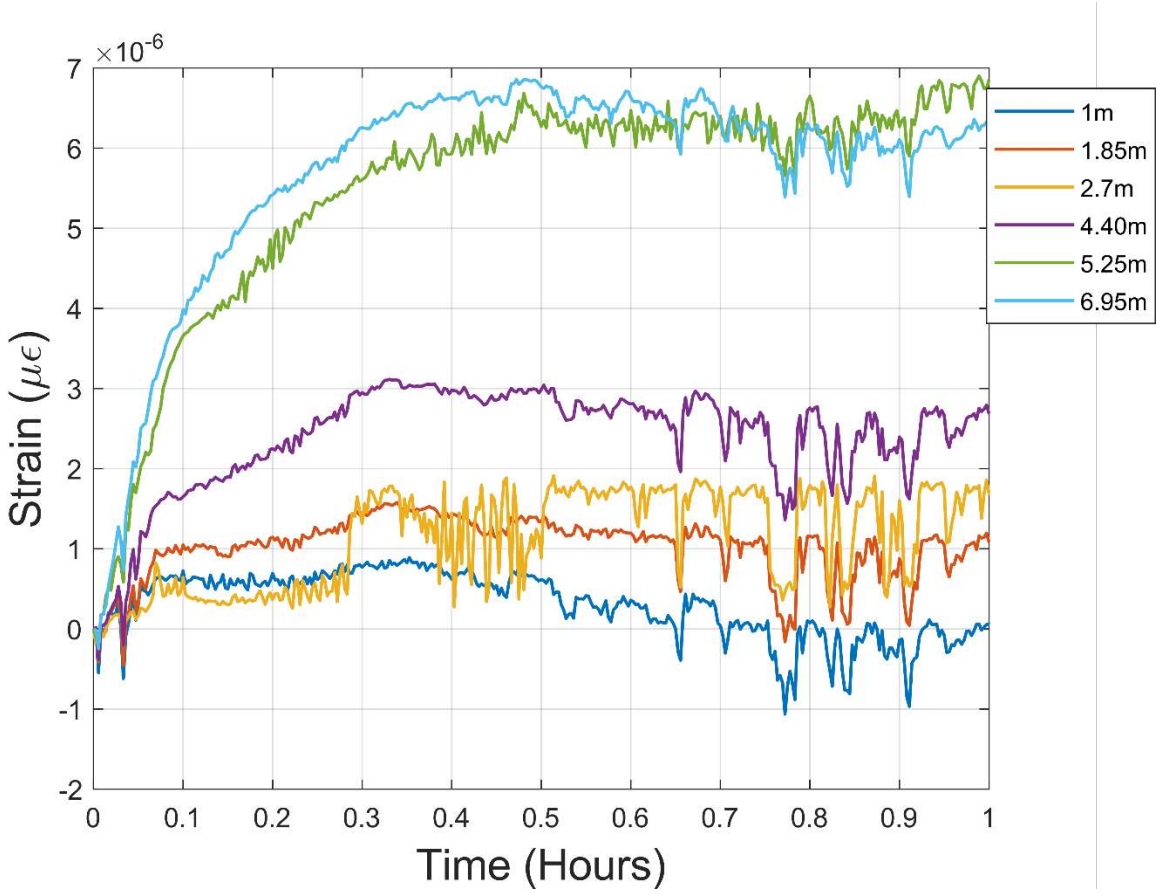

Figure 12-65: Strain measured during the first hour of the constant rate pumping test shown in Figure 12-64.

The general pattern of vertical strain follows the pattern of drawdown. The strain increases (becomes tensile) when the pump starts and the strain rate is greatest during the first 6 minutes (0.1 hr in Figure 12-65). This is when the rate of drawdown near the well is the greatest. The strain rate is greatest at the deepest reflector pair (0.01 με/s at 6.95 m) and it slows progressively upward to 0.002 με/s at the upper two reflector pairs at 1.85 and 1 m depth (Figure 12-65). The rate of increase of the strain slows after 6 minutes (0.1 hr) and the strain reaches maximum values at $0.5 < t < 2$ hr. The greatest strain is 8 με at a depth of 5.25 m and the maximum strain decreases upward to approximately 1 με at the shallowest sensor at 1 m depth (Figure 12-64 Figure 12-63).

The magnitude of the strain response during the first half hour of pumping is greatest at the greatest depth (6.95 m), but then the magnitude at 6.95 m starts to decrease while the magnitude at the overlying sensor pair (5.25 m) continues to increase. The maximum strain reached by the

6.95 m sensor pair is approximately 7 με at 0.5 hr, whereas the maximum at 5.25m is 8 με a few hours later. Interestingly, the strain at 6.95m steadily drops from 7 με at t = 0.5 hr to 2 με at the end of pumping at t = 6 hrs.

When pumping is stopped at t = 6 hr (Figure 12-64) the strain abruptly decreases, but the rate of decrease slows with time just as it did during pumping. The strain continues to become more compressive through hour 10 as the pressure in the underlying aquifer recovers from pumping (Figure 12-62).

The exception is at the 6.95m sensor where the strain increases slightly during recovery, so the response of the deepest sensor, at 6.95 m, is anomalous during both pumping and recovery. Pressure changes during pumping and recovery in the underlying aquifer will propagate upward into the vadose zone, but the distance that the pressure changes will be limited by the low relative permeability of the partially saturated saprolite. It seems likely that pressure changes associated with pumping and recovery reach the sensor at 6.95 m depth, but not the overlying sensor, and this accounts for the anomalous behavior.

High frequency fluctuations are common in all the strain records, with fluctuations of +/- 0.5 με occurring over time periods of minutes or longer. On many occasions, the fluctuations at all the sensors are similar (e.g. between 0.7 and 0.9 hrs in Figure 12-65). Increasing barometric pressure will compress the vadose zone, while decreasing pressure will cause the vadose zone to expand. It seems likely that high frequency fluctuations occurring in multiple sensors are a result of barometric pressure fluctuations. Barometric pressure is known to fluctuate on time scales of seconds to minutes in response to wind gusts, but it also fluctuates over time scales of many hours in response to diurnal variations. Gradual increases in barometric pressure during pumping could account for the slight decreases in strain.

Strain is roughly linearly correlated to barometric pressure and it is possible to remove many of the effects of barometric pressure using a linear correction factor (Murdoch et al. 2015). This correction is done routinely, but barometric pressure measurements are unavailable during the time of the test so no correction was done.

12.9.2 Sinusoidal Pumping Tests

Eight pumping tests utilizing a sinusoidal flow rate were performed between March and June 2020. All tests performed involved pumping the well for at least 6 hours while monitoring pressure and strain. The pumping tests were categorized into two series: variable amplitude pumping tests (Tests 1-6) and variable period pumping tests (Tests 1, 7, and 8).

12.9.2.1 Variable Amplitude Tests

Each test used a period of 30 minutes (0.5 hours) and the amplitudes ranged from 0.12 gpm to 2.5 gpm (Table 12-18 and Figure 12-66). The flow rates in the periodic tests were varied around a mean flow rate of 3.3 gpm, which was the flow rate used in the constant rate pumping test.

Table 12-18. Amplitude and period of the flow rate during tests 1 through 6.

Test	Amplitude (± gpm)	Period (minutes)
1	2.5	30
2	1.5	30

3	0.7	30
4	0.5	30
5	0.25	30
6	0.12	30

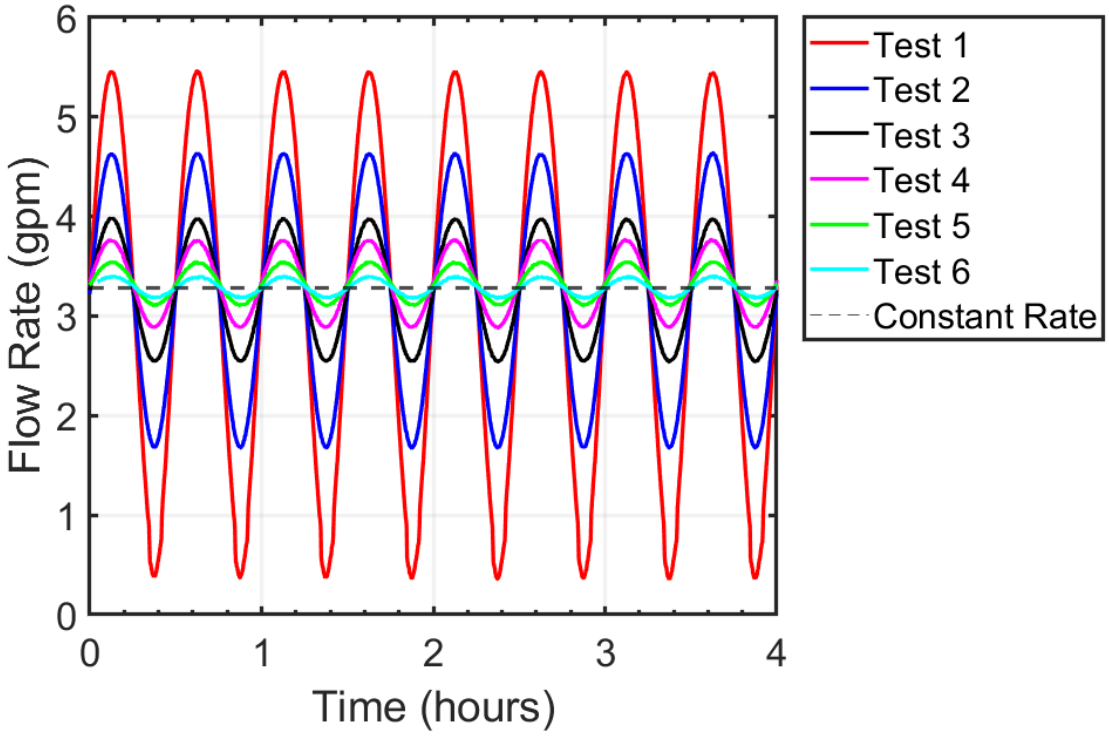

Figure 12-66: Flow rate with time measured with a flowmeter during the six variable amplitude pumping tests. The flow rate during the constant-rate test (dashed) was the mean of the sinusoidal rates.

12.9.2.1.1 Pressure Response

The pressure response for each test, Test 1 through Test 6, was measured in the three piezometers: WL-4, WL-5, and WL-7 (Figure 12-67). The first hour of the test was discarded to avoid the large transients that occur early in the tests.

A signal with the same period as the pumping rate was observed at each of the monitoring wells. The amplitude of the periodic pressure response largest in WL-5 for each of the three tests,

and in general the amplitude of the pressure response decreased with the amplitude of pumping and distance from the pumping well.

The variation of drawdown during Test 1 (Q = ±2.5 gpm) was +/- 0.1 m at WL-5, but it was ±0.003 m at WL-4 and ± 0.002 m at WL-4, which are further from the pumping well than WL-5. The variation in drawdown dropped in proportion to the pumping amplitude. For example, the pumping rate amplitude was Q = ±0.12 gpm during Test 6, which is 1/20 of the amplitude during Test 1. The variation of drawdown at WL-5 dropped from +/-0.1m during Test 1 to +/- 0.005 m during Test 6, a reduction by a factor of 1/20. The drawdown at WL-4 varies erratically in the range of +/- 0.001m and there is a sharp increase and fall in drawdown, but these variations appear to be unrelated to the 0.5 hr period of pumping.

The drawdown data were analyzed using a Fast Fourier Transform (FFT) to determine the magnitudes of the different spectral components. This process identifies the dominant periods that make up the drawdown signal (Figure 12-68).

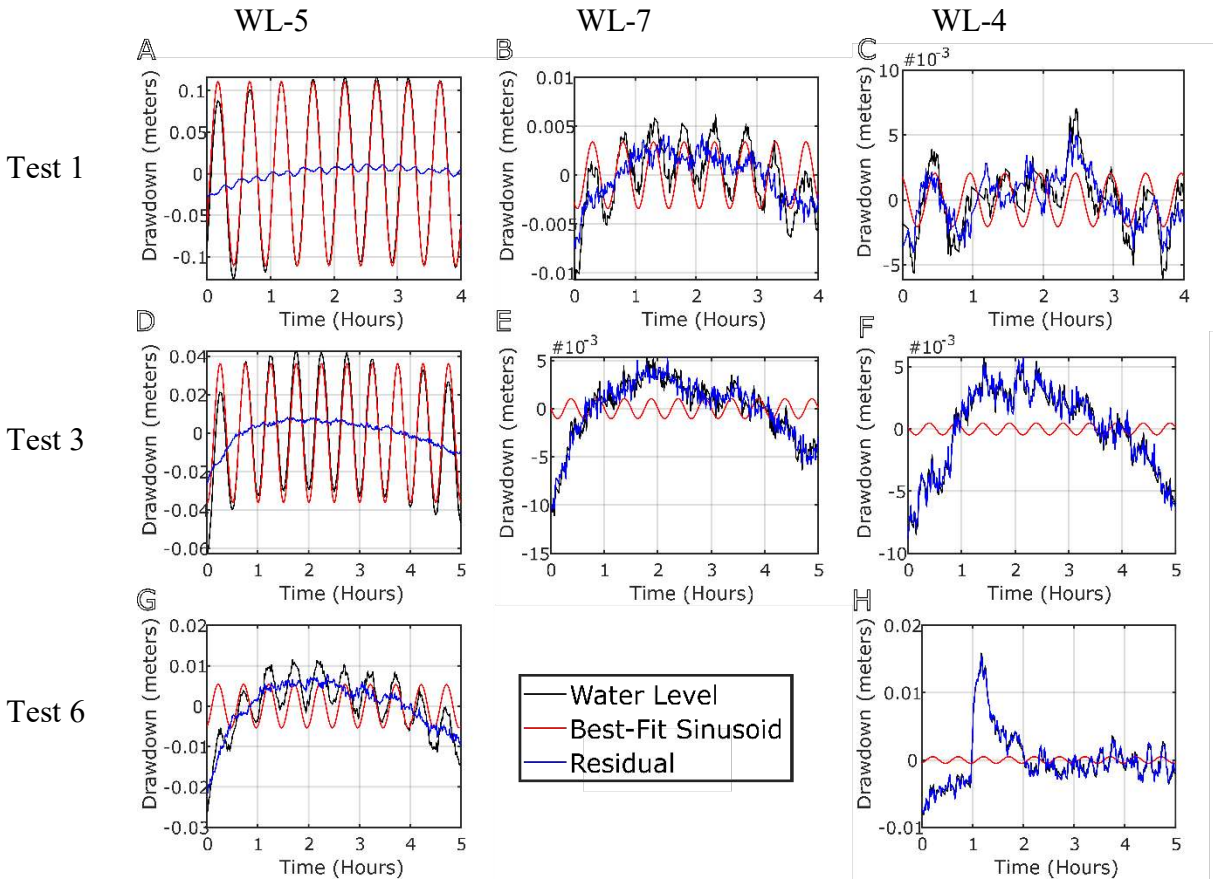

Figure 12-67: Drawdown in the three piezometers during Test 1 (Q =±2.5 gpm), Test 3 (Q = ± 0.7 gpm), and Test 6 (Q = ±0.12 gpm) as functions of time. Data from the first hour of pumping (first two periods) was omitted. Field data (black), best-fit sinusoid (red), residual (blue). Data from WL-7 was not recorded during Test 6.

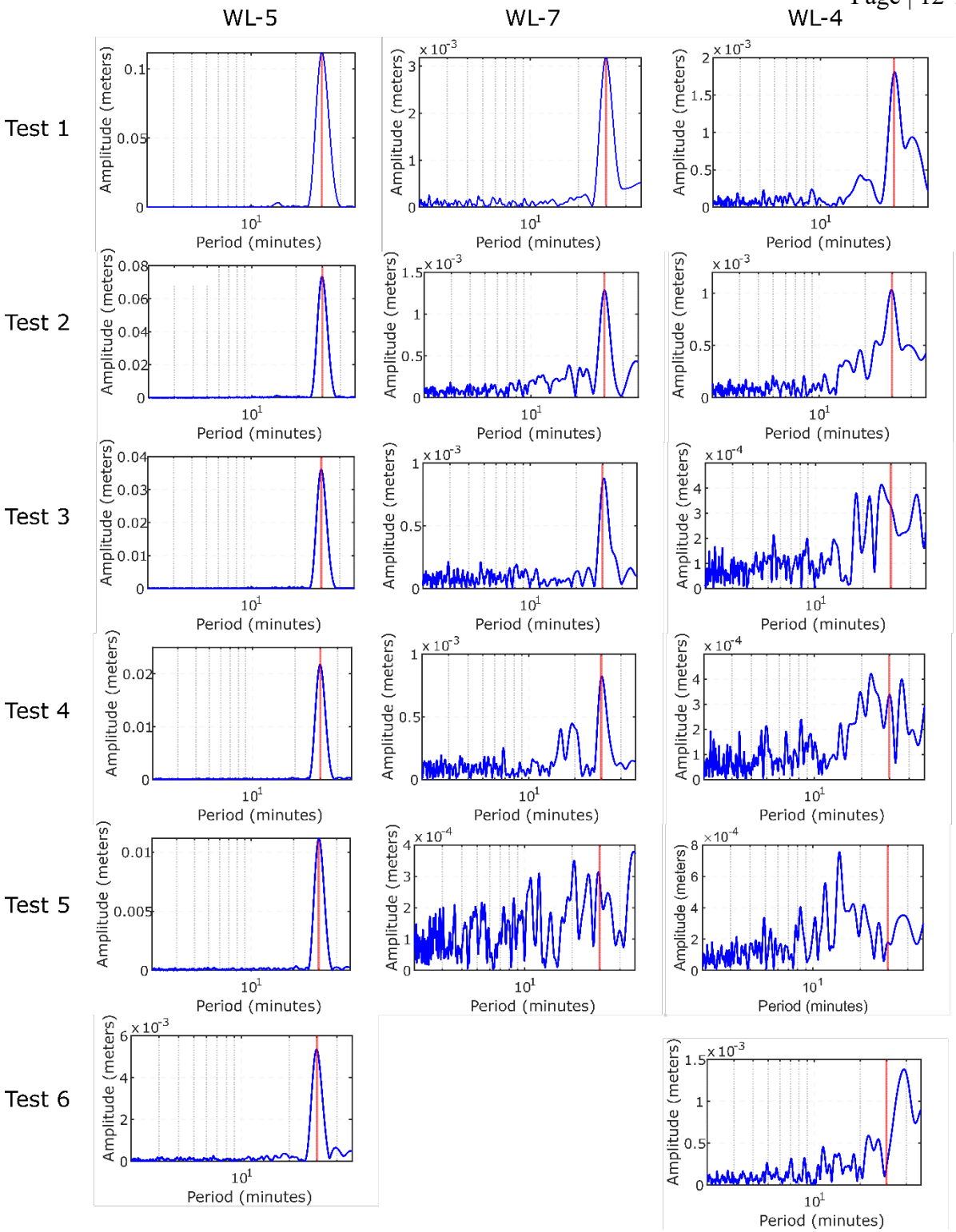

Figure 12-68: Magnitude spectra of the drawdown during the six variable rate pumping tests. The pumping period for each test was 30 minutes. The red vertical line is the period of the pumping.

A period of 30 minutes has the largest magnitude in the spectra of all three piezometers for Tests 1 and 2 (Figure 12-68). Amplitudes for the 30-minute period decrease with pumping rate, and the amplitudes for the 30-minute period at WL-4 for Tests 3 through 6 are less than the amplitudes at other periods. There is a secondary peak at 30 minutes during Test 4 at WL-4, but a discernable peak at 30 minutes is absent at WL-4 during the other tests. The amplitude of the 30-minute period is greater than background at WL-7 for all but Test 5. During Test 5, there is secondary peak at approximately 28 minutes, which is flanked by slightly larger peaks with periods of 20 and 45 minutes (Figure 12-68).

Table 12-19. Amplitudes and phases of the hydraulic head, P_h, in different piezometers during periodic tests of different pumping amplitudes.

Tests # +/- pumping amplitude	Piezometer, radial distance (m)	P_h, Amplitude (m)	P_h,Phase Lag (min)
Test 1 ±2.5 gpm	WL-5, 6.7	0.11	7.4
	WL-7, 9.1	0.003	15.1
	WL-4, 20.9	0.002	24.6
Test 2 ±1.5 gpm	WL-5, 6.7	0.073	7.6
	WL-7, 9.1	0.0013	16.1
	WL-4, 20.9	0.0008	N/A
Test 3 ±0.7 gpm	WL-5, 6.7	0.036	7.5
	WL-7, 9.1	0.001	14.9
	WL-4, 20.9	N/A	N/A
Test 4 ±0.5 gpm	WL-5, 6.7	0.021	N/A
	WL-7, 9.1	0.001	13.7
	WL-4, 20.9	N/A	N/A
Test 5 ±0.25 gpm	WL-5, 6.7	0.010	7.55
	WL-7, 9.1	N/A	15.5
	WL-4, 20.9	N/A	N/A
Test 6 ±0.12 gpm	WL-5, 6.7	0.005	8.0
	WL-7, 9.1	N/A	N/A
	WL-4, 20.9	N/A	N/A

The results of the Fourier transform indicate that noise of 0.4 to 0.8 mm amplitude occurred in the range of periods similar to the 30-minute pumping period and was apparently unrelated to pumping (Figure 12-68). In some cases, there are signals with periods similar to the pumping period, but their periods are different enough so they appear unrelated to pumping. For example, at WL-4 during Test 6 the dominant signal has a 38-minute period and 1.4 mm amplitude, and during Test 4 there are peaks at periods of 22 min and 36 min, along with a peak at 30 min (Figure 12-68). I reviewed the spectra and was unable to identify any periods other than 30 minutes that

appear consistently, so I conclude the other periods are noise that is unrelated to pumping. Variations in barometric pressure could cause the small variations in hydraulic head that appear as noise in the spectra.

During Test 1, the phase lag time ranges from 7.4 min at the closest piezometer, WL-5 (6.7 m), to 15.1 min at WL-7 (9.1 m), and 24.6 min at the furthest piezometer, WL-4 (20.9 m). The lag time is largely unaffected by the magnitude of pumping, however. At WL-7 the lag ranges from 13.7 to 15.5 min, but variation appears to be unrelated to the pumping rate (Table 12-19). Similar results occur in data from WL-5.

In contrast to the lag time, the amplitude of the drawdown decreases with both radial distance and the magnitude of the pumping rate (Table 12-19). The effect of distance is illustrated during Test 1 when the amplitude decreases from 0.11m at WL-5(6.7 m) to 0.002 m at WL-4 (20.9 m). The head amplitude decreases approximately in proportion to the pumping amplitude. The smallest amplitude that can be detected is limited by the resolution of the instrument (<0.001 m) (Table 12-19).

12.9.2.1.2 Strain Response

Vertical strain was measured at six locations along a vertical line at approximately 4.4m from the pumping well, as outlined in section 12.9.1.2. Vertical strain in the vadose zone varies as a sinusoidal function of time with a 30-minute period (Figure 12-69). The first hour of data was omitted to reduce the effects of transients and the amplitude and phase of the strain data were estimated using the same least-squares fitting approach applied to the pressure data. The magnitude of strain variations during Test 1 is approximately 2.5 με at 6.95m below ground surface and it decreases upward to approximately 0.2 με (200 nε) at a depth of 1.0 m. Trends and noise levels in the data vary between the sensors. The noise level is less than 10 nε in sensors at 6.95m and 4.40m, but it is 20 to 40 nε at sensor 2.7 m and 1 m (Figure 12-69).

The strain signal at each sensor includes small fluctuations of approximately +/- 10 nε. (Figure 12-71).

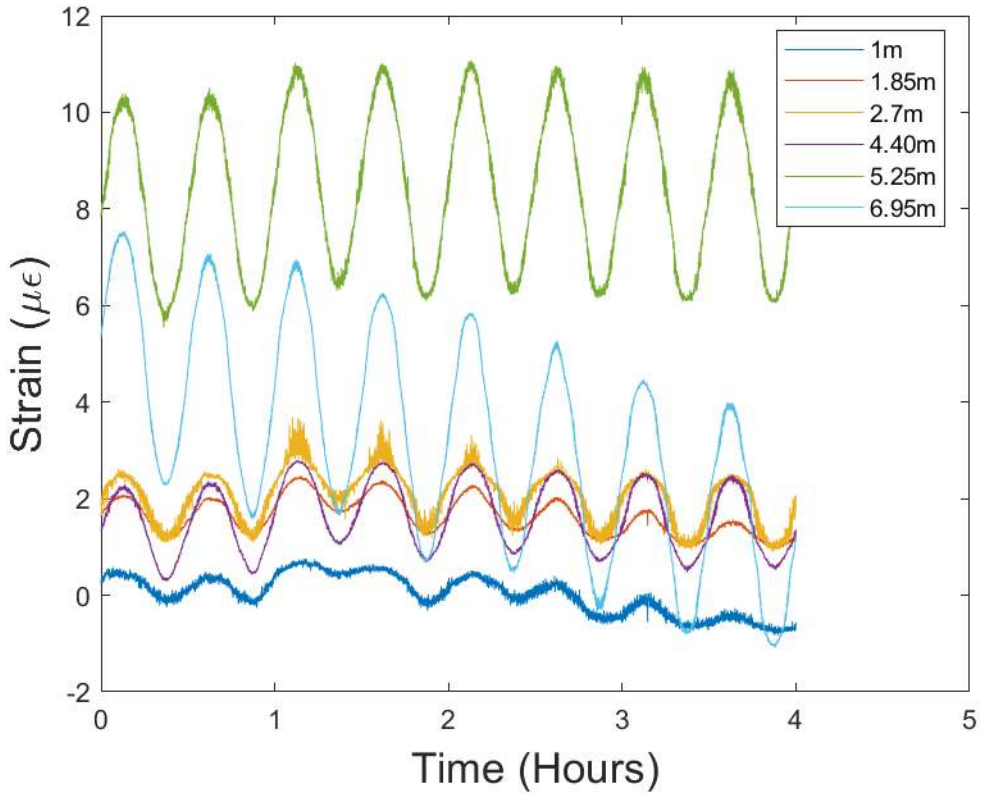

Figure 12-69: Strain measured at different depths during pumping Test 1. Data from the first hour of pumping (first two periods) was omitted. Strain is offset by arbitrary amounts. No correction for trend or barometric pressure.

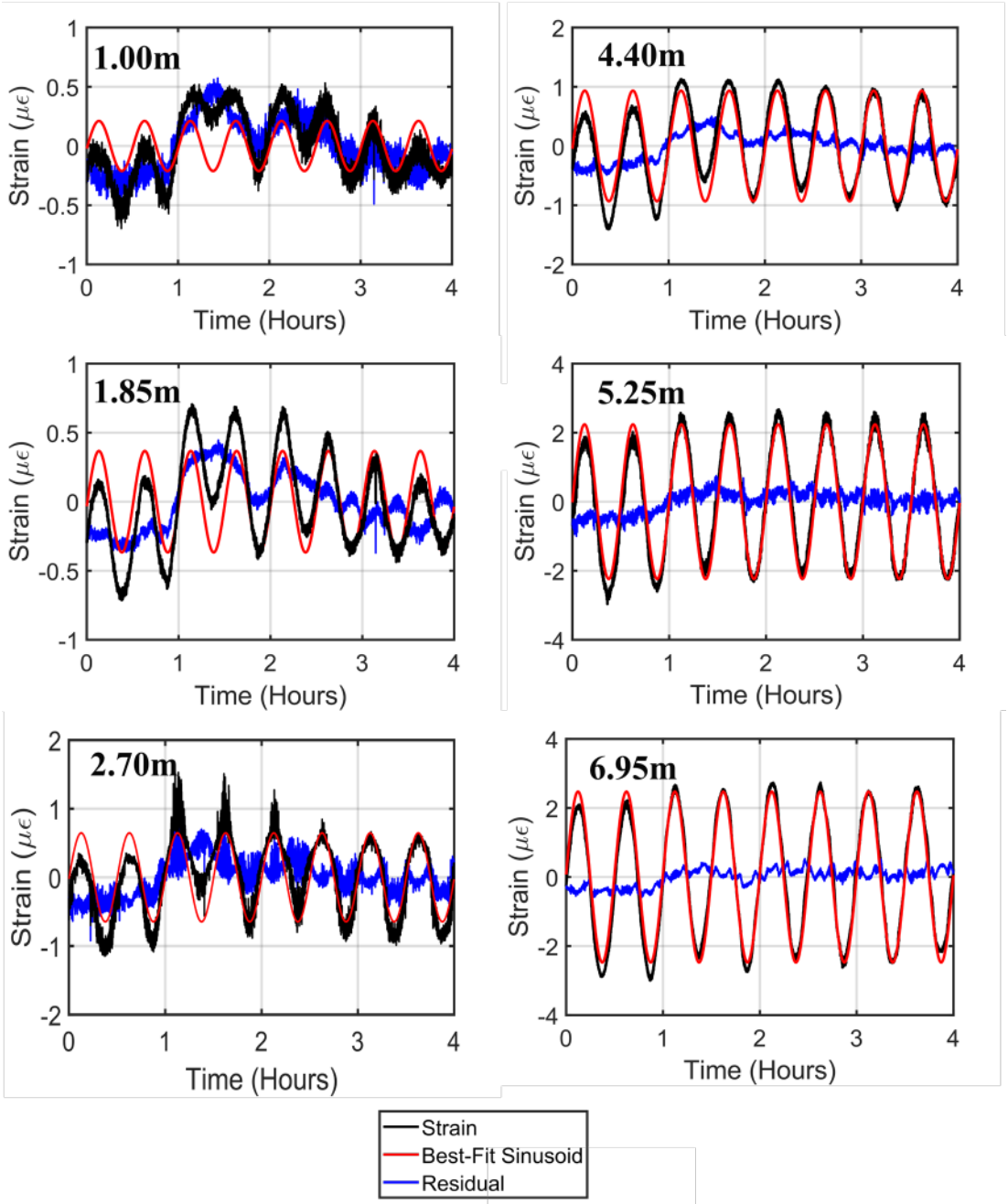

Figure 12-70: Vertical strain during Test 1 (rate, +/- 2.5 gpm). Depths to the midpoints of the sensors on the left. Field data (black), best-fit sinusoid (red), residual (blue).

The amplitude of the strain increases with depth and pumping rate, and these effects are illustrated with selected examples from three depths and three tests that used different pumping rates (Figure 12-71). The strain appears as nearly a pure sinusoid at the highest pumping rate and deepest strainmeter (Figure 12-71). In this case, the amplitude of the sinusoid is approximately 2 με

and the residual resulting from noise in the strain signal is a few tenths of a με. The ratio of signal to noise increases as the pumping rate decreases. In Test 6, the strain variations are minor and difficult to discern from the background strain.

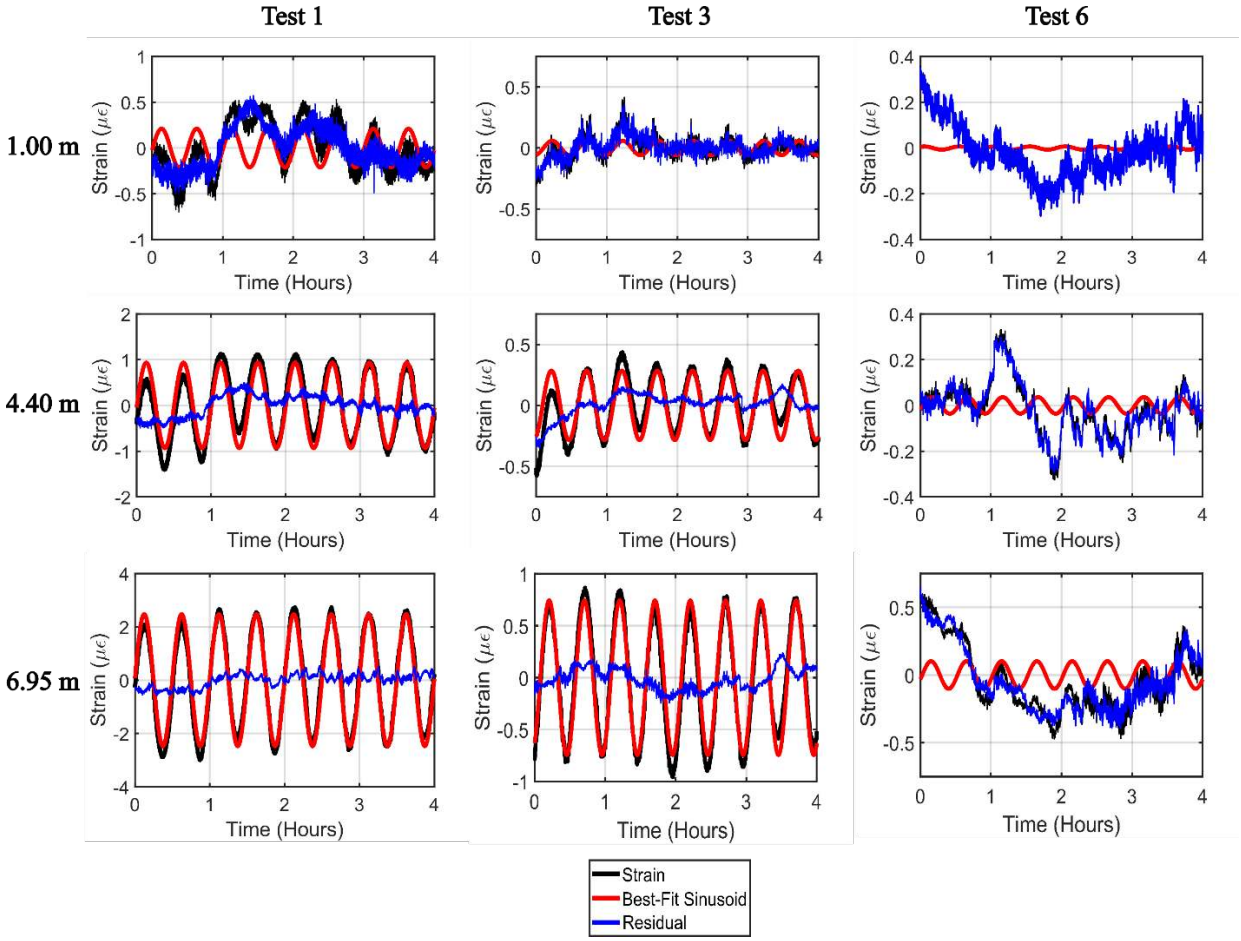

Figure 12-71: Strain response in the vadose zone during Test 1, Test 3, and Test 6 at depths (below ground surface): 1.0m 4.4m, and 6.95m. Field data (black), best-fit sinusoid (red), residual (blue).

A Fourier transform of the strain data was performed to calculate the magnitude spectra and this indicates that the maximum amplitude occurs in most cases at a 30 minute period, which is the period used at the pumping well (Figure 12-72). The amplitude increases with depth, and when the pumping rate is low there are peaks at periods less than 30 minutes that are larger than the peak at 30 minutes at the shallowest sensors. For example, during Tests 4, 5 and 6 there are peaks in the range of 10 to 30 minutes that are greater than the peaks at 30 minutes at the shallowest few sensors. Nevertheless, the peaks at the shallow sensors are readily identified in the spectra. This indicates that a Fourier transform should be capable of identifying the magnitude of the signal at the pumping period at all depths.

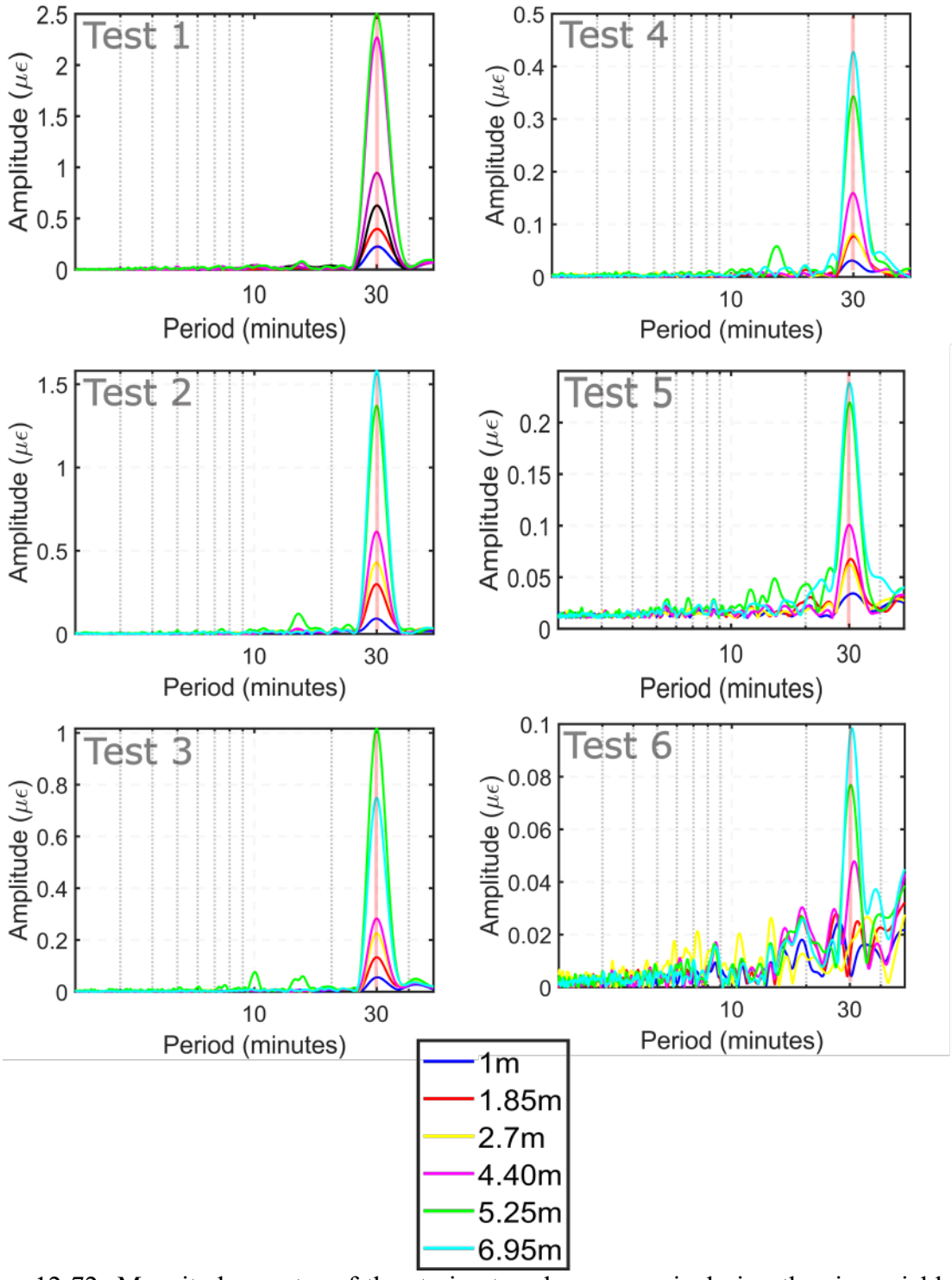

Figure 12-72**:** Magnitude spectra of the strain at each sensor pair during the six variable rate pumping tests. The pumping rate had a period of 30 minutes. The vertical red line represents the pumping period.

The amplitude spectrum during Test 6 includes a wider range of periods than in the other tests (Figure 12-72). There are multiple peaks of 0.02 to 0.04 με in the range of 15 to 40 minutes during Test 6. This noise in the signal is probably a result of strain caused by variations in barometric pressure. The amplitudes at 30 minutes at the lowest three sensors are greater than 0.04 me, and they are clearly discernable above the noise. However, strains at the shallowest three sensors at 30 minutes are of the same magnitude as the noise. Indeed, scrutiny of the spectrum from Test 6 indicates that all the peaks in the vicinity of 30 minutes are shifted slightly from 30 minutes, and the shift is greatest in the data from the shallow sensors. This is probably because the barometric pressure causes strains over a broad band of periods and this causes small shifts in the phase of the signal induced by the pumping test.

A summary of the strain analysis indicates that amplitude increases as the depth of the sensor pair increases (Figure 12-73). The amplitude is a linear function of depth down to 4.4 m and the gradient increases with the pumping rate. For example, the amplitude above 4.4 m depth increases at a gradient of 0.25 με/m for a pumping rate 2.5 gpm, and 0.14 με/m for a pumping rate of 1.5 gpm, and the gradient progressively decreases with the pumping rate. Between 4.4m and 5.25m depth there is a sharp increase in gradient that occurs during each test. Below this jump, the gradient of the amplitude is similar to the slope at shallow depth.

The phase delay time is roughly 5 minutes, but it decreases with depth, and is largely independent of pumping rate (Figure 12-73). The gradient of the delay is approximately -0.11 min/m (the negative sign indicates the delay decreases with depth). The vertical phase velocity of the strain is the inverse of the gradient and is 9 m/min upward at this location.

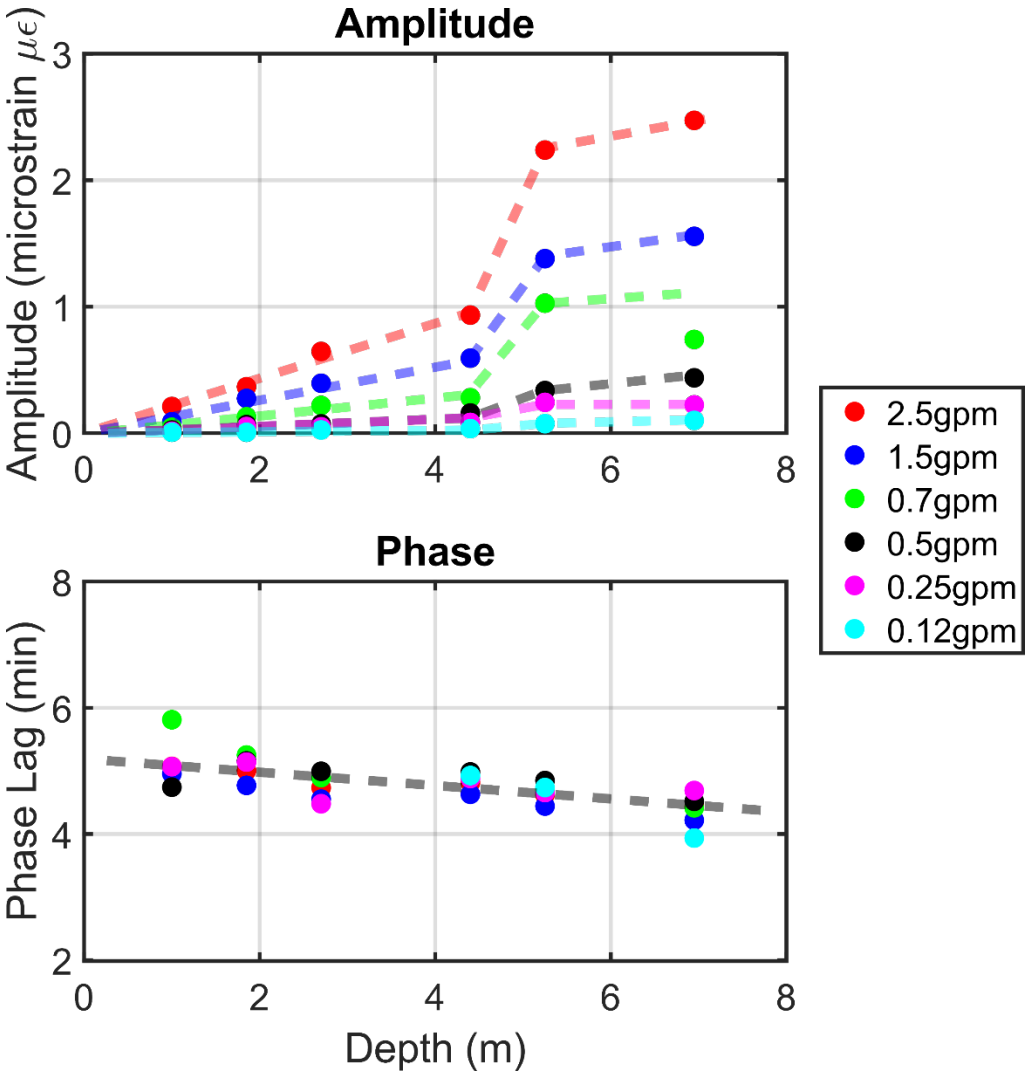

Figure 12-73: Amplitude and phase lag as functions of depth for the six different periodicity tests (Test 1 through Test 6). Best fit line of the Phase Lag for all 6 tests is

y=-0.11(m/min)x(min)+5.2(min)

12.9.2.2 Variable Period Tests

Three pumping tests were conducted using a sinusoidal rate at different periods and a flow rate amplitude of 2.5 gpm. (Table 12-20 and Figure 12-74).

Table 12-20. Characteristics of pumping rates using during variable period tests.

Test	Amplitude (± gpm)	Period (minutes)
1	2.5	30
7	2.5	15
8	2.5	60

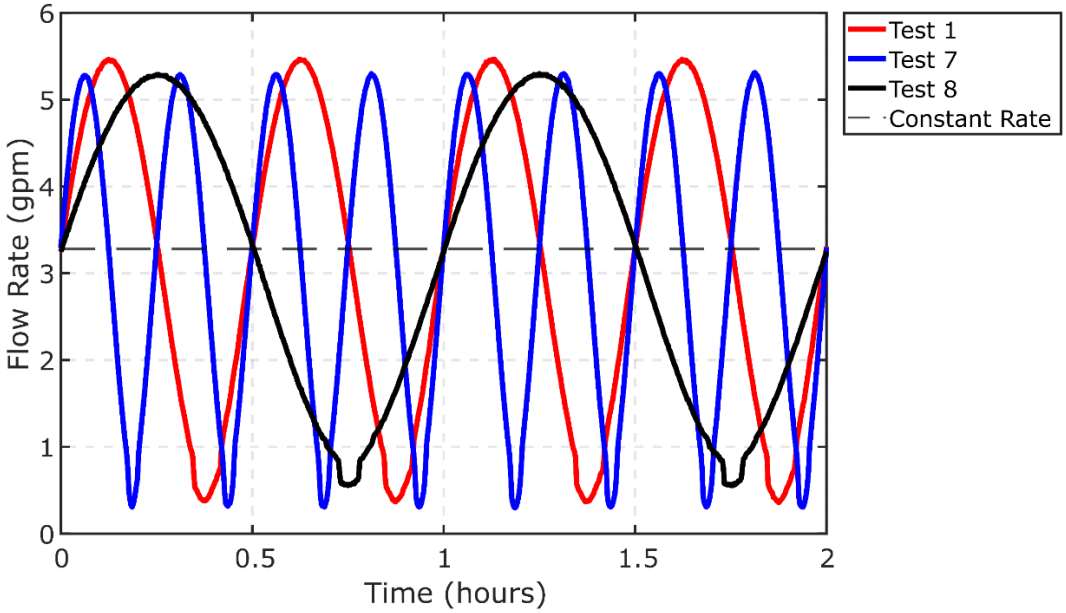

Figure 12-74: Flow rates measured with a flow meter during the three variable period pumping tests. Test 1 (red line) has a period of 30 minutes, Test 7 (blue line) has a period of 15 minutes, and Test 8 (black line) has a period of 60 minutes. The constant rate test (3.3 gpm) is also shown (black dashed line) for reference.

The flow rates were varied around a mean flow rate of 3.3 gpm, which was the flow rate used in the constant rate pumping test. The rates varied as nearly a sinusoidal function of time, but there were slight deviations from a pure sinusoid at the low end of the rates. The deviations apparently occurred because 1 gpm is the lower end of the range of operation for the flowmeter, but they are expected to have no effect on the results.

12.9.2.2.1 Pressure Response

The magnitude of drawdown increases with the period of the pumping rate, and decreases with distance from the well (Figure 12-75). There was an unknown pumping issue at approximately 1.4 hrs into Test 7 and this caused the drawdown to decrease unexpectedly. A clear sinusoidal response occurs at WL-5 during all three periods, and sinusoidal response is evident at WL-7. The sinusoidal response at WL-4 is clear in the time series from Test 8 with a period of 60 minutes, but it is obscured by noise during tests with shorter periods (Figure 12-75).

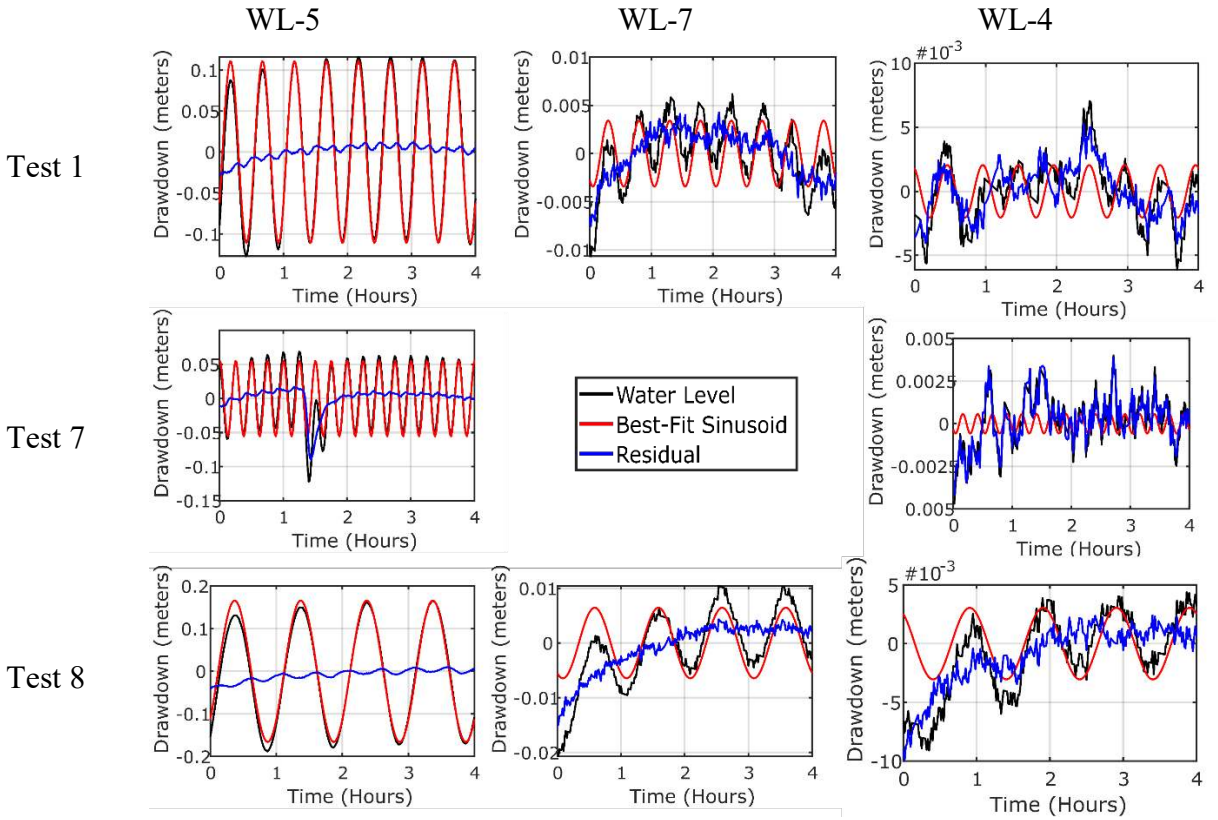

Figure 12-75: Drawdown the three piezometers for Test 1 (period = 30 min), Test 7 (period = 15 min), and Test 8 (period = 60 min). Observed head (black), best fit sinusoid (red), residual (blue). No data were recorded at WL-7 during Test 7. Field data (black), best-fit sinusoid (red), residual (blue).

The dominant period in the amplitude spectra of the pressure is the same as the pumping rate in all cases, except during Test 7 at WL-4 (Figure 12-76). The largest amplitude during that test is 6×10^{-4} m at 18 min, and a slightly smaller amplitude occurs at a 15-minute period. The amplitudes during Test 7 at WL-4 are small (smaller than the reported accuracy of the transducer) and the largest amplitude is probably created by variations in barometric pressure. Nevertheless, there is a relatively well defined peak at the pumping period (Figure 12-75).

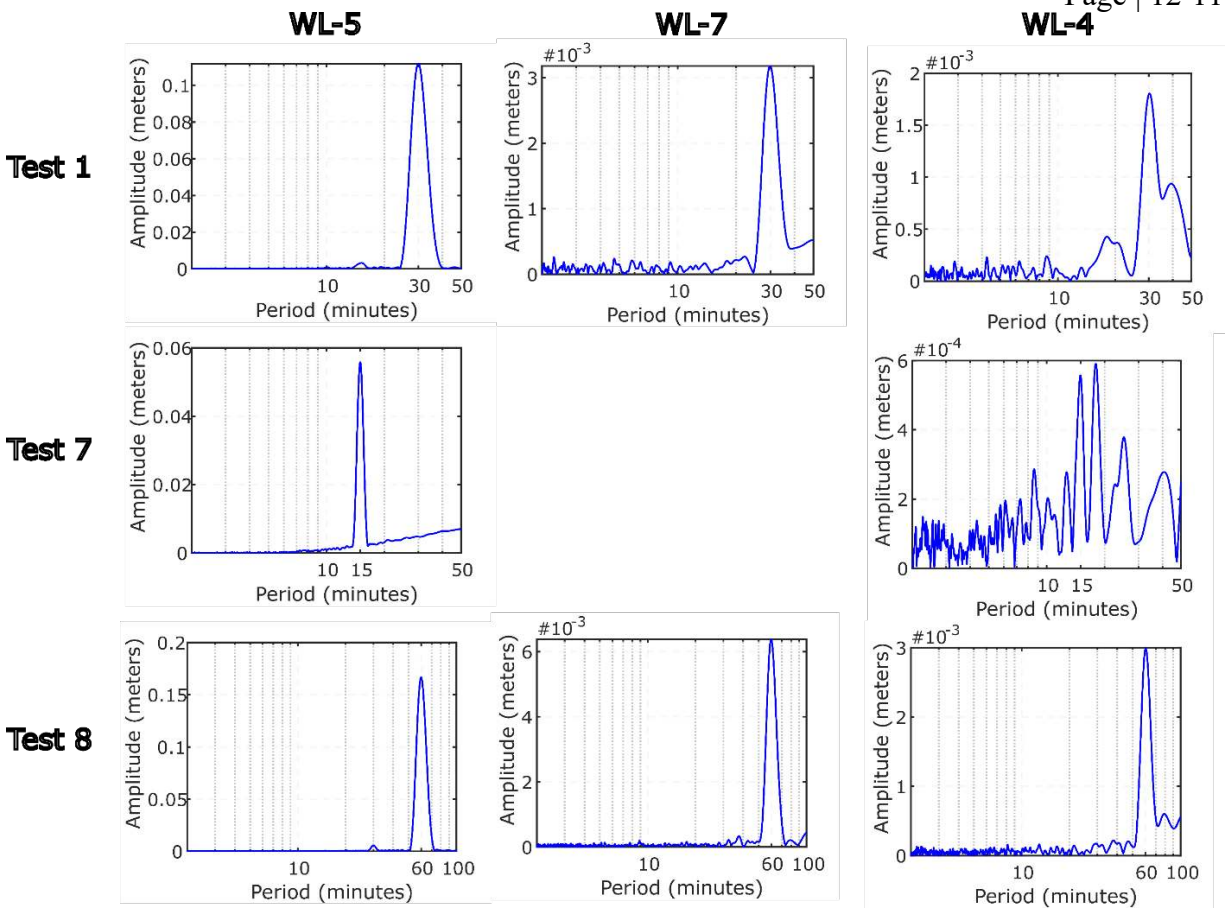

Figure 12-76: Magnitude spectrum plots of the drawdown in during the three variable period pumping tests. The pumping rate had a period of 30 minutes (Test 1), 15 minutes (Test 7), and 60 minutes (Test 8). No data were recorded at WL-7 during Test 7.

The phase delay increases with distance from the pumping well, from 7.4 minutes at r = 6.7 m to 25 min at r = 20.9 m during Test 1 (Table 12-21). This gives an average gradient of the delay of 1.2 min/m. The horizontal phase velocity, v_{ph}, of the pressure is the inverse of the phase gradient, so the horizontal phase velocity is 0.8 m/min for the 30 minute period, λ = 30 min. The gradient is steeper (approximately 2.2 min/m), and the phase velocity of the pressure is slower, 0.44 m/min for λ = 60 min. The effect of the period on the phase velocity can be addressed by defining

$$\xi_p = v_{ph}\sqrt{\lambda} \qquad 12\text{-}33$$

gives $3.1 < \xi_p < 5.2$ where the variation occurs in data from the different piezometers and but variations in ξ_p independent of the pumping period (Table 12-21).

Table 12-21. Amplitude and period of pressure measurements, and associated variables during periodic pumping tests of different periods.

Period, λ (min)	Well	r (m)	P_h Amplitude (m)	P_h, Phase Lag (min)	Phase velocity, v_{ph} (m/min)	$\xi_p = v_{ph}$ sqrt(λ) (m/min$^{1/2}$)
15	WL-5	6.7	0.05	9.5	1.34	5.2
15	WL-7	9.1	N/A	N/A	N/A	N/A
15	WL-4	20.9	N/A	N/A	N/A	N/A
30	WL-5	6.7	0.11	7.4	0.91	5.0
30	WL-7	9.1	0.003	15.1	0.60	3.3
30	WL-4	20.9	0.002	24.6	0.85	4.7
60	WL-5	6.7	0.17	10.1	0.66	5.1
60	WL-7	9.1	0.006	23.1	0.39	3.1
60	WL-4	20.9	0.003	42.2	0.50	3.8

The phase lag increases with distance from the pumping well, from 7.4 minutes at 6.7 m to 24.9 min at 20.9 m during Test 1. This gives an average gradient of 1.2 min/m. The horizontal phase velocity of the pressure is the inverse of the phase gradient. This gives a horizontal phase velocity of 0.8 m/min for the 30 minute period. The gradient is steeper (approximately 2.2 min/m), and the phase velocity of the pressure is 0.44 m/min for the 60 minute period.

12.9.2.2.2 Strain Response

The effect of varying the pumping period on the strain is similar to the effect on the drawdown: increasing the period increases the amplitude of the strain and increases the ratio of signal to noise (Figure 12-77). This result is also apparent in the magnitude spectra, which are dominated by peaks at the pumping period (Figure 12-78)

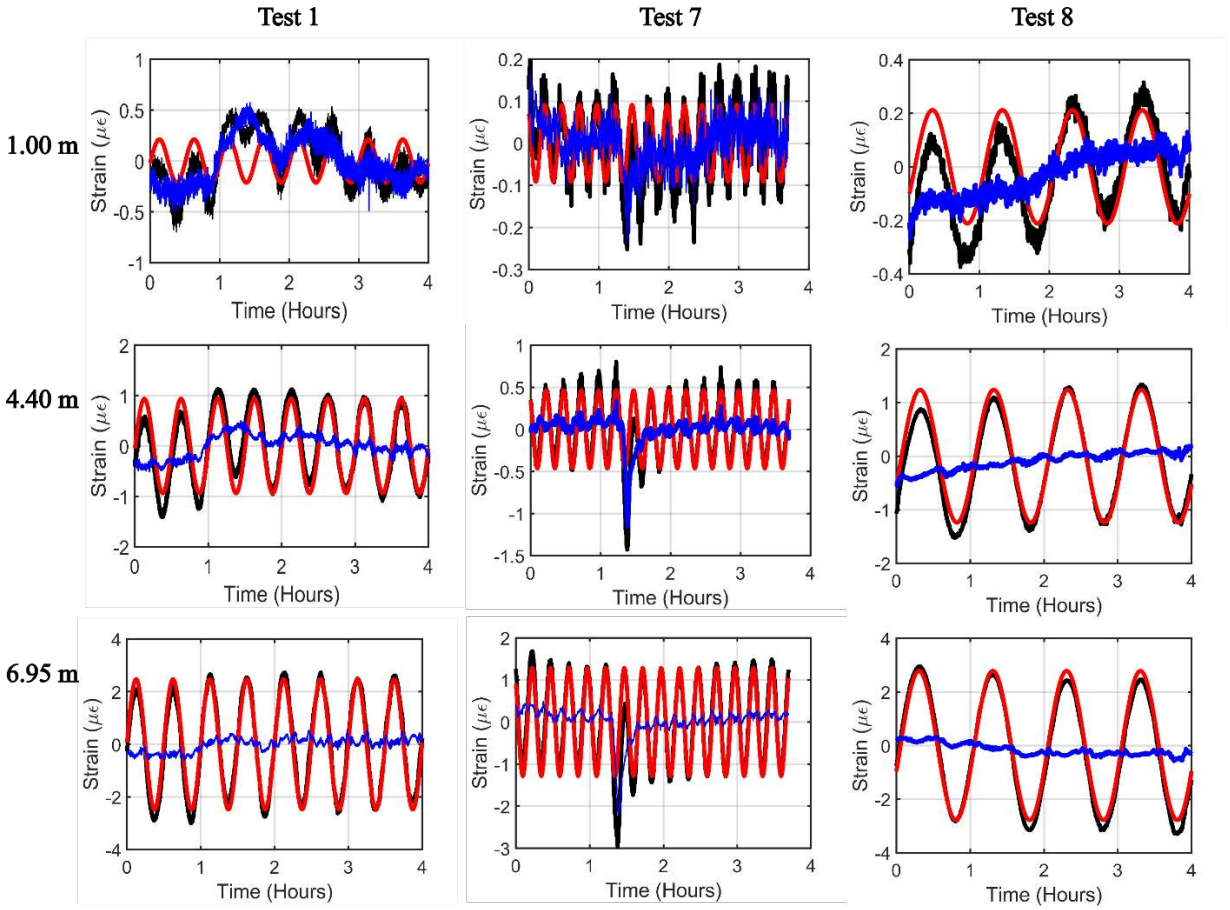

Figure 12-77: Strain response in the vadose zone during Test 1, Test 7, and Test 8 at depths (below ground surface): 1.0m 4.4m, and 6.95m. Field data (black), best-fit sinusoid (red), residual (blue).

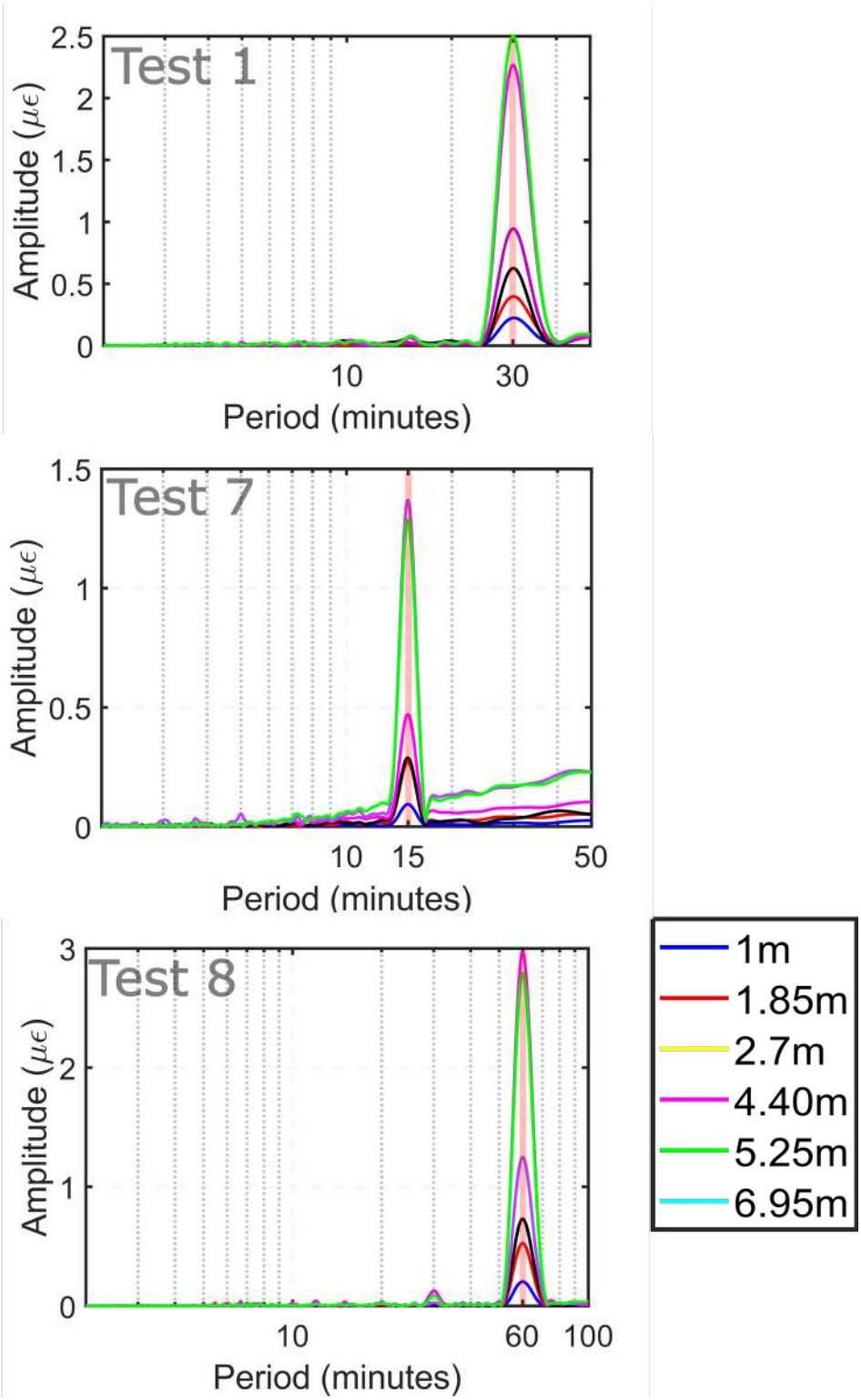

Figure 12-78: Magnitude spectrum plots of the strain at each sensor pair during pumping tests with different periods (Test 1 [30 min], Test 7 [15 min], and Test 8 [60 min]). The vertical red line represents the pumping period.

Table 12-22. Amplitudes and phase lags of the strain during pumping tests of different periods.

r = 4.4m	Depth (m)	ε_v Amplitude (με)	ε_v, Phase Lag (min)	Average Phase Lag (min) +/- range (min)	Phase velocity, $v_{\varepsilon h}$ (m/min) +/- range (m/min)	$\xi_\varepsilon = v_{\varepsilon h}$ sqrt(λ) (m/min$^{1/2}$)
Test 7	1	0.09	3.49			
λ=15 min	1.85	0.26	3.46			
	2.7	0.3	3.37			
	4.4	0.46	3.44			
	5.25	1.4	3.34			
	6.95	1.28	3.27	3.4 +/- 0.11	1.3 +/- .03	5.0
Test 1	1	0.21	5.07			
λ=30 min	1.85	0.36	5			
	2.7	0.64	4.73			
	4.4	0.93	4.81			
	5.25	2.23	4.62			
	6.95	2.47	4.43	4.8 +/- 0.23	0.92 +/- 0.05	5.0
Test 8	1	0.21	7.54			
λ=60 min	1.85	0.52	7.55			
	2.7	0.72	6.86			
	4.4	1.23	7.07			
	5.25	2.97	6.67			
	6.95	2.78	6.22	7.0 +/- 0.44	0.63 +/- 0.10	4.9

The amplitude of the strain response increases with the pumping period (Figure 12-79). The response is particularly well developed at the lower sensors where amplitude increases from approximately 1.4 με to 2.9 με as the period increases from 15 to 60 min. The amplitude decreases upward for the tests that used different pumping periods (Figure 12-79) in a pattern that resembles the pattern from the tests conducted with different pumping amplitudes.

The phase delay increases from 3.4 +/- 0.11 min for a pumping period of 15 minutes to 7 +/- 0.44 min for the 60 minutes period (Figure 12-79) and it follows that the horizontal phase velocity of the strain decreases from $v_{\varepsilon h}$ = 1.3 +/- 0.03 m/min to $v_{\varepsilon h}$ = 0.63 +/- 0.1 m/min over that range of periods.

The product of the strain phase velocity and the square root of the period

$$\xi_\varepsilon = v_{\varepsilon h}\sqrt{\lambda} \qquad 12\text{-}34$$

is essentially constant at 5.0 m/min$^{1/2}$ (Table 12-22), which is similar to upper end of the range of values for the pressure (Table 12-21).

The phase delay increases with depth, and the gradient in the vertical delay increases with the pumping period (Table 12-22). This indicates that the upward vertical phase velocity, $v_{\varepsilon v}$, of the strain also decreases with the pumping period, but it is significantly faster than the horizontal phase velocity. For example, for a 15 minute pumping period the vertical phase velocity ($v_{\varepsilon v}$ = 33 m/min) is roughly 25x faster than the horizontal velocity and it slows as the period increases but it remains 7x faster ($v_{\varepsilon v}$ = 5 m/min) than $v_{\varepsilon h}$ for the 60 minute pumping period (Table 12-22).

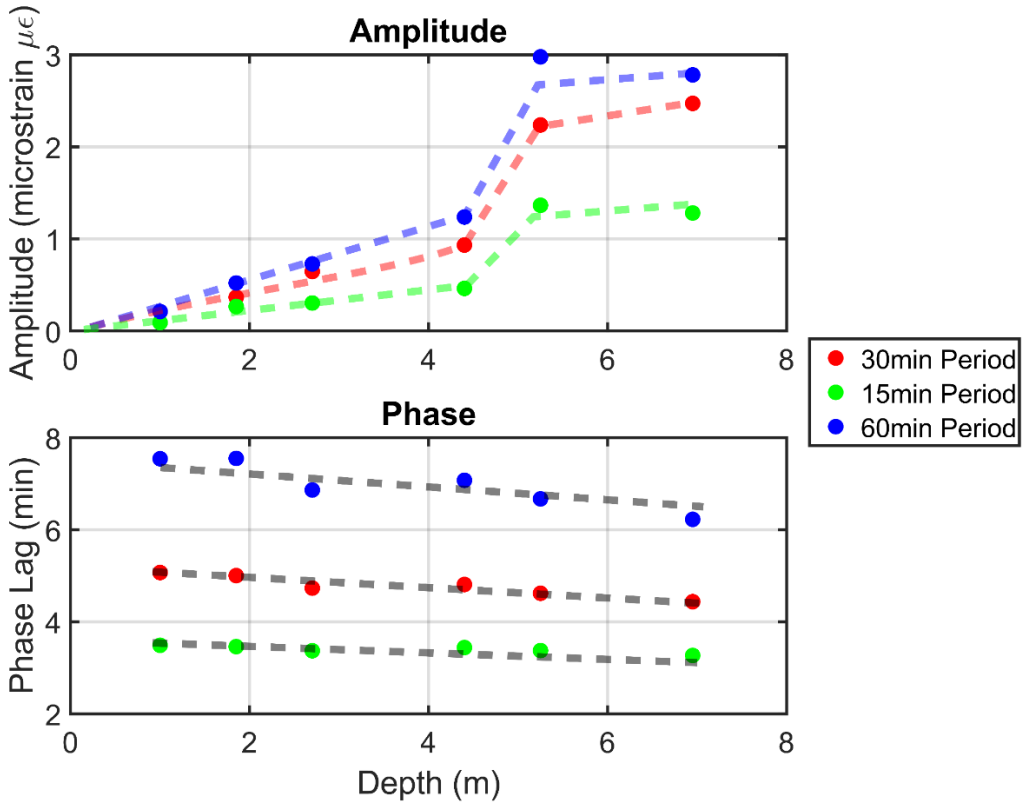

Figure 12-79: Amplitude and phase of the strain during Test 1 (red), Test 7 (green) and Test 8 (blue). The gradients of the phase delay are: -0.03 min/m (15 minutes); -0.1 min/m (30 minutes); -0.21 (60 minutes).

12.10 PART 2 DISCUSSION

This investigation demonstrated that distributed vertical strain could be measured in the vadose zone during a periodic pumping test using the newly developed CMPI optical fiber measurement system. The strain in the vadose zone shares important similarities with the pressure in the underlying aquifer. They both vary periodically with the same period as the pumping rate, and the amplitudes of both pressure and strain increase with the pumping rate. The delay times of both the pressure and strain increase with distance from the well and with the period of the pumping rate.

Table 12-23. Summary of D_h values calculated using delay time of pressure (P), strain at 6.95 m (S1), strain averaged over all depths (S2), calculated using either the Rasmussen (R) or Streltsova (S) solutions. D_h also estimated from a constant rate pumping test (PC). Values in parentheses are standard deviations.

			Diffusivity [m^2/s]		
Pumping Test	Location	id	Neuman	Rasmussen (R)	Streltsova (S)
Constant Rate	All Piezometer		0.039		
Test 1	WL-5	P		0.051	0.031
30-minute period	WL-7	P		0.03	0.023
	WL-4	P		0.033	0.028
	Average (std dev)			0.036 (0.011)	0.027 (0.004)
	Strain @ 6.95m	S1		0.01	0.042
	Strain average	S2		0.082 (0.01)	0.036 (0.003)
Test 7	WL-5	P		0.011	0.01
15-minute Period	WL-7	P		0.181	0.119
	WL-4	P		-	-
	Average (std dev)			0.096 (0.12)	0.065 (0.07)
	Strain @ 6.95m	S1		0.07	0.038
	Strain average	S2		0.062 (0.004)	0.035 (0.001)
Test 8	WL-5	P		0.071	0.033
60-minute period	WL-7	P		0.027	0.02
	WL-4	P		0.023	0.019
	Average (std dev)			0.040 (0.026)	0.024 (0.008)
	Strain @ 6.95m	S1		0.153	0.042
	Strain average	S2		0.109 (0.03)	0.034 (0.02)
	Constant Rate	D	**0.039**		
	Ave (std dev) A	P		**0.053 (0.05)**	**0.035 (0.03)**
	Ave (std dev) B	S1		**0.078 (0.07)**	**0.041 (0.002)**
	Ave (std dev) C	S2		**0.08 (0.022)**	**0.035 (0.001)**

The amplitude and phase lag of pressure in an aquifer during periodic pumping tests are commonly analyzed to estimate properties of aquifers (Rasmussen et al. 2003, Streltsova 1988), and the similarity between pressure and strain suggests that it may also be feasible to estimate aquifer properties using strain data.

12.10.1Aquifer Properties

To evaluate this suggestion, pressure and strain lag time data were compiled from three periodic tests that used different periods (Test 1, Test 7, and Test 8) and analyzed to calculate D_h in Table 12-23 using the solutions from Rasmussen et al. (2003; (12-24)) and from Streltsova (1988; (12-30)). D_h was calculated using lag time at each piezometer, and these data were averaged, and it was also calculated using strain measured at the bottom sensor pair on the strain ribbon (at 6.95 m depth) and using average phase lag of the strain over the six sensor pairs (Table 12-23). The strain phase lag decreased with depth, so D_h calculated using the average is less than D_h calculated using the strain at the bottom of the vadose zone. The hydraulic diffusivity estimated by fitting data from all three monitoring wells measured during a constant rate pumping test to the Neuman (1973) solution served as a baseline.

The average hydraulic diffusivity across all tests using pressure data and the Rasmussen solution is 0.053 (0.05) m^2/s, where the standard deviation is given in parentheses. The average D_h value using pressure and the Streltsova solution is 0.035 (0.03) m^2/s, which is less than that calculated using the Rasmussen solution but the two average values are withing one standard deviation of each other so the null hypothesis that there is no significant difference between the means was tested using a two-tailed, paired Student t-test. The result of comparing the two means is $p = 0.10$, so we would accept the null hypothesis assuming a critical value of $p = 0.05$.

There is no statistical difference between D_h calculated using pressure (P-R or P-S) and values calculated using time delays from strain, assuming $p < 0.05$ is a significant difference (first two rows in Table 12-24) except for between P-S and S2-R where $p = 0.03$. The case with the most significant difference between D_h values ($p = 0.02$) is between *S1* (strain averaged over the different locations) and P-CRS (pressure during constant rate test that analyzed the three piezometers simultaneously). This low p value occurs because the three values determined using strain are remarkably consistent ($\sigma = 0.001$), and only one value of D_h for P-CRS is used. However, the average value of D_h from *S2* is only a few percent different from the D_h value from P-CRA, so this approach for comparing results to D_h from a constant rate test may be too conservative. An alternative approach is to use the values of D_h determined by analyzing data from the three monitoring wells during the constant rate tests individually. This gives a value of D_h for each of the three piezometers. p values were calculated using this dataset and the results are in column P-CRI in **Error! Reference source not found.**. All the values of D_h calculated using pressure or strain from the periodic tests are essentially the same as D_h values calculated from the constant rate test, according to p values determined using P-CRI in D_h (Table 12-24; rightmost column).

Table 12-24. Summary of average and standard deviations of D_h from pressure (P) and strain at 6.95m (S1) and average strain (S2) lag time calculated using solutions in Rasmussen (R) and Streltsova (S). P-CR is calculated from pressure data measured during a constant-rate tests in upper three rows. P values giving probability comparing means of different data sets in lower six rows. Bold fonts highlight $p< 0.05$, grey font highlights $p >0.1$.

	P-R	P-S	S1-R	S1-S	S2-R	S2-S	P-CRA	P-CRI
average	0.053	0.035	0.078	0.041	0.083	0.035	0.039	0.070
std dev	0.055	0.035	0.072	0.002	0.021	0.001		0.056
P-R		*0.05*	0.63	0.53	0.28	0.37	0.48	0.69
P-S			*0.42*	0.68	**0.03**	0.98	0.78	0.40
S1-R				0.47	0.91	0.41	0.45	0.89
S1-S					*0.07*	**0.04**	0.34	0.46
S2-R						*0.06*	*0.07*	0.40
S2-S							**0.02**	0.44

12.10.2 Simulations of Pressure and Strain

The data analyzed above indicates that delay times of strain in the vadose zone are similar to the delay of pressure in the underlying aquifer at the same radial distance(Table 12-23Table 12-24), and this leads to similar estimates of D_h (Table 12-23Table 12-24) . That result suggests that under the conditions of the field test, strain measured in the vadose zone could be used to estimate D_h in the underlying aquifer, but the field data are only available for the vertical component of strain measured at one radial distance so the generality of this result is unclear. Simulations were conducted of an idealized representation of the field site to further evaluate this effect.

Simulations used two rectangular domains in axial symmetry where the physics in each domain are related, but different. The lower domain includes fluid flow through porous media and deformation coupled through poroelasticity and it represents the aquifer. The upper rectangular domain is the vadose zone. It includes elastic deformation, but the fluid pressure is assumed to be constant. This is justified for short well tests because the relative liquid phase permeability in the vadose zone would limit upward pressure diffusion from the aquifer, and the air phase would create a highly compressible pore fluid that would limit pressure changes due to deformation. We have conducted simulations where fluid pressure in the vadose zone is allowed to change as represented by the Richards equation. Results of the model using Richards equation shows that pressure changes in the lower part of the vadose zone can be affected by pressure changes in the underlying aquifer, but those changes are small and limited to the lower few meters so they will be ignored here.

The thickness of the aquifer and vadose zones are both 10 m, which is similar to the field site, and the lateral extent is 10 km, which is large enough to eliminate effects of lateral boundaries. Other boundary conditions for the fluid and displacements are standard and summarized in Figure 12-80.

The well is represented using a boundary condition that includes wellbore storage. This is accomplished by assuming water volume is conserved in a wellbore of finite volume, where the diameter is assumed to be 0.0762 m based on field conditions. The hydraulic head is assumed to be uniform over a fully penetrating well screen, and the head in the well bore is above the top of the screen so the change in head is equal to the change in storage in the well bore.

The pumping rate varies periodically, starting with a pumping stage followed by an injection stage of equal rate, but opposite sign (Figure 12-81). This gives a net pumping rate of zero after every completed sinusoidal cycle of pumping and injection. Changes in wellbore storage cause the flowrate leaving the wellbore and entering the aquifer to be less than the pumping or injection rate, particularly early in a pumping or injection cycle (red line in Figure 12-81). The hydraulic head in the well drops with time during the pumping cycle and reaches a minimum at the end of the pumping stage. It then increases and reaches a maximum at the end of the injection stage (blue line in Figure 12-81).

The pumping rate and wellbore pressure are both sinusoids with the same period, and in the absence of wellbore storage the wellbore pressure will lag behind the pumping rate by $3\pi/2$, or 3/4 of the period, λ (Streltsova, 1988). This difference in phase occurs because the head in the well drops whenever the pumping rate is positive, so the peak pressure occurs at the end of the pumping stage. Wellbore storage causes the flow at the well screen to lag behind the flow from the pump (Figure 12-81), and this causes the wellbore pressure to lag further than $3\pi/2$ behind the pumping rate. This causes problems when using the pumping rate as a reference for the delay time. The pressure head in the wellbore can be easily measured in the field, so it will serve at the baseline time for calculating phase delay in both the simulations and the field data analysis.

The pressure and strains vary periodically at reference points in the aquifer and vadose zone (Figure 12-13). The signs of the pressure and most of the strains are generally similar, so an increase in pressure occurs with an increase in strain, which implies that the strain is becoming increasingly tensile at an overlying point. The exception is the vertical strain, which decreases when the pressure increase. The delays of pressure and strain components all increase with distance from the well, and this is manifested by a delay in the time when the maxima or minima occur in the time series (Figure 12-13). Even though they share similar general characteristics, the shapes, magnitudes and delays of each strain component are distinct from each other and from the pressure (Figure 12-13).

The strain tensor field at the end of the injection stage, ranges from roughly -10 $\mu\varepsilon$ to 1 $\mu\varepsilon$ and each component forms a unique pattern (Figure 12-83). The maximum strains are in the lower left corner, slightly above the well screen, and they decrease upward and radially within approximately 5 m of the well. In the mid-distance of $5 < r < 15$m, the strains decrease in approximately a horizontal direction (the contours are roughly vertical). At larger radial distances the strains decrease downward. Both the vertical and radial strains, and the horizontal average strain change sign with distance (the thick red line is zero strain, but the sign of the circumferential strain is positive throughout the domain in Figure 12-83.

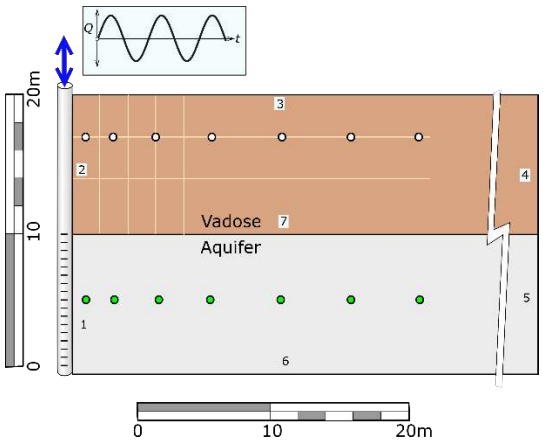

Figure 12-80. Conceptual model of simulation in axial symmetric coordinates with a well at the axis. Pressure analyzed in the aquifer. Pressure assumed constant in vadose. Strain occurs everywhere and is coupled to the fluid pressure in the aquifer. Light colored lines in vadose zone are section lines used for plotting. White circles are locations of strain and green circles are location of pressure time series. Boundary conditions for pressure and mechanics: (1) periodic flux as shown in inset from wellbore with storage, normal traction equal to pressure; (2) zero normal displacement (roller); (3) zero normal traction (4) roller @ r = 10km (5) roller, specified head @ r = 10km (6) no flow, roller (7) no flow, continuity.

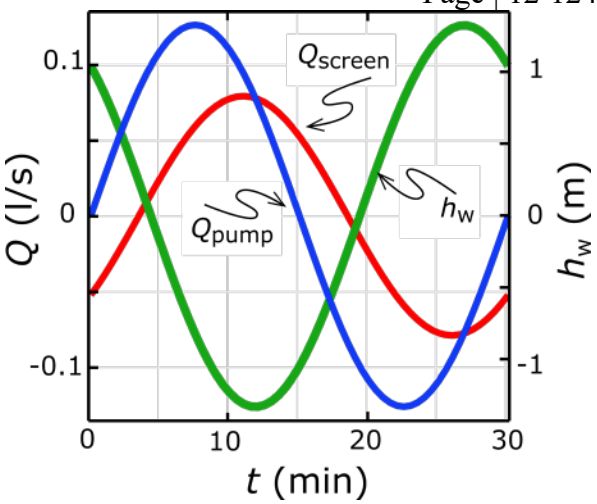

Figure 12-81. Flowrate and pressure at the wellbore. The flowrate pumped from the well (Q_{pump}) is a sinusoid with zero net rate. The flowrate through the well screen (Q_{screen}) is exchanged between the well and the aquifer. It differs from the Q_{pump} because of wellbore storage.

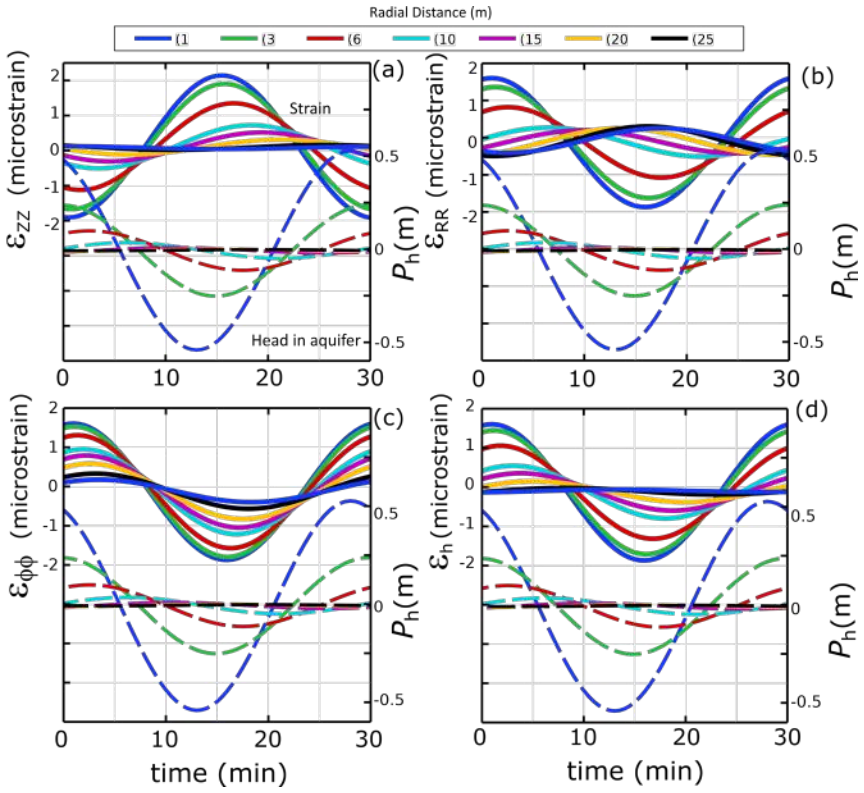

Figure 12-82. Strain components (solid lines) at reference points at different radial distances indicated by color in the vadose zone (z = -3m) and hydraulic heads (dashed lines) in the aquifer (z = -15m) at radial distances indicated by color. Sinusoidal pumping with a period of 30 min. Reference points in Figure 12-80.

A unifying pattern emerges that appears to persist in the strain field throughout a sinusoidal well test (Figure 12-83). In general, there are four regions in the vadose zone where the direction of decreasing strain are consistent, whereas the direction of decreasing pressure is always horizontal away from the well in the aquifer (Figure 12-84). Strain decreases upward in the Near Well region, whereas it decreases in a horizontal direction in the Shallow and Mid-Distance regions. Strain decreases downward in the region that is far from the well (Figure 12-84).

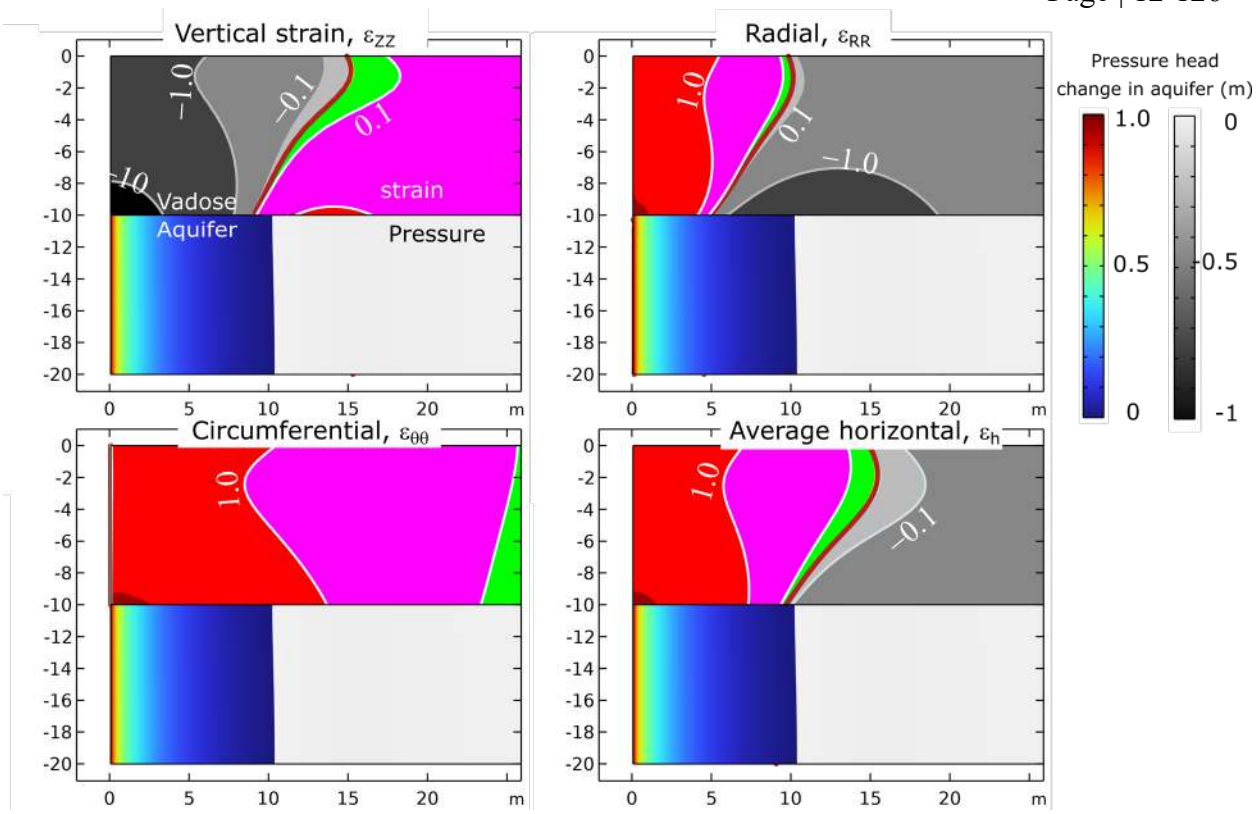

Figure 12-83. Strain components in the vadose zone (labeled in units of microstrain) and hydraulic head change in the aquifer in cross-section at the end of the injection stage of a sinusoidal cycle. Negative strain is compression and is shown in grey tones, positive strain is tension and shown as colors. Sinusoidal pumping with a period of 30 min.

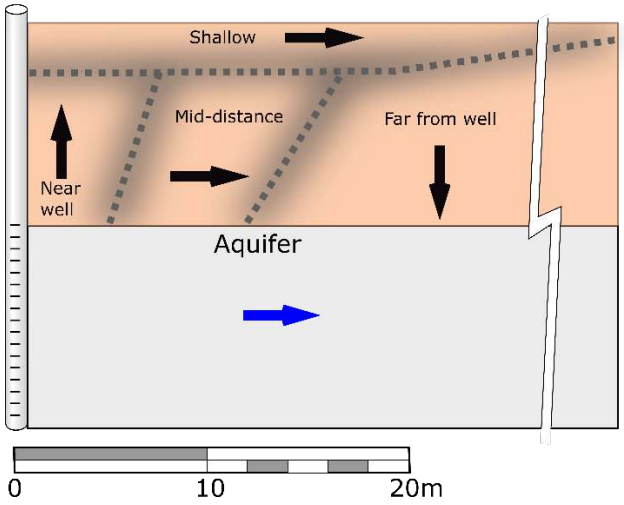

Figure 12-84. Conceptual model of regions of different hydraulic head and strain gradients in the vadose zone and aquifer. Arrows show direction of decreasing strain (black) or hydraulic head (blue).

12.10.2.1 Delay times

Phases of the strain components in the vadose zone were calculated using a Fourier transform. The phase of the pressure at the well face was taken as zero and phases were converted to time delay following the pressure. A half period was added to the phase of ε_{zz} to facilitate plotting with the other strains.

The delay of the pressure increases as a roughly linear function of distance from the well (blue lines in Figure 12-85). The delay of the vertical and average horizontal strains, ε_{ZZ} and ε_h, at shallow depth (3m) in the vadose zone are non-linear functions of distance, but they cross the delay of the pressure at two locations and they are generally within 20 percent of the delay of the pressure within 25 m of the well (Figure 12-85a). The delay of the circumferential strain $\varepsilon_{\phi\phi}$ is significantly less than, and the delay of the radial strain ε_{RR} is significantly greater than the pressure delay. This suggests that the pressure delay in the aquifer could be estimated to within roughly 20 percent using the delay of ε_{ZZ} or ε_h measured at shallow depth in the vadose zone.

The delays of the ε_{ZZ} and ε_h are similar to the delay of p at mid-depth and near the bottom of the vadose zone in proximity to the well, although at r > 8m the delays for those strains at the bottom of the vadose zone exceeds that of the pressure (Figure 12-85b and c). The simulation used here assumes the pressure change in the aquifer is isolated from the vadose zone, whereas in most cases a pressure change in the aquifer is expected to propagate upward into the overlying vadose zone. This will affect the strains in the vadose zone, particularly at the bottom of the vadose zone. The strains shown in Figure 12-85c do not include this effect.

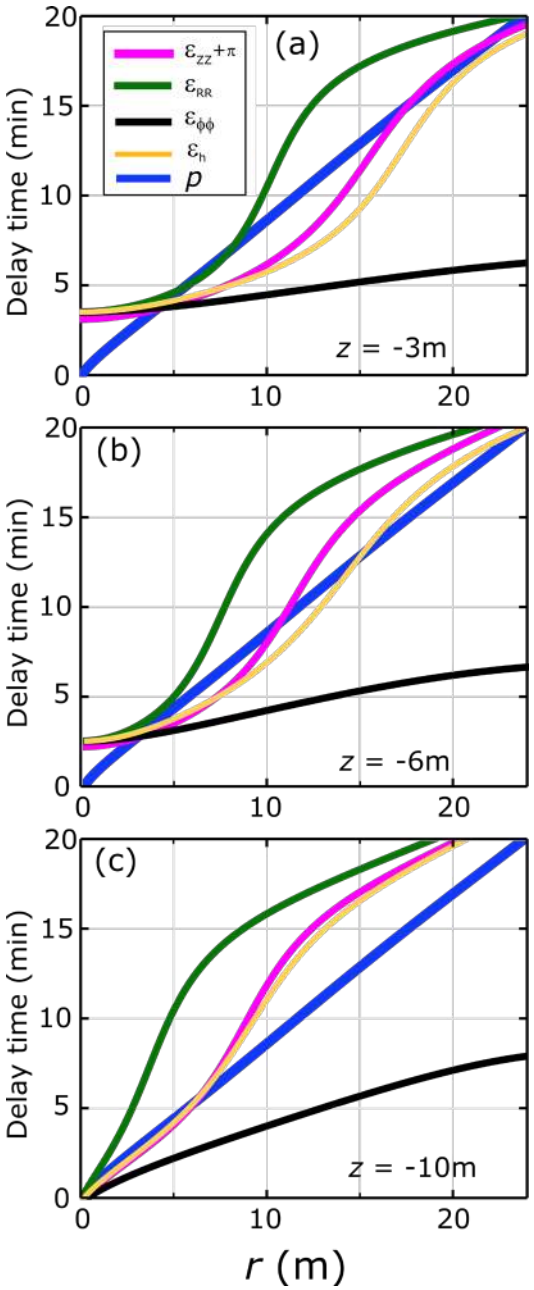

Figure 12-85. Delay time of the strain and pressure behind the pressure in the well along horizontal lines at different depths. Pressure measured at mid-height in aquifer. (a) strain at 3m depth and (b) strain at 6m depth. (c) strain at 10m depth, which is the bottom of vadose zone. Sinusoidal pumping with a period of 30 min.

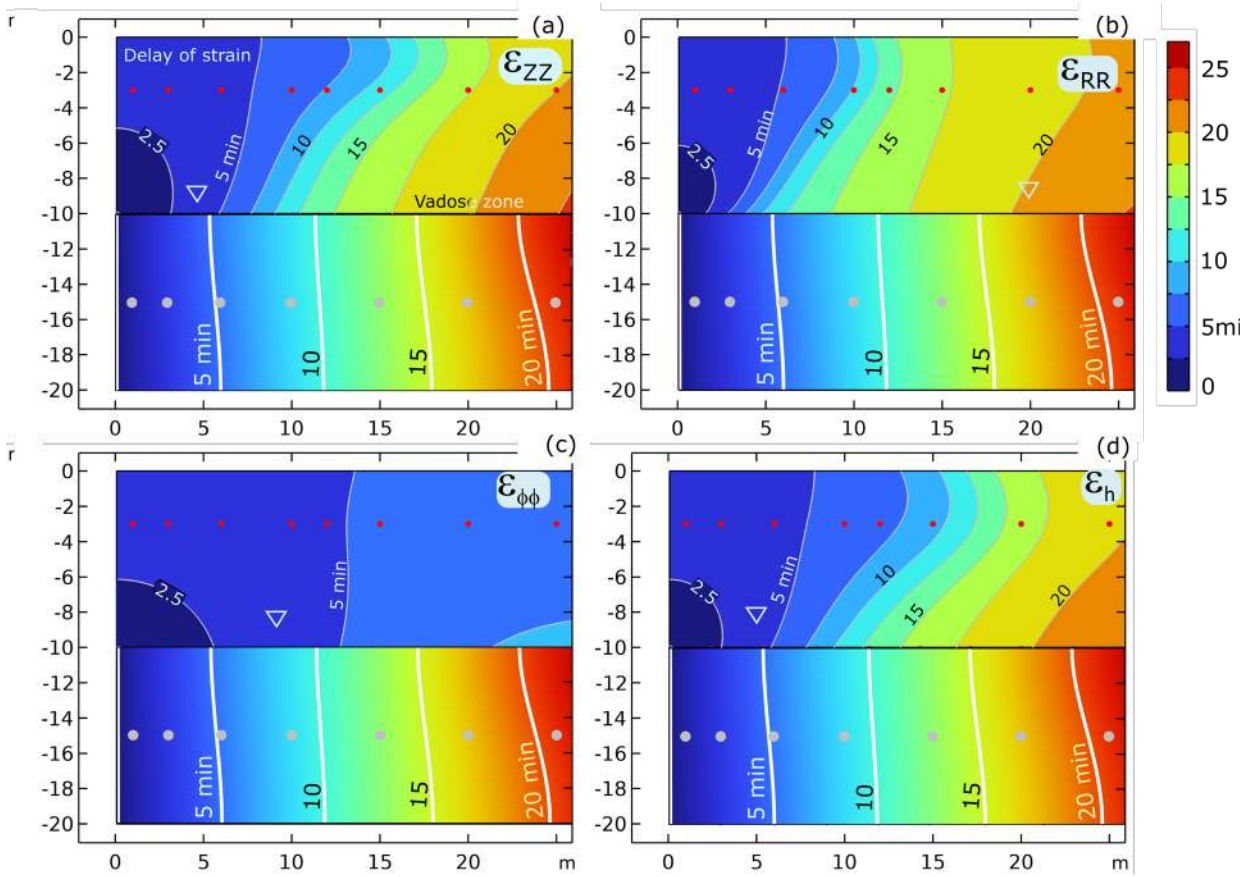

Figure 12-86. Delay of the pressure and different strain components in minutes behind the pressure at the well face for simulations that used a sinusoidal rate with a period of 30 min. Delay of strain in the vadose zone with filled contours, delay of pressure in aquifer with color flood. Dots are locations of time series in Figure 12-80.

12.10.2.2 Phase velocity

The patterns of the delays of the strain components are broadly consistent, but each one is distinct from the others (Figure 12-86). The delays generally increase upward and horizontally from a point in the vadose zone closest to the well screen (r = 0.1, z = -10m). This gives rise to upward phase velocities within a few meters of the well (Figure 12-86). Contours of the delays are roughly vertical in the range of 6 < r <10m, and they curve upward and outward away from the well at greater radial distances (Figure 12-86Figure 12-87).

The phase velocity of the strain is normal to the contours shown in Figure 12-86, and this supports the general conceptual model in Figure 12-84. The horizontal phase velocity of the pressure is 1.2 m/min, according to Figure 12-85. This is slightly larger than was observed in the field (0.9 m/min). The horizontal phase velocity determined using delay measurements of strain in the vadose zone will be within approximately +/- 20% of the phase velocity of the pressure. At 3 < r < 6 m from the well, the delay times of the strain at shallow depth are essentially the same as the delay times of the pressure in the underlying aquifer. This explains the similarity in delay times,

and D_h values, between the vertical strains at r = 4.4m and the pressure in the field data (Table 12-23Table 12-24).

The upward velocity of the ε_{zz} is approximately 3 m/min at r = 2m, and it increases to 6 to 9 m/min at r = 4m. It is downward at -0.6 m/min at r = 14m. The delay is slightly variable, but essentially independent of depth at r = 8m (Figure 12-87). Velocity is the inverse of the gradient in Figure 12-87, which implies that the phase velocity is large, and it changes sign at $r \sim$ 8m.

12.10.3 Implications

The simulations explain the field data and provide some insights into relationships between pressure and strain. In general, but the time delay of ε_{zz} and ε_h are similar (within 20%) of the delay time of the pressure in the underlying aquifer (Figure 12-85 and Figure 12-86). ε_{zz} can be measured using a strain ribbon and the CMPI technique, as we showed here. We expect that other methods of measuring strain with optical fibers, using distributed acoustic sensing, for example, could also be used with the strain ribbon to measure vertical strains in the vadose zone. It is feasible to measure ε_h using cylindrical strainmeters that are pushed into vertical borings made with a direct-push drilling rig and recovered after testing. This means that it should be straight-forward to measure ε_{zz} and ε_h.

The delay times of ε_{RR} and $\varepsilon_{\phi\phi}$ differ significantly from the underlying strain, so they would be less useful as surrogates for pressure. However, the relative magnitudes of the horizontal strains will be sensitive to the location and orientation of perturbations in the underlying pressure caused by aquifer heterogeneities. As a result, we expect that these components of the strain tensor will also be useful in characterizing aquifers during periodic well tests.

Although the delay times for ε_{zz} and ε_h are similar to the delay times for pressure in the underlying aquifer, the time are by no means the same. This is because the pressure propagates radially at approximately a uniform velocity, whereas the strain in the vadose zone follows a more circuitous route, propagating upward near the well, horizontally at mid distance and downward at a larger distance where the pressure in the underlying aquifer as largely decayed (Figure 12-84). Upward propagation causes the delay times of the strain to be less than the pressure close to the well (r < 3m in Figure 12-85). The strain speeds up and propagates faster than the pressure resulting in delay times that are less than pressure in the mid-distance. These effects occur because the vadose zone is deformed by the aquifer expanding both outward and upward when the pressure in the aquifer is increasing, and contracting inward and downward when the pressure is decreasing. These effects are manifested in patterns of different strain components that are complex (Figure 12-83), but that can be readily simulated using poroelastic analyses. This suggests that measurements of ε_{zz} and ε_h in the vadose zone during periodic well tests can be using directly with the analytical solutions of Streltsova or Rasmussen to provide an approximate estimate of D_h, and then numerical inversion of poroelastic simulations can be used to refine those estimates and potentially identify heterogeneities or other features not included in the analytical solutions.

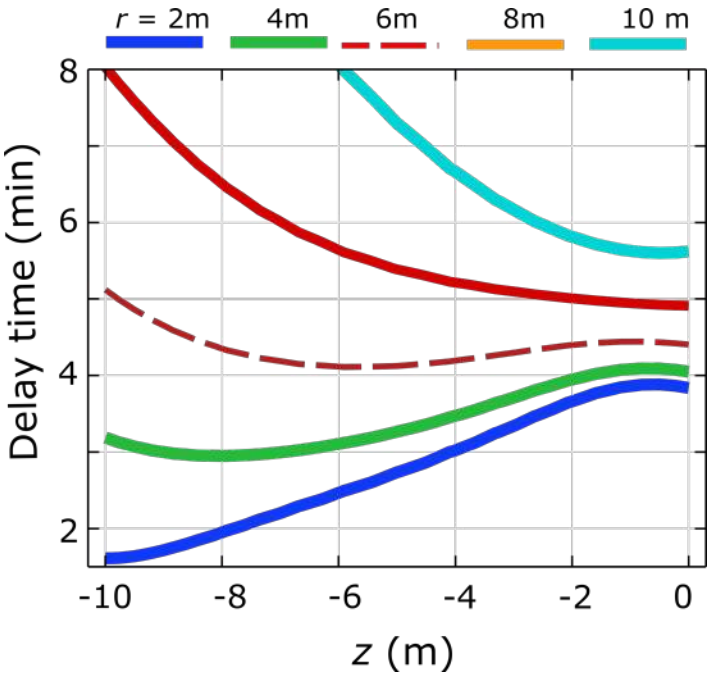

Figure 12-87. Delay of strain as function of depth along vertical lines at different radial distances (legend). Positive slope indicates strain advancing upward, negative indicates strain advancing downward. Phase velocity of the strain at r = 2 m is 2 m/min, and phase velocity at r = 14m is –0.6 m/min.

12.11 REFERENCES

Agnew, D. C. 2007. "Earth Tides." In Treatise on Geophysics, 163-195: Elsevier B.V.

Ajo-Franklin JB, Peterson J, Doetsch J and Daley TM (2013). High-resolution characterization of a CO2 plume using crosswell seismic tomography:Cranfield, MS, USA. Int J Greenhouse Gas Control 18:497–509.

Althen Sensors and Controls (2023). 500 Self-Leveling Borehole Tiltmeter (Lily) https://www.althensensors.com/sensors/inclinometers-tiltmeters/geotechnical- inclinometers/4740/500-self-leveling-borehole-tiltmeter-lily/.

Arts R, Eiken O, Chadwick A, Zweigel P, van der Meer L and Zinszner B (2004).

Bakhos, T., Cardiff, M., Barrash, W., & Kitanidis, P. K. (2014). Data processing for oscillatory pumping tests. Journal of Hydrology, 511, 310-319.Barker-Black 1984 solution in fractured rock.

Bakker, M. (2009). Sinusoidal pumping of groundwater near cylindrical inhomogenei-ties. Journal of Engineering Mathematics, 64(2), 131-143.

Ben Zekry, S., Lawrie, G., Little, S., Zoghbi, W., Freeman, J., Jajoo, A., ... & Azencott, R. (2012). Comparative evaluation of mitral valve strain by deformation tracking in 3D-echocardiography. Cardiovascular Engineering and Technology, 3, 402-412.

Bierschenk, W. H. 1963. Determining well efficiency by multiple step-drawdown tests. International Association of Scientific Hydrology Publication, 64, 493-507.

Black JH, Kipp KL Jr (1981). Determination of hydrogeological parameters using sinusoidal pressure tests: a theoretical appraisal. Water Resources Research 17(3):686-692.

Blais, R. (2023). Evaluating the Feasibility of Using Strain Measured During Sinusoidal-Rate Pumping Tests, MS Thesis [Master of Science]. Clemson University.

Blais, R., Murdoch, L. C., DeWolf, S., Germanovich, L. N., Hua, L., & Moak, R. (2020, December). Using Strain in the Vadose Zone During Sinusoidal-Rate Well Tests to Characterize an Aquifer. In AGU Fall Meeting Abstracts (Vol. 2020, pp. H062-0008).

Bouwer, H. (1989). The Bouwer and Rice Slug Test—An Update a. Groundwater, 27(3), 304-309.Bruggeman 1999.

Bouwer, H., and R.C. Rice (1976). A slug test for determining hydraulic conductivity of unconfined aquifers with completely or partially penetrating wells. Water Resour. Res. 12, no. 3: 423-428.

Bredehoeft, J. D. 1967. "Response of Well-Aquifer Systems to Earth Tides." Journal of Geo-physical Research (1896-1977) 72 (12): 3075-3087.

Butler Jr, J. J., & Healey, J. M. (1998). Relationship between pumping-test and slug-test pa-rameters: Scale effect or artifact?. Groundwater, 36(2), 305-312.Carr and van der Kemp 1969.

Butler, J.J., Jr. (1997). The Design, Performance, and Analysis of Slug Tests. Boca Raton, Lewis Publishers.

Butsch R, Brown AL, Bryans B, Kolb C and Hovorka S (2013). Integration of well-based subsurface monitoring technologies:Lessons learned at SECARB study, Cranfield, MS. Int J Greenhouse Gas Control 18:409–420.

Cardiff, M., & Barrash, W. (2015). Analytical and semi-analytical tools for the design of oscillatory pumping tests. Groundwater, 53(6), 896-907.

Cardiff, M., & Sayler, C. (2016). Strategies for avoiding errors and ambiguities in the analysis of oscillatory pumping tests. Journal of Hydrology, 540, 1016-1021.

Cardiff, M., Bakhos, T., Kitanidis, P., Barrash, W. (2013). Aquifer heterogeneity characteriza-tion with oscillatory pumping: sensitivity analysis and imaging potential. Water Resour. Res. 49 (9), 5395–5410.

Cartwright, D. E. and R. J. Tayler. 1971. "New Computations of the Tide-Generating Potential." Geophysical Journal International 23 (1): 45-73.

Cleveland, T., R. Bravo, and J. Rogers. 1992. "Storage Coefficients and Vertical Hydraulic Conductivities in Aquitards using Extensometer and Hydrograph Data." Ground Water 30 (5): 701-708.

Cooper Jr, H. H., & Jacob, C. E. (1946). A generalized graphical method for evaluating for-mation constants and summarizing well-field history. Eos, Transactions American Geo-physical Union, 27(4), 526-534.

Cooper, H. H., J.D. Bredehoeft, I.S. Papadopulos, and R. R. Bennett. 1965. "The Response of Well-Aquifer Systems to Seismic Waves." Journal of Geophysical Research (1896-1977) 70 (16): 3915-3926.

Cooper, Hilton H., J.D. Bredehoeft, and I.S. Papadopulos. 1967. "Response of a Finite-Diameter Well to an Instantaneous Charge of Water." Water Resources Research 3 (1): 263-269.

Costantino, O. L. (2021). Evaluating the Feasibility of Measuring and Analyzing Strain Caused by Changes in Barometric Pressure in the Vadose Zone (Clemson University).

Cutillo, P.A. and J.D. Bredehoeft. 2011. "Estimating Aquifer Properties from the Water Level Response to Earth Tides." Groundwater 49 (4): 600-610

Davis, S., F. Peterson, and A. Halderman. 1969. "Measurements of Small Surface Displace-ments Induced by Fluid Flow." Water Resources Research 5 (1): 129-138.

Dietz, D.N. 1943. "De Toepassing Van Invloedsfuncties Bij Het Berekenen Van De Verlaging Van Het Groundwater Ten Gevolge Van Wateronttrekking." Water 27 (6): 51 57.

Eden, R. N., & Hazel, C. P. (1973). Computer and graphical analysis of variable discharge pumping tests of wells. Institution of Engineers Australia.

FBGS. (2023). https://fbgs.com/technology/.

Ferris, J. G. (1952). Cyclic fluctuations of water level as a basis for determining aquifer transmissibility (No. Note 1). US Geological Survey.

Ferris, J. G., Knowles, D. B., Brown, R. H., & Stallman, R. W. (1962). Theory of aquifer tests (pp. 69-174). Denver, CO, USA: US Government Printing Office.

Fokker, P. A., Borello, E. S., Serazio, C., & Verga, F. (2012). Estimating reservoir heterogeneities from pulse testing. Journal of Petroleum Science and Engineering, 86, 15-26.

Fokker, P.A., E.S. Borello, F. Verga, and D. Viberti. 2018. "Harmonic Pulse Testing for Well Performance Monitoring." Journal of Petroleum Science and Engineering 162: 446-459.

Fokker, P.A., Renner, J., Verga, F. (2013). Numerical modeling of periodic pumping tests in wells penetrating a heterogeneous aquifer. Am. J. Environ. Sci. 9 (1), 1.

Fourier, J. B. J. (1822). Théorie analytique de la chaleur. Firmin Didot.

GEOPROBE. (2023). Macro-Core® MC5 Soil Sampling System (LWCR). https://geoprobe.com/tooling/macro-corer-mc5-soil-sampling-system-lwcr.

Haborak, K. G. (1999). Analytical solutions to flow in aquifers during sinusoidal aquifer pumping tests (Doctoral dissertation, University of Georgia).

Hack, J. T. (1982). Physiographic divisions and differential uplift in the Piedmont and Blue Ridge (No. 1265). USGPO.

Hantush, M. S. (1960). Modification of the theory of leaky aquifers. Journal of Geophysical Research, 65(11), 3713-3725.

Hantush, M. S. (1961). Aquifer tests on partially penetrating wells. Journal of the Hydraulics Division, 87(5), 171-195.

Hantush, M. S., & Jacob, C. E. (1955). Non-steady radial flow in an infinite leaky aquifer. Eos, Transactions American Geophysical Union, 36(1), 95-100.

Hantush, M.S. 1959. "Analysis of Data from Pumping Wells Near a River." Journal of Geo-physical Research (1896-1977) 64 (11): 1921-1932.

Hantush, M.S. 1964. Hydraulics of wells, in: Advances in Hydroscience, V.T. Chow (editor), Academic Press, New York, pp. 281-442.

Hollaender, F., Hammond, P. S., & Gringarten, A. C. (2002, September). Harmonic testing for continuous well and reservoir monitoring. In SPE Annual Technical Conference and Exhibition. OnePetro.

Horne, R.N. and A.J. Rosa. 1997. "Reservoir Description by Well Test Analysis using Cyclic Flow Rate Variation." SPE Formation Evaluation 12 (4): 247-254.

Hosseini, S. A., & Alfi, M. (2016). Time-lapse application of pressure transient analysis for monitoring compressible fluid leakage. Greenhouse Gases: Science and Technolo-gy, 6(3), 352-369.

Hovorka SD, Meckel TA and Treviño RH (2013). Monitoring a large-volume injection at

Hsieh, P. A., Bredehoeft, J. D., & Farr, J. M. (1987). Determination of aquifer transmissivity from Earth tide analysis. Water resources research, 23(10), 1824-1832.

Hua, L., X. Zhu, S. DeWolf, J. Lei, Q. Zhang, L. Murdoch, and H. Xiao. 2020. "Phase Demodulation by Frequency Chirping in Coherence Microwave Photonic Interferometry." IEEE Journal of Selected Topics in Quantum Electronics 27 (2): 1-9.

Hua, L., Y. Song, B. Cheng, W. Zhu, Q. Zhang, and H. Xiao. 2017. "Distributed Optical Fiber Sensing Based on Coherence-Length Gated Microwave Photonics Interferometry.".

Huang, C. S., Tsai, Y. H., Yeh, H. D., & Yang, T. (2019). A general analytical model for head response to oscillatory pumping in unconfined aquifers: effects of delayed gravity drainage and initial condition. Hydrology and Earth System Sciences, 23(3), 1323-1337.

Huling, S. G., & Weaver, J. W. (1991). Dense nonaqueous-phase liquids. Ground-water is-sue (No. PB-91-195974/XAB). Environmental Protection Agency, Ada, OK (United States). Robert S. Kerr Environmental Research Lab.

Hvorslev, M.J. 1951. Time lag and soil permeability in ground-water observations. U.S. Army Corps of Engineers Waterways Exper. Sta. Bull. No. 36.

HydroSOLVE, Inc. 2023. AQTESOLV. http://www.aqtesolv.com/.

Innovative Remediation Technologies, Inc. (2009). ISOC. https://www.innrt.com/isoc.html.

Istok, J. D., & Dawson, K. J. (1991). Aquifer testing: design and analysis of pumping and slug tests. CRC Press.

Jacob, C. E. (1940). On the flow of water in an elastic artesian aquifer. Eos, Transactions American Geophysical Union, 21(2), 574-586.

Jacob, C.E. (1947). Drawdown Test to Determine Effective Radius of Artesian Well. Trans. Am. Soc. Civ. Eng. 112, 1047–1070.

Jiao, J. J., & Tang, Z. (1999). An analytical solution of groundwater response to tidal fluctua-tion in a leaky confined aquifer. Water Resources Research, 35(3), 747-751.

Johnson, C. R., R. A. Greenkorn, and E. G. Woods. 1966. "Pulse-Testing: A New Method for Describing Reservoir Flow Properties between Wells." Journal of Petroleum Technology 18 (12): 1599-1604.

Kantha, L. 2006. "Time to Replace the Saffir-Simpson Hurricane Scale?" Eos, Transactions American Geophysical Union 87 (1): 3-6.

Kasich, J., M. Taylor, and C. Butler. 2018. Technical Guidance Manual for Hydrogeologic Investigations and Ground Water Monitoring: Pumping and Slug Tests.

Kruseman, G.P. and N. de Ridder. 1994. Analysis and Evaluation of Pumping Test Data. International Institute for Land Reclamation and Improvement : ILRI Publication. 2. ed., (completely rev.), reprinted ed. Vol. 47. Wageningen: ILRI.

Kuang, X., Jiao, J. J., Zheng, C., Cherry, J. A., & Li, H. (2020). A review of specific storage in aquifers. Journal of Hydrology, 581, 124383.

Kudryavtsev, S. M. 2004. "Improved Harmonic Development of the Earth Tide-Generating Potential." Journal of Geodesy 77 (12): 829-838.

Kuo, C. H. 1972. "Determination of Reservoir Properties from Sinusoidal and Multirate Flow Tests in One Or More Wells." Society of Petroleum Engineers Journal 12 (06): 499-507. doi:10.2118/3632-PA.

Malama, B., K.L. Kuhlman, R. Brauchler, and P. Bayer. 2016. "Modeling Cross-Hole Slug Tests in an Unconfined Aquifer." Journal of Hydrology 540: 784-796.

Mehnert, E., A. J. Valocchi, M. Heidari, S. G. Kapoor, and P. Kumar. 1999. "Estimating Transmissivity from the Water Level Fluctuations of a Sinusoidally Forced Well." Ground Water 37 (6): 855-860.

Melchior, P. J. and M. Toba. 1978. The Tides of the Planet Earth Elsevier Science & Technology.

Merritt, M. 2004. Estimating Hydraulic Properties of the Floridan Aquifer System by Analysis of Earth-Tide, Ocean-Tide, and Barometric Effects, Collier and Hendry Counties, Florida.

Micron Optics. (2023). FBG Sensors. http://micronoptics.ru/sensors_products.html.

Minitab. (2016). Understanding Analysis of Variance (ANOVA) and the F-test. https://blog.minitab.com/en/adventures-in-statistics-2/understanding-analysis-of-variance-anova-and-the-f-test

Moak, R., Murdoch, L. C., Thrash, C. J., Germanovich, L. N., DeWolf, S., & Jun, F. (2016, December). Characterizing Subsurface Deformation from Changes in Moisture Content during Infiltration Experiments. In AGU Fall Meeting Abstracts (Vol. 2016, pp. H23D-1577).

Moench, A. F. (1984). Double-porosity models for a fissured groundwater reservoir with frac-ture skin. Water Resources Research, 20(7), 831-846.

Murdoch, L. C., & Franco, J. (1994). The analysis of constant drawdown wells using instantaneous source functions. Water resources research, 30(1), 117-124.

Murdoch, L. C., Freeman, C. E., Germanovich, L. N., Thrash, C., & DeWolf, S. (2015). Using in situ vertical displacements to characterize changes in moisture load. Water Resources Research, 51(8), 5998-6016.

Murdoch, L. C., Germanovich, L. N., DeWolf, S. J., Moysey, S. M. J., Hanna, A. C., Kim, S., & Duncan, R. G. (2020). Feasibility of using in situ deformation to monitor CO2 storage. International Journal of Greenhouse Gas Control, 93, 102853. https://doi.org/10.1016/j.ijggc.2019.102853

Murdoch, L. C., Germanovich, L. N., Roudini, S., DeWolf, S. J., Hua, L., & Moak, R. W. (2021). A Type-Curve Approach for Evaluating Aquifer Properties by Interpreting Shal-low Strain Measured During Well Tests. Water Resources Research, 57(9), e2021WR029613.

Murdoch, L. C., Richardson, J. R., Tan, Q., Malin, S. C., & Fairbanks, C. (2006). Forms and sand transport in shallow hydraulic fractures in residual soil. Canadian Geotechnical Journal, 43(10), 1061-1073.

Murdoch, L. C., Scott, D. W., Germanovich, L., Hanna, A., Moak, R., & Moysey, S. (2019). Characterizing and interpreting the in situ strain tensor during CO2 injection (p. 252). Final Report for DOE Project DE-FE 0023313. https://10.2172/1529100

Murdoch, L.C., C.E. Freeman, L.N. Germanovich, C. Thrash, and S. DeWolf. 2015. "Using in Situ Vertical Displacements to Characterize Changes in Moisture Load." Water Resources Research 51 (8): 5998-6016.

Murdoch, L.C., J.R. Richardson, C. Fairbanks, S.C. Malin, and Q.Tan. 2006. "Forms and Sand Transport in Shallow Hydraulic Fractures in Residual Soil." Canadian Geotechnical Journal 43 (10): 1061-1073.

Nelson, A.E., Horton, J.W., and Clarke, J.W. 1998. Geologic map of the Greenville quadrangle, South Carolina, Georgia and North Carolina. US Geological Survey, Miscellaneous Investigation Series Map I-2175. Scale 1 : 250 000. 13 pp.

Neuman, S. P. (1974). Effect of partial penetration on flow in unconfined aquifers considering delayed gravity response. Water resources research, 10(2), 303-312.

NOAA. "Where is the Highest Tide?", https://oceanservice.noaa.gov/facts/highesttide.html.

Onset. (2023). Onset HOBO and InTemp Data Loggers. https://www.onsetcomp.com/.

Patterson, J., & Cardiff, M. (2021). Period Dependence in Flow Properties of a Frac-tured Bedrock Aquifer: Investigating Heterogeneity, Fluid Exchange, and Poroelasiticity as Potential Sources. In AGU Fall Meeting Abstracts (Vol. 2021, pp. H42E-06).

Plunkett, G. (2021). A Novel Technique for Distributed Measuring of Strain in the Vadose Zone (Doctoral dissertation, Clemson University).

Rabinovich, A., Barrash, W., Cardiff, M., Hochstetler, D. L., Bakhos, T., Dagan, G., & Kitanidis, P. K. (2015). Frequency dependent hydraulic properties estimated from oscil-latory pumping tests in an unconfined aquifer. Journal of Hydrology, 531, 2-16.

Ramirez A and Foxall W, (2014). Stochastic inversion of InSAR data to assess the

Rasmussen, T., K. Haborak, and M. Young. 2003a. "Estimating Aquifer Hydraulic Properties using Sinusoidal Pumping at the Savannah River Site, South Carolina, USA." Hydrogeology Journal 11 (4): 466-482.

Rasmussen, T., K. Haborak, and M. Young. 2003b. "Estimating Aquifer Hydraulic Properties using Sinusoidal Pumping at the Savannah River Site, South Carolina, USA." Hydrogeology Journal 11 (4): 466-482.

Renner, J., Messar, M. (2006) Periodic pumping tests. Geophys. J. Int. 167 (1), 479–493.

Rice, J. A. (2006). Mathematical statistics and data analysis. Cengage Learning.

Riffenburgh, R. H. (2012). Statistics in medicine. Academic press.

Riley, F. 1987. "Developments in Borehole Extensometry." International Journal of Rock Mechanics and Mining Sciences & Geomechanics Abstracts 24 (5): 169-186.

Robson, S. G. and E. R. Banta. 1970. "Determination of Specific Storage." Ground Water 28: 686-674.

Rodrigues, R., Betelu, S., Colombano, S., Tzedakis, T., Masselot, G., & Ignatiadis, I. (2020). In situ chemical reduction of chlorinated organic compounds. Environmental Soil Remediation and Rehabilitation: Existing and Innovative Solutions, 283-398.

Rojstaczer, S. 1988a. "Determination of Fluid Flow Properties from the Response of Water Levels in Wells to Atmospheric Loading." Water Resources Research 24 (11): 1927-1938.

Rojstaczer, S. 1988b. "Intermediate Period Response of Water Levels in Wells to Crustal Strain: Sensitivity and Noise Level." Journal of Geophysical Research: Solid Earth 93 (B11): 13619-13634.

Rojstaczer, S. and D. Carr Agnew. 1989. "The Influence of Formation Material Properties on the Response of Water Levels in Wells to Earth Tides and Atmospheric Loading." Journal of Geophysical Research 94 (B9): 12403-12411.

Rorabaugh, M. I. (1953). Graphical and theoretical analysis of step-drawdown test of artesian well. In Proceedings of the American Society of Civil Engineers (Vol. 79, No. 12, pp. 1-23). ASCE.

Rosa, A. J., & Horne, R. N. (1997). Reservoir description by well test analysis using cyclic flow rate variation. SPE Formation Evaluation, 12(04), 247-254.

Rotzoll, K., A. El-Kadi, and S. B. Gingerich (2008). Analysis of an Unconfined Aquifer Subject to Asynchronous Dual-Tide Propagation. Ground Water 46 (2): 239-250.

Shakiba, M., & Hosseini, S. A. (2016). Detection and characterization of CO2 leakage by multi-well pulse testing and diffusivity tomography maps. International Journal of Green-house Gas Control, 54, 15-28.

Sheahan, N. T. (1971). Type-curve solution of step-drawdown test. Groundwater, 9(1), 25-29.

Smith-Jones, A. (2023). Evaluation of Zero-Net-Rate Pumping Tests [Master of Science]. Clemson University.

Strang, G. (1994). Wavelets. American Scientist, 82(3), 250-255.

Streltsova, Tatiana D. Well Testing in Heterogeneous Formations. Wiley, 1988.

Sun, A. Y., Lu, J., & Hovorka, S. (2015). A harmonic pulse testing method for leakage detec-tion in deep subsurface storage formations. Water Resources Research, 51(6), 4263-4281.

Theis, C.V. 1935. The relation between the lowering of the piezometric surface and rate and duration of discharge of a well using ground water storage. Transactions of the Ameri-can Geophysical Union 16, 519–524.

Townley, L. R. (1995). The response of aquifers to periodic forcing. Advances in water Resources, 18(3), 125-146.

Trefry, M. G. (1999). Periodic forcing in composite aquifers. Advances in Water Re-sources, 22(6), 645-656.

Valois, R., Rau, G. C., Vouillamoz, J. M., & Derode, B. (2022). Estimating hydraulic properties of the shallow subsurface using the groundwater response to Earth and atmospheric tides: a comparison with pumping tests. Water Resources Research, 58(5), e2021WR031666.

Van der Kamp, G., & Gale, J. E. (1983). Theory of earth tide and barometric effects in porous formations with compressible grains. Water Resources Research, 19(2), 538-544.

Vandenberg, A. 1976. Tables and Type Curves for Analysis of Pump Tests in Leaky Parallel-Channel Aquifers. Ottawa: Environment Canada, Inland Waters Directorate, Water Resources Branch.

Vandenberg, A. 1977. "Type Curves for Analysis of Pump Tests in Leaky Strip Aquifers." Journal of Hydrology 33 (1): 15-26.

Wang, H.F. 2000. Theory of Linear Poroelasticity with Applications to Geomechanics and Hydrogeology Princeton University Press.

Xing, Y., Liu, Q., Hu, R., Gu, H., Taherdangkoo, R., Yang, H., & Ptak, T. (2022). A general numerical model for water level response to harmonic disturbances in aquifers considering wellbore effects. Journal of Hydrology, 609, 127678.

Zhou, Y., & Cardiff, M. (2017). Oscillatory hydraulic testing as a strategy for NAPL source zone monitoring: Laboratory experiments. Journal of contaminant hydrology, 200, 24-3

CHAPTER THIRTEEN

EVALUATING STRAIN CAUSED BY AIR PRESSURE CHANGES IN THE VADOSE ZONE

Contents

13.1 Abstract 13-2
13.2 Introduction 13-2
13.3 Distributed sensing using optical fibers with microwave photonics 13-4
13.3.1 Architecture and theoretical basis of CMPI 13-4
13.3.2 CMPI for strain measurement 13-8
13.3.3 CMPI system hardware 13-10
13.3.4 System specification tradeoffs and limitations 13-11
13.4 Strains caused by small fluctuations in air pressure measured by CMPI 13-12
13.4.1 Experimental Methods 13-12
13.4.2 Results 13-15
13.5 Discussion 13-27
13.6 Conclusion 13-30
13.7 References 13-31

EVALUATING STRAIN CAUSED BY AIR PRESSURE CHANGES IN THE VADOSE ZONE

13.1 ABSTRACT

Distributed strain measurements appear to hold significant potential for monitoring hydrologic processes. Coherence-length-gated Microwave Photonics Interferometry (CMPI) is a distributed sensing technique that measures strain in an optical fiber by reading optical interference phase changes in the microwave domain. The technique provides 10nε resolution when cm spatial resolution is applied. CMPI was used to measure the strain caused by small periodic variations in air pressure (25 Pa amplitude and 4 Hz) in a sand-filled laboratory column used to represent barometric loading in the vadose zone. The strain varied as a periodic function with an amplitude that decreased and a phase that increased with depth. The distribution of amplitude and phase of the strain depended on the water saturation, permeability, and presence of a barrier at the top of the sand. A theoretical analysis suggests that the air pressure diffusivity estimated from pressure data is similar to the diffusivity estimated from the distributed strain. These results indicated that the CMPI distributed strain measurement system could be used to improve monitoring and characterization of the vadose and underlying saturated zone.

13.2 INTRODUCTION

Understanding changes in water content and pore pressure in geologic media is a central theme to much of hydrology and related fields, and this has motivated the development of a wide range of monitoring methods (Dobriyal et al., 2012; Lekshmi et al., 2014). The typical approach is to use a sensor that measures a local property, such as transducer to measure the fluid pressure or a capacitance gauge to measure dielectric properties. Changes in pore pressure or water content deform porous media, and measurements of this deformation have potential as an alternative monitoring signal (Murdoch et al., 2020). One example of this approach is the use of Interferometric Synthetic Aperture Radar (InSAR) or Global Positioning System (GPS) to measure deformation at the ground surface caused by fluid pumping or injection in underlying aquifers or reservoirs (Khakim et al., 2012; Vasco et al., 2022; Galloway & Burbey, 2011; Monfared & Rothenburg, 2011).

It is also possible to measure strain in the subsurface using discrete or distributed sensors (Murdoch et al., 2020b). The deformation that can be resolved by subsurface sensors is many orders of magnitude higher than InSAR or GPS, providing a mechanism for detecting effects of small changes in pressure or water content. Distributed strain sensors typically involve uniaxial measurements along an optical fiber (Becker et al., 2017, 2023; Sun et al., 2020; Xue & Hashimoto, 2017a), although twisting multiple fibers together can provide some strain components normal to the axis of the fibers (Murdoch et al., 2020b). Optical fiber can also be packaged in discrete instruments to measure multiple components of the strain tensor with high precision (Murdoch et al., 2023).

Many applications have been focused on evaluating strains cause by pressure changes in the saturated zone. Well tests used to characterize aquifers or reservoirs cause tilt or strain that can be measured and inverted to help the characterization process (Becker et al., 2017; Cappa et al., 2007; Fabian & Kümpel, 2003; Guglielmi et al., 2014; Hisz et al., 2013; Jin et al., 2021;

Karasaki et al., n.d.; Murdoch et al., 2020a; Schweisinger et al., 2009, 2011; Sun et al., 2020, 2021; Svenson et al., 2008; Vasco et al., 2001; Xue & Hashimoto, 2017b). Leaks of CO_2 may also cause a strain signal that could be used to help locate the leak and characterize its severity (Rutqvist & Tsang, 2002; Xue & Hashimoto, 2017b).

Deformation also occurs in the vadose zone in response to hydrologic processes or surface loads (Keller et al., 2012; Murdoch et al., 2015). Changes in pore pressure in an underlying aquifer will cause characteristic patterns of deformation in the vadose zone (Murdoch et al., 2015). Evaluating small strains in the subsurface can be complicated by changes in barometric pressure. An increase in barometric pressure acting on the ground surface causes negative vertical strain (compression), but an increase in the pressure in pore space cause a positive strain (tension). The net observed strain is a combination of these two offsetting effects. Changes in water content will increase the weight of shallow soils, compressing the underlying formation (Marin et al., 2010; Van Der Kamp & Schmidt, 1997), and is will also affect the strain by altering the air phase relative permeability.

We measured vertical strain in the vadose zone with the intent of estimating changes in water content in overlying soils due to rainfall or evaporation (Murdoch et al., 2015). We found that changes in water content correlated with strains in underlying soil, but the effect was complicated by changes in barometric pressure. Our initial approach was to account for changes in barometric pressure by assuming it only acted at the ground surface. This explained some effects, but the correlation between barometric pressure and strain changed with time, and this complicated the interpretation. The change in correlation between barometric pressure and strain in the subsurface appeared to be a result of changes in the air pressure diffusivity caused by changes in water content. Barometric pressure could diffuse relatively deep into the subsurface when soils are dry, but pressure diffusion was negligible in wet soils because the gas phase pressure diffusivity (and relative permeability) was essentially zero. In a related process, diffusion of air pressure through the vadose zone is widely recognized to affect water levels in wells in unconfined aquifers (Quilty & Roeloffs, 1991; Rasmussen & Crawford, 1997; Rojstaczer, 1988; Rojstaczer & Riley, 1990; Weeks, 1979; Yusa, 1969).

This motivated us to seek a method that could measure the strain caused by barometric pressure fluctuations as a function of depth. Our initial motivation was to improve the interpretation of the strain data in Murdoch et al (2015), but this raised an even more intriguing possibility: If the strain caused by barometric pressure fluctuations was affected by moisture content, then perhaps it could be used to monitor moisture content changes in the vadose zone? This would have important applications in hydrology, but it would require measuring small, distributed strains with high spatial and temporal resolution (nε strain resolution with cm spatial resolution and 100 Hz sampling). Those measurement requirements exceeded capabilities of available technology at the time, so we evaluated the feasibility of developing a new distributed strain sensing technique using microwave photonics (Hervás et al., 2017; Hua et al., 2017).

The objective of this chapter is to describe a microwave photonics technique for measuring distributed strain using optical fibers with applications to hydrologic sensing. The first part of the chapter describes the optical sensing method, named Coherence-length-gated Microwave Photonics Interferometry (CMPI)(Hua et al., 2017, 2021, 2022, 2023; Zhu et al., 2021). The method provides high-sensitivity measurements by recording optical interference signals from time-multiplexed interferometers in the microwave domain. This is followed by a section

describing experiments where the CMPI method was used to measure small strains caused by changes in air and water pressure in a laboratory column configured like the vadose zone. This section is based on Costantino (2023) We also describe a field application of the CMPI system used to characterize strain during a well test, which is based on Blais (2023).

13.3 DISTRIBUTED SENSING USING OPTICAL FIBERS WITH MICROWAVE PHOTONICS

Microwave photonics modulates light in the microwave band and then it synchronizes the optical detection system with the microwave modulation frequency (Hervás et al., 2017). As a result, the system has a high SNR and thus an improved detection limit. Microwave photonics-based sensing technologies have been demonstrated to measure temperature(Huang et al., 2015; Tian et al., 2022), strain (Hua et al., 2015), and displacement,(Dong et al., 2018 Hou et al., 2022), among others. Due to their extensive measurement range and relatively low implementation cost, microwave photonics sensing technologies have emerged as promising contenders for detecting hydrologic and geophysical processes (Bogris et al., 2022; Dauson et al., 2022).

The phase of the microwave-modulated light can be measured and Fourier transformed to find the time-of-arrival information for distributed sensing. The highly stable microwave phase determines locations along the signal path and thus enables a measurement range of more than 10 km (Clement et al., 2019). Frequency modulation in the GHz bandwidth enables spatial resolution in the cm range(Huang et al., 2014). Distributed systems based on this approach have been developed for interrogating Rayleigh scattering (Liehr et al., 2010), fiber Bragg grating (FBG) arrays(Cheng et al., 2015; Clement Bellido et al., 2018; Ricchiuti et al., 2014), and interferometers(Hua et al., 2017; Huang et al., 2014; Wu et al., 2021; C. Zhu & Huang, 2023).

The CMPI method provides high-sensitivity sensing by recording optical interference signals from time-multiplexed interferometers in the microwave domain. The coherence length of the light source is carefully chosen or controlled to eliminate crosstalk, or gate the signal between adjacent interferometers such that distributed sensing can be achieved. A frequency-time joint method is used to separate interferometers in the time domain. As a result, a maximum measurable frequency of tens of kilohertz for distributed strain sensing can be obtained(Hua, et al., 2021). The CMPI interrogation mechanism can be combined with low-coherence interferometry (LCI) to achieve fully distributed sensing(X. Zhu et al., 2021).

The following section outlines the components and architecture of the CMPI system along with the theoretical basis of the method. It describes how the CMPI method acquires signals from distributed interferometers. The next section outlines the approach for determining strain from the interferometer data, and in particular, it describes how CMPI can measure strain from static to acoustic frequencies. The section concludes with a description of the CMPI performance characteristics and trade-offs affecting spatial resolution, number of sensing units, strain resolution, frequency constraints, and other characteristics.

13.3.1 Architecture and theoretical basis of CMPI

A typical CMPI system includes a microwave source, a vector microwave detector, a light source, an electro-optical modulator, a photodetector (PD), and distributed sensors formed by interferometers (Fig. 1a). A continuous-wave (CW) laser with a center frequency of ω is used as

the light source. The light intensity is modulated by a microwave signal. The light launches into an optical fiber sensing network and is reflected by reflectors with respective time delays τ. Any two reflections that have a lag (τ_{k2}-τ_{k1}) much smaller than the coherence time of the laser produce optical interference, so the responsive light paths form an interferometer IF_k. Light reflections are injected into a PD, which converts the light power into electric voltage and sends it back to the vector microwave detector. The frequency of the microwave signal is swept over a designed range. At each modulation frequency Ω, synchronized detection is conducted, and the amplitude variation and phase shift of the modulation envelope is measured.

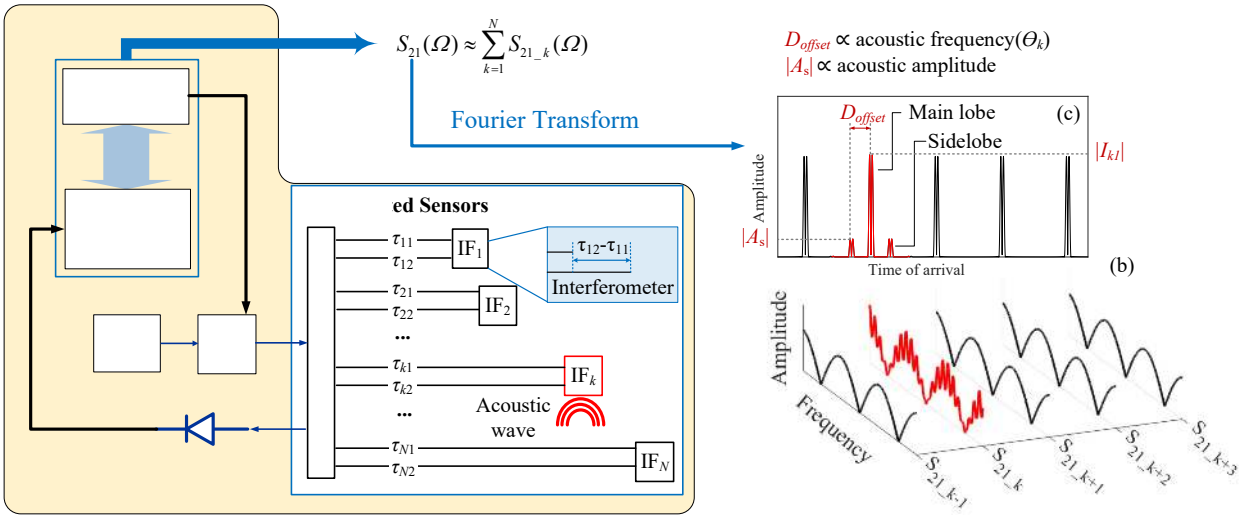

Figure 1 (a) Schematic of the CMPI system for distributed strain sensing (DDS) and distributed acoustic sensing (DAS). PD: Photodetector, EOM: electro-optic modulator, CW laser: continuous-wave laser. (b) The amplitude of the decomposed frequency domain signal from each interferometer. (c) The amplitude of the time domain signal.

The optical path difference (OPD) for each interferometer IF_k (k =1, 2.., N) is designed to be much smaller than the coherence length of the light source (Lc); the separation distance between adjacent interferometers is designed to be much larger than Lc. Therefore, the optical interference only occurs within each interferometer, and it is negligible among different interferometers. The complex frequency response of the system S_{21} can be approximately expressed as

$$S_{21}(\Omega) \approx \sum_{k=1}^{N} S_{21_k}(\Omega), \quad (1)$$

where $S_{21_k}(\Omega)$ is the frequency response from the kth interferometer, which is expressed as

$$S_{21_k}(\Omega) = m\begin{bmatrix}\left(A_{k1}{}^2 + A_{k1}A_{k2}\cos\Delta\phi_k\right)e^{-j\tau_{k1}\Omega} \\ +\left(A_{k2}{}^2 + A_{k1}A_{k2}\cos\Delta\phi_k\right)e^{-j\tau_{k2}\Omega}\end{bmatrix}, \quad (2)$$

where m is a constant decided by the modulation depth of the electro-optic modulator (EOM); A_{k1} and A_{k2} are the amplitudes of the two reflected waves; $\Delta\phi_k$ is the optical phase difference between the two waves. When the interference phase of the kth interferometer varies sinusoidally as a function of time with frequency Θ_k, amplitude δ_k , and the initial phase Φ_0, we can express it as

$$\Delta\phi_k = \Delta\phi_{k_static} + \delta_k cos(\Theta_k t + \Phi_0), \tag{3}$$

where $\Delta\phi_{k_static}$ is a constant within each S_{21} measurement window; $\delta_k cos(\Theta_k t + \Phi_0)$ is the dynamic phase, and t is the time variable. Assume the microwave modulation frequency is linearly scanned from Ω_{start} with a step of $\Delta\Omega$ and a constant sampling time Δt, we can express t as

(4)

When $\delta_k \ll 1$, $\cos\Delta\phi_k$ can be simplified through Fourier-Bessel expansion and linear approximation and expressed as

$$\cos\Delta\phi_k \approx cos\,\Delta\phi_{k_{static}} - \delta_k sin\,\Delta\phi_{k_{static}}\, cos\left(\frac{\Theta_k \Delta t}{\Delta\Omega}\Omega + \Phi_{cons}\right), \tag{5}$$

where

$$\Phi_{cons} = \Phi_0 - \frac{\Theta_k \Delta t}{\Delta\Omega}\Omega_{start}. \tag{6}$$

Substitute Eq. 5 into Eq. 2. The result indicates the amplitude of the microwave interferogram S_{21_k} is modulated by a sinusoidal signal that has a frequency of $\frac{\Theta_k \Delta t}{\Delta\Omega}$ as illustrated in Fig. 1 b . The inverse Fourier transform of $S_{21}(\Omega)$ is expressed as

$$F(t_z) = m\sum_{k=1}^{N} F_k(t_z), \tag{7}$$

which includes 'Static' and 'Dynamic' components as

$$F_k(t_z) = \{I_{k1}\delta(t_z - \tau_{k1}) + I_{k2}\delta(t_z - \tau_{k2})\}_{\text{Statistic}}$$
$$-\begin{Bmatrix} A_s\delta(t_z - \tau_{k1} + D_{offset}) + A_s{}^*\delta(t_z - \tau_{k1} - D_{offset}) \\ +A_s\delta(t_z - \tau_{k2} + D_{offset}) + A_s{}^*\delta(t_z - \tau_{k2} - D_{offset}) \end{Bmatrix}_{\text{Dynamic}} \tag{8}$$

where

$$I_{k1(2)} = {A_{k1(2)}}^2 + A_{k1}A_{k2}\, cos\, \Delta\phi_{k_static} \quad (9.a)$$

$$A_s = \delta_k A_{k1}A_{k2}\, sin\, \Delta\phi_{k_static}\, e^{j\Phi_{cons}};\ \text{and}\ \ D_{offset} = \Theta_k \frac{\Delta t}{\Delta\Omega} \quad (9.b)$$

The 'Static' component in Eq. 8 includes two time-pulses (main lobes) that are generated by the two reflected waves from interferometer IF$_k$, and they are centered at $\tau_{k1}$and τ_{k2}, respectively. The amplitude of the main lobe $|I_{k1(2)}|$ is determined by the average interference phase $\frac{L_k\omega}{c}$ within the S_{21} measurement window.

The 'Dynamic' component is formed by time pulses generated by the dynamic interference changes. Those pulses occur at both sides of the respective main lobes (side lobe, Fig. 1c). The offset between a side lobe and the corresponding main lobe (D_{offset}) is proportional to the acoustic frequency Θ_k with a scaling coefficient . The amplitude of the dynamic interference phase change δ_k is proportional to the amplitude of the sidelobes $|A_S|$.

The average interference phase can be calculated using the chirp effect of the EOM to perform quadrature-phase demodulation (Hua, et al., 2021). This is done by tuning the EOM bias to add opposite phase shifts of π/4 to the optical interference phase, so the peak values of the two main lobes are in quadrature as and . The standard quadrature-phase demodulation method can be used to calibrate the conic coefficients (${A_{k1}}^2$,${A_{k2}}^2$, $A_{k1}A_{k2}$, and the quadrature error) and calculate the interference phase(Požar et al., 2011).

$S_{21_k}(\Omega)$ can be extracted from $S_{21}(\Omega)$ through Fourier transform of the gated time-domain signal as

$$S_{21_k_g}(\Omega) = \mathcal{F}[F(t_z)g_k(t_z)]. \quad (11)$$

where $g_k(t_z)$ is a time-domain gate function that selects the time pulses generated by the kth interferometer. The temporal signal can be reconstructed by applying a high-pass filter to $\left|S_{21_k_g}(\Omega)\right|$. The time is linearly converted from Ω using Eq. 4, and the amplitude is also corrected by using the calculated interference phase.

The individual reflected wave from one interferometer cannot be resolved in the time domain when the microwave bandwidth becomes small. Consequently, Eq. 8 can be approximated as

$$F_k(t_z) \approx \{(I_{k1} + I_{k2})\delta(t_z - \overline{\tau_k})\}_{\text{Static}}$$

$$-\left\{2A_s\delta\left(t_z - \overline{\tau_k} + D_{offset}\right) + 2{A_s}^*\delta\left(t_z - \overline{\tau_k} - D_{offset}\right)\right\}_{\text{Dynamic}} \quad (12)$$

where .

13.3.2 CMPI for strain measurement

CMPI-distributed sensors are created with cascaded weak reflectors in single-mode optical fiber(SMF). Any two reflectors with a separation distance smaller than the coherence length of the light source (Fig. 2a) form an intrinsic Fabry-Perot interferometer (IFPI). The strain applied to the IFPI changes the distance between the reflector pair and changes the interference phase, which is expressed as(Butter & Hocker, 1978)

$$d\Delta\phi_k = \frac{2n\omega(1-P_{eff})}{c}\Delta l_k \varepsilon \quad (13)$$

where c is the speed of light, n is the refractive index of the fiber, ω is the frequency of the optical light, P_{eff} is the effective strain-optic coefficient, and Δl_k is the cavity length of IFPI. Static strain changes can be measured by monitoring the static interference phase change. The sensitivity of the static strain is $\frac{2n\omega(1-P_{eff})}{c}\Delta l_k$, which is linearly proportional to Δl_k. Dynamic strain results in an interference phase change at the strain change frequency, which can be calculated from the $D_{_offset}$. The amplitude of the dynamic strain can be calculated using A_s.

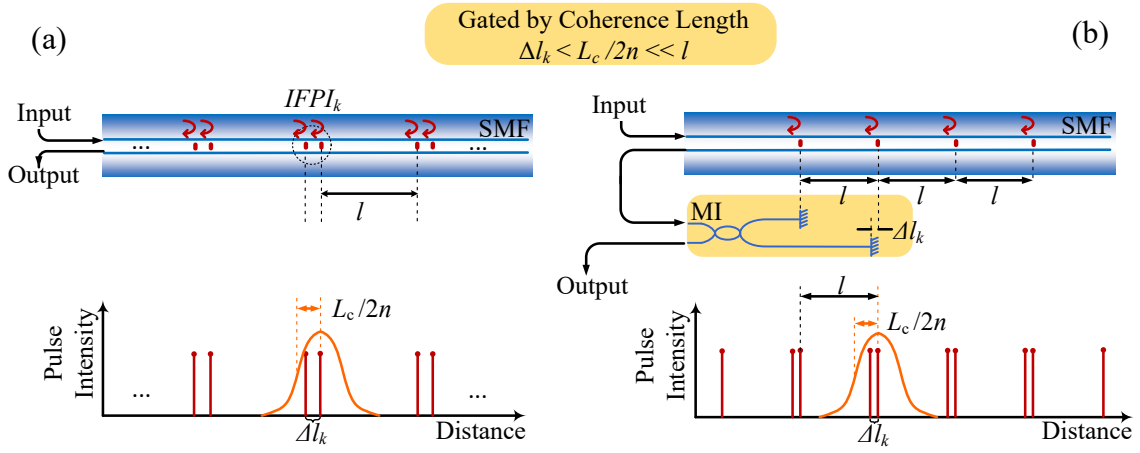

Figure 2. Schematic of the interferometers formed by cascaded weak reflectors (red dots) in optical fiber (blue bad). (a) Cascaded IFPIs with a separation distance of l. (b) Low-coherence interferometry from a weak in-fiber reflector array and a local Michelsen interferometer (MI). L_c is the coherent length of the light source, n is the refractive index of the optical fiber

CMPI provides high strain sensitivity and a large dynamic frequency measurement range. A set of lab tests has been performed to demonstrate strain sensing using an array of weak reflectors in optical fiber. In one setup, a weak reflector array was pre-strained and fixed on two linear translation stages. Strains were applied to the sensor array by moving the stage axially. Results show that the interference phase increases linearly as a function of the applied strain. The characterized static strain resolution was 0.6 με for a 1.5 cm cavity IFPI sensor, and the resolution increased to 10^{-8}ε when the cavity length was 1m (Hua et al., 2017; Hua, et al., 2021). In another setup, the fiber reflector array was wrapped around a piezoceramic cylinder (PCC), which was driven by a waveform generator to create acoustic signals. Acoustic signals of frequency up to 15.6 kHz were detected. The experimental results show that the sensing system

can locate an acoustic source. The recovered acoustic signals match the excitation signals in frequency, amplitude, and phase (Hua et al., 2021).

One major concern is the crosstalk among CMPI sensors. To avoid crosstalk the separation between the IFPIs needs to be larger than the coherence length, as illustrated in Fig. 2. Therefore, the regions between adjacent IFPIs are insensitive to the strain, and those regions are so-called dark zones. Dark zones reduce the number of sensor units, increase the cost of the sensor array, and make the sensor package complicated.

Low-coherence interferometry has been adapted into the original CMPI system to tackle the dark zone problem. Low-coherence interferometry (LCI) was originally used for absolute remote measurement of displacement (Rao & Jackson, 1996), in which a local receiving interferometer (LRI) is connected in-line with the remote sensing interferometer. The OPD of LRI is adjusted to match that of the sensing interferometer within the coherence length of the source, such that the interference occurs at the output of the LRI.

A local Michelson interferometer (MI) is implemented as the LRI in the CMPI architecture (Fig. 2). Cascaded IFPIs are formed by two weak reflectors with a similar cavity length, l. The cavity length is designed to match the OPD of the MI, and Δl represents the maximum matching deviation. The coherent length of the light source is larger than the maximum matching deviation and much smaller than the cavity length (). The interference occurs between the pair of lightwaves: one reflected by the first reflector and the long arm of the MI; the other reflected by the second reflector and the short arm of the MI. As such, the OPD and the separation distance of these combined interferometers are still Δl and l. Dark zones along the sensing fiber are eliminated using this approach. If there are N weak reflectors along the fiber, this configuration creates N-1 low-coherent interferometers. The relationship between interference phase change and the applied strains becomes

$$\mathrm{d}\Delta\phi_k = \frac{2n\omega(1-P_{eff})}{c} l\varepsilon \qquad (14)$$

Here, the local MI, as a LRI, is used to enable the IFPIs, which have a similar cavity length as the arm length difference of the MI. As such, we can also increase the arm length difference of the MI to il, where i is an integer, so the IFPIs with a cavity length of il are enabled. The relationship between interference phase change and the applied strains becomes

$$\mathrm{d}\Delta\phi_{k_i} = \frac{2n\omega(1-P_{eff})}{c} il\varepsilon \qquad (15)$$

Equations 14 and 15 indicate that the strain sensitivity is proportional to the MI cavity length. Consequently, the number of sensors decreases to N-i. MI works as a low pass filter to enable the average strain reading over the MI cavity length. The spatial resolution is always decided by the separation between the adjacent reflectors. One can use this feature to trade-off the system specs in terms of the number of sensing units, cutoff spatial frequency, and strain sensitivity.

13.3.3 CMPI system hardware

Hardware for the CMPI system includes three primary components, an interrogator, a reference Michelson Interferometer and a sensing fiber (Fig. 4). A single longitude mode of the F-P laser is filtered out by a bandpass filter (BPF1) and used as the light carrier. The selected mode has a center wavelength of 1543 nm and a coherence length of 6 cm. The light was intensity-modulated by a microwave signal via an EOM (Lucent, X2623Y). The modulation signal was generated by a vector network analyzer (VNA). The bias voltage of the EOM was provided by an external DC power supply. An inline polarization controller (Thorlabs, US) was used to optimize the modulation depth of the EOM. The microwave-modulated light output from the EOM was first amplified by an Erbium-doped fiber amplifier 1 (EDFA1) and then launched into the distributed sensors. Reflected signals from the distributed fiber sensors were then coupled into the MI, which was made of a coupler and two Faraday rotation mirrors (FRMs). The MI was well confined and stabilized in a black box using epoxy to minimize the effects of environmental vibrations. The output light was amplified by the EDFA2 and filtered by the BPF2. A high-speed photodetector detected the filtered signal and passed over the converted electrical signal to VNA through port 2.

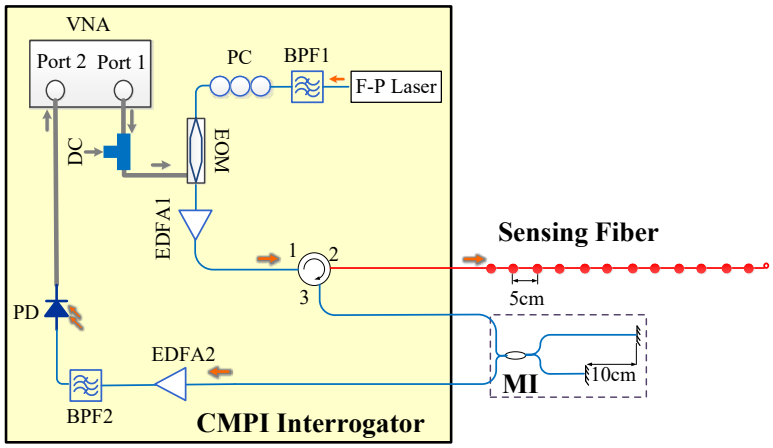

Figure 3. Hardware used in the CMPI system including an interrogator, Michelson Interferometer (MI), and sensing fiber. The interrogator includes a Vector Network Analyzer (VNA), a laser, an electro-optical modulator (EOM), a photodetector (PD), and two Erbium-doped fiber amplifiers (EDFA).

The system was validated by applying known strain to the sensor. A 10-cm cavity MI was used to select reflectors every 10 cm apart. In the static strain testing, a SMF that has 6 weak reflectors 10 cm apart was attached along a cantilever beam. Strains along the cantilever beam were measured and compared with the theoretical value. The results show that the system provides a static strain resolution of 95 nε at a spatial resolution of 10 cm (X. Zhu et al., 2021). To test the dynamic strain sensing, a piece of SMF with an array of 12 weak reflectors 5 cm apart was wrapped on two piezo-ceramic cylinders (PCCs) driven at frequencies of 1700 Hz and 3430 Hz as acoustic sources. The experimental results show that the sensing system can locate multiple acoustic sources. The system resolves 20 nε when the spatial resolution is 5 cm. The recovered acoustic signals match the excitation signals in frequency, amplitude, and phase(Hua, et al., 2021).

13.3.4 System specification tradeoffs and limitations

Dynamic strain (acoustic signal) is sampled during microwave frequency scanning, so the sampling rate is determined by the frequency scanning sampling time (Δt). Therefore, the maximum measurable frequency is . An acoustic signal centered at any frequency between DC and Θ_{max} can be detected. However, the sidelobes generated by different sensors may overlap when the acoustic signal bandwidth (B_a) approaches the upper limit as shown in Fig. 4a. These overlaps (spatial aliasing) cause crosstalk among sensors, and more sophisticated signal processing methods are required to identify the frequency components and recover the temporal signal. The reception bandwidth that avoids spatial aliasing (B_r), is expressed as

$$B_r = \frac{S_R}{2\gamma}, \text{ where } \gamma = \frac{cN\Delta t}{2B_\Omega n}. \quad (16)$$

The reception bandwidth can be increased by fabricating reflectors with larger intervals (Fig. 4b), decreasing γ (Fig. 4c) by either increasing the frequency scanning bandwidth (B_Ω), decreasing the scanning points (N), or reducing the sampling time (Δt). These four parameters also affect other aspects of system performance, such as the range sampling resolution (Sr), maximum measurement range ($L_r = {cN}/{2B_\Omega n}$), and signal-to-noise ratio (inversely proportional to Δt). The tradeoffs among the different aspects of system performance can be tuned to satisfy the requirements of different applications.

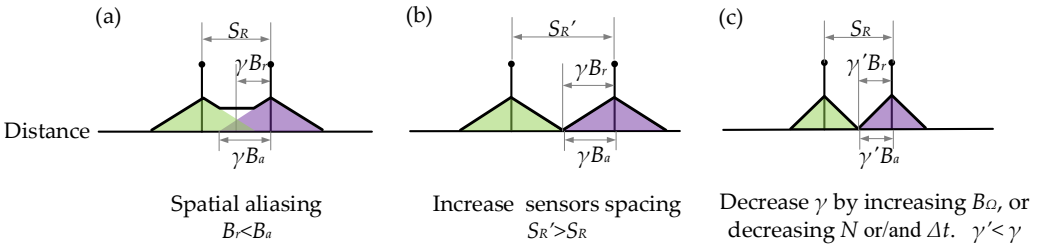

Figure 4 Relationship between the spatial resolution (S_R) and reception bandwidth (B_r). (a) Spatial aliasing when $S_R < 2\gamma B_a$. (b) Increase S_R or (c) decrease γ to avoid spatial aliasing.

The maximum number of sensing units N_C in the system is the ratio of the maximum measurement range and the spatial resolution (). Using Eq.(16) gives

$$N_c = (2B_r\Delta t)^{-1} \quad (17)$$

Equation 17 indicates that the number of sensing units is inversely proportional to the reception bandwidth and Δt. The loss from the sensing cable can also limit the N_c, but this factor is minor when the reception bandwidth is greater than several Hz.

There is a time delay between the waveform reading and the occurrence due to the frequency sweeping and signal post-processing. The delay is usually from milliseconds to seconds, which can be minimized by choosing a small number of modulation frequencies.

13.4 STRAINS CAUSED BY SMALL FLUCTUATIONS IN AIR PRESSURE, AN APPLICATION OF CMPI

Barometric pressures fluctuate due to atmospheric tides, heating and cooling of air from daily solarization, short- and long-term fluctuations from storm systems and weather patterns, and annual fluctuations from seasonal changes in the atmosphere, among other factors (Kuang et al., 2013; Massmann & Farrier, 1992). These effects cause diurnal to semi-diurnal fluctuations (12 or 24 hr period) of roughly +/- 300 Pa near the equator, and the magnitude decreases with latitude and can be nearly zero at latitudes above 60° (Massmann & Farrier, 1992). Variations of 1000 Pa to several 1000 Pa can occur over several hours during severe storms or during several days in response to weather fronts.

Changes in barometric pressure have long been known to affect the water level in wells (Jacob, 1940); increases in barometric pressure acting on the ground surface cause a drop in the water level in a well completed in a confined aquifer, and vice versa. This effect is more complicated in an unconfined aquifer where the barometric pressure change diffuses downward through the vadose zone (Davis & Rasmussen, 1993; Quilty & Roeloffs, 1991; Rasmussen & Crawford, 1997; Rojstaczer, 1988; Rojstaczer & Riley, 1990; Weeks, 1979; Yusa, 1969), which damps the effect of barometric pressure change on the water level. Interestingly, the connection between the diffusion of air pressure through the vadose zone and water level changes in wells was recognized (Tolman, 1937) long before methods for analyzing this process were available.

Pressure diffusion through the vadose zone also affects strain in the vadose zone. We showed that changes in water content correlated with strains in the underlying soil, but the effect was complicated by changes in barometric pressure (Murdoch et al., 2015). Our initial approach was to account for changes in barometric pressure by assuming it only acted at the ground surface. This explained some effects, but the correlation between barometric pressure and strain changed with time, and this complicated the interpretation. The change in correlation between barometric pressure and strain in the subsurface appeared to be a result of changes in the air pressure diffusivity caused by changes in water content. Barometric pressure could diffuse relatively deep into the subsurface when soils are dry, but pressure diffusion was negligible in wet soils because the gas phase pressure diffusivity (and relative permeability) was essentially zero. This seemed to be a reasonable explanation, but little work was available describing the effects of barometric pressure on strain in the vadose zone.

The objective of the experiments described here is to evaluate the feasibility of measuring and evaluating strains caused by barometric pressure fluctuations. This would build on our earlier work where we needed to improve the barometric calibration of in-situ strain data. However, it became apparent that the effects of barometric pressure diffusing into the vadose zone would be controlled by variations in pneumatic diffusivity, which depends on water content and relative permeability. As a result, a secondary motive is to evaluate the sensitivity of distributed strain to basic vadose zone processes, such as changes in water content.

13.4.1 Experimental Methods

The approach was to evaluate the strains and pressure in a column in the laboratory before proceeding to the field. A cylindrical PVC pipe 0.2 m in diameter and 1.03 m long was fitted with flanges at the end and tapped holes along the side (Fig. 5). The tapped holes were used to secure air pressure transducers, and the distance from the top of the cylinder was used as a

reference (Fig. 5) to locate the transducer (Costantino, 2021). Water could be injected or drained through a fitting in the bottom flange. A pipe fitting in the upper flange was attached to a plate bolted to the face of an 8-inch acoustic speaker wired to a signal generator (Fig. 5).

The strain was measured in the sand using an optical fiber interrogated with a CMPI system, as described above. The optical fiber was a single-mode fiber with reflectors spaced 5 cm apart. The reflectors were fabricated using femtosecond laser micromachining, which created reflectivity from -35 to -45dB (Song et al., 2016). A 10-cm-long cavity MI was used to select reflectors every 10 cm apart to form an IFPI.

The fiber was packaged to improve the frictional strain transfer with the porous media and to provide protection from breakage during deployment. The packaging consisted of laminating the fiber between two layers of 100-micron-thick polyester film with a contact adhesive. This was accomplished using a purpose-built device that dispensed the optical fiber between two rolls of 3M 396 tape (Plunkett, 2021). This created a uniform ribbon 2.5 cm wide with the optical fiber along its axis laminated between two pieces of film for a total thickness of 200 microns. The coefficient of friction between the strain ribbon and sand is 0.35 +/- 0.1, and the axial compliance of the ribbon is 80 με/N, according to measurements described in Plunkett (2021).

Air pressure was measured with Bourns BPS110 Series Analog Low-Pressure Sensors rated to measure between 1-6.89 kPa with 0.25% accuracy and a total error band of 1.5%. The transducers were attached to a short piece of vinyl tubing attached to a brass tube inserted through the wall of the column (Fig. 5). The transducer was mounted slightly above the brass tube so that air was trapped next to the transducer when the water level in the column was above the level of the transducer. This protected the transducer, which is designed to measure air pressure and is damaged when exposed to water. It also caused the air pressure transducers to continue to measure pressure changes when the sand was completely saturated, even though the air pressure in the column would have been zero.

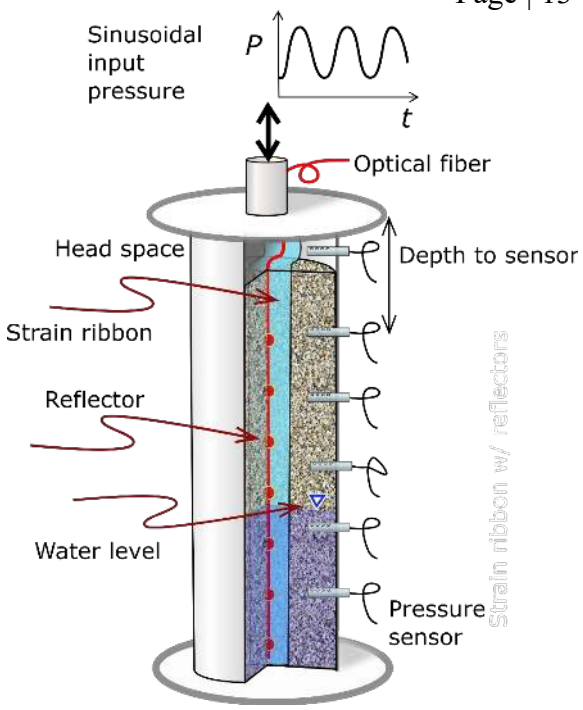

Figure 5. Schematic of the sand-packed column with a sinusoidal air pressure applied to the head space in the laboratory experiments. A strain ribbon containing an optical fiber with uniformly spaced reflector extends along the axis of the column to measure strain.

Experiments were conducted by configuring the column and attaching the speaker to a signal generator and attaching the pressure transducers to a data acquisition system (LabJack T7). The signal generator was set up to drive the speakers with a 4 Hz sinusoid. The frequency of 4 Hz was selected to ensure that the wavelength of the pressure wave is slightly longer than the column height, thereby enabling differentiation of the phase at adjacent sensors. Additionally, this helps minimize the difference between phases to below 2π, thus avoiding any potential ambiguity. The strain was measured using the CMPI interrogator, as outlined above, and the data were sampled and stored in Matlab. The VNA measured the amplitude and phase of the electrical signal at the modulation frequency, which was set to 40001 sampling points in the microwave band from 0.3 kHz to 9 GHz. The IFBW was set to 10 kHz, and the sampling time for each modulation frequency was set as 1 ms. The bandwidth for each sensing section is solely dependent on the sampling time, which was 500 Hz for each sensing unit. The LabJack was triggered by the VNA to start the pressure signal sampling. The pressure signal was applied for several minutes and then sampled over approximately 10s. The resulting S_{21} and pressure data were saved to a local drive and processed offline.

The experimental program includes six configurations of different water content and materials in the column. The baseline configuration was created by attaching the strain ribbon to the center of the bottom flange and then tensioning the ribbon with a 10N weight. A 2-cm-thick layer of gravel was placed at the bottom of the column and the rest was filled with dry, medium-grained, well-sorted sand to approximately 7 cm from the top. This created a head space between the upper flange and the top of the sand. The brass tubes used for air pressure measurements were in place as the column was filled. The strain ribbon extended along the axis of the column (Fig. 5) and the measurement fiber passed through a pressure seal in the upper flange.

A suite of the following six configurations was tested.

1) **Dry**: This is the baseline outlined above—the column is filled with dry, medium-grained sand. All configurations used this sand, except the Silt-to-48 configuration.

2) **Fill to 42**: Water was injected and filled the column to a depth of 42 cm from the top of the column. The point of zero pressure (PZP) in the column was measured at 42 cm using an external standpipe. A capillary fringe is expected to extend approximately 10 cm above the PZP (Plunkett, 2021). The PZP is similar to the water table in a unconfined aquifer.
3) **Drained**: Water in the Fill-to-42 experiment was drained and the test was repeated.
4) **Fill to 29**: Water was injected into the column to fill it to a depth of 29 cm. This is the level of the uppermost strain and pressure sensors.
5) **Barrier**: A thin plastic film was placed across the column and sealed to the sides creating a barrier to air flow. A few cm of sand was placed on top of the film to hold it firmly against the underlying sand. The film is flexible so it can transmit effective stress to the underlying sand, but it reduces the transmission of air pressure.
6) **Silt to 48**: The upper 48 cm of sand was removed from the column and replaced with a mixture of sand and silt. This created a two-layer system with the permeability of the upper layer less than that of the underlying layer.
7) **Fill and Drain**: The speaker is removed and the top of the column is vented. Water is injected at a constant rate using a peristaltic pump until water is ponded on the sand. The pump is then turned off, the system is allowed to equilibrate and then the pump is reversed and the water removed.

13.4.2 Results

Pressure and strain were monitored as functions of depth during the experiments and the results were compiled as time series, which were then processed and summarized as variations in amplitude and phase delay. The summaries were used to facilitate a comparison between the experimental configurations.

13.4.2.1 Dry Experiment

The pressure at the sensor closest to the speaker and located in the head space (depth = 6 cm from the top of the column) fluctuates with the greatest amplitude, approximately 55 Pa from peak to trough (Fig. 6a), and the amplitude progressively decreases approximately as a negative exponential function of depth with a semi-log slope of s_p = -1.2 1/m (Fig. 7a). The maximum pressure is 10 Pa at a depth of 67 cm (Fig. 6a).

The pressure in the sand is also periodic and the signal is delayed behind the pressure in the headspace (Fig. 6a). The delay relative to the pressure in the headspace, $P_{r,}$ increases with depth at a gradient of 130 ms/m (Fig. 8a), which indicates an air pressure phase velocity of approximately v_{pp} = 8 m/s. The period is 0.25 s, which implies a wavelength of λ_p = 2 m.

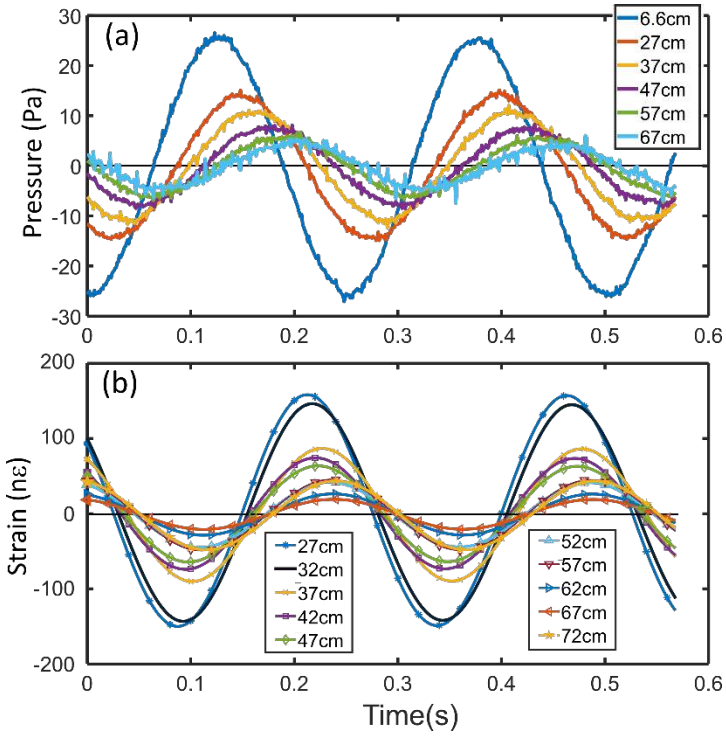

Figure 6. Air pressure (a) and strain (b) at different depths as a function of time when applying a sinusoidal pressure at the top of the column of dry sand. The air pressure at 7 cm is used as a reference, P_r.

The vertical strain also varies as a periodic function of time (Fig. 6b) with the same period as the pressure. The largest strain amplitude is 200 nε and it occurs at the sensor closest to the top of the column (27 cm). The strain amplitude decreases with depth and is 25 nε at the lowest strain sensor (72 cm in Fig. 6). The strain amplitude attenuates as approximately a negative exponential with a semi-log slope of s_ε = -2.0 1/m.

The strain minima at the shallowest sensor occur slightly before the pressure maxima in the headspace, and the strain minima occur progressively later as the depth of the strain sensor increases (Fig. 6). When the air pressure loads only the surface of the sand and does not pressurize the sand (e.g. if the sand was impermeable), the air pressure and strain should be exactly opposite in sign; an increase in air pressure in the head space is associated with a decrease in strain (compression), and tension occurs when the air pressure decreases. We will use the air pressure in the head space, P_r, as a reference, and a positive strain delay will be taken as the time when a strain minima occurs after the pressure maxima in the headspace.

The strain delay is negative at the shallowest sensor and it increases with depth, according to the time series (Fig. 6). The strain delay is approximately linear with depth and the gradient is 85 ms/m (Fig. 8b), which is flatter than that of the pressure. It follows that the phase velocity, $v_{p\varepsilon}$, of the strain is $v_{p\varepsilon}$ =12 m/s, and the strain wavelength is λ_ε = 3m.

Loading on the surface of the sand will create an elastic *p* wave that propagates downward. According to (Barrì et al., 2012), the velocity of *p* waves in the sand is approximately 150 m/s, which is an order of magnitude faster than the phase velocity of the

strain. As a result, it appears that the strain waves are a result of the pressure propagating into the sand, even though the phase velocity of the strain is faster than that of the pressure.

13.4.2.2 Fill-to-42 Experiment

The time series for this and the other experiments are similar to Fig. 6 with variations in amplitude and delay that appear to result from the configuration of the experiment. The amplitude of the pressure in the upper part of the Fill-to-42 experiment is greater, and then amplitude decreases more slowly with depth than in the Dry experiment (Figs. 7a and b). The slope of the pressure delay in this experiment is slightly less than in the Dry experiment (Figs. 7a and b). The pressure amplitude decreases sharply below the point of zero pressure (PZP). The pressure data where the column is saturated are uncertain because the measurements were made with transducers designed to measure air pressure.

The volume of air-filled pores in this experiment is significantly smaller than in the Dry experiment. The smaller volume apparently lessened the decrease in pressure with depth compared to the Dry experiment.

The amplitude of the strain signal above the PZP is greater than in the Dry experiment, but the amplitude of the strain decays sharply below the PZP (Fig. 7b). This is consistent with the pressure amplitude, which is relatively large in the zone above the PZP.

The delay of the strain above the PZP decreases with depth (Fig. 8). Everywhere else in this, and in the other experiments, the strain delay increases with depth, so this effect is unusual. Below the PZP, the strain delay increases sharply with depth at a slope of 270 ms/m ($v_{p\varepsilon}$ = 4 m/s, λ_{ε} = 1 m). This indicates that the velocity of the strain in saturated conditions slows to approximately 1/3 that of dry conditions.

13.4.2.3 Drained Experiment

The water that was injected to partially fill the column in the Fill-to-42 experiment was drained and another experiment was conducted. The amplitude and delay of the pressure in the upper half of the column during the Drained experiment are essentially the same as during the Dry experiment (Figs. 7 and 8). The pressure delay in the lower half of the column is longer than in the Dry experiment, probably because the saturation there is higher.

The strain delay rate is also similar to that of the Dry experiment in the upper half and greater than the Dry experiment in the lower half of the column. The saturation in the lower half of the column during the Drained experiment is greater than in the Dry experiment and this would have reduced the pneumatic diffusivity. This could explain the increase in the delay of the pressure in the lower half of the experiment.

The amplitude of the strain decreases with depth in the Drained experiment, but it does so at a semi-log slope that is less than in the Dry experiment (Fig. 7c).

13.4.2.4 Fill-to-29 Experiment

This experiment involved filling the column so the point of zero pressure was at 29 cm, so it is similar to the Fill-to-42 Experiment. The pressure in the uppermost pressure sensor (27 cm) was less than, and the delay was significantly greater than in the previous experiments. The PZP was below the 27-cm pressure sensor, but the saturation would have been elevated in the

zone up to 10 cm above the PZP because of capillarity (Plunkett, 2021) and this likely affected the pressure amplitude and delay.

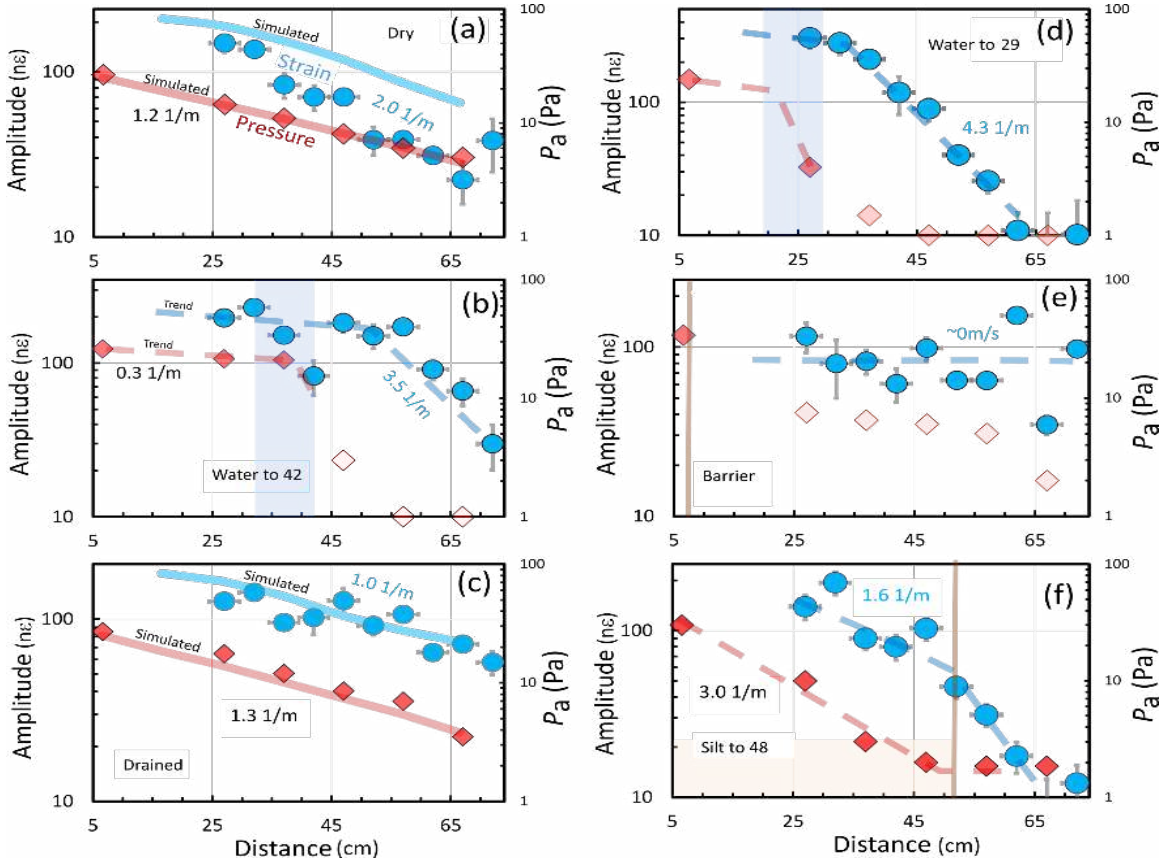

Figure 7. Amplitude of periodic pressure (red) and strain (blue) signals as functions of distance in different configurations of a sand-filled column. Surface of the sand at x = 6cm. (a) Dry sand, (b) Water filled to 42 cm; (c) Water drained after filling; (d) Water filled to 29 cm; (e) Barrier at surface of sand; (f) Silty sand to 48 cm underlain by sand. Numbers are semi-log slope. Data shown as symbols, numerical simulation as thick solid lines in Dry and Drained plots, trend of data estimated manually as thick dashed line. Vertical bands are water level or contact between sand and silty sand. Lightly shaded red symbols are uncertain pressure measurements.

The strain amplitude attenuates with a semi-log slope of approximately s_ε = -4.3 1/m, which is the steepest of any of the experiments. The strain delay is also the steepest of any experiments, approximately 300 ms/m ($v_{p\varepsilon}$ = 3 s/m and λ_ε = ¾ m). These results are similar to the amplitude decay and delay in the saturated region of the Fill-to-42 experiment. They indicate that going from dry to saturated conditions slows the velocity, reduces the wavelength, and increases the amplitude attenuation of the strain.

13.4.2.5 Barrier Experiment

The barrier experiment was conducted by sealing a thin, compliant plastic film to the walls of the column near the top of the sand. The film was covered with a few cm of sand to hold it in

place. The film was intended to transmit stresses, but prevent air pressure from propagating through the sand.

The pressure is attenuated with depth much more in this experiment than in the others (Fig. 7d). Interestingly, a periodic pressure response occurs even with the barrier in place. This may have been because of small unrecognized leaks in the film, or because the film was displaced enough to transmit a slight change in pressure.

The strain response in this experiment is significantly different from the responses in the other experiment. The strain amplitude (60-90 nε) and phase (+/- 10 ms) are somewhat variable, but they are essentially independent of depth (Figs. 7d and 8d). To account for a possible delay resulting from synchronization between the strain and pressure measurements, an assumed offset was applied to the strain delay in Fig. 8d. This was done because the delay could have affected the accuracy of the dataset. Nevertheless, it is clear that the increase in delay with depth that occurred in the other experiments was absent in this one.

13.4.2.6 Silt to 48 Experiment

The sand was removed from the column and replaced with dry silty sand with a lower permeability than the original sand. The strain ribbon was tensioned in place and the silty sand was packed in lifts as the column was filled.

The air pressure in the silty sand attenuates more rapidly and the delay is greater than in the sand. This effect appears to change when crossing the contact between the silty sand and the sand at 48cm depth (Fig. 7f and 8f).

The strain in the silty sand attenuates more rapidly than in the Drained experiment, but less rapidly than in the Dry experiment. The strain delay in the silty sand increases with depth 2 to 3 times faster than in sand (Figs. 7f and 8f). This indicates that $v_{p\varepsilon}$ is approximately 4.5 m/s in the dry silty sand, but it is much faster, 12 m/s, in the dry and drained sand.

13.4.2.7 Fill and Drain Experiment

This experiment involved injecting water into the bottom of the column at a constant rate with a peristaltic pump until a small volume of water ponded on the surface of the sand, and then reversing the pump to remove the water. The strain was measured between 10 reflectors spaced 5cm apart in a strain ribbon along the axis of the column.

There is a systematic variation in strain with time as the column fills, ponding occurs, and then is drained (Fig. 9). Early in the experiment, a few με of tensile strain occur in the lower part of the column and compressive strain occurs in the top. Strain above approximately 25cm increases by 5 to 10 με and reaches a maximum at times that increase progressively with height above the column. The maximum strain at each reflector pair occurs approximately when the water level or PZP in the column reaches the reflector pair. For example, at the reflector pair between 40-45 cm, the strain increases and reaches a maximum at approximately 1300 s, and the scaled water volume at this time is at 50 cm, slightly above the top reflector (Fig. 9).

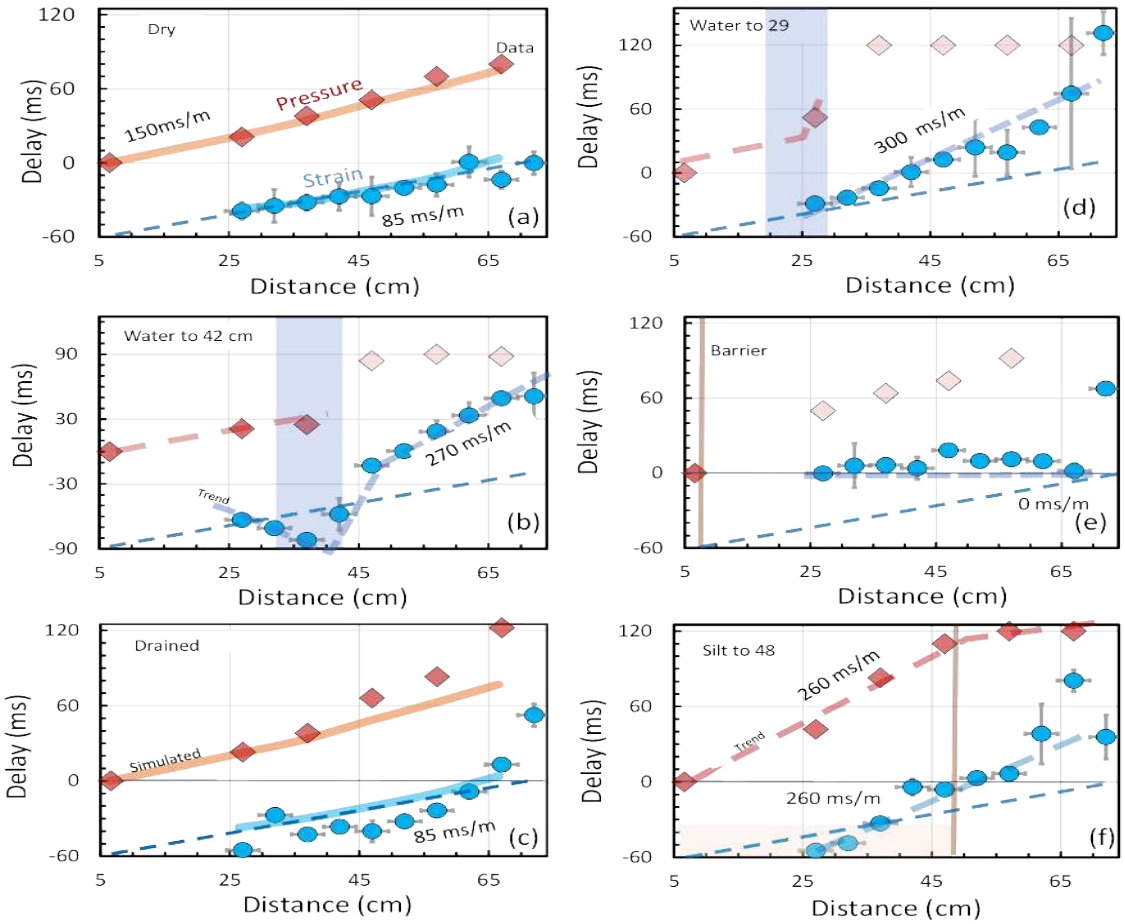

Figure 8. Delay of the periodic pressure (red) and strain (blue) signals as functions of distance in different configurations of a sand-filled column. The surface of the sand at x = 6cm. (a) Dry sand, (b) Water filled to 42 cm; (c) Water drained after filling; (d) Water filled to 29 cm; (e) Barrier at the surface of sand; (f) Silty sand to 48 cm underlain by sand. Best-fit slopes as shown. Data are shown as symbols, an analytical solution for Dry baseline as a thin dashed line, numerical simulation as thick solid lines in Dry and Drained plots, and trend of data estimated manually as thick dashed line. Vertical bands are water level or contact between sand and silty sand. Lightly shaded red symbols are uncertain pressure measurements.

The scaled water volume is roughly equal to the height of the point of zero pressure (PZP) in the column. The PZP is analogous to the water table in an aquifer. A pressure transition zone extends 10 to 15cm above the point of zero pressure (Plunkett, 2021)and is similar to the capillary fringe above an aquifer. The results during the filling of the column indicate that the sand is compressed slightly above a rising water table, but then is starts to expand as the pore pressure increases in the capillary fringe. The sand expands as the pore pressure increases and then it decreases slightly as the point of zero pressure rises above the upper reflector pair (Fig. 9).

The process outlined above occurs progressively upward as the pore pressure increases, but a striking change occurs as the column becomes filled with water (Fig. 9). A slight increase in

compression occurs as the capillary fringe starts to interact with the ground surface, but then a large and rapid increase in compression occurs when ponding starts to occur at the ground surface. The greatest compressive strain is 40-50 με and occurs at the upper reflector pair, but compression occurs throughout the upper half of the column when ponding occurs. The compression abruptly stops when water covers the surface of the column, and the strain rate essentially goes to zero before the pump is turned off (Fig. 9).

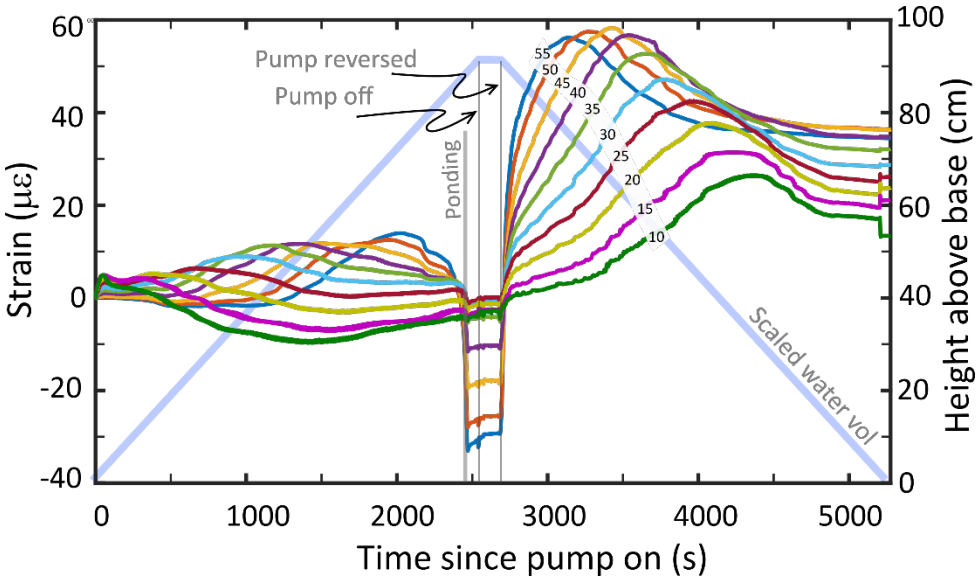

Figure 9. Axial strain measured with a strain ribbon and CMPI at different elevations (numbers on colored lines are cm above the datum) in a sand-filled column as functions of time when the column is filled and drained at a constant rate. Ponding occurs approximately 90 s before the pump is turned off. Injected water volume is scaled to the cross-sectional area and porosity to give and effective height above the base of the column (blue line).

An abrupt tensile strain occurs when the pump is reversed and the surface pond is fully drained (Fig. 9). The strain at the upper reflector pair increases by more than 80 me at the onset of draining. It reaches a peak and then decreases, and this pattern is repeatedly progressively downward as the column is drained (Fig. 9).

The sharp compression as the column filling nears completion was surprising, but it appears to be related to capillary exclusion (Philip et al., 1989; Plunkett, 2021) of the rising pressure transition zone. Capillary exclusion causes the ground surface to behave as a no-flow boundary and this increases the pore pressure as the pressure transition zone interacts with the free surface. The pressure increases by approximately 1000 Pa from this effect, according to the measurements in a similar experiment by Plunkett (2021). The observed compression is consistent with a load of 1000Pa acting on the upper boundary, suggesting that the pressure caused by capillary exclusion causes the compression observed in the experiments.

The experimental data described above and shown in Figs. 6-9 indicate that changes in pore pressure representing fluctuations of barometric pressure or changes in the height of the water table cause strains that can be characterized with distributed strain measurements made

with CMPI. These results suggest that distributed strains could offer insights into hydrologic processes in the vadose zone.

13.4.2.8 Analysis

The strain and pressure in the lab experiments were analyzed using a simple analytical solution that describes the basic process, and a numerical solution that has the potential to include more details. Both analyses are one dimensional with a pressure that varies periodically, with amplitude A_p, and period λ, at one end. The analytical solution assumes the pressure and strain are uncoupled and the properties of the porous media are homogeneous and isotropic. We assume the pressure variations can be described using the diffusion equation with uniform and constant pressure diffusivity, D. This requires that the change in pressure is small enough to ignore fluid compressibility. The pressure is uncoupled from the strain rate in the solid because of the high compressibility of the air in the pores. This boundary value problem is solved by Carslaw & Jaeger (1986) for an analogous problem in heat conduction. The pressure in the half-space, P, is given in dimensionless form as

$$P^* = \frac{P}{A_p} = e^{-z^*} \sin\,(t^* - z^*) \tag{18}$$

where the characteristic time and length

$$t_c = \frac{\lambda}{2\pi} \tag{19}$$

$$L_c = \sqrt{\frac{\lambda D}{\pi}} \tag{20}$$

are used to define

$$t^* = \frac{t}{t_c} = \frac{t}{\frac{\lambda}{2\pi}} = \frac{2\pi t}{\lambda} \tag{21}$$

$$z^* = \frac{z}{L_c} = \frac{z}{\sqrt{\frac{\lambda D}{\pi}}} = z\sqrt{\frac{\pi}{\lambda D}} \tag{22}$$

The total strain is the sum of the strain caused by the pressure loading at the ground surface and the strain caused by the change in pore pressure. The strain caused by the pressure loading at the ground surface is

$$\varepsilon_s = -B \sin(t^*) \tag{23}$$

where

$$B = \frac{A_p(1+\nu)(1-2\nu)}{E(1-\nu)} \tag{24}$$

and E is Young's modulus and ν is Poisson's ratio of the porous medium. The strain caused by the pore pressure change is

$$\varepsilon_p = B\alpha_b e^{-z^*} \sin(t^* - z^*) \tag{25}$$

where α_b is the Biot-Willis coefficient. We will assume $\alpha_b = 1$, which is reasonable for materials like soils with a bulk modulus much less than the grain modulus, and saturation effects on the apparent α_b will be ignored. The total strain is the sum of the two components, so in dimensionless form

$$\varepsilon^* = \frac{\varepsilon_s + \varepsilon_p}{B} = e^{-z^*} \sin(t^* - z^*) - \sin(t^*) \tag{26}$$

The trigonometric identity for an arbitrary phase shift, φ_ε, gives

$$\varepsilon^* = e^{-z^*} \sin(t^* - z^*) - \sin(t^*) = c_\varepsilon \sin(t^* + \varphi_\varepsilon) \tag{27}$$

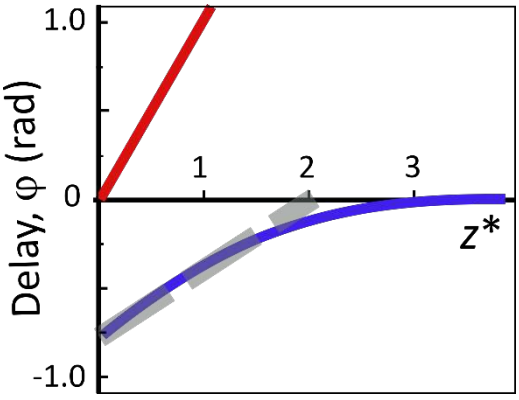

Figure 10. Phase delay in radians of the strain (blue) and pressure (red) relative to the pressure at the ground surface. Positive delay means the signal arrives after, negative means it arrives before the reference signal. Phase lag of the strain can be approximated by the grey dashed line for $z^*<1$.

where c_e is the observed strain amplitude. It follows that

$$c_\varepsilon = \sqrt{e^{-2z^*} - 2e^{-z^*} \cos z^* + 1} \tag{28}$$

and the amplitude of the pressure is $c_p = e^{-z^*}$.

The delay of the strain also follows from (27). Changing the sign to write the phase as a delay in keeping with the experimental data

$$\varphi_\varepsilon = -\tan^{-1}\left(\frac{e^{-z^*}\sin z^*}{1-e^{-z^*}\cos z^*}\right) \tag{29}$$

It is apparent that the delay of the strain is approximately linear for $z^* < 1$ (dashed line in Fig. 10). The slope is ½ at $x^*=0$ and the slope of a best-fit line

$$\varphi_\varepsilon \approx \frac{\pi}{4}\left(\frac{1}{2}z^* - 1\right) \tag{30}$$

is π/8. For comparison, the delay for the pressure is (Fig. 10)

$$\varphi_p = z^* \tag{31}$$

The experimental results for the delay appear to be generally consistent with Eqs. (30-31). The strain and pressure delays for uniform sand are approximately linear with depth. The slope of the pressure delay is steeper than that of the strain, and the strain delay is less than that of the pressure (Fig. 8 and Fig. 10).

Substituting and then solving for D in terms of air pressure phase velocity

$$D_{vp} = \frac{\lambda v_p^2}{4\pi} \tag{32}$$

and in terms of the strain phase velocity

$$D_{ve} = S_1 \frac{v_\varepsilon^2 \lambda}{4\pi} \tag{33}$$

where the coefficient is $0.15 < S_1 < 0.25$ using the different approximations for the slope of the phase velocity. D can also be estimated from the semi-log slope of pressure decay

$$D_{sp} = \frac{0.59}{s_p^2 \lambda} \tag{34}$$

Using values for the air pressure from the Dry and Drained experiments, $v_p = 7.6$ m/s gives $D_{vp} = 1.1$ m^2/s and s_p=1.3 1/m gives $D_{sp} = 1.4$ m^2/s. The phase velocity of the strain is $v_\varepsilon = 12$ m/s, which gives 0.4 m^2/s < $D_{v\varepsilon}$ < 0.7 m^2/s.

The values of D determined using the air pressure (1.1 - 1.4 m^2/s) are slightly greater than values estimated from the strain delay, but the values are remarkably similar. The values differ by approximately a factor of 2, which could be because friction on the wall of the column slowed v_ε compared to the semi-infinite case in the analytical solution.

13.4.2.9 Numerical simulation

Results from the analytical solution are encouraging, but they omit a variety of factors that limit the application of the results to uniform materials. In many cases, field conditions would be characterized by soil materials with different textures and water pore pressure. This will cause the soil properties to vary in space. Changes in air pressure cause changes in water pressure, which may also cause the properties to change—most of the relevant properties in the analysis are functions of pore pressure. It follows (Costantino, 2021) that these conditions are described using two non-homogeneous diffusion equations for the liquid and gas phases,

$$-\nabla \cdot D_l \nabla (P_l + \rho_l g z) + \frac{\partial P_l}{\partial t} = -\Gamma_l \tag{35a}$$

$$-\nabla \cdot D_g \nabla \left(P_g + \rho_g g z\right) + \frac{\partial P_g}{\partial t} = -\Gamma_g \tag{35b}$$

where the diffusivities of the liquid and gas pressure are respectively,

$$D_l = \frac{k k_{rl}}{\mu (S_l \mathrm{S}_{\sigma l} - C_m)} = \frac{k k_{rl}}{\mu (S_l \mathrm{S}_{\sigma l} + |C_m|)} \tag{36a}$$

$$D_g = \frac{k k_{rg}}{\mu (S_g \mathrm{S}_{\sigma g} - C_m)} = \frac{k k_{rg}}{\mu (S_g \mathrm{S}_{\sigma l} + |C_m|)} \tag{36b}$$

with the terms on the right side serving to couple changes the liquid and gas phase pressures

$$\Gamma_l = \frac{C_m}{(S_w \mathrm{S}_\sigma - C_m)} \frac{\partial P_g}{\partial t} \tag{37a}$$

$$\Gamma_g = \frac{C_m}{(S_g \mathrm{S}_\sigma - C_m)} \frac{\partial P_l}{\partial t} \tag{37b}$$

P_n is the pressure of the *n*th phase, were *n*=*l* for the liquid and *n* = *g* for the gas phases, respectively. ρ is the fluid density, μ is fluid viscosity, *g* is gravity, *k* and k_r are the intrinsic and relative permeabilities, S_n is the saturation of the nth phase, and the elastic storage term is $S_{\sigma n} = \phi \beta_n + \left(\frac{1}{K} - \frac{1}{K_s'}\right)$, C_m is the specific moisture capacity (derivative of the soil water retention curve with respect to pressure).

Stresses are determined using momentum conservation for quasi-static conditions

$$\frac{\partial \sigma_{ij}}{\partial x_i} = -F_i \tag{38}$$

where σ_{ij} is the total stress tensor, and F_i is the body force vector. The *ij* subscript assumes Einstein notation where repeated subscripts indicate summation. The total stress depends on the effective stress on the solid, σ_{eij} and the effective pore pressure, P (Borja, 2006, Eq. 3.42)

$$\sigma_{ij} = \sigma_{eij} - \alpha P \qquad (39)$$

where α is the Biot-Willis parameter. The effective pressure in the unsaturated zone is weighted between the water and the air pressures (Borja, 2006, Eq. 3.24; and Lu et al., 2010, Eq. 18)

$$P = S_e P_l + (1 - S_e) P_g \qquad (40)$$

where S_e is the effective liquid saturation. The material parameters are characterized by constitutive functions of the capillary pressure. Saturation, specific moisture capacity and permeability were determined using the van Genuchten functions. Young's Modulus was characterized as a power function given by Lu & Kaya (2014). Poisson's ratio was described using the function given by Thota et al. (2021). More information is in Murdoch et al. (2023).

13.4.2.10 Results

Simulations were conducted for a 1D case resembling the experiments, and the parameters were adjusted manually so the results were similar to results from the Dry and Drained experiments.

The resulting strain in the experiments has components caused by the surface load and the pore pressure (Fig. 11). The component from the surface load at 0.2 m depth fluctuates between +/- 400 nε while the pressure fluctuates between +/- 25 Pa. The phase of the surface load component is always delayed by ½ period relative to P_r (pressure in the head space). However, the pressure load component of strain is only delayed slightly relative to P_r and its magnitude is slightly less than the surface load component. The result of adding the two components is that the resulting strain minima occurs before the maxima in P_r (Fig. 11a).

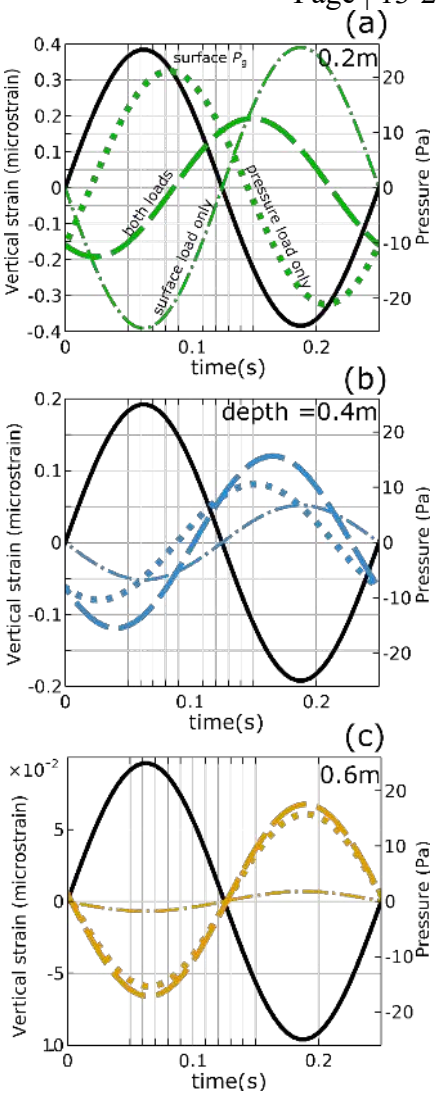

Figure 11. Components of the vertical strain from an air pressure fluctuation on the surface. The black solid line is P_r, the pressure at the ground surface used for reference, dashed-dot line is the strain component from surface loading only, the dotted line is the strain component from pressure in the porous media only, and thick dashed line is the sum of the two components. From numerical simulations based on Eqs. 19 – 24.

The phase of the two components moves closer together at 0.4 m and they are nearly in phase from one another at 0.6 m (Figs. 11b and c) The

magnitude of the strain from surface load also decreases with depth. This is because the lower boundary condition prevents displacement. The resulting total strain at 0.4 m is approximately half of that from the 0.2 m depth while the resulting total strain at 0.6 m is barely fluctuating at all.

Interactions between the surface and pressure loads cause the time series of the strain to lead the pressure, and the results of the simulations resemble those of the experiments (Figs. 12 and 6). The simulations of the pressure and strain magnitudes and delays are also similar to the experimental data (Figs. 7a and c, and Figs. 8a and c).

A key aspect controlling the strain response is the pore pressure that is created by the fluctuating air pressure at the ground surface. The simulations show that the air pressure perturbation is transferred to the water pressure and continues to propagate downward causing a strain response. The pressure propagation depends on the air and water pressure diffusivity D_w, which varies with depth and saturation. The air pressure diffusivity, D_a, is approximately 1.4 m^2/s in dry sand, and the D_w is approximately 0.12 m^2/s in saturated conditions (Fig. 13). Interestingly, both D_a and D_w decrease and are small in the transition zone at the water table, suggesting the water table would impede downward propagation of barometric pressure.

The numerical analysis is capable of representing the partially saturated conditions and resulting non-linear material properties in the other experiments, and analyses of those experiments are ongoing.

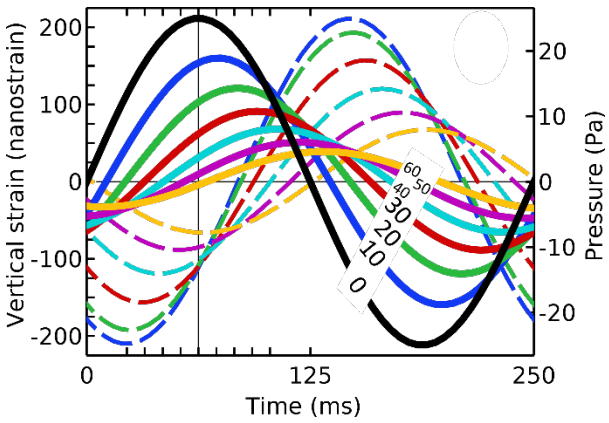

Figure 12. Pressure (thick solid lines) and strain (dashed lines) at different depths in cm (numbers) in dry sand using numerical simulation based on Eqs. 35 – 40.

13.5 Discussion

The experiments and simulations outlined above indicate that strains in soil are closely related to small periodic changes in air pressure and saturation at the cm-to-meter scale. Strain amplitudes in the sand caused by small fluctuations in air pressure (+/- 25 Pa) were as small as 10 nε during a 4 Hz signal and spatial variations in strain were detected with a 5 cm spacing. The effects of fluctuating barometric pressure on water levels is widely known, but to our knowledge, the effects of barometric pressure on strain in partially saturated media have not been documented. One reason for this is that detecting these signals challenges the available measurement capabilities (strain resolutions in the nε range, sampling rates of at least 100 Hz, and spatial resolutions at the cm scale in a package that could be deployed in the field). The development of the CMPI methods with optical fiber packaged in a strain ribbon has made it feasible to measure these signals.

The experimental results show that a periodic fluctuation of air pressure at the ground surface will cause a strain signal that penetrates into and responds to the properties of an underlying porous medium. The phase velocity (inverse of s_p) of the strain is roughly twice that

of the pressure under dry conditions (Figs. 8a and c), and it decreases by a factor of roughly 1/3 when the sand becomes saturated (Figs. 8a, c and b, d). D_w is expected to be significantly less than D_a, according to Fig. 13 and Eq. 21, and this may explain why the strain phase velocity is slower in saturated than dry conditions.

The effects of air pressure diffusing into the subsurface are illustrated by comparing results from the Barrier (Figs. 7 and 8e) and the other experiments (Figs. 7 and 8). Strain delay and magnitude are variable but essentially independent of depth in the Barrier experiment where a membrane was used to seal the downward diffusion of pressure but allow stress to be transmitted. In contrast, the delay and magnitude of the strain varied with depth in the other experiments where the pressure barrier was omitted. According to the theoretical analyses (e.g. Eq. 6), strain is independent of depth when only the surface load is considered. This is consistent with the experiments and confirms that systematic variations of strain with depth are due to pressure variations.

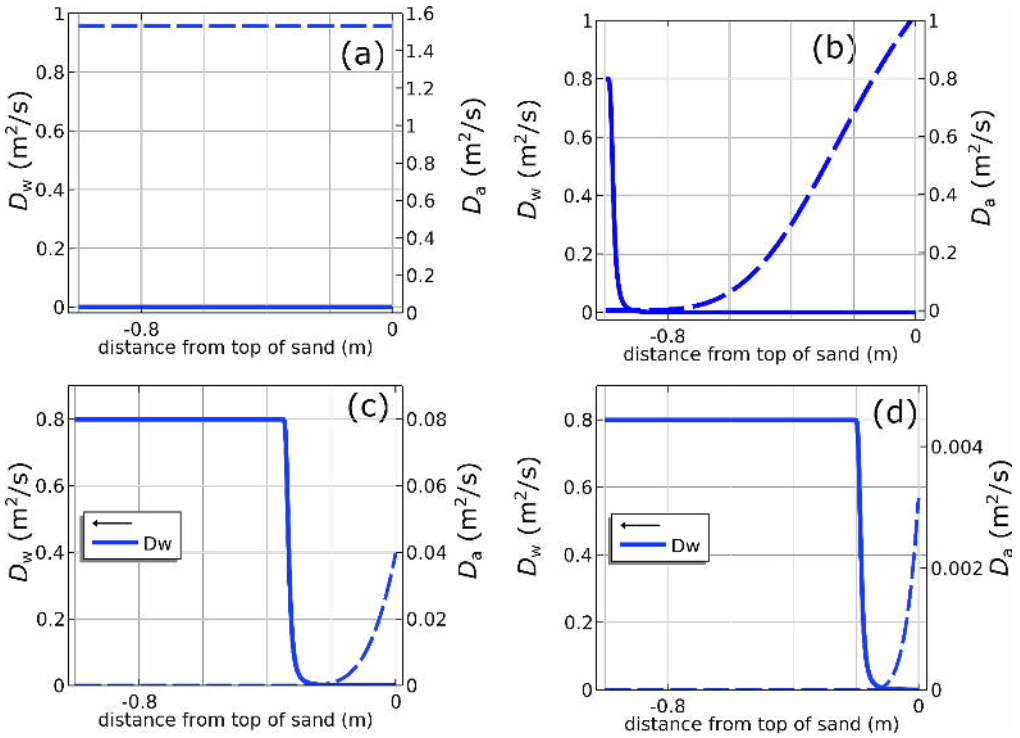

Figure 13: Initial pressure diffusivity for water, D_w, and are, D_a, as a function of depth for different initial conditions. a.) dry. b.) gravity drainage. c.) PZP at d = 0.35m. d.) PZP at d = 0.2m. From numerical simulations using Eq. 35-40.

The amplitude of the strain varies with saturation, with smaller strain magnitudes occurring in Dry conditions and larger strains in saturated conditions (3a, c and b, d). The strain magnitude will be affected by both the pressure magnitude and the elastic modulus, and both of these parameters are functions of pore pressure (Eq. 20; Borja, 2006; Lu and Kaya, 2012).

The experiments conducted here used pressure fluctuations that are smaller and faster than fluctuations of barometric pressure where diurnal variations of several hundred Pa are common, and larger variations in the kPa range occur over longer periods. The characteristic length of a diurnal variation in the dry sand used in the experiment would be more than 100m, and it would

be more than 10 m when the pressure diffusivity was 2 orders of magnitude less than in the experiments. This suggests that strain variations caused by variations in barometric pressure could extend to significant depths in the vadose zone. We have shown that the strain signal is affected by the pore pressure and water content, and this raises an important point for both the potential and the challenges of interpreting strains caused by barometric pressure variations. It appears that variations in strain caused by barometric pressure fluctuations could be used to continuously interrogate changes in pore pressure and properties in the vadose zone, which would have wide applications for environmental characterization and monitoring. However, the quantitative interpretation would likely require inverting numerical analyses similar to those described above. The key material parameters in that analysis are all non-linear functions of pore pressure, which will raise challenges during the inversion process.

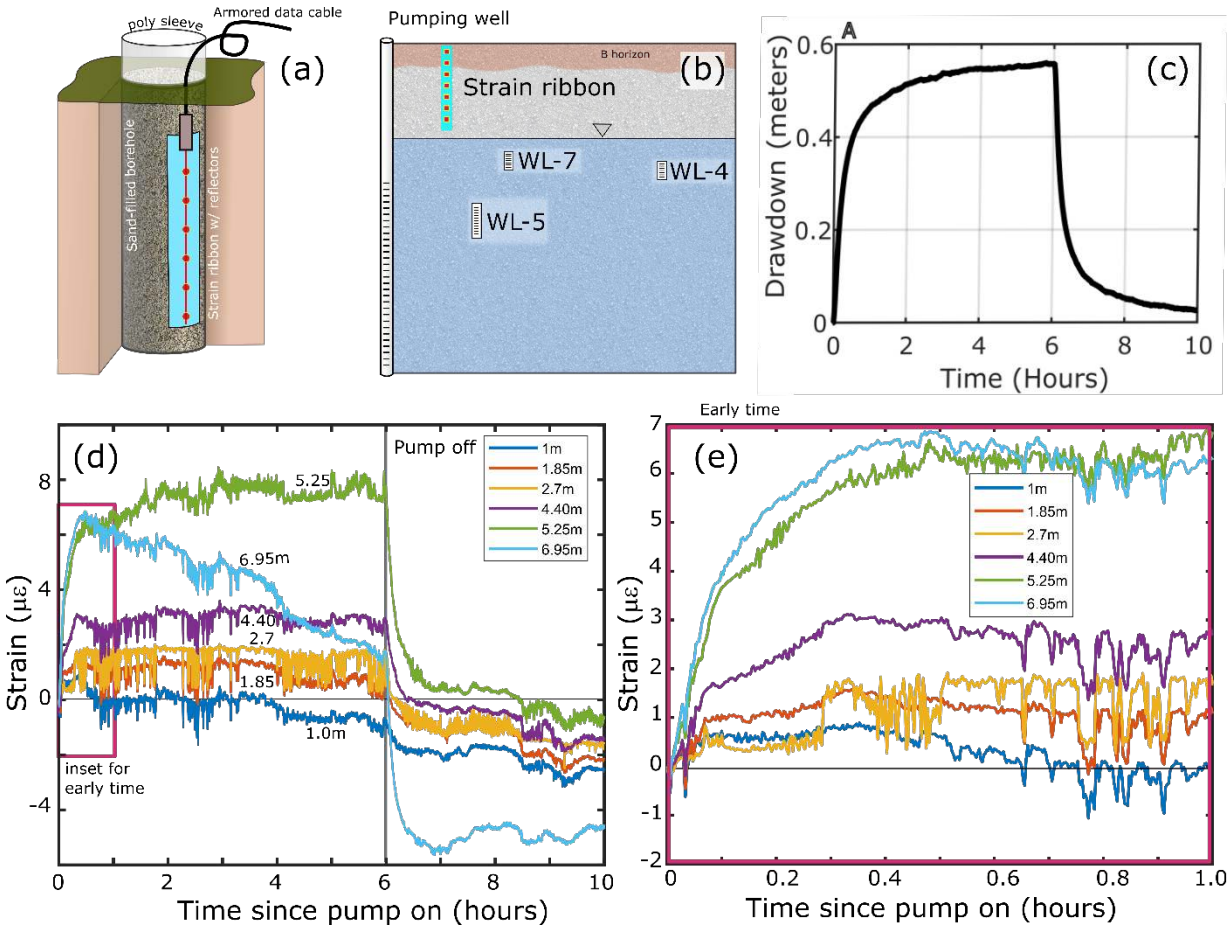

Figure 14. Field test of a CMPI strain ribbon used to characterize a pumping test. (a) schematic of the strain ribbon pressed against the wall of a borehole by a sand-filled polyethylene sleeve. (b) Cross-section of the field site. (c) drawdown at monitoring well WL-5. (d) vertical strain at different depths below the ground surface during pumping and recovery after the pump is turned off. The red box frames the data in panel (e). (e) strains as a function of time during the first hour of the pumping test.

We are optimistic that measurements of strain made with optical fibers could have important applications for monitoring processes in the vadose zone, but there are also important potential

applications in the saturated zone. The Fill and Drain experiments show a strong and distinctive strain signal associated with a rising water table that reaches the ground surface. In addition, we have used the CMPI technique with a strain ribbon in the field to monitor transient well tests. One experiment was conducted by deploying a strain ribbon along the wall of a borehole and then filling a polyethylene sleeve in the borehole with sand to couple the ribbon to the wall of the boring (Fig. 14). Becker et al (2017) describe a similar technique for pressing a fiber cable against the wall of a borehole with a water-filled sleeve. The strain ribbon was deployed in the vadose zone from the ground surface to a depth of 8m in saprolite. The water table of the unconfined aquifer in the saprolite was at a depth of approximately 9m and a pumping well was drilled 4m from the strain ribbon. We conducted a constant-rate pumping test for 6 hrs and we monitored the strain in the vadose zone and the drawdown in monitoring well WL-5 at 5m m from the pumping well.

The drawdown in the monitoring well increased sharply soon after the pump was started and the rate of increase diminished with time in a pattern (Fig. 14c) typical of pumping tests in an unconfined aquifer (Neuman, 1975). The vertical strain in the vadose zone increased as soon as pumping started and then the rate diminished with time in a pattern that resembles the drawdown (Figs. 14d and e). The strain is greatest at the bottom of the ribbon near the water table where it reaches a maximum of approximately 7 με. The strain decreases upward, but the CMPI ribbon resolves a clear strain signal surface that reaches a maximum of approximately 0.6 με 1 m from the ground surface (Fig. 14).

Poroelastic analyses of pressure and strain in the vicinity of a well being pumped at a constant rate were conducted using methods outlined in (Murdoch et al., 2020) and configured to the field site. Those analyses show that the strain signal resembles the drawdown, confirming the results in Murdoch et al., (2021). The results also show that the strain magnitude increases with depth, except near the water table where pumping drops the pore pressure causing compression and a reduction in strain magnitude resembling Fig. 14 (blue curve from 6.95 m depth). Similarities between the observed strain and the simulations suggest that strain data distributed with depth in the vadose zone could be used with inversion to characterize results of pumping tests in an underlying aquifer.

13.6 Conclusion

Distributed strain and acoustic measurements outlined throughout this AGU volume have provided new insights into geophysics. In this chapter, we have shown how an approach for measuring distributed strain, called Coherence-length-gated Microwave Photonics Interferometry (CMPI), has enabled new insights into hydrologic processes in the vadose and saturated zones.

CMPI measures strain by reading optical interference phase change in the microwave domain. A local Michelson interferometer was implemented to eliminate the dark zones for high spatial resolution sensing. A frequency-to-time-domain mapping signal processing method was developed to increase the sensor bandwidth for distributed acoustic sensing. Sensing performance of centimeter spatial resolution, up to 10nε sensitivity, and kHz strain measurement rate was achieved.

CMPI was used to measure the strain caused by small periodic variations in air pressure (25 Pa amplitude and 4 Hz) in a sand-filled laboratory column used to represent pressure changes in the vadose zone caused by barometric fluctuations. The amplitude of the pressure decreased as

an exponential function of depth, and the phase delay of the pressure increased as a linear function of depth in the experiments. The amplitude and phase delay of the strain followed similar functions of depth in dry sand. Strain amplitudes decreased from roughly 200 nε at shallow depths to roughly 10 nε near the bottom of the column. The phase velocity of the pressure in dry sand was approximately 7.6 m/s and the velocity of the strain was faster, approximately 12 m/s. Saturating the sand reduced the phase velocity of the strain to 3-4 m/s, and the velocity increased to 12 m/s when the water was drained. Changing the material from a permeable, clean sand, to a lower permeability silty sand reduced the strain phase velocity from 12 to 4.5 m/s. The strain varied periodically but was essentially independent of depth when a pressure barrier was placed at the top of the sand.

The results of the experiments show how the strain distribution with depth caused by air pressure fluctuation is affected by the saturation and permeability distribution in the underlying porous media. An analytical solution used to interpret the data gives similar results for the air pressure diffusivity estimated from the air pressure and the strain, suggesting that distributed strain could be used to characterize vadose zone properties. Inverting a numerical analysis that includes variable material properties appears to offer a path forward for more detailed interpretation. These results will help future investigations account for the effects of barometric pressure on data from strainmeters, and they suggest that the constant interrogation by a fluctuating barometric pressure may lead to a new strategy for monitoring the vadose zone.

13.7 REFERENCES

Barrì, J., Bordes, C., Brito, D., Sénéchal, P., & Perroud, H. (2012). Laboratory monitoring of P waves in partially saturated sand. *Geophysical Journal International Geophys. J. Int*, *191*, 1152–1170. https://doi.org/10.1111/j.1365-246X.2012.05691.x

Becker, M. W., Ciervo, C., Cole, M., Coleman, T., & Mondanos, M. (2017). Fracture hydromechanical response measured by fiber optic distributed acoustic sensing at milliHertz frequencies. *Geophysical Research Letters*, *44*(14), 7295–7302. https://doi.org/10.1002/2017GL073931

Becker, M. W., Harris, B., & Pevzner, R. (2023). Characterization of Aquifer Poroelastic Response to Impulse and Oscillatory Well Pressure Using Distributed Acoustic Sensing. *Geophysical Research Letters*, *50*(1). https://doi.org/10.1029/2022GL100904

Blais, R. (2023). *Evaluating the Feasibility of Using Strain Measured During Sinusoidal-Rate Pumping Tests, MS Thesis* [Master of Science]. Clemson University.

Bogris, A., Nikas, T., Simos, C., Simos, I., Lentas, K., Melis, N. S., Fichtner, A., Bowden, D., Smolinski, K., Mesaritakis, C., & Chochliouros, I. (2022). Sensitive seismic sensors based on microwave frequency fiber interferometry in commercially deployed cables. *Scientific Reports*, *12*(1). https://doi.org/10.1038/s41598-022-18130-x

Borja, R. I. (2006). On the mechanical energy and effective stress in saturated and unsaturated porous continua. *International Journal of Solids and Structures*, *43*(6), 1764–1786. https://doi.org/10.1016/j.ijsolstr.2005.04.045

Butter, C. D., & Hocker, G. B. (1978). Fiber optics strain gauge. *Applied Optics*, *17*(18), 2867–2869. https://doi.org/10.1364/AO.17.002867

Cappa, F., Guglielmi, Y., & Virieux, J. (2007). Stress and fluid transfer in a fault zone due to overpressures in the seismogenic crust. *Geophysical Research Letters*, *34*(5). https://doi.org/10.1029/2006GL028980

Carslaw, H. S., & Jaeger, J. C. (1986). *Conduction of Heat in Solids* (2nd ed.). Oxford University Press.

Cheng, R., Xia, L., Yan, J., Zhou, J., Wen, Y., & Rohollahnejad, J. (2015). Radio Frequency FBG-Based Interferometer for Remote Adaptive Strain Monitoring. *IEEE Photonics Technology Letters*, *27*(15), 1577–1580. https://doi.org/10.1109/LPT.2015.2406112

Clement Bellido, J., Peralta, J. H., Madrigal, J. M., Vicente, H. M., Penalva, G. T., Fernandez-Pousa, C. R., & Maicas, S. S. (2018). Fast incoherent OFDR interrogation of FBG arrays using sparse radio frequency responses. *Journal of Lightwave Technology*. https://doi.org/10.1109/JLT.2018.2821199

Clement, J., Maestre, H., Torregrosa, G., & Fernández-Pousa, C. R. (2019). Incoherent Optical Frequency-Domain Reflectometry Based on Homodyne Electro-Optic Downconversion for Fiber-Optic Sensor Interrogation. *Sensors*, *19*(9), 2075.

Costantino, O. (2021). *Evaluating the Feasibility of Measuring and Analyzing Strain Caused by Changes in Barometric Pressure in the Vadose Zone* [Master of Science]. Clemson University.

Dauson, E., Donahue, C., DeWolf, S., Hua, L., Xiao, H., Murdoch, L., & Johnson, P. (2022). Damage detection in a laboratory-scale wellbore applying Time Reversal and Nonlinear Elastic Wave Spectroscopy (TR NEWS). *NDT and E International*, *126*. https://doi.org/10.1016/j.ndteint.2021.102573

Davis, D. R., & Rasmussen, T. C. (1993). A comparison of linear regression with Clark's Method for estimating barometric efficiency of confined aquifers. *Water Resources Research*, *29*(6), 1849–1854. https://doi.org/10.1029/93WR00560

Dobriyal, P., Qureshi, A., Badola, R., & Hussain, S. A. (2012). A review of the methods available for estimating soil moisture and its implications for water resource management. *Journal of Hydrology*, *458–459*, 110–117. https://doi.org/10.1016/J.JHYDROL.2012.06.021

Dong, H., Liu, S., Yang, L., Peng, J., & Cheng, K. (2018). Optical fiber displacement sensor based on microwave photonics interferometry. *Sensors (Switzerland)*, *18*(11). https://doi.org/10.3390/s18113702

Fabian, M., & Kümpel, H.-J. (2003). Poroelasticity: observations of anomalous near surface tilt induced by ground water pumping. *Journal of Hydrology*, *281*(3), 187–205. https://doi.org/10.1016/S0022-1694(03)00234-8

Galloway, D. L., & Burbey, T. J. (2011). Review: Regional land subsidence accompanying groundwater extraction. *Hydrogeology Journal*, *19*(8), 1459–1486. https://doi.org/10.1007/s10040-011-0775-5

Guglielmi, Y., Cappa, F., Lancon, H., Janowczyk, J. B., Rutqvist, J., Tsang, C. F., & Wang, J. S. Y. (2014). ISRM suggested method for step-rate injection method for fracture in-situ properties (SIMFIP): Using a 3-components borehole deformation sensor. *Rock Mechanics and Rock Engineering*, *47*(1), 303–311. https://doi.org/10.1007/s00603-013-0517-1

Hisz, D. B., Murdoch, L. C., & Germanovich, L. N. (2013). A portable borehole extensometer and tiltmeter for characterizing aquifers. *Water Resources Research*, *49*(12), 7900–7910. https://doi.org/10.1002/wrcr.20500

Hua, L., Song, Y., Cheng, B., Zhu, W., Zhang, Q., & Xiao, H. (2017). Coherence-length-gated distributed optical fiber sensing based on microwave-photonic interferometry. *Optics Express*, *25*(25), 31362–31376.

Hua, L., Song, Y., Huang, J., Lan, X., Li, Y., & Xiao, H. (2015). Microwave interrogated large core fused silica fiber Michelson interferometer for strain sensing. *Applied Optics*, *54*(24), 7181–7187.

Hua, L., Xiao, H., & Murdoch, L. (2022). *Phase demodulation by frequency chirping in coherence microwave photonic interferometry*.

Hua, L., Zhu, X., Cheng, B., Song, Y., Zhang, Q., Wu, Y., Murdoch, L. C., Dauson, E. R., Donahue, C. M., & Xiao, H. (2021). Distributed acoustic sensing based on coherent microwave photonics interferometry. *Sensors*, *21*(20). https://doi.org/10.3390/s21206784

Hua, L., Zhu, X., Dewolf, S., Lei, J., Zhang, Q., Murdoch, L., & Xiao, H. (2021). Phase Demodulation by Frequency Chirping in Coherence Microwave Photonic Interferometry. *IEEE Journal of Selected Topics in Quantum Electronics*, *27*(2), 1–9. https://doi.org/10.1109/JSTQE.2020.2975575.

Hua, L., & Murdoch, L. C. (2023). A Microwave Photonics Optical Fiber Method for Measuring Distributed Strain for Hydrologic Applications in the Vadose and Saturated Zones. In G. Zhan (Ed.), *Distributed Acoustic Sensing in Borehole Geophysics*. American Geophysical Union. In review.

Huang, J., Lan, X., Luo, M., & Xiao, H. (2014). Spatially continuous distributed fiber optic sensing using optical carrier based microwave interferometry. *Optics Express*, *22*(15), 18757. https://doi.org/10.1364/OE.22.018757

Huang, J., Lan, X., Song, Y., Li, Y., Hua, L., & Xiao, H. (2015). Microwave interrogated sapphire fiber michelson interferometer for high temperature sensing. *IEEE Photonics Technology Letters*, *27*(13), 1398–1401. https://doi.org/10.1109/LPT.2015.2422136

Jacob, C. E. (1940). *On the flow of water in an elastic artesian aquifer* (Vol. 21).

Jin, G., Ugueto, G., Wojtaszek, M., Guzik, A., Jurick, D., & Kishida, K. (2021). Novel Near-Wellbore Fracture Diagnosis for Unconventional Wells Using High-Resolution Distributed Strain Sensing during Production. *SPE Journal*, *26*(05), 3255–3264. https://doi.org/10.2118/205394-PA

Karasaki, K., Freifeld, B., Cohen, A., Grossenbacher, K., Cook, P., & Vasco, D. (n.d.). *A multidisciplinary fractured rock characterization study at Raymond field site, Raymond, CA*. www.elsevier.com/locate/jhydrol

Keller, T., Arvidsson, J., Schjønning, P., Lamandé, M., Stettler, M., & Weisskopf, P. (2012). *In Situ Subsoil Stress-Strain Behavior in Relation to Soil Precompression Stress*. https://doi.org/10.1097/SS.0b013e318262554e

Khakim, M. Y. N., Tsuji, T., & Matsuoka, T. (2012). Geomechanical modeling for InSAR-derived surface deformation at steam-injection oil sand fields. *Journal of Petroleum Science and Engineering*, *96–97*, 152–161. https://doi.org/10.1016/j.petrol.2012.08.003

Kuang, X., Jiao, J. J., & Li, H. (2013). Review on airflow in unsaturated zones induced by natural forcings. *Water Resources Research*, *49*(10), 6137–6165. https://doi.org/10.1002/WRCR.20416

Kumar Thota, S., Duc Cao, T., & Vahedifard, F. (2021). Poisson's Ratio Characteristic Curve of Unsaturated Soils. *Journal of Geotechnical and Geoenvironmental Engineering*, *147*(1), 04020149. https://doi.org/10.1061/(asce)gt.1943-5606.0002424

Lekshmi, S. S. U., Singh, D. N., & Baghini, M. (2014). A critical review of soil moisture measurement. *Measurement*, *54*, 92–105. https://doi.org/10.1016/J.MEASUREMENT.2014.04.007

Liehr, S., Nöther, N., & Krebber, K. (2010). Incoherent optical frequency domain reflectometry and distributed strain detection in polymer optical fibers. *Measurement Science and Technology*. https://doi.org/10.1088/0957-0233/21/1/017001

Lu, N., Godt, J. W., & Wu, D. T. (2010). A closed-form equation for effective stress in unsaturated soil. *Water Resources Research*, *46*(5). https://doi.org/10.1029/2009wr008646

Lu, N., & Kaya, M. (2014). Power Law for Elastic Moduli of Unsaturated Soil. *Journal of Geotechnical and Geoenvironmental Engineering*, *140*(1), 46–56. https://doi.org/10.1061/(asce)gt.1943-5606.0000990

Marin, S., van der Kamp, G., Pietroniro, A., Davison, B., & Toth, B. (2010). Use of geological weighing lysimeters to calibrate a distributed hydrological model for the simulation of land–atmosphere moisture exchange. *Journal of Hydrology*, *383*(3–4), 179–185. https://doi.org/10.1016/J.JHYDROL.2009.12.034

Massmann, J., & Farrier, D. F. (1992). Effects of atmospheric pressures on gas transport in the vadose zone. *Water Resources Research*, *28*(3), 777–791. https://doi.org/10.1029/91WR02766

Monfared, K. A., & Rothenburg, L. (2011). Ground surface displacements and tilt monitoring for reconstruction of reservoir deformations. *International Journal of Rock Mechanics and Mining Sciences*, *48*(7), 1113–1122. https://doi.org/10.1016/j.ijrmms.2011.07.003

Murdoch, L. C., DeWolf, S., Germanovich, L. N., Moysey, S., Hanna, A., Roudini, S., & Moak, R. (2023). Using the Shallow Strain Tensor to Characterize Deep Geologic Reservoirs. *Water Resources Research*. https://doi.org/10.1029/2022wr032920

Murdoch, L. C., Freeman, C. E., Germanovich, L. N., Thrash, C., & Dewolf, S. (2015). Using in situ vertical displacements to characterize changes in moisture load. *Water Resources Research*, *51*(8), 5998–6016. https://doi.org/10.1002/2015WR017335

Murdoch, L. C., Germanovich, L. N., DeWolf, S. J., Moysey, S. M. J., Hanna, A. C., Kim, S., & Duncan, R. G. (2020a). Feasibility of using in situ deformation to monitor CO2 storage. *International Journal of Greenhouse Gas Control*, *93*. https://doi.org/10.1016/j.ijggc.2019.102853

Murdoch, L. C., Germanovich, L. N., DeWolf, S. J., Moysey, S. M. J., Hanna, A. C., Kim, S., & Duncan, R. G. (2020b). Feasibility of using in situ deformation to monitor CO2 storage. *International Journal of Greenhouse Gas Control*, *93*. https://doi.org/10.1016/j.ijggc.2019.102853

Neuman, S. P. (1975). Analysis of pumping test data from anisotropic unconfined aquifers considering delayed gravity response. *Water Resources Research*, *11*(2), 329–342. https://doi.org/10.1029/WR011I002P00329

Philip, J. R., Knight, J. H., & Waechter, R. T. (1989). Unsaturated seepage and subterranean holes: Conspectus, and exclusion problem for circular cylindrical cavities. *Water Resources Research*, *25*(1), 16–28. https://doi.org/10.1029/WR025i001p00016

Plunkett, G. (2021). *A Novel Technique for Distributed Measuring of Strain in the Vadose Zone* [Master of Science]. Clemson University.

Požar, T., Gregorčič, P., & Možina, J. (2011). A precise and wide-dynamic-range displacement-measuring homodyne quadrature laser interferometer. *Applied Physics B: Lasers and Optics*, *105*(3), 575–582. https://doi.org/10.1007/s00340-011-4512-5

Quilty, E. G., & Roeloffs, E. A. (1991). Removal of barometric pressure response from water level data. *Journal of Geophysical Research*, *96*(B6). https://doi.org/10.1029/91JB00429

Rao, Y. J., & Jackson, D. A. (1996). Recent progress in fibre optic low-coherence interferometry. *Measurement Science and Technology*, *7*(7), 981–999. https://doi.org/10.1088/0957-0233/7/7/001

Rasmussen, T. C., & Crawford, L. A. (1997). Identifying and removing barometric pressure effects in confined and unconfined aquifers. *Ground Water*, *35*(3), 502–511. https://doi.org/10.1111/J.1745-6584.1997.TB00111.X

Ricchiuti, A. L., Hervas, J., Barrera, D., Sales, S., & Capmany, J. (2014). Microwave Photonics Filtering Technique for Interrogating a Very-Weak Fiber Bragg Grating Cascade Sensor. *IEEE Photonics Journal*, *6*(6), 1–10. https://doi.org/10.1109/JPHOT.2014.2363443

Rojstaczer, S. (1988). Determination of fluid flow properties from the response of water levels in wells to atmospheric loading. *Water Resources Research*, *24*(11), 1927–1938. https://doi.org/10.1029/WR024i011p01927

Rojstaczer, S., & Riley, F. S. (1990). Response of the water level in a well to Earth tides and atmospheric loading under unconfined conditions. *Water Resources Research*, *26*(8), 1803–1817. https://doi.org/10.1029/WR026I008P01803

Rutqvist, J., & Tsang, C. F. (2002). A study of caprock hydromechanical changes associated with CO2-injection into a brine formation. *Environmental Geology*, *42*(2–3), 296–305. https://doi.org/10.1007/s00254-001-0499-2

Schweisinger, T., Svenson, E. J., & Murdoch, L. C. (2009). Introduction to hydromechanical well tests in fractured rock aquifers. *Ground Water*, *47*(1), 69–79. https://doi.org/10.1111/j.1745-6584.2008.00501.x

Schweisinger, T., Svenson, E. J., & Murdoch, L. C. (2011). Hydromechanical behavior during constant-rate pumping tests in fractured gneiss. *Hydrogeology Journal*, *19*(5), 963–980. https://doi.org/10.1007/s10040-011-0728-z

Song, Y., Hua, L., Lei, J., Zhang, Q., Liu, J., Ye, L., & Xiao, H. (2016). An IFPI Temperature Sensor Fabricated in an Unstriped Optical Fiber with Self-Strain-Compensation Function. *Journal of Sensors*, *2016*. https://doi.org/10.1155/2016/6419623

Sun, Y., Xue, Z., Hashimoto, T., Lei, X., & Zhang, Y. (2020). Distributed Fiber Optic Sensing System for Well-Based Monitoring Water Injection Tests—A Geomechanical Responses Perspective. *Water Resources Research*, *56*(1), e2019WR024794. https://doi.org/10.1029/2019WR024794

Sun, Y., Xue, Z., Hashimoto, T., & Zhang, Y. (2021). Optically quantifying spatiotemporal responses of water injection-induced strain via downhole distributed fiber optics sensing. *Fuel*, *283*, 118948. https://doi.org/10.1016/J.FUEL.2020.118948

Svenson, E., Schweisinger, T., & Murdoch, L. C. (2008). Field evaluation of the hydromechanical behavior of flat-lying fractures during slug tests. *Journal of Hydrology*, *359*(1–2), 30–45. https://doi.org/10.1016/j.jhydrol.2008.06.004

Tian, X., Wang, Y., Zhu, D., & Shi, J. (2022). Radio-Frequency Intensity Interrogation for Temperature Measurement. *IEEE Photonics Technology Letters*, *34*(18), 973–976. https://doi.org/10.1109/LPT.2022.3195960

Van Der Kamp, G., & Schmidt, R. (1997). Monitoring of total soil moisture on a scale of hectares using groundwater piezometers. *Geophysical Research Letters*, *24*(6), 719–722. https://doi.org/10.1029/97GL00521

Vasco, D. W., Karasaki, K., & Kishida, K. (2001). A coupled inversion of pressure and surface displacement. *Water Resources Research*, *37*(12), 3071–3089.

Vasco, D. W., Kim, K. H., Farr, T. G., Reager, J. T., Bekaert, D., Sangha, S. S., Rutqvist, J., & Beaudoing, H. K. (2022). Using Sentinel-1 and GRACE satellite data to monitor the hydrological variations within the Tulare Basin, California. *Scientific Reports*, *12*(1). https://doi.org/10.1038/s41598-022-07650-1

Weeks, E. P. (1979). Barometric fluctuations in wells tapping deep unconfined aquifers. *Water Resources Research*, *15*(5), 1167–1176. https://doi.org/10.1029/WR015I005P01167

Wu, N., Xia, M., Wu, Y., Li, S., Qi, R., Huang, Y., & Xia, L. (2021). Microwave photonics interrogation for multiplexing fiber Fabry-Perot sensors. *Optics Express*, *29*(11), 16652. https://doi.org/10.1364/oe.424059

Xue, Z., & Hashimoto, T. (2017a). Geomechanical Monitoring of Caprock and Wellbore Integrity Using Fiber Optic Cable: Strain Measurement from the Fluid Injection and Extraction Field Tests. *Energy Procedia*, *114*, 3305–3311. https://doi.org/10.1016/j.egypro.2017.03.1462

Xue, Z., & Hashimoto, T. (2017b). Geomechanical Monitoring of Caprock and Wellbore Integrity Using Fiber Optic Cable: Strain Measurement from the Fluid Injection and Extraction Field Tests. *Energy Procedia*, *114*, 3305–3311. https://doi.org/10.1016/j.egypro.2017.03.1462

Yusa, Y. (1969). The fluctuation of the level of the water table due to barometric change. *Special Contributions, Geophysical Institute, Kyoto University*, *9*, 15–28.

Zhu, C., & Huang, J. (2023). Multiplexed optical fiber tip refractive index sensor interrogated by microwave photonics. *Optics and Lasers in Engineering*, *163*. https://doi.org/10.1016/j.optlaseng.2023.107477

Zhu, X., Hua, L., Lei, J., Tang, J., Murdoch, L., & Xiao, H. (2021). Microwave-photonic Low-coherence Interferometry for Dark Zone Free Distributed Optical Fiber Sensing. *Optics Letters*, *46*(5), 1173–1176. https://doi.org/10.1364/ol.414699

CHAPTER FOURTEEN

EFFECTS OF CHANGES IN WATER PRESSURE ON STRAIN IN THE VADOSE ZONE

Contents

14.1 Abstract 14-1
14.2 Introduction 14-4
14.2.1 Vadose Zone Moisture Measurements 14-4
14.2.2 Strain Measurements 14-5
14.2.3 Objective 14-7
14.2.4 Approach 14-7
14.2.5 Organization of the Chapter 14-8
14.3 Apparatus and Experimental Methods 14-9
14.3.1 Data Processing 14-9
14.3.2 Apparatus 14-9
14.3.3 Soil Parameters 14-19
14.3.4 Grain Size Distribution 14-20
14.3.5 Dry Bulk Density 14-22
14.3.6 Water Retention Curve 14-22
14.4 Column Loading Tests 14-28
14.4.1 Column Loading Test 14-28
14.5 Column Fill and Drain Tests 14-33
14.5.1 Partial-fill Injection Test 14-33
14.5.2 Complete-Fill Tests: Fill and Drain with Ponding 14-50
14.5.3 Results 14-51
14.5.4 Patterns and Repeatability 14-71
14.5.5 Displacement Over the Sensor 14-80
14.5.6 Pressure and Strain Behavior 14-81
14.5.7 Outside Strain Sensor 14-83
14.5.8 Infiltration 14-87
14.5.9 Infiltration Open Drainage 14-94
14.5.10 Separation of Effects and Commonalities 14-96
14.6 Conceptual Model 14-97
14.6.1 Stage One 14-100
14.6.2 Stage Two 14-100
14.6.3 Stage Three 14-101
14.6.4 Stage Four 14-101
14.6.5 Surface Wetting Stage (w) 14-101
14.6.6 Ponded No-Flow 14-103
14.6.7 Summary 14-107
14.7 Summary and Conclusions 14-108
14.8 References 14-110

EFFECTS OF CHANGES IN WATER PRESSURE ON STRAIN IN THE VADOSE ZONE

14.1 ABSTRACT

Characterizing water content and pressure changes in the vadose zone is important to understanding a variety of geologic processes, ranging from storage and drainage, to evapotranspiration, and recharge. Changes in water content, or pressure, cause strain in the solid porous medium of the vadose zone, and it is possible that measuring those strains could be used as a characterization tool. The Coherence-length-gated Microwave Photonics Interferometry (CMPI) technique measures strain at high resolution along many intervals defined by pairs of reflectors distributed along an optical fiber. This technique was developed for this project, and it appears to have the spatial and temporal resolution to characterize strains that are expected to occur with hydrologic changes in the vadose zone. However, the technique has never been used to measure strain in porous media, so its capabilities remain uncertain. The objective of this chapter is to evaluate the ability of using CMPI to measure strain in the vadose zone.

The research approach consists of conducting laboratory tests using a column filled with sand that is subjected to changes in water content and pressure. An optical fiber with CMPI reflectors was laminated in a high-surface-area ribbon and deployed along the axis of the column. The column was made from 8-inch, Schedule 40 PVC pipe (75 cm tall, 20 cm inner diameter) and filled with medium-grained sand ($K = 2.5\text{x}10^{-6}$ m/s, porosity = 0.28, Coefficient of Uniformity = 2, van Genuchten ($n = 4.34$, $\alpha = 0.00039$ m^{-1}, $\theta_s = 0.28$, and $\theta_r = 0.08$), Young's Modulus = 18 –30MPa). Five pressure and four temperature sensors were inserted through the wall of the column. The optical fiber strain measurements include five reflectors spaced 10 cm apart in a ribbon on the inside, and 5 addition reflectors on the outside along the axis of the column. Strain measurements are made between pairs of reflectors. The reflectors are created in 250-micron-diameter acrylate-coated single mode Corning SMF28e+ optical fiber using a femtosecond laser. The optical fiber was laminated between two pieces of polyester film creating a large surface area to transfer strain from the porous media to the optical fiber. The experiments were conducted by filling the column from the bottom or infiltrating water from the top. The water was allowed to equilibrate to room temperature prior to each test in order to limit thermoelastic strain.

Five injection tests with a rate of 250 ml/min and three infiltration tests at varying rates were conducted, and the results show patterns of strain and pressure are generally similar. Hydrologic conditions define three zones based on the pressure magnitude and distribution.

1.) *Ambient Zone* where the pressure heads are quasi-static, and the pressure gradient is roughly unity (head gradient of zero). This is the uppermost zone and is characterized by negative pressures. The pressure head gradient is approximately 1.

2.) *Transition Zone* where the pressures increase from ambient to zero, are changing relatively rapidly and the pressure gradient is relatively steep (pressure head gradients of 2). The Transition zone is 10 to 15 cm thick.

3.) *Positive Pressure Zone* where the pressure is positive, the rate of change is slower than in the transition zone and the gradient is flatter (pressure head gradient 1.1 to 1.2). This is the lowest zone in the column.

Injection of water causes the pressure to increase and the three pressure zones to move upward. The Transition zone moves at a rate of approximately $2x10^{-4}$ +/- $0.5x10^{-4}$ m/s, according to analyses of pressure profiles. This is the same as the ratio of the volumetric flux ($5.4x10^{-5}$ m/s) and the porosity (0.28).

Strain signals in the range of 10s of με were observed with a noise level of generally less than 0.1 με (signal to noise ratio of greater than 100) during injection and drainage. The strain generally increases during injection and decreases during drainage. The strain rate, and how the strain relates to changes in pore pressure varies considerably, however. These changes are repeatable and were used to define four stages in the strain time series during filling and four stages during draining. An additional three stages were identified in the time series of tests that involved filling the column until water ponded on the surface of the sand.

The spatial and temporal distributions of strain caused by injection depend on the location of the moving pressure zones. The locations of the different pressure zones were determined from pressure profiles at different times and these data were transferred to strain time series. This shows that the pressure zones occur in consistent locations relative to the strain sensor during the different stages, which indicates that the changing pore pressure is controlling the strain. This was expected, but how the pressure controls the strain was unexpected. In some locations, the strain increases with increasing pressure, which is consistent with Hooke's Law. In other locations, however, the strain is unchanged or decreases when the pore pressure increases. It is inferred that this is a result of stress transfer, where an increase in stress in one location causes a decrease in stress in another location to maintain equilibrium.

An interesting effect occurs when the upper surface of the sand becomes saturated. Significant compression (several 10s of με) occurs as the pressure and saturation increase at the upper surface. Compression occurs throughout the column, but the effect is greatest at the top of the column. The rate of compression is fastest slightly before ponding occurs, but it slows markedly and nearly stops when water starts to accumulate at the surface (ponding). This effect reverses when the surface of the sand is drained, resulting in tension throughout the column. The compression caused by this effect can be as large or larger than the tensile strain that accumulated during filling. This effect was unexpected because increasing pressure is normally associated with tensile strain. Nevertheless, this effect was observed consistently in all tests where the pressure changes at the upper surface, including tests where water was injected from below or infiltrated from above. This effect behaves as if the pore pressure at the upper surface of the sand exerts a normal force on the boundary (increasing pore pressure exerts a downward compression on the boundary).

Results of the laboratory experiments indicate that CMPI can measure strain caused by fluid pressure changes in the vadose zone with a signal to noise ratio of 100 or more. Injection and drainage cause a strain signal that is complex, but repeatable. The magnitudes of the strain signal are consistent with magnitudes that are expected based on poroelastic calculations using independently measured properties of the sand. The strain signal can be explained with a conceptual model that recognizes three basic effects: 1.) strain in proportion to pressure change (Hooke's Law); 2.) strain independent of local pressure change due to stress transfer; 3.) strain caused by a load applied at the ground surface that is proportional to the pressure change. These results indicate that the CMPI technique with an optical fiber laminated in a polyester ribbon generates data that represent the strain distribution during hydrologic processes of imbibition and

drainage in variably saturated sand. This suggests that distributed strain measurements using CMPI could be a viable approach for evaluating processes in the vadose zone, laying the groundwork for future field implementation. This chapter is based on research by Grant Plunkett for his MS thesis research (Plunkett, 2021)

14.2 INTRODUCTION

Understanding water content and movement in the vadose zone has applications from agriculture, to environmental monitoring (Baram et al., 2012), to resource management. Soil moisture measurement techniques range in their scales. The largest scale remote sensing techniques use satellites to record electromagnetic radiation coming from the ground which can be interpreted to give soil moisture values for scales ranging from 10^3 to 10^4 m (Ochsner et al., 2013). Ground-based sensing has a greater resolution than remote sensing. Techniques such as capacitance probes and time domain reflectometry can measure soil moisture at the 10^{-1} m scale (Blonquist et al., 2005).

Changes in pressure or water content in the subsurface cause strain (Hisz et al., 2013). It is possible to use strain as a in situ measurement of water content in the vadose zone because a change in water content will alter the total stress. Point measurements of strain have been made using an instrument developed at Clemson University, called the DEL-x (Thrash, 2016), however a new method can measure the strain in regions distributed over a length of optical fiber (Hua et al., 2017). This distributed strain measurement method needs to be tested for use in the vadose zone. Laboratory tests will evaluate this technique and report findings on strain and how it varies during changes in pressure.

14.2.1 Vadose Zone Moisture Measurements

The vadose zone by definition is the region between the water table and the ground surface (Martin & Koerner, 1984). This region is where many interesting dynamics occur between the groundwater and porous media. Fluctuations in the water table induce changes in the vadose zone. These fluctuations can come from raising and lowering the pressure in the saturated zone from below, or infiltration from above.

Methods have been developed for characterizing hydrogeologically relevant properties and processes in the vadose zone over scales ranging from kilometers to milimeters. These include characterizing the amount of cosmic ray absorption to infer water contents (Zreda et al., 2012), to neutron probes in boreholes (Dobriyal et al., 2012), to classical well testing characterizing aquifer properties.

Water content can vary over the cm scale in the vadose zone. Sensors can measure these fluctuations. However, in situ moisture sensors can be bulky and disturb the material they are situated in and have the potential to alter the material and measurements. Tensiometers are often used to measure suction pressure in unsaturated soils. This works as long as the tubing and porous cup of the tensiometer remains saturated. Time domain reflectometry (TDR) can measure water content in a subsurface sensor at a scale of around 10 cm (depending on the probe) (Blonquist et al., 2005). However, installing the instrument can disturb the sample and affect reported water content (Topp et al., 2001). Distributed measurements are possible with a cascaded TDR sensor (Aharoni et al., 2017)

14.2.2 Strain Measurements

Measuring strain in the subsurface has applications that include geotechnical measurements of slope stability (Nitzsche & Herle, 2020), structural health of dams (Prakash et al., 2018), and modeling of subsidence (Hall & Fox, 2018). Strain measurements can monitor seismic events (Hagiwara, 1974), enhance the study of plate tectonics (Weiss et al., 2020), and monitor volcanism (Luttrell et al., 2013). Measuring the stress-strain relationship in reservoirs is important for the oil and gas industry (Gambolati et al., 1999). Soil compaction is a problem in agriculture negatively affecting crop growth (Keller et al., 2012).

14.2.2.1 InSAR

Satellites using Interferometric Synthetic Aperture Radar (InSAR) can measure strain rates and plate velocities (Weiss et al., 2020). These can be used to monitor tectonically active regions to better understand orogeny and crustal deformation. Naturally, this has potential use in hazard mapping for earthquakes and related disasters (e.g. Fattahi & Amelung, 2016). InSAR has also been used in measuring subsidence (Hongdong et al., 2011).

14.2.2.2 Tiltmeters

Tiltmeters have been used in diverse applications such as monitoring volcanos and monitoring hydraulic fracturing (Warpinski et al., 1997). Rainfall and changes in barometric pressure can induce measurable deformations in the subsurface, with up to 0.5 με measured in solid rock at a depth of 60 m during a rainfall event. (Dal Moro & Zadro, 1998).

14.2.2.3 DEL-x

An instrument has been recently developed at Clemson to measure small scale deformation in the subsurface. This instrument, the DELTA-extensometer, known as the DEL-x can measure vertical changes in the subsurface down to a resolution of 0.01 μm (Murdoch et al., 2016: Freeman, 2012; Thrash, 2016).

One finding that emerged from the DEL-X is that strain is affected by changes in water content, weight in overlying soil, changes in pore pressure (water or air), changes in surface load by barometric pressure, and temperature. However, signals need to be separated. Signals migrate with time, so one way to help separate signals and improve interpretation is to measure strain at multiple locations with depth. This is possible with DEL-X but limited by scale and logistics to 1-2 m spacing. Higher resolution is needed to resolve wetting and barometric fronts (Thrash, 2016).

14.2.2.4 Optical Fiber Strain sensors

Optical fibers have been used as strain sensors for some time to measure strain. Mainly in civil engineering applications such as structural health monitoring (Inaudi & Glisic, 2006), but increasingly including geomechanical relevance.

14.2.2.5 Distributed Brillouin Sensing systems

Distributed Brillouin Sensing systems (DBSs) have been used in subsurface strain measurements. Madjdabadi et al., 2016 explores using DBSs in mining applications measuring strain in a rock mass. The strains measured are in the 1000s of με with a noise level of approximately 80 με.

14.2.2.6 Fiber Bragg Grating

Recently, Fiber Brag Grating (FBG), an optical fiber sensor, has been explored for real time measurement of strain in unsaturated aeolian sands (You et al., 2019). Temperature and strain results show that the strain is greatly affected by temperature, however, most of the temperature change occurs near the surface of the sand.

14.2.2.7 Challenges to Measuring Strain in the Vadose Zone

A technique for measuring meaningful strain needs to be able to clearly resolve strain magnitudes expected in the vadose zone without affecting the material in a way that overly complicates the reading. Many vadose zones are soft, unconsolidated porous media. Sensors need to couple to the subsurface formation using a material with compliance high enough to not affect the measurement. The DEL-X measured displacements of a couple microns during rainfall events (Thrash, 2016). An instrument would need to have a sub-micron resolution to resolve these fronts. Problems and additional challenges arise when electrical components are placed in the ground, an ideal instrument would have its electrical components on the surface.

14.2.2.8 Coherence-length-gated Microwave Photonics Interferometry

Coherence-length-gated Microwave Photonics Interferometry (CMPI) is a technology that measures strain between reflectors etched into optical fiber (Hua et al., 2017). These measurements are distributed and can be spaced at a desired location. Earlier experiments of CMPI being used to measure strain have yielded encouraging results, however, there is currently no application involving loading or flow in porous media.

14.2.2.8.1 Description of technique

CMPI technology works by using a laser and an electro-optic modulator (EOM) to create light modulated in the microwave band. The light is injected into an optical fiber, and back scattered light from reflectors in the fiber is detected by a photodetector. The amplitude and phase of the reflected light at the modulated frequency is resolved through synchronized detection. After scanning the designated modulation band, the complex reflection spectrum is obtained. The time domain signal is obtained by Fourier transform of the complex reflection spectrum. Reflected waves that separate within the coherence length of the laser produce optical interference, which is sensitive to the localized strain (Hua et al., 2017) . The chirp effect of the EOM is used to create two quadrature signals for the interference phase demodulation in the CMPI system, which allows the strain to be measured between the reflector locations without complicated coherent detection schemes (Hua et al., 2020). An external interferometer (EI) can be added into the system to enable fully distributed sensing capability. CMPI has several unique advantages including high strain sensitivity, high signal quality, relieved requirement on fabrication, low dependence on the types of optical waveguides, insensitivity to variations of polarization, and high spatial resolution.

14.2.2.8.2 CMPI Applications in Hydrogeology

Microwave photonics used with optical fiber has a diverse set of applications including structural monitoring (Leung et al., 2015). Potential applications in the subsurface include monitoring CO_2 injections for leaks, determining aquifer characteristics from pumping tests, and monitoring infiltration in the vadose zone. Advancing strain measurement capabilities from point measurements to distributed measurements over a length is important to understanding the

movement of pressure fronts. For field applications to advance, CMPI strain sensing capabilities in porous media need to be evaluated first in the laboratory.

14.2.3 Objective

This chapter has two distinct, but related objectives. One is to evaluate the feasibility of measuring strain caused by hydrologic processes in unconsolidated, variably saturated porous media. Another objective to evaluate the performance of the new sensing method Coherence-length-gated Microwave Photonics Interferometry as a technique for measuring strain in variably saturated porous media.

14.2.4 Approach

The general approach to achieving the objective of the research is to use laboratory experiments to mimic hydrologic processes under ideal conditions and then measure the resulting distributions of pressure, temperature, and strain. The experiments will be configured by stretching a distributed optical fiber sensor through a sand-filled column and vary water pressure and saturation under controlled conditions in the laboratory to broadly resemble imbibition and draining processes in the vadose zone. The optical fiber is packaged in compliant strip that extends along the axis of the column.

The column contains features to allow instruments inside and outside as well as filling and draining from the bottom and infiltration from the top. It contains ports on the side where temperature and pressure sensors are inserted, and a port in the bottom where water can be injected and removed. Supports on the top of the column allow for a sprinkler head to infiltrate water from above.

This configuration allows water to be injected and either pumped out or drained by gravity out the bottom. It also allows water to be infiltrated in the top. The sand is filled to within a few cm of the top of the column, so water can pond on the sand.

Laboratory experiments conducted in the Advanced Materials Research Laboratory were used to evaluate the distributed strain under room temperature. A pair of optical fibers were used to measure the distributed strain using the CMPI method. An optical fiber with reflectors was packaged in a compliant strip with high surface area designed to couple the fiber to strain in the sand inside the column. The high compliance allows for the strip and optical fiber to stretch as the material in the column deforms. High surface area helps to couple the strip to the porous media using friction. Another set of optical fiber reflectors are taped to the outside of the column. This is used to measure strain changes that may occur in the column itself.

The column was loaded with static weight to test the system and the resulting strain was used to estimate the elastic properties of the sand. Water was then injected in the bottom of the column to increase the water content and pressure in the column. Pressure and temperature were monitored with sensors along the column, and the distributed strain was measured with the optical fiber. These data were also measured upon drainage of the column. These are called “Fill and Drain” tests. Most Fill and Drain tests involve completely filling the column until water ponded on top of the sand. One test involved partially filling the column with water and then draining it.

Another set of tests were conducted by adding water to the top of the column to simulate infiltration. These tests involved sprinkling water over the top of the column using a shower head. Infiltration was tested at different rates. One test occurred where the drain at the bottom of the column was closed, allowing the column to fill up completely. Another set of tests created a continuous drainage scenario by opening the bottom drain throughout the test.

14.2.5 Organization of the Chapter

The following chapter is organized into seven sections, including this abstract and this introductory section. Section 14.3 describes the setup for the experiments and the physical characteristics and properties of the porous media used in the experiments. Section 14.4 describes a loading experiment used to test the strain ribbon. Section 14.5 describes tests involving varying the saturation in the column, and 14.6 introduces a conceptual model to help explain what the data from the experiments. The chapter concludes with Section 14.7.

14.3 APPARATUS AND EXPERIMENTAL METHODS

Experiments were conducted to test the equipment and reproduce hydrogeologically relevant situations during loading/unloading, injection/drainage, and infiltration/drainage. Loading/unloading tests were conducted by applying and removing different weights on the top of the column. The strain caused by these loads was measured to evaluate repeatability and to estimate material parameters. Injection/drainage tests were conducted by filling the column with water injected from the base, whereas infiltration/drainage tests were conducted by applying water to the top of the column. Water added during these tests was drained by either pumping or gravity. These tests were intended to simulate imbibition and infiltration.

14.3.1 Data Processing

The raw data was processed using a combination of programs, mainly MATLAB and Microsoft Excel. The data acquisition from the CMPI and LabJack data acquisition system used for the pressure and temperature sensors needed to be synchronized. The CMPI measured data at frequencies of 2 to 10 Hz depending on the experiment. The LabJack measured at 2 to 4 Hz. Timetables were made in MATLAB to synchronize the time to the start of the experiment and interpolate data points for the relevant data at intervals of every 0.25 seconds. These new data points are the linear interpolations of the raw data found between these points and accurately represent the data that would have been acquired at these time intervals.

14.3.2 Apparatus

The experimental apparatus consists of a column filled with sand and fitted with sensors for pressure, temperature, and strain, and it also includes equipment for pumping and weighing water. The column used for the experiments is a 75 cm-long, 20 cm-diameter (8-inch nominal) PVC pipe (Figure 1). The column was sealed into a small basin using epoxy to provide structural stability and a watertight seal.

14.3.2.1 Column Configuration

The holes are drilled and tapped ¼ NPT in the side of the column to accommodate tubing and sensors. Two holes are on opposite sides of the column and approximately 2 cm from the bottom. One is used to attach tubing from a pump and is used for filling and draining water. The other is used for pressure measurement and a sighting manometer. A needle valve at the base of the sighting manometer can be used to isolate the manometer, which is necessary to prevent air from entering the column through the manometer during drainage. Two rows of holes extend along the axis on opposite sides of the column. The holes are 13, 29, 44, and 60 cm from the base. These holes were used for pressure and temperature sensors, and the name of the sensor includes the height of the access hole above the base.

A MasterFlow peristaltic pump equipped with 0.25-inch diameter tubing was used to inject, drain, and infiltrate the column. The peristaltic pump provided a nearly constant flow rate of 100 ml/min. The pump was attached to a tank that is weighed. Weighing the tank using the load cell array and assuming a constant density provided data on the water volume during injection or drainage.

To stabilize apparatus components and to lessen temperature fluctuations caused by air current convection, a frame was constructed around the column. This frame is made of T-Slotted

aluminum bars. Panels made from polystyrene foam and transparent polycarbonate plastic are on the side of the frame to reduce air movement, and resulting temperature changes, at the column.

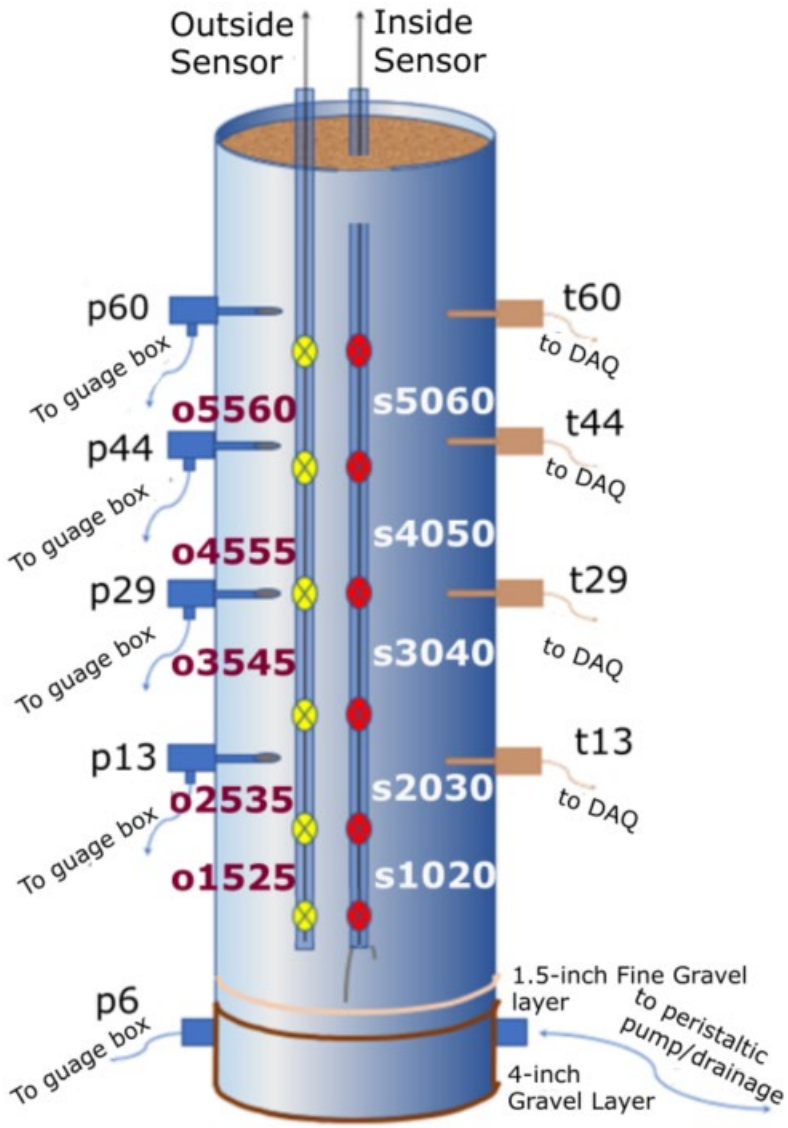

Figure 1: Column apparatus used for experiments, p6-p60 are pressure sensors. t13-t60 are temperature sensors. The five red points indicate the reflectors on a strain ribbon in sand inside of the column; yellow points indicate reflectors attached to the outside of the column.

Infiltration is conducted using a 15 cm diameter shower head that is placed on a piece of polycarbonate supported by the frame 8 cm over the top of the column. The system evenly distributes water over the surface of the column except for the area below the fiber optic strain ribbon. This area is blocked out of the shower head to lessen the number of drops of water disturbing the optical fiber.

The column was filled to a depth of 5 cm with gravel. The gravel has a higher hydraulic conductivity than the sand. Water is injected into the side of the gravel layer and the high

hydraulic conductivity causes the head to be essentially uniform over the gravel layer. This causes the upward flow rate to be essentially uniform over the column. On top of the gravel layer is a fine mesh overlain by, a centimeter-deep layer of coarse-grained, well sorted sand. The rest of the column is filled with fine to medium-grained sand. Soil Properties of these materials are presented in section Three.

The column was leveled by placing spacers under the base and measuring with a bubble level.

14.3.2.2 Pressure, Temperature, Water Volume Measurement

Strain, pore pressure, temperature, and volume of water injected/drained were measured and recorded during the experiments. These quantities were measured with sensors and the data were recorded using a data acquisition system.

14.3.2.2.1 Pressure Sensors

Pore pressure is measured in the column using Honeywell (model ABPDANT005PGAA5) pressure transducers. These are board-mount transducers with a 0-35 kPa (0-5 psi) span, an accuracy of 0.25% of the span and a total error band of 1.5% of the span. They are designed to work with wet media, are temperature compensated and have an amplified analog output. These transducers are inexpensive and well suited to measuring pore pressure in the range of the experiments. They can accommodate an overpressure of ~1 MPa (150 psi), which makes them robust in an experimental setting.

Even though the Honeywell transducers were well suited to measuring pressures over the expected range during the experiments, they only measure positive pressure, and the pressure in the column was expected to range from +/- 6 kPa. The transducers were mounted on a horizontal frame below the column to accommodate this discrepancy, which ensured that the pressure signal would remain within their measurement range

The transducers are attached to plastic tubing that extends to a porous ceramic cup, which contacts the soil in the column. The porous ceramic cup is 0.635 cm (0.25 inch) in diameter by 2.858 cm long, 1 bar standard flow (Soilmoisture 0652X03-B01M1). The cup is sealed onto an aluminum (the aluminum corroded during use, so in retrospect these tubes should have been made from brass or stainless steel) tube, which is connected to a four-way brass fitting (Clippard 15002-3-BLK). The assembly functions like a miniature tensiometer, with the high air-entry pressure of the porous ceramic cup ensuring the tubing remains filled with water when the pressure drops below zero. The fitting is sealed with 10-32 bolts on the top and back, and a barb fitting on the bottom is attached vinyl tubing (3 mm (1/8 inch) outer, by 1.5 mm (1/16 inch) inner diameter) that extends to a transducer (Figure 2). The aluminum tube is inserted into a compression fitting that allows it to be sealed in the side of the column.

The system must be filled with water from the transducer to the porous cup in order to make an accurate measurement. To accomplish this, the transducers are filled with water using a syringe attached to a small capillary tube, then the 3 mm tubing is filled with water an attached to the transducer. The bolt on the end of the aluminum tube is removed and the capillary tube is inserted the full length of the porous cup and water is injected to displace air. The bolt on the end is attached and then the bolt on the top of the four-way fitting is removed. The capillary tubing is inserted down into the 3 mm tubing and water is injected to displace remaining air. The bolt is then replaced, and the system is ready to use.

The lowest gauge (p6) is connected adjacent to the gravel layer in the column opposite of the injection site. The other four sensors are connected to tensiometers like the one shown in Figure 2.

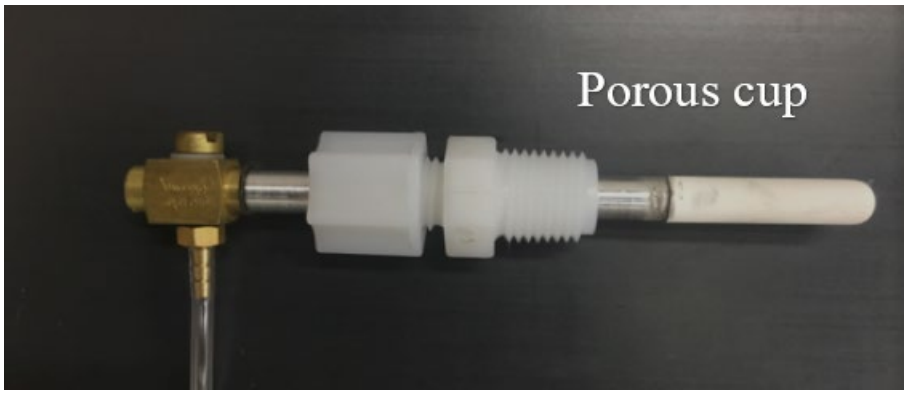

Figure 2: Tensiometer used to measure pressure in the sand on P2-P5. The porous ceramic cup shown on the end of the tensiometer allows suction to be measured.

The voltages recorded from the Data Acquisition system or DAQ are converted into pressures in Pascals by the using the relationship

$$Pressure(Pa) = \frac{voltage - 0.5}{4} * 34474 \qquad (14\text{-}1)$$

Initial calibration of the sensors found that eq. (1) was accurate to within 10 Pa, which is sufficient for application in the experiments.

The pressure transducers were located at a common datum elevation below the bottom of the column, and as a result, the data from the transducers was proportional to the total hydraulic head. The pressure determined from eq. (1) was converted to total head by dividing by the unit weight of water. The pressure head at each tensiometer was determined by subtracting the height of the tensiometer above the datum from the total head. This resulted in measurements of both pressure and total heads as functions of time at each tensiometer.

14.3.2.2.2 Temperature Sensors

The column contains four temperature sensors. These sensors are made by embedding thermistors (EPCOS B57861S0303F040) into brass tubes filled with epoxy. An epoxy with a high metal content forms the contact between the sand and the thermistor. This is done to give the area around the thermistor a high thermal mass and thermal conductivity.

The electrical resistance in a thermistor changes with temperature, which needs to be converted to a voltage to be measured by the data acquisition system (LabJack U6-Pro). This is done by including the thermistor as one resistor in a basic voltage divider circuit where the output voltage varies as a function of the input voltage V_{in} as

$$V_{out} = \frac{R_0}{R_0 + R(T)} V_{in} \qquad (2)$$

where $R(T)$ is the thermistor resistance and R_0 is a fixed "reference" resistance. These EPCOS thermistors are designed to have a reference value of 30 kOhms and a decreasing resistance with increasing temperature. In this configuration, for example, when $R(T) = R_0$ the output voltage is one-half the input and increases with decreasing resistance.

The Steinhart–Hart equation combined with the voltage divider equation gives a way to convert from the voltages measured by the DAQ to the temperature. The electrical resistance as a function of temperature for these thermistors can be modeled as

$$\frac{1}{T} = \left(\frac{1}{B}\right)\ln\left(\frac{R}{R_0}\right) \qquad (3)$$

where T is the temperature, R is the measured resistance, R_0 is the reference resistance (30 kOhms) and B is the thermistor specific calibration factor. For the thermistors used in the experiments, (B = 3964° Kelvin).

The thermistors are calibrated by filling the column up with water and placing a calibrated temperature and pressure transducer (HOBO U20) into the water. The thermistors temperature was calibrated to the temperature recorded by the HOBO U20 (Figure 3).

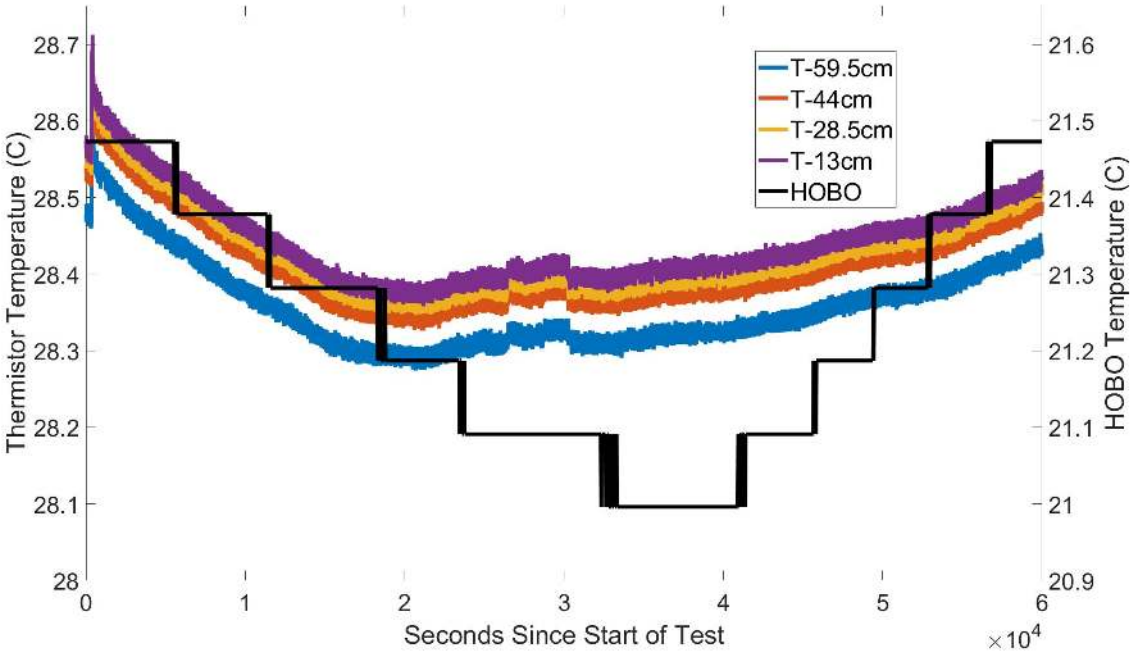

Figure 3: Temperature time series for the temperature measured with thermistors and the HOBO U20. The data respond together and have similar amounts of changes in temperature. The difference between the temperature found using the thermistors and HOBO gives constants subtracted from the Steinhart–Hart equation.

The temperature measured by the thermistors are slightly different, but they follow the same trend of decreasing by 0.3 °C over 2 x 10^4 s and then increasing slowly. The temperature measured by the HOBO follows those measured by the thermistors over the first 2x10^4 s, but there is a consistent difference of 7.1 °C between the data. This is accounted for by subtraction from the thermistor data. Then the temperature measured by the HOBO continued to decrease

while the temperature measured by the transducers started to increase slightly. The temperature measured by the HOBO started to increase at t =3.5 x 10^4 s, and it is similar to temperatures measured by the thermistors at the end of the test. The step-like pattern of the time series indicates that the temperature change during the test is small compared to the analog to digital resolution of the HOBO U20. The calibration test showed that the temperatures measured by the thermistors differ by approximately 0.1 ºC, even though the temperature in the column was assumed to be uniform. This difference was accounted for by including an offset for each temperature measurement.

A temperature change can manifest as thermoelastic strain signal. To estimate the thermal expansion coefficients, a test recorded both the temperature and strain in the column filled with partially saturated sand over the course of a day (Figure 4). The temperature and strain fluctuate periodically during the test, with a period that ranges from 6 to 9 hrs. The total variation in strain is approximately 15 με, and the variation in temperature is 0.1 to 0.3 ºC. This indicates a coefficient of thermal expansion of approximately 50 to 100 με/ºC. Thermal expansion coefficients were determined by correlating the temperature and strain at each position along the column. This tacitly assumes the temperature is uniform at each elevation.

The thermal expansion coefficients at each elevation (Table 1) were used with temperature measurements to estimate the strain due to thermoelastic effects. These strains were subtracted from the measured strains during the tests to correct for effects due to temperature change.

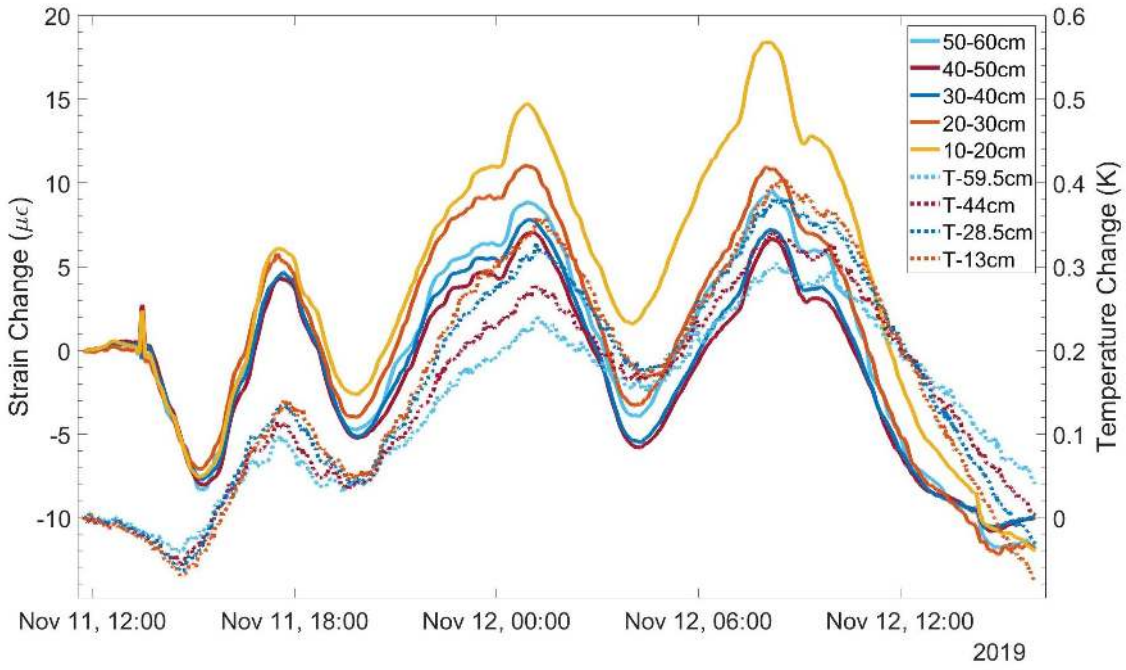

Figure 4: Strain change and temperature change time series during ambient conditions over one day. The peaks and dips in temperature and strain were used to find the coefficients of thermal expansion reported in Table 1.

Reflector Pair	Temperature Compensation
10-20cm	13με /C
20-30cm	100με /C
30-40cm	90με /C
40-50cm	65με /C
50-60cm	100με /C

Table 1: Coefficient of Thermal Expansion of the strain sensing regions determined during ambient conditions.

The temperature measured at the upper most temperature sensor (t60) is routinely higher compared to the other data during most of the experiments. The temperature at the sensor second from the top (t44) is used to characterize the temperature at the upper strain sensor (s5060).

14.3.2.2.3 Characterizing water flow using load cells

The water used during an experiment was measured as a function of time by logging the weight of a tank used to store water for the test. Three load cells with a capacity of 15 N each (Honeywell FSG15N1A) were placed between two square polycarbonate plates (30 x 30 x 1 cm thick). (Honeywell, n.d.). A 19 L tank was placed on the polycarbonate plate, and the apparatus was calibrated by adding known volumes of water to the tank and recording the voltage change.

For injection and pumping out, a 5-gallon bucket holds the water. During gravity drainage, a lower bin had to be used so the outlet hose could be placed at a lower height. In the raw data mass data, these changes are noticeable in the raw time series data.

The load cell data can be used as one method to approximate the water level in the column. This is done by taking the volume of water injected to reach the final height of the water level during the tests, around 73 cm, and dividing by the total volume of the column over this interval. This ratio is the average fillable porosity. It is less than the true porosity due to water already being present in unsaturated portions of the column. Data Acquisition System

Data from the pressure, temperature, and load sensors were recorded using a LabJack U6-Pro data acquisition system with 2 CB-37 expansion boards. This 5-volt data acquisition system works by recording voltages from voltage output sensors. The system has 16 channels and records data with 32-bit precision. It was configured using the manufacturer software LJLogUD. This program was used to measure the 16 channels at a rate of 2 or 4 Hz depending on the experiment.

14.3.2.3 Strain Measurement

14.3.2.3.1 Fiber Packaging

The coupling between porous media and optical fiber is poor because there is a small frictional force associated with the small surface area of the fiber. The fiber needs to be packaged in a way to allow the strain to be transferred and also to provide protection from breaking. Preliminary work shows that laminating fiber between polyester film can create a large surface area that generates frictional forces that couple the fiber to the sand. The polyester film also strengthens the fiber and reduces risk of breakage.

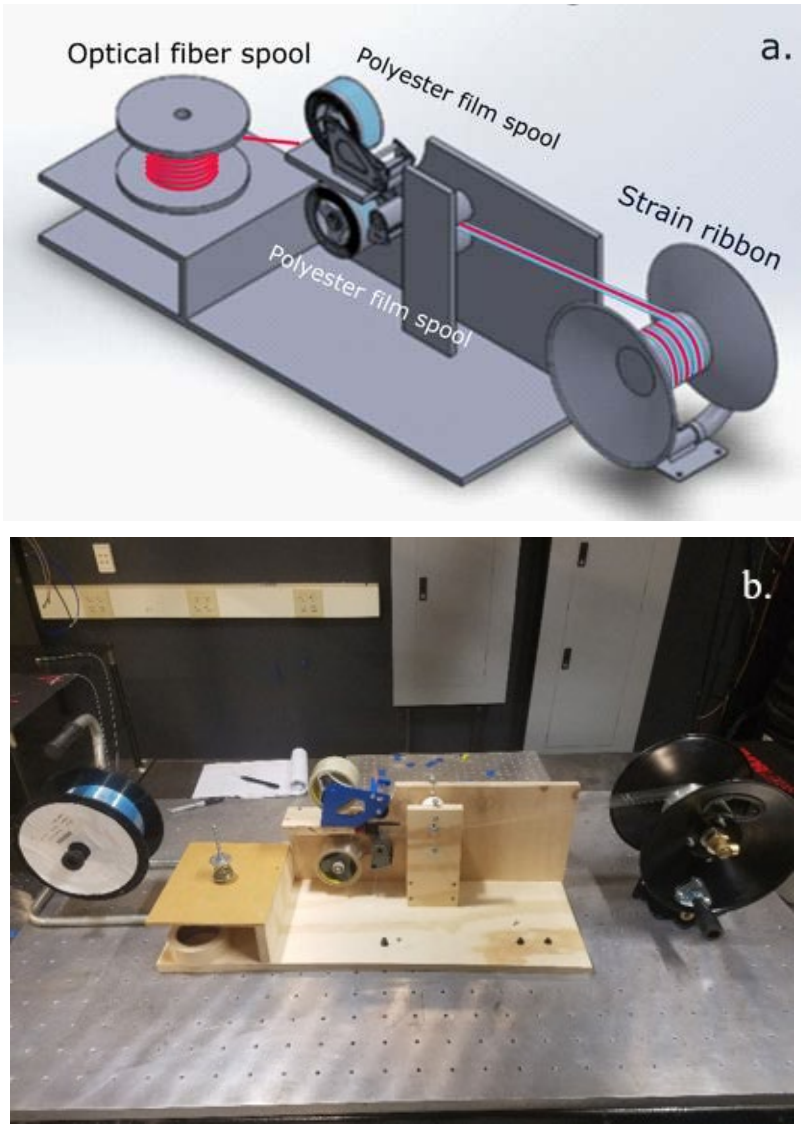

Figure 5: a. Computer generated model of laminating for assembling the optical fiber ribbon. b. Photograph of the actual device.

The fiber is packaged using 3M 396 tape. This tape sticks particularly well to itself and to the fiber. Daniel Hestenes, a collaborator, created a device to attach the fiber to the tape. The tape goes through a series of rollers that laminate the fiber between two pieces of tape (Figure 5).

The laminating device laminates optical fiber between two pieces of tape to create a strain ribbon. Two spools are attached to a mounting bracket, which is slotted to accommodate several sizes of tape. The mounting bracket has a centered hole through its length which places the fiber near the center of the tape. The fiber is then further aligned to the center of the tape with a small eyelet. The tape with the fiber passes through two plastic rollers. The plastic rollers are mounted in a vertically slotted hole and are manually tensioned using a pair of bolts. The packaged fiber is collected on a reel, which is used to pull the tape through the device.

This device aligns the two pieces of tape. It also minimizes the bubbles formed from incomplete contact between the two pieces of tape while keeping adequate tension on both the fiber and tape.

The strain ribbon used in these experiments was made from 2-inch-wide 3M 396 tape, which was subsequently trimmed to 1-inch wide. The fiber used on the inside of the inside of the column is not properly attenuated at the bottom. Some of the light leaks through causing an incomplete reflection. This was partially mitigated by blotting the bottom end of the fiber with black ink. Resultant from this, there are some instances where the signal from the bottom pair of reflectors ‘jumps’ or anomalously responds. This was fixed in subsequent designs by using an open knot at the bottom of the fiber.

A device was constructed a device to measure the coefficient of friction between the strain ribbon and sand. A normal force is placed on the ribbon, which itself rests on a brick with sand bonded to its surface. The axial force on the ribbon is incrementally increased with a dead weight, and displacement is monitored with a dial indicator. The axial force required to initiate displacement is recorded and then the test is repeated. The normal force is then increased, and additional tests are conducted.

Results show that the shear force increases with the axial force (Figure 6). The coefficient of friction is the ratio of the shear force required to initiate displacement under a certain normal force. The coefficient of friction between the tape and sand 0.37 +/- 0.05.

This finding is consistent with a test conducted by MCG Geotechnical Engineering Inc. and the Bureau of Reclamation in Colorado on the coefficient of friction between polyethylene sleeves that line pipes and various porous media. Their value of coefficient of friction between polyethylene sleeves and sand is between 0.22 and 0.49 (Gemperline & Rinehart, 2018).

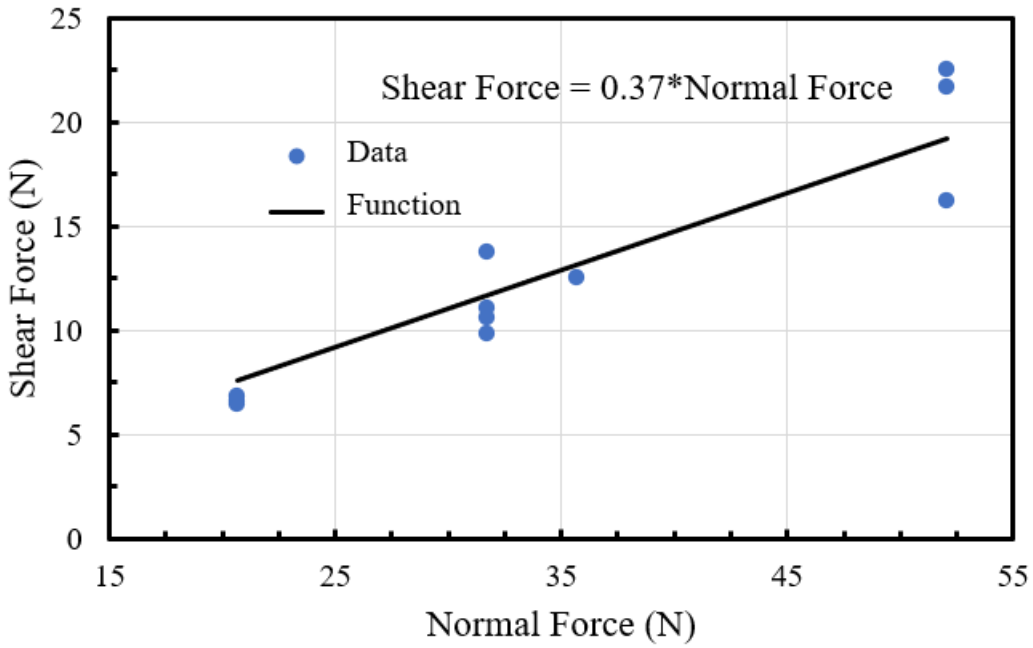

Figure 6: Shear force plotted with the normal force for friction tests. The coefficient of friction is the ratio of the shear force and normal force.

The compliance of the fiber packaging was measured using a loading machine. The machine pulls the material at a very precise load and strain is recorded by a Fiber Bragg grating sensor. The compliance is the ratio between the strain and the load.

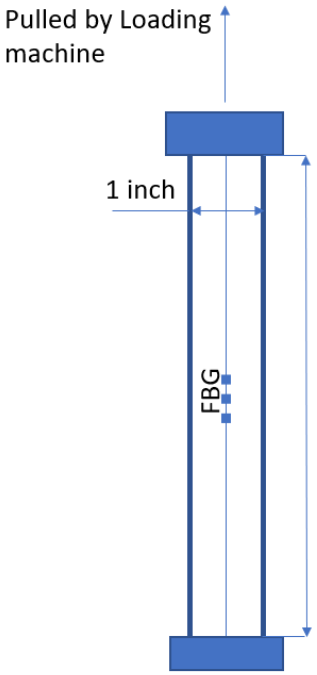

Figure 7: Simple model showing the device for measuring compliance.

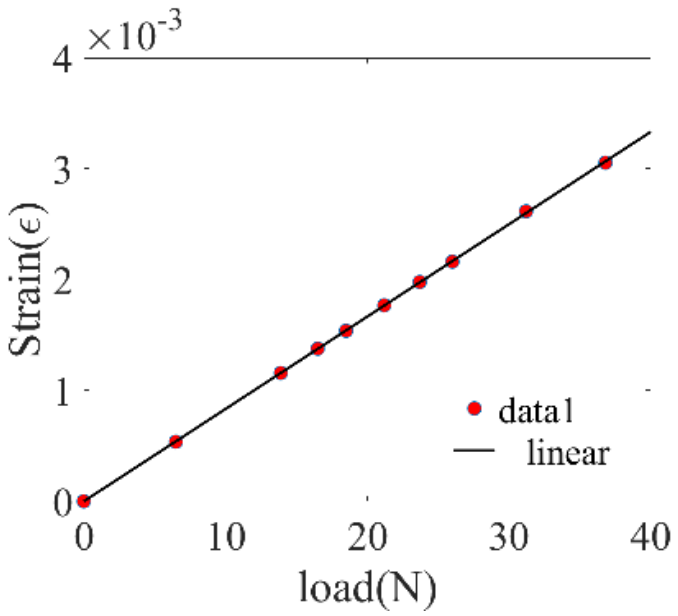

Figure 8: Strain measured using the FBG and the load on the machine stretching the optical fiber packaging.

The data are near linear under these loads and the compliance is approximately 80 με/N.

14.3.2.3.2 Fiber Sensor Geometry and Installation

The strain ribbon contains two sets of reflectors. One set of reflectors was embedded in sand along the center axis of the column and another was attached to the outer wall of the column. The strain ribbon was attached to the bottom of the column by a hook that is embedded in the epoxy base. The fiber was under tension with a force of 10 N while the column was filled with sand. The reflector spacing is 0.1 m. Heat-shrink tubing was used to reinforce the fiber where the fiber comes out of the sand. The other set of reflectors were taped along the outside of the column to measure changes in strain on the column itself. These outer reflectors also have a spacing of 0.1 m.

14.3.3 Soil Parameters

Hydromechanical parameters of the sand are needed to describe the flow and deformation during the experiments. These parameters were measured using laboratory methods.

14.3.3.1 Saturated Hydraulic Conductivity

The saturated hydraulic conductivity of soil was measured using a falling head test. For this test, the PVC column used in preliminary investigations was used. It was fully saturated from below and standing water formed with a depth of 10.8 cm. The head was recorded, and an outflow tube was place above the water level. The end of the outflow tube was lowered to 1.2 cm above the surface of the sand, and the water was drained into a pan on load cells. The sand remained fully saturated during the test, and the weight of the accumulating water was recorded using the load cells.

This testing method measures saturated hydraulic conductivity in a setting similar to the experiments.

The hydraulic conductivity was determined by assuming mass conservation at constant density, which leads to

$$h = h_0 e^{-t\frac{K}{L}}$$

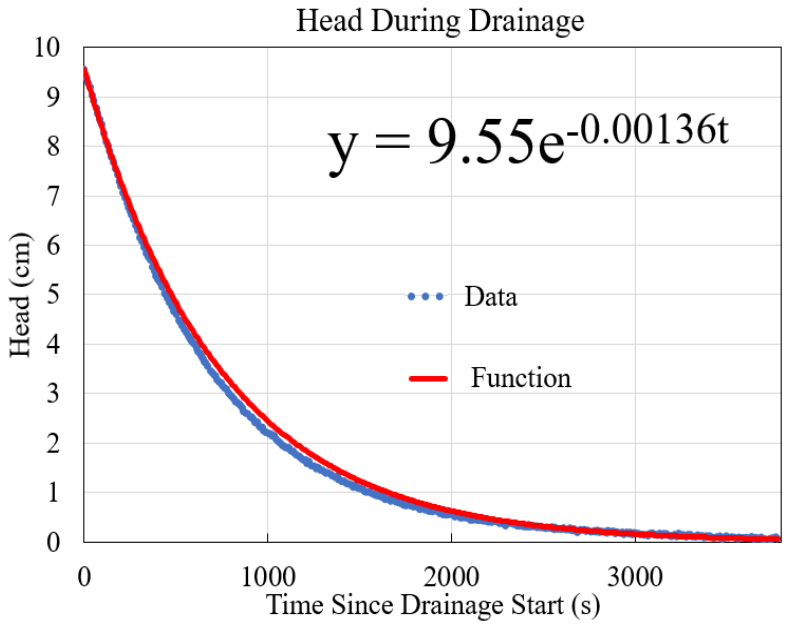

Figure 9: Head in outflow column time series with exponential decay function.

Using Equation 22 and the best fit line in Figure 9 the hydraulic conductivity of the sand is approximately K = 0.025 cm/s. The volume of water used to fill the column during the test gives the porosity. The packed sand in this smaller column has a porosity of approximately 0.28.

14.3.4 Grain Size Distribution

Sieve tests were conducted to measure the grain size distribution. A mass of porous media was poured into a series of sieves on a shaker designed to vibrate the material allowing for maximum separation. The grain size distributions for the different materials present in the column are shown below.

14.3.4.1 Sand

The sand forms the region in the column where strain is measured. 4562 grams was sorted using 63, 125, 250, 300, 500, 710, 1000, and 1180 micron sieves. The distribution of sand grain sizes is shown in Figure 10.

The grain size data indicate that this is a medium-grained (median grain size is 400 micron), well sorted (coefficient of uniformity, D60/D10 = 450/200 = 2.25) sand. This material was obtained from a local hardware store.

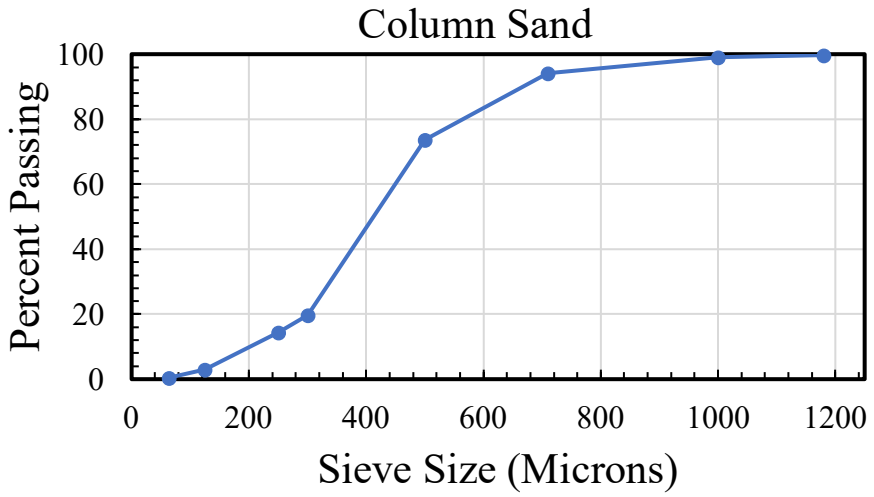

Figure 10: Grain size distribution for the sand used to fill the column.

14.3.4.2 Middle Layer Gravel

The gravel separates the column sand from the injection gravel. 4000 grams was sorted using 250, 300, 500, 710, 1000, 1180, 2000, and 2830 micron sieves. The distribution of gravel sizes is shown in Figure 11.

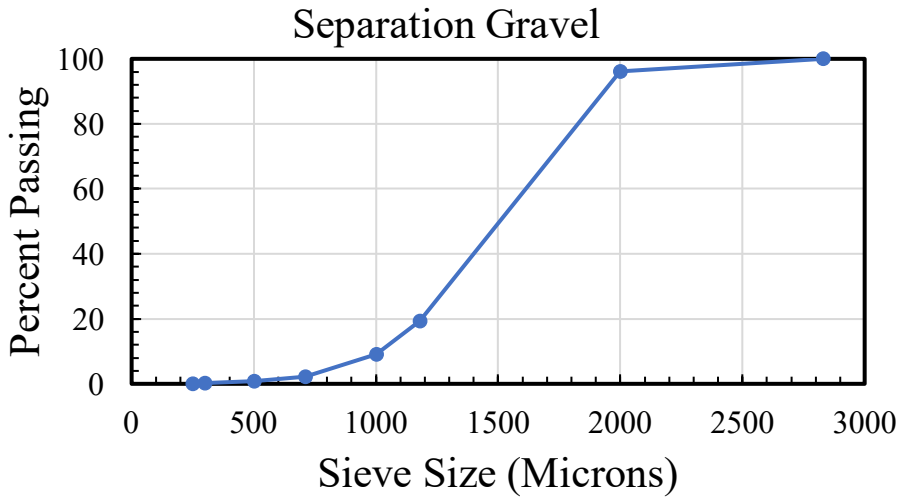

Figure 11: Grain size distribution for the separation gravel layer.

The separation gravel is what forms the layer between the injection gravel and the column sand. It is made of commercially available well sorted sand.

14.3.4.3 Injection Layer Gravel

This layer is where the water is injected from a peristaltic pump. 4500 grams was sorted using 300, 500, 710, 1180, 2000, 2830, and 4000 micron sieves. The distribution of gravel sizes is shown in Figure 12.

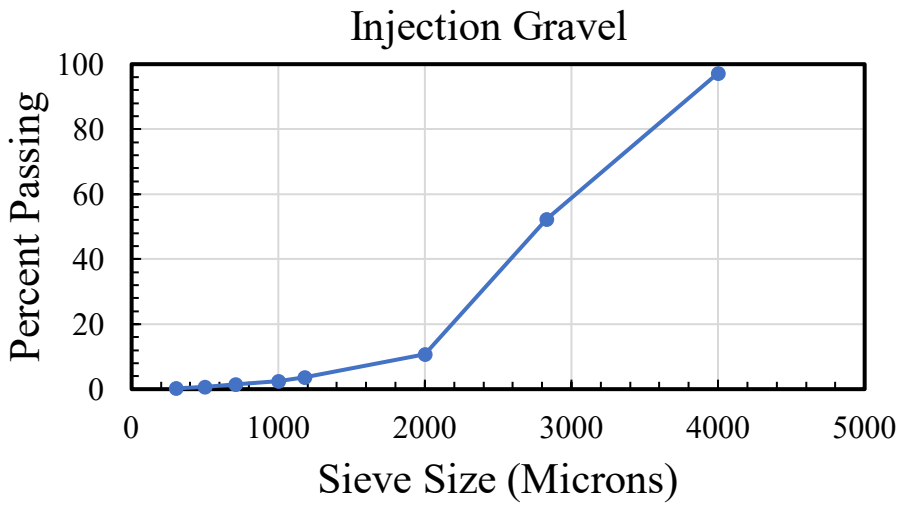

Figure 12: Grain size distribution for the gravel used as the injection site for the column.

The median grain size for the gravel is considerable larger than that of the sand. The hydraulic conductivity of this gravel layer should also be much higher.

14.3.5 Dry Bulk Density

The dry bulk density of the medium-grained sand used in the experiments was measured as loose, unpacked material, and after packing and gentle agitation similar to that used when the column was packed. The tests were completed three times and the results indicate that the bulk density of the loose sand in an air-dry condition is 1.54 +/- 0.02 gm/ml. The bulk density of the same material after packing is 1.64 +/- 0.02 gm/ml. Packing increases the density by approximately 6 percent.

14.3.6 Water Retention Curve

The soil water retention curve (SWRC) is important to determining how water is stored in the column. The SWRC was measured using a hanging column and aspects of the procedure outlined in the ASTM standard method for determining the Soil Water Characteristic Curve (ASTM, 2003). A Buchner funnel was used to hold the sand and prevent air entry when suction was applied. The pressure applied during the experiment was well below this limit. A graduated burette is used to record the volume of water pulled from the sample with drops in head. This gives results accurate to the nearest 0.1 ml.

Two different retention curves were made. One retention curve with the sand in a non-packed state and one with a higher resolution with the sand in a compacted state similar to what is seen in the column.

Curve fitting software TableCurve 2.0 was used to estimate parameters in the van Genuchten equation (van Genuchten, 1980).

14.3.6.1 Ambient Conditions

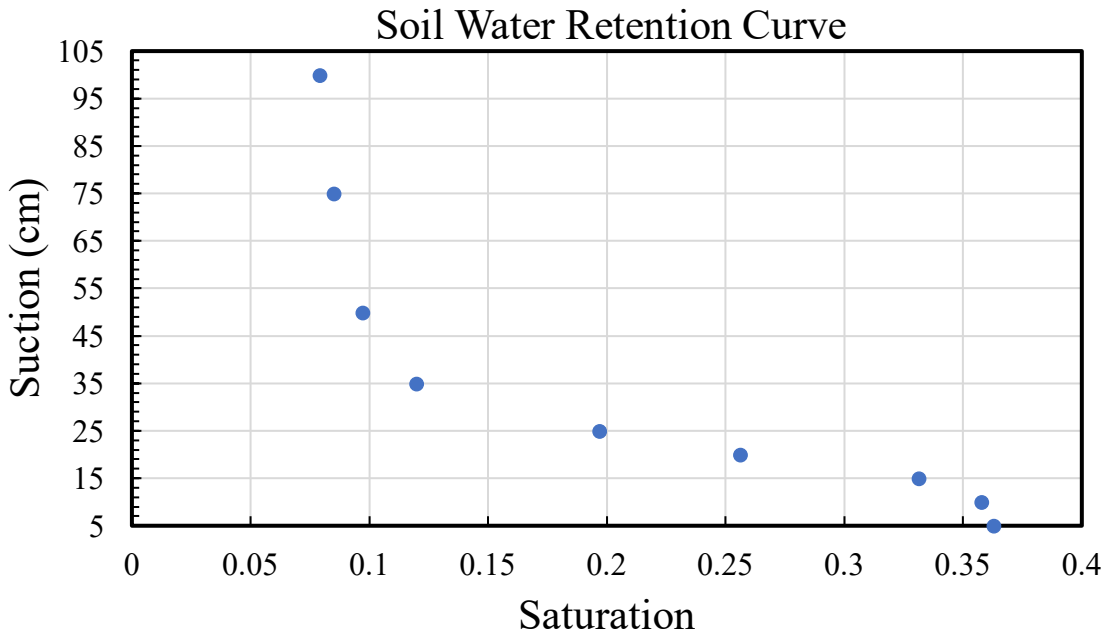

Figure 13: Soil Water Retention Curve under loose sand conditions (porosity of approximately 0.36) and a suction to 1 m of head.

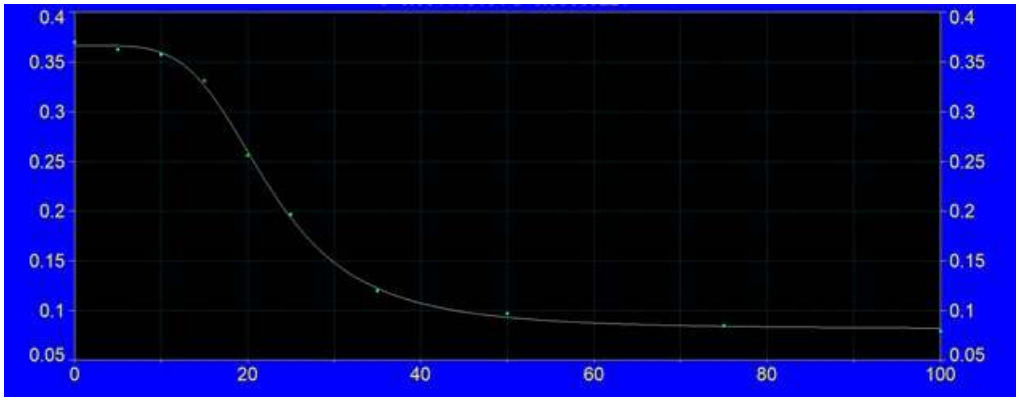

Figure 14: Curve fitting of the van Genuchten equation to the data above. Resultant values are $\alpha = 0.048\ cm^{-1}$, $\eta = 4.65$, $\theta_s = 0.36$ and $\theta_r = 0.08$. Curve fitted using the software TableCurve. $r^2 = 0.999$.

14.3.6.2 Packed Sand

Samples of sandwere packed using the samed methods used to pack the column and the retention experiments were repeated (Figure 15Figure 16).

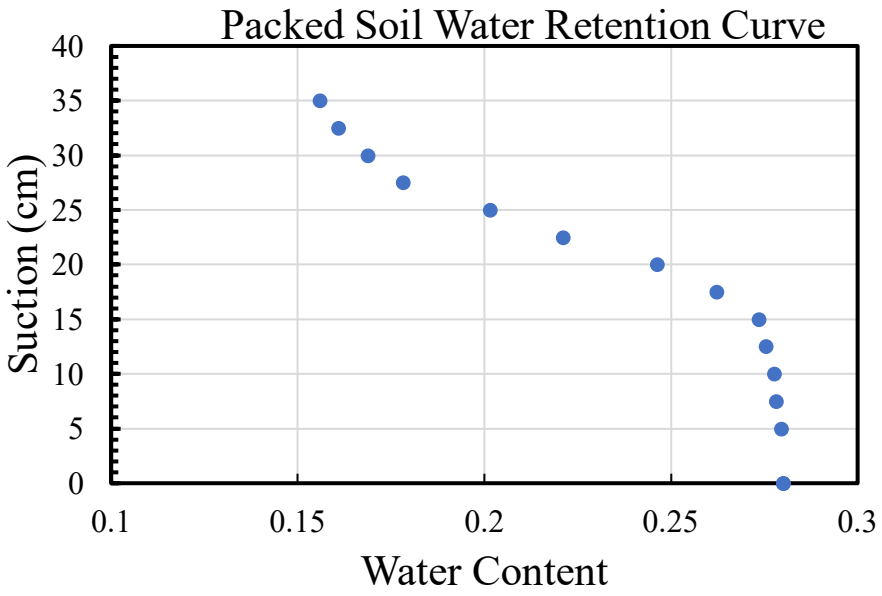

Figure 15: Soil water retention curve with packed sand similar to what is seen in the column. Porosity is approximately 0.28.

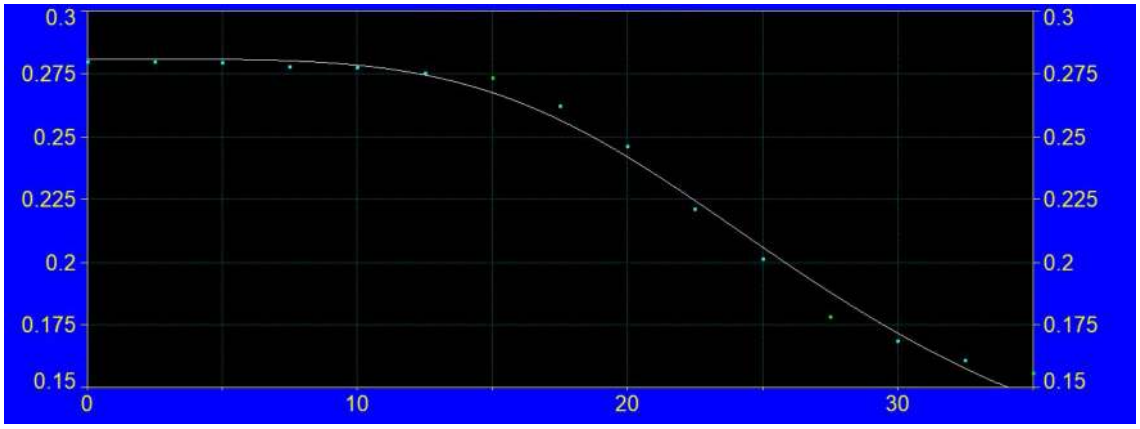

Figure 16: Curvefitting of the van Genuchten equation to the data above. Resulting values are $\alpha = 0.039$ cm^{-1}, $\eta = 4.34$, $\theta_s = 0.28$, and $\theta_r = 0.08$. Curve fitted using the software TableCurve. $r^2 = 0.990$.

14.3.6.3 Elastic Moduli

A staged quasi-consolidated drained (QCD) triaxial shear test was performed to estimate the elastic modulus. The specimen was prepared by gently hand tamping the material in an air-dry state into a membrane-lined vacuum split mold. The mold with porous stones and end caps on the top and bottom of the tamped material was placed on the base of a triaxial cell. A vacuum was applied to the bottom of the sample before releasing the mold-membrane vacuum and removing the mold. The triaxial cell was then filled with water and the mold vacuum was released.

The test was conducted in stages under loading conditions similar to the experiments. Each stage involved loading the specimen, under a given effective confining stress, at a target strain rate of 0.003 in/hr to a target 0.07% shear strain. All testing was performed under drained conditions. A formal saturation and consolidation stage, as would be performed in a consolidated drained triaxial shear test such as ASTM D7181, was not performed at any stage of the testing. However, the material was gently 'saturated' in the second stage and some consolidation occurs as a function of an applied effective confining stress and load. Thus, this testing is referred to as staged 'quasi-consolidated' drained triaxial shear testing.

The first stage was performed with the material at the as prepared air-dry state under 0.5 psi effective confining stress. Upon completion, the specimen was unloaded to a load equal to the effective confining stress.

The material was then 'saturated' by injecting de-aired water into the specimen, from bottom to top, using a small pressure head (burette water column with no backpressure). The specimen was considered 'saturated' after at least one pore-volume of water was passed through the specimen, assuming 28% porosity.

The effective stress was maintained at 0.5 psi for the second stage, and the specimen was once again deformed to 0.07% strain. Upon completion, the specimen was unloaded until the load was equal to the effective confining stress (0.5 psi at this stage). The effective stress was then increased to 2 psi, sheared to 0.07% strain, and unloaded to the effective confining stress (2 psi at this stage) for the third stage. This process was repeated under 5 psi and 15 psi effective confining stresses for the fourth and fifth stages. Each stage was terminated at 0.07% strain.

The axial strain was essentially a linear function of the axial stress during all the tests, suggesting that the tests were within the elastic range of the sand. The slopes of axial stress as a function of axial strain were measured for the different stages, and the slopes were assumed to be the effective Young's modulus. The results (Figure 17-22) range from 18 to 40 MPa. The modulus increases with confining pressure, and the modulus of the saturated sand is less than that of the air-dry sand.

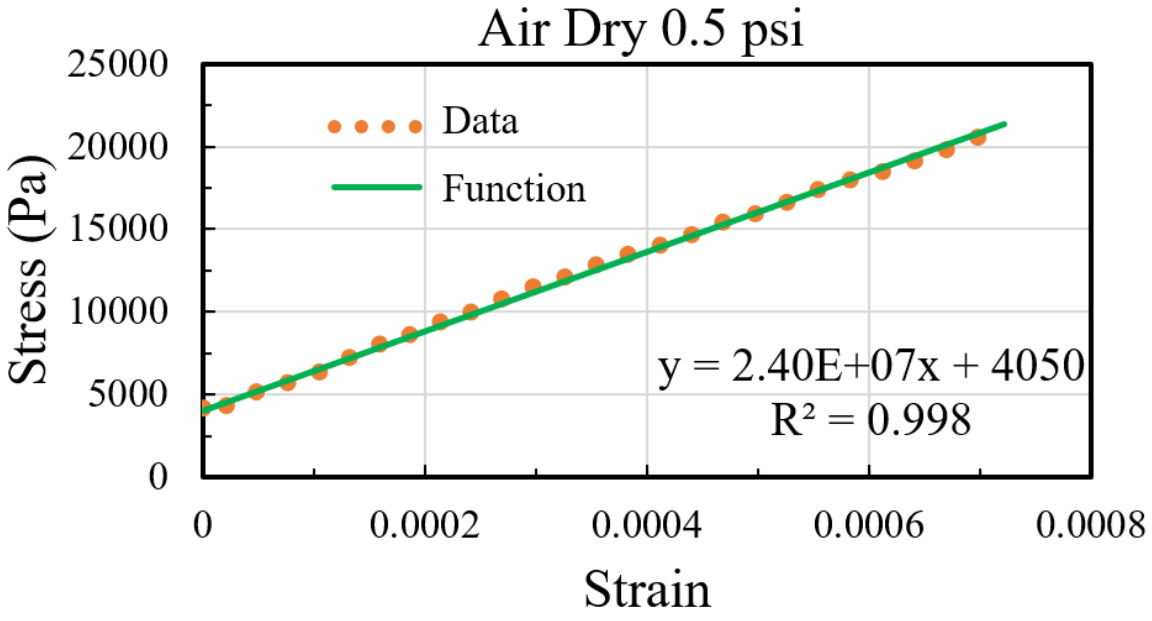

Figure 17: Stress and strain during triaxial test. The Young's Modulus is 24 MPa.

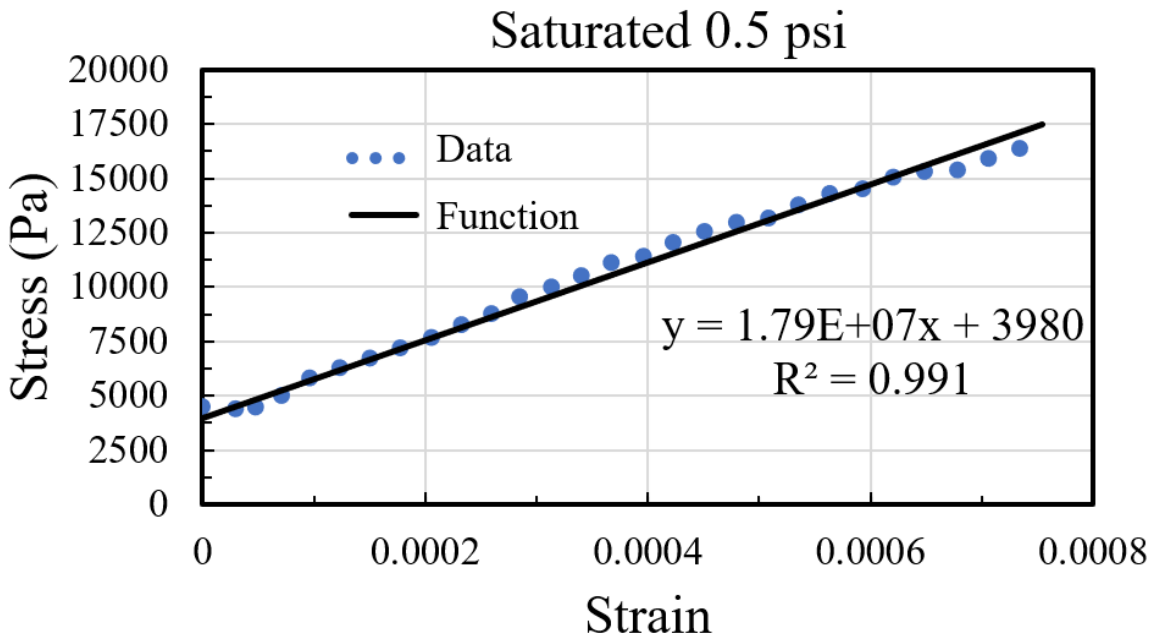

Figure 18: Stress and strain during triaxial test. The Young's Modulus is 18 MPa.

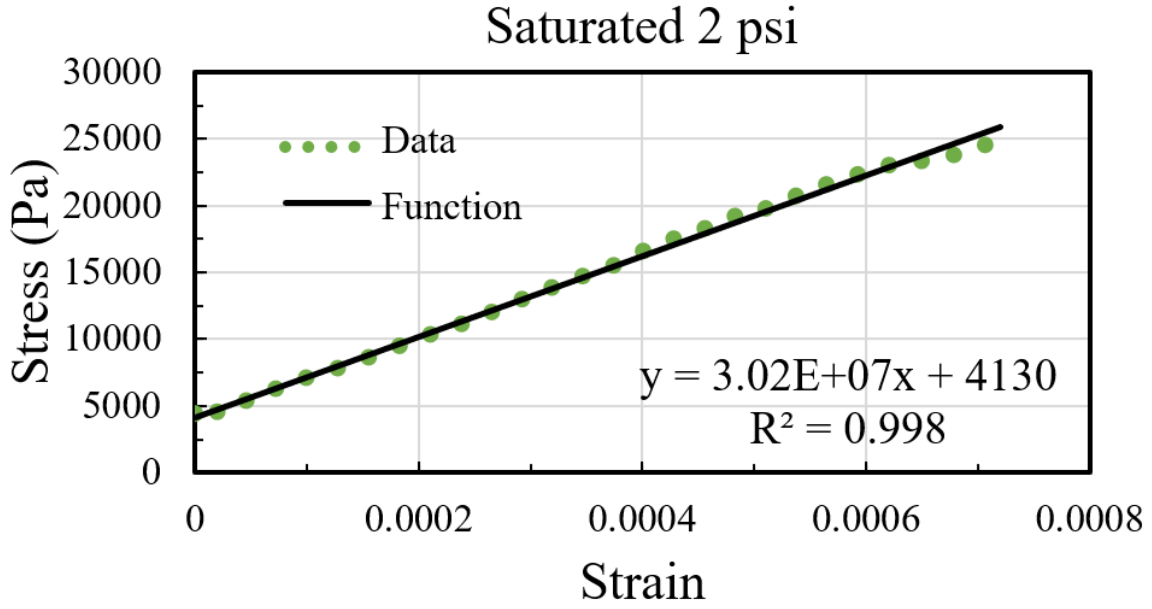

Figure 19: Stress and Strain during triaxial test. The Young's Modulus is 30 MPa.

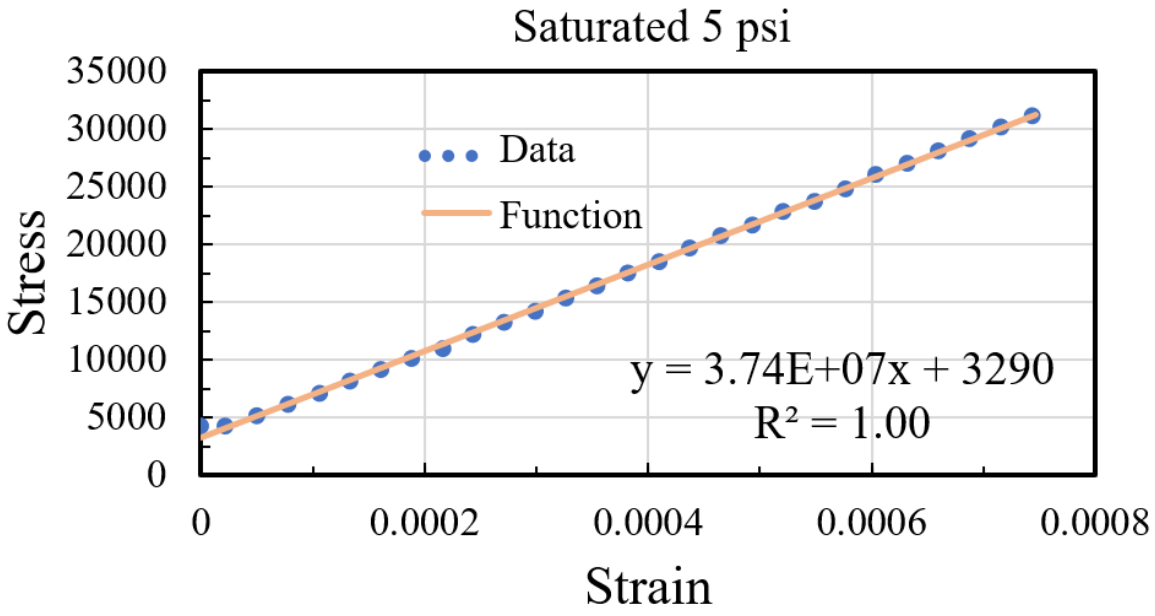

Figure 20: Stress and strain during triaxial test. The Young's Modulus is 37 MPa.

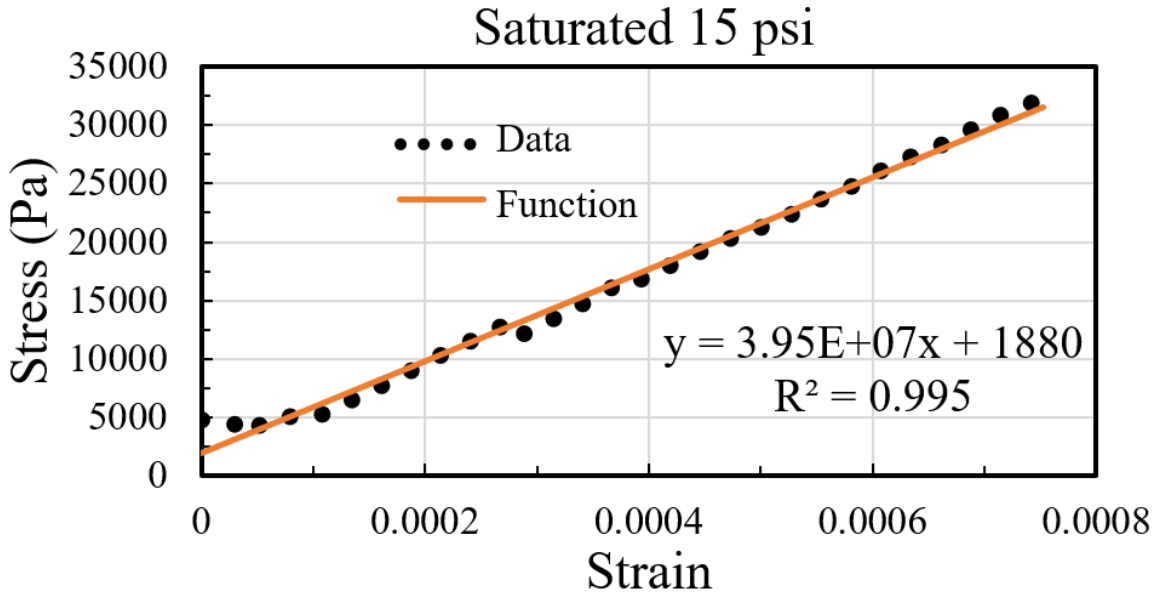

Figure 21: Stress and strain during triaxial test. The Young's Modulus is 40 MPa.

14.4 COLUMN LOADING TESTS

14.4.1 Column Loading Test

Strain was measured at five intervals in the sand, and at five intervals along the outer wall of the pipe. The strain was measured as displacement between two reflectors separated by 10 cm. This gives the strain averaged over a 10-cm-long interval. The midpoints of the reflectors occur at distances of 15, 25, 35, 45, 55 cm above the base of the column, and the sand extended to a height of 72 cm. The total height of the column is 75 cm.

The column was loaded with weights and the strain was measured in the sand and in the wall of the column. The load was applied by placing weights on a polystyrene cylinder with a diameter that is approximately 1 cm less than the inside of pipe. A 2.5-cm-wide slot was cut along the radius of the loading column and the strain ribbon was put in the slot during loading. This allowed the load to be applied without contacting the strain ribbon. Steel disks were placed on the loading cylinder to generate forces of 1.4, 2.8, 5.4 and 11.4 N. A loading test was conducted by placing steel disks on the loading cylinder, measuring the strain at each reflector pair for approximately 5 seconds. Then the weights were removed for 5 seconds, and the test was repeated approximately 10 times. This produced a step-like time series of increasing and decreasing strain. Trends in the strain also occurred during the test, presumably because of temperature changes. The average strain resulting from the applied load was determined with a trend lines that were manually fit to the upper and lower steps in the time series.

Four suites of tests were conducted using loads applied to dry sand soon after the column was filled. Three suites of tests were conducting later when the sand was completely saturated. Additional tests were conducted by applying load to the wall of the column instead of on the sand. The tests are named for where the load was applied (LS=load on sand; LW=load on wall) the moisture state of the sand (DS = dry sand, WS = wet and fully saturated sand) and the applied load in grams force. So, test LS-DS-560 applied a weight of 560 g to the dry sand.

14.4.1.1 Observed Strains

The strains at a particular elevation increased with the applied load. This is the expected response, so the strains were normalized to the applied load to facilitate plotting (Figure 22). The strain in the sand increases markedly with elevation in all the tests. Strains in the saturated sand are generally greater than strains in the dry sand at the same elevation. The maximum ratio is approximately 0.7 1/N at the upper end of the column when the sand is saturated, and the ratio decreases to approximately 0.1 1/N at lower end of the column (Figure 22).

In contrast, the strain ratio in the wall of the column ranges from 0.02 to 0.1 1/N. The strain ratio in the wall appears to be independent of elevation and there appears to be negligible difference between tests using dry and saturated sand (Figure 23).

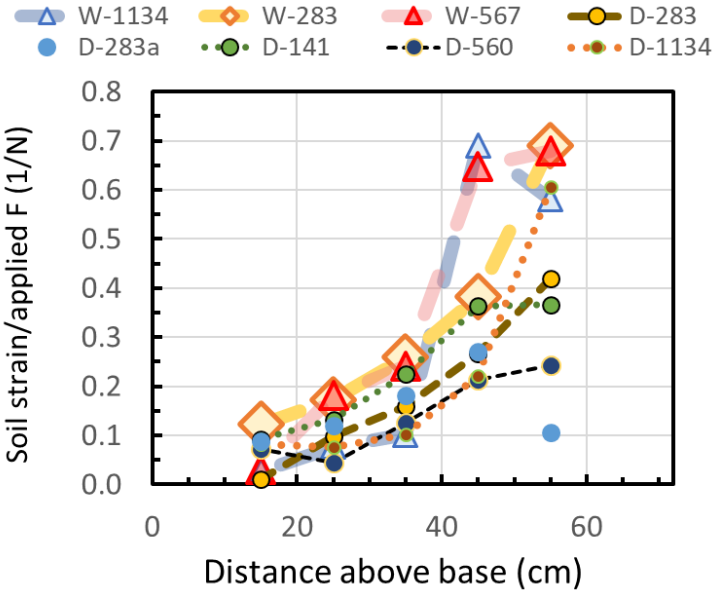

Figure 22: Ratio of the strain in sand to the applied force as a function of distance above the column base for tests with different applied loads and different saturation states (D=dry; W = saturated). The x axis extends over the full height of the column.

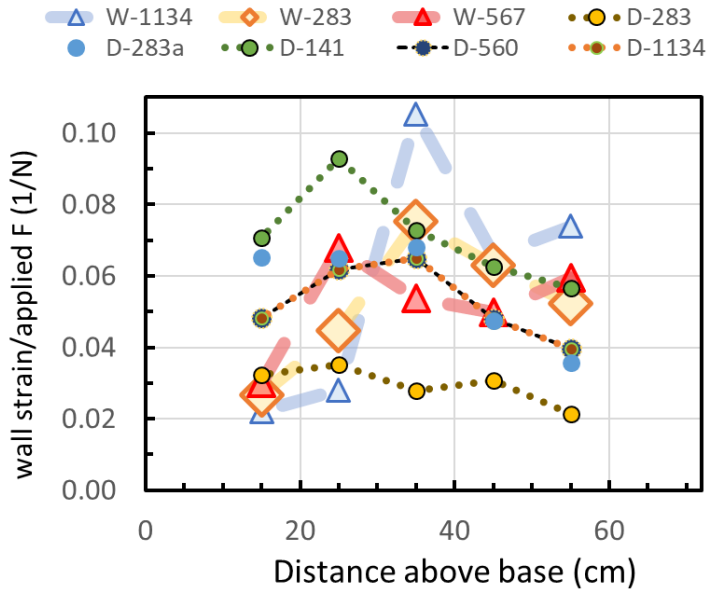

Figure 23: Ratio of the strain in wall of the PVC column to the applied force as a function of distance above the column base for tests with different applied loads and different saturation states (D=dry; W = saturated). The x axis extends over the full height of the column.

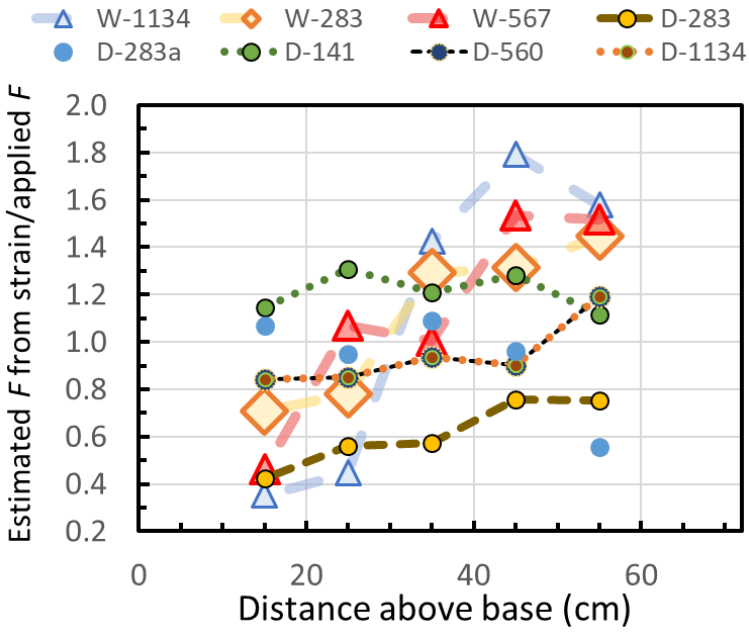

Figure 24: Ratio of the total force estimated from the strain to the applied force as a function of distance above the column base for tests with different applied loads and different saturation states (D=dry; W = saturated). The x axis extends over the full height of the column.

14.4.1.2 Estimated force

It was assumed that the applied force was uniformly distributed at a particular elevation within the sand and also within the PVC column. It was also assumed that the applied force could transfer from the sand to the PVC column. So, for example, the fraction of the load carried by the sand could increase if the fraction carried by the column decreased with elevation, providing the total force summed to the applied load. A force balance indicates that the average force in the sand at the elevation of sensor *i* is

$$F_{si} = \varepsilon_{si} E_i' A_c \qquad 14\text{-}2$$

where ε_{si} is the strain in the sand at sensor *i*, E_i' is the effective elastic modulus at sensor *i*, and A_c is the cross-sectional area of the column (0.0314 m^2). The average force in the wall of the column is

$$F_{wi} = \varepsilon_{wi} E_{PVC}' A_w \qquad 14\text{-}3$$

where ε_{wi} is the strain in the sand at wall sensor *i, E_{PVC}'* is the effective elastic modulus of PVC, and A_w is the cross-sectional area of the wall (0.0066 m^2).

The total force at the elevation of each sensor is assumed to equal the force generated by the applied weight

$$F_a = F_s + F_w \qquad 14\text{-}4$$

We assumed that the effective elastic modulus of the sand could vary with depth as a result of packing, interaction with the wall, or other factors. The effective modulus of the PVC wall was assumed to be uniform.

A series of optimization analyses was conducted by determining the elastic moduli E'_{PVC} and the five E'_{si}. The objective function was the sum of the squared residuals between the applied force and the sum of $Fs+Fw$. Analyses were conducted for all the test conducted using wet sand, all the tests conducted using dry sand, and all the tests as an aggregate.

The elastic modulus of the PVC pipe is in the range of 2 to 3 GPa, whereas the sand is in the range of 5 to 30 MPa according to the results. The results also indicate that the force carried by the PVC column can be greater than that in the sand, even though the weight was applied to the sand. The ratio of F_s/F_{applied} is generally less than 0.2, and it is less than 0.1 at the bottom of column, according to the analysis. The ratio F_w/F_s decreases with elevation, which is consistent with Figure 22.

The ratio of $(F_w+F_s)/F_{applied}$ typically increases with elevation and it generally ranges between 0.4 and 1.6 (Figure 24). Ideally, this ratio would equal unity.

The optimization analysis estimates an effective elastic modulus, E' at each depth. Assuming the PVC column restricts horizontal strain to zero, vertical force is related to the vertical strain according to uniaxial Hooke's Law (Wang, 2000) using

$$F_a = A_s\sigma_{zz} = A_s\frac{E}{(1+\nu)}\frac{(1-\nu)}{1-2\nu}\epsilon_{zz} \qquad 14\text{-}5$$

$$F_a = E'A_s\epsilon_{zz} \qquad 14\text{-}6$$

$$E' = \frac{E}{(1+\nu)}\frac{(1-\nu)}{1-2\nu} \qquad 14\text{-}7$$

$$E = C_1E' \qquad 14\text{-}8$$

$$C_1 = \frac{(1+\nu)(1-2\nu)}{(1-\nu)} \qquad 14\text{-}9$$

Assuming the Poisson's ratio for sand ranges from 0.25 to 0.4 implies that C_1 ranges from 0.83 to 0.47, and using ν=0.3 gives $C_1 = 0.75$. This allows Young's modulus to be estimated from the strain data (Figure 25). The results indicate that Young's modulus decreases slightly from the middle to the top of the column. Estimates based on all the data are in the range of E_s =15 MPa to 20 MPa, and E_{PVC} =2.4 GPa. Estimates using only the data from dry sand indicate a stiffer modulus for sand, in the range of E_s = 30 MPa, and E_{PVC} =2.2 GPa. In contrast, estimate using only the data from wet sand indicate a softer modulus for sand, in the range of E_s =5 MPa to 10 MPa, and E_{PVC} =2.4 GPa.

The results of the loading tests are consistent with both general published values and those measured using geotechnical tests. Published estimates for the Young's modulus of loose sand range from 10 to 80 MPa depending on axial strain (Satoshi Yamashita,1 Michele Jamiolkowski, 2000). Values for E of PVC pipes range from 2.4 to 2.9 GPa, according to (Neelam & Kalaga, 2002). The Young's modulus of saturated sand used in the experiments ranged from 18 to 30

MPa as the confining stress increased from 0.5 psi to 2 psi in a triaxial test, which is consistent with the average values of *E* from the loading tests (Figure 22). The triaxial tests indicated that Young's modulus of wet sand is less than (approximately ¾) that of dry sand. The loading tests also indicate that dry sand is stiffer than wet sand, although they indicate the difference between the dry and saturated conditions is larger than it was in the triaxial tests.

The results of the loading tests indicate that the strain measured by the optical fiber ribbon is approximately equal to the values expected from elastic deformation of sand in a tube of PVC. This is an initial confirmation that the strain data measured by the optical fiber is meaningful. The results also indicate that there is significant interaction between the load carried by the sand and the enveloping PVC tube, and this interaction will affect the results of strain measurements in the sand. This interaction likely accounts for much of the variability in the strain data, and uncertainty in moduli estimates.

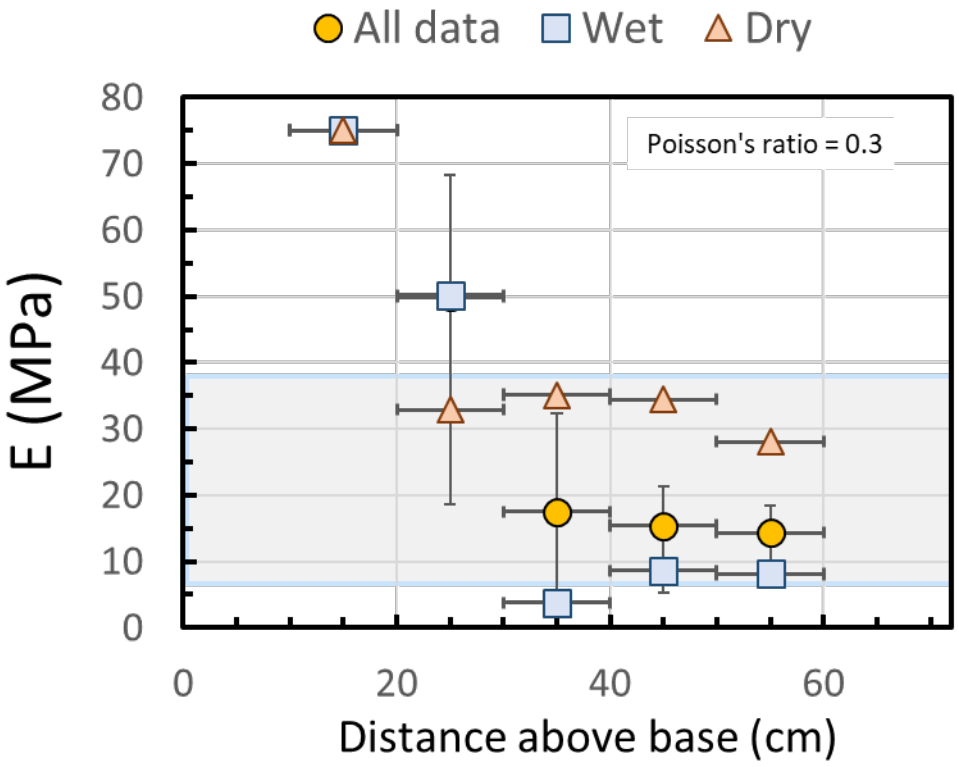

Figure 25: Young's modulus of sand using parameter estimation that requires internal forces to sum to the applied force. ν = 0.3 is assumed. Grey band is the range of moduli in the mid to upper parts of the column.

14.5 COLUMN FILL AND DRAIN TESTS

A suite of tests was conducted by increasing saturation and then draining the column while measuring pressure and strain. These were conducted in two ways, either by injecting into the base of the column or by infiltrating from above. The water was then either drained by gravity or pumped out of the column. Strain, pressure, temperature, and mass of water injected/drained were measured. The water used for injection was taken from tap and was left overnight in a basin, so the water temperature equilibrates with the room temperature. This was done to minimize strain due to temperature fluctuations in the column.

The suite of injection tests includes four tests where water was injected at 0.1 L/min for approximately 2,000 seconds to completely fill the column and cause ponding at the surface of the sand. One test was conducted where water was injected for approximately 1,600 seconds to partially fill the column. The tests were conducted over a three-month period, from October 2019 to January 2020, with several days to several weeks between each test. An initial goal was to evaluate the effects of completely filling the column, but it was realized near the end of the testing program that it would also be useful to have results from a test where the column was partially filled to avoid complications that occurred when the water level approached the top of the column. Only one of the partially filled tests was completed because of time constraints, but it provided a useful baseline and will be described first.

14.5.1 Partial-fill Injection Test

An injection test was conducted to evaluate the strain response during injection and drainage without incurring effects associated with the injected water reaching the surface. The test was conducted 28 days after the previous injection test and the initial hydraulic head was nearly uniform over the height of the column, indicating no flow and that the water was in gravity equilibrium.

The test consisted of injecting at a constant rate for 1,610 s (27 min), shutting off the pump for approximately 600 s (10 min) and then starting it again in reverse at t =2,277 s (38 min). The water level in the sight tube attached to the bottom of the column started at an elevation of 11 cm and it was at 47 cm after the pump was turned off at the end of the test. This was sufficiently below the surface of the sand (elevation of 72 cm) so the interaction between the wetting front and the sand was expected to be minimal. The pump was turned on and off two more times, once between t =4,500 s and 4,700 s, and again between t =5,300 s and 5,400 s.

14.5.1.1 Results

Filling the column with water generally caused pore pressure and axial strain to increase (become more tensile), and these trends reversed during draining. These are the expected effects, but the details of the pressure and strain responses vary among the different sensors and lead to some insights about the filling and draining process.

14.5.1.1.1 Pore pressure

Pore pressure was measured using tensiometers in the column that were connected to transducers at a common datum below the bottom of the column. As a result, the pressure measured at the transducers was proportional to the total head. The pore pressure head at the

tensiometers was determined by subtracting the elevation head from the measurements made by the transducers. The transducer locations were determined by measuring up from the bottom of the column, and this measurement is used in the name of the transducer. The bottom of the column was 0.5 cm above the transducers, so the elevation head used to convert total head to pressure head used the transducer location plus 0.5 cm.

The pressure head at the start of the test was -30 cm at the p44 tensiometer and +11.3 cm at the bottom tensiometer (p6) (Figure 27). The pressure heads at the lower three tensiometers are roughly linear with a gradient of 1.1. This is slightly greater than the expected value of 1.0 during hydrostatic conditions. The difference is probably because of a slight offset in the transducers. The pressure head at the p44 tensiometer is approximately 8 cm above the projection of 1.1 gradient at the start of the test. This is probably because the p44 tensiometer was filled before the test and water from the porous cup elevated the head. Data from the p60 sensor was erratic during this test, so those data are omitted.

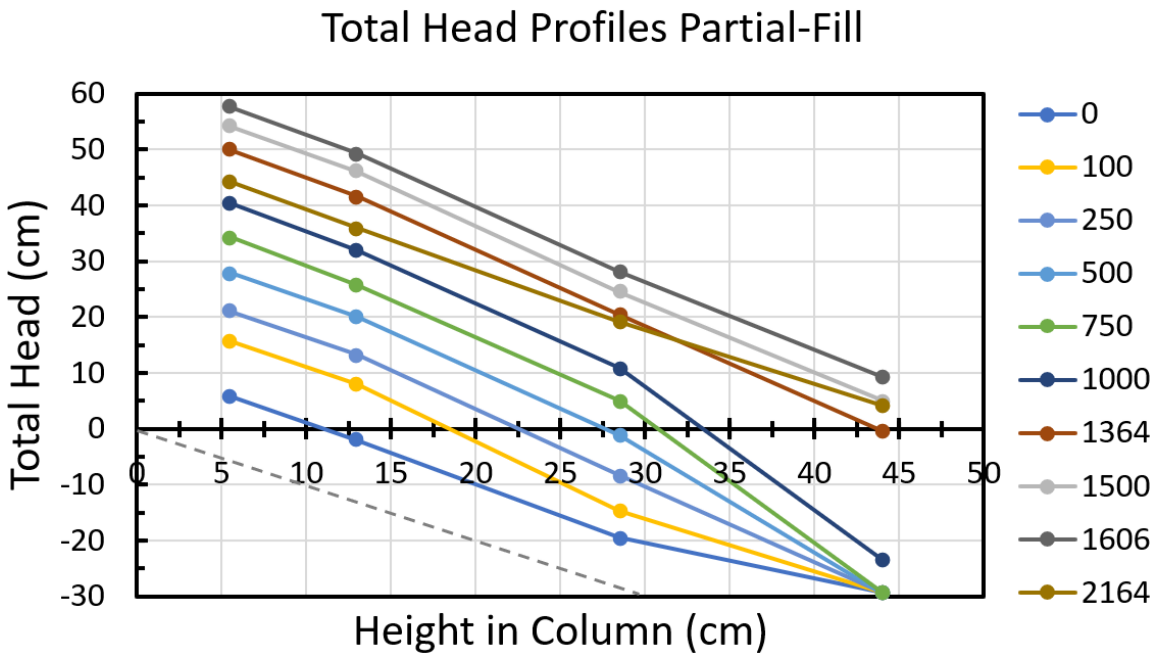

Figure 26: Pressure head profiles at different times during the partial-fill injection test. The times in seconds relative to turning on the pump are shown in the legend. The dashed line is a reference with a slope of -1.

The pressure head gradient increased from 1.1 before injection to approximately 1.3 during injection (Figure 26). The heads in the bottom three sensors increase with time, but the gradient is similar. This indicates that the total head gradient change due to pumping is approximately 0.20 during injection. The volumetric flux is ($Q = 1.66 \times 10^{-6}$ m^3/s); $A = 0.031$ m^2, 5.4×10^{-5} m/s, which indicates a saturated hydraulic conductivity of 2.7×10^{-4} m/s. This is consistent with independent measurements of *K* (Figure 9).

The pressure head increases at the 28 cm sensor within a few tens of seconds after the start of injection, and it increased at the sensor 44 cm approximately 800 s later. This indicates the pressure was propagating and at rate of approximately 16 cm over 800 s, or 0.02 cm/s. The elevation change in the equilibrium head was 39 cm during injection, and it occurred over 1,600

seconds, which is an average rate of rise of 0.024 cm/s. The ratio of the flux/velocity 0.54/2.0 = 0.27 is the average fillable porosity, which is consistent with the retention curve.

The elevation of the point of zero pressure (PZP) corresponds to the height of the water table in an aquifer and can be identified by interpolation of the data in Figure 26. The elevation where the pressure profiles cross the zero-pressure axis is the PZP. The PZP is at 12 cm initially, and it is at 32 cm after 750 s, according to Figure 27. The PZP was determined at different times as one measure of how the pressure propagates up the column.

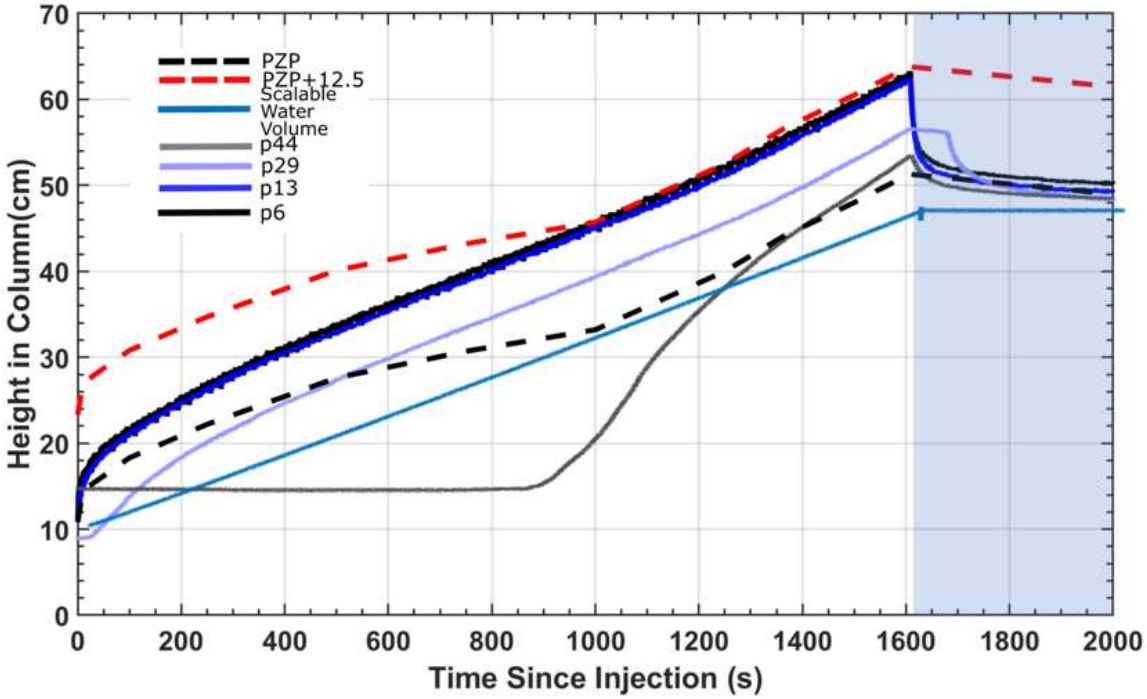

Figure 27: Pressure head, scaled water volume, and transition zone (PZP to PZP + 12.5 cm) height as functions of time for the injection portion of the infiltration fill-up test. Blue band is the period of no-flow

The time series of the total head (Figure 27), the data measured at the horizontal bank of transducers for the lower three transducers (p6, p13, p29), starts at essentially the same value of 11 cm, which is consistent with equilibrium conditions (Figure 26). The total head increases first at the bottom and then the transducers that are progressively higher in the column increase. The total head increases sharply during the first tens of seconds, but then the rate drops to approximately 0.022 cm/s (2.2 Pa/s) at the bottom transducers (p6, p13 and p29) and this rate is roughly constant during injection. The total head is unchanged initially in the upper transducer, p44, but it rapidly increases to approximately 0.05 cm/s (5 Pa/s) at approximately 850 seconds.

The weight of the injected water was determined with a load cell and those data are plotted on Figure 27 using normalization. The normalization procedure involves converting the weight to volume of water and dividing by the cross-sectional area of the pipe, *A*. This value was then divided by the average fillable porosity, which was determined from tests where the water level reached the surface of the sand. In those tests, the average fillable porosity was determined as

$$n_f = \frac{V_t}{A(h - hi)} \qquad 14\text{-}10$$

where n_f is 0.25, h_s is the total height of the sand in the column, h_i is the initial height of the water level in the column, and V_T is the total volume injected when the water level reaches the surface of the sand. The normalized volume of water is

$$V = An(h - h_i) \qquad 24$$

The rate of injection was constant, so the normalized volume of injected water increases linearly with time, is steady when the pump is turned off, and then decreases linearly with time during the pumping out portion of the test.

The PZP was determined by interpolation at multiple times and compiled into a time series. These data show that the PZP started at an elevation of 12 cm and moved upward during filling to a maximum height of 51 cm, and then it dropped during draining (Figure 28). It generally followed the scaled water volume, but there are systematic variations. For example, the PZP rises faster than the volume curve at the beginning of injection and it is 6.5 cm above the curve after 100 seconds. However, the PZP flattens and falls below the volume curve with time (Figure 28). This behavior is reasonable because the volume curve is normalized to the average fillable porosity. The fillable porosity is less than the average near the bottom of the column, whereas it is greater than the average near the top of the column because the water content has redistributed by gravity drainage prior to the test. The PZP is at approximately 32 cm at t =850 s, and the data indicate (Figure 26) that the pressure at p44 first starts to change at this time. This indicates that the zone where the pressure transitions to ambient is approximately 12 cm high.

The PZP reaches a maximum elevation of 51 cm when the pump is turned off. The data indicate that the maximum height of transition zone is approximately 12 cm higher at 63 cm. This is approximately 9 cm below the surface of the sand, ensuring that there is negligible pressure interaction with the surface.

The data from the transducers indicates that there are three main zones defined by pressure during imbibition; 1.) Ambient, 2.) Transition and 3.) Positive. In general, where the pore pressure is initially negative, the pressure remains at ambient conditions and then it increases sharply when the transition zone arrives. The rate of pressure increase diminishes when the pressure becomes positive. The pressure and head gradients are steeper in the transition zone than in the ambient and positive pressure zones (Figure 26). These profiles indicate the transition zone is between 10 cm and 15 cm wide. Combining this with other pressure data, an average value of 12.5 cm is used for the height of the transition zone.

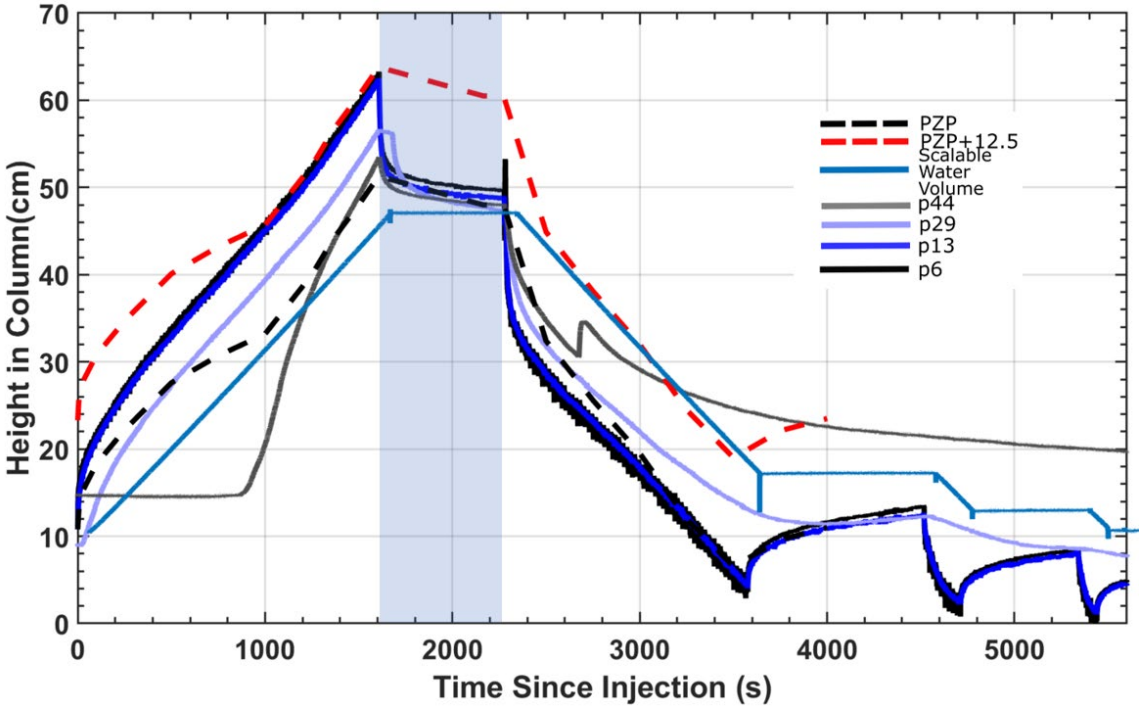

Figure 28: Total heads (solid lines), scaled water volume (straight blue line), and transition zone (PZP to PZP + 12.5 cm) height as functions of time for the partial-fill test. Blue band is the period of no-flow.

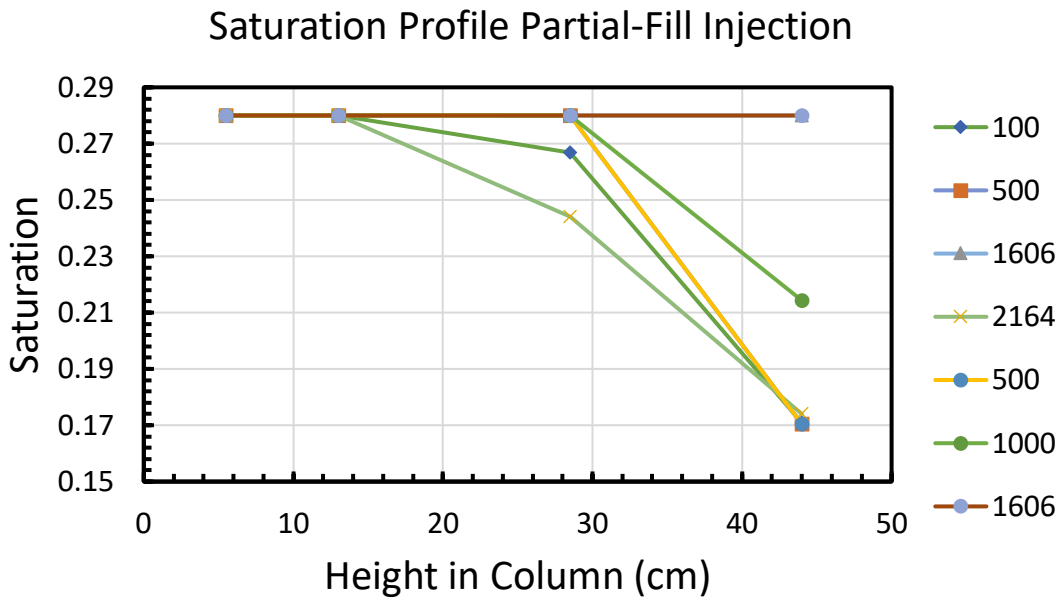

Figure 29: Saturation profile during partial fill injection determined using the retention curve in Figure 15. The times in seconds relative to turning on the pump are shown in the legend.

The pressure data along with the retention data can be used to estimate the water content as a function of elevation. The sand at the p6 and p13 tensiometers is completely saturated at the start

of the test (Figure 29). The water content at p29 is 0.24 and at the p44 transducer has an initial saturation of 0.17. The maximum change in water content is approximately 0.1 and occurs at the top sensor, p44. All sensors are saturated at the end of injection t =1,600 s.

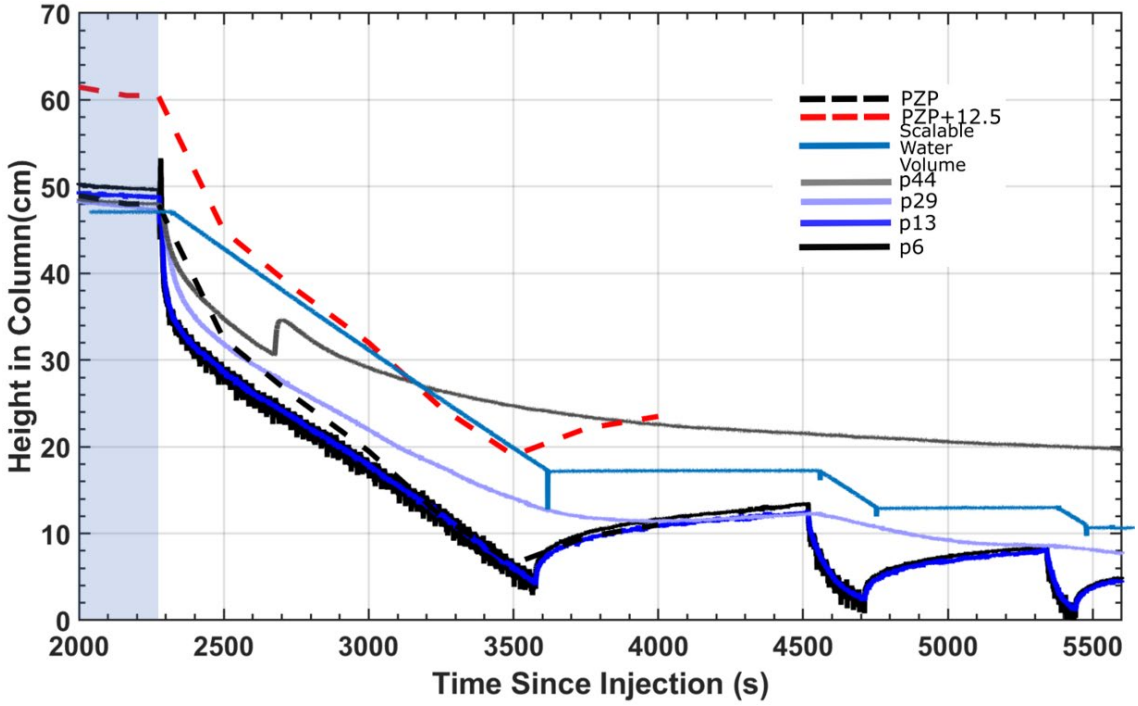

Figure 30: Total head, scaled water volume, and transition zone (PZP to PZP + 12.5 cm) height as functions of time for the drainage portion of the infiltration fill-up test. Blue band is the period of no-flow.

Pumping out from the base of the column initiates drainage and causes a rapid pressure decrease for approximately 20 seconds (Figure 30). After this period, the pressure in p6 and p13 begin dropping at a rate of 0.023 cm/s. The pressure at p29 drops at a similar rate that diminishes over time. The pressure at p44 initially follows the similar rate but it also slows from this trend. The pressures at p28 and p44 lags that of the lower two transducers and the rate of drop diminishes, particularly when the PZP drops below the level of the tensiometer. The initial drop in head is consistent with the development of a vertical head gradient of 10/40=0.25, which is similar to the 0.2 head gradient determined during filling. The PZP also drops rapidly during the first tens of seconds, but this rate diminishes and approaches the 0.02 cm/s rate recorded by the transducers after a few hundred seconds of pumping out (Figure 30).

Water is pumped out of the column for approximately 1,000 s and the pump is turned off at t = 3,600 s. The total head at p6 and p13 increase abruptly when the pump is turned off, but there is only a slight effect at p28 and negligible effect at p44 (Figure 30). A head increase of approximately 5 cm occurs in a few seconds, but the head continues to rise at a slower rate for nearly 1,000 seconds. The rapid initial increase in head likely occurs as the head gradient flattens when the flow stops. Water will continue to drain out of the partially saturated sand, and this is assumed to cause the continued rise in head at p6 and p14 and the slight drop in head at p29 (Figure 30).

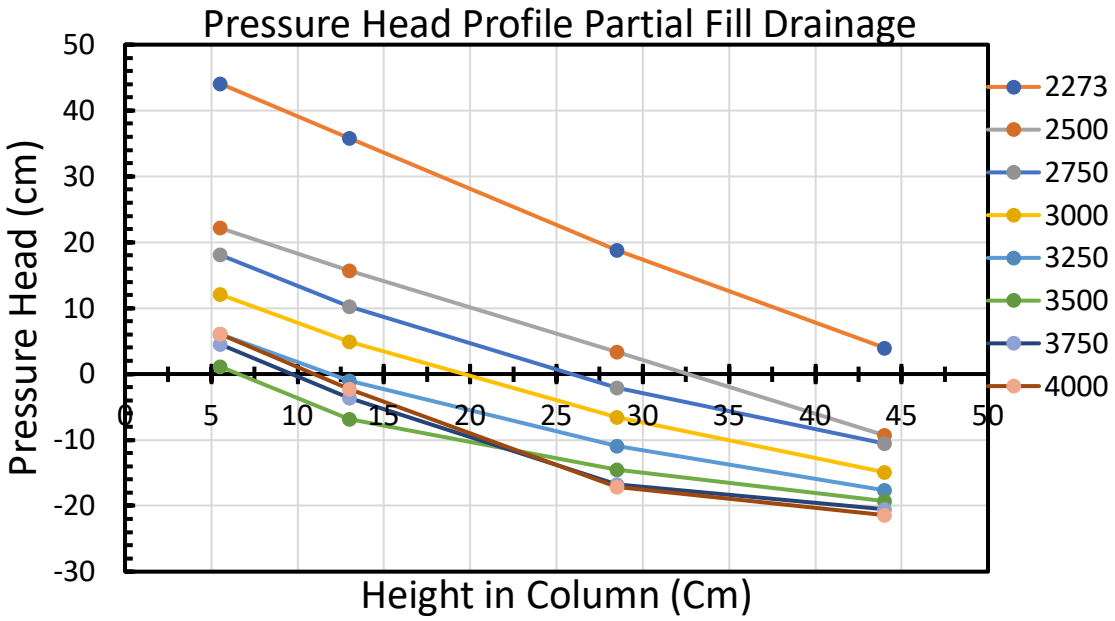

Figure 31: Pressure head profiles at different times during the drainage portion of the partial-fill injection test. The times in seconds relative to turning on the pump are shown in the legend.

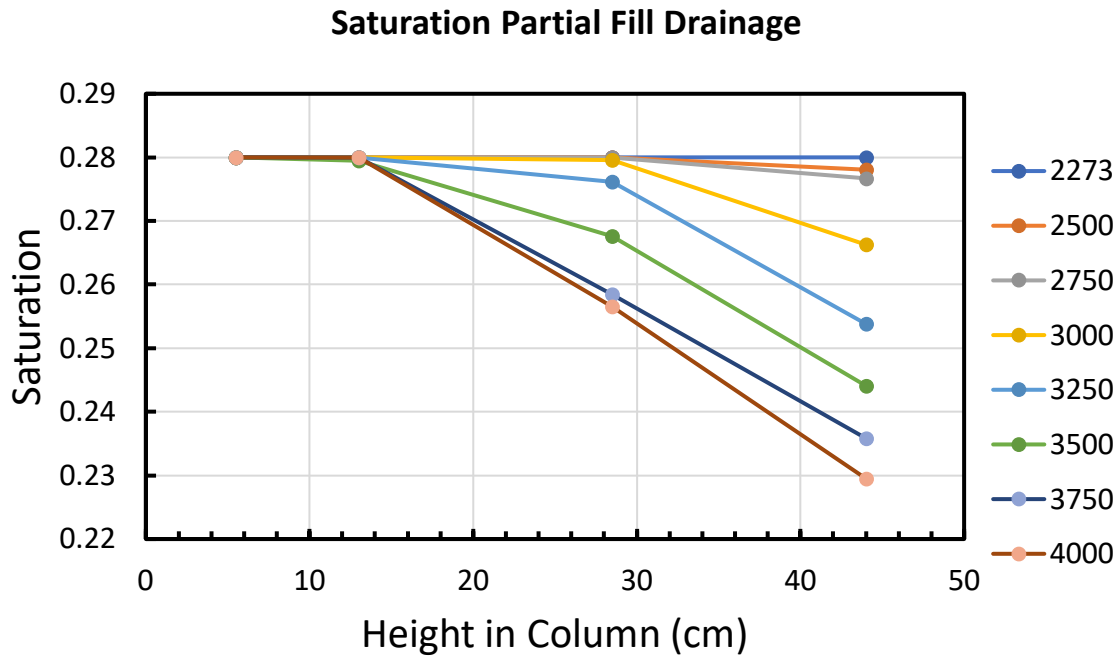

Figure 32: Saturation profile partial fill drainage. The times in seconds relative to turning the pump on at the start of the test are shown in the legend. P5 and p13 are almost fully saturated throughout the test.

The scaled water volume is higher than the pressure heads at the lower three tensiometers (p6, p14, p29) and less than the pressure head at p44. The PZP is slightly higher than the pressure head at the lower pressure sensors at earlier drainage times but begins to follow it after 800 seconds of drainage (t = 3,100 s).

The head continues to drop at p44 and p29 after the pump is shut off and this causes the water content to decrease (Figure 32). At 4,000 s the water content reaches a low of 0.23 in p44. Water content at p29 drops to 0.26 at t = 4,000 s. Sand at p13 and p6 remain almost fully saturated during drainage.

Turning on the pump causes an abrupt change in head as the hydraulic head gradient of 0.2 to 0.25 becomes established. After that, the head advances at a rate of approximately 0.02 cm/s, which is consistent with the velocity expected from the flow rate and average fillable porosity. This corresponds to a pressurization rate of 2 Pa/s. The head gradient is negative and induces upward flow during injection, it goes to zero when the pump is turned off. The total head gradient changes sign and causes downward flow when the pump is reversed. The head gradient caused by the pump dissipates within 100 to 200 seconds after the pump is turned off, and this causes the head to stabilize. However, gravity drainage occurs when the pump is turned off after pumping water out of the column, and this causes the pressure to increase over a longer time period (at least 1,000 seconds).

14.5.1.2 Strain

Strain data were recorded between five pairs of reflectors in an optical fiber between 10 and 60 cm above the datum. Elevations of the pressure sensors roughly correspond with the elevations of the strain sensing regions (Figure 1). The PZP was at 12 cm and the top of the pressure transition zone is inferred to occur at approximately 25 cm at the start of pumping. The lowest pair of strain sensors, at 10 cm and 20 cm and labeled “s1020”, was within the transition zone at the start, and s2030 also contained part of the transition zone. The height of the transition zone increased to approximately 63 cm during the test. As a result, sensor s4050 was completely below the transition zone at the end of the test, and the interval spanned by sensor s5060 was within the pressure transition zone.

14.5.1.2.1 Strain during filling

Soon after the start of pumping, tensile (positive) strain occurred at the lowest two sensors (s1020 and s2030), essentially no strain occurred at the middle sensors (s3040 and s4050) and slight compressive strain occurred at the uppermost sensor (s5060). The tensile strain rate was initially roughly constant (~0.02 με/s) at the lower two (s1020 and s2030) sensors, the rate abruptly decreased after several hundred seconds. In contrast, the strain rate at the other sensor was small initially, but then it progressively increased to approximately 0.02 με/s followed by a flattening, a pattern similar to the strain at the lower sensors. The increase in slope occurs first in s3040, then s4050 followed by s5060. The linear portion of the increasing strain between each pair of sensors can be fit by a curve with the same slope ~0.02 με/s, and the curves are offset by approximately 400 s. The sensors are 10 cm apart, so that indicates the linear portion of the increasing strain moves at a rate of approximately 10cm/400s or 0.025 cm/s. (Figure 33). This indicates the band of linearly changing strain is moving at a rate similar to the velocity of the water.

Strain is expected to increase as the sand dilates due to an increase in pore pressure. The period when the strain increases linearly at each sensor occurs at approximately the time when the transition pressure zone is between the reflectors on the fiber sensor. The pressure increases at approximately 2 Pa/s in the lower tensiometers where the strain rate is approximately 0.02 με/s. Assuming the sand column behaves as an ideal, 1D poroelastic material, the ratio of pressure change to strain leads to

$$C_1 = \frac{1-\nu}{(1+\nu)(1-2\nu)} \qquad 14\text{-}11$$

$$\frac{\Delta P}{\epsilon_{zz}} = C_1 E \qquad 14\text{-}12$$

where E is Young's modulus, α is the Biot-Willis coefficient, and ν is Poisson's ratio (Wang, 2000). Assuming α is unity and ν could range between 0.25 and 0.45 as a result of changes in saturation constrains C_1 to $1.2 < C_1 < 3.8$. The ratio of the pressurization and strain rates gives (2.5 Pa/s)/(2x10^{-8} 1/s) = 125 MPa and using C1 leads to an estimate of Young's modulus of 30 MPa $< E <$ 100 MPa, with the lower value associated with saturated conditions. Measurements of Young's modulus during the column loading tests indicate values in the range of $7 < E <$ 37 MPa. The values from the triaxial test indicate $18 < E <$ 40 MPa, depending on saturation and confining pressures (Figure 17-Figure 21). Each method covers a significant range, but all three indicate $E \sim$ 30 MPa.

These results indicate that the periods of linear increase of strain are consistent with the linear increases in pressure that occur simultaneously, but the magnitude of the observed strain rate less than what is expected from Young's modulus measurements measured independently. It is possible that the relatively stiff PVC tube could have caused the sand to behave as if it were stiffer than indicated by the triaxial test. It is also feasible that the effective modulus at the small strains (less than 10 με) that occur during the partial-fill is stiffer than the modulus at the larger strains (greater than 100 με) used in the triaxial test.

The transition zone is bounded by the PZP on the bottom and is assumed to be 12 cm thick, and the position of this zone is related to the strain signal. The position of the pressure transition zone was plotted on the time series (Figure 33) and compared to the strain time series. This shows, for example, that the top of the transition zone (PZP +12.5 cm) is at roughly 35 cm at t = 400 s when the strain at s3040 first starts to increase. The top of the transition zone is at approximately the bottom of the sensing interval for s4050 when the strain at that sensor starts to increase at approximately t = 700 s (Figure 33). Interestingly, the strain at s5060 becomes slightly negative during injection and it starts to increase when the top of the transition zone reaches 50 cm height at approximately t =1,100 s.

Each strain curve flattens when it reaches 10 to 15 με, and the time when this occurs is approximately equal to the time when the PZP arrives at the top reflector in the strain sensing pair. For example, the slope of the signal from s2030 flattens at approximately t =800 s. and the PZP is at 30 cm at this time, and a similar effect occurs at s3040 (Figure 33).

14.5.1.2.2 Pump off

The pressures drop sharply when the pump is turned off as the water returns to hydrostatic conditions, and this is accompanied by slight drops in strain. After that, the strain increases slowly by several με during the period the pump is off.

14.5.1.2.3 Strain during draining

When the pump is reversed and turned back on, the strain initially becomes tensile in the lower sensors, but it reverses and becomes compressive with time. Data from the lowest sensor, s1020, was erratic, however, the general trend occurs through despite the erratic data points. The largest tensile strain occurs in the lowest sensor, and it lasts the longest. The strain at s2030 increases by approximately 10 με and reaches a maximum at 2,850 s, approximately 600 s after the pump was turned on. A similar effect occurred at s3040, but the strain only increased by 8 με and the peak was reached after 350 s, and the effect was even smaller and briefer at s4050 (Figure 33). No tensile strain was observed at the upper sensor, which started to compress as soon as the pump was turned on (Figure 33 and 35). The peak compressive strain propagates from one sensor to another in approximately 250 s, giving a propagation rate of 0.04 cm/s.

After the initial tensile period is over, the strain decreases (becomes compressive) at a rate of 0.02 to 0.03 με/s at the lower three sensors (with the exception of s1020). The strain at s5060 during draining decreases at a slower rate (0.01 με/s) than at the sensors below it, just as the strain at that sensor increased at a slower rate during filling.

The strain decreases during draining and it drops below the original strain in all but s2030. When the pump is turned off at approximately t = 3,500 s, the strains rebound in all the sensors, increasing at a rate that is several times slower than the rate of decrease. Strains decrease again when the pump is turned back on at t = 4,500 s, and then increase again when it is turned off at t = 4,700 s. This pattern is repeated through another cycle of recovery from t = 4,700 to 5,300 s, and pumping from t = 5,300 to 5,400 s and subsequent recovery (Figure 33 and 35). Strain at the upper sensor, s5060, recovers to essentially the value at the beginning of the test. Strain in the other sensors are compressive, within 10 με of the starting strain, but the trends are increasing and they may recover to within a few με with sufficient time. Strain at s2030 is 15 to 20 με more tensile at the end of the test than at the beginning (Figure 33 and 35).

14.5.1.3 Summary

The observations from the partial-fill test indicate

1) Pore pressure during injection and draining forms three zones: 1.) positive pressure; 2.) transition from positive to ambient; 3.) ambient pressure. The transition zone is bounded on the bottom by the point of zero pressure and on the top by ambient pressure. The height of the transition zone is approximately 12 cm, based on pressure data during filling. The transition zone moves upward at an average velocity of approximately 0.02 cm/s, which results in a pressurization rate of 2 Pa/s. The initial pressurization rate is faster than this, around 7 Pa/s at the upper two sensors, but it decreases with time.
2) The sand expands and experiences tensile strain when the pressure increases during imbibition, and it contracts with compressive strain during drainage. The occurrence of strain appears to be related to the location of the pressure transition zone. Changes in strain progress up the column at approximately the velocity of the water during

injection. The strain is negligible or negative in the region above the transition zone, but it increases roughly linearly as the transition zone passes between the strain sensing region between the reflectors. The linear portion of the strain rate is 0.15 με/Pa.

3) The strain rate decreases and, in some cases, it changes sign when the pressure transition zone rises above the strain sensing interval.

4) There are several exceptions to the occurrence of tensile strain associated with increasing pressure. One of these occurs after the transition zone has moved past the strain sensors and the strain is either unchanged or decrease while the pressure continues to increase.

5) Another exception occurs when the pump is first shut off. The pressures drop due to the flattening of the negative vertical head gradient caused by the upward flow, and this generally causes strain to increase.

6) One more exception occurs as the head gradient increases later in the experiment. This occurs when the pump is first turned on to drain the column. This causes the pressures to drop abruptly, and this results in an abrupt increase in strain.

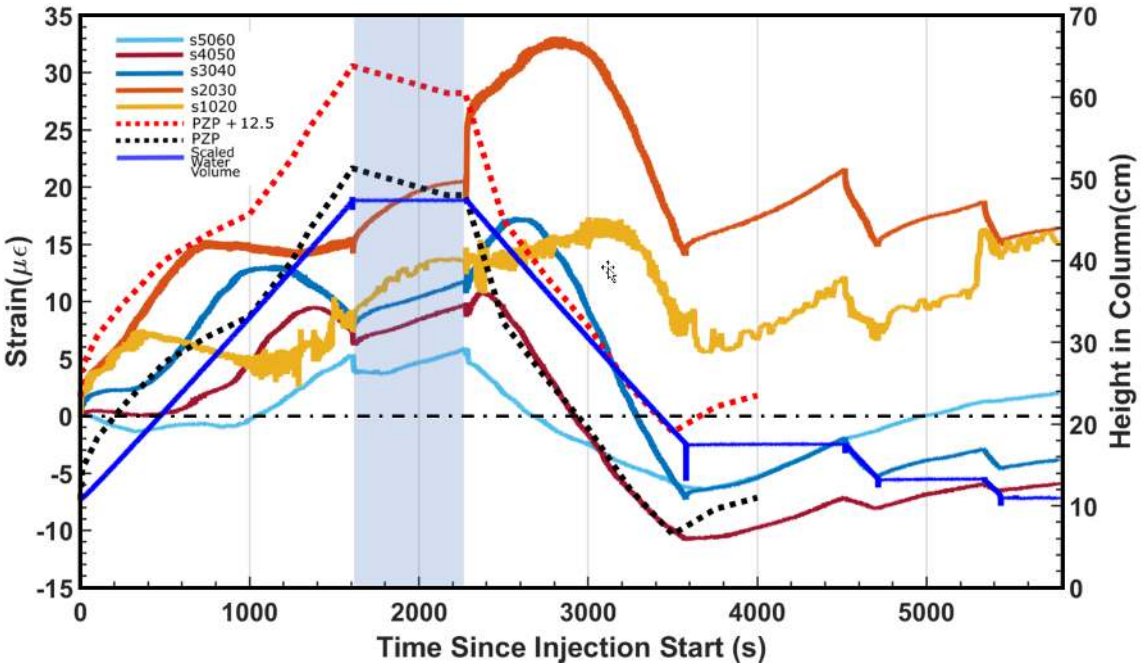

Figure 33: Strain, scaled water volume, and transition zone (PZP to PZP + 12.5 cm) height as functions of time for the infiltration fill-up test. Blue band is the period of no-flow.

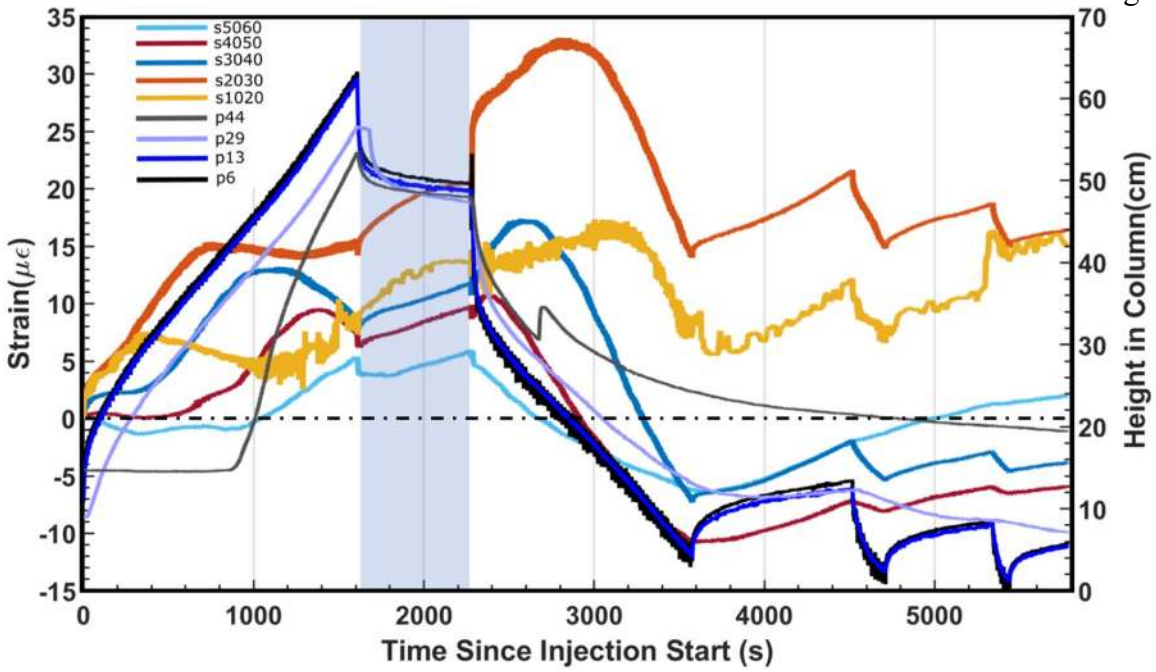

Figure 34: Strain and total head as functions of time for Partial-Fill test. Blue band is the period of no-flow.

14.5.1.4 Distributed Strain and Pressure in the Column

The strain and pressure at different sensors create a complex dataset that is difficult to fully appreciate when plotted together (e.g. Figure 33 and Figure 34). As a result, subsets of the data from similar height intervals along the column are described separately to identify relevant details.

The s1020 sensor is the lowest in the column and the bottom reflector is slightly (5 cm) above the gravel, the p6 pressure sensor is below the s1020 interval in the gravel.

The data at s1020 includes high frequency fluctuations of variable amplitude (up to several με/s) and abrupt jumps (up to 5 με/s) that complicated the signal compared to the data from the other sensors (Figure 35 and Figure 36). The heads measured at p6 includes a regular periodic fluctuation with an amplitude of up to 4 cm and a period of 2 seconds. This period corresponds to the rotation rate of the pump and the periodicity is due a result of pulsation caused by the peristaltic pump. Some of the variation in strain in s1020 may also be caused by the pump. Abrupt offsets in the data from s1020 were corrected manually.

This region is tensioned initially by 2 με when the pump is turned on. This initial shock lasts for 1 seconds. After this period, the strain increases in a linear fashion of 0.2 με/s. This abruptly stops at t =350 s and the region is gradually compressed by 2 με. This continues until the pump is turned off.

The strain is more erratic data during drainage (Figure 33 and Figure 34). These jumps downwards are assumed to be artifacts and are ignored for this graphical analysis. Upon drainage, the strain gradually tensions to a value of 17 με 900 seconds after drainage begins (t = 3,100 s). After this tension peak, the region compresses at a rate of 0.02 με/s until the pump is turned off. Tensioning occurs when the pump is turned off as the saturation increases from delayed yield from storage.

14.5.1.4.1 10-20cm

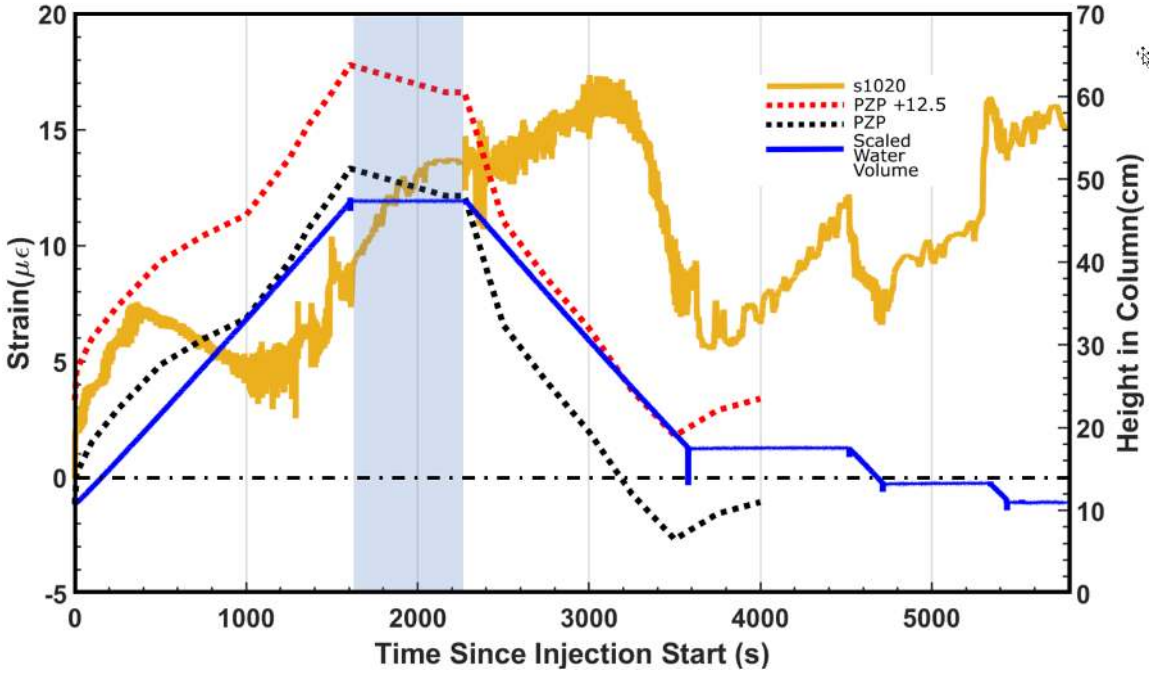

Figure 35: Strain at s1020, scaled water volume, and transition zone (PZP to PZP + 12.5 cm) height as functions of time for the Partial-Fill test. Blue band is the period of no-flow.

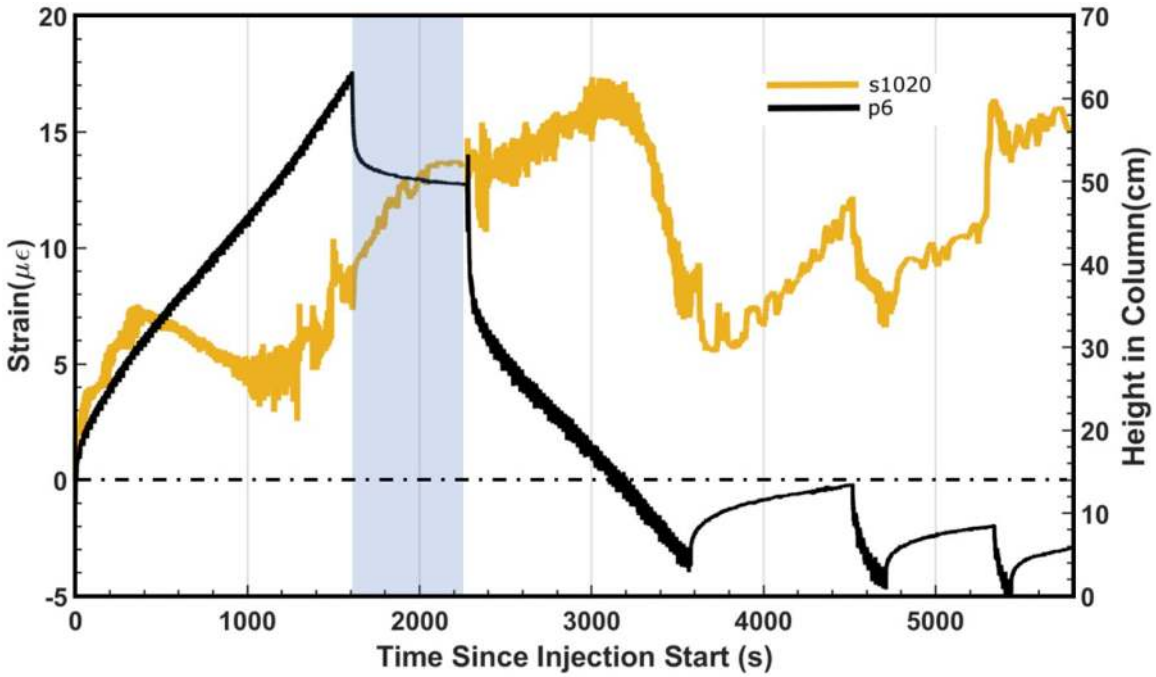

Figure 36: Strain at s1020 and total head at p6 as functions of time for Partial-Fill test. Blue band is the period of no-flow.

14.5.1.4.2 20-30cm

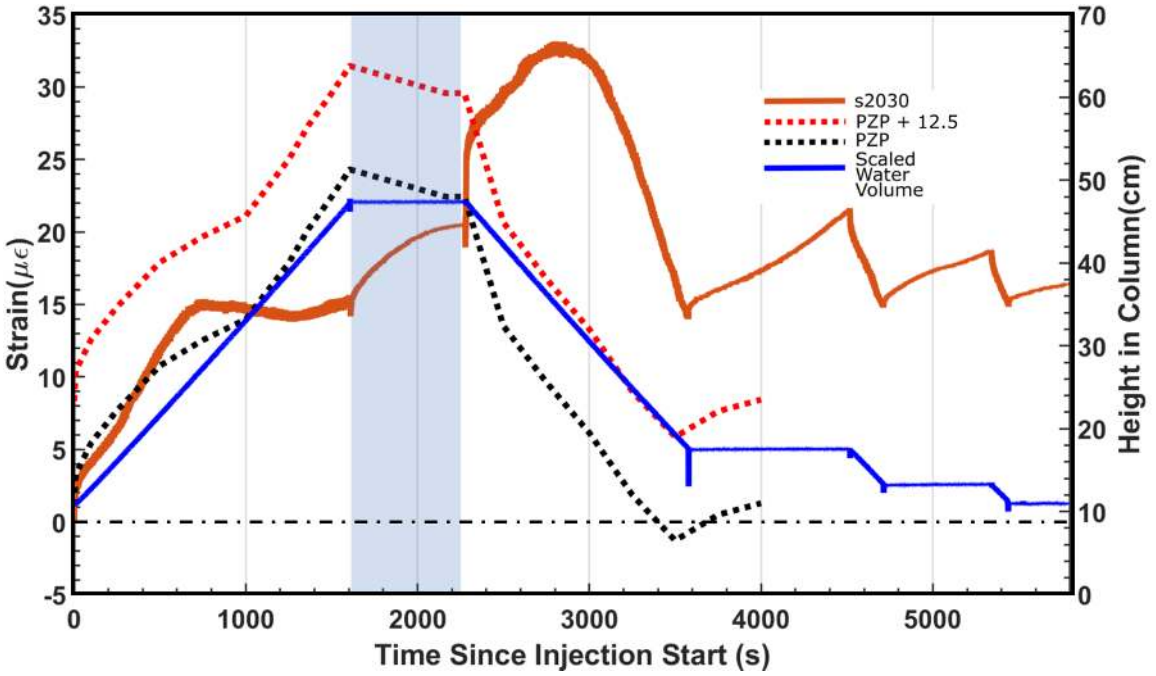

Figure 37: Strain at s2030, scaled water volume, and transition zone (PZP to PZP + 12.5 cm) height as functions of time for Partial-Fill test. Blue band is first the period of no-flow.

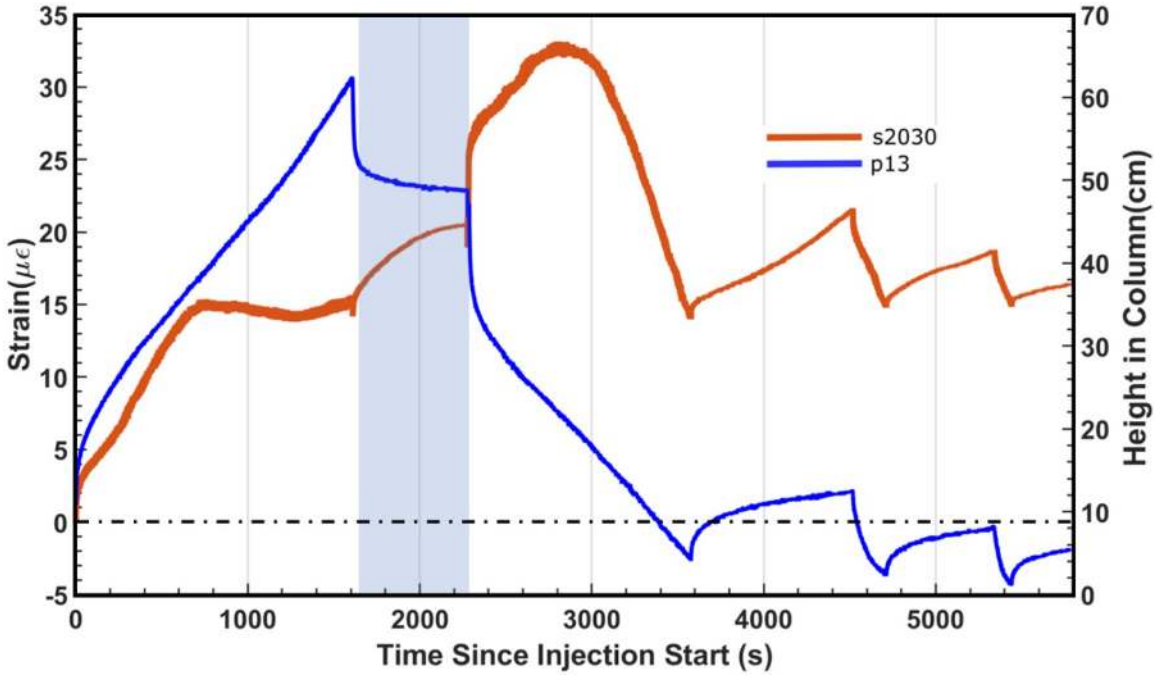

Figure 38: Strain at s2030 and total head at p13 as functions of time for Partial-Fill test. Blue band is the period of no-flow.

The region between 20 and 30 cm is initially tensioned by 1.5 με when the pump is turned on (Figure 37 and Figure 38). The strain increases at a rate of 0.2 με/s from time 50 to 700 s.

Then the region begins slowly compressing at a rate of 0.007 με/s. Slight tensioning occurs around 1,300s.

When the pump is turned on in reverse, the strain tensions sharply by 5 με at the start of drainage. After this, the strain increases at a rate of 0.02 με/s and reaches a maximum net of 15 με 600 seconds after drainage began (t = 2,600 s). The region is linearly compressed at a rate of 0.035 με/s until the pump is again turned off (t = 3,600 s).

Tension occurs when the pump is off and water continues to drain from upper regions of the column. Tensioning is immediate after the pump is turned off and jumps to a steady rate of 0.0057 με/s. Turning the pump back on to pump out remaining water causes compression at a rate of 0.034 με/s.

14.5.1.4.3 30-40cm

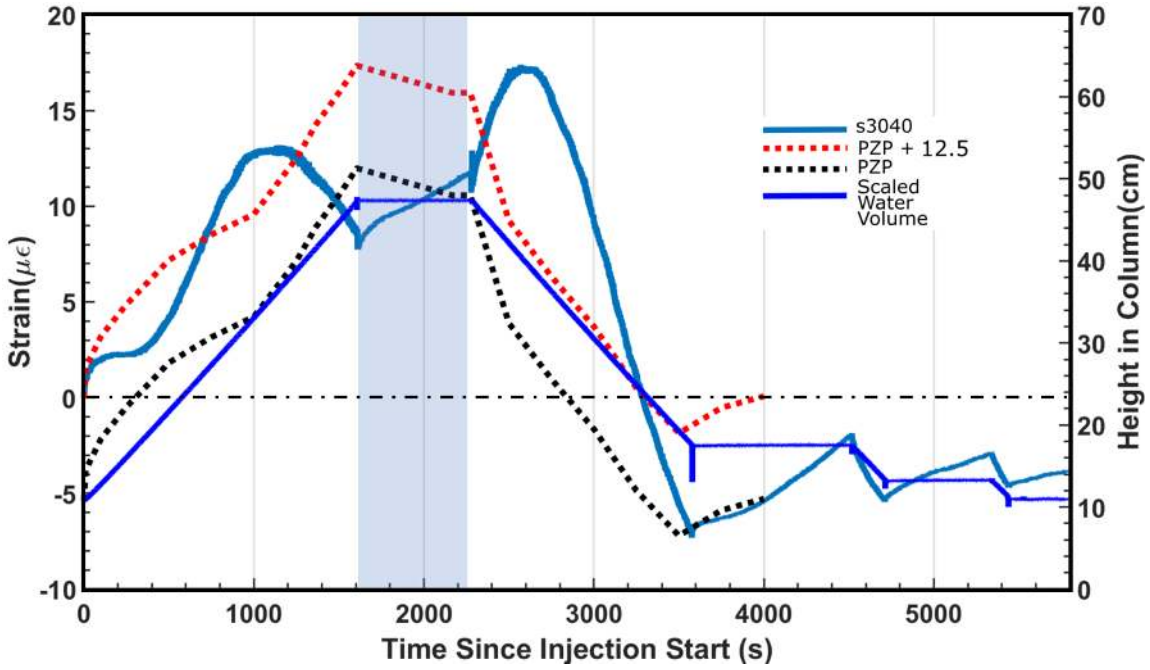

Figure 39: Strain at s3040, scaled water volume, and transition zone (PZP to PZP + 12.5 cm) height as functions of time for Partial-Fill test. Blue band is the period of no-flow.

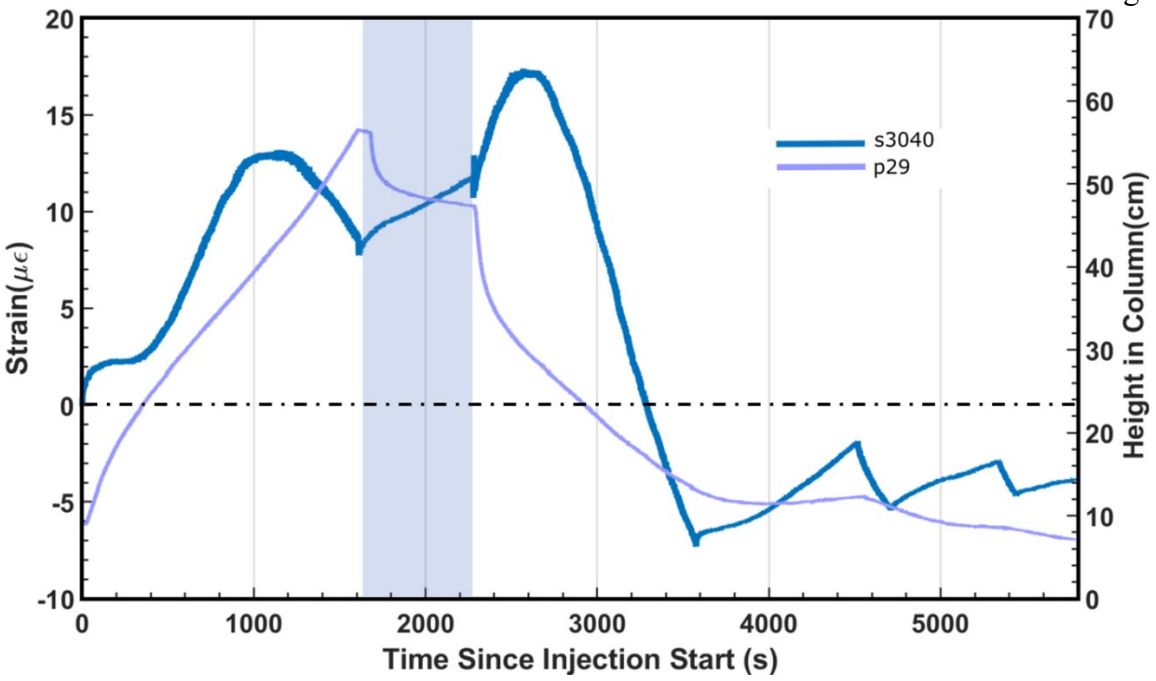

Figure 40: Strain at s3040 and total head at p29 as functions of time for Partial-Fill test. Blue band is the period of no-flow.

The region between 30 and 40 cm experiences a small increase of strain (0.5 με) from the pump being turned on (Figure 39 and Figure 40). The strain stabilizes with slight tensioning until time 330 s when it begins increasing linearly at a rate of 0.2 με/s. This stops at 1,000 s. The tension rounds out into compression and then decreases linearly at a rate of 0.011 με/s until the pump is turned off.

Tensioning occurs during drainage at a rate of 0.03 με/s rounding off to a maximum tension of 6 με greater than before drainage at a time of 300 seconds after drainage (t = 2,700 s). After rounding off, the strain compresses linearly at a rate of 0.029 με/s until the pump is shut off.

Immediate tensioning occurs when the pump is shut off. This is similar to the underlying sensor, but the magnitude is less than in the lower regions. This starts as a jump moving to a tensioning rate of roughly 0.0054 με/s. Compression at a rate of 0.018 με/s occurs when the pump is turned on again to remove the remaining water.

Strain remains stable in the 40 to 50 cm region, compressing slightly, after the pump is turned on (Figure 41 and Figure 42). Tension begins at t = 500 s and begins to linearly increase at a rate of 0.02 με/s. This tensioning reaches a maximum at time 1,500 seconds and decreases until the pump is turned off.

The pressure is constant until t = 900 s, and then it increases sharply. The increase in pressure occurs 350 s after the increase in strain. This occurs because the pressure sensor is 4 cm above the lower reflector in the strain sensor. The leading edge of the pressure transition zone is at an elevation of 40 cm at t = 500 s and it is at 44 cm at t = 900 s (Figure 42).

14.5.1.4.4 40-50cm

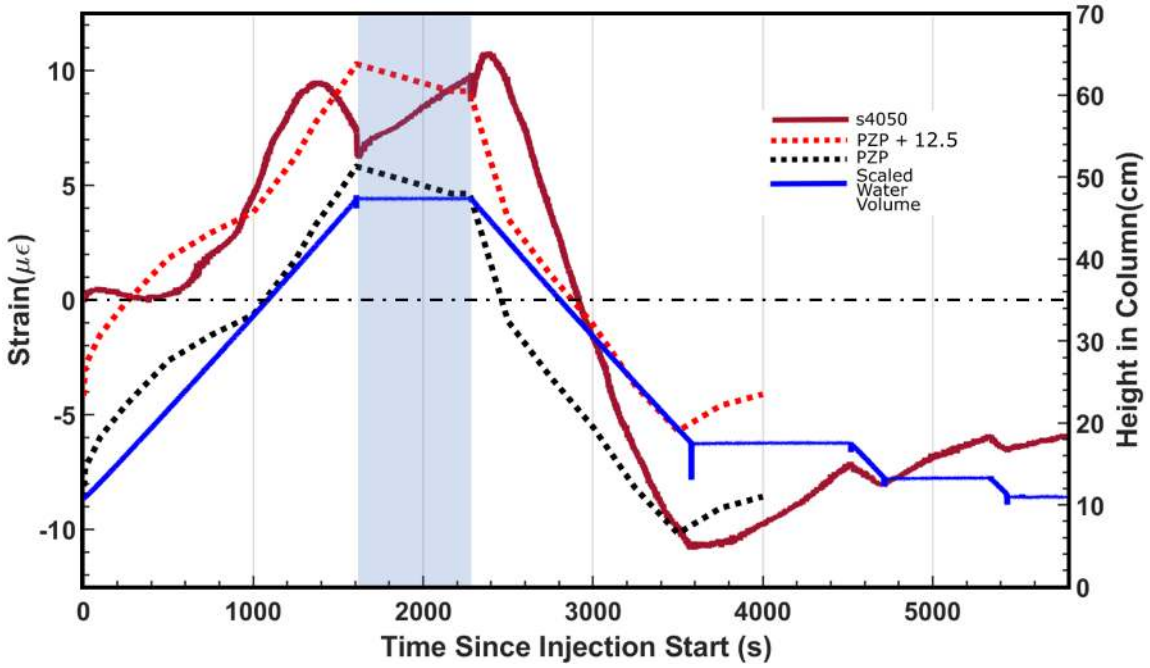

Figure 41: Strain at s4050, scaled water volume, and transition zone (PZP to PZP + 12.5 cm) height as functions of time for Partial-Fill test. Blue band is the period of no-flow.

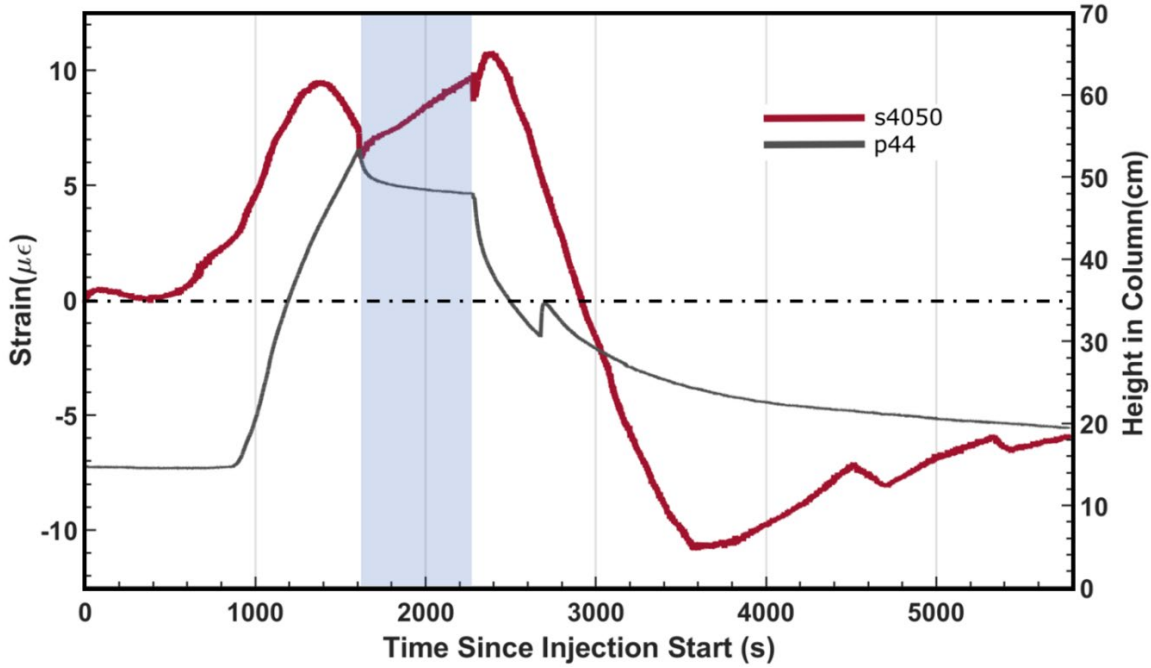

Figure 42: Strain at s4050 and total head at p44 as functions of time for Partial-Fill test. Blue band is the period of no-flow.

Slight tensioning occurs during drainage up to a value of 1 με 90 seconds after drainage starts (t = 2,400 s). After this, the region is compressed at a rate of approximately 0.02 με/s until the pump is again turned off. Around t = 3,200 seconds, the rate of compression slows.

Turning the pump off at t = 3,600 s ceases compression. Compression occurs at a rate of 0.004 με/s when the pump is turned back on.

14.5.1.4.5 50-60cm

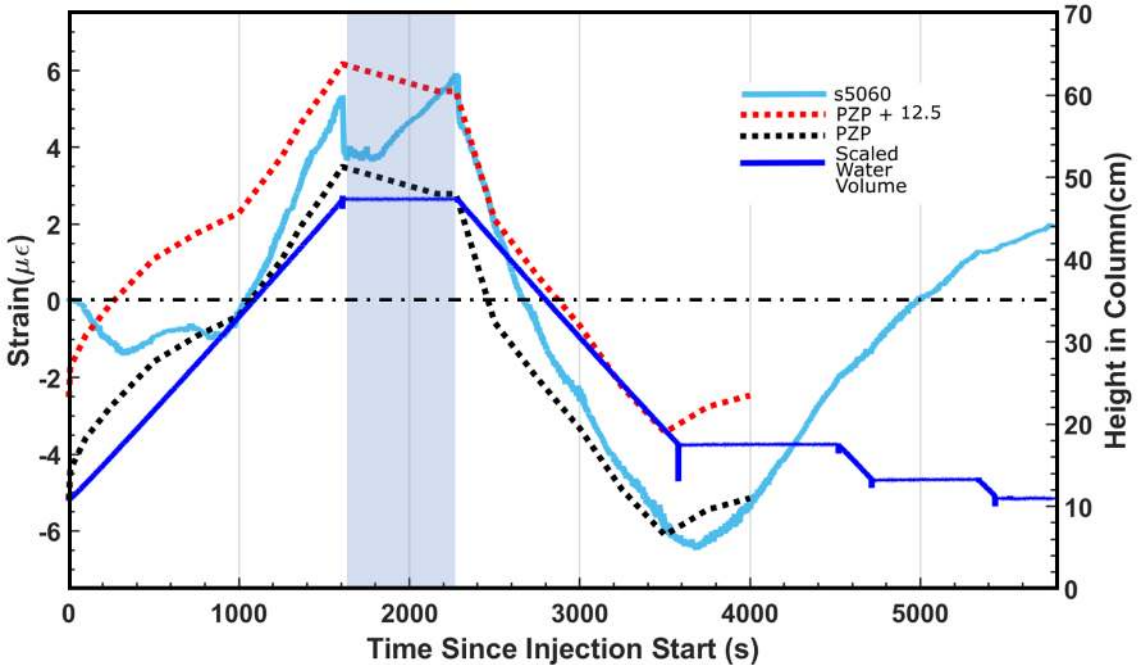

Figure 43: Strain at s5060, scaled water volume, and transition zone (PZP to PZP + 12.5 cm) height as functions of time for Partial-Fill test. Blue band is the period of no-flow.

Compression occurs during the first part of this experiment reaching a value of 3 με. At t = 1000 s, tensioning occurs and linearly increases at a rate of 0.02 με/s. Turning the pump off causes s slight compression of 1.3 με.

Instant compression of 1 με occurs when the pump is turned on to drain the column. After this, the strain decreases at a rate of roughly 1.2 με/s.

Compression slows when the pump is turned off. This compression stops and tensioning begins 90 seconds after the pump is turned off. This tensioning has a rate of roughly 0.0065 με/s. The tension rate slows when the pump is turned back on.

14.5.2 Complete-Fill Tests: Fill and Drain with Ponding

A series of tests was conducted by completely filling the column until water accumulated at the surface and then draining it by pumping or gravity.

The tests were conducted by injecting until water reached depths of around 1 cm at the surface of the sand, which will be referred to as “ponding”. The pump was turned off and injection stopped after ponding occurred. No water flows in or out of the column when the pump is turned off. This period of no flow continues for five to ten minutes. After this the column is

either drained using the pump by gravity. The outflow tubing from the column is monitored for air entry, and the pump is turned off when air enters the outflow tubing. Sometimes the pump is turned back on after the total head rises above the injection port. Gravity drainage tests are typically allowed to drain for several hours. Most of the drainage occurs shortly after the drain is opened. The water that accumulates during drainage is measured as a function of time using a load cell.

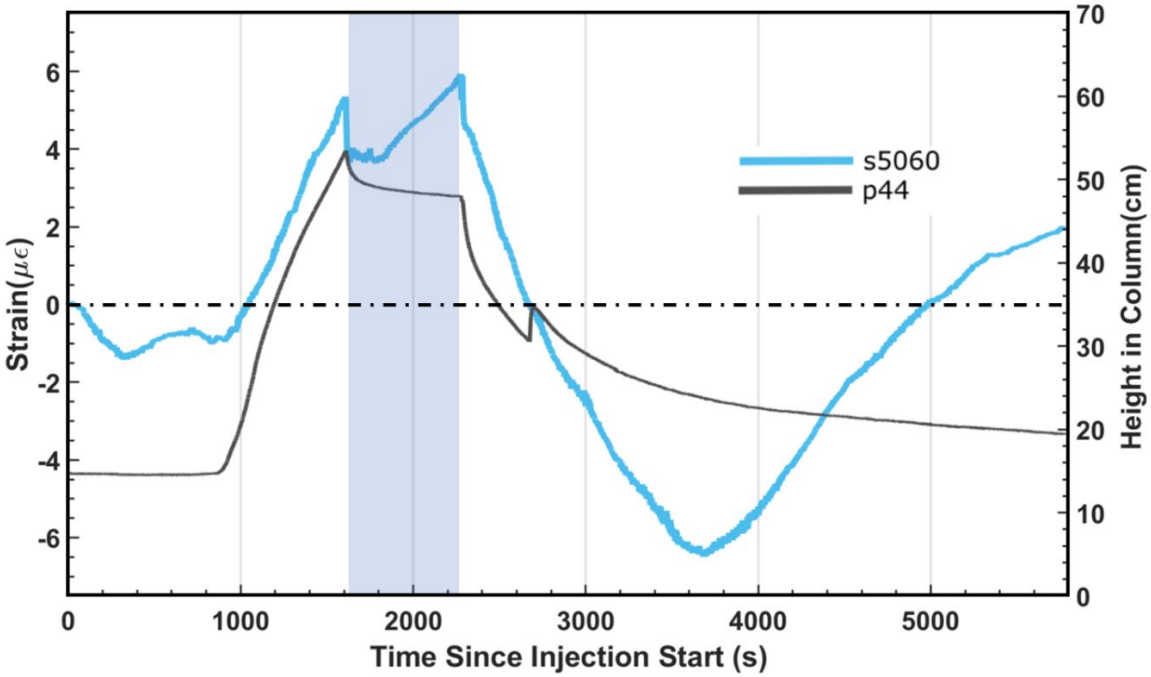

Figure 44: Strain at s5060 and total head at p44 as functions of time for Partial-Fill test. Blue band is the period of no-flow.

14.5.3 Results

The pore pressure increases during injection, is nearly constant during the no-flow period when the pump is turned off and decreases during drainage. The axial strain becomes tensile as the pore pressure increases during injection, and this trend is reversed with compressive strains occurring when the pore pressure decreases during draining. These effects are expected and are similar to the partial-fill test, but details of the pore pressure and strain response vary among the different sensors and unexpected effects occur during ponding.

Many of the basic aspects of the tests with ponding are similar to the partial-fill test. These similarities will be noted in some cases, but in other cases the details of the complete-fill test will be repeated even though they are similar to those described earlier. This was done to put clarity before brevity.

14.5.3.1 Pore Pressure

The pore pressure data during the complete-fill test on October 19, 2019 (referred to as the 10/16 test) will be described below. The data from this test are used because all the sensors were working, the temperature change is small, and the data are representative of the other injection

tests. The gravity drainage description is taken from a test on October 25, 2019 (referred to as the 10/25 test), and it is generally typical of the other gravity drainage tests.

Pore pressure was measured using tensiometers that were connected to transducers at a common datum below the bottom of the column. As a result, the pressure measured at the transducers was proportional to the total head. The pore pressure head at the tensiometers was determined by subtracting the elevation head from the measurements made by the transducers. The transducer locations were determined by measuring up from the bottom of the column, and this measurement is embedded in the name of the transducer. The bottom of the column was 0.5 cm above the transducers, so the elevation head used to convert total head to pressure head used the transducer location plus 0.5 cm. This is the same approach used for the partial-fill test.



Figure 45: Pressure head profile before the 10/16 injection test.

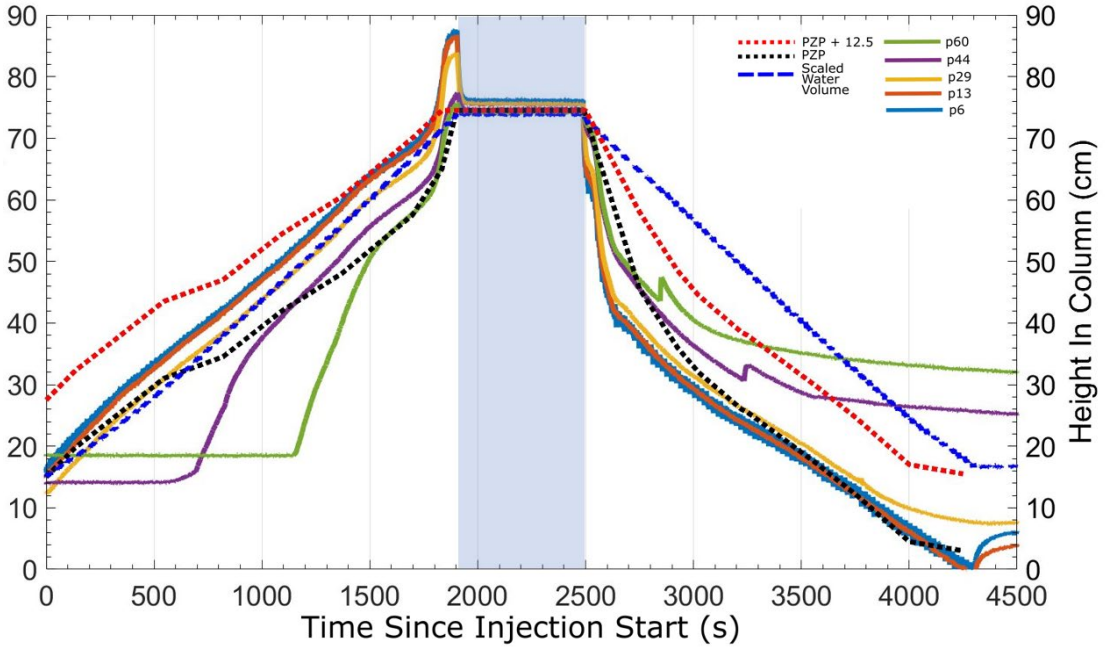

Figure 46: Total head, scaled water volume, leading edge, and point of zero pressure (PZP) as a function of time. Blue shaded regions are when the pump was off.

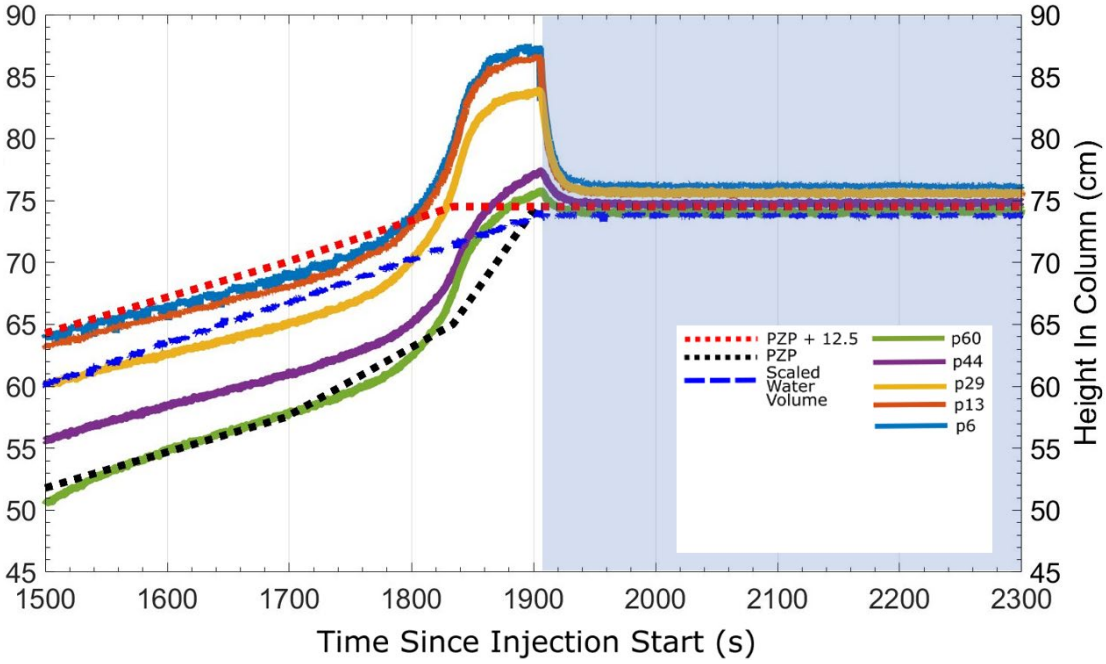

Figure 47: Detail of data series as a function of time. Detail is of the ponding event and no flow region.

14.5.3.1.1 Initial Conditions and Procedures

This suite of Complete Fill experiments included four tests conducted between October and November of 2019. The total head measured above the transducers at the beginning of the tests generally ranged between 10 and 15cm depending on the time since the last test. This means that

the point of zero pressure started at an elevation of 10 to 15 cm. Slow drainage occurs for several days after a test, so the initial heads during tests conducted in this time period were higher than heads conducted after the heads have fully equilibrated.

Water was added to the top two tensiometers (p44 and p60) the beginning of each test. This was necessary because air entered these transducers between tests in some cases. The start of injection was delayed for tens of minutes after filling the transducers to give the transducers time to equilibrate. Nevertheless, this time may have been insufficient for full equilibration to occur and may explain why the initial total heads in the upper tensiometers are higher than in the lower three transducers. The water content around p44 and p60 was likely increased by flow from the porous cup on the tensiometer. The conclusion is that the pore pressure was in equilibrium in most of the column, and it was slightly elevated in the upper part of the column because of filling of the tensiometers.

Pressure head data are available for five sensor locations during the 10-16 test.
Data from the lower four transducers prior to injection (Figure 45) can be fit with a line with a slope of 1.0. The pressure heads at p44 and p60 are a few cm above the line with a slope of 1.0.

In the time series of the total head for the 10/16 test, the data measured at the horizontal bank of transducers start between 1,000 and 1,500 Pa, which is expected to be equilibrium conditions. Pressure in the lower three tensiometers (p6, p13, and p29) increases at roughly a constant rate of 3.4 Pa/second when the pump is turned on, while the pressure at the upper two transducers remains constant (Figure 46). The pressure at p44 starts to increase at 700 s and at p60 it increases at t =1150 s. The transducers are separated by 15 cm, so the pressure front is advancing at approximately 15 cm/450 s =0.03 cm/s. The pressure at p44 and p60 initially increases at approximately double the rate of the underlying transducers, approximately 7 Pa/s, and the rate drops to around 3.5 Pa/s after approximately 300 s. The rate of advance of the pressure front (0.03 cm/s) is consistent with the pressurization rate of 3.5 Pa/s. This indicates that the faster rate of initial pressurization occurs while the transducer is sampling the transition zone. Assuming a rate of 0.03 cm/s and a duration of 300 s indicates the transition zone is approximately 9 cm long, which is consistent with other estimates (within a few cm).

The head gradient is steeper in the transition zone than in the underlying positive pressure zone. The steepest pressure head gradient in the transition zone is between 2 and 2.4 (e.g. times 545 and 1,094 in Figure 49).

The rate of pressure change increases sharply at approximately 1,750 s in p60, p44 and p29, and it starts to increase slightly later (at t = 1,750 s) in the deeper tensiometers, p13 and p6 (Figure 47). The pressure reaches a maximum rate of 30 Pa/s, approximately ten times faster than during most of the test. This rapid pressurization occurs when the top of the transition zone, as indicated by the PZP + 12.5 line, reaches the top of the sand at z = 72 cm (grey line in Figure 47) This rapid pressurization is brief, however, as the rate diminishes to 2 Pa/s in the upper three tensiometers, and it is several times greater than this in the lower two at t = 1,880 s when the PZP reaches the surface of the sand. The rates continue to diminish until the pump is turned off at 1,900 s.

The head reaches a maximum value of 87 cm at p6 when the pump is turned off. The heads drop abruptly when the pump is turned off and the sensors drop to 74 cm. This indicates that there is no flow during this time when the column is fully saturated and the pump is turned off.

The pressure head gradient is 1.0 when the column is fully saturated (Figure 49). During injection, the pressure head gradient is 1.2, an increase of 0.2 due to flow. The flux is 5.4 x 10^{-5} m/s, so the hydraulic conductivity is 2.7 x 10^{-4} m/s, which is the same as during the partial-fill test, and essentially the same as measured during the falling head test (2.5 x 10^{-4} m/s; Figure 9)

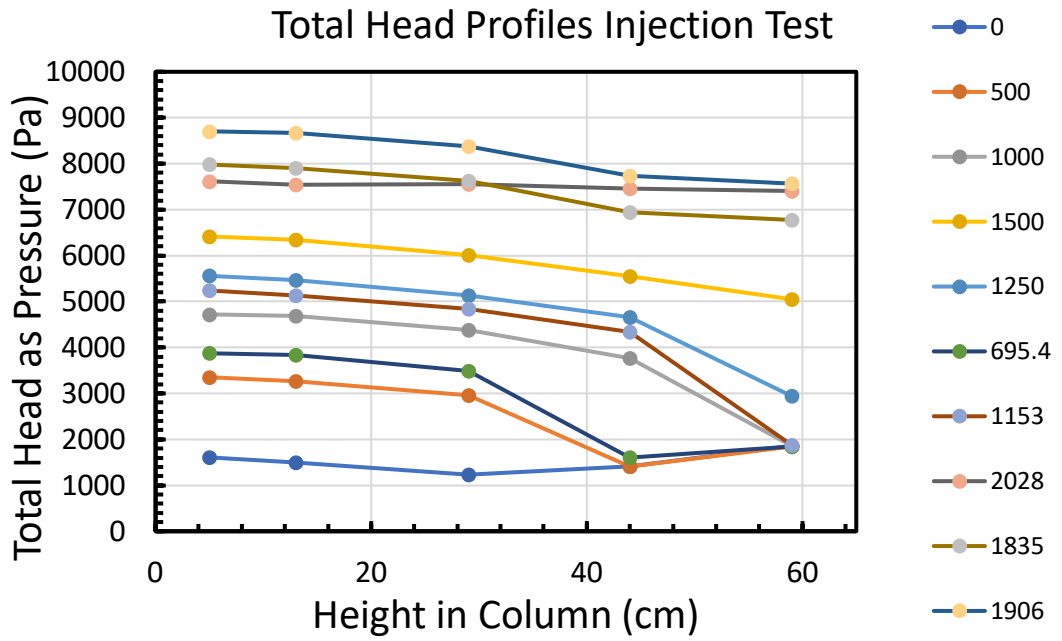

Figure 48: Total head profiles during the injection portion of the 10/16 test.

The partial-fill test described earlier resulted in data that indicates the pore pressure occurs in three zones: 1.) positive pressure, 2.) transition; 3.) ambient. The length of the transition region is estimated using the profiles of the pressure head during injection (Figure 49). The pressure head gradient is roughly uniform and equal unity in the bottom of the column and it varies slightly about unity in the overlying tensiometers before injection starts (Figure 48). A line with a slope of unity is shown in Figure 48 for reference. The point of zero pressure is at approximately 15 cm before the pump is turned on (Figure 49). The pressure head increases at the bottom three tensiometers, but it remains unchanged in the top two transducers when the pump is turned on. The pressure head gradient steepens to at least 2 in the transition zone, and it flattens above this point.

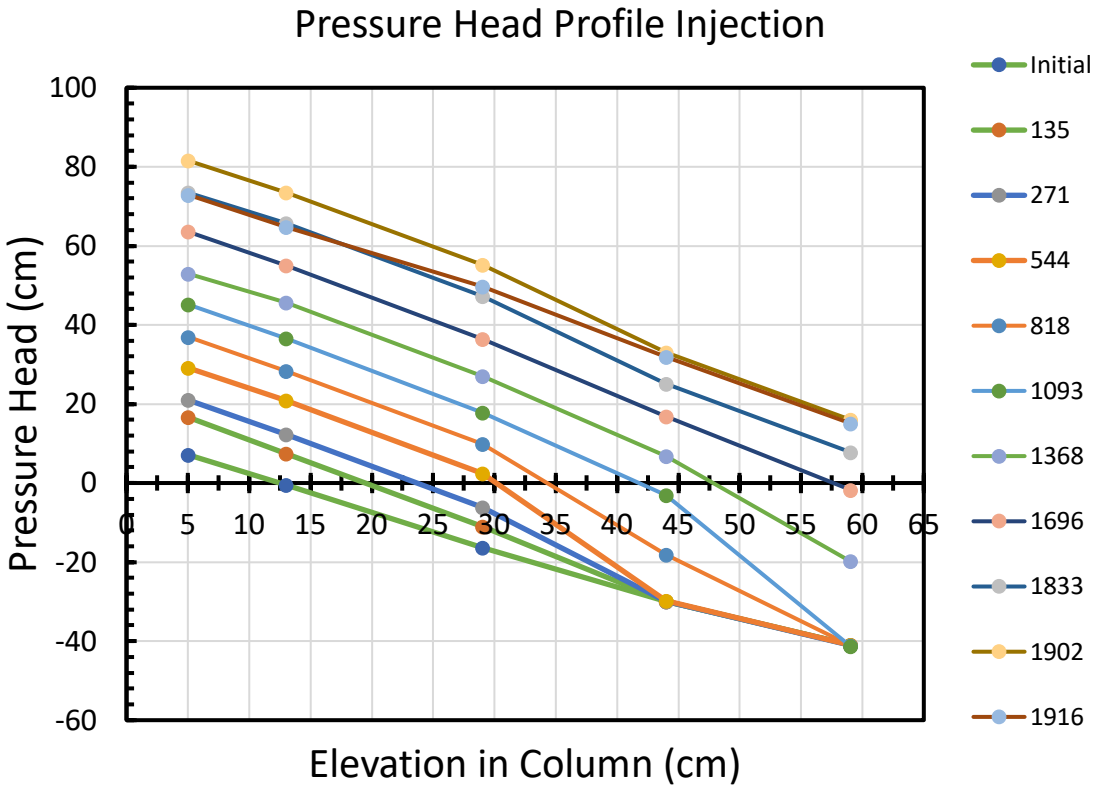

Figure 49: Pressure head profiles for injection test. Legend corresponds to seconds since injection started.

This plot (Figure 49) shows regions where the pressure gradient changes with transducer height in the column. The rectangle drawn shows a region where the pressure gradient breaks from the gradient in the lower 3 transducers. The 44cm transducer records a pressure of slightly above initial equilibrium conditions at this time. It is inferred that the wetting front transition zone is just arriving at this transducer. From this, the transition zone length is estimated to be around 13cm.

Water content profiles are created using the pressure head values along with the moisture retention data (Figure 50). Sand at the p5 and p13 sensor is fully saturated from before the start of the test. The initial water content at p29 is slightly less than the saturated water content (0.28). The sand at p44 and p60 have initial suctions of 0.17 and 0.12 respectively. Suction pressure decreases as the wetting front moves up the column. The saturation increases to the porosity, 0.28. The saturation for a tensiometer can be found at a particular time using this method. Increasing saturation appears to occur at a tensiometer when the PZP is between 8 and 15 cm below that tensiometer.

Combining data from the pressure and saturation profiles during injection, the length of the transition zone is estimated to be 12.5 cm above the PZP.

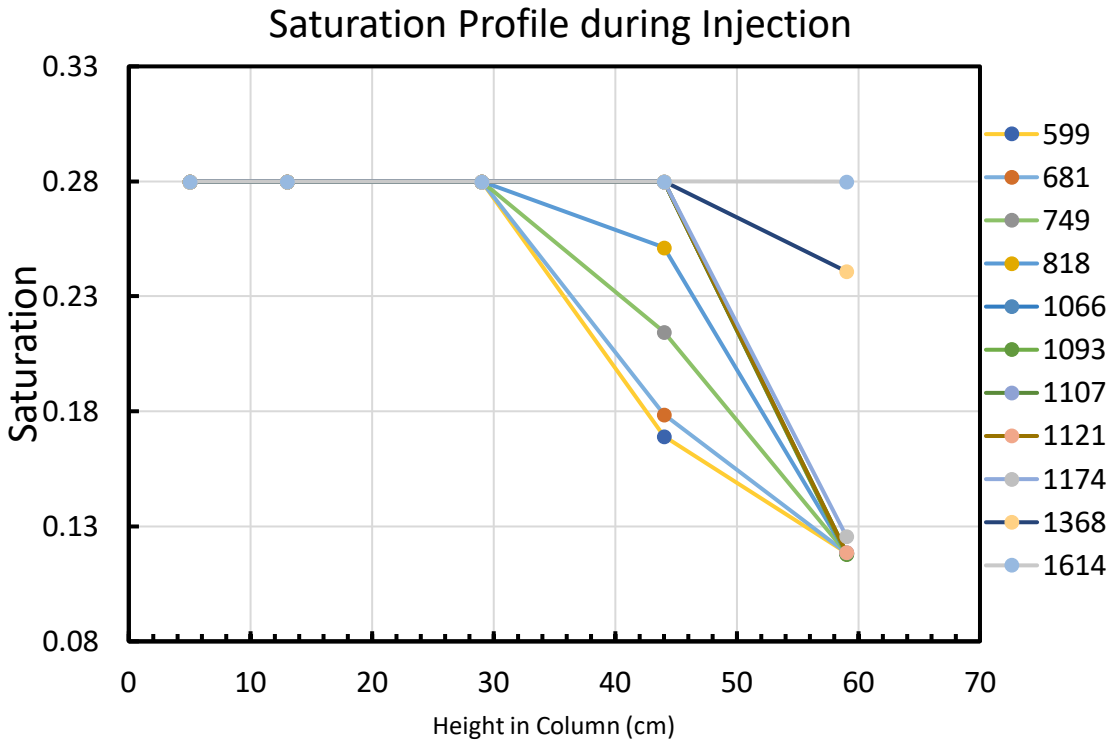

Figure 50: Saturation profiles during injection. a=0.039 cm^{-1} and n=4.3.

14.5.3.1.1.1Drainage by Pumping Out

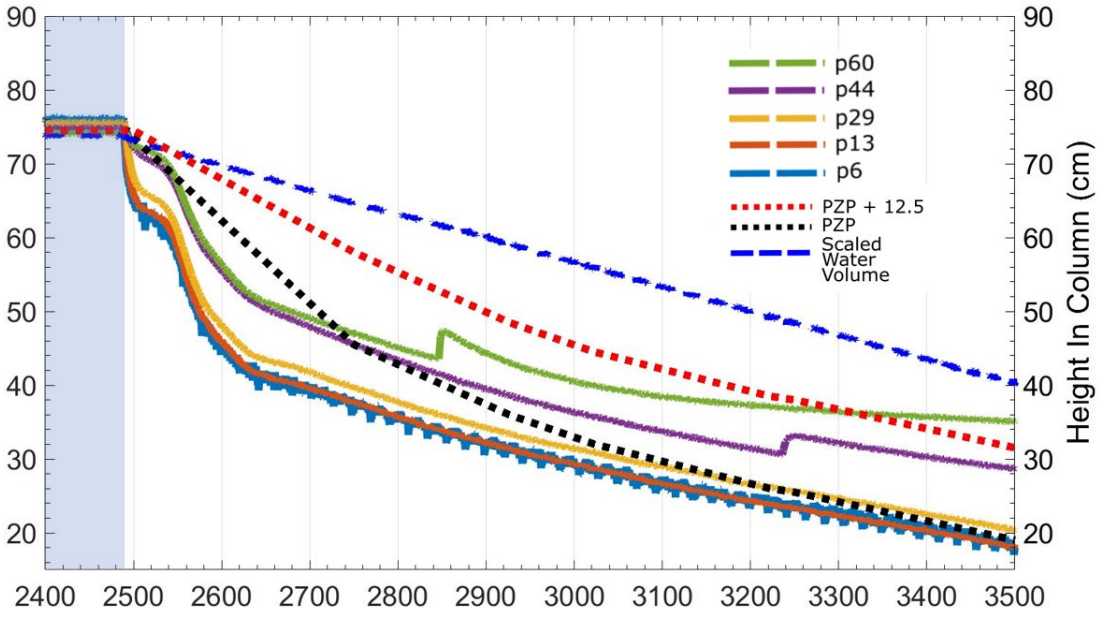

Figure 51: Total head, normalized water volume, point of zero pressure (PZP) and PZP +12.5 cm as functions of time during drainage of the 10-16 complete fill test. The pump was turned on at *t* =2480 s to drain water from the column. Water is ponded on the sand up to *t* =2540 s.

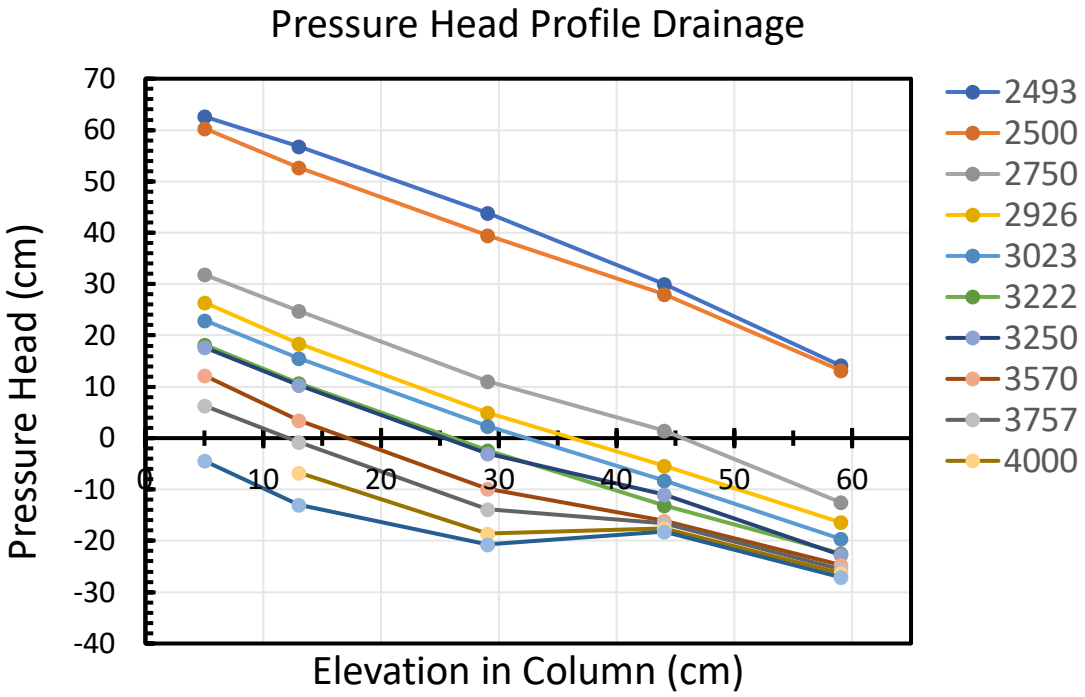

Figure 52: Pressure head profiles for the drainage portion of the injection test.

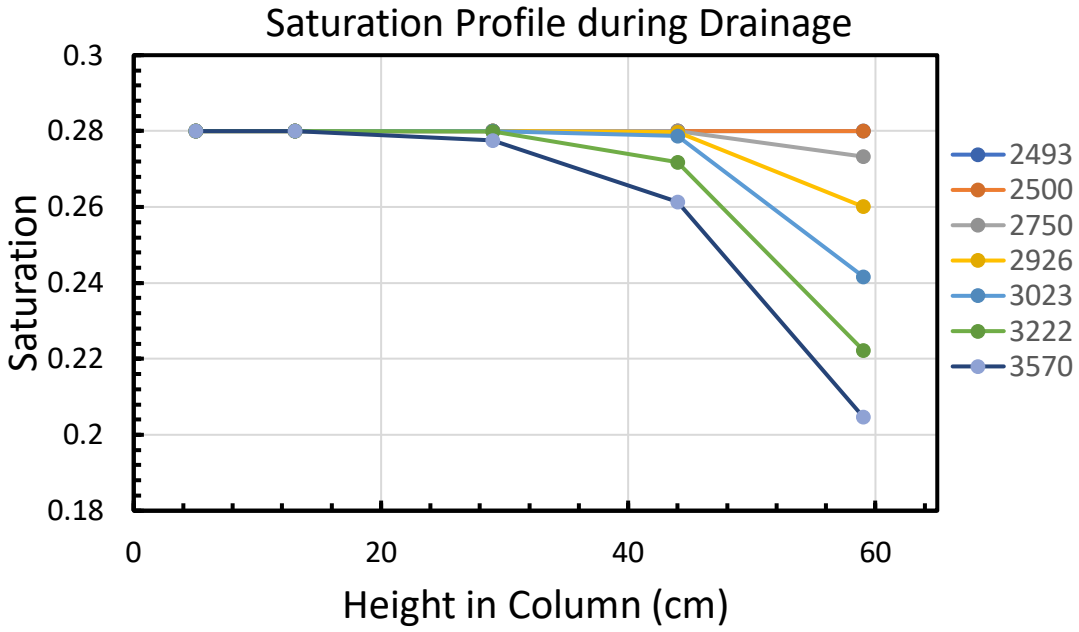

Figure 53: Saturation profile for the drainage portion of the injection test.

Drainage of the column by pumping out causes a sharp initial drop in pressure. The p6 transducer records a drop of 1,000 Pa (Figure 51). The drop slows for a brief period, presumably as the pond drains, and then sharply drops again. The pressure in the lower three transducers

drops at a similar rate. The topmost sensor breaks from the trend first at around t = 2,630 s. After that the sensor second from the top breaks from the trend 930 seconds later. The upper two sensors jump in pressure during drainage events. These events are not completely understood but reliably happen in every test. The gradient of drainage by pumping out is 0.87 (Figure 52).

Pressures in the bottom three transducers rise when the pump is turned off. The rise is sharp at first and then slows. The upper two transducers do not respond to continued cycles of drainage.

Saturation in the column drops in the upper three transducers (p60, p44, p29). At time 3,570 s, p60 drops to a saturation of 0.21, p44 drops to a saturation of 0.26, and p29 drops to a saturation of 0.275. The lower two transducers do not drop appreciably below complete saturation (0.28) (Figure 53).

14.5.3.1.2 Gravity Drainage

Pressure drops more quickly during gravity drainage than during drainage by pumping out. The ponded water drains much more quickly, and the effects of its drainage are absent from the data. The pressure first drops in lower points of the column and the drop propagates upward. The pressure in p6 drops by 3,500pa in 5 seconds after the drain is opened (Figure 54 and Figure 55). This initial drop can be seen in the pressure head profile of the gravity drainage (Figure 56). The total head at the p6 and p13 tensiometers drops by over 20 cm between the t = 3,185 and t = 3,187 second profiles while the total head at the p44 and p60 tensiometers stays nearly constant (Figure 56).

The total head changes little after 4,500 seconds in p6, p13, and p29. The total head at p44 and p60 continues to drop throughout the test (Figure 56).

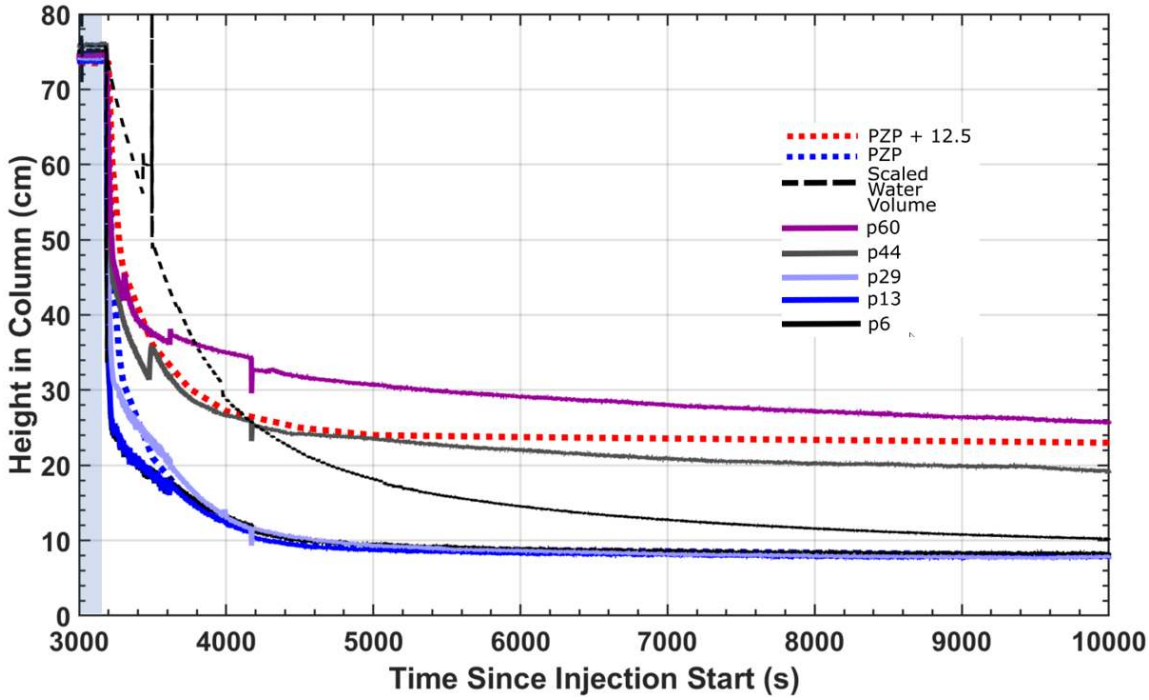

Figure 54: Total head, normalized water volume, point of zero pressure (PZP) and PZP +12.5 cm as functions of time during gravity drainage of the 10/25 complete fill test. The drain was opened at t = 3,185 s.

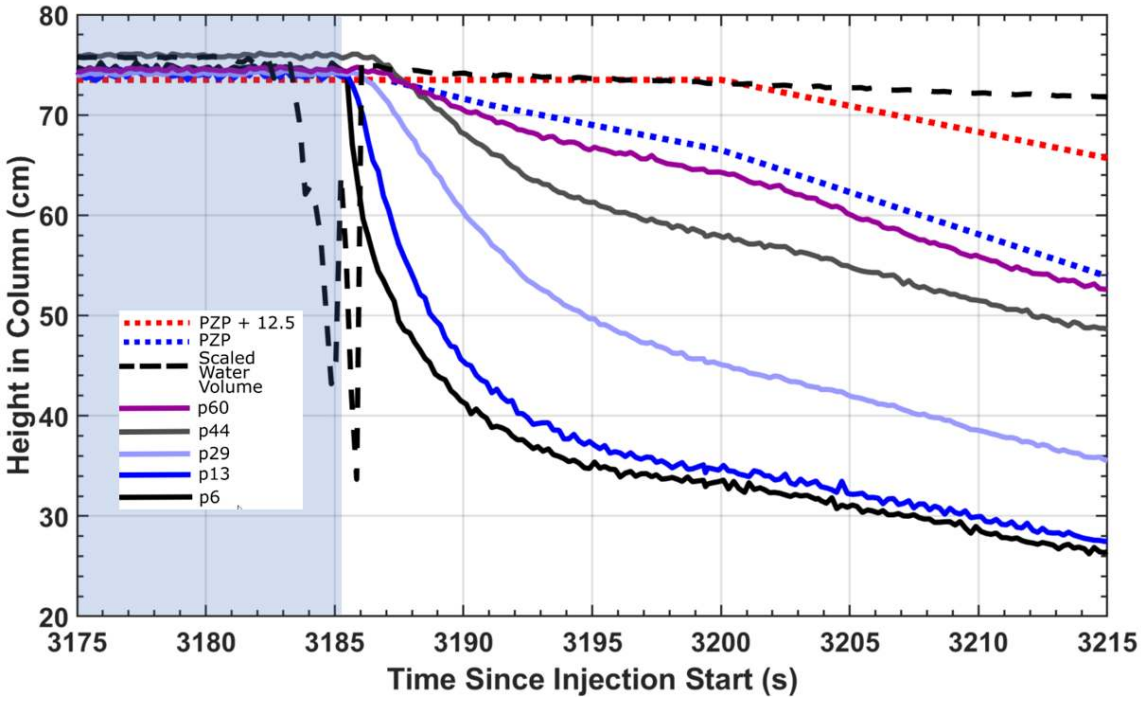

Figure 55: Total head, normalized water volume, point of zero pressure (PZP) and PZP +12.5 cm as functions of time during gravity drainage of the 10/25 complete fill test. Plot shows detail of the drain initially being opened at t = 3,185 s.

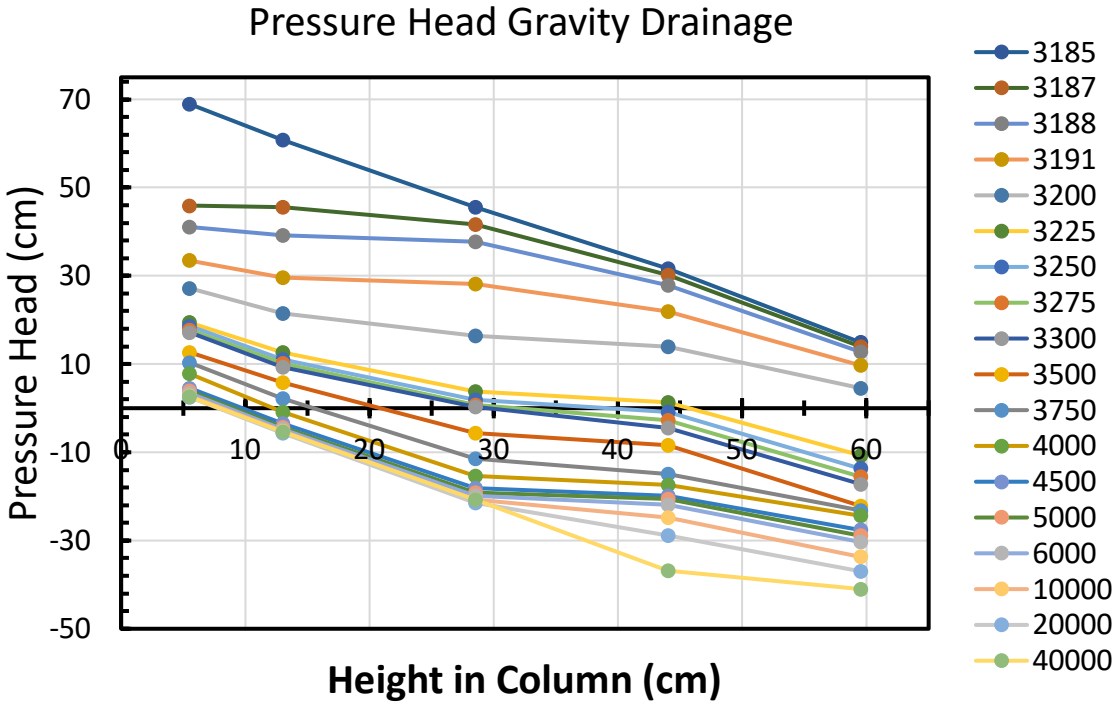

Figure 56: Pressure head during the gravity drainage of the 10/25 fill and drain test.

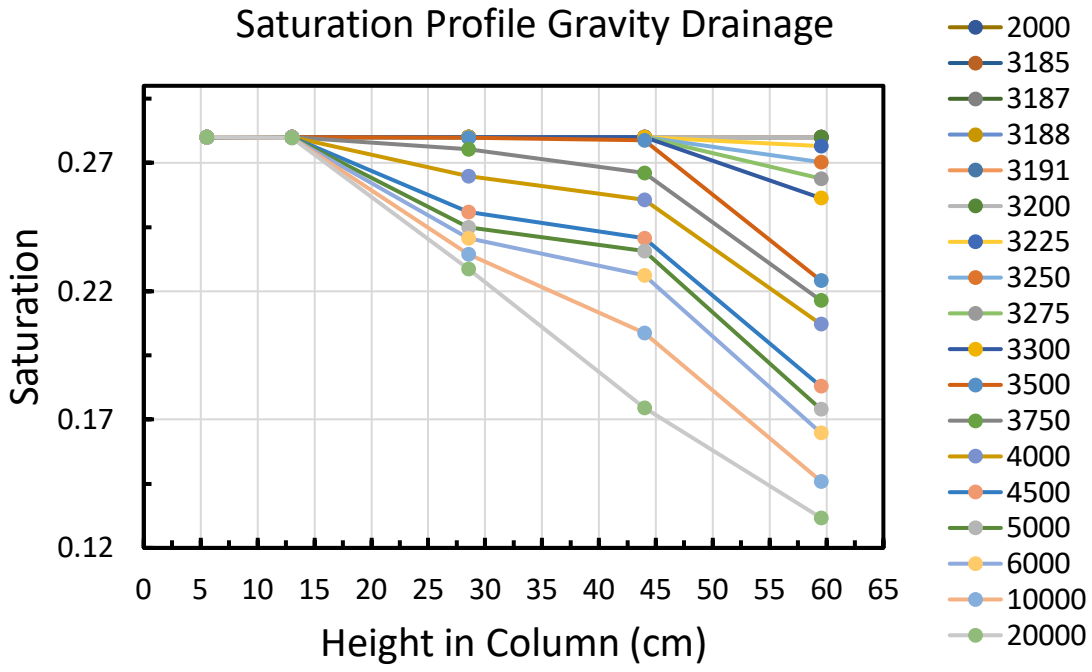

Figure 57: Saturation during the drainage portion of the 10/25 fill and drain test.

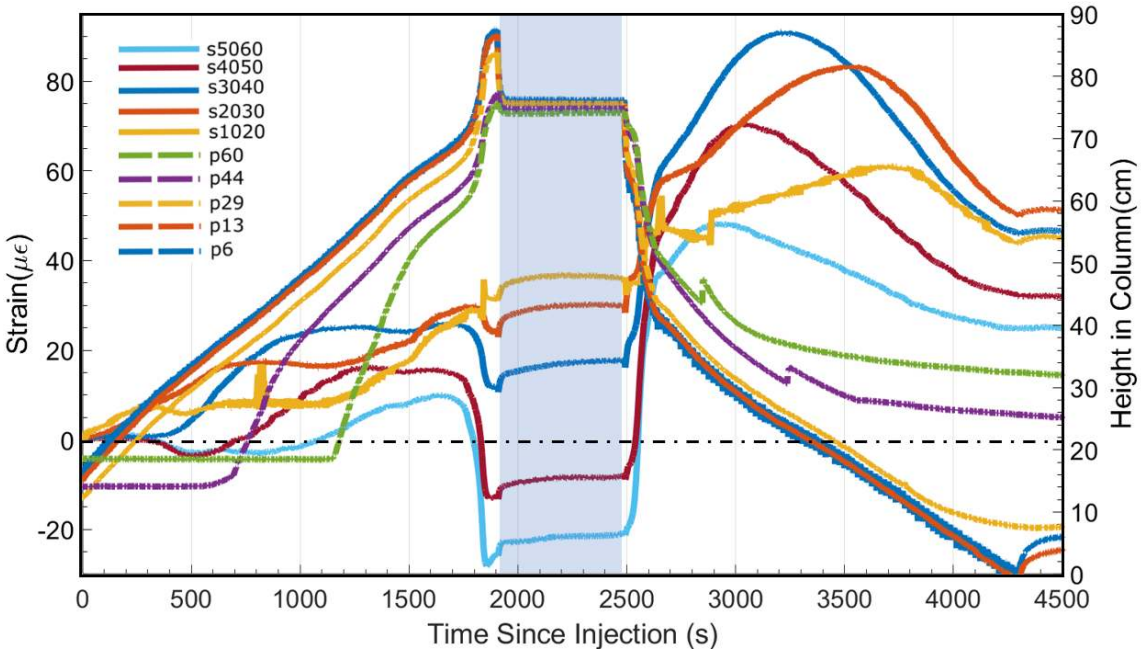

Figure 58: Strain and total head time series for the 10/16 fill and drain test. Blue band is the period of no-flow. Drainage by pumping out starts at t = 2,480 s.

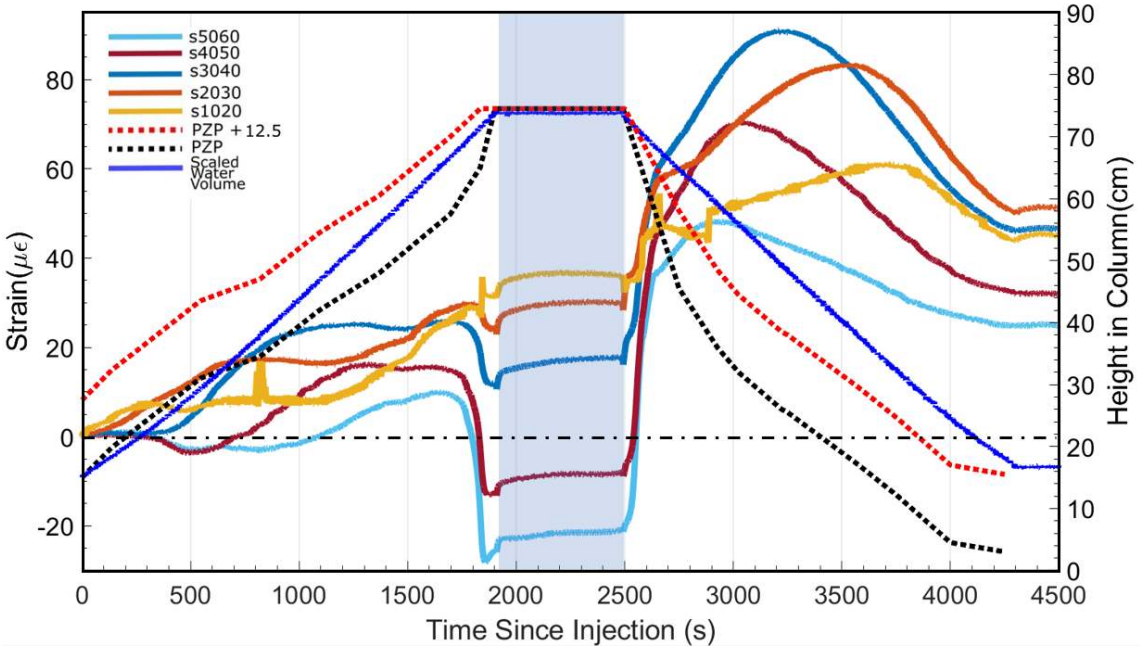

Figure 59: Strain, scaled water volume, and transition zone (PZP to PZP + 12.5 cm) height as functions of time for the 10/16 test. Blue band is the period of no-flow. Drainage by pumping out starts at t = 2,480 s.

Saturation quickly drops in the sand at the p60 transducer (Figure 57). Saturation several hours after injection (t = 20,000 s) is similar to ambient saturation in the sand (Figure 15). The sand is saturated near the p6 and p13 transducers during the entirety of the test (Figure 57).

14.5.3.2 Strain

Strain data was recorded between five pairs of reflectors between 10 and 60 cm above the datum. The PZP initially occurs between 7-15 cm due to residual saturation from previous tests. The top of the pressure transition zone is inferred to occur 20-25 cm above the datum at the start of pumping. The lowest pair of strain sensors, s1020 and s2030, lie within the transition zone at the start of the test. As pumping occurs, the transition zone moves up through the column encompassing all the sensors.

14.5.3.2.1 Strain During Filling

Strain occurs in the column during injection as the transition zone and PZP moves upwards through the column. Tensioning occurs when the transition zone reaches within +/- 5 cm of the bottom of the sensing region. The strain increases linearly during this period at a rate between 0.02 and 0.05 με/s. When the PZP reaches the top of the sensor (within +/-5 cm) strain rate lessens and either goes to zero or into slight compression.

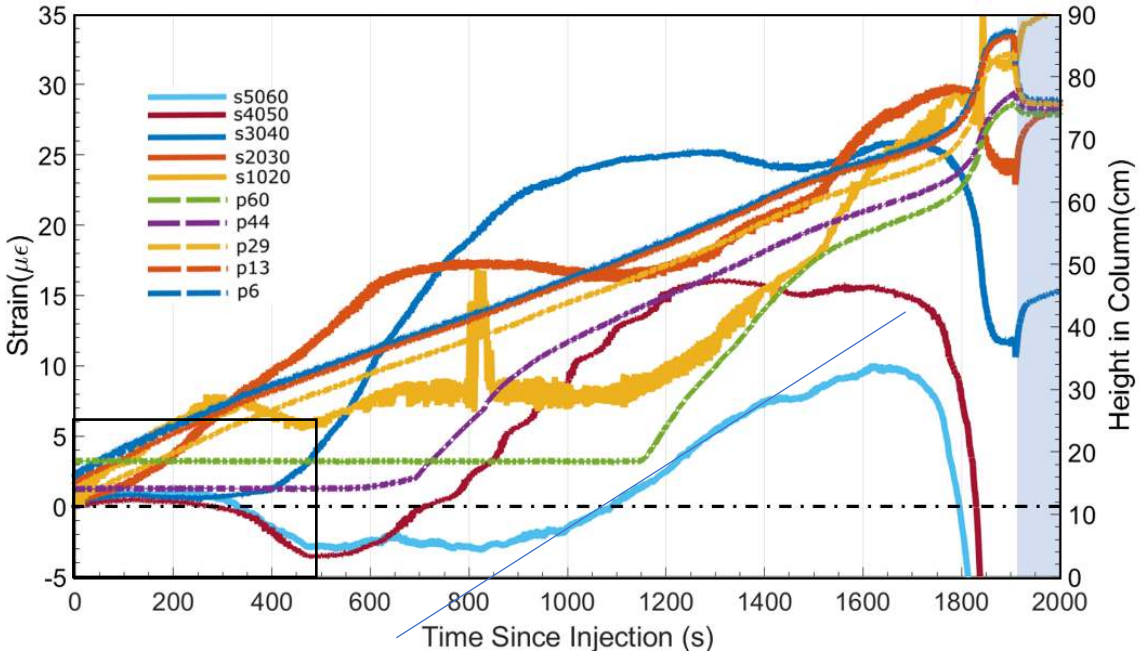

Figure 60: Strain and total head as functions of time for the 10/16 test. Blue band is the period of no-flow.

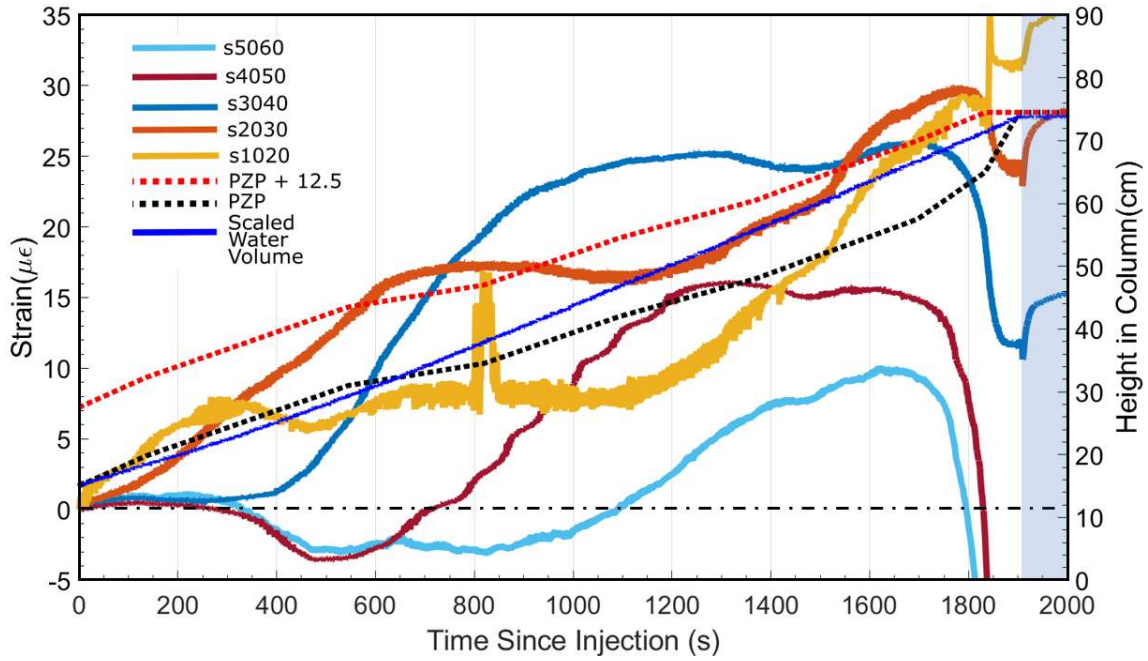

Figure 61: Strain, scaled water volume, and transition zone (PZP to PZP + 12.5 cm) height as functions of time for the injection portion of the 10/16 test. Blue band is the period of no-flow.

Strain early in the 10/16 test is similar to the Partial-Fill (Figure 26). Immediate tensile strain of between 1 and 3 με occurred when the pump was turned on at the lower three sensors with the highest tension in the lowest sensor (though this event is somewhat obscured by the line

thickness). Essentially no strain occurs at the upper two strain sensing regions (s4050 and s5060). The strain at s2030, the second lowest sensor, increased at a rate of approximately 0.025 με/s for 600 s then leveled out and was roughly constant at 17 με over 600 s < *t* < 1200 s. The strain then increased a second time (1200s t < 1800s) at a rate similar to the first period of increase. This pattern of increasing, leveling out, and increasing again also occurred in the lowest sensor, s1020, but the signal is noisier than the one from s2030 and this reduces the confidence in the repeatability of the signal. The strain rate at s3040 was small initially, but then at *t* = 400 s it progressively increased to approximately 0.05 με/s and 600 s later the rate decreased to essentially zero (*t* = 1,000 s,). This resulted in a total of 25 με during test, which is the largest of any of the sensors. The strain started to increase roughly 600 s later (*t* = 1,600 s) but the strain was affected by interactions with the free surface, so it is unclear if the second period increasing strain that occurred at s1020 and s2030 would have also occurred at s3040.

The strain at the other two sensors, s4050 and s5060, was also constant at the start of the test, but it became compressive at roughly the same time the strain in the underlying s3040 became tensile. The strain decreased at a rate of -0.03 με/s, which is approximately half the rate of expansion at the underlying s3040 sensor. for approximately 100 s, resulting on 3 to 4 με of compression. This trend at s4050 reversed at approximately *t* = 600 s when the strain rate started to increase, reaching a rate of 0.035 με/s for a period that lasted 600 s and then flattening back to zero rate (at t = 1,200 s). PZP+12.5 at *t* = 600 s was at *z* = 44 cm, which is approximately at the bottom of the sensing interval, and the PZP at t = 1200 s was at *z* = 48 cm, which is approximate at the top of the sensing interval of s4050. These observations indicate that compression occurs in front of the leading edge of the transition zone, and it supports the findings from the partial fill test that a linear increase in strain occurs when the transition zone is within the sensing interval.

A similar effect occurs in the data from s5060 (Figures 61 and 62). Here the period of initial compression lasts until approximately *t* = 900 s, which is when PZP + 12.5 cm is at z = 50 cm, the bottom of the sensing interval. The strain rate then increases to 0.025 με/s, and the strain becomes affected by interaction with the free surface before this period ends.

14.5.3.2.2 Interactions with the free surface

The pressure and strain progress up the column as relatively uniform fronts, as outlined above, but these signals change sharply as the transition zone interacts with the free surface of the column. Four tests were conducted where the saturation increased upward and reached the free surface and the strain and pressure signals were generally similar. A video camera recorded the appearance of the free surface during wetting and ponding of a test on 10/27, so those data will be used to describe this response. The pressure and strain during all the tests where water ponded at the free surface resemble the results from the 10/27 test.

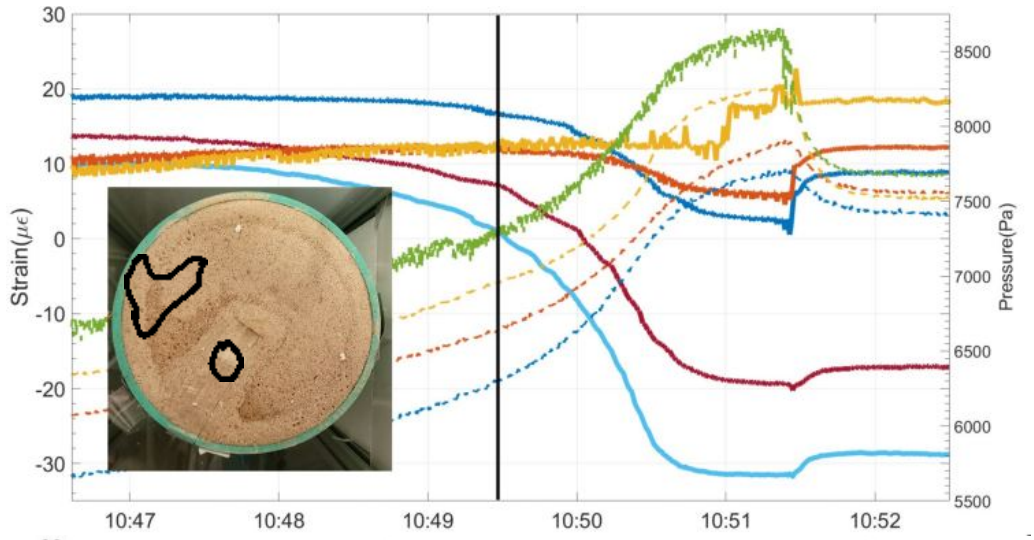

a. Initial appearance of surface wetting (circled)

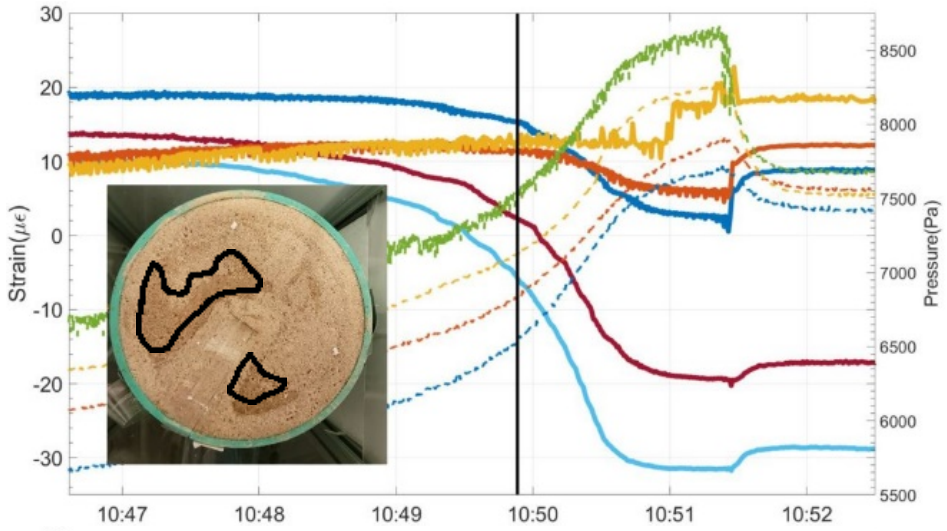

b. Continuation of surface wetting

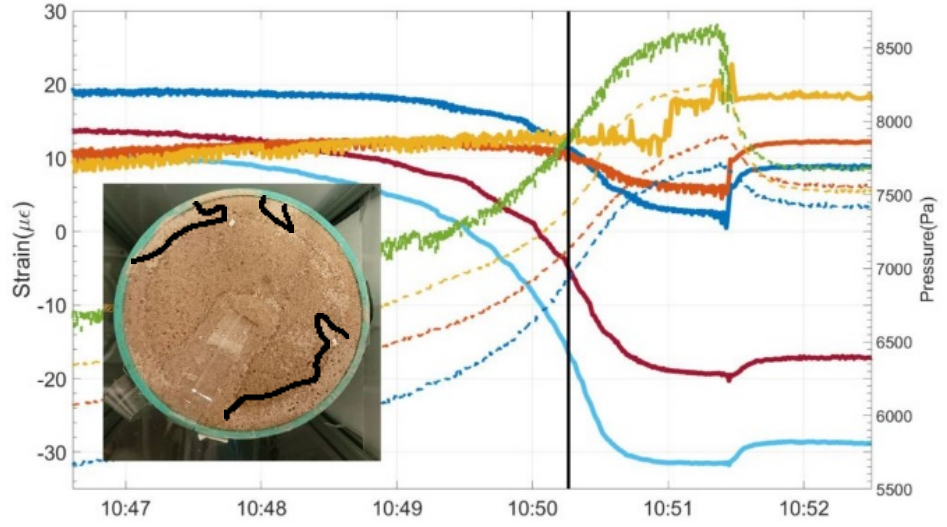

c. Continuation of surface wetting. Dry areas circled.

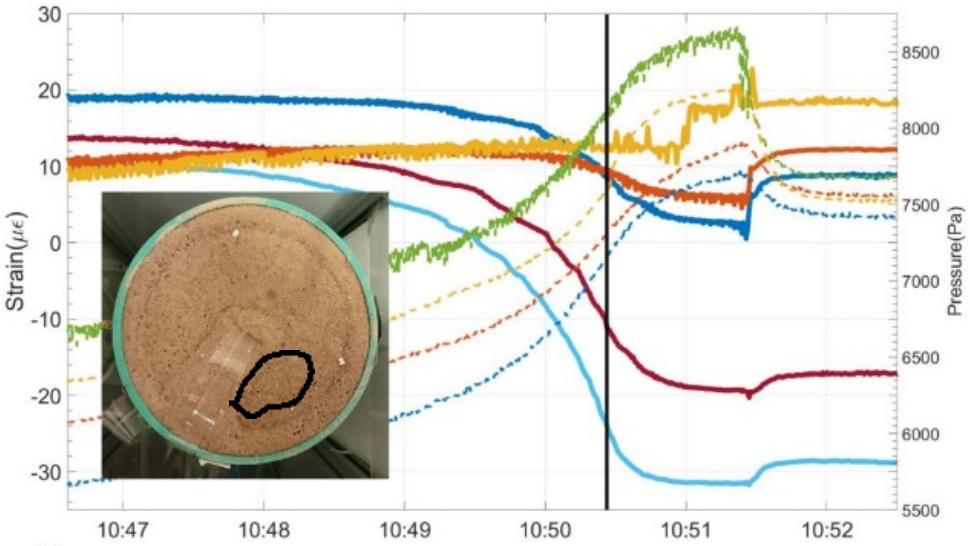

d. Appearance of surface saturation in lower regions of the surface. Saturation circled.

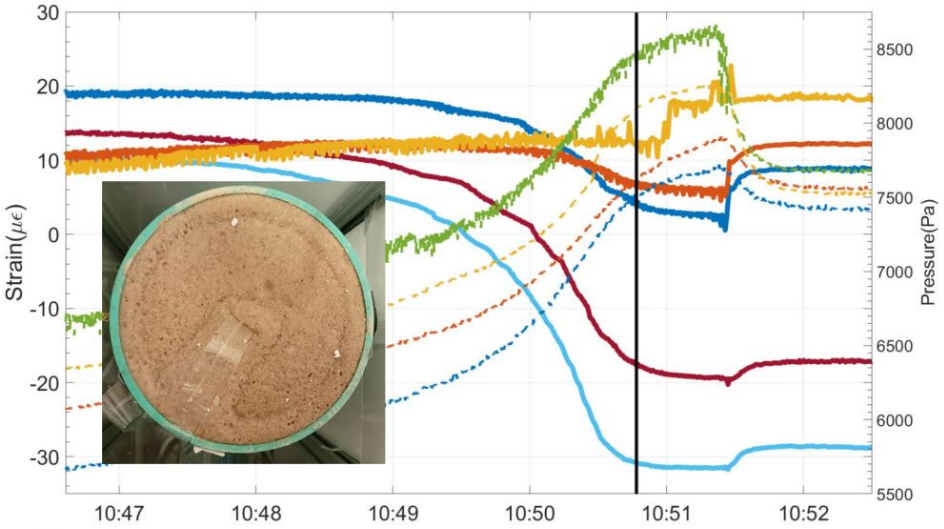

e. Full saturation of the surface.

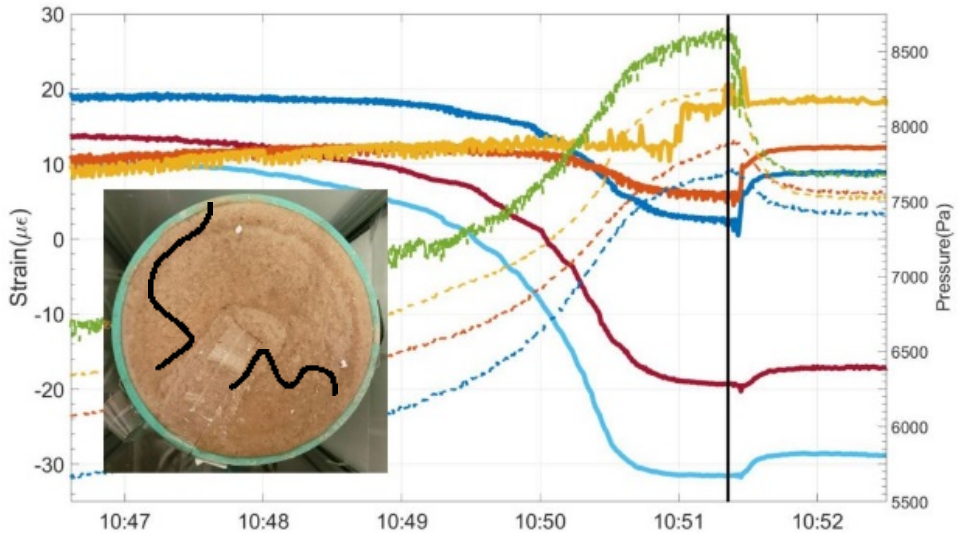

f. Maximum saturation of surface. Areas of deep standing watter are circled.

Figure 62: Photographs taken from above the column during surface interactions along with strain and pressure time series from 10/27 test (pumping starts at *t* = 10:16). Image from time specified with vertical black line.

Compression of the sand in the column occurs as the pressure transition zone approaches the free surface and continues as the surface becomes saturated and covered by ponded water (Figure 62 a.-f.). For example, the strain at s5060 starts to decrease (become more compressive) at approximately t = 10:47 and the rate steepened for the next few minutes resulting in a total of 40 με of compression (-30 με relative to the initial conditions). The strain rate increases steadily for several minutes and reaches a maximum of approximately -45 με/minute (-0.75 με/s) at *t* = 10:50. This is more than an order of magnitude faster than the dilational strain that occurred before the free surface interaction. This fast strain rate abruptly stops at approximately *t* =10:50:30, and the strain is essentially constant during the last 30 seconds of injection at s5060. The strain signal at the underlying sensors is similar to the one at s5060, the strain becomes increasingly compressive and then it abruptly stops before the pump is turned off. The time when this effect starts increases, and the magnitude of the strain change decreases with depth, however. This suggests that interactions with the free surface affect strain throughout the column, and this effect propagates downward from the free surface.

The pressure throughout the column is also affected during this period, and the changes in the strain signal outlined above appear to be related to changes in pressure and saturation. In general, pore pressure increases roughly linearly behind the pressure transition zone, but the slopes increase during interaction with the free surface. This appears to occur at roughly the same time as the decrease in the strain rate in Figure 63, although the increase in the pressurization rate appears to occur 100 s or more later than the decrease in the strain rate in the 10/16 test, as shown in Figures 61 and 62. The pressure increases and reaches maximum positive rates at the same time that the strain rate reaches maximum negative rates (e.g. at 10:50:30 for s5060 and p60, Figure 63d). Both the pressurization and strain rates flatten after this time.

The appearance of the surface of the sand changes as the water content increases and free water appears (images in Figure 63). The change is apparent at t = 10:49:30 when two arcuate bands become darker than the rest of the sand. The darker bands are slight depressions in the surface of the sand, and the color change occurred because the water content increased in those regions (Figure 63a). The darkened region expanded with time, following the lowest lying topography in the surface, and by 10:50:15 it covered much of the interior of the column (Figure 63c). Free water appeared first as glistening droplets at the bottom of the arcuate bands at approximately 10:50:30, and then it progressively filled the shallow depressions in the surface (Figures 63 d-f). Free water covered the entire surface of the sand when the pump was turned off at *t* =10:51:25.

Images of the surface of the sand offer an explanation for the pressure and strain data. The data suggests that the pressure rate increased when the transition zone reached the sand surface. This caused the water content to increase and the surface to darken. Flow of water out of the sand was initially inhibited, however, and this caused the pore pressure to increase. A similar effect occurs where infiltrating water is initially excluded from entering a cavity (Philip & Knight, 1989). The maximum rate of pressure increase occurred just as the first signs of free

water appeared at the surface of the sand. The rate of pressurization then quickly diminished to small values as the free ponded water spread across the surface of the sand.

The capillary exclusion effect appears to explain the changes in the pressurization rate, and the pressurization rate is related to the strain rate. Strain and pressurization rates are related during filling of the column, but the effect that occurs during interaction with the free surface is different from the earlier occurrences. Perhaps the most striking difference is that strain is positively correlated with pressure during most of the test, but they are negatively correlated during the period characterized by interaction with the free surface—that is, an increase in pressure in the interior of the column is associated with an increase in strain (dilation), but an increase in pressure at the free surface is increasing is associated with compression. Moreover, the strain rate that occurs during the free surface interaction is much faster than when the pressure is changing within the column.

Turning off the pump causes the pressures to decrease as the 0.2 head gradient caused by the upward flow of water collapses. This means that the pressure drop is greatest in the bottom of the column and diminishes upward. The pressures measured by the sensors return to within 250 Pa of each other, which corresponds to essentially uniform head in the column (cite figure). Turning off the pump is accompanied by sharp tensioning in lower parts and a more gradual effect in the upper regions of the column. Presumably, these strains are a result of the pressure changes associated with stopping flow. Interestingly, the pressure and strain are negatively correlated during this period, just as they were during the interaction with the free surface. After this, strain and pressure stabilize until the drainage of the column is initiated.

14.5.3.2.3 Pump Off

The strain changes little when the pump is turned off.

14.5.3.2.4 Pumping Out Drainage

When the pump is turned on in reverse to drain the column, sharp initial tensioning occurs. A more gradual tensioning rate occurs after this that lessens and eventually turns negative (compresses). s5060 reaches a tension maximum first and then begins compressing. This effect moves downwards to the lower sensors with progressively lower tensioning and peaks later in time (Figure 63 and Figure 64).

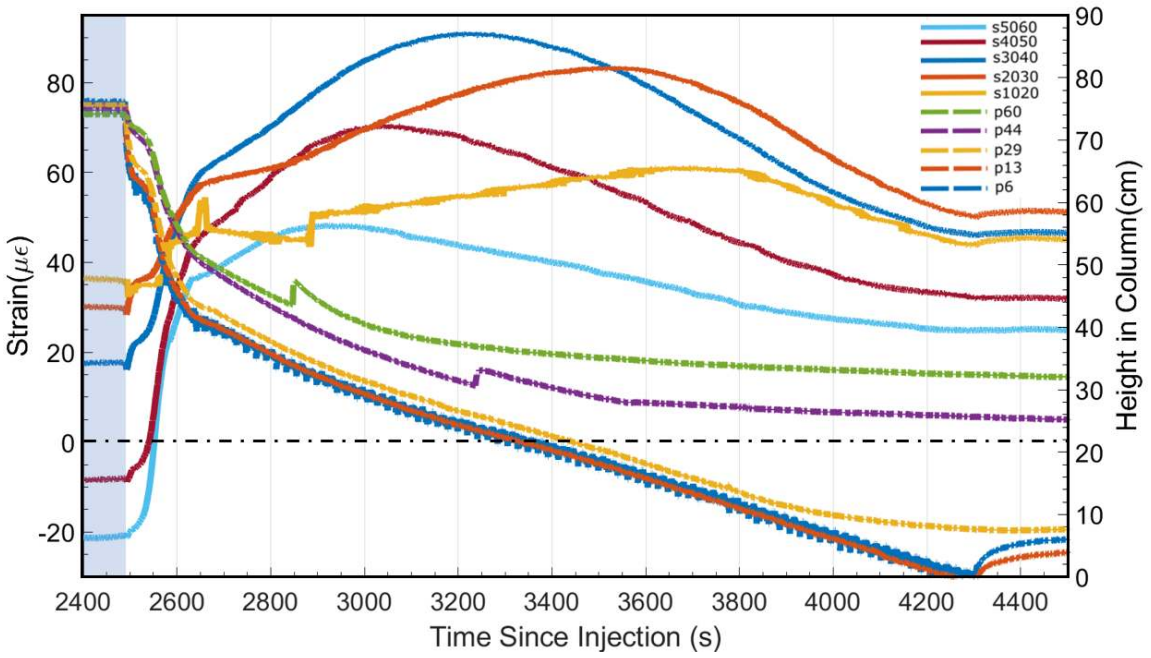

Figure 63: Strain and total head during the drainage portion of the 10/16 test. Blue band is the period of no-flow. Drainage by pumping out starts at t = 2,480 s.

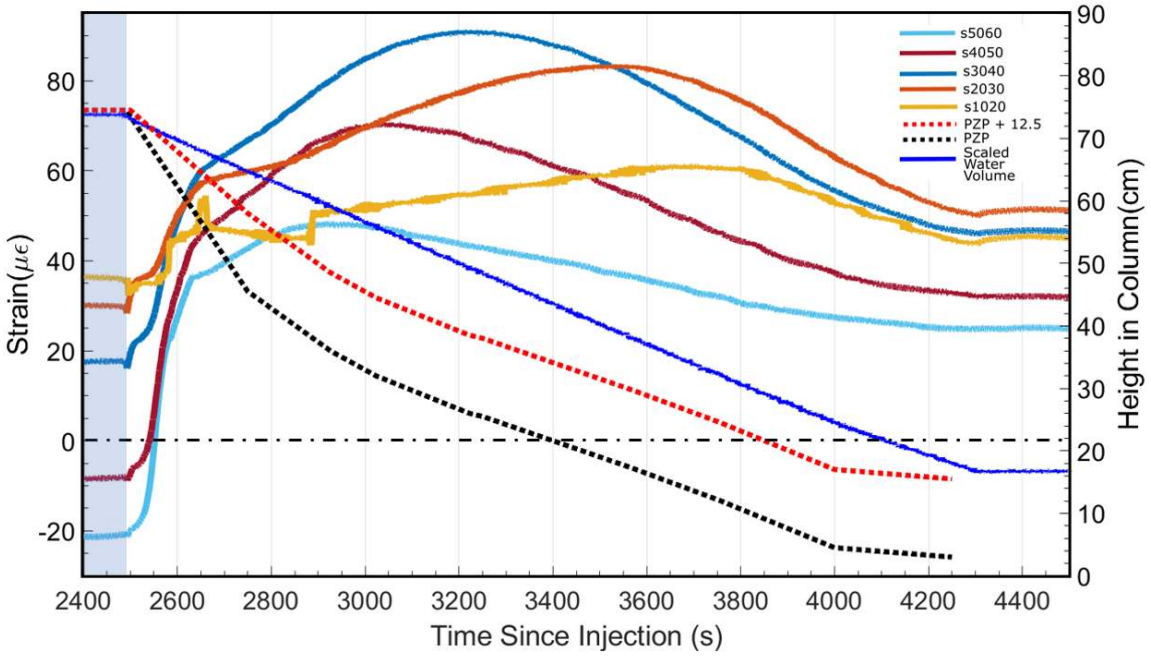

Figure 64: Strain, scaled water volume, and transition zone (PZP to PZP + 12.5 cm) height as functions of time for the drainage portion of the 10/16 test. Blue band is the period of no-flow. Drainage by pumping out starts at t = 2,480 s.

14.5.3.2.5 Gravity Drainage

The start of gravity drainage coincides with rapid tensioning. this tensioning rate lessens, reaches a maxima of as much as 65 με and then decreases. s5060 reaches a maximum (50 με) first and s1020 reaches a maximum (15 με) last with the sensors in between reaching the maximum in order of height above the datum. The largest strains occur at s3040 and s4050 and reach 65 με. The maxima reached from gravity drainage are less than the maxima reached during drainage by pumping in reverse. For example, the maximum strains that occurs at s3040 and s4050 during pumping in reverse are between 80 and 85 με, approximately 15 to 20 με greater than during gravity drainage. After the maximum is reached, compression occurs more gradually than tensioning (Figure 65 and Figure 66).

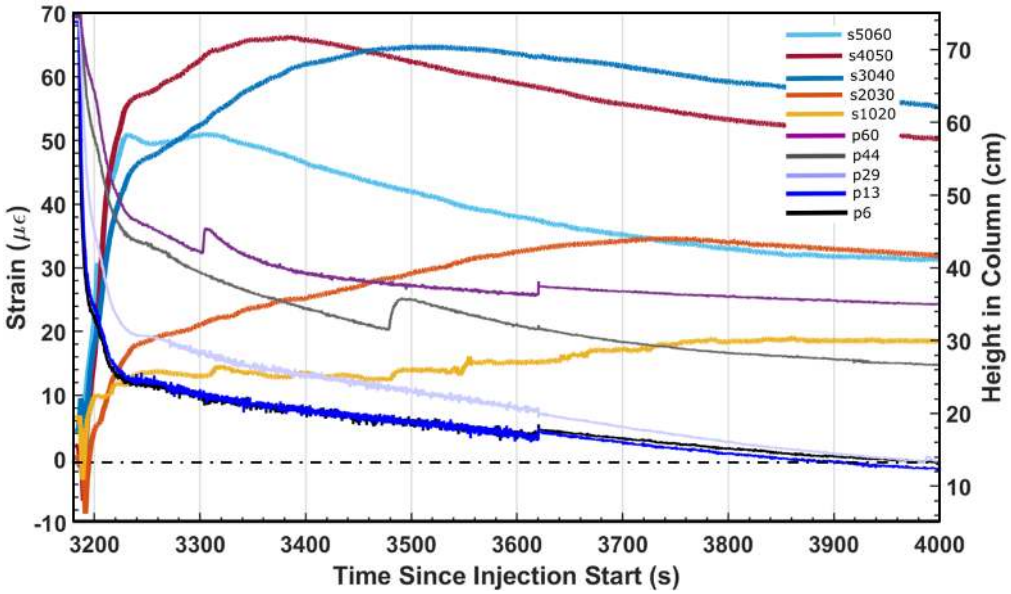

Figure 65: Strain and total head time-series for the drainage portion of the 10/25 gravity drainage test.

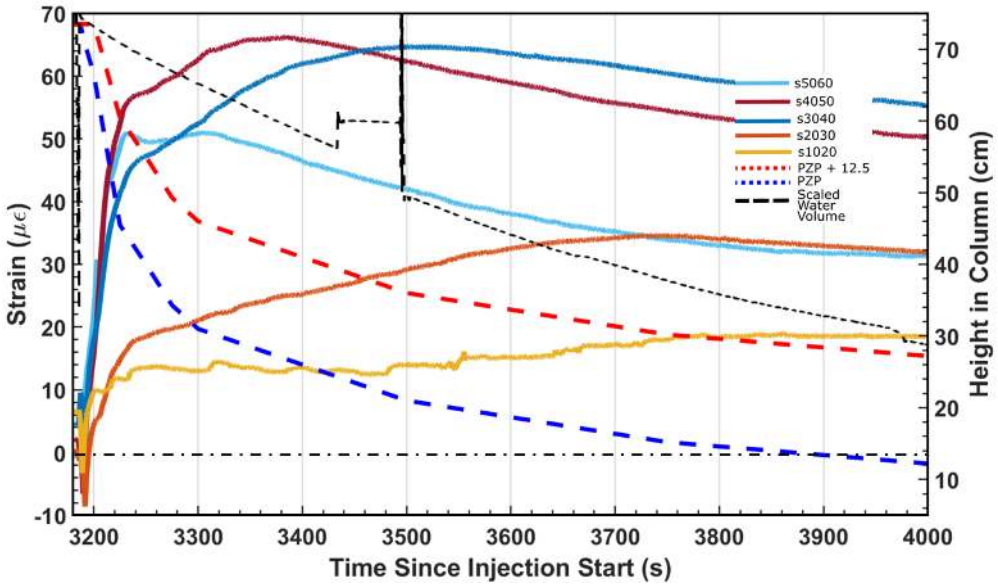

Figure 66: Strain, scaled water volume, and transition zone (PZP to PZP + 12.5 cm) height as functions of time for the gravity drainage portion of the 10/25 test. Blue band is the period of no-flow.

14.5.4 Patterns and Repeatability

Repeatable patterns in the time-series emerge from the data. These changes in strain seem to be due to changes in pressure and the movement of the transition zone. The general pattern for the column is tensioning when the PZP/wetting front enters the reflection zone. When the PZP moves above the reflector zone, the tensioning rate slows and then generally stops. Slight compression or tension can occur as the PZP moves higher. At a certain point, tensioning occurs again most likely due to the increase in pressure.

To better envision the patterns found from the data, the injection tests were conglomerated with normalized start times with zero being the start of injection. Differences occur during the tests supposedly due to differences in the starting conditions of the column. Because these tests were conducted on the same column separated by days, the column has a starting PZP and saturation curve above it. This results in the PZP reaching the surface of the column at different times. These times differ by up to 600 seconds.

Five tests were compiled for the series. The before mentioned Partial-Fill test and 10/16 test, as well as three gravity drainage tests. The 10/23 test was the first gravity drainage test conducted. Drainage had to be stopped a few seconds after the drain was opened dur to an improper placement of the outflow tubing resulting in a higher outflow head than planned. This issue was resolved, and the drainage continued as planned. The 10/25 test filled up quicker than the other injection tests, due to a higher starting saturation and PZP and appears numerically apart from the rest of the tests during injection. The column was then drained by gravity. The overall patter of the 10/25 test is consistent with the other tests shown. The 10/27 gravity drainage test had no issues or inconsistent data.

The software Inkscape is used here to create graphs of the standard responses to injection and drainage. The thick black line represents the 10/16 injection/pumping out test earlier

described. Grey shading represents the variability found during injection and ponding stages of the different tests. The blue dashed line is the typical gravity drainage response, formed graphically by comparing the 3 gravity drainage tests. The red dashed line represents the partial injection test described earlier extrapolated out in time to better compare with the other tests.

Different stages appear in the patterns of strain data related to the position of the transition zone and PZP. These regions are labeled and shaded for easier viewing. The stages shown correspond to the 10/16 test.

Stages 1-4 and Stage w represent stages during injection. Stage 1 represents the injection stage where little response occurs. The transition zone is below the sensor during this stage. Stage 2: Tensioning begins, the transition zone reaches the bottom reflector, and the stage continues until the PZP is above the top reflector. Stage 3: The PZP is above the top reflector and tensioning slows, stops, or even reverses into compression. Stage 4: The PZP is far above the sensor. Stage w: The transition zone reaches the surface of the column and continues until the PZP reaches the surface resulting in ponding. This results in large compression throughout the column.

Stages a-d represent stages during drainage. Stage a: Pumping out starts and the column tensions. This stage continues until the pond is fully drained from the surface. Stage b: This stage starts with the drainage of the surface resulting in the PZP being below the surface and a transition zone. This continues until PZP reaches the top reflector. Stage c: The PZP reaches the top reflector and continues until the transition zone passes the bottom reflector. Stage d: The transition zone is beyond the bottom reflector and continues until the pump is shut off.

14.5.4.1 s1020

The s1020 sensor starts tensioning at the start of injection (Figure 67). This tensioning slows and sometimes stops. It later resumes again and continues until surface wetting (Figure 68).

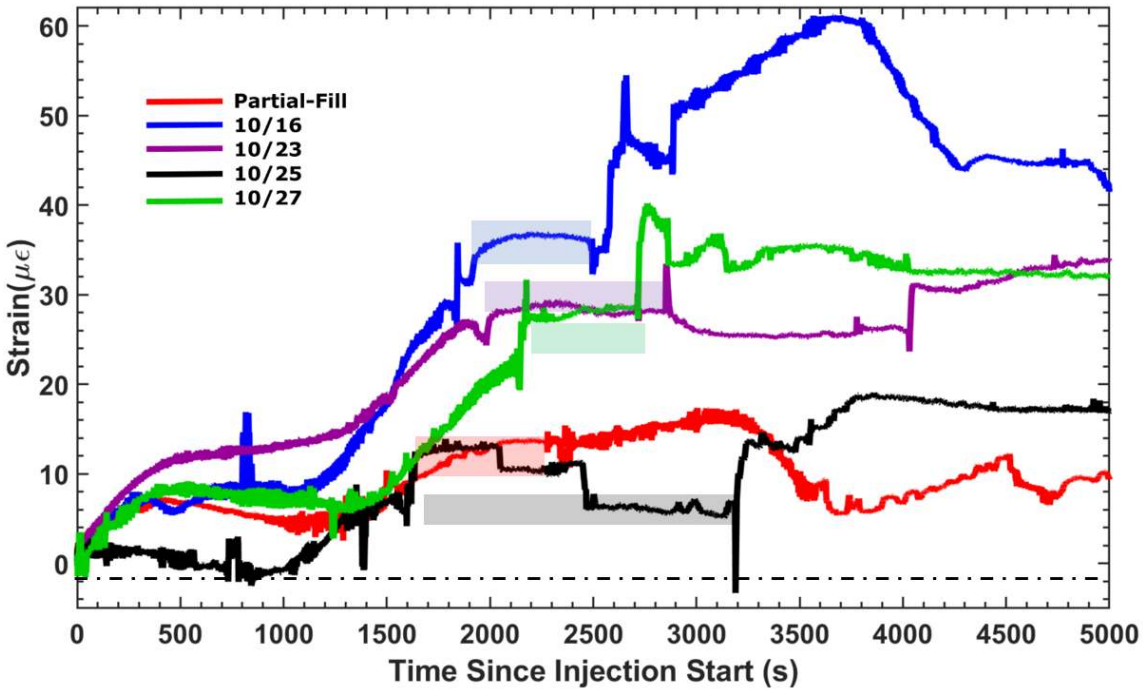

Figure 67: Strain time-series at s1020 sensor for five injection tests conducted on different dates with normalized start times. The No-Flow interval is represented by the transparent bands of the same color.

Stage 1 is absent in this data set. The strain at s1020 is rapidly tensioned by approximately 2 με at the start of pumping (best seen n Figure 36 and somewhat in Figure 60). The reflector and p6 tensiometer is below the PZP at the start of the experiment. After turning on the pump, tensioning occurs linearly at a rate of approximately 0.025 με/s during Stage 2. Strain stabilizes after this period beginning Stage 3. Slight compression or tensioning can occur. Tensioning occurs during Stage 4 after Stage 3 at a rate of slightly higher than the first tensioning period (0.03 με/s). All injection tests have the pattern of early tensioning, a period of little change, and a later period of tensioning (Figure 67). The strain at s1020 decreases by approximately 2 με when the pressure transition zone reaches the surface of the sand during Stage w, a response that is much less than the compression that occurs at the overlying strain sensors. The strain then stabilizes and is constant at a 30 +/- 5 με during the period of No-Flow (Figure 67).

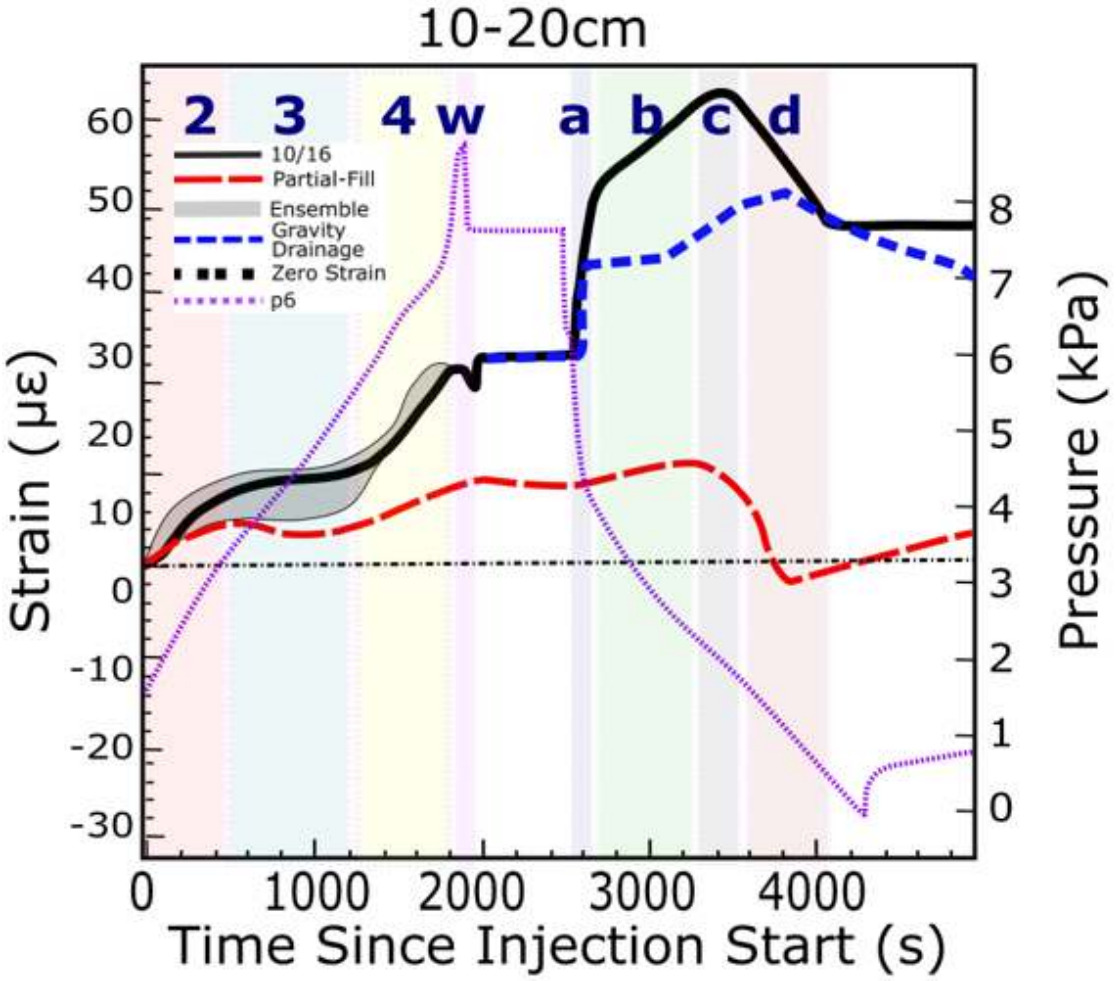

Figure 68: Ensemble strain and total head as pressure time-series for s1020 and p6. The white band is the no-flow interval.

Upon drainage the region undergoes tension during Stage a. Drainage causes interactions between the PZP and the surface of the sand, similar to the interactions during injection and the surface wetting. Sharp tensioning occurs during this initial drainage period. Two different types of tensioning occur after this. The pumping out case shows a gradual tensioning at a rate of 0.017 με/s. The tensioning during pump out peaks at around 900 seconds after the start of pumping in reverse. After this peak, compression occurs at a rate of 0.028 με/s. This continues until the pump is turned off.

The gravity drainage case shows a slight sharp initial tensioning followed by a gradual tensioning that eventually peaks and turns to compression.

14.5.4.2 s2030

The s2030 sensor begins tensioning at the start of injection (Figure 69). It later slows and sometimes compresses. Tensioning then resumes until surface wetting (Figure 70).

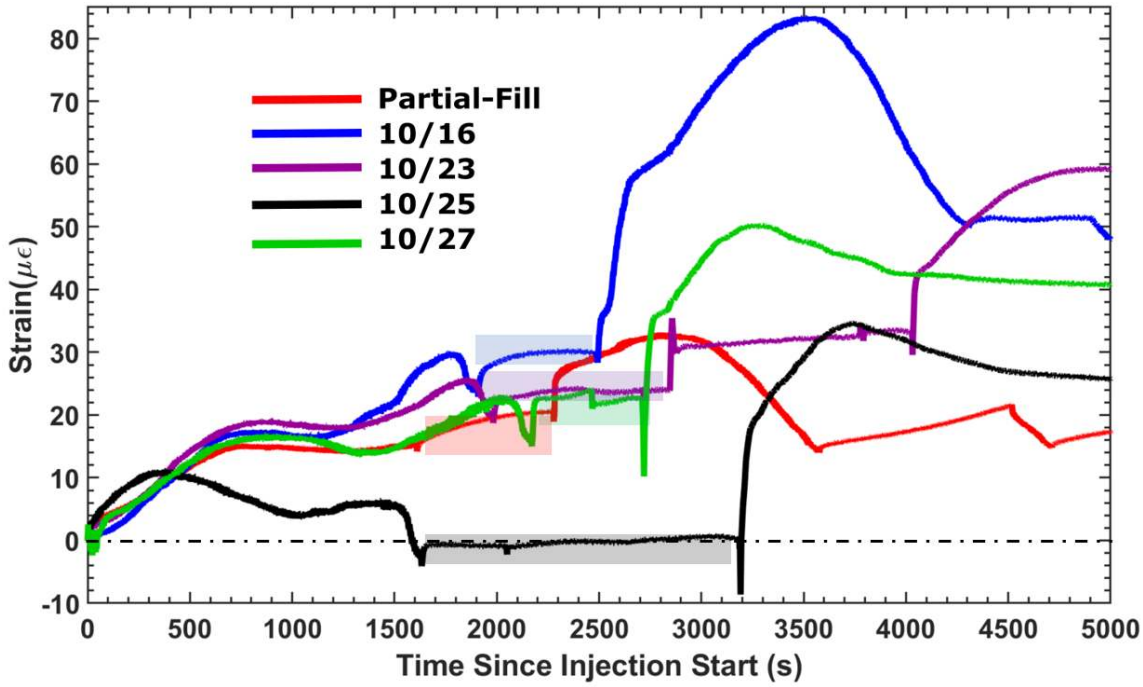

Figure 69: Strain time-series at s2030 sensor for five injection tests conducted on different dates with normalized start times. The No-Flow interval is represented by the transparent bands of the same color.

This sensor responds similarly to the bottom strain sensor. An initial tensioning occurs of approximately 1 με when injection starts (Figure 70). Linear tensioning occurs at around 50 seconds after the start of injection at a rate of 0.025 με/s during Stage 2. The tensioning rate begins slowing and rounding off to a period of stability (Stage 3). During this stage slight compression can occur. At around 1,300 seconds, Stage 4 begins, and a second period of tension occurs. This has a similar rate of tensioning as before 0.025 με/s.

This region compresses slightly by 6 με when the transition zone reaches the surface of the sand at the top of the column, more than the sensor below it (Stage w). When drainage starts, sharp tensioning occurs (Stage a). The pumping out case shows a tensioning rate of 0.044 με/s

during Stage b. This peaks at 35 με at t = 1,050 s during Stage c. This is higher than the lower sensor. The strain compresses at a rate of 0.050 με/s during Stage d and continues until the pump is turned off (Figure 70).

The gravity drainage case shows sharper strain rate change initially that then linearly tensions at a rate of 0.050 με/s. This peaks at 38 με 530 seconds after drainage starts and then compresses gradually as water is drained from the column (Figure 70).

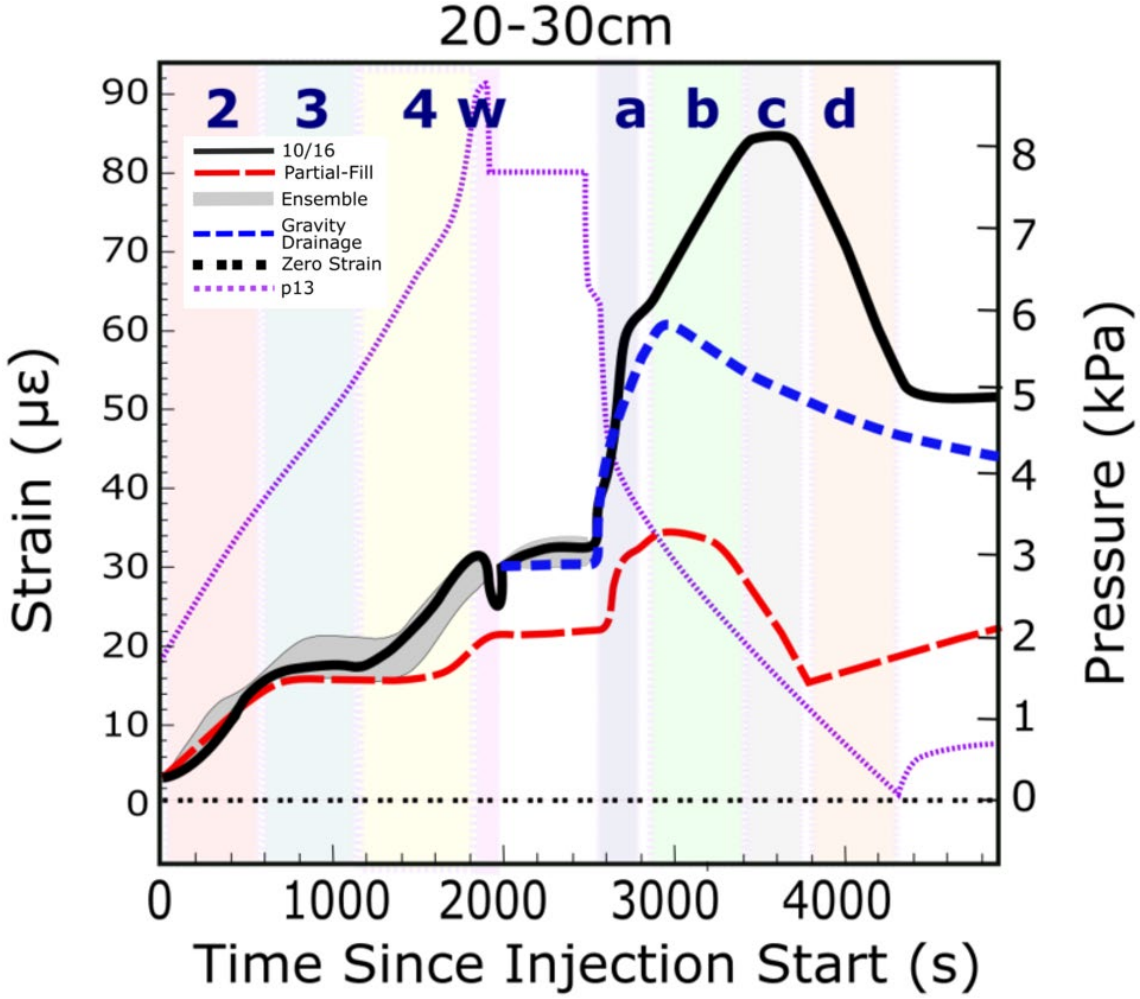

Figure 70: Ensemble strain and total head as pressure time-series for s2030 and p13. The white band is the no-flow interval.

14.5.4.3 s3040

The s3040 sensor usually does not begin increasing at the immediate start of injection (Figure 71). Tensioning starts later and reaches a maximum. After this it stabilizes and can compress. Tensioning can resume after this period and continue till surface wetting (Figure 72).

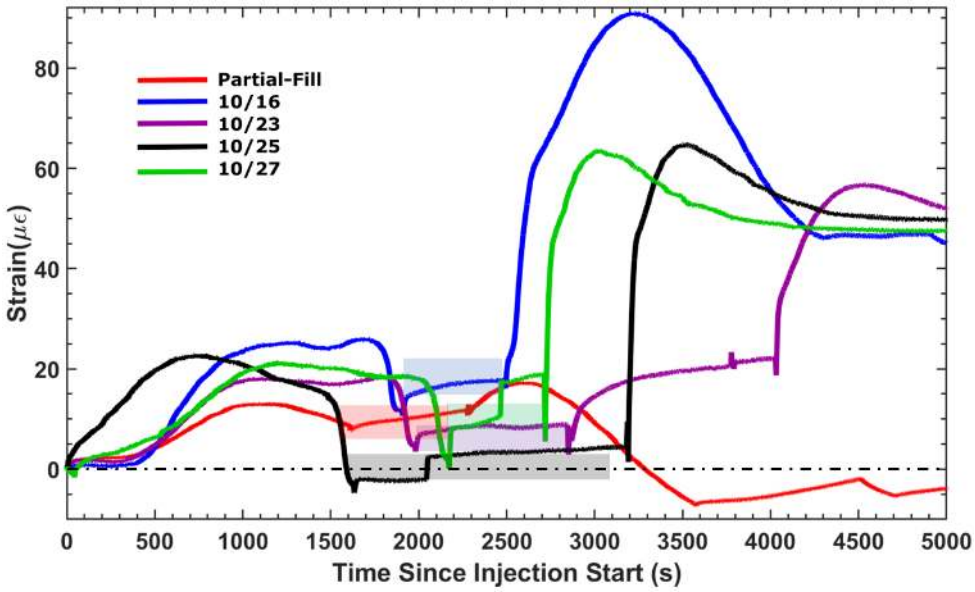

Figure 71: Strain time-series at s3040 sensor for five injection tests conducted on different dates with normalized start times. The No-Flow interval is represented by the transparent bands of the same color.

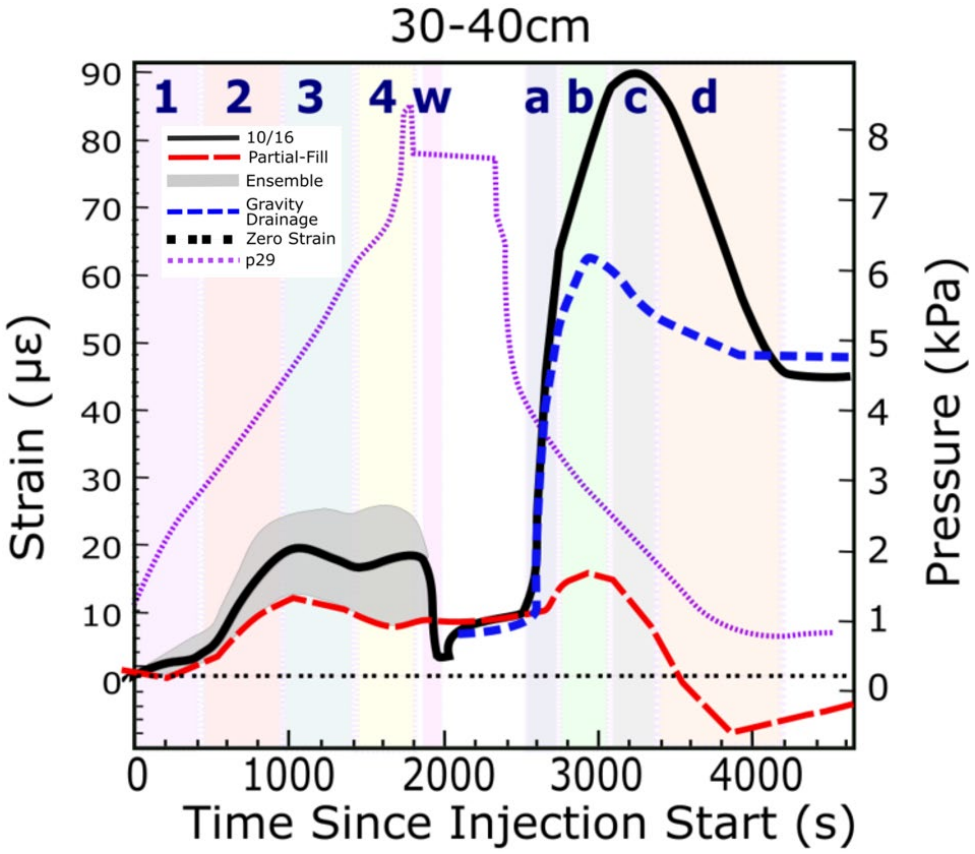

Figure 72: Ensemble strain and total head as pressure time-series for s3040 and p29. The white band is the no-flow interval.

Often initial tension occurs when the pump is first turned on, approximately 0.5 με, followed by a period of stability (Figure 72). Stage 1 is first present in this sensor. The strain goes into linear tension at around t = 400 to 900 s during Stage 2. The rate of tensioning is approximately 0.037 με/s. This corresponds to the transition zone reaching the area between the reflectors and ends with complete saturation in the length between the reflectors. After this stage, the tensioning rate flattens and can slightly compress (Stage 3). At around t = 1,500 s, Stage 4 begins, and new tensioning occurs. This rate is similar to the start of the first tensioning period before linearity occurs. Interactions between the transition zone and the surface in Stage w coincide compression of approximately 15 με. The injection tests, other than the 10/25 test, show the pattern of little initial change, tensioning, a decrease of the tensioning rate, followed by

Once drainage begins, a sharp tensioning occurs of approximately 42 με (Stage a). Tension rate slows to 0.068 με/s after this in Stage b. The strain reaches a maximum of 73 με above pre-drainage values 350 seconds after the start of drainage in Stage c. After this maximum, the region compresses at a rate of 0.057 με/s in Stage d until the pump is shut off (Figure 72).

In the gravity drainage scenario, the tension maximum is reached sooner but is less than in the pumping out case (60 με). After the maximum, the region compresses gradually (Figure 72).

14.5.4.4 s4050

The s4050 sensor remains relatively stable (though compression sometimes occurs) from the start of injection until approximately t = 600 s when tensioning occurs. Tensioning reaches a maximum and then stabilizes and slightly compresses. (Figure 73) and ensemble (Figure 74).

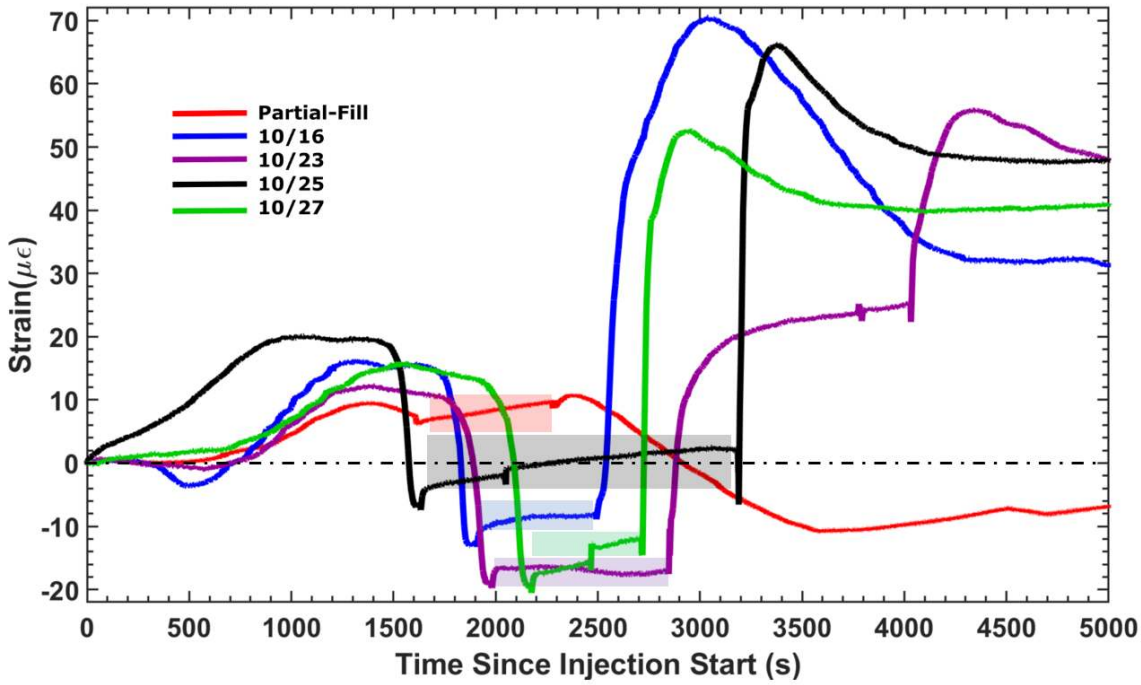

Figure 73: Strain time-series at s4050 sensor for five injection tests conducted on different dates with normalized start times. The No-Flow interval is represented by the transparent bands of the same color.

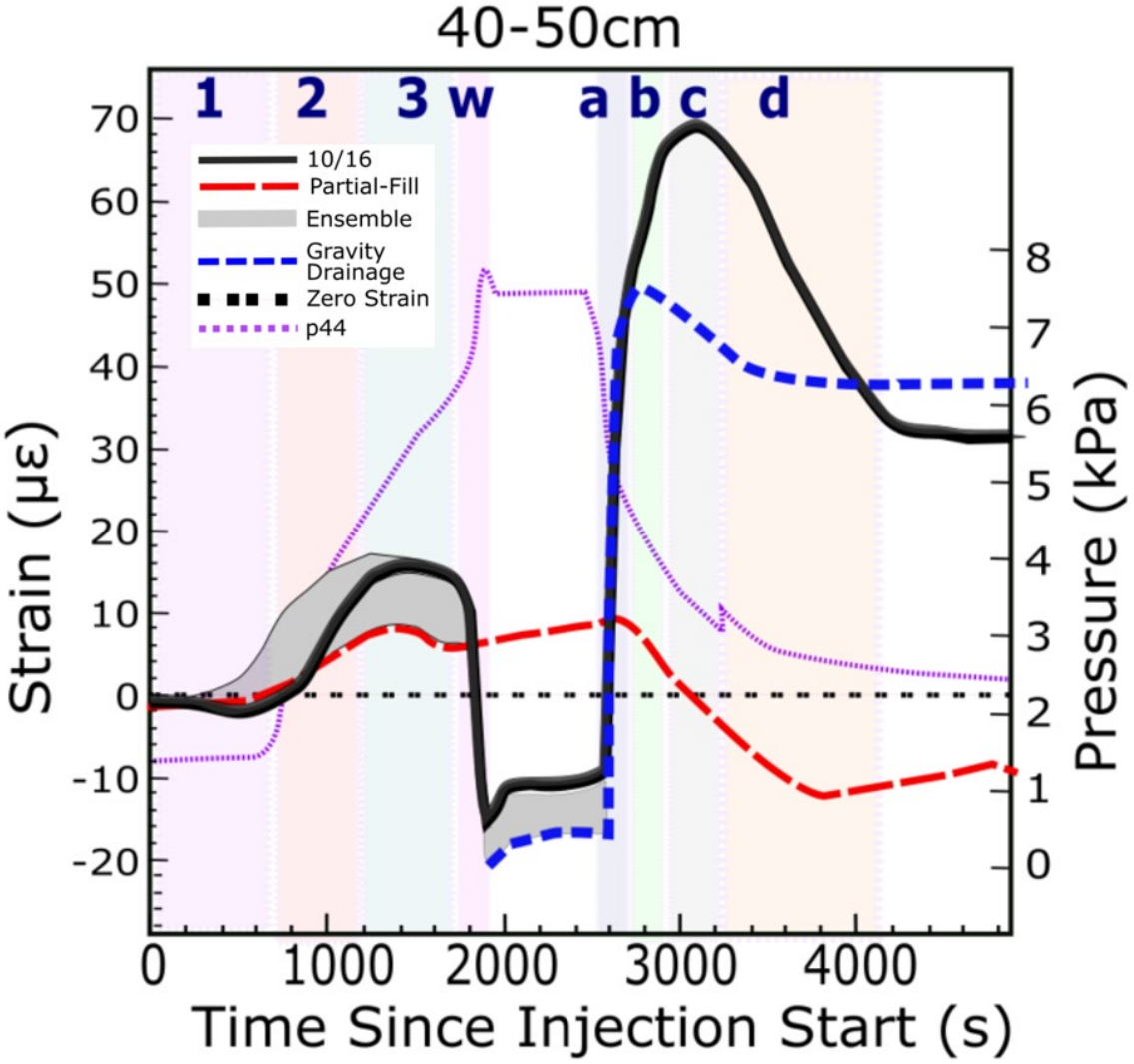

Figure 74: Ensemble strain and total head as pressure time-series for s4050 and p44. The white band is the no-flow interval.

The s4050 reflector and p44 tensiometer data remain unchanged (although very slight compression can occur) when the pump is turned on at t =0 to t ~700 s (Stage 1) (Figure 74). After this point, the strain during Stage 2 increases at a rate of roughly 0.026 με/s for 500 s (until t ~ 1,200 s), and then the strain rate diminishes to zero or slightly negative (Stage 3). Stage 4 is absent in this sensor. The strain compresses by approximately 30 με during surface interactions (Stage w).

Pumping out the column coincides with a sharp tensioning of 53 με over 150 seconds (Stage a). The tensioning rate slows to a rate of 0.087 με/s during Stage b. This tension reaches a maximum of 80 με during Stage c 300 seconds after the start of drainage. After this maximum, compression occurs at a rate of 0.040 με/s during Stage d (Figure 74).

Gravity drainage of the column shows a sharper initial tensioning, 50 με over 50 seconds. After the initial tensioning, linear tensioning of 0.16 με/s occurs. Tensioning peaks at 64 με. Gradual non-linear compression then occurs (Figure 74).

14.5.4.5 s5060

The s5060 sensor (Figure 75) is gradually compressed at the start of injection and then begins tensioning. This continues until surface wetting (Figure 76).

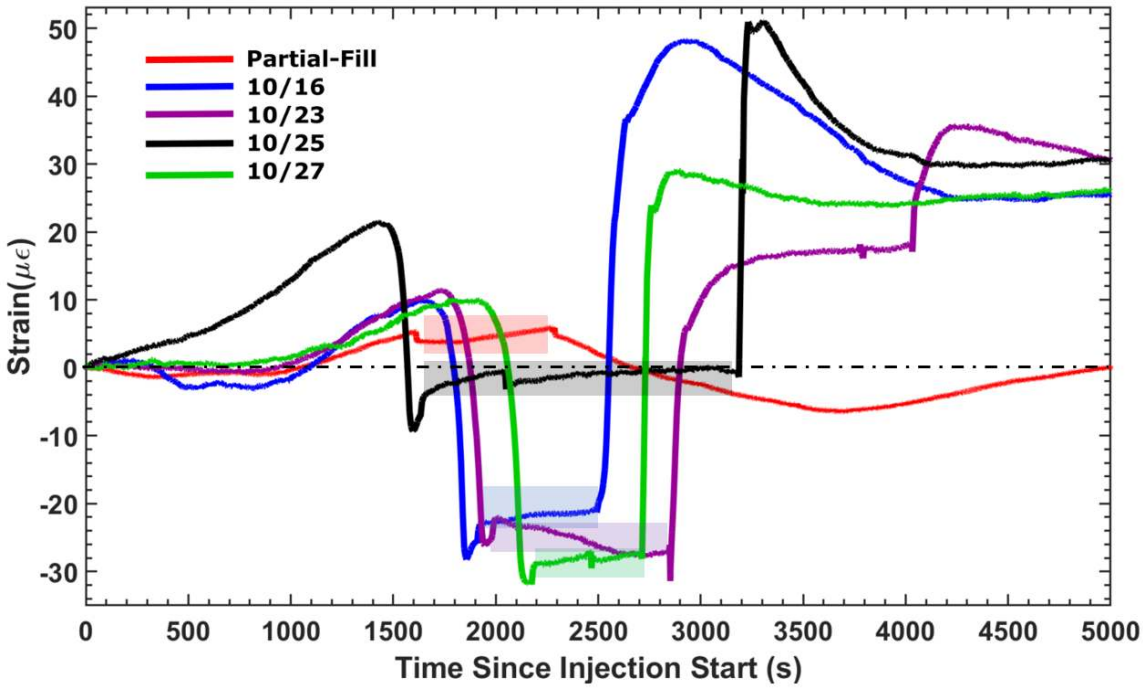

Figure 75: Strain time-series at s5060 sensor for five injection tests conducted on different dates with normalized start times. The No-Flow interval is represented by the transparent bands of the same color.

No response is recorded when the pump is turned on at the start of the experiment from s5060 and p60 (Figure 76). During Stage 1, slight compression can occur as the PZP moves through the column. Tension occurs linearly during Stage 2 when the transition zone moves between the reflecting region at approximately 0.018 με/s beginning at t = 900 s. This tensioning slows and stops as the transition zone moves above the top reflector (Stage 3). Typically, this happens at t = 1,800 s. Rapid compression occurs as the transition zone reaches the surface of the sand. The compression during Stage w is greatest in this sensor at approximately 35 με.

Upon pumping out in Stage a, an initial tensioning of 58 με occurs over 150 seconds. During Stage b, gradual tensioning occurs at a rate of 0.040 με/s. This rounds out to a peak of 69 με in Stage c 250 s after the pump is turned on. Compression occurs at a rate of 0.022 με/s in Stage d (Figure 76).

Draining of the column by gravity initially shows rapid tensioning in this sensor. The value of this tensioning is approximately 51 με over 50 seconds. Linear tensioning occurs for 50 seconds after this at approximately 0.083 με/s. Slight gradual compression occurs after this (Figure 76).

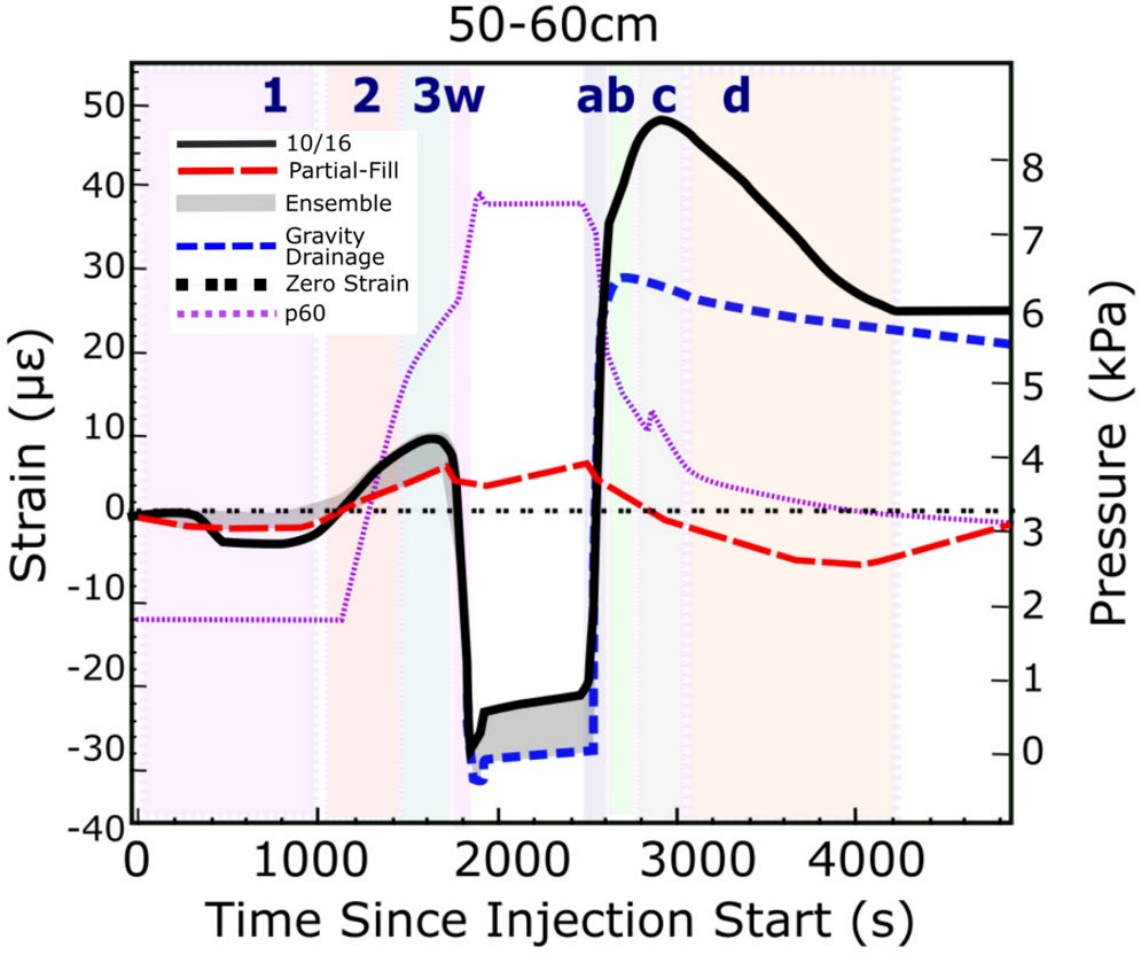

Figure 76: Ensemble strain and total head as pressure time-series for s5060 and p60. The white band is the no-flow interval.

14.5.5 Displacement Over the Sensor

Disregarding the distributed nature of the optical fiber sensor further illustrates repeatability. The total displacement is parallel to the total strain. The total displacement of the optical fiber can be found by converting the individual strains into displacements by multiplying by the length between the reflectors (0.1 m) and adding the individual displacements up.

The pattern of total displacements shows a lengthening during injection of between 5 and 10 µm (Figure 77). The fiber is compressed by a similar amount during the surface wetting stage. Dropping the pressure during drainage after complete surface saturation lengthens the fiber by 15 to 20 µm. The resulting displacement at the end of the experiments in the complete fill and drain tests is roughly 20 µm in added length. The optical fiber during the partial fill test with no surface interaction returned to approximately its original length.

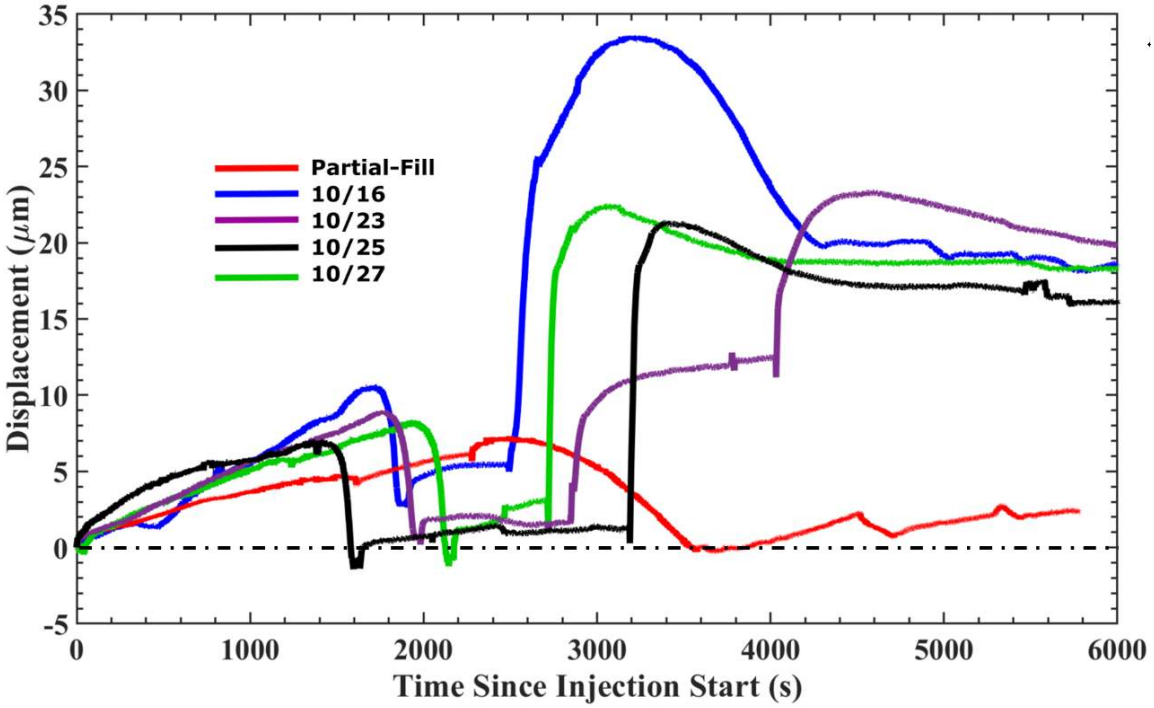

Figure 77: Total displacement time-series of the five tests.

14.5.6 Pressure and Strain Behavior

As seen in the experiments, changes in pressure result in changes in strain. Changes in strain during injection have some linearity to them when the transition zone passes between the reflectors. Strain and pressure changes during surface interactions (Stage 4) is comparatively large and occurs over a short period of time. When the strain is plotted against the pressure, the path the strain sensors go through can be seen. Surface interactions lead to repeatable responses that are clearly different from pressure and strain changes seen in other times in the experiments. These surface interaction events are shown as linear paths in the strain and pressure. Particularly in s2030 s3040 s4050 and s5060, the path the strain and pressures take seems somewhat repeatable. The erratic nature of s1020 makes this analysis unpredictable during stage 4 at this sensor. The slope of these linear paths reveals something resembling a modulus for the sand. This slope can be between 37 and 112 MPa. This is not exactly the moduli predicted for the sand but is within the range of reasonable values.

Stage b of drainage shows a similar modulus in the linear regions of roughly 47 MPa s5060, s4050, and s3040. s2030 has a modulus of 67 MPa. S1020 has a stiffer modulus of 112 MPa. The moduli increase with depth (greater confining pressure). These moduli are reasonable compared to the values for Young's modulus obtained during the triaxial test and the Loading Test and further confirm that these are real interactions between the water pressure and strain in the sand.

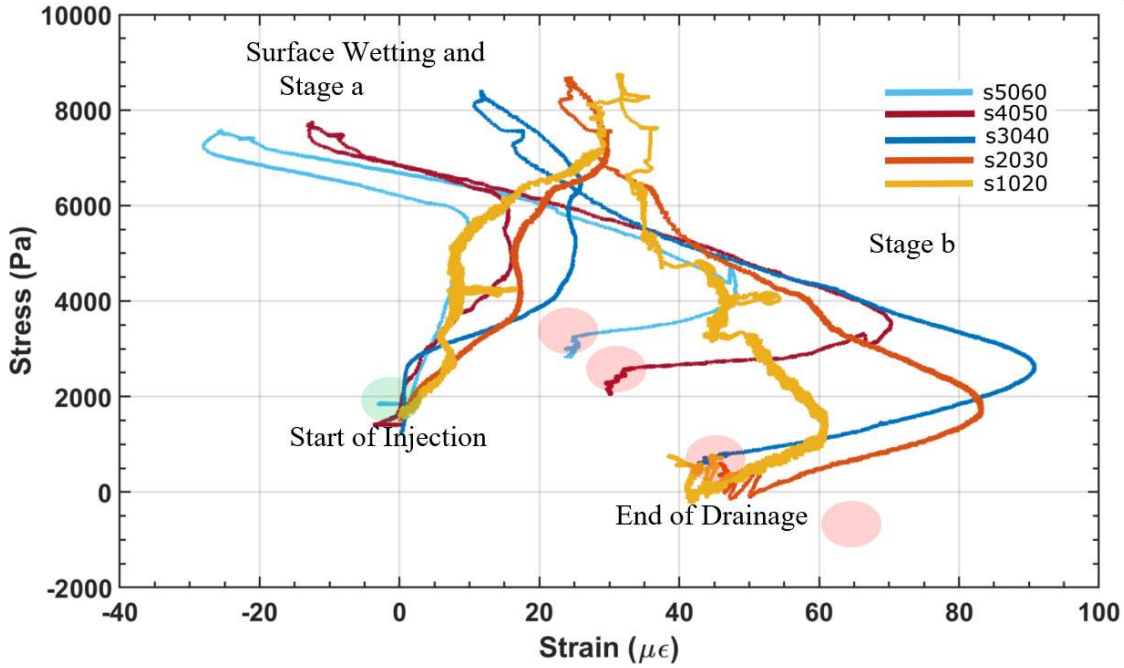

Figure 78: Strain and pressure during injection and pumping out for the 10/16 Injection Test. Surface wetting occurs at roughly t = 1800 s.

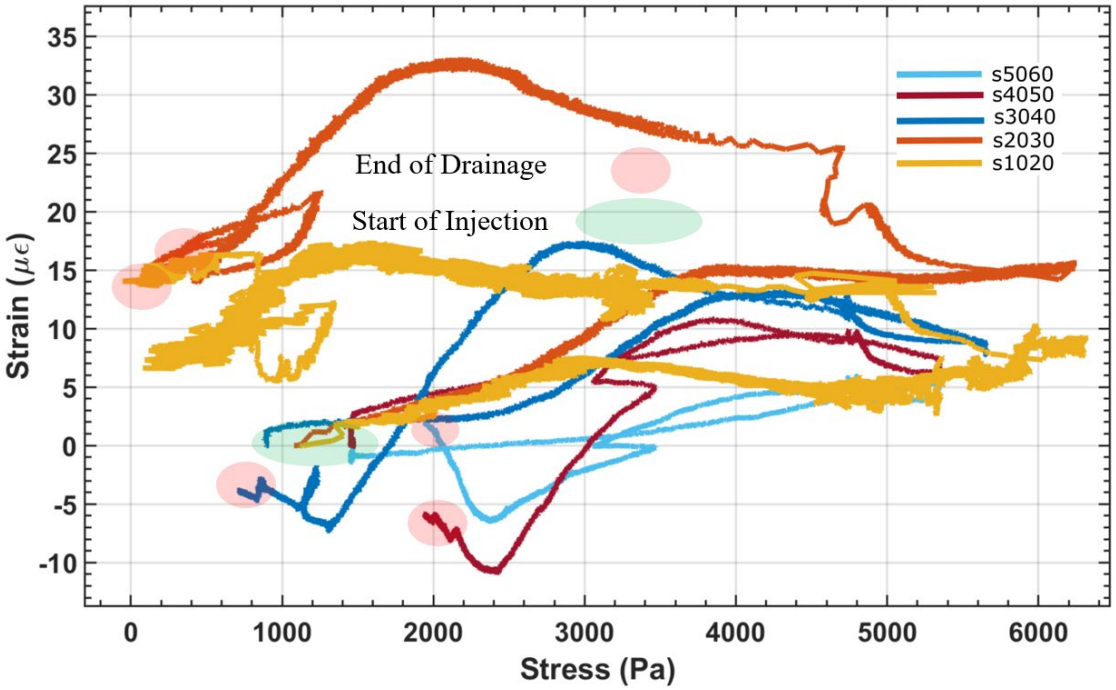

Figure 79: Strain and pressure during the Partial-Fill test.

The stress/strain relationship during the Partial-Fill test is more symmetric than the 10/16 test where surface interactions occurred. More of the strain is recovered with s3040, s4050, and s5060 ending within roughly 5 με of values at the start of injection.

14.5.7 Outside Strain Sensor

The outside strain sensor shows changes in strain during injection and drainage tests. The best results from these sensors come from the 10/16 injection and pump out drainage test (Figure 80). This strain ribbon generally shows stretching during injection and compression during drainage.

The data have trends throughout the test. Temperature correction was not done on the strain data for the outside of the column. The temperature on directly the outside of the column is not the same temperature as on the inside temperature sensors or the temperature of the room. This is the most likely reason for the trends seen in the data. The 10/16 test shows a trend in the strain of 0.0015 με/s. These trends were removed. The trend correction is not all encompassing, but the overall pattern of the data is preserved.

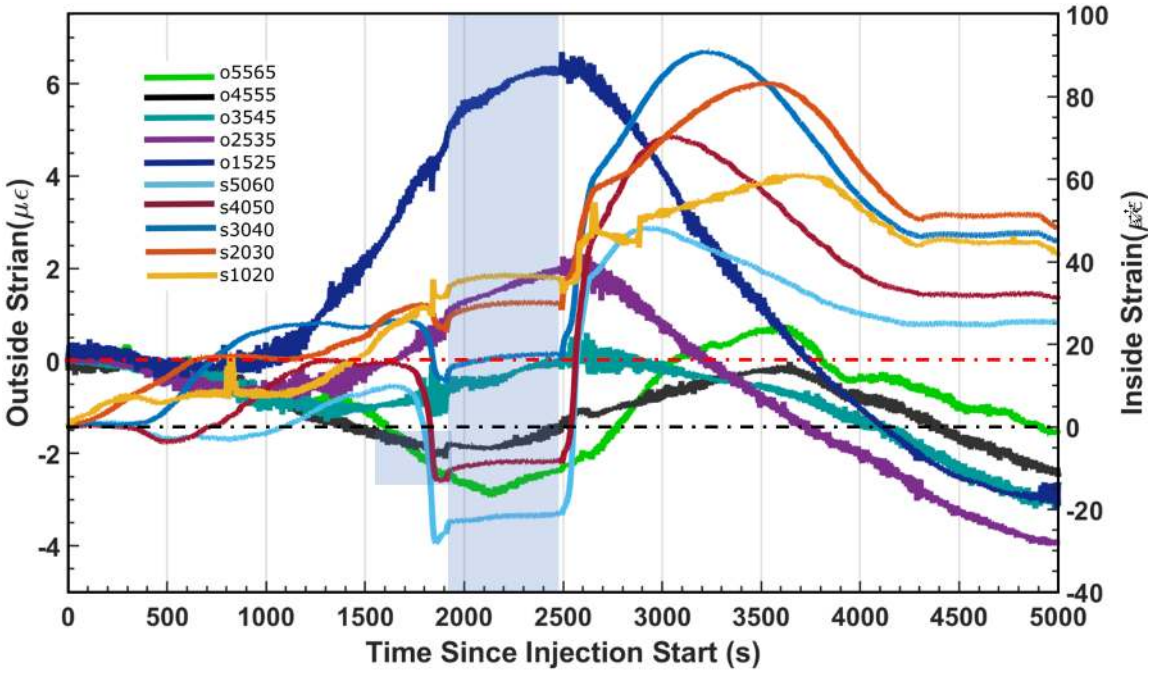

Figure 80: Time-series of the strain both inside and outside for the 10/16 test. Blue band is the period of no flow. Red dashed line is zero outside strain. Black dashed line is zero inside strain.

The patterns of data appear to be indicative of the column bulging in the lower regions and compressing in the upper regions where it is lowest. The lowest sensor is tensioned by the most and at the highest rate (Figure 81). Sensors progressively higher are tensioned by less (Figure 81-Figure 85). A midpoint between compression and tension is likely reached near o3545 due to this sensor being only slightly compressed (Figure 83). Sensors above this are compressed during injection with o5565 compressing the most (Figure 84 and Figure 85). During drainage, the lower regions of the column compress and the upper regions tension (Figure 80).

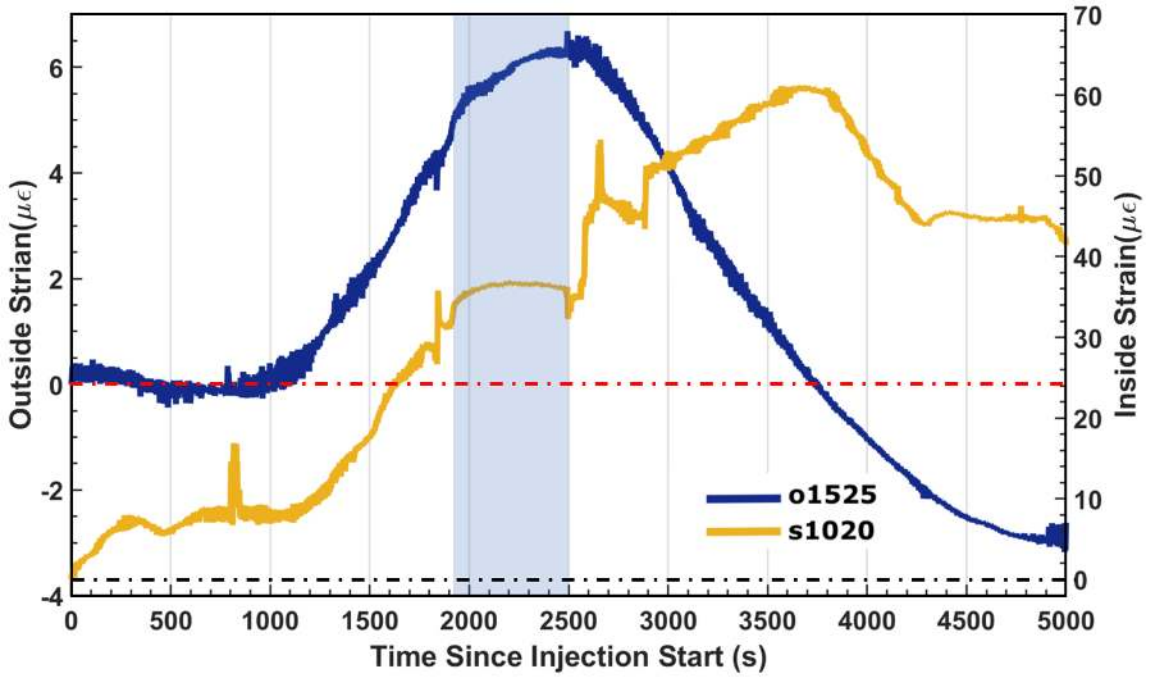

Figure 81: Strain in the sand (s1020) and PVC (o1525) for the 10/16 test. Blue band is the period of no flow. Red dashed line is zero outside strain. Black dashed line is zero inside strain.

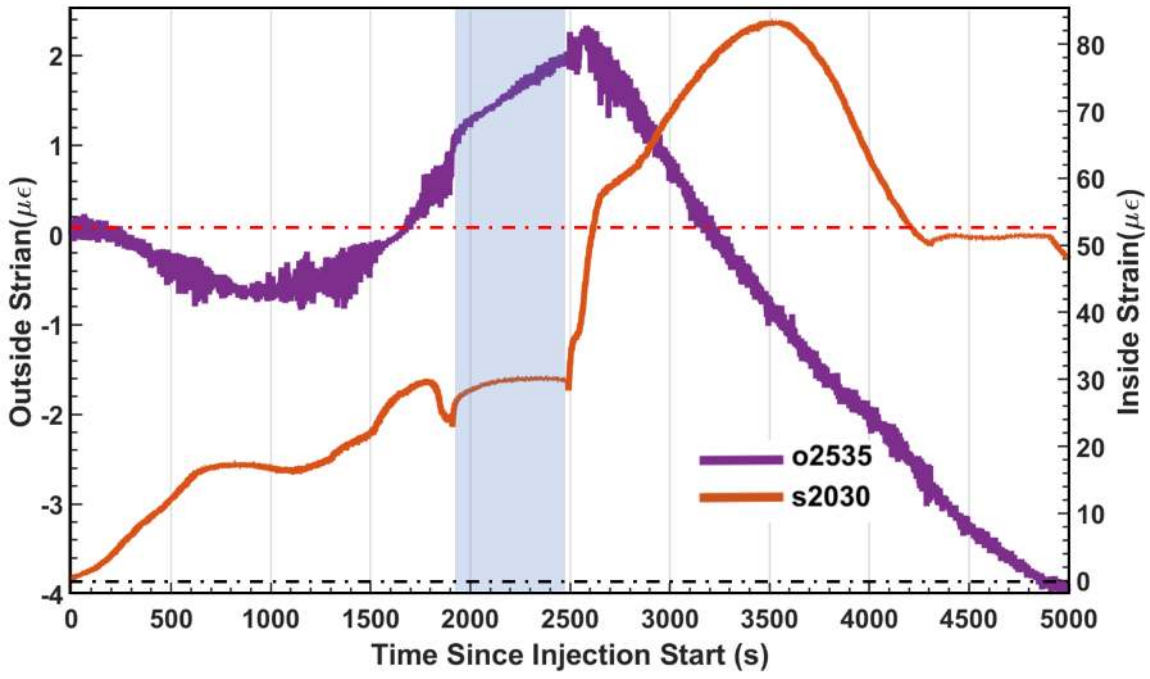

Figure 82: Strain in the sand (s2030) and PVC (o2535) for the 10/16 test. Blue band is the period of no flow. Red dashed line is zero outside strain. Black dashed line is zero inside strain.

14.5.7.1

14.5.7.2 o1525/s1020

The greatest tensioning occurs in the lower sensor. Tensioning of approximately 0.007 με/s occurs at t = 1,000 s and continues until t = 2,000 s. This reaches a maximum of approximately 8 με. Compression of 0.008 με/s occurs after the no flow period (Figure 81).

14.5.7.3 o2035/s2030

Tensioning occurs in the 20-30cm strain sensor at t = 1,300 s and continues until the no flow period at a rate of 0.004 με/s. Compression occurs once the pump is turned on in reverse (Figure 82).

14.5.7.4 o3545/s3040

The 30-40cm region does not appear to be affected much by the injection during the 10/16 test, however slight compression of approximately 1 με occurs followed by tensioning at t = 1,400 s (Figure 83).

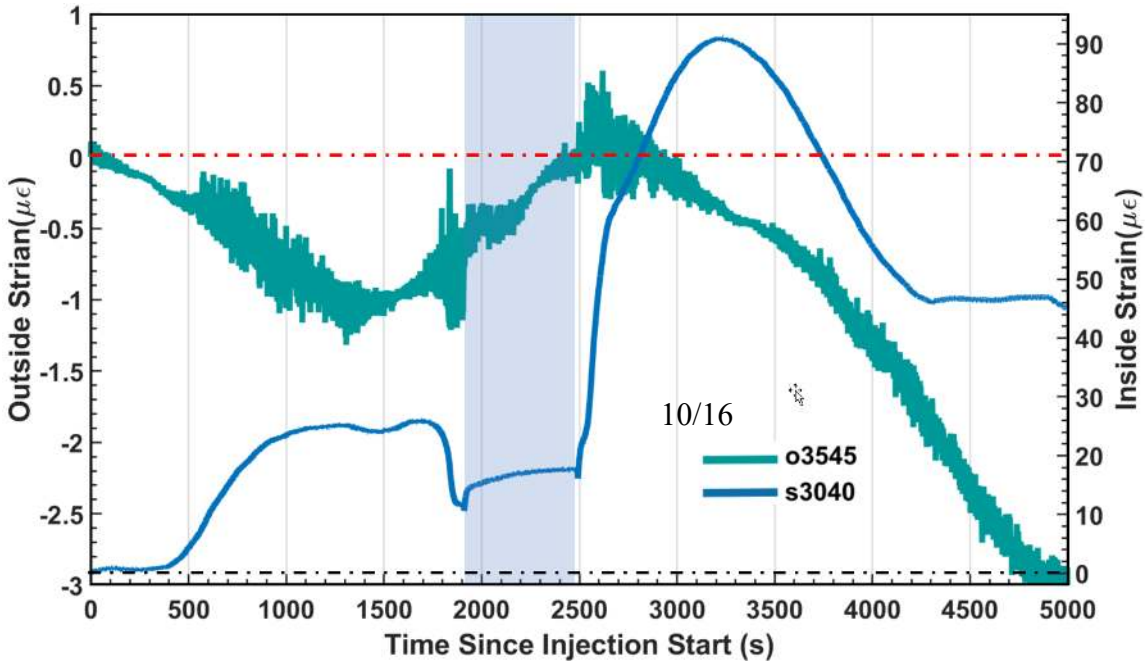

Figure 83: Strain in the sand (s3040) and PVC (o3545) for the 10/16 test. Blue band is the period of no flow. Red dashed line is zero outside strain. Black dashed line is zero inside strain.

14.5.7.5 o4555/s4050

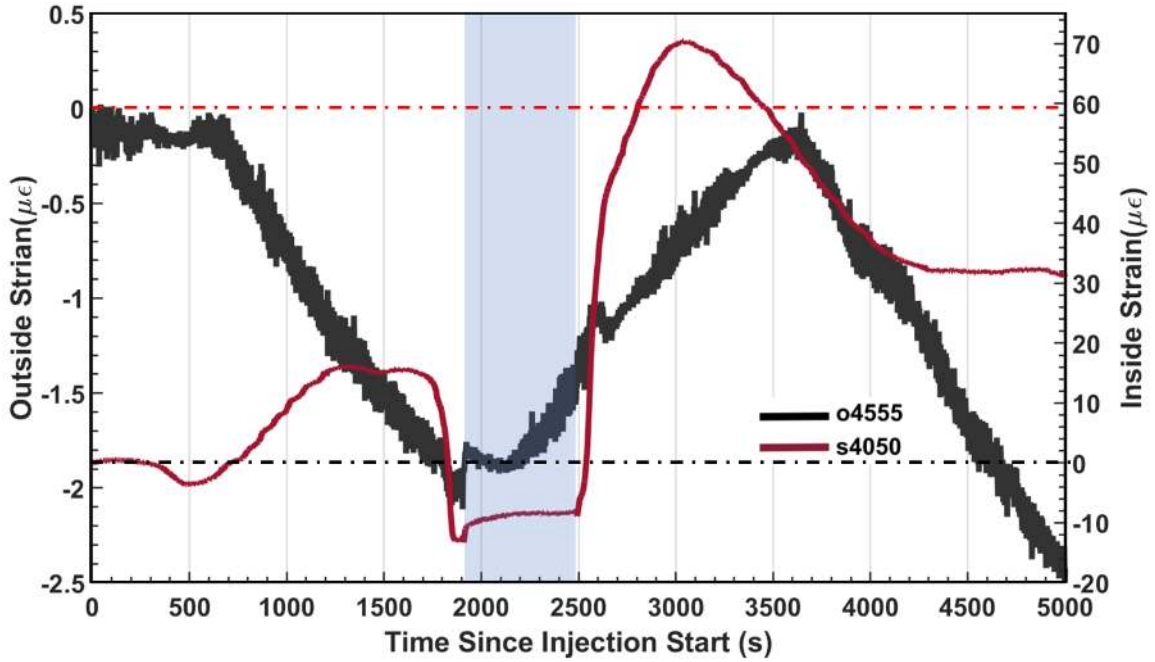

Figure 84: Strain in the sand (s4050) and PVC (o4555) for the Partial-Fill and 10/16 test. Blue band is the period of no flow. Red dashed line is zero outside strain. Black dashed line is zero inside strain.

Compression occurs t = 600 s and continues for until the pump is turned off. Some tensioning occurs when the pump is turned on in reverse that reaches a maximum and reverses t = 3,600 s (Figure 84).

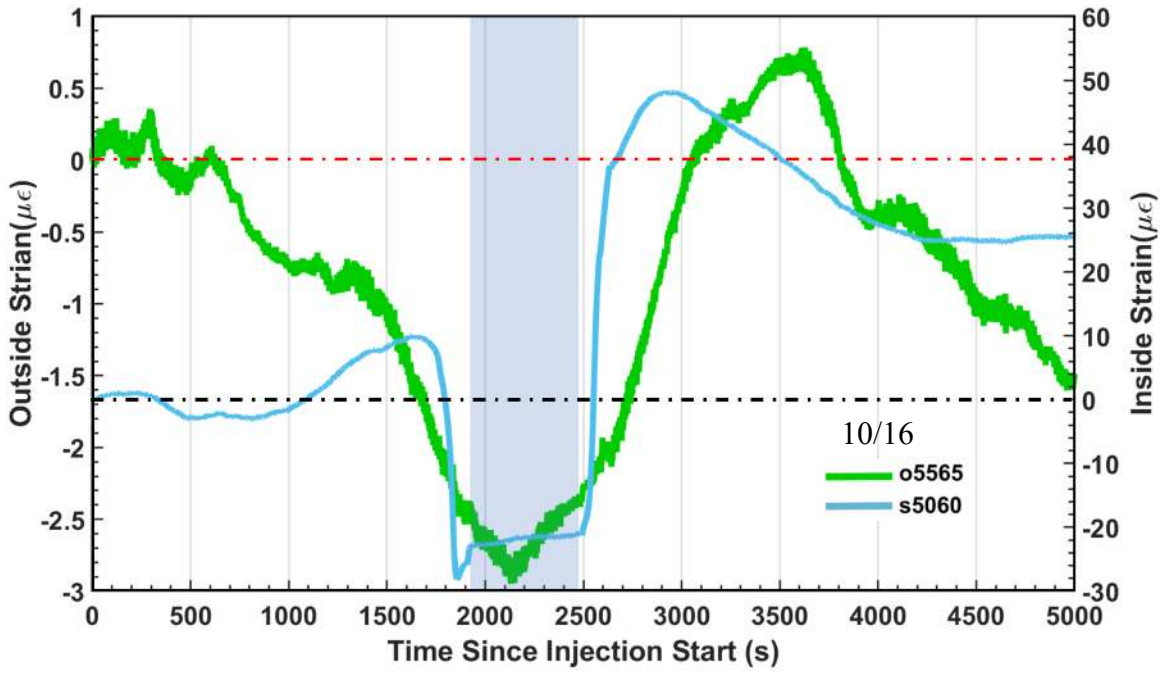

Figure 85: Strain in the sand (s5060) and PVC (o5565) for the Partial-Fill and 10/16 test. Blue band is the period of no flow. Red dashed line is zero outside strain. Black dashed line is zero inside strain.

14.5.7.6 o5565/s5060

Compression occurs in the upper outside strain sensor throughout injection reaching approximately 3 με (Figure 85). This is reversed during drainage.

14.5.8 Infiltration

Infiltration tests were conducted to simulate possible rainfall events (however, the rates of infiltration are much higher than in most natural settings). A showerhead sprinkles water onto the surface of the column. This showerhead is supported over the top of the column by the frame. A section of the showerhead is blocked off to protect the optical fiber tape from being directly rained on. Some of the sand at the top of the column has been removed to where there is a 2.5 cm gap between the top of the sand and the top of the PVC column. A protecting layer of separation gravel is place on top of the sand that's only a couple grains deep. This helps protect the sand from gouging from the infiltrating water.

These tests had two different set ups and various infiltration rates. The first set up involved closing the drain at the bottom of the column, allowing it to completely fill up during infiltration. The other set up features an open drain where water continuously flows out of the column.

14.5.8.1 Infiltration Fill-Up test

An infiltration test was conducted with a closed drain to fill up the column. Infiltration was stopped after a 2.5 cm pond was formed. Ten minutes after filling, the column is drained using gravity.

14.5.8.2 Results

14.5.8.2.1 Pore Pressure

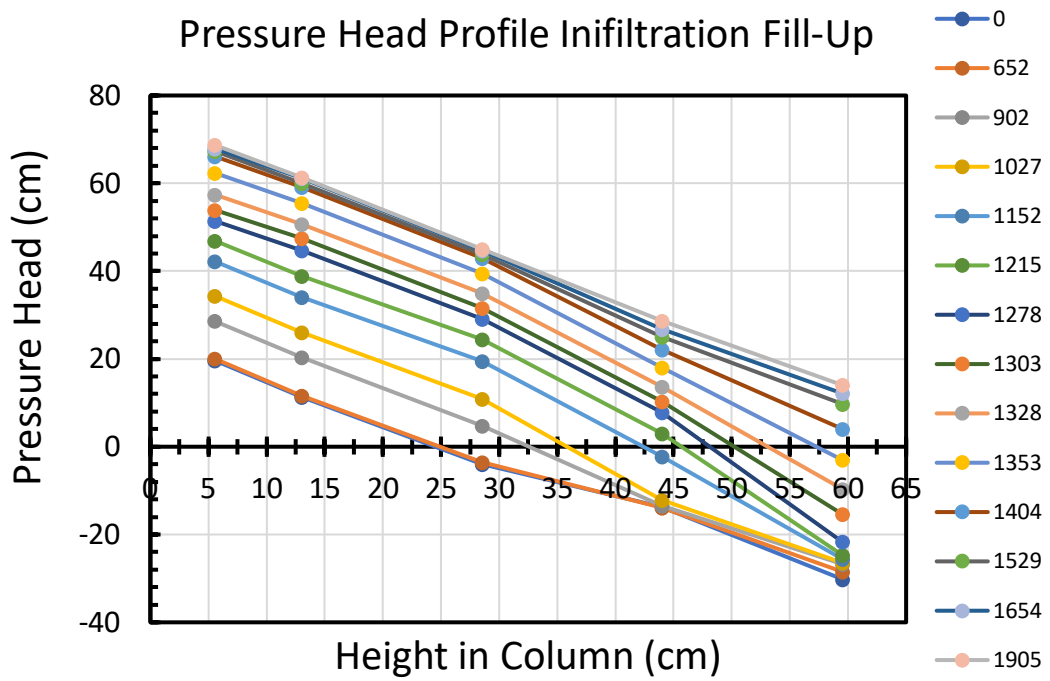

Figure 86: Pore pressure head profile for the infiltration fill-up test.

The infiltration rate during this test was 0.1 liters/min. This rate was lower than the rate of uptake in the sand, preventing the formation of a pond until the PZP reached the surface. The p60 tensiometer shows slight increase in pressure at time 450 seconds due to wetting from water flowing thought the column. The bottom three pressure sensors begin increasing around 675 seconds. This corresponds to the wetting front reaching the static PZP which then begins increasing in height. The pressure increases at a rate of 6.5 Pa/s. Around 1,050 seconds p44 begins increasing at the same rate as the lower three. The pressure gradient during infiltration is roughly 1.05. This is lower than the injection tests. As the PZP reaches the top of the column, the pressure begins to increase more rapidly as the wetting front reaches the top of the column. Infiltration continues until a pond 2.5 cm deep forms. When the pump is shut off and infiltration stops, the bottom 3 pressure sensors stabilize but the top two slightly increase. The pressure heads approach the same value of 74 cm.

After the infiltration, the drain is opened, and the column drains under gravity. The pond is deeper in this test than the other tests. While the pond drains, the pressure head forms a gradient of 1.77. Once the pond is drained the pore pressure responds similarly to the other gravity drainage tests.

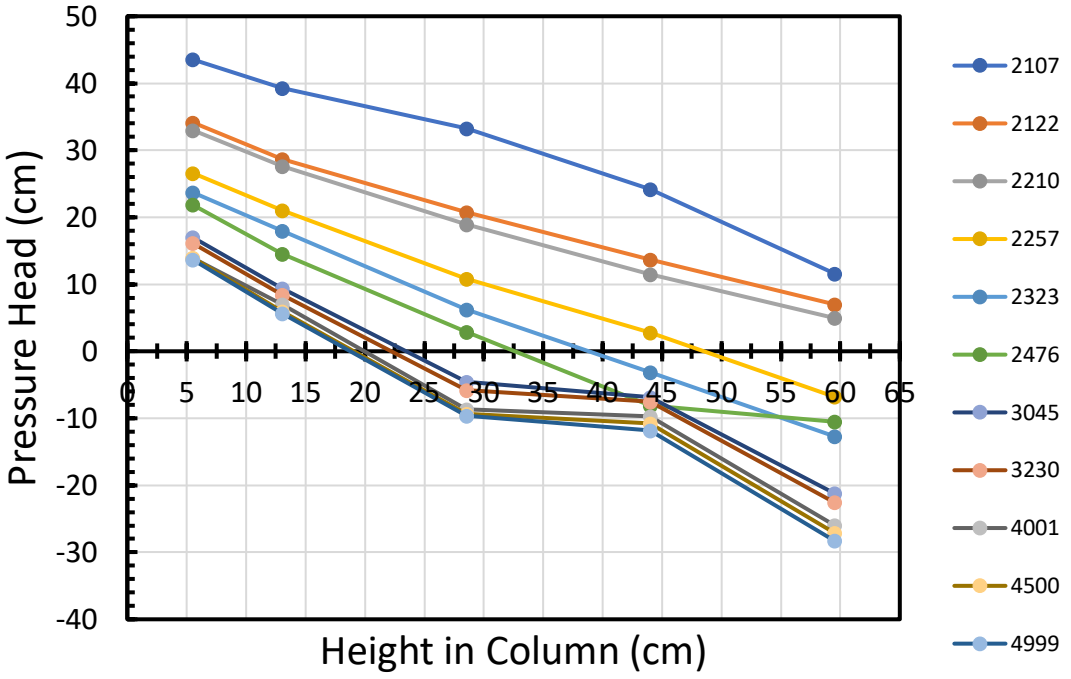

Figure 87: Pore pressure head profile for the drainage portion of the infiltration fill-up test.

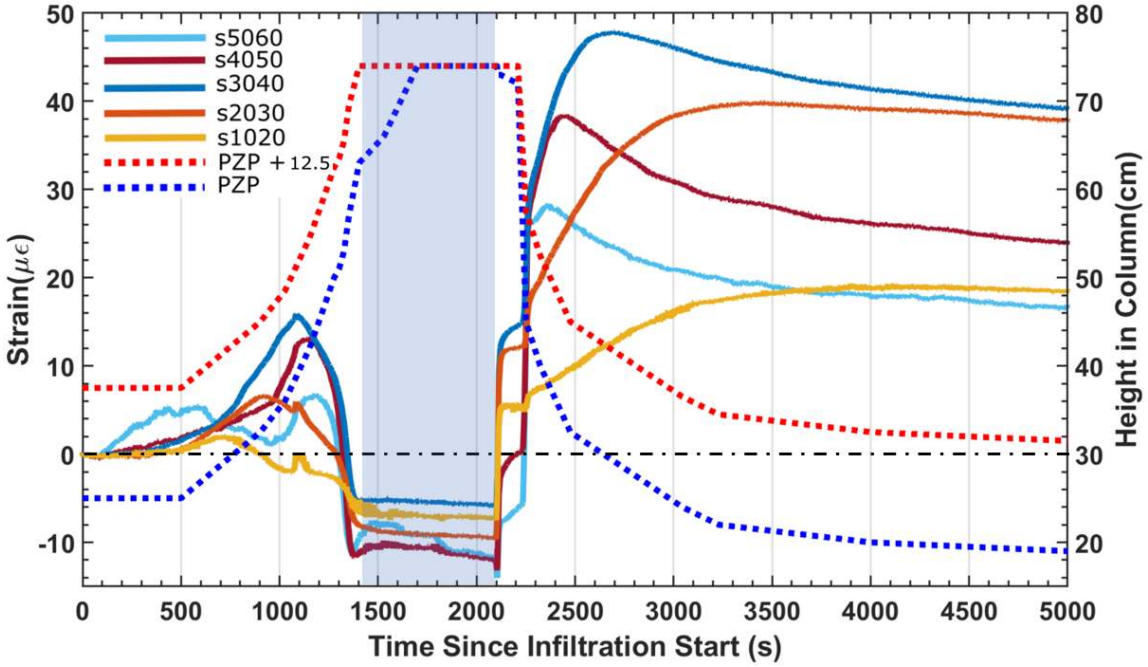

Figure 88: Strain and transition zone (PZP to PZP + 12.5 cm) height as functions of time for the infiltration fill-up test. Blue band is the period of no-flow.

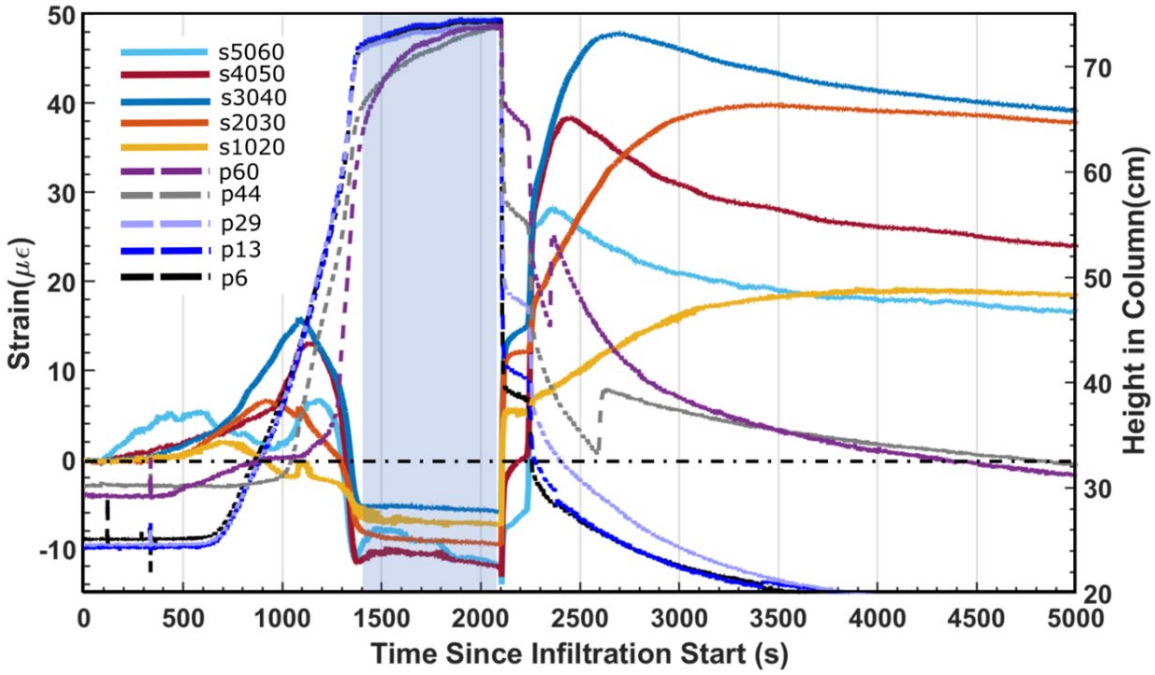

Figure 89: Strain and total head as functions of time for the infiltration fill-up test. Blue band is the period of no-flow.

14.5.8.2.2 Strain

The filling up of the column during infiltration produces a somewhat similar response to filling the column up during injection. Tensioning occurs as the wetting front from infiltration moves down the column. s5060 tensions the most during this period (upwards of 5 mu/s). The lower sensors increase more gradually. The rate of tensioning increases when the infiltrating front reaches the PZP causing it to rise. The strain reaches a maximum and begins compressing once the PZP reaches the top reflector (+/- 5 cm). The effect of ponding causes the rapid compression seen in the injection tests. After infiltration is stopped, the strain stabilizes and changes little until drainage begins.

After the infiltration, the drain is opened, and the column drains under gravity. Similar to other tests, starting drainage coincides with rapid initial tensioning. A period of stability occurs as the pond drains. This effect occurs for a longer time period due to a deeper pond than in the injection tests. Once the pond is drained tensioning occurs similarly to the other tests involving gravity drainage with tensioning followed by compression as the transition zone through the column.

The s1020 sensor initially begins to tension at the time when the PZP begins increasing. After this point, it compresses until the formation of the pond. Little change occurs during the no flow region. Opening the drain coincides with approximately 15 με of tension. Little change occurs after this as the pond drains. After this, the sensor tensions similar to other gravity drainage tests.

14.5.8.3 Strain in the Column

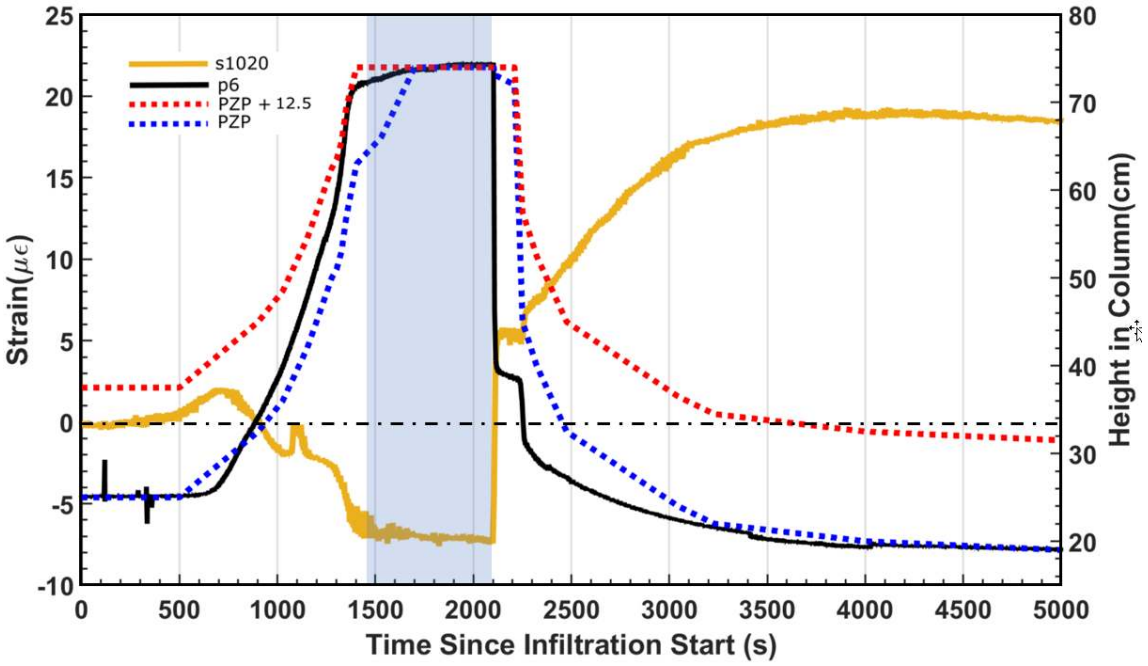

Figure 90: Strain at s1020, total head at p6, and transition zone (PZP to PZP + 12.5 cm) height as functions of time for the infiltration fill-up test. Blue band is the period of no-flow. Height or pressure head right axis label.

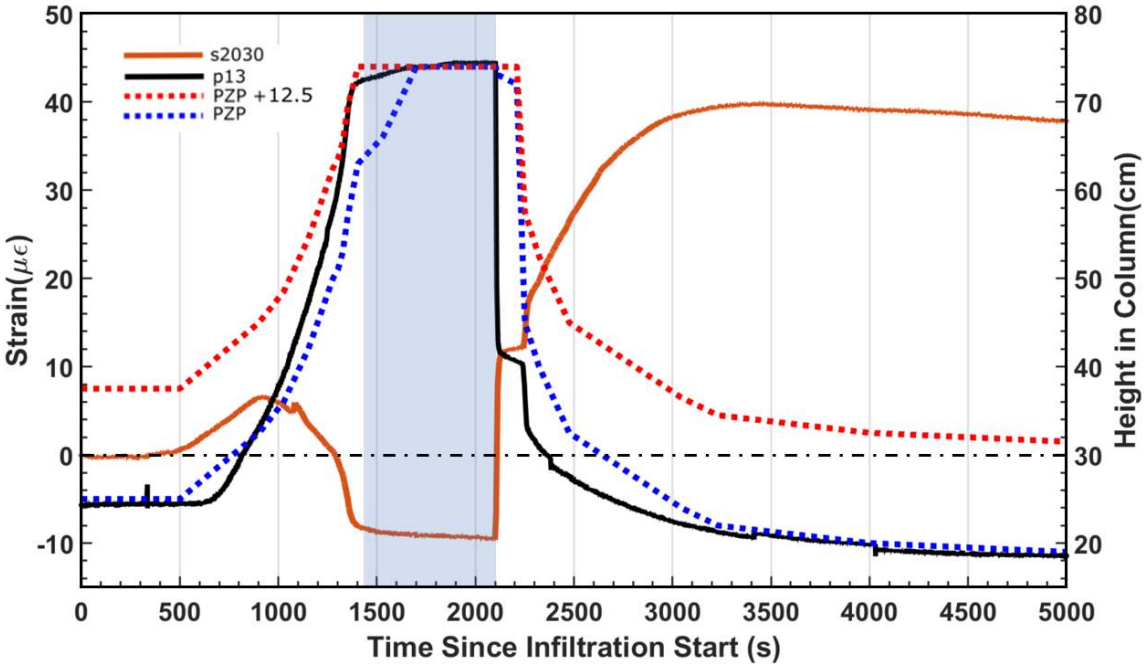

Figure 91: Strain at s2030, total head at p13, and transition zone (PZP to PZP + 12.5 cm) height as functions of time for the infiltration fill-up test. Blue band is the period of no-flow. Height or pressure head right axis label

The s2030 sensor begins increasing around the time the PZP starts increasing. It then begins compressing which continues until ponding occurs. Little change occurs during the no flow point. Opening the drain coincides with approximately 20 με of tension. Little change occurs after this while the pond drains. After this the response is similar to other gravity drainage tests.

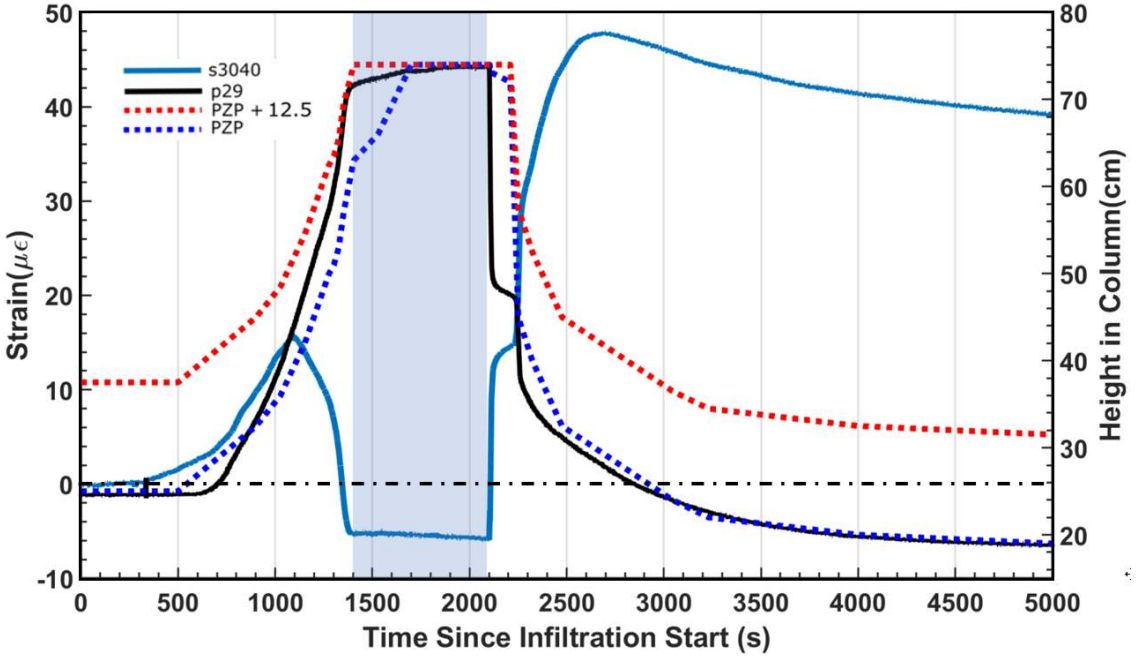

Figure 92: Strain at s3040, total head at p29, and transition zone (PZP to PZP + 12.5 cm) height as functions of time for the infiltration fill-up test. Blue band is the period of no-flow.

The s3040 sensor begins tensioning before the infiltrating water reaches the PZP causing it to increase in height. After a point, the sensor begins compressing. Ponding causes a larger rate of compression. Little change occurs during the no flow point. Opening the drain coincides with 20 με of tensioning. 2 με of tensioning occur while the pond drains. The response after this is similar to other gravity drainage tests.

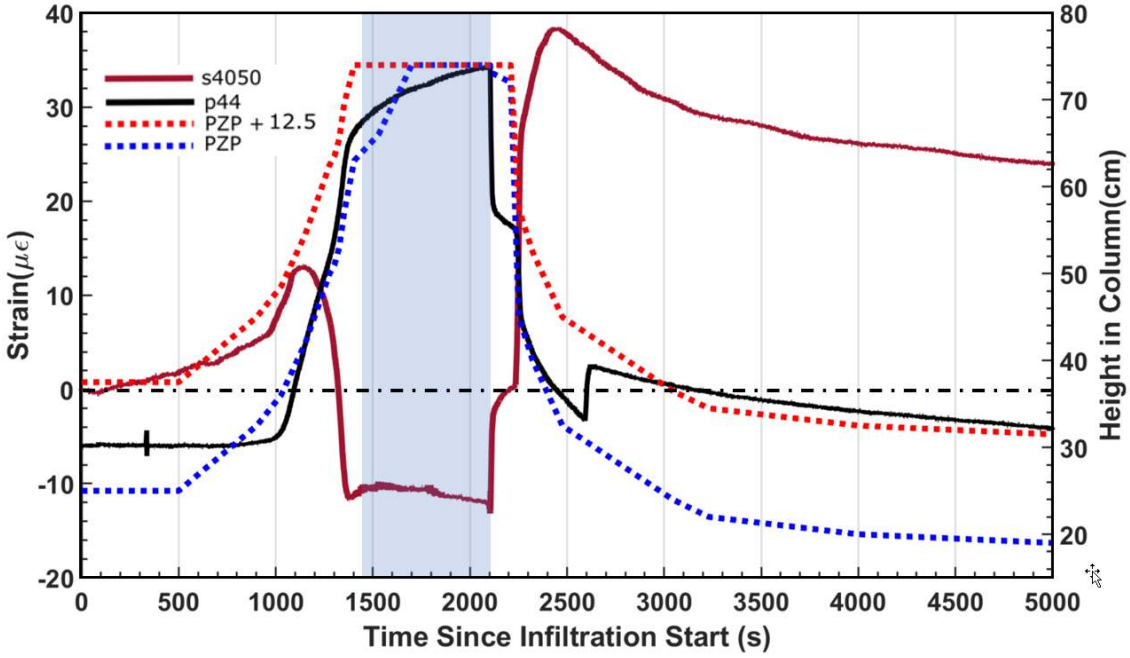

Figure 93: Strain at s4050, total head at p44, and transition zone (PZP to PZP + 12.5 cm) height as functions of time for the infiltration fill-up test. Blue band is the period of no-flow.

The s4050 sensor begins tensioning well before the wetting front reaches the PZP. Tensioning occurs more quickly at around t =1,000 s. Pond formation causes compression. Little change occurs during the do flow period. Opening the drain coincides with approximately 10 με of tensioning. Approximately 5 με of tensioning occurs while the pond drains. After complete drainage of the pond, the response is similar to other gravity drainage tests.

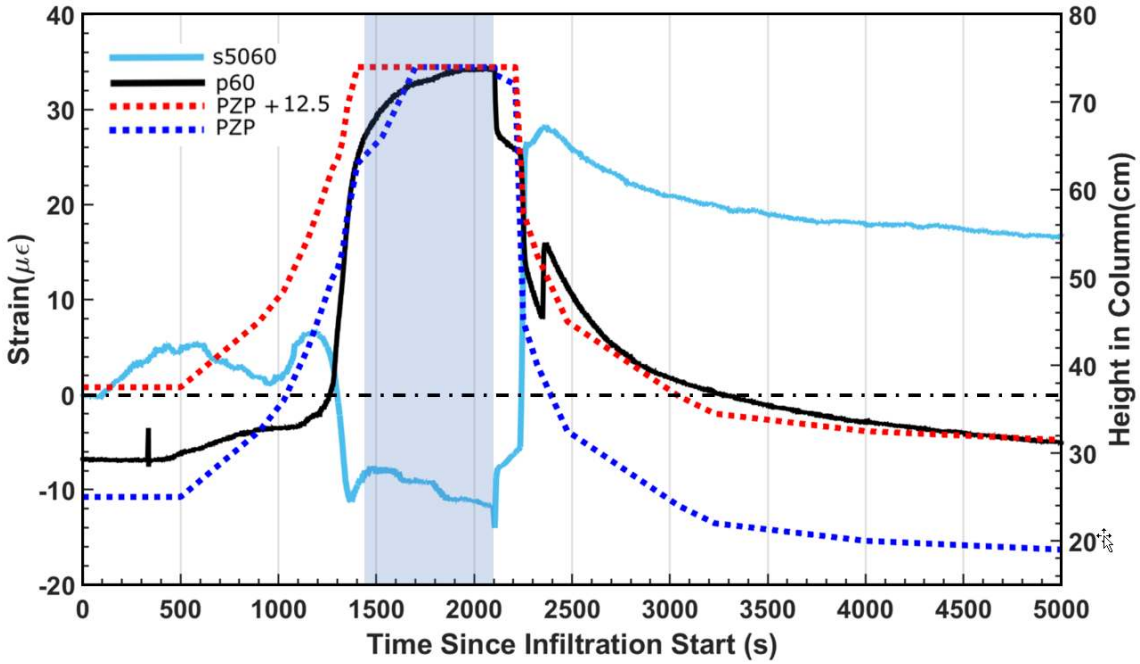

Figure 94: Strain at s5060, total head at p60, and transition zone (PZP to PZP + 12.5 cm) height as functions of time for the infiltration fill-up test. Blue band is the period of no-flow.

The strain at s5060 begins increasing at t =100 s and the pressure at p60 starts to increase slightly at t =400 s. The strain increases sharply at t =1,000 s and peaks at t =1150 s rounding off to compression. Ponding causes sharp compression as seen in other tests. Slight erratic change occurs during the no flow period. Opening the drain coincides with 5 με of tensioning. Another 5 με of tensioning happens as the pond drains. After complete drainage of the pond, the s5060 sensor responds similar to other gravity drainage tests.

14.5.9 Infiltration Open Drainage

Open drainage tests were conducted with various infiltration rates. These rates have varying effects on ponding. Ponding occurs when the rate of infiltration is greater than the rate of uptake. Infiltration was conducted at a rate of 0.7 l/min. This is a high enough rate to create a pond on the surface.

14.5.9.1.1 Results High Rate

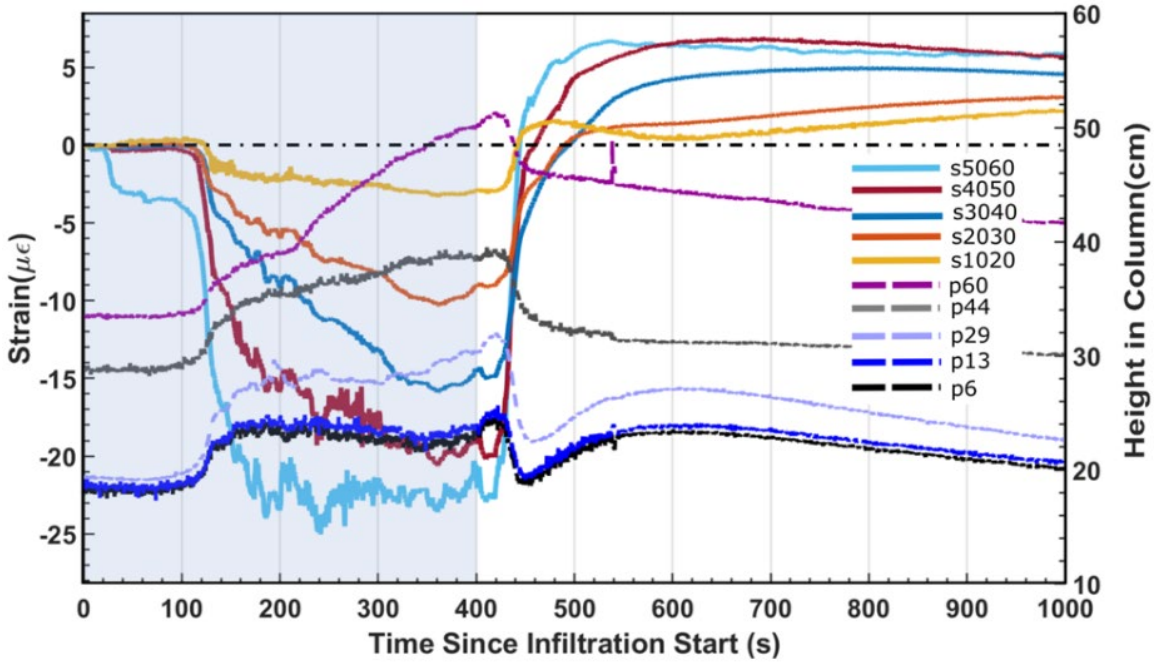

Figure 95: Infiltration test were the infiltration rate was greater than the uptake rate. This causes ponding on the surface. Strain and total head time series shown. Infiltration is on during the blue band.

14.5.9.1.1.1 Pore Pressure

Pressure jumps positively as soon as a pond is formed on the surface of the column. During the ponding, while infiltration is still on, pressures increase as water moves through the column. p60 increases the most with regions having a lower head. Pressure rapidly decreases after the pond sinks and completely goes away. After this drop, the pressure slowly increases as more water moves downward through the column.

14.5.9.1.1.2 Strain

s5060 compresses by 3 με 20 seconds after infiltration starts. Interestingly, ponding coincides with compression even when the rest of the column is unsaturated. Compression occurs when the uppermost grains of sand are completely saturated. This compression first happens at the top of the column and continues to the bottom. The compression is greatest in the upper regions of the column. When the infiltration is turned off, the pond drains. When the pond fully drains and the water moves beyond the top grains, tensioning occurs. Sharp tensioning happens throughout the column. The amount of tensioning increases with height in the column with the strain approaching between 0 and 5 με above pre-infiltration values.

14.5.9.1.2 Results Lower Rate

An infiltration scenario was created where ponding occurs and but due to the infiltration rate 0.35 l/min and drainage rate reach an equilibrium and the PZP forms at 30 cm.

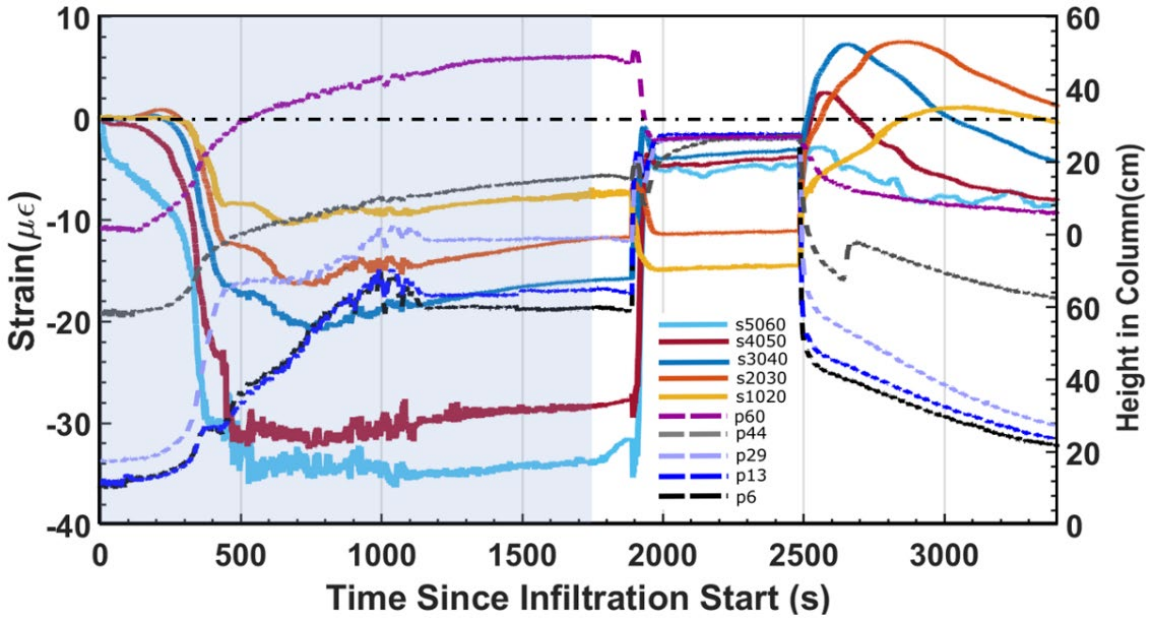

Figure 96: Strain and total head time series. This test had a lower infiltration rate but high enough to cause ponding. Drainage was stopped and restarted during the test. Infiltration is on during the blue band.

14.5.9.1.2.1Pore Pressure

Pressure begins to increase 100 seconds after infiltration starts. The pressure increases to a point and then stabilizes. At time 1,750 s the infiltration is stopped. 150 seconds later the pond fully drains. After 10 seconds drainage is stopped. This causes the pressure to stabilize at the same value throughout the column. At 2,500 seconds the drain is opened again, and the drainage is similar to other gravity drainage situations.

14.5.9.1.2.2Strain

s5060 is compressed by 4 με/s almost immediately following the start of infiltration. s4050 is compressed more gradually shortly after infiltration starts. s3040 compresses later and even more gradually. s2030 and s1020 compress begin compressing at roughly the same time when the pond forms. The formation of the pond compresses all sensors in the column.

s5060 begins tensioning slightly when infiltration is shut off. When the pond fully drains, all sensors tension. The tensioning is cut off when drainage is stopped. When drainage is resumed, the strain behaves similar to other gravity drainage tests with the exception of s5060, which is most likely due to the PZP already being below it.

Breaking the drainage of the column into two events illustrates that two separate events cause tensioning in the column. First, opening the drain causes an initial shock to the system with a pressure wave propagating up the column. This causes the initial tensioning.

14.5.10Separation of Effects and Commonalities

The infiltration experiments allow for some of the effects seen in the injection tests to be separated and further studied.

Ponding during infiltration corresponds to compression throughout the column. This occurs in both infiltration conditions where the wetting front rises from below, and where the infiltration rate is high enough to form a pond on top of an unsaturated column. The pattern of the magnitude of compression decreasing with depth in the column also occurs with s5060 compressing the most and s1020 compressing the least.

The drainage of the pond corresponds with tensioning throughout the column. In the Infiltration-Fill up test, two separate tensioning events are seen. One corresponding with the drain opening, and one corresponding with the pond being fully drained. In the other infiltration tests, immediate tensioning occurred as soon as the pond was drained.

The drainage curves of the Infiltration-Fill Up and the Lower rate infiltration Open Drain test follows the same pattern as the injection tests drained using gravity.

14.6 CONCEPTUAL MODEL

The experimental observations can be integrated to a conceptual model that provides some insight into processes affecting strain during changes in saturation. Basic mechanics indicates that increasing pore pressure displaces grains of sand away from each other, reducing effective stress and causing tension. Decreasing the pressure has the opposite effect as the sand grains move closer to each other, causing compression. This concept is expressed in Hooke's Law, where vertical strain is given under uniaxial conditions as

$$\varepsilon_{zz} = C_u(\sigma_{zz} + \alpha p) \qquad 14\text{-}13$$

where σ_{zz} is the total vertical stress, α is the Biot-Willis coefficient, and

$$C_u = \frac{(1-2\nu)(1+\nu)}{(1-\nu)E} \qquad 14\text{-}14$$

with ν is Poisson's ratio and E is Young's modulus. Uniaxial strain means the horizontal strain is zero, which could be approximated by the relatively stiff tube used constrain the sand in the column. Assuming that the total vertical stress remains constant, it is apparent that the pressure compliance is

$$\frac{\partial \varepsilon_{zz}}{\partial p} = \frac{\alpha(1-2\nu)(1+\nu)}{(1-\nu)E} \qquad 14\text{-}15$$

In the experiments, $\alpha = 1$ and $0.25<\nu<0.45$, and 10MPa < *E* < 40MPa. This indicates that the strain increases (becomes more tensile) when the pressure increases, which is consistent with the concept outlined above. It also shows that the expected pressure compliance is in the range $0.006\frac{\mu\varepsilon}{Pa} < \frac{\partial \varepsilon_{zz}}{\partial p} < 0.08\frac{\mu\varepsilon}{Pa}$.

Another important effect that can cause strain is related to the observation that the stress change in one area is transferred to another area in order to maintain equilibrium (Wang, 2000). For example, when the far-field stress remains constant, a stress increase in one area will decrease the stress in the neighboring region in order to maintain equilibrium with the far-field stress. So, an increase in pressure that causes local tensile strain and expansion in the pressurized area can result in compression in a neighboring region. This non-local strain can itself cause a change in pressure. An example of this effect is the pressure increase in confining

units that occurs when pumping causes pressure to drop in an underlying aquifer, a process called the Noordbergum effect (summary in Wang, 2000; 218-221). A similar effect can cause a pressure reversal during injection into a single fracture (Murdoch and Germanovich, 2013). Pressurizing a borehole in tight rocks causes the pressure to decrease as a result of this stress transfer effect (Wang, 2000, Fig 8.8).

A third effect that can cause strain is a changing load on the boundary. Increasing the total stress normal to the free surface will increase the strain within the sand. The total stress is the sum of the effective stress and the pore pressure, so changing the pore pressure at the boundary will change the boundary condition and create strain within the sand.

These considerations identify three effects:

Hooke's law effect: strain is proportional to the local change in pressure, so the pressure compliance is positive.

Stress transfer effect: strain is caused by stress transfer from a neighboring region, so the strain can be independent of the local change in pressure. The pressure compliance can be zero or negative in this case.

Boundary load effect: Strain is a result of changes in the load applied to a boundary. Strain can be independent of the local pressure.

Several aspects of the experiments complicate interpretation of the results. All of the important parameters (Young's modulus, Poisson's ratio, permeability, effective Biot-Willis parameter) are non-linear functions of saturation. This may cause basic inferences to differ from expectations. Moreover, the experiments were conducted inside a tube that is more rigid than the sand used in the experiment. This will tend to make the deformation uniaxial, which simplifies interpretations, but friction on the wall of the column will introduce effects that may be difficult to anticipate.

The conceptual model will be described using both Stages in time and Zones in space. A representative set of reflectors are assumed to be in the middle of the column, and Stages are identified based on characteristic changes in the strain time-series associated with the sensing region between those reflectors. Zones are identified based on the characteristics of the pore pressure distribution (Ambient Zone, Transition Zone, Positive Pressure Zone).

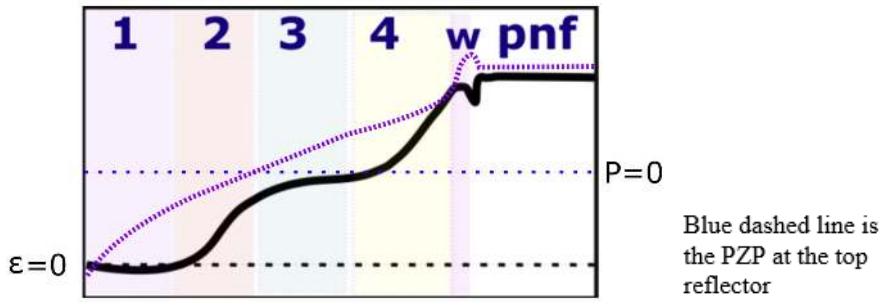

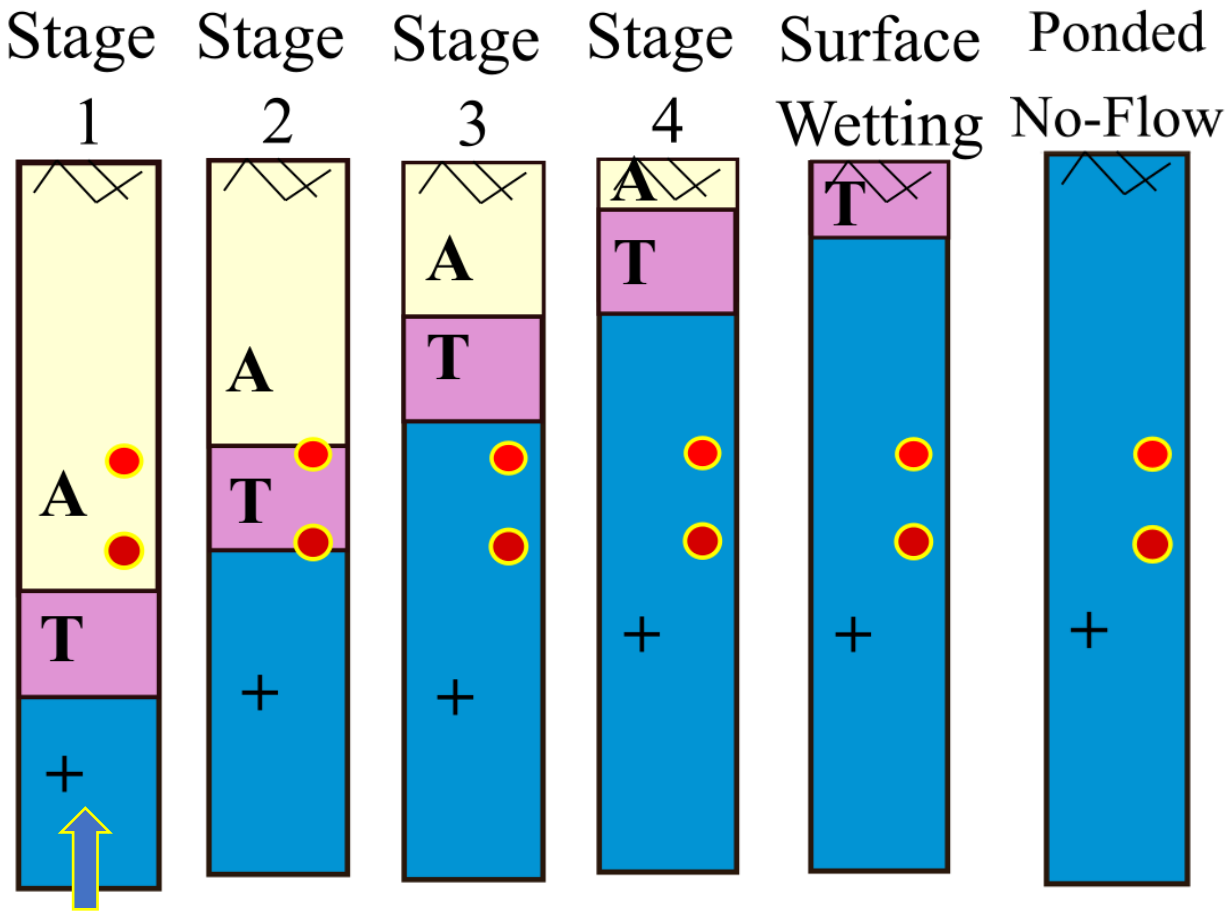

Figure 97: Strain time-series with stages (labeled colors) and sketches of different stages (Ambient, Transition, and Positive pressure (+)) in the column during injection. Red dots are a representative strain sensor. P=0 is for the top of the reflector.

14.6.1 Stage One

Stage One starts with the strain in the sensing region at ambient conditions. The strain then becomes negative (compression) reaching several με of compressive strain before the strain starts to increase. For example, s4050 and s5060 in Figure 74 and Figure 76 (Figure 34 and 59). This stage is absent from sensors below the transition zone at the start of the test (e.g. s1020 and s2030 in Figure 68 and Figure 70).

The pressure transition zone underlies the strain sensing region throughout Stage One, but the increase in strain that marks the end of the Stage occurs as the leading edge of the pressure transition zone arrives at the lower reflector (Figure 98). Strain appears to be unaffected by the rising pressure when the transition zone is significantly below the sensing region, but the region is compressed as the transition zone approaches. This appears to be a strain transfer effect from expansion in the advancing underlying transition zone. The rate of compression during Stage One is roughly half the rate of expansion in the underlying transition zone, but this may be because the elastic modulus in the relatively dry sand under ambient saturation is stiffer than under the more saturated conditions in the transition zone. The pressure compliance during Stage One is zero or negative. This is consistent with strain caused by the stress transfer effect.

14.6.2 Stage Two

The beginning of Stage Two is marked by an increase in strain that continues until the strain is increasing at a roughly constant rate of approximately 0.02 με/s. The slope flattens and goes to approximately zero at the end of the stage.

The pore pressure is negative at the start of this stage and it increases first at the bottom of the interval between the reflectors and then throughout the interval. The pressure head reaches zero at the bottom reflector at approximately the end of Stage Two. The rate of pressure head change ranges from 0.025cm/s at the lower transducers (p6, p13, p29) to 0.08 cm/s in the upper two transducers (p44 and p60 in Figure 59). The upper two transducers appear to represent far-field conditions at the start of the tests, whereas the lower ones may be influenced by the initial position of the transition and positive pressure zones. As a result, the relatively rapid pressure increase measured at the upper two transducers is inferred to be representative of Stage Two.

Stage Two appears to be controlled by the location of the pressure transition zone. The PZP+ 12.5 (top of transition zone) is approximately at the level of the bottom reflector at the start of Stage Two (e.g. Figure 66). The PZP(bottom of the transition zone) is approximately at the level of the top reflector at the end of the end of Stage Two. The duration of Stage Two is approximately 800s. The velocity of the water is approximately 0.027 cm/s, the transition zone is 12 cm high and the spacing between the reflectors is 10 cm. As a result, the time for the transition zone to transit the sensing interval is 22cm/0.027 cm/s =814 s, which is consistent with the observed duration of the Stage Two.

The vertical pressure head gradient in the transition zone is approximately 2 to 2.5, according to the data. This is the steepest pressure head gradient of the three pressure zones. The gradient is approximately 1.2 in the positive pressure zone and 1.0 in the ambient zone. The rate of injection is constant, so the steep pressure gradient in the transition zone caused the rate of pressure increase during Stage Two to be several times faster than during the other Stages; the rate of change of pressure head is approximately 0.08 cm/s in Stage Two and it drops to 0.025 cm/s in Stage Three.

The pressure compliance determined from the ratio of the strain and pressurization rates is 0.01 με/Pa, and it ranges from 0.05 to 0.02 (e.g. slopes of the lines in Figure 79 and 80). This is in the range expected for strain caused by a pressure increase, as calculated above.

14.6.3 Stage Three

This stage begins with the slowing of the strain rate and continues until the rate is essentially zero, and in some cases the rate drops to negative values (Figure 59). The Stage ends in the records from the upper sensors when the pump is turned off, but strain in the lower two sensors increases prior to turning off the pump. As a result, we infer that a significant increase in strain marks the end of Stage Three (Figure 97). This indicates that the duration of Stage Three is 500s to 700s (Figures 59 and 60). It follows that this increase in strain would have occurred in the upper sensors if the duration of pumping was longer.

The pore pressure is positive in this stage and the pressure head is increasing at a rate of approximately 0.025cm/s (2.5 Pa/s). The sand is saturated and the pressure gradient is uniform and approximately 1.2. The PZP is approximately at the upper reflector at the beginning of this Stage and it is 13 to 19 cm above the upper reflector at the end of the Stage.

The pressure compliance decreases to zero and becomes negative in Stage Three. This is inconsistent with strain caused be a local pressure change. It is consistent, however, with compression caused by stress transfer from the expansion in the overlying pressure transition zone. Although the pressurization rate is positive during Stage Two, it is roughly one third of the rate of pressurization that occurs during Stage Two. This is a result of a flattening of the pressure head gradient by roughly half from Stage Two to Stage Three. The interpretation is that the expansion that occurs in the pressure transition zone is sufficient to counter the expansion that would have occurred due to the increasing pressure during Stage Three.

14.6.4 Stage Four

This Stage is marked by an increase in strain to 0.02 to 0.03 με/s, approximately the same rate that occurred during Stage Two. This stage only occurs in data from the lower sensors, s1020, s2030, and s3040 (Figure 68, Figure 70, and Figure 72). The pressure continues to increase at a rate of approximately 2.5 Pa/s, and the pressure gradient remains constant at 1.2. This implies that the pressure compliance is 0.008 to 0.012 με/Pa, which is in the expected range for strain change according to Hooke's Law.

It appears that the process causing strain has returned to the same process as during Stage Two. The PZP and transition zone are more than 20 cm above the upper reflector during Stage Four.

One explanation for this behavior is that expansion in the transition zone compresses the sand above and below it. This effect causes compression observed during Stages One and Three. The effect diminishes with distance, however, and it appears to be negligible beyond 20 cm below the PZP where the sand expands in proportion to the increasing pressure.

14.6.5 Surface Wetting Stage (w)

Interaction with the free surface begins with a decrease in the slope of the strain time series that marks the beginning of the Surface Wetting Stage, Stage *w* in Figure 97. The slope

decreases and the rate drops as low as -0.7 με/s, as the strain becomes increasingly compressive. The magnitude of the compressive strain is greatest near the free surface where it is up to 30 με more compressive than the initial conditions (it drops from 10 με to -30 με). The rates and final magnitude diminish with depth, however, and the strain at s2030 drops by only a few με and the change is negligible at s1020. The negative slope abruptly flattens, and the strain is essentially constant by the time the pump is turned off to mark the end of the Stage Four (Figure 76 and Figure 68).

The pressurization rate increases from 2.5 Pa/s during Stage Four to a maximum of 25Pa/s during the Surface Wetting Stage. The maximum pressurization rate coincides with the largest negative strain rate. The pressurization rate diminishes and drops back to the original rate of 2.5 Pa/s as the strain rate drops to zero at the end of the Stage. The change in slope produces a sigmoidal pattern where approximately 1000 Pa of pressure is gained relative to projected pressure change caused by filling the column with water. This anomalous increase in pressure is roughly independent of depth, unlike the magnitude of the strain change, which decreases with depth.

The appearance of the surface of the sand changes through this stage, initially darkening as the moisture content increases first in the lowest areas. The moisture content continues to increase through the period of increasing pressurization rate and diminishing strain rate. The inflection in these curves appears to coincide with the development of free water ponding on the sand. The rates of both the pressure and strain diminish as the extent of ponding expands and the rates drop to essentially zero when free water covers the full sand surface.

The location of the PZP can be extrapolated from measurements at the p60 pressure sensor, and this indicates that the beginning of the Surface Wetting Stage occurs when the PZP+12.5 point reaches the free surface of the sand. The appearance of free water at the surface of the sand occurs approximately when the PZP reaches the free surface.

The effects observed in the Surface Wetting Stage appear to be a result of interactions between the pressure transition zone and the free surface of the sand. The change in appearance of the surface of the sand is a result of increasing moisture content that occurs as the transition zone moves upward. Even though the moisture content increases at the surface, flow of water out onto the surface of the sand is inhibited for most of this Stage. This causes the pressure to increase up to 10x faster that it would have otherwise increased.

The increase in pressure and the large decrease in strain that occur during the Surface Wetting stage occurred in all tests where then the rise in the water level was sufficient to cause ponding. These effects are absent from the Partial Fill test where ponding did not occur. This is strong evidence that these effects are a result of interactions between the pressure transition zone and the free surface.

Capillary exclusion was originally recognized by Philip & Knight, (1989) as a process where water in unsaturated soil is prevented from entering a buried cavity, like a macropore, cave or tunnel. The water is excluded from entering the cavity so long as the water pressure is less than atmospheric pressure. Capillary exclusion of downward flowing water has received considerable attention because it explains the conditions required for water to flow across the free surface of a cavity in the vadose zone. Capillary exclusion will also occur when upward flowing water encounters a free surface, as in the experiments. Extrapolating pressure data

measured at p60 indicates that the PZP reaches the sand surface at approximately the same time free water was observed accumulating at the surface. This is consistent with expectations from the capillary exclusion effect. The observed excess increase in pressure of approximately 1000 Pa appears to be a consequence of capillary exclusion.

Mechanical processes associated with capillary exclusion are poorly known, but they can be inferred from the experimental observations. The pressure compliance during surface wetting is negative, roughly -0.028 με/Pa, ruling out the possibility that the strain is a result of local pressure changes. It is also unlikely that strain transfer is an explanation because there is no indication of a region undergoing the rapid expansion that would be needed to explain the observed rapid compression. The observed strain behaves as if a compressive stress is applied at the upper boundary. The effects of a boundary load would diminish with depth as a result of friction along the wall of the column, as was observed in the loading tests (Figure 22).

One possibility is the boundary load is related to the change in pressure that occurs due to capillary exclusion. The magnitude of the pressure increase is approximately 1000 Pa. Assuming this pressure is applied downward at the surface, this would cause strain of approximately $\varepsilon_{zz} = C_u 1000Pa$. C_u depends on E and ν for saturated conditions. Assuming E=18MPa and ν=0.35 in eq. gives $C_u = 3.5\text{x}10^{-8}$ Pa^{-1}. This indicates that the expected strain is $3.5\text{x}10^{-5} = 35$ με. Approximately 40 με of compression was observed at the upper strain sensor, s5060 (Figure 58). As a result, the boundary load hypothesis appears to explain the magnitude of the compressive strain observed during the Surface Wetting Stage.

14.6.6 Ponded No-Flow

The strain rate goes to essentially zero when free water covers the top of the column (ponding), and turning off the pump causes slight, but immediate tensioning throughout the column. Strain and pressure stabilize during the Ponded No-Flow stage. The pressure head gradient collapses to 1.

14.6.7

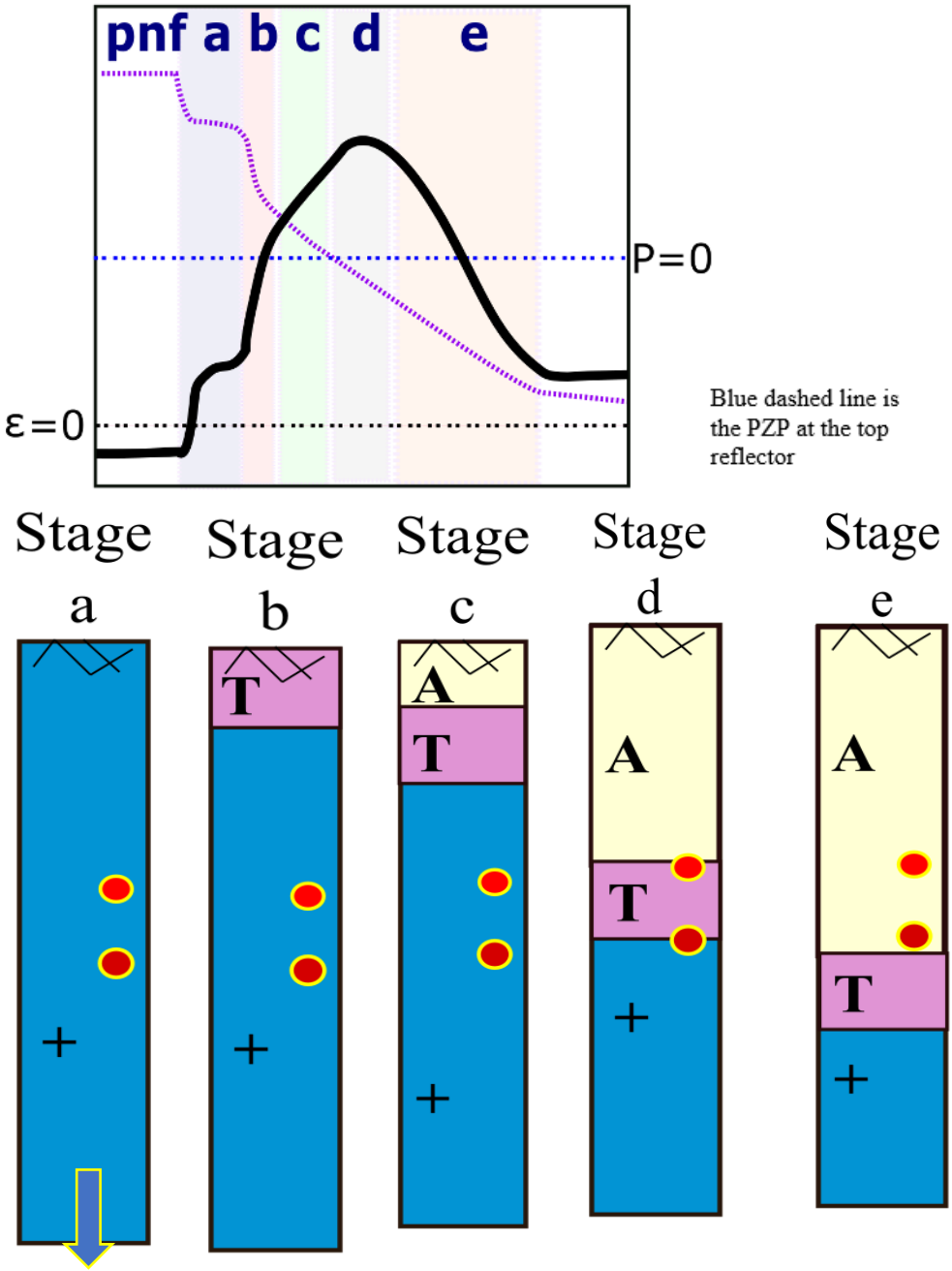

Figure 98: Strain time-series with stages (labeled colors) and sketches of different stages (Ambient, Transition, and Positive pressure (+)) in the column during drainage. Red dots are a representative strain sensor.

14.6.7.1 Drainage Stages

Drainage occurs when water is removed from the bottom of the column, either by pumping or by opening a valve and allowing gravity drainage. This process results in four stages, designated *a, b, c, d*, and defined by characteristics of the strain signal (Figure 98).

14.6.7.1.1 Stage *a*

The strain time series during the onset of drainage resembles a tangent function (sigmoid rotated by 90°), with an initial rapid increase at the onset of drainage followed by a decrease in the rate and a subsequent increase. Stage *a* begins with the start of drainage and ends at the inflection point in the sigmoid. All of the experiments where Stage *a* occurred start with water ponded on the surface of the sand. The depth of the ponded water decreases when drainage starts, and the ponded water is completely drained from the surface at approximately the same time as the inflection in the strain signal. As a result, the end of Stage *a* is characterized by the inflection point in the strain signal, but that time was selected because it coincides with the drainage of the ponded water.

The shape of the strain time series when drainage occurs by pumping differs significantly from the shape when drainage occurs by gravity, although both shapes resemble tangent functions, and they share the characteristic that ponded water is depleted at the inflection point. The strain rate increases at the outset of drainage, but the rate is faster and the overall strain that occurs during gravity drainage (Figure 90) is larger than when draining by pumping (Figure 64).

The changes in pressure in the two experiments also have similarities and differences. In both the gravity drainage and the pumping cases, the pressure is sigmoidal with a rate that is initially steeply negative, flattens with time and then steepens. The pressure drops much faster at the start of gravity drainage (Figure 90) compared to the drainage by pumping (Figure 64). The hydraulic head measured at different locations along the column is uniform during the no-flow period and the head drops first at the bottom of the column when drainage starts. The head drops by approximately 10 cm at the start of pumping, but it drops by over 60 cm at the start of gravity drainage (the outflow tube was approximately 65 cm below the top of the initial water level). These differences in the head account for the differences in the strain between these two cases. Nevertheless, the cases share a sigmoidal shape with an inflection point that occurs when the ponded water drains from the surface of the sand.

The pressure compliance is negative throughout Stage *a* with tensile strain accompanying a drop in pressure. This effect is explained by a stress transfer that is related to inferred compressive strain at the bottom of the column. The pressure drop during drainage will be greatest at the bottom of the column, and this is inferred to cause negative strain (compression). This is similar to subsidence caused by reducing pressure in an aquifer. Negative strain at the bottom of the column would initially cause positive strain in the overlying sand. The rates and magnitudes of the strain increase with the rates and magnitudes of the pressure change, which accounts for the differences between the gravity and pumping cases. Friction between the sand and the wall of the column may increase the magnitude of the effect.

14.6.7.1.2 Stage *b*

Stage *b* starts with an increase in the strain rate following Stage *a* and it includes a period of rapidly increasing strain. The end of Stage *b* is marked by an abrupt decrease in the strain rate. The strain rate during Stage *b* is among the most rapid during the test. It reaches 0.9 με/s during the pump out (Figure 64) and it is even faster during gravity drainage (Figure 90). This fast strain rate persists for up to a few tens of seconds and results in tensile strain of up to tens of με. The tensile strain that occurs during Stage *b* is greater than the compression that occurs during the Surface Wetting stage.

The pressure drops rapidly during Stage *b,* reaching a rate of -0.3 cm/s (-30Pa/s) (Figure 64). Interestingly, this rate is similar to, but opposite in sign to the rate of pressure increase during the Surface Wetting stage. The PZP starts at the top and moves downward into the column during Stage *b*. The pressure is positive during Stage *b*.

Stage *b* shares some important similarities with the Surface Wetting stage. They both occur as the pressure at the surface of the column changes significantly. The pressure increases and approaches zero as the transition zone approaches the free surface during the Surface Wetting stage, and it starts at zero (when the ponded water drains) and decreases during Stage *b*. However, the pressure drop during Stage *b* is larger than the pressure increase during Surface Wetting (e.g. Figure 59). This difference in pressure change may explain why the strain increase during Stage *b* is greater than the decrease during the Surface Wetting stage.

The similarity between the Surface Wetting stage and Stage *b* implies that the capillary boundary load inferred to occur during the Surface Wetting stage also occurs during Stage *b*. This means that the sharp decrease in pressure that occurs at the surface of the sand behaves like a tensile boundary load.

14.6.7.2 Stage *c*

Stage *c* is marked by a rapid decrease in both the strain and pressure rates by approximately and order of magnitude. The strain rate drops to 0.07 με/s and the rate of change of the pressure head increases to -0.03 cm/s (-3Pa/s), and these rates are similar for the upper three sensors during the pump out test. These data lead to a pressure compliance of -0.23 με/Pa.

The pressure transition zone during filling (imbibition) is a region where the pressure increases rapidly and expansion occurs, but during drainage it is a region where the pressure drops and contraction occurs. The regions bordering the pressure transition zone appeared to experience compression during filling, and this is manifested by compression during Stage 1 and reduced extension to compression during Stage 3. A similar effect appears to occur during draining. In this case, the pressure transition zone undergoes contraction and this causes the region below it to expand.

As a result, the strain during Stage c appears to result from a stress transfer effect underlying the pressure transition zone. This is analogous to Stage 3 during filling.

14.6.7.3 Stage *d*

Stage d is characterized by a sharp decrease and a change in sign of the strain rate (Figure 98). The strain reaches a maximum value, which is roughly twice the maximum strain at the time when the column was filled with water.

The boundaries of Stage d are related to the location of the PZP. The stage begins when the PZP arrives at the upper reflector and it ends when the PZP reaches the lower reflector in the strain sensing interval.

The pressure decreases at approximately a steady rate of 0.02 Pa/s, which is typical of pumping conditions. As a result, the pressure compliance changes sign from negative to positive during Stage *d*.

The maximum strains occur at times that increase progressively with depth in the column. This is consistent with an effect that is associated with the location of the downward moving PZP.

The effects outlined for Stage d occur in tests that involve complete filling and ponding, as well as the Partial Fill test (Figure 34). This further supports the conclusion that this stage is controlled by the moving transition zone, and it demonstrates that the effects during this stage are independent of the extent to which the column is filled.

The data indicate that the stress transfer effect that was controlling strain during Stage *c* is also important at the beginning of Stage d. This changes however as the transition zone moves through the zone between the reflectors on the strain sensor. The Hooke's Law effect controls the strain at the end of Stage *d*.

14.6.7.4 Stage *e*

Both the pressure and the strain decrease during Stage e. The rates diminish with time. Stage e starts in the upper sensors sooner than in the lower sensors, so the rates at shallow depths are slower than at greater depth. The pressure compliance is similar at the different depths, even though the rates are different. For example, the strain rate at the lower sensors is -0.06 με/s when the pressure rate is -2.5 Pa/s at t = 3400s during the 10/16 tests, while the strain rate at the s5060 sensor is -0.02me/s and the pressure rate is -0.8 Pa/s. The pressure compliance is 0.025 με/Pa at both locations.

These results indicate that the strain during Stage *e* is consistent with Hooke's Law.

14.6.8 Summary

Strain during the experiments appears to be controlled by effects associated with the pressure transition zone (Figure 99). During the imbibition that accompanies filling, the pressure is increasing in the transition zone and tl Blue dashed line is pand while the regions above and below are compressed. This effect dimi the PZP at the top and the strains are tensile in the region more than 20 cm below the transition zo reflector sure is increasing. These effects explain Stages 1, 2, 3, and 4.

Sharp changes occur as the pressure transition zone approaches the free surface. Capillary exclusion causes the pressure to increase. A capillary boundary effect that behaves like a compressive stress approximately equal to the change in pore pressure causes compressive strain that increases until the surface becomes saturated. The strain rate goes to zero and the pressurization rate slows significantly when the surface of the sand is fully covered in ponded water.

Strain during drainage controlled by the same effects as during filling. The strain is sensitive to draining of ponded water, and a sharp tension occurs when the pressure at the surface of the sand drops below zero. This is equivalent to the sharp increase in compression as the transition zone reaches the surface during filling. The transition zone compresses during draining the causes expansion in the underlying sand. As a result, the downward moves transition zone causes tension as it approaches and compression when it arrives and passes a strain measurement location.

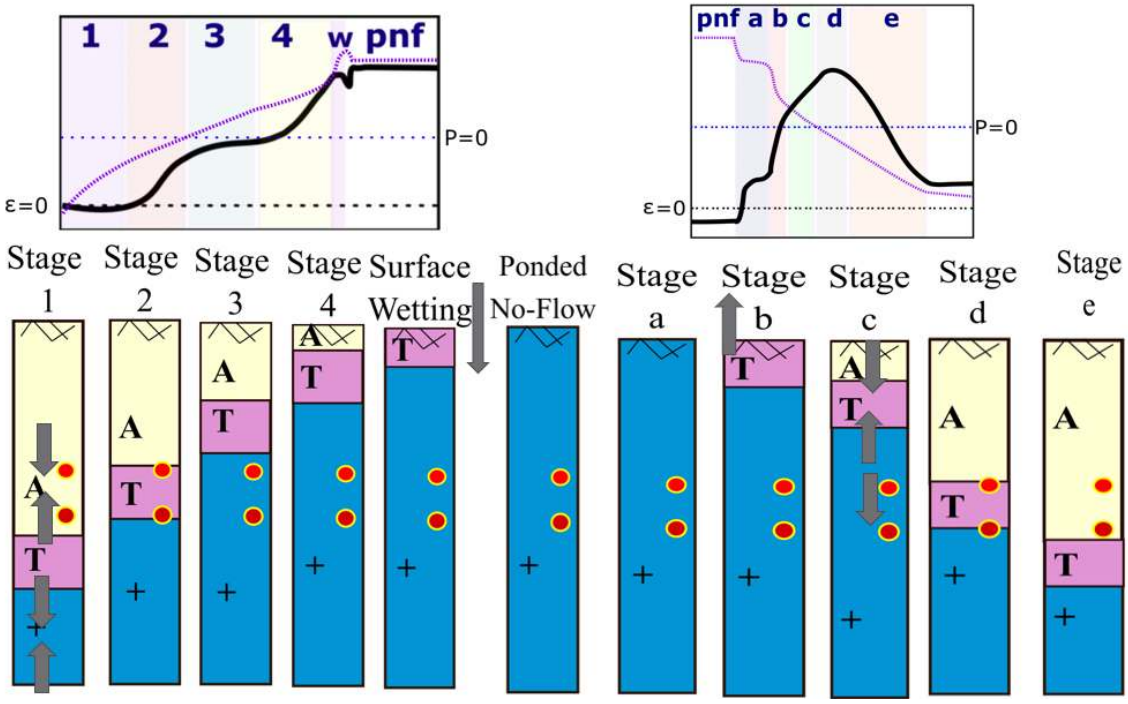

Figure 99: Graphical summary of strain and pressure events during imbibition and drainage. Grey arrows represent dilation or contraction.

14.7 Summary and Conclusions

A new method of measuring strain in unconsolidated materials was developed and evaluated using laboratory experiments. The method uses 250 μm optical fiber laminated in a thin compliant ribbon of polyester film 2.5 cm wide. Reflectors on the optical fiber are interrogated using a novel strain sensing technique called CMPI. The strain ribbon is embedded in sand and coupled to strain in the sand through friction.

A strain ribbon with reflectors spaced every 10 cm was placed along the axis of a plastic cylinder filled with sand and instrumented with pressure and temperature sensors. Water was injected into the bottom of the sand-filled column and then drained while the pressure, temperature and strain were measured.

An initial suite of tests was conducted by placing weights on top of the sand and measuring the resulting strain. The results indicate that the strain is proportional to the applied load and the proportionality is generally consistent with the expected elastic properties of the sand. The strain in the sand decreases with depth, and strain can be measured in the wall of column. This suggests that some stress in the sand is transferred to the column.

A suite of tests was conducted where the column was filled until water ponded on the surface of the sand, and then it was drained. Another test was conducted where the column was partially filled with water, and additional tests were conducted where water was infiltrated from the top of the column.

The results show that the strain and pressure increase during filling and decrease during drainage of the column. The pressure occurs in three zones: an *ambient* zone where the pressure is unchanged from the initial conditions, a *pressure transition* zone where the pressure is greater than ambient but less than zero, and a *positive pressure* zone.

Although the records of strain distributed along the column generally increase during injection and decrease during drainage, details of these records are complex but generally repeatable. Some aspects of the records are repeated even during experiments that are quite different. Repeatability of the general pattern of strain indicates that the sensors are measuring a signal that reflects strain processes within the sand.

Eleven stages were identified in the strain signals and pressure signals of experiments where water completely filled the column. Stages 1,2,3,4, and *w* occur during filling, Stage pnf occurs when the injection pump is turned off, and Stages *a,b,c,d,e* occur during draining. Strain during these stages appears to be controlled by effects associated with the pressure transition zone. During the imbibition that accompanies filling, the pressure is increasing in the transition zone and this causes it to expand while the region above and below are compressed. This effect diminishes with depth and the strains are tensile in the region more than 20 cm below the transition zone when the pressure is increasing. These effects explain Stages 1, 2, 3, and 4.

Sharp changes occur as the pressure transition zone approaches the free surface. Capillary exclusion causes the pressure to increase. A capillary boundary effect that behaves like a compressive stress approximately equal to the change in pore pressure causes compressive strain that increases until the surface becomes saturated. The strain rate goes to zero and the pressurization rate slows significantly when the surface of the sand is fully covered in ponded water.

Strain during drainage controlled by the same effects as during filling. The strain is sensitive to draining of ponded water, and a sharp tension occurs when the pressure at the surface of the sand drops below zero. This is equivalent to the sharp increase in compression as the transition zone reaches the surface during filling. The transition zone compresses during draining that causes expansion in the underlying sand. As a result, the downward moving transition zone causes tension as it approaches, and compression when it arrives and passes a strain measurement location.

This work demonstrates a new method for measuring strain in unconsolidated materials. The strain ribbon is minimally invasive, inexpensive, and robust. The compliance is similar to soil, so strain in the soil is expected to be readily transferred to the optical fiber. Previous methods for measuring strain in unconsolidated materials require much larger devices with complex anchors. The strain ribbon will enable strains at many locations separated by dm to be measured with a resolution of 10^{-8}. Applications are envisioned in hydrogeology, soil science, agriculture, geotechnical engineering, and other fields where strain in soil is of interest.

This work also demonstrates new insights into strains that occur during changes in saturation. Conventional expectations that strain is proportional to the local pressure change, according to Hooke's Law, are met in some locations, but other processes also affect strain. In particular, stress transfer, where the strain in one location is affected by fluid pressure in another location, is also important. This work also identified a possible boundary condition associated with capillary effects near a free surface that appears to be previously unrecognized.

The new technology and new insights it provides set the stage for evaluations of this approach in the field. The ultimate significance of this work will be the role it played preparing a new method for monitoring strains in hydrogeologic field applications.

14.8 REFERENCES

Aharoni, I., Siebner, H., & Dahan, O. (2017). Application of vadose-zone monitoring system for real-time characterization of leachate percolation in and under a municipal landfill. *Waste Management*, *67*, 203–213. https://doi.org/10.1016/j.wasman.2017.05.012

ASTM. (2003). *Standard Test Methods for Determination of the Soil Water Chararcteristic Curve for Desorption Using a Hanging Column, Pressure Extractor, Chilled Mirror Hygrometer, and/or Centrifuge*. *04*(February).

Baram, S., Kurtzman, D., & Dahan, O. (2012). Water percolation through a clayey vadose zone. *Journal of Hydrology*, *424–425*, 165–171. https://doi.org/10.1016/j.jhydrol.2011.12.040

Blonquist, J. M., Jones, S. B., & Robinson, D. A. (2005). A time domain transmission sensor with TDR performance characteristics. *Journal of Hydrology*, *314*(1–4), 235–245. https://doi.org/10.1016/j.jhydrol.2005.04.005

Dal Moro, G., & Zadro, M. (1998). Subsurface deformations induced by rainfall and atmospheric pressure: Tilt/strain measurements in the NE-Italy seismic area. *Earth and Planetary Science Letters*, *164*(1–2), 193–203. https://doi.org/10.1016/S0012-821X(98)00203-9

Dobriyal, P., Qureshi, A., Badola, R., & Hussain, S. A. (2012). A review of the methods available for estimating soil moisture and its implications for water resource management. *Journal of Hydrology*, *458–459*, 110–117. https://doi.org/10.1016/j.jhydrol.2012.06.021

Fattahi, H., & Amelung, F. (2016). InSAR observations of strain accumulation and fault creep along the Chaman Fault system, Pakistan and Afghanistan. *Geophysical Research Letters*, *43*(16), 8399–8406. https://doi.org/10.1002/2016GL070121

Freeman, C. (2012). *Estimating Water Flux and Storage Using Displacement Measurements*.

Gambolati, G., Teatini, P., & Tomasi, L. (1999). *Stress-Strain Analysis in Productive Gas/Oil Reservoirs*. *1519*(October 1997), 1495–1519.

Gemperline, M. C., & Rinehart, R. V. (2018). *Soil-Pipe Interface Friction Coefficients for Buried PE4710 Pipe.*

Hagiwara, Y. (1974). Probability of earthquake occurrence as obtained from a Weibull distribution analysis of crustal strain. *Tectonophysics*, *23*(3), 313–318. https://doi.org/10.1016/0040-1951(74)90030-4

Hall, K. M., & Fox, P. J. (2018). Large Strain Consolidation Model for Land Subsidence. *International Journal of Geomechanics*, *18*(11), 06018028. https://doi.org/10.1061/(asce)gm.1943-5622.0001267

Hisz, D. B., Murdoch, L. C., & Germanovich, L. N. (2013). A portable borehole extensometer and tiltmeter for characterizing aquifers. *Water Resources Research*, *49*(12), 7900–7910. https://doi.org/10.1002/wrcr.20500

Honeywell. (n.d.). *FSG Series Force Sensor* (pp. 268–270).

Hongdong, F., Kazhong, D., Chengyu, J., Chuanguang, Z., & Jiqun, X. (2011). Land subsidence monitoring by D-InSAR technique. *Mining Science and Technology*, *21*(6), 869–872. https://doi.org/10.1016/j.mstc.2011.05.030

Hua, L., Song, Y., Cheng, B., Zhu, W., Zhang, Q., & Xiao, H. (2017). Coherence-length-gated distributed optical fiber sensing based on microwave-photonic interferometry. *Optics Express*, *25*(25), 31362–31376.

Hua, L., Zhu, X., DeWolf, S., Lei, J., Zhang, Q., Murdoch, L., & Xiao, H. (2020). Phase demodulation by Frequency Chirping in Coherence Microwave Photonic Interferometry. *IEEE Journal of Selected Topics in Quantum Electronics*, *27*(2), 7700109. https://doi.org/10.1109/jstqe.2020.2975575

Inaudi, D., & Glisic, B. (2006). Distributed fiber optic strain and temperature sensing for structural health monitoring. *Proceedings of the 3rd International Conference on Bridge Maintenance, Safety and Management - Bridge Maintenance, Safety, Management, Life-Cycle Performance and Cost*, *July*, 963–964. https://doi.org/10.1201/b18175-412

Keller, T., Arvidsson, J., Schjønning, P., Lamandé, M., Stettler, M., & Weisskopf, P. (2012). In Situ Subsoil Stress-Strain Behavior in Relation to Soil Precompression Stress. *Soil Science*, *177*(8). https://journals.lww.com/soilsci/Fulltext/2012/08000/In_Situ_Subsoil_Stress_Strain_Behavior_in_Relation.3.aspx

Leung, C. K. Y., Wan, K. T., Inaudi, D., Bao, X., Habel, W., Zhou, Z., Ou, J., Ghandehari, M., Wu, H. C., & Imai, M. (2015). Review: optical fiber sensors for civil engineering applications. *Materials and Structures/Materiaux et Constructions*, *48*(4), 871–906. https://doi.org/10.1617/s11527-013-0201-7

Luttrell, K., Mencin, D., Francis, O., & Hurwitz, S. (2013). Constraints on the upper crustal magma reservoir beneath Yellowstone Caldera inferred from lake-seiche induced strain observations. *Geophysical Research Letters*, *40*(3), 501–506. https://doi.org/10.1002/grl.50155

Madjdabadi, B., Valley, B., Dusseault, M. B., & Kaiser, P. K. (2016). Experimental evaluation of a distributed Brillouin sensing system for measuring extensional and shear deformation in rock. *Measurement: Journal of the International Measurement Confederation*, *77*, 54–66. https://doi.org/10.1016/j.measurement.2015.08.040

Martin, J. P., & Koerner, R. M. (1984). The influence of vadose zone conditions in groundwater pollution. Part II: Fluid movement. *Journal of Hazardous Materials*, *9*(2), 181–207. https://doi.org/10.1016/0304-3894(84)80017-5

Murdoch, L., Falta, R., & Moysey, S. (2016). *MEASURING AND INTERPRETING VERTICAL DISPLACEMENTS RELATED TO SHALLOW HYDROLOGIC PROCESSES A Proposal Presented to The Graduate School of Clemson University In Partial Fulfillment of the Requirements for the Degree Master of Science Hydrogeology by Colby T. May*.

Neelam, M. K., & Kalaga, S. (2002). Elastic properties of PVC pipes. *Journal of Structural Engineering (Madras)*, *29*(2), 91–96.

Nitzsche, K., & Herle, I. (2020). Strain-dependent slope stability. *Acta Geotechnica*, *15*(11),

3111–3119. https://doi.org/10.1007/s11440-020-00971-3

Ochsner, T. E., Cosh, M. H., Cuenca, R. H., Dorigo, W. A., Draper, C. S., Hagimoto, Y., Kerr, Y. H., Larson, K. M., Njoku, E. G., Small, E. E., & Zreda, M. (2013). State of the Art in Large-Scale Soil Moisture Monitoring. *Soil Science Society of America Journal*, *77*(6), 1888–1919. https://doi.org/10.2136/sssaj2013.03.0093

Philip, J. R., & Knight, J. H. (1989). Unsaturated Seepage and Subterranean Holes: Conspectus, and Exclusion Problem for Circular Cylindrical Cavities. *Water Resources Research*, *25*(1), 16–28.

Plunkett, G. (2021). *A Novel Technique for Distributed Measuring of Strain in the Vadose Zone* [Master of Science]. Clemson University.

Prakash, G., Sadhu, A., Narasimhan, S., & Brehe, J. M. (2018). Initial service life data towards structural health monitoring of a concrete arch dam. *Structural Control and Health Monitoring*, *25*(1), 1–19. https://doi.org/10.1002/stc.2036

Satoshi Yamashita,1 Michele Jamiolkowski, 2 and Diego C. F. Lo Presti3. (2000). Stiffness Nonlinearity of Three Sands. *JOURNAL OF GEOTECHNICAL AND GEOENVIRONMENTAL ENGINEERING*, *126*(October), 929–938.

Thrash, C. (2016). *Measuring and Interpreting Vertical Displacements Related to Shallow Hydrologic Processes*. 1–161.

Topp, G. C., Lapen, D. R., Young, G. D., & Edwards, M. (2001). Evaluation of shaft-mounted TDT readings in disturbed and undisturbed media. *TDR 2001 - Second International Symposium and Workshop on Time Domain Reflectometry for Innovative Geotechnical Applications, Northwestern University, Evanston, Ill., 5-7 September 2001*, *2000*, 62–71.

van Genuchten, M. T. (1980). A Closed-form Equation for Predicting the Hydraulic Conductivity of Unsaturated Soils. *Soil Science Society of America Journal*, *44*, 892–898.

Wang, H. F. (2000). *Theory of Linear Poroelasticity with Applications to Geomechanics and Hydrogeology*. Princeton University Press. http://www.jstor.org/stable/j.ctt1jktrr4

Warpinski, N. R., Branagan, P. T., & Engler, B. P. (1997). *Evaluation of a Downhole Tiltmeter Array for Monitoring Hydraulic Fractures*. *34*(329), 3–4.

Weiss, J. R., Walters, R. J., Morishita, Y., Wright, T. J., Lazecky, M., Wang, H., Hussain, E., Hooper, A. J., Elliott, J. R., Rollins, C., Yu, C., González, P. J., Spaans, K., Li, Z., & Parsons, B. (2020). High-Resolution Surface Velocities and Strain for Anatolia From Sentinel-1 InSAR and GNSS Data. *Geophysical Research Letters*, *47*(17). https://doi.org/10.1029/2020GL087376

Western, A. W., Grayson, R. B., & Blöschl, G. (2002). Scaling of soil moisture: A hydrologic perspective. *Annual Review of Earth and Planetary Sciences*, *30*, 149–180. https://doi.org/10.1146/annurev.earth.30.091201.140434

You, R., Ren, L., & Song, G. (2019). A novel fiber Bragg grating (FBG) soil strain sensor. *Measurement: Journal of the International Measurement Confederation*, *139*, 85–91. https://doi.org/10.1016/j.measurement.2019.03.007

Zreda, M., Shuttleworth, W. J., Zeng, X., Zweck, C., Desilets, D., Franz, T., & Rosolem, R.

(2012). COSMOS: The cosmic-ray soil moisture observing system. *Hydrology and Earth System Sciences*, *16*(11), 4079–4099. https://doi.org/10.5194/hess-16-4079-2012